Molecular Imaging and Biology (2022) 24 (Suppl 2):S63–S480
https://doi.org/10.1007/s11307-022-01794-2

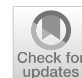

ABSTRACTS

World Molecular Imaging Congress 2022

Published online: 17 January 2023
© The Author(s), under exclusive licence to World Molecular Imaging Society 2022

2022 World Molecular Imaging Congress Program

Title: World Molecular Imaging Congress 2022

Date: September 28-October 1, 2022

Location: Miami, FL, USA

Sponsorship: Publication of this supplement was sponsored by the World Molecular Imaging Society. All content was reviewed and selected by the WMIC Program Committee and the WMIC Review Committee, which held full responsibility for the abstract selections.

001-Endoscopic Visualization of Colorectal Adenomas In Vivo

Presenter: Jashim Uddin, Vanderbilt University

Jashim Uddin
Vanderbilt University, Nashville, TN

Colorectal cancer (CRC) is the third leading cause of cancer-related mortality in men and women, and it is projected to cause > 50,000 deaths during the year 2019 in the United States (1). Screening tests for colorectal cancer are recommended at the age of 50, and it is expected that by the use of early screening procedures colorectal tumors can be detected and removed before they become cancerous, making colorectal cancer one of the only truly preventable types of cancer (2, 3). Current screening procedures include white light colonoscopy, chromoendoscopy, narrow-band imaging, etc., all of which aim to detect solid colon tumors and precursor lesions, but only raised solid tumors and matured CRC can typically be visualized and removed, but precursor lesions, such as adenomas are frequently missed(4-6). Uncontrolled cell proliferation is pivotal in colorectal tumorigenesis and cyclooxygenase-2 (COX-2) is an important regulatory enzyme in this process(7). It has been confirmed that precursor lesions such as aberrant crypt foci, hyperplastic polys, and macro- or micro-adenomas are COX-2 overexpressing and is absent from most normal adult human tissues, and that makes it an attractive molecular target for early detection of colorectal carcinogenesis by molecular imaging(8). Various radio- or fluorophore-labeled small molecules targeted to COX-2 have been reported, but none reached to the clinic. Towards addressing this need, we have developed a novel nanobody-based strategy – single chain antibodies functionalized with fluorophores – for *in vivo* optical imaging of cyclooxygenase-2 (COX-2), a biomarker overexpressed in early stages of colorectal carcinogenesis. We hypothesize that imaging probes tagged to nanobodies specific for COX-2 protein would selectively accumulate in colorectal adenomas, resulting in specific and sensitive of detection, while reducing background and off-target systemic toxicity. To test this hypothesis, we developed fluorescent derivatives of COX-2-targeted nanobodies derived from heavy chain-only antibodies originated in Alpaca. We evaluated their COX-2 binding affinity and their use in targeted visualization early lesions of CRC in an azoxymethane and dextran sodium sulfate- induced colorectal adenoma mouse model. For site-specific bioconjugation, we performed site-directed mutagenesis study to generate mutant nanobodies followed by conjugation with fluorescent tags. We determined the structural and functional basis of COX-2 binding by X-ray co-crystal analysis. We validated the specificity and sensitivity of the fluorescent COX-2 nanobody in detection of colorectal adenomas in a clinically relevant adenoma model. This demonstrate the 1st COX-2-targeted fluorescent nanobodies exhibiting high affinity for COX-2, and offering significant advantages over standard endoscopic imaging. This study establishes a framework for the clinical development of molecularly-targeted (COX-2-targeted) fluorescent nanobodies for early detection of CRC and facilitates personalized medicine tailoring of therapeutic strategies to the patient based on molecular profiling.

References

1. Key Statistics for Colorectal Cancer: American Cancer Society; 2019. Available from: https://www.cancer.org/cancer/colon-rectal-cancer/about/key-statistics.html.
2. Liang PS, Dominitz JA. Colorectal Cancer Screening: Is Colonoscopy the Best Option? Med Clin North Am. 2019;103(1):111'-23. Epub 2018/11/24. doi: 10.1016/j.mcna.2018.08.010. PubMed PMID: 30466668.
3. Nishihara R, Wu K, Lochhead P, Morikawa T, Liao X, Qian ZR, Inamura K, Kim SA, Kuchiba A, Yamauchi M, Imamura Y, Willett WC, Rosner BA, Fuchs CS, Giovannucci E, Ogino S, Chan AT. Long-term colorectal-cancer incidence and mortality after lower endoscopy. N Engl J Med. 2013;369(12):1095-105. Epub 2013/09/21. doi: 10.1056/NEJMoa1301969. PubMed PMID: 24047059; PMCID: PMC3840160.
4. Abegunde AT. Chromoendoscopy, White-Light, or Narrow-Band Imaging Colonoscopy in Colorectal Cancer Surveillance in Inflammatory Bowel Disease: True Illumination or Game of Shadows. Clin Gastroenterol Hepatol. 2016;14(7):1062. Epub 2015/10/11. doi: 10.1016/j.cgh.2015.09.035. PubMed PMID: 26453956.
5. Zhao S, Wang S, Pan P, Xia T, Chang X, Yang X, Guo L, Meng Q, Yang F, Qian W, Xu Z, Wang Y, Wang Z, Gu L, Wang R, Jia F, Yao J, Li Z, Bai Y. Magnitude, Risk Factors, and Factors Associated With Adenoma Miss Rate of Tandem Colonoscopy: A Systematic Review and Meta-analysis. Gastroenterology. 2019. Epub 2019/02/10. doi: 10.1053/j.gastro.2019.01.260. PubMed PMID: 30738046.
6. van Rijn JC, Reitsma JB, Stoker J, Bossuyt PM, van Deventer SJ, Dekker E. Polyp miss rate determined by tandem colonoscopy: a

systematic review. Am J Gastroenterol. 2006;101(2):343-50. Epub 2006/02/04. doi: 10.1111/j.1572-0241.2006.00390.x. PubMed PMID: 16454841.
7. Sinicrope FA, Gill S. Role of cyclooxygenase-2 in colorectal cancer. Cancer Metastasis Rev. 2004;23(1-2):63-75. Epub 2004/03/06. PubMed PMID: 15000150.
8. Takayama T, Katsuki S, Takahashi Y, Ohi M, Nojiri S, Sakamaki S, Kato J, Kogawa K, Miyake H, Niitsu Y. Aberrant crypt foci of the colon as precursors of adenoma and cancer. N Engl J Med. 1998;339(18):1277-84. Epub 1998/10/29. doi: 10.1056/NEJM199810293391803. PubMed PMID: 9791143.

Oral Presentation

Disclosures: The authors have disclosed no financial interest.

002-Preclinical PET imaging studies of metabotropic glutamate receptor 2 function using [11C]mG2P001

Presenter: Gengyang Yuan,Massachusetts General Hospital

Gengyang Yuan[1], Maeva Dhaynaut[2], Nicolas J. Guehl[2], Ramesh Neelamegam[3], Sung-Hyun Moon[2], Pekka Poutiainen[4], Sepideh Afshar[5], Georges El Fakhri[6], Marc D. Normandin[7], Anna-Liisa Brownell[7]

[1]*Massachusetts General Hospital, Charlestown, MA*
[2]*Massachusetts General Hospital, Boston, MA*
[3]*PharmaLogic Holdings, Aurora, CO*
[4]*Kuopio*
[5]*Massachusetts General Hospital, Boston*
[6]*Massachusetts General Hospital*
[7]*Gordon Center for Medical Imaging (MGH/HMS), Boston, MA*

Objectives

Metabotropic glutamate receptor 2 (mGluR2) has been implicated in several neurological and psychiatric disorders, including schizophrenia, anxiety, depression, and Alzheimer's disease.[1-2] Radiotracers for imaging mGluR2 density and distribution would enable studies of the receptor's function and facilitate development of treatments for mGluR2-related diseases. The aim of this study was to investigate the mGluR2 function using PET imaging with the 2-((4-(2-[^{11}C]methoxy-4-(trifluoromethyl)phenyl) piperidin-1-yl)methyl)-1-methyl-1*H*-imidazo[4,5-*b*]pyridine ([^{11}C] mG2P001), which is a selective probe developed from a positive allosteric modulator (PAM).[3]

Methods

The positive allosteric modulation of mGluR2 was first investigated based on modulation of [^{11}C]mG2P001 accumulation between the baseline and blocking conditions in eight normal Sprague Dawley rats (male, weight 360-420 g, age 9-11 weeks). The unlabeled mG2P001, a potent mGluR2 PAM (IC_{50} = 7.6 nM, EC_{50} = 51 nM),[3] was used as a blocking agent at a dose of 4 mg/kg iv. 10 min before tracer injection. The behavior of [^{11}C]mG2P001 was further mimicked by the tritiated [^{3}H]mG2P001 in the transfected CHO-K1 cells expressing human mGlu2 receptors. In these studies, cellular binding of [^{3}H]mG2P001 was investigated by different concentrations of co-incubated glutamate and unlabeled mG2P001, respectively. Furthermore, the mGluR2 functional expression was investigated with eight PET/CT imaging studies in three monkeys (Cynomolgus fascicularis, female, weight 4.6-6.0 kg, age 5-6 yrs). In the blocking studies, different doses of mG2P001 (i.e., 0.2 mg/kg or 1.69 mg/kg) were administrated via either simultaneous infusion or pre-injection bolus 10 min before the tracer injection. Arterial blood was collected for tracer metabolism analysis and the generation of the metabolite corrected arterial input function. The 1- and 2-tissue compartment models and Logan graphical analysis were used for invasive kinetic modeling of the brain PET data.

Results

PET imaging in rats showed that accumulation of [^{11}C]mG2P001 was significantly enhanced in all the regions of interest (ROIs) of the brain, ranging from 23.5% to 53.2%, with the highest enhancement observed in the hypothalamus and the lowest one in the olfactory bulb. In the CHO cells, the specific binding of [^{11}C]mG2P001 toward the mGlu2 receptor was significantly enhanced by increasing the amount of glutamate with a maximum of 2-fold enhancement compared to the control value at a glutamate concentration of 10 μM. Similarly, the specific binding of [^{11}C]mG2P001 was also increased with more unlabeled mG2P001 in the incubation media. In primates, the arterial blood analysis revealed the moderate metabolism stability of [^{11}C]mG2P001 with only one primary highly polar radiometabolite. As a PET radiotracer, [^{11}C]mG2P001 had excellent brain permeability (SUV_{max} > 3 at 15 min) and moderate heterogeneous distribution across the monkey brain. Both the 2-tissue compartment model and Logan graphical analysis fitted well for the acquired PET data and provided the stable regional total volume of distribution V_T estimates under both baseline and blocking conditions. Based on the Logan V_T estimates, all the blocking experiments showed an enhanced accumulation of [^{11}C]mG2P001 across the investigated brain ROIs with a representative study showing a 33% enhancement after pretreatment with 0.6 mg/kg mG2P001 iv.

Conclusion

The PET imaging studies in rats and nonhuman primates evidenced the enhanced specific binding of [^{11}C]mG2P001 to mGluR2 following the pretreatment with unlabeled mG2P001. These results were unusual and unique for the mGluR2 PAMs. The *in vitro* cell studies further indicated the glutamate binding cooperativity and positive allosteric modulation in enhancing the specific radioligand binding. Altogether, [^{11}C] mG2P001 is a sensitive biomarker for mGluR2 functional expression and it can be further analyzed for diagnostic and therapeutic purposes.

Acknowledgment This project was financially supported by NIH grants 1R01EB021708, 1R01NS100164, 1S10RR023452-01, 1S10OD025234-01, S10OD018035, and P41EB022544.

References

1. Niswender CM and Conn PJ. Metabotropic glutamate receptors: physiology, pharmacology, and disease. Annu Rev Pharmacol Toxicol 2010; 50: 295-322.
2. Muguruza C, Meana JJ and Callado LF. Group II metabotropic glutamate receptors as targets for novel antipsychotic drugs. Front Pharmacol 2016; 7: 130.
3. Yuan G, Qu X, Zheng B, et al. Design, synthesis, and characterization of benzimidazole derivatives as positron emission tomography imaging ligands for metabotropic glutamate receptor 2. J Med Chem 2020; 63: 12060-12072.

Oral Presentation

Disclosures: The authors have disclosed no financial interest.

003-Evaluation of [18F]FSPG versus [18F]FDG PET imaging for predicting malignancy of solitary pulmonary nodules

Presenter: Ophir Vermesh, Stanford University

Ophir Vermesh[1], Harmeet Bedi[2], Alice Fan[2], Andrei Iagaru[1], Carina Mari[1]

[1]Stanford University, Stanford, CA
[2]Stanford University School of Medicine, Stanford, CA

Purpose/Background:

Solid pulmonary nodules (SPNs), <3-cm isolated round opacities surrounded by lung parenchyma, are often detected incidentally on routine chest radiographs and computed tomography (CT) and frequently seen on screening chest CTs in high-risk patients (*1, 2*). While the majority of SPNs are benign, their detection requires further workup to assess for possible malignancy, including follow-up CT and/or positron emission tomography (PET)/CT imaging, and biopsy for lesions that are large, fast-growing, have suspicious morphologic characteristics, or demonstrate high 18-fluorodeoxyglucose (18F-FDG) avidity (*1*). While FDG PET is valuable in further characterizing SPNs, it suffers from relatively high false positive and false negative rates due to high FDG uptake in infectious and inflammatory processes, and low or variable uptake in certain lung cancer subtypes as well as in low grade cancers (*1, 3*). A PET tracer that could more accurately predict whether an SPN is malignant would obviate unnecessary repeat imaging and invasive biopsies. [18F]FSPG, a glutamate analogue containing an [18F]fluoropropyl group, is used to image expression of the cystine/glutamate (x_C^-) transporter, which is upregulated in a variety of tumors, including non-small cell lung cancer, breast cancer, and liver cancer and has been associated with poor outcomes (*4, 5*). 18F-FSPG is stable in human plasma for up to 4 hours, has no measurable radiometabolites, is rapidly cleared via the kidneys, and has low background uptake, ideal characteristics for high contrast tumor imaging (*6-9*). The goal of this study is to evaluate whether [18F]FSPG is superior [18F]FDG in predicting whether an SPN is malignant.

Methods:

Fifteen patients with SPNs discovered on routine or screening chest CT were recruited as part of a phase 2 clinical trial to undergo both [18F]FDG PET and [18F]FSPG PET clinical imaging within 2 weeks of each other. We evaluated [18F]FDG and [18F]FSPG activity of lung nodules on PET imaging as well as histopathologic diagnosis, tumor grade, and stage. Inclusion criteria: 1) nodule size 7-30 mm, 2) age ≥ 45 years, 3) current or former smoker with ≥ 20 pack year history. Exclusion criteria: 1) history of lung cancer, 2) other cancer within the previous 5 years, 3) pregnant or nursing. Of 15 patients, 14 patients underwent tissue biopsy, resulting in a diagnosis of non-small cell lung cancer (NSCLC) in 10 patients (8 patients with adenocarcinoma and 2 patients with squamous cell carcinoma) and benign findings in 4 patients. One patient has a slow-growing nodule that lacks suspicious morphologic characteristics and is undergoing active surveillance./

Results:

On average, SPNs had higher activity (SUVmax) on [18F]FDG PET than on [18F]FSPG PET imaging (median SUV max 3.4 vs. 1.5)(p = 0.01)(**Fig. 1A, B**). There was a statistically significant difference between malignant and benign tumors in uptake of [18F]FDG (median SUVmax 4.7 vs. 1.8, p = 0.03) and [18F]FSPG-PET (SUVmax 1.9 vs. 1.0, p = 0.002). Background signals with [18F]FSPG were lower than with [18F]FDG. Using SUVmax cutoff values for [18F]FDG and [18F]FSPG-PET of 2.5 and 1.1, respectively, the sensitivity, specificity, positive predictive value (PPV), and negative predictive value (NPV) for detection of high grade malignancy by [18F]FDG PET were 70%, 100%, 100%, 57% and for [18F]FSPG PET were 100%, 100%, 100%, and 100% (**Fig. 1C**). [18F]FSPG PET detected all lesions that were detected by [18F]FDG and also correctly classified 3 malignancies that were incorrectly classified by [18F]FDG. Receiver operating characteristic (ROC) curves for [18F]FDG and [18F]FSPG yielded areas under the curve (AUC) of 0.84 (p = 0.05) and 1.0 (p = 0.004), respectively.

Conclusion:

[18F]FSPG PET has comparable, if not higher, sensitivity than [18F]FDG in predicting malignancy in patients with SPNs. A larger sample size is needed to detect differences in specificity between the two PET tracers.

References

1. W. R. Webb, C. B. Higgins, Thoracic imaging: pulmonary and cardiovascular radiology. (Lippincott Williams & Wilkins, 2010).
2. S. J. Swensen, M. D. Silverstein, D. M. Ilstrup, C. D. Schleck, E. S. Edell, The probability of malignancy in solitary pulmonary nodules: application to small radiologically indeterminate nodules. Archives of internal medicine 157, 849-855 (1997).
3. A. Culverwell, A. Scarsbrook, F. Chowdhury, False-positive uptake on 2-[18F]-fluoro-2-deoxy-D-glucose (FDG) positron-emission tomography/computed tomography (PET/CT) in oncological imaging. Clinical radiology 66, 366-382 (2011).
4. K. Vanhove et al., Glutamine addiction and therapeutic strategies in lung cancer. International journal of molecular sciences 20, 252 (2019).
5. S. Baek et al., Exploratory Clinical Trial of (4S)-4-(3-[18F] fluoropropyl)-l-glutamate for Imaging xC− Transporter Using Positron Emission Tomography in Patients with Non–Small Cell Lung or Breast CancerPET Imaging of xC− Transporter in Lung and Breast Cancer. Clinical cancer research 18, 5427-5437 (2012).
6. M. Wardak et al., 18F-FSPG PET/CT Imaging of System xC– Transporter Activity in Patients with Primary and Metastatic Brain Tumors. Radiology 303, 620-631 (2022).
7. N. Koglin et al., Specific PET Imaging of xC− Transporter Activity Using a 18F-Labeled Glutamate Derivative Reveals a Dominant Pathway in Tumor MetabolismPET Imaging of System xC− Activity. Clinical Cancer Research 17, 6000-6011 (2011).
8. K. Smolarz et al., (S)-4-(3-18F-Fluoropropyl)-l-glutamic acid: An 18F-labeled tumor-specific probe for PET/CT imaging—Dosimetry. Journal of Nuclear Medicine 54, 861-866 (2013).
9. E. S. Mittra et al., Pilot preclinical and clinical evaluation of (4S)-4-(3-[18F] Fluoropropyl)-L-Glutamate (18F-FSPG) for PET/CT imaging of intracranial malignancies. PLoS One 11, e0148628 (2016).

Oral Presentation

Disclosures: The authors have disclosed no financial interest.

004-Biohybrid Tissue-Engineered Vascular Prosthesis: Reporting on Their Remodeling by 1H/19F MRI

Presenter: Elena Rama, RWTH Aachen University

Elena Rama[1], Saurav Ranjan Mohapatra[2], Asmaa Elshafei[3], Christian Apel[2], Stefan Jockenhoevel[2], Fabian Kiessling[4]

[1]RWTH Aachen University, Germany
[2]RWTH Aachen University, Aachen, Nordrhein-Westfalen, Germany
[3]RWTH Aachen University, Aachen, Germany
[4]RWTH Aachen University, Aachen, NRW, Germany

Labelling scaffolds for ^{1}H magnetic resonance imaging (MRI) poses challenges with respect to detection, sensitivity, specificity, and quantification. These key aspects have increasingly motivated the application and investigation of ^{19}F-MRI parallel to the development of new biochemical compounds. Indeed, although ^{19}F-MRI provides high image contrast due to the almost complete lack of fluorine background in living organisms, fluorine probes with high content of highly mobile and chemically equivalent fluorine atoms are needed. In addition, novel imaging approaches combining hybrid imaging modalities and new materials are highly required in routine clinical applications [1]. Therefore, this study aims to enhance and strengthen the monitoring of biohybrid tissue-engineered vascular grafts' (TEVG) resorption and remodeling via innovative hybrid $^{1}H/^{19}F$ MRI. As a proof-of-concept and to enhance the visibility and longitudinal monitorability of our TEVG, multifilaments of highly fluorinated thermoplastic polyurethane (^{19}F-TPU) were added to the textile scaffold. Consequently, our new TEVG consisted of i) non-degradable polyvinylidene fluoride (PVDF) monofilaments coated with ii) biodegradable poly(lactic-co-glycolic acid) (PLGA) fibers labeled with superparamagnetic iron oxide nanoparticles (SPION), to which iii) non-degradable ^{19}F-TPU multifilaments were added, and finally moulded with iv) fibrin gel containing human endothelial and smooth muscle cells (hECs and hSMCs). First, the biocompatibility of the ^{19}F-TPU fibers was assessed on hSMCs via XTT and compared to the Food-and-Drug-Administration-approved PLGA fibers and a negative control. Subsequently, a systematic investigation was carried out to determine the amount of ^{19}F-TPU needed to generate a high signal-to-noise ratio via $^{1}H/^{19}F$ 7T MRI. Therefore, textile scaffolds containing a different number of ^{19}F-TPU filaments were embedded in 10% gelatin (w/v) and then imaged with a dual-tuned $^{1}H/^{19}F$ transmit/receive volume coil. Furthermore, the degradation of the biocompatible and biodegradable SPION-labeled PLGA coating was longitudinally assessed with and without cellular components at 37°C for 7 days and at 70°C for 3 weeks, respectively. The evaluation of the release and possible cytotoxic effects of extractables and leachables on cells revealed the biocompatibility and safety of ^{19}F-TPU filaments (A). Interestingly, the XTT results for these fibers showed slightly higher signals than those for PLGA, which might be due to the acidic effect of its degradation debris [1,2]. The superimposition of the grayscale T2W and "hot spot" ultrashort echo time (UTE) sequences of the gelatin phantoms containing a different number of ^{19}F-TPU fibers showed both enhanced visibility of the PLGA layer due to the SPION labeling and ^{19}F signal intensity corresponding to a higher number and different positioning of ^{19}F-TPU fibers (B). Surprisingly, the visualization of the structure of individual ^{19}F-TPU fibers was successfully enabled by image post-processing. The longitudinal monitoring of the degradation of the SPION-labeled PLGA and the permanent signal given by the ^{19}F-TPU fibers was carried out concomitantly (C-F). In both experimental setups, with and without cells, the R2 analyses showed a gradual decrease in the MRI signal after 7 days and 3 weeks, respectively, indicating swelling and hydrolysis of the PLGA, leading to SPION release. As postulated, no significant changes could be observed regarding the non-degradable ^{19}F-TPU signal intensity. Additional histological analyses supported the PLGA degradation and the constant presence of the ^{19}F-TPU filaments. Herein, we present an additional non-invasive imaging method to strengthen the investigation of the remodeling and resorption of vascular prostheses via hybrid imaging techniques. We demonstrated the novel employment of innovative fluorinated and biocompatible MRI-traceable fibers. Indeed, our findings report the successful visualization of individual fluorinated filaments and the critical possibility of monitoring both biodegradable and non-biodegradable textile components of our TEVG. Therefore, the presented approach might play a critical role in our TEVG theranostic and therapeutic application. Acknowledgement: This work was supported by Deutsche Forschungsgemeinschaft (DFG) (403039938).

References

1. Rama et al. "Monitoring the Remodeling of Biohybrid Tissue-Engineered Vascular Grafts by Multimodal Molecular Imaging." Advanced Science 9.10 (2022): 2105783.
2. Casey et al. "Sensors and regulators of intracellular pH." Nature reviews Molecular cell biology 11.1 (2010): 50-61.

Oral Presentation

Disclosures: The authors have disclosed no financial interest.

005-A bioluminescence reporter mouse model for visualizing and quantifying CD8+ T cells in vivo

Presenter: Kimberly Bettano, Merck

Kimberly A. Bettano[1], Raquel Sevilla

[1]Merck, Boston, Ma

Cytotoxic CD8+ T cells are the primary effector cells mediating anti-tumor responses. In vivo monitoring of CD8+ T cells has broad implications for the development of novel cancer therapies. Here we describe the development of a genetically engineered mouse model (GEMM) in which CD8+ T cells are labeled with an optical reporter, enabling in vivo, longitudinal monitoring using bioluminescence imaging (BLI). Firefly luciferase (Luc2), human diphtheria toxin receptor (DTR), and enhanced green fluorescence protein (eGFP) cDNAs are engineered under the CD8α promoter to generate a transgenic mouse line. Luciferase mRNA and CD8α mRNA were generally correlated in various tissues from these mice. Sorted splenic CD8+ T cells, CD4+ T cells and CD3- non-T cells verified that the luciferase signal is specific to CD8+ T cells. In vivo imaging showed that luciferase signal was detected in various immune organs, such as lymph nodes, thymus, and spleen, and the detection was confirmed by ex vivo examination. Administration of diphtheria toxin markedly reduced luciferase signal systemically, confirming the function of the DTR. In the MC38 mouse syngeneic model, we observed significant increases in CD8+ T cells with mDX400 treatment, an anti PD-1 mouse monoclonal antibody that correlated with tumor growth inhibition. This novel reporter GEMM is a valuable drug discovery tool for profiling compounds and understanding mechanisms of action in immunotherapy of cancer.

Oral Presentation

Disclosures: The authors have disclosed no financial interest.

006-Investigation of crucial influence of the meta-substituted analogs of a potential game changer – 18F-AF78, a novel NET targeting radiotracer

Presenter: Saskia Mühlig, Julius Maximilian University of Wurzburg

Saskia Mühlig[1], Xinyu Chen[2], Anna Tutov[1], Rudolf A. Werner[3], Andreas Buck[2], Michael Decker[1], Takahiro Higuchi[2]

[1]Julius Maximilian University of Wurzburg, Würzburg, Bayern, Germany
[2]Würzburg, Bayern, Germany
[3]Hannover Medical School, Hannover, Lower Saxony, Germany

Introduction:

Fluorine-18-labelled radiotracers targeting norepinephrine transporter (NET) have potential applications in the diagnosis and assessment of cardiac sympathetic nerve conditions as well as the delineation of neuroendocrine tumors. Recently, we developed and reported AF78(F) as a novel tracer of this kind [1]. As a step forward, five new AF78 analogs were characterized in vitro and in vivo to understand the relationship with NET affinity.

Materials and Methods:

Radiolabeling was performed using a one-pot-two-steps protocol as previously described by Chen et. al. [2]. Non-radioactive analogs, i.e., meta-Cl, Br, I and OH substitution, of AF78(F) were newly synthesized. Competitive uptake assay was performed with ^{3}H-NE and human neuroblastoma SK-N-SH cell line to characterize uptake via NET. Cells were treated with 3H-NE, containing non-radioactive compounds in various concentrations for 60 min at 37°C, in the presence of pyrogallol and pargyline. After washing with PBS, cells were lysed in NaOH, followed by measurement of radioactivity. Non-radioactive meta-iodobenzylguanidine (MIBG), and neurotransmitter norepinephrine (NE) were used as references for the target compounds. For PET imaging, [^{18}F]AF78 was injected via teil vein following a 10 min dynamic PET scan. In vivo biodistribution was performed in healthy male wistar rats (n=3-6 each radiotracer). Radiotracers were administered via tail vein. After 10 min tracer injection, hearts, livers, and bloods were obtained for tissue counting study.

Results/Discussion:

The uptake studies showed IC_{50} values for NE (0.50 ± 0.16μM), MIBG (1.75± 0.47μM), AF78(F) (0.42 ± 0.14μM), AF78(Cl) (0.94± 0.28μM), AF78(Br) (3.32 ± 0.72μM), AF78(I) (6.51 ± 3.32μM) and AF78(OH) (22.67 ± 3.58μM), respectively, with AF78(F) showing highest uptake affinity. Consequently, the data reveal that the uptake of nonradioactive compounds against 3H-NE is inversely proportional to the size of non-polar halogen substituent, while polar hydroxyl group dramatically decreases the IC_{50} value. Heart to blood ratios support the results of the cell studies with AF78(F) (13.2±1.2), AF78(Cl) (10.4±0.4), AF78(Br) (8.7±1.5) and AF78(I) (5.9±0.4), respectively. In the healthy rat, PET/CT imaging showed homogeneous radiotracer distribution throughout the left ventricular wall, even the delineation of the right ventricular wall is visible. Because thermogenesis is predominantly driven by the SNS, specific uptake via NET was further proven by uptake in brown adipose tissue. Moreover, it has been reported that MIBG is not selective towards NET but can also be taken up by organic cation transporters (OCTs) in non-target organs, which will reduce the effective radiation dosage for the target organ while causing an unnecessarily higher utilization of radioactivity [3]. Therefore, the evaluation of their affinity on OCTs is currently in process.

Conclusion:

Our results show a remarkable trend between the meta-substitution on AF78 and their NET affinities, which correlates with the halogen´s space hindrance, non-polarity as well as negative inductive effect. These findings would pave the way for further tracer development, by using non-polar meta-halogen and radiotracers with higher NET selectivity over OCTs for better imaging accuracy and therapeutic specificity.

References

1. Chen X, Fritz A, Werner RA, Nose N, Yagi Y, Kimura H, Rowe SP, Koshino K, Decker M, Higuchi T. Initial Evaluation of AF78: a Rationally Designed Fluorine-18-Labelled PET Radiotracer Targeting Norepinephrine Transporter. Mol Imaging Biol. 2020 Jun;22(3):602-611. doi: 10.1007/s11307-019-01407-5.
2. Chen, X., Fritz, A., Werner, R. A., Nose, N., Yagi, Y., Kimura, H., Rowe, S. P., Koshino, K., Decker, M., & Higuchi, T. (2020). Initial Evaluation of AF78: a Rationally Designed Fluorine-18-Labelled PET Radiotracer Targeting Norepinephrine Transporter.Molecular imaging and biology,22(3), 602–611. doi:10.1007/s11307-019-01407-5
3. Bayer M, Kuçi Z, Schömig E, Gründemann D, Dittmann H, Handgretinger R, Bruchelt G. Uptake of mIBG and catecholamines in noradrenaline- and organic cation transporter-expressing cells: potential use of corticosterone for a preferred uptake in neuroblastoma- and pheochromocytoma cells. Nucl Med Biol.;36(3):287-94. doi: 10.1016/j.nucmedbio.2008.12.010

Oral Presentation

Disclosures: The authors have disclosed no financial interest.

007-Radioimmunotherapy Targeting Hypoglycosylated MUC16 in High Grade Serous Ovarian Cancer

Presenter: Kyeara Mack, Memorial Sloan Kettering Cancer Center

Kyeara Mack[1], Komal Mandleywala[2], Zachary Samuels[3], Madi Madiyalakan[4], Cory Brooks[5], Prakash Radhakrishnan[6], Michael Hollingsworth[7], Jason Lewis[3]

[1]*Memorial Sloan Kettering Cancer Center*
[2]*Memorial Sloan Kettering Cancer Center, NYC, NY*
[3]*Memorial Sloan Kettering Cancer Center, New York, NY*
[4]*Quest PharmaTech Inc*
[5]*California State University, Fresno, Fresno, California*
[6]*University of Nebraska Medical Center, Omaha, Nebraska*
[7]*University of Nebraska Medical Center, Omaha, NE*

Objectives:

MUC16 continues to rank among viable targets for the diagnosis and treatment of high grade serous (HGS) ovarian adenocarcinomas. Aberrantly expressed *O*-linked glycans on hypoglycoslyated forms of mucins such as MUC16 are implicated in the biology that promotes the malignancy of tumors of epithelial origin. Current therapies for ovarian cancer have not significantly improved overall survival, thus there is a critical need for additional treatment methods. We hypothesize that truncated MUC16 isoforms are a potential target for radioimmunotherapy treatment of HGS ovarian cancer. Here, we utilized a Lutetium-177 (^{177}Lu) labeled humanized antibody, huAR9.6, that targets fully-glycosylated and hypoglycosylated isoforms of MUC16 to treat ovarian tumors with varying MUC16 expression levels.

Methods:

huAR9.6 was conjugated to CHX-A”-DTPA and radiolabeled with ^{177}Lu for radioimmunotherapy experiments in mice bearing MUC16^{+} subcutaneous OVCAR3 tumors & medium MUC16 expressing OVCAR5 tumors. OVCAR3 xenografted mice were placed into three cohorts for administration of 250 μCi, 500 μCi, or 750 μCi of ^{177}Lu-labeled huAR9.6 to evaluate dose dependent efficacy. OVCAR5 xenografted mice were placed into a single 500 μCi dose cohort. Toxicity of the treatment was assessed by monitoring hematologic parameters throughout the study.

Results

In this study, [^{177}Lu]Lu-CHX-A”-DTPA-huAR9.6 significantly suppressed tumor growth in all three dose cohorts of the OVCAR3

xenografts. The 500 µCi and 750 µCi doses were curative in OVCAR3 tumor bearing mice, but showed toxic side effects (petechiae, hair loss, and death). [^{177}Lu]Lu-CHX-A"-DTPA-huAR9.6 slowed tumor growth in mice bearing OVCAR5 tumors in comparison to saline control. WBC, RBC, and platelet counts decreased within 2-3 weeks post-injection, but all cell counts recovered to normal range by weeks 3-5.

Conclusion:

Here, we show that [^{177}Lu]Lu-CHX-A"-DTPA-huAR9.6 has strong anti-tumor effects in high MUC16 expressing tumors. These findings demonstrate great potential for using ^{177}Lu-labeled huAR9.6 for radioimmunotherapy treatment in ovarian cancer.

Acknowledgments: This work was supported by the NIH R35 CA232130 and Quest PharmaTech for providing the antibody.

References

1. D. Thomas et al. Mol Ther. 2021 April 7;29(4):1557-1571.
2. M.A. Hollingsworth et al. Nat Rev Cancer. 2004 Jan;4(1):45-60.
3. Sharma S.K. et al. Clin Cancer Res 2022 March 1; 28 (5): 948–959.

Oral Presentation

Disclosures: The authors have disclosed no financial interest.

008-89Zr-trastuzumab-PET/CT imaging of HER2-positive breast cancer for predicting pathologic complete response after neoadjuvant systemic therapy

Presenter: Martijn van Dam, Leiden University Medical Center (LUMC)

Martijn van Dam[1], Daan G. Linders[2], Marion M. Deken[3], Marieke Straver[4], Denise Hilling[5], Danielle J. Vugts[6], Martin Wasser[5], E.M.C. Voormolen[7], Danielle Cohen[7], Lioe-Fee de Geus-Oei[5], Lenka. M. Pereira Arias-Bouda[8], Alexander Vahrmeijer, Gerrit-Jan (G.J.) Liefers[7]

[1]*Leiden University Medical Center (LUMC), Leiden, Zuid-Holland, Netherlands*
[2]*Leiden University Medical Center (LUMC), Netherlands*
[3]*Leiden University Medical Center (LUMC), Leiden, Leiden, Netherlands*
[4]*Haaglanden Medisch Centrum, The Hague, Netherlands*
[5]*Leiden University Medical Center (LUMC), Leiden, Nederland, Netherlands*
[6]*Amsterdam University Medical Center (UMC), Amsterdam, Zuid-Holland, Netherlands*
[7]*Leiden University Medical Center (LUMC), Leiden, Netherlands*
[8]*Leiden University Medical Center, Leiden, Netherlands*

Background:

To date, breast cancer (BC) is the world's most prevalent cancer type and the leading cause of cancer-related mortality in women[1]. Approximately 20% of all BCs show amplification of the human epidermal growth factor receptor-2 (HER2/neu) gene, which is critical for tumor proliferation and disease progression[2]. HER-2-positive (HER2+) BC often exhibits aggressive clinicopathologic features. Nonetheless, with the introduction of neoadjuvant systemic chemo- and HER2-directed therapies, pathological complete response (pCR) rates in up to 60-65% of patients have been reported[3,4]. This leads to the suggestion for future non-surgical treatment strategies in case of pCR after neoadjuvant systemic therapy (NST)[5]. Pivotal herein is accurate preoperative prediction of pCR. Currently used modalities, such as MRI, lack sensitivity for predicting pCR in HER2+ BC, corresponding to a pCR in only 73% of patients[6-9]. HER2-targeted PET/CT-imaging using zirconium-89 (^{89}Zr)-radiolabeled trastuzumab holds potential as a technique to improve the diagnostic accuracy. This trial evaluates the feasibility of ^{89}Zr-trastuzumab-PET/CT for accurate non-invasive prediction of pCR in HER2+ BC.

Methods:

This multicenter interventional prospective trial was approved by the Dutch medical ethics committee. Female patients aged >18 years with HER2+ BC scheduled to undergo NST and surgical resection were included. HER2-status was scored based on standard-of-care immunohistochemistry analysis of the diagnostic biopsy specimen. All subjects underwent a pre- and post-NST ^{89}Zr-trastuzumab-PET/CT scan. For both scans, patients received 37 MBq (±10%), 50 mg of clinical grade ^{89}Zr-trastuzumab intravenously four days prior to scanning. Dose and timing were based on previous phase I studies[10,11]. The standard-of-care MRI images before and after NST were evaluated using the RECIST1.1 guidelines, and evaluated for tumor size, lymph nodes, as well as speed and intensity of (pathological) contrast enhancement, washout, and diffusion restriction. ^{89}Zr-trastuzumab-PET/CT scans were assessed for ^{89}Zr-trastuzumab uptake in the primary tumor and involved lymph nodes, quantified as Metabolic Tumor Volume (MTV), Standardized Uptake Value Ratio (SUV_R) and $SUV_{mean/max}$ using semi-automatic tumor segmentation, based on subject individual thresholding. SUV_R is SUV_{max} of the BC lesion divided by SUV_{mean} of healthy tissue in the contralateral breast. Radiologic complete response (rCR) was defined as visual disappearance of ^{89}Zr-trastuzumab uptake in the tumor region. All diagnostic biopsies and resection specimens were assessed by a board-certified pathologist. A pCR was defined as the absence of invasive tumor cells in the resected specimen, irrespective of remaining in situ lesions (ypT0/ypTis). For the quantification of residual disease, the Residual Cancer Burden (RCB) score was used[12].

Results:

To date, five patients with NST-treated HER2+ BC lesions have been included. No adverse events were reported during administration and follow-up. Figure 1 shows examples of the diagnostic MRI- and ^{89}Zr-Trastuzumab-PET/CT images pre- and post-NST correlated to definitive histopathologic results. In total 4/5 patients had a pCR, the accuracy of ^{89}Zr-trastuzumab-PET/CT and MRI was respectively 80% and 100%. The MTV of BC lesions pre-NST was heterogeneous and ranged from 1.5-21.6 mm^3 (median 6.3). SUV_R and SUV_{max} pre-NST respectively ranged from 7.0-95.5 (median 22.3) and 1.4-19.1 (median 6.7). The percentage decrease (Δ, delta) of SUV_R pre- and post NST was -94%, -91%, -88%, -83% in cases with pCR, in contrast to pPR which showed a decrease of -57%.

Conclusions:

These preliminary results showed proof-of-concept for the diagnostic evaluation of neoadjuvant treated HER2+ BC lesions using ^{89}Zr-trastuzumab-PET/CT with a favorable safety and tolerability profile. Based on this limited series ^{89}Zr-trastuzumab-PET/CT may be non-inferior compared to MRI for response assessment based on diagnostical accuracy[9]. Nonetheless, in this series MRI outperformed ^{89}Zr-trastuzumab-PET/CT based on visual analysis. A more robust conclusion on the added diagnostic value of ^{89}Zr-trastuzumab-PET/CT for accurate response assessment in HER2+ BC should be drawn after inclusion of all intended participants.

References

1. Sung, H., et al. Global Cancer Statistics 2020: GLOBOCAN Estimates of Incidence and Mortality Worldwide for 36 Cancers in 185 Countries. CA Cancer J Clin 71, 209-249 (2021).
2. Arteaga, C.L., et al. Treatment of HER2-positive breast cancer: current status and future perspectives. Nat Rev Clin Oncol 9, 16-32 (2011).
3. Chang, H.R. Trastuzumab-based neoadjuvant therapy in patients with HER2-positive breast cancer. Cancer 116, 2856-2867 (2010).
4. Untch, M., et al. Neoadjuvant treatment with trastuzumab in HER2-positive breast cancer: results from the GeparQuattro study. J Clin Oncol 28, 2024-2031 (2010).
5. Shin, H.C., et al. Breast-conserving surgery after tumor downstaging by neoadjuvant chemotherapy is oncologically safe for stage III breast cancer patients. Ann Surg Oncol 20, 2582-2589 (2013).
6. Schaefgen, B., et al. Can Routine Imaging After Neoadjuvant Chemotherapy in Breast Cancer Predict Pathologic Complete Response? Ann Surg Oncol 23, 789-795 (2016).
7. Sheikhbahaei, S., et al. FDG-PET/CT and MRI for Evaluation of Pathologic Response to Neoadjuvant Chemotherapy in Patients With Breast Cancer: A Meta-Analysis of Diagnostic Accuracy Studies. Oncologist 21, 931-939 (2016).
8. van Loevezijn, A.A., et al. Minimally Invasive Complete Response Assessment of the Breast After Neoadjuvant Systemic Therapy for Early Breast Cancer (MICRA trial): Interim Analysis of a Multicenter Observational Cohort Study. Ann Surg Oncol 28, 3243-3253 (2021).
9. van Ramshorst, M.S., et al. MRI predicts pathologic complete response in HER2-positive breast cancer after neoadjuvant chemotherapy. Breast Cancer Res Treat 164, 99-106 (2017).
10. Dijkers, E.C., et al. Biodistribution of 89Zr-trastuzumab and PET imaging of HER2-positive lesions in patients with metastatic breast cancer. Clin Pharmacol Ther 87, 586-592 (2010).
11. Laforest, R., et al. [(89)Zr]Trastuzumab: Evaluation of Radiation Dosimetry, Safety, and Optimal Imaging Parameters in Women with HER2-Positive Breast Cancer. Mol Imaging Biol 18, 952-959 (2016).
12. Symmans, W.F., et al. Measurement of residual breast cancer burden to predict survival after neoadjuvant chemotherapy. J Clin Oncol 25, 4414-4422 (2007).

Oral Presentation

Disclosures: The authors have disclosed no financial interest.

009-Quantitative postmortem autoradiography of multiple markers in Alzheimer's disease

Presenter: Anat Biegon, Stony Brook University

Anat Biegon[1], Jasbeer Dhawan[2], Aviram Nessim[2], Vanessa A. Carter[2], Erin Sundermann[3]

[1]*Stony Brook University, Stony Brook*
[2]*Stony Brook Medicine, Stony Brook, NY*
[3]*University of California, San Diego, San Diego*

Introduction:

Amyloid and tau deposits are the hallmarks of Alzheimer's disease (AD) since its first discovery and the basis for a diagnosis of "definitive AD" obtained postmortem. More recently, we have seen accumulating evidence of a relationship between disease progression, neuroinflammation and loss of glutamate NMDA receptors, gathered from disparate studies using PET *in vivo* and immunohistochemistry or autoradiography *in vitro*. In the present study, we set out to perform the first fully quantitative analysis of all four markers and their interrelationship in brains of subjects who died with AD, mild cognitive impairment (MCI) or cognitively normal controls. Notably, the NMDA receptor is relatively rarely studied in the context of AD although it is directly and profoundly linked to memory formation. The hypothesis driving the study is that excessive deposition of both amyloid and tau is necessary but not sufficient to cause hippocampal structural (atrophy) and functional (memory loss) pathology, and the latter are predicated on hippocampal neuroinflammation and loss of NMDA receptors.

Methods:

Hippocampal samples from 72 individuals were obtained from two brain repositories. Samples were equally divided among men and women and the three disease categories, resulting in a group size of 24 subjects/diagnosis, 12 men and 12 women. Antemortem neuropsychological test results and detailed pathological evaluation were available for all subjects. Brains with pathological findings indicative of diseases other than AD (e.g. Lewy body disease, Parkinson's, other dementias) were not included. Each hippocampus was cryosectioned to provide 10 consecutive slides which were labeled with radioligands for tau, amyloid, TSPO (translocator protein, a marker of neuroinflammation/microglial activation) and NMDA receptors using published methodologies (1-3). Sections were also stained with cresyl violet to assess anatomy and histopathology. Autoradiograms were scanned and analyzed using FIJI (originally NIH Image) software. To facilitate quantification, commercial tritium standards were included in all experiments using tritiated ligands, ([3H]PK11195 and [3H]MK801 for TSPO and NMDA receptors, respectively) while experiments with F18 labeled tracers ([18F]T807 and [18F]Florbetaben for tau and amyloid respectively) were accompanied by freshly prepared [18F] standards. Results: As expected, diagnosis of AD was associated with significant increases in hippocampal tau and TSPO and a decreases in NMDA receptor density relative to non-demented controls. Amyloid density was higher in AD cortex and control white matter relative to hippocampus and did not match the anatomical distribution of changes in the other three markers. Patterns of AD-related changes in tau, TSPO and NMDA receptors were grossly similar, all showing relative preservation of the dentate compared to the CA1 and subiculum. As a group, subjects with MCI demonstrated intermediate levels of TSPO and NMDA receptors, with some subjects demonstrating profound changes similar to those observed in AD and other subjects demonstrating no change relative to non-demented controls.

Conclusions:

In vitro autoradiography is a reliable and quantitative tool enabling simultaneous assessment of multiple markers in brains of subjects along the AD trajectory which may contribute to a better understanding and prediction of disease progression from MCI to AD.

References

1. Kravitz E., Gaisler-Salomon I., Biegon A. PLoS One 8(11):e81244. doi: 10.1371/journal.pone.0081244 (2013)
2. Lowe VJ, Curran G, Fang P, et. al. Acta Neuropathol Commun. 2016 Jun 13;4(1):58.
3. Ni R, Röjdner J, Voytenko L, Dyrks T, Thiele A, Marutle A, Nordberg A. J Alzheimers Dis. 2021;80(4):1723-1737.

Oral Presentation

Disclosures: The authors have disclosed no financial interest.

010-Dual mode magnetic resonance imaging of aneurysmal inflammation using a ROS-responsive molecular sensor.

Presenter: Alexei Bogdanov, UMass Chan Medical School

Alexei A. Bogdanov[1], Eric Gale[2], Robert King[3], Anita Leporati[4], Matthew Gounis[3]

[1]UMass Chan Medical School, Worcester, MA
[2]Massachusetts General Hospital, Boston
[3]UMass Chan Medical School, Worcester, Massachusetts
[4]UMass Chan Medical School, Sterling, MA

Non-invasive detection of inflammation in vascular disease and cancer *in vivo* is one of the major goals of molecular imaging. Addressing this need requires developing and *in vivo* testing of novel probes in realistic models of human disease. Recently developed reactive oxygen species (ROS)-responsive redox imaging probe Fe-PyC3A enabled MRI of acute internal organ inflammation in several animal models [1]. Fe-PyC3A undergoes nearly instantaneous oxidation of Fe(II) to Fe(III) by ROS released by the activated cells of innate immunity leading to a rapid increase of longitudinal relaxivity (r1) and consequently, MR signal intensity. The feasibility of rapid (dynamic) MRI after Fe(II) PyC3A administration has not been tested yet in large animal models of inflammation even though near-real time MRI is the most important application of Fe-PyC3A in terms of clinical translation. In general, unlike most inflammation-specific probes Fe-PyC3A would not require a pre-injection and delayed image acquisition. In this work we tested dynamic as well as delayed MRI for imaging unstable and inflamed rabbit aneurysms, which undergo expansion and sustained inflammation [2]. A group of NZ rabbits (n=8) underwent aneurysm creation at the base of right common carotid artery [3] using consecutive elastinolysis and decellularization as described in [2]. Two groups of animals (n=4 each) were imaged- at 4 and 12 weeks after aneurysm creation. At 12 wks the healing of vascular injury was higher according to pathology. Fe-PyC3A was injected IV at the dose of 0.15-0.2 mmol/kg. 3T MRI was performed by using T1-FFE (TR/TE: 21/4ms, FA: 20°), and axial MSDE MR pulse sequence (SR prepulse 650 ms, TR/TE: 2500/6ms, FA: 90° V-enc: 1), with respiratory gating, and acquired immediately as well as 3 h post contrast injection. Dynamic images were analyzed by using SNR calculations in two animal groups. MSDI aneurysm enhancement ratios (ER) were calculated as a quotient of mean aneurysm MR signal intensities (normalized by mean in-plain MR signal of the muscle), measured before and after injection of Fe-PyC3A. Model aneurysms were excised and processed for histology as described in [4]. Test experiments in vitro showed that the oxidation of low-Fe(II)PyC3A by hydrogen peroxide resulted in a robust 15-times increase of r1 at 3T, suggesting that ROS released locally *in vivo*can produce SNR increase on 3T MR images. In a rabbit model of continuous aneurysmal inflammation the injection of Fe-PyC3A resulted in a transient increase of SNR with time-to-peak enhancement of 1.07±0.11 min in both 4- and 12 wk groups. SNR increase did not reach significant levels in one animal, while in the 12-week group a lower but significant ($p<0.05$) increase of SNR was observed in all animals (n=4), (Figure 1A,B). An I.V. injection of Gadavist (non-specific enhancement) resulted in high but nonspecific SNR, which plateaued after 3 min according to dynamic MRI acquisitions. Delayed MRI of the lumens on MSDE (Figure 1C) showed an increase with ER=1.33±0.09 after Fe-PyC3A administration (Figure 1B) with a statistically significant enhancement still present after a 3h delay. Histology identified the presence of MPO- and S100A8/A9 positive inflammatory cells at the level of 115±18 cells/section at 4 wk early time point which remained nearly constant for 12 weeks (109±23 cells) in the thrombi as well as in the blood vessel wall. In conclusion, dynamic and delayed MRI acquired after the administration of iron chelate - based ROS sensors allowed to detect a strong increase of SNR peak proving the feasibility of non-invasive molecular MRI of vascular inflammation due to ROS release by infiltrating inflammatory cells. Further detailed quantitative analysis of Fe-PyC3A sensor – assisted MRI with correlates of innate immune system markers will enable differentiation of low- and high-grade inflammation by both dynamic and delayed MRI techniques.

References

1. Wang H, Jordan VC, Ramsay IA, et al. (2019) Molecular Magnetic Resonance Imaging Using a Redox-Active Iron Complex. J Am Chem Soc 141:5916-5925.
2. King RM, Caroff J, Langan ET, et al. (2021) In situ decellularization of a large animal saccular aneurysm model: sustained inflammation and active aneurysm wall remodeling. J Neurointerv Surg 13:267-271.
3. Krings T, Moller-Hartmann W, Hans FJ, et al. (2003) A refined method for creating saccular aneurysms in the rabbit. Neuroradiology 45:423-429.
4. Wadghiri YZ, Hoang DM, Leporati A, et al. (2018) High-resolution Imaging of Myeloperoxidase Activity Sensors in Human Cerebrovascular Disease. Sci Rep 8:7687.

Oral Presentation

Disclosures: The authors have disclosed no financial interest.

011-Imaging of senescent pancreatic cancer with uPAR ImmunoPET

Presenter: Edwin Pratt, Memorial Sloan Kettering Cancer Center

Edwin C. Pratt[1], Riccardo Mezzadra[1], Tara D. Viray[2], Spencer A. Kaminsky[1], Amanda Kulick[1], Scott W. Lowe[1], Jason Lewis[1]

[1]Memorial Sloan Kettering Cancer Center, New York, NY
[2]Memorial Sloan Kettering Cancer Center, North Brunswick, NJ

Senescence is a newly identified hallmark of cancer[1], whereby the cancer cells undergo a type of proliferation arrest yet also increase the secretion of inflammatory markers known as the senescence associated secretory phenotype (SASP)[2]. Despite an array of antibodies clinically approved that target SASP antigens, senescence imaging has been limited to the nonspecific small molecule beta-galactosidase. Urokinase plasminogen activator surface receptor (uPAR) is an internalizing membrane bound antigen that has garnered tremendous interest in oncology and recently senescence. Prior research has shown uPAR targeting CAR-T cells to act as a senolytic in a lung adenocarcinoma model, prolonging survival[3]. Here the use of both murine and human targeting uPAR antibodies were investigated as potential markers of senescence for pancreatic cancer under a senescence inducing combination of Trametinib and Palbociclib (TP). Using Zirconium-89 with the chelator desferoxamine (^{89}Zr-DFO), murine and human targeting uPAR antibodies were radiolabeled with a specific activity between 5-10mCi/mg. Species cross reactivity of ^{89}Zr-DFO labeled huPAR and muPAR was determined by magnetic bead based binding assay bearing human and murine uPAR antigens. High reactivity with the muPAR antibody was seen against mouse, human and control targets,

while huPAR antibody bead binding was most selective for human uPAR (persuasive data 1a). Cell uptake of 1 µCi ^{89}Zr-DFO-muPAR antibody increased two-fold (32 to 65 µCi/µg) in KPC cells undergoing senescence inducing TP treatment (persuasive data 1b). In vivo, administration of 10-40 µg, 75 µCi-250 µCi of radiolabeled huPAR or muPAR was imaged by PET/CT at 24, 48, 72, and 144h followed by terminal biodistribution in several flank pancreatic tumor models. Strong accumulation in subcutaneously implanted KPC pancreatic tumors were seen in both untreated and TP treated mice (persuasive data 1c) with uptake between 15-20 percent injected dose per gram in each image slice. It was noted that in TP treated mice, lower liver and blood activity was seen by PET/CT and confirmed by terminal biodistribution at 144 h. Human uPAR targeting antibody in nude mice bearing flank MiaPaCa2 tumors showed strong antibody uptake by 144 h, with increased uptake for mice undergoing TP therapy (Persuasive Date 1d). Additional imaging and biodistribution were performed in BxPC3 and PANC1 tumor bearing mice, though tumor uptake was less than that seen for MiaPaCa2. Preloading studies at 10 µg, 40 µg, and 100µg at 4h prior to injection of the radiotracer showed improved tumor uptake kinetics at 24 hours with the highest preloading level, though 144h terminal biodistribution differences were more modest (data not shown). While uPAR is not considered an antigen specific to senescence, moderate to high uptake was observed three different pancreatic lines over the normal pancreas and TP therapy increased tumor uPAR uptake in tumors. The development and optimization of ^{89}Zr-DFO-uPAR antibodies for human and murine targets allows a new way to identify pancreatic cancer in addition to the uPAR increase as part of senescence inducing therapy. Future directions include testing other pancreatic models, senescence inducing drug combinations, and possible antibody conjugated senolytic or endoradiotherapy strategies.

References

1. Hanahan, D. Hallmarks of Cancer: New Dimensions. Cancer Discov 12, 31-46, doi:10.1158/2159-8290.CD-21-1059 (2022).
2. Ruscetti, M. et al. Senescence-Induced Vascular Remodeling Creates Therapeutic Vulnerabilities in Pancreas Cancer. Cell 181, 424-441 e421, doi:10.1016/j.cell.2020.03.008 (2020).
3. Amor, C. et al. Senolytic CAR T cells reverse senescence-associated pathologies. Nature 583, 127-132, doi:10.1038/s41586-020-2403-9 (2020).

Oral Presentation

Disclosures: The authors have disclosed no financial interest.

012-13C-MRS metabolic markers of response to immunotherapy in YUMMER 1.7 melanoma xenografts

Presenter: Chantale Farah, Catholic University of Louvain, Belgium

Chantale Farah[1], Lionel Mignion[1], Marie-Aline Neveu[1], Bénédicte Jordan[1]

[1]Catholic University of Louvain, Belgium, Woluwe saint lambert, Brussels, Belgium

There is today no consensus to determine which advanced melanoma patient will benefit from immune or targeted therapy. If BRAF targeted therapy is efficient in most of the patients, resistance occurs in almost all cases, whereas immune checkpoint inhibitors show a lower response rate yet with a long-term benefit. To identify the subset of melanoma patients who will achieve durable clinical benefit with checkpoint blockade, the development of biomarkers of response to immune checkpoint blockade is crucial. The aim of this work was to evaluate metabolic imaging using ^{13}C-MRS (Magnetic Resonance Spectroscopy) as a marker of response to immunotherapy in a syngeneic melanoma model. Showing significant tumor growth delay when treated with anti-PD1 antibody compared to isotype control antibody, the YUMMER1.7 melanoma xenograft model has been selected as a responsive model to immunotherapy for this study. ^{13}C-MRS was performed *in vivo* after injection of hyperpolarized (HP) ^{13}C-pyruvate, at baseline and after 1 cycle of immunotherapy, to evaluate dynamic changes in pyruvate-lactate exchange. Furthermore, *ex vivo* ^{13}C-MRS steady state metabolic tracing experiments were performed after U-^{13}C-glucose injection at the same time-points. A significant decrease in the HP ^{13}C-lactate to ^{13}C-pyruvate ratio was observed *in vivo* after one cycle of immunotherapy, that was not observed in the isotype control group. With respect to steady state measurements, there was a lack of change in the *ex vivo* metabolite concentrations (^{13}C lactate, ^{13}C alanine, ^{13}C glutamate) after ^{13}C glucose injection in response to immunotherapy. Altogether these results suggest that HP ^{13}C-pyruvate could be used as an early maker of response in melanoma patients treated with immunotherapy. The current data also further illustrate that steady state metabolite concentrations are only one aspect of metabolism and do not necessarily reflect the activity of a metabolic pathway, contrarily to HP metabolic imaging. Further IHC studies are ongoing to assess metabolic transporters and glycolytic enzymes, including GLUT1, MCT1, MCT4, and LDH-A.

References

1. Farah, C.; Neveu, M.-A.; Yelek, C.; Bouzin, C.; Gallez, B.; Baurain, J.-F.; Mignion, L.; Jordan, B.F. Combined HP 13C Pyruvate and 13C-Glucose Fluxomic as a Potential Marker of Response to Targeted Therapies in YUMM1.7 Melanoma Xenografts. Biomedicines 2022, 10, 717. https://doi.org/10.3390/biomedicines10030717
2. Wang, J.; Perry, C.J.; Meeth, K.; Thakral, D.; Damsky, W.; Micevic, G.; Kaech, S.; Blenman, K.; Bosenberg, M. UV-Induced Somatic Mutations Elicit a Functional T Cell Response in the YUMMER1.7 Mouse Melanoma Model. Pigment Cell Melanoma Res. 2017, 30, 428–435, doi:10.1111/pcmr.12591.

Oral Presentation

Disclosures: The authors have disclosed no financial interest.

013-18F-FDG PET imaging as a pharmacodynamic biomarker of KRAS inhibition in xenograft and genetically engineered mouse models of cancer

Presenter: Ziyue Karen Jiang, Pfizer

Ziyue Karen Jiang[1], Catherine Lee[2], Lisa Manzuk[1], Kavon Noorbehesht[3], Gabriel Troche[1], Nathan Ihle[2], Anand Giddabasappa

[1]Pfizer, San Diego, CA
[2]San Diego, CA
[3]Vertex Pharmaceuticals, Boston, MA

KRAS is one of the most commonly mutated oncogenes in human cancers, with the highest prevalence in pancreatic, colorectal, and lung cancer (ref 1). Although once considered "undruggable", a renewed and growing interest is now in pursuing KRAS-targeted compounds. We developed a KRAS G12C mutation-specific inhibitor that had

shown promising pharmacology and efficacy results. It will be referred to as "KRasi" hereinafter. KRAS activation controls three major signaling axes: PI3K-AKT, MAPK-ERK, and Ral-GEF (ref 2), and both PI3K and ERK pathways regulate glucose metabolism. So, here, we aim to explore PET imaging with 18F-FDG, a well validated glucose analog imaging probe, as a pharmacodynamic biomarker of KRAS inhibition first in a xenograft pancreatic tumor model and then in a genetically engineered mouse (GEM) model of non-small cell lung cancer (NSCLC). KRAS G12C-harboring MiaPaca2 human pancreatic tumors were established in nude mice and treated with escalating doses of KRasi for three consecutive days. 18F-FDG PET imaging was performed prior to drug treatment (baseline) and immediately (1 hour) after the final dose. As shown in Figure (a-b), image analysis and ex vivo gamma counting demonstrated a significant decrease in tumor uptake of 18F-FDG in the KRAS inhibited groups (mean ex vivo tumor uptake of 2.50 and 2.56 %ID/g in the low- and high-dose groups, respectively, versus 4.56 %ID/g in the vehicle control). While ~90% of pancreatic cancers harbor KRAS mutations, G12C only accounts for ~1% of them. In contrast, it is the most prevalent KRAS mutation in NSCLC, yet most GEM models available are driven by KRAS G12D. To address this gap, KrasLSL-G12D/wt p53fl/fl knock-in mouse (commonly known as the KP model) was modified to replace the G12D mutation with G12C. Development of lung tumors in the resulting animals was induced by administering Cre-expressing Adenovirus intranasally. Subsequent tumor growth was monitored by longitudinal microCT imaging and quantified by an automated segmentation algorithm (ref 3). Compared to its G12D counterpart, the new, G12C-driven model showed a marked delay in tumor latency (~18 versus 12 weeks post induction for the first detection of discernible tumor nodules) and significantly longer survival time (median survival of 27.7 versus 36.6 weeks post induction). However, the speed of tumor progression to death did not differ drastically, and both models were decently avid for glucose/18F-FDG at baseline. To assess the pharmacodynamic effect of Kras inhibition in the KRas G12C/p53 GEM model of NSCLC, mice with distinct lung tumor nodules were treated with high dose KRasi for 7 consecutive days, with PET imaging performed at baseline and post-treatment. As shown in Figure (c-e), all animals demonstrated a moderate baseline level of tumor 18F-FDG uptake. After treatment, while the vehicle groups exhibited continuous tumor growth and a moderate increase in their tumor 18F-FDG uptake (average post-to-baseline fold change: 1.18), most of the KRas inhibitor treated animals had either stable disease or tumor size reduction, and either no change or a decrease in 18F-FDG PET signal compared to baseline (average post-to-baseline fold change: 0.87). Taken together, these results showcased the value of 18F-FDG PET imaging as pharmacodynamic readout of KRas inhibition in mouse models of cancer. Of note, this is beyond its "regular" use in the clinic as a tool to assess tumor burden. Given that G12C-specific inhibitors are currently in clinical trials for lung cancer, but only about half of patients have shown partial responses to treatment (Ref 4), there is still a need to further understand the mechanisms of resistance. The imaging strategy presented here could aid in the elucidation of molecular and metabolic mechanisms in the preclinical setting.

References

1. Karachaliou et al, Clinical Lung Cancer2013 May;14(3):205-14.
2. Liu et al, Acta Pharm Sin B. 2019 Sep;9(5):871-879
3. Montgomery et al, PLoS One 2021 Jun 17;16(6):e0252950
4. Skoulidis et al, N Engl J Med 2021 Jun 24; 384:2371-2381

Oral Presentation

Disclosures: The authors have disclosed no financial interest.

014-Correlation of PCASL with FDG and FDOPA in various neurodegenerative conditions – An MR/PET study

Presenter: Sandhya Mangalore, National Institute of Mental Health and Neurosciences

Sandhya Mangalore[1], Kavish K. Chaurasia[2], Venkatesh Murthy[2]

[1]National Institute of Mental Health and Neurosciences, bangalore, karnataka, India
[2]National Institute of Mental Health and Neurosciences, Bengaluru, Karnataka, India

Background:

Pseudo Continuous Arterial Spin Labelling (pCASL) MR is a perfusion imaging biomarker and reflects molecular level process. It is a contrast free & radiation free technique.

Methods:

The standardised PCASL sequence was acquired along with routine neuro-degenerative protocol. We had 60 cases of variety of neurodegenerative diseases referred for FDG PET between April 2020- December 2021 & 22 cases of movement disorder referred for FDOPA PET scan between April 2021- December 2021.

Results:

Based on FGD-PET we could phenotype cases based on the perfusion profile as AD(18), FTD(28), DLB(3),Parkinsonian disorders such as PDD, CBD, PSP(10), Vascular dementia(1).We could also subtype AD as PCA AD(5), AD- VaD (1) and FTD as svFTD(7), bvFTD(7), FTDPSP(1),PNFA(2), FTD-NPH(1), CBDAD(1).Detailed clinical – structural – functional imaging correlation was done for all these cases . Based on FDOPA we subdivided the patients into: Idiopathic Parkinson disease (IPD, n = 10), Atypical Parkinson disease (corticobasal degeneration, n = 02), Secondary /other movement disorders with reduced dopaminergic activity in basal ganglia (Vascular n=01, drug induced PD n=02 & Mangenese toxicity n=01) & Scan negative for dopaminergic deficits without reduced dopaminergic activity in basal ganglia (n= 06).Among 10 IPD cases, PCASL & FDOPA –PET findings correlated in 7 cases for reduced perfusion & dopaminergic activity in caudate nucleus & putamen, with additional information on cortical gray-matter symmetrical hypoperfusion without atropy in parietooccipital region in 1 case. FDOPA showing reduced dopaminergic activity activity in basal ganglia, hypoperfusion revelled by PCASL in parietal lobes along with basal ganglia differentiated IPD from 2 cases of AtypicalParkinson disease as cortico-basal degeneration.

Conclusion:

pCASL provides brain perfusion profile, so profiling patients before gross morphological changes, thus helpful in early & correct diagnosis of multiple conditions. Syngergistic effect of ASL with FDOPA as DOPA gives basal ganglia information whereas ASL being analogue of FDG gave lobar information too hence sensitivity specificity was increased of PET to make further phenotype analysis between IPD/APD .

References

1. Huang CW, Hsu SW, Chang YT, Huang SH, Huang YC, Lee CC, Chang WN, Lui CC, Chen NC, Chang CC. Cerebral Perfusion Insufficiency and Relationships with Cognitive Deficits in Alzheimer's Disease: A Multiparametric Neuroimaging Study. Sci

Rep. 2018 Jan 24;8(1):1541. doi: 10.1038/s41598-018-19387-x. PMID: 29367598; PMCID: PMC5784155.
2. Fällmar D, Lilja J, Velickaite V, Danfors T, Lubberink M, Ahlgren A, van Osch MJ, Kilander L, Larsson EM. Visual Assessment of Brain Perfusion MRI Scans in Dementia: A Pilot Study. J Neuroimaging. 2016 May;26(3):324-30. doi: 10.1111/jon.12296. Epub 2015 Sep 16. PMID: 26376736.

Oral Presentation

Disclosures: The authors have disclosed no financial interest.

015-CAN ABSENT SWALLOW TAIL (AST) SIGN BE USED AS A BIOMARKER FOR IDIOPATHIC PARKISONS DISEASE AMIDST A WIDE VARIETY OF PARKINSONIAN SYNDROMES: 3D FLAIR MRI - 6-[18F]-FDOPA PET CORRELATION

Presenter: Sandhya Mangalore, National Institute of Mental Health and Neurosciences

Sandhya Mangalore[1], Kavish K. Chaurasia[2], Priyanka Priyadarshini[2]

[1]National Institute of Mental Health and Neurosciences, bangalore, karnataka, India
[2]National Institute of Mental Health and Neurosciences, Bengaluru, Karnataka, India

OBJECTIVE:

To evaluate the presence of Absent Swallow Tail sign (AST) in Parkinsonian syndromes and correlate it with ^{18}F-DOPA- PET and whether AST can be used as an imaging biomarker to differentiate IPD from APD, secondary Parkinsonian disorders (Essential tremors, drug induced PD, Vascular PD etc) and other movement disorders.

MATERIALS AND METHODS:

A total of 24 cases with clinical features of Parkinsonism were taken for the study. The control group comprised of 8 cases of supratentorial tumours not involving basal ganglia and midbrain. In all cases and controls, 3D FLAIR and ^{18}FDOPA PET was done. PET images were co-registered on 3D T1 MPRAGE. 3D FLAIR images were reformatted in axial plane in such a way that the imaging plane lies perpendicular to the tangential plane of red nucleus on the sagittal 3D FLAIR images. AST sign was evaluated on right and left Substantia Nigra (SN) separately and correlated with ^{18}F-DOPA images. **RESULTS:**Out of the 24 cases with Parkinsonian syndromes, 10 cases were IPD. All the cases of IPD had bilateral AST sign with abnormal FDOPA findings, comprising the true positive group for AST sign, except one case wherein clinical suspicion was young onset PD, where AST was present only on the left side with F-DOPA abnormality in bilateral striatum. This one case was considered as false negative in our study.3 cases were APD**.** In these 3 cases, AST was absent except in 1 case where it was equivocal on one side due to presence of type I VR spaces. ^{18}F-DOPA was abnormal in all the cases.7 cases were of secondary Parkinsonian syndromes (i.e. essential tremors, drug induced PD) without dopaminergic deficits. In all these cases ^{18}F-DOPA uptake was normal. AST was absent in all except 2 cases. 4 cases were of movement disorders due to other causes (2 were manganese toxicity and 1 was DYT23 dystonia, 1 was vascular PD). In these cases ^{18}F-DOPA uptake was abnormal. AST was present in 1 case of manganese toxicity and in the dystonia case.These cases of APD, secondary PD and movement disorders where AST was present were considered as false positive.AST was negative in all the controls with normal DOPA uptake. This group comprised true negative cases for AST sign. Specificity and sensitivity was calculated bases on performance of AST in correlation with FDOPA. AST was 90% sensitive and 71 % specific with a positive predictive value of 69% and negative predictive value of 90% in differentiating IPD from APD, secondary PD and other causes of movement disorders.

LEARNING POINTS

1. Presence of AST indicates IPD
2. Absence of AST indicates APD, secondary PD, toxic and genetic causes of movement disorders.
3. ^{18}F-DOPA PET can differentiate IPD/APD from secondary causes of PD.
4. In all cases of toxic and genetically associated movement disorders, ^{18}F-DOPA PET was abnormal with variable AST sign. This group mandates further research to derive conclusions.
5. Reconstruction in the described plane is important to increase sensitivity and specificity of AST

CONCLUSION: AST can be used as a reliable biomarker for differentiating IPD from APD, secondary PD and other causes of movement disorders.

Oral Presentation

Disclosures: The authors have disclosed no financial interest.

016-Virtual histology of brain pathologies: Crucial impact of sample preparation techniques

Presenter: Matthieu Chourrout, University Claude Bernard Lyon 1 (UCBL)

Matthieu Chourrout[1], David Meyronet[2], Thierry Baron[3], Gaëlle Hugon[4], Timm Weitkamp[5], Emmanuel Brun[6], Marlene Wiart[7], Fabien CHAUVEAU[8]

[1]University Claude Bernard Lyon 1 (UCBL), BRON, Rhône, France
[2]University Claude Bernard Lyon 1, Lyon, France
[3]Lyon, France
[4]Paris Saclay University, Orsay, France
[5]Saint-Aubin, France
[6]Grenoble Alpes University, Grenoble, Rhones-Alpes, France
[7]Claude Bernard University Lyon 1, Bron, France, France
[8]Lyon Neuroscience Research Center, BRON, Auvergne-Rhône-Alpes, France

Introduction:

Virtual histology is a pioneer means for the study of intact biological samples, digitally browsing the tissue in 3D to screen and examine pathological hallmarks. X-ray phase-contrast tomography (XPCT) is ideally suited for this purpose. XPCT is a cutting-edge fast imaging technique with an isotropic resolution of 5–10μm. It makes use of x-ray refraction instead of absorption, thus achieving a higher sensitivity within soft tissues such as the brain, in a similar way to phase-contrast microscopy. XPCT can reveal microstructural and anatomical features of the healthy brain [1–3] or quantitatively highlight diverse alterations caused by neurological diseases, for instance demyelination or amyloid plaque burden, without the need for cutting or staining [4–8]. For all these reasons, XPCT might become a novel complementary imaging tool for 3D neuropathological evaluation of brain samples.

In a standardization perspective, it is crucial to determine whether routine preparation of anatomopathological samples is compatible with XPCT imaging and how sample preparation determines the quality and contrast of images. To date, the preparation process is poorly described nor standardized, which limits reproducibility and widespread use of the technique. We hereby present our work to fine-tune the sampling and preparation processes and provide a comprehensive framework for clinical and pre-clinical applications in the field of neuropathology.

Methods:

Preparation of brain samples were varied to investigate the impact of:

- Freezing methods (isopentane, dry ice) vs. no freezing;
- Fixation (4% formaldehyde (FA) vs. 10% FA);
- Pretreatment with blood clot removal agent (CHAPS/NMDEA mix [9]) in order to prevent artifacts due to the lack of washing of the intravascular space in case of autopsic tissue;
- Ethanol dehydration kinetics (monitored at 5 time points throughout the process);
- Paraffin embedding vs. 96%-ethanol immersion.

These tests were performed on human and rodent brain samples. Human brains from deceased patients with neurodegenerative diseases (Alzheimer's disease, dementia with Lewy bodies) were selected and collected by an expert clinician (N=5). Whole excised brains from rodents were also collected (N=3) and hemispheres with different preparations were compared.
XPCT was performed at 2 synchrotron radiation facilities: ESRF – The European Synchrotron Radiation Facility (ID-19 beamline) and SOLEIL (ANATOMIX beamline). 3D images were generated with the PyHST2 toolbox then were analyzed with Fiji and ThermoScientific AMIRA.

Results:

We here confirm that ethanol dehydration is a crucial step to obtain contrast between white matter and gray matter in the brain parenchyma. Interestingly, ethanol-induced contrast formation was not immediate, particularly in corpus callosum and striatum, but appeared progressively once immersed in ethanol: 32 hours are required for the white-matter signal to be maximized. Fixation with higher percentage of FA did not modify the contrast, thus suggesting that anatomopathologists may use their usual preparation method. The paraffin embedding process degraded both anatomical contrast and image quality. Therefore, we tested alternative freezing techniques. However, differences were observed on adjacent human brain samples depending on the freezing method; the nature of these differences is under investigation with our expert clinician and will be confirmed with immuno-histochemistry and histochemistry analysis. Prior to imaging, the CHAPS/NMDEA-treated samples turned white, suggesting that blood removal was efficient; this was further confirmed by XPCT, enabling artifact-free analysis of the major blood vessels. Assessment of blood removal within the capillary network is in progress.

Conclusion:

XPCT-based virtual histology is a powerful tool that perfectly fits between in vivo 3D imaging and standard 2D immuno-histochemistry with respect to resolution and sample integrity. Standardizing preparation now is an opportunity to provide high-quality protocols as open-source material. This will contribute to fostering the use of XPCT by the neuroscience/neuroimaging communities and to encouraging further developments to fully exploit the potential of this approach, for which new contrasts still need to be discovered and deciphered.

References

1. Töpperwien, M., Krenkel, M., et al. 2017, 'Three-dimensional mouse brain cytoarchitecture revealed by laboratory-based x-ray phase-contrast tomography', Scientific Reports, 7 (1), 42847.
2. Xi, Y., Lin, X., et al. 2015, 'High-Resolution and Quantitative X-Ray Phase-Contrast Tomography for Mouse Brain Research', Computational and Mathematical Methods in Medicine, 2015 1–12.
3. Shi, S., Zhang, H., et al. 2019, '3D digital anatomic angioarchitecture of the mouse brain using synchrotron-radiation-based propagation phase-contrast imaging', Journal of Synchrotron Radiation, 26 (5), 1742–1750.
4. Cedola, A., Bravin, A., et al. 2017, 'X-Ray Phase Contrast Tomography Reveals Early Vascular Alterations and Neuronal Loss in a Multiple Sclerosis Model', Scientific Reports, 7 (1), 5890.
5. Noda-Saita, K., Yoneyama, A., et al. 2006, 'Quantitative analysis of amyloid plaques in a mouse model of Alzheimer's disease by phase-contrast X-ray computed tomography', Neuroscience, 138 (4), 1205–1213.
6. Chourrout, M., Rositi, H., et al. 2022, 'Brain virtual histology with X-ray phase-contrast tomography Part I:whole-brain myelin mapping in white-matter injury models', Biomedical Optics Express, 13 (3), 1620.
7. Chourrout, M., Roux, M., et al. 2022, 'Brain virtual histology with X-ray phase-contrast tomography Part II:3D morphologies of amyloid-β plaques in Alzheimer's disease models', Biomedical Optics Express, 13 (3), 1640.
8. Eckermann, M., Schmitzer, B., et al. 2021, 'Three-dimensional virtual histology of the human hippocampus based on phase-contrast computed tomography', Proceedings of the National Academy of Sciences, 118 (48), e2113835118.
9. Zhao, S., Todorov, M.I., et al. 2020, 'Cellular and Molecular Probing of Intact Human Organs', Cell, 180 (4), 796-812.e19.

Oral Presentation

Disclosures: The authors have disclosed no financial interest.

017-In vivo molecular imaging of chemokine-like receptor 1 (CMKLR1) to monitor ongoing inflammation in a preclinical bleomycin-induced lung injury model

Presenter: Philip Mannes, University of Pittsburgh School of Medicine

Philip Mannes[1], Clayton Barnes[1], Kathryn Day[2], Joseph D. Latoche[3], Jessie Nedrow[4], Carolyn Anderson [5], Janet Lee[4], Sina Tavakoli[6]

[1]*University of Pittsburgh School of Medicine*
[2]*University of Pittsburgh, Pittsburgh, Pennsylvania*
[3]*University of Pittsburgh, Pittsburgh, PA*
[4]*University of Pittsburgh*
[5]*University of Missouri, Columbia, Missouri*
[6]*University of Pittsburgh, Pittsburgh*

Introduction:

Lung diseases driven by non-resolving inflammation represent a significant burden on the US healthcare system (*1*) that is highlighted by the COVID-19 pandemic. There are currently few clinical tools to monitor ongoing lung inflammation, and stratify patient care using a personalized medicine approach. A promising target is chemokine-like receptor 1 (CMKLR1), a GPCR expressed by various leukocytes including monocytes/macrophages and natural killer cells, that binds to ligands chemerin and the omega-3 lipid mediator resolvin E1 released during

inflammation (*2*). The CMKLR1-chemerin axis has been implicated in various lung diseases and modulation of CMKLR1 signaling results in altered inflammatory responses (*3-5*). We evaluated a novel CMKLR1-targeted positron emission tomography (PET) radiotracer in a preclinical model of bleomycin-induced lung injury to non-invasively measure ongoing lung inflammation in the context of fibrotic lung injury. We further characterized CMKLR1 expression over the course of the inflammatory and fibrotic phases of bleomycin-induced lung injury.

Methods:

CMKLR1-targeted peptide ligands NODAGA-CG34 and 6CF-CG34 (6-carboxyfluorescein-CG34) were synthesized using solid phase peptide chemistry. For PET/CT imaging, NODAGA-CG34 was radiolabeled with ^{64}Cu to give ^{64}Cu-NODAGA-CG34 in radiochemical purity >95%. PET/CT with ^{64}Cu-NODAGA-CG34 was conducted in a bleomycin-induced murine model of lung injury, and the radiotracer uptake in the lungs was quantified by percent injected dose per gram (%ID/g) using Inveon Research Workspace. Specific uptake of the radiotracer was confirmed by co-injection of 100x molar excess of non-radiolabeled NODAGA-CG34. Following imaging studies, radiotracer uptake in individual organs (%ID/g) was measured with ex vivo gamma counting. In select mice, *ex vivo* autoradiography of the lungs was performed and adjacent lung sections were stained for immunofluorescence microscopy. Cellular patterns of CMKLR1 expression throughout the course of bleomycin-induced lung injury was determined by flow cytometry quantification of 6CF-CG34, a fluorescent analog of NODAGA-CG34, by lung leukocytes.

Results:

In vivo lung uptake of ^{64}Cu-NODAGA-CG34 both globally (%ID/g_{mean}) and focally (%ID/g_{max}) was highest at 1 week (%ID/g_{mean} = 2.47±0.67, %ID/g_{max} = 4.04±0.87) and 2 weeks (%ID/g_{mean} = 1.83±0.30, %ID/g_{max} =3.35±0.47) following bleomycin treatment, and decreased nearly to baseline by 4 weeks (%ID/g_{mean} = 0.70±0.06 and 1.03±0.10, %ID/g_{max} =1.38±0.10 and 1.96±0.19, respectively). ^{64}Cu-NODAGA-CG34 uptake was near-completely blocked upon co-injection with excess non-radiolabeled NODAGA-CG34, confirming its specificity. Quantification of ^{64}Cu-NODAGA-CG34 uptake in the lungs by *ex vivo* gamma counting strongly correlated with *in vivo* uptake obtained by PET (R^2 = 0.77, $P < 0.0001$), confirming the accuracy of quantitative PET imaging. Additionally, ^{64}Cu-NODAGA-CG34 uptake measured by *in vivo* PET and high-resolution *ex vivo* autoradiography spatially co-localized within regions of lung inflammation and increased CMKLR1 expression determined by histology. Further, we found that the increased CMKLR1 expression, measured by 6CF-CG34 uptake, in the lungs of mice at 1- and 2-weeks post-bleomycin was mostly driven by interstitial and monocyte-derived macrophages, and to a lesser degree natural killer cells, and matches the observed kinetics of radiotracer uptake determined by *in vivo* PET.

Conclusion:

In vivo molecular imaging of CMKLR1 with ^{64}Cu-NODAGA-CG34 measures ongoing inflammation in the context of a preclinical fibrotic lung injury model. PET imaging of CMKLR1 provides a potential strategy to non-invasively quantitate, spatially localize and monitor the dynamics of lung injury.

References

1. M. A. Matthay et al., Acute respiratory distress syndrome. Nat Rev Dis Primers 5, 18 (2019).
2. A. J. Kennedy, A. P. Davenport, International Union of Basic and Clinical Pharmacology CIII: Chemerin Receptors CMKLR1 (Chemerin1) and GPR1 (Chemerin2) Nomenclature, Pharmacology, and Function. Pharmacol Rev 70, 174-196 (2018).
3. S. Provoost et al., Pro- and Anti-Inflammatory Role of ChemR23 Signaling in Pollutant-Induced Inflammatory Lung Responses. J Immunol 196, 1882-1890 (2016).
4. B. Bondue et al., ChemR23 dampens lung inflammation and enhances anti-viral immunity in a mouse model of acute viral pneumonia. PLoS Pathog 7, e1002358 (2011)
5. S. Luangsay et al., Mouse ChemR23 is expressed in dendritic cell subsets and macrophages, and mediates an anti-inflammatory activity of chemerin in a lung disease model. J Immunol 183, 6489-6499 (2009).

Oral Presentation

Disclosures: The authors have disclosed no financial interest.

018-Preclinical evaluation of an integrin αvβ6- targeted photodynamic therapy agent

Presenter: Hua Zhang, University of California, Davis

Hua Zhang[1], Tanushree (Nina) Ganguly[1], Rebecca Harris[1], Luciana Kovacs[2], Yng (Sarah) Tang[3], Ryan A. Davis[4], Sven Hausner[5], Julie Sutcliffe[1]

[1]*University of California, Davis, Sacramento, CA*
[2]*University of California, Davis, Berlin, Berlin, Germany*
[3]*University of California, Davis, San Jose*
[4]*University of California, Davis, Sacramnento, CA*
[5]*UC Davis Health, Sacramento, CA*

Introduction:

Photodynamic therapy (PDT) is a non-invasive therapeutic approach in which an external light source activates an injected photosensitizer (PS) to generate reactive oxygen species causing localized cell death and reduced off-target toxicity. Although PDT has proven to be effective in treating some cancers clinically, the non-specific uptake and poor pharmacokinetic profiles of PSs often limit its clinical applications [1-3]. The integrin $\alpha_v\beta_6$ is an epithelial-specific cell surface receptor that is highly expressed in a wide range of tumors, but has low/undetectable expression in healthy adult tissue, making it an attractive target for cancer specific treatment [4, 5]. Here, we report the development and preclinical evaluation of a PS conjugated to an $\alpha_v\beta_6$-targeting peptide, for targeted-delivery to $\alpha_v\beta_6$-expressing tumors.

Methods:

An $\alpha_v\beta_6$-targeted PS, **1** (IR700-ABM-5G; Fig. 1A) was synthesized by conjugating the hydrophilic PS (IRDye700DX NHS, Li-Cor) onto an $\alpha_v\beta_6$-targeting peptide (NH_2-ABM-5G) in solution via NHS chemistry. The *in vitro* phototoxicity of **1** was assessed by WST-1 assay using DX3puroβ6 ($\alpha_v\beta_6$+) and DX3puro ($\alpha_v\beta_6$ -) cells, using a red light-emitting diode (LED, 690 ± 20 nm, Marubeni model L690-66-60) as the light source, against controls (LED light alone, **1** alone, and non-targeted IR700 with LED). *In vivo* imaging was performed in *nu/nu* nude mice bearing paired DX3puroβ6 and DX3puro xenograft tumors. Mice were injected with 10 μg of **1**, followed by imaging at 1, 2, 4, and 24 h. Biodistribution (24 h) data were collected post sacrifice. The *in vivo* therapeutic effect of **1** was studied in mice bearing DX3puroβ6 and DX3puro xenograft tumors: Group 1 - DX3puroβ6 tumor, saline; Group 2 - DX3puroβ6 tumor, LED only (no **1**); Group 3 - DX3puroβ6 tumor, **1** only (no LED); Group 4 - DX3puro tumor, **1** + LED; and Group 5 - DX3puroβ6 tumor, **1** + LED. For Groups 3-5, mice were

injected with 10 μg of **1**; for Groups 2, 4, and 5, mice were subjected to 20 min LED, and for all animals the treatments were performed once.

Results: **1**

demonstrated targeted phototoxicity to DX3puroβ6 ($\alpha_v\beta_6$ +) cancer cells. With light activation, **1** had an EC_{50} of 1.6 nM for DX3puroβ6 cells and ≥250 nM for the DX3puro cells. The toxicity of **1** without light activation was similar to that of free (non-targeted) IR700, i.e., not detectable at concentrations <100 nM, with only a moderate viability decrease (~20%) at a concentration of 250 nM. Fluorescent intensity measurements obtained from *in vivo* imaging and biodistribution confirmed selective uptake and retention of the **1** in the DX3puroβ6 tumors (Fig. 1B): the fluorescence intensity of DX3puroβ6 tumors was 2.9-fold higher than that of DX3puro tumors, and 2.5- to 6-fold higher than that of the other organs, except kidneys and stomach. A significant delay in tumor growth was observed following a single treatment with **1** + LED in mice bearing a DX3puroβ6 ($\alpha_v\beta_6$ +) tumor vs a DX3puro ($\alpha_v\beta_6$ -) tumor (38 vs 18 days, respectively, to reach tumor volume of 200 mm^3, $p < 0.001$), resulting in an increased median survival (61 vs 50 days respectively, $p < 0.05$). No therapeutic effect was observed in any of the control groups (Fig. 1C).

Conclusion: **1**

showed $\alpha_v\beta_6$-selective uptake and retention in integrin $\alpha_v\beta_6$-expressing DX3puroβ6 tumors in mice. The promising *in vivo* pharmacokinetics and superior therapeutic efficacy of **1** validate its potential as an $\alpha_v\beta_6$-targeted PDT agent and warrant further investigation for clinical translation.

References

1. Li, X.S., et al., Clinical development and potential of photothermal and photodynamic therapies for cancer. Nature Reviews Clinical Oncology, 2020. 17(11): p. 657-674.
2. Alsaab, H.O., et al., Progress in Clinical Trials of Photodynamic Therapy for Solid Tumors and the Role of Nanomedicine. Cancers, 2020. 12(10): p. 26.
3. Gunaydin, G., M.E. Gedik, and S. Ayan, Photodynamic Therapy-Current Limitations and Novel Approaches. Frontiers in Chemistry, 2021. 9: p. 25.
4. Desnoyers, A., et al., Integrin alpha nu beta 6 Protein Expression and Prognosis in Solid Tumors: A Meta-Analysis. Molecular Diagnosis & Therapy, 2020. 24(2): p. 143-151.
5. Hausner, S.H., et al., Preclinical Development and First-in-Human Imaging of the Integrin alphavbeta6 with 18F alphavbeta6-Binding Peptide in Metastatic Carcinoma. Clinical cancer research: an official journal of the American Association for Cancer Research, 2019. 25(4): p. 1206-1215.

Oral Presentation

Disclosures: The authors have disclosed no financial interest.

019-Evolution-guided peptide engineering for tumor-targeted extracellular vesicles using a BRET reporter platform

Presenter: Masamitsu Kanada, Michigan State University

Masamitsu Kanada[1], Lauren Linenfelser[1], Kylie Maxton[1], Alexander R. Bricco[2], Assaf Gilad[1]

[1]Michigan State University, East Lansing, MI
[2]Michigan State University, East Lansing

Extracellular vesicle (EV)-mediated transfer of biomolecules plays an essential role in intercellular communication and may improve targeted drug delivery. In the past decade, various approaches to EV surface modification for targeting specific cells or tissues have been proposed, including genetic engineering of parental cells or postproduction EV engineering. However, due to technical limitations, targeting moieties of engineered EVs have not been thoroughly characterized. We developed the bioluminescence resonance energy transfer (BRET) EV reporter, PalmReNL-based dual-reporter platform for characterizing the cellular uptake of tumor homing peptide (THP)-engineered EVs, targeting PDL1, uPAR, or EGFR proteins expressed in MDA-MB-231 breast cancer cells, simultaneously by bioluminescence measurement and fluorescence microscopy [1]. Bioluminescence analysis of cellular EV uptake revealed the highest binding efficiency of uPAR-targeted EVs, whereas PDL1-targeted EVs showed slower cellular uptake. EVs engineered with two previously reported EGFR-binding peptides via lipid nanoprobes did not increase cellular uptake, indicating that designs of EGFR-binding peptide conjugation to the EV surface are critical for functional EV engineering. Fluorescence analysis of cellular EV uptake allowed us to track individual PalmReNL-EVs bearing THPs in recipient cells. These results demonstrate that the PalmReNL-based EV assay platform can be a foundation for high-throughput screening of tumor-targeted EVs. Taking advantage of the BRET EV reporter system, we designed 24 scrambled amino acid sequences derived from the uPAR-binding peptide for EV engineering, followed by assessing their cellular uptake by MDA-MB-231 cells in vitro. Interestingly, two scrambled peptides dramatically improved cellular uptake of engineered EVs relative to the original uPAR-binding peptide (Fig. 1). We use these data sets for evolving peptides with better tumor targeting capacity using a novel computational algorithm called Protein Optimization Evolving Tool (POET), which we recently developed [2]. With further investigation, our research will expand synthetic biology approaches for improving tumor-targeted drug delivery by EVs and other nanocarriers.

References

1. Kanada M, Linenfelser L, Cox E, Gilad AA. A Dual-reporter Platform for Screening Tumor-targeted Extracellular Vesicles. Pharmaceutics, 2022, 14(3), 475.
2. Bricco AR, Miralavykomsari I, Bo S, Perlman O, Farrar CT, McMahon MT, Banzhaf W, Gilad AA. Protein Optimization Evolving Tool (POET) based on Genetic Programming. bioRxiv 2022.03.05.483103; doi: https://doi.org/10.1101/2022.03.05.483103.

Oral Presentation

Disclosures: The authors have disclosed no financial interest.

020-Labelling primary murine hepatocytes with a near-infrared dye facilitates repeat non-invasive in vivo tracking of engraftment and survival in an acute model of liver injury

Presenter: Candice Ashmore-Harris, University of Edinburgh

Candice Ashmore-Harris[1], Victoria Gadd[2], Janet Man[3], Rhona Aird[3], Mark MacMillan[3], Daniel Rodrigo Torres[3], Stuart Forbes[4]

[1]University of Edinburgh, Edinburgh, United Kingdom
[2]The University of Edinburgh, Edinburgh, United Kingdom
[3]The University of Edinburgh, United Kingdom
[4]University of Edinburgh, United Kingdom

Introduction:

To alleviate the reliance on whole organ transplant, cell therapies are increasingly considered as candidates to repair damaged organs and tissues. Primary hepatocyte transplants (HTx) are an established, safe cell therapy for liver disease patients, but graft survival is often transient with patients eventually requiring whole organ transplant. Strategies that improve initial engraftment, and reduce transient graft loss, require robust protocols to enable non-invasive *in vivo* tracking of transplanted cells in real-time. Unfortunately, primary hepatocytes lose their mature phenotype and function *ex vivo,* thus excluding labelling strategies requiring *in vitro* culture. To overcome this challenge we have developed a protocol suitable for labelling freshly isolated primary murine hepatocytes, with a near-infrared (NiR) dye prior to transplant, to facilitate *in vivo* fluorescence imaging.

Methods:

Labelling efficiency and impact on viability were assessed by flow cytometry; with phenotypic and functional capacity assessed *in vitro* by plating capacity (monolayer attachment to collagen-I), and immunostaining for hepatic markers.

We performed HTx in the MDM2 mouse model of liver injury[1,2] to test if the NiR signal from labelled hepatocytes was sufficient to enable *in vivo* fluorescence imaging in situ and whether labelling impacted cell transit to the liver. The widespread hepatocyte senescence and block to hepatocyte replication seen in human liver disease is mimicked by AhCre-mediated loss of Mdm2 expression in the adult mouse liver in this model; resulting in hepatocyte necrosis, apoptosis and senescence, thereby facilitating therapeutic cell engraftment. Freshly isolated TdTomato+ hepatocytes (control HTx), or TdTomato+/NiR labelled hepatocytes were intrasplenically transplanted into MDM2 mice 7 days following injury induction. Mice were NiR imaged post-transplant, with a subset culled for organ imaging *ex vivo* to validate *in vivo* imaging signals (N=2-3 per group), remaining mice were reimaged 4 hours post-transplant, with organs imaged *ex vivo* to validate *in vivo* imaging signals (N=3 per group). The impact of labelling on overall engraftment and survival, and the capacity for repeat imaging, was assessed in a pilot study, with HTx transplanted MDM2 mice repeat imaged post-surgery and 1, 3, 5 and 7 days post-transplant (N=1 control HTx, N=2 NiR labelled HTx).

Immunostaining for transplanted hepatocytes (cells dual stained for Tdtomato and hepatocyte nuclear factor 4α ($Tdtomato^+/HNF4A^+$)) was performed in all collected livers to validate *in vivo* and *ex vivo* imaging results.

Results:

Our protocol efficiently labels hepatocytes (≥95% cells, N=3 independent experiments) with limited impact on viability (87% relative to cells from the same isolation, N=3 independent experiments), phenotype ($HNF4A^+$ cells) or functional capacity. *In vivo* imaging studies demonstrate rapid cell transit from the spleen to the liver post-transplant with NiR fluorescence anatomically associated with the liver and spleen *in vivo* and *ex vivo*. Immunostaining showed no difference in the number of donor cells in the liver between control and NiR labelled HTx mice at 4 hours post-transplant, suggesting NiR labelling does not interfere with cell transit to the liver (n≥15 fields of view quantified per mouse, N=3 mice per group, p>0.05 t-test). *In vivo* imaging also showed retained NiR signal over 7 days in the liver of NiR labelled HTx mice, with immunostaining of explanted livers demonstrating comparable engraftment/survival of $TdTomato^+HNF4A^+$ cells relative to control HTx mice.

Summary:

This study is the first to demonstrate the capacity for NiR fluorescence based tracking of HTx *in vivo*. It offers an accessible and affordable means to facilitate assessment of cell engraftment, whilst retaining cell phenotypic and functional capacity. It offers the potential to be a valuable tool to address wider questions in the liver cell therapy field, such as whether use of different cell administration routes (e.g. intrasplenic vs intraportal) or immunoprotective matrices improve initial cell engraftment.

References

1. Raven, A. et al. Cholangiocytes act as facultative liver stem cells during impaired hepatocyte regeneration. Nature 547, 350–354 (2017).
2. Lu, W. Y. et al. Hepatic progenitor cells of biliary origin with liver repopulation capacity. Nat. Cell Biol. 17, 973–983 (2015).

Oral Presentation

Disclosures: The authors have disclosed no financial interest.

021-A PET imaging approach to develop and study a new therapy for multiple sclerosis (MS)

Presenter: Peter Clark, University of California, Los Angeles

Peter M. Clark[1], Bao Ying Chen[2], Jessica Salas[3]

[1]*University of California, Los Angeles, Los Angeles, CA*
[2]*City of Hope*
[3]*Crump Institute for Molecular Imaging, Los Angeles, CA*

Introduction:

Multiple sclerosis (MS) is a chronic autoimmune disease that affects nearly three million people worldwide[1]. Current MS therapies can be effective but also cause serious side effects and only work in some patients. New treatments for MS and new ways of identifying these treatments are needed. We took the innovative approach of studying a pathway using PET imaging for which there exists a clinically relevant inhibitor and using the knowledge we gained through our PET imaging studies to inform on the use of this inhibitor. Deoxyribonucleoside salvage is a pathway in which cells consume deoxyribonucleosides from extracellular space for intracellular metabolism[2]. Deoxycytidine kinase (dCK) is the rate-limiting enzyme in the deoxyribonucleoside salvage pathway. dCK is required for proper lymphocyte development, and dCK activity is upregulated in the lymph nodes and spleen in mouse models of autoimmune hepatitis and systemic lupus erythematosus[3–5]. Various PET radiotracers including [^{18}F]FAC in mice and [^{18}F]CFA in humans can be used to visualize and quantify deoxyribonucleoside salvage and dCK activity *in vivo*[4,6]. The small molecule TRE-515 is a first-in-class inhibitor of dCK activity currently in Phase I clinical trials for solid tumors.

Hypothesis:

We hypothesized that dCK activity would be upregulated in lymphoid organs in mouse models of MS and that treating these models with TRE-515 would limit disease.

Methods and Results:

We imaged with [^{18}F]FAC PET the MOG_{35-55} progressive experimental autoimmune encephalomyelitis (EAE) and the $PLP_{139-151}$ EAE relapsing-remitting mouse model of MS. In both models, [^{18}F]FAC accumulation was elevated in the lymph nodes but absent in most other organ systems throughout the disease course. *Ex vivo* biodistribution studies confirmed these results. Additional *ex vivo* studies demonstrated that during immune activation in the MOG_{35-55} model, dCK activity was

specifically elevated in T and B lymphocytes. Based on these results, we predicted that targeting dCK would (i) limit symptoms of MS in these models while (ii) causing limited side effects by (iii) significantly affect B and T lymphocytes. We tested these predictions using the dCK inhibitor TRE-515. PET imaging with [^{18}F]FAC confirmed that TRE-515 can block dCK activity in the lymphoid organs of mice. TRE-515 treatments increased plasma levels of the dCK substrate deoxycytidine, suggesting a potential liquid biomarker for drug-target engagement. TRE-515 limited clinical symptoms in both MS mouse models with no observable side effects, demonstrating dCK as a potential new therapeutic target in MS. Mass cytometry (CyTOF) studies of the immune system showed that TRE-515 selectively decreases the levels of activating and proliferation T and B lymphocytes without affecting the levels of other immune cell populations including naïve T and B lymphocytes, regulatory T and B cells, and innate immune cells.

Conclusions:

These studies demonstrate the therapeutic potential of targeting dCK in mouse MS models and do so using a clinically relevant dCK inhibitor. Additionally, our results show (i) that PET can be used to identify new targetable pathways in mouse models of MS and (ii) how the information gained through these PET studies can inform on important aspects of targeting these pathways including potential drug side effects and mechanism-of-action.

References

1. Thompson AJ, et al. Lancet. 2018.
2. Arnér ES, et al. Pharmacol Ther. 1995.
3. Toy G, et al. Proc Natl Acad Sci USA. 2010.
4. Radu CG, et al. Nat Med. 2008.
5. Salas JR, et al. J Nucl Med. 2018.
6. Kim W, et al. Proc Natl Acad Sci USA. 2016.

Oral Presentation

Disclosures: The authors would like to disclose that TRE-515 is an investigational drug.

022-18F-fluciclovine Delineates PSMA-Suppressed Castration Resistant Prostate Cancer

Presenter: Martin Bakht, Dana-Farber Cancer Institute/ Harvard Medical school

Martin Bakht[1], Yasutaka Yamada[2], Sheng-Yu Ku[2], Varadha Balaji Venkadakrishnan[2], Josh Korsen[3], Teja Muralidhar Kalidindi[4], Kei Mizuno[2], Shin Hye G. Ahn[5], Ji-Heui Seo[2], Maria Mica Garcia[2], Francesca Khani[6], Olivier Elemento Elemento[6], Henry Long[2], Matthew Freedman[2], Alain Chaglassian[7], Anthony P. Belanger[2], Quang-De Nguyen[2], NagaVaraKishore Pillarsetty[3], Jason Lewis[3], Himisha Beltran[2]

[1]Dana-Farber Cancer Institute/ Harvard Medical school, Boston, MA
[2]Dana-Farber Cancer Institute, Boston, MA
[3]Memorial Sloan Kettering Cancer Center, New York, NY
[4]Memorial Sloan Kettering Cancer Center, Hastings on Hudson, NY
[5]Dana-Farber Cancer Institute
[6]Weill Cornell Medicine, New York, NY
[7]Blue Earth Diagnostics Inc., Burlington, MA

Prostate-specific membrane antigen (PSMA) has emerged as an important theranostic in castration resistant prostate cancer (CRPC)[1-3]. However, not all patients respond to PSMA-targeted therapy, in part due to heterogeneity or suppression of PSMA[4]. Neuroendocrine prostate cancer (NEPC) is an androgen receptor (AR)-negative subtype of CRPC that arises in up to 20% of patients with CRPC in later stages of their disease as a mechanism of treatment resistance, and is associated with PSMA-suppression[5,6]. Based on an increased understanding of the biology of NEPC, there are several clinical trials testing new drugs for patients with NEPC. Patient selection for these studies will be critical and the development of a noninvasive means to PET-CT imaging of NEPC is an unmet clinical need. ^{18}F-fluciclovine is another PET radiotracer approved in prostate cancer for the detection of hormone naïve recurrent disease, with limited data in the CRPC setting[7,8]. ^{18}F-fluciclovine uptake in tumors is associated with activity of the amino acid transporters such as L-type amino acid transporter1 (LAT1). In this study, we evaluated PSMA regulation across metastatic CRPC lesions and in the context of AR-driven and AR-negative disease. We also used four NEPC patient-derived xenograft (PDX) models and one PSMA-suppressed CRPC model to evaluate if ^{18}F-fluciclovine PET-CT can detect models with low ^{18}F-rh-PSMA. We developed an in vivo orthotopic xenograft model using the AR-positive, PSMA-positive cell line 22Rv1. When orthotopically implanted into the left anterior prostate lobe of a castrated mouse, an AR-positive, PSMA-positive prostate tumor develops. This tumor subsequently metastasizes to various sites, including the development of distinct PSMA-high, PSMA-low, and PSMA-negative liver metastases that are all AR-positive. The PSMA-low tumor was used as a PSMA-suppressed CRPC model. We evaluated transcriptomic concordance between PDXs and corresponding PDX tumors standardized uptake value (SUV) values for ^{18}F-fluciclovine and ^{18}F-rh-PSMA. In PSMA-expressing CRPC patient tumors, as well as a PSMA-positive orthotopic xenograft model of CRPC, we observed lower PSMA expression in liver lesions versus other sites of metastatic disease, suggesting a potential role of the microenvironment in modulating PSMA expression. While PSMA expression in prostate cancer is thought to require the presence of AR, we identified a subset of AR-negative NEPC tumors with high PSMA expression and ^{18}F-rh-PSMA uptake. Irrespective of PSMA level, all NEPC models could be delineated with ^{18}F-fluciclovine PET-CT. The SLC7A5 gene (encoding LAT1) was identified among the most differentially expressed genes in PSMA-suppressed CRPC and confirmed by Western blot and immunohistochemistry. Gene Ontology (GO) enrichment analysis revealed that the elevation of neutral amino acids transporters in 22Rv1 PSMA-suppressed CRPC model is not limited to LAT1. While ^{18}F-rh-PSMA could not delineate 22Rv1 PSMA-suppressed CRPC xenograft models, this model was effectively detectable using ^{18}F-fluciclovine PET-CT.

In summary, we discovered that PSMA-suppressed, AR-negative NEPC and PSMA-suppressed, AR-positive CRPC models may be visualized using ^{18}F-fluciclovine as a result of elevation of amino acid transporters. This study support ^{18}F-fluciclovine PET as a possible alternative imaging modality for both PSMA-low CRPC and NEPC.

References

1. Miyahira, A. K. et al. Meeting report from the Prostate Cancer Foundation PSMA theranostics state of the science meeting. Prostate, doi:10.1002/pros.24056 (2020).
2. Narayan, V. et al. PSMA-targeting TGFβ-insensitive armored CAR T cells in metastatic castration-resistant prostate cancer: a phase 1 trial. Nature Medicine, doi:10.1038/s41591-022-01726-1 (2022).
3. Sartor, O. et al. Lutetium-177–PSMA-617 for Metastatic Castration-Resistant Prostate Cancer. New England Journal of Medicine 385, 1091-1103, doi:10.1056/NEJMoa2107322 (2021).
4. Paschalis, A. et al. Prostate-specific Membrane Antigen Heterogeneity and DNA Repair Defects in Prostate Cancer. Eur Urol 76, 469-478, doi:10.1016/j.eururo.2019.06.030 (2019).

5. Beltran, H. et al. Divergent clonal evolution of castration-resistant neuroendocrine prostate cancer. Nat Med 22, 298-305, doi:10.1038/nm.4045 (2016).
6. Bakht, M. K. et al. Neuroendocrine differentiation of prostate cancer leads to PSMA suppression. Endocrine-related cancer 26, 131-146 (2019).
7. Gusman, M. et al. Review of 18F-fluciclovine PET for detection of recurrent prostate cancer. Radiographics 39, 822-841 (2019).
8. Saarinen, I. et al. Correlation between 18F-1-amino-3-fluorocyclobutane-1-carboxylic acid (18F-fluciclovine) uptake and expression of alanine-serine-cysteine-transporter 2 (ASCT2) and L-type amino acid transporter 1 (LAT1) in primary prostate cancer. EJNMMI Research 9, 50, doi:10.1186/s13550-019-0518-5 (2019).

Oral Presentation

Disclosures: The authors have disclosed no financial interest.

023-Together or apart: Optimising pre-targeting strategies for nanomedicines using molecular imaging

Presenter: Nicholas Fletcher, University of Queensland

Nicholas L. Fletcher[1], Gayathri Ediriweera[2], Kristofer Thurecht[2]

[1]*University of Queensland, Australia*
[2]*University of Queensland*

Introduction:

Nanomedicine therapeutic delivery represents the opportunity for a step-change in cancer treatment. Recent advances highlight the benefits of including targeting ligands such as antibodies within the nanomedicine to enhance retention at, and delivery to, the tumour. However, such approaches are double-edged, with studies showing a higher-degree of ligand functionalization commensurately increases clearance by the mononuclear phagocytic system (MPS), limiting the material available to accumulate at the tumour (1). We propose two approaches to overcome this requirement for a trade-off between targeting and MPS clearance. We demonstrate effective pre-targeting strategies for incorporating biorthogonal chemistries for conventional pre-targeting [A], as well as novel pre-targeting approaches using bispecific antibodies [B]. By temporally separating administration of the targeting ligand from the imaging probe and consequent therapeutic component, these pre-targeting approaches demonstrate enhanced tumour retention with reduced clearance organs accumulation.

Methods:

Nanomedicines in this work are ~10 nm hyperbranched polymers (HBP) which are archetypical soft polyethyleneglycol (PEG)ylated nanoparticles. These are well studied, able to incorporate a variety of functionalities including chemotherapies (2), fluorescence (3) and PET probes (4). Advances in targeting ligand engineering have now produced bispecific antibodies (BsAbs) whereby one portion binds to methoxy PEG (mPEG) epitopes present on synthetic nanomedicines, while the other binds to molecular disease markers of interest (5). In this way noncovalent complexes of nanomedicine HBP core, of primarily mPEG, decorated with targeting ligands are able to be produced.
Herein, a small molecule tetrazine probe [A] or nanomedicine core [B] were labelled with ^{64}Cu or ^{89}Zr respectively. Tumour bearing murine xenograft tumours were then pre-targeted with targeted nanomedicines [A] or BsAb [B] and preclinical PET-CT imaging of labelled materials following their subsequent administration was used to validate each pre-targeting approach.

Results and Discussion:

In the conventional pre-targeting system [A], a rapidly clearing ^{64}Cu-labelled tetrazine probe was produced which is reactive towards transcyclooctene (tCO) functionalized nanomedicines. This undergoes a rapid Inverse electron demand Diels-Alder reaction to both release doxorubicin and retain the imaging probe in a theranostic system. By first administering BsAb targeted HBP which accumulated at the tumour site, ^{64}Cu-probe retention and consequent drug release could then be specifically triggered within the tumour and imaged using ^{64}Cu-PET. In an MCF7 xenograft model, this demonstrated almost 2-fold higher tumour:spleen ratio compared to a control unreactive system. Conversely, if a pre-targeting approach was not used, liver and spleen uptake of the complex was greatly enhanced. This tetrazine-tCO biorthogonal click reaction approach combines both enhanced tumour accumulation of the probe with selectively triggered and quantifiable therapeutic release in a true theranostic approach.
While BsAB targeting of HBPs is efficacious, coating of "stealthy" polymeric materials with proteinaceous targeting ligands not only improves interactions with target cancer cells, but also enhances unwanted MPS clearance. The second pre-targeting system [B] focuses on overcoming this dichotomy by combining the stealthy carrier and targeting components in situ. In this novel pre-targeting approach using bispecific antibodies, mice were pre-administered targeting anti-EGFR BsAb in an MDA-MB-468 xenograft model. The time between pre-targeting and administration of ^{89}Zr-labelled HBP was then varied to optimize the pre-targeting approach. This resulted in retaining effective tumour retention while also halving the accumulation in MPS clearance organs such as the liver and spleen, 4-fold increasing the tumour:liver ratio.

Conclusions:

These imaging results demonstrate two pathways to overcome one of the key shortcomings in current nanomedicine targeting. By utilising either biorthogonal chemistries for conventional pre-targeting [A] or novel bispecific antibody pre-targeting [B], we are able to modulate targeting and clearance of administered nanomaterials. Such control over not just nanomaterial synthesis but subsequent interactions and therapeutic delivery will be key in the next generation of materials.

References

1. Sivaram, A. J.; Wardiana, A.; Alcantara, S.; et al., Controlling the Biological Fate of Micellar Nanoparticles: Balancing Stealth and Targeting. ACS Nano 2020, 14 (10), 13739-13753.
2. Zhao, Y.; Fletcher, N. L.; Gemmell, A.; et al., Investigation of the Therapeutic Potential of a Synergistic Delivery System through Dual Controlled Release of Camptothecin–Doxorubicin. Advanced Therapeutics 2020, 1900202
3. Pearce, A. K.; Simpson, J. D.; Fletcher, N. L.; et al., Localised delivery of doxorubicin to prostate cancer cells through a PSMA-targeted hyperbranched polymer theranostic. Biomaterials 2017, 141, 330-339. Humphries, J.; Pizzi, D.; Sonderegger, S. E.; et al., Hyperbranched Poly(2-oxazoline)s and Poly(ethylene glycol): A Structure–Activity Comparison of Biodistribution. Biomacromolecules 2020, 21 (8), 3318-3331.
4. Fletcher, N.; Houston, Z.; Simpson, J.; Veedu, R.; Thurecht, K., Designed multifunctional polymeric nanomedicines: long-term biodistribution and tumour accumulation of aptamer-targeted nanomaterials. Chemical Communications 2018, 54 (82), 11538-11541.
5. Howard, C. B.; Fletcher, N.; Houston, Z. H.; et al., Overcoming Instability of Antibody-Nanomaterial Conjugates: Next Generation Targeted Nanomedicines Using Bispecific Antibodies. Advanced Healthcare Materials 2016, 5 (16), 2055-2068.

Oral Presentation

Disclosures: The authors have disclosed no financial interest.

024-The Chicken Chorioallantoic Membrane (CAM) as a Low-Cost, High-Throughput Model for PET Radiotracer Development.

Presenter: Lydia Smith, King's College London

Lydia Smith[1], Hannah Greenwood[2], Will Tyrrell[2], Richard Edwards[3], Friedrich Baark[3], George Firth[3], Muhammet Tanc[2], Richard Southworth[3], Anne Herrmann[4], Timothy H. Witney[3]

[1] *King's College London, London, United Kingdom*
[2] *King's College London, School of Imaging Sciences and Biomedical Engeneering, London, United Kingdom*
[3] *King's College London, London, London, United Kingdom*
[4] *University of Liverpool, Liverpool, United Kingdom*

Introduction:

Novel PET radiotracer development for cancer imaging follows a well-defined path, using widely available cell and murine models. *In vitro* models are useful for preliminary evaluation but provide limited insight into clinical translatability. Animal models overcome these limitations; however, mice are expensive, low throughput, require large holding spaces and are restricted by extensive ethical regulation[1]. Therefore, lower cost, higher throughput animal models of cancer are desirable. One potential alternative is the chicken chorioallantoic membrane (CAM) [1], which enables growth of xenografted tumours on the highly-vascularised membrane inside chicken eggs (**Fig.1a**). This model is amenable for imaging applications as tumours develop on the CAM within seven days, while cost savings of up to 25-fold can be achieved compared to murine models, supporting higher-powered experimental design[2]. Moreover, using an evolutionary lower species reduces ethical concerns and makes the model available to all[2]. Here, we describe the use of the chick CAM for PET radiotracer development, assess [^{18}F]FDG pharmacokinetics in *in ovo* tumours, and evaluate chick CAM tumour redox status with [^{18}F]FSPG[3].

Methods:

Following published methods for *in ovo* tumour engraftment[4], multiple inoculation methods using physical or chemical supports were tested to optimise NCI-H460 Fluc lung cancer tumour growth. Eggs were maintained at 37°C and 48% humidity throughout. On embryonic day 3 (E3), a window was cut in the shell to access the CAM. On E7, the CAM was inoculated with 3×10^6 NCI-H460 Fluc cells and allowed to grow until E14, when tumour-bearing eggs were imaged by BLI (IVIS Spectrum, PerkinElmer). Tumours were subsequently excised and weighed prior to *ex ovo* analysis. Separately, dynamic [^{18}F]FDG PET/CT (Mediso nanoScan; 1-5 coincidence mode; 3D reconstruction; CT attenuation corrected; scatter corrected) was performed following an i.v. injection of ~3 MBq to derive time activity curves (TAC) for tumour-bearing eggs. Mice bearing 100 mm^3 subcutaneous NCI-H460 Fluc tumours were also imaged with [^{18}F]FDG PET/CT under the same protocol for comparison. Finally, dynamic [^{18}F]FSPG PET imaging was performed using eggs bearing NCI-H460 Fluc tumours (~3 MBq). Following imaging, tumours were snap-frozen and protein expression assessed by western blotting.

Results:

NCI-H460 Fluc cells implanted with matrigel created reproducible tumours which were similar in size to those used for conventional small animal imaging (**Fig.1b**), as confirmed by BLI (**Fig.1c**). Following i.v. administration, [^{18}F]FDG PET imaging showed high radiotracer uptake in the CAM-grown tumour and a tumour-to-albumin ratio of 14.7 (**Fig. 1d**). [^{18}F]FDG tumour uptake followed a similar pattern both *in ovo* and *in vivo*, with rapid delivery in the first 5 min proceeding a slower rate of uptake over the remaining 55 min. [^{18}F]FDG tumour uptake was higher in the CAM tumours at 10.0 ± 2.1 %ID/g compared to 6.0 ± 1.4 %ID/g in mice at 60 min p.i. (**Fig. 1f**). Area under the TACs showed comparable uptake in the brains of both mice and the chick (**Fig. 1f**). [^{18}F]FSPG PET imaging of NCI-H460 Fluc tumours, which provides a measure of system x_c^- activity (**Fig. 1g**), showed high but variable uptake in NCI-H460 Fluc tumours (14.0 ± 5.5 %ID/g at 60 min p.i.; **Fig. 1h&i**). This variability may be accounted for by altered transporter expression in these tumours (**Fig. 1j**).

Conclusions:

Here, we have shown it possible to reproducibly cultivate *in ovo* tumours for imaging using matrigel as a matrix just seven days after implantation. Chick CAM tumours were avid for both [^{18}F]FDG and [^{18}F]FSPG, providing high signal-to-background ratios. This work supports the case for the use of the chick CAM as a more sustainable, low-cost substitute to tumour xenograft mouse models and has the potential to expedite novel radiotracer development.

References

1. Warnock, G., Turtoi, A., Blomme, A., Bretin, F., Bahri, M. A., Lemaire, C., & Plenevaux, A. R. (2013). In vivo PET/CT in a human glioblastoma chicken chorioallantoic membrane model: a new tool for oncology and radiotracer development. Journal of Nuclear Medicine, 54(10), 1782-1788.
2. Haller S, Ametamey SM, Schibli R, Müller C. Investigation of the chick embryo as a potential alternative to the mouse for evaluation of radiopharmaceuticals. Nucl Med Biol. 2015; 42(3):226-33.
3. McCormick PN, Greenwood HE, Glaser M, et al. Assessment of Tumor Redox Status through (S)-4-(3-[18F]fluoropropyl)-L-Glutamic Acid PET Imaging of System xc- Activity. Cancer Res. 2019;79(4):853-863.
4. Herrmann A, Moss D, Sée V. The Chorioallantoic Membrane of the Chick Embryo to Assess Tumor Formation and Metastasis. Methods Mol Biol. 2016;1464:97-105

Oral Presentation

Disclosures: The authors have disclosed no financial interest.

025-Antibody fragment-based theranostics targeting prostate stem cell antigen (PSCA): using 89Zr-immunoPET to guide the development of 177Lu-radioimmunotherapy

Presenter: Kirstin Zettlitz, City of Hope

Kirstin A. Zettlitz[1], Felix Salazar[1], Jennifer Chean[1], Deirdre La Placa[1], Saad Ahmed[2], Vikram Adhikarla[2], Bao Ying Chen[2], Sunidhi Jaiswal[1], Tove Olafsen[3], Anna M. Wu[1]

[1] *City of Hope, Duarte, CA*
[2] *City of Hope*
[3] *City of Hope, Duarte*

Targeted radioimmunotherapy (RIT) aims to deliver a cytotoxic radiation dose to the tumors while reducing the absorbed dose to normal tissues (therapeutic index). The long half-life of full length antibodies results in the highest tumor uptake, but can also cause hematological

toxicities. Smaller antibody fragments show better tumor penetration and shorter plasma half-lives but renal clearance can cause dose-limiting nephrotoxicity. We have re-engineered an antibody fragment (A2 scFv-Fc2 double mutant, A2DM) with optimized pharmacokinetics to improve the therapeutic index for RIT of prostate stem cell antigen (PSCA) expressing tumors (e.g. cancers of the prostate, pancreas or bladder). The scFv-Fc fusion protein (110 kDa) clears through the hepatobiliary route and spares the more radiosensitive kidneys. Point mutations introduced to disrupt FcRn binding result in rapid clearance from the blood, thereby reducing the absorbed dose to the bone marrow. In this study, we use surrogate 89Zr-immunoPET to profile pharmacokinetics and for initial dose estimation and compare to the subsequent full biodistribution study using the therapeutic compound 177Lu-DTPA-A2DM in nude mice bearing prostate cancer xenografts. Based on these results we conducted a preliminary radioimmunotherapy study with a single dose of 177Lu-DTPA-A2DM. METHODS A2DM conjugation with p-SCN-Bn-CHX-A”-DTPA was optimized to yield a chelate-to-antibody ratio of 0.7 and confirmed by SEC and LC/MS. Chelation of [177Lu]LuCl3 (labeling efficiency: 99.4%, n=7) resulted in high specific activity (45.34 ± 1.7 µCi/µg). For biodistribution studies, mice (Nu/J, 22Rv1-PSCA) were injected with 10 µCi/10 µg and groups of 4-5 mice were analyzed (10 min - 96 h p.i.). Tumors and tissues were weighed, gamma counted and the %ID/g calculated based on decay-corrected standards. For a preliminary therapy study tumor bearing mice (tumor size ~40 mm3) were injected with a single dose (500 µCi/11.5 µg, n=7) of 177Lu-DTPA-A2DM, the control group (n=12) did not receive treatment. Mice were monitored for tumor volume and toxicity (body weight). RESULTS 89Zr-DFO-A2DM immunoPET and ex vivo biodistribution studies in prostate cancer models (Nu/J mice with subcutaneous 22Rv1-PSCA xenografts and hPSCA knock-in mice with syngeneic RM9-PSCA tumors) confirmed rapid hepatic clearance (t1/2 ~12 h) and specific uptake in PSCA-positive tumors, resulting in high tumor-to-blood ratios (25-30 at 96 h p.i.). Dose estimates based on the 89Zr-DFO-A2DM biodistribution predicted the liver to be dose-limiting with a maximum tolerated dose (MTD) of approximately 460 µCi for the respective 177Lu-DTPA-A2DM. Full biodistribution of 177Lu-DTPA-A2DM showed tumor uptake peaking around 20 h p.i. (10.6 ± 1.1 %ID/g) and rapid clearance resulted in a tumor-to-blood ratio of 36.8 at 92 h p.i., similar to the biodistribution of 89Zr-DFO-A2DM. The tissue with the highest 177Lu-DTPA-A2DM uptake was the liver, reaching around 20% ID/g at 8 h p.i. and retaining that activity until starting to slowly decrease at 44 h p.i. The preliminary radioimmunotherapy study showed significantly slowed tumor growth in mice that received a single dose of 177Lu-DTPA-A2DM (day 0-1: ns; day 2-4: p≤0.002; day 5-7: p≤0.0002; day 8-17: p≤0.0001). No toxicity or body weight loss was observed during the study. Future RIT studies will include dose escalation/de-escalation and control groups. Surrogate 89Zr-immunoPET profiled the pharmacokinetics, biodistribution and tumor targeting of the novel anti-PSCA antibody fragment and correctly predicted the liver as the dose limiting organ. The A2 scFv-Fc2 DM was successfully conjugated with DTPA and radiolabeled with 177Lu at high specific activities suitable for RIT. Biodistribution studies using 177Lu-DTPA-A2DM showed similar pharmacokinetics and tumor targeting as 89Zr-DFO-A2DM, confirming that 89Zr is an adequate surrogate/companion diagnostic to guide 177Lu-RIT. Radioimmunotherapy with a single dose (500 µCi) of of 177Lu-DTPA-A2DM showed tumor growth inhibition compared with untreated mice. In conclusion, 177Lu-DTPA-A2DM could provide an improved therapeutic index for RIT of PSCA-positive prostate and pancreatic cancer.

Oral Presentation

Disclosures: The authors have disclosed no financial interest.

026-Multifunctional PAMAM dendrimer-drug conjugates for management of prostate cancer

Presenter: Wojciech Lesniak, Johns Hopkins University School of Medicine

Wojciech Lesniak[1], Gabriela Lofland[2], Srikanth Boinapally[3], Anna Jablonska[4], Babak Behnam Azad[1], Mauro Garcia[5], Martin Pomper[3]
[1]*Johns Hopkins University School of Medicine, Baltimore, MD*
[2]*Johns Hopkins University School of Medicine*
[3]*Johns Hopkins Univeristy, Baltimore, MD*
[4]*University of Maryland*
[5]*Johns Hopkins Univeristy*

Background:

Prostate-specific membrane antigen (PSMA) is a useful biomarker for management of prostate cancer (PC). In the context of PC, PSMA has been leveraged for diagnosis, radiopharmaceutical therapy and targeted drug delivery by antibody-drug conjugates and poly-lactic acid-polyethylene glycol (PLA-PEG)-based nanoparticles. Poly(amidoamine) [PAMAM] dendrimers serve as versatile nanoplatforms that can be tailored to different sizes and compositions depending on the application. Lesniak et al. demonstrated that generation-4 PAMAM dendrimers conjugated with a low-molecular-weight (LMW) PSMA-targeted agent, lysine-glutamate-urea (KEU), have suitable pharmacokinetics for targeting of PSMA-expressing tumors with imaging or therapeutic agents.[1] More recently, PSMA-targeted dendrimers conjugated with multiple near-infrared dyes were shown to enable detection of PSMA expression with optical and photoacoustic imaging.[2] Here, we present development of multifunctional PSMA-targeted dendrimer-drug conjugates (PT-DDCs) and their evaluation in an experimental model of PC.

Methods:

The PT-DDCs were synthetized through consecutive conjugation of maytansine (DM1, a highly potent antimitotic agent commonly used for formulation of antibody-drug conjugates[3]), Cy5 for optical evaluation, NOTA for radiolabeling with ^{64}Cu for PET-CT imaging or ^{67}Cu for endoradiotherapy and KEU moieties with generation-4 PAMAM dendrimers. The remaining terminal primary amines were capped with butane-1,2-diol to minimize non-specific *in vivo* uptake and toxicity of resulting PT-DDCs. The design of PT-DDCs enables comprehensive evaluation of their *in vivo* properties using optical and nuclear imaging. Non-targeted control dendrimer-drug conjugates (Ctrl-DDC) were formulated without conjugation of KEU. Physicochemical properties of all DDCs were assessed using high performance liquid chromatography, matrix assisted laser desorption ionization mass spectrometry and dynamic light scattering. PT-DDCs were evaluated using isogenic human prostate cancer PSMA$^+$ PC3 PIP and PSMA$^-$ PC3 flu cell lines *in vitro* and in mice bearing the corresponding xenografts.

Results:

PT-DDCs showed high *in vitro* uptake by PSMA$^+$ PC3 PIP cells that could be blocked by ZJ-43 LMW, a potent PSMA inhibitor.[4] PT-DDCs also showed concentration dependent accumulation and cytotoxicity in PSMA$^+$ PC3 PIP cells with K_D of 203 ± 25 nM (95% CI 151 - 254 nM) and IC_{50} of 4.57 nM (95% CI 2.48 - 128.4 nM). PT-DDCs did not accumulate in PSMA$^-$ PC3 flu cells and showed higher IC_{50} of 89.9 (95% CI 43.5 - 185.8 nM) against this cell line. Ctrl-DDC did not accumulate in either of cell lines and provided higher IC_{50} values of 338.8 nM (95% CI 59.5 - 1,924 nM) for PSMA$^+$ PC3 PIP cells and 84.6 nM (95% CI 37.7 - 189.7 nM) for PSMA$^-$ PC3 flu cells. Evaluation of stability indicated that PT-DDCs did not release DM1 in PBS and human blood plasma during 24 h incubation at 37°C and required addition of

glutathione, an intracellular reducing agent. Therapy studies indicated selective accumulation of PT-DDCs in PSMA+ PC3 PIP tumors, as confirmed by non-invasive optical imaging, and dose-dependent tumor growth inhibition (TGI), reaching 82.62 ± 8.25 % for 10 mg/kg dose. We did not detect either accumulation of PT-DDCs in PSMA- PC3 flu tumors or therapeutic response in mice treated with a 10 mg/kg dose. Positron emission tomography/computed tomography (PET/CT) studies in mice bearing PSMA+ PC3 PIP and PSMA- PC3 flu tumors confirmed *in vivo* specificity of PT-DDCs and its potential for concurrent DM1 and radionuclide delivery to PSMA+ tumors.

Future plans:

PT-DDCs will be pursued further *in vivo* in relevant PSMA-expressing tumor model systems for theranostic applications.

References

1. Lesniak, W. G.; Boinapally, S.; Banerjee, S. R.; Behnam Azad, B.; Foss, C. A.; Shen, C.; Lisok, A.; Wharram, B.; Nimmagadda, S.; Pomper, M. G. Mol Pharm (2019), doi: 10.1021/acs.molpharmaceut.9b00181
2. Lesniak, W.G., Wu Y., Kang, J., Boinapally, S., Banerjee, S.R., Lisok, A., Jablonska, A., Boctor, E.M., Pomper, MG. Nanoscale (2021) doi: 10.1039/d1nr00669
3. Rinnerthaler, G.; Gampenrieder, S.P.; Greil, R. HER2 Directed Antibody-Drug-Conjugates beyond T-DM1 in Breast Cancer. (2019) DOI: 10.3390/ijms20051115
4. Yamamoto, T. et al., Antinociceptive effects of N-acetylaspartylglutamate (NAAG) peptidase inhibitors ZJ-11, ZJ-17 and ZJ-43 in the rat formalin test and in the rat neuropathic pain modelEur. J. Neurosci., (2004) doi: 10.1111/j.1460-9568.2004.03504.x.

Oral Presentation

Disclosures: The authors have disclosed no financial interest.

027-Targeted Molecular Imaging of Bacterial Lung Infections via Copper-64 labeled Pyochelin Siderophore

Presenter: Alec Ventrola, University of Cincinnati

Alec Ventrola[1], Nalinikanth Kotagiri[2], Nabil Siddiqui[2]

[1]*University of Cincinnati, Cincinnati*
[2]*University of Cincinnati, Cincinnati, Ohio*

There is a lack of clinically available PET probes able to accurately visualize, differentiate, and monitor bacterial lung infections. One of the most widely available PET probes, fluorinated glucose (18FDG), is unable to differentiate mammalian cells from bacterial cells in vivo. Distinct metabolic pathways involving the transportation of metals into the bacterial cell can be utilized to differentiate between bacterial and mammalian cells within the lungs. Bacterial cells produce high affinity metal chelators called siderophores to transport metals from the extracellular environment into the cell via highly specific protein receptors. For example, *Pseudomonas aeruginosa* produces a high affinity metal chelator called pyochelin (Pch) to transport Fe (III) through the fptA receptor and into the cell. We hypothesized that ^{64}Cu-labeled Pch can be imported intracellularly in bacterial cells expressing the fptA receptor to allow for targeted PET imaging. To evaluate this process, high performance liquid chromatography was performed using ^{64}Cu-Pch to measure purity and stability. The presence of two peaks at >95% purity at pH 7 and 37°C (Figure 1A) indicated acceptable probe conditions, and the siderophore pyochelin exists as diastereomers. For *in vitro* stability studies, we incubated the ^{64}Cu-Pch probe in mouse serum for 0, 0.5, 1, 6, and 24 hours and confirmed the presence of at least 91% of intact ^{64}Cu-Pch 24 hours after the initial incubation (Figure 1B). We first administered ^{64}Cu-Pch retro-orbitally into mice infected with a mucoid and non-mucoid variant of *Pseudomonas aeruginosa*, *Klebsiella pneumoniae, E. coli* Nissle wild-type, *E. coli* UTI89, or *Staphylococcus aureus* (Figure 1, C-I). There were significantly higher PET signals from the lungs in the fptA expressing *P. aeruginosa* mice compared to the non-fptA expressing bacteria. Cooperatively, there was a significant difference between the lung biodistribution of *Pseudomonas aeruginosa* non-mucoid and all other bacteria tested (Figure 1, J). We then administered ^{64}Cu-Pch retro-orbitally into mice infected with mucoid *P. aeruginosa* to investigate whether ^{64}Cu-Pch probe can be used to monitor antibiotic treatment. Treated groups were given two oral doses of ciprofloxacin compared to the untreated groups of mice. Mice that received mucoid *P. aeruginosa* showed a significant difference in biodistribution in the lungs between the untreated and treated.

References

1. Hayen, Heiko, and Dietrich A. Volmer. "Different Iron-Chelating Properties of Pyochelin Diastereomers Revealed by LC/MS." Analytical and Bioanalytical Chemistry, vol. 385, no. 3, 2006, pp. 606-611., https://doi.org/10.1007/s00216-006-0443-0.
2. Braud, Armelle, et al. "The Pseudomonas aeruginosa Pyochelin-Iron Uptake Pathway and Its Metal Specificity." Journal of Bacteriology, vol. 191, no. 11, 2009, pp. 3517-3525., https://doi.org/10.1128/jb.00010-09.

Oral Presentation

Disclosures: The authors would like to disclose that the Cu-64 PcH Probe is an investigational device.

028-Zr-89-Labeled pH-Responsive Ultrasmall Gold Nanoclusters for Cancer Diagnosis and Radiosensitization Therapy

Presenter: Yifei Jiang, Shanghai Jiao Tong University

Yifei Jiang[1], Qinghe Wu[2], Chunfu Zhang[2]

[1]*Shanghai Jiao Tong University, China*
[2]*Shanghai Jiao Tong University, Shanghai, Shanghai, China*

Introduction:

Ultrasmall gold nanoclusters show great potentials as the carriers of radionuclides due to their effective renal clearance[1]. However, low tumor targeting efficiency caused by too rapid clearance still hampers its use for tumor theranostics[2]. In this study, we synthesized ^{89}Zr-labeled, GSH and L-Cysteine-coated ultrasmall gold nanoclusters (^{89}Zr-GSH/ L-Cysteine@AuNCs), which has swiftly pH-responsive aggregation property and is renal clearable. Since acidic tumor microenvironment is the universal hallmark of solid tumors[3], ^{89}Zr-GSH/ L-Cysteine@AuNCs could highly accumulate in the tumor sites with long-term retention. As a result, ^{89}Zr labeled ultrasmall gold nanoclusters showed precise diagnosis of tumors. Meanwhile, due to the high atomic number of Au, ^{89}Zr-GSH/ L-Cysteine@AuNCs was further employed as the nanosensitizer for tumor radiation therapy (RT).

Materials and methods:

^{89}Zr-GSH/ L-Cysteine@AuNCs was prepared by by a co-reduction of $HAuCl_4$ by GSH and L-Cysteine in the presence of $^{89}ZrCl_3$. The sizes,

morphologies and pH-responsive ability were examined in vitro. The tumor targeting ability of the probe was evaluated by PET/CT imaging and its biodistribution was assessed by using region of interest (ROI) functions (Inveon Research Workplace software) to quantify its retention in different organs. Tumor radiotherapy (8 Gy) was performed 24 h after the tumor-bearing mice were intravenously injected with ^{89}Zr-GSH/ L-Cysteine@AuNCs (10 mg Au/kg b. w.).

Results and discussion:

GSH/ L-Cysteine@AuNCs was ultrasmall in neutral condition (PBS, pH=7.4), while agglomerated into large aggregations in acidic condition (PBS, pH=6.5). The protonation of carboxylic acid groups in GSH and L-Cysteine caused the surface charge dropped from -32.9 mv (pH=7.4) to -2.7 mv (pH=6.5), which resulted in pH-induced aggregation under acidic conditions. ^{89}Zr could be effectively and stably doped into the AuNCs with relatively high radiolabeling efficiency (> 80%). PET/CT imaging of tumors within six days demonstrated that ^{89}Zr-GSH/ L-Cysteine@AuNCs could efficiently accumulate in tumors and retain for long term. Meanwhile, in contrast to the traditional large-sized nanoparticles, ^{89}Zr-GSH/ L-Cysteine@AuNCs with ultrasmall sizes was eliminated primarily by the kidney and no accumulations were found in the liver and spleen.
The tumors treated with ^{89}Zr-GSH/ L-Cysteine@AuNCs and RT were also significantly inhibited compared to the control group, primarily due to radiosensitization of ultrasmall AuNCs. Tumor cells in ^{89}Zr-GSH/ L-Cysteine@AuNCs + X-ray therapy groups were extensively apoptotic, as demonstrated by TUNEL staining. Moreover, no abnormity of major organs was found post-treatment, implying the high biocompatibility of our nanoprobes.

Conclusion:

^{89}Zr-GSH/ L-Cysteine@AuNCs with sensitive pH-responsibility could highly efficiently accumulate in the tumor sites with long-term retention and be effectively cleared by kidney, showing the great potential as carriers of radionuclides for enhanced tumor diagnosis and therapeutic effect of radiation.

References

1. Yu M, Xu J, Zheng J. Renal clearable luminescent gold nanoparticles: from the bench to the clinic[J]. Angewandte Chemie International Edition, 2019, 58(13): 4112-4128.
2. Zhang X D, Luo Z, Chen J, et al. Ultrasmall Au10−12 (SG)10−12 nanomolecules for high tumor specificity and cancer radiotherapy[J]. Advanced Materials, 2014, 26(26): 4565-4568.
3. Kato Y, Ozawa S, Miyamoto C, et al. Acidic extracellular microenvironment and cancer[J]. Cancer Cell International, 2013, 13(1): 1-8.

Oral Presentation

Disclosures: The authors have disclosed no financial interest.

029-A deep learning approach for real-time intraoperative detection of peripheral nerves

Presenter: Alex Ngai Nick Wong, Hong Kong Polytechnic University

Alex Ngai Nick Wong[1], ZeBang He[2], Minfeng YANG[3], Jung Sun Yoo[4]

[1]*Hong Kong Polytechnic University, Hung hom, Hong Kong*
[2]*Hong Kong Polytechnic University, Hong Kong, Hong Kong*
[3]*Hong Kong Polytechnic University*
[4]*Hong Kong Polytechnic University, Hung Hom, Kowloon, Hong Kong SAR*

Nerve preservation is vital for surgical treatment to reduce postoperative adverse effect. Real-time visualization of nerves with high specificity is indispensable to guide surgeon to avoid accidental nerve transection. A label-free imaging strategy using optical reflectance [1] was recently developed to provide accurate and safe intraoperative guidance for detecting peripheral nerves. However, wavelength-specific strong reflectance signal is often observed not only in nerve tissues but also in similar layered structures such as tendon tissues. To address this issue and increase nerve imaging specificity, we applied artificial intelligence techniques for classification and segmentation of surgical reflectance images to highlight nerve tissues with pseudo-color in real-time. Here, we provide a multi-task deep learning-based nerve imaging technique for accurate real-time nerve delineation via neural network training based on representative surgical video data.

METHOD

Intraoperative reflectance nerve imaging was performed using Nikon SMZ18 stereomicroscope with customized reflectance filter for specific nerve illumination (450±20nm). Nerve surgery video was captured through the entire operation of dissection of sciatic nerve using xenograft model of murine breast cancer with 4T1 cell line. The whole process of surgery was recorded using 17 mice and the video data were saved with 17.39-18.39 fps. After collecting the mice dissection surgery video data, total 11,113 video frames were extracted with time interval of 600 ms and labelled manually into different categories, i.e., general field, tendon, and nerve for various surgical actions. For annotation of the nerve segments, each image from "nerve" class was manually labelled and prepared as ground truth mask using the online annotation service "Supervisely." To design the multi-task pipeline deep learning model, we first fine-tuned DenseNET201 deep learning model [2] for "nerve" category image recognition. Then, fine-tuning of DoubleUNet model [3] was performed for pseudo-colored nerve delineation from the previously recognized "nerve" category images. The classification performance was evaluated based on Matthews Correlation Coefficient (MCC) and Area Under Curve (AUC). The segmentation performance was evaluated based on Intersection over Union (IoU) and Dice Similarity Coefficient (DSC). The image processing time of our proposed multi-task pipeline was also provided to evaluate its actual performance for real time surgical guidance. The student's t-test was used for all the comparisons in different models for "nerve" category recognition and nerve delineation. All the statistics were assumed two-sided and a P-value less than 0.05 was considered statistically significant.

RESULTS

DenseNET201 showed high confidence for recognizing "nerve" category images and depicted MCC of 0.8312 and AUC of 0.9654. DoubleUNet demonstrated excellent performance for nerve delineation with IoU of 0.8312 and DSC of 0.965. Leveraging our proposed multi-task pipeline, fast image processing speed (~14.7 fps) was achieved proving genuine capability for real-time intraoperative guidance in detecting peripheral nerves in operating room.

CONCLUSIONS

The developed multi-task deep learning-based nerve imaging technique enables highly specific nerve visualization in real-time during surgery. Representative surgical video recording provided sufficient features and patterns for effective model training of the proposed multi-task pipeline without any extensive data preparation. The presented multi-task pipeline consists of two steps, classification and segmentation which make nerve delineation robust and reproducible due to prior elimination of non-nerve images before segmentation process. Such design was also crucial to achieve real time functionality. Reflectance nerve imaging equipped with deep learning could facilitate imaging-guided surgery in clinics and empower better patient outcome.

References

1. Ntziachristos, V., J.S. Yoo, and G.M. van Dam, Current concepts and future perspectives on surgical optical imaging in cancer. J Biomed Opt, 2010. 15(6): p. 066024.
2. Huang, G., Liu, Z., Van Der Maaten, L., & Weinberger, K. Q, Densely connected convolutional networks. In Proceedings of the IEEE conference on computer vision and pattern recognition, 2017: p. pp. 4700-4708.
3. Jha, D., Riegler, M. A., Johansen, D., Halvorsen, P., & Johansen, H. D., Doubleu-net: A deep convolutional neural network for medical image segmentation. 2020 IEEE 33rd International Symposium on Computer-Based Medical Systems, 2020: p. pp. 558-564.

Oral Presentation

Disclosures: The authors have disclosed no financial interest.

030-Combined HP 13C Pyruvate and 13C-Glucose Fluxomic as a Potential Marker of Response to Targeted Therapies in YUMM1.7 Melanoma Xenografts

Presenter: Chantale Farah, Catholic University of Louvain, Belgium

Chantale Farah

Catholic University of Louvain, Belgium, Woluwe saint lambert, Brussels, Belgium

A vast majority of BRAF V600E mutated melanoma patients will develop resistance to combined BRAF/MEK inhibition after initial clinical response. Resistance to targeted therapy is described to be accompanied by specific metabolic changes in melanoma. The aim of this work was to evaluate metabolic imaging using ^{13}C-MRS (Magnetic Resonance Spectroscopy) as a marker of response to BRAF/MEK inhibition in a syngeneic melanoma model. Tumor growth was significantly delayed in mice bearing YUMM1.7 melanoma xenografts treated with the BRAF inhibitor vemurafenib, and/or with the MEK inhibitor trametinib, in comparison with the control group. ^{13}C-MRS was performed in vivo after injection of hyperpolarized (HP) ^{13}C-pyruvate, at baseline and 24 h after treatment, to evaluate dynamic changes in pyruvate-lactate exchange. Furthermore, ex vivo ^{13}C-MRS steady state metabolic tracing experiments were performed after U-^{13}C-glucose or 5-^{13}C-glutamine injection, 24 h after treatment. The HP ^{13}C-lactate-to-pyruvate ratio was not modified in response to BRAF/MEK inhibition, whereas the production of ^{13}C-lactate from ^{13}C-glucose was significantly reduced 24 h after treatment with vemurafenib, trametinib, or with the combined inhibitors. Conversely, ^{13}C-glutamine metabolism was not modified in response to BRAF/MEK inhibition. In conclusion, we identified ^{13}C-glucose fluxomic as a potential marker of response to BRAF/MEK inhibition in YUMM1.7 melanoma xenografts. Besides targeted therapy, immunotherapy with immune checkpoint inhibitors have become a standard therapy for melanoma, the aim of the ongoing work is to evaluate metabolic imaging as a marker of response to immune checkpoint blockade (anti-PD1) in another melanoma model sensitive to immunotherapy (YUMMER1.7).The in vivo experiments are still ongoing.

References

1. Farah, C.; Neveu, M.-A.; Yelek, C.; Bouzin, C.; Gallez, B.; Baurain, J.-F.; Mignion, L.; Jordan, B.F. Combined HP 13C Pyruvate and 13C-Glucose Fluxomic as a Potential Marker of Response to Targeted Therapies in YUMM1.7 Melanoma Xenografts. Biomedicines 2022, 10, 717. https://doi.org/10.3390/biomedicines10030717
2. Acciardo, S.; Mignion, L.; Lacomblez, E.; Schoonjans, C.; Joudiou, N.; Gourgue, F.; Bouzin, C.; Baurain, J.-F.; Gallez, B.; Jordan, B.F. Metabolic Imaging Using Hyperpolarized 13 C-Pyruvate to Assess Sensitivity to the B-Raf Inhibitor Vemurafenib in Melanoma Cells and Xenografts. J. Cell. Mol. Med. 2020, 24, 1934–1944.

Oral Presentation

Disclosures: The authors have disclosed no financial interest.

031-PET/MR Imaging of a Lung Metastasis Model of Clear Cell Renal Cell Carcinoma with (2S,4R)-4-[18F]Fluoroglutamine

Presenter: Niki Zacharias Millward, MD Anderson Cancer Center

Niki Zacharias Millward[1], Alyssa Pollard[2], Vincenzo Paolillo[3], Bhasker Radaram[4], Sarah Qureshy[4], Li Li[3], Tapati Maity[3], Lei Wang[3], Md. N. Uddin[3], Jose Karam[3], Marty Pagel[5], David Piwnica-Worms[6], Steven W. Millward[3], Natalie Wall Fowlkes[3], William Norton[3], Brian Engel[3], Federica Pisaneschi[7]

[1]*MD Anderson Cancer Center, Houston*
[2]*MD Anderson Cancer Center, Smithtown, NY*
[3]*University of Texas MD Anderson Cancer Center, Houston, TX*
[4]*GlaxoSmithKline, Collegeville, PA*
[5]*MD Anderson Cancer Center, Houston, TX*
[6]*University of Texas MD Anderson Cancer Center, Houston, Texas*
[7]*University of Texas MD Anderson Cancer Center, Houston*

Purpose:

Kidney cancer is one of the 10 most common cancers in the United States, and approximately 90% of kidney malignancies are diagnosed as renal cell carcinoma (RCC) [1]. Clear cell renal cell carcinoma (ccRCC) is the most common RCC subtype (≈ 70%). Even after nephrectomy, distant ccRCC metastases occur frequently, with the lungs being the most common site. ccRCC has recurrence rates of up to 30% with the highest risk of recurrence occurring within the first 3 years following surgery. However, RCC metastases have been found up to 37 years after surgical resection [2]. Metabolic reprogramming plays an important role in the tumorigenesis of ccRCC. Currently, positron emission tomography (PET) reporters are not used clinically to visualize altered glutamine metabolism in ccRCC, which greatly hinders detection, staging, and real-time therapeutic assessment. We sought to determine if (2S,4R)-4-[18F]fluoroglutamine ([18F]FGln) could be used to interrogate altered glutamine metabolism in ccRCC lesions in the lung.

Procedures:

We generated a novel ccRCC lung lesion model using the ccRCC cell line UMRC3 stably transfected with GFP and luciferase constructs. This cell line was used for characterization of [18F]FGln uptake and retention by transport analysis in cell culture and by PET/MRI (magnetic resonance imaging) in animal models. Lung tumors were generated by injecting 3 million UMRC3 cells expressing luciferase and GFP into the lower left lung of nude mice [3,4]. Tumor growth in animal models was monitored using bioluminescence (BLI) and MRI. After necropsy, UMRC3 tumor growth in lung tissue was verified by fluorescence imaging and histology.

Results:

In UMRC3 cells, [18F]FGln cell uptake was 2-fold higher than cell uptake in normal kidney HEK293 cells. Tracer cell uptake was reduced by 60-90% in the presence of excess glutamine in the media and by 20-50% upon treatment with V-9302, an inhibitor of the major glutamine transporter alanine-serine-cysteine transporter 2 (ASCT2). Furthermore, in UMRC3 cells, [18F]FGln cell uptake was reduced by siRNA knockdown of ASCT2 to levels obtained by the addition of excess exogenous glutamine. Conversely, [18F]FGln cellular uptake was increased in the presence of the glutaminase inhibitor CB-839. In our ccRCC lung animal model, we observed an engraftment rate ranging from 50 to 87 % for different cohorts, and BLI was observed five days post-injection and remained constant or increased for all animals over the 1-2 month imaging duration. Using simultaneous PET/MRI for visualization, retention of [18F]FGln in vivo in ccRCC lung tumors was 1.5-fold greater than normal lung tissue and 2-fold greater than muscle. In ccRCC lung tumors, [18F]FGln retention did not change significantly upon treatment with CB-839.

Conclusions:

We report one of the first direct orthotopic mouse models of ccRCC lung lesions. Using PET/MR imaging, lung tumors were easily discerned from normal tissue. Higher uptake of [18F]FGln was observed in a ccRCC cell line and lung lesions compared to HEK293 cells and normal lung tissue, respectively. [18F]FGln cell uptake was modulated by exogenous glutamine, V-9302, siRNA knockdown of ASCT2, and CB-839. Interestingly, in a pilot therapeutic study with CB-839, we observed no difference in treated tumors relative to untreated controls. This was in contrast to cellular studies, where CB-839 increased glutamine uptake.

References

1. Hsieh JJ et al. (2017) Renal cell carcinoma. Nat Rev Dis Primers 17009.
2. Tamburrini A et al. (2017) A record-breaking lung metastasis from renal cell carcinoma 37 years after nephrectomy. J Surg Case Rep 10: rjx205.
3. Onn A et al. (2003) Development of an orthotopic model to study the biology and therapy of primary human lung cancer in nude mice. Clin Cancer Res 15: 5532-5539.
4. Wilson AN et al. (2022) A method for orthotopic transplantation of lung cancer in mice. Methods Mol Biol 231-242.

Oral Presentation

Disclosures: The authors have disclosed no financial interest.

032-Engineered nanomaterials with enhanced splenic retention for the cardiac immune modulation

Presenter: Jason McCarthy, Masonic Medical research institute

Jagathesh Chandra Bose Rajendran[1], **Jason McCarthy[2]**, Chase W. Kessinger[3], Tajinder Dhammu[4], Toolika Singh[4], Sebastian Himbert[5], Fernando J. Garcia-Marques[6], Natalia Oleinik[4], Maria I Kontaridis,[2], Maikel Rheinstadter[5], Besim Ogretmen[4], Donald Menick[4], Bing Xu[2], Khanh Ha[7]

[1]Masonic Medical research institute, NEW HARTFORD, NY
[2]Masonic Medical research institute, Utica, NY
[3]Masonic Medical Research Institute, Utica, New York
[4]Medical University of South Carolina, Charleston, SC
[5]McMaster University, Hamilton,ON, ON
[6]Stanford University, Palo Alto, CA
[7]Massachusetts General Hospital, Boston, Massachusetts

The spleen is an important mediator of both adaptive and innate immunity. As such, attempts to modulate the immune response provided by this organ may be conducive to improved outcomes for numerous diseases throughout the body. Bioinspired nanomaterials, based upon a senescent erythrocyte mimicking strategy, thus have the potential to enhance the retention of drugs within the spleen. Fluorescent polymeric nanomaterials were generated encapsulating the histone deacetylase inhibitor suberoylanilide hydroxamic acid (SAHA) featuring a coating material derived from engineered red blood cell (RBC) membranes, isolated through a controlled freeze-thaw process and modified with phosphatidyl serine lipids to give engineered senescent erythrocyte-like nanotheranostics (eSENTs). Extensive physical (dynamic light scattering, transmission electron microscopy) and biophysical characterization of these particles (Lipidomics, proteomics, and molecular simulations) confirmed that our synthetic strategy provided nanosized (116 nm) materials featuring an 11.5 nm thick surface lipid layer, while in vitro experimentation demonstrated that the nanoparticle surface mimicked that of a senescent RBC. In vivo in naive animals, the materials demonstrated significantly enhanced retention within the spleen, as compared to the non-coated control particles. This behavior translated to therapeutic efficacy in the murine model of myocardial infarction, with the coated particles demonstrating a significant reduction in infarct size (14% at 72-hours post-myocardial infarction). Importantly, using both flow cytometric and fluorescent microscopic analysis, the trafficking of the splenic cells to the heart was obviated, providing a potential mechanism for the efficacy of the generated therapeutic.

References

1. Engineered Cell-Derived Vesicles Displaying Targeting Peptide and Functionalized with Nanocarriers for Therapeutic microRNA Delivery to Triple-Negative Breast Cancer in Mice (Adv. Healthcare Mater. 5/2022)
2. A Microfluidics-Based Scalable Approach to Generate Extracellular Vesicles with Enhanced Therapeutic MicroRNA Loading for Intranasal Delivery to Mouse Glioblastomas
3. Reconstructed Apoptotic Bodies as Targeted "Nano Decoys" to Treat Intracellular Bacterial Infections within Macrophages and Cancer Cells

Oral Presentation

Disclosures: The authors have disclosed no financial interest.

033-HER2- endoradiotherapy combined with statins reverses drug resistance in esophagogastric cancers

Presenter: Yi Rao, Memorial Sloan Kettering Cancer Center

Yi Rao[1], Zachary Samuels[2], Lukas Carter[2], Patricia M. Ribeiro Pereira[3], Jason Lewis[2]

[1]Memorial Sloan Kettering Cancer Center, New York
[2]Memorial Sloan Kettering Cancer Center, New York, NY
[3]Washington University in St. Louis

In 2020, more than 1,000,000 new cases of esophagogastric (EG) cancer were diagnosed and 769,000 deaths worldwide[1]. Although HER2-targeting trastuzumab is commonly used in HER2+ EG cancer patients,

intrinsic and acquired trastuzumab resistances inevitably develop over time. Lovastatin, a cholesterol-lowering drug, is reported to elevate cell surface HER2[2]. Hence, we hypothesize that the combination of statin and [^{177}Lu]Lu-DOTA-trastuzumab endoradiotherapy would improve the therapeutic efficacy in low HER2 patients and overcoming trastuzumab resistance. First, to evaluate the impact of pharmacological modulation of membrane HER2, we performed biodistribution studies of [^{177}Lu]Lu-DOTA-trastuzumab with or without lovastatin pre-treatment in mice with HER2+ EG patient-derived esophagogastric (EG) xenografts (PDXs). The PDXs used in our studies were obtained from esophagogastric patients that demonstrated clinical resistance to trastuzumab. We found that tumor uptake of [^{177}Lu]Lu-DOTA-trastuzumab was increased by ~ 48% in lovastatin pre-treated cohort compared to the saline control (Fig. 1a), which closely matching previous NCI-N87 tumor model. Hence, 28 Mbq [^{177}Lu]Lu-DOTA-trastuzumab (the previous determined optimal dose) was used in the PDXs therapeutic study. Furthermore, to evaluate the efficacy of [^{177}Lu]Lu-DOTA-trastuzumab therapy combined with statin, we performed radioimmunotherapies in mice bearing HER2-positive gastric PDXs (n = 9-10 mice/cohort). Mice treated with either a single dose of 50mg trastuzumab (median survival = 17 days) or 50mg trastuzumab combined with 4.15mg/kg lovastatin (median survival = 19.5 days) showed the fasted tumor growths and poorest overall survival compared to [^{177}Lu]Lu-DOTA-trastuzumab treated cohorts (Fig. 1b-d). Furthermore, more than 50% mice from [^{177}Lu]Lu-DOTA-IgG isotype control cohort experienced severe petechiae and lethargy, which were indicators of severe radiotoxicity within 3 weeks after endoradiotherapy (Fig. 1c). In addition, tumor growths inhibitions were observed in both [^{177}Lu]Lu-DOTA-trastuzumab treated cohorts, wherein the combination of [^{177}Lu]Lu-DOTA-trastuzumab and lovastatin cohort demonstrated sustained tumor growth inhibition and remarkably prolonged survival amongst all cohorts (Fig. 1b-d). In contrast, tumor growths of [^{177}Lu]Lu-DOTA-trastuzumab monotherapy cohort exhibited initial suppression, but eventually relapsed 40 days post treatment (Fig. 1b), suggesting that the statin treatment rendered more durable [^{177}Lu]Lu-DOTA-trastuzumab responses in HE2+ EG PDXs.

References

1. Bray, F., et al. Global cancer statistics 2018: GLOBOCAN estimates of incidence and mortality worldwide for 36 cancers in 185 countries. CA Cancer J Clin 68, 394-424 (2018).
2. Pereira, P.M.R., et al. Caveolin-1 mediates cellular distribution of HER2 and affects trastuzumab binding and therapeutic efficacy. Nat Commun 9, 5137 (2018).

Oral Presentation

Disclosures: The authors have disclosed no financial interest.

034-Quantitative T2 mapping as a biomarker of neuropathology resulting from acute organophosphate intoxication in a rat model

Presenter: Alita D Almeida, University of California, Davis

Alita J. D Almeida[1], Brad A. Hobson[2], Valerie A. Porter[2], Joel R. Garbow[3], Pamela J. Lein[4], Abhijit J. Chaudhari[2]

[1]University of California, Davis
[2]University of California, Davis, Sacramento, CA
[3]Washington University School of Medicine, Saint Louis, MO
[4]University of California, Davis School of Veterinary Medicine, Davis, CA, California

Introduction: Organophosphate (OP) nerve agents and pesticides represent a major public health issue and are of significant concern as chemical warfare agents [1]. Acute intoxication with OPs trigger both peripheral and central cholinergic effects that underlie life threatening seizures and long-term neurologic consequences [2],[3]. Therefore, quantitative metrics for assessing the spatiotemporal progression and resolution of OP-induced injury across multiple brain regions are needed to evaluate neuroprotective therapies. The pathology observed following acute OP intoxication includes neuronal necrosis, neuroinflammation, edema, blood brain barrier dysfunction, and hemorrhage, all of which impact magnetic resonance imaging (MRI) T_2 (spin-spin) relaxation time constants [4]. Therefore, direct quantification of T_2 relaxation time (termed T_2-mapping) may provide valuable information regarding the spatiotemporal effects of OP intoxication and therapies on different pools of hydrogen nuclei found in the brain, mainly in myelin, intra/extracellular water, and cerebrospinal fluid. We tested the hypothesis that brain T_2 maps of OP-intoxicated rats can quantitatively detect neuropathology, and thus, provide biomarkers to evaluate the effectiveness of therapeutics for attenuating OP-induced neuropathology.

Methods:

Adult Sprague Dawley rats were imaged at days 3, 7 and 28 post-OP (diisopropylfluorophosphate, DFP)-intoxication. Three therapies were investigated: midazolam (a benzodiazepine anticonvulsant; MDZ, n=29), allopregnanolone (a neurosteroid; ALO, n=28), and the combination of MDZ and ALO (DUO, n=28). Untreated DFP-exposed animals (DFP, n=32) and vehicle controls (VEH, n=13) were also imaged. The data was acquired on a 7T MRI scanner using a rat brain phased array coil and a spin-echo pulse sequence with 15 echo times (TEs). To generate T_2 values, a mono-exponential curve fit using the equation: $\mathbf{y = a*exp(-x/b)}$ was performed from MRIs at various TEs, such that 'x' was the TE, 'y' was the signal intensity, 'b' was the sought T_2 relaxation time and 'a' was a constant representing signal gain or attenuation by the scanner and proton density [5]. The hippocampus (H) and piriform cortex (PC) were manually delineated as regions-of-interest (ROIs) given their known significance as targets of acute OP intoxication. Curve fitting was carried out with MATLAB using 2 approaches: (1) Voxel-wise quantification: curve fitting was performed on intensity-TE curves for each voxel, providing a voxel-wise map of T_2 values; and (2) Regional quantification: Voxel intensity values in each ROI were averaged at each TE and a curve fit was performed to estimate a T_2 value for each ROI.

Results:

For both quantification methods, the T_2 values in VEH were within the range reported in the literature [4],[6]. OP-intoxicated rats had longer T_2 values (voxel-wise- H: 57.23 ms, PC: 71.21 ms and regional- H: 57.4 ms, PC: 59.09 ms) compared to the averaged treatment groups (voxel-wise- H: 54.02 ms, PC: 62.37 ms and regional- H: 54.5 ms, PC: 55.44 ms) and vehicles (voxel-wise- H: 53.8 ms, PC: 57.86 ms and regional- H: 54.3 ms, PC: 55.24 ms). T_2 values were longest on day 3 and decreased with time. Treatment administration resulted in a reduction in T_2 values compared to the DFP group ($p<0.05$). The pattern of distribution of T_2 values was relatively uniform in regions across days and groups. The voxel-wise quantification method showed a larger variation in T_2 values within ROIs than the regional quantification method, suggestive of intra-regional heterogeneity of neuronal damage that was consistent with visible lesions on T_2-weighted images.

Conclusion:

This study demonstrates the potential of T_2 mapping as a quantifiable biomarker to track neuropathology resulting from OP-intoxication over time and to assess the impact of therapies. Future work will involve validation of these methods against measures from other modalities

(histology, diffusion MRI) and evaluation in studies assessing spatiotemporal response to novel therapies to mitigate OP-induced neuronal damage.

References

1. R. A. Young and A. Watson, "Organophosphate nerve agents," in Handbook of Toxicology of Chemical Warfare Agents, Elsevier, 2020.
2. M. Guignet et al., "Persistent behavior deficits, neuroinflammation, and oxidative stress in a rat model of acute organophosphate intoxication," Neurobiology of Disease, vol. 133. Academic Press Inc., p. 104431, Jan. 01, 2020, doi: 10.1016/j.nbd.2019.03.019.
3. S. Sisó et al., "Spatiotemporal progression and remission of lesions in the rat brain following acute intoxication with diisopropylfluorophosphate," Toxicol. Sci., vol. 157, no. 2, pp. 330–341, Jun. 2017, doi: 10.1093/toxsci/kfx048.
4. S. Liachenko and J. Ramu, "Quantification and reproducibility assessment of the regional brain T 2 relaxation in naïve rats at 7T," J. Magn. Reson. Imaging, vol. 45, no. 3, pp. 700–709, Mar. 2017, doi: 10.1002/jmri.25378.
5. S. Liachenko, J. Ramu, T. Konak, M. G. Paule, and J. Hanig, "Quantitative Assessment of MRI T 2 Response to Kainic Acid Neurotoxicity in Rats in vivo," Toxicol. Sci., vol. 146, no. 1, pp. 183–191, Jul. 2015, doi: 10.1093/toxsci/kfv083.
6. K. Lee et al., "Quantitative T2 MRI is predictive of neurodegeneration following organophosphate exposure in a rat model," Sci. Rep., vol. 10, no. 1, Dec. 2020, doi: 10.1038/s41598-020-69991-z.

Oral Presentation

Disclosures: The authors have disclosed no financial interest.

035-Detection of Residual Peritoneal Metastases following Cytoreductive Surgery Using the pH-sensitive Micellar Imaging Agent Pegsitacianine: An Interim Review of an Ongoing Phase 2 Study

Presenter: Patrick Wagner, Allegheny Health Network Cancer Institute

Patrick Wagner[1], Edward Levine[2], Alex Kim[3], Perry Shen[4], Nicole D. Fleming[5], Shannon N. Westin[6], Madeline Olson[7], Brian Madajewski[8], Brian Ostrander[9], Kartik Krishnan[7], Baran D. Sumer[10], Tian Zhao[11], Jinming Gao[12], David Bartlett[13]

[1]Allegheny Health Network Cancer Institute, Pittsburgh, PA
[2]Wake Forest University, Winston-Salem, North Carolina
[3]Ohio State University Wexner Medical Center, Columbus
[4]Wake Forest University, Winston Salem, NC
[5]University of Texas MD Anderson Cancer Center, Houston, TX
[6]UT MD Anderson Cancer Center, Houston, TX
[7]OncoNano Medicine Inc, Southlake, TX
[8]OncoNano Medicine Inc, Southlake
[9]OncoNano Medicine Inc, Southlake, Texas
[10]University of Texas Southwestern Medical Center, Dallas, TX
[11]OncoNano Medicine Inc, Dallas
[12]University of Texas Southwestern Medical Center, Dallas, Texas
[13]Allegheny Health Network, Pittsburgh, PA

Background:

Pegsitacianine (ONM-100) is an ultra pH-sensitive polymeric micellar fluorescent nanoprobe designed to aid in the real-time localization and detection of tumor in the surgical setting using near-infrared (NIR) imaging. Pegsitacianine is comprised of pH-sensitive amphiphilic polymers with the NIR dye, indocyanine green, covalently attached to the hydrophobic segment. At physiological pH, pegsitacianine circulates as intact micelles in a fluorescently "OFF" state. Tumor accumulation of the micelles lead to dissociation and activation of fluorescence by the acidic tumor microenvironment (i.e., Warburg effect). Acidic microenvironments are ubiquitous in most solid tumors and provide pegsitacianine the potential to function in an agnostic manner, with all imaging systems FDA-cleared for use with indocyanine green. Previously studied in six tumor types at intravenous doses ranging from 0.1 – 1.2 mg/kg administered 24 hours prior to surgery, pegsitacianine has been well tolerated, fluoresced in all tested tumor types, detected positive surgical margins, and demonstrated favorable sensitivity and specificity measurements. The current Phase 2 study (NCT04950166) is designed to evaluate the ability of pegsitacianine to detect residual tumors following cytoreductive surgery (CRS), an operation to completely resect peritoneal metastatases from GI caners. The completeness of cytoreduction is scored at the conclusion of surgery and is a key indicator of the efficacy of surgery and long-term prognosis. Methods for detecting residual disease following intended surgery could allow surgeons to more accurately evaluate the completeness of surgery, or even enhance the results by removing additional tumors.

Methods:

The ongoing Phase 2 study is a non-randomized, open-label, multicenter study being conducted in the United States. The study is planned to be conducted in two Parts. Part 1 is designed to investigate the ability of pegsitacianine to detect solid peritoneal metastases (i.e., <=50% mucin) and Part 2 is designed to investigate the ability of pegsitacianine to detect mucinous lesions (i.e., >50% mucin). The primary performance metric of pegsitacianine is the rate of detection of residual disease following intended CRS. A total of ten (10) suspected tumor lesions and five (5) normal tissue samples will be imaged for fluorescence during CRS. After completion of intended surgery, the peritoneal cavity will be re-examined using the NIR camera to evaluate for residual fluorescent tissue. Removal of residual tumor indicates a clinically significant event, and correlation of fluorescence with final pathology results will be used to calculate the performance of pegsitacianine.

Results:

A total of 13 patients have been administered pegsitacianine at a dose of 1 mg/kg with imaging occurring between 24- and 72-hours post-dose. Pegsitacianine has been well-tolerated in all dosed patients with no drug-related SAEs. To date, seven patients (53.8%) have demonstrated a clinically significant event. All clinically significant events have been a result of the detection of residual disease following the completion of intended surgery with an augmentation to the completeness of cytoreduction score occurring in one patient (15.3%) Pegsitacianine performance calculated at the level of the individual specimens has demonstrated favorable sensitivity (89%) negative predictive (81%) and positive predictive (68%) values, as well as a low patient-level false positive rate (23%).

Conclusions:

Pegsitacianine exploits the ubiquitous acidic microenvironment of solid tumors to function as a tumor-agnostic adjunct to CRS for peritoneal carcinomatosis, which can arise from a wide variety of primary tumor types. In this ongoing study, pegsitacianine continues to be well-tolerated with no observed drug-related SAEs, and has detected residual disease that otherwise would have been unresected, following CRS in 53.8% of evaluable patients. With a high rate of residual disease detection and it's promising performance, pegsitacianine holds great potential to enhance the efficacy of CRS by detecting residual tumors, leading to improvement in surgical efficacy and patient outcomes.

Oral Presentation

Disclosures: The authors would like to disclose that the drug Pegsitacianine is an investigational drug.

036-Combining HP-MRS and PET Imaging to interrogate Prostate Cancer Metabolism

Presenter: Prasanta Dutta, MD Anderson Cancer Center

Prasanta Dutta[1], José Enriquez[2], Jenny Han[1], Peter Shepherd[1], Nora Navone[3], Christopher Logothetis[2], Daniel Frigo[2], Mark Titus[2], Federica Pisaneschi[4], Pratip Bhattacharya[2]

[1]*MD Anderson Cancer Center, Houston, TX*
[2]*University of Texas MD Anderson Cancer Center, Houston, TX*
[3]*MD Anderson Cancer Center, Houston, Texas*
[4]*University of Texas MD Anderson Cancer Center, Houston*

Background:

There is an unmet clinical need for robust imaging biomarkers to distinguish indolent from aggressive prostate cancer (PCa). It is growing recognition that dysregulated cell metabolism as a key driver for PCa progression and resistance to therapy. Androgen receptor (AR) signaling regulated by androgen ligands is one of the critical pathways for PCa pathogenesis, aggressiveness and progression. Comprehensive metabolic imaging and metabolomics study were performed on Androgen Receptor dependent (AR+) and AR independent (AR-) patient derived xenograft (PDX) tumors by employing [1-^{13}C]-pyruvate hyperpolarized magnetic resonance spectroscopy (HP-MRS), [^{18}F]-fluorodeoxyglucose positron emission tomography (FDG-PET), [^{18}F]-fluoro-pivalic acid positron emission tomography (FPIA-PET), ^{1}H Nuclear Magnetic Resonance (NMR) spectroscopy and **liquid chromatography with tandem mass spectrometry (LC-MS-MS)** to interrogate PCa dysregulated metabolism.

Methods:

[1-^{13}C]-labeled pyruvic acid was hyperpolarized using a commercial DNP HyperSense polarizer following standard protocol (1). Anatomical MRI and ^{13}C-MRS were obtained using a Bruker 7T scanner. The high-resolution ^{1}H-NMR spectroscopy were performed on a 500 MHz spectrometer coupled with cryogenic temperature probe. PET images were acquired on an Albira trimodal PET/SPECT/CT image station (2).

Results:

AR (+/-) PCa-PDX tumors those are sensitive and resistance to enzalutamide were employed in this *in vivo*metabolic imaging study. The dynamic metabolic flux ratio, lactate-to-pyruvate (Lac/Pyr) was determined *in vivo* and used as a treatment response marker. The Lac/Pyr ratios were significantly higher in resistant tumors compared to sensitive tumors ($p<0.01$) as shown in Figure (A-C). A significant difference in [^{18}F]-FDG uptake between these two cohorts of AR (+/-) mice was also observed. PET imaging revealed that [^{18}F]-FPIA is transported into the tumors (Figure D). FPIA interrogated the fatty acid oxidation in tumor cells and we are currently exploring how its uptake varies between AR (+/-) PCa-PDX tumors. *Ex vivo* NMR and mass spectrometry-based metabolomics depicted higher lactate concentration in drug resistant tumors.

Conclusion:

Metabolic imaging combining [1-^{13}C]-pyruvate HP-MRS and [^{18}F]-PET presents an exciting opportunity to realize imaging-based personalized medicine in different AR (+/-) PCa-PDX preclinical models by interrogating glycolysis and fatty acid oxidation pathways.

References

1. Zacharias N et al. Androgen Receptor Signaling in Castration-Resistant Prostate Cancer Alters Hyperpolarized Pyruvate to Lactate Conversion and Lactate Levels In Vivo. Mol Imaging Biol. 2019;21(1):86-94.
2. Witney TH et al. Preclinical evaluation of 3-18F-fluoro-2,2-dimethylpropionic acid as an imaging agent for tumor detection. J Nucl Med. 2014;55(9):1506-12.

Oral Presentation

Disclosures: The authors have disclosed no financial interest.

037-Molecular magnetic resonance imaging (MRI) of myeloperoxidase activity to identify plaques prone to rupture in a rabbit model of atherothrombosis

Presenter: Xiaoying Wang, King's College London, School of Imaging Sciences and Biomedical Engeneering

Xiaoying Wang[1], Prakash Saha[2], Mohammed Chowdhury[3], Gastao Lima da Cruz[4], Carlos Velasco Jimeno[4], Sergey Tumanov[5], Claudia Prieto Vasquez[4], René M. Botnar[6], Roland Stocker[5], Alkystis Phinikaridou[7]

[1]*King's College London, School of Imaging Sciences and Biomedical Engeneering, United Kingdom*
[2]*King's College London, London, United Kingdom*
[3]*University of Cambridge, Cambridge, United Kingdom*
[4]*King's College London, School of Imaging Sciences and Biomedical Engeneering, London, United Kingdom*
[5]*The Heart Research Institute, Newtown, Australia*
[6]*King's College London, London, Please select an option below, United Kingdom*
[7]*King's College London, London, -None-, United Kingdom*

Introduction:

Disruption of unstable atherosclerotic plaque with subsequent thrombosis is primarily responsible for acute cardiovascular events [1]. Detecting unstable plaque with clinical imaging modalities and stabilising the plaques at risk is crucial for reducing plaque rupture-related mortality. The activity of myeloperoxidase (MPO), a pro-inflammatory enzyme expressed in advanced human plaques [2], has been shown to contribute to the formation of unstable plaque and to be suitable for detecting unstable plaque by molecular MRI in a mouse model of plaque instability [3]. Here, we investigated whether molecular MRI of MPO activity could identify plaques prone to rupture in a rabbit model of atherothrombosis.

Methods:

Aortic atherosclerosis was induced in male New Zealand White rabbits (n=10) with aortic balloon injury and dietary modification including 8 weeks of 1% cholesterol-containing chow followed by 4 weeks of normal chow. *In-vivo*T1-weighted black blood (T1BB), inversion recovery (IR), and T1 mapping images were acquired with a 3-Tesla MRI scanner at 8 and 12 weeks using *bis*-5-hydroxytryptamide-DTPA-Gd (MPO-Gd, 0.1mmol/kg) to assess plaque MPO activity 1-2 h after injection. Following the 12-week MRI scan, Russell viper venom and

histamine were administered to trigger plaque erosion/rupture [4] and rabbits were scanned post-trigger without contrast agent to identify thrombi. Vessel wall area (VWA, cm^2), late gadolinium enhancement (LGE) area (mm^2), mean signal intensity (SI), and relaxation rate (R1, s^{-1}) were quantified. Tissue-to-muscle contrast ratio (TMCR) was calculated as: $TMCR=(SI_{Aortic\ Wall} - SI_{Muscle})/SI_{Muscle}$

Results/Discussion:

All rabbits developed atherosclerosis and four advanced to atherothrombosis. Imaged aortic segments (n=196) were classified as plaque-free (n=77) or plaque-containing (n=119) by comparing the vessel wall area to healthy age-matched controls on pre-trigger T1BB images (**Fig.1a**). Plaques were then separated into stable (n=98) and rupture-prone (n=21) based on the presence of thrombus on the post-trigger T1BB images (**Fig.1d**). Compared with plaque-free aorta, segments containing plaques showed higher enhancement and R1s after MPO-Gd injection, suggesting higher MPO activity (**Fig.1b-c**).

Quantitative MRI analysis (**Fig. 1e**) showed similar VWA and LGE area in stable and rupture-prone plaques at weeks 8 and 12. However, rupture-prone plaques had significantly higher TMCR than stable plaques and plaque-free segments at both weeks 8 and 12, while no TMCR difference was observed between the stable and plaque-free groups. Moreover, rupture-prone plaques had significantly higher R1 values compared with stable plaques at both time points. Both ruptured and stable plaques had higher R1 values compared with plaque-free tissue.

Conclusion:

The data showed that MPO activity could be detected *in-vivo* with a clinical MRI scanner using MPO-Gd. Rupture-prone plaques tend to accumulate more MPO-Gd, suggesting a relationship between local MPO activity and atherothrombosis. Thus, clinical MRI using a molecular probe that selectively quantifies MPO activity is a very promising tool to identify high-risk plaques, and guide treatment to reduce the risk of acute cardiovascular events.

References

1. Falk, E., P.K. Shah, and V. Fuster, Coronary plaque disruption. Circulation, 1995. 92(3): p. 657-71.
2. Teng, N., et al., The roles of myeloperoxidase in coronary artery disease and its potential implication in plaque rupture. Redox Rep, 2017. 22(2): p. 51-73.
3. Rashid, I., et al., Myeloperoxidase is a potential molecular imaging and therapeutic target for the identification and stabilization of high-risk atherosclerotic plaque. Eur Heart J, 2018. 39(35): p. 3301-3310.
4. Phinikaridou, A., et al., A robust rabbit model of human atherosclerosis and atherothrombosis. J Lipid Res, 2009. 50(5): p. 787-97.

Oral Presentation

Disclosures: The authors have disclosed no financial interest.

038-A highly efficient Myeloperoxidase-activatable MRI probe (heMAMP) revealed D-mannose treatment effects in experimental stroke

Presenter: Negin Jalali Motlagh, Massachusetts General Hospital

Negin Jalali Motlagh[1], Hyung-Hwan Kim[2], Cuihua Wang[1], Gregory R. Wojtkiewicz[2], John W. Chen[2]

[1]*Massachusetts General Hospital, Charlestown, MA*
[2]*Massachusetts General Hospital, Boston, MA*

Purpose:

Stroke is a major human disease burden that can lead to death or life-long disability. Inflammation and oxidative stress are two critical pathological processes in stroke. Myeloperoxidase (MPO) is an important oxidative inflammatory enzyme that plays important roles in promoting tissue damage and affecting adverse neurological outcome. Unlike other simple sugars, D-mannose has been shown to have unique immune regulatory functions. We aimed to determine the effect of D-mannose on myeloperoxidase (MPO) in a stroke mouse model using molecular MRI targeting myeloperoxidase activity.

Methods:

All animal experiments were approved by the local subcommittee on research animal care. Focal cerebral ischemia was induced by transiently occluding the right middle cerebral artery for 30 minutes followed by reperfusion in twenty 8-10 weeks old C57BL/6J male mice. On the day of surgery, mice were randomly divided into two treatment groups: 1) D-mannose (450mg/kg) injected i.p. daily and 2) PBS i.p. daily as control. To evaluate MPO activity *in vivo*, mice were imaged on a 4.7T MRI scanner on day 10 after stroke induction. T1-weighted imaging was performed before and after the intravenous injection of 0.1mmol/kg of heMAMP[1], a new generation of MPO-specific MRI agents. Contrast-to-noise-ratio (CNRs) were computed for each region of interest (ROI) with the formula: CNR (postcontrast $ROI_{ischemic\ brain}-$ postcontrast $ROI_{contralateral\ brain})/SD_{noise}-$ (precontrast $ROI_{ischemic\ brain}-$ precontrast $ROI_{contralateral\ brain})/SD_{noise},$ where $ROI_{ischemic\ brain}$ is enhancing area and SD_{noise} is the standard deviation of noise measured from an ROI placed in an empty area of the image. Flow cytometry and MPO protein assays were also performed after imaging. $P<0.05$ was considered statistically significant.

Results:

D-mannose treatment improved neurological deficit scores compared to those treated with PBS. D-mannose decreased heMAMP MRI enhancement in the infarcted area (Figure A, p=0.0027). This result was corroborated by *ex vivo* MPO protein assays of the ischemic brains (p=0.04). Interestingly, on flow cytometry, the percentage of MPO-positive cells was not different between the two groups (p=0.48). Taken together, our data revealed that D-mannose treatment in stroke did not change the number of pro-inflammatory cells recruited to the inflammation site, but each of these cells generated less active MPO.

Conclusion:

Molecular imaging with heMAMP MRI revealed that D-mannose treatment in stroke improved neurological outcome by decreasing the amount of active MPO secreted from inflammatory leukocytes at the infarcted site, even as the number of MPO-positive cells was not significantly altered by D-mannose treatment. The highly efficient MPO-activatable MRI probe (heMAMP), which is significantly more stable than the previous linear MPO-Gd agent and up to 3-fold more sensitive to MPO activity, allowed highly sensitive differentiation between the treatment groups and played an important role in elucidating these observations. These findings suggest that D-mannose may be a potential new therapeutic direction for the treatment of ischemic stroke.

References

1. Wang, C.; Cheng, D.; Jalali Motlagh, N.; Kuellenberg, E. G.; Wojtkiewicz, G. R.; Schmidt, S. P.; Stocker, R.; Chen, J. W., Highly Efficient Activatable MRI Probe to Sense Myeloperoxidase Activity. J Med Chem 2021, 64 (9), 5874-5885.

Oral Presentation

Disclosures: The authors would like to disclose that D-mannose (MRI Gadolinium imaging agent), PF-2999, and 18F-MAPP are investigational devices.

039-18F-Labeled PET radiotracer for imaging CSF1R

Presenter: Deepankar Das, Johns Hopkins University School of Medicine

Deepankar Das[1], Ravi Naik[2], IL Minn[3], Yong Du[3], Wojciech Lesniak[1], Paige Finley[2], Daniel H. Holt[4], Robert F. Dannals[4], Martin Pomper[3], Andrew Horti[3]

[1]*Johns Hopkins University School of Medicine, Baltimore, MD*
[2]*Johns Hopkins Univeristy, Baltimore, Maryland*
[3]*Johns Hopkins Univeristy, Baltimore, MD*
[4]*Johns Hopkins University School of Medicine, Baltimore, Maryland*

In the past PET imaging of neuroinflammation mainly used radiotracers that targeted the translocator protein (TSPO). Recently, researchers have developed PET radiotracers targeting other cellular receptors relevant to neuroinflammation[1] including microphage colony stimulating factor 1 receptor (CSF1R)[2-6]. Here we present a new ^{18}F-labelled PET radiotracer 4-cyano-N-(4-(2-[^{18}F]fluoroethyl)piperazin-1-yl)-2-(4-methylpiperidinyl)phenyl)-1H-pyrrole-2-carboxamide ([^{18}F]**1**) with high binding affinity at CSF1R (IC_{50}= 3.1 ± 0.5 nM). The imaging properties of [^{18}F]**1** were evaluated in mouse and non-human primate neuroinflammation models induced with lipopolysaccharide (LPS). [^{18}F]**1** was prepared in a one-pot radiolabeling procedure using an automated module with high molar radioactivity (203-1290 GBq/μmol) and radiochemical purity > 97%. [^{18}F]**1** demonstrated robust brain uptake in control mice that peaked (3.6%ID/g tissue) at 5 min post-administration followed by rapid washout. A comparison of control mice versus LPS-treated mice showed a 46% increase in brain uptake of [^{18}F]**1** in the LPS group. Brain uptake of [^{18}F]**1** in the LPS-treated mice was blocked with CSF1R inhibitor, suggesting specific binding to CSF1R in the inflamed case. PET studies with [^{18}F]**1** were performed in healthy baboon and LPS-treated baboon. The comparison of baseline and blocking studies showed that in the control baboon brain, [^{18}F]**1** labels CSF1R with a moderate level of specificity (5%-38%). In the LPS-treated baboon, the radiotracer distribution volume (V_T) was higher in all brain regions versus control. The regional baseline LPS/healthy V_T ratios were in the range of 1.4-1.9. A blocking study in the LPS-treated baboon demonstrated that [^{18}F]**1** binding was specific for CSF1R. Regional baseline/blocking V_T ratio in LPS-treated baboon was greatest in the thalamus, followed by hippocampus, cerebellum, caudate, and occipital cortex (1.4-1.6). These data indicate that [^{18}F]**1** is promising for translation to enable quantification of brain CSF1R receptor density in human subjects.

Oral Presentation

Disclosures: The authors have disclosed no financial interest.

040-Expanding and Evolving Magnetogenetic Tools Toward in vivo Imaging Applications

Presenter: Connor Grady, Michigan State University

Connor Grady[1], Enrique A. Castellanos Franco[2], Ryan Ashbaugh[3], Lalita Udpa[3], Galit Pelled[3], Assaf Gilad[1]

[1]*Michigan State University, East Lansing, MI*
[2]*Michigan State University, East Lansing*
[3]*Michigan State University*

Background:

Synthetic biology plays a major role in the field of molecular imaging[1]. A major challenge in the field is the ability to effectively control reporter enzymes remotely in a non-invasive manner. Many tools have been developed using the split protein approach utilizing optogenetics and chemogenetics means to activate and control these enzymes, although these systems can lack penetration depth and have a lack of temporal control of the reporters. To overcome this, we created an adaptation on the split-protein method and utilize magnetic fields as the stimulus for activation. With the magnetogenetic approach we have created an improved split-NanoLuc and a split-Herpes Simplex Virus type 1 Thymidine Kinase (HSV1-TK). Both constructs set the stage for the magnetogenetic approach to be utlized through *in vivo* applications.

Methods:

All constructs were cloned with the EPG[2] gene and Gibson Assembly creating fusion proteins to the N and C terminals of EPG. The split constructs were expressed in pcDNA3.1(+) or pTwist vectors for mammalian expression in RIN m5F, rat insulinoma, or 4T1 cells, mouse breast cancer. NanoLuc imaging with electromagnetic stimulation was performed using IVIS (Perkin Elmer). Firefly Luminescence for viability following ganciclovir treatment was measured using the Spark (Tecan). Magnetic fields were induced with electromagnetic coils[3] for imaging experiments and static magnets were used for long term stimulation.

Results and Discussion:

Building on a prototype (Fig. P2) that showed the possibility to use EPG with a split-NanoLuc[4], we decided to improve the brightness of the construct by using the NanoBiT split site of NanoLuc. The split-EPG-NanoBiT construct was cloned with varying linker combinations between the EPG and split luciferase fragments to determine optimal conditions. This construct was expressed in RIN-m5F cells and measured using the IVIS with electromagnetic fields (EMF) induction. Reads were taken every 10 seconds with an open filter with 4 periods of 2 minute constant EMF stimulation followed by 6 minutes of no stimulation. EPG constructs showed a 17%-23% (Fig. P3D) change from the minimum luminescence to the final read and a luminescent recovery of 87%- 96% (Fig. P3C) of initial luminescence depending on linker variant compared to the native NanoLuc construct which only maintained 57% of initial luminescence (N=6 wells). A split version of HSV1-TK was fused to two versions of the EPG protein using varying linker combinations. One version uses the full EPG (Fig. 1A, iii) with predicted signal sequence and transmembrane domains, while the short version (Fig 1A, iv) removes these features as they are not believed to play a role in magnetoreception, but act as longer linkers for the construct. 4T1 Cells stably expressing firefly luciferase and transiently expressing the EPG-split-HSV1-TK construct were treated with ganciclovir for 72 hours and luminescence was used to quantify cell viability. Two linker combinations showed a 13% change in cell luminescence (Fig. 1B) when stimulated with a magnet compared to the non-stimulated cells (N=6 wells). This effect with magnetic stimulation was shown to be significantly increase cell death ($p<0.05$) which was not seen in the positive control HSV1-TK or mock transfected cells. Moreover, the EPG-split-HSV1-TK can be explored further for temporal and spatial control of theranostic genes *in vivo*. Either by utilizing radiotracers such as [124]FIAU for PET imaging or selectively controlling cancer treatment in tumors using ganciclovir.

Conclusions:

We are developing a novel magnetogenetic platform to remotely control enzymatic activity *in situ* utilizing split-protein approach controlled

by the EPG protein. By evolving the EPG-split-NanoLuc construct to be brighter and creating an EPG-split-HSV1-TK, we envision that this system combined with molecular imaging can play a key role in monitoring neuromodulation as well as cell therapies.

References

1. Gilad, A. A. & Shapiro, M. G. Molecular Imaging in Synthetic Biology, and Synthetic Biology in Molecular Imaging. Mol Imaging Biol 19, 373-378, doi:10.1007/s11307-017-1062-1 (2017).
2. Krishnan, V. et al. Wireless control of cellular function by activation of a novel protein responsive to electromagnetic fields. Scientific reports 8, 8764, doi:10.1038/s41598-018-27087-9 (2018).
3. Ashbaugh, R. C., Udpa, L., Israeli, R. R., Gilad, A. A. & Pelled, G. Bioelectromagnetic Platform for Cell, Tissue, and In Vivo Stimulation. Biosensors 11, 248 (2021).
4. Grady, C. in World Molecular Imaging Congress (2021). Inagaki, S. et al. Genetically encoded bioluminescent voltage indicator for multi-purpose use in wide range of bioimaging. Scientific reports 7, 42398, doi:10.1038/srep42398 (2017).
5. Han, Y. et al. Directed Evolution of Split APEX2 Peroxidase. ACS Chem Biol 14, 619-635, doi:10.1021/acschembio.8b00919 (2019).

Oral Presentation

Disclosures: The authors have disclosed no financial interest.

041-The Assessment of Incipient Cardiac Damage using PET Imaging Biomarkers in a Doxorubicin Cardiotoxicity Model

Presenter: Chul-Hee Lee, Weill Cornell Medicine

Chul-Hee Lee[1], Luisa Rubinelli[2], Onorina Manzo[2], Thomas M. Jeitner[2], Juan A. Azcona[3], John W. Babich[2], Annarita Di Lorenzo[2], James M. Kelly[4]

[1]Weill Cornell Medicine, NY
[2]Weill Cornell Medicine
[3]Weill Cornell Medicine, New York
[4]Weill Cornell Medicine, New York, NY

Introduction:

Although anthracycline chemotherapy is highly effective in treating a variety of cancers, it is substantially associated with dose-dependent cardiotoxicity. Cardiotoxicity encompasses several pathologies that can eventually lead to heart failure[1]. Echocardiography is commonly used to assess cardiac health and to clinically diagnose cardiotoxicity. Typically, this technique detects dysfunction only after pathological remodeling has occurred. Early detection of cardiac damage may allow therapeutic interventions that could prevent heart failure. Thus, we hypothesize that PET probes interacting with early pathological markers can detect the onset of myocardial damage before the heart becomes dysfunctional. To this aim, we evaluated in a mouse model doxorubicin-induced cardiotoxicity, the following biomarkers: [^{18}F]DPA-714, a translocator protein (TSPO) ligand, [^{68}Ga]Ga-FAPI-04, a fibroblast activation protein (FAP) ligand, and [^{18}F]MFBG, a norepinephrine transporter (NET) ligand, as candidate imaging biomarkers of inflammation, fibrosis, and sympathetic neuron activity, respectively.

Methods:

We induced chronic cardiotoxicity in male C57BL/6J mice by administering 8x3 mg/kg doxorubicin intraperitoneally (total dose 24 mg/kg) over 2 weeks[2]. The body weights of mice were measured on a weekly basis. Over 12 weeks, the DOX mice were imaged serially with echocardiography and [^{68}Ga]Ga-FAPI-04, [^{18}F]DPA-714, or [^{18}F]MFBG PET and compared to age- and sex-matched controls. We calculated parameters such as left ventricular ejection fraction (LVEF), fractional shortening (FS), and quantified tracer uptake in the heart over time by drawing volumes of interest (VOI). Blood samples were collected at each time point, and mice (n=4-5 per time point) were sacrificed and their hearts fixed in 4%PFA for histological analysis. Heart sections were stained with hematoxylin and eosin (H&E) and Masson's trichrome to assess histopathological changes. In addition, expression of cellular target proteins was evaluated by western blot.

Results:

Our doxorubicin regimen was well tolerated, with an overall mortality rate of <20%. DOX-treated mice exhibited decreased body weight and heart weight-to-tibia length (HW/TL) ratio and reduced topoisomerase-2β (TOP2B) expression[3], which is a marker of DOX-induced cardiotoxicity, while fibrotic scarring increased. [^{18}F]DPA-714 signal in the heart increased in DOX mice relative to controls within 2 weeks of end-of-treatment and peaked at 5 weeks. However, the signal-to-noise ratio (SNR) was low due to physiological uptake in the liver and lung[4]. Cardiac [^{68}Ga]Ga-FAPI-04 signal increased within 2 weeks, similar to [^{18}F]DPA-714, but the SNR of [^{68}Ga]Ga-FAPI-04 is high due to low uptake in normal tissues. Contrary to our expectations, [^{18}F]MFBG uptake significantly increased in the heart of DOX animals compared to controls. By contrast, no cardiac dysfunction was evident by echocardiography until 10 weeks after end-of-treatment, at which point FS was significantly reduced relative to healthy controls.

Conclusions:

Our model results in chronic cardiotoxicity characterized by decreased HW/TL, FS, expression of TOP2B, and increased fibrosis. Starting from 2 weeks [^{68}Ga]Ga-FAPI-04, [^{18}F]DPA-714, and [^{18}F]MFBG signals increased in the damaged hearts and lasted up to 10 weeks after the end-of-treatment, when echocardiographic analysis detected cardiac dysfunction. These findings suggest that PET imaging biomarkers may be useful in identifying patients at risk of cardiotoxicity early on during anthracycline chemotherapy allowing therapeutic interventions to prevent or reduce heart failure.

Acknowledgments: This work was supported by a R21 Award (R21CA246409-01) received from the National Cancer Institute at the National Institutes of Health. The authors wish to thank Illumina Radiopharmaceuticals, LLC for the provision of materials for the preparation of [18F]MFBG.

References

1. Pietzsch S, Wohlan K, Thackeray JT, et al. Anthracycline-free tumor elimination in mice leads to functional and molecular cardiac recovery from cancer-induced alterations in contrast to long-lasting doxorubicin treatment effects. Basic Res Cardiol. 2021;116:61.
2. Amgalan D, Garner TP, Pekson R, et al. A small-molecule allosteric inhibitor of BAX protects against doxorubicin-induced cardiomyopathy. Nat Cancer. 2020;1:315-328.
3. Zhang, S., Liu, X., Bawa-Khalfe, T. et al. Identification of the molecular basis of doxorubicin-induced cardiotoxicity. Nat Med. 2012;18:1639–1642

Oral Presentation

Disclosures: The authors have disclosed no financial interest.

042-Radiopaque Nanoparticles Influence Biomaterial Properties in Tissue Engineering Scaffolds

Presenter: Kendell Pawelec, Michigan State University

Kendell Pawelec[1], Laney Buchanan[2], Foster J. Buchanan[2], Legend E. Kenney, Erik Shapiro[1]

[1]Michigan State University, East Lansing, MI
[2]Michigan State University, East Lansing, Michigan

Implantable medical devices from polymeric materials stabilize and repair tissue after trauma or disease. While their use is widespread, it remains difficult to evaluate devices after implantation to ensure proper positioning and determine subsequent device damage, to potentially prevent life-threatening complications. Incorporating radiopacity into biomedical devices significantly improves radiologists' success rate for identifying implant location and potential damage [1]. Nanoparticle contrast agents offer a facile way of adding radiopacity in a variety of imaging modalities [2-3]. However, the addition of nanoparticles to a polymer matrix can affect device properties, like mechanics and degradation rate, both crucial to implant functionality. This study was designed to assess the long-term effects of nanoparticle contrast agents on polymeric devices.

Methods:

Cylindrical scaffolds (4.7mm diameter, 2m thick) were produced via salt leeching, giving porous features (100-300µm) mimicking clinical polymeric devices. Three FDA-approved polymers with differing degradation rates were used as matrices: poly(lactide co-glycolide)(PLGA) 50:50, PLGA 85:15 and polycaprolactone (PCL). The range of CT-visible hydrophobic TaO_x was 0-40wt%. During the study, scaffolds were hydrated (37°C) in 3 buffers, covering the range of physiological pH values: phosphate buffered saline (PBS, pH 7.4), 50mM sodium citrate (pH 6.5), and 50mM sodium citrate (pH 5.5). Hydrated scaffolds were monitored longitudinally with micro-computed tomography (µCT) at 90keV, 88 µA, voxel size < 20µm, to quantify x-ray intensity and scaffold volume. Simultaneously, scaffold mechanical properties and mass loss were tracked over 20 weeks.

Results & Discussion:

In µCT, only implants incorporating a nanoparticle were visible. The features that could be tracked were dependent on the amount of TaO_x incorporated. At ≤ 5wt%, overall scaffold dimensions could be tracked, but no information could be gathered on fine features like porosity. At ≥20wt% TaO_x, x-ray intensity remained significantly larger than background, as long as scaffolds remained intact, up to 20 weeks. As TaO_x particles have negligible degradation under physiological conditions [4], the polymer matrix determined the scaffold degradation kinetics. While approximating the in vivo environment, in vitro degradation in PBS is not a good predictor for in vivo device degradation, as it cannot mimic inflammation or mechanical loading at the implant site. Thus, citrate at pH 6.5 was used to mimic an inflammatory environment and citrate pH 5.5 mimicked a lysosomal environment. The buffer pH and the wt% TaO_x affected the mechanical strength and degradation time of the polymer devices. To illustrate, at pH 5.5, the fastest degrading polymer (PLGA 50:50) lost all mechanical strength by week 4 post-hydration with 40wt% TaO_x, compared to week 7 when 0wt% TaO_x was present. The higher TaO_x content likely influenced the scaffold mechanics and degradation by reducing the amount of polymer available to hold together a coherent structure. Additional TaO_x incorporation > 20wt% did not significantly improve the ability to monitor features and affected mechanics, setting an upper limit on contrast incorporation. Importantly, scaffolds lost compressive strength several weeks prior to significant mass loss, highlighting the need to consider multiple metrics when evaluating changes to biomedical devices.

Conclusion:

Contrast agents are critical for the ability of radiologists to identify device features once implanted. Scaffolds incorporating radiopaque nanoparticles could be monitored for over 20 weeks via CT, with a range of 5-20wt% TaO_x ideal for imaging without significantly affecting device properties. Degradation time and mechanics were controlled by the polymer matrix and were significantly impacted by pH, highlighting the potential impact of inflammation and cellular interaction when designing implants. With increased imaging functionality, the next generation of devices may provide radiologists the opportunity to identify potential device damage before catastrophic failure.

References

1. Pawelec KM, Chakravarty S, Hix JML, Perry K, van Holsbeeck L, Fajardo R, Shapiro EM. Design considerations to facilitate clinical radiological evaluation of implantable biomedical structures. ACS Biomater. Sci. Eng. 2021, 7(2): 718-726.
2. Baetke, S. C.; Lammers, T.; Kiessling, T. Applications of nanoparticles for diagnosis and therapy of cancer. Br. J. Radiol. 2015, 88, No. 20150207.
3. Wolf, F.; Paefgen, V.; Winz, O.; Mertens, M.; Koch, S.; Gross-Weege, N.; Morgenroth, A.; Rix, A.; Schnoering, H.; Chalabi, K.; Jockenhoevel, S.; Lammers, T.; Mottaghy, F.; Kiessling, F.; Mela, P.MR and Pet-CT monitoring of tissue-engineered vascular grafts in the ovine carotid artery. Biomaterials 2019, 216, No. 119228.
4. Chakravarty, S; Hix, JML; Wieweora, KA; Volk, M; Kenyon, E; Shuboni-Mulligan, DD; Blanco-Fernandez, B; Kiupel, M; Thomas, J; Sempere, L; Shapiro, EM. Tantalum Oxide Nanoparticles as Versatile Contrast Agents for X-ray Computed Tomography. Nanoscale. 2020, 12(14): 7720–7734.

Oral Presentation

Disclosures: The authors have disclosed no financial interest.

043-Development of Radioligands for Imaging and Quantifying Phosphodiesterase 4D in Brain with Positron Emission Tomography

Presenter: Meijuan Jiang, National Institutes of Health

Meijuan Jiang[1], Shiyu Tang[2], Madeline D. Jenkins[3], Bruny Kenou[4], Paolo Zanotti Fregonara[4], Jeih-San Liow[4], Sami S. Zoghbi[4], Robert Innis[5], Sanjay Telu[4], Victor W. Pike[5]

[1]National Institutes of Health, Bethesda, MD
[2]National Institute of Mental Health, Bethesda, MD
[3]National Institute of Mental Health, Bethesda, Maryland
[4]Bethesda, Maryland
[5]National Institutes of Health, Bethesda, Maryland

Phosphodiesterase-4 (PDE4) enzymes specifically hydrolyze the intracellular secondary messenger cAMP. Inhibition of PDE4 enzymes significantly increases intracellular cAMP levels, thereby triggering downstream signaling events. These enzymes have become important targets for the treatment of neuropsychiatric disorders, such as neurodegeneration (cognitive impairment) and major depressive disorder.[1] Early PDE4 inhibitors, such as rolipram, bind to all PDE4 subtypes (A, B, C, and D) and have dose-limiting side-effects

(nausea and vomiting) that limit their clinical application. Recently, PDE4D-selective inhibitors have been developed and used as cognition enhancers and antidepressants with improved tolerability.[2, 3] One example, BPN14770, has recently entered phase II clinical trials for the treatment of Fragile X Syndrome.[3, 4] An ability to image and quantify PDE4D in human brain with positron emission tomography (PET) could be of benefit for further drug development and for the investigation of neuropsychiatric disorders. Previously, 4 radioligands have been labeled with cyclotron-produced carbon-11 ($t_{1/2}$ = 20.4 min). Two of them gave sizeable PDE4D-specific PET signals in monkey brain.[5] However, evidence for the accumulation of radiometabolites in brain was found in subsequent human experiments, rendering the best probe [^{11}C]T1650 unsuitable for quantifying PDE4D. Hence, further structural modification of T1650 is needed to avoid problematic radiometabolites. Based on the known structure of PDE4D, the structure of T1650 may be considered to have four interacting parts with the enzyme, namely the planar methoxypyridinyl scaffold (P1), the 3-nitrophenyl group (P2), the methylene linker (P3), and the pyrazolyl group (P4). In a structure-activity relationship study, we systematically varied the four sub-components of the T1650 structure by bioisosteric replacements to produced 58 new inhibitors. 4 different structures were explored for P1, 9 for P2, 4 for P3, and 15 for P4. The synthesized compounds were subjected to inhibitory assays with a mutationally activated, dimeric form of PDE4D, denoted PDE4D7-S129D (PDE4D*) and also for the PDE4B isoform, denoted PDE4B1-S133D (PDE4B*). Among them, eight compounds were found to have high PDE4D* affinity (IC_{50} < 10 nM), selectivity for inhibition of PDE4D* over PDE4B* of >50 fold, a PET CNS MPO score > 3, and amenability to labeling with ^{11}C or ^{18}F at high molar activity.[6-8] Five of the new inhibitors were labeled by methylation of readily synthesized phenol precursors with [^{11}C]iodomethane. Radiosyntheses took about 40 min and gave useful yields and high molar activities (230~750 GBq/μmol). Evaluation of these five ^{11}C radioligands in monkey with PET revealed that they all showed sizable PDE4D-specific signals in brain by comparing baseline study and pre-blocking experiments with rolipram. Two radioligands showed quite stable distribution volume (V_T) after 90 min in monkey brain, an important requirement for PDE4D quantification. These two radioligands are considered promising for further evaluation of metabolic behavior and of brain PDE4D imaging performance.

References

1. Sun, J., et al., J. Med. Chem., 2021. 64(11): p. 7083-7109.
2. Burgin, A.B., et al., Nat. Biotechnol., 2010. 28(1): p. 63-70.
3. Gurney, M.E., et al., J. Med. Chem., 2019. 62(10): p. 4884-4901.
4. Zhang, C., et al., Neuropsychopharmacology, 2018. 43(11): p. 2299-2309.
5. Wakabayashi, Y., et al., ACS Chem. Neurosci., 2020. 11(9): p. 1311-1323.
6. Zhang, L., et al., J. Med. Chem., 2017. 60(20): p. 8538-8551.
7. Zhang, L., et al., J. Med. Chem., 2013. 56(11): p. 4568-79.
8. Pike, V.W., Curr. Med. Chem., 2016. 23(18): p. 1818-1869.

Oral Presentation

Disclosures: The authors have disclosed no financial interest.

044-Development of [18F]F-5-OMe-Tryptophans through Photoredox Radiofluorination: A New Method to Access Trp-based PET Agents

Presenter: Xuedan Wu, University of North Carolina at Chapel Hill

Xuedan Wu[1], Xinrui Ma[1], Yaofeng Zhong[1], Wei Chen[1], Muyun Xu[1], He Zhang[1], Li Wang[1], Xianshuang Tu[1], Zhaoguo Han[1], Zhanhong Wu[1], Moschos Stergios[1], Zibo Li[1]

[1]University of North Carolina at Chapel Hill, Chapel Hill, NC

Abstract

Indoleamine 2, 3-dioxygenase 1 (IDO1) plays an important role in the biology of melanoma and other cancers, which catalyzes the degradation of *L*-tryptophan (Trp) to resist immune destruction[1]. Although various radiolabeled Trp analogs have been developed to monitor Trp metabolism in vivo using positron emission tomography (PET), the lack of IDO1 specificity or complicated synthesis has limited their applications[2]. In this study, we report the development of [^{18}F]F-5-OMe-tryptophans using photoredox radiofluorination and their initial evaluation in B16F10 mouse models.

Methods:

Photoredox radiofluorination is a newly developed method that allows PET agents to be generated from simple precursors under mild conditions[3-5]. To block the TPH metabolic site, 4-F-5-OMe-tryptophan (*L*/*D*-T**13**) and 6-F-5-OMe-tryptophan (*L*/*D*-T**18**) were prepared as optically pure enantiomers. The four agents' metabolic pathways were evaluated in vitro using IDO/TPH enzyme assays. After photocatalyzed radiofluorination and deprotection, the [^{18}F]-agents were evaluated in vivo by small animal PET studies.

Results:

L/*D*-[^{18}F]-T**18** and *L*/*D*-[^{18}F]-T**13** could be produced by photoredox radiofluorination in radiochemical yields (RCYs) ranging from 2.6±0.5% to 32.4±4.1% (3 ≤ n ≤ 5, ee ≥ 99.0%) with over 98.0% radio chemical purity (RCP). Compared with *L*-Trp, both *L*-T**13** and *L*-T**18** showed improved IDO1 specificity because their TPH pathway was potentially blocked by methoxyl group at 5 position. Small animal PET images demonstrated that [^{18}F]-*L*-T**13** reached 9.57±0.26 %ID/g tumor uptake in B16F10 mouse models with very good tumor/muscle uptake ratio (4.57±0.2).

Conclusions:

Photoredox radiofluorination allowed us access novel tryptophan-based PET agents in good RCY from readily available precursors. Initial evaluation suggested [^{18}F]-*L*-T**13** had preferential IDO1 selectivity and prominent tumor uptake in B16F10 models, which warranted further evaluations in applications including immunotherapy prognosis.

References

1. Moujaess, E.; Haddad, F. G.; Eid, R.; Kourie, H. R., The emerging use of immune checkpoint blockade in the adjuvant setting for solid tumors: a review. Immunotherapy 2019, 11 (16), 1409-1422.
2. John, F.; Muzik, O.; Mittal, S.; Juhasz, C., Fluorine-18-Labeled PET Radiotracers for Imaging Tryptophan Uptake and Metabolism: a Systematic Review. Mol Imaging Biol 2020, 22 (4), 805-819.
3. Chen, W.; Wang, H.; Tay, N. E. S.; Pistritto, V. A.; Li, K. P.; Zhang, T.; Wu, Z.; Nicewicz, D. A.; Li, Z., Arene radiofluorination enabled by photoredox-mediated halide interconversion. Nat Chem 2021.
4. Tay, N. E. S.; Chen, W.; Levens, A.; Pistritto, V. A.; Huang, Z.; Wu, Z.; Li, Z.; Nicewicz, D. A., (19)F- and (18)F-Arene Deoxyfluorination via Organic Photoredox-Catalysed Polarity-Reversed Nucleophilic Aromatic Substitution. Nat Catal 2020, 3 (9), 734-742.

5. Chen, W.; Huang, Z.; Tay, N. E. S.; Giglio, B.; Wang, M.; Wang, H.; Wu, Z.; Nicewicz, D. A.; Li, Z., Direct arene C-H fluorination with (18)F(-) via organic photoredox catalysis. Science 2019, 364 (6446), 1170-1174.

Oral Presentation

Disclosures: The authors have disclosed no financial interest.

045-Optimized Doxycycline-Inducible Gene Expression System for Genetic Programming of Tumor-Targeting Bacteria

Presenter: DINH HUY NGUYEN, Chonnam National University

Dinh Huy Nguyen

Chonnam National University, Gwangju, Jeonranamdo, South Korea

Purpose:

In the programming of tumor-targeting bacteria, various therapeutic or reporter genes are expressed by different gene-triggering strategies. Previously, we engineered pJL87 plasmid with an inducible bacterial drug delivery system that simultaneously co-expressed two genes for therapy and imaging by a bidirectional tet promoter system only in response to the administration of exogenous doxycycline (Doxy). In this multi-cassette expression approach, tetA promoter (PtetA) was 100-fold higher in expression strength than tetR promoter (PtetR). In the present study, we developed pJH18 plasmid with novel Doxy-inducible gene expression system based on a tet promoter.

Procedures:

In this system, Tet repressor (TetR) expressed by a weak constitutive promoter binds to tetO operator, resulting in the tight repression of gene expressions by PtetA and PtetR, and Doxy releases TetR from tetO to de-repress PtetA and PtetR.

Results:

In Salmonella transformed with pJH18, the expression balance of bidirectional tet promoters in pJH18 was remarkably improved (PtetA:PtetR = 4~6:1) compared with that of pJL87 (PtetA:PtetR = 100:1) in the presence of Doxy. Also, the expression level by novel tet system was much higher in Salmonella transformed with pJH18 than in those with pJL87 (80-fold in rluc8 and 5-fold in clyA). Interestingly, pJH18 of the transformed Salmonella was much more stably maintained than pJL87 in antibiotic-free tumor-bearing mice (about 41-fold), because only pJH18 carries bom sequence with an essential role in preventing the plasmid-free population of programmed Salmonella from undergoing cell division.

Conclusions:

Overall, doxycycline-induced co-expression of two proteins at similar expression levels, we exploited bioluminescence reporter proteins with preclinical but no clinical utility. Future validation with clinically compatible reporter systems, for example, suitable for radionuclide imaging, is necessary to develop this system further towards potential clinical application.

Oral Presentation

Disclosures: The authors have disclosed no financial interest.

046-Blood Plasma metabolites as possible biomarker/s for diagnosis of metastatic prostate cancer using NMR spectroscopy

Presenter: Virendra Kumar, All India Institute of Medical Sciences (AIIMS)

Virendra Kumar[1], Pradeep Kumar[2], Rajeev Kumar[2], Sanjay Thulkar[2], Sanjay Sharma[2], Maroof A. Khan[1]

[1]*All India Institute of Medical Sciences (AIIMS), India*
[2]*All India Institute of Medical Sciences (AIIMS), New Delhi, Delhi, India*

Prostate cancer (PCa) with metastases remains incurable. The 5-year survival rate of patients with metastatic PCa on initial diagnoses is less than 30%. PCa usually metastasize to the bones and lymph nodes. Current diagnostic methods cannot predict metastatic PCa at a treatable stage of the disease. Thus, sensitive and specific diagnostic and prognostic tumor biomarker/s for PCa metastases will help in clinical management. Therefore, the objective of the present study is to investigate the blood plasma metabolomic profiles to distinguish PCa patients with metastases from those without metastases using ^{1}H-NMR spectroscopy for establishing potential biomarker/s. Blood samples were collected from PCa patients with metastases [(n =12 mean age: 66.67 ± 10.63 years), PSA; 205.38 (50.20- 1361.10) ng/mL] and from those without established metastases [(n =25, mean age: 66.52 ± 7.10 years), PSA; 23.37 (4.39- 100) ng/mL], in morning pre-prandial after overnight fasting. An informed consent was taken and the study was approved by Institute Ethics Committee. Each blood sample was centrifuged at 5000 rpm for 10 minutes at 4°C and plasma was separated and stored at -80°C until NMR experiments were carried out. Proton NMR spectra of blood plasma samples were acquired at 700 MHz spectrometer (Agilent, USA) using 1D CPMG with pre-saturation. The following parameters were used for 1D NMR: 64 scan, with a 70s relaxation delay and a spectral width of 9124.1 Hz with an echo time of 15ms. Two dimensional (2D) COSY and TOCSY experiment was carried out for assignments of resonance peaks. For comparison between these two patient groups, unpaired Mann-Whitney U test was carried out. A p-value <0.05 was considered significant. Univariate (receiver operating characteristics (ROC) curve analysis) and multivariate (orthogonal partial least squares–discriminate analyses (OPLS-DA), variable importance to projection (VIP) score statistical analysis was carried out using MetaboAnalyst 5.0. The metabolic profile analysis showed significantly higher concentration of phosphocreatine (PCr), choline (Cho), betaine, acetate (Ace), pyruvate (Pyr), 3hydroxybutyrate (3HOB), lactate (Lac), dimethylamine (DMA), glycine (Gly) and glycerophosphocholine (GPC) in PCa patients with metastases as compared to non-metastases. The univariate ROC curve analyses indicated phosphocreatine, choline, betaine with AUC of 0.89, 0.88 and 0.84 respectively, had the highest diagnostic accuracy. These three metabolites also showed high VIP scores (1.57, 1.55 and 1.51, respectively). A significantly higher concentration of membrane components such as Cho, GPC and betaine observed in patients with metastases and those without metastases, suggests an alteration in phospholipids metabolism associated with the cancer progression and tumorogenesis[1]. Higher concentrations of DMA in blood plasma of patients with metastases indicate alterations in membrane biosynthesis needed for proliferation of cancer cells[2]. Further, elevated level of Lac and Pyr were observed in blood plasma of PCa patients with metastases as compared to non-metastases[3]. Lac and Pyr are intermediates of glycolysis and TCA cycle, which suggested that the higher consumption of glucose by metastases stage is in response to the stimulated aerobic glycolysis or due to Warburg effect with a conversion through Pyr to Lac. Higher concentrations of 3HOB and Ace in blood plasma of metastases PCa patients with indicate utilization of lipids and ketone bodies as energy

source[4-5]. Further, Gly is an important source of one carbon unit for nucleic acid synthesis to promote rapid cell proliferation and tumorigenesis in advance PCa. Pathway enrichment analysis using the KEGG (Kyoto Encyclopedia of Genes and Genomes) and SMPDB (The Small Molecule Pathway Database) revealed most dominated involvement of phospholipids, glycolysis, gluconeogenesis, TCA cycle, and fatty acid oxidation & glycine serine and threonine metabolism in PCa with metastases condition. In conclusion, NMR-based metabolomics profiling provides novel insights into the pathophysiological mechanism of cancer progression to metastases stage of PCa to monitor and treatment outcomes.

References

1. Glunde K, Bhujwalla ZM, Ronen SM. Nat Rev Cancer. 2011; 11:835-48.
2. Pérez RC, Puchades CL, García FM et al. Metabolomics. 2017;13:52.
3. Gatenby RA, Gillies RJ .Nat Rev Cancer. 2004;4:891-9.
4. Nagrath D, Caneba C, Karedath T et al. Biochim Biophys Acta. 2011; 1807:650-63.
5. Puchalska, P. & Crawford, P. A. Cell Metabolism. 2017; 25:262–284.

Oral Presentation

Disclosures: The authors have disclosed no financial interest.

047-In vivo minibody PET allows noninvasive monitoring of CD8+ and CD4+ cells during the development of diet-induced non-alcoholic steatohepatitis

Presenter: Vera Jörke, Eberhard Karls University of Tuebingen

Vera Jörke[1], Stefania Pezzana[2], Dominik Sonanini[3], Dominik Seyfried[3], Alessandro Mascioni[4], Andreas Maurer[5], Andreas M. Schmid[6], Irene Gonzalez Menendez[7], Leticia Quintanilla-Fend[7], Mathias Heikenwälder[8], Manfred Kneilling[7], Bernd Pichler[9], Johannes Schwenck[10]

[1]*Eberhard Karls University of Tuebingen, Tübingen, Germany*
[2]*University Hospital Tuebingen, Tübingen, Germany, Germany*
[3]*University of Tuebingen, Tuebingen, Baden-Wuerttemberg, Germany*
[4]*ImaginAb, Inglewood, California*
[5]*Werner Siemens Imaging Center, Tübingen, Baden Württemberg, Germany*
[6]*Werner Siemens Imaging Center, Tübingen, BaWue, Germany*
[7]*Eberhard Karls University of Tuebingen, Tübingen, Baden Württemberg, Germany*
[8]*German Cancer Research Center (DKFZ), Heidelberg, Germany*
[9]*Werner Siemens Imaging Center, Tuebingen, Germany*
[10]*University of Tuebingen, Tübingen, BW, Germany*

The shift to a more sedentary lifestyle and unhealthy diets in recent years led to rising incidences in non-alcoholic steatohepatitis (NASH) and subsequently hepatocellular carcinomas (HCC) which will further increase in the upcoming years. Disease predisposition and outcome is mainly influenced by lipid-mediated toxicity and the dynamics of the hepatic immune cell infiltrate with $CD8^+$ and $CD4^+$ T cells as main mediators. Therefore, our aim was to characterize non-invasively the dynamics of these T cells *in vivo* by positron-emission tomography (PET) using a ^{89}Zr radiolabeled anti-murine CD8 ([^{89}Zr]Zr-df-IAB42) and CD4 minibodies ([^{89}Zr]Zr-df-IAB46). NASH was induced by feeding C57BL/6J mice a choline-deficient high- fat diet (CD-HFD) over a time course of 12 months[1,2]. Controls received standard chow (ND). After 3, 6, 9 and 12 months of CD-HFD/ ND, static PET scans combined with subsequent magnetic resonance imaging (MRI) were performed 24h after *i.v.* injection of either [^{89}Zr]Zr-df-IAB42 or [^{89}Zr]Zr-df-IAB46 (n=8-18). At each time point, liver tissue (n=3) was harvested and flow cytometry (FC) as well as histopathology (H&E), and CD8 and CD4 immunohistochemistry (IHC) was conducted. The non-alcoholic fatty liver disease (NAFLD) activity score (NAS) was determined by an experienced pathologist. All data are presented as mean ± SEM. Independent of the time point the CD-HFD and the ND group showed an increased [^{89}Zr]Zr-df-IAB42 or [^{89}Zr]Zr-df-IAB46 uptake in the lymphatic tissue 24h after tracer injection. Further, no differences were detected in the hepatic $CD8^+$ T cell infiltrate at 3, 6, and 9 months between CD-HFD and ND fed animals. Nonetheless, liver uptake of the [^{89}Zr]Zr-df-IAB42 was significantly increased after 12 months in CD-HFD animals compared to ND-fed animals. On the contrary, no differences in hepatic uptake of [^{89}Zr]Zr-df-IAB46 representing the $CD4^+$ T cell infiltrate between CD-HFD and ND were found at any of the investigated time point. Histopathological analysis (H&E staining) revealed typical features of NASH and an elevated NAS score in liver tissue samples of CD-HFD mice starting from 6 months. Moreover, *ex vivo* analysis of livers confirmed the increased $CD8^+$ T cell infiltrate at 12 months in CD-HFD animals by IHC and FC, while no differences in the $CD8^+$ T cell infiltrate were detected at 3, 6, and 9 months after onset of diet. Consistent with the results from the [^{89}Zr]Zr-df-IAB46 PET, $CD4^+$ IHC and FC analyses revealed no differences between CD-HFD and ND mice at all time points of investigation. Concluding, we demonstrated $CD8^+$ and $CD4^+$ minibody PET as potential tool for the non-invasive monitoring of the T cell infiltrate in NASH development which can be applied also in a translational setting. This offers the opportunity to study *in vivo* the T cell infiltrate and their role during disease progression from steatosis to NASH and HCC, which has not been fully understood yet.

References

1. Wolf, Monika Julia, et al., … Heikenwalder M. "Metabolic activation of intrahepatic CD8+ T cells and NKT cells causes nonalcoholic steatohepatitis and liver cancer via cross-talk with hepatocytes." Cancer cell 26.4 (2014): 549-564.
2. Pfister, Dominik, et al., … Heikenwalder M. "NASH limits anti-tumour surveillance in immunotherapy-treated HCC." Nature. 2021 Apr; 592(7854):450-456. doi: 10.1038/s41586-021-03362-0. Epub 2021 Mar 24.

Oral Presentation

Disclosures: The authors have disclosed no financial interest.

048-Assessment of lipids contents in brain tumor patients using CEST-MRI of two Tsat's

Presenter: Chu Wang, Tsinghua University

Chu Wang[1], Chuyu Liu[1], Benqi Zhao[2], Zhuozhao Zheng[2], Xiaolei Song[1]

[1]*Tsinghua University, China*
[2]*Beijing Tsinghua Changgung Hospital, China*

Abstract Body:

CEST-MRI at 3T shows potential in detection of lipids and myeline content in human brain through quantitative NOE imaging. Herein, we propose a novel quantitation method using two saturation lengths (T_{sat}), which could produce contrast maps similar to AREX method but without needs for a T1 map. Clinical Relevance— A type of CEST-MRI, termed as amide proton transfer, have been proved for grading gliomas in patients at 3T, without injection of contrast agents. Our method aims to quantitative imaging of NOE that originated from brain lipids, by further tuning the imaging parameters and analysis. Introduction CEST-MRI is a promising molecular imaging tool that allows sensitive detection of endogenous metabolic changes. For CEST spectra acquired at 3T with a lower saturation B_1, the signals originated from aliphatic protons on lipids become prominent through NOE (Nuclear Overhauser effect). White matter displayed greater NOE values than gray matter, owing to the higher lipid content in myeline [1]. NOE imaging is showing promise in subtyping of brain tumors. e.g., A study showed that gliomas exhibited hypointense on NOE-weighted maps while meningiomas did not have such obvious difference [2]. Previous methods on NOE quantification include LD (Lorentzian difference), three-offsets and AREX [1]. Among them, AREX obtained the highest CNR by compensating T1. However, an additional T1 map need to be acquired. Herein, we developed an alternative analysis approach free of T1 map, which employed CEST dataset of two saturation lengths, that could be acquired using a fast MeLOVARS method [3]. Methods

The method can be divided into 2 parts. First is to bridge the gap between LD and analytical PTR (proton transfer ratio). After that is using this relationship for quantitation. The workflow is shown in Fig.1a and Fig.1b.

For analytical 2-pool PTR as shown in Fig.1a, f is the concentration ratio between the exchangeable solute protons and water protons, k is solute-water exchange rate. T_{sat}*m is the actual saturation time. M is set to 5 and a single T_{sat} is 0.4 s. For parameters to be calculated in Fig.1b, k*f is related to concentration ratio since k is relatively stable in this situation.

To evaluate the results, a normal volunteer and 10 patients (5 with high-grade glioma and 5 with low-grade meningioma) were scanned using a CEST-MRI sequence with EPI readout at 3T. The study protocol was approved by the institutional review board and written informed consent was obtained from each subject. MR experiments were performed on a 3T Ingenia MRI system (Philips Healthcare) with a 32-channel phase array coil. For patients, the CEST slice were centered at the largest areas of the tumors shown on T2w images. Imaging parameters were as follows: B_1 = 0.7 μT, TR = 5500ms, slice thickness = 7 mm, with in-plane resolution of 3×3 mm^2. In total, 31 saturation offsets with uneven intervals were collected, so that the amide and NOE contrast could be quantified using the Lorentzian difference.

Results:

Fig.1c and Fig.1d show the error analysis of our method. Fig.2 shows the results on a normal volunteer and two patients. NOE k*f is hypointense in glioblastoma and is slightly different from meningioma, which is consistent with previous research. Fig.3a and Fig.3b show the significant difference of k*f between tumor ROI and normal ROI in high-grade glioma and low-grade meningioma. Fig.3c and Fig.3d show that our method can successfully distinguish high-grade glioma and low-grade meningioma.

Conclusion:

Using two T_{sat} and the analytical calculations, we proposed a CEST quantitative method with reduced T_1 contamination. The comparison of NOE indicate it may be useful in oncology diagnosis.

References

1. Zaiss M., et al. NeuroImage 112(2015):180-188.
2. Shen Y., et al. Nmr in Biomedicine (2017): e3735.
3. Song X., et al. Magn. Res. Med. 73.2(2015):488-496.

Oral Presentation

Disclosures: The authors have disclosed no financial interest.

049-Efficacy of ICG fluorescence for real-time surgical margin assessment during minimally invasive resections of colorectal liver metastases: A multicenter, single-arm clinical trial (MIMIC)

Presenter: Okker Bijlstra, Leiden University Medical Center (LUMC)

Okker Bijlstra[1], Friso Achterberg[1], Maxime Slooter[2], Mark Boonstra[2], Stefan Bouwense[3], Koop Bosscha[4], Marielle Coolsen[3], Wouter Derksen[5], Michael Gerhards[6], Paul Gobardhan[7], Jeroen Hagendoorn[5], Daan Lips[8], Hendrik Marsman[6], Sven Mieog[9], Alexander Vahrmeijer, Rutger Jan Swijnenburg[10]

[1]Leiden University Medical Center (LUMC), Leiden, Zuid-Holland, Netherlands
[2]Amsterdam University Medical Center (UMC), Amsterdam, Zuid-Holland, Netherlands
[3]Maastricht University, Maastricht, Netherlands
[4]Den Bosch, Netherlands
[5]Univeristy Medical Center Utrecht, Utrecht, Netherlands
[6]Amsterdam, Netherlands
[7]Breda, Netherlands
[8]Enschede, Netherlands
[9]Leiden University Medical Center (LUMC), leiden, z-h, Netherlands
[10]Amsterdam University Medical Center (UMC), Amsterdam, Noord-Holland, Netherlands

Background:

Near-infrared fluorescence (NIRF) imaging with indocyanine green (ICG) has provided surgeons with the possibility to (1) identify up to 12% additional colorectal liver metastases (CRLM) and (2) assess the tumor-margin in real-time during surgery [1-5]. Recent pilot studies show that the presence of fluorescence at the parenchymal transection plane indicates a too close proximity to the malignant lesion predicting a potential tumor-positive resection margin [6, 7]. In the prospective multicenter MIMIC trial, we evaluated the accuracy of in vivo ICG fluorescence-guided liver surgery.

Materials and methods:

The MIMIC trial was designed as a single-arm prospective interventional trial in 8 Dutch liver surgery centers. Patients scheduled to undergo minimally invasive (either laparoscopic or robot-assisted) resections for CRLM were eligible for inclusion. Patients with recurrent CRLM at the site of previous ablation or resection were excluded. Twenty-four hours prior to surgery, 10 mg of ICG was administered intravenously enabling the formation of a fluorescent rim around the metastatic lesion(s). The primary aim of the study was to document the radical resection rate (R0). Secondary aims were the diagnostic accuracy of intraoperative imaging compared to gold standard histopathological resection margin determination, and the effect of NIRF imaging on change of surgical management (i.e. wider resection or resection of additional liver tissue).

Results:

A total of 204 patients were included this study. No significant differences in baseline characteristics, intraoperative variables and postoperative outcomes were observed between patients operated either by laparoscopy (n=75) or robot-assisted surgery (n=129). In these patients, a total of 315 CRLM were resected (mean 1.54 lesions per patient). Overall, the initial R0 (≥1 mm) resection rate was 83%. Based on ICG fluorescence, in 18 of 55 (33%) initial R1 resections, additional liver tissue was resected which converted the resection margin from R1 into R0, increasing the total R0 rate to 88%. The negative predictive value (absence of fluorescence in the resection plane) of NIRF was 92% for an R0 resection. In 21% of CRLM resections a change of surgical management was documented based on ICG fluorescence.

Conclusions:

In patients undergoing minimally invasive CRLM resections, the absence of ICG fluorescence predicts a tumor-negative margin with high accuracy and leads to a change of surgical strategy in more than one-fifth of patients.

References

1. Handgraaf HJM, Boogerd LSF, Hoppener DJ, Peloso A, Sibinga Mulder BG, Hoogstins CES, et al. Long-term follow-up after near-infrared fluorescence-guided resection of colorectal liver metastases: A retrospective multicenter analysis. European journal of surgical oncology: the journal of the European Society of Surgical Oncology and the British Association of Surgical Oncology. 2017;43(8):1463-71.
2. van der Vorst JR, Schaafsma BE, Hutteman M, Verbeek FP, Liefers GJ, Hartgrink HH, et al. Near-infrared fluorescence-guided resection of colorectal liver metastases. Cancer. 2013;119(18):3411-8.
3. Ishizawa T, Fukushima N, Shibahara J, Masuda K, Tamura S, Aoki T, et al. Real-time identification of liver cancers by using indocyanine green fluorescent imaging. Cancer. 2009;115(11):2491-504.
4. Ishizawa T, Saiura A, Kokudo N. Clinical application of indocyanine green-fluorescence imaging during hepatectomy. Hepatobiliary surgery and nutrition. 2016;5(4):322-8.
5. He K, Hong X, Chi C, Cai C, An Y, Li P, et al. Efficacy of Near-Infrared Fluorescence-Guided Hepatectomy for the Detection of Colorectal Liver Metastases: A Randomized Controlled Trial. Journal of the American College of Surgeons. 2022;234(2):130-7.
6. Achterberg FB, Sibinga Mulder BG, Meijer RPJ, Bonsing BA, Hartgrink HH, Mieog JSD, et al. Real-time surgical margin assessment using ICG-fluorescence during laparoscopic and robot-assisted resections of colorectal liver metastases. Ann Transl Med. 2020;8(21):1448.
7. Bijlstra OD, Achterberg FB, Grosheide L, Vahrmeijer AL, Swijnenburg R-J. Fluorescence-guided minimally-invasive surgery for colorectal liver metastases, a systematic review. Laparoscopic Surgery. 2021;5.

Oral Presentation

Disclosures: The authors have disclosed no financial interest.

050-Magnetic Resonance Imaging of Inflammation Driven by Cationic Lipid Nanoparticles during SARS-CoV-2 mRNA delivery in Rats

Presenter: Saaussan Madi, GlaxoSmithKline

Stephanie Slania[1], **Saaussan Madi[2]**, Shalini Saxena[3], Tolulope A. Aweda[4], Tina Skedzielewski[4], Mary Rambo[5], Tammy Lambert[6], Austin Cole[3], Andrew Gehman[3], Andrzej Pitek[3], Beat Jucker[4], Russell Johnson[7], Hasan Alsaid

[1]Johnson&Johnson
[2]GlaxoSmithKline, Collegeville
[3]GlaxoSmithKline
[4]gsk, Collegeville, PA
[5]GlaxoSmithKline, King of Prussia, PA
[6]Collegeville, [7]Rockville

Introduction:

The COVID-19 pandemic enabled rapid development of messenger RNA (mRNA)-based vaccines, with most mRNA-based vaccines in development and in clinic relying on lipid nanoparticles (LNP) with ionizable cationic lipids to enable mRNA delivery[1]. Several studies have shown that LNP-mediated delivery of nucleic acids may incite innate immune activation; however, LNPs that use biodegradable cationic lipids may reduce injection site reactions[2,3]. Magnetic resonance imaging (MRI) and T2-weighted (T2W) imaging has been employed to evaluate inflammation response to acute drug deposition and long acting injectables[4,5]. In this study, T2/T2W MRI was used to examine the inflammation profiles of LNP formulations with different ionizable cationic lipids that have varying biodegradability profiles (RV39 << RV75 < RV94).The inflammatory response of both empty LNPs and LNPs loaded with SARS-CoV-2 self-amplifying mRNA (SAM) was assessed via MRI and cytokine analysis. Additionally, antibody response to vaccination with SAM-loaded LNPs was measured to confirm the potency of these formulations and the impact of cationic lipid degradability on inflammatory response.

Methods:

Male Sprague-Dawley rats (250-300g) were randomly assigned to treatment groups (n=5 per group). Animals received a 50 µL injection into the right gastrocnemius muscle (RM) on Day 0 (prime dose) of either empty LNP (RV94, RV75, or RV39) or LNP loaded with 3 µg SARS-CoV-2 SAM (RV94-SAM or RV75-SAM). On Day 22, the SAM-loaded LNP groups received a second dose (boost dose). Serial T2/T2W MRI of the injection site and draining right popliteal lymph node (RLN) was performed on a 4.7T Bruker magnet at baseline, 24, 48, 72, and 168 hours post-prime dose. Plasma was collected at each imaging timepoint and at 4 hours post-prime dose for cytokine analysis. Antibody response to vaccination was assessed on days 14, 21, and 35 post-prime dose in groups treated with SAM-loaded LNPs to confirm the potency of these formulations. Statistical analysis was performed using a mixed-effect model for all comparisons.

Results:

Treatment was well tolerated by all groups and resulted in rapid MRI signal enhancement at 24 hours post-prime dose in the RM (Figure 1A) and RLN. Compared to other empty LNPs, treatment with RV94 resulted in the least amount of inflammation as indicated by a significant decrease in RM signal enhancement volumes. In contrast, treatment with RV39 exhibited the most inflammation as indicated by the highest RM signal enhancement volumes (Figure 1B). When comparing loaded vs. unloaded LNP (RV94-SAM vs. RV94 and RV75-SAM vs. RV75), treatment with SAM-LNPs resulted in significantly increased inflammation (Figure 1A) as indicated by significantly higher RM signal enhancement volumes (Figure 1C). Minimal differences were observed between the empty LNP groups in the RLN (Figure 1D). However, the loaded LNPs (RV94-SAM and RV75-SAM) showed significantly larger RLN volumes when compared to their corresponding empty LNPs (Figure 1E). In contrast to marked differences in MRI

signal enhancement, cytokine analysis showed no differences between the empty LNP groups. However, IL-6, IL-13, and TNF-alpha showed significant increase in the SAM-loaded vs. empty LNPs at 24 and/or 48 hours post-prime dose. Antibody responses following the prime dose of RV75-SAM and RV94-SAM vaccines were comparable between the treatment groups and, following a boost dose, both vaccines yielded a large and significant increase in antibody titers (Figure 1F).

Conclusions:

Imaging biomarkers, especially right muscle MRI signal enhancement volume, were a more sensitive measure of local innate immune activation than cytokine readouts. MRI endpoints were sensitive enough to detect differences in immune activation between both empty and loaded LNPs, supporting the use of this imaging modality to act as a sensitive, local safety readout for vaccination.

References

1. Chaudhary N et al. Nat Rev Drug Discov 2021;1-22.
2. Abrams MT et al. Molecular Therapy 2010;18:171-180.
3. Hassett J et al. Mol Ther Nucleic Acids 2019;15:1-11.
4. Jucker et al. Journal of Controlled Release 2017;268:102-112.
5. Jucker et al. Br J Clin Pharmacol 2021;1-12.

Oral Presentation

Disclosures: The authors have disclosed no financial interest.

051-T1-weighted magnetic resonance imaging of liver fibrosis with collagen-targeting single-nanometer iron oxide nanoparticles

Presenter: Yingying Ning, Harvard Medical School

Yingying Ning[1], Juanye Zhang[2], Iris Y. Zhou[3], Nicholas Rotile[4], Stephen C. Barrett[4], Mozhdeh Sojoodi[5], Kenneth K. Tanabe[5], Peter Caravan[6], Moungi G Bawendi[2]

[1]*Harvard Medical School, Boston*
[2]*Massachusetts Institute of Technology, Boston, MA*
[3]*Massachusetts General Hospital, Charlestown, MA*
[4]*Massachusetts General Hospital*
[5]*Massachusetts General Hospital Cancer Center, Boston, MA*
[6]*Harvard Medical School, Charlestown, MA*

Introduction:

Superparamagnetic iron oxide nanoparticles (SPION) have been extensively studied for their applications in T_2 weighted MRI, as SPIONs have larger r_2/r_1 ratio than Gd(III). However, the high r_2/r_1 also leads to more significant signal loss of SPIONs in positive contrast T_1-weighted imaging. In addition, most SPIONs have long circulation in the blood stream and/or high liver accumulation due to their large, >10 nm sizes and because they are phagocytosed by macrophages. As a result, targeted imaging with SPIONs takes hours to days for sufficient probe accumulation at target and background washout, and targeted imaging of the liver is precluded by high background signal. We showed that single-nanometer iron oxide (SNIO) nanoparticles are potent probes for T_1-weighted imaging in vivo, with fast blood clearance and low liver uptake.[1] Here, we report SNIO-CBP, a SNIO nanoparticle functionalized with a type I collagen-binding peptide, for detection of liver fibrosis, which is the outcome of most chronic hepatic injury including viral hepatitis B or C infection, autoimmune and biliary diseases or alcoholic and nonalcoholic steatohepatitis.[2]

Results and Discussions:

SNIO-CBP was prepared via conjugation of alkyne-functionalized SNIO (SNIO-alkyne) with type I collagen binding peptide CBP-azide via copper-catalyzed alkyne-azide reaction (Fig. A). Small-angle X-ray scattering (SAXS) established that the iron oxide core of SNIO-CBP had a mean diameter of 1.5 nm (Fig. B). Gel filtration chromatography showed a mean hydrodynamic diameter of 3.8 nm (Fig. C). SNIO-CBP has near-zero zeta potential and exhibited minimal non-specific binding in plasma after incubation with fetal bovine serum (FBS) (Fig. D). The SNIO/CBP ratio was determined to be 1/1.2, according to ^{56}Fe ICP-MS and *L*-amino acid quantification. SNIO-CBP shows a dissociation constant of 23.2 μM in binding with type-I collagen (Fig. E). Longitudinal relaxivity (r_1) of SNIO-CBP was measured to be 4.5 s^{-1} (mM Fe)$^{-1}$ at 1.41 T and 37 °C, or 145 s^{-1}(mM peptide)$^{-1}$. Dynamic T_1-weighted MRI following intravenous administration (2 nmol/g based on CBP concentration), showed immediate blood pool enhancement with a blood elimination half-life of 5.7 min, followed by rapid renal elimination. Importantly, SNIO-CBP showed only transient and slight liver enhancement consistent with an extracellular distribution and renal clearance (Fig. F).

Then we investigated the ability of SNIO-CBP to detect liver fibrosis in two different mouse models: CCl_4 induced liver fibrosis and choline-deficient, L-amino acid defined, high fat diet (CDAHFD) model. SNIO-CBP enhanced T1-weighted MRI could specifically and robustly detect liver fibrosis in both toxin- (Fig. G) and dietary-induced (Fig. H) mouse models. The change in ΔCNR of fibrotic liver induced by SNIO-CBP was in good agreement with the increasing hydroxyproline content and elevated collagen proportional area (CPA) in liver. Prussian blue staining showed localization of SNIO-CBP in fibrotic regions. Importantly, we compared the sensitivity of SNIO-CBP in detecting liver fibrosis in CCl_4 mice with CM-101, a CBP modified gadolinium based contrast agent.[3] We found that SNIO-CBP provided equivalent enhancement of fibrotic liver compared to CM-101, even at a 2.5-fold lower dose, indicating the higher sensitivity of the gadolinium-free SNIO-CBP.

Conclusion:

We reported the novel design of a collagen-targeting iron oxide nanoparticle with single-nanometer core sizes for MRI diagnosis of liver fibrosis. We showed that SNIO-CBP has ideal properties as a targeted T_1-weighted contrast agent: good affinity to type I collagen, minimal non-specific binding to plasma biomolecules, fast blood elimination, and minimal nonspecific liver enhancement. These properties enabled rapid (minutes post injection) detection and quantification of liver fibrosis in two different mouse models with higher sensitivity than the state of the art Gd-based probe. Taken together, SNIO-CBP is a promising candidate as a gadolinium free contrast agent for sensitive detection of liver fibrosis.

References

1. Wei H, Wiśniowska A, Fan J, Harvey P, Li Y, Wu V, Hansen EC, Zhang J, Kaul MG, Frey AM, Adam G, Frenkel AI, Bawendi MG, Jasanoff A. PNAS. 2021, 118, e2102340118;
2. A. Pellicoro, P. Ramachandran, J. P. Iredale, J. A. Fallowfield. Nat Rev Immunol 2014, 14, 181-194;
3. Farrar CT, Gale EM, Kennan R, Ramsay I, Masia R, Arora G, Looby K, Wei L, Kalpathy-Cramer J, Bunzel MM, Zhang C, Zhu Y, Akiyama TE, Klimas M, Pinto S, Diyabalanage H, Tanabe KK, Humblet V, Fuchs BC, Caravan P. Radiology. 2018, 287, 581-589.

Oral Presentation

Disclosures: The authors have disclosed no financial interest.

052-A Generative Adversarial Network for Accelerated and Quantitative 3D Molecular MRI: a Multi-Center Brain and Leg Human Study

Presenter: Or Perlman, Tel Aviv University

Jonah Weigand-Whittier[1], Maria Sedykh[2], Kai Herz[3], Jaume Coll-Font[4], Elizabeth Gerstner[5], Christopher Nguyen[4], Moritz Zaiss[6], Christian Farrar[7], **Or Perlman[8]**

[1]Massachusetts General Hospital
[2]University Hospital Erlangen
[3]University of Tuebingen, Tübingen, Germany
[4]Athinoula A. Martinos Center for Biomedical Imaging
[5]Massachusetts General Hospital, Boston, USA
[6]University of Tuebingen, Erlangen, Germany
[7]Massachusetts General Hospital, Charlestown, MA
[8]Tel Aviv University, Tel Aviv, Israel

Introduction:

Chemical exchange saturation transfer (CEST) is a molecular MRI technique capable of detecting the signals stemming from dilute labile protons on various metabolites, proteins, and peptides[1]. The CEST contrast mechanism has shown promise for cancer applications[2], such as tumor detection, grading, and treatment response monitoring, as well as for stroke management[3], the study of neurodegenerative disease, and muscle metabolism imaging[4]. Alongside CEST imaging, the semisolid magnetization transfer (MT) contrast can provide complementary molecular information, depicting the immobile macromolecule content, thus, constituting a tool for the characterization of lipids and white matter tissue, and showing benefit for multiple sclerosis diagnosis and cancer imaging[5]. Although CEST-weighted protocols are being increasingly investigated in clinical studies and were recently FDA approved for some vendors[6], the semi-quantitative nature of the typical CEST analysis metric may bias the interpretation of the observed effects. Recently, semisolid MT and CEST MR-fingerprinting (MRF) were developed, allowing a quantitative reconstruction of the proton exchange parameters[7,8,9]. Nevertheless, the prolonged acquisition time required for applying this approach for 3D imaging is still a limiting factor for adoption into clinical routine.

Objective:

The goal of this work was to considerably shorten the acquisition time required for quantitative 3D CEST and semisolid MT imaging and validate the robustness of the developed method under multiple imaging scenarios, scanner hardware, and imaging sites.

Methods:

Three-dimensional CEST and semisolid MT MRF datasets of L-arginine phantoms, in-vivo human whole-brains (5 volunteers and 3 GBM patients), and in-vivo human leg calf-muscles (5 volunteers and 1 cardiac rehabilitation subject) were acquired using the open-source pulseq-CEST framework[10], implemented in 3T clinical scanners at 3 different sites, using 3 different scanner models. A generative adversarial network supervised framework (GAN-CEST) was then designed and trained to learn the mapping from a reduced input data space to the quantitative exchange parameter space while preserving perceptual and quantitative content.

Results:

The total acquisition time for GAN-CEST was 33%-80% shorter than CEST-MRF. Excellent agreement was observed between the GAN-CEST estimated L-arginine concentrations and the known concentrations (Pearson's r = 0.967, normalized root mean squared error (NRMSE) =0.018), and between the estimated proton exchange rates and the reference QUESP calculated values (Pearson's r = 0.967, NRMSE=0.017). GAN-CEST images from a brain tumor subject at an unseen site and scanner model yielded a semi-solid volume fraction and exchange rate NRMSE of 0.036±0.010 and 0.065±0.021, respectively, and structural similarity index (SSIM) of 0.966±0.014 and 0.950±0.021, respectively. The mapping of the calf-muscle exchange parameters from an unseen cardiac rehabilitation patient, yielded NRMSE of 0.036±0.0102 and 0.046±0.014 for the semi-solid volume fraction and exchange rates, respectively, and SSIM of 0.966±0.015 and 0.947±0.024, respectively. In regions with large susceptibility artifacts, GAN-CEST has demonstrated improved performance and reduced noise compared to MRF.

Conclusions:

GAN-CEST has demonstrated the ability to substantially reduce the acquisition time for quantitative semisolid MT/CEST mapping while reducing artifacts and retaining performance across imaging sites, unseen scanners models, and pathology.

References

1. Wu et al., EJNMMI Physics 3 (2016): 1-21.
2. Zhou et al., Journal of Magnetic Resonance in Imaging, 50.2 (2019): 347-364.
3. Sun et al., Journal of Cerebral Blood Flow & Metabolism, 27.6 (2007): 1129-1136.
4. Haris et al., Nature Medicine, 20. 2 (2014): 209-214.
5. Henkelman et al., NMR in Biomedicine, 14.2 (2001): 57-64.
6. 3D APT U.S. FDA web site. https://www.accessdata.fda.gov/cdrh_docs/pdf17/K172920.pdf.
7. Cohen et al., Magnetic Resonance in Medicine 80.6 (2018): 2449-2463.
8. Heo et al. Neuroimage 189 (2019): 202-213.
9. Perlman et al. Nature Biomedical Engineering (2021): 1-10. https://doi.org/10.1038/s41551-021-00809-7
10. Herz et al. Magnetic Resonance in Medicine 86.4 (2021): 1845-1858.

Oral Presentation

Disclosures: The authors have disclosed no financial interest.

053-Macrophage PET imaging using an apolipoprotein A1-mimicking radiotracer

Presenter: Abraham Teunissen, Icahn School of Medicine at Mount Sinai

Abraham J. Teunissen[1], Geoffrey Prévot[2], Yohana C. Toner[1], Mandy van Leent[1], Jazz Munitz[1], Yuri van Elsas[1], Thomas Reiner[3], Zahi Fayad[1], Willem Mulder[1], Carlos Perez-Medina[4]

[1]Icahn School of Medicine at Mount Sinai, New York, NY
[2]Icahn School of Medicine at Mount Sinai, New York, New York
[3]Novartis, Switzerland, [4]Mount Sinai, New York, NY

Macrophages are key inflammatory mediators in many pathological conditions, including cardiovascular disease (CVD)

and cancer.[1,2] Therefore, macrophages are not just an appealing therapeutic target but also a valuable diagnostic marker. Several approaches to monitor macrophage burden have been reported (*e.g.*, MRI, PET, or optical methods).[3-5] Although some of these approaches produced promising results, a pressing need exists for quantitative and non-invasive macrophage-specific imaging agents for diagnosing and prognosing inflammatory diseases. Apolipoprotein A1 (apoA1), the most predominant protein on high-density lipoprotein (HDL), displays high affinity for scavenger receptor type B-1 and adenosine triphosphate-binding cassette transporters A1, all abundantly expressed on macrophages.[6-8] Capitalizing on this, radiolabeled reconstituted HDL has been used to study macrophages in atherosclerosis, cancer and other diseases.[9] However, good manufacturing practice (GMP) production of apoA1-based nanomaterials is problematic due to their heterogeneity and the challenges associated with purifying apoA1. Here, we report the development and *in vivo* validation of an apoA1-inspired PET tracer for studying macrophage burden in mouse models of CVD and cancer. Specifically, we functionalized an apoA-1 mimetic peptide (mA1, ~5.5 kDa vs. 28 kDa for endogenous apoA1) with the chelator deferoxamine (DFO) to enable its radiolabeling with zirconium-89 (^{89}Zr), thereby creating ^{89}Zr-mA1 (**Figure 1A-B**). Our results corroborate a mechanism that involves the *in vivo* binding of our probe to lipoproteins and its subsequent uptake by macrophages (**Figure 1C**). We demonstrated ^{89}Zr-mA1's propensity and selectivity for lipoprotein binding by mixing it with albumin, low-density lipoprotein (LDL), or HDL and analyzing these mixtures by size exclusion chromatography (SEC, **Figure 1D**). We similarly administered ^{89}Zr-mA1 *i.v.* to C57BL/6 mice and analyzed their plasma 30 minutes later by SEC. Results showed that the ^{89}Zr-mA1 predominantly associates with large (>500 kDa) structures, corroborating *in vivo* lipoprotein binding (**Figure 1E**). Pharmacokinetic studies by *ex vivo* gamma counting revealed weighted blood half-lives of 55.9 and 367.8 min in C57BL/6 and *Apoe*$^{-/-}$ mice, respectively (**Figure 1F**). As *Apoe*$^{-/-}$ mice inherently have elevated lipoprotein levels, these results further support *in vivo* lipoprotein binding. Biodistribution analyses by PET imaging and *ex vivo* gamma counting revealed high tracer uptake in the liver and kidneys (**Figure 1G-H**). We subsequently focused on ^{89}Zr-mA1's cell-specific uptake and applicability for studying disease. Myocardial infarction (MI) results in inflammation due to tissue damage, which is mainly mediated by macrophages.[10] We used a mouse MI model to image this increased macrophage burden in the infarcted area using ^{89}Zr-mA1. Two days after LAD ligation, mice were injected with the radiotracer and PET scanned at 1 and 24 hours post-injection. (**Figure 1I**). Tracer accumulation in the infarcted area was clearly visible at 24 hours post-injection as indicated by a 2-fold stronger signal than observed in the remote myocardium (P=0.03). These results we corroborated by *ex vivo* gamma counting (not shown). We also labeled mA1 with ^{nat}Zr to study its cellular specific by CyTOF, showing the tracers' high selectivity for macrophage uptake (**Figure 1J**). Next, we investigated ^{89}Zr-mA1's applicability for studying macrophage burden in cancer. C57BL/6 mice were inoculated with B16F10 melanoma and ^{89}Zr-mA1 administered 14 days later. Static PET scans were performed at 1 and 24 hours post-injection. Results showed that tumor uptake increased over time, from an SUV of 0.4 ± 0.3 at 1 h to 0.5 ± 0.2 at 24 h post-injection (**Figure 1K**). These data were confirmed *ex vivo* by gamma counting (not shown). mA1's macrophage targeting was again corroborated by CyTOF (**Figure 1L**). To summarize, our results demonstrate that ^{89}Zr-mA1 has a lipoprotein affinity and thereby favorably accumulates in macrophages *in vivo*. This makes it a promising tool for non-invasively and quantitatively studying diseases characterized by marked changes in macrophage burden. Our study is currently under review at the Journal of Nuclear Medicine.

References

1. Epelman, S., Lavine, K. J. & Randolph, G. J. Origin and Functions of Tissue Macrophages. Immunity 41, 21–35 (2014).
2. Wynn, T. A. & Vannella, K. M. Macrophages in Tissue Repair, Regeneration, and Fibrosis. Immunity 44, 450–462 (2016).
3. Weissleder, R., Nahrendorf, M. & Pittet, M. J. Imaging macrophages with nanoparticles. Nat. Mater. 13, 125–138 (2014).
4. Foss, C. A., Sanchez-Bautista, J. & Jain, S. K. Imaging Macrophage-associated Inflammation. Seminars in Nuclear Medicine 48, 242–245 (2018).
5. Li, Y. & Liu, T. M. Discovering macrophage functions using in Vivo optical imaging techniques. Frontiers in Immunology 9, (2018).
6. Wasan, K. M., Brocks, D. R., Lee, S. D., Sachs-Barrable, K. & Thornton, S. J. Impact of lipoproteins on the biological activity and disposition of hydrophobic drugs: implications for drug discovery. Nat. Rev. Drug Discov. 7, 84–99 (2008).
7. Linsel-Nitschke, P. & Tall, A. R. HDL as a target in the treatment of atherosclerotic cardiovascular disease. Nat. Rev. Drug Discov. 4, 193–205 (2005).
8. Kingwell, B. A., Chapman, M. J., Kontush, A. & Miller, N. E. HDL-targeted therapies: progress, failures and future. Nat. Rev. Drug Discov. 13, 445–464 (2014).
9. Mulder, W. J. M. et al. High-Density Lipoprotein Nanobiologics for Precision Medicine. Acc. Chem. Res. 51, 127–137 (2018).
10. Swirski, F. K. & Nahrendorf, M. Leukocyte Behavior in Atherosclerosis, Myocardial Infarction, and Heart Failure. Science. 339, 161–166 (2013).

Oral Presentation

Disclosures: The authors have disclosed no financial interest.

054-Optical redox imaging of ex vivo hippocampal slices differentiates normal from Alzheimer's disease in mouse models

Presenter: He Nucleus Xu, University of Pennsylvania

He Nucleus N. Xu[1], Sarah Gourmaud[2], Allison Podsednik[2], Xiaofan Li[2], Huaqing Zhao[3], Frances Jensen[2], Delia Talos[2], Lin Z. Z. Li[4]

[1]*University of Pennsylvania, Philadelphia*
[2]*Perelman School of Medicine at the University of Pennsylvania, Philadelphia, PA*
[3]*Philadelphia, PA*
[4]*University of Pennsylvania*

Compared to normal control, more prominent decline of nicotinamide adenine dinucleotide (NAD^+) with age has been reported in brain tissue homogenates and neurons isolated from Alzheimer's disease (AD) models [1]. As essential coenzymes, the redox pair NAD^+ and NADH together with flavin adenine dinucleotide (FAD and $FADH_2$) critically support energy metabolism and maintain mitochondrial redox homeostasis. Furthermore, only NADH and FAD are intrinsically fluorescent whereas NAD^+ and $FADH_2$ are not. Optical redox imaging (ORI) is a well-established technique that detects fluorescent intensities of NADH and FAD-containing flavoproteins (Fp) to yield cellular redox and metabolic information and provides biomarkers for a variety of pathological conditions [2]. However, its utility in AD has not been characterized at the tissue level. We hypothesized that wide-field microscopy imaging of NADH and Fp from ex vivo brain slices as a low-cost and convenient technique differentiates AD from

normal brain. We tested the hypothesis on a well-characterized AD mouse model with 5 Familial Alzheimer's disease mutations (5XFAD) and wild type (WT) control littermates at various ages (average 2, 3.5, 7, 14 months). These ages are related to 5XFAD brain neuropathological and phenotypical changes: amyloid-β accumulation starting from 1.5-2 months; behavioral and synaptic impairment from 4 months; synaptic and neuronal loss from 7 months onward. We dissected the hippocampi and cut ~1 mm thick slices and immediately placed them in glass-bottom dishes each containing 1 mL Live Cell Imaging Solution (Invitrogen™) supplemented with 22 mM glucose. Another portion of the hippocampus was snap-frozen for amyloid-β (Aβ42) assay. Employing an inverted EVOS wide-field microscope equipped with proper filters (357/44 nm excitation and 447/60 nm emission for NADH and 470/22 nm excitation and 510/42 nm emission for Fp channels), we performed tile-imaging of the hippocampal slices with a 4X objective (2343 μm × 1849 μm per field of view). All samples were imaged at least 3 times over ~2 hours to establish a relationship between the redox indices (NADH, Fp, the redox ratio Fp/(NADH+Fp)) and time elapsed from dissection. Data were compared at the same time lapse after dissection. We found 1) immediate significant redox responses of the hippocampal slices to the metabolic modulations by mitochondrial oxidative phosphorylation uncoupler FCCP followed by mitochondrial inhibitors rotenone plus antimycin A; 2) a significant increase in Fp and the redox ratio with age in the hippocampi of both WT and 5XFAD with a more prominent redox shift in AD hippocampi and a significant decrease in NADH in 5XFAD hippocampi; 3) a higher NADH in 5XFAD versus WT hippocampi at the pre-symptomatic age of 2 (mean1.83 ± 0.52, range 1.2 to 2.5) months ($p<0.05$) and significantly higher Fp ($p<0.01$) and redox ratio ($p<0.001$) in 5XFAD hippocampi than that in WT at 7 (mean 7.17 ± 0.59, range 6.5-8) months of age, and 4) a negative correlation of NADH ($p<0.05$) and a positive correlation of Fp ($p<0.0001$) and redox ratio ($p<0.0001$) with Aβ42 level in AD hippocampi. These findings indicate early changes of NADH metabolism during AD progression and suggest that the ORI can be further optimized to conveniently study the metabolism of freshly dissected brain tissues in animal models to identify early AD biomarkers.

References

1. Lautrup S, Sinclair DA, Mattson MP, Fang EF (2019) NAD+ in Brain Aging and Neurodegenerative Disorders. Cell Metabolism 30:630-655.
2. Heikal AA (2010) Intracellular coenzymes as natural biomarkers for metabolic activities and mitochondrial anomalies. Biomark Med 4:241-263.

Oral Presentation

Disclosures: The authors have disclosed no financial interest.

055-Translation potential of molecular MRI quantification of extracellular aldehyde pairs in detection of liver fibrogenesis

Presenter: Yingying Ning, Harvard Medical School

Yingying Ning[1], Iris Y. Zhou[2], Jesse Roberts[3], Nicholas Rotile[4], Matthew Barr[5], Tracy Punshon[5], Hannah Drescher[3], Stephen C. Barrett[4], Mozhdeh Sojoodi[6], Brian Jackson[5], Kenneth K. Tanabe[6], Peter Caravan[7]

[1]Harvard Medical School, Boston
[2]Massachusetts General Hospital, Charlestown, MA
[3]Massachusetts General Hospital, Boston, MA
[4]Massachusetts General Hospital
[5]Dartmouth College, Hanover, NH
[6]Massachusetts General Hospital Cancer Center, Boston, MA
[7]Harvard Medical School, Charlestown, MA

Introduction:

Liver fibrosis is a hallmark of most chronic liver diseases that account for approximately 2 million deaths worldwide per year. Liver fibrosis is progressive and can lead to cirrhosis, primary liver cancer, liver failure, and death.[1] No noninvasive clinical methods exist to detect the early onset of liver fibrosis, and no methods exist that can measure disease activity, e.g. fibrogenesis. During liver fibrogenesis, lysyl oxidase (LOX) oxidizes lysine amino pairs in close proximity on collagens to aldehyde (Lys^{Ald}) pairs.[2] **Gd-1,4**, a probe that targets two Lys^{Ald} simultaneously can robustly detect the onset of liver fibrogenesis and treatment to response in mouse (Fig. S1).[3] Herein, we use **Gd-1,4** to assess the liver fibrogenesis in a rat model of obstructive cholestatic disease and explore its translation potential using human fibrotic liver specimens.

Results and Discussions:

Liver fibrosis was induced in male CD rats (n = 7) by bile duct ligation (BDL), and control animals (n = 4) underwent a sham procedure (Fig. 1A). Animals were imaged with a 4.7 Tesla Bruker MRI scanner. T1 weighted MRI and liver R1 maps were acquired prior to and up to 30 minutes post i.v. 100 μmol/kg **Gd-1,4**. **Gd-1,4** enhanced MRI showed significantly higher liver signal in BDL rats than in sham-operated rats at 30 min p.i. (Fig. 1B). Both the change of liver longitudinal relaxation rate ΔR1 and ΔCNR were significantly enhanced in the BDL animals, compared to sham rats. Liver fibrosis/fibrogenesis in the BDL rats was confirmed by the presence of elevated collagen, LOX, Lys^{Ald} and hydroxyproline content (Fig. S1). *Ex vivo* analyses on rat liver tissues using LA-ICP-MS showed that the probe specifically accumulates in the fibrotic septa which colocalized with the presence of Lys^{Ald} (Fig. 1C). When we incubated an adjacent slice with additional **Gd-1,4** and $NaBH_3CN$ to make an irreversible linkage, it resulted in further increased Gd concentration in fibrotic septa; when we co-incubated **Gd-1,4** with a 100-fold excess of hydrazine, it blocked further binding of **Gd-1,4** and demonstrated the specificity of the probe for tissue aldehyde. We next investigated the applicability of **Gd-1,4** to assess fibrogenesis in human fibrotic/cirrhotic liver associated with NASH ($n = 5$) and normal liver tissue ($n = 4$). Significantly increased Lys^{Ald} levels were observed in fibrotic regions of fibrotic specimens, while there was negligible staining in normal liver (Fig. 1D-E). Positive staining of collagen and LOX were also observed in the fibrotic septa (Fig. 1F). We incubated adjacent slices from the fibrotic liver with **Gd-1,4** or **Gd-1,4** with excess N_2H_4. LA-ICP-MS imaging showed that the average Gd concentration in Lys^{Ald} positive areas (30-200 ppm) was significantly higher than in regions with low Lys^{Ald} (< 30 ppm, Fig. 1F-G), but excess N_2H_4 blocks **Gd-1,4** binding, demonstrating the specificity of the probe to fibrotic human liver. Across all samples, the average Gd concentration in fibrotic human liver was 80.4 ± 15.5 ppm, compared to 23.7 ± 10.8 ppm in normal liver (Fig. 1H-I).

Conclusion:

The MR signal change observed with **Gd-1,4** is robust across different models and species. *Ex vivo* analysis of human liver specimens shows absence of extracellular aldehyde in healthy liver, but high concentrations in fibrotic liver. LA-ICP-MS experiments on human fibrotic liver reveal Gd concentrations similar to that observed in rat model, strongly suggesting that robust MR signal changes would be seen in patients with chronic liver disease, indicating the high clinical translation potential of **Gd-1,4**.

References

1. Pellicoro, P. Ramachandran, J. P. Iredale, J. A. Fallowfield. Nat Rev Immunol 2014, 14, 181-194
2. W. Chen et al. Hepatology 2020, 72, 729-741
3. Ning. et al. GA 290, GA312, WMIC 2021

Oral Presentation

Disclosures: The authors have disclosed no financial interest.

056-Adapting primary and engineered macrophages for tumor visualization: a dual approach

Presenter: Giorgia Zambito, Erasmus Medical Center

Chintan chawda[1], **Giorgia Zambito[2]**, Roisin McMorrow[3], Clemens Lowik[4], Laura Mezzanotte[3]

[1]Erasmus Medical Center, Netherlands
[2]Erasmus Medical Center, Rotterdam, Zuid-Holland, Netherlands
[3]Erasmus Medical Center, Rotterdam, Netherlands
[4]Erasmus University Rotterdam, Rotterdam, Zuid Holland, Netherlands

Macrophage, a key component of the immune cell population, owing to its cellular plasticity is found to be a contributing factor both in cancer progression[(1,2)] and suppression[(3,4)]. A seminal work proposed injected macrophages as a pan-cancer sensors due to their preference to accumulate in breast tumors[(5)]. However, evidence of this behavior is still lacking in different other tumor models, let alone a transgenic mice model dedicated to visualizing this.

Design objective of the study

The primary aim of this project is to visualize the accumulation of genetically engineered macrophages injected in melanoma tumor mouse models. Secondly, applying this proof of concept, a dedicated reporter mouse model is developed that allows visualizing transgenic macrophages by dual-modality optical imaging, i.e. fluorescence (Fl) and bioluminescence (Bl) imaging.

Methodology and Results

Firstly, the BMC2 macrophages (Cellosaurus, CVCL_2I36, derived from C57BL/6 mice) and metastatic melanoma tumor cells (B16F10, ATCC CRL-6475) were transduced by lentiviral vectors for equimolar expression of CBG2 (click beetle red) (λ=680nm) and CBR2 (near-infra-red click beetle) (λ=740nm) luciferases, respectively[(6,7)]. For in vivo experiments, CBR2 expressing B16F10 melanoma cells (4 x 10^4 cells) were injected intravenously (iv) in C57BL/6 mice. Tumor growth was monitored over time by CBR2-specific bioluminescence. BMC2-CBG2 macrophages were pre-labeled with a near-infrared fluorescent dye (Xenolight DiR, 320 µg/mL) and injected iv (10 x 10^6 cells) at day 14 post melanoma injection. Naphthyl luciferin substrate (NH_2NPLH2) was injected intraperitoneally (ip) (220mg/kg) that was used as a single substrate for CBG2 and CBR2 detection. The Fl emissions from BMC2-CBG2 and from B16-CBR2 metastatic melanoma were detected in the lungs at 72 h (Figure 1a). This was performed also at 24, 48 and 72 h post BMC2-CBG2 injection. The Bl spectral unmixing algorithm was applied to distinguish co-localized bioluminescent signals of BMC2-CBG2 and B16F10-CBR2 in the lungs (Figure 1b). Ex vivo BL quantification show metastasis (magenta color) and BMC2-CBG2 macrophages (green color) co-localized in the lungs (Figure 1c). Secondly, a transgenic macrophage reporter mouse was developed for visualization of primary macrophage during pancreatic carcinoma progression and metastasis (in the persuasive data). To do so, CRISPR/CAS knock-in of the MRC-1 promoter was performed. This promoter drives the expression of a reporter gene fusion consisting of click beetle red luciferase (CBR2) and mKate2 fluorescent protein. To ensure stable expression this entire gene cassette is introduced in the ROSA26 locus of albino black/6 mice. MRC1 (mannose receptor C-type 1) also known as CD206, is a type 1 membrane receptor [(8)] expressed in macrophages making MRC1 an ideal promoter to report macrophages in our model.

Conclusion

Together, engineered and primary reporter macrophages could successfully visualize both melanoma and pancreatic tumor models (persuasive data) separately through optical non-invasive imaging modalities.

References

1. Laoui D, Movahedi K, Van Overmeire E, Van den Bossche J, Schouppe E, Mommer C, Nikolaou A, Morias Y, De Baetselier P, Van Ginderachter JA. Tumor-associated macrophages in breast cancer: distinct subsets, distinct functions. Int J Dev Biol. 2011;55(7-9):861–7.
2. DeNardo DG, Ruffell B. Macrophages as regulators of tumour immunity and immunotherapy. Nat Rev Immunol (2019) 19(6):369–82. doi: 10.1038/s41577-019-0127-6
3. Bruns H, Büttner M, Fabri M, Mougiakakos D, Bittenbring JT, Hoffmann MH, et al. Vitamin D-dependent induction of cathelicidin in human macrophages results in cytotoxicity against high-grade B cell lymphoma. Sci Transl Med (2015) 7(282):282ra47. doi: 10.1126/scitranslmed.aaa3230
4. Beatty GL, Chiorean EG, Fishman MP, Saboury B, Teitelbaum UR, Sun W, et al. CD40 agonists alter tumor stroma and show efficacy against pancreatic carcinoma in mice and humans. Science. 2011;331:1612–16.]
5. Aalipour, Amin et al. "Engineered immune cells as highly sensitive cancer diagnostics." Nature biotechnology (2019) 37,5: 531-539.
6. Hall MP, Woodroofe CC, Wood MG, et al. Click beetle luciferase mutant and near infrared naphthyl-luciferins for improved bioluminescence imaging. Nature Communications (2018); 9:132.
7. Zambito, G. et al. Red-shifted click beetle luciferase mutant expands the multicolor bioluminescent palette for deep tissue imaging. iScience (2021); 24.
8. Feinberg, Hadar et al. "Structural analysis of carbohydrate binding by the macrophage mannose receptor CD206." The Journal of biological chemistry vol. 296 (2021): 100368. doi:10.1016/j.jbc.2021.100368

Oral Presentation

Disclosures: The authors have disclosed no financial interest.

057-Deuterated choline tracks choline kinase α activity and enables non-invasive assessment of response to therapy in gliomas in vivo

Presenter: Celine Taglang, University of California, San Francisco

Celine Taglang[1], Georgios Batsios[2], Meryssa Tran[3], Anne Marie Gillespie[3], Sabrina Ronen[1], Pavithra Viswanath[3]

[1]University of California, San Francisco, San Francisco, CA
[2]University of California, San Francisco, San Francisco
[3]University of California, San Francisco, San Francisco, California

Introduction:

Aberrant choline phospholipid metabolism is a metabolic hallmark of cancer[1,2]. Choline is a dietary nutrient that is metabolized to phosphocholine (PC) by choline kinase α (CKα) and subsequently incorporated into phosphatidylcholine, which is the primary membrane phospholipid in mammalian cells[1,2]. Due to the high membrane turnover associated with uncontrolled proliferation, tumor cells upregulate PC and phosphatidylcholine biosynthesis[1]. ^{1}H-MRS detects steady-state metabolite levels but does not interrogate metabolic pathway activity. Recent studies suggest that ^{2}H-MRS following administration of ^{2}H-choline can be used to monitor production of tCho *in vivo*[3,4]. The goal of the current study was to determine whether tCho production from ^{2}H-choline reflects CKα activity and establish the utility of ^{2}H-choline for monitoring glioma response to therapy *in vivo*.

Methods Cell Studies:

Patient-derived high-grade glioblastoma (GBM1), low-grade oligodendroglioma (BT88) and low-grade astrocytoma (BT257) cells were maintained as previously described[5-8]. CKα expression was silenced by RNA interference using a mix of Smartpool siRNAs against CKα[9,10]. Silencing was confirmed by measuring CKα (gene *CHKA*) mRNA levels using quantitative RT-PCR[11]. Cells were incubated in media containing 56mM [$^{2}H_9$]-choline for 48h. ^{2}H-MR spectra were acquired from live cell suspensions on a Varian 14.1T scanner using a 16mm ^{2}H surface coil and a pulse-acquire sequence. Data was analyzed in Mnova. Peak integrals were corrected for saturation and normalized to the natural abundance of semi-heavy water (HDO, 4.75 ppm) collected from a vial containing saline. ***In vivo* studies**: We examined mice bearing orthotopic BT257 tumors generated as described earlier[8]. Tumor volume was determined by T2-weighted MRI using a 14.1T scanner equipped with a single-channel ^{1}H volume coil and a spin echo multi-slice sequence[12]. For treatment response assessment, BT257 tumor-bearing mice were treated with temozolomide (50 mg/kg, 6 days/week, intraperitoneally). Following injection of [$^{2}H_9$]-choline (200mg/kg) (at days 0 and 7 of treatment) via a tail-vein catheter over 2.5 min, non-localized ^{2}H-MR spectra were acquired over 50 min with a pulse-acquire sequence. Normalized tCho levels were calculated by dividing tCho peak integrals by pre-injection HDO. **Statistical analysis**: All results are expressed as mean±standard deviation. Statistical significance was assessed using an unpaired two-tailed Student's t-test with $p<0.05$ considered significant. **Results** [$^{2}H_9$]-choline provides a readout of CKα activity**:** First, we confirmed that CKα mRNA and activity were significantly reduced in siCKα cells relative to siCtrl. Importantly, silencing CKα abrogated tCho production from [$^{2}H_9$]-choline in both GBM1 and BT88 models. These results suggest that PC produced via CKα activity is the predominant component of the ^{2}H-tCho peak produced from [$^{2}H_9$]-choline, consistent with previous studies indicating that CKα is a key rate-limiting enzyme in choline phospholipid biosynthesis in cancer[1,2].

[$^{2}H_9$]-choline can be used to non-invasively monitor response to therapy in patient-derived glioma models: As shown in the representative ^{2}H-MR spectra and quantification, tCho labeling was significantly higher in BT257 tumors relative to normal brain. Temozolomide (TMZ), standard of care for glioma patients[13], induced tumor shrinkage as assessed by T2-weighted MRI in BT257 tumor-bearing mice, an effect that was apparent by D15. Importantly, [$^{2}H_9$]-choline flux to tCho was reduced in BT257 tumor-bearing mice at D7 of TMZ treatment, when no difference in tumor volume was detectable.

Conclusions:

PET-based radiolabeled choline tracers interrogate choline uptake while ^{1}H-MRS monitors steady-state choline metabolism. Our results showing that silencing CKα abrogates tCho production from [$^{2}H_9$]-choline in multiple patient-derived tumor models indicates that [$^{2}H_9$]-choline tracks the activity of CKα. Importantly, our studies show that [$^{2}H_9$]-choline provides an early readout of response to therapy, prior to MRI-detectable volumetric alterations. These results suggest that [$^{2}H_9$]-choline has the potential to assess pseudoprogression, which is a major challenge in glioma imaging[10].

References

1. Cheng, M., Bhujwalla, Z. M. & Glunde, K. Targeting Phospholipid Metabolism in Cancer. Frontiers in oncology 6, 266, doi:10.3389/fonc.2016.00266 (2016).
2. Glunde, K., Bhujwalla, Z. M. & Ronen, S. M. Choline metabolism in malignant transformation. Nature reviews. Cancer 11, 835-848, doi:10.1038/nrc3162 (2011).
3. De Feyter, H. T., Thomas, M., Ip, K., Behar, K. & de Graaf, R. Delayed mapping of 2H-labeled choline using Deuterium Metabolic Imaging (DMI) reveals active choline metabolism in rat glioblastoma. 2021 Annual Meeting of the International Society for Magnetic Resonance in Medicine (2021).
4. Veltien, A. et al. Simultaneous Recording of the Uptake and Conversion of Glucose and Choline in Tumors by Deuterium Metabolic Imaging. Cancers (Basel) 13, doi:10.3390/cancers13164034 (2021).
5. Mancini, A. et al. Disruption of the beta1L Isoform of GABP Reverses Glioblastoma Replicative Immortality in a TERT Promoter Mutation-Dependent Manner. Cancer cell 34, 513-528 e518 (2018).
6. Giannini, C. et al. Patient tumor EGFR and PDGFRA gene amplifications retained in an invasive intracranial xenograft model of glioblastoma multiforme. Neuro-oncology 7, 164-176 (2005).
7. Kelly, J. J. et al. Oligodendroglioma cell lines containing t(1;19)(q10;p10). Neuro-oncology 12, 745-755, doi:10.1093/neuonc/noq031 (2010).
8. Mazor, T. et al. Clonal expansion and epigenetic reprogramming following deletion or amplification of mutant IDH1. Proceedings of the National Academy of Sciences of the United States of America 114, 10743-10748, doi:10.1073/pnas.1708914114 (2017).
9. Viswanath, P. et al. Mutant IDH1 gliomas downregulate phosphocholine and phosphoethanolamine synthesis in a 2-hydroxyglutarate-dependent manner. Cancer & metabolism 6, 3, doi:10.1186/s40170-018-0178-3 (2018).
10. Viswanath, P. et al. 2-hydroxyglutarate-mediated autophagy of the endoplasmic reticulum leads to an unusual downregulation of phospholipid biosynthesis in mutant IDH1 gliomas. Cancer research, doi:10.1158/0008-5472.can-17-2926 (2018).
11. Viswanath, P. et al. Non-invasive assessment of telomere maintenance mechanisms in brain tumors. Nature communications 12, 92, doi:10.1038/s41467-020-20312-y (2021).
12. Batsios, G. et al. PI3K/mTOR inhibition of IDH1 mutant glioma leads to reduced 2HG production that is associated with increased survival. Sci Rep 9, 10521, doi:10.1038/s41598-019-47021-x (2019). 13 Stupp, R. et al. Radiotherapy plus

Oral Presentation

Disclosures: The authors have disclosed no financial interest.

058-[18F]pFBC is a Covalent CLIPTag Radiotracer for PET Reporter Gene Imaging of Viral Gene Transfer in the Murine Brain

Presenter: Sophie Stotz, University of Tuebingen

Sophie Stotz[1], Gregory D. Bowden[2], Sabrina Buss[3], Gina Dunkel[4], Bettina Weigelin[1], Kristina Herfert[3], Bernd Pichler[5], Andreas Maurer[6]

[1]*University of Tuebingen, Tuebingen, Germany*
[2]*Werner Siemens Imaging Center, Germany*
[3]*Eberhard Karls University of Tuebingen, Tuebingen, Baden-Wuerttemberg, Germany*
[4]*Werner Siemens Imaging Center, Tuebingen, Baden-Wuerttemberg, Germany*
[5]*Werner Siemens Imaging Center, Tuebingen, Germany*
[6]*Werner Siemens Imaging Center, Tübingen, Baden Württemberg, Germany*

Introduction:

Preclinical models of neurological diseases and gene therapy suffer from the lack of nuclear reporter systems, and only very few radiotracers that readily cross the blood-brain barrier (BBB) are available [1,2]. We developed a reporter system based on CLIPTag [3] and [^{18}F]*p*FBC [4], an ^{18}F-labeled CLIPTag-ligand. We show specific binding of [^{18}F]*p*FBC in a HEK293 tumor model as well as in a murine adeno-associated virus (AAV) model of viral gene transfer and aim to quantify reporter expression with light sheet microscopy.

Methods:

We designed and automated the synthesis of [^{18}F]*p*FBC. HEK293 cells were engineered to stably express membrane-tethered CLIPTag protein (HEK-CLIP) and characterized it extensively *in vitro*. NOD.CB17-Prkdc^{scid} mice (n=5 per group) carrying either HEK-CLIP or HEK293 subcutaneous xenografts underwent dynamic PET and MR imaging and the residual activity in the organs was assessed *ex vivo* with gamma-counting. To determine whether [^{18}F]*p*FBC is suitable as a PET tracer for the central nervous system (CNS), *in vivo* metabolite analysis by radio-HPLC in plasma and brain homogenate was performed 5, 15 and 30 minutes after [^{18}F]*p*FBC administration in healthy mice (n=3 per time point). To demonstrate specific binding in the brain, an AAV containing the CLIPTag sequence was injected in the right striatum (n=9) and after 5 and 10 weeks, transfection efficiency was assessed by dynamic PET imaging as well as autoradiography of frozen brain slices. To quantify CLIPTag expression, remaining brains were extracted, stained with antibodies and cleared for light sheet microscopy.

Results:

[^{18}F]*p*FBC was synthesized in good yields and excellent radiochemical purity (25 %RCY and >95% RCP) with high molar activity (>200 GBq/µmol at EOS). Expression of CLIPTag on the cell surface was confirmed by Western blot analysis and confocal microscopy. *In vitro* binding studies showed significant (p=0.0037) uptake of [^{18}F]*p*FBC by HEK-CLIP cells compared to control cells which was blockable to baseline by co-incubation with non-radioactive *p*FBC (p=0.0145). PET data showed a 2-fold increased absolute uptake (p=0.0267) and a significantly higher mean tumor-to-muscle ratio (p=0.0379) in the HEK-CLIP xenografts compared to controls. Metabolite analysis revealed appearance of one polar metabolite in plasma and no radio-metabolite crossing the BBB. In AAV-injected mice, [^{18}F]*p*FBC showed fast uptake and rapid clearance from the brain, but no right to left (R-L) uptake difference in the striata in the PET data. In contrast, the autoradiograph showed a clear accumulation of radioactivity in the AAV-CLIP injected right striatum compared to the sham-injected left striatum. In control animals injected with an AAV containing GFP only, no R-L uptake differences were observed with autoradiography.

Conclusions:

Here, we successfully established a novel reporter gene system for PET imaging of gene expression in the brain and periphery and demonstrated its great potential for a wide range of applications, in particular in neurobiological research and gene therapy with viral vectors. We hypothesize that the fast efflux of [^{18}F]*p*FBC hampers the detection via PET, thus, further studies including PgP inhibition and careful modification of the radiotracer are required. Our reporter system could strengthen evaluation of preclinical models and, as development of CNS PET tracers is highly challenging, aid in understanding neurological processes in advance, before developing a target-specific radiotracer.

ACKNOWLEDGEMENTS The authors would like to thank Elena Kimmerle, Ramona Stremme, Natalie Hermann, and Matthias Dahms for excellent technical support.

References

1. Vandeputte C, et al. J Nucl Med 2011 Jul;52(7): 1102-9.
2. Haywood T, et al. PNAS 2019 May;116(23): 11402-7.
3. Gautier A, et al. Chem Biol 2008 Feb, 15(2): 128-36
4. Bowden GD, et al. Sci Rep 2019 Aug, 9(1): 11370

Oral Presentation

Disclosures: The authors have disclosed no financial interest.

059-New Somatostatin Receptor 2 (SSTR2)-Targeted Probe for Near-Infrared Fluorescence Guided Meningioma Surgery

Presenter: Merle Weitzenberg, Helmholtz Zentrum Munchen

Merle M. Weitzenberg[1], Gina Fürtjes[2], Hannes Rolbieski[3], Kristoffer Riecken[4], Oliver Plettenburg[5], Volker Neuschmelting[6], Oliver Bruns[7]

[1]*Helmholtz Zentrum Munchen, Germany*
[2]*Helmholtz Zentrum München, München, Bayern, Germany*
[3]*Helmholtz Zentrum Munchen, Munich, Germany*
[4]*University Hospital Hamburg-Eppendorf, Hamburg, Hamburg, Germany*
[5]*Helmholtz Zentrum Munchen, Hannover, Germany*
[6]*University Hospital Cologne, Köln, Nordrhein-Westfahlen, Germany*
[7]*NCT Dresden, Dresden, Sachsen, Germany*

Meningioma are the most common primary tumors of the central nervous system. Tumor resection as first line therapy is often not curing.[1] Recurrences mostly arise at the surgical margin presumably from small tumor lesions that are currently invisible to the surgical eye.[2] Objective of this study is the development of a highly specific fluorescent probe for intraoperative meningioma imaging in order to make tumor remnants resectable and thus lower recurrence rates.
Labeling of meningioma shall be accomplished by targeting reliably overexpressed somatostatin receptor type 2 (SSTR2) with octapeptide TATE, a synthetic somatostatin analogue.[3] ^{68}Ga-DOTA-TATE is already clinically used for pre- and post-operative diagnostics via SSTR-PET/CT.[4] Due to low spatial resolution and radioactivity of the tracer, PET is not suitable for intraoperative labeling of tumor remnants. Conjugation of TATE to a Near-Infrared (NIR) dye, on the other hand, should allow detection of SSTR2-expressing tissue with high spatial resolution in real time up to few millimeters in depth. Two different heptamethine cyanines were used for conjugation; IRDye800, a commercially available NIR-dye whose conjugates are currently

propelling more than 20 Phase I and Phase II clinical trials,[5] and sNIR, a newly developed NIR-dye. Despite similarities in terms of structure, net charge and optical properties, sNIR and its TATE-conjugate have higher photostability than IRDye800 and its TATE-conjugate, both *in vitro* and *in vivo*. The decisive advantage of TATE-sNIR over TATE-IRDye800, however, is its noticeably faster tissue clearance when injected intravenously in anesthetized mice (**Figure 1**). Tissue half-life of TATE sNIR (28 ± 2 min, n = 3) is one-sixth of TATE-IRDye800 (180 ± 42 min, n = 2), indicating that there is a retention of TATE-IRDye800 that TATE-sNIR is not subjected to. Rapid clearance of non and unspecifically bound probe is prerequisite for detection of specifically bound probe in a beneficial target-to-background ratio. Therefore, further experiments were conducted with TATE-sNIR. The probe showed high affinity for SSTR2 in a filtration based radioligand competition assay (low nanomolar K_i). To evaluate the ability of labeling SSTR2-expressing tissues *in vivo*, mice were intravenously injected with TATE-sNIR, sacrificed 3 h post injection (equals six tissue half-lives) and organs were imaged *ex vivo*. Specific signal uptake was observed in pancreas, gastric epithelium, and pituitary gland, which highly express SSTR2 according to immunohistochemistry (IHC) (**Figure 2a**)). The negative control scrambled-TATE-sNIR (not bearing the SSTR2-targeting pharmacophore) did not enrich in these tissues (**Figure 2b**)). Moreover, the uptake of TATE-sNIR could be blocked through simultaneous injection of a 100 fold excess of non-fluorescent SSTR2-targeting Octreotide (**Figure 2c**)).
For further validation, IOMM-Lee cells (human malignant meningioma cell line with low SSTR2 expression) were stably transduced to overexpress both SSTR2 and an Infrared fluorescent protein (iRFP). An ectopic tumor model was established by subcutaneous injection of normal and transduced IOMM-Lee cells in the left and right flanks of mice. Tumor-bearing mice were intravenously injected with TATE-sNIR, sacrificed 3 h post injection and tumors were imaged *ex vivo*. SSTR2-positive tumors were up to 35-times as bright as SSTR2-negative tumors. Furthermore, an orthotopic meningioma mouse model was developed by intracranial injection of transduced IOMM-Lee cells in order to perform labeling and blocking experiments with TATE-sNIR and Octreotide as well as to investigate unspecific binding with scrambled-TATE-sNIR. Additionally, endogenous expression of iRPF by the tumor cells was used to further validate the labeling of TATE-sNIR using microscopy. Moreover, washout and blocking experiments with freshly excised human meningioma tissue *ex situ* are currently being performed.
The preliminary preclinical results demonstrate that TATE-sNIR is capable of specifically targeting SSTR2 *in vitro* and *in vivo* potentially enabling sensitive and specific meningioma fluorescence guided surgery in the future.

References

1. Goldbrunner, R. et al. EANO guidelines for the diagnosis and treatment of meningiomas. Lancet Oncol. 17, e383–e391 (2016).
2. Lemée, J. M. et al. Extent of Resection in Meningioma: Predictive Factors and Clinical Implications. Sci. Rep. 9, 1–6 (2019).
3. de Oliveira Silva, C. B. et al. Expression of somatostatin receptors (SSTR1-SSTR5) in meningiomas and its clinicopathological significance. Int. J. Clin. Exp. Pathol. 8, 13185–13192 (2015).
4. Boy, C. et al. DGN-Handlungsempfehlung (S1-Leitlinie) Somatostatinrezeptor-PET/CT. (2017).
5. https://www.licor.com/bio/reagents/irdye-800cw-infrared-dyes, accessed 27/04/22.

Oral Presentation

Disclosures: The authors have disclosed no financial interest.

060-Allysine-targeted molecular MR imaging enables early evaluation of pancreatic cancer neoadjuvant chemotherapy response

Presenter: Hua Ma, Harvard Medical School

Hua Ma[1], Shadi Esfahani[2], Shriya Krishna[3], Nicholas Rotile[4], Bahar Ataeinia[5], Jonah Weigand-Whittier[4], Avery T. Boice[6], Iris Y. Zhou[5], Peter Caravan[7]

[1]*Harvard Medical School, Somerville*
[2]*Massachusetts General Hospital, Bosotn, MA*
[3]*Massachusetts General Hospital, boston*
[4]*Massachusetts General Hospital*
[5]*Massachusetts General Hospital, Charlestown, MA*
[6]*Massachusetts General Hospital, Charleston, Massachusetts*
[7]*Harvard Medical School, Charlestown, MA*

Introduction:

Pancreatic ductal adenocarcinoma (PDAC) is a highly morbid cancer with a 5-year survival of less than 5%.[1] Neoadjuvant chemotherapy with FOLFIRINOX has become the standard of care for patients with borderline resectable or locally advanced disease. FOLFIRINOX induces a dense fibrotic reaction in PDAC, replacing tumor cells with mainly cross-linked collagen type I. Therefore, collagen production and deposition may represent valuable biomarkers to monitor treatment response and assist with prognostication and clinical management decisions.[2] In this work, we aim to evaluate molecular MRI of tumor fibrogenesis using a hydrazine bearing Mn(II)-based MRI probe to study response to conventional chemotherapy in two mouse models of human PDAC.

Materials and Methods:

MnL3 is a Mn(II)-PC2A derivatized with an allysine-targeting hydrazine moiety and MnL4 is a nonbinding control probe (Figure 1A). Condensation kinetics of MnL3 with butyraldehyde at pH 6.5 or 7.4 were measured by UV spectroscopy (25 °C, PBS). Relaxivities of MnL3 and MnL4 in PBS, BSA, and allysine-modified BSA solutions were measured at 1.4 T, 37 °C. Protein-bound MnL3 was isolated by ultrafiltration and relaxivity was measured. Mouse PDAC models: 1×10^7 patient-derived metastatic PDAC6 or primary PANC1 cancer cells were injected into the subcutaneous space of the right lower back of male nude (nu:nu) mice. Approximately 4 weeks post tumor implantation, animals underwent 4.7T MRI prior to, 3 days and 7 days after intravenous administration of FOLFIRINOX (Folinate 50 mg/kg, Oxaliplatin 2.5 mg/kg, Irinotecan 25 mg/kg, Fluorouracil 25 mg/kg) every 3 days. T2 RARE (TR/TE/FA=1400 ms/ 60 ms/ 180°, 0.3 mm isotropic spatial resolution) was used to define the tumor region of interest (ROI) excluding the areas of tumor necrosis. Pre- and dynamic 60 min post-probe (i.v. bolus of 100 μmol/g MnL3 or MnL4) T1-weighted FLASH (TR/TE/FA=16 ms/ 2 ms/ 300°, 0.4 mm isotropic spatial resolution) was used to quantify tumor signal enhancement in the ROI, normalized to an external, adjacent phantom and expressed as the percentage increase in normalized signal (%nSI) at each time point. Tumor allysine concentration was measured according to previously reported assay.[3]

Results:

MnL3 reacts twice as fast with butyraldehyde at pH 6.5 (10.4 $M^{-1}s^{-1}$) compared to pH 7.4 (4.6 $M^{-1}s^{-1}$) suggesting higher selectivity in the acidic tumor microenvironment. Relaxivity (Figure B) of MnL3 and MnL4 was similar in PBS (3 $mM^{-1}s^{-1}$), consistent with the presence of one coordinated water ligand. MnL3 relaxivity was not enhanced in BSA solution, but dramatically increased in the presence of BSA-Ald (and 4-fold higher when bound to BSA-Ald), demonstrating specific

binding to BSA-Ald and low/no nonspecific protein binding. The relaxivity of MnL4 was unchanged in BSA or BSA-Ald solutions.
In PDAC6 tumor-bearing mice, MnL3 demonstrated persistent tumor enhancement over 60 min of imaging post-injection, with a significantly higher signal compared to MnL4 (Figure C, E), confirming the specificity of the MnL3 probe for detection of fibrogenesis. MnL3 tumor enhancement was significantly increased at 3- and 7-days post FOLFIRINOX treatment compared to pre-treatment MRI, and correspond well with allysine concentration (Figure 1H). While MnL4 tumor enhancement remained low and not significantly changed from pre-treatment MRI (Figure 1E). Additionally, in PANC1 tumors, MnL3 tumor enhancement was significantly higher 3 days post FOLFIRINOX compared to 3 days post vehicle treatment (Figure D, F). Fibrotic response to treatment on both tumor types was confirmed by increased allysine concentration (Figure G) and Sirius Red stained collagen deposition (Figure I, J).

Conclusion:

MnL3 exhibits a "turn-on" in relaxivity upon allysine binding. MnL3 molecular MRI is specific for PDAC and signal enhancement increases with increasing tumor fibrogenesis. MnL3 detects early (3 day) changes to FOLFIRINOX chemotherapy, highlighting the potential of allysine as a noninvasive biomarker to predict treatment response.

References

1. Pandol, S.; Edderkaoui, M.; Gukovsky, I.; Lugea, A.; Gukovskaya, A., Desmoplasia of pancreatic ductal adenocarcinoma. Clinical Gastroenterology and Hepatology 2009, 7 (11), S44-S47.
2. Erstad, D. J.; Sojoodi, M.; Taylor, M. S.; Jordan, V. C.; Farrar, C. T.; Axtell, A. L.; Rotile, N. J.; Jones, C.; Graham-O'Regan, K. A.; Ferreira, D. S., Fibrotic response to neoadjuvant therapy predicts survival in pancreatic cancer and is measurable with collagen-targeted molecular MRI. Clinical Cancer Research 2020, 26 (18), 5007-5018.
3. Waghorn, P. A.; Oliveira, B. L.; Jones, C. M.; Tager, A. M.; Caravan, P., High sensitivity HPLC method for determination of the allysine concentration in tissue by use of a naphthol derivative. Journal of Chromatography B 2017, 1064, 7-13.

Oral Presentation

Disclosures: The authors have disclosed no financial interest.

061-First-in-human intra-cavity imaging of 5-aminolevulinic acid-induced fluorescence during breast cancer surgery

Presenter: Christopher Gibson, University Health Network

Christopher Gibson[1], Shirley Wang[1], Arcturus Phoon[1], Nayana Thalanki[1], Kathryn Ottolino-Perry[1], Stephen Petropoulos[1], Zuha Qureshi[2], Vasanth Subramanian[3], Anam Shahid[1], Cristiana O'Brien[4], Steven Carcone[4], Suzanne Chung[2], Teresa Tsui[2], Viktor Son[1], Mayleen Sukhram[1], Fannong Meng[1], Susan Done[1], Tulin Cil[1], Michael Reedijk[1], Alexandra Easson[1], Wey Leong[1], Ralph DaCosta[5]

[1]*University Health Network, Toronto, ON*
[2]*University Health Network*
[3]*University Health Network, Brampton, ON*
[4]*University Health Network, Toronto*
[5]*University Health Network, Toronto, Ontario*

Breast-conserving surgery (BCS) is the standard surgical treatment for patients with early-stage breast cancers [1]. Currently, surgeons distinguish tumors from healthy tissue by visual inspection and palpation within the surgical cavity, which is subjective and inconsistent. Positive tumor margins are determined by histology, a process that is impractical and can take several weeks to complete. As a result, approximately 23% of patients require reoperation (8,854 in 2007-2010; range: 17-56% across Canada) within 1y to remove residual tumour cells not detected in the initial surgery [2*]*. Re-excisions increase poor cosmesis, complications, discomfort, adjuvant delay, medical costs, and local recurrence [3]. An urgent clinical need exists for real-time BCS imaging to assess the surgical cavity. Visualization of grossly occult breast cancer based on 5-aminolevulinic acid (ALA)-induced protoporphyrin IX (PpIX) fluorescence in resected tissues has been demonstrated previously [4]. ALA is a prodrug that promotes tumour-specific accumulation of PpIX, which fluoresces bright red when excited with violet light. Our novel fluorescence imaging device (see Figure) contains 405 nm LEDs for PpIX excitation and an imaging filter to block the excitation while transmitting green and red wavelengths to an 8 MP image sensor. An accompanying surgical drape was designed with a transparent optical window to ensure sterility. ***Study objective:*** To assess the clinical utility of a novel handheld fluorescence imaging device for first-in-human, real-time intraoperative imaging during index BCS, particularly within the surgical cavity. ***Method:*** To date, n = 14 patients have received 20 mg/kg bodyweight ALA 2-4 h prior to imaging. Surgical cavities as well as intact and sectioned lumpectomy specimens were imaged with the prototype device. Biopsies were collected from the surgical cavity and sectioned specimens to correlate tissue types with imaged appearance. ***Results:*** Using the prototype device, adipose and connective tissues were differentiated from healthy breast tissues: in n_c = 8 biopsies suspected to be connective tissues based on fluorescence imaging, seven had connective tissue proportion ≥50% in the biopsy section analyzed. Adipose tissues were correctly identified in 100% of n_a = 14 biopsies suspected to contain adipose tissues predominantly. Breast tumours in sectioned lumpectomies appeared red due to the accumulation of PpIX, which contrasted against the green connective tissues and orange-brown adipose tissues (see Figure). In addition, ductal carcinoma in situ (DCIS) was identified at the surgical margin, which was not discovered by the intraoperative standard of care. The DCIS was < 1 mm below the surface of the lumpectomy specimen, which the SSO-ASTRO guidelines would deem a positive margin. In addition to the encouraging imaging results, artifacts unique to the clinical setting were discovered. These artifacts include ambient light leakage, undesirable sources of fluorescence, condensation, blood within the surgical cavity, and image blur. The cause of each artifact has been identified and solutions proposed. Future work includes the continuation of the clinical trial until observation of true positive red fluorescence within the surgical cavity is achieved and iteration of the prototype device to eliminate or mitigate the effects of imaging artifacts.

References

1. Habermann E et al. Are Mastectomy Rates Really Increasing in the United States? Journal of Clinical Oncology. 2010;28(21):3437-3441.
2. Porter G et al. Rates of breast cancer surgery in Canada from 2007/08 to 2009/10: retrospective cohort study. CMAJ Open. 2014;2(2):E102-E108.
3. Clough KB et al. Oncoplastic Surgery: Pushing the Limits of Breast-Conserving Surgery. The Breast Journal. 2015.
4. Ottolino-Perry K et al. Intraoperative fluorescence imaging with aminolevulinic acid detects grossly occult breast cancer: a phase II randomized controlled trial. Breast Cancer Research 2021;23(1):1-20.

Oral Presentation

Disclosures: The authors have disclosed no financial interest.

062-Specific detection of pathogenic myeloid cells in a mouse model of multiple sclerosis using [18F]OP-801 before and after treatment with a CSF1R inhibitor

Presenter: Mackenzie Carlson, Stanford University

Mackenzie Carlson[1], Isaac M. Jackson[2], Israt S. Alam[3], Mausam Kalita[3], Corinne Beinat[1], Christopher J. Acosta[4], Irene N. Falk[5], Samantha Reyes[6], Sydney Nagy[1], Carmen Azevedo[7], Natacha Le Moan[8], Rishi Sharma[9], Jeffrey Cleland[9], Bin Shen[10], Michelle L. James[1]

[1]*Stanford University, Stanford, CA*
[2]*Stanford University, San Bruno, CA*
[3]*Stanford University, Stanford*
[4]*Stanford University*
[5]*Stanford University, Mountain View, CA*
[6]*Stanford University School of Medicine, Stanford, CA*
[7]*Washington University in St. Louis, St. Louis, MO*
[8]*Ashvattha Therapeutics*
[9]*Ashvattha Therapeutics, Redwood City, CA*
[10]*Molecular Imaging Program at Stanford (MIPS), Stanford, CA*

Background:

Immune-mediated neurodegeneration is a key pathological hallmark of multiple sclerosis (MS), a chronic, demyelinating disease of the central nervous system (CNS). Although there are several disease-modifying immunomodulatory therapies available for MS, selection and monitoring of interventions is hindered by a lack of specific *in vivo* imaging biomarkers. We identified [^{18}F]OP-801, a radiolabeled synthetic hydroxyl dendrimer that crosses the blood-brain barrier in the presence of inflammation (and is selectively [>95%] taken up by reactive macrophages/microglia), as a candidate PET tracer to accurately monitor innate immune activation in MS. Here we evaluate [^{18}F]OP-801 for its ability to detect pathogenic myeloid cells in an experimental autoimmune encephalomyelitis (EAE) murine model of MS at both pre-symptomatic and symptomatic disease stages.

Methods:

Female C57BL/6 mice were induced with EAE by administering an emulsion of $MOG_{35\text{-}55}$ and CFA subcutaneously, followed by two intraperitoneal injections of pertussis toxin 1h and 24h later. EAE mice were weighed and scored daily based on levels of paresis/paralysis. On Day 8, static PET/CT images were acquired for EAE (n=15) and naïve (n=5) mice 50 min after injection of [^{18}F]OP-801 (150-250 μCi). Signal was quantified in spinal cord and brain. To assess specificity of [^{18}F]OP-801, we treated a subset of EAE mice (n=10) with a hydroxyl dendrimer CSF1R inhibitor conjugate (to deplete macrophages/microglia via 200mg/kg/day intraperitoneal injections from Day 9 onwards); the remaining EAE mice (n=5) were given vehicle. On Day 19, all mice were imaged using [^{18}F]OP-801-PET, then perfused with saline. Organs were dissected, weighed, and gamma counted to measure associated radioactivity. [^{18}F]OP-801 distribution in CNS tissues were further evaluated using high resolution *ex vivo* autoradiography. Tissue slices used for autoradiography were subsequently stained with H&E to assess immune cell infiltrates/lesions.

Results:

PET images of pre-symptomatic EAE mice revealed significantly higher signal in lumbar spinal cord of EAE compared to naïve mice (p=0.002, Suppl. Fig. 1), consistent with known innate immune cell trafficking and activation in this model[1]. Elevated signal in lumbar spinal cord was also observed in high-scoring (≧2.5) EAE mice on day 19 (p=0.011). No significant differences were found in brain PET signal. Biodistribution results revealed significantly higher spinal cord-to-blood and brain-to-blood ratios of symptomatic EAE mice ($p<0.05$, Suppl. Fig. 1). Whole spinal cord autoradiography images demonstrated visually higher uptake in vehicle EAE mice compared to treated EAE and naïve mice (Fig. 1). Sectioned lumbar spinal cord autoradiography showed significantly different signal in vehicle EAE, treated EAE, and naïve mice (ANOVA p=0.03, Fig. 1) with significantly higher signal in vehicle EAE compared to naïve mice by post-hoc analysis (p=0.03) and higher-trending signal in vehicle compared to treated EAE mice (p=0.07), supporting specificity of [^{18}F]OP-801 for activated macrophages/microglia. H&E-stained spinal cord sections revealed inflammatory lesions corresponding with tracer signal (Fig. 1). Brain autoradiography shows higher levels of [^{18}F]OP-801 binding in EAE mice in the hypothalamus and brain stem, although differences in these regions were not apparent using PET. Importantly, there was no significant difference in [^{18}F]OP-801 binding in peripheral tissues, including blood and spleen which exhibit fluctuations in T cells, B cells, monocytes, and neutrophils (but not macrophages) in EAE, further confirming specificity of [^{18}F]OP-801 for activated microglia/macrophages[2].

Conclusion: [

^{18}F]OP-801 is a promising tracer for imaging activated macrophages/microglia with high sensitivity in the lumbar spinal cord of EAE mice. Importantly, our studies using the dendrimer-CSF1R inhibitor verified the specificity of [^{18}F]OP-801 for macrophages/microglia while also demonstrating the ability of this new therapy to deplete pathogenic immune cells in EAE mice. Future work will involve investigating which cell subtypes endocytose [^{18}F]OP-801 in different neuroinflammatory models, including EAE, in addition to commencing clinical imaging studies with this tracer.

References

1. Constantinescu CS, et al. British journal of pharmacology. 2011.
2. Barthelmes J, et. al. Journal of visualized experiments. 2016.

Oral Presentation

Disclosures: The authors would like to disclose that [18F]OP-801 with Ashvattha Therapeutics And Ivuxolimab are investigational drugs/devices.

063-PET imaging of metformin-induced modulation of cell-surface HER

Presenter: Sandeep Surendra Panikar, Washington University School of Medicine

Sandeep Surendra Panikar[1], Nai C. Keltee[2], Emma L. Brown[3], Abbey Zidel[2], Zachary T. Fisher[2], Alex Mabry[2], Patricia M. Ribeiro Pereira[3]

[1]*Washington University School of Medicine, St. Luois*
[2]*Washington University School of Medicine, St. Louis, MO*
[3]*Washington University in St. Louis*

Objective:

Trastuzumab and Panitumumab are therapeutic mAbs that target the epidermal growth factor receptor 1 (EGFR) and 2 (HER2)[1, 2]. Trastuzumab is the standard-of-care treatment for metastatic and early-stage HER2-positive breast cancer and first-line therapy in combination with chemotherapy for gastric cancer. Panitumumab treats EGFR-mutant lung cancer, KRAS wild-type colorectal cancer, and head and neck squamous cell carcinoma. Previous studies have shown that caveolae-mediated HER endocytosis and recycling processes affect Trastuzumab- or Panitumumab-tumor binding and subsequent efficacy[3, 4]. Others have shown that metformin, a type 2 diabetes treatment, enhances caveolin-1 (CAV-1, the main structural protein of caveolae) protein levels in cancer cells. In the present study, we used HER2 and EGFR-targeted PET imaging to annotate metformin-induced changes in Trastuzumab and Panitumumab-tumor binding.

Methods: Western blot analyses:

Total, membrane, and internalized cell extracts of $HER2^+$ NCIN87 gastric cancer cells or $EGFR^+$ A431 epidermoid cancer cells were analyzed for changes in HER2 or EGFR. Radiolabeling: Trastuzumab or Panitumumab coupled with the DFO chelator were labeled with ^{89}Zr. Imaging: PET/CT images and *ex vivo* biodistribution were acquired at 24 and 72 h post-injection of [^{89}Zr]Zr-DFO-antibody (50–80 µg protein, >99% RCP). Animals: NCIN87 or A431 cancer cells (5 million cells/mice) were injected subcutaneously on the right shoulder of athymic nude mice. Acute metformin administration: Metformin (250 mg/kg) was orally administered 12 h prior to and at the same time as the tail vein injection of [^{89}Zr]Zr-DFO-antibody. Daily metformin administration: Metformin (200 mg/kg) was intraperitoneally administered for 11 consecutive days prior to the tail vein injection of [^{89}Zr]Zr-DFO-antibody.

Results:

Retrospective analyses have shown that high CAV-1 protein levels in tumors correlate with low Trastuzumab efficacy in preclinical cancer models and patients[4]. Our data validate previous studies showing metformin-induced changes in CAV-1 (**Fig 1**)[5]. In our studies, metformin induces a ~2-fold increase in CAV-1 expression at early time points (*i.e*., 2 to 12 h). At incubation times longer than 12 h, CAV-1 protein levels were similar in metformin-treated cells when compared with control (**Fig 1**). Additional western blot analyses demonstrated a decrease in membrane HER after 4 h of incubation with metformin (**Suppl Fig 1A**). Metformin-induced HER membrane depletion demonstrates to be transient, and HER is restored to the surface of cancer cells at 12 h after removing metformin (**Suppl Fig 1A**). Western blot analyses showing metformin-induced changes in membrane HER and antibody-tumor binding were further validated in immunofluorescence, fractionation, and PET imaging assays. At 24 h post-injection of ^{89}Zr-labeled Trastuzumab, NCIN87 control tumors had ~1.6 higher %ID/g when compared with tumors from mice treated with an acute dose of metformin. Similarly, the uptake of ^{89}Zr-labeled Panitumumab in A431 xenografts was ~1.8 higher in control tumors vs. in metformin-treated tumors. The differences in antibody-tumor uptake with an acute dose of metformin are temporal and similar uptake values were observed at 72 h post antibody injection vs control. Since metformin is clinically prescribed once daily, we performed additional immuno-PET studies administering metformin for 11 consecutive days prior of ^{89}Zr-labeled antibody injection. PET imaging of these mice revealed that the tumor uptake of **[^{89}Zr]Zr-DFO-Trastuzumab** is 3.7-fold lower in metformin-treated mice when compared with control mice. (Suppl Fig 1B-C).

Conclusions:

Metformin induces changes in CAV-1 protein levels, which ultimately interferes with HER surface availability for binding Trastuzumab or Panitumumab. The findings that metformin alters the cellular distribution of HER have direct clinical implications in the therapeutic outcomes of antibodies targeting membrane HER2 or EGFR and in their use for molecular imaging. PET imaging demonstrated that a daily administration of metformin significantly reduces the uptake of [^{89}Zr]Zr-DFO-Trastuzumab in NCIN87 tumors. Future studies will explore the impact of metformin in antibody response to HER-targeting antibody therapies.

References

1. Yarden, Y.; Pines, G., The ERBB network: at last, cancer therapy meets systems biology. Nat Rev Cancer 2012, 12 (8), 553-63.
2. Chegu, A.; Panikar, S. S.; Pereira, P. M. R., Mini-review: Antibody-PET of receptor tyrosine kinase interplay and heterogeneity. Nuclear Medicine and Biology 2022, 108-109, 70-75.
3. Pereira, P. M. R.; Mandleywala, K.; Monette, S.; Lumish, M.; Tully, K. M.; Cornejo, M.; Mauguen, A.; Ragupathi, A.; Mattar, M.; Janjigian, Y. Y.; Lewis, J. S., Caveolin-1 temporal modulation enhances trastuzumab and trastuzumab-drug conjugate efficacy in heterogeneous gastric cancer. bioRxiv 2021, 2021.07.13.452260.
4. Pereira, P. M. R.; Mandleywala, K.; Monette, S.; Lumish, M.; Tully, K. M.; Panikar, S. S.; Cornejo, M.; Mauguen, A.; Ragupathi, A.; Keltee, N. C.; Mattar, M.; Janjigian, Y. Y.; Lewis, J. S., Caveolin-1 temporal modulation enhances antibody drug efficacy in heterogeneous gastric cancer. Nature Communications 2022, 13 (1), 2526.
5. Chung, Y.-C.; Chang, C.-M.; Wei, W.-C.; Chang, T.-W.; Chang, K.-J.; Chao, W.-T., Metformin-induced caveolin-1 expression promotes T-DM1 drug efficacy in breast cancer cells. Scientific reports 2018, 8 (1), 3930-3930.

Oral Presentation

Disclosures: The authors have disclosed no financial interest.

064-Detection of a new resonance in down-field 1HMRS of human brain in vivo at 7.0T

Presenter: Ravi Prakash Reddy Nanga, University of Pennsylvania
Ravi Prakash Reddy Nanga[1], Mark Elliott[2], Anshuman Swain[1], Neil E. Wilson[2], Sophia Swago[1], Narayan Datt Soni[3], Walter Witschey[3], Ravinder Reddy[2]

[1]*University of Pennsylvania, Philadelphia, PA*
[2]*University of Pennsylvania, Philadelphia, Pennsylvania*
[3]*Perelman School of Medicine at the University of Pennsylvania, Philadelphia, PA*

Introduction:

Downfield ^{1}HMRS (DFMRS) is an emerging technique for detection of *in vivo* metabolites with protons that resonate beyond 4.7ppm. Since most of the DF metabolites have protons that either have chemical exchange or cross-relax with water, typically non-water suppressed methods are used to perform DFMRS[1-3]. In the current study while performing DFMRS studies at 7.0T, we have detected a new resonance that was previously not reported. Preliminary results obtained from healthy human brain are presented here.

Methods:

Six subjects (4 Male, 2 Female) in the age range of 26-43Y participated in the IRB approved study after explaining the study protocol and obtaining the consent form. All the DFMRS data were obtained

at 7.0T Siemens Terra scanner (Siemens Healthcare, Erlangen, Germany) using a single-channel transmit/32-channel receive phased array knee radio frequency coil (Nova Medical, Wilmington, MA, USA). A spectrally selective 90° E-BURP pulse[4] centered at 10ppm with a band width of 2 ppm was used to excite the downfield metabolites (TR/TE: 1000/18ms, 256 averages, BW: 600Hz), and 3 narrow spatially selective refocusing 180° Shinnar-Le Roux (SLR) pulses (BW: 800Hz) were used for localization as described in a previous study[3]. Number of averages was 256 and total acquisition time was ~7 min including long TR (10s) water reference scan. A large voxel was positioned within the brain avoiding the sinus cavity and the voxel dimensions varied across the volunteers (200 – 350 cm^3). L-Tryptophan phantom was prepared for *in vitro* studies.

Results:

In all the six volunteers scanned, we have consistently identified a new resonance with peak center at ~10.1ppm. A representative spectrum from one of the volunteers is shown in Figure 1 along with the anatomical image and the newly identified peak is shown at ~10.1 ppm. Another observation is the well resolved NAD^+ peaks when the excitation radio frequency was centered at 10.0 ppm. Phantom studies also showed resonance at ~10.1 ppm coming from indole -NH proton of L-Tryptophan and when a water saturation is applied this peak disappears indicating that it either has chemical exchange or cross-relaxation with water which is in line with the in vivo findings on the human brain.

Discussion:

Based on our phantom studies and a literature review of *in vivo* metabolites, we attribute that the new resonance at 10.1 ppm to L-Tryptophan (L-TRP). L-TRP is an essential amino acid in the human brain and is also a major precursor for production of NAD^+ through *de novo* synthesis pathway [5-8] and also serves as a precursor for the production of the important brain neurotransmitter serotonin. A recent CEST study on *in vitro* phantoms of L-TRP and the downstream intermediate metabolites in serotonin synthesis showed a z-spectrum with a small reduction in the water magnetization varying from 5.11 to 5.47 ppm for these metabolites with respect to water [9]. The absolute chemical shift resonances for the indole (-NH) proton of these metabolites reported in that study was 10.17, 10.02, 9.99 and 9.81 ppm for L-Tryptophan, 5-Hydroxytryptophan, Serotonin and 5-Hydroxyindoleaceticacid, respectively. Based on this study and our *in vitro* findings and the *in vivo* concentrations of all the metabolites mentioned above, we believe that the major potential contributor to the 10.1 ppm resonance is from L-TRP. Further characterization of this newly identified resonance (T_1, T_2 and its concentration) are in progress.

Conclusion:

We have detected a new resonance that was not reported previously with a chemical shift of ~10.1 ppm occurring in the down-field ^{1}HMRS from the human brain *in vivo at 7.0T*. This is for the first time that this peak is observed and based on the phantom data and literature, we attribute that this resonance to be from the indole -NH proton of L-Tryptophan.

References

1. de Graaf, R. A., Behar, K. L. Detection of cerebral NAD(+) by in vivo (1)H NMR spectroscopy. NMR Biomed. 2014, 27(7): 802-809.
2. de Graaf, R. A., de Feyter, H. M., Brown, P. B., et al. Detection of cerebral NAD(+) in humans at 7T. Magn Reson Med. 2017, 78(3): 828-835.
3. Bagga, P., Hariharan, H., Wilson N. E., et al. Single-Voxel 1H MR spectroscopy of cerebral nicotinamide adenine dinucleotide (NAD+) in humans at 7T using a 32-channel volume coil. Magn Reson Med. 2020, 83(3): 806-814.
4. Geen, H., Freeman, R. Band-selective radiofrequency pulses. J Magn Reson (1969). 1991, 93(1): 93-141.
5. Badawy, A. A-B. Kynurenine pathway of tryptophan metabolism: regulatory and functional aspects. Int J Tryptophan Res. 2017, 10:1178646917691938.
6. Bender, D. A. Biochemistry of tryptophan in health and disease. Mol Aspects Med. 1983, 6(2):101-197.
7. Badawy, A. A-B. Tryptophan metabolism in alcoholism. Nutr Res Rev. 2002, 15(1):123-152.
8. Katsyuba, E., Mottis, A., Zietak, M., et al, De novo NAD+ synthesis enhances mitochondrial function and improves health. Nature. 2018, 563(7731), 354-359.
9. Oglesby, R. T., Lam, W. W., Stanisz, G. J. In vitro characterization of the serotonin biosynthesis pathway by CEST MRI. Magn Reson Med. 2020, 84(5):2389-2399.

Oral Presentation

Disclosures: The authors have disclosed no financial interest.

065-Complex gold-silver nanostructures for imaging and therapy of biofilm infections

Presenter: Maryam Hajfathalian, Stanford University

Maryam Hajfathalian[1], Christiaan Devries[2], Yuxi Dong[3], Ahmad Amirshaghaghi[4], Zhi Ren[4], Pallavi Jonnalagadda[5], Jessica Hsu[6], Yong Li Yong Li[5], Yuan Liu Yuan Liu[5], Aimen Zlitni[7], Paul L. Bollyky[8], Hyun Koo[9], David Cormode[4]

[1]*Stanford University, MOUNTAIN VIEW, CA*
[2]*Stanford School of Medicine, Stanford, California*
[3]*University of Pennsylvania, PHILADELPHIA, Pennsylvania*
[4]*University of Pennsylvania, Philadelphia, PA*
[5]*University of Pennsylvania*
[6]*Philadelphia, PA*
[7]*Stanford University, Stanford, CA*
[8]*Stanford University School of Medicine, Stanford, California*
[9]*University of Pennsylvania, philladelphia, PA*

Introduction:

Biofilms are microbial aggregates embedded in a self-produced matrix of extracellular polymeric substances (EPS) that can grow on natural surfaces such as teeth, heart valves, and wounds. These biofilms are difficult to treat with existing clinical therapies due to antimicrobial resistance. Studies indicate that biofilm infections once established cannot be treated by antibiotics alone in most cases. Therefore, a critical need exists to effectively diagnose and treat biofilm infections. Here, we present a theranostic agent to image and treat harmful biofilms. We developed Wulff in cage gold nanoparticles (PTNP) with enhanced photothermal (PTT) and photoacoustic imaging (PA) properties that are promising candidates for biofilm detection, treatment, and infectious disease control. We found PTNP can control virulent biofilms and treat infectious disease via activation with near infrared region (NIR) laser with precise spatial control and in a short timeframe. A strong biocidal effect against Streptococcus mutans (*S. mutans*) and Staphylococcus aureus (*S. aureus*) within biofilms was observed, which caused elimination of 99.99% of bacteria, considerably more effective than currently clinically used oral and skin antimicrobials. Therefore, here for the first time, we introduce a flexible, fast, precise, and unique topical

therapeutic method to image and treat costly oral and skin biofilm-associated infections.

Methods:

Multifunctional gold-silver photothermal nanocages (PTNP) were synthesized by transformation of gold Wulff-shaped seeds into complicated Wulff in a cage nanoparticle via galvanic replacement of a silver shell with gold (S1).[1] After synthesizing the PTNP and purification, the collected nanoparticles were coated with dextran-10kDa (DEX) to provide stability in biological media (S2). The effect of the PTNP on the viability of several cell lines was investigated via the MTS assay (S3). These structures were characterized using transition electron microscopy (TEM), energy dispersive X-ray spectroscopy (EDS), and UV-visible spectroscopy. CT, PA and PTT *in vitro* imaging were carried out to demonstrate the feasibility of PTNP as a contrast agent for these modalities (S4). The anti-biofilm efficacy of the PTNP was examined *in vitro* using S. *mutans* and *S. aureus* biofilms as models of oral and skin infections, respectively (S5). The untreated or treated biofilm with PTNP was analyzed using high-resolution confocal fluorescence imaging and live-dead staining, while PA imaging of biofilms treated with PTNP was carried out to investigate the theranostic potential of these structures within the biofilm *in vivo* and *ex vivo* (S6). Furthermore, PTNP was examined for its efficacy as an anti-biofilm agent to control, image, and treat wound infections and severe dental caries using rodent models.

Results:

TEM of PTNP showed the Au seeds core and the shells that contains AuAg alloys with some porosities (A, B). The optical extinction spectra of PTNP showed the plasmonic peak at 808 nm (C). Uptake of PTNP by *S. mutans* biofilms was confirmed by SEM in backscattered electron (BSE) mode which showing the morphology of PTNP-treated biofilm (D). We found almost complete bacteria killing in biofilms incubated with PTNP and after 30 s laser irradiation, while no dead cells were observed in the area without laser irradiation (E, F). We found an exceptionally strong biocidal effect against *S. mutans* and *S. aureus* within biofilms when exposed to NIR laser irradiation and PTNP (G, S5). Treatment of *S. aureus* infected mouse wounds was studied using bioluminescence imaging (BLI) (H), which showed potent *in vivo* bacterial killing. Robust PA contrast can be seen in both wound and oral infection treated with PTNP (I-N).

Conclusion:

PTNP is a promising approach as a theranostic anti-biofilm agent.

Oral Presentation

Disclosures: The authors have disclosed no financial interest.

066-Deep-BioD: A Deep learning-based method for automated quantification of radioactivity in major mouse organs using CT and PET whole body scans

Presenter: Vibha Nasery, Regeneron Pharmaceuticals

Vibha V. Nasery[1], Mary Germino[2], Sai Kiran Sharma[3], Kevin Guley[1], Richard Tavare[3], Johnathon Walls[3], Nicholas Gale[1]

[1]*Regeneron Pharmaceuticals*
[2]*Regeneron Pharmaceuticals, Ossining, New York*
[3]*Regeneron Pharmaceuticals, Tarrytown, NY*

Introduction:

Per-organ radioactivity concentration is a routinely desired endpoint from preclinical PET/CT studies. Longitudinal imaging experiments are especially important to study antibody distribution over time for therapeutic antibodies development. However, it can be difficult to manually delineate the organs of interest in large datasets. Deep learning based[1,2,3,4] models are currently state-of-the-art for such segmentation tasks. In our pipeline, 3D UNets[3,4] were employed to perform organ segmentation in CT images which enabled per-organ quantification of the corresponding PET dataset. The segmentation performance was compared with previously published 2D UNet approach.[1]

Methods:

The quantification pipeline consists of two stages: 1. Organ segmentation from CT images using deep learning Three UNet based models- 2D UNet, 3D UNet and 3D Attention UNet were trained to segment 10 different organs- heart, liver, stomach, lungs, brain, bladder, kidneys, spleen and femur bone in CT images. The PET/CT data that came from a Zr-89 radiolabeled antibody (immune-PET) that was imaged over 7 timepoints in 8 mice was used for training and testing these models. Manual annotations for organs were available for 54 CT scans. The data was randomly divided into training, testing and validation sets with 40, 7 and 7 scans in each, making sure that all time points of any animal belonged to the same set. The models were trained with soft Dice loss for 30 epochs. The validation loss was evaluated for each epoch, and the model with the least validation loss was chosen for testing the performance. Standard data augmentations[5] including random affine transformations were applied to the images during training. 2. Mean radioactivity quantification from PET images: The PET and CT scan pairs were co-registered and the mean radioactivity concentration per organ was calculated from PET, based on the organ segmentation masks generated by the deep learning model.

Results and Discussion:

3D deep learning models take 3D volume images as input, and the subsequent operations like convolutions are also performed in 3D. 2D models on the other hand, use a single slice as an input, and don't leverage context from adjacent slices. 3D Attention UNet[4] modifies the vanilla UNet architecture to include trainable "attention gates", which help to focus on the regions where organs of interest are present. The test dataset for the models included the same mice imaged over 7 different time points. It was observed that all three models performed well, with the 3D models performing better. The median Dice score for 3D models was greater than or equal to 0.89 for all organs except spleen, which had a median score of 0.8. The heart and lungs were segmented very accurately with Dice scores 0.96 and 0.92 respectively for the 3D models. Overall, these models show improvement over the existing published methods for organ segmentation in native contrast micro CT images[1]. 3D models had higher Dice scores for all organs than 2D model, and showed major improvements for heart, kidneys (4-6%) and bladder (23%). Bladder is difficult to segment because of the variability in size. The caveat with 3D models is that they were difficult to train and had to be trained multiple times to obtain the best performance and they were computationally expensive.
For mean radioactivity quantification, high correlations (with R^2 values ranging from 0.95 to 1) were observed between the values obtained by using manually annotated masks and the values obtained by using deep learning model generated masks for all organs except stomach. Even for stomach, there was a good correlation with R^2 of 0.84.

Conclusions:

Using 3D architectures provide modest improvements in deep-learning based segmentations of organs from murine CT, as compared to a simpler 2D approach.

References

1. Schoppe, Oliver et al. "Deep learning-enabled multi-organ segmentation in whole-body mouse scans." Nature communications vol. 11,1 5626. 6 Nov. 2020, doi:10.1038/s41467-020-19449-7
2. Ronneberger, Olaf, Philipp Fischer, and Thomas Brox. "U-net: Convolutional networks for biomedical image segmentation." International Conference on Medical image computing and computer-assisted intervention. Springer, Cham, 2015.
3. Çiçek, Özgün, et al. "3D U-Net: learning dense volumetric segmentation from sparse annotation." International conference on medical image computing and computer-assisted intervention. Springer, Cham, 2016.
4. Oktay, Ozan, et al. "Attention u-net: Learning where to look for the pancreas." arXiv preprint arXiv:1804.03999, 2018.
5. Buslaev, Alexander, et al. "Albumentations: Fast and Flexible Image Augmentations." Information, vol. 11, no. 2, Feb. 2020, p. 125. Crossref, https://doi.org/10.3390/info11020125.

Oral Presentation

Disclosures: The authors have disclosed no financial interest.

067-The role of the near-infrared fluorescent dye in the pharmacokinetic behavior of fluorescent nanobody-based tracers for intra-operative cancer imaging

Presenter: Noemi Declerck, Vrije Universiteit Brussel

Noemi B. Declerck[1], Sofie Declercq[2], Pieterjan Debie[3], Julie Du Ville[2], Lukasz Mateusiak[4], Marcus CM Stroet[2], Rida Tariq Akhtar[2], Michael P. Luciano[5], Dong-Hao Li[6], Martin J. Schnermann, Bradley Smith[7], Sophie Hernot[8]

[1]Vrije Universiteit Brussel, Jette, Belgium
[2]Vrije Universiteit Brussel, 1090 Jette, Belgium
[3]Vrije Universiteit Brussel, Jette, België, Belgium
[4]Vrije Universiteit Brussel, Brussels (Jette), Brussels-Capital Region, Belgium
[5]National Cancer Institute, FREDERICK, MD
[6]University of Notre Dame, Notre Dame, Indiana
[7]University of Notre Dame, Indiana
[8]Vrije Universiteit Brussel, Brussels, Brussels, Belgium

Introduction:

Near-infrared fluorescence molecular imaging is a propitious tool aimed at supporting intra-operative decision-making during cancer resection. Most targeted contrast agents currently under development are labelled with IRDye800CW®, however this dye is known to cause non-specific background signals. [1-5] Here, tumor-specific Nanobodies (Nbs) were labelled with alternative dyes, namely ZW800-1 [4,5], FNIR-Tag [6] and s775z [7], and a side-by-side comparison of their *in vivo* biodistribution and tumor targeting was performed to determine whether these dyes possess improved characteristics for the development of fluorescent Nb-based tracers. Furthermore, the impact of a higher dye density on the tracer's pharmacokinetics was investigated.

Methods:

An anti-EGFR Nb was randomly labeled with NHS-activated IRDye800CW, ZW800-1, FNIR-tag or s775z. Excess of the dyes was adapted to yield a degree of labeling (DOL) of 1 or 2 on average. Following the *in vitro* assessment of purity, composition, spectral properties, functionality, and serum protein binding, the *in vivo* behavior of all fluorescent tracers was evaluated in EGFR+ tumor-bearing mice (n=4/group, N=32). At 1, 3, 6, 12, and 24 hours after intravenous injection of 2 nmol of the anti-EGFR tracer or a control tracer, 2D images were acquired using the Fluobeam. In addition, major organs and tissues excised at 1h and 24h post-injection were imaged *ex vivo*. For all images, mean fluorescent signals and tumor-to-background ratios (TBRs) were determined. An analogous protocol was applied to prepare and evaluate fluorescent anti-HER2 and anti-CEA Nbs.

Results/Discussion:

The Nbs were successfully labeled with IRDye800CW, ZW800-1, FNIR-tag or s775z. The *in vivo* evaluation of the tracers with a DOL1 showed that FNIR-Tag- and s775z-Nbs clearly accumulate in the tumor at 1h post-injection with little background signal, except in the kidneys due to renal clearance of the tracer. In comparison IRDye800CW- and ZW800-1-tracers demonstrate considerable aspecific accumulation, mainly in the liver, leading to low TBRs within the rapid imaging timeframe Nb-based tracers aim at. The *ex vivo* analysis confirmed the in vivo results, showing tumor-to-liver of 1.7 ± 0.1 and 9.0 ± 0.9, respectively for FNIR-Tag and s775z-labeled Nbs. (Fig.1) Similar findings were observed for the anti-HER2 and -CEA Nbs. As compared to Nbs labeled with a DOL1, Nbs labeled with on average 2 FNIR-Tag dyes showed higher mean fluorescent tumor signals, but no increased TBRs, because of a higher background, mainly in the liver. Nbs labeled with on average 2 s775z show similar results, albeit the increase in aspecific liver accumulation was more limited.

Conclusions:

FNIR-Tag- and s775z-labeled Nbs possess a clinically relevant biodistribution profile with rapid tumor visualization and low background signals. Thus, these dyes can be used as a platform technique for the development of translatable Nb-based tracers. We could not show a clear benefit for conjugating more than 1 dye per Nb. However, our data further underlines the importance of the chosen dye on the pharmacokinetic profile of a molecular tracer.

References

1. Hernot S, van Manen L, Debie P, Mieog JSD, Vahrmeijer AL. Latest developments in molecular tracers for fluorescence image-guided cancer surgery. Lancet Oncol. 2019;20(7):e354-e367. doi:10.1016/S1470-2045(19)30317-1
2. Debie P, Hernot S. Emerging fluorescent molecular tracers to guide intra-operative surgical decision-making. Front Pharmacol. 2019;10(MAY). doi:10.3389/fphar.2019.00510
3. Debie P, Van Quathem J, Hansen I, et al. Effect of Dye and Conjugation Chemistry on the Biodistribution Profile of Near-Infrared-Labeled Nanobodies as Tracers for Image-Guided Surgery. Mol Pharm. 2017;14(4):1145-1153.
4. Choi HS, Gibbs SL, Lee JH, et al. Targeted zwitterionic near-infrared fluorophores for improved optical imaging. Nat Biotechnol. 2013;31(2):148-153. doi:10.1038/nbt.2468
5. Choi HS, Nasr K, Alyabyev S, et al. Synthesis and in vivo fate of zwitterionic near-infrared fluorophores. Angew Chem Int Ed Engl. 2011;50(28):6258-6263. doi:10.1002/anie.201102459
6. Li D-H, Schreiber CL, Smith BD. Sterically Shielded Heptamethine Cyanine Dyes for Bioconjugation and High Performance Near-Infrared Fluorescence Imaging. Angew Chem Int Ed Engl. 2020;59(29):12154-12161. doi:10.1002/anie.202004449.
7. Luciano MP, Crooke SN, Nourian S, et al. A Nonaggregating Heptamethine Cyanine for Building Brighter Labeled Biomolecules. ACS Chem Biol. 2019;14(5):934-940. doi:10.1021/acschembio.9b00122

Oral Presentation

Disclosures: The authors have disclosed no financial interest.

068-Characterization of the Glutamate transporter GLT-1 and PS1/γ-secretase interaction by FLIM and EM in Alzheimer's disease

Presenter: Florian Perrin, Massachusetts General Hospital

Florian Perrin[1], Priyanka Sinha[2], Calina Glynn[2], Noe Quittot[2], Shane Mitchell[2], Oksana Berezovska[2]

[1]Massachusetts General Hospital, Charlestown, MA
[2]Massachusetts General Hospital, Boston, MA

Rational

Mutations in Presenilin 1 (PS1), the catalytic sub-unit of γ-secretase, cause early-onset familial Alzheimer's disease (fAD) by inducing a "closed" structural conformation in PS1 and production of longer Aβ species [1]. Interestingly, clinical data revealed that patients with presenilin mutation carriers have significantly higher incidence of epileptiform activity, suggesting that fAD PS1 mutations (Aβ-related or not) could contribute to hyperactivity [2]. We have recently discovered an interaction between PS1, and the major CNS glutamate transporter GLT-1/EAAT2 in AD context [3]. This interaction plays a role in GLT-1 trafficking and function where PS1 acts as a chaperone. This interaction is weakened in AD patients compared to control patients. Here we aim to investigate: i) Where the interaction site is located; ii) Designing a cell permeable peptide (CPP) to modulate this interaction iii) Establish a 3D structure of the GLT-1/PS1 interaction and CPP binding site by cryo-EM.

Methods

To identify the PS1/GLT-1 interaction site, fluorescence lifetime imaging microscopy assay (FLIM) has been used in intact cells *in vitro*. Based on protein structure and amino acids properties, several amino acids within GLT-1 and PS1 proteins that could potentially be the interaction sites have been mutated to alanine. Next, we sought to determine if it is possible to block these interaction sites using CPP. These CPPs present sequence from HIV and sequence from native GLT-1/PS1 proteins, coupled to a fluorophore for cells uptake monitoring. Finally, a protocol for GLT-1 and PS1 purification has been created to establish the cryo-EM structure of the PS1/GLT-1 complex and the exact binding site of the CPP.

Results

Based on the alanine mutants scanning performed by FLIM, we discovered two potential interaction sites in GLT-1 transmembrane domain (TM) 4 and TM5, while PS1 presents one interaction site in the TM6. The purification protocol allowed to observe the GLT-1/PS1 complexes by EM.

Conclusions

The identification of PS1/GLT-1 interaction sites are critical for modulation of both PS1 and GLT-1 function. CPP as drug could potentially induce functional changes in GLT-1 and PS1. The regulation of glutamate uptake in the synaptic cleft could be beneficial for controlling epileptiform activity in AD patients and beyond.

Reference

1. Berezovska O, Lleo A, Herl LD, Frosch MP, Stern EA, Bacskai BJ, Hyman BT (2005) Familial Alzheimer's disease presenilin 1 mutations cause alterations in the conformation of presenilin and interactions with amyloid precursor protein. The Journal of neuroscience: the official journal of the Society for Neuroscience 25: 3009-3017 Doi 10.1523/jneurosci.0364-05.2005
2. Larner AJ, Doran M (2006) Clinical phenotypic heterogeneity of Alzheimer's disease associated with mutations of the presenilin-1 gene. J Neurol 253: 139-158 Doi 10.1007/s00415-005-0019-5
3. Zoltowska KM, Maesako M, Meier J, Berezovska O (2018) Novel interaction between Alzheimer's disease-related protein presenilin 1 and glutamate transporter 1. Scientific reports 8: 8718 Doi 10.1038/s41598-018-26888-2n

Oral Presentation

Disclosures: The authors have disclosed no financial interest.

069-In vivo 31P-MRS reveals NAD deficiency in a mouse model of Alzheimer's disease

Presenter: Lin Z. Li, University of Pennsylvania

Lin Z. Z. Li[1], Kavindra Nath[2], Fernando Arias-Mendoza[3], He Nucleus N. Xu[4], Frances Jensen[3], Delia Talos[3]

[1]University of Pennsylvania
[2]University of Pennsylvania, Philadelphia, PA
[3]Perelman School of Medicine at the University of Pennsylvania, Philadelphia, PA
[4]University of Pennsylvania, Philadelphia

Nicotinamide adenine dinucleotide (NAD) is vital for maintaining brain energy homeostasis and decreases substantially with age and prominently in Alzheimer's disease (AD) [1, 2]. This NAD deficiency contributes to AD progression, while its supplementation normalizes the NAD redox status, mitigates neuropathology, and restores cognitive deficits in AD animal models [1-3]. NAD supplementation is under phase I/II clinical trials for treating AD. However, elucidation of the NAD's role in AD progression and the evaluation of the supplementation response are severely undercut by the lack of techniques to monitor NAD in vivo. It is unknown at which stage brain NAD starts to decline or how it changes with the disease course. Phosphorous-31 magnetic resonance spectroscopy (^{31}P-MRS) has been successfully applied to measure brain NAD indices (oxidized form NAD^{+}, reduced form NADH, and the redox ratio NAD^{+}/NADH) in both animals and human subjects *in vivo* [4-7]. Nevertheless, such measurements have not been reported in AD brains. We hypothesize that in vivo ^{31}P-MRS detects abnormal NAD metabolism in AD mouse models. Mice with five times familiar AD mutations (5XFAD) [8] and their wildtype (WT) littermates were scanned on a 9.4 T, 31 cm Bruker horizontal bore animal MR scanner, using a 11 mm ^{31}P surface coil and a 35 mm quadrature ^{1}H volume coil. ^{1}H-MRI was used to position a voxel (~150-200 mm^{3}) in the mouse brain to mainly cover the cerebrum although a slight contribution (~10-15%) of cerebellum was present. Multiple blocks of Image Selected In vivo Spectroscopy ^{31}P-MRS spectra were acquired every 21 min (time of repetition 4 s, number of acquisitions 40, 512 acquisition points, and bandwidth 4202 Hz). Individual raw data blocks were post-processed with a Lorentzian filter of 30 Hz and phase correction before summing

up the spectra [9]. By referencing the phosphocreatine peak at -2.5 ppm, the brain NAD^+, NADH, and αATPs were fit from the sum spectra (-8~-12.8 ppm) using Lorentzian functions [4, 6, 10]. The uridine diphosphate glucose or galactose around -12.3 ppm were below or comparable to the noise level and thus not included in the spectral fitting. Using αATP to represent the ATP level, we determined the brain NAD^+/ATP, NADH/ATP, (NAD^++NADH)/ATP, and NAD^+/(NAD^++NADH). We identified a significant decrease of brain NAD^+/ATP and the redox ratio NAD^+/(NAD^++NADH) in the 7-month 5XFAD mice compared to the age-matched WT (n=4/group). Furthermore, compared to WT, 5XFAD mouse brains exhibit cognitive deficits at 6-7 months. Thus, our data, demonstrating NAD deficiency in vivo for the first time, are correlating with the age-dependent cognitive dysfunction in AD reported in the literature. In a subgroup of the same mice (n=3/group), we performed the ^{31}P-MRS measurement again when they reached 9 months. This time the brain voxels were positioned to include the cerebrum only and avoid the cerebellum. At the 9 months, cerebral NADH trended higher, and the redox ratio was significantly lower in 5XFAD mice compared to WT mice. These in vivo data consistently support a depression of brain NAD and bioenergetics in the AD mice compared to WT mice. Taken together, our preliminary ^{31}P-MRS studies of AD mice demonstrated the feasibility of quantifying brain NAD in vivo longitudinally to differentiate AD from WT brains. Work is in progress to measure NAD redox status at young ages and establish the temporal profile of brain NAD as well as bioenergetics (ATP) during the full disease progression in AD mouse models.

Reference

1. Wang, X., et al., NAD+ in Alzheimer's Disease: Molecular Mechanisms and Systematic Therapeutic Evidence Obtained in vivo. Frontiers in Cell and Developmental Biology, 2021. 9(1960).
2. Lautrup, S., et al., NAD^+ in Brain Aging and Neurodegenerative Disorders. Cell Metabolism, 2019. 30(4): p. 630-655.
3. Hou, Y., et al., NAD(+) supplementation normalizes key Alzheimer's features and DNA damage responses in a new AD mouse model with introduced DNA repair deficiency. Proc Natl Acad Sci U S A, 2018. 115(8): p. E1876-E1885.
4. Lu, M., et al., Intracellular redox state revealed by in vivo (31) P MRS measurement of NAD(+) and NADH contents in brains. Magn Reson Med, 2014. 71(6): p. 1959-72.
5. Zhu, X.-H., et al., In vivo NAD assay reveals the intracellular NAD contents and redox state in healthy human brain and their age dependences. Proceedings of the National Academy of Sciences, 2015. 112(9): p. 2876-2881.
6. Kim, S.Y., et al., Redox dysregulation in schizophrenia revealed by in vivo NAD+/NADH measurement. Schizophr Bull, 2017. 43(1): p. 197-204.
7. de Graaf, R.A., et al., Detection of cerebral NAD(+) in humans at 7T. Magn Reson Med, 2017. 78(3): p. 828-835.
8. Oakley, H., et al., Intraneuronal β-Amyloid Aggregates, Neurodegeneration, and Neuron Loss in Transgenic Mice with Five Familial Alzheimer's Disease Mutations: Potential Factors in Amyloid Plaque Formation. The Journal of Neuroscience, 2006. 26(40): p. 10129-10140.
9. Skupienski, R., K.Q. Do, and L. Xin, In vivo (31)P magnetic resonance spectroscopy study of mouse cerebral NAD content and redox state during neurodevelopment. Sci Rep, 2020. 10(1): p. 020-72492.
10. Nath, K., et al., (31) P and (1) H MRS of DB-1 melanoma xenografts: lonidamine selectively decreases tumor intracellular pH and energy status and sensitizes tumors to melphalan. NMR Biomed, 2013. 26(1): p. 98-105.

Oral Presentation

Disclosures: The authors have disclosed no financial interest.

070-Pre-Clinical MRI radiomics and machine learning to predict survival after immunotherapy treatment

Presenter: Vlora Riberdy, Dalhousie University

Vlora Riberdy[1], Alessandro Guida[2], James Rioux[3], Kimberly Brewer[2]

[1]Dalhousie University
[2]Dalhousie University, Halifax
[3]Biotics Research Canada, Halifax, NS

Introduction:

Glioblastoma is an aggressive form of brain cancer with poor long-term survival[1]. Current methods of treatment involve surgical resection followed by radiation and/or chemotherapy[1]. However, survival is typically less than a year after diagnosis[1], with a two-year survival rate of 26-33%[2]. The use of novel immunotherapies in combination with temozolomide (TMZ) chemotherapy has shown promising results with glioblastoma[1,2]. Molecular magnetic resonance imaging (MRI) allows for treatment monitoring via longitudinal characterization of the tumour micro-environment. Magnetic Resonance Fingerprinting (MRF) is a specialized MR sequence capable of simultaneous T_1, T_2, and T_2^* relaxation measurements[3]. With these parameter maps we can simultaneously quantify the concentration of gadolinium and superparamagnetic iron-oxide based agents. With such a large amount of quantitative imaging data, analysis becomes more complex. A radiomics approach can simplify the task by representing a large multi-dimensional set of images with a much smaller set of engineered features[4,5]. Machine learning algorithms can then be applied to determine if there are any correlations between features and treatment outcomes. We can apply binary classifiers to the data based on survival metrics to determine if any features can be used as early markers of treatment success.

Methods:

Fifteen female mice C57BL/6 mice (5 mice/treatment group) were intracranially implanted with $5x10^4$ gl261 glioma cells. Treatment groups were as follows: 1) untreated/control, 2) treated with anti-PD-1 (200 µg/kg/mouse/dose every 3 days for up to 8 doses) or 3) treated with anti-PD-1 and TMZ (25 µg/kg/mouse/day for 10 days). Mice received MRI brain scans twice weekly (pre- and post-contrast) for up to 6 weeks. Scans included an anatomical T_2-weighted FSE and MRF (which generated T_1, T_2, T_2^*, gadolinium and iron concentration maps). Mice received an injection of 100 µL SPIO Rhodamine B (Biopal) 24 hours before the post-contrast scan and injections of MultiHance (gadobentate dimeglumine, Bracco) during the post-contrast scan prior to MRF imaging. Regions of interest were drawn outlining either the whole brain (brain ROI) and tumour (tumour ROI) contours for each mouse at each time point and were passed into the radiomics pipeline to extract approximately 100 features per image volume. These features were then passed into a logistic regression model with a binary classifier related to the survival endpoint. This classifier stated whether a subject survived to the study endpoint or not. Model performance was evaluated with a leave-one-group-out cross validation technique, to estimate accuracy, and a receiver operating characteristic (ROC) curve.

Results:

Using all 100 of the extracted features, we tested each scan type and found the best performance was obtained from the T_2^* tumour ROI data with a prediction accuracy of 76% and an area under the curve (AUC)

of the ROC curve of 0.74. We are currently investigating whether earlier time points can also yield predictive features with similar accuracy.

Conclusions:

In this preliminary study, we examined the use of radiomics and machine learning on preclinical MRI data to predict survival outcomes in female mice treated for glioblastoma. Further optimization of this algorithm will involve feature selection to remove redundant features, which helps avoid overfitting and testing additional classifiers related to flow cytometry data. We will also be expanding this methodology to male mice to explore potential sex-based differences.

Reference

1. Walid M et al. Prognostic Factors for long-term survival after glioblastoma. Perm J. 2008;12(4).
2. Fernandes C et al. Current standards of care in glioblastoma. In: Glioblastoma. Codon Publications. 2017;197-241.
3. Marriott A, et al. Simultaneous quantification of SPIO and gadolinium contrast agents using MR fingerprinting. MRI. 2021;79:121-129.
4. Gillies RJ, Kinahan PE, Hricak H. Radiomics: Images are more than pictures, they are data. Radiology. 2016:278:563-577.
5. Kniep HC, Madesta F, Schneider T, Hanning U, Schonfeld MH, Schon G, Fiehler J, Gauer T, Werner R, Gellissen S. Radiomics of brain MRI: utility in prediction of metastatic tumor type. Radiology. 2019;290:479-487.

Oral Presentation

Disclosures: The authors have disclosed no financial interest.

071-Promoting Cancer Nanomedicine Clinical Translation via Imaging, Biopsy Biomarkers and Machine Learning

Presenter: Twan Lammers, RWTH Aachen University Hospital

Twan Lammers

RWTH Aachen University Hospital, Aachen, Germany

Introduction:

Nanomedicine formulations, such as liposomes and micelles, are extensively used for tumor-targeted drug delivery. To promote the efficiency of cancer nanomedicine clinical translation, probes and protocols for patient stratification are urgently needed [1]. It was recently demonstrated that theranostic polymeric micelles enable EPR monitoring during treatment [2], and can be used to visualize and quantify nanomedicine tumor targeting in patients [3]. Reasoning that radionuclide-based imaging may not be optimal for clinical translation and routine use, we set out to explore tumor tissue biomarkers for cancer nanomedicine patient stratification.

Methods:

Tumor-bearing mice (A431, MLS, CT26) were injected with fluorophore-labeled polymeric nanocarriers and tumor accumulation was imaged via CT-FMT (Fig. 1a). Histological stainings were performed to screen for tissue biomarkers and evaluated by gradient tree boosting-based machine learning. The most important features, i.e. blood vessels and macrophages, were verified in 10 additional tumor models, visualizing and quantifying the tumor accumulation of doxorubicin-loaded liposomes (Fig. 2a,b). Moreover, tumor tissue derived from head and neck, breast and lung cancer patients from the RWTH Aachen Biobank was histologically evaluated, and features were correlated with the accumulation patterns of radiolabeled liposomes visualized and quantified in patients with similar types of cancer [4].

Results:

Polymer accumulation in three initial tumor models varied between 4 and 11 %ID (Fig. 1b,c). More than 20 histological biomarkers in tumors were stained, quantified and correlated with polymer tumor accumulation (Fig. 1d-i). The prominence of blood vessels (CD31) and macrophages (F4/80) as the most important tissue biomarkers was confirmed by machine learning (Fig. 1j-l). Upon scoring blood vessels and macrophages in 10 additional tumor models, tumors with high vs. low levels of liposome tumor accumulation could be clearly differentiated (Fig 2a-f). This notion was validated in a clinical data set, showing that blood vessel and macrophage densities in patient tumor biopsies correlate well with liposome tumor targeting values previously reported in the literature (Fig. 2g-k; [4]).

Conclusion:

We show that histopathological assessment of tumor tissue biopsy biomarkers can be employed to predict nanomedicine tumor accumulation in mouse models and patients. This strategy expands the theranostic armamentarium to promote cancer nanomedicine patient stratification and clinical translation.

Reference

1. Van der Meel, R., et al., Smart cancer nanomedicine. Nature Nanotechnology 14, 1007-1017 (2019)
2. Biancacci, I., et al Monitoring EPR effect dynamics during nanotaxane treatment with theranostic polymeric micelles. Advanced Science e2103745 (2022)
3. Miedema, I., et al. PET-CT imaging of polymeric nanoparticle tumor accumulation in patients. Advanced Materials e2201043 (2022)
4. Harrington, K., et al. Effective targeting of solid tumors in patients with locally advanced cancers by radiolabeled pegylated liposomes. Clinical Cancer Research 7, 243-54 (2001)

Oral Presentation

Disclosures: The authors have disclosed no financial interest.

072-PET imaging of demyelination in the human brain with the radiotracer [18F]3F4AP: A first-in-human study in healthy controls and subjects with multiple sclerosis

Presenter: Nicolas Guehl, Massachusetts General Hospital

Nicolas J. Guehl[1], Yang Sun[1], Andrew Russo[1], Karla M. Ramos Torres[1], Maeva Dhaynaut[1], Eric Klawiter[1], Georges El Fakhri[2], Marc D. Normandin[3], Pedro Brugarolas[1]

[1]Massachusetts General Hospital, Boston, MA
[2]Massachusetts General Hospital
[3]Gordon Center for Medical Imaging (MGH/HMS), Boston, MA

Introduction:

MRI is the gold standard for imaging demyelinating diseases as it offers excellent sensitivity to brain lesions and high resolution, however, MRI lacks specificity to demyelination, inflammation and axonal loss and

it is not fully quantitative[1,2]. [^{18}F]3F4AP is a PET tracer based on the multiple sclerosis (MS) drug 4-aminopyridine that binds to K^+ channels on demyelinated axons and may provide a specific and quantitative marker of demyelination[3]. We previously demonstrated that [^{18}F]3F4AP can detect chemically-induced demyelinated lesions in rodent models as well as a focal traumatic brain injury in a rhesus macaque[3,4]. Given these promising findings, we recently advanced this tracer to human studies. Here we report the first brain imaging results with [^{18}F]3F4AP in healthy volunteers and subjects with MS.

Methods:

Three healthy control subjects (2 females and 1 male) and three subjects with MS (1 female and 2 males) underwent a 120 min dynamic PET acquisition on a GE Discovery MI PET/CT starting with a bolus injection of [^{18}F]3F4AP. Mean injected activity was 8.16 mCi (range: 7.13-10.19 mCi). Radioactivity concentration in whole-blood (WB) and total plasma (PL) was measured throughout the duration of the scan and radiometabolite analysis was performed on selected plasma samples to derive individual metabolite-corrected arterial input functions for subsequent kinetic modeling analysis. Participants also underwent a structural T1-weighted sequence for anatomical reference (pre and post Gadolinium contrast), T2-FLAIR. Structural MR and dynamic PET images were aligned to the Montreal Neurological Institute (MNI) template space for extraction of regional time activity curves. Various compartment models as well as the Logan graphical method with arterial plasma input function were investigated for determination of the total volume of distribution V_T.

Results:

Radioactivity time courses measured in WB and PL were consistent across subjects and WB-to-PL ratio was 0.88 ± 0.01 after 15 min (range: 0.84-0.94). Relatively rapid *in vivo* metabolism was observed by Radio-HPLC analysis with on average 31% (range 24-34%) of radioactivity corresponding to the parent compound at 90 min post tracer injection. In the brain of control subjects, [^{18}F]3F4AP peaked quickly (2-4 SUV in white matter and 5-7 SUV in gray matter at ~3 min) and was followed by fast washout with little heterogeneity across brain regions after 20 min. A one-tissue (1T) model was found to be sufficient to describe [^{18}F]3F4AP kinetics in the healthy brain tissues and provided stable V_T estimates ranging from 1.52-1.69 mL.cm^{-3} in gray matter and 1.22-1.29 mL.cm^{-3} in white matter. In one MS subject, [^{18}F]3F4AP was able to clearly detect two of the lesions seen on the T2-FLAIR and T1-weighted MR, which were not Gd positive. In the two lesions, [^{18}F]3F4AP kinetics was best described by a two-tissue (2T) model and were slower compared to any other brain regions, thus leading to elevated V_T values (2.24 and 2.26 mL. cm^{-3}).

Conclusion: [

^{18}F]3F4AP readily entered the human brain, displayed fast kinetics in healthy brain tissues, and was able to clearly identify two of the MS lesions seen on the MR sequences on one of the MS subjects. More studies are underway to elucidate the nature of the MR lesions detected by [^{18}F]3F4AP PET. The fact that [^{18}F]3F4AP PET only accumulated in a subset of the MR lesions may suggest specificity towards demyelinated lesions, which could be very useful for understanding the contribution of demyelination in various neurological diseases as well as for monitoring remyelinating therapies.

Acknowledgment This project was financially supported by NIH grants: R01NS114066, T32EB013180, S10OD026987, S10OD018035, and P41EB022544; and the Innovation award from the Polsky Center from University of Chicago.

Reference

1. Filippi M & Rocca MA MR imaging of multiple sclerosis. Radiology 259, 659–681, doi: 10.1148/radiol.11101362 (2011)
2. Fox RJ, Beall E, Bhattacharyya P, Chen JT & Sakaie K Advanced MRI in multiple sclerosis: current status and future challenges. Neurol Clin 29, 357–380, doi: 10.1016/j.ncl.2010.12.011 (2011).
3. Brugarolas P et al. Development of a PET radioligand for potassium channels to image CNS demyelination. Sci Rep 8, 607, doi: 10.1038/s41598-017-18747-3 (2018).
4. Guehl NJ et al. Evaluation of the potassium channel tracer [18F]3F4AP in rhesus macaques. J Cereb Blood Flow Metab, 271678X20963404, doi: 10.1177/0271678X20963404 (2020).

Oral Presentation

Disclosures: The authors have disclosed no financial interest.

073-TRAIL-armoring enhances CAR-T cell immunotherapy in Malignant Pleural Mesothelioma

Presenter: Alessia Volpe, Memorial Sloan Kettering Cancer Center

Alessia Volpe[1], Mayuresh M. Mane[1], Juan Zurita[1], Larissa Shenker[1], Maxim A. Moroz[2], Anna Moroz[3], Prasad S. Adusumilli[1], Dmitri V. Rozanov[4], Vladimir Ponomarev[1]

[1]*Memorial Sloan Kettering Cancer Center, New York, NY*
[2]*Stanford University, Fremont, United States*
[3]*Stanford University, Stanford, CA*
[4]*Oregon Health and Science University, Portland, OR*

Introduction:

Malignant pleural mesothelioma is the most common type of mesothelioma in the US, accounting for >150,000 new cases each year. Mesothelin (MSLN) expressing mesothelioma is less likely to respond to conventional treatments but does show a long-lasting response to MSLN-specific chimeric antigen receptor (CAR)-T cells alone or as a combination treatment.[1] However, this approach fails to treat MSLN-negative cells. The TNF-related apoptosis-inducing ligand (TRAIL) exhibits a strong anti-tumor activity in preclinical and in clinical settings.[2] Here we describe a synergistic theranostic approach for tumor sensitization to adoptive T cell immunotherapies combining translatable membrane-bound and soluble TRAILs with MSLN-directed CAR-T therapy in a model of MSTO-211H malignant pleural mesothelioma.

Methods:

Membrane-bound (MB-) and a soluble (s-) TRAILs with active trimerization motifs coupled with a MSLN-directed CAR (M28z) were retrovirally transduced into human T lymphocytes and cytolytic activity was assessed by cell killing assays. CAR-T cells and MSLN+/- targets were engineered with membrane anchored Cypridina luciferase (maCluc), Click Beatle Green luciferase (CBG) and Renilla luciferase (Rluc) bioluminescence reporters, respectively, thereby enabling long-term *in vivo* whole-body bioluminescence imaging (BLI) of all three transduced populations within the same animal.[3] MSTO-211H human metastatic pleural mesothelioma tumors with heterogeneous MSLN expression were intraperitoneally injected into young adult male NSG mice, followed by regional administration 5x10^5 CAR-T cells at day 6 post tumor establishment. *In vivo* BLI imaging of MSLN+/- tumors allowed a reliable assessment of TRAIL-armored MSLN-directed CAR-T cells therapeutic efficacy, thereby enabling to differentiate responders from mild and non-responders early during treatment using

a lesion-based BLI imaging quantification approach. The latter also correlated to CAR-T cell kinetics.

Results:

In line with previous findings,[4] all MSLN-targeted CAR-T cells killed MSLN+ cells due to anti-MSLN CAR:MSLN engagement **(Fig.1 A)**, with MB- and s-TRAIL M28z CAR-T cells showing a remarkably enhanced cytolytic activity. **(B)** Importantly, only MB- and s-TRAIL M28z CAR-T cells were able to kill also MSLN- cells. **(C)** Triple BLI imaging revealed MSLN+ tumor regression 22 days post CAR-T cells administration in all groups **(Fig.1 C**/top**)**. However, M28z failed to cure MSLN- tumor, resulting in its progression and mice death **(C**/mid**)**. Only animals treated with MB- and s-TRAIL M28z CAR-T cells showed a regression of MSLN- tumor burden due to the TRAIL-mediated tumor targeting and proapoptotic effect **(C**/mid**)**, also correlating to CAR-T cell accumulation at the site of the lesion **(C**/bottom**)**. **(D)** Lesion-based imaging BLI imaging quantification allowed stratification of treated mice and revealed the inverse correlation between tumor burden and CAR-T cell retention in the responders group (top). Notably, only mice treated with MB- and s-TRAIL M28z CAR-T cells resulted in reduced tumor burden as a result of CAR-T cells residing at the lesion (bottom). **(E)** 38% of the mice treated with s-TRAIL M28z CAR-T cells were still alive 66 days post-treatment compared to the untreated group (median survival: 72 vs 27 days; p<0.0001).

Conclusions:

We employed the real-time imaging paradigm to show that TRAIL-armored mesothelin-specific CAR-T cells are superior to the already therapeutic and trialled MSLN-targeted CAR-T cells by providing additional proapoptotic stimuli to both antigen positive and negative tumor targets, thereby enhancing anti-tumor targeting and increasing overall response. TRAIL-armored CAR-T cell therapy is a readily translatable strategy rendering mesothelioma patients with heterogeneous mesothelin expression more amenable to adoptive T cell therapy, thereby improving outcomes.

Acknowledgements: This work was supported by the EIO Fellowship Award from the Center for Experimental Immuno-Oncology and the Tow Foundation Postdoctoral Fellowship from the MSKCC Center for Molecular Imaging and Nanotechnology to A.V., as well as an NIH/NCI grant to V.P.

Reference

1. Adusumilli PS, Zauderer MG, Riviere I, et al. A phase I trial of regional mesothelin-targeted CAR T-cell therapy in patients with malignant pleural disease, in combination with the anti-PD-1 agent pembrolizumab. Cancer discovery 2021 doi: 10.1158/2159-8290.Cd-21-0407 [published Online First: 2021/07/17].
2. Bellail AC, Qi L, Mulligan P, et al. TRAIL agonists on clinical trials for cancer therapy: the promises and the challenges. Rev Recent Clin Trials 2009;4(1):34-41. doi: 10.2174/157488709787047530 [published Online First: 2009/01/20].
3. Moroz MA, Zurita J, Moroz A, et al. Introducing a new reporter gene, membrane-anchored Cypridina luciferase, for multiplex bioluminescence imaging. Molecular therapy oncolytics 2021;21:15-22. doi: 10.1016/j.omto.2021.03.004 [published Online First: 2021/04/15].
4. Adusumilli PS, Cherkassky L, Villena-Vargas J, et al. Regional delivery of mesothelin-targeted CAR T cell therapy generates potent and long-lasting CD4-dependent tumor immunity. Science translational medicine 2014;6(261):261ra151. doi: 10.1126/scitranslmed.3010162 [published Online First: 2014/11/08].

Oral Presentation

Disclosures: The authors have disclosed no financial interest.

074-A Novel Radiopharmaceutical, [18F]fluoromannitol, for Imaging Diverse Pathogenic Bacteria in vivo

Presenter: Spenser Simpson, St. Jude Children's Research Hospital

Spenser R. Simpson[1], Alexandria Kesterson[1], Justin Wilde[2], Zoraiz Qureshi[3], Bijoy Kundu[4], Mark Simons[5], Kiel Neumann[1]

[1]*St. Jude Children's Research Hospital, Memphis, TN*
[2]*University of Virginia*
[3]*University of Virginia, Charlottesville*
[4]*University of Virginia, Charlottesville, VA*
[5]*Uniformed Services University of the Health Sciences*

Introduction:

Infectious disease remains the main cause of morbidity and mortality throughout the world(*1*). Of growing concern is the rising incidence of multidrug-resistant bacteria(*2,3*). Many of these bacterial infections are hospital-acquired and have prompted the Center for Disease Control and Prevention (CDC) in 2019 to reclassify several pathogens as urgent threats, its most perilous assignment(*4*). Consequently, there is an urgent need to improve the clinical management of bacterial infection, via new methods to specifically identify bacteria and monitor antibiotic efficacy *in vivo*. While biopsy remains the current gold standard for confirming the presence and identity of a pathogenic microorganisms, deep-seated infections that are difficult to access or identify often rely upon non-invasive imaging techniques. PET imaging utilizing [^{18}F]FDG is increasingly used for identification purposes; however, it is unable to distinguish active infection from cancer or inflammation. Many radiopharmaceuticals have recently been reported to address this challenge, such as sugar/sugar alcohol metabolism(*5-7*), folic acid biosynthesis(8,*9*), D-amino acid metabolism(*10,11*), and labeled antibiotics(*12*). While these imaging agents represent monumental advances, there is a persistent need for imaging agents that meet the challenges of clinical infectious diseases practice; a major advance would be an imaging agent with broad bacterial strain sensitivity, optimal PK for contrast, and widely deployable/available for clinical use. We have developed a novel radiopharmaceutical, [^{18}F]fluoromannitol ([^{18}F]FMtl), that is incorporated into a diverse set of pathogens with high specificity and sensitivity and meets these metrics.

Methods:

[^{18}F]FMtl was synthesized from a 3-step, two-pot radiosynthesis from a commercially-available chemical precursor. Chemical and radiochemical purity were determined by HPLC. *In vitro* assays were performed using *S.aureus*, *A.baumannii*, and *P.aeruginosa* serial bacterial strains received from the Naval Medical Research Center derived from military service members with combat wounds. Commercially available strains were purchased from ATCC. Murine myositis models were generated by inoculating the right triceps brachii with a live strain of bacteria and the left triceps brachii with 10X heat killed bacteria. [^{18}F]FMtl was administered via tail vein 10-12 hours post infection. Dynamic and static *in vivo* imaging were performed with a Bruker Albira Si Trimodal scanner and imaging results were validated post imaging via biodistribution and CFU analysis e*x vivo*. Parametric total body rate of tracer uptake (Ki) maps with partial volume correction were computed using methods as described(*13*).

Results/Discussion:

[^{18}F]FMtl was successfully synthesized and isolated in >99% radiochemical purity in a 23±2% radiochemical yield (n=14, EOS). *In vitro* assays showed uptake of [^{18}F]FMtl in all strains tested with the exceptions of *P.aeruginosa* and *E.faecium*. *In vivo* studies showed that [^{18}F]FMtl was specifically accumulated in the site of infection in both gram-positive and gram-negative strains, whereas [^{18}F]FDG was predictably unable to distinguish active infection from sterile inflammation. Dynamic imaging revealed rapid accumulation and significant differences in PET signal in as little as 5 minutes post-injection in both gram-positive (*S.aureus*) and gram-negative (*E.coli*) strains. *Ex vivo* gamma counting confirmed the increased accumulation of PET signal in the infected tissue compared to inflamed tissue. *Ex vivo* biodistribution showed the highest nonspecific accumulation of [^{18}F]FMtl were in the kidneys and bladder, which is consistent with PET imaging data demonstrating that any [^{18}F]FMtl not accumulated at the site of infection is rapidly cleared through the urinary tract. *In vivo* data indicate that using the clinical standard semi-quantitative analysis, SUV, [^{18}F]FMtl can reliably detect as little as $5\log_{10}$CFU/mL of bacteria.

Conclusions:

We synthesized and characterized a novel radiopharmaceutical, [^{18}F]FMtl. The production is straightforward, robust, and high yielding. We showed the uptake of [^{18}F]FMtl in a broad range of gram positive and gram negative bacteria *in vitro*. *In vivo* experiments showed the selectivity of [^{18}F]FMtl to detect active infections over sterile inflammation in both gram positive (*S.aureus*) and gram negative (*E.coli*) bacteria.

Reference

1. G. A. Roth et al., Global, regional, and national age-sex-specific mortality for 282 causes of death in 195 countries and territories, 1980–2017: a systematic analysis for the Global Burden of Disease Study 2017. The Lancet 392, 1736-1788 (2018).
2. P. W. Stone, Economic burden of healthcare-associated infections: an American perspective. Expert Review of Pharmacoeconomics & Outcomes Research 9, 417-422 (2009).
3. A. A. Ordonez et al., Molecular imaging of bacterial infections: Overcoming the barriers to clinical translation. Science Translational Medicine 11, eaax8251 (2019).
4. Antibiotic resistance threats in the United States, 2019 (2019).
5. X. Ning et al., PET Imaging of Bacterial Infections with Fluorine-18-Labeled Maltohexaose. Angewandte Chemie International Edition 53, 14096-14101 (2014).
6. E. A. Weinstein et al., Imaging Enterobacteriaceae infection in vivo with ^{18}F-fluorodeoxysorbitol positron emission tomography. Science Translational Medicine 6, 259ra146-259ra146 (2014).
7. G. Gowrishankar et al., Specific Imaging of Bacterial Infection Using 6″-^{18}F-Fluoromaltotriose: A Second-Generation PET Tracer Targeting the Maltodextrin Transporter in Bacteria. Journal of Nuclear Medicine 58, 1679-1684 (2017).
8. C. A. Mutch et al., [11C]Para-Aminobenzoic Acid: A Positron Emission Tomography Tracer Targeting Bacteria-Specific Metabolism. ACS Infectious Diseases 4, 1067-1072 (2018).
9. Z. Zhang et al., Positron Emission Tomography Imaging with 2-[18F]F-p-Aminobenzoic Acid Detects Staphylococcus aureus Infections and Monitors Drug Response. ACS Infectious Diseases 4, 1635-1644 (2018).
10. K. D. Neumann et al., Imaging Active Infection in vivo Using D-Amino Acid Derived PET Radiotracers. Scientific Reports 7, 7903 (2017).
11. M. F. L. Parker et al., Sensing Living Bacteria in Vivo Using d-Alanine-Derived 11C Radiotracers. ACS Central Science 6, 155-165 (2020).
12. M. A. Sellmyer et al., Bacterial infection imaging with [^{18}F] fluoropropyl-trimethoprim. Proceedings of the National Academy of Sciences 114, 8372-8377 (2017).
13. Q. Huang, J. C. Massey, K. Mińczuk, J. Li, B. K. Kundu, Phys Med Biol 64, 165010 (2019).

Oral Presentation

Disclosures: The authors have disclosed no financial interest.

075-A Multichannel Joint Reconstruction Technique Allows for Artifact-free Focused Small Field of View Magnetic Particle Imaging

Presenter: Julia Gevaert, Western University

Julia J. Gevaert[1], Corby Fink[2], Donna M. Fong[3], Justin J. Konkle, Patrick -. Goodwill, Jimmy Dikeakos[4], Gregory A. Dekaban[5], Paula Foster[6]

[1]*Western University, London*
[2]*Robarts Research Institute, London, Ontario*
[3]*Magnetic Insight, ALAMEDA, CA*
[4]*Western University, London, Ontario*
[5]*Robarts Research Institute, London, Ontario, CANADA, ON*
[6]*Robarts Research Institute, London*

Introduction:

Magnetic Particle Imaging (MPI) directly detects superparamagnetic iron oxide (SPIO) labeled cells. We have used MPI to detect SPIO-labeled dendritic cells (DC) migrated to the popliteal lymph nodes (pLN) after injection into the hind footpads. However, in some cases the low pLN signal could not be resolved from nearby higher footpad signal where window leveling to pLN signal oversaturated the footpad signal (Fig. 1C). The same limitation occurs when SPIO is injected intravenously, accumulates in the liver, and prevents isolation of regions of interest with lower signals. Previous studies have reported on the issue of resolving a wide range of differing iron concentration.[1–4] A small focused field of view (FOV), to exclude high sources of nearby signal, cannot be performed with the standard reconstruction algorithm equipped on the Momentum™ MPI scanner because it is assumed that there is no signal at the edge of the FOV and these values are set to zero for each line along the transmit axis. However, when there is signal at the FOV edge, an inverted negative artifact is created (Suppl. Fig. 3B). The multichannel joint reconstruction method uses an iterative reconstruction technique to recover edge information using information from an orthogonal axis, preventing this artifact and allowing the user to prescribe a small FOV on the region of interest. Here we describe the implementation of this method to detect and quantify DC migration in mice.

Methods:

Mouse bone marrow-derived immature DC were labeled with Synomag-D™ (Micromod GmbH).[5–8] Synomag-D+ DC (3 x 10^5 (n = 3) or 5 x 10^5 (n = 3)) were injected into each mouse hind footpad. MPI was conducted on day 0 and 2 using the Momentum™ scanner (Magnetic Insight, Inc.) to identify migrated DC to the draining popliteal lymph nodes (pLNs). For day 0, 2, MPI was done using a 3.0 T/m selection field gradient, drive field strengths 20 mT (X) and 23 mT (Z), and a 12 x 6 cm FOV. Additionally, on day 2, MPI was done using a 2 cm small FOV centered on the pLNs with the same parameters and with a stronger gradient strength (5.7 T/m). Multichannel joint reconstruction

was used for 2 cm FOV images which uses an iterative technique with replication, convolution, and edge pinning operations to recover fully constructed images for each channel and transmit direction.

Results:

Signal from Synomag-D+ DC in the left and right hind footpads was detected on Day 0 MPI in all mice (Fig. 1A, B). On day 2, signal was resolved and quantified in the pLN for 5/6 mice (left) and 4/6 mice (right) when using a 12 cm FOV and standard reconstruction (Fig 1C). When using a 2 cm FOV focused on the pLNs with the higher gradient strength and the new reconstruction method the signal could be resolved and quantified in all pLNs (Fig. 1D-F). The mean iron content was 15 ng or 3400 DC. The use of a 2 cm FOV also reduced the scan time from 30 to 15 minutes. Ex vivo MPI showed signal in all excised pLNs, validating the presence of migrated DC (Fig. 1G).

Conclusion:

Here we describe the implementation of a multichannel joint reconstruction method on the Momentum™ system which will allow users to resolve and quantify discrete sources of signal without interference from proximate, varying iron concentrations which are not of interest. We have used this approach to quantify DC migration to lymph nodes without interference from the large signal at the injection site. Since the number of migrated DC is proportional to the anti-tumor response in immunotherapy the ability to measure this robustly is essential.

Reference

1. Gevaert, J. J., Fink, C., Dikeakos, J. D., Dekaban, G. A. & Foster, P. J. Magnetic Particle Imaging Is a Sensitive In Vivo Imaging Modality for the Detection of Dendritic Cell Migration. Mol Imaging Biol (2022) doi:10.1007/s11307-022-01738-w.
2. Franke, J. et al. System Characterization of a Highly Integrated Preclinical Hybrid MPI-MRI Scanner. IEEE Transactions on Medical Imaging 35, 1993–2004 (2016).
3. Graeser, M., Knopp, T., Sattel, T. F., Gruettner, M. & Buzug, T. M. Signal separation in magnetic particle imaging. in 2012 IEEE Nuclear Science Symposium and Medical Imaging Conference Record (NSS/MIC) 2483–2485 (2012). doi:10.1109/NSSMIC.2012.6551566.
4. Herz, S. et al. Selective Signal Suppression in Traveling Wave MPI: Focusing on Areas with Low Concentration of Magnetic Particles. International Journal on Magnetic Particle Imaging 3, (2017).
5. Boberg, M. et al. Simultaneous imaging of widely differing particle concentrations in MPI: problem statement and algorithmic proposal for improvement. Phys. Med. Biol. 66, 095004 (2021).
6. Thu, M. S. et al. Self-assembling nanocomplexes by combining ferumoxytol, heparin and protamine for cell tracking by magnetic resonance imaging. Nature Medicine 18, 463–467 (2012).
7. De Chickera, S. N. et al. Labelling dendritic cells with SPIO has implications for their subsequent in vivo migration as assessed with cellular MRI. Contrast Media & Molecular Imaging 6, 314–327 (2011).
8. de Chickera, S. et al. Cellular MRI as a suitable, sensitive non-invasive modality for correlating in vivo migratory efficiencies of different dendritic cell populations with subsequent immunological outcomes. Int Immunol 24, 29–41 (2012).

Oral Presentation

Disclosures: The authors have disclosed no financial interest.

076-A Preliminary Study on Hyperpolarized 13C Whole-Abdomen Metabolic Imaging of a Pancreatic Cancer Patient

Presenter: Guannan Zhang, Memorial Sloan Kettering Cancer Center

Guannan Zhang[1], Kofi Deh[2], Angela Hijin Park, Nadia Bragagnolo[3], Serge K. Lyashchenko[1], Shake Ahmmed, Avigdor Leftin[4], Vesselin Miloushev, Marius Mayerhoefer, Charles H. Cunningham[5], Kayvan Keshari[2]

[1]Memorial Sloan Kettering Cancer Center, New York
[2]Memorial Sloan Kettering Cancer Center, New York, NY
[3]Sunnybrook Research Institute
[4]Memorial Sloan Kettering Cancer Center, NY, NY
[5]Sunnybrook Research Institute, Toronto, ON

Introduction:

Detection and treatment of pancreatic ductal adenocarcinoma (PDAC) remains a major challenge in clinics due to the aggressiveness of the disease associated with a high potency of metastatic dissemination to adjacent organs.[1] Abdominal magnetic resonance imaging (MRI) plays an important role in the diagnosis of PDAC. The large field-of-view of whole-abdomen coverage offers the opportunity of evaluating abdominal pathology for PDAC patients and therefore allowing the detection of metastatic lesions in the abdomen. Yet, one of the challenges of MRI that limits its widespread applicability is the inherently low sensitivity of magnetic resonance at thermal equilibrium. Hyperpolarization by dissolution dynamic nuclear polarization is an emerging technique that significantly improves the signal to noise ratio by several orders of magnitude. This technique has been successfully developed in conjunction with MRI to image metabolism in humans by administering hyperpolarized [1-^{13}C] pyruvate.[2] Here, we show dynamics of hyperpolarized [1-^{13}C] pyruvate in the abdomen of a PDAC patient, demonstrating the applicability of the method to detect the spread of metastatic cancer.

Methods:

All MR data were acquired on a wide-bore 3 T scanner (MR750w, GE healthcare). T_1 – weighted images were acquired for anatomical reference using a spin-echo sequence. The jacket coil (Clinical MR Solutions, Figure a) was custom-designed for ^{13}C hyperpolarization studies. It was used for excitation and detection on ^{13}C. Immediately following the injection, hyperpolarized ^{13}C images were acquired using a spectrally-selective 3D echo planar imaging (EPI) sequence (Table 1).[3]

Results:

The metabolite maps of hyperpolarized [1-^{13}C] pyruvate and [1-^{13}C] lactate summed through time were overlaid with a T_1-weighted anatomical reference where the slice containing the pancreas is displayed in Figure b. Pyruvate signals were highest in the kidneys and the aorta. Highest lactate signals were further exhibited in the kidneys. Due to an increased glycolytic rate in the presence of the pancreatic tumor, lactate was accumulated in the pancreas, resulting in a strong lactate signal and a higher k_{PL} in the tumor compared to the surrounding tissues. The use of D_2O as a dissolution solvent leads to *in vivo* $T_{1,pyr}$ ~ 50 s which is longer than that (~ 30 s) using H_2O.[4] Furthermore, the time-to-peak and k_{PL} were compared in different organs as shown in Figure c. No significant difference was observed in time-to-peak pyruvate and lactate between organs which is ~ 5-15 s. Liver exhibits the highest k_{PL} (0.022 s^{-1}) compared to other organs which is consistent with the literature results.[5] The ~ 3.5 times higher k_{PL} in pancreas (0.021 s^{-1}) compared to the literature value (~ 0.006 s^{-1}) is probably due to the presence of the tumor.

Discussion:

Hyperpolarized pyruvate imaging have been safely performed in humans for cancer studies. These studies investigated cancer metabolism in a region of interest within the body by monitoring the change of the hyperpolarized metabolic flux. However, for patients diagnosed with metastatic cancer, it often requires to image for multiple regions of interest since metastases in cancer spans a wide range of the body and therefore results in lesions in multiple areas. Here we present the preliminary work on acquiring dynamics of hyperpolarized [1-^{13}C] pyruvate in the abdomen of a PDAC patient, with the purpose of demonstrating the applicability of the method to detect spread of metastatic cancer. The jacket coil provides coverage and ^{13}C RF excitation over the whole abdominal area and therefore allowing to detect lesions in multiple areas. Additionally, this is the first study that a patient was injected using hyperpolarized [1-^{13}C] pyruvate in D_2O (Table 2). The observed longer $T_{1,pyr}$ *in vivo* offers opportunities to capture the complete dynamics of pyruvate perfusion and metabolism for future studies.

Reference

1. Ayres Pereira, M. & Chio, I. I. C. Metastasis in Pancreatic Ductal Adenocarcinoma: Current Standing and Methodologies. Genes 11, 6 (2019).
2. Wang, Z. J. et al. Hyperpolarized 13C MRI: State of the Art and Future Directions. Radiology 291, 273–284 (2019).
3. Geraghty, B. J., Lau, J. Y. C., Chen, A. P. & Cunningham, C. H. Dual-Echo EPI sequence for integrated distortion correction in 3D time-resolved hyperpolarized 13C MRI. Magn. Reson. Med. 79, 643–653 (2018).
4. Gordon, J. W., Chen, H., Dwork, N., Tang, S. & Larson, P. E. Z. Fast Imaging for Hyperpolarized MR Metabolic Imaging. J. Magn. Reson. Imaging 53, 686–702 (2021).
5. Lee, P. M. et al. Whole-Abdomen Metabolic Imaging of Healthy Volunteers Using Hyperpolarized [1-13C] pyruvate MRI. J. Magn. Reson. Imaging. (2022). DOI: 10.1002/jmri.28196

Oral Presentation

Disclosures: The authors would like to disclose that HP pyruvate is an investigational device.

077-An MRI-based Titi Monkey Brain Atlas for Analyzing Pair-bonding Studies

Presenter: Sarah Tam, University of California, Davis

Sarah Tam[1], Pauline Zablocki-Thomas[2], Sara Freeman[3], Karen Bales[4], Abhijit J. Chaudhari[5], Brad A. Hobson[5]

[1]*University of California, Davis, Davis*
[2]*University of California Davis, Davis, CA*
[3]*Logan, UT*
[4]*University of California, Davis, Davis, CA*
[5]*University of California, Davis, Sacramento, CA*

Introduction:

In vivo molecular neuroimaging in coppery titi monkeys (*Plecturocebus cupreus*) using positron emission tomography (PET) offers a unique opportunity to study the neurobiology of pair-bonding that is highly relevant to human behavior [1]. These socially monogamous South American monkeys display adult pair-bonding, a form of attachment which is not exhibited by commonly imaged laboratory models such as rodents or rhesus monkeys. Previous studies using PET and magnetic resonance imaging (MRI) have characterized changes in titi monkey brain metabolism [2] and neurotransmitter pathways in response to behavioral stimuli [3,4]. However, dedicated tools for the efficient analysis of titi monkey imaging data are lacking. Brain image segmentation is a fundamental step for the analysis of *in vivo* imaging data. Currently, there are no publicly available segmentation templates/atlases for titi monkey neuroimaging data necessitating time consuming, labor intensive, and subjective manual delineation of limited regions of interest. To address this significant limitation, the objective of the current study was to generate a first-of-its-kind MRI-based atlas of the titi monkey brain with a particular focus on brain areas relevant to pair-bonding neurobiology.

Methods:

Adult, female titi monkeys were born and housed at the California National Primate Research Center (Davis, CA). Imaging included *in vivo* T_1-weighted 3D RF-spoiled, gradient-recalled echo MRI scans (TR, 22 ms; TE, 8 ms; flip angle, 30°; matrix size, 256 x 256 x 70; voxel size, 0.31 x 0.31 x 1.0 mm) acquired on a 1.5 T scanner equipped with a 3-inch surface coil (General Electric Corporation, Milwaukee, WI), and [^{18}F]FDG PET brain scans acquired on the πPET dedicated brain scanner (Brain Biosciences, Rockville, MD, spatial resolution ~2.0 mm). Atlas regions were manually delineated on a single, representative MR image of a 5-year-old titi monkey (Amira software, Thermo Scientific, Waltham, MA, USA) by consensus of three experts in titi brain neuroanatomy. Labels included the entire brain (40 mm) and were based on titi monkey histologic data [9] and the NeuroNames [5,6] and Calabrese et al. (2015) [7] macaque MR atlases. To assess the utility of the atlas, MRI scans of 6 monkeys were manually segmented, each into fourteen brain regions, to generate ground truth. Separately, the atlas was warped to the 6 scans by a blinded investigator using semi-automated, non-rigid image registration (3D Slicer with Elastix Toolbox [8]). The regional labels thus generated were propagated to [^{18}F]FDG PET scans co-registered to the MRIs and average standardized uptake values (SUV) were derived per region. SUVs of regions common to manual delineation and the atlas-based analysis were compared. PET analysis used PMOD v4.302 (PMOD Technologies, Zurich, CHE) while statistical analysis was performed in Graphpad Prism v9.3.1 (GraphPad Software, San Diego, CA, USA). Data are reported as mean±SD.

Results and Conclusions:

The completed atlas consists of 46 brain regions spanning the full titi brain volume. Regions include extensive subdivisions of the cerebral cortex, limbic, and subcortical areas. A high positive correlation ($r=0.987$, $p<0.0001$) was observed across regions between regional [^{18}F]FDG SUVs calculated using manual segmentation and the atlas-based method. Regional SUVs were lower (paired t-test: $p=0.0018$) for atlas-based segmentation (2.504 ± 0.783) compared to manual segmentation (2.551 ± 0.817) although the magnitude of the effect was minor (0.047 ± 0.1344). Differences in regional SUVs between methods ranged from 11.07% to -11.23% across all scans and regions, with an average of -1.58 ± 4.68%. Bland–Altman agreement analysis indicated 95% limits of agreement from -0.311 to 0.2163 in calculated SUVs, and most points (80/84) are within the ±1.96 SD limit, which is indicative of high agreement. This study suggests that robust semi-automated segmentation can be achieved using this first-of-its-kind MR atlas of the titi monkey.

Reference

1. Bales KL, et al. Titi Monkeys as a Novel Non-Human Primate Model for the Neurobiology of Pair Bonding. Yale J Biol Med, 2017. 90(3): p. 373-387. PMID: 28955178.

2. Maninger N, et al. Pair bond formation leads to a sustained increase in global cerebral glucose metabolism in monogamous male titi monkeys (Callicebus cupreus). Neuroscience. 2017 Apr 21;348:302-312. doi: 10.1016/j.neuroscience.2017.02.028. Epub 2017 Feb 24. PMID: 28242440.
3. Hostetler CM, et al. Effects of pair bonding on dopamine D1 receptors in monogamous male titi monkeys (Callicebus cupreus). Am J Primatol. 2017 Mar;79(3):1-9. doi: 10.1002/ajp.22612. Epub 2016 Oct 18. PMID: 27757971.
4. Rothwell ES, et al. Dopamine D1-like receptors regulate agonistic components of pair bond maintenance behaviors in male titi monkeys (Callicebus cupreus). Psychoneuroendocrinology. 2019 Aug;106:259-267. doi: 10.1016/j.psyneuen.2019.04.012. Epub 2019 Apr 13. PMID: 31022585.
5. Dubach MF, Bowden DM. BrainInfo online 3D macaque brain atlas: a database in the shape of a brain. Society for Neuroscience Annual Meeting 2009, Chicago, IL Abstract No. 199.5.
6. Rohlfing T, et al. The INIA19 Template and NeuroMaps Atlas for Primate Brain Image Parcellation and Spatial Normalization. Frontiers in Neuroinformatics, 2012. 6:27. [doi 10.3389/fninf.2012.00027].
7. Calabrese E, et al. A diffusion tensor MRI atlas of the postmortem rhesus macaque brain. Neuroimage 2015, 117:408–416. [doi 10.1016/j.neuroimage.2015.05.072].
8. Klein S, Staring M, Murphy K, Viergever MA, Pluim JP. elastix: a toolbox for intensity-based medical image registration. IEEE Trans Med Imaging. 2010 Jan;29(1):196-205. doi: 10.1109/TMI.2009.2035616. Epub 2009 Nov 17. PMID: 19923044.

Oral Presentation

Disclosures: The authors have disclosed no financial interest.

078-Preclinical development of a novel fluorescent imaging agent for real-time intraoperative detection of pancreatic cancer

Presenter: Craig Ramirez, Illumaras

Craig Ramirez[1], Andrew Hauser[2]

[1]Illumaras, [2]Illumaras, Inc.

Mutant RAS is responsible for approximately 95% of pancreatic ductal adenocarcinoma (PDAC) incidences, and is an early genetic event during tumorigenesis.[1] Surgical treatment with the goal of tumor-free excision margins (clean margins) is the only potentially curative approach to PDAC. Approximately 15-20% of PDAC patients are eligible for surgery at the time of diagnosis.[2] However, for these patients that undergo surgery, tumor recurrence is frequent and the 5-year survival rates are dismal.[3] The inability to obtain clean margins, as well as the inability to identify and remove small metastatic lesions, directly impacts recurrence.[3] Fluorescence-guided surgery (FGS) is a young and promising field, with the aim of increasing the accuracy of conventional surgery. The potential value of FGS has been highlighted by the recently approved imaging agent for ovarian cancer, which was able to identify additional lesions in 27% of patients in a Phase III trial.[4] However, for RAS cancers, reliable targets for FGS are scarce. In the past decade, there has been a renewed interest in a metabolic adaptation of RAS cancers called macropinocytosis. This process enables mutant RAS tumors to scavenge extracellular proteins that can be broken down and provide an amino acid supply in poor nutrient conditions.[5] The central hypothesis behind ILR-103 is that by the attachment of a fluorescent probe (Cy5.5) to a macropinocytosis-specific carrier protein, mutant RAS tumor lesions can be more efficiently identified for surgical resection. ILR-103 showed macropinocytosis specificity in cell culture models, and preclinical data showed that ILR-103 preferentially labeled mutant RAS tumors compared to wildtype RAS tumors in human xenograft models. Immunofluorescence performed on frozen tissue sections validated tumor cell internalization. ILR-103 was also tested in the $Kras^{G12D}$;$Trp53^{R172H}$;$p48^{Cre}$ (KPC) mouse model, a well-validated, clinically relevant mouse model of PDAC.[6] The tumors generally have a moderately differentiated ductal morphology with extensive stromal desmoplasia, similar to the most common morphology observed in humans. *Ex vivo* analysis confirmed the presence of ILR-103 in the diseased pancreas (KPC) but absence in the healthy pancreas (wildtype mice). H&E staining of the tumor sections validated the ability of ILR-103 to label tumor lesions within the diseased pancreas. CK8 staining of the tumor sections verified specific internalization by the tumor cells and not the surrounding normal tissue. Importantly, ILR-103 labeled metastatic tumor cells in the liver and lungs, but not surrounding normal tissue, suggesting ILR-103 can be used for identification of metastatic lesions. The mechanism of action behind ILR-103 represents a significant departure from the current-state of surgery for RAS cancers, leveraging a synthetic protein technology for tumor-specific 'labeling' and detection by fluorescence. ILR-103 represents a new approach to combat PDAC, and has the potential to be applied to various tumor types with RAS pathway activation (i.e. mutant RAS or PTEN-deficiency).

Reference

1. Zeitouni D, Pylayeva-Gupta Y, Der CJ, Bryant KL. KRAS mutant pancreatic cancer: no lone path to an effective treatment. Cancers. 2016;8(4):E45. PMCID: PMC4846854.
2. Tummers WS, Willmann JK, Bonsing BA, Vahrmeijer AL, Gambhir SS, Swinjenburg R-J. Advances in diagnostic and intraoperative molecular imaging of pancreatic cancer. Pancreas. 2018; 47(6):675-689. PMID:29894417.
3. Bengtsson A, Andersson R, Ansari D. The actual 5-year survivors of pancreatic ductal adenocarcinoma based on real-world data. Scientific Reports. 2022; 10(1):16425. PMID: 33009477.
4. Voelker R. Lighting the way for improved detection of ovarian cancer. JAMA. 2022; 327(1):27. PMID:34982136.
5. Commisso C, et al. Macropinocytosis of protein is an amino acid supply route in Ras-transformed cells. Nature. 2013;497(7451):633-637. PMCID: PMC3810415.
6. Lee JW, Komar CA, Bengsch F, Graham K, Beatty GL. Genetically engineered mouse models of pancreatic cancer: the KPC model (LSL-KrasG12D/+;LSL-Trp53R172H/+;Pdx-1-Cre), its variants and their application in immuno-oncology drug discovery. Curr Protoc Pharmacol. 2017; 73:14.39.1-14.39.20. PMCID: PMC4915217.

Oral Presentation

Disclosures: The authors have disclosed no financial interest.

079-Functional Segmentation of Occupancy Images Improves Precision of EC50 Images

Presenter: Alaaddin Ibrahimy, Yale University

Alaaddin Ibrahimy[1], Jocelyn Hoye[2], Bart de Laat[1], Hao Wu[3], David L. Wilson[3], Evan Morris[4]

[1]Yale University, New Haven, CT
[2]Yale University, New Havebn, CT

[3]*Case Western Reserve University, Cleveland, OH*
[4]*Yale University, Madison, CT*

Background:

PET is used productively by pharmaceutical companies to measure drug occupancy, in vivo. The outcome measure is usually a whole-brain EC_{50}. We recently introduced voxel-level occupancy images (Occ) from PET which can be used to generated EC_{50} *images* by applying an E_{max} model at each voxel (de Laat 2020; 2021)

Aim:

Our goal is to evaluate image segmentation via the SLICR algorithm to denoise the Occ and produce more precise EC_{50} *images*.

Method:

We created a 4D digital phantom containing 10 Occ (corresponding to 10 different plasma concentrations of drug). The Occ were constructed to include two bilateral local hot-spots of high EC_{50} (region-1: 25; region-2: 50; background: [6-10] ng/ml) . An established noise model was applied to the simulated images to make noisy Occ (de Laat 2021). SLICR, a k-means clustering algorithm, was modified to segment Occ into "k" clusters. EC_{50}, *images* were created by nonlinear estimation at each voxel. Coefficient of variation images, CV(EC_{50}), were estimated from the covariance matrix of the parameters at each voxel. EC_{50}, and CV(EC_{50}) *images* were created from the noisy and the segmented versions of the Occ.

Results/Conclusions:

Variability in EC_{50} values was lower using segmented Occ with SLICR while the increase in bias was minimal (see Figure). Using SLICR, the overall computation time decreases by orders of magnitude. Our results suggest that segmentation of Occ with SLICR could produce more precise EC_{50} *images* and improve our ability to identify 'hot-spots' of high effective affinity of a drug for target(s).

Reference

1. de Laat B, Morris ED. A local-neighborhood Lassen plot filter for creating occupancy and non-displaceable binding images. J Cereb Blood Flow Metab. 2021;41(6):1379-1389. doi:10.1177/0271678X20950486
2. de Laat B, Hoye J, Liu H, Morris ED. EC50images, a novel endpoint from PET target occupancy studies, reveal spatial variation in apparent drug affinity. Eur J Nucl Med Mol Imaging. 2022;49(4):1232-1241. doi:10.1007/s00259-021-05561-3

Oral Presentation

Disclosures: The authors have disclosed no financial interest.

080-Multispectral short-wave infrared imaging of fluorescently labelled anti-GD2 targeted probes enables high-contrast fluorescence-guided surgery in neuroblastoma

Presenter: Dale Waterhouse, University College London

Dale J. Waterhouse[1], Laura Privitera[2], Alessandra Preziosi[2], Olumide Ogunlade[2], Chiara Da Pieve[3], Marta Barisa[3], Olumide Ogunbiyi[2], Ciaran Hutchinson[2], Irene Paraboschi[2], Kate Cross[2], Paul Beard[2], Gabriela Kramer-Marek[4], Danail Stoyanov[1], Neil Sebire[1], Paolo De Coppi[1], John Anderson[1], Stefano Giuliani[1]

[1]*University College London, London, United Kingdom*
[2]*University College London*
[3]*Institute of Cancer Research*
[4]*Institute of Cancer Research, Sutton, Surrey, United Kingdom*

Rationale:

Fluorescence-guided surgery (FGS) is a cutting-edge innovation set to play a pivotal role in next-generation neuroblastoma (NB) surgery. Fluorescence imaging using short-wave infrared (SWIR) wavelengths has shown advantages over conventional near-infrared (NIR) fluorescence due to reduced tissue scattering and negligible autofluorescence. Our preclinical study aims to develop and compare the performance of two near-infrared dyes (IRDye800CW and IR12-NHS), with long tails emitting in the SWIR range when conjugated to a clinical-grade anti-GD2 monoclonal antibody (Dinutuximab beta), using NIR-I and SWIR imaging devices.

Methods:

Dinutuximab was conjugated with IRDye800CW and IR12-NHS dyes (degree of labelling 1.0–1.5). *In vitro* validation and specificity assessment of the two conjugates was performed by flow cytometry and fluorescence microscopy. A custom multispectral NIR-I/SWIR fluorescence imaging device was constructed (**Fig. 1A**). System sensitivity and depth penetration were assessed with the use of phantom models. *In vivo,* the fluorescence signal was assessed in a LAN-1 subcutaneous NSG mouse model using a gold standard preclinical imaging system (IVIS®Spectrum, n=26), a commercial clinical NIR-I imaging device (EleVision™, n=2) and the novel multispectral NIR-I/SWIR device (n=10) at 24, 48, 72 and 96 hours **(Fig. 1B)**. Tumour mean fluorescence intensity (MFI) and tumour-to-background ratio (TBR) were evaluated. Histopathological analyses were performed on the resected tumours. R&D approval 20DC07.

Results:

The novel NIR-I/SWIR fluorescence imaging device showed a minimum detectable number of 250,000 cells and was able to resolve cells at depths up to 5 mm. *In vivo,* FGS using a commercially available clinical NIR-I fluorescence imaging system (EleVision™) helped identify a macroscopic tumour residual (~5mm), which was confirmed to be viable NB by histopathology **(Fig. S1)**. Biological validation using a gold standard preclinical imaging system **(Fig. S2)** showed that whilst MFI decreased with time ($p=4.2x10^{-6}$), and anti-GD2-IR800 was consistently brighter, ($MFI_{IR800}/MFI_{IR12}=2.0\pm0.5$, $p=2.7x10^{-6}$), the tumour remained detectable above background tissue at all time points (TBR>1.5). Fluorescence imaging using the novel NIR-I/SWIR device showed high TBR at all time points for both dyes (2.3<$tbr_{IR800/MFIIR12}=3.0\pm0.7$, p=0.013). Crucially, the multispectral NIR-I/SWIR fluorescence imaging system enabled higher TBR at SWIR wavelengths compared with NIR-I ($TBR_{900nm}=2.6\pm0.4$ versus $TBR_{1300nm}=4.6\pm1.0$, p=3</tbrx10^{-5}), resulting in a higher-contrast definition of tumour margins (**Fig. 1C–E**).

Conclusions:

This study presents *in vivo* validation for anti-GD2-IR800 as a promising probe for FGS in NB and introduces a novel targeted fluorescent probe, anti-GD2-IR12. Anti-GD2-IR800 and anti-GD2-IR12 allow bright and high-contrast visualisation of NB and identification of small clusters of cancer cells, which might be particularly useful during the surgical removal of small cancer residuals from high-risk areas. Crucially, we demonstrate both the anti-GD2-IR800 and the anti-GD2-IR12 can be repurposed as SWIR fluorescent probes, supporting a straightforward translation of SWIR imaging techniques into clinical practice. By combining the high-specificity of anti-GD2 antibodies, the availability and translatability of existing NIR-I dyes, and

the advantages of SWIR in terms of depth and signal-to-background ratio, we were able to demonstrate the exciting potential for SWIR FGS to transform surgery for NB.

Oral Presentation

Disclosures: The authors have disclosed no financial interest.

081-Ultrasonic Reporter for Protein Kinase Activity

Presenter: Jee Won Yang, California Institute of Technology (Caltech)

Jee Won Yang[1], Zhiyang Jin[2], Ruby Zhang[3], Dina Malounda[4], Mikhail G. Shapiro

[1]*California Institute of Technology (Caltech), PASADENA, CA*
[2]*California Institute of Technology (Caltech), Pasadena, California*
[3]*California Institute of Technology (Caltech)*
[4]*California Institute of Technology (Caltech), San Gabriel, CA*

Background:

Although protein kinases control nearly every facet of cellular function, current approaches to understanding their tightly controlled spatiotemporal regulation of multiple cellular processes are limited to *in vitro* assays due to the lack of robust, deep-tissue *in vivo* biomolecular tools. As aberrant kinase signaling is linked to numerous pathologies, novel tools for imaging live kinase activity are increasingly needed to study the rapid dynamics of and complex mechanisms behind aberrant signal transduction pathways[1]. While advances in fluorescent proteins and live-cell optical imaging have allowed spatiotemporally precise kinase activity measurements in living cells, they do not enable noninvasive deep-tissue imaging due to the physical limitation of light scattering[2]. Alternatively, ultrasound has unique advantages for cellular response imaging due to its ability to penetrate much deeper into tissue (several cm) than light with relatively high spatial and temporal resolution (<100 μm and 1 ms). Additionally, genetically encoded contrast agents for ultrasound-based on gas vesicles (GVs) [3,4], a unique class of air-filled protein nanostructures derived from buoyant microbes, have been developed as acoustic reporter genes[5,6] and as acoustic biosensors for enzymatic activity[7]. Here, we have engineered GVs as the first ultrasonic reporter for kinase activity (UReKA), enabling dynamic monitoring of Protein Kinase A (PKA) activity reversibly and repeatably when UReKA is administered. The hypothesis is that upon phosphorylation by PKA, the outer structural proteins of UReKA undergo an allosteric conformational change with a loss of binding to GV shells, resulting in reduced GV shell stiffness, increased mechanical deformation behavior (e.g., buckling), and enhanced detection of a non-linear signal (**persuasive data, Fig. S1d**). Future experiments include demonstrating the functionality of UReKA *in vitro* in mammalian cells and *in vivo* to measure upregulated PKA activity.

Innovation:

The key innovation is the development of the first ultrasonic reporter for kinase activity (UReKA) that enables real-time, *in situ* detection of dynamic molecular states. These sensors are reversible to capture the full dynamics of kinase/phosphatase activity. One of the two types of GV structural proteins is engineered to become responsive to PKA (**persuasive data, Fig. S1c**), inducing a conformational shift, and loss of binding. This PKA-induced "shedding" of outer structural proteins enables GV shells to generate non-linear ultrasound signals in response to acoustic pressure[8–10] that can be detected selectively using specific ultrasound pulse sequences[8,11] (**persuasive data, Fig. S1a**). This shedding is demonstrated to be reversible when lambda protein phosphatase (LPP) is added (**persuasive data, Fig. S1e-g**).

Method:

Our basic design of UReKA relies on an alpha-helical structural protein called GvpC, bound to the GV shell surface, which acts as a mechanical stiffener, controlling the extent of GV buckling and non-linear contrast generated[9,11] (**persuasive data, Fig. S1b**). GvpC was modified to incorporate a peptide domain recognized and phosphorylated by PKA (**persuasive data, Fig. S1c**). Purified UReKA were analyzed for their mechanical properties and reversibility.

Results:

Purified UReKA showed approximately 100% enhancement in non-linear contrast signal when incubated with 1 mM ATP and cyclic-AMP-activated PKA at 37°C, compared to an ATP-only control. The contrast was reversed by the addition of LPP, which removed GvpC phosphorylation (**persuasive data, Fig. S1e-g**).

Impact:

These results provide the first demonstration of a fully reversible ultrasonic PKA activity sensor, UReKA, enabling real-time, *in situ* detection of transient molecular concentrations, with the potential to visualize live intracellular PKA activity in deep tissue.

Reference

1. Zhang, JF., Liu, B., Hong, I. et al. An ultrasensitive biosensor for high-resolution kinase activity imaging in awake mice. Nat Chem Biol 17, 39–46 (2021).
2. Maryu, G. et al. Live-cell Imaging with Genetically Encoded Protein Kinase Activity Reporters. Cell structure and function vol. 43,1 (2018).
3. Shapiro, M. G. et al. Biogenic gas nanostructures as ultrasonic molecular reporters. Nat. Nanotechnol. 9, 311–316 (2014).
4. Lakshmanan, A. et al. Molecular Engineering of Acoustic Protein Nanostructures. ACS Nano 10, 7314–7322 (2016).
5. Bourdeau, R. W. et al. Acoustic reporter genes for noninvasive imaging of microorganisms in mammalian hosts. Nature 553, 86–90 (2018).
6. Farhadi, A., Ho, G. H., Sawyer, D. P., Bourdeau, R. W. & Shapiro, M. G. Ultrasound imaging of gene expression in mammalian cells. Science 365, 1469 (2019).
7. Lakshmanan, A. et al. Acoustic biosensors for ultrasound imaging of enzyme activity. Nat Chem Biol 16, 988–996 (2020).
8. Maresca, D. et al. Nonlinear ultrasound imaging of nanoscale acoustic biomolecules. Applied Physics Letters 110, 073704 (2017).
9. Cherin, M. et al. Acoustic behavior of Halobacterium salinarum gas vesicles in the high frequency range: experiments and modeling. Ultrasound in Medicine and Biology 43, 1016–1030 (2017).
10. Zhang, S. et al. The Vibration Behavior of Sub-Micrometer Gas Vesicles in Response to Acoustic Excitation Determined via Laser Doppler Vibrometry. Advanced Functional Materials n/a, 2000239.
11. Maresca, D., Sawyer, D. P., Renaud, G., Lee-Gosselin, A. & Shapiro, M. G. Nonlinear X-Wave Ultrasound Imaging of Acoustic Biomolecules. Physical Review X 8, 041002 (2018).

Oral Presentation

Disclosures: The authors have disclosed no financial interest.

082-Towards Real-Time Monitoring of the Immune Response in ICI Immunotherapy with a Wireless Fluorescence Microscope-on-Chip

Presenter: Rozhan Rabbani, University of California, Berkeley

Rozhan Rabbani[1], Micah Roschelle[1], Efthymios P. Papageorgiou[1], Hui Zhang[2], Vladimir Stojanovic[1], Mekhail Anwar[3]

[1]University of California, Berkeley, Berkeley, CA
[2]University of California, San Francisco, San Francisco, CA
[3]University of California, San Francisco, San Francisco

Introduction:

Access to cellular-level information from the immune system in real-time is critical in evaluating Immunotherapy, an effective therapeutic that unlocks the immune system to attack cancer [1]. Although only ~30% of patients respond [2], intratumoral information can rapidly recognize non-responders and provide insight into the mechanism of resistance, enabling rapid personalization of therapy to convert a non-responding tumor into a responding one. Activation of the immune system after the injection of T-cell-targeted immune-checkpoint inhibitors (ICI) such as anti-CTLA and anti-PD1 can destroy tumors systematically, producing durable responses [3]. To quantify the dynamic infiltration of stimulating and suppressing immune cells, a miniaturized imaging system capable of 1) simultaneous detection of **multiple cell types** 2) with **cellular-level resolution** 3) in **real-time** is critical. Fluorescence microscopy (via injection of fluorescently-tagged cell-specific antibodies) circumvents low sensitivity (centimeter-scale) and long delays (months) of the current modalities (MRI/CT, etc.), but is yet to be deployed on a platform compatible with long-term implantation. Given recent advances in CMOS technology, INSITE, a lensless fluorescence microscope-on-chip that eliminates conventional optics for both wired intraoperative and implantable applications is proposed [4,5]. The proof-of-concept wireless INSITE consists of a chip-scale imager, a sub-mm-sized laser diode and a piezoceramic transceiver for power and data transfer via an ultrasonic link. In this work, we use INSITE to visualize the response of MC38 mouse models of colorectal cancer to ICIs. Specifically, we monitor CD8 T-cells and neutrophils [6] ex vivo over time and verify the results by comparing images from INSITE to the microscope images of the same tissue.

Methods:

30 MC38 mice are injected with anti-PD1 and anti-CTLA4 at time points ranging from 0 to 18 days with an interval of 2 days in-between injections. At each time point, tumors and lymph nodes of 3 mice are harvested and stained for CD8 T-cells and neutrophils. Compared to untreated mice, ICI-treated mice are expected to show significant traces of CD8 T-cells indicating immune system activation. To demonstrate multiplexed imaging, Cd11b markers representing immunosuppressive cell populations are included. In this study, as a proof of concept, one mouse from the latest time point is compared against an untreated mouse leaving the statistics of the rest for future work.

The images are taken using the wired intraoperative 36x80-pixel INSITE [4] after a 50ms exposure time with fiber-optic lasers with wavelengths of 633nm and 488nm. Additionally, CD8 T-cell populations in lymph nodes are imaged with the 36x40-pixel wireless INSITE prototype after an exposure time of 64ms. In this case, illumination is provided with a 635nm laser diode, controlled by the sensor, and the 11.5kbit data is streamed out within 700ms.

Results:

The images show CD8 densities of 35% and 42% in the lymph nodes of untreated and ICI-treated mice, respectively. A 20% increase in CD8 T-cell density together with a 2.8x higher average signal intensity indicates immune system activation in response to ICI. The results for CD11b are 26% and 33% for untreated and ICI-treated mice. Repeating the same procedure with the wireless sensor for the CD8-stained lymph nodes demonstrates densities of 38% and 51% (34% increase) for untreated and ICI-treated mice.

Conclusion:

Monitoring the multiplexed immune response with cellular-level resolution in real-time enables rapid assessment of resistance and its mechanism enabling personalization of immunotherapy to achieve durable responses. This work presents the application of custom-designed wired intraoperative and implantable imagers in evaluating immunotherapy. The performance of the sensor is verified by comparing CD8 T-cell and neutrophil profiles in images taken with INSITE with ground truth microscope images. The images show higher densities and average intensities of CD8 in ICI-treated mouse compared to untreated mouse indicating successful activation of the immune system.

Reference

1. S. A. Rosenberg, “Shedding Light on Immunotherapy for Cancer,” New England Journal of Medicine, vol. 350, no. 14, pp. 1461-1463, 2004.
2. F. K. Krebs, et al. Immune signature as predictive marker for response to checkpoint inhibitor immunotherapy and overall survival in melanoma. Cancer Med. 2021;10(5):1562-1575.
3. Robert, C. A decade of immune-checkpoint inhibitors in cancer therapy. Nat Commun 11, 3801 (2020)
4. E. P. Papageorgiou, B. E. Boser and M. Anwar, “Chip-Scale Angle-Selective Imager for In Vivo Microscopic Cancer Detection,” IEEE Transactions on Biomedical Circuits and Systems, vol. 14, no. 1, pp. 91-103, 2020.
5. R. Rabbani et al., "Towards an Implantable Fluorescence Image Sensor for Real-Time Monitoring of Immune Response in Cancer Therapy," 2021 43rd Annual International Conference of the IEEE Engineering in Medicine & Biology Society (EMBC), 2021, pp. 7399-7403
6. K.J, Hiam-Galvez, B.M. Allen, & M.H. Spitzer, “Systemic immunity in cancer.” Nat Rev Cancer 21, 345–359 (2021).

Oral Presentation

Disclosures: The authors have disclosed no financial interest.

083-Doubly 13C-labeled ethyl acetyl carbonate for simultaneous measurements of pH and acetate metabolism in tissues by hyperpolarized 13C MR

Presenter: Nesmine Maptue, University of Florida

Nesmine R. Maptue[1], Crystal Harrison[2], Gaurav Sharma[2], Alex Funk[3], Chalermchai Khemtong[1]

[1]University of Florida, Gainesville, FL
[2]University of Texas Southwestern Medical Center, Dallas
[3]University of Texas Southwestern Medical Center

Introduction:

Abnormal metabolism is present in many disease states. Additionally, the altered metabolism is often associated with impaired acid-base homeostasis, resulting in abnormal tissue pH. The ability to

noninvasively assess tumor pH and energy metabolism would therefore be greatly beneficial to the diagnosis and treatment of metabolic diseases. In this study, we developed hyperpolarized (HP) doubly ^{13}C-labeled ethyl acetyl carbonate (Fig. 1A) as an esterase-sensitive metabolic imaging agent for simultaneous assessment of tissue pH and energy metabolism in functioning tissues.

Experimental Methods:

Doubly ^{13}C-labeled ethyl acetyl carbonate ($^{13}C_2$-EAC) was synthesized in-house. The compound was polarized without a glassing matrix in a HyperSense polarizer using BDPA as the radical. ^{13}C NMR spectra were acquired on a 9.4T vertical-bore spectrometer. HP $^{13}C_2$-EAC was dissolved in ethanol for T_1 measurements. Real-time production of hyperpolarized of the hyperpolarized ^{13}C-bicarbonate and $^{13}CO_2$ (for pH measurements) and HP ^{13}C-acetate were evaluated in isolated perfused rat hearts. MR imaging of tissue pH and acetate metabolism using HP $^{13}C_2$-EAC was demonstrated in isolated perfused rat kidneys.

Results and Discussion:

Results show that $^{13}C_2$-EAC can be highly polarized by dynamic nuclear polarization (DNP) using BDPA as the radical. It was also found that the polarization of $^{13}C_2$-EAC was extremely fast with the maximum polarization levels achieved within ~15 minutes of polarization. T_1's of both carbonate and acetyl carbons are comparable, 30 s at 9.4T. Single ^{13}C NMR and arrayed spectra of HP $^{13}C_2$-EAC in ethanol acquired with a 5-deg pulse are shown in Fig. 1B-C. The mechanism of esterase-induced production of HP $^{13}CO_2$/$H^{13}CO_3^-$ and [1-^{13}C]acetate from HP $^{13}C_2$-EAC is illustrated in Fig. 1A. A single ^{13}C spectrum acquired at 20s after the beginning of the injection HP $^{13}C_2$-EAC (2 mM) is shown in Fig. 1D, showing that HP $^{13}C_2$-EAC was readily hydrolyzed in the perfused heart. In this spectrum, the pH probes $^{13}CO_2$/$H^{13}CO_3^-$ are clearly detectable. Additionally, a strong resonance of [1-^{13}C]acetate is observed at 182.2 ppm, confirming the release of the HP ^{13}C-short chain fatty acid following esterase hydrolysis of the injected probe HP $^{13}C_2$-EAC. More importantly, ^{13}C-acetyl-CoA and ^{13}C-acetylcarnitine are also detected at 200.7 ppm 174.9 ppm, respectively. This confirms that the freshly produced HP [1-^{13}C]acetate is readily metabolized in the perfused heart. Resonance of the expected [5-^{13}C]glutamate produced from metabolism of [1-^{13}C]acetate via the TCA cycle overlaps with the acetate peak and cannot be analyzed. However, the metabolism of [1-^{13}C]acetate produced in situ was confirmed by high-resolution ^{13}C NMR of heart tissue extracts. Preliminary imaging evaluations of HP $^{13}C_2$-EAC were done in isolated perfused rat kidneys. pH and ^{13}C-acetyl carnitine intensity maps are shown in Fig. 1E. A ^{13}C spectrum of a region-of-interest highlighted in the ^{1}H density image is shown in Fig. 1F. These results confirm that simultaneous measurements of tissue pH, by imaging $^{13}CO_2$ and $H^{13}CO_3^-$, and detection of [1-^{13}C]acetate metabolism produced from esterase-hydrolysis of HP $^{13}C_2$-EAC metabolism in viable tissues in real-time are feasible.

Conclusions:

We have demonstrated the potential of using HP doubly $^{13}C_2$-EAC as a bifunctional metabolic imaging agent for HP ^{13}C-MR applications. T_1 of both the carbonate and acetyl carbons was relatively long. HP $^{13}C_2$-EAC was rapidly hydrolyzed by esterase in isolated perfused hearts and kidneys, producing HP $^{13}CO_2$ and $H^{13}CO_3^-$, [1-^{13}C]acetate for measuring pH and detecting short-chain fatty acid metabolism, respectively. The results demonstrate the feasibility of developing enzyme-sensitive HP substrates for in situ production of HP metabolic imaging probes.

Reference

1. Wikehooley, J.L. et al. Radiotherapy and Oncology, 1984. 2(4): p. 343-366.;
2. Raghunand, N., et al. Br J Radiol, 2003. 76 Spec No 1: p. S11-22.;
3. Korenchan, D.E., et al., Chem Commun, 2016. 52(14): p. 3030-3.; 10.,
4. Maptue, N. et al. ACS Sens.; 2018, 3, 2232-2236.

Oral Presentation

Disclosures: The authors have disclosed no financial interest.

084-Understanding antitumor immunity by measuring granzyme biochemistry in vivo with a restricted interaction peptide

Presenter: Apurva Pandey, University of California, San Francisco

Michael J. Evans[1], Ning Zhao[2], Charles Craik[3], Conner Bardine[3], **Apurva Pandey[1]**

[1]University of California, San Francisco, San Francisco, CA
[2]University of California, San Francisco, South San Francisco, CA
[3]University of California, San Francisco, San Francisco, California

Purpose/Background:

Despite the recent approvals of cancer immunotherapies, interpreting which patients are undergoing productive responses is currently challenging with standard of care diagnostics. Thus, there is an urgent unmet need to develop new biomarkers to distinguish responsive and resistant patients, as well as to detect undesired immune related adverse events. We hypothesized that an imaging technology capable of selectively measuring the biology utilized by T cells to impart cytotoxicity could predict early tumor responses. Since T cell cytotoxicity against tumor cells is primarily conferred by the pro-apoptotic serine protease granzyme B (GZMB), we have developed a novel probe termed GRIP B that measures the biochemistry of GZMB as it traverses the pericellular space at the immunological synapse. GRIP B is modeled after a "restricted interaction peptide", a technology that we recently pioneered to enable the first spatiotemporal measurements of endoprotease biochemistry in vivo with PET. Mechanistically, an inactive "pro-form" of radiolabeled GRIP B is administered systemically, whereupon cleavage by GZMB releases a radiolabeled (non-toxic) antimicrobial peptide that spontaneously adopts a helical conformation to immediately associate with nearby phospholipid membranes (i.e. the plasma membrane of the tumor cell). Thus, sequestration of the radiotracer by the endoprotease provides a readout of the relative units of enzyme activity within a region of interest. The specificity of GRIP B is driven by the biochemistry of GZMB, which is the only known extracellular protease in humans that can cleave a peptide with an aspartic acid at the P1 site.

Methods:

Multisubstrate profiling with mass spectrometry was applied to identify an optimal 8 mer P4-P4' cleavage sequence for GZMB. The sequence was flanked by Temporin L (membrane binding module) and a PAR1 sequence we previously showed to inhibit Temporin L folding. The peptide was conjugated to DOTA and Cu-64 for imaging studies. Mice bearing subcutaneous CT26, MC38, TRAMP C2, EMT6, or B16F10 tumors were treated with vehicle or immune checkpoint inhibitors. Mice with imaged with 64Cu-GRIP B or 64Cu-D-GRIP B, an uncleavable control. Treatment and imaging studies were also performed with tumor bearing GZMB knockout mice. Post treatment changes in

tumoral uptake of 64Cu-GRIP B were correlated with tumor volume changes.

Results:

GRIP B was efficiently cleaved by recombinant human and mouse GZMB. In vivo, dynamic PET acquisitions showed 64Cu-GRIP B rapidly cleared from blood via the kidneys, and did not appreciably bind normal mouse tissues, as expected. PET and biodistribution studies in tumor bearing mice showed that checkpoint inhibitor treatment activated 64Cu-GRIP B in tumor and normal tissues, for example the spleen. The uncleavable probe was not activated by GZMB in vivo. No tumoral uptake of 64Cu-GRIP B was observed in GZMB knockout mice, confirming the probe's mechanism of action. Post treatment changes in tumoral uptake of 64Cu-GRIP B correlated with tumor responses

Conclusion:

We describe here in a first in class radiotracer that measures granzyme proteolysis in vivo using an imaging modality that can be translated into patients. We are currently exploring additonal applications for the probe as well as performing IND enabling studies for a first in human imaging study.

Oral Presentation

Disclosures: The authors have disclosed no financial interest.

085-Microbubble Shape Affects Margination, Circulation and Focused Ultrasound-induced Blood-Brain Barrier Permeation

Presenter: Anshuman Dasgupta, RWTH Aachen University

Anshuman Dasgupta[1], Tao Sun[1], Roberto Palomba[1], Diana Möckel[2], Fabian Kiessling[3], Paolo Decuzzi[3], Nathan McDannold[4], Samir Mitragotri[4], Twan Lammers[5]

[1]*RWTH Aachen University, Germany*
[2]*Institute for Experimental Molecular Imaging, Aachen, Germany*
[3]*RWTH Aachen University, Aachen, NRW, Germany*
[4]*Brigham and Women's Hospital*
[5]*RWTH Aachen University Hospital, Aachen, Germany*

Introduction:

Microbubbles (MB) are 1-10 µm-sized gas-filled vesicles which are extensively used for ultrasound (US) imaging and drug delivery. To enhance US imaging and drug delivery, a wide range of MB physicochemical characteristics including size, surface chemistry, shell rigidity and gas volume have been explored [1]. Shape is another physicochemical property that may have important implications in US imaging and drug delivery. We here studied the impact of MB shape on flow dynamics, macrophage uptake and US-mediated blood-brain barrier (BBB) permeation.

Methods:

Spherical-shaped MB were synthesized by anionic polymerization of n-butyl cyanoacrylate [2]. Rod-shaped MB were synthesized by stretching spherical-shaped MB unidirectionally above their glass transition temperature [3]. Spherical- and rod-shaped MB were characterized and compared with regards to their margination propensity, macrophage uptake, circulation time and BBB permeation upon US treatment.

Results:

Confocal, cryo-SEM and STED microscopy confirmed the successful formation of spherical- and rod-shaped MB. Upon injecting the MB in the presence of blood into a straight microfluidic channel, we observed that rod-shaped MB show enhanced margination (i.e., the propensity to move closer to the vessel walls) and exhibit tumbling motion. We furthermore observed that rod-shaped MB exhibit reduced macrophage uptake and this finding also translated into longer in-vivo circulation times. Exploiting these features, we finally demonstrated that both standard and antibody-targeted rod-shaped MB were significantly more efficient than their spherical counterparts in mediating focused US-induced BBB permeation.

Conclusion:

The findings presented here indicate that tailoring MB shape is a promising strategy for modulating flow dynamics, phagocytosis and BBB permeation. The rod-shaped MB and other non-spherical shapes can be considered to be useful for potentiating US-mediated drug delivery across the BBB and to improve the treatment of brain disorders.

Reference

1. Dasgupta et al. Drug Discov Today: Technologies. 2016:41-48.
2. Liu et al. Mol Pharmaceutics. 2020:2840-2848.
3. Champion et al. Proc Natl Acad Sci. 2007:11901-11904.

Oral Presentation

Disclosures: The authors have disclosed no financial interest.

086-Oxidation of hyperpolarized [1-13C]pyruvate in isolated rat kidneys

Presenter: Chalermchai Khemtong, University of Florida

Gaurav Sharma[1], Nesmine R. Maptue[2], Mohsin Rahim[3], Miriam Trigo[4], Thomas Hever[4], Xiaodong Wen[4], Alex Funk[4], Craig Malloy[5], Jamey Young[3], **Chalermchai Khemtong**[2]

[1]*University of Texas Southwestern Medical Center, Dallas*
[2]*University of Florida, Gainesville, FL*
[3]*Vanderbilt University*
[4]*University of Texas Southwestern Medical Center*
[5]*University of Texas at Dallas, Dallas*

Kidneys play a central role in numerous disorders but current imaging methods have limited utility to probe renal metabolism. Hyperpolarized (HP) ^{13}C magnetic resonance imaging is uniquely suited to provide metabolite-specific information about key biochemical pathways and it offers the further advantage that renal imaging is practical in humans. HP ^{13}C MR imaging of [1-^{13}C]pyruvate metabolism has been demonstrated in rats and humans. Downstream metabolites of HP [1-^{13}C]pyruvate, i.e. ^{13}C-bicarbonate, [1-^{13}C]lactate, and [1-^{13}C]alanine, have all been detected in the kidneys. Renal perfusion is very high relative to other organs and a challenge remains in separating signals of the metabolites produced via renal metabolism from those of the same metabolites produced in distant organs and delivered to the kidneys via the circulation, potentially lactate and bicarbonate (via CO_2). We evaluated the feasibility of hyperpolarization exams in a widely-used model for analysis of renal physiology, the isolated perfused rat kidney, which enables isolation of renal metabolism from the effects of

other organs and validation of HP results by independent measurements. Isolated kidneys were supplied with either HP [1-^{13}C]pyruvate only or HP [1-^{13}C]pyruvate plus octanoate. Two groups were studied after 20 minutes of perfusion with either 2 mM [U-$^{13}C_3$]pyruvate or 2 mM [U-$^{13}C_3$]pyruvate plus 0.2 mM [2,4,6,8-$^{13}C_4$]octanoate. Metabolic activity in both groups was confirmed by stable renal oxygen consumption. HP exams were performed in a 9.4 T NMR system, followed by freeze-clamping of the kidney. Subsequently, frozen kidneys were pulverized, extracted, freeze-dried, resuspened, and analyzed by ^{1}H and ^{13}C NMR spectroscopy. Representative ^{13}C NMR spectra (Figure) show that HP [1-^{13}C]pyruvate is readily metabolized under both perfusion conditions as confirmed by the appearances of downstream metabolites of [1-^{13}C]pyruvate. The evolution of ^{13}C signals confirms the metabolism of HP [1-^{13}C]pyruvate by lactate dehydrogenase, alanine transaminase, and pyruvate dehydrogenase followed by the $^{13}CO_2$ - $H^{13}CO_3^-$ equilibration catalyzed by carbonic anhydrase. Summed spectra of the first 40 consecutive timepoints of each array are shown. Small signals from TCA cycle intermediates, [1-^{13}C]malate and [1-^{13}C]aspartate, are also visible, confirming activity of pyruvate carboxylase. Figure panels C-E show comparisons of total normalized signals of ^{13}C-bicarbonate, [1-^{13}C]lactate, and [1-^{13}C]alanine between the two perfusion groups. Kidneys perfused with only pyruvate produced ~2-fold higher HP ^{13}C-bicarbonate signal than the kidneys receiving a mixture of pyruvate and octanoate (panel C). Octanoate suppressed but did not eliminate the production of HP [^{13}C]bicarbonate from [1-^{13}C] pyruvate. Steady-state flux analyses using non-HP ^{13}C substrates of tissue extracts from the same kidneys confirmed utilization of HP [1-^{13}C] pyruvate as observed by HP ^{13}C NMR. Interestingly, the tissue extract studies found that in the presence of octanoate, lactate is generated from a TCA cycle intermediate, oxaloacetate. We found that, unlike the heart, octanoate does not fully suppress oxidation of HP [1-^{13}C] pyruvate. The isolated rat kidney is an excellent model for investigating and establishing new HP ^{13}C metabolic probes for future kidney imaging applications.

Oral Presentation

Disclosures: The authors have disclosed no financial interest.

087-Simultaneous PET/MRI imaging of liver function using radiometal labeled OATP-transportable chelates

Presenter: Legend Kenney, Michigan State University

Erik Shapiro[1], Janaki Ramulu B[1], Shatadru Chakravarty[2], Nathan Kauffman[1], Christiane Mallett[1], Kurt Zinn[1], Jinda Fan[1], **Legend E. Kenney**

[1]Michigan State University, East Lansing, MI
[2]Michigan State University, East Lansing, Michigan

Chronic liver diseases (**CLD**) are a morbid ensemble of diseases with dire outcomes including liver failure or cancer. Early detection and accurate disease staging of CLD are critical for timely and appropriate treatment options which can potentially slow or reverse disease course. One promising technique for determining early liver dysfunction is to measure the hepatic flux of an imageable molecule. Parametric estimation techniques of dynamic imaging data with physiologically based pharmacokinetic (**PBPK**) models can evaluate liver functional parameters such as k_{influx} – the rate constant of contrast agent influx into hepatocytes via OATPs, and k_{efflux} – the rate constant of contrast agent efflux from hepatocytes to bile via the MRP2 transporter. Accurate estimations of k_{influx} and k_{efflux} are important as changes in these values are sensitive to early changes in transporter expression in CLD and can enable early disease detection. The key inputs to PBPK models are the dynamic hepatic and vascular concentrations of the imageable molecule. Dynamic contrast enhanced-MRI (**DCE-MRI**) with the hepato-specific MRI contrast agent Gd-EOB-DTPA, has been investigated for non-invasively assessing liver function (1), however determining concentration of MRI contrast agent in the blood and tissue is complicated due to uncertainty and changes in contrast agent relaxivity, and intrinsic imaging errors. Taken together, propagation of these errors results in poor ability of DCE-MRI to detect early CLD or discriminate stages of CLD (2). Unlike MRI contrast agents, PET tracer concentrations can be measured directly from images without a-priori tissue information, and without intrinsic MRI artifacts such as in-flow errors and RF inhomogeneity. Thus, we hypothesize that dynamic PET imaging of the hepatic influx and efflux of a PET imageable hepto-specific substrate more accurately measures the concentration flux of hepato-specific probes in the liver and in the vasculature, enabling more accurate measurements of hepatic k_{influx} and k_{efflux}. We synthesized two PET radiometal-chelate hepatospecific tracers based on EOB-DTPA. The first new agent is ^{86}Y-EOB-DTPA, simply substituting the non-radioactive Gd with ^{86}Y. ^{86}Y-EOB-DTPA has the advantage of preserving the original chelate structure and we determined using simultaneous PET/MRI that ^{86}Y-EOB-DTPA mirrors the hepatic influx of Gd-EOB-DTPA following intravenous delivery of both compounds concomitantly. Yet, ^{86}Y is a non-ideal isotope for PET due to spurious gamma rays near the PET detection window and relatively low availability compared to other PET isotopes (3). The second new agent we synthesized is ^{64}Cu-EOB-NOTA. We used ^{64}Cu as it is the highest resolution PET radiometal, important to measure image derived vascular input function by confining the PET signal within small blood vessels. The ethoxybenzene (EOB) substituent confers hepato-specificity, as Gd-DTPA is non-hepatospecific, and other EOB-tagged chelates also exhibit hepato-specificity (4, 5). Cu is poorly complexed by DTPA but is stable in NOTA (6). ^{64}Cu-EOB-NOTA was synthesized from two separate chemical components – a reactive EOB component and bis-protected NOTA to ensure mono-substitution. Radiolabeling with ^{64}Cu in high yield was accomplished by addition of $^{64}CuCl_2$ to free chelate in buffered, aqueous solution.
We validated the hepatobiliary transport of ^{64}Cu-EOB-NOTA using simultaneous PET/MRI in mice (n=3) following intravenous injection of a cocktail containing Gd-EOB-DTPA. Peak hepatic uptake occurred at ~ 20 minutes, with slow washout over an hour. Measurement of ^{64}Cu in the biological waste revealed 50:50 hepatic:renal agent clearance. ^{64}Cu-EOB-NOTA hepatic flux was slower than Gd-EOB-DTPA, but still exhibited influx and efflux within standard dynamic imaging time frame. A control mouse injected with rifampicin to block OATPs demonstrated highly reduced hepatic uptake and more renal excretion. PET imaging of ^{64}Cu-EOB-NOTA and future compounds of this class is promising new approach for measuring changes in liver function in early liver diseases.

Reference

1. Juluru K, Talal AH, Yantiss RK, Spincemaille P, Weidman EK, Giambrone AE, et al. Diagnostic accuracy of intracellular uptake rates calculated using dynamic Gd-EOB-DTPA-enhanced MRI for hepatic fibrosis stage. J Magn Reson Imaging. 2017;45(4):1177-85.
2. Forsgren MF, Karlsson M, Dahlqvist Leinhard O, Dahlstrom N, Noren B, Romu T, et al. Model-inferred mechanisms of liver function from magnetic resonance imaging data: Validation and variation across a clinically relevant cohort. PLoS Comput Biol. 2019;15(6):e1007157.
3. Le Fur M, Caravan P. (86)Y PET imaging. Methods Enzymol. 2021;651:313-42.
4. Baek AR, Kim HK, Park S, Lee GH, Kang HJ, Jung JC, et al. Gadolinium Complex of 1,4,7,10-Tetraazacyclododecane-1,4,7-

trisacetic Acid (DO3A)-Ethoxybenzyl (EOB) Conjugate as a New Macrocyclic Hepatobiliary MRI Contrast Agent. J Med Chem. 2017;60(12):4861-8.
5. Nyström NN, Liu H, Martinez FM, Zhang X-a, Scholl TJ, Ronald JA. Gadolinium-free Magnetic Resonance Imaging of the Liver using an Oatp1-targeted Manganese(III) Porphyrin. bioRxiv. 2021:2021.08.04.455144.
6. Cai Z, Anderson CJ. Chelators for copper radionuclides in positron emission tomography radiopharmaceuticals. J Labelled Comp Radiopharm. 2014;57(4):224-30.

Oral Presentation

Disclosures: The authors would like to disclose that FDG has been approved.

088-Re-engineered bio-tropical peptide for fluorescence-guided surgery of neck peripheral nerves

Presenter: JUNIOR GONZALES, Memorial Sloan Kettering Cancer Center

Junior Gonzales[1], Paula Demetrio de Souza Franca[2], Dauren Adilbay[3], Raik Artschwager[3], Thomas Reiner[4], NagaVaraKishore Pillarsetty[3]

[1]*Memorial Sloan Kettering Cancer Center, Flushing, NY*
[2]*Memorial Sloan Kettering Cancer Center, New York*
[3]*Memorial Sloan Kettering Cancer Center, New York, NY*
[4]*Novartis, Switzerland*

More than 360 million of individuals in the world and twenty-two million Americans suffer from peripheral nerve injury caused by domestic/traumatic lesions, and derived from medical errors and/or genetic predisposition, resulting in a broad spectrum of potentially debilitating side effects in patients, affecting their quality of life. Intuitively, any substance with the power to light up nerves to guide surgery would help improve surgical outcomes at conserving nerves tremendously; perhaps the use of an exogeneous contrast agent will address the formidable nerve-damage challenge in surgery. In the clinical practice, however, the current standard of care – visual examination and palpation – remains unchanged – confined to optical magnifying lenses and electrical stimulation. To address this unmet clinical need, we (i) make use of the exclusive expression of voltage-gated sodium channel NaV1.7 as an intraoperative marker to access peripheral nerve structures in vivo and (ii) shuttle to the sodium channel via NaV1.7-selective reputed (Tarantula species Peru) Tsp1a peptide. From the translational angle, we further modify Tsp1a peptides with red and near-infrared chromophores to align with the available technology used nowadays in fluorescence-guided surgeries and we show that expression of channel NaV1.7 is very high in several human peripheral nerves harvested from the torso and extremities. Herein, we have repurposed, engineered and prepared a library of 10 fluorescent Tsp1a compounds with clinically employed fluorophores which maintained affinity for human NaV1.7 in vitro and serve as targeted vectors for delivering fluorescent sensors to delineate peripheral nerves in vivo. First, we observe a high signal-to-noise ratio for all in-house prepared fluorescently labeled Tsp1a peptides injected in mice, which accumulate in peripheral nerve sites in vivo. Second, we simulate a human- thyroidectomy in a non-human primate to resemble a surgical extenuating event happening in the daily basis, where the vagus and recurrent laryngeal nerves are normally damaged and blood turbidity and vasculature are undifferentiable by the surgeon, nevertheless our tool/technology lighted up these peripheral nerves in vivo and were also successfully differentiated. Ex vivo analysis on resected nerves and surrounding tissue from the primates corroborates the detectable fluorescence signal observed in vivo. The successful localization of neck nerves in the thyroidectomy suggests that fluorescently labeled Tsp1a tracers could be used to discriminate and demarcate nerves from their surrounding tissues in a routine clinical setting which as a whole holds potential to revolutionize/transform the standard of care of nerve surgery.

Reference

1. Li, H., Liu, Z. & Ge, J. Scientific research progress of COVID-19/SARS-CoV-2 in the first five months. J Cell Mol Med 24, 6558-6570 (2020).
2. Crombie, I.K., Davies, H.T.O. & Macrae, W.A. Cut and thrust: antecedent surgery and trauma among patients attending a chronic pain clinic. Pain 76, 167-171 (1998).
3. Castiglione, F., Ralph, D.J. & Muneer, A. Surgical Techniques for Managing Post-prostatectomy Erectile Dysfunction. Curr Urol Rep 18, 90 (2017).
4. Grinsell, D. & Keating, C.P. Peripheral nerve reconstruction after injury: a review of clinical and experimental therapies. Biomed Res Int 2014, 698256 (2014).
5. Campbell, W.W. Evaluation and management of peripheral nerve injury. Clin Neurophysiol 119, 1951-1965 (2008).
6. Lee, S.K. & Wolfe, S.W. Peripheral nerve injury and repair. J Am Acad Orthop Surg 8, 243-252 (2000).
7. Antoniadis, G. et al. Iatrogenic nerve injuries: prevalence, diagnosis and treatment. Dtsch Arztebl Int 111, 273-279 (2014).
8. Kretschmer, T., Heinen, C.W., Antoniadis, G., Richter, H.P. & Konig, R.W. Iatrogenic nerve injuries. Neurosurg Clin N Am 20, 73-90, vii (2009).
9. Tasmuth, T., von Smitten, K., Hietanen, P., Kataja, M. & Kalso, E. Pain and other symptoms after different treatment modalities of breast cancer. Ann Oncol 6, 453-459 (1995).
10. Karydas, I., Fentiman, I.S., Habib, F. & Hayward, J.L. Sensory changes after treatment of operable breast cancer. Breast Cancer Res Treat 8, 55-59 (1986).
11. Downing, R. & Windsor, C.W. Disturbance of sensation after mastectomy. Br Med J (Clin Res Ed) 288, 1650 (1984).
12. Echternach, M. et al. Laryngeal complications after thyroidectomy: is it always the surgeon? Arch Surg 144, 149-153; discussion 153 (2009).
13. Sosa, J.A. et al. The importance of surgeon experience for clinical and economic outcomes from thyroidectomy. Ann Surg 228, 320-330 (1998).
14. Varaldo, E., Ansaldo, G.L., Mascherini, M., Cafiero, F. & Minuto, M.N. Neurological complications in thyroid surgery: a surgical point of view on laryngeal nerves. Front Endocrinol (Lausanne) 5, 108 (2014).

Oral Presentation

Disclosures: The authors have disclosed no financial interest.

089-Development and evaluation of a clinically translatable human OX40 immunoPET tracer for highly specific detection of T cell activation

Presenter: Israt Alam, Stanford University

Israt S. Alam[1], Mausam Kalita[1], Samantha Reyes[2], Irene N. Falk[3], Carmen Azevedo[4], Ophir Vermesh[5], Bin Shen[6], David A. Anders[5], Emily Deal[2], Anand Giddabasappa[7], Edmund Keliher[8], Derek Bartlett[9], Kevin P. Maresca[8], Michelle L. James[5]

[1]Stanford University, Stanford
[2]Stanford University School of Medicine, Stanford, CA
[3]Stanford University, Mountain View, CA
[4]Washington University in St. Louis, St. Louis, MO
[5]Stanford University, Stanford, CA
[6]Molecular Imaging Program at Stanford (MIPS), Stanford, CA
[7]Pfizer, SAN DIEGO, CA
[8]Pfizer, Cambridge, MA
[9]Pfizer

Objectives:

T cell priming and activation are central to the success of cancer immunotherapies (IOTs), and an early indicator of downstream expansion, trafficking, and tumor cell killing. Current standard-of care immunomonitoring techniques are limited in their ability to allow non-invasive, whole-body, real-time monitoring of T cell activation in response to IOTs. We previously identified the OX40 receptor (CD134) as a highly specific, cell surface biomarker of $CD4^+$ and $CD8^+$ activated T cells and showed that murine OX40-immunoPET was able to visualize T cell activation *in vivo* and predict therapeutic response across a range of IOT models. This promising data warrants clinical evaluation of OX40 imaging. Here, we report the development and validation of the first *human* OX40 immunoPET tracer based on the OX40 therapeutic monoclonal antibody (mAb) Ivuxolimab, currently in Phase II trials [1].

Methods:

DFO-conjugation of the human OX40 specific mAb (Ivuxolimab) and subsequent ^{89}Zr-radiolabeling was conducted in metal-free buffers and optimized to produce [^{89}Zr]huOX40mAb. To assess target binding of the radiotracer *in vitro*, cell binding studies were performed using primary human T cells. [^{89}Zr]huOX40mAb binding to human embryonic kidney 293 (HEK293) cells, and to HEK293 cells stably expressing human OX40 ($OX40^+$ HEK293), was also evaluated. Female NOD.Cg-Prkdc-scid Il2rgtm1Wjl /SzJ (NSG) mice were implanted with $1x10^7$ HEK293 or $OX40^+$ HEK293 cells subcutaneously in the flank. When tumors grew to ~150 mm3, mice were injected with [^{89}Zr]huOX40mAb (63.5+2.6 µCi intravenously, n=8-9/group). PET/CT images were acquired every 24 hours and up to 5 days post injection (p.i.). Immediately after imaging, key tissues were harvested for *ex vivo* gamma counting and autoradiography to confirm tracer biodistribution.

Results:

Ivuxolimab showed reproducible DFO-conjugation (**Fig. S1A**) and radiolabeling ([^{89}Zr]huOX40mAb final molar activity: 15 µCi/µg; final radiochemical purity: >99%, **Fig. S1B**). [^{89}Zr]huOX40mAb demonstrated 10.8 fold higher binding to human activated (OX40+) T cells versus resting T cells (p=0.0022) and 26.8 fold higher binding to $OX40^+$ HEK293 versus parental HEK293 cells (p=0.0002). Blocking with 25-fold excess cold mAb dramatically reduced tracer binding to activated T cells (by 88%, p<0.01) and to $OX40^+$ HEK293 cells (by 87%, p<0.0001) further confirming radiotracer specificity (**Fig. S1C**). *In vivo* assessment of [^{89}Zr]huOX40mAb specificity and biodistribution revealed markedly higher signal in $OX40^+$ HEK293 tumors versus HEK293 tumors (**Fig. 1A**). Quantification of PET images using region-of-interest analysis confirmed significantly higher tracer binding to $OX40^+$ HEK293 tumors compared to HEK293 tumors, as determined by the injected dose per gram of tissue (10.5+6.6% ID/g and 2.5+0.7 %ID/g respectively at 72 hours p.i., p=0.0006) (**Fig. 1B**). Notably, increasing tumor to muscle ratios were only observed in $OX40^+$ HEK293 tumors over time, indicating clearance of the unbound tracer (**Figs. 1C, S1D**). Biodistribution analysis using *ex vivo* gamma counting of tissues and autoradiography of tumor and muscle at 72 hours p.i. further corroborated PET results (**Fig. S1E**).

Conclusion:

Varying spatiotemporal immune behaviors in response to cancer IOTs render monitoring of therapeutic response and prediction of clinical outcomes challenging. T cell activation is an early and critical event in IOT-induced anti-cancer responses. [^{89}Zr]huOX40mAb is a promising new radiotracer for visualizing activated human T cells with highly specific target binding *in vitro* and *in vivo*. These data, along with future evaluation in human T cell activation models, estimation of detection sensitivity, radiation dosimetry studies and the ability to leverage existing pharmacokinetic and safety data for the clinically-evaluated therapeutic parent mAb, will ensure timely investigational new drug (IND) approval for our eventual goal of clinical translation. [^{89}Zr]huOX40mAb has the potential to allow early, accurate, and sensitive monitoring of global T cell responses to evaluate IOT responses and guide patient management, ultimately improving their outcomes.

Reference

1. Diab A, Hamid O, Thompson JA, et al. A Phase I, Open-Label, Dose-Escalation Study of the OX40 Agonist Ivuxolimab in Patients with Locally Advanced or Metastatic Cancers. Clin Cancer Res. 2022;28(1):71-83.

Oral Presentation

Disclosures: The authors would like to disclose that Ivuxolimab is an investigational drug.

090-Dynamic Trimodal Imaging of Mesenchymal Stem Cells with Magnetic Particle Imaging, Positron Emission Tomography, and Bioluminescence Imaging

Presenter: Nourhan Shalaby, Western University

Nourhan Shalaby[1], John J. Kelly[2], Olivia Sehl[3], Julia J. Gevaert[2], Matthew S. Fox[4], Qi Qi[2], Jonathan D. Thiessen[5], Justin W. Hicks[6], Paula Foster[3], Timothy J. Scholl[7], John Ronald[8]

[1]Western University, London, ON
[2]Western University, London
[3]Robarts Research Institute, London
[4]Lawson Health Research Institute, London, Ontario
[5]Lawson Health Research Institute, London
[6]Lawson Health Research Institute, London, ON
[7]Robarts Research Institute, London, Ontario
[8]Robarts Research Institute, London, ON

Introduction:

Mesenchymal stem cells (MSCs) have been used to treat many pathologies[1]. While remarkably successful, there are still hurdles to overcome for optimum clinical potential. Current post-administration monitoring methods (blood tests and biopsies) are invasive and lack information on the number, biodistribution and viability of administered cells [2]. In this work, we propose a non-invasive multi-modal approach to monitor mesenchymal stem cells using a multi-modal imaging technique comprising magnetic particle imaging (MPI), bioluminescence imaging (BLI) and positron emission tomography (PET).

Methods:

MSCs were transduced to express a lentiviral plasmid containing a tdTomatoe (tdT) fluorescence gene and a BLI reporter gene, Akaluc. MSCs were sequentially transduced with a second lentiviral plasmid

containing genes for zsGreen (zsG) fluorescence protein and a Sodium Iodide Symporter (NIS) PET imaging reporter. Flow cytometry and fluorescence-activated cell sorting were performed to assess transduction efficiency and collect a 97%-pure population of MSCs expressing both tdT-Akalus and zsG-NIS. These MSCs were labeled *in vitro* by incubation with a super-paramagnetic iron oxide, Synomag-D for detection with MPI. Mice (n=5) were injected with 10^6 tdT-Akaluc-zsG-NIS-MSCs in the hind limb. Longitudinal imaging of these mice with MPI, BLI and PET was performed over a duration of 30 days.

Results/ Discussion:

At early time points, MPI and BLI showed high sensitivity while PET did not show significantly higher tracer uptake than background. MPI detection of iron-labeled MSCs declined over time, likely due to iron label dilution, and clearance. BLI and PET signals showed similar early signal decreases (mainly due to initial cell death post-administration) and eventual increase of BLI and PET at later time points (Fig.1). Post-mortem tissue collection and staining with Pearl's Prussian Blue showed iron within MSCs. MSCs and control hind limbs were also imaged for tdT and zsG fluorescence. We report correlation between MPI and BLI (R^2=0.677) and BLI and PET (R^2=0.864) at earlier timepoints. At later time points, MPI and BLI showed no correlation (R^2=0.002), while PET and BLI showed strong correlation (R^2=0.987). Thus, we show the feasibility of using MPI as an early cell detection technique, while PET can be used at later time points, for long-term tracking applications.

Conclusions:

MSCs were engineered with a BLI and PET reporter gene and iron-labeled to allow MPI detection. We tracked biodistribution, viability and proliferation of MSCs with MPI, BLI and PET. MPI was successful in cell detection at earlier timepoints, while PET and BLI can be used for longitudinal tracking. We show that a multi-modal imaging approach allows for sensitive imaging over longer time frames with different unique advantages for each modality.

Reference

1. Wang LLW, Janes ME, Kumbhojkar N, et al (2021) Cell therapies in the clinic. Bioeng Transl Med 6:e10214. https://doi.org/10.1002/BTM2.10214
2. Manley NC, Steinberg GK (2012) Tracking Stem Cells for Cellular Therapy in Stroke. Curr Pharm Des 18:3685. https://doi.org/10.2174/138161212802002643

Oral Presentation

Disclosures: The authors have disclosed no financial interest.

091-Dehydroascorbic acid: A multifaceted substrate for developing efficient DNP formulations for simultaneous assessment of multiple metabolic pathways using Hyperpolarized Magnetic Resonance Imaging

Presenter: Saket Patel, Memorial Sloan Kettering Cancer Center

Saket Patel[1], Nathaniel Kim[2], Paola Porcari[3], Thasin Peyear[3], Marjan Berishaj[3], Elizabeth Coffee[3], Kayvan Keshari[3]

[1]*Memorial Sloan Kettering Cancer Center*
[2]*Memorial Sloan Kettering Cancer Center, New York*
[3]*Memorial Sloan Kettering Cancer Center, New York, NY*

Introduction:

After two decades of advancements in the field of hyperpolarized magnetic resonance spectroscopy (MRS), there are still very few substrates like [1-^{13}C]pyruvate ([1-13C]PA) that meets the standard for clinical translation. The main hinderance in expanding the HP substrate library arises due to the issues of solubility in physiological solvents, low polarization, low substrate concentration post dissolution, and short spin lattice relaxation time (T_1). Herein, we report a way to improve the polarization of key metabolites using another metabolite dehydroascorbic acid (DHA). Role of DHA as an efficient HP probe for assessing oxidative stress, as a co-dissolved probe for simultaneous monitoring of three metabolic pathways, and as a glassing matrix/physiological solvent for highly efficient HP MRS of other crucial substrates namely [2-^{13}C]Fructose and [1-^{13}C]Glycerate has been demonstrated.

Methods:

The hyperpolarization was carried out on SpinLab polarizer (5 T, 0.8 K) using microwave irradiation at 139.88 GHz. The four samples were investigated: **1)** [1-^{13}C]DHA/PA (40/60; v/v); **2)** [1-^{13}C]DHA/[1-^{13}C]PA/[2-^{13}C]PA (40/30/30; v/v/v); **3)** [2-^{13}C]Fructose/DHA/H_2O (55/15/30; v/v/v); **4)** [2-^{13}C]glycerate/DHA/H_2O (3.5 M glycerate and 1.48 M DHA). Sample **1-2** was doped with 15 mM of AH111501 radical, and samples **3-4** were doped with 15 mM OX063 radical. The frozen sample was polarized for about 1.5-2 hours and dissolved in 12 mL of D_2O (sample **1-2** neutralized using equimolar amount of 4M NaOAc to neutralize PA). Polarization and ^{13}C T_1 of each the hyperpolarized substrate was measured at 1T (Magritek) by recording a ^{13}C NMR spectra every 3s using a 5-degree flip angle. The ^{13}C polarization and ^{13}C T_1 calculations were carried out using MATLAB software. *Simultaneous in vivo Chemical Shift Imaging (CSI) of HP [1-^{13}C]DHA, [1-^{13}C]PA, and [2-^{13}C]PA was performed* using a 3T MRI system (Bruker, Billerica, MA) equipped with a 40 mm inner-diameter, quadrature double-tuned ^{1}H/^{13}C volume coil and ^{13}C Urea phantom as a chemical shift reference. 250 μL of HP solution (containing *1-^{13}C]DHA, [1-^{13}C]PA, and [2-^{13}C]PA in* 43 mM, 46 mM, 47 mM concentration, respectively) was injected to a nude mice over 10s and MRS acquisition was carried out 25 seconds after injection. Data was analyzed using MATLAB and SIVIC.

Results and discussion:

DHA monomer was synthesized via the air oxidation of vitamin C using charcoal (**Figure A**). A ~7 times boost in ^{13}C polarization of DHA was observed compared to previous reports using DHA dimer.[1] (**Figure B**) Metabolic products of all three metabolites were observed in nude mice brain, in a single experiment by injecting HP solution from sample **2** into a nude mice. (**Figure C**)
The Polarization of [2-^{13}C]Fructose in DHA/H_2O was improved by a factor of two (**Figure D**) and a 1.5x times for [2-^{13}C]glycerate (**Figure E**).[2, 3] The reason for this boost in polarization of fructose and glycerate sample in DHA is because of good glassing nature of DHA monomer, which allows efficient polarization transfer via spin diffusion. The ^{13}C T_1 of Fructose can be further increased using deuterated analogue of [2-^{13}C]Fructose.[2]

Conclusion:

We have developed the potential of DHA monomer as a multiuse DNP probe. A new method to simultaneously hyperpolarize multiple substrates using DHA monomer and, for the first time, a simultaneous investigation of three probes has been demonstrated. The huge polarization boost for DHA, fructose, and glycerate demonstrate the efficiency of DHA as a substrate as well as glassing agent. These developments pave way of imaging multiple metabolic pathways simultaneously, which could provide crucial clinically relevant information. *In vivo* MRI studies using HP [2-^{13}C]Fructose and HP [2-^{13}C]Glycerate to

investigate glycolysis are ongoing. Sample **1** have all the characteristics for clinical translation such as high polarization, high concentration, long ^{13}C T_1, no toxic solvent, and removable radical.

Reference

1. Keshari, K. R., Kurhanewicz, J., Bok, R., Larson, P. E. Z., Vigneron, D. B., Wilson, D. M. (2011). Hyperpolarized 13C dehydroascorbate as an endogenous redox sensor for in vivo metabolic imaging. PNAS, 150(46), 18606-18611.
2. Bohndiek, S. E., Kettunen, M. I., Hu, D., Kennedy, B. W. C., Boren, J., Gallagher, F. A., Brindle, K. M. (2011). Hyperpolarized [1-13C]-ascorbic and dehydroascorbic acid: vitamin C as a probe for imaging redox status in vivo. JACS, 133(30), 11795-11801.
3. Timm, K. N., Hu, D., Williams, M., Wright, A. J., Kettunen, M. I., Kennedy, B. W. C., Larkin, T. J., Dzien, P., Marco-Rius, I., Bohndiek, S. E., Brindle, K. M. (2017). Assessing oxidative stress in tumors by measuring the rate of hyperpolarized [1-13] dehydroascorbic acid reduction using 13C magnetic resonance spectroscopy. Journal of Biological Chemistry, 292(5), 1737-1748.
4. Keshari KR, Wilson DM, Chen AP, Bok R, Larson PE, Hu S, Van Criekinge M, Macdonald JM, Vigneron DB, Kurhanewicz J (2009). Hyperpolarized [2-13C]-fructose: a hemiketal DNP substrate for in vivo metabolic imaging. J Am Chem Soc., 131(48), 17591-6.
5. Tee SS, Kim N, Cullen Q, Eskandari R, Mamakhanyan A, Srouji RM, Chirayil R, Jeong S, Shakiba M, Kastenhuber ER, Chen S, Sigel C, Lowe SW, Jarnagin WR, Thompson CB, Schietinger A, Keshari KR. Ketohexokinase-mediated fructose metabolism is lost in hepatocellular carcinoma and can be leveraged for metabolic imaging. Sci Adv., 8(14), eabm7985.
6. Park JM, Wu M, Datta K, Liu SC, Castillo A, Lough H, Spielman DM, Billingsley KL.(2017). Hyperpolarized Sodium [1-13C]-Glycerate as a Probe for Assessing Glycolysis In Vivo. J Am Chem Soc., 39(19), 6629–6634.

Oral Presentation

Disclosures: The authors would like to disclose that HP pyruvate is an investigational device.

092-Preliminary results of the first microtubule-based PET imaging studies in cognitively normal and impaired older adult subjects

Presenter: Kiran Kumar Solingapuram Sai, Wake Forest School of Medicine

Naresh Damuka[1], Bhuvanachandra Bhoopal[2], Mack Miller[3], Ivan Krizan, Avinash H. Bansode[3], Melissa Rundle[4], Krishna Gollapelli, Samuel N. Lockhart[4], Akiva Mintz[5], Suzanne Craft[6], **Kiran Kumar Solingapuram Sai**

[1]Wake Forest School of Medicine, Winston Salem
[2]Wake Forest School of Medicine, Winston Salem, NC
[3]Wake Forest School of Medicine, Winston-Salem, NC
[4]Wake Forest School of Medicine
[5]Columbia University, New York, New York
[6]Wake Forest School of Medicine, Winston Salem, North Carolina

Introduction:

Disruption of the structural integrity of the microtubule (MT) network and impairment of MT function are critical for the pathophysiology of Alzheimer's disease (AD) and related disorders (ADRDs). Additionally, MT-based pathophysiology is commonly associated with tauopathies. Our lab reported the first brain-penetrant PET radiotracer [^{11}C]MPC-6827 to image MTs *in vivo* in both rodent and non-human primate models of AD. Our mechanistic studies demonstrated that [^{11}C]MPC-6827 uptake is elevated with destabilized tubulins. We reported the dosimetry of [^{11}C]MPC-6827 in healthy adults (WMIC 2021). Here we report the first clinical [^{11}C]MPC-6827 PET imaging study in age-matched cognitively normal and impaired male older adult subjects.

Methods:

Two cognitively normal (both [^{11}C]PiB Aβ and [^{18}F]flortaucipir [FTP] tau-PET negative) and two cognitively impaired (both Aβ-PET-positive and n=1 FTP positive) male subjects (79-85 y) with brain MRI brain scans were recruited from Wake Forest Alzheimer's Disease Research Center (ADRC) Clinical Cohort. [^{11}C]MPC-6827 was produced from the corresponding phenol precursor following our reported methods. Dynamic 0-60 min brain PET imaging was obtained with an intravenous injection of [^{11}C]MPC-6822 (9±0.5 mCi, <10 μg) using the GE Discovery PET/CT scanner. ROIs were drawn on the whole brain, cortex, thalamus, putamen, cerebellum, hypothalamus, and hippocampus from the fused PET/MR DICOM images using the PMOD software. Time activity curves (TACs), and standard uptake values (SUV) were determined and correlated closely with FTP tau, PiB Aβ PET, and age. As FTP primarily measures phosphor-tau expression in AD brains, we closely correlated its uptake with our destabilized MT tracking radiotracer, [^{11}C]MPC-6827.

Results:

[^{11}C]MPC-6827 was produced with high radiochemical purity (>99.8%) and specific activity (3960 ± 100 mCi/μmol). Based on the SUV analysis, uptake of radiotracer was higher in the cognitively impaired subjects compared to the controls in all the studied brain regions. Radiotracer uptake was positively correlated with their age, Aβ, and tau uptake—validating its relevance with existing AD biomarkers. When examined with the Braak-based analyses (tau staging scheme) with SUVRs from both FTP (80-100 min post-injection) and [^{11}C]MPC-6827 (28-60 min post-injection) with inferior cerebellar reference for both radiotracers, [^{11}C]MPC-6827 and FTP SUVR values were positively correlated ($^{*}p$=0.077) and the scatter plot exhibited an L-shaped association, such that elevated FTP (phosphor-tau) uptake was present only when [^{11}C]MPC-6827 (MT destabilization) uptake was already present.

Conclusion:

Our strong preliminary results here suggest that MT destabilization precedes paired helical filaments of tau in neurofibrillary tangles. We are currently collecting data on more subjects to exploit the clinical significance of the MT-based PET in AD imaging--a potential new platform for early detection of the neurodegeneration process in AD.

Reference

1. WMIC 2021; First-in-human PET imaging of BBB permeable beta-tubulin tracer
2. Mol 2020, 25(10), 2289
3. Alzheimer's Dement., 17: 2021

Oral Presentation

Disclosures: The authors have disclosed no financial interest.

093-Multimodal imaging platform for quantification of the pharmacokinetics and transduction of engineered AAVs

Presenter: Jai Woong Seo, Stanford University

Jai Woong Seo[1], Javier Ajenjo[2], Bo Wu[3], Raie Marina[1], Elise Robinson[4], James Wang[5], Corinne Beinat[4], Michelle L. James[4], Bin Shen[6], Timothy Miles[7], Viviana Gradinaru[7], Katherine W. Ferrara[1]

[1]*Stanford University, Palo Alto, CA*
[2]*Stanford University*
[3]*Stanford Universtiy, Palo Alto, CA*
[4]*Stanford University, Stanford, CA*
[5]*Stanford University, Palo Alto, California*
[6]*Molecular Imaging Program at Stanford (MIPS), Stanford, CA*
[7]*California Institute of Technology (Caltech)*

Adeno-associated viruses (AAVs) delivering single-stranded deoxyribonucleic acids (ssDNA) within a 25-nm capsid protein are widely employed for gene therapy. Novel engineered AAVs targeting the brain transduced primarily neurons and astrocytes in preclinical models with minimal integration into peripheral and clearance tissues[1,2]. The influence of capsid characteristics on delivery pharmacokinetics (PK) and gene transduction efficiency is not fully understood due to a lack of methods to visualize the process. Here, we report a multimodal AAV imaging platform combining optical and positron emission tomography (PET) reporter genes along with capsid tagging[3] to assess the 1) temporal and spatial distribution and 2) transduction of AAVs. Combined optical and PET imaging allows the pharmacokinetics, cellular specificity, and protein expression kinetics of engineered AAV vectors to be assayed *in vivo* for the first time. Multimodal imaging of AAVs (PHP.eB and CAP-B10 engineered from AAV9) reveals insight of clearance, zonal and cellular localization.

Methods:

Surface lysines on AAVs were modified with tetrazine-NHS ester (Tz-NHS) to yield Tz-AAVs. After overnight dialysis of the mixture, Tz-AAVs were reacted with ($[^{64}Cu]Cu\text{-}NOTA)_8$-TCO or Cy5-TCO. Labeled AAVs were purified and concentrated with an Amicon spin filter (MWCO, 100 kDa) with multiple 15 mL PBS (0.01% Pluronic F-68) washes. The number of AAV vectors was determined by qPCR. $[^{64}Cu]$Cu-AAVs (AAV9 n=3, PHP.eB n=4, CAP-B10 n=4) and Cy5-AAVs (AAV9 n=2, PHP.eB n=2, CAP-B10 n=2) were administered to C57BL/6 mice through tail-vein injection. PET/CT scans were performed at 0, 4, and 21 h p.i. for PK and biodistribution. For optical studies, tissues were harvested at 4 h p.i. after perfusion.

Results*:*

The radiochemical purity of AAVs was >98% on instant thin-layer chromatography (ITLC). The recovery yields of $[^{64}Cu]$Cu- and Cy5-AAVs were 51% and 19%, respectively. Brain accumulation of $[^{64}Cu]$Cu-PHP.eB and -CAP-B10 (P <0.0001 at 0, 4 and 21 h) was greater at all time points than that of AAV9 (**Fig. A** and **B**). The liver accumulation of $[^{64}Cu]$Cu-PHP.eB was 8.7%ID/cc (P=0.038), which was greater than $[^{64}Cu]$Cu-CAP-B10 (5.6%ID/cc, P=0.038) and $[^{64}Cu]$Cu-AAV9 (3.1%ID/cc, P=0.0026) (**Fig. C**). On fluorescence microscopy, Cy5-PHP.eB and -CAP-B10 capsids were sequestered within Kupffer cells (**Fig. D** and **F**) which resulted in reduced transduction of both genes in the liver (**Fig. E** and **G**) compared to Cy5-AAV9. PET reporter gene and capsid imaging provide a longitudinal assessment of gene transduction within the brain.

Methods*:*

PHP.eB (n=4) and AAV9 (n=4), both with the EF1A-PKM2 transgene, or saline (n=4) were systemically injected ($2x10^{11}$ vg/mouse), and PKM2 transduction was assessed by $[^{18}F]$DASA-23 at 1, 3, 16, and 34 weeks p.i. mRNA and protein expression were measured by RT-qPCR and western blot, respectively (n_{total}= 60).

Results:

By PET image analysis, PKM2 expression at 1 week p.i. was significantly higher in PHP.eB-dosed mice (p = 0.033) than in AAV9-dosed mice. $[^{18}F]$DASA-23 uptake was elevated 1.7 fold at 1 week (p = 0.033), 2.2 fold at 3 weeks (p = 0.020), and remained at >2 fold until 34 weeks p.i. of PHP.eB (**Fig. H**). mRNA and protein expression levels resulting from PHP.eB administration were significantly higher than that of AAV9 throughout the study.

In conclusion,

the multimodal AAV imaging platform facilitated the assessment of the PK and transduction of engineered AAV variants in mice. This report lays the groundwork for larger animal and human studies to provide mechanistic insight and characterization of species-related differences.

Reference

1. Chan, K. Y. et al. Engineered AAVs for efficient noninvasive gene delivery to the central and peripheral nervous systems. Nat. Neurosci. 20, 1172–1179 (2017).
2. Goertsen, D. et al. AAV capsid variants with brain-wide transgene expression and decreased liver targeting after intravenous delivery in mouse and marmoset. Nat. Neurosci. (2021). doi:10.1038/s41593-021-00969-4
3. Seo, J. W. et al. Positron emission tomography imaging of novel AAV capsids maps rapid brain accumulation. Nat. Commun. 11, 2102 (2020).

Oral Presentation

Disclosures: The authors have disclosed no financial interest.

094-Preclinical evaluation of [203Pb]VMT-α-NET and [212Pb] VMT-α-NET as imaging-guided alpha-particle radiotherapy for SSTR2-positive tumors

Presenter: Mengshi Li, Viewpoint Molecular Targeting, Inc.

Mengshi Li[1], Dijie Liu[2], Brianna Cagle[2], Nicholas Baumhover[2], Dongyoul Lee[3], Frances L. Johnson[1], Michael K. Schultz[4]

[1]*Viewpoint Molecular Targeting, Inc., Coraville, IA*
[2]*Viewpoint Molecular Targeting, Inc.*
[3]*Human Toxicology, University of Iowa, Iowa City, IA*
[4]*University of Iowa, Iowa City, IA*

Objective:

Pb-203 and Pb-212 have been emerging as a promising elementally-matched theranostic pair for imaging-guided alpha-particle radiotherapy. VMT-alpha-NET (*i.e.,* VMT-α-NET; **Figure 1**) is a somatostatin receptor 2 (SSTR2)-targeted bifunctional peptide coupled with novel Pb specific chelator (PSC) that is designated for Pb (II) radiocomplex. In the current study, preclinical *in vitro* and *in vivo* evaluation of ^{203}Pb- and ^{212}Pb-labeled VMT-α-NET was conducted.

Methods:

Radiosynthesis of $[^{203}Pb]$VMT-α-NET and $[^{212}Pb]$VMT-α-NET was conducted in 0.5 M sodium acetate buffer (pH=5.4). Radiochemical

stability of [^{203}Pb]VMT-α-NET and [^{212}Pb]VMT-α-NET in human serum was determined. Stability of ^{212}Bi daughter in VMT-α-NET during the ^{212}Pb-to-^{212}Bi decay was also determined. Binding affinity (*i.e.*, Kd) of [^{203}Pb]VMT-α-NET was determined by Scatchard plot Bmax binding assays in AR42J cells. *In vivo* SSTR2-mediated tumor targeting of [^{203}Pb]VMT-α-NET was determined by SPECT imaging in athymic nude mice bearing AR42J xenografts. *In vivo* biodistribution of [^{212}Pb]VMT-α-NET in normal organs and potential redistribution of ^{212}Bi daughter were determined in CD-1 Elite mice.

Results:

Rapid incorporation of ^{203}Pb and ^{212}Pb in VMT-α-NET was observed after reactions under 80ºC within 15 min. Greater than 95% radiochemical stability was observed in both [^{203}Pb]VMT-α-NET and [^{212}Pb]VMT-α-NET after incubation in human serum for 55 hours and 24 hours, respectively. Specifically, stable decay product [^{212}Bi]VMT-α-NET with minimal free ^{212}Bi was observed. [^{203}Pb]VMT-α-NET demonstrated superior binding affinity to SSTR2 with K_d=0.59 nM. In *in vivo* studies, rapid tumor uptake and renal clearance of [^{203}Pb]VMT-α-NET were observed in athymic nude mice bearing AR42J xenograft. In the biodistribution study, nearly identical biodistribution profiles of [^{212}Pb]VMT-α-NET and progeny [^{212}Bi]VMT-α-NET were found. No redistribution of ^{212}Bi activity was identified, indicating that ^{212}Bi remained co-localized with parent [^{212}Pb]VMT-α-NET *in vivo*.

Conclusion:

In the current study, high radiochemical stability, tumor targeting were observed in [^{203}Pb]VMT-α-NET and [^{212}Pb]VMT-α-NET. In addition, ^{212}Bi remained stable in the VMT-α-NET chelator during the ^{212}Pb-to-^{212}Bi decay. Therefore, [^{203}Pb]VMT-α-NET and [^{212}Pb]VMT-α-NET demonstrate great potential for image-guide alpha-particle therapy for SSTR2 positive NET tumors. Preclinical alpha-particle radiotherapy of [^{212}Pb]VMT-α-NET is ongoing to determine the optimized dosing regimen for [^{212}Pb]VMT-α-NET.

Oral Presentation

Disclosures: The authors have disclosed no financial interest.

095-Optical- and MRI-detectable USPIO-5D3-DM1 nano-constructs for prostate cancer therapy

Presenter: Sudath Hapuarachchige, Johns Hopkins University School of Medicine

Sudath Hapuarachchige[1], Ge Si[2], Cyril Ba?inka[3], Dmitri Artemov[2]

[1]*Johns Hopkins University School of Medicine, BALTIMORE, Maryland*
[2]*Johns Hopkins University School of Medicine, BALTIMORE, MD*
[3]*Institute of Biotechnology of the Czech Academy of Sciences, Vestec, Czech Republic*

Introduction:

Prostate cancer (PC) has the second highest cancer related mortality in men.[1] Primary PC eventually becomes castrate resistant (CRPC) stage and progresses rapidly to lethal metastatic form (mCRPC).[2] In mCRPC stage, common chemotherapeutics such as docetaxel and cabazitaxel show an insufficient therapeutic efficacy. They also exhibit significant non-specific toxicities for vital organs and side effects. Prostate-specific membrane antigen (PSMA) are cell surface receptors expressed in prostate tissues; they are overexpressed in almost all PCs compared to non-prostatic tissues.[3] This expression level is also corelated with cancer aggressiveness, androgen blockage and deprivation. Therefore, PSMA is widely used as a natural biomarker for PC targeted drug delivery. PSMA-specific biomacromolecules such as anti-PSMA antibodies and peptides, and target-specific small molecules are currently used as bioligands for PSMA.[4] In this study, an original antibody-targeted ultrasmall iron oxide (USPIO) nanoparticle-based drug delivery system was developed for image-guided drug delivery in PC. A recently developed anti-PSMA monoclonal antibody (mAb), 5D3, was used as the bioligand.[5-6] 5D3 mAb has improved PSMA binding affinity and internalization characteristics compared to other existing anti-PSMA mAbs.[7] USPIO have high loading capacity and biocompatibility, as a drug delivery platform. They can be detected *in vivo* by magnetic resonance imaging (MRI) as well.

Methods:

First, 5D3 mAb was conjugated with USPIO nanoparticles and loaded with mertansine (DM1), an anti-tubulin agent, as the chemotherapeutic drug to obtain USPIO-5D3-DM1. The nano-construct was further labeled with near-infrared (NIR) fluorophore, CF-750 for optical imaging and tracking the delivery. The final USPIO-5D3-DM1-CF750 (Figure 1A) nano-construct has both therapeutic and diagnostic capabilities. The biodistribution and tumor uptake of USPIO-5D3-DM1-CF750 were evaluated in PSMA(±) xenograft mouse models. Bilateral tumor mouse models were prepared by the inoculation of PSMA(+) PC3-PIP and PSMA(-) PC3-Flu cells. Mice were administered with USPIO-5D3-DM1-CF750 nano-constructs (5.0 mg/kg in Saline, i.v.) and imaged using Xenogen *in vivo* live animal optical imaging system. **Results:** The results show high tumor uptake of nano-construct in PSMA(+) PC3-PIP tumor (Figure 1B). After 24 h, mice were euthanized and tumors and vital organs, brain, heart, lungs, liver, kidneys, spleen, and intestine were extracted and imaged *ex vivo* using Xenogen (Figure 1C). High uptake of the probe was confirmed in PSMA(+) tumor, as well as in the liver and kidneys. MR images were taken after systemic administration of USPIO-5D3-DM1-CF750 (10.0 mg/kg, i.v.) in bilateral tumor mouse models using a 9.4T Bruker Biospin MRI system. A significant change in T1 contrast was observed in tumors compared to the pre-scan (Figure 1D). T2-weighted images exhibited considerably higher contrast of USPIO-5D3-DM1-CF750 uptake in PSMA(+)than in PSMA(-) tumors. Currently, MR relaxation properties of the nano-constructs and tumor uptake of drugs are being investigated.

Conclusions:

This study establishes a strong foundation for the development of highly effective image-guided drug delivery system, using biocompatible, high-capacity USPIO drug carrier nanoparticles, high PSMA affinity 5D3 targeting mAb, and highly potent DM1 chemotherapeutics to treat PSMA-overexpressing PC.

Reference

1. Siegel, R. L.; Miller, K. D.; Jemal, A. Cancer Statistics, 2020. CA Cancer J Clin. 2020; 70: 7-30.
2. Cho, S.; Zammarchi, F.; Williams, D. G. et al. Antitumor Activity of MEDI3726 (ADCT-401), a Pyrrolobenzodiazepine Antibody-Drug Conjugate Targeting PSMA, in Preclinical Models of Prostate Cancer. Mol Cancer Ther. 2018; 17: 2176-2186.
3. Israeli, R. S.; Powell, C. T.; Corr, J. G. et al. Expression of the Prostate-Specific Membrane Antigen. Cancer Res. 1994; 54: 1807-1811.
4. Boinapally, S.; Ahn, H.; Cheng, B. et al. A Prostate-Specific Membrane Antigen (PSMA)-Targeted Prodrug with a Favorable in vivo Toxicity Profile. Sci. Rep. 2021; 11: Article No. 7114.
5. Hapuarachchige, S. Huang, C. T.; Donnelly, M. C. et al. Cellular Delivery of Bioorthogonal Pretargeting Therapeutics in PSMA-Positive Prostate Cancer. Mol Pharm 2020; 17: 98-108.

6. Colin, T. H. Guo, X.; Barinka, C. et al. Development of 5D3-DM1: A Novel Anti-Prostate-Specific Membrane Antigen Antibody-Drug Conjugate for PSMA-Positive Prostate Cancer Therapy. Mol. Pharmaceutics 2020; 17: 3392–3402.
7. Novakova, Z.; Foss, C. A.; Copeland, B. T. et al. Novel Monoclonal Antibodies Recognizing Human Prostate-Specific Membrane Antigen (PSMA) as Research and Theranostic Tools. Prostate 2017; 77: 749-764.

Oral Presentation

Disclosures: The authors have disclosed no financial interest.

096-Magnetic resonance imaging of the retention of biohybrid extracellular vesicles in the brain for sustained drug release in the repair of radiotherapy-induced brain injury

Presenter: Wenshen Wang, Kennedy Krieger Institute

Wenshen Wang[1], Safiya Aafreen[2], Chantelle Terrilion[2], Guanshu Liu[3], Ethel J. Ngen[4]

[1]*Kennedy Krieger Institute*
[2]*Johns Hopkins Univeristy*
[3]*Johns Hopkins University School of Medicine, Baltimore*
[4]*Johns Hopkins University School of Medicine, Baltimore, MD*

Introduction:

Up to 90% of brain tumor patients treated with radiotherapy experience radiotherapy-induced brain injury (RIBI) and neurocognitive impairment, later in life.[1,2] RIBI is a chronic side effect which severely impacts the quality of life of brain tumor survivors.[1,2] With more pediatric brain tumor patients surviving cancer, there is currently a need for RIBI prophylactic and therapeutic strategies.[1,2]

Hypothesis:

Neuroinflammation is a key contributor to RIBI.[1,3] Consequently, strategies to reduce neuroinflammation are being explored.[1,3] Although stem cell therapies are promising, there are concerns associated with their use.[4] This includes the possibility of teratoma formation.[5] Thus, alternative therapeutic and regenerative strategies are concurrently being explored, such as stem cell-derived extracellular vesicles (EVs) and drug loaded nanocarriers.[6, 7] EVs provide the therapeutic advantages of stem cells, while eliminating the risk of teratoma formation.[6, 7] EV-biohybrid nano drug delivery systems (DDS), are obtained by the fusion of EVs with synthetic nano DDS and provide an even greater advantage: the possibility of combining the biotherapeutic payloads from regenerative stem cells with neuroprotective drugs for enhanced therapeutic outcomes.[8, 9]

Objective:

Here, we developed a novel liposome-EV biohybrid for use as a magnetic resonance imaging (MRI) nanotheranostic agent in the repair of RIBI. This EV biohybrid synergizes the regenarative ability of stem cells with the anti-inflammation ability of interleukin 10 (IL-10) and phosphatidylserine (PS). We also evaluated its safety and retention in the brain for sustained drug release after intracranial administration, in a preclinical mouse model of RIBI.

Method:

Induced pluripotent stem cell (iPSCs)-derived EVs were isolated from conditioned medium of iSPC as described previously.[10] Western blots were used to confirm the collection and purification of EVs according to MISEV2018.[11] Phosphatidylserine liposomes (PC: PS = 2.5:1) were prepared using the thin-film hydration and extrusion method. The liposomes were loaded with 20 nm superparamagnetic paramagnetic iron oxide nanoparticles (SPIONs), functionalized with histidine tags.[10] IL-10 was loaded to the PS-liposomes by post-insertion of IL-10 conjugated palmitic acid.[12] Hybrid EVs were prepared by incubating 100 µl EVs, 100 µl 1010 liposomes containing SPIONs and 200 µl 40% PEG-8000 for 2 hrs. The size and concentration of the resulting hybrid EVs were assessed using nanoparticle tracking analysis. The EVs were next tested in mice: 8 week old male C57Bl/6J mice were treated with computed tomography (CT)-guided radiotherapy (IR) at a treatment dose of 80 Gy and a dose rate of 1.7Gy/ min.[13,14] EVs at a concentration of 10^8 EVs / 2µL,were stereotactically implanted in the irradiated brain hemispheres, two days after radiotherapy and before brain injury detection on MRI. The retention of the EVs was then monitored over four weeks, using multi-parametric MRI. EV-treated mice (Group 1) were studied in comparison to Group 2 mice, treated with radiotherapy and a vehicle (PBS); and Group 3 mice (a control untreated group). The survival and weight changes in all groups was also monitored.

Results:

Compared to other liposome-EV fusion technologies such as freeze-thaw[15] and extrusion[16], the PEG-mediated fusion can reserve many characteristics of the naïve EVs while loading therapeutics and imaging agents efficiently, as demonstrated in this study. The size of hybrid EVs is approximately the same as the naïve EVs at around 120- 130 nm diameter range. Our preliminary results showed that hybrid EVs can be readily detected in the brain on T_2*-weighted MRI after 10^8 EV particles were administrated intracranially. This MRI signal persisted throughout the imaging period.

Conclusion:

These results suggest that IL-10-loaded biohybrid EVs are retained in the brain for up to a month after intra-cranial administration. This suggests that these EV-based biohybrid systems could be used for sustained drug release in the long-term repair of RIBI and neurocognitive decline.

Reference

1. Makale MT, et al. Nature reviews Neurology 2017, 13(1):52-64.
2. Stavinoha PL, et al. Bioengineering (Basel) 2018, 5(3):73.
3. Zhao W, R et al. Curr Med Chem 2009, 16(2):130-143.
4. Smith SM, et al. Curr Stem Cell Rep 2017, 3(4):342-347.
5. Blum B, et al. In: Advances in Cancer Research. Volume 100, edn.: Academic Press; 2008: 133-158.
6. Baulch JE, et al. Proc Natl Acad Sci U S A 2016, 113(17):4836-4841.
7. Leavitt RJ, et al. Cancer Res 2020, 80(19):4266-4277.
8. Ou Y-H, et al.Seminars in Cancer Biology 2021, 74:45-61.
9. Li Y-J, et al. Journal of Nanobiotechnology 2021, 19(1):242.
10. Han Z, L et al. J Extracell Vesicles 2021, 10(3):e12054.
11. Thery C, et al. J Extracell Vesicles 2018, 7(1):1535750.
12. Toita R, et al. Biomaterials 2016, 110:81-88.
13. Ngen EJ, et al. J Neurooncol 2016, 128(2):225-233.
14. Ngen EJ, et al. Sci Rep 2015, 5(1):13628.
15. Sato YT, et al. Scientific Reports 2016, 6(1):21933.
16. Hu M, et al. ACS Nano 2021, 15(2):3123-3138.

Oral Presentation

Disclosures: The authors have disclosed no financial interest.

097-A newly designed hyperpolarized molecular probe enables the in vivo detection of aminopeptidase N activity from the tumor regions in animals

Presenter: Hiroyuki Yatabe, University of Tokyo

Hiroyuki Yatabe[1], Yutaro Saito[1], Iori Tamura[1], Yohei Kondo[2], Ryo Ishida[3], Tomohiro Seki[4], Keita Hiraga[1], Akihiro Eguchi[5], Yoichi Takakusagi[6], Keisuke Saito[6], Nobu Oshima[7], Hiroshi Ishikita[1], Kazutoshi Yamamoto[8], Murali Krishna[8], Shinsuke Sando[8]

[1]*University of Tokyo, Japan*
[2]*University of Tokyo, Tokyo, Japan*
[3]*National Institutes of Health, Japan*
[4]*Josai University, Sakado, Saitama, Japan*
[5]*University of Copenhagen, Denmark*
[6]*National Institutes for Quantum Science and Technology, Chiba, Chiba, Japan*
[7]*Kyoto University, Japan*
[8]*National Institutes of Health, Bethesda, Maryland*

Dissolution dynamic nuclear polarization (dDNP) is a technique for hyperpolarization that enhances nuclear magnetic resonance/magnetic resonance imaging (NMR/MRI) signals by five to six orders of magnitudes [1]. By utilizing molecular probes hyperpolarized with dDNP, biological events can be observed in real-time by MRI. Various DNP-NMR molecular probes have been reported, but most are naturally occurring molecules [2-4]. This situation has led to the limited scope of targets by DNP-NMR. To achieve diagnosis impossible with conventional DNP-NMR molecular probes, it is desired to develop novel DNP-NMR molecular probes targeting new biomarkers related to diseases, especially cancer. Here, we report the design and development of a new DNP-NMR molecular probe, Ala-[1-^{13}C]Gly-d_2-NMe$_2$, to detect and visualize aminopeptidase N (APN) activity *in vivo* [5]. APN is an enzyme that cleaves peptides at the N-terminus by recognizing neutral residues such as alanine and is known to be involved in tumor angiogenesis and metastasis [6]. A DNP-NMR molecular probe for detecting APN activity, [1-^{13}C]Ala-NH$_2$, has previously been reported [7]. [1-^{13}C]Ala-NH$_2$ could be used for the detection of APN activity *in vitro* but was not applicable *in vivo* mainly because of its slow enzymatic reaction. We considered this slow enzymatic reaction was attributed to the low affinity of the probe to APN. Therefore, in this research, we began with the calculation of the binding affinity of probe candidates (Ala-NH$_2$, Ala-Gly, and Ala-Gly-NMe$_2$) in the APN active pocket by QM/MM analysis. The results showed that the carbonyl group at the second residue from N-terminus of a probe contributed to the interaction with E384 in APN, resulting in a high affinity with APN. Next, we measured the kinetic parameters (K_m, k_{cat}) of each probe for APN. The K_m value of Ala-NH$_2$ (15.7 ± 4.4 mM) was higher than those of Ala-Gly (3.6 ± 0.3 mM) and Ala-Gly-NMe$_2$ (1.9 ± 0.1 mM), suggesting that Gly moiety is essential for high affinity with APN, as computational results indicated. The k_{cat} value of Ala-Gly-NMe$_2$ (255 ± 22 s^{-1}) was around eight-fold higher than that of Ala-Gly (32 ± 2 s^{-1}), and Ala-Gly-NMe$_2$ showed high selectivity for APN. Therefore, Ala-Gly-NMe$_2$ was selected as a potential probe candidate. To develop a practical DNP-NMR molecular probe, spin-lattice relaxation time (T_1), which determines the hyperpolarization lifetime, needs to be long enough. To achieve long T_1, the carbonyl carbon at Gly moiety in Ala-Gly-NMe$_2$ was selected as a ^{13}C-labeled position, and the alpha-position at Gly moiety was deuterated. The developed probe, Ala-[1-^{13}C]Gly-d_2-NMe$_2$, showed sufficiently long T_1 of 56.7 ± 8.7 s at 3 T. Next, hyperpolarization studies were conducted. The solution of Ala-[1-^{13}C]Gly-d_2-NMe$_2$ (4–5 M) was hyperpolarized. After the dissolution, the probe solution was intravenously injected into tumor xenograft mice (MIA PaCa-2) and ^{13}C magnetic resonance spectra were acquired from the tumor region. The distinct probe and product ([1-^{13}C]Gly-d_2-NMe$_2$) signals were observed. When pre-administrating phebestin [8], an inhibitor of APN, the product signal was suppressed, suggesting that Ala-[1-^{13}C]Gly-d_2-NMe$_2$ can detect APN activity *in vivo*. Finally, we performed chemical shift imaging. The results showed that the product to probe ratio from the tumor region was higher than that from the muscle region, indicating that this developed probe can detect site-specific APN activity *in vivo*. This is the first time to detect and image APN activity *in vivo* with DNP-MRI. We developed a practical DNP-NMR molecular probe with a sufficient conversion to detect APN activity *in vivo*. Since APN is known to be a multifunctional enzyme and is related to various diseases such as hypertension, inflammation, and cancer, the developed probe Ala-[1-^{13}C]Gly-d_2-NMe$_2$ has the potential to be utilized to diagnose these diseases.

Reference

1. J. H. Ardenkjær-Larsen et al. Proc. Natl. Acad. Sci. U. S. A., 2003, 100, 10158–10163.
2. Y. Kondo et al. Angew. Chem., Int. Ed. 2021, 60, 14779–14799.
3. K. R. Keshari et al. Chem. Soc. Rev. 2014, 43, 1627–1659.
4. C. Mu et al. Mol. Imaging Biol. 2021, 23, 323–334.
5. Y. Saito et al. Sci. Adv. 2022, 8, eabj2667.
6. S. A. Amin et al. J. Med. Chem. 2018, 61, 6468–6490.
7. R. Hata. et al. Angew. Chem., Int. Ed. 2016, 55, 1765–1768.
8. M. Nagai et al. J. Antibiot. 1997, 50, 82–84.

Oral Presentation

Disclosures: The authors have disclosed no financial interest.

098-Clinical fluorescence lifetime imaging using exogeneous cancer targeted probes

Presenter: Anand Kumar, Massachusetts General Hospital

Rahul Pal[1], Thinzar M. Lwin[2], Yu-Jin Lee[3], Marisa Hom[3], Eben Rosenthal[3], **Anand T. Kumar**[4]

[1]*Athinoula A. Martinos Center for Biomedical Imaging, Charlestown, Massachusetts*
[2]*City of Hope*
[3]*Stanford University, Palo Alto, CA*
[4]*Massachusetts General Hospital*

Fluorescence molecular imaging, using tumor targeted fluorescent dyes, is being widely explored for tumor detection during surgeries and for cancer staging. Besides allowing enhanced accuracy for tumor margin assessment and identifying distant metastases (e.g., lymph nodes) in various surgical settings, the use of probes excitable in the near infrared (NIR) can allow non-invasive imaging of cancer in superficial lymph nodes and in intact organs such as the breast. A wide range of fluorescent agents have been developed for tumor targeting, with some of these agents currently in late stage clinical trials [1-3]. Despite significant progress in developing new cancer targeted contrast agents, non-specific probe accumulation in normal tissue results in poor tumor fluorescence

contrast, precluding widespread clinical adoption. Here we present the first clinical evidence [4] that fluorescence lifetime (FLT) imaging can provide tumor specificity at the cellular level in patients systemically injected with panitumumab-IRDye800CW, an epidermal growth factor receptor (EGFR) targeted NIR fluorescent probe. We performed wide-field and microscopic fluorescence lifetime imaging of resection specimens from patients injected with panitumumab-IRDye800CW under an FDA directed clinical trial. We show that the FLT within EGFR overexpressing cancer cells is significantly longer than the FLT of normal tissue, providing high sensitivity (>98%) and specificity (>98%) for tumor vs. normal tissue classification, despite the presence of significant non-specific probe accumulation. We further show microscopic evidence that the mean tissue FLT is spatially correlated (r > 0.85) with tumor-specific EGFR expression in tissue and is consistent across multiple patients. These tumor cell-specific FLT changes can be detected through thick biological tissue, allowing highly specific tumor detection and non-invasive monitoring of tumor EFGR expression in vivo. Our data indicate that FLT imaging is a promising approach for enhancing tumor contrast using an antibody targeted NIR probe with a proven safety profile in humans, suggesting a strong potential for clinical applications in image guided surgery, cancer diagnostics, and staging. To determine the tumor specificity of panitumumab-IRDye800CW FLT in human head and neck cancers, we performed an imaging study of tissue specimens from surgery of oral squamous cell carcinoma (OSCC) patients who received a systemic injection of panitumumab-IRDye800CW, 48 hours prior to surgery. Figure 1 shows Fluorescence lifetime imaging microscopy (FLIM, left), EGFR IHC (center) and H&E stained histology (right) images from a representative specimen, illustrating the longer FLT in OSCC tumors corresponding to the higher EGFR expression in the tumor region. Fig. 1a shows a large field of view region of interest (ROI). Long FLT (red) is observed in two EGFR overexpressing tumor clusters (Fig. 1a, arrows). Low EGFR expressing normal tissue surrounding the tumor showed shorter FLTs (green/blue) consistent with the FLTs of nonspecific panitumumab-IRDye800CW and tissue autofluorescence. Figures 1b and 1c show higher magnification regions of interest (ROIs, shown as dashed boxes) from Fig. 1a and Fig. 1b, respectively. The FLIM images show long FLTs spatially colocalized within high EGFR expressing tumor cells and the tumor specificity of FLT enhancement can be observed in individual OSCC cell clusters down to single cell resolution (Fig. 1c, Arrows). We have performed several clinical trials to evaluate the safety of panitumumab-IRDye800CW probe in humans. The optical imaging technique used in our work employs safe and non-ionizing NIR light. Several NIR fluorescence devices have previously been FDA approved for image guided surgery, and could serve as predicates for future FDA clearance of FLT imaging devices. The translational relevance of this work therefore lies in the fact that fluorescence lifetime imaging in conjunction with panitumumab-IRDye800CW can be potentially extended to intraoperative image-guided surgery upon successful validation in clinical trials

Reference

1. Azari, F., G. Kennedy, E. Bernstein, C.G. Hadjipanayis, A.L. Vahrmeijer, B.L. Smith, E.L. Rosenthal, B.D. Sumer, J. Tian, and E.R. Henderson, Intraoperative molecular imaging clinical trials: a review of 2020 conference proceedings. Journal of biomedical optics, 2021. 26(5): p. 050901.
2. Lee, J.Y., S.S. Cho, W. Stummer, J.L. Tanyi, A.L. Vahrmeijer, E.L. Rosenthal, B. Smith, E.R. Henderson, D.W. Roberts, and A. Lee, Review of clinical trials in intraoperative molecular imaging during cancer surgery. Journal of biomedical optics, 2019. 24(12): p. 120901.
3. Pogue, B.W. and E.L. Rosenthal, Review of successful pathways for regulatory approvals in open-field fluorescence-guided surgery. Journal of Biomedical Optics, 2021. 26(3): p. 030901.
4. Pal, R., M. E Hom, N.S. van den Berg, T. M Lwin, Y.-J. Lee, A. Prilutskiy, W. Faquin, E. Yang, S.V. Saladi, M.A. Varvares, E.L. Rosenthal, and A.T.N. Kumar, First Clinical Results of Fluorescence Lifetime-Enhanced Tumor Imaging Using Receptor-targeted Fluorescent ProbesEGFR-targeted Lifetime Imaging of Cancers. Clinical Cancer Research, 2022: p. OF1-OF12.

Oral Presentation

Disclosures: The authors have disclosed no financial interest.

099-Antigen-dependent inducible T cell reporter system for PET imaging of breast cancer and glioblastoma

Presenter: Jaehoon Shin, University of California San Francisco

Jaehoon Shin[1], Matthew Parker[2], Joseph E. Blecha[3], Suzanne Lapi[4], Robert R. Flavell[3], David M. Wilson[3]

[1]University of California San Francisco, San Francisco, CA, [2]University of California, San Francisco, San Francisco, California, [3]University of California, San Francisco, San Francisco, CA, [4]University of Alabama at Birmingham, Birmaingham, Alabama

For the past several decades, chimeric antigen receptor T cell (CAR T) therapies have shown promise in the treatment of cancers. These treatments would greatly benefit from companion imaging biomarkers to follow the trafficking of T cells *in vivo*. Using synthetic biology, we engineered T cells with a chimeric receptor SyNthetic Intramembrane Proteolysis Receptor (SNIPR) that induces overexpression of an exogenous reporter gene cassette upon recognition of specific tumor markers. We then applied a SNIPR-based positron emission tomography (PET) reporter system to two cancer-relevant antigens, human epidermal growth factor receptor 2 (HER2) and epidermal growth factor receptor variant III (EGFRvIII), commonly expressed in breast and glial tumors respectively. Antigen-specific reporter induction of the SNIPR-PET T cells was confirmed *in vitro* using GFP fluorescence, luciferase luminescence, and the HSV-TK PET reporter with [^{18}F]FHBG. T cells associated with their target antigens were successfully imaged using PET in dual xenograft HER2+/HER2- and EGFRvIII+/EGFRvIII- animal models, with > 10-fold higher [^{18}F]FHBG signals seen in antigen-expressing tumors versus the corresponding controls. The main innovation described is therefore PET detection of T cells via specific antigen-induced signals, in contrast to reporter systems relying on constitutive gene expression.

References

1. Shin, J. et al. Antigen-dependent inducible T cell reporter system for PET imaging of breast cancer and glioblastoma. bioRxiv, 2022.2002.2016.480729, doi:10.1101/2022.02.16.480729 (2022).
2. Zhu, I. et al. Modular design of synthetic receptors for programmed gene regulation in cell therapies. Cell 185, 1431-1443 e1416, doi:10.1016/j.cell.2022.03.023 (2022).
3. Roybal, K. T. et al. Engineering T Cells with Customized Therapeutic Response Programs Using Synthetic Notch Receptors. Cell 167, 419-432 e416, doi:10.1016/j.cell.2016.09.011 (2016).
4. Roybal, K. T. et al. Precision Tumor Recognition by T Cells With Combinatorial Antigen-Sensing Circuits. Cell 164, 770-779, doi:10.1016/j.cell.2016.01.011 (2016).

Oral Presentation

Disclosures: The authors have disclosed no financial interest.

100-TREM1-targeted PET imaging of tumor-associated macrophages in an orthotopic murine model of intracranial metastatic melanoma

Presenter: Irene Falk, Stanford University

Irene N. Falk[1], Aisling M. Chaney[2], Mackenzie Carlson[3], Rohit Verma[4], Carmen Azevedo[2], Mausam Kalita[5], Isaac M. Jackson[6], Michael Lim[7], Michelle L. James[3]

[1]*Stanford University, Mountain View, CA*
[2]*Washington University in St. Louis, St. Louis, MO*
[3]*Stanford University, Stanford, CA*
[4]*Stanford University School of Medicine, Palo Alto, CA*
[5]*Stanford University, Stanford*
[6]*Stanford University, San Bruno, CA*
[7]*Stanford University Medical Center, Palo Alto, CA*

Objectives:

Metastatic brain tumors have been demonstrated to suppress anti-tumor T-cell activation through immune modulation of tumor-associated macrophages (TAMs). Triggering receptor expressed on myeloid cells 1 (TREM1) is a membrane receptor involved in immune signaling that is highly expressed on TAMs, but not cancer cells, and is therefore a promising imaging target for the highly specific detection of TAMs. Because TREM1 levels are intimately associated with cancer recurrence, progression, metastasis, and poor survival rates, imaging this target could also provide insight into the functional status of myeloid cells in the tumor microenvironment. Here we evaluate a TREM1-targeted PET tracer for its ability to detect TAMs in an intracranial model of metastatic melanoma.

Methods:

C57Bl/6 mice (n=6) were stereotactically implanted supratentorially in the left hemisphere with 200,000 B16-F10 cells suspended in 20 µl of PBS. Sham mice (n=5) received stereotactic injections of an equivalent volume of PBS. After 6 days, mice received an intravenous injection of [^{64}Cu]TREM1-mAb (197 ± 6 mCi) and were imaged 24- and 48- hours later using MR and PET/CT. To quantify non-specific antibody binding, a subsequent study compared [^{64}Cu]TREM1-mAb-injected tumor-bearing mice (n=7) to tumor-bearing mice injected with a [^{64}Cu]-conjugated isotype control-mAb (n=5). After imaging, mice were perfused to remove unbound intravascular [^{64}Cu]TREM1-mAb, and radioactivity in dissected tissues was measured using a gamma counter. Brain sections from selected tumor and sham mice were further analyzed via *ex vivo* autoradiography and stained with H&E. Tumor PET signal was identified by co-registering brain PET and T2-weighted MR.

Results:

At 24 hours post-injection, TREM1-PET signal was significantly higher within the brain tumors of tumor-bearing mice than in the contralateral parenchyma (n=6) or the normal brains of sham mice (n=5) (3.72±0.18%ID/g; contralateral brain: 2.01±0.35%ID/g; sham brain: 0.78±0.18%ID/g, p<0.01, **Fig 1a and c**). Significant differences were also seen at 48 hours post-injection (p<0.0001, **Suppl Fig 1a**). Similarly, *ex vivo* gamma counting at 48 hours revealed significantly elevated radioactive signal in the brains of tumor-implanted mice relative to shams (tumor: 1.85±0.32, sham: 0.28±0.03, p=0.01, **Fig 1b**). Specifically, *ex vivo* gamma counting demonstrated significantly higher radioactive signal in the left and right hemispheres of tumor-bearing animals when compared to the corresponding hemispheres of sham mice (left tumor: 1.50±0.21%ID/g; left sham: 0.16±0.03%ID/g, right tumor: 0.44±0.06%ID/g, right sham: 0.16±0.01%ID/g, p<0.001, **Suppl Fig 1c**). Autoradiography in tumor-bearing mice likewise showed significantly increased [^{64}Cu] TREM1-mAb binding within the left hemisphere when compared to the contralateral brain and the corresponding hemispheres of sham mice (p<0.0001) (**Fig 1d**, **Suppl Fig 1c**), and increased signal was found to localize to the site of the tumor on H&E (**Suppl Fig 1d**). Importantly, [^{64}Cu]-isotype control-mAb binding in tumor-bearing brains was found to be significantly lower than [^{64}Cu]TREM1-mAb binding (p=0.009) (**Suppl Fig 1c**).

Conclusion:

Our studies demonstrate that [^{64}Cu]TREM1-mAb can be used to detect increases in TREM1+ cells in the tumor microenvironment of tumor-bearing mice. The ability to image TREM1-positive cells *in vivo* in the tumor microenvironment could profoundly impact our understanding of the functional role of TAMs in the development of brain metastases, as well as our ability to select and monitor chemotherapies.

Reference

1. Xie et al. Frontiers in endocrinology, 2021,12; 646793.
2. Jain et al. Journal of Nuclear Medicine. 2020; 61(8): 2207-1112.

Oral Presentation

Disclosures: The authors would like to disclose that [18F]OP-801 with Ashvattha Therapeutics is an investigational device.

101-Size-Changeable Nanoprobes for the Combined Radiotherapy and Photodynamic Therapy of Tumor

Presenter: Zhenyu Hou, Southeast University

Zhenyu Hou
Southeast University, Nanjing, China

Purpose:

Radiation therapy (RT) and photodynamic therapy (PDT) are promising while challenging in treating tumors. The potential radiation resistance of tumor cells and side effects to healthy tissues restrict their clinical treatment efficacy. Effectively delivery of therapeutic agents to the deep tumor tissues would be available for tumor-accurate therapy and promising for the tumor therapy. Thus, developing nanoprobes with effectively delivering radiotherapy sensitizers and photosensitizers to the interior of tumors is needed for the accurate combined RT and PDT of tumor.

Methods:

The size-changeable nanoprobes of Gd 2 O 3 @BSA-BSA-Ce6 (BGBC) were synthesized with a crosslinking method. Magnetic resonance imaging (MRI) and in vivo near-infrared (NIR) imaging were measured to evaluate the nanoprobes' tumor accumulation and intratumor penetration effect. The tumor suppression effect of combined RT and PDT with these nanoprobes was also studied for the 4T1 bearing Balb/c mice.

Results:

The nanoprobes BGBC showed high tumor accumulation and disintegrated into small particles responding to the photo irradiation produced reactive oxygen species (ROS), allowing for tumor penetration. Abundant radiotherapy sensitizers and photosensitizers were delivered to the deep tumor tissues, which is available for the accurate therapy of tumor. In addition, the BGBC displayed outstanding MRI and fluorescence imaging effects for evaluating the biodistribution and tumor- suppression effect of nanoprobes. Consequently, significant tumor suppression effect was obtained based on the accurate tumor treatment with the combined RT and PDT.

Conclusion:

The designed size-changeable nanoprobes BGBC showed excellent tumor accumulation and deep tumor penetration, resulting in a significant tumor-suppression effect based on the combined RT and PDT. This study provides a novel strategy for dual delivery of radiotherapy sensitizers and photosensitizers into the deep tumor tissues and is promising for the accurate theranostics of tumor.

Reference

1. Baskar R, Lee KA, Yeo R, et al. Cancer and radiation therapy: current advances and future directions. Int J Med Sci. 2012;9(3):193-9.
2. Abshire D, Lang MK. The Evolution of Radiation Therapy in Treating Cancer. Semin Oncol Nurs . 2018 May;34(2):151-157.
3. Kayali M, Jaoude JA, Mohammed M, et al. Post-mastectomy radiation therapy in Triple-negative beast cancer patients: Analysis of the BEATRICE Trial. Ann Surg Oncol. 2021.
4. Gensheimer MF, Loo BW Jr. Optimal Radiation Therapy for Small Cell Lung Cancer. Curr Treat Options Oncol. 2017 Apr;18(4):21.
5. Babaei M, Ganjalikhani M. The potential effectiveness of nanoparticles as radio sensitizers for radiotherapy. Bioimpacts. 2014;4(1):15-20.
6. Kim ES, Choi JY, Hwang SJ, Bae IH. Hypermethylation of miR-205-5p by IR governs aggressiveness and metastasis via regulating bcl-w and src. Mol Ther Nucleic Acids. 2019;14:450-464.
7. Yadav P, Shankar BS. Radio resistance in breast cancer cells is mediated through TGF-β signalling, hybrid epithelial-mesenchymal phenotype and cancer stem cells. Biomed Pharmacother. 2019;111:119-130.
8. Herrera FG, Bourhis J, Coukos G. Radiotherapy combination opportunities leveraging immunity for the next oncology practice. CA Cancer J Clin. 2017; 67(1):65-85.
9. Schaue D, McBride WH. Opportunities and challenges of radiotherapy for treating cancer. Nat Rev Clin Oncol. 2015;12(9):527-40.
10. Baumann M, Krause M, Overgaard J, Debus J, et al. Radiation oncology in the era of precision medicine. Nat Rev Cancer. 2016;16(4):234-49.
11. Connell PP, Hellman S. Advances in radiotherapy and implications for the next century: a historical perspective. Cancer Res. 2009;69(2):383-92.
12. Hernandez-Rivera M, Kumar I, Cho SY, et al. High-performance hybrid bismuth-carbon nanotube based contrast agent for X-ray CT imaging. ACS Appl Mater Interfaces. 2017;9(7):5709-5716.
13. Popovtzer A, Mizrachi A, et al. Actively targeted gold nanoparticles as novel radiosensitizer agents: an in vivo head and neck cancer model. Nanoscale. 2016; 8(5):2678-85.
14. Jeremic B, Aguerri AR, Filipovic N. Radiosensitization by gold nanoparticles. Clin Transl Oncol. 2013;15(8):593-601.

Oral Presentation

Disclosures: The authors have disclosed no financial interest.

102-Multimodality detection and treatment for breast cancer with a biodegradable "one-for-all" nanoparticle contrast agent

Presenter: Jessica Hsu, University of Pennsylvania

Jessica C. Hsu[1], Diego Barragan[2], Alexander Tward[2], Katherine Mossburg[1], Maryam Hajfathalian[3], Yuxi Dong[4], Emma Cruz[5], Ahmad Amirshaghaghi[2], Joann Miller[2], Mathilde BOUCHE, Alexander Andrianov[6], David Cormode[2]

[1]*University of Pennsylvania*
[2]*University of Pennsylvania, Philadelphia, PA*
[3]*Stanford University, Mountain View, CA*
[4]*University of Pennsylvania, Philadelphia, Pennsylvania*
[5]*Philadelphia, PA*
[6]*University of Maryland, Rockville, MD*

Purpose:

Current screening and treatment standards for breast cancer may result in delayed diagnosis and incomplete tumor eradication, worsening the disease outcome and chance of survival. Herein, we synthesized ultrasmall, near-infrared fluorescent silver sulfide nanoparticles (Ag_2S-NP) for efficient renal clearance and encapsulated them in larger, biodegradable polymeric nanoparticles (AgPCPP) for improved optical properties. AgPCPP have potent contrast properties for preoperative x-ray (DEM and CT) and optical (PA and NIRF) based detection modalities, as well as intraoperative NIRF image-guided surgical techniques (FLARE). Their remarkable photothermal conversion activity is suitable for postoperative anticancer therapy via localized thermal ablation. Importantly, we found that AgPCPP, or aggregated forms of Ag_2S-NP, increased the absorption of NIR light, thereby producing enhanced PA/NIRF signals and photothermal heating effects. Thus, we present a "one-for-all" theranostic agent that is multifunctional and gradually degrades into small components for elimination from the body (Fig. A).

Methods and Materials:

AgPCPP were formed by encapsulating hydrophilic 2 nm Ag_2S-NP (Fig. S1) in PCPP polymers with 10% PEGylated PCPP block copolymers. The nanoparticles were characterized using TEM, fluorimetry, UV-vis spectroscopy, DLS, and SEM/EDX. Contrast production was evaluated via phantom imaging using clinical DEM (Hologic 3Dimensions) and CT (Siemens Force), as well as preclinical PA (VisualSonics), NIRF (IVIS Spectrum), and FLARE (Curadel) imaging systems. *In vitro* biocompatibility was examined via MTS assays using Renca, HepG2, and MDA-MB-231 cells. *In vitro* photothermal effects were investigated using an 808 nm laser. *In vivo* multimodal imaging, photothermal therapy, and biodistribution studies were performed in a murine model of breast cancer.

Results:

The size of AgPCPP could be varied between 40-300 nm by adjusting the amount of PEG-PCPP copolymers used in the synthesis (B). For this study, we used an AgPCPP formulation with an average core diameter of 95 nm. From EDX analysis, AgPCPP include several elemental components such as silver, sulfur, calcium, and phosphorous. Interestingly, polymer encapsulation induces a red shift in absorption (Fig. S2) and increases the fluorescence emission of Ag_2S-NP in the NIR region (Fig. S3). We found that both Ag_2S-NP and AgPCPP are biocompatible with all cell types. We also found that approximately

90% of Ag_2S-NP payload are released within 7 days, indicating the biodegradability of AgPCPP. While Ag_2S-NP and AgPCPP provide similar x-ray contrast, AgPCPP generate higher PA (Fig. C) and NIRF signals (Fig. D, S4) as well as greater photothermal killing compared to free Ag_2S-NP (Fig. S5) due to higher temperature elevation under laser irradiation (Fig. S6). AgPCPP are also stable under repeated cooling/heating cycles (Fig. S7). Moreover, AgPCPP enhanced the tumor contrast as evidenced by *in vivo* NIRF and CT imaging (Fig. E). AgPCPP further raise tumor hyperthermia (Fig. F) and reduce tumor growth post photothermal treatment (Fig. G). Biodistribution results indicate that more AgPCPP are found in the tumors than Ag_2S-NP (Fig. S8), suggesting that larger size is beneficial for increasing tumor accumulation.

Conclusions:

AgPCPP may improve the optical and photothermal properties of free Ag_2S-NP. AgPCPP can fulfill diagnostic, surgical, and therapeutic tasks before breaking down and releasing Ag_2S-NP for renal excretion, thus providing good prospects for translation to clinical use.

Oral Presentation

Disclosures: The authors have disclosed no financial interest.

103-Reversible and Irreversible Detection of Reactive Oxygen Species by Fluorescence and Photoacoustic Methods

Presenter: Srinivas Banala, University Hospital RWTH Aachen

Srinivas Banala[1], Jean Michel Merkes[1], Alexa Hasenbach[1], Christopher Cremer[2], Frederic W. Patureau[2], Sven Hermann[3], Fabian Kiessling[2]

[1]*University Hospital RWTH Aachen, Aachen, Germany*
[2]*RWTH Aachen University, Aachen, NRW, Germany*
[3]*European Institute for Molecular Imaging (EIMI), Münster, North-Rhine Westfalia, Germany*

Introduction:

Reactive oxygen and nitrogen species (ROS, RNS) are important messenger molecules and involved in a variety of physiological and pathological conditions.[1] Over production of ROS/RNS often indicates onset of diseases or response to different therapies.[2] Non-invasive direct detection of ROS/RNS is currently not possible. Only probes trapping or reacting with ROS/RNS enable their detection in indirect ways. Currently known probe designs suffer often from issues of either under- or over- estimation and selectivity.[3] Exploiting the broad reactivity of 2,6-di-^{tert}-butyl-4-hydroxy toluene (BHT) towards ROS/RNS, we explored revesible and irreversible ROS/RNS detections using fluorogenic methylene blue and acoustogenic BODIPY probes respectively.[4]

Results and Discussion:

We have used two synthetic routes to attach 2,6-di-^{tert}-butyl-4-hydroxy phenyl (BHP) unit to our chromophore cores (Figure 1A): a C-N coupling chemistry with leucomethylene blue (LMB) and bromo-BHP,[5a] and Knoevenagel condensation with BODIPY and BHP-CHO.[5b] Further polar probes, LMB with sulfonate side chain and BODIPY with tri (PEGylation) were synthesized, to circumvent the hydrophobicity issue of BHT. All probes were purified by chromatography and RP-HPLC, characterized by NMR and ESI-MS, and their cell viability (XTT, MTT) was determined. The BHP-LMBs (**1**, **2**) are non-fluorescent and exhibited absorption in the UV-range. When treated with ROS/RNS in DMSO or H_2O (Figure 1B), lipophobic $_l$BHP-LMBs **1** exhibited a broad spectrum ROS/RNS activity converting to methylene blue (MB), with more than a 1000-fold gain in fluorescence emission (Figure 1C). However, the hydrophilic $_h$BHP-LMBs **2**, in H_2O, in reaction with H_2O_2, ^{t}BuOOH and OH*, gave a new non-fluorescent species with absorption maximum at 800 nm (Figure 1B, right), and yielded MB with a high gain in fluorescence in presence of $ONOO^-$, KO_2 and OCl^-. Cell uptake of **1** was excellent, and intracellularly produced ROS/RNS (induced by IFN-γ, LPS) could be detected, but **2** could not be internalized in cells. The BHT-BODIPY dyes (**3**, **4**) were fluorescent and exhibited absorption maximum at 690 nm. This absorption maximum was shifted to ~810 nm, when treated with a variety of ROS ($OH^\bullet$, ^{t}BuO$^\bullet$, $O_2^{\bullet-}$, OCl^- and $ONOO^-$). Hydrophobic **3** was formulated in cremophore EL (1 mg / nmol) for cellular uptake, and *in vitro* menadione induced ROS could be detected by PAI (Figure 1E). *In vivo* studies using $O_2^{\bullet-}$ activated biogel-dye pellet showed absence of fluorescence and after 2h, a gain in fluorescence in that pellet, confirming the reversibility *in vivo*, as measured by FRI. In parallel, unmixing *in vivo* PA signals confirmed that no overlap of **3** and **3**+$O_2^{\bullet-}$ signals, though unmixing was found be difficult in the activated pellet.

Conclusions:

We showed that detection of ROS/RNS was possible with reversibly activateable acoustogenic BHT-BODIPY probes and irreversibly fluorogenic BHT-LMB probes. ROS/RNS caused a redshift in PA signal with a large gain in signal intensity of BHT-BODIPY, and over a 1000-fold increase in fluorescence emission of LMB-BHT, yielding red fluorescent methylene blue. As the BHT synthon is highly hydrophobic, we are exploring BHT-mimics towards (ir)reversibly acoustogenic and fluorogenic probes for ROS/RNS detections. Further, engineering a BHT-mimic may allow stabilization of radical or anionic derivatives of BHP-LMB, that might open new possibilities for reversible ROS detection by photoacoustic imaging.

Reference

1. S. I. Ahmad, ed., Reactive Oxygen Species in Biology and Human Health, CRC Press, New York, 2016
2. a) S. Dikalov, K. K. Griendling and D. G. Harrison, Hypertension, 2007, 49, 717-727. b) S. Di Meo, T. T. Reed, P. Venditti and V. M. Victor, Oxid. Med. Cell. Longev., 2016, 2016, 1245049.
3. a) P. L. Zamora and V. F. A., in Measuring Oxidants and Oxidative Stress in Biological Systems, eds. L. Berliner and N. L. Parinandi, Springer, Cham, 2020, vol. 34, pp. 13-38. b) M. G. Bonini, C. Rota, A. Tomasi and R. P. Mason, Free Radical Biol. Med., 2006, 40, 968-975. c) Q. Zheng, S. Jockusch, Z. Zhou and S. C. Blanchard, Photochem. Photobiol., 2014, 90, 448-454
4. a) C. Crammer, J.M. Merkes, C. Bub, D. Rommel, F. Patureau, S. Banala, RCS Advances, 2021, 11, 32295-32299; b) J.M. Merkes, A. Hasenbach, S. Herman, F. Kiessling, S. Banala, ACS Sensors, 2021, 6, 4379-4388.

Oral Presentation

Disclosures: The authors have disclosed no financial interest.

104-A Positron Emission Tomography (PET) approach to identifying and developing new therapies in mouse models of multiple sclerosis (MS)

Presenter: Bao Ying Chen, City of Hope

Bao Ying Chen[1], Peter M. Clark[2]

[1]*City of Hope*
[2]*University of California, Los Angeles, Los Angeles, CA*

Introduction:

Multiple sclerosis (MS) is a debilitating disease in which the immune system attacks the body's healthy tissue in the central nervous system, leading to vision loss, fatigue, and paralysis. MS therapies only cover a subset of patients and can take up to 96 weeks to determine whether therapies are working effectively. There is a need for not only more effective and safe therapies but also an imaging strategy to determine, early on, if a therapy is effective. Positron emission tomography (PET) imaging non-invasively images biochemical processes *in vivo*. [^{18}F]FAC is a deoxycytidine analogue PET radiotracer that measures deoxyribonucleoside salvage, a pathway that is enriched in activated immune cells and controlled by the rate-limiting enzyme deoxycytidine kinase (dCK).

Objective:

Demonstrate the use of [^{18}F]FAC PET to profile and confirm the functional relevance of deoxyribonucleoside salvage in mouse models of MS.

Methods:

To induce EAE, mice were injected with myelin oligodendrocyte glycoprotein (MOG_{35-55}) or (MOG_{1-125}) in Freund's complete adjuvant and pertussis toxin. MOG_{35-55} induces a T cell dependent response. MOG_{1-125} induces a B cell dependent response.
To study [^{18}F]FAC PET across disease progression, EAE and control mice were imaged on Day 7 (pre-symptomatic state), Day 14 (peak disease), Day 21 (stabilized state), and Day 28 (late disease) post-induction.
TRE-515 is a dCK inhibitor. To determine the functional relevance of deoxyribonucleoside salvage in EAE, mice were induced with EAE and treated with TRE-515 once a day, every day, for up to 28 days.

Results:

[^{18}F]FAC PET profiles deoxyribonucleoside salvage activity in multiple T cell and B cell dependent mouse models of MS.

- In a T cell dependent mouse model of MS, [^{18}F]FAC accumulation was increased two-fold in the spleen, and lymph nodes by day 7, even before clinical symptoms. This accumulation was maintained in the spleen and lymph nodes through day 28. Similar results were observed in a B cell dependent model of MS (Fig. 1). At day 14 post-immunization, [^{18}F]FAC accumulation was increased in the spleen and lymph nodes (Fig. 2). [^{18}F]FAC PET results suggests that the deoxyribonucleoside salvage pathway is utilized in disease induction and progression in MS.

[^{18}F]FAC PET suggests that targeting the deoxyribonucleoside salvage pathway may lead to therapeutic efficacy in MS.

- Whether targeting deoxyribonucleoside salvage can alleviate symptoms in MS mice was determined.
- TRE-515 is a small molecule inhibitor of deoxycytidine kinase (dCK). dCK is the rate-limiting enzyme in the deoxyribonucleoside salvage pathway.
- Pharmacodynamic studies with [^{18}F]FAC PET demonstrate that targeting dCK with TRE-515 blocks deoxyribonucleoside salvage activity (Fig 3).
- Blocking deoxyribonucleoside salvage, MS mice developed symptoms later, had fewer symptoms at peak disease stage, and had fewer symptoms overall compared to mice treated with vehicle. Similar results seen in multiple mouse models of MS (Fig 3).

[^{18}F]FAC PET identifies several potential cellular targets in MS mice

- [^{18}F]FAC PET confirms that deoxyribonucleoside salvage is functionally relevant in multiple models of MS. Results from cytometry time of flight (CyTOF) suggests that early in the disease, proliferating CD4 T cells and B cells are most affected when deoxyribonucleoside salvage is blocked, suggesting that these cell types utilize this pathway during the early disease stages. T and B cells are important contributors of MS.

Innovation/impact:

We demonstrate a PET imaging strategy to identify important pathways in mouse models of MS. This imaging strategy identified potential targets that can be targeted to limit symptoms. Imaging results that we learn here are not only applicable to MS but also to other types of autoimmune disease, such as irritable bowel syndrome and rheumatoid arthritis.

Oral Presentation

Disclosures: The authors would like to disclose that TRE-515 is an investigational drug.

105-Doped-BaF2 Nanocrystals as Novel Multifunctional Imaging Probes for In Vivo 19F-MRI and CT Applications

Presenter: Dana Cohen, Weizmann Institute of Science

Dana Cohen[1], Andrea Galisova[2], Lothar Houben[2], Vlad Brumfeld[3], Amnon Bar-Shir[4]

[1]*Weizmann Institute of Science, Rehovot, HaMerkaz, Israel*
[2]*Weizmann Institute of Science, Rehovot, Israel, Israel*
[3]*Weizmann Institute of Science, Israel*
[4]*Weizmann Institute of Science, Rehovot, Israel*

Introduction:

Proposing small (d ~10nm) nanofluorides as inorganic colloids, result with a new type of nanotracers for ^{19}F-MRI applications[1]. This opens multitude opportunities for new designs that were not accessible beforehand, including the use of ultra-small sugar-coated nanofluorides for mapping neuroinflammation and the exploitation of the difference in ^{19}F-NMR chemical shifts of CaF_2 (δ = - 109 ppm) and SrF_2 (δ = - 88 ppm) for "multicolor" ^{19}F-MRI *in vivo* [2]. Interestingly, BaF_2 express a unique ^{19}F chemical shift, δ = -14 ppm, that is further shifted from the other fluorides, [3] which raise the possibility to expand the range of nanofluorides uses in multiplexed ^{19}F MRI. In addition, the similar atomic number of Barium (z = 56) to Iodine (z = 53) makes it applicable for computed tomography (CT) applications [4, 5]. However, pure BaF_2 cannot be obtained as stable colloid in solution[6] and have not been studied before with ^{19}F-NMR, thus, their use in either CT or MRI studies was not demonstrated.

Results and Discussion:

As BaF_2-based nanomaterials tend to undergo phase transition, we first rationalize their fabrication to obtain them as spherical colloids. La^{3+} ions were used as non-paramagnetic dopants to control the phase transition and shape of the fabricated BaF_2. **Fig.1a** shows

how gradual increase in the amount of La^{3+} dopant affects the size and shape of BaF_2 NCs formation while a 20%La doped-BaF_2 resulted in a rounded shape colloids. Next, after determining the T_1 relaxation time of La: BaF_2 to be very long, which limits signal averaging at a given time of acquisition and therefore compromised ^{19}F-MRI SNR, we set to shorten their T_1 with the aid of paramagnetic dopant. We have substituted 5% of the diamagnetic La^{3+} dopant with the moderate paramagnetic dopant Sm^{3+}, to obtain 15%La,5%Sm:BaF_2 NCs (La:Sm:BaF_2). Interestingly, the 5% Sm^{3+} dopant resulted in a dramatic shortening of the T_1 of BaF_2 from 7 sec to only 0.1 sec (**Fig.1b**), which is crucial for their further implementation in *in vivo* applications. High-resolution ^{19}F-NMR spectrum (**Fig.1c**) of La:Sm:BaF_2 showed a well-defined peak at -14 ppm, which further shifted from that of SrF_2 (-88 ppm) and CaF_2 (-109 ppm). Such a large range of chemical shifts allows the use of these nanofluorides in a multicolor ^{19}F-MRI experiments (**Fig.1c, bottom**). Using the phospholipid incorporation approach, resulted with water soluble, fluorescently labeled and targeted NCs (**Fig.1d**). In this regard, folate-modified phospholipids were used, resulted with FA-La:Sm:BaF_2 NCs, for the targeting of cancerous cells within a tumor site, that highly express folate receptors. After intravenously administration, we were able to detect ^{19}F MRI signal of FA-La:Sm:BaF_2 that perfectly overlaid over a ^{1}H image at the exact location of the tumor site, also validated by fluorescence imaging (**Fig. 1e**). Finally, as a proof of concept, we demonstrated the potentiality of using La:Sm:BaF_2 as an agent also for CT by comparing its CT contrast as compared to Iohexol within the same concentration, using a microCT scanner. Interestingly, we were able to detect an increase in the CT signal attenuation while increasing La:Sm:BaF_2 concentration, in a slightly greater slope than Iohexol (**Fig. 1f**).

Conclusion:

Our engineered multifunctional La:Sm:BaF_2 NCs (δ = -14ppm), which were designed to obtain extremely short T_1 relaxation times (100 msec) and colloidal stability can be used as ^{19}F agents for multicolor ^{19}F MRI studies, in addition to the previously proposed Sm:SrF_2 (δ = -88ppm) and Sm:CaF_2 (δ = -109ppm) NCs. Furthermore, we demonstrate their targeted ability within a tumor site. Moreover, nanofluorides based on Ba atoms having a high atomic number, allows their use in a CT setup thus making them applicable agents for multimodal imaging studies.

Reference

1. Ashur, I., H. Allouche-Arnon, and A. Bar-Shir, Calcium Fluoride Nanocrystals: Tracers for In Vivo 19F Magnetic Resonance Imaging. Angewandte Chemie International Edition, 2018. 57(25): p. 7478-7482.
2. Cohen, D., et al., Glyconanofluorides as Immunotracers with a Tunable Core Composition for Sensitive Hotspot Magnetic Resonance Imaging of Inflammatory Activity. ACS Nano, 2021. 15(4): p. 7563-7574.
3. Sadoc, A., et al., NMR parameters in alkali, alkaline earth and rare earth fluorides from first principle calculations. Physical Chemistry Chemical Physics, 2011. 13(41): p. 18539-18550.
4. Wang, J., et al., BaHoF5 nanoprobes as high-performance contrast agents for multi-modal CT imaging of ischemic stroke. Biomaterials, 2015. 71: p. 110-118.
5. Liu, Z., et al., Direct visualization of gastrointestinal tract with lanthanide-doped BaYbF5 upconversion nanoprobes. Biomaterials, 2013. 34(30): p. 7444-52.
6. Chen, D., et al., Modifying the size and shape of monodisperse bifunctional alkaline-earth fluoride nanocrystals through lanthanide doping. J Am Chem Soc, 2010. 132(29): p. 9976-8.

Oral Presentation

Disclosures: The authors have disclosed no financial interest.

106-The Feasibility of Using L-boronophenylalanine-mediated Boron Neutron Capture Therapy for the Treatment of Colorectal Peritoneal Metastases

Presenter: Ting-Yu Chang, National Yang Ming Chiao Tung University

Ting-Yu Chang[1], Wen-Yi Chang[1], Chun-Yi Wu[2]

[1]*National Yang Ming Chiao Tung University, Taipei, Taiwan*
[2]*National Yang Ming Chiao Tung University, Taipei, Taiwan, Taiwan*

Objective:

Colorectal cancer, especially that develops peritoneal metastases, is one of the top leading causes of cancer-related death in the world. Boron neutron capture therapy (BNCT) is a binary strategy that can eliminate tumors without causing severe normal tissue damage. We determined the boron concentration in peritoneal metastases after an intraperitoneal boronophenylalanine-fructose (BPA-fructose) administration and discover the therapeutic efficacy after BNCT.

Methods:

Approximately 5´10^5 CT-26 cells in 500 µL serum-free RPMI-1640 medium were intraperitoneally injected to conduct peritoneal metastases on day 0. ^{18}F-FBPA-fructose microPET/MR imaging, biodistribution study, and ICP-MS analysis were performed to determine the distribution of BPA-fructose (BPA-Fr) in tumor-bearing mice. BPA-fructose (1 g/kg) was intraperitoneally administered at 3 h before neutron irradiation, and the mice were irradiated with neutrons at a flux of 1×10^9 neutron/(cm^2·s) for 30 min at Tsing Hua Open Pool Reactor (THOR).

Results:

The T2-weighted MRI imaging can clearly visualize the peritoneal metastases grown on the surface of the intestine and mesentery on day 5. In ^{18}F-FBPA imaging, the tumor uptakes of the mice receiving an intraperitoneal (at 3 h post-injection) and intravenous injections (at 1 h post-injection) were 9.4±2.6 and 9.3±2.1%ID/g, respectively. These two groups also had a similar tumor-to-muscle ratio (5.5 and 5.6), suggesting that intraperitoneal injection may be an alternative to deliver BPA for patients with peritoneal metastases. The boron content of the tumor, determined by ICP-MS, was around 42±13 ppm at 3h after intraperitoneal injection. After neutron irradiation, the group that received BPA-Fr exhibited a superior antitumor effect without severe body weight loss. Kaplan-Meier survival curve showed significantly improved survival in the treated group when compared to the controls ($p<0.01$). All mice in control groups (the groups injected with normal saline and received neutron alone) died before day 20; however, the treated mice were still alive. The extended lifespan was approximately 20 d. Besides, this apparent tumor reduction effect was not noticed in the tumor-bearing immunodeficient mice, implying the underlying immune response should be discussed in further studies.

Conclusion:

We demonstrated the potential of using BPA-mediated BNCT to treat the mice with colorectal peritoneal metastases. The strategy could be immediately considered for further translational research to improve the survival and life quality of patients with advanced colorectal cancer.

Oral Presentation

Disclosures: The authors have disclosed no financial interest.

107-The Apparent Discrepancy Between Spatial Metabolomics and Hyperpolarised 13C-MRI In Prostate Cancer Can Be Explained By Differences In Perfusion and Cellularity

Presenter: Nikita Sushentsev, University of Cambridge

Nikita Sushentsev[1], Ines Horvat-Menih[2], Mary McLean[3], Anne Y. Warren[4], Vincent Gnanapragasam[5], Tristan Barrett[6], Ferdia Gallagher[6]

[1]*University of Cambridge, Cambridge, United Kingdom*
[2]*Department of Radiology, University of Cambridge, Cambridge, United Kingdom*
[3]*Cancer Research UK Cambridge Institute, Cambridge, Cambridgeshire, United Kingdom*
[4]*Cambridge University Hospital NHS Foundation Trust, Cambridge, Cambridgeshire, United Kingdom*
[5]*University of Cambridge*
[6]*University of Cambridge, Cambridge, Cambridgeshire, United Kingdom*

Background:

Hyperpolarized [1-^{13}C]pyruvate magnetic resonance imaging (HP-^{13}C-MRI) is an emerging clinical imaging technique that can probe cellular lactate production in vivo[1]. Clinical studies of HP-^{13}C-MRI have been pioneered in prostate cancer[2] (PCa), where the technique can non-invasively assess intergrade[3] and intragrade[4] tumour aggressiveness. Importantly, all studies in localized PCa have shown exclusive [1-^{13}C]lactate labelling in tumors, which appears inconsistent with their established oxidative metabolism, as compared to the glycolytic benign prostate (BP)[5]. **Objective.** This study used desorption electrospray ionization mass spectrometry imaging (DESI-MSI) and HP-^{13}C-MRI in patients with early-stage PCa to compare pyruvate and lactate metabolism in the BP and PCa.

Methods:

Fresh frozen prostatectomy samples containing histopathologically-proven BP and early-stage PCa areas underwent DESI-MSI for the identification of endogenous epithelial pyruvate and lactate within regions-of-interest (ROIs) drawn by an experienced genitourinary pathologist. A separate cohort of patients with matched early-stage PCa lesions underwent 3 T HP-^{13}C-MRI following intravenous injection of hyperpolarized [1-^{13}C]pyruvate prior to radical prostatectomy. Tumor-derived signal-to-noise ratios (SNR) for pyruvate and lactate, alongside ^{1}H-MRI-derived K^{trans} and apparent diffusion coefficient (ADC) measures of vascular permeability and cellularity were extracted from BP and PCa based on ROIs drawn by expert radiologists. The ROIs were matched to those drawn on whole-mount surgical sections, from which immunohistochemical expression of the monocarboxylate transporter 1 (MCT1) and mitochondrial pyruvate carrier 2 (MPC2) were derived, along with RNAscope-derived mRNA expression of lactate dehydrogenase (LDH) subunits A/B and pyruvate dehydrogenase E1 subunit alpha 1 (PDHA1). The data are presented as median, with P derived using the Mann-Whitney test and units described in the Supplementary File.

Results:

10 prostatectomy samples including BP (n=5) and PCa (n=5) tissues were cut at three separate positions within the biopsy core, with the resulting n=30 spatially distinct slices analyzed using DESI-MSI, which showed significantly higher epithelial pyruvate and lactate in BP compared to PCa (400.6 vs. 205.8; P<0.0001). This contrasted sharply with HP-^{13}C-MRI that showed significantly higher pyruvate SNR and lactate SNR in PCa (n=11) compared to BP (n=11) (33.0 vs. 1.0 for pyruvate SNR; 12.0 vs. 1.0 for lactate SNR; P<0.0001 for both). At the tissue level, the glycolytic phenotype of BP in the HP-^{13}C-MRI cohort was confirmed by its significantly higher combined epithelial LDH density and *LDHA/PDHA1* ratio compared to PCa (7.9 vs. 5.6, P=0.02; 1.9 vs. 0.8, P=0.04, respectively). Moreover, PCa epithelium showed a significantly higher capacity for mitochondrial pyruvate import as evidenced by its MPC2 expression compared to BP (58.6 vs. 34.7, P=0.005). In addition, the two tissue types showed no difference in epithelial MCT1 density (925.0 vs. 716.0 for PCa and BP, respectively; P>0.99). Simultaneously, PCa showed significant differences in K^{trans} and ADC values compared to BP (0.39 vs. 0.11 for Ktrans, 921.5 vs. 1348.0 for ADC; P<0.005 for both).

Conclusions:

Human prostate cancer presents unique metabolic challenges for the interpretation of metabolic imaging. This study highlights an apparent discrepancy between spatial metabolomics measured on ex vivo samples and in vivo HP-^{13}C-MRI for differentiating glycolytic BP from oxidative PCa based on pyruvate and lactate measurements. The observed discrepancy may be explained by a significantly higher [1-^{13}C]pyruvate delivery to a dense cellular tumor, compared to the normal tissue. While probe delivery is key for [1-^{13}C]lactate labelling to occur, increased epithelial cell density may further amplify the visible tumor lactate signal on HP-^{13}C-MRI. Overall, these results highlight the importance of considering key biological factors within the tumor microenvironment when interpreting HP-^{13}C-MRI, in addition to the intrinsic cellular metabolic changes that occur within the tumor.

Reference

1. Kurhanewicz, J. et al. Hyperpolarized 13C MRI: Path to Clinical Translation in Oncology. Neoplasia (United States) vol. 21 1–16 (2019).
2. Nelson, S. J. et al. Metabolic imaging of patients with prostate cancer using hyperpolarized [1-13C]pyruvate. Science Translational Medicine vol. 5 198ra108 (2013).
3. Granlund, K. L. et al. Hyperpolarized MRI of Human Prostate Cancer Reveals Increased Lactate with Tumor Grade Driven by Monocarboxylate Transporter 1. Cell Metab. 31, 105-114.e3 (2020).
4. Sushentsev, N. et al. Hyperpolarised 13C-MRI identifies the emergence of a glycolytic cell population within intermediate-risk human prostate cancer. Nat. Commun. 2022 131 13, 1–12 (2022).
5. Bader, D. A. & McGuire, S. E. Tumour metabolism and its unique properties in prostate adenocarcinoma. Nat. Rev. Urol. 2020 174 17, 214–231 (2020).

Oral Presentation

Disclosures: The authors have disclosed no financial interest.

108-Differentiating Individual Fluorophores from a Heterogenous Signature on a Fibre-based Time Resolved Fluorescence Spectroscopy (TRFS) System

Presenter: Alexandra Adams, The University of Edinburgh

Alexandra Adams[1], Andras Kufcsak[1], Katjana Ehrlich[2], Keith Finlayson[1], Kev Dhaliwal[3], Sohan Seth[1]

[1]*The University of Edinburgh, Edinburgh, United Kingdom*
[2]*Edinburgh, United Kingdom*
[3]*Queens Medical Research Institute, Edinburgh, Scotland, United Kingdom*

Introduction:

Variation in tissue autofluorescence originates from structural, metabolic, and environmental differences. Current clinical fluorescence diagnostic devices detect spectral intensity changes in tissue fluorophores. Challenges in spectroscopy data collection include the overlapping spectra of individual fluorophores and in the heterogeneity of tissue fluorescence itself [4]. Fluorescence lifetime, independent of absolute intensity and fluorophore specific, overcomes some limitations. Recent technological advancements have seen point-based fluorescence lifetime devices accepted onto clinical studies [5, 7]. Further development in detector technology will see the clinical devices transition from a few detector channels to many hundreds [2, Table 1], providing extremely information-rich tissue profiles, and requiring sophisticated algorithms to fully interrogate them. Given the complexity of the biological environment, a specific excitation wavelength will excite a limited number of endogenous fluorophores which fluorescence emission will undoubtedly be overlapping. We present, Multichannel Fluorescence Lifetime Estimation, MuFLE, a tool to unmix these fluorophores with overlapping signatures simultaneously in both the spectral and temporal domain. This will allow further investigation of the changes of individual tissue fluorophores [6], and provide highly detailed, instantaneous information unrivalled by any current surgical fluorescence information.

Method:

The time resolved fluorescence spectroscopy (TRFS) system is comprised of a pulsed laser (485nm, 20MHz repetition rate, 200µW average power), coupling and collection optics, and a grating based spectrometer and a complementary metal-oxide semi-conductor (CMOS) single-photon avalanche diode (SPAD) line sensor [3] (Fig. 1A). The line sensor has 512 channels and allows single photon acquisition in time-correlated single photon counting (TCSPC) mode with a time resolution of 50ps. Each channel records a single fluorescence decay of a given wavelength range of 0.5nm. The spectrometer covers a spectral range from 474nm – 735nm. To demonstrate proof of concept, we use a mixture of Rhodamine B and Fluorescein. These fluorophores were chosen as they have overlapping emission spectra. The time-resolved emission spectra (TRES) histogram over wavelength channels and time bins was pre-processed to only include time bins in which a signal was observed (552.03nm – 627.51nm), and the data was normalised.
The fluorescent decay traces in each channel are expressed as a composition of fluorescence from each fluorophore present in the sample, convolved with the instrument response function (IRF) with an additive bias for detector noise (dark counts) and background signal from the optical fibre (delivering the laser pulses to sample and the fluorescence response to the detector). A smooth spectral intensity structure across the wavelength channels is assumed for individual fluorophores and fitted using B-Splines [1] (Fig. 1B). In addition, a linear trend is assumed for the two fluorescence lifetimes (Fig. 1C). Both the spectral intensity and lifetimes are fitted simultaneously by minimizing a squared error loss function using a gradient descent algorithm.

Results:

Assessing the spectrum (Fig. 1B, red plot), or single decay (Fig. 1B, purple plot) alone show no obvious trend of either fluorophore. In addition, the intensity and lifetime parameters from the individual channels (green, Fig. 1C) shows less intensity differentiation when the individual decays are fit independently. The two MuFLE intensity and lifetime coefficients differentiate between Fluorescein (emission peak 550nm) and Rhodamine B (emission peak 585 nm) (Fig. 1C). These results show MuFLE reliably unmixing individual fluorophores from a mixed sample.

Conclusion:

Using a mix of Rhodamine B and Fluorescein, we show that MuFLE can reliably unmix individual fluorophores in a heterogeneous sample. Translational applications of MuFLE will allow individual fluorophore detection in tissue, increasing the precision of diagnostic devices and their surgical accuracy in differentiating between the underlying fluorophores originating from metabolically differentiated targets such as malignant, benign and healthy tissue.

Reference

1. M. G. Cox. The numerical evaluation of b-splines. IMA Journal of Applied mathematics, 10(2):134–149, 1972.
2. R. Datta, A. Gillette, M. Stefely, and M. C. Skala. Recent innovations in fluorescence lifetime imaging microscopy for biology and medicine. Journal of Biomedical Optics, 26(7):070603, 2021.
3. A. T. Erdogan, R. Walker, N. Finlayson, N. Krstajić, G. Williams, J. Girkin, and R. Henderson. A cmos spad line sensor with per-pixel histogramming tdc for time-resolved multispectral imaging. IEEE Journal of Solid-State Circuits, 54(6):1705–1719, 2019.
4. L. Marcu. Fluorescence Lifetime Techniques in Medical Applications. Annals of Biomedical Engineering, 40(2):304–331, Feb. 2012.
5. M. Marsden, T. Fukazawa, Y.-C. Deng, B. W. Weyers, J. Bec, D. G. Farwell, and L. Marcu. Flimbrush: dynamic visualization of intraoperative free-hand fiber-based fluorescence lifetime imaging. Biomedical Optics Express, 11(9):5166–5180, 2020.
6. M. Monici. Cell and tissue autofluorescence research and diagnostic applications. Biotechnology annual review, 11:227–256, 2005.
7. G. O. Williams, E. Williams, N. Finlayson, A. T. Erdogan, Q. Wang, S. Fernandes, A. R. Akram, K. Dhaliwal, R. K. Henderson, J. M. Girkin, et al. Full spectrum fluorescence lifetime imaging with 0.5 nm spectral and 50 ps temporal resolution. Nature communications, 12(1):1–9, 2021.

Oral Presentation

Disclosures: The authors have disclosed no financial interest.

109-In vivo Activated Microglia in Early Stage of Parkinson's Disease (PD): Revealed by PET/MRI Imaging by [18F]DPA-714 Targeting TSPO

Presenter: Peizhen Ye, Fifth Affiliated Hospital of Sun Yat-sen University

Peizhen Ye[1], Lei Bi[1], Min Yang[2], Yifan Qiu[1], Guolong Huang[1], Zhijun Li[3], Hongjun Jin[4], Mengchao Cui[5]

[1]*Fifth Affiliated Hospital of Sun Yat-sen University, Zhuhai, China*
[2]*Fifth Affiliated Hospital of Sun Yat-sen University, Zhuhai, Guangdong Province, China*

[3]*Sun Yat-sen University, Zhuhai, Guangdong province, China*
[4]*The Fifth Affiliated Hospital, Sun Yat-sen University, Zhuhai City, Guangdong, China*
[5]*Beijing Normal University, Beijing, China, China*

Background:

Parkinson's disease (PD) is one of progressive neurodegenerative diseases, characterized by symptoms of the loss of dopaminergic (DA) neurons and the appearance of Lewy body [1]. The most extensively studied rodent model of PD is the 6-hydroxydopamine (6-OHDA) treated rat, and stable PD-like rotation behavior the 6-OHDA treated rat induced by apomorphine (APO) were observed 3-4 weeks after 6-OHDA treatments [2]. Reports suggest that neuroinflammation associated with microglia play a role in PD neuronal degeneration [3], however, the relationship between activated microglia and behavioral abnormality in PD still remain to be explored. Translocator protein (TSPO) is a biomarker of activated microglia, and [^{18}F]DPA-714 was a new developed radiotracer for TSPO [4]. We hypothesized that quantification of *in vivo* activated microglia in early stage would be helpful for monitoring the pathological process of PD by evaluating the rodent brain imaging of [^{18}F]DPA-714 and [^{18}F]D6-FP-(+)-DTBZ through positron emission tomography (PET)/magnetic resonance imaging (MRI).

Methods:

The synthesis of radiotracer [^{18}F]DPA-714 and [^{18}F]D_6-FP-(+)-DTBZ was prepared from corresponding precursors according to previous reports [5]. Thirty-three healthy adult SD rats were assigned for the sham group (n = 17) and 6-OHDA partial lesion group (n = 16). The needles were introduced with vehicle solution for sham group and 6-OHDA solution (12 μg 6-OHDA) for 6-OHDA partial lesion group into the right striatum **(Figure 1A)**. PD-like rotation behaviors were examined and video-recorded for 30 min after i.p injection of APO solution **(Figure 1A)**. The neuroinflammation of the right striatum was quantified by the 30-min post-injection static brain PET scans followed intravenous [^{18}F]DPA-714 **(Figure 1A)**. [^{18}F]FDG PET scans were performed at the same time points **(Figure 1A)**. The loss of DA neurons of the striatum was quantified by 0-30 min dynamic [^{18}F]D_6-FP-(+)-DTBZ PET imaging at the 4th week after 6-OHDA treatment **(Figure 1A)**. MRI images were co-registered to the PET images to quantify the radioactivity in striatum. Normalization of PET imaging analysis was conducted by $SUV_R^{Ips/Con}$ (SUV of the ipsilateral striatum/SUV of the contralateral striatum). TSPO immunofluorescence staining at the same time points post-lesion was also performed **(Figure 1A)**.

Results:

PET/MRI imaging indicated that the SUV of [^{18}F]DPA-714 was significantly higher in right striatum comparing with the left in 6-OHDA treated rats during 1-3 weeks after 6-OHDA treatment **(Figure 1B)**. $SUV_R^{Ips/Con}$ of [^{18}F]DPA-714 in striatum of 6-OHDA treated groups reached the peak at the 2nd week (1.523±0.148) from the 1st week (1.401±0.128), then slowly decreased for the 3rd week (1.450±0.217) to the 4th week (1.166±0.131) (**Figure 1B, E**). Results of immunofluorescence also showed the activation of microglia in the ipsilateral striatum **(Figure 1F, G)**. There was no difference between bilateral striatum in the sham group **(Figure 1B, E)**. There was no uptake difference observed in bilateral striatum in [^{18}F]FDG PET/MRI images during entire time points **(Figure 1C)**. Time activity curve (TAC) of [^{18}F]D_6-FP-(+)-DTBZ revealed that approximately 60% DA neurons loss for the 6-OHDA treated right stratum, indicating the successful establishment of this model **(Figure 1D)**. The behavior tests indicated rotations increased from the 1st week (6.4 ± 2.4 turns/ min) to the 3rd week (11.3±4.3 turns/ min), and then stable during the 3rd to the 4th week at around 11 turns/ min (**Figure 1E**).

Conclusion:

The neuroinflammation quantified by [^{18}F]DPA-714, but not [^{18}F]FDG PET/MRI imaging, was observed increasing in affected side striatum as early as 1st-3rd week post 6-OHDA treatments, when PD-like rotation behaviors were not reached stable conditions **(Figure 1E)**. The results of this study may be important in investigating the mechanism of activated microglia for neuroinflammation in the degenerative process of PD.

Reference

1. Sonninen, T.M., et al., Metabolic alterations in Parkinson's disease astrocytes. Sci Rep, 2020. 10(1): p. 14474.
2. Su, R.J., et al., Time-course behavioral features are correlated with Parkinson's disease-associated pathology in a 6-hydroxydopamine hemiparkinsonian rat model. Mol Med Rep, 2018. 17(2): p. 3356-3363.
3. Hirsch, E.C. and S. Hunot, Neuroinflammation in Parkinson's disease: a target for neuroprotection? Lancet Neurol, 2009. 8(4): p. 382-97.
4. Rodríguez-Chinchilla, T., et al., [(18)F]-DPA-714 PET as a specific in vivo marker of early microglial activation in a rat model of progressive dopaminergic degeneration. Eur J Nucl Med Mol Imaging, 2020. 47(11): p. 2602-2612.
5. Zhao, C., et al., An Efficient Automated Radiosynthesis and Bioactivity Confirmation of VMAT2 Tracer [(18)F]FP-(+)-DTBZ. Mol Imaging Biol, 2020. 22(2): p. 265-273.

Oral Presentation

Disclosures: The authors have disclosed no financial interest.

110-Non-invasive stratification of colon cancer by metabolic PET imaging

Presenter: Gaurav Malviya, Beatson Institute for Cancer Research

Gaurav Malviya[1], Tamsin Lannagan[1], Agata Mrowinska[1], Emma Johnson[1], Robert Bielik[1], Gavin Brown[1], Colin Nixon[1], Kathryn Gilroy[1], Andrew Campbell[1], Dmitry Soloviev[1], Owen Sansom[1], David Y. Lewis[2]

[1]*Beatson Institute for Cancer Research, Glasgow, United Kingdom*
[2]*Beatson Institute for Cancer Research, Glasgow, Lanarkshire, United Kingdom*

Gene expression profiling is the current basis for molecular subtyping of colon cancer but it relies on biopsy or surgical resection and provides limited insight into subtype dynamics or spatial heterogeneity [1, 2]. To overcome these limitations we investigated non-invasive PET imaging signatures for colon cancer stratification as surrogates for gene-expression based subtyping. The ultimate aim of molecular stratification is to support the application of subtype-specific therapies for different patient subgroups. We initially classified five colon cancer organoid models derived from genetically engineered mouse models (GEMM) with multiple conditional alleles present in the majority of human colon cancer patients: *Apc*$^{fl/+}$ *Kras*$^{G12D/+}$ (AK), *Apc*$^{fl/+}$ *Kras*$^{G12D/+}$ *Trp53*$^{fl/fl}$ *Tgfbr1*$^{fl/fl}$ (AKPT), *Apc*$^{fl/+}$ *Kras*$^{G12D/+}$ *Trp53*$^{fl/fl}$*Rosa26*$^{N1icd/+}$ (AKPN), *Braf*$^{V600E/+}$ MLH$^{fl/fl}$ *Tgfbr1*$^{fl/fl}$ (BMT) and *Kras*$^{G12D/+}$ *Trp53*$^{fl/fl}$ *Rosa26*$^{N1icd/+}$ (KPN). To differentiate models we used a complementary panel of four PET tracers imaging glucose uptake ([^{18}F]FDG), amino acid uptake ([^{18}F]FET), proliferation ([^{18}F]FLT) and fatty acid synthesis ([^{11}C]acetate;

ACE) (Figure 1a). We observed significant inter-model heterogeneity in imaging signatures, each model had a unique profile of tracer uptake, e.g. [^{18}F]FDG and [^{18}F]FET uptake were highest in AK and [^{18}F]FLT and [^{11}C]ACE were highest in AKPN (Figure 1b and 1c), each tracer provided unique information (tracer correlations $R^2 = 0.30 – 0.47$; Figure 1d). Overall Receiver Operating Characteristic (ROC) curves showed that [^{18}F]FDG and [^{18}F]FET were more effective than [^{18}F]FLT and [^{11}C]ACE for stratifying colon cancer models. BMT was best separated from the other models by [^{18}F]FLT (AUC = 0.98 +/- 0.02; p = 0.0005), KPN was best separated by [^{18}F]FET (AUC = 0.79; p = 0.05) and AKPN by [^{11}C]ACE (AUC = 0.88; p = 0.02) (Figure 1e and 1f). GLUT-1 IHC correlated with [^{18}F]FDG uptake across the five models ($R^2 = 0.28$; p = 0.01), for other tracers, uptake could not be resolved down to a single protein.

We next investigated if imaging signatures were dependent on tissue context and microenvironment by using the same genetic lesions (KPN) in different locations: subcutaneous implantation, orthotopic (intracolonic injection), or autochthonously driven directly from conditionally expressed oncogenes (GEMM). Higher fidelity models had higher [^{18}F]FDG but not [^{18}F]FET uptake, GEMM > orthotopic > subcutaneous (F = 8.2; p = 0.009). We checked consistency in other genotypes (i.e. AKPT). While [^{18}F]FDG uptake in orthografts was again higher than subcutaneous (74.2% of variation; p < 0.0001) the extent of the increase varied by genotype (KPN v AKPT) (9.8% of variation; p = 0.0067), suggesting the relative contribution of genes and environment to imaging signatures was, at last partially, dependent on tumor genetics.

To determine if imaging signatures changed during tumor evolution, we imaged KPN GEMM tumors early (on day 43) and late (on day 85) post-tamoxifen induction. [^{18}F]FDG but not [^{18}F]FET increased over time (p = 0.008). To check if imaging signatures were associated with aggressivity we compared the uptake of four PET tracers in organoids from matched KPN primary and liver metastasis. [^{18}F]FDG (p = 0.028) and [^{18}F]FET (p = 0.008), but not [^{11}C]ACE and [^{18}F]FLT were higher in the metastatic setting. We repeated this in another two matched KPN primaries and metastasis, this time showing no difference in [^{18}F]FDG and [^{18}F]FET. PET imaging has the potential to differentiate metastatic colon cancer but cancer evolution is heterogeneous.

We measured metabolic PET imaging signatures (207 PET scans) in a broad spectrum of fifteen different colon cancer models showing distinct imaging differences depending on genotype, environment and tumor evolution. This is the first colon stratification study using a panel of PET imaging biomarkers. The metabolic heterogeneity in colon cancer subtypes provides a novel approach for future clinical colon cancer stratification and advances the development of subtype-based precision medicine.

Reference

1. Guinney J, Dienstmann R, Wang X, de Reyniès A, Schlicker A, Soneson C, et al. 2015. The consensus molecular subtypes of colorectal cancer. Nature Medicine; 21(11):1350-6.
2. Isella C, Brundu F, Bellomo SE, Galimi F, Zanella E, Porporato R et al. Selective analysis of cancer-cell intrinsic transcriptional traits defines novel clinically relevant subtypes of colorectal cancer. Nat Commun. 2017;8:15107.

Oral Presentation

Disclosures: The authors have disclosed no financial interest.

111-SWIR ratiometric fluorescence in vivo imaging of physiology in freely-moving mice

Presenter: Joycelyn Yiu, UC San Diego

Joycelyn Yiu[1], Bernardo Arús[2], Emily Cosco[3], Ellen Sletten[4], Thomas Bischof[5], Oliver Bruns[6]
[1]UC San Diego

[2]Helmholtz Zentrum München, Neuherberg, Germany
[3]University of California, Los Angeles, Los Angeles, California
[4]University of California, Los Angeles
[5]Helmholtz Pioneer Campus, Neuherberg, Bayern, Germany
[6]Helmholtz Zentrum Munchen, München, Bayern, Germany

Anesthesia and stress affect general animal physiology.[1,2] However, the current noninvasive methods to measure physiology typically rely on anesthesia or physical restraint due to either insufficient temporal resolution or signal variation derived from motion.[3] Here, a shortwave infrared (SWIR) fluorescence imaging method is used to tackle these limitations.[4,5] We have recently set the record for SWIR fluorescence imaging speeds (<3 ms, 300 fps), enabling the resolution of features such as blood vessels even as the mice exhibited fast movements. To address variations in signal dependent of mouse pose, a ratiometric approach was devised. The emission of two orthogonal fluorescent dyes was measured: the sample and reference fluorophores. The former consists of well-established fluorescent probes of physiological activity in organs of interest, while the latter exhibits stable signal in the same organ and acts as a reference to the sample probe. After *in vitro* and *ex vivo* validation, this approach was tested *in vivo* by measuring indocyanine green (ICG) clearance, a clinically-used liver physiology assay.[6,7] ICG clearance kinetics is used as a proxy for liver function, and ICG fluorescence was measured in two different compartments by imaging, tracking, and extracting fluorescence intensity from blood vessels and liver.[8,9] Chrom7, a cyanine orthogonal to ICG, was deployed as the reference probe.[5] A machine learning-based approach was used to track the organs.[10] Our SWIR ratiometric imaging was able to reproduce in the awake mice the results observed in isoflurane-anesthetized ones for both ICG blood half-life (isoflurane: mean 2.56 min ± sd 0.28, n=4; awake: 2.81 min ± 0.73, n=4) and liver clearance (18.44 min ± 2.50, n=3; 18.71 min ± 3.29, n=9), in line with the clinical literature. Our work paves the way to free researchers from the confounding effects of anesthesia by enabling the quantitative measurement of organ physiology in freely-moving mice.

Reference

1. Lundgaard, I. et al. Direct neuronal glucose uptake heralds activity-dependent increases in cerebral metabolism. Nat. Commun. 6, 6807 (2015).
2. Bachmann, S. B., Proulx, S. T., He, Y., Ries, M. & Detmar, M. Differential effects of anaesthesia on the contractility of lymphatic vessels in vivo. J. Physiol. 597, 2841–2852 (2019).
3. Hildebrandt, I. J., Su, H. & Weber, W. A. Anesthesia and Other Considerations for in Vivo Imaging of Small Animals. ILAR J. 49, 17–26 (2008).
4. Thimsen, E., Sadtler, B. & Berezin, M. Y. Shortwave-infrared (SWIR) emitters for biological imaging: a review of challenges and opportunities. Nanophotonics 6, 1043–1054 (2017).
5. Cosco, E. D. et al. Bright Chromenylium Polymethine Dyes Enable Fast, Four-Color In Vivo Imaging with Shortwave Infrared Detection. J. Am. Chem. Soc. 143, 6836–6846 (2021).
6. Carr, J. A. et al. Shortwave infrared fluorescence imaging with the clinically approved near-infrared dye indocyanine green. Proc. Natl. Acad. Sci. U. S. A. 115, 4465–4470 (2018).
7. Wiegand, B. D., Ketterer, S. G. & Rapaport, E. The use of indocyanine green for the evaluation of hepatic function and blood flow in man. Am. J. Dig. Dis. 5, 427–436 (1960).

8. Ben-Moshe, S. & Itzkovitz, S. Spatial heterogeneity in the mammalian liver. Nat. Rev. Gastroenterol. Hepatol. 16, 395–410 (2019).
9. Narasaki, H. et al. Intraoperative Real-Time Assessment of Liver Function with Near-Infrared Fluorescence Imaging. Eur. Surg. Res. Eur. Chir. Forsch. Rech. Chir. Eur. 58, 235–245 (2017).
10. Mathis, A. et al. DeepLabCut: markerless pose estimation of user-defined body parts with deep learning. Nat. Neurosci. 21, 1281–1289 (2018).

Oral Presentation

Disclosures: The authors have disclosed no financial interest.

112-Automated PSMA-Positive Lesion Detection with 68Ga PSMA PET in Patients with Metastatic Prostate Cancer

Presenter: Omer Aras, Memorial Sloan Kettering Cancer Center

Omer Aras[1], Burcin Agridag Ucpinar[1], Yuhang Shi[1], Ezgi Gokdemir[2], Cetin Demirdag[2], Richard Ting[3], Ulku Korkmaz[4], Lance Hu[5], Haluk Sayman[6]

[1]Memorial Sloan Kettering Cancer Center
[2]Trakya University, Turkey
[3]Weill Cornell Medicine
[4]Trakia University
[5]United Imaging Healthcare
[6]Istanbul University-Cerrahpasa Cerrahpasa Medical Faculty, Turkey

Aim:
Prostate membrane-specific membrane antigen positron emission tomography (PSMA PET) is an established modality for the evaluation of PSMA-positive prostate cancer, with excellent diagnostic sensitivity. The aim of this study was to determine the feasibility of automated PMSA positive lesion detection using ^{68}Ga PSMA PET in patients with metastatic prostate cancer.

Materials and methods:
This retrospective study included 10 patients with prostate metastatic cancer who underwent PSMA positron emission tomography/computed tomography (PET/CT) and/or positron emission tomography/magnetic resonance imaging (PET/MRI). Neural networks were trained to segment organs on PET/CT or PET/MR images. PSMA avid foci were automatically segmented by applying a threshold of 45% of the maximum standard uptake value (SUVmax). Thus, PSMA foci within organs of physiologic PSMA uptake were automatically excluded from the analysis. PSMA-derived tumor volume (PSMA-TV), TL-PSMA (based on total lesion glycolysis (TLG)) SUVmax, SUVmean, and other whole-body imaging biomarkers were calculated for each patient. Automatically derived results were compared with manual readings in a subsample of patients by two nuclear medicine physicians.

Results:
A total of 17 PSMA-positive lesions were accurately detected from either PSMA PET/CT or PET/MRI, resulting in a diagnostic sensitivity of 100%. There was one false positive result (tracer extravasation at the site of injection). ^{68}Ga PSMA PET identified neoplastic lesions in 80% of patients, two patients with biochemical recurrence did not show any suspicious PSMA positive foci. The median TL-PSMA was 13777.9 mm^3 (6244.21–23510.79). The correlation between PSMA-TV and PSA levels was statistically significant ($p < 0.05$).

Conclusion:
Automated PSMA-positive lesion detection on ^{68}Ga PSMA PET is feasible. Accurate and automated PSMA-positive tumor detection on ^{68}Ga PSMA PET while providing whole-body tumor loads is feasible; such an automatic, robust, and fast approach may be used to inform the treatment of prostate cancer and be employed routinely.

Oral Presentation

Disclosures: The authors have disclosed no financial interest.

113-Molecular imaging of PDGFR-β and imatinib therapy in renal fibrosis

Presenter: Diana Möckel, Institute for Experimental Molecular Imaging

Diana Möckel[1], Barbara M. Klinkhammer[2], Simon W. Otten[3], Maike Baues[4], Peter Boor[2], Fabian Kiessling[5], Twan Lammers[6]

[1]Institute for Experimental Molecular Imaging, Aachen, Germany
[2]Institute of Pathology, RWTH Aachen University Hospital, Aachen, NRW, Germany
[3]Institute of Pathology, RWTH Aachen University Hospital, Aachen, Germany
[4]Institute for Experimental Molecular Imaging, Aachen, NRW, Germany
[5]RWTH Aachen University, Aachen, NRW, Germany
[6]RWTH Aachen University Hospital, Aachen, Germany

Introduction:
Millions of patients suffer from chronic kidney disease (CKD), which affects about 10% of the world's population and is associated with high mortality and morbidity. The best predictor of CKD progression is the extent of fibrosis, i.e., pathological deposition of extracellular matrix (ECM) and loss of functional renal tissue. Currently, there are no specific treatment options and invasive biopsies remain the gold standard for diagnosis. Multiple signaling pathways are involved in fibrosis, including platelet-derived growth factor (PDGF) signaling. Mesenchymal stromal cells express both PDGF receptors PDGFR-α and PDGFR-β, whose activation drives proliferation, migration and production of extracellular matrix, i.e., key processes involved in fibrosis initiation and progression. Based on these notions, we set out to study the bicyclic PDGFR-β-binding peptide (BiPPB) [1-3] for diagnosis, staging and treatment monitoring of renal fibrosis (Fig. 1a).

Methods:
The biodistribution and kidney accumulation of Cy7-labeled BiPPB and a scrambled peptide control were visualized and quantified using computed tomography - fluorescence molecular tomography (CT-FMT), fluorescence reflectance imaging (FRI) and microscopy. This was done in three different mouse models for kidney fibrosis: the unilateral ischemia/reperfusion injury (I/R), the adenine-induced nephropathy (Adenine) and a transgenic model with constitutive PDGFR-β activation specifically in renal mesenchymal cells (Mutant; Fig. 1b) [4]. In the latter model, we also monitored pharmacological PDGFR-β inhibition with imatinib. Kidney fibrosis and therapeutic efficacy findings were verified by immunohistochemistry (IHC).

Results:
In vivo 3D CT-FMT imaging and *ex vivo* 2D FRI showed strong accumulation in fibrotic kidneys for Cy7-labeled BiPPB, whereas only moderate amounts accumulated in the contralateral (I/R) and healthy

kidney (Adenine) over 48 hours after i.v. injection (Fig. 1c-d). The accumulation of the scrambled BiPPB was also significantly lower compared to the specific BiPPB. In transgenic mutant mice with specific activation of mesenchymal cells and primary renal scarring significantly more Cy7-BiPPB accumulated in the kidneys in comparison to healthy wildtype littermates. In combination with imatinib treatment for 3 weeks (mutant imatinib) the accumulation of Cy7-BiPPB is decreased (Fig. 1e-g). This was confirmed *ex vivo* by significantly increased probe accumulation (2D FRI; Fig. 1h) and PDGFR-β expression (immunohistochemistry (IHC) Fig. 1i) in fibrotic kidneys, which was diminished by imatinib treatment.

Conclusion:
Our findings confirm the PDGFR-β signaling pathway as a prominent pathway and therapeutic target in renal fibrosis. Here we demonstrate the potential of PDGFR-β-based imaging agents for non-invasive, quantitative and longitudinal monitoring of renal fibrosis progression and therapy response.

Acknowledgements: This work was supported by the DFG (SFB/TRR57, 445703531 CRU5011), ERC (StG309495-NeoNaNo) and START (124/14, 152/12).

Reference

1. Bansal R et al., PLoS One. 2014;9(2):e89878
2. Bansal R et al., J Control Release. 2014;179:18-24
3. Poosti F et al., Oncotarget. 2016;7(34):54240-54252
4. Buhl EM et al., EMBO Molecular Medicine. 2020 Mar 6;12(3):e11021

Oral Presentation

Disclosures: The authors have disclosed no financial interest.

114-PET Imaging of P2X7 Receptor (P2X7R) for Neuroinflammation with Newly Radiosythesized [18F]GSK1482160 in APP/PS1 Transgenic Mice

Presenter: Guolong Huang, Fifth Affiliated Hospital of Sun Yat-sen University

Guolong Huang[1], Yifan Qiu[1], Lei Bi[1], Kehao Gong[1], Peizhen Ye[1], Yanfang Shen[2], Yongshan Liu[2], Min Yang[3], Junbin Han[4], Hongjun Jin[5]

[1]*Fifth Affiliated Hospital of Sun Yat-sen University, Zhuhai, China*
[2]*Fifth Affiliated Hospital of Sun Yat-sen University*
[3]*Fifth Affiliated Hospital of Sun Yat-sen University, Zhuhai, Guangdong Province, China*
[4]*Fudan University*
[5]*The Fifth Affiliated Hospital, Sun Yat-sen University, Zhuhai City, Guangdong, China*

Introduction:
The overexpression of purinergic receptor P2X7 ligand-gated ion channel type 7 (P2X7R) is strongly associated with the activation of microglia, which plays an important role in the development of Alzheimer's disease (AD). GSK1482160 is a well-reported P2X7R modulator with nanomolar binding affinity and high selectivity. The previous radiosynthesis of this compound faced challenges. In this study, the [^{18}F]GSK1482160 was radiosynthesized based on nucleophilic aromatic (SNAr) radiofluorination. PET/CT with newly radiosythesized [18F]GSK1482160 was applied to explore the P2X7R expression in APP/PS1 transgenic mice of AD compared to age-matched controls.

Methods:
The [18F]GSK1482160 was synthesized as shown in Figure 1A and radiopharmaceuticals were analyzed by Radio-HPLC to detect the radiochemical purity (RCP) and radiochemical yield (RCY). Four 12-month-old APP/PS1 transgenic mice (AD, n = 4) and aged match C57BL/6 mice (WT, n = 4) were assigned for this study. A 10 min CT scan was conducted to confirm the positioning of the animal, followed by a 5 min transmission scan for attenuation correction. Each mouse was given ~8.15 MBq [18F]GSK1482160 tail intravenous injection, and a 30 min dynamic (10×3s; 3×10s; 4×60s; 6×150s; 2 ×300s) emission scan was performed on nanoPET (Mediso Inc., Hungary). Each mouse was given a pre-treatment of cyclosporin A (CsA) (25 mg/kg) 30 minutes before the PET scan. The brain MRI image of each mouse was collected through 9.4T microMRI scanner (Bruker Inc, USA). The three-dimensional volume of interests (VOIs) was transformed into the PET space and then overlaid on all reconstructed PET images. Activity measures were standardized to the mice body weight, and injected dose of radioactivity yielded a standardized uptake value (SUV). Brain regions' time active curves (TACs) were quantified based on PMOD (Technologies LLC, Zurich, Switzerland). The area under curves (AUCs) were calculated based on TACs from the different region of interests (ROIs).

Results:
[18F]GSK1482160 was successfully synthesized with RCY 25-30%, R CP ? 98%, and molar activity (Am) 55-85 GBq/?mol. PET/MRI imaging showed these brain regions that the AD mice had significantly higher brain uptake than the WT mice (**Figure 1B and 1C**): basal forebrain septum (28.78 vs 20.51), amygdala (30.07 vs 22.04), cortex (26.62 vs 18.19), olfactory bulb (32.85 vs 23.30), hippocampus (23.39 vs 16.30), striatum (28.28 vs 17.03), midbrain (24.88 vs 18.09) (**Figure 1D and 1E**).

Conclusions:
New PET tracer [18F]GSK1482160 was successfully achieved with good RCY, RCP, and Am. The PET imaging of [18F] GSK1482160 revealed that the expression of P2X7R was significantly higher in the AD mice. Therefore, this improved method for this novel tracer warrants further validation for potential PET imaging agents for neuroinflammation of AD.

References

1. Chen YH, Lin RR, Tao QQ. The role of P2X7R in neuroinflammation and implications in Alzheimer's disease. Life Sci. 2021 Apr 15;271:119187.
2. Han J, Liu H, Liu C, Jin H, Perlmutter JS, Egan TM, Tu Z. Pharmacologic characterizations of a P2X7 receptor-specific radioligand, [11C]GSK1482160 for neuroinflammatory response. Nucl Med Commun. 2017 May;38(5):372-382.

Oral Presentation

Disclosures: The authors have disclosed no financial interest.

115-Collagen-based radiotracer for the specific detection of Gram-positive bacteria by SPECT/CT imaging

Presenter: Mario González-Arjona, Fundación Investigación Biomédica del Hospital Gregorio Marañón

Mario González-Arjona[1], Gorka Sobrino[2], María Guembe[3], Lorena Cussó[2], Daniel Calle[4], Emilio Bouza[5], Patricia Muñoz[5], Manuel Desco[3], Beatriz Salinas[6]

[1]*Fundación Investigación Biomédica del Hospital Gregorio Marañón, Madrid, Spain*
[2]*Instituto de Investigación Sanitaria Gregorio Maranon, Madrid, Madrid, Spain*
[3]*Instituto de Investigación Sanitaria Gregorio Maranon, Madrid, Spain*
[4]*Centro Nacional de Investigaciones Cardiovasculares (CNIC), Madrid, Spain*
[5]*Instituto de Investigación Sanitaria Gregorio Maranon, Madrid, Comunidad de Madrid, Spain*
[6]*Fundación Investigación Biomédica del Hospital Gregorio Marañón, Madrid, Madrid, Spain*

Introduction:
Infective endocarditis (IE) is one of the main complications of nosocomial bacteremia [1], frequently caused by Gram-positive bacteria *Staphylococcus aureus,* infecting patients during surgical procedures or associated with intravascular devices [2]. Early detection of infection allows for more efficient treatment and a more effective approach to the pathology. Nuclear imaging is rising as a noninvasive and selective tool for diagnosis. However, gold standard radiotracer [^{18}F]-FDG fails to discern infection from inflammation [5], causing false positives. Based on the presence of Collagen binding proteins (CnBP) in the cell wall of Gram-positive bacteria and to overcome those limitations in IE detection, we propose the development of novel radiotracer based on the radiolabeled collagen type I for the selective detection of gram-positive bacteria associated with IE, as it has a proved and specific interaction with *S. aureus* thanks to the presence of CnBP on its cell membrane [6,7].

Methods:
Rat Tail Collagen I was conjugated to DTPA-bis-anhydride chelator in $NaHCO_3$ 0.1M buffer at 37ºC and purified using 100kDa-Amicon filters. Radiolabeling was performed with sodium [^{99m}Tc]$NaTcO^4$, reduced to ^{99m}Tc(IV) using $SnCl_2$, at 37ºC/30 min, and filtered employing 100kDa Amicon. The reaction was optimized with different collagen and $SnCl_2$ concentrations. Purity and *In-vitro* stability were assessed by Radio-TLC (90:10 MeOH:H_2O). Hydrophobicity was established by LogP calculation. Blood circulation half-life was performed in SD rats by blood extraction (2 weeks). Selectivity of the tracer towards Gram-positive bacteria and fungi was evaluated *In-vitro* using ATCC strains of: *S. aureus* 29213*, Staphylococcus epidermidis* 35984*, Enterococcus faecalis* 35186, *Escherichia coli* 25922 (Gram-negative, control) and *Candida albicans* 14053 (yeast, control) as controls. Binding of [^{99m}Tc]-DTPA-Collagen and [^{18}F]-FDG to *S. aureus* was evaluated *In-vitro*. *In-vivo* validation of the radiotracer was performed by SPECT/CT in infective endocarditis model of SD rats, employing sterility Sham model as control. Radiotracer (1.03±0.20mCi, 250µL, 1X PBS) was administered intravenously 24h post-surgery. *Ex-vivo* biodistribution and autoradiography studies were performed after imaging. Finally, microbiological studies and H&E histology were performed to confirm the infection.

Results/Discussion:
[^{99m}Tc]-DTPA-Collagen was successfully synthetized, with an optimal radiochemical-yield of 43±6% (Collagen 2mg/mL, $SnCl_2$ $2x10^{-4}$M). Radio-TLC assessment confirmed a purity of 96±2% and a stability higher than 90% after 50h post-incubation. LogP revealed a hydrophilic behavior of the tracer (LogP value: -3.69±0.58), suitable for *In-vivo* studies. *In-vitro* uptake showed a high specificity for Gram-positive bacteria (63±7%), in contrast to Gram-negative (9±2%) and fungi (12±3%); and three times greater sensitivity of [^{99m}Tc]-CDTPA-Collagen to *S. aureus* (66±3%) compared to [^{18}F]-FDG (21±1%). Blood-circulation assay revealed a half-life of the tracer lower than 20 min (19±2min), which indicates a fast metabolism. *Ex vivo* biodistribution studies showed main uptake in liver (6.1±2.8%ID/g) and spleen (2.1±0.2%ID/g), confirming hepatobiliary excretion of the tracer. Prelimina*ry in-vivo* SPECT/CT imaging showed a very localized uptake in the cardiac valve, not present in the damaged region of sham rats, proving the selectivity of the tracer towards infected regions, avoiding false positives by inflamed tissue. Autoradiography, confirmed higher uptake in infected cardiac tissue, with an infected:sham uptake ratio of 1.4:1 ($5.2\pm0.1x10^4$: $3.6\pm0.8x10^4$). Microbiological studies and H&E histology confirmed the infected/inflamed status of the models.

Conclusions:
We have synthesized and fully characterized the SPECT radiotracer [^{99m}Tc]-DTPA-Collagen based on the ^{99m}Tc-radiolabeled Collagen I protein. We validated *in-vitro* the selectivity of the tracer towards Gram-positive bacteria and higher binding than "Gold-standard" [^{18}F-FDG]. *In-vivo* SPECT/CT assessment of the probe in an infective endocarditis model and further *ex-vivo* studies have confirmed its ability to selective detect the active infectious processes and avoid false positives by inflammatory uptake.

Reference
1. Tleyjeh, I.M.; Baddour, L.M. Staphylococcus aureus bacteremia and infective endocarditis: old questions, new answers? In Proceedings of Mayo Clinic Proceedings; pp. 1163-1164.
2. Widmer, E.; Que, Y.-A.; Entenza, J.M.; Moreillon, P. New concepts in the pathophysiology of infective endocarditis. Current infectious disease reports 2006, 8, 271-279.
3. Fowler Jr, V.G.; Sanders, L.L.; Sexton, D.J.; Kong, L.; Marr, K.A.; Gopal, A.K.; Gottlieb, G.; McClelland, R.S.; Corey, G.R. Outcome of Staphylococcus aureus bacteremia according to compliance with recommendations of infectious diseases specialists: experience with 244 patients. Clinical Infectious Diseases 1998, 27, 478-486.
4. Reunes, S.; Rombaut, V.; Vogelaers, D.; Brusselaers, N.; Lizy, C.; Cankurtaran, M.; Labeau, S.; Petrovic, M.; Blot, S. Risk factors and mortality for nosocomial bloodstream infections in elderly patients. European journal of internal medicine 2011, 22, e39-e44.
5. Brøndserud, M.B.; Rosenvinge, F.S.; Høilund-Carlsen, P.F.; Hess, S. Clinical value of FDG-PET/CT in bacteremia of unknown origin with catalase-negative gram-positive cocci or Staphylococcus aureus. European journal of nuclear medicine and molecular imaging 2019, 46, 1351-1358.
6. Di Lullo, G.A.; Sweeney, S.M.; Korkko, J.; Ala-Kokko, L.; San Antonio, J.D. Mapping the ligand-binding sites and disease-associated mutations on the most abundant protein in the human, type I collagen. Journal of Biological Chemistry 2002, 277, 4223-4231. 7. Holderbaum, D.; Spech, R.A.; Ehrhart, L.A. Specific binding of collagen to Staphylococcus aureus. Collagen and Related Research 1985, 5, 261-271.

Oral Presentation

Disclosures: The authors have disclosed no financial interest.

116-Translational evaluation of a next-generation fluorescent somatostatin analog for intraoperative imaging

Presenter: Servando Hernandez Vargas, University of Texas Health Science Center at Houston

Servando Hernandez Vargas[1], Solmaz AghaAmiri[2], Sukhen C. Ghosh[3], Michael P. Luciano[4], Luis Borbon[4], Po Ear[4], James Howe[4], Jennifer Bailey-Lundberg[4], Gregory Simonek[4], Daniel Halperin[4], Hop Tran Cao[4], Naruhiko Ikoma[4], Martin J. Schnermann, Ali Azhdarinia[1]

[1]*University of Texas Health Science Center at Houston, Houston*
[2]*University of Texas Health Science Center at Houston, Houston, TX*
[3]*McGovern Medical School, Institute of Molecular Medicine, Houston, Texas*
[4]*National Cancer Institute, FREDERICK, MD*

Introduction:
Fluorescence-guided surgery (FGS) is an imaging specialty capable of identifying tumors that would otherwise be undetected [1]. Patients with neuroendocrine tumors (NETs) are excellent candidates for tumor-targeted FGS since up to 45% of surgical cases have partial resection and most overexpress the somatostatin receptor subtype-2 (SSTR2). Here we introduce two key advances in the translational evaluation of an FGS approach for NETs. First, we developed a second-generation near-infrared fluorescent (NIRF) somatostatin analog, MMC(FNIR-Tag)-TOC, to enhance tumor specificity. Second, we examined agent performance using novel animal models and simulated a clinical workflow to bridge preoperative nuclear imaging with SSTR2-targeted FGS.

Methods:
The SSTR2-targeting peptide, TOC, was conjugated to a multimodality chelator (MMC) [2] on solid-phase, and followed by FNIR-Tag (charge balanced dye [3]) conjugation *via* click chemistry. The fluorescent conjugate was radiolabeled with ^{67}Ga as previously described [2]. SSTR2-mediated binding was confirmed using established radioligand assays [2]. To determine the optimal dose and time, we injected increasing doses (2, 5 and 10 nmol) of dual-labeled agent into nude mice with NCI-H69 xenografts and performed *in vivo* imaging up to 24 h post-injection (p.i.) ($n = 4$/group). Key tissues were resected for *ex vivo* imaging and gamma counting. To simulate a patient selection protocol, we used an orthotopic pancreatic tumor model (BON1-SSTR2; $n = 5$) and performed surgical planning on day 0 *via* PET/CT scan using ^{68}Ga-DOTA-TOC (1 h p.i.; 200 µCi; 0.5 nmol). Two days later, we injected mice with 5 nmol of MMC(FNIR-Tag)-TOC, acquired *in vivo* fluorescence images 3 h p.i., and harvested tumors under white light. After direct visual inspection of the wound bed, we identified and harvested suspicious lesions for multiscale imaging and immunohistopathology. To assess imaging performance in a translational setting, we first used our novel patient-derived xenograft (PDX) models, NEC913 (SSTR2+) and NEC1452 (SSTR2-) [4], and performed NIRF imaging studies *in vivo* ($n = 3$) as described above. Finally, we examined specific binding in frozen sections from freshly resected pancreatic NETs, metastatic lesions (liver), and involved lymph nodes.

Results/Discussion:
The dose-time finding study showed that agent uptake in tumor and nontumor tissues varied slightly as a function of dose or time, suggesting saturable tumor binding (1.5-2.0 %IA/g) and efficient clearance (<0.25 and <0.50 %IA/g in muscle and blood at 3 h, respectively). On average, fluorescent TBRs were >3.5 and >5.5 in pancreas and small intestine, respectively, with no differences ($P > 0.05$) associated with dose or time. From these experiments, we identified 5 nmol and 3 h as preferred parameters. Using a theranostic approach for "patient" selection with a FDA-approved radiopharmaceutical, we observed excellent correlation between nuclear and fluorescence imaging findings in the BON1-SSTR2 orthotopic model. *Ex vivo* imaging yielded a tumor-to-pancreas ratio of 17.7±9.3, suggesting strong potential for visual contrast in an intraoperative setting. Furthermore, we detected fluorescent focal points in the spleen and small intestine suspected to be metastatic disease. Analysis of tumor and suspicious lesions confirmed cancer status (H&E) and SSTR2-positive regions (IHC) that correlated with mesoscopic NIRF imaging. In the PDX imaging study, agent accumulation was only observed in SSTR2+ tumors, with minimum to no signal in tumors lacking the receptor (SSTR2+ tumor/SSTR2- tumor ratio >4). MMC(FNIR-Tag)-TOC staining of surgical biospecimens showed excellent co-localization with IHC.

Conclusions:
Using multiple translational models and a combination of fluorescent and radioactive readouts, we observed excellent correlation between preoperative nuclear imaging, fluorescence-guided surgery, and histopathology, indicating strong potential of MMC(FNIR-Tag)-TOC for clinical applications.

Reference
1. Hernot, S., et al., Lancet Oncol., (2019), DOI: 10.1016/S1470-2045(19)30317-1
2. Hernandez Vargas, S., et al., Clin. Cancer Res., (2019), DOI: 10.1158/1078-0432.CCR-18-3312
3. Luciano, M. P., et al., ACS Chem. Biol., (2019), DOI: 10.1021/acschembio.9b00122
4. Tran, C. G., et al., Cancers, (2022), DOI: 10.3390/cancers14081910

Oral Presentation

Disclosures: The authors have disclosed no financial interest.

117-Early identification of life-threatening soft-tissue infection using dynamic fluorescence imaging: first-in-kind clinical study of first-pass kinetics

Presenter: Samuel Streeter, Dartmouth College

Samuel Streeter[1], Gabrielle Ray[2], Logan Bateman[3], Kendra Hebert[1], Fallon Bushee[2], I Leah Gitajn[4], Jaimo Ahn[5], Sunil Singhal[6], Niels Martin[7], William Obremskey[8], Jonathan Schoenecker[8], Jonathan Elliott[4], Eric Henderson[9]

[1]*Dartmouth College, Hanover, New Hampshire*
[2]*Geisel School of Medicine at Dartmouth, Hanover, New Hampshire*
[3]*Thayer School of Engineering at Dartmouth, Hanover, New Hampshire*
[4]*Dartmouth-Hitchcock Medical Center, Lebanon, NH*
[5]*University of Michigan Medical School, Ann Arbor, Michigan*
[6]*Perelman School of Medicine at the University of Pennsylvania, Philadelphia, PA*
[7]*Perelman School of Medicine at the University of Pennsylvania, Philadelphia, New Hampshire*
[8]*Vanderbilt University School of Medicine, Nashville, Tennessee*
[9]*Dartmouth College, Lebanon, NH*

Necrotizing fasciitis (NF) is an aggressive form of a necrotizing soft-tissue infection (NSTI)—commonly known as 'flesh-eating bacteria'—with a cumulative mortality rate of 34% (6-76%) (1, 2). NF occurs with an inoculation of virulent bacteria in or around fascia, the connective tissue layer investing our muscle and organ compartments. With some bacterial strains, this tissue layer provides an ideal environment for bacterial growth, facilitating rapid advancement along fascial planes.

The result is a soft-tissue infection that quickly spreads centrally—often within hours—leading to sepsis, multi-organ failure, and death. Immediate, aggressive surgical debridement is considered standard-of-care. Patients with NF present with non-specific findings—fever, pain, and elevated inflammatory laboratory values—and the overlying skin can appear normal (Figure 1A). Therefore, diagnosis is often delayed, increasing morbidity and mortality. A key feature of NF is prominent blood vessel thrombosis in affected tissues. Because of this phenomenon, we hypothesized that perfusion imaging using indocyanine green (ICG) would show diminished blood flow in NF-affected tissues, particularly compared to non-necrotizing superficial infections (*e.g.,* cellulitis). We therefore undertook a first-in-kind and Institutional Review Board-approved pilot study in patients presenting to the Emergency Department at Dartmouth Health (ClinicalTrials.gov Identifier: NCT04839302). Patients presenting with clinical features of NSTI and Laboratory Risk Indicator for Necrotizing Fasciitis score ≥ 6 were educated about the study. Consenting patients received intravenous administration of ICG (0.1-0.5 mg/kg) and immediate imaging of the affected site. ICG is an established perfusion fluorophore that can be used to distinguish perfused tissues from non-perfused tissues and has been used extensively for angiography and various surgical subspecialties (3, 4). Early results support our hypothesis that ICG signal voids occur in NF-affected tissues (peak fluorescence intensity at 50 s post-injection of <100 a.u. vs. >250 a.u. for NF-affected and unaffected tissues, respectively; Figure 1A-D) and dynamic contrast-enhanced fluorescence parameters reveal tissue kinetics that can be related to disease progression and extent (*e.g.,* egress slope (ES) of >0.8 vs. <0.2 near leading edge of disease and beyond disease extent, respectively; Figure 1H). Future work will involve the identification of ICG fluorescence-to-histopathology correlates in NF-affected tissues that indicate bacterial burden and delineate appropriate surgical debridement. Once robust histopathological correlates are determined, we aim to initiate a prospective, non-randomized, multi-center observational trial of ICG fluorescence in patients presenting to tertiary Emergency Departments with soft-tissue infections. ICG will be administered with the goals of, first, accurately distinguishing NF and non-NF infections, and second, correlating the use of ICG fluorescence with initial surgical debridement success.

Reference

1. C.-H. Wong, L.-W. Khin, K.-S. Heng, K.-C. Tan, C.-O. Low, The LRINEC (Laboratory Risk Indicator for Necrotizing Fasciitis) score: a tool for distinguishing necrotizing fasciitis from other soft tissue infections. Crit Care Med 32, 1535–1541 (2004).
2. C. R. McHenry, J. J. Piotrowski, D. Petrinic, M. A. Malangoni, Determinants of mortality for necrotizing soft-tissue infections. Ann Surg 221, 558–565 (1995).
3. J. T. Alander, et al., A review of indocyanine green fluorescent imaging in surgery. Int J Biomed Imaging 2012, 940585 (2012).
4. M. B. Reinhart, C. R. Huntington, L. J. Blair, B. T. Heniford, V. A. Augenstein, Indocyanine Green: Historical Context, Current Applications, and Future Considerations. Surg Innov 23, 166–175 (2016).

Oral Presentation

Disclosures: The authors have disclosed no financial interest.

118-Radio Frequency Sweeps at uT Fields allow for cheap and efficient Parahydrogen Induced Polarization of Biomolecules

Presenter: Stephan Knecht, NVision Imaging Technologies GmbH

Stephan Knecht[1], Martin Gierse[2], Michael Keim[3], Alastair Marshall[3], Alon Salhov[4], Sebastian Lucas[3], Jochen Scheuer[5], Christoph Müller[6], John Blanchard[5], Ilai Schwartz[3]

[1]NVision Imaging Technologies GmbH, Ulm, Germany
[2]NVision Imaging Technologies GmbH, Baden-Wuerttemberg, Germany
[3]NVision Imaging Technologies GmbH, Germany
[4]NVision Imaging Technologies GmbH, Israel
[5]NVision Imaging Technologies GmbH
[6]NVision Imaging Technologies GmbH, Ulm, Baden-Würtemberg, Germany

Magnetic resonance imaging (MRI) of the metabolic processes within the human body opens up new methods of studying cancers by assessing tumors. It is accomplished through the monitoring of the 13C NMR signal of a metabolite, used as a tracer (e.g., pyruvate), and its downstream metabolic products. This has such a low signal intensity that measuring it is almost impossible, and hyperpolarization offers an attractive solution. Parahydrogen-induced polarization (PHIP), where parahydrogen is chemically added to an unsaturated precursor molecule, generates a high-purity entangled spin state in the product molecule. A transfer step is then undertaken to convert the spin-order of the hyperpolarized protons into observable ^{13}C magnetization. To facilitate an efficient transfer several pulsed coherence transfer schemes have been developed in the past[1,2]. While very efficient, they often require complex and often expensive hardware and are difficult to scale to volumes needed for prospective clinical development of PHIP. As a cost-efficient and scalable alternative, adiabatic manipulation of a static field in the nano Tesla to micro Tesla rage have been suggested and used in the past [3]. Unfortunately, this approach is not compatible with molecules containing quadrupolar relaxation sinks (such as deuterium) and does not allow the decoupling of different spin species. Both these factors greatly limit its potential for PHIP. Here, we present a novel method using adiabatically ramped radio-frequency (RF) sweeps at low static magnetic fields (several uT). These RF sweeps are a robust, effective and cost-efficient method of polarization transfer. We demonstrate this method on a variety of molecules and find that its performance either matches or exceeds the performance of magnetic field sweeps and can provide ^{13}C polarization in excess of 30%. The experimental process and setup is shown in figure 1. Additionally, we show that spin species can be decoupled from each other by RF-Irradiation, further increasing the performance of the polarization transfer for some molecules. Additionally, we demonstrate, that side specific deuteration can break the symmetry of spin coupling networks in pyruvate side-arms. This in combination with the presented transfer method allows for 50% higher transfer of polarization.

Reference

1. Goldman, Maurice, et al. "Hyperpolarization of 13C through order transfer from parahydrogen: a new contrast agent for MRI." Magnetic resonance imaging 23.2 (2005): 153-157.
2. Korchak, Sergey, Salvatore Mamone, and Stefan Glöggler. "Over 50% 1H and 13C Polarization for Generating Hyperpolarized Metabolites—A para-Hydrogen Approach." ChemistryOpen 7.9 (2018): 672-676.
3. Eills, James, et al. "Polarization transfer via field sweeping in parahydrogen-enhanced nuclear magnetic resonance." The Journal of chemical physics 150.17 (2019): 174202.

Oral Presentation

Disclosures: The authors have disclosed no financial interest.

119-Preclinical Evaluation of 4-[18F]Fluoroglutamine PET predicts response to combined Inhibition of EGFR and glutaminolysis in KRAS wild-type metastatic colorectal cancer

Presenter: Seong-Woo Bae, University of Texas MD Anderson Cancer Center

Seong-Woo Bae[1], Allison Cohen[1], Mohammed N. Tantawy[2], Gregory D. Ayers[2], Robert Coffey[3], Jordan Berlin[3], Scott Kopetz[1], H. Charles Manning

[1]*University of Texas MD Anderson Cancer Center, Houston, TX*
[2]*Vanderbilt University, Nashville, TN*
[3]*Vanderbilt University Medical Center, Nashville, Tennessee*

Monoclonal antibodies (mAbs) against the epidermal growth factor receptor (EGFR) have been developed for metastatic colorectal cancer (mCRC) therapy. However, the benefit of anti-EGFR mAbs was limited in patients with mCRC (Cetuximab: 0% KRAS mutant mCRC, 17% KRAS wild-type mCRC; Panitumumab: 10.8% mCRC). Therefore, a profound understanding of CRC characteristics based on a comprehensive exploration is an unmet need. The sensitive and quantitative nature of positron emission tomography (PET), coupled with the ability to produce targeted PET tracers, allow us to interrogate tumor metabolism non-invasively. We hypothesize that PET imaging with complementary genomics can confer new insights into mCRC milieu to improve targeted therapy. Altered glutaminolysis of cancer cells links signal transduction with nutrient accumulation, which can stimulate mitogen activated protein kinase (MAPK)-dependent proliferation irrespective of EGFR, and may contribute to resistance to anti-EGFR therapy. Given the significance of glutamine to cancer cells, targeting glutaminolysis represents a promising therapeutic approach. We aim to develop a preliminary signature based on combined PET imaging and genomics to predict response to combined inhibition of EGFR and glutamine metabolism in KRAS wild-type (WT) CRC. We have evaluated the feasibility of ^{18}F-4-Fluoro-glutamine (^{18}F-Gln) to detect metabolic activity of tumors in preclinical mouse models. We have imaged numerous CRC cell line xenograft models with ^{18}F-Glnpre- and post-treatment with two drugs targeting different aspects of glutamine metabolism. V-9302 is a small molecule inhibitor of ASCT2, the primary glutamine transporter in cancer cells (Schulte et al. *Nat Med*. 2018; 24(2):194-202), while CB-839 targets glutaminase, the enzyme responsible for conversion of glutamine to glutamate. In prior work, we have observed a decrease in ^{18}F-Gln uptake following treatment with V-9302 reflecting a pharmacodynamic response (Supporting Information Figure S1A). Here, we examined the correlation between baseline ^{18}F-Gln-PET and *SLC1A5* (ASCT2) gene expression in patient-derived xenograft (PDX) models and observed a positive correlation (Supporting Information Figure S1B). Furthermore, we are conducting a co-clinical trial evaluating ^{18}F-Gln PET to detect response to the combination of anti-EGFR mAbs and CB-839. Preclinically, we are evaluating ^{18}F-Gln PET pre- and post-treatment with combined CB-839 and panitumumab or cetuximab in CRC PDXs. We have observed changes in ^{18}F-Gln avidity in each PDX following the combination treatment (Figure 1A and B). CRC can be divided into four gene expression-based biologically distinct consensus molecular subtypes (CMS). A genomic landscape of PDXs with mutational status and transcriptomic profiles allows us to better understand each tumor phenotype (Figure 1C). We have identified resistance to the combination treatment in CMS1 with hypermutation and immune signature. PDXs with CMS2, which is a canonical subtype with *WNT* and *MYC*activation, were more likely to have ^{18}F-Gln PET uptake. In agreement with its CMS3 classification, which is a metabolic subtype, we observed better efficacy of the combination treatment in a CRC PDX with high expression of glutaminolysis-related genes and were able to predict its response using ^{18}F-Gln PET. Clinically, we are conducting a Phase II clinical trial combining panitumumab with CB-839 (NCT03263429). As part of this trial, we have successfully imaged patients with ^{11}C-glutamine PET for the first time and showed that this tracer allows non-invasive visualization of metastatic colon cancer lesions in multiple organs (Cohen et al. *J Nucl Med*. 2022; 63(1):36-43, Supporting Information Figure S1C). In conclusion, we have evaluated the feasibility of ^{18}F-Gln PET imaging for predicting response to combined inhibition of EGFR and glutaminolysis in KRAS WT CRC. To elucidate the underlying molecular underpinnings of colorectal cancer, we will further investigate metabolomic changes of tumors under a perturbed metabolic milieu by the therapeutic approach. These studies could lead to important advances in overcoming resistance to anti-EGFR therapies in CRC.

Oral Presentation

Disclosures: The authors have disclosed no financial interest.

120-Multiparametric Immunoimaging Maps Inflammatory Signatures in Murine Myocardial Infarction Models

Presenter: Mandy van Leent, Icahn School of Medicine at Mount Sinai

Mandy van Leent[1], Willem J. M. Mulder[2], Zahi Fayad[1], Alexander Maier[3], Claudia Calcagno[1]

[1]*Icahn School of Medicine at Mount Sinai, New York, NY*
[2]*Eindhoven University of Technology, Eindhoven, Netherlands*
[3]*Icahn School of Medicine at Mount Sinai*

Introduction:
The immune response following acute myocardial infarction (MI) encompasses a delicate balance between inflammatory and reparative programs. Our knowledge of these complex mechanisms is mainly derived from studies using a murine model of permanent coronary artery occlusion. In this study we developed, validated and implemented multiparametric imaging methods to investigate cardiac function and the systemic immune response in transient or permanent coronary artery occlusion mouse models.

Materials and Methods:
The MI models encompassed either transient (40 min, refered to as ischemia reperfusion, IR) or permanent occlusion (PO) of the left coronary artery, and non-infarcted mice were used as controls (Persuasive data file panel a). Both models were applied to male C57BL/6 mice. One, two or three days after MI, the animals subjected to systemic immunoimaging of the bone marrow, spleen and myocardium. We performed late gadolinium-enhanced (LGE) and ^{19}F-cardiac magnetic resonance imaging (cMRI), ^{18}F-fluorodeoxyglucose (FDG) positron emission tomography (PET) and ^{18}F-fluorothymidine (FLT) PET. We also performed PET imaging using a ^{64}Cu-labeled tracer targeting chemokine receptor 2 (CCR2) and an ^{89}Zr-labeled nanobody targeting CD11b. Finally, the same MI models were applied to atherosclerosis-prone *Apoe*$^{-/-}$ mice and systemic inflammation and plaque progression were assessed by flow cytometry and immunohistochemistry four weeks after infarction.

Results:
Through LGE cMRI, we observed that IR resulted in a smaller infarct size, better cardiac function and reduced survival as compared to PO (Panel a, Persuasive data file panel b). ^{89}Zr-CD11b nanobody and ^{64}Cu-CCR2 PET demonstrated that mice subjected to IR had less immune

cell influx to the ischemic myocardium compared to mice subjected to PO (Panels b and c). This finding was confirmed by flow cytometry analysis of the infarct zone (Persuasive data file panel c). In contrast, both MI models cause a similar systemic immune response in the bone marrow and spleen as observed with multimodal imaging (Panels d and e, Persuasive data file panels d-f). Both IR and PO aggravate atherosclerosis in *Apoe*$^{-/-}$ mice with higher macrophage and Ly6C^{hi} monocyte numbers in aortas and larger plaque size compared to *Apoe*$^{-/-}$ mice without MI (Panel f). The cardiac phenotypes and survival were similar to wildtype mice (Persuasive data file panels g and h).

Conclusions:
We developed and employed multimodal, multiparametric imaging protocols to characterize the immune response in the heart, bone marrow and spleen in two models of myocardial infarction. While cardiac function was superior in the IR model, both types of MI accelerated atherosclerosis.

Oral Presentation

Disclosures: The authors have disclosed no financial interest.

121-Radiosynthesis and PET imaging of [F-18]Sutezolid in Mouse Models of Pulmonary Tuberculosis and Tuberculous meningitis

Presenter: Patricia De Jesus, Johns Hopkins University School of Medicine

Patricia De Jesus[1], Camilo A. Ruiz-Bedoya[2], Filipa Mota[3], Anil Shelke[4], Melissa Bahr[5], Dylan Boone[6], Kelly Flavahan[7], Joel Freundlich[8], Sanjay K. Jain[2]

[1]*Johns Hopkins University School of Medicine, Upper Marlboro*
[2]*Johns Hopkins Univeristy, Baltimore, MD*
[3]*Johns Hopkins University School of Medicine, Baltimore, Maryland*
[4]*Rutgers University*
[5]*Johns Hopkins Univeristy*
[6]*Johns Hopkins Univeristy, Baltimore, Maryland*
[7]*Johns Hopkins University School of Medicine*
[8]*Rutgers University, Newark, NJ*

Background:
Mycobacterium tuberculosis remains the second most deadly pathogen after SARS-CoV-2. While this pathogen affects mainly the lungs, it can also affect the brain, causing tuberculous (TB) meningitis, the deadliest form of the disease. Sutezolid (PNU100480) is an oxazolidinone antimicrobial thiomorpholine analog of linezolid, a commonly used antimicrobial. It is potent against drug-resistant *M. tuberculosis* clinical isolates. Studies have shown that sutezolid is less toxic than linezolid and generates a sulfoxide metabolite that is also active against extracellular bacteria(1, 2). While drug dosing is commonly determined by pharmacokinetic studies based on plasma and cerebrospinal fluid (CSF), this traditional approach provides no information regarding drug delivery and biodistribution into privileged tissues, such as brain parenchyma and diseased lung areas (i.e., pulmonary cavities, granulomas). Here, we developed a [^{18}F]sutezolid radiotracer, chemically identical to the parent drug, to perform multicompartment pharmacokinetic quantification of the drug by positron emission tomography (PET) in healthy mice and mouse models of pulmonary TB and TB meningitis.

Methods:
[^{18}F]Sutezolid was obtained by copper-catalyzed radiofluorination of a boronic acid precursor, as previously reported for [^{18}F]-Linezolid(3). [^{18}F]Sutezolid was purified by preparative-HPLC in 4 % RCY (non-decay corrected) and formulated for *in vivo* injection. Mice [C3HeB/FeJ, female, healthy (n=4), pulmonary TB (n=3), TB meningitis (n=3)] were administered with a single dose of [^{18}F]Sutezolid (2.3 ± 0.5 MBq) intravenously. A 60 min dynamic PET/CT scan [nanoScan PET/CT (Mediso)] was acquired. 3D regions of interest (ROIs) were drawn to quantify radioactivity using VivoQuant 3.5 (Invicro). *Ex-vivo* biodistribution was measured using an automated gamma counter.

Results:
Whole-body [^{18}F]sutezolid PET imaging demonstrated rapid distribution to all organs with fast drug clearance via hepatobiliary and renal pathways, as early as 3 min post-injection. *Ex-vivo* biodistribution showed similar findings. In mice with pulmonary TB, [^{18}F]sutezolid demonstrated high lung penetration and spatial heterogeneity, with significantly lower penetration in the lung lesions (e.g., pneumonia, granulomas) compared to the unaffected lung ($P< 0.05$). In the mouse model of TB meningitis, [^{18}F]sutezolid penetrated the brain parenchyma and spatial heterogeneity was also observed, with higher concentration being found within the area of infection.

Conclusion:
We report the first radiosynthesis of [^{18}F]sutezolid and an *in vivo* PET imaging study in mouse models of pulmonary TB and TB meningitis. Further studies will be conducted to fully characterize the biodistribution of [^{18}F]sutezolid and optimize its use in novel chemotherapy regimens for multi-drug resistant pulmonary TB and TB meningitis.

Reference
1. Wallis RS, Dawson R, Friedrich SO, Venter A, Paige D, Zhu T, et al. Mycobactericidal activity of sutezolid (PNU-100480) in sputum (EBA) and blood (WBA) of patients with pulmonary tuberculosis. PLoS One. 2014;9(4):e94462.
2. Zhu T, Friedrich SO, Diacon A, and Wallis RS. Population pharmacokinetic/pharmacodynamic analysis of the bactericidal activities of sutezolid (PNU-100480) and its major metabolite against intracellular Mycobacterium tuberculosis in ex vivo whole-blood cultures of patients with pulmonary tuberculosis. Antimicrob Agents Chemother. 2014;58(6):3306-11.
3. Mota F, Jadhav R, Ruiz-Bedoya CA, Ordonez AA, Klunk MH, Freundlich JS, et al. Radiosynthesis and Biodistribution of (18) F-Linezolid in Mycobacterium tuberculosis-Infected Mice Using Positron Emission Tomography. ACS Infect Dis. 2020;6(5):916-21.

Oral Presentation

Disclosures: The authors have disclosed no financial interest.

122-Tracking biodistribution of [89Zr]Zr labeled extracellular vesicles by PET reveals organ-specific biodistribution based upon the route of administration

Presenter: Suchul Jang, Codiak BioSciences

Shil Patel[1], Karl Schmidt[2], Mohammed Farhoud[3], Tong Zi[2], **Suchul Jang**[4], Kevin Dooley[4], Dustin Kentala[5], Dobson Howard[6], Silvia Siso[2], Kyriakos Economides[2], Douglas Williams[2]

[1]*Codiak BioSciences, Cambridge*
[2]*Codiak BioSciences*
[3]*Sofie Biosciences, Inc, Culver City, California*

[4]*Codiak BioSciences, Cambridge, MA*
[5]*Invicro, Needham, Massachusetts*
[6]*Invicro, boston, ma*

Introduction:
Extracellular vesicles (EVs) have generated interest as delivery vehicles for multiple classes of therapeutics based on their ability to shuttle cargo and to mediate intercellular communication. We recently have described an engineered EV platform with overexpression of prostaglandin F2 receptor negative regulator (PTGFRN) which allows delivery of therapeutics to various immune cells. In this study, the biodistribution of engineered EVs was examined using *in vivo* and *ex vivo* techniques after systemic and compartmental administration.

Methods:
EVs were surface-labeled with ^{89}Zirconium deferoxamine ([^{89}Zr]Zr-DFO) and/or Cy7-scrambled antisense oligonucleotide (Cy7-ExoA-SOscr), or luminally loaded with GFP by fusion to PTGFRN. Labeled EVs were administered to rodents and non-human primates (NHP) via multiple routes. Positron Emission Tomography (PET) followed by immunohistochemistry (IHC) and autoradiography cross-validation enabled the assessment of the anatomical and cellular distribution of labeled EVs both spatially and temporally.

Results:
Systemic or local administration of EVs distributed preferentially to the liver and spleen (Intravenous, IV), gastrointestinal tract and lymph nodes (Intraperitoneal, IP), or local/regional lymph nodes (Subcutaneous, SC) in both rodents and NHP. Immunostaining of dissected organs displaying PET signal revealed co-localization of an EV marker (PTGFRN) with a subset of macrophage markers (CD206, F4/80, IBA1). While a homogeneous distribution of compartmentally dosed labeled EVs was observed in rodents, dosing into the cerebrospinal fluid in NHP resulted in a heterogenous distribution of EVs depending on the route of administration, specifically intrathecal (ITH) versus intracisterna magna (ICM) and intracerebroventricular (ICV). Anatomically, ITH administration in NHP revealed meningeal distribution of EVs along the neuraxis to the base of the skull. In contrast, ICM and ICV administration resulted in meningeal distribution of EVs around the skull and to the cervical and thoracic spinal column. Further characterization using IHC showed uptake of these EVs associated within a subset of meningeal macrophages.

Conclusions:
The present study provides a comprehensive assessment of the fate of engineered EVs across several mammalian species. The *in vivo* distribution was robustly and reproducibly observed to be both spatially and temporally dependent upon the route of administration providing insight into potential targeting opportunities for engineered EVs carrying a therapeutic payload.

Oral Presentation

Disclosures: The authors have disclosed no financial interest.

123-New insights in the mechanism of imaging cathepsin S-positive tumors in vivo

Presenter: Berit Blume, Helmholtz Zentrum Munchen

Berit Blume[1], Bernardo Arús[2], Oliver Bruns[3], Oliver Plettenburg[4]

[1]*Helmholtz Zentrum Munchen, Germany*
[2]*Helmholtz Zentrum München, Neuherberg, Germany*
[3]*Helmholtz Zentrum Munchen, München, Bayern, Germany*
[4]*Helmholtz Zentrum Munchen, Hannover, Germany*

One of the leading causes of death worldwide is cancer accounting for nearly 10 million deaths in 2020 [1]. To enhance the progression-free survival and overall survival after surgery it is important to determine the tumor-free margin, which is often not visible. Thus there is a demand for selective optical methods for image-guided surgery [2]. One possible approach is targeting cysteine proteases, especially cathepsin cysteine proteases, which are known to play a major role in cancer. Studies have shown that cathepsin S, which is expressed in brain cancer, gastric cancer, hepatocellular carcinomas, gioblastomas, melanoma and pancreatic islet cell cancer, plays a role in tumor invasion, resistance to apoptosis and in tumor angiogenesis [3]. Furthermore, it was shown that this protease is expressed on the surface of carcinoma cells and remains associated with the membrane. Development of a lipidated activatable cathepsin S probe (quenched fluorophore, probe **2**) for tumor imaging leads to a good signal/background ratio due to internalization of the cleaved fluorescent part (figure **A**) [4]. To further investigate the mechanism of labeling cathepsin S positive tumors new probes were designed and validated *in vitro* and *in vivo*. First we asked, if cleavage of the protease is required for labeling of 4T1 cells. Therefore, the product of proteolytic cleavage was synthesized and compared to the literature reported probe **2** (figure **B**). In cell assays with 4T1 tumor cells it was evident that in contrast to various other cleavable probes (**2**-**5**) the cleavage product **6** did not label the cells (figure **C**). That indicates that for *in vitro* labeling of cathepsin S-positive tumor cells cleavage of the probe by the protease is required for uptake into 4T1 cells. Second, both probes were tested *in vivo* in 4T1 tumor bearing mice (persuasive data, figure **C**). Interestingly, in the *in vivo* model, both probes (**2** and **6**) were capable of labeling the tumor, suggesting two different, possibly synergistic mechanisms acting *in vivo* and *in vitro*. In another aspect of this work we studied the influence of the lipidation on the efficacy of labeling. A set of different lipidated probes was synthesized (figure **B**) and the quenched probes were validated in a protease assay (persuasive data, figure **A**). The results suggested that an inversion of the stereochemistry (probe **1**) at the amino acid next to the cleavage side suppresses cleavage and thus activation of the probe. All other tested probes (**2**-**5**) were processed by the protease, shorter chain lengths displaying quicker cleavage. In a next step, the probes were tested *in vitro* on murine 4T1 tumor cells to investigate in the impact of lipidation on cellular labeling (figure **C**). C12 and C14 sidechains did display optimal labeling in this assay; the short chain analog **5** (bearing an acetyl chain) did show minimal cellular labeling despite being quickly processed in biochemical cathepsin assays. Probes **1** and **2** structurally only differ in stereochemistry at one center. In accordance with the *in vitro* results before, we could show that *in vivo* signal obtained for **1** was significantly lower than observed for **2**, underlining specificity of cleavage (persuasive data, figure **B**). Further work is warranted to investigate the specific uptake mechanisms in more detail, in particular since cathepsin probes are advancing in clinical trials for cancer imaging [5].

Reference

1. WHO – Cancer: https://www.who.int/news-room/fact-sheets/detail/cancer (27.04.2022, 17:18)
2. Keereweer, S., Kerrebijn, J.D.F., van Driel, P.B.A.A. et al. Optical Image-guided Surgery—Where Do We Stand? Mol Imaging Biol 13, 199–207 (2011).
3. Wilkinson, Richard D.A., Williams, Rich, Scott, Christopher J. and Burden, Roberta E.. "Cathepsin S: therapeutic, diagnostic, and prognostic potential" Biological Chemistry, vol. 396, no. 8, 2015, pp. 867-882.

4. Tan, G. J., Peng, Z. K., Lu, J. P., & Tang, F. Q. (2013). Cathepsins mediate tumor metastasis. World journal of biological chemistry, 4(4), 91–101.
5. Hu HY, Vats D, Vizovisek M, Kramer L, Germanier C, Wendt KU, Rudin M, Turk B, Plettenburg O, Schultz C. In vivo imaging of mouse tumors by a lipidated cathepsin S substrate. Angew Chem Int Ed Engl. 2014 Jul 14;53(29):7669-7673.
6. Whitley, M. J., Cardona, D. M., Lazarides, A. L., Spasojevic, I., Ferrer, J. M., Cahill, J., Lee, C. L., Snuderl, M., Blazer, D. G., 3rd, Hwang, E. S., Greenup, R. A., Mosca, P. J., Mito, J. K., Cuneo, K. C., Larrier, N. A., O'Reilly, E. K., Riedel, R. F., Eward, W. C., Strasfeld, D. B., Fukumura, D., … Brigman, B. E. (2016). A mouse-human phase 1 co-clinical trial of a protease-activated fluorescent probe for imaging cancer. Science translational medicine, 8(320), 320ra4

Oral Presentation

Disclosures: The authors have disclosed no financial interest.

124-Precision control and monitoring of cancer chemotherapy based on magnetic particle imaging

Presenter: Yapei Zhang, Michigan State University

Yapei Zhang[1], Bryan R. Smith[2], Sesha Lakshmi Arathi Paluri[3], Leo Barrios[4]

[1]Michigan State University, East Lansing
[2]Michigan State University, East Lansing, MICHIGAN
[3]Michigan State University, East Lansing, MI
[4]Michigan State University

Many commonly-used cancer drugs, such as Doxorubicin, are toxic to normal tissues and have narrow therapeutic windows—a dose range between minimum effective drug dose (MED) and the minimum toxic drug dose (MTD)[1]. Drug concentrations ideally should constantly remain between MED and MTD to minimize adverse effects. Currently, the clinically-injected dosage for chemotherapy treatment is computed based on body surface area, an overly simplistic one-size-fits-all-type strategy that results in widely heterogeneous patient responses[2]. In general, administration of too much drug (above MTD) causes serious side effects on normal human organs; too little drug (below MED) results in lack of treatment efficacy and may result in drug-induced cancer drug resistance—likely the most important reason for chemotherapy failure[3]. In particular, given that only a median ~0.7% of an average administered nanoparticle dose reaches the tumor site[4], nanomedical drug concentrations are likely to remain below the therapeutic window, rendering them ineffective with potential induced tumor drug resistance[5]; this also means the most nanodrug will enter normal tissues, leading to off-target effects and toxicity. Drug release monitoring may provide a solution. Drug release monitoring efforts have tested several imaging modalities: magnetic resonance imaging (MRI) is generally not linearly quantitative and intrinsic/background signal can convolute drug distribution signals[1]; optical imaging and photoacoustic imaging are limited by penetration depth and signal convolution[6]. Magnetic particle imaging (MPI), a novel non-invasive imaging modality employing superparamagnetic nanoparticles (NPs) as contrast agents, offers excellent imaging depth, linearly-quantifiable signal, and real-time imaging capability[7]. Moreover, MPI displays near-infinite contrast and high sensitivity[8]. Based on these merits, MPI has broad potential for quantitative monitoring of drug release *in vivo* at large depths. However, drug release monitoring alone is insufficient to maintain drug concentrations in the therapeutic window because it cannot adjust said dose. Remote-controlled actuation of treatments using NPs in combination with imaging to monitor drug release has the potential to address cancer treatment issues with precision-delivered dosages to the relevant disease sites and not to off-target sites. Importantly, precision-remote drug release monitoring represents a significant opportunity for physicians to better track/control drug doses in a more timely and accurate manner in cancer patients[1], allowing real-time adjustments of already-administered doses by modulating the irradiation time of incident near-infrared (NIR) laser light in order to ensure maintenance of local tumor drug concentrations within the therapeutic window. Our remote-controlled precision medical combination treatment and monitoring consists of a nanocomposite comprising a core of clustered superparamagnetic Fe_3O_4 nanoparticles and Doxorubicin with a poly(lactide-co-glycolide acid) (PLGA) shell (SPNCD) (Fig1a). As PLGA shells degrade, Doxorubicin release and disassembly of clustered Fe_3O_4 nanoparticles in the core occur simultaneously. This yields a linear correlation between the released Doxorubicin and disassembled clustered Fe_3O_4 (R^2=0.98, Fig1b), allowing precise, whole-body image-based quantification of drug release (Fig1c). When the intratumoral drug concentration is lower than MED, we deposit energy precisely to the tumor region bearing nanoparticles using NIR (808nm, 1W) to controllably accelerate nanoparticle degradation, thereby boosting the local drug concentration (e.g., controlled acceleration of drug release up to 40% within 7 mins) to within the therapeutic window and maintain it there using MPI to estimate drug localization/release. Importantly, <2% Doxorubicin released at neutral pH 7.4 serum over 48 h, indicating that SPNCD nanocomposites are stable at neutral extracellular environmental pH and can reduce off-target toxicity of Doxorubicin. Our nanoplatform has great potential for clinical translation as: i) all materials comprising SPNCD are FDA-approved; ii) our imaging approach means dosage regimens may be optimized and personalized to maintain Doxorubicin concentrations within the therapeutic window of each patient by adjusting NIR irradiation time/intensity, both reducing side effects and reliably maintaining sufficient local doses to kill tumor cells (Fig1d).

Reference

1. Zhu, X., Li, J., Peng, P., Hosseini Nassab, N. & Smith, B. R. Quantitative Drug Release Monitoring in Tumors of Living Subjects by Magnetic Particle Imaging Nanocomposite. Nano Lett. 19, 6725–6733 (2019).
2. Mathijssen, R. H. J. et al. Flat-Fixed Dosing Versus Body Surface Area–Based Dosing of Anticancer Drugs in Adults: Does It Make a Difference? Oncologist 12, 913–923 (2007).
3. Scire, J., Hozé, N. & Uecker, H. Aggressive or moderate drug therapy for infectious diseases? Trade-offs between different treatment goals at the individual and population levels. PLoS Computational Biology vol. 15 (2019).
4. Lammers, T. et al. Cancer nanomedicine: Is targeting our target? Nat. Rev. Mater. 1, 1–2 (2016).
5. Wang, X., Zhang, H. & Chen, X. Drug resistance and combating drug resistance in cancer. Cancer Drug Resist. 2, 141–160 (2019).
6. Wang, R., Zhou, L., Wang, W., Li, X. & Zhang, F. In vivo gastrointestinal drug-release monitoring through second near-infrared window fluorescent bioimaging with orally delivered microcarriers. Nat. Commun. 8, (2017).
7. Panagiotopoulos, N. et al. Magnetic particle imaging: Current developments and future directions. Int. J. Nanomedicine 10, 3097–3114 (2015).
8. Zheng, B. et al. Magnetic particle imaging tracks the long-term fate of in vivo neural cell implants with high image contrast. Sci. Rep. 5, 1–9 (2015).

Oral Presentation

Disclosures: The authors have disclosed no financial interest.

125-Magnetic/radiopaque nanoparticles for in vivo MPI/CT tracking of mesenchymal stem cells as delivery vehicle for cancer treatment

Presenter: Chao Wang, Johns Hopkins University

Chao Wang[1], Ali Shakeri-Zadeh[2], Behnaz Ghaemi[3], Jeff Bulte[3]

[1]Johns Hopkins University, Baltimore, MD
[2]Johns Hopkins Univeristy, Baltimore
[3]Johns Hopkins University School of Medicine, Baltimore

Introduction:
Targeting of therapeutic nanoparticles (NPs) toward cancer cells has not been completely successful, and attempts are being undertaken to develop an effective targeting strategy that would ensure uniform distribution of NPs throughout the tumor. The utilization of stem cells with inherent trophic characteristics for homing to tumors has been suggested as a promising technique for NP delivery to cancer cells (1, 2). Monitoring the homing and intratumoral distribution of transplanted cells, as well as off-target site biodistribution in the rest of the body, might be addressable by *in vivo* hybrid imaging. The goal of this study was to develop a bimodal cell tracking approach based on a new superparamagnetic radiopaque nanocomplex that can be detected by magnetic particle imaging (MPI) and computed tomography (CT).

Methods:
Through a step-by-step solvothermal decomposition method, a **BBS** nanocomplex composed of bovine serum albumin (**B**SA), radiopaque $\mathbf{Bi}_2S_3$ nanoparticles and superparamagnetic iron oxide (**S**PIO) was synthesized. BBS nanocomplexes were characterized with different techniques. Human mesenchymal stem cells (hMSCs) were labeled with poly-L-lysine as transfection agent and the BBS nanocomplexes for 24 hours. Naked BBS or BBS-labeled hMSCs were injected intratumorally (i.t.) or intravenously (i.v.) in DU145 (human prostate cancer)-bearing mice. Thirty minutes and 48 hours after injection, mice were imaged with MPI and CT. Two days after i.t. injection or four days after i.v. injection, mice were sacrificed and tumors were excised for *ex vivo* imaging.

Results:
Spherical BBS nanocomplexes (average size: 90 nm) were characterized with even distribution of bismuth, iron and sulfur across the spheres (**Fig. 1A**). In vivo MPI/CT images of mice receiving naked BBS nanocomplexes or BBS-hMSCs after i.t. injection are shown in **Fig. 1B**. I.t. injection of BBS-hMSCs demonstrated that labeled cells moved throughout the entire tumor and kept strong signal intensity over 48 hours, while naked BBS nanocomplexes remaining as a focal point near the injection site with decreasing signal intensity. For i.v. injection, we observed the homing of cells to the lung 2 hours after injection and in the liver 24 hours later (**Fig. 1C**). No obvious signal could be noticed in the tumor for i.v. injection. Ex vivo imaging showed the highest amount of MPI signal intensity was obtained for i.t. injection of BBS-hMSCs (**Fig. 1D**).

Conclusion:
Using CT and MPI, we demonstrated the feasibility and the disparity of in vivo bimodal imaging of naked BBS and BBS-labeled hMSCs. We are now exploring different protocols for MPI/CT-guided hyperthermal treatment employing BBS nanocomplexes delivered by stem cells.

Reference
1. Y. Su, et al. Int. J. Pharm. 2021; 600:120477.
2. X. Wang, et al. Acta Pharm. Sin. B. 2019; 9(1): 167
3. J.W.M. Bulte. Adv. Drug Deliv. Rev. 2019; 138:293.

Oral Presentation

Disclosures: The authors have disclosed no financial interest.

126-Streamlined Production of [18F]OP-801 and Radiation Dosimetry to Enable Clinical Translation for Imaging Neuroinflammation

Presenter: Isaac Jackson, Stanford University

Isaac M. Jackson[1], Mackenzie Carlson[2], Corinne Beinat[2], Mausam Kalita[3], Samantha Reyes[4], Carmen Azevedo[5], Sydney C. Nagy[2], Israt S. Alam[3], Rishi Sharma[6], Santiago Appiani La Rosa[7], Farshad Moradi[2], Jeffrey Cleland[6], Bin Shen[8], Michelle L. James[2]

[1]Stanford University, San Bruno, CA
[2]Stanford University, Stanford, CA
[3]Stanford University, Stanford
[4]Stanford University School of Medicine, Stanford, CA
[5]Washington University in St. Louis, St. Louis, MO
[6]Ashvattha Therapeutics, Redwood City, CA
[7]Ashvattha Therapeutics, Baltimore, MD
[8]Molecular Imaging Program at Stanford (MIPS), Stanford, CA

Objectives:
There is a critical need for tools that enable specific detection and tracking of neuroinflammation in neurodegenerative diseases such as Alzheimer's Disease (AD) and Amyotrophic Lateral Sclerosis (ALS). Unfortunately, existing PET tracers for imaging activated microglia and macrophages, key elements of the innate immune response, are severely limited. A novel dendrimer PET tracer [^{18}F]OP-801, known to be selectively (>95%) taken up by activated macrophages and microglia, has recently been studied in mouse models of sepsis and AD and was demonstrated to be sensitive for imaging early stage neuroinflammation[1]. Motivated by this promising preclinical data, we endeavored to optimize the radiosynthesis of [^{18}F]OP-801 and complete radiation dosimetry studies in anticipation of clinical translation. Here we describe the automated, high-yield radiosynthesis and quality control (QC) analyses of [^{18}F]OP-801 for routine clinical production, in addition to analysis of its stability in human plasma, and human dosimetry estimates.

Methods:
[^{18}F]OP-801 was synthesized in two steps using a FX-FN synthesis module (General Electric) with adjacent customized module. In brief, [^{18}F]fluoride and 3-azidopropyl-4-methylbenzenesulfonate in acetonitrile were reacted to yield [^{18}F]3-fluoropropylazide, which was subsequently purified via HPLC and transferred to a second reactor containing alkyne-functionalized dendrimer precursor for copper catalyzed click chemistry. The reaction mixture was purified via HPLC and reformulated to furnish pure [^{18}F]OP-801 in saline/EtOH (10 mL/1 mL). This optimized synthetic route was used to perform three validation runs followed by complete QC analysis to confirm identity, stability, and purity in compliance with USP283 for submission as part of a Drug Master File (DMF) application to support a human clinical trial. Aliquots of 15 mCi of [^{18}F]OP-801 in 70 mL human plasma

were incubated at 37 °C and stability assessed via HPLC at 0, 5, 15, 30, 60, and 90 minutes. Radiation-absorbed dose for a human subject was calculated via image-based dosimetry in male (n=4) and female (n=5) C57BL/6 mice. 60-minute dynamic PET scans were performed, and images reconstructed via OSEM3D/MAP. %ID/g values were converted to %ID/organ and underwent an animal-to-human biokinetic extrapolation using the percent kg/g method[2]. Final projected human doses were calculated with OLINDA.

Results:

Prior to optimization and dosimetry, a single intravenous GLP dose toxicology study was conducted in rats and a greater than 500-fold safety factor for [^{19}F]OP-801 was determined for the proposed maximum human mass dose (100 µg). [^{18}F]OP-801 was reproducibly synthesized in suitable yield (76.36 mCi, 6.89% decay-corrected at end of beam, n=3) and radiochemical purity (>99%) (**Fig 1A**). QC analysis, including radiochemical identity and purity, residual solvent analysis, pH, and stability in formulation at 0 and 4 hours after end of synthesis, confirmed that [^{18}F]OP-801 is suitable for injection and human use. [^{18}F]OP-801 was found to be stable *in vitro* in human plasma, with >99% tracer intact after 90 minutes (**Fig 1B**). Dosimetry calculations provided human dose estimates for 24 organs of interest and identified kidneys (0.117 rem/mCi in females, 0.167 rem/mCi in males) and urinary bladder wall without bladder voiding (0.198 rem/mCi in females, 0.033 rem/mCi in males) as dose limiting (**supplemental fig**). Clinical imaging of [^{18}F]OP-801 will include bladder voiding, making kidneys the dose limiting organ in humans.

Conclusion:

Here, we describe a high-yielding, automated synthesis of [^{18}F]OP-801 that is amenable to regular implementation for *in vivo* imaging studies. *In vitro* stability in formulation and plasma, as well as human dosimetry estimates based on mouse imaging models, are conducive to translation and clinical imaging of [^{18}F]OP-801. Based on these data, validation runs for clinical dose manufacturing were completed and submitted as part of a DMF application, with the goal of conducting clinical imaging with [^{18}F]OP-801 in healthy humans and ALS patients in 2022.

Reference

1. Alnasser et al. Molecules, 2018. 23(5): 1025.
2. Kirschner et al. J Nucl Med,1975. 16(3):248–249.

Oral Presentation

Disclosures: The authors would like to disclose that [18F]OP-801 with Ashvattha Therapeutics And Ivuxolimab are investigational drugs/devices.

127-Development of [18F]DASA-10 for Enhanced Imaging and Detection of Pyruvate Kinase M2 Expression in Glioblastoma

Presenter: Christopher Acosta, Stanford University

Christopher J. Acosta[1], Michelle L. James[2], Carmen Azevedo[3], Lawrence Recht[1], Mustafa Tansel Kendirli[4], Corinne Beinat[2]

[1]*Stanford University*
[2]*Stanford University, Stanford, CA*
[3]*Washington University in St. Louis, St. Louis, MO*
[4]*Stanford University, PALO ALTO, CA*

Cancer's atypical metabolism is an imperative part of its ability to ensure the rapid growth and survival of cancer cells. Pyruvate kinase catalyzes the last and physiologically irreversible step in glycolysis, converting phosphoenolpyruvate to pyruvate. The ubiquitous expression of the pyruvate kinase M2 (PKM2) isoform in cancer, a key step in tumor metabolism and growth, makes it a promising target for molecular imaging. Recently we reported the development and translation of a novel positron emission tomography (PET) tracer ([18F]DASA-23) for visualizing PKM2 in living subjects. While the successful imaging of PKM2 in patients with [18F]DASA-23 is promising and highlights the importance of imaging PKM2, we observed several limitations with [18F]DASA-23. Most notably, high non-specific binding in normal brain and high radiation dose to the gallbladder wall. We hypothesized that the reduced lipophilicity and improved PKM2 functional activity of [18F]DASA-10 would lead to a more effective strategy for imaging of PKM2, while still retaining the favorable specificity of DASA-based molecules. Due to the limitations of [18F]DASA-23, we set out to develop an enhanced F-18 labeled version of this tracer, [18F]DASA-10, with the goal of improved physicochemical properties and detection of PKM2 in mind. Herein, we report the radiosynthesis of 1-((2,3-dihydrobenzo[b][1,4]dioxin-6-yl)sulfonyl)-4-((2-fluoro-6-(fluoro18F)phenyl)sulfonyl)piperazine ([18F]DASA-10) and our initial radiotracer validation studies. We synthesized [18F]DASA-10 via fluorination of the corresponding nitro-containing precursor with K[18F]F/K2.2.2.) (Fig. 1A). [18F]DASA-10 was prepared in 5.61 ± 1.8% radiochemical yield (n = 5, non-decay corrected at end of synthesis) with molar activity >5 Ci/µmol and radiochemical purity greater than 98%. Cellular uptake studies showed significantly increased cellular uptake of [18F]DASA-10 relative to [18F]DASA-23 in U87 and GL26 glioma cells at both 30- and 60-min post addition of tracer (Fig. 1B). Removal of tracer from cell media resulted in significant differences in tracer efflux of [18F]DASA-10 relative to [18F]DASA-23, with increased retention of [18F]DASA-10 in both U87 and GL26 glioma cells in dedicated efflux studies (Fig. 1C). To determine specificity of [18F]DASA-10 for PKM2, we transiently modulated PKM2 expression in DU145 cells using PKM2-siRNA, employing conditions previously studied with [18F]DASA-23. Gratifyingly, we detected a 72.70% reduction of cellular uptake in cells lacking PKM2 and reduced non-specific binding compared to our prior work with [`18F]DASA-23. Given the favorable results of [18F]DASA-10 and specificity in cellular work, we next moved to in vivo studies. Healthy nude mice were imaged to determine brain penetrance and biodistribution of [18F]DASA-10 using micro PET/CT (Fig. 1D). We completed 60-min dynamic imaging immediately following intravenous administration of 100 µCi [18F]DASA-10 and observed it passively crossed the blood brain barrier (BBB) and then rapidly cleared the healthy brain (Fig. 1E). We detected significantly lower levels remaining in the brain at the 30- and 60-min time points relative to [18F]DASA-23 (Fig. 1F). We observed predominantly hepatobiliary clearance of [18F]DASA-10 and some renal clearance. Importantly, a significant reduction in [18F]DASA-10 gallbladder uptake relative to [18F]DASA-23 (12.3 ± 6.1%ID/g vs 88.4 ± 11.8 %ID/g at 60 minutes post injection of tracer, p=0.0006) was observed. Lastly, we characterized the in vivo radiometabolite profile of [18F]DASA-10 at 30-min post administration of radiotracer. We tested the radiometabolite profile in key tissues including brain, plasma, and liver. We observed [18F]DASA-10 remained largely intact in brain tissue (72.4 ± 15.5% intact), while it underwent degradation in plasma after 30-min in circulation (34.1 ± 9.6% intact) and substantial degradation in liver (4.5 ±0.6% intact). In conclusion, [18F]DASA-10 demonstrated improved physiochemical properties, greater specificity in cell culture for measuring PKM2, and favorable biodistribution in mice. Ongoing studies are comparing the ability of [18F]DASA-10 and [18F]DASA-23 to visualize tumor associated PKM2 in preclinical models of GBM.

Oral Presentation

Disclosures: The authors have disclosed no financial interest.

128-Whole-brain imaging of tumor-brain interactions using acoustic reporter genes and fUSI

Presenter: Claire Rabut, California Institute of Technology (Caltech)

Claire Rabut[1], Shirin Shivaei[1], Mikhail G. Shapiro[1]

[1]California Institute of Technology (Caltech), Pasadena, CA

Motivation

Brain tumor patients often experience impacted neural function. However, the complex interplay between brain tumor progression and aberrant neural activity remains poorly understood. Existing fluorescent labelling modalities distinguishing tumor from healthy tissue in the brain fail to provide in vivo in-depth information. Magnetic resonance reporter genes can non-invasively enable tumor imaging. However, the difficulty of studying behaving mammals inside MRI scanners restricts the monitoring of tumor-related perturbed circuit dynamics. In contrast, ultrasound readily permeates the brain, interacts with tissue with a fundamental resolution on the order of 100µm and 1ms, and enables scans in awake and behaving subjects. Based on power doppler imaging, functional ultrasound imaging (fUSi) is a recently developed neurovascular imaging technology [1] that provides a highly sensitive method to image dynamic deep brain neural activity. Furthermore, recent breakthroughs in molecular engineering showed the feasibility to connect ultrasound to cells at the genetic level for biomolecular acoustic imaging of gene expression [2]. In this study, we leverage these emerging new capabilities of ultrasound to study the biology of brain tumors by simultaneously imaging tumor gene expression, vascular perfusion and neural activity.

Methods

To localize brain tumor in the whole-brain with high sensitivity, we engineered a glioblastoma cell line with genetically integrated acoustic reporter genes. The acoustic contrast is obtained through the expression of gas vesicles (GVs). GVs are a unique class of genetically encoded air-filled protein nanostructures derived from buoyant bacteria, which can scatter sound waves in the nonlinear regime, and thereby produce ultrasound contrast distinguishable from the linear scattering of tissue [3]. Using lentiviral transduction, we created a stable U87 cell line (human glioblastoma [4]) expressing GVs under a Tet-inducible promoter (**Fig.a**).

To demonstrate the ability of GVs to report gene expression in vivo, we stereotaxically implanted GVs-transfected-U87 cells in the right ventral thalamic nucleus of 8-weeks-old immunodeficient mice (N=6). Nonlinear ultrasound scans were performed on days 8, 12 and 16 (transgene expression was induced by intraperitoneal injections of doxycycline before each session), while simultaneously recording fUSi functional response to visual stimuli. Baseline ultrasound scans were also performed before tumor implantation. All acquisitions were performed transcranially and non-invasively in anesthetized mice.

Results

GVs-expressing-tumor was readily distinguishable from healthy brain tissue in ultrasound images acquired on day 8 after implantation, and the tumor growth was monitored over multiple days (day 12, day 16). Functional ultrasound acquisitions enabled simultaneous mapping of the cerebral vascular network, and of functional visual regions (**Fig.b**). Both right and left lateral geniculate nuclei (LGN) were localized following visual-evoked activation before the tumor implantation (day-1), and on day 8 after implantation. As the tumor grew (day 12, day 16), the right LGN disappeared from the imaging plane.

Finally, the spatial distribution of gene expression was evaluated via fluorescence imaging of histological sections of the brain (**Fig. c**) and confirmed the borders of tumor located with ultrasound.

Conclusion

Our results establish gas vesicles as the first genetically encoded acoustic reporter for brain tumor. GVs-dependent contrast of implanted brain tumor was readily observed non-invasively in mice and enabled the monitoring of tumor growth over the course of multiple days. Simultaneous hemodynamic functional recording showed a displacement of visual-evoked regions in the tumor-based hemisphere suggesting a reorganization of the functional atlas during disease progression. Further work in three dimensions [5] and in awake behaving animals [6] would enable a complete understanding of the functional reorganization of the brain during disease progression. Finally, studying more invading tumor models would allow a better modelling of wild-type brain tumors in human.

Reference

1. Deffieux, T., Demene, C., Pernot, M. & Tanter, M. Functional ultrasound neuroimaging: a review of the preclinical and clinical state of the art. Current Opinion in Neurobiology 50, 128–135 (2018).
2. Farhadi, A., Ho, G. H., Sawyer, D. P., Bourdeau, R. W. & Shapiro, M. G. Ultrasound imaging of gene expression in mammalian cells. Science 365, 1469–1475 (2019).
3. Shapiro, M. G. et al. Biogenic gas nanostructures as ultrasonic molecular reporters. Nature Nanotech 9, 311–316 (2014).
4. Clark, M. J. et al. U87MG Decoded: The Genomic Sequence of a Cytogenetically Aberrant Human Cancer Cell Line. PLoS Genet 6, e1000832 (2010)
5. Rabut, C. et al. 4D functional ultrasound imaging of whole-brain activity in rodents. Nat Methods 16, 994–997 (2019).
6. Urban, A. et al. Real-time imaging of brain activity in freely moving rats using functional ultrasound. Nat Methods 12, 873–878 (2015).

Oral Presentation

Disclosures: The authors have disclosed no financial interest.

129-Longitudinal monitoring of synaptic health following a stroke using [18F]-SynVesT-1 PET and chemical exchange saturation transfer MRI

Presenter: Qi Qi, Western University

Qi Qi[1], Matthew S. Fox[2], Ruo Yan Chen[3], Patrick Lim[2], Justin W. Hicks[4], Austyn Roseborough[5], Lynn Wang[3], Shawn N. Whitehead[5], Jonathan D. Thiessen[6]

[1]Western University, London
[2]Lawson Health Research Institute, London, Ontario
[3]Western University, London, Ontario
[4]Lawson Health Research Institute, London, ON
[5]Schulich School of Medicine and Dentistry, London, Ontario
[6]Lawson Health Research Institute, London

Introduction:

Synapses are critical signal transmission microstructures within the nervous system. Following a stroke, synaptic degeneration is expected

to correspond to cognitive decline **[1]**. A novel position emission tomography (PET) radiotracer, [^{18}F]-SynVesT-1, targeting synaptic vesicle glycoprotein 2A (SV2A) could help in tracking the progression of synaptic loss and recovery after stroke **[2]**. Chemical exchange saturation transfer (CEST) MRI is sensitive to endogenous metabolites that provide complementary information about synaptic deficits within the surrounding microenvironment after stroke, including glutamate with GluCEST **[3]**, amide proton transfer (APT) **[4]** and the intracellular pH (pH_i) environment with amine and amide concentration independent detection (AACID) CEST **[5]**. This study aimed to monitor the effect of stroke on synaptic density and the synaptic microenvironment using both PET and CEST MRI.

Methods:
T_2-weighted and CEST MRI was acquired in healthy wild-type Fischer 334 rats (N=6) using a 9.4 T Bruker MRI. GluCEST was calculated using the magnetization transfer ratio asymmetry (MTR_{assym}) at 3.5 ppm. Amide CEST signal was calculated using APT CEST and pH_i environment was evaluated using AACID CEST. PET (Siemens Inveon) was performed the following day. A 60-minute dynamic PET acquisition was started immediately prior to a bolus injection of 30 MBq [^{18}F]-SynVesT-1. The last 15 minutes of PET data was normalized by the mean activity from the cerebellum to compute standardized uptake value ratio (SUVR). After the baseline imaging experiment, endothelin-1 (600 pmol/3 µl saline) was injected into the right dorsal striatum (RDS) of each rat to induce stroke. The same series of imaging experiments (MR + PET) was repeated 7 and 30 days after surgery. PET and CEST images were manually registered to the T_2-weighted MRI using 3D Slicer. RDS, left dorsal striatum (LDS), right cerebral cortex (RCX) and left cerebral cortex (LCX) were delineated using T_2-weighted MRI (delineated by the red, white, blue and pink dotted lines respectively in Figure 1).

Results (Figure 2):
After surgery, hyperintense T_2-weighted signal spanned the RDS and RCX. SUVR in the RDS at Day 7 and 30 were significantly lower than baseline ($P = 0.042$ and 0.001 respectively). SUVR in the LDS was higher than RDS 30 days ($P = 0.001$) after the surgery. GluCEST MTR_{assym} measured in the RCX on Day 7 was significantly higher than baseline and Day 30 ($P < 0.001$); it was also significantly higher than LCX ($P < 0.001$). GluCEST MTR_{assym} in the RDS was higher than in the LDS on Day 30 ($P < 0.001$). LDS APT signal was significantly higher than RDS on Day 7 and 30 ($P = 0.018$ and 0.032 respectively); APT signal in the LCX was also significantly higher than RCX on Day 7 and 30 ($P = 0.012$ and 0.018 respectively). RDS pH_i decreased from baseline to Day 7 and increased on Day 30. LDS pH_i was higher than RDS on Day 7 and 30 ($P < 0.001$ and $= 0.038$ respectively); LCX pH_i was significantly higher than RCX ($P = 0.012$).

Discussion:
This study demonstrated the highly complementary nature of combined PET and CEST-MRI measurements of both synaptic density and the synaptic microenvironment following a stroke. In ischemic brain injury, excess glutamate is released, often leading to a vicious cycle of glutamate excitotoxicity and neuronal death. Our results reflect the expected time course in the stroke region, with elevated glutamate, decreased pH, and decreased synaptic density in the acute phase (Day 7) and some recovery by the chronic phase (Day 30). Similarly, increased SUVR, APT, and pH in the contralateral region of the brain could reflect compensatory effects. These *in vivo* results will be compared to immunostaining for synaptic proteins, activated microglia, and reactive astrocytes.

Reference

1. Murphy TH and Corbett D, Plasticity during stroke recovery: from synapse to behaviour. Nat Rev. 2009; 10:861-872.
2. Sadasivam P, Fang XT, Toyonaga T, et al., Quantification of SV2A binding in rodent brain using [18F]-SynVesT-1 and PET imaging. Mol Imaging and Biol. 2020; 23: 372-381.
3. Chen YZ, Dai ZZ, Shen ZW, et al., Magnetic resonance imaging of glutamate in neuroinflammation. Radiol Infect Dis. 2016; 3(2): 92-97.
4. Zhou J, Heo HY, Knutsson L, et al., APT-weighted MRI: techniques, current neuro applications, and challenging issues. J Magn Reson Imaging 2020; 50(2): 347-364.
5. McVicar N, Li AX, Gonçalves DF, et al., Quantitative Tissue pH Measurement during Cerebral Ischemia using Amine and Amide concentration-independent Detection (AACID) with MRI. NMR Biomed. 2015; 28:566 –575.

Oral Presentation

Disclosures: The authors have disclosed no financial interest.

130-D2/D3 receptor trafficking is implicated by [11C]raclopride PET of Beta-arrestin knock-out mice

Presenter: Joseph Mandeville, Athinoula A. Martinos Center for Biomedical Imaging

Yinching I. Chen[1], Jonah Weigand-Whittier[2], **Joseph B. Mandeville[3]**

[1]Athinoula A. Martinos Center for Biomedical Imaging, Charlestown
[2]Massachusetts General Hospital
[3]Athinoula A. Martinos Center for Biomedical Imaging, Cambridge, MA

Background:
PET measurements infer receptor occupancy through changes in binding potential (BP_{ND} when using reference region models) associated with a drug or task. Because BP_{ND} depends upon both receptor availability and ligand-receptor affinity, agonist-induced receptor desensitization and internalization can shift radioligand affinities and confound interpretation of results within a classical occupancy model [1, 2]; in fact, many PET radiotracers are not sensitive to even large doses of exogenous agonists. Beta-arrestin knock-mice (KO) do not readily internalize receptors, and one prior PET study used these mice to demonstrate less prolonged depression of ^{11}C-MNPA and [18F] Fallypride BP_{ND} following amphetamine stimulation [3]. We employed mouse PET/MR and the most commonly used dopaminergic radiotracer, [11C]raclopride, to test the hypothesis that BP_{ND} would show prolonged displacement in KO mice and that the change in BP_{ND} due to a second amphetamine challenge could also provide an index of receptor trafficking in vivo.

Methods:
PET/MR scans were performed in 48 mice using a Bruker 4.7T BioSpec MRI scanner with a Bruker PET insert. Wild-type (WT) and Beta-arrestin KO mice were compared using simultaneous multi-mouse (n=6 per study) following injection of [11C]raclopride. A within-scan challenge design was employed (n=33 of 48 mice, double tail vein catheters) to determine changes in binding potential (ΔBP_{ND}) due to IV amphetamine injection (1 mg/kg) in mice that were either naïve to amphetamine or had been treated IP with 3.3 mg/kg at 2.5 hours prior to the second amphetamine challenge (Fig 1a). Colocalized MRI and PET data were extracted from the multi-mouse field-of-view, aligned to the Allen Mouse Brain space using a multi-subject MRI template [4], corrected for partial volume effects using the geometric transfer

matrix approach [5], and analyzed by the two-parameter multi-linear reference model with striatum and cerebellum as the target and reference regions, respectively. Group data for either BP_{ND} or ΔBP_{ND} were analyzed by a random-effects general linear model including regressors for average, genotype, pretreatment, and the interaction of genotype and pretreatment.

Results:

Figure 1 shows a map of BP_{ND} in space (b) and derivation of BP_{ND} and ΔBP_{ND} in the time domain (c). Baseline BP_{ND} was smaller for KO mice than WT mice, while BP_{ND} was larger in KO than WT mice at 2.5 hours after AMP pretreatment (Fig 1d, e); the same relative orders were observed for the AMP-induced change ΔBP_{ND} (Fig 1d,e). Relative to average values of BP_{ND} and ΔBP_{ND} in the naïve state, KO animals exhibited larger recovery at 2.5 hours in BP_{ND} and in the response to a second AMP challenge (Fig. 1f). Both BP_{ND} and ΔBP_{ND} showed highly significant changes associated with amphetamine treatment ($p<<0.001$). Groups were differentiated by genotype (BP_{ND}, $p<0.01$; ΔBP_{ND}, $p<0.05$). Most informatively, groups were differentiated by the interaction of pretreatment and genotype ($p<0.05$ for BP_{ND}, ΔBP_{ND}), showing that WT and KO animals responded differently to amphetamine pretreatment.

Discussion:

An insensitive or paradoxical response to receptor agonists (neurotransmitters or exogenous drugs) has confounded PET occupancy studies for many radiotracers and receptor systems. Here, we employed a fast and well characterized D2/D3-receptor radiotracer to show two phenomena consistent with dopamine-induced affinity shifts: a prolonged reduction in BP_{ND} and a decreased response to a second dopamine challenge. The change ΔBP_{ND} to a second challenge showed a larger relative effect size than BP_{ND} but had slightly less discriminating power due to larger variance. These results implicate receptor desensization and internalization as prospective confounds for the interpretation of functional changes in BP_{ND} in the context of a classical occupancy model, and the methods are readily extensible to other radiotracers and receptor systems.

Reference

1. Laruelle M. Imaging synaptic neurotransmission with in vivo binding competition techniques: a critical review. J Cereb Blood Flow Metab 2000; 20: 423-451.
2. Sander CY, Hooker JM, Catana C, et al. Imaging Agonist-Induced D2/D3 Receptor Desensitization and Internalization In Vivo with PET/fMRI. Neuropsychopharmacology 2016; 41: 1427-1436. DOI: 10.1038/npp.2015.296.
3. Skinbjerg M, Liow JS, Seneca N, et al. D2 dopamine receptor internalization prolongs the decrease of radioligand binding after amphetamine: a PET study in a receptor internalization-deficient mouse model. Neuroimage 2010; 50: 1402-1407.
4. Ma D, Cardoso MJ, Modat M, et al. Automatic structural parcellation of mouse brain MRI using multi-atlas label fusion. PLoS One 2014; 9: e86576. 2014/01/30. DOI: 10.1371/journal.pone.0086576.
5. Erlandsson K, Buvat I, Pretorius PH, et al. A review of partial volume correction techniques for emission tomography and their applications in neurology, cardiology and oncology. Phys Med Biol 2012; 57: R119-159. 2012/10/18. DOI: 10.1088/0031-9155/57/21/R119.

Oral Presentation

Disclosures: The authors have disclosed no financial interest.

131-Optimization of an Allysine-Targeted PET Probe for the Measurement of Fibrogenesis in a Mouse Model of Pulmonary Fibrosis

Presenter: Nicholas Rotile, Massachusetts General Hospital

Nicholas Rotile[1], Peter Caravan[2], Yingying Ning[3], Sergey Shuvaev[4], Hua Ma[5], Matthew Drummond[6], Rachel Knipe[6]

[1]*Massachusetts General Hospital*
[2]*Harvard Medical School, Charlestown, MA*
[3]*Harvard Medical School, Boston*
[4]*Athinoula A. Martinos Center for Biomedical Imaging, Charlestown, MA*
[5]*Harvard Medical School, Somerville*
[6]*Massachusetts General Hospital, Boston, MA*

Introduction:

Idiopathic Pulmonary Fibrosis (IPF) is a destructive lung disease which results in thickening of the lung interstitium, abolition of alveolar spaces and eventual respiratory failure.[1] It is accompanied by upregulation of lysyl oxidase (LOX) enzymes which catalyze oxidation of lysine e-amino groups on extracellular matrix proteins to form the aldehyde containing amino acid allysine. An aminooxy-indole derived PET probe was shown to bind allysine in vivo and robustly staged and quantified pulmonary fibrogenesis in a mouse model.[2] However, limitations of that probe included very high reactivity/instability and high hepatobiliary elimination which makes PET imaging of the lower lung challenging. Herein, we report a systematic study to optimize allysine-targeted PET probes for imaging pulmonary fibrogenesis.

Methods:

8 novel allysine-binding chelators, **PIF-1-8** were devised and synthesized (Fig 1A). Radiolabeling procedures using $^{68}GaCl_3$ and $^{64}CuCl_2$ were developed and optimized. The performance of these radiotracers was validated in naïve and fibrotic C57BL/6J male mice 14 days after intratracheal bleomycin instillation. PET/MR studies at 4.7T were performed to compare their pharmacokinetics and specificity in detecting pulmonary fibrogenesis. Tissues were harvested 90 min post injection for ex vivo analysis including gamma counting and biochemical analysis of lungs to quantify allysine and collagen content by hydroxyproline assay.

Results and discussions:

In vivo comparison of different probes were based on their uptake in the lung of bleomycin injured mice as compared to liver (Fig 1B) and heart (Fig 1C). Results showed that **^{68}Ga-PIF3** and **^{68}Ga-PIF7** showed much higher sensitivity than the other probes in detecting pulmonary fibrogenesis with rapid renal clearance and low liver uptake. In comparison, there was negligible uptake in the lungs of naïve mice (Fig 1D). To account for model heterogeneity, a cross-over PET/MR comparison of **^{68}Ga-PIF3** and **^{68}Ga-PIF7** showed that **^{68}Ga-PIF7** has consistent higher uptake in fibrotic lungs (Fig 1E). A pair-wise comparison between **^{68}Ga-PIF7** and an aldehyde unreactive control compound **^{68}Ga-PIFCtrl** confirmed the specificity of the probe to fibrotic tissue (Fig 1F-G). Moreover, substituting ^{64}Cu for ^{68}Ga did not affect the uptake of the **PIF-7** probe in fibrotic lungs (Fig 1H-I), indicating the robust PET signal of the probe in detecting pulmonary fibrogenesis. As **^{68}Ga-PIF-7** has a α-carboxylate moiety near the hydrazine moiety, these results demonstrated the benefit of acid catalysis to promote the condensation reaction with allysine in vivo. Ex vivo analysis of the lung showed elevated lung allysine and hydroxyproline levels in bleomycin injured mice over naïve mice, indicating the presence of pulmonary fibrogenesis/fibrosis after bleomycin injury. The uptake of **^{68}Ga-PIF7** in lung correlated well with the allysine concentration

in bleomycin injured animals (Fig 1J) and gave **^{68}Ga-PIF7** as the most promising candidate probe for clinical translation.

Conclusion:
A series of allysine-binding PET tracers with variations in the aldehyde reactive moiety were evaluated in a preclinical model of lung fibrosis. The hydrazine-bearing tracer with a α-carboxylate moiety **^{68}Ga-PIF7** exhibited consistent higher uptake in fibrotic lungs than other probes which correlated well with the expression of the biomarker of the disease activity (allysine). The probe showed high uptake in bleomycin injured lung, but low signal in normal lung, liver and blood pool, suggesting it will be effective for delineating disease activity in the lower lung where fibrosis is more prevalent in IPF.

Reference

1. C. Kuhn, J. Boldt, T. E. King, E. Crouch, T. Vartio and J. A. McDonald, Am. Rev. Respir. Dis., 1989, 140, 1693–1703;
2. J. Wahsner, P. Desogere, E. Abston, K. A. Graham-O'Regan, J. Wang, N. J. Rotile, M. D. Schirmer, D. D. Santos Ferreira, J. Sui, B. C. Fuchs, M. Lanuti and P. Caravan, J Am Chem Soc 2019, 141, 5593-5596.

Oral Presentation

Disclosures: The authors have disclosed no financial interest.

132-Detecting in vivo cell-cell communication using an inducible antigen-dependent synthetic blood biomarker

Presenter: YangHao Fu,Robarts Research Institute

YangHao Fu[1], TianDuo Wang[2], John Ronald[1]

[1]Robarts Research Institute, London, ON
[2]Robarts Research Institute, London

Introduction:
The field of cellular immunotherapy has made major improvements to cancer treatment over recent years. For instance, chimeric antigen receptor (CAR) T-cell therapy has been proven to be the paradigm for engineered T-cell therapies due to its efficacy in treating blood-based cancers such as leukemia and lymphoma.[1] Although the state-of-the-art CAR T-cell therapies have shown high success in most patients, it is difficult to understand why they have minimal effect in others. Clinically, blood tests are often used to monitor immunotherapies to detect circulating immune cells, which doesn't accurately capture treatment efficacy. This study aims to build a new activatable system that secretes a unique blood biomarker when engineered therapeutic immune cells interact with target cancer cells within tumors. The synthetic notch (SynNotch) receptor is one of the most mechanistically versatile systems that signal cell-cell contact via transcriptional modulation of desired genes in response to SynNotch receptor-antigen binding (Fig. 1A).[2] Our approach is to engineer immune cells with a SynNotch receptor that, upon cancer antigen binding, activates the expression of secreted embryonic alkaline phosphatase (SEAP) – a safe and sensitive human-derived blood-based reporter.[3] Our goal is to engineer immune cells with a SynNotch system that will activate the expression of SEAP upon cancer binding, allowing for blood-based detection of *in vivo* cell-cell communication.

Methods:
We engineered Jurkat cells, a human T cell line, via sequential lentiviral transduction of two components: (1) a SynNotch receptor directed against the B cell leukemia antigen CD19, and (2) a reporter response element encoding SEAP. The B-cell surface antigen CD19 was chosen as it is the most successful target of CAR-T immunotherapy in humans currently.[4] Successfully dual-engineered T cells were isolated using fluorescence-activated cell sorting and expanded. To validate this activatable system *in vitro*, 10^5 T cells were co-cultured in well plates with $CD19^+$ Nalm6 B-cell leukemia cells at a 1:1 ratio. As a negative control, we used CRISPR-knockout to generate $CD19^-$ Nalm6 cells. In media, SEAP concentration was assessed every 24 hours for 4 days using the Great EscAPe SEAP Chemiluminescence Assay kit 2.0. Translating this system *in vivo*, Nod-scid-gamma (NSG) mice were implanted with either $CD19^+$ or $CD19^-$ Nalm6 cells subcutaneously. Once tumours reached ~100mm^3, mice received an intratumoural injection of engineered Jurkat cells ($1x10^7$), and blood samples were taken from the left flank for SEAP assays.

Results:
Co-culturing of dual-engineered T cells with $CD19^+$ Nalm6 cells resulted in significantly higher SEAP activity on all days, only day 2 is shown here ($p < 0.001$, Fig. 1B). In contrast, reporter expression was minimal when T cells engineered with the reporter gene only or naïve T cells when co-cultured with $CD19^+$ cells. Co-culturing with $CD19^-$ cells resulted in no detectable SEAP levels above the background. No SEAP activity was also observed prior to engineered cell injection in tumor-bearing mice (Fig. 1C). Importantly, significantly elevated SEAP activity was observed post-T cell injection in mice bearing $CD19^+$ tumors, but not $CD19^-$ tumors.

Discussion:
We have established a synthetic biology reporter system that is activated upon antigen binding, which allows for the detection of immune cell interactions with cancer cells through a simple and convenient blood test. Future work includes transferring this system into primary T-cells as well as expanding the potential target antigen. The development of this system would allow for a specific monitoring tool for many cell-based cancer immunotherapies, ultimately improving our understanding of those treatment dynamics as well as the presence of side effects in individual patients.

Reference

1. June et al., Science, 2018, 359(6382):1361-1365.
2. Maude et al., NEJM, 2014, 371: 1507-1517.
3. Berger et al., Gene, 1988, 66(1):1-10.
4. Sadelain et al., J Clin Invest, 2015, 125(9): 3392-3400.

Oral Presentation

Disclosures: The authors have disclosed no financial interest.

133-A new time-domain camera system for video-rate near-infrared fluorescence imaging

Presenter: Hans Ingelberts, Vrije Universiteit Brussel

Hans Ingelberts[1], Sophie Hernot[2], Thomas van den Dries[2], Thomas Lapauw[2], Maarten Kuijk[2]

[1]Vrije Universiteit Brussel, Elsene, Belgium
[2]Vrije Universiteit Brussel, Brussels, Brussels, Belgium

Introduction:
Near-infrared (NIR) fluorescence has emerged as a safe tool in various stages of research and clinical translation for applications such as tumor imaging. To suppress unwanted light or to image multiple dyes simultaneously, conventional *spectral* systems rely on optical filters and multiple light sources and cameras [1]. Fluorescence, however, also exhibits a specific time-domain behavior, the fluorescence lifetime, which can be used as additional contrast [2]. A new time-domain fluorescence camera system is demonstrated which can image fluorescence lifetime at video-rate acquisition times.

Methods:
The imaging system is built around the *tau*CAM, a novel fast-gated camera, housing a custom 64x64-pixel CAPS fast-gated CMOS image sensor with a quantum efficiency (QE) of 60% at 700 nm [3]. This sensor can image the time-behavior of fluorescence by synchronizing to a pulsed excitation source and capturing light in nanosecond gate-windows that can be controlled with picosecond precision. The system is optimized for the 800 nm NIR fluorescence channel employing a 775 nm LASER emitting 35-ps pulses at 40 MHz with an average power up to 1 watt and detection through a 70 nm optical bandpass filter around 835 nm. The imaging system is compact and can image a field-of-view of 10x10 cm at a working distance of 30 cm. The capabilities of the system are demonstrated using commercially available fluorescence imaging standardization phantoms which contain ICG-equivalent fluorescence in different concentrations and at different depths with tissue mimicking optical properties. Additionally, custom made phantoms have been constructed to demonstrate the fluorescence-lifetime capability. These phantoms contain different NIR dyes (ICG, IRDye 800CW, s775z) in gelatin and epoxy and can be imaged at the same wavelength but are discernable by their fluorescence-lifetime contrast. Finally, this fluorescence-lifetime contrast is demonstrated in video, imaging phantoms that structurally mimic a tumor and blood vessels to demonstrate the potential for fluorescence-guided surgery. For video-rate imaging fluorescence-lifetime images are calculated from *tau*CAM time-gated images by a novel calibrated rapid-lifetime determination (CRLD) method. To validate the CRLD images, fluorescence-lifetime images are also calculated using a conventional non-linear fitting approach.
The sensitivity of the imaging system is compared to a commercially available conventional NIR fluorescence imaging system (Fluoptics Fluobeam) and the accuracy of the fluorescence-lifetime measurements is verified with a time-correlated photon counting fluorescence-lifetime spectrometer (Edinburgh Instruments Mini Tau).

Results/Discussion:
It is demonstrated that the imaging system has a NIR fluorescence sensitivity down to nano molar concentrations, on par with conventional fluorescence imaging systems [4] but adding fluorescence-lifetime imaging capabilities. Accurate fluorescence lifetimes can be measured with a precision down to less than 20 ps and it is shown that this capability can be used to discern different NIR dyes at different concentrations based on their specific fluorescence lifetimes. In the gelatin phantom, the fluorescence lifetimes of the NIR dyes are similar to the sub-nanosecond lifetimes which are typically observed in vivo. These small but distinct lifetime differences are sufficient to provide clear contrast between the tumor and blood vessel mimicking phantoms at 15 frames per second.

Conclusion:
The *tau*CAM-based NIR fluorescence imaging system can image fluorescence and fluorescence lifetime with a high NIR QE efficiency bringing the advantages of fluorescence-lifetime imaging towards in vivo applications on moving subjects. These capabilities have been demonstrated on phantoms, but in vivo experiments are being planned in which the fluorescence-lifetime contrast will be used to increase tumor-to-background contrast or simultaneous imaging of two NIR nanobody contrast agents.

Reference

1. DSouza AV, Lin H, Henderson ER, Samkoe KS, Pogue BW. Review of fluorescence guided surgery systems: identification of key performance capabilities beyond indocyanine green imaging. J Biomed Opt. 2016 Aug 1;21(8):80901. doi: 10.1117/1.JBO.21.8.080901. PMID: 27533438; PMCID: PMC4985715.
2. Kumar AT, Carp SA, Yang J, Ross A, Medarova Z, Ran C. Fluorescence lifetime-based contrast enhancement of indocyanine green-labeled tumors. J Biomed Opt. 2017 Apr 1;22(4):40501. doi: 10.1117/1.JBO.22.4.040501. PMID: 28397959; PMCID: PMC5387867.
3. Thomas Van den Dries, Thomas Lapauw, Arnaud Juliens, Jan Coosemans, Pooria Iranian, Gobinath Jegannathan, Maarten Kuijk, Hans Ingelberts, "Compact sub-nanosecond time-gated camera based on a new 64x64 Current-Assisted Photonic Sampler (CAPS) sensor with improved quantum efficiency," Proc. SPIE 12006, Silicon Photonics XVII, 120060B (5 March 2022); https://doi.org/10.1117/12.2608704
4. Alberto J. Ruiz, Mindy Wu, Ethan Philip M. LaRochelle, Dimitris Gorpas, Vasilis Ntziachristos, T. Joshua Pfefer, Brian W. Pogue, "Indocyanine green matching phantom for fluorescence-guided surgery imaging system characterization and performance assessment," J. Biomed. Opt. 25(5) 056003 (21 May 2020) https://doi.org/10.1117/1.JBO.25.5.056003

Oral Presentation

Disclosures: The authors have disclosed no financial interest.

134-Evaluating a suite of novel OATP-targeted manganese contrast agents for liver MRI

Presenter: Sean McRae, Western University

Sean McRae[1], Francisco Martínez?Santiesteban[2], Eric Gale[3], Peter Caravan[4], John Ronald[5], Timothy J. Scholl[6]

[1]*Western University*
[2]*Robarts Research Institute, London, Ontario*
[3]*Massachusetts General Hospital, Boston*
[4]*Harvard Medical School, Charlestown, MA*
[5]*Robarts Research Institute, London, ON*
[6]*Western University, London, Ontario*

Introduction:
Magnetic resonance imaging (MRI) is a clinical standard for *in vivo* detection of many macroscopic pathologies. Its sensitivity and specificity for small lesions can often be improved by the administration of paramagnetic contrast agents. For instance, gadolinium-ethoxybenzyl-diethylenetriamine-pentaacetatae (Gd-EOB-DTPA;*Primovist*) is a liver-targeted agent that is transported into healthy human hepatocytes primarily through organic anion transporting polypeptide (OATP) 1B1 and 1B3. Reduced OATP expression in liver lesions results in regions of hypointense contrast compared with healthy liver on T_1-weighted MR images. Our group has also shown that engineering cells to synthetically express human OATP1B1 or 1B3 increases their detectability on T_1-weighted images upon administration of Gd-EOB-DTPA. However, concerns over gadolinium deposition in patients with renal impairments, has shifted the focus in the field to the development

of new agents containing alternative paramagnetic ions, such as manganese. This study describes the development of five novel amphiphilic manganese agents (arbitrarily named Mn 1 – 5), the evaluation of OATP uptake both *in vitro* using human OATP isoforms, and *in vivo* liver uptake through endogenous OATP expression in mice.

Methods:

Human breast cancer (MDA-MB-231) cells were engineered using a lentiviral vector expressing fluorescent zsGreen to facilitate cell sorting, and either the human OATP1B1 or OATP1B3. ***In vitro* agent characterization:** Agent relaxivity (r_1) was measured at low field (0.23 mT – 1 T) using fast-field cycling relaxometry, and at our imaging field strength (3 T) using a fast-spin echo inversion-recovery sequence (FSE-IR) at 37ºC. Naïve and engineered MDA-MB-231 cells containing either of the two OATP isoforms were incubated with one of the novel manganese-agents (1.6 mM) for 90 minutes, then washed and collected for analysis. An FSE-IR sequence was used to acquire R_1maps of cell pellets to assess agent uptake through OATP. Agent uptake was estimated by dividing the change in relaxation rates between the naïve and treated cells by the relaxivity of the agent at 3 T and normalized to the uptake of Primovist through OATP1B3 (our benchmark probe-reporter combination). Based on the *in vitro* uptake data, Mn-2, Mn-3, and Mn-5 were selected for *in vivo* evaluation. ***In vivo* MRI:** Healthy BALB/c mice were imaged using a custom-built whole-body linear birdcage coil at 3 T. Pre-contrast images were taken before agent administration using a 3D spoiled gradient recalled steady state acquisition (3D-SPGR). After administration of 0.1 mmol/kg dose of agent, repeated whole-mouse T_1-weighted images (300 m isotropic resolution) were acquired every 138 s over 70 minutes to assess agent biodistribution and contrast enhancement in various organs.

Results:

The measured mean relaxivity of the five manganese agents at 3 T was $2.99 \pm 0.3\ mM^{-1}s^{-1}$. *In vitro* uptake assays through human transporters showed uptake of all five manganese-based agents compared to cells lacking the transporter. Higher uptake of Mn agents was observed through OATP1B1 compared to our Gd-EOB-DTPA-OATP1B3 benchmark. *In vivo* MRI showed mixed renal/hepatobiliary clearance of all three agents with peak contrast enhancements in the liver of 126%, 151%, and 185% compared to precontrast, and estimated half-lives of 24.73 mins, 20.03 mins, and 21.22 mins for Mn-2, Mn-3, and Mn-5 respectively.

Conclusions:

These next-generation Mn-based contrast agents display promising properties for MR imaging and offer a potential solution to reduce Gd-specific concerns that are associated with commercially available agents. The novel agents investigated showed good uptake through human OATP1B1 *in vitro* and successfully generated strong liver contrast *in vivo*, showing fast clearance, and no evident toxicity at 0.1 mmol/kg. Future work will include evaluating these novel agents for OATP1 reporter gene imaging in various applications.

Reference

1. Patrick P, et al. Dual-modality gene reporter for in vivo imaging. Proceedings of the National Academy of Sciences, 2014.
2. Nyström N et al. Longitudinal Visualization of Viable Cancer Cell Intratumoral Distribution in Mouse Models Using Oatp1a1-Enhanced Magnetic Resonance Imaging. Invest Radiol, 2019.
3. Grobner T. Gadolinium-a specific trigger for the development of nephrogenic fibrosing dermopathy and nephrogenic systemic fibrosis? Nephrol Dial Transplant, 2006.

Oral Presentation

Disclosures: The authors have disclosed no financial interest.

135-NIR 2nd window imaging to assess the impact of inherited Notch-DLL4 expression on pulmonary radiation injury

Presenter: Mir Hadi Razeghi Kondelaji, Medical College of Wisconsin-Biomedical Engineering

Mir Hadi Razeghi Kondelaji[1], Guru Sharma[2], Chris Hansen[3], Brian Fish[2], Tracy Gaperetty[2], Heather Himburg[2], Amit Joshi[3]

[1]*Medical College of Wisconsin-Biomedical Engineering, Milwaukee, WI*
[2]*Medical College of Wisconsin, Milwaukee, Wisconsin*
[3]*Medical College of Wisconsin, Milwaukee, WI*

Introduction:

Ionizing radiation causes lung injury by increasing vascular permeability. Recently we reported a physiologically based pharmacokinetic (PBPK) model based on non-invasive dynamic NIR imaging to estimate vascular function and permeability in lungs [PMID: 28567545]. However, the role of inherited genes in pulmonary radiation injury and recovery has not been fully studied. We report the influence of inherited endothelial notch-DLL4 expression on radiation injury via NIR-2nd window dynamic imaging of ICG dye kinetics in consomic rat models. Consomic strains were generated by the substitution of the brown Norway (BN) rat (DLL4-low) chromosome 3 into the salt sensitive (SS, DLL4-high) background (referred to as SS-BN3 consomic). We demonstrate the divergent effect of DLL4 expression on radiation induced vascular permeability, which further led to mortality differences, where SS rats (DLL4-high) exhibited high pulmonary mortality compared to SS.BN3 rats following whole thoracic radiation.

Method:

SS and SSBN3 rats were bred to differ in the inheritance of 3rd chromosome (Figure 1- A). Animals in each group were divided into two groups, where one group was exposed to 13.5 Gy leg out partial body irradiation. NIR-2nd window dynamic fluorescence imaging of ICG dye uptake and clearance was conducted with a NIRVANA camera (15 minutes, 10.6 frame/second, and 808 nm excitation, 950 nm longpass emission) at 42 days and 90 days post irradiation. Time dependent images were analyzed by principal component analysis (PCA) to detect lung ROI and time courses across groups were compared (Figure 1-B, and C). PBPK compartmental model parameters were estimated to quantify the permeability- surface area product (PS). Figure 1-D. To evaluate the endothelial cellularity, and the sensitivity of cells to the irradiation, and to evaluate the role of DLL4 expression on the irradiation response, flow cytometry was performed for selected animals from each group. Also, about ten million lung cells per animal were used for $CD31^+$ enrichment to assess the effect of irradiation injury on the $CD31^+$ count in radiated and control groups.

Results:

42 days post injury, the PS value increased to 6.85 ± 1.89 [CL: 2.76- 10.94] mL/min for SS rats after 13 Gy irradiation, compared to 2.36 ± 0.20 [CL: 1.94- 2.78] mL/min for non- irradiated SS rats (p-value<0.05). While, the PS for SSBN3 rats was 2.56 ± 0.21 [CL: 2.11- 3.01] mL/min, and 3.50 ± 0.69 [CL: 2.06- 4.94] mL/min for control and radiated groups(Figure 1-E). This suggests SS.BN3 pulmonary vasculature was resistant to radiation injury. The surviving animals has PS values reduce to match control at 90 day. We examined the endothelial cellularity (EC) in lung by flow cytometry (Figure 1-H).

In SS rats EC reduced from 9.87% in 0Gy to 5.65% in 13Gy. However, BN3 rats showed a nonsignificant reduction in EC from 7.08% in 0Gy to 5.46% in 13Gy, suggesting radioprotective effects in consomic SSBN3 rats (Figure 1-F). There was significant decrease in Dll4 mRNA in SS rats upon radiation compared to that in SSBN3 rats. Notably, in non-radiated groups, SS rats have higher EC counts and Dll4 mRNA expression than SSBN3 rats (Figure 1-G) suggesting higher DLL4 expression increases radiation injury. Also, the morbidity analysis of animals shows higher rate for irradiated SS rats compared to non- irradiated SS and radiated SSBN3 groups (Figure 1-H).

Conclusion:
Our study suggests a significant dependence of radiation injury to the inherited notch-DLL4 expression, which can be imaged in 200g rats with NIR 2nd window imaging.

Oral Presentation

Disclosures: The authors have disclosed no financial interest.

136-Development of a Highly Efficient Modular and Multiplexed CRISPR Editing System for Multimodal Tracking of CAR-T Cells

Presenter: John Kelly, Western University

John J. Kelly[1], Nourhan Shalaby[2], Rafael E. Sanchez Pupo[3], Ying Xia[4], Francisco Martínez?Santiesteban[4], Qi Qi[1], Matthew S. Fox[5], Justin W. Hicks[6], Jonathan D. Thiessen[7], Timothy J. Scholl[4], John Ronald[3]

[1]*Western University, London*
[2]*Western University, London, ON*
[3]*Robarts Research Institute, London, ON*
[4]*Robarts Research Institute, London, Ontario*
[5]*Lawson Health Research Institute, London, Ontario*
[6]*Lawson Health Research Institute, London, ON*
[7]*Lawson Health Research Institute, London*

Introduction:
Chimeric antigen receptor T (CAR-T) cells have shown remarkable efficacy in treating blood-based cancers[1]. However, current challenges of these transformative therapies include low effectiveness in many patients, accumulation in normal tissues leading to serious side effects, and insufficient migration into and treatment of solid tumours. Translationally relevant imaging technologies that allow one to monitor the fate of CAR-T cells could enable prediction of patient response and side effects, as well as better evaluate CAR-T designs. Our objective was to develop a highly efficient CRISPR system for editing human T cells with multiple transgenes at loci known to improve both safety and efficacy of CAR-T cells, whilst also making them “visible” with clinically relevant imaging modalities. As described by *Eyquem et al.*[2], T cells were edited at the *TRAC* locus to knock-in a CAR and simultaneously knock-out the endogenous T cell receptor (TCR) to improve CAR-T cell potency and delay exhaustion. Human MRI (*OATP1B3*), PET (*NIS*) or preclinical bioluminescent (*Akaluc*) reporter genes were included in our CRISPR system to allow for multi-modal molecular-genetic imaging of edited CAR-T cells.

Methods:
Human T cells were nucleofected with ribonucleoprotein complexes (RNPs) targeted to the *TRAC* or *AAVS1* safe-harbor loci. Adeno-associated viral (AAV) vectors were designed to carry CD19CAR and *OATP 1B3*, *NIS* or *Akaluc* reporter genes to the *TRAC* or *AAVS1* loci. Editing efficiency was determined by flow cytometry and integration by PCR analysis. CD19+ human B cell lymphoma (NALM6) cells expressing either firefly luciferase (FLuc) or Antares BLI genes were engineered for CAR-T targeted kill assays and *in vivo* preclinical moue models. Uptake of the PET tracer [18F]tetrafluoroborate (TFB, 1 MBq/1M cells, 45 mins) into NIS expressing cells was measured with a gamma counter. Uptake of the MRI contrast agent Gd-EOB-DTPA (5.2 mM, 90 mins) was determined using a 3T clinical MRI scanner. Akaluc expression was determined by BLI using an IVIS imaging system and its substrate, akalumine (5 mM).

Results:
Flow cytometry analysis showed >85% editing efficiency when targeting CD19CAR AAV to the *TRAC* locus. CD19CAR+/TCR- T cells significantly delayed cancer progression and extended survival in a NALM6-Fluc leukemia mouse model. CD19CAR-OATP1B3, -NIS and -Akaluc CAR-T cells had functional reporter gene expression downstream of the CAR, as confirmed by uptake of Gd-EOB-DTPA into OATP1B3 expressing cells, [18F]TFB into NIS expressing cells and bioluminescence in Akaluc expressing cells (Fig.1 A-C). Multiplexed editing with CD19CAR-OATP1B3 or -NIS at the *TRAC* locus and NIS- or OATP1B3-LNGFR at the *AAVS1* locus together produced 50-74% TCR-/LNGFR+ duel edited cell populations (Fig.1 D). Single and dual edited CAR-T cells effectively killed NALM6-Fluc cells, whereas naïve and RNP only control T cells did not (Fig. 1 E). These data indicate that both the CAR and reporter gene components were functional in single and dual-edited T cells. Correct integration at *TRAC* and/or *AAVS1* loci was confirmed by junction PCR analysis. For preclinical mouse models, a dual BLI imaging system was employed that showed homing of CD19CAR-Akaluc T cells to subcutaneous NALM6-Antares expressing cancer cells.

Conclusion:
Our work demonstrates the first CRISPR-Cas system for highly efficient editing of cancer-killing CAR-T cells with clinically relevant human reporter genes. Ongoing efforts are extending these studies to MRI and PET of edited CAR-T cells in preclinical mouse cancer models. These advanced CRISPR tools should have broad utility for co-editing primary cells with therapeutic genes and reporter genes to make trackable therapeutic cells with improved efficacy and safety profiles.

Reference

1. Vitale, C. and Strati, P., Frontiers in Oncology, 2020
2. Eyquem, J. et al., Nature, 2017

Oral Presentation

Disclosures: The authors have disclosed no financial interest.

137-Preliminary results of hyperpolarized MRI of [1-13C] pyruvate in D2O in the normal human brain

Presenter: Kofi Deh, Memorial Sloan Kettering Cancer Center

Kofi Deh[1], Guannan Zhang[2], Angela Hijin Park, Shake Ahmmed, Serge K. Lyashchenko[2], Nadia Bragagnolo[3], Charles H. Cunningham[4], Vesselin Miloushev, Marius Mayerhoefer, Kayvan Keshari[1]

[1]*Memorial Sloan Kettering Cancer Center, New York, NY*
[2]*Memorial Sloan Kettering Cancer Center, New York*
[3]*Sunnybrook Research Institute*
[4]*Sunnybrook Research Institute, Toronto, ON*

Background:
Although dissolution dynamic nuclear polarization generates high spin polarizations for feasible clinical magnetic resonance imaging (MRI) of 13C-metabolites, this hyperpolarization is non-renewable, and the effective relaxation time of hyperpolarized metabolites limits the achievable image SNR and spatial resolution. Our group has demonstrated a preclinical method of increasing the polarization lifetime by dissolving 13C-pyruvate in deuterium (D2O) [1]. Here, we perform a translation of this method into humans to study its safety and imaging characteristics.

Methods:
Several tests were performed to verify it was safe to inject humans with D2O. The results of the trials submitted for an IND approval are shown in Figure 1a. Three healthy volunteers (ages:29.5± 2.5 years) were imaged under IRB#21-309 on a GE Discovery MR750w 3.0T using a dual-tuned transmit/receive quad 1H/13C head coil. The pyruvate dose was prepared by loading 1.54 grams of [1-13C]-pyruvate/EPA solution into a cryostat vial, and 37 grams of D2O into a fluid path which was polarized in a 5T Spinlab Hyperpolarizer (GE Healthcare) for about two hours. After polarization, the [1-13C]-pyruvic acid was neutralized with 42 grams of 0.276 M NaOH and 0.153 M Tris in D2O in a receiver vessel. The solution was terminally sterilized into the patient administration syringe. After performing quality control (see Figure 1b), 0.43 ml/kg of the dose was injected at 5 mL/s into the volunteer followed by 20 mL of saline flush using a Medrad power injector. Image acquisition was initiated immediately following the saline flush using a spectrally-selective dual-echo 3D dynamic EPI sequence [2]. 12 timepoints of 13C images were acquired for 24 image slices over a field of view of 25 x 25 x 48 cm3 and an image size of 16 x 16 x 24 voxels at a repetition interval (TR) of 5 seconds with flip angles of 80° on 13C-bicarbonate and 13C-lactate, and 11° on 13C-pyruvate. An axial T1-weighted image was acquired for anatomic localization. The kinetics of pyruvate perfusion and conversion to lactate was determined by fitting the imaging time series to an inputless two-site kinetic tissue model[3].

Results:
We have injected 3 volunteers with no adverse effects. However, only two image acquisitions were successful. Pyruvate and lactate were readily detected (Figure 1 d), but the bicarbonate SNR was poor and this may have been due to a miscalibration of the bicarbonate frequency. Good kinetic parameter maps were obtained in the interior of the brain, but the fit at the edge was poor (Figure 1c). Average time-to-peak (TTP) values for pyruvate and lactate measured over a region-of-interest (ROI) on the central slices were found to be 6.41 and 15.94 seconds. Mean pyruvate to lactate conversion rate (kPL) was found to be 0.017/second and the mean effective T1 for pyruvate ($T1_{pyruvate}$) was 47.5 seconds (Fig. 1e)

Discussion:
We have verified the safety and determined the imaging characteristics of HP [1-13C-pyruvate] in D2O in the normal human brain. Despite the small number of subjects, it is interesting to note that the mean pyruvate to lactate conversion rate (kPL) is comparable to that reported in another work [4]. More notably, the effective T1 of pyruvate in D20 obtained is almost 50 seconds which is about twice that reported for pyruvate in H20 in [3] and [4]. This suggests the increase in effective T1 of pyruvate from solvation in D2O may be maintained in the human brain.

Reference

1. Cho et al. J. Magn Reson. 2019
2. Geraghty et al. MRM 2018
3. Larson et al. NMR in Biomedicine, 2018
4. Mammoli et al., IEEE Trans. Med. Imaging, 200

Oral Presentation

Disclosures: The authors would like to disclose that HP pyruvate is an investigational device.

138-uSPIO nanocarrier for dual PET-MRI image-guided pretargeting theranostic platform

Presenter: Ge Si, Johns Hopkins University School of Medicine

Ge Si[1], Sudath Hapuarachchige[2], Dmitri Artemov[1]

[1]*Johns Hopkins University School of Medicine, Baltimore, MD*
[2]*Johns Hopkins University School of Medicine, Baltimore, Maryland*

Introduction:
HER2(+) metastatic breast cancer (BC) is one of the most aggressive and lethal cancer type amongst female. HER2 targeted therapies such as monoclonal antibodies and antibody-drug conjugates lack long-term efficacy and/or can cause severe off-target toxicity. Therefore, the development of novel targeted delivery strategies that minimize toxicity and increases therapeutic localization is critical to improve treatment outcomes. Pretargeting delivery separates a traditional single targeted delivery step into a pretargeting step followed by the subsequent delivery of therapeutic components with optimized clearance and circulation time that can reduce off-target accumulation and associated toxicity.[1] The delivery components are functionalized with bioorthogonal reactive groups that quickly react *in situ*. In the pretargeting step, a high-affinity mAb ligand targets HER2 markers on the cancer cell membrane. In the second step, drug carrier molecules are administered and selectively react with the pretargeted receptors forming cross-linked cluster on the cell surface, facilitating rapid internalization and intracellular delivery of therapeutics. We have reported a click-chemistry based pretargeting platform for HER2(+) BC with dual-modality PET-SPECT image guidance.[2] An enhanced localization of the therapeutic components and improved treatment response was observed in pretargeted tumors.[1, 2] However, an interference between PET/SPECT channels; an increased radiation exposure; and complex logistics of imaging lead us to developing new PET-MRI guided pretargeting platform, that takes advantages of dual PET-MRI systems, reduced radioactivity dose, and improved soft-tissue contrast. Biocompatible uSPIO-based nanocarriers are used as the drug delivery platform due to their high MR relaxivity, high loading capacity, and non-toxicity.

Methods:
Hydrophilic uSPIO carriers were constructed from an oleic-acid capped hydrophobic sub-5nm iron-oxide core. A bifunctional hydrophilic ligand was synthesized having strong affinity towards iron-oxide core and bearing free amine group. A ligand exchange method was used to strip the native oleic acid cap with the synthesized ligand. TCO-tetrazine click chemistry was selected for pretargeting delivery due to its fast kinetics with no side reactions or products.[3] Pegylated click-reactive linkers and/or DM1 (Mertansine) drug were conjugated onto uSPIO post-ligand exchange. TEM and DLS were used for measuring uSPIO core size and hydrodynamic diameter. T_1 and T_2 uSPIO relaxivity was determined in a phantom study. The uSPIO-Tetrazine carrier was tested in preclinical models of HER2(+) BT-474 BC using pretargeting ^{89}Zr radiolabeled trastuzumab conjugated with TCO click reactive group (Tz-^{89}Zr-TCO). uSPIO was delivered 20h after pretargeting trastuzumab and PET-MRI images were acquired on a Bruker 7 Tesla PET-MRI system at 1 to 24h post administration.

Results: The developed uSPIO construct has a core size of 3.5nm and a hydrodynamic diameter of 15nm (Figure 1A). It produces strong positive T_1 contrast in MR images with T_1 relaxivity comparable to Gd-based contrast agents (1 vs 3 s^{-1}•mM^{-1}) (Figure 1C). Surface amine conjugation with PEG-tetrazine linker and drug does not induce significant structural change to the uSPIO core, as confirmed by TEM (Figure 1B). MRI of pretargeted and non-pretargeted tumors is shown in Figure 1D. A 15% T_1 drop with the first hour and a 95% signal recovery after 4 hours of administration was detected in non-pretargeted tumors suggesting passive EPR-based delivery and rapid washout of the carrier. Over 40% T_1 drop was detected in Tz-^{89}Zr-TCO pretargeted tumors and the signal did not fully recover till 24 hours post injection, suggesting specific tumor retention of pretargeted uSPIO-PEG-Tt carriers. Co-registration of PET and MRI signals was observed only in the tumor region (Figure 1D).

Conclusion:
This study builds a solid foundation for further development of the uSPIO-based drug carrier platform for pretargeting image-guided theranostic approach to simultaneously visualize biodistribution and enhance therapeutic localization using dual PET-MR imaging.

Reference

1. Hapuarachchige, S., Kato, Y. & Artemov, D. Bioorthogonal two-component drug delivery in HER2(+) breast cancer mouse models. Scientific reports 6, 24298 (2016).
2. Hapuarachchige, S. et al. Dual-Modality PET-SPECT Image-Guided Pretargeting Delivery in HER2(+) Breast Cancer Models. Biomacromolecules (2021).
3. Oliveira, B.L., Guo, Z. & Bernardes, G.J.L. Inverse electron demand Diels-Alder reactions in chemical biology. Chemical Society Reviews 46, 4895-4950 (2017).

Oral Presentation

Disclosures: The authors have disclosed no financial interest.

139-Monitoring protein aggregation in neurological proteopathies with a highly sensitive chemiluminescence probe

Presenter: Biyue Zhu, Massachusetts General Hospital

Biyue Zhu[1], Jing Zhang[2], shi kuang[3], Jun Yang[4], Chongzhao Ran[4]

[1]Massachusetts General Hospital, boston, MA
[2]Harvard Medical School, Charlestown, MA
[3]Massachusetts General Hospital, Charlestown, MA Massachusetts
[4]Harvard Medical School

Neurological proteopathies are diseases characterized by abnormal assembly of misfolded proteins, including Alzheimer's disease (AD), Parkinson disease (PD), and prion disease.[1] Fluorescence staining with Thioflavin T (ThT) is a gold standard method for detecting various misfolded proteins and is widely applied in *in vitro* testing and etiology elucidation.[2] However, the high background signal, short emission wavelength, and poor blood-brain barrier permeability hamper it's *in vitro* and *in vivo* applications.[3] In contrast, chemiluminescence imaging requires no excitation, which can significantly enhance signal to noise ratio (SNR) and thus facilitate deep tissue imaging.[4] Currently, there are no chemiluminescence probe for monitoring proteopathies. In the present study, we first demonstrated that ADLumin-1, a highly sensitive chemiluminescence probe (Fig. 1a),[5] could target the long-axis of beta-sheet structure and serve as an excellent alternative to ThT. When interacting with amphiphile peptide PA-K/K2, ADLumin-1 showed selective binding to beta-sheet-rich PA-K2 (Fig. 1b) and displayed over 100-fold signal amplification compared to the gold standard ThT (Fig. 1c). ADLumin-1 also showed excellent capability to detect a broad spectrum of misfolding-prone protein biomarkers (Fig. 1d) and molecular docking indicated that ADLumin-1 bind along the long axis of beta-sheet structure (Fig. 1e). By using α-synuclein, the biomarker in PD, as an example, ADLumin-1 was successfully applied to monitor α-synuclein aggregation ($Kd = 0.76$ μM) and direct detection of α-synuclein aggregates with the lower limit of detection at 1 pg/mL (Fig. 1f). By coupling with protein misfolding cyclic amplification (PMCA) technology, ADLumin-1 enabled attomole level detection of α-synuclein aggregates in human cerebrospinal fluid (Fig. 1g), which could not be achieved with ThT. Moreover, the probe could label α-synuclein inclusions in brain slides of a PD patient (Fig.1h). In addition, ADLumin-1 could differentiate transgenic A53T mice from wildtype mice, evidenced by significantly higher chemiluminescence signal from brain region (Fig. 1i,j). Lastly, ADLumin-1 enabled noninvasive monitoring of disease progression and α-synuclein aggregation in transgenic PD mice (Fig.1k). In summary, ADLumin-1 is a highly sensitive chemiluminescence probe for detection of neurological proteopathies both in vitro and in vivo.

Reference

1. Jucker M, Walker L C. Propagation and spread of pathogenic protein assemblies in neurodegenerative diseases[J]. Nat. Neurosci., 2018, 21(10): 1341-1349.
2. Biancalana M, Koide S. Molecular mechanism of Thioflavin-T binding to amyloid fibrils[J]. Biochim. Biophys. Acta - Proteins Proteom., 2010, 1804(7): 1405-1412.
3. Zhu B, Cheng Y, Li G, et al. Synthesis and evaluation of styrylpyran fluorophores for noninvasive detection of cerebral β-amyloid deposits[J]. Bioorganic Med. Chem. Lett., 2016, 24(4): 827-834.
4. Miao Q, Xie C, Zhen X, et al. Molecular afterglow imaging with bright, biodegradable polymer nanoparticles[J]. Nat. Biotechnol., 2017, 35(11): 1102-1110.
5. Yang J, Yin W, Van R, et al. Turn-on chemiluminescence probes and dual-amplification of signal for detection of amyloid beta species in vivo[J]. Nat. Commun., 2020, 11(1): 1-14.

Oral Presentation

Disclosures: The authors have disclosed no financial interest.

140-1Visualizing in vivo cell-cell communication with activatable magnetic resonance imaging

Presenter: TianDuo Wang, Robarts Research Institute

TianDuo Wang[1], Yuanxin Chen[2], Nivin Nystrom[2], Shirley Liu[3], John Ronald[2]
[1]Robarts Research Institute, London
[2]Robarts Research Institute, London, ON
[3]Western University, London

Introduction:
Cellular therapies rely on proper communication between delivered cells and their target. Cancer immunotherapies harness the innate tumour-homing ability of immune cells to better target and kill malignant cells. To improve cancer killing, immune cells can be engineered with targeting receptors, such as chimeric antigen receptors (CAR), to

recognize specific cancer antigens. CAR-T cells have already shown remarkable clinical success in treating B-cell cancers1, with the potential to treat other cancer types on the horizon. However, some patients still suffer from inadequate efficacy and/or serious side effects, thought to be due to sub-optimal tumour-homing and off-targeting of normal tissues by immune cells. This study aims to develop a non-invasive and clinically-relevant imaging tool to visualize when immune cells interact with their targeted antigen – the prerequisite for inducing cancer killing. The synthetic notch (SynNotch) receptor is a uniquely versatile system that signals cell-cell contact via activatable transcriptional expression of desired transgenes2 (Fig. 1A). The objective of this work was to engineer immune cells with a SynNotch system that activates the expression of multimodal imaging reporter genes in response to cancer antigen binding.

Methods:
Human Jurkat T cells were engineered via sequential lentiviral transduction of two components: (1) SynNotch directed against the B-cell surface antigen CD193, and (2) an activatable response element containing tdTomato (tdT) for fluorescence, firefly luciferase (Fluc) for bioluminescence (BLI), and organic anion transporting polypeptide 1B3 (OATP1B3) for MRI4. Successfully engineered T cells were isolated using fluorescence activated cell sorting. For in vivo evaluation, Nod-scid-gamma mice were implanted with either CD19+ or CD19- Nalm6 leukemia cells subcutaneously. Once tumours reached >100mm3, mice received an intratumoural injection of 10 million engineered T cells. BLI and gadolinium-enhanced T1-weighted MRI was performed to assess Fluc and OATP1B3 reporter activation in tumours, respectively. Contrast-to-noise ratio (CNR) measurement of MR images was performed by a blinded observer by drawing regions representing the enhanced cells and tumour background on individual slices and averaged per mouse.

Results:
BLI revealed minimal background Fluc activity in subcutaneous tumours prior to T cell injection (Fig. 1B). Excitingly, as early as 12 hours post-intratumoural T cell injection, mice carrying CD19+ tumours showed significantly elevated Fluc signal compared to mice with CD19- tumours at all timepoints. Following administration of the gadolinium agent Primovist, MRI revealed localized regions of contrast enhancement within CD19+ tumours whereas CD19- tumours showed no notable enhancement (Fig 1C). These enhanced regions in CD19+ tumours exhibited significantly higher contrast-to-noise over the tumour background compared to CD19- tumours (Fig 1D).

Discussion:
This work describes an activatable molecular imaging system to visualize cell-cell communication between cells in vivo using clinically-relevant imaging modality for the first time. The results demonstrate selective activation of reporter genes in immune cells interacting with cancer cells in an antigen-dependent manner with minimal off-target activity. Notably, MRI revealed discernable regions of contrast enhancement within CD19+ tumours, but not CD19- tumours, reflective of OATP1B3 expression in T cells interacting with their target antigens. Future work for this imaging system includes adapting it for other immune cell types like natural killer cells and CAR-T cells. Moreover, the modularity of SynNotch can easily target antigens on solid tumours antigens instead, allowing this system to be used across a wide range of cancer types. Further refinement of this technology will provide a clinically-relevant imaging tool which could provide valuable insight into how cells communicate in multicellular organisms, and ultimately help to improve the safety and efficacies of cell therapies as a whole.

Reference

1. Maude et al., NEJM, 2014, 371: 1507-1517.
2. Morsut et al., Cell, 2016, 164: 780-791.
3. Sadelain et al., J Clin Invest, 2015, 125(9): 3392-3400.
4. Nystrom et al., Invest Radiol, 2019, 54(5): 302-311.

Oral Presentation

Disclosures: The authors have disclosed no financial interest.

141-1Magnetic particle imaging of cerebrovascular functional changes in rats

Presenter: Eli Mattingly, Massachusetts Institute of Technology

Eli Mattingly[1], Erica E. Mason[2], Konstantin Herb[3], Monika ?liwiak[3], John Drago[1], Emiri T. Mandeville[4], Joseph B. Mandeville[5], Lawrence L. Wald[4]

[1]Massachusetts Institute of Technology, Cambridge, MA
[2]Massachusetts General Hospital, Charlestown, Massachusetts
[3]Athinoula A. Martinos Center for Biomedical Imaging, Charlestown, MA
[4]Massachusetts General Hospital, Charlestown, MA
[5]Athinoula A. Martinos Center for Biomedical Imaging, Cambridge, MA

Background:
Magnetic particle imaging (MPI) utilizes the nonlinear magnetic response of superparamagnetic iron oxide nanoparticle (SPION) tracers, and is notable for its high sensitivity and lack of biological background signal. These traits, together with the SPION's restriction to the cerebral blood spaces, make it an attractive modality for cerebral blood volume (CBV) imaging including mapping functional changes. Modeling analysis [3] as well as preliminary experiments of rats undergoing a hypercapnia challenge supported the use of MPI for functional neuroimaging [1, 2]. Here, we present a study of MPI's ability to image hypercapnia induced CBV changes in 5 rats using improved MPI hardware with increased sensitivity and temporal resolution.

Methods:
The mechanically rotating field-free line (FFL) MPI system used in this experiment is described in the Open-Source MPI project[5] (seen in Fig. 1A), and utilizes a receive chain from the University Medical Center Hamburg Eppendorf. MPI images are acquired every 5.0 sec. The imaging parameters are: drive amplitude = 8 mT pk, field of view (FOV) ≈ 30 mm diameter, and the images are reconstructed with an inverse radon transform. Synomag-D 70 nm SPIONs (micromod, Germany) were injected into 5 adult male Sprague-Dawley rats. Availability of the particles necessitated the use of 2 batches (16321104-02, 08522104-01) of SPIONs. Spatial resolution is ~2 mm. Each rat underwent two rounds of the hyper-/hypocapnia protocol, with a 10 mg/kg dose before each, with doses ~1 hr apart. The hyper-/hypocapnic protocol is as follows: Hypercapnia was induced by ventilating the rat with 5% CO_2 + enriched (30% O_2) air at 35 breaths per minute (BPM); hypocapnia was induced by hyperventilation (55 BPM) on enriched air. Each state lasted 5 minutes (repetition period = 10 min), and the experimental protocol for each rat involved three full periods (30 min total). For each rat, a volume MPI scan was acquired (see Fig. 1B). Finally, 3T MRI data was obtained for each rat on the same bed used in the MPI system (3D GRE, TE=2.67 ms, TR=20 ms, isotropic 0.5 mm). The MR images

were then coregistered to the MPI. To analyze the imaging time sequence, a generalized linear model (GLM) was built for the experiment with constant, linear, initial transient decay, scan direction, and "activation" terms. The "activation" term is the square-wave corresponding to hyper-/hypocapnia convolved with a hemodynamic response function and a particle decay term. The resultant activation model fit and the measured data with other regressors (constant, linear, etc.) subtracted, is shown in Fig. 1D. The contrast-to-noise ratio (CNR) is defined as the peak-to-peak activation divided by the standard deviation of the residual error from the GLM.

Results:

The maximum positive CNR is located in the brain for each of the 5 rats, and the values are: [13.6, 19.9, 11.5, 10.0, 10.4]. Within the brain, the percent signal change is ~20-30%. Each corresponds to a Bonferroni corrected p-value of $< 10^{-12}$. Fig. 1C shows the CNR map coregistered on the MRI for a representative rat, and for all 5 rats in the persuasive data file.

Discussion:

The results show strong activation, localized to the brain, consistent with the expected physiological response of hyper-/hypocapnia. These are the first MPI imaging of cerebrovascular functional changes in rats *in vivo*, localized to the brain as confirmed by MRI coregistration. Next steps include imager developments to accommodate larger rats, and reconstruction improvements (e.g. [4]) to mitigate artifacts, e.g. due to rat positioning near the edge of the FOV or out of plane signal. This study motivates future work such as 1) MPI imaging of localized neural activation, and 2) scaling to larger animals.

Funding: NIBIB U01EB025121-02, NSF GRFP 1122374.

Reference

1. C. Z. Cooley, J. B. Mandeville, E. E. Mason, E. T. Mandeville, and L. L. Wald. Rodent Cerebral Blood Volume (CBV) changes during hypercapnia observed using Magnetic Particle Imaging (MPI) detection. NeuroImage, 178(April):713–720, 2018.
2. K. Herb, E. E. Mason, E. Mattingly, J. B. Mandeville, E. T. Mandeville, and L. L. Wald. Functional MPI (fMPI) of hypercapnia in rodent brain with MPI time-series imaging. In International Workshop for Magnetic Particle Imaging.
3. E. E. Mason, C. Z. Cooley, S. F. Cauley, M. A. Griswold, S. M. Conolly, and L. L. Wald. Design analysis of an MPI human functional brain scanner. International Journal of Magnetic Particle Imaging, 3(1), 2017.
4. E. E. Mason, Stephen, F. Cauley, E. Mattingly, M. Sliwiak, and L. L. Wald. Side Lobe Informed´ Center Extraction (SLICE): a projection-space forward model reconstruction for a 2D imaging system. International Journal on Magnetic Particle Imaging, 8(1), 2022.
5. E. Mattingly, E. E. Mason, K. Herb, M. Sliwiak, K. Brandt, C. Z. Cooley, and L. L. Wald. OS-MPI: An´ open-source magnetic particle imaging project. International Journal on Magnetic Particle Imaging, 6(2):1–3, 2020.

Oral Presentation

Disclosures: The authors have disclosed no financial interest.

142-Characterization of [6,6'-2H2] Fructose as a Novel Deuterium Metabolic Imaging Probe in Subcutaneous Liver Cancer Mouse Models: a Comparative Study with [6,6'-2H2] Glucose

Presenter: Guannan Zhang, Memorial Sloan Kettering Cancer Center

Guannan Zhang[1], Quinlan Cullen[2], Marjan Berishaj[3], Kofi Deh[3], Nathaniel Kim[1], Kayvan Keshari[3]

[1]Memorial Sloan Kettering Cancer Center, New York
[2]Memorial Sloan Kettering Cancer Center
[3]Memorial Sloan Kettering Cancer Center, New York, NY

Introduction:

Early detection and treatment of hepatocellular carcinoma (HCC), one of the leading causes of cancer-related deaths due to its aggressive malignancy, remains a major challenge in healthcare. Considerable effort has been devoted to developing diagnostic tools,[1] such as ^{1}H MRI, FDG-PET, CT, for targeting and imaging HCCs. Yet, none of the methods provide insights into tumor metabolism, which is critical for tumor detection and evaluation of therapeutic treatment. Most recently, deuterium metabolic imaging, or DMI, has been demonstrated as a powerful and simple technique for non-invasive imaging of tumor metabolism in vivo.[2] Fructose, which is mainly metabolized by the liver,[3] is a promising reporter of metabolism in liver tumors. Here, we show quantitative assessment of [6,6'-$^{2}H_{2}$] fructose metabolic flux in subcutaneous HepG2 mouse models at 9.4 T and the comparison with [6,6'-$^{2}H_{2}$] glucose, exploring the possibility of developing deuterated fructose as a novel deuterium imaging probe for detecting liver tumors in vivo.

Results and Discussion:

Kinetics of [6,6'-$^{2}H_{2}$] fructose and [6,6'-$^{2}H_{2}$] glucose metabolism in liver cancer cells were investigated *in vitro* for the quantification and comparison of metabolic rates derived from glycolytic and fructolytic pathways. Human-derived HepG2 liver cells were incubated with 10 mM [6,6'-$^{2}H_{2}$] fructose and 10 mM [6,6'-$^{2}H_{2}$] glucose, respectively. ^{2}H signals of the metabolic products of the precursors were observed in the culture media (Figure 1a-c), indicating HepG2 cells actively metabolize both precursors. The production rate of [3,3'-$^{2}H_{2}$] lactate is 2 times less of the consumption rate of the precursors, indicating half of the precursor was converted into [3,3'-$^{2}H_{2}$] lactate during glycolysis, or fructolysis (Table 1). As the production rate of lactate reflects the contribution of the precursors to anaerobic pathways, the 3 times faster [3,3'-$^{2}H_{2}$] lactate production rate of [6,6'-$^{2}H_{2}$] glucose implies that [6,6'-$^{2}H_{2}$] glucose metabolism dominates anaerobic glycolysis, and [6,6'-$^{2}H_{2}$] fructose is contributed more to other pathways. The visualization of [6,6'-$^{2}H_{2}$] fructose and [6,6'-$^{2}H_{2}$] glucose metabolism *in vitro* allows further study of their metabolism *in vivo*. Kinetics of the metabolism were monitored in subcutaneous HepG2 mouse models in vivo by 2D CSI using a ^{2}H surface coil (Figure 1d). After the arrival of the precursors, an increase in the HDO production was observed, which correlates well with the consumption of the precursors in the initial ~35 mins (Figure 1e-i), implying HDO arising from the TCA cycle can be served as a robust reporter of the uptake of the precursors in the tumor. The *in vivo* HDO production rate of glucose is comparable to that of fructose (Table 1), indicating their contribution to *in vivo* TCA cycle is similar. After the initial period, HDO continues to increase rapidly which could be attributed to the second round of TCA cycle producing additional HDO, or the influx of HDO generated from metabolism of the precursors in the surrounding tissues. The lactate signal was observed by summing the ^{2}H signal from the time points (Figure 1j), where *in vivo* lactate production rates were obtained (Table 1). The ratio of $v_{\text{lac-glu,in vivo}}/v_{\text{lac-fru,in vivo}}$ and $v_{\text{HDO-glu,in vivo}}/v_{\text{HDO-fru,in vivo}}$ is comparable to that observed *in vitro*. However, the metabolic rates *in vivo* are slower than that *in vitro*, which could be caused by the differences between an *in vivo* and *in vitro* environment as well as the perfusion of precursors in tumors and a constant concentration of precursors in the cell culture.

Conclusion:

In summary, we have evaluated and compared the metabolic flux between [6,6'-$^2H_2$] fructose, and [6,6'-$^2H_2$] glucose which is the most widely used probe to study *in vivo* metabolism using DMI, demonstrating the feasibility of using [6,6'-$^2H_2$] fructose as a deuterium imaging probe to detect liver tumors.

Reference

1. Llovet, J. M. et al. Hepatocellular carcinoma. Nat. Rev. Dis. Primers 7, 6 (2021).
2. De Feyter, H. M. & de Graaf, R. A. Deuterium metabolic imaging – Back to the future. J. Magn. Reson. 326, 106932 (2021).
3. Krause, N. & Wegner, A. Fructose Metabolism in Cancer. Cells 9, 2635 (2020).

Oral Presentation

Disclosures: The authors would like to disclose that HP pyruvate is an investigational device.

143-Multi-color on-chip fluorescence microscopy for real-time surgical guidance

Presenter: Micah Roschelle, University of California, Berkeley

Micah Roschelle[1], Rozhan Rabbani[1], Efthymios P. Papageorgiou[1], Hui Zhang[2], Matthew Cooperberg[2], Bradley Stohr[3], Ali Niknejad[1], Mekhail Anwar[4]

[1]*University of California, Berkeley, Berkeley, CA*
[2]*University of California, San Francisco, San Francisco, CA*
[3]*University of California San Francisco, San Francisco, CA*
[4]*University of California, San Francisco, San Francisco*

Introduction:

A hallmark of a successful tumor resection surgery is the complete removal of all gross and microscopic disease with minimal damage to neighboring healthy tissue. Nevertheless, surgical guidance is largely accomplished by visual examination and palpitation, lacking contrast and sensitivity. As a result, patients suffer from increased risks of: recurrence through high positive margin rates[1], metastases from undetected nodal disease, and long-term damage to healthy tissue such as neighboring nerves[2]. Thus, fluorescence-guided surgery (FGS) systems—which can provide high-contrast, cell-specific imaging of multiple targets—are poised to significantly improve clinical outcomes[3]. Current FGS systems, however, face tradeoffs between microscopic detection and maneuverability. Surgical microscopes are capable of microscopic resolution but require bulky optics that obstruct the surgical workflow[4]. In contrast, laparoscopes achieve integration in minimally invasive procedures with miniaturized optics that cover a large field of view (FoV), but are limited to macroscopic detection[5]. Alternatively, contact imaging chips eliminate optical lenses and their associated tradeoffs by maintaining direct tissue contact, capturing fluorescence emissions before they diverge[6]. In this way, contact imagers achieve high collection efficiencies necessary for microscopic detection while maintaining a compact form factor. Moreover, the FoV (sensor size) is scalable without significant sacrifices in resolution. Despite these advantages, contact imaging chips require thin, planar alternatives to conventional emission filters and focusing optics. Collimators can be used to enhance resolution[7]. However, high-performance interference filters show severe performance degradations at oblique angles of incidence (AOIs), precluding their use in lens-less systems[8]. Prior works, therefore, use absorption filters, which exhibit weaker rejection and wavelength selectivity and require complex designs for multiplexed imaging[9,10]. Here we demonstrate a fluorescence contact imaging chip with a novel emission filter design which is capable of multiplexed and microscopic intraoperative imaging in a thin and planar form factor, allowing for easy integration on surgical tools. Our filter design consists of a low-NA fiber optic plate (LNA-FOP) and a multi-bandpass interference filter. The LNA-FOP acts as a collimator, compensating for the angle-sensitive interference filter while also improving resolution.

Methods:

The filter is fabricated by directly coating a dual-bandpass (500-575nm, 675-775nm) interference filter on a 500µm-thick LNA-FOP. It is then epoxied to our custom-designed 5x2.5mm CMOS image sensor with 80x36 pixels at a 55µm pitch. To characterize resolution, we image a standard fluorescent USAF 1951 target. To determine sensitivity, we prepare fluorescently stained PC3-PIP cell culture slides and image cell clusters of 10-1000 cells. As an illustration of clinical relevance, we image slide-mounted resected prostate tissue, fluorescently stained for tumor cells (anti-PSMA/anti-rabbit-IRDye680LT) and for nerves (anti-S100/anti-mouse-AlexaFluor488).

Results:

Measurements of filter performance demonstrate at least 6 orders of magnitude rejection of excitation at 488nm and 633nm across AOIs and a line resolution of 110µm. Sensitivity measurements show detection of clusters of less than 100 cells with 50ms exposures and excitation intensities of 28mW/cm^2 at signal-to-noise ratios (SNRs) of 4-20x depending the fluorophore used. Finally, *ex vivo* imaging results illustrate three clinically relevant scenarios: (1) the detection of microscopic disease (<100 cells) at the surgical margin, (2) simultaneous visualization and identification of both tumor and nerves within the same FoV, and (3) the identification of a nodal metastasis.

Conclusion:

This work presents a highly sensitive intraoperative imaging chip with a novel filter design that enables high-resolution, multi-target imaging within a from factor suitable for imaging hard-to-access areas in minimally invasive procedures. We demonstrate the potential of this technology to detect microscopic disease along the resection margin, undetected nodal disease, and at-risk healthy structures in real-time during surgery, fulfilling a critical need in surgical oncology.

Reference

1. Orosco, R. K. et al. Positive Surgical Margins in the 10 Most Common Solid Cancers. Scientific Reports 8, (2018).
2. Lima, T. F. N., Bitran, J., Frech, F. S. & Ramasamy, R. Prevalence of post-prostatectomy erectile dysfunction and a review of the recommended therapeutic modalities. International Journal of Impotence Research vol. 33 401–409 (2021).
3. Nagaya, T., Nakamura, Y. A., Choyke, P. L. & Kobayashi, H. Fluorescence-guided surgery. Frontiers in Oncology vol. 7 (2017).
4. Ma, L. & Fei, B. Comprehensive review of surgical microscopes: technology development and medical applications. Journal of Biomedical Optics 26, (2021).
5. Pogue, B. W. Perspective review of what is needed for molecular-specific fluorescence-guided surgery. Journal of Biomedical Optics 23, 1 (2018).
6. Greenbaum, A. et al. Imaging without lenses: Achievements and remaining challenges of wide-field on-chip microscopy. Nature Methods vol. 9 889–895 (2012).

7. Papageorgiou, E. P., Boser, B. E. & Anwar, M. An angle-selective CMOS imager with on-chip micro-collimators for blur reduction in near-field cell imaging. in Proceedings of the IEEE International Conference on Micro Electro Mechanical Systems (MEMS) vols. 2016-February 337–340 (Institute of Electrical and Electronics Engineers Inc., 2016).
8. Dandin, M., Abshire, P. & Smela, E. Optical filtering technologies for integrated fluorescence sensors. Lab on a Chip vol. 7 955–977 (2007).
9. Papageorgiou, E. P., Boser, B. E. & Anwar, M. Chip-Scale Angle-Selective Imager for in Vivo Microscopic Cancer Detection. IEEE Transactions on Biomedical Circuits and Systems 14, 91–103 (2020).
10. Sasagawa, K. et al. Highly sensitive lens-free fluorescence imaging device enabled by a complementary combination of interference and absorption filters. Biomedical Optics Express 9, 4329 (2018).

Oral Presentation

Disclosures: The authors have disclosed no financial interest.

144-Adapting Primary and Engineered Macrophages for Tumor Visualization: a dual approach

Presenter: Giorgia Zambito, Erasmus Medical Center

Chintan Chawda[1], **Giorgia Zambito[2]**, Clemens Lowik[3], Laura Mezzanotte[4]

[1]Erasmus Medical Center, Netherlands
[2]Erasmus Medical Center, Rotterdam, Zuid-Holland, Netherlands
[3]Erasmus University Rotterdam, Rotterdam, Zuid Holland, Netherlands
[4]Erasmus Medical Center, Rotterdam, Netherlands

Abstract Body:
Macrophage, a key component of immune cell population, owing to its cellular plasticity is found to be a contributing factor both in cancer progression(1,2) and suppression(3,4). A seminal work proposed injected macrophages as pan-cancer sensor due to their preference to accumulate in breast tumors(5). However, evidence of this behavior is still lacking in different tumor models, let alone a transgenic mice model dedicated to visualize this.

Design Objective of the Study:
The primary aim of this project is to visualize accumulation of genetically engineered macrophages injected in melanoma tumor mouse models. The second aim would follow this proof of concept to dedicate a reporter mouse model that allows visualization of transgenic macrophages by dual-modality optical imaging, i.e. fluorescence (Fl) and bioluminescence (Bl) imaging. Transgenic macrophages would then be used to visualize pancreatic cancer.

Methodology and Results:
Firstly, the BMC2 macrophages (Cellosaurus, CVCL_2I36, derived from C57BL/6 mice) and metastatic melanoma tumor cells (B16F10, ATCC CRL-6475) were transduced by lentiviral vectors for equimolar expression of CBG2 (click beetle red) (λ=680nm) and CBR2 (near-infra-red click beetle) (λ=740nm) luciferases, respectively (Fig.a) (6,7). For in vivo experiments, CBR2 expressing B16F10 melanoma cells (4 x 104 cells) were injected intravenously (iv) in C57BL/6 mice. Tumor growth was monitored over time by CBR2-specific bioluminescence. BMC2-CBG2 macrophages were pre-labeled with a near-infrared fluorescent dye (Xenolight DiR, 320 µg/mL) and injected iv (10×10^6 cells) at day 14 post melanoma injection. Naphthyl luciferin substrate (NH_2NPLH2) was injected intraperitoneally (ip) (220mg/kg) that was used as a single substrate for CBG2 and CBR2 detection. The Fl emissions from BMC2-CBG2 and from B16-CBR2 metastatic melanoma were detected from the lungs at 72 h (Fig.1b). This was performed also at 24, 48 and 72 hour post BMC2-CBG2 injection. The Bl spectral unmixing algorithm was applied to distinguish co-localized bioluminescent signals of BMC2-CBG2 and B16F10-CBR2 in the lungs (Fig. 1c). Ex vivo BL quantification show metastasis (magenta color) and BMC2-CBG2 macrophages (green color) co-localized in the lungs (Fig. 1d). Secondly, a transgenic macrophage reporter mouse was developed for visualization of primary macrophage during pancreatic carcinoma progression and metastasis. To do so, CRISPR/CAS knock in of MRC-1 promoter was performed. This promoter drives the expression of a reporter gene fusion consisting of click beetle red luciferase (CBR2) and mKate2 fluorescent protein. To ensure stable expression this entire gene cassette is introduced in the ROSA26 locus of albino black/6 mice. MRC1 (mannose receptor C-type 1) also known as CD206, is a type 1 membrane receptor (8) expressed in macrophages making MRC1 as an ideal as promoter to report macrophages in our model. Based on this model, bone marrow derived myeloid progenitor cells when polarized to macrophage lineage (naïve-macrophage) using mCSF1factor (50ng/ml), yielded 99.3% macrophage population (Figure 1d). This was based from CD11b gating in FACS analysis. In addition, these naïve macrophages could be further polarized to pro-inflammatory (M1-like) macrophages using lipopolysaccharides (LPS) (100ng/ml) and INF-γ (50ng/ml) (Figure 1e, right). Likewise, polarization towards anti-inflammatory (M2-like) macrophages were possible when exposed to IL-4 (10ng/ul) (persuasive data). This reflects the cellular plasticity of macrophage towards the micro-environmental (M.E) stimuli. Furthermore, the naïve transgenic macrophages (10×10^6 cells) pre-labeled DiR dye were injected in C57BL/6 mice engrafted with subcutaneous pancreatic cancer cells (3×10^5 cells) (persuasive data). Lastly, macrophages were visualized for the hour 24th, 48th, 72nd and day 7 th and 9 th. Bl and Fl imaging demonstrated a significant accumulation of injected macrophages around tumor from 48 to 72 hours (persuasive data).

Conclusion:
Together, both the engineered and the primary reporter macrophages could be successfully visualized in both metastatic melanoma and pancreatic tumor.

Reference

1. Laoui D, Movahedi K, Van Overmeire E, Van den Bossche J, Schouppe E, Mommer C, Nikolaou A, Morias Y, De Baetselier P, Van Ginderachter JA. Tumor-associated macrophages in breast cancer: distinct subsets, distinct functions. Int J Dev Biol. 2011;55(7-9):861–7.
2. DeNardo DG, Ruffell B. Macrophages as regulators of tumour immunity and immunotherapy. Nat Rev Immunol (2019) 19(6):369–82. doi: 10.1038/s41577-019-0127-6
3. Bruns H, Büttner M, Fabri M, Mougiakakos D, Bittenbring JT, Hoffmann MH, et al. Vitamin D-dependent induction of cathelicidin in human macrophages results in cytotoxicity against high-grade B cell lymphoma. Sci Transl Med (2015) 7(282):282ra47. doi: 10.1126/scitranslmed.aaa3230
4. Beatty GL, Chiorean EG, Fishman MP, Saboury B, Teitelbaum UR, Sun W, et al. CD40 agonists alter tumor stroma and show efficacy against pancreatic carcinoma in mice and humans. Science. 2011;331:1612–16.]

5. Aalipour, Amin et al. "Engineered immune cells as highly sensitive cancer diagnostics." Nature biotechnology (2019) 37,5: 531-539.
6. Hall MP, Woodroofe CC, Wood MG, et al. Click beetle luciferase mutant and near infrared naphthyl-luciferins for improved bioluminescence imaging. Nature Communications (2018); 9:132.
7. Zambito, G. et al. Red-shifted click beetle luciferase mutant expands the multicolor bioluminescent palette for deep tissue imaging. iScience (2021); 24.
8. Feinberg, Hadar et al. "Structural analysis of carbohydrate binding by the macrophage mannose receptor CD206." The Journal of biological chemistry vol. 296 (2021): 100368. doi:10.1016/j.jbc.2021.100368

Oral Presentation

Disclosures: The authors have disclosed no financial interest.

145-Targeted multicolor in vivo imaging over 1,000 nm enabled by nonamethine cyanines

Presenter: Mara Saccomano, Helmholtz Zentrum Munchen

Mara Saccomano[1], Michael P. Luciano[2], Venu G. Bandi, Martin J. Schnermann, Oliver Bruns[3]

[1]Helmholtz Zentrum Munchen, Munich, Germany
[2]National Cancer Institute, Frederick, MD
[3]Helmholtz Zentrum Munchen, München, Bayern, Germany

Recent progress has shown that using wavelengths between 1000 and 2000 nm, referred to as the Shortwave Infrared range (SWIR), can enable in vivo imaging at depths and resolution not possible with conventional optical wavelengths such as visible (<700nm) and near infrared (NIR, 700-1000 nm) 1. However, a critical bottleneck in this field is access to biologically compatible and targeted fluorescent probes that operate in this range with well-separated absorbance maxima and efficient emission in the SWIR region – properties critical especially for in vivo multiplexing experiments. In this context, indocyanine dyes are broadly used in multiplexed fluorescence-based experiments. Moreover, derivatives of heptamethine- indocyanines (e.g. Cy7, IRDye800CW and indocyanine green, ICG), which are the most broadly applied molecules not only for preclinical in vivo NIR imaging but also for clinical use [2], were recently found to exhibit substantial emission beyond 1,000nm [3]. The use of heptamethine indocyanine "tail imaging" in the SWIR has been also investigated in the clinic using the FDA-approved NIR fluorophore, ICG [4]. This study extends the biological utility of the indocyanine scaffold to longer wavelengths for performing fluorescence guided surgery (FGS) in multicolor in tumor mice, with negligible crosstalk between the channels. Enabled by a rational design process, persulfonated indocyanine dyes (FNIR-872 and FNIR1072) were generated with absorbance maxima at 872 and 1072 nm through catechol- and aryl-ring fusion, respectively, onto the nonamethine scaffold. Both dyes were successfully conjugated to a therapeutic monoclonal antibody (Panitumumab, against the epidermal growth factor receptor (EGFR) overexpressed in multiple cancers) or to a glucan molecule such as dextran, commonly used in microscopy experiments for vasculature imaging. Both conjugates were tested in orthotopically transplanted breast tumor mice (MDA-MB-468, highly expressing EGFR) in combination with the heptamethine dye ICG. These chemical and biological studies were supported by complementary advances in a custom-built SWIR imaging setup and software package for multicolor real-time imaging in vivo that incorporates different NIR laser excitation sources specific for each dye (λex = 785 nm for ICG, λex = 892 nm for FNIR-872 and λex = 968 nm for FNIR-1072), as well as a 1300 nm LED for reflectance imaging. Lasers and LEDs were sequentially triggered and long-pass emission filters (>1050nm) were used to detect the fluorescence emission of these dyes (excitation multiplexing). Panitumumab targeted- tumor imaging was successfully performed using FNIR-872-mAb and FNIR-1072-mAb, revealing comparable tumor to background (TBR) and tumor signal to clinically used IR-800CW-mAb.

In addition, multiplexed three- colors in vivo imaging using monoclonal antibody Panitumumab and dextran- conjugates with FNIR-872 or FNIR-1072 in tumor mice illustrate the benefits of concurrent labeling of the tumor mass as well as the macro and micro vasculature in the surroundings. Moreover, these conjugates were multiplexed against ICG dye for labeling in parallel lymphatic vessels, while the reflection channel was used for room light visualization of the surface of the mouse.

These efforts demonstrate the potential of two novel bioconjugatable indocyanines derived dyes suitable for targeted- SWIR- FGS in multicolor in combination with existing heptamethine indocyanines. The high acquisition speed allowed us to precisely perform fluorescence-guided resection of tumor mass and associated lymph-node in tumor mice. These molecules in combination with the multi-color real time visualization software tool we have developed will have applications in diverse preclinical and clinical contexts where multiplexed information of targeted biological structures is needed.

Reference

1. Zhu, B.; Kwon, S.; Rasmussen, J. C.; Litorja, M.; Sevick-Muraca, E. M., Comparison of NIR Versus SWIR Fluorescence Image Device Performance Using Working Standards Calibrated With SI Units. IEEE Trans Med Imaging 2020, 39 (4), 944-951.
2. Barth, C. W.; Gibbs, S. L., Fluorescence Image-Guided Surgery - a Perspective on Contrast Agent Development. Proc SPIE Int Soc Opt Eng 2020, 11222.
3. Carr, J. A.; Franke, D.; Caram, J. R.; Perkinson, C. F.; Saif, M.; Askoxylakis, V.; Datta, M.; Fukumura, D.; Jain, R. K.; Bawendi, M. G.; Bruns, O. T., Shortwave infrared fluorescence imaging with the clinically approved near-infrared dye indocyanine green. Proc Natl Acad Sci U S A 2018, 115 (17), 4465-4470.
4. Hu, Z.; Fang, C.; Li, B.; Zhang, Z.; Cao, C.; Cai, M.; Su, S.; Sun, X.; Shi, X.; Li, C.; Zhou, T.; Zhang, Y.; Chi, C.; He, P.; Xia, X.; Chen, Y.; Gambhir, S. S.; Cheng, Z.; Tian, J., First-in-human liver-tumour surgery guided by multispectral fluorescence imaging in the visible and near-infrared-I/II windows. Nat Biomed Eng 2020, 4 (3), 259-271.

Oral Presentation

Disclosures: The authors have disclosed no financial interest.

146-Co-hyperpolarization of [1-13C]dehydroascorbate and [1-13C] pyruvic acid enhances the signal lifetime of hyperpolarized dehydroascorbate and enables simultaneous dynamic molecular imaging of brain redox and glycolytic activity

Presenter: Nathaniel Kim, Memorial Sloan Kettering Cancer Center

Nathaniel Kim[1], Saket Patel[2], Marjan Berishaj[3], Elizabeth Coffee[3], Paola Porcari[3], Kayvan Keshari[3]

[1]Memorial Sloan Kettering Cancer Center, New York
[2]Memorial Sloan Kettering Cancer Center
[3]Memorial Sloan Kettering Cancer Center, New York, NY

Introduction:

Hyperpolarized dehydroascorbate (HP DHA) was first reported as a potential redox sensor more than a decade ago[1] but has since found limited use in preclinical magnetic resonance spectroscopy.[2-4] This is due to the low polarization levels and limited concentration achievable by previous formulations. We sought to increase the polarization of DHA by generating a new formulation combining DHA with pyruvic acid (PA) and co-hyperpolarizing both substrates simultaneously. We herein demonstrate this fully developed method which allows for the metabolic imaging of glycolytic activity and redox status simultaneously *in vivo.*

Method:

Co-hyperpolarization of [1-^{13}C]DHA and [1-^{13}C]PA – 150μL of a 40:60 v/v mixture of monomeric [1-^{13}C]DHA and [1-^{13}C]PA containing 15 mM AH111501 trityl radical was hyperpolarized on a SpinLab polarizer (GE) for 2 hours. The frozen sample was dissolved in 13mL D_2O and collected in a flask containing an equimolar amount of sodium acetate resulting in a pH 5 solution containing 40 mM HP DHA and 100 mM HP PA. Polarization and ^{13}C T_1 of the hyperpolarized DHA/PA solution was measured at 1T (Magritek) by recording ^{13}C spectra every 3s using a 5 degree flip angle. The polarization and T_1 for [1-^{13}C] DHA and [1-^{13}C]pyruvic acid were measured as 25%, 92s and 30%, 99s respectively.

In vivo magnetic resonance spectroscopy (MRS) of co-hyperpolarized [1-^{13}C]DHA and [1-^{13}C]PA – Time-resolved MRS studies centered on a 10 mm axial slice across the brain were carried out on a 3T MRI spectrometer (Bruker) with a ^{13}C urea phantom present for chemical shift reference. ^{13}C MRS spectra were acquired every second and resonances of bicarbonate, pyruvate, DHA, alanine, vitamin C, and lactate were observed throughout the time course of this study.

Dynamic magnetic resonance imaging of co-hyperpolarized [1-^{13}C] DHA and [1-^{13}C]PA – NSG mice were injected with 250μL of 40mM HP DHA and 100 mM HP pyruvate. ^{13}C HP MRS was performed using an axial 2D EPSI (3s TR) centered on a 10mm slice across the brain at the start of injection for 90s. Lactate/(Lactate + Pyruvate + Bicarbonate) (HP Lac/Total), bicarbonate-to-total pyruvate and Vitamin C/(Vitamin C + DHA) (HP VitC/Total) ratios were calculated for representative brain voxels at 0s post-injection and 30s post-injection by taking the area under the curve of every metabolite for both time-points. The correlation between time of acquisition, glycolytic activity, and redox status were statistically compared.

Results:

The performance of DHA with the developed formulation shows 7 times better polarization efficiency compared to previous reports of HP DHA (**Figure A**). Additionally, the sample does not contain an external compound for glassing and is made of only endogenous substrates, affording a dissolution of HP DHA and HP pyruvate with prolonged hyperpolarized lifetimes. All pyruvate metabolites classically observed in HP MRI were observed and were chemical shift resolved from DHA and ascorbate (**Figure B**). The increased signal enhancement allowed for dynamic MRS of DHA and pyruvate (**Figure C**). Significant differences in the signal intensity of pyruvate and DHA metabolite resonances are observed over time. The HP Lac/Total ratios at 0s and 30s post-injection are 0.095±0.035 and 0.192±0.042 (P=0.0002), respectively. The HP VitC/Total ratios at 0 seconds and 30s post-injection are 0.104±0.028 and 0.187±0.052 (P=0.0014), respectively (**Figure D**). There is moderate correlation between the observed HP Lac/Total and HP VitC/Total ratios (linear fit, R^2=0.562) 0s post-injection.

Conclusion:

We demonstrated a new method for co-hyperpolarizing DHA and pyruvic acid. This method greatly enhances the signal lifetime of hyperpolarized DHA. Redox status and glycolytic activity can be metabolically imaged simultaneously for the first time. Conversion rates of pyruvate and DHA can be compared and correlations between them afford new information about the metabolic status of the brain.

Reference

1. Keshari, K. R., Kurhanewicz, J., Bok, R., Larson, P. E. Z., Vigneron, D. B., Wilson, D. M. (2011). Hyperpolarized 13C dehydroascorbate as an endogenous redox sensor for in vivo metabolic imaging. PNAS, 150(46), 18606-18611.
2. Bohndiek, S. E., Kettunen, M. I., Hu, D., Kennedy, B. W. C., Boren, J., Gallagher, F. A., Brindle, K. M. (2011). Hyperpolarized [1-13C]-ascorbic and dehydroascorbic acid: vitamin C as a probe for imaging redox status in vivo. JACS, 133(30), 11795-11801.
3. Timm, K. N., Hu, D., Williams, M., Wright, A. J., Kettunen, M. I., Kennedy, B. W. C., Larkin, T. J., Dzien, P., Marco-Rius, I., Bohndiek, S. E., Brindle, K. M. (2017). Assessing oxidative stress in tumors by measuring the rate of hyperpolarized [1-13] dehydroascorbic acid reduction using 13C magnetic resonance spectroscopy. Journal of Biological Chemistry, 292(5), 1737-1748.
4. Qin, H., Carroll, V. N., Sriram, R., Villanueva-Meyer, J. E., von Morze, C., Wang, Z. J., Mutch, C. A., Keshari, K. R., Flavell, R. R., Kurhanewicz, J., Wilson, D. M. (2018). Imaging glutathione depletion in the rat brain using ascorbate-derived hyperpolarized MR and PET probes. Scientific Reports, 8, 7928.

Oral Presentation

Disclosures: The authors would like to disclose that HP pyruvate is an investigational device.

147-A New Library of Nano-Probes to Enable Highly Multiplexed Spatial Profiling using Raman Imaging

Presenter: Olga Eremina, University of Southern California

Olga Eremina[1], Cristina Zavaleta[2], Alexander Czaja[3], Augusta Fernando[3], Dmitry Eremin[1], Arjun Aron[2]

[1]*University of Southern California, Los Angeles, CA*
[2]*University of Southern California Viterbi School of Engineering, Los Angeles, CA*
[3]*University of Southern California*

Objectives:

With the advent of several new targeted and immuno-therapies, knowing the molecular expression profile of an individual patient's tumor is more important than ever to properly stratify patients and ensure an effective treatment response. Precision medicine seeks advancements in molecular spatial profiling techniques with highly multiplexed imaging capabilities and sub-cellular resolution. Surface-enhanced Raman spectroscopy (SERS) imaging offers promise through the utilization of nano-based contrast agents that exhibit narrow spectral features and molecular specificity.[1] SERS makes Raman scattering intensities competitive with fluorescence methods while offering the added benefit of unsurpassed multiplexing capabilities. Here, we present the largest library of 26 individually distinct SERS nanoparticles (NPs) bearing high spectral uniqueness to arm researchers and clinicians facilitating unmixing of up to 26 components in a single imaging pixel. We demonstrated the utility of our SERS NPs for targeting specific biomarkers on cultured cells and profiling cancerous human tissue sections for highly multiplexed optical imaging. This study showcases the far-reaching capabilities of SERS-based Raman

imaging in molecular profiling to improve personalized medicine and patient outcome.

Methods:
Fabrication of SERS NPs: De-novo synthesized NPs were prepared by: (1) creation of 60-nm spheric AuNPs; (2) labeling of AuNPs with unique Raman reporter; (3) silica coating; (4) thiolation; (5) conjugation with biotargeting species; (6) capping remaining thiols; (7) purification. *SERS spectra simulation:* Density functional theory (DFT) facilitated selection of Raman reporters which met the key criterion of high spectral uniqueness.[2] *Multiplexed imaging assessment:* A computer-controlled x–y translation stage was used to raster scan various SERS NP mixtures. *Cancer cell imaging:* Each cell line (200,000 cells) was incubated with 10 µL of 1.5 nM NP staining solution for 15 min. *In-vivo imaging:* Mice were injected with 8 fmol of 26 equally mixed SERS NP flavors. *Human tissue imaging*: Human cancerous breast tissue sections were stained with SERS NPs for HER2.

Results:
We demonstrated that, when both spatially separated and colocalized, our library of 26 SERS NPs can be successfully unmixed in a single Raman spectrum acquisition **(Fig. 1A)**. Notable multiplexing capacity and high sensitivity, with limits of detection in 10^{-18} M range, of SERS NPs break new ground in molecular spatial profiling (**persuasive data**). Active biomarker targeting was assessed with flow cytometry and Raman imaging of various types of cancer cells showing excellent spatial co-registration with the cells depicted in the white light images **(Fig. 1B)**. We observed high specific-to-nonspecific ratios of NPs targeting cells based on protein overexpression profiles: EGFR 11.3±0.8 (n=35), CD47 7.4±0.3 (n=32), integrin $\alpha_v\beta_3$ 6.1±0.6 (n=27), cMET 3.8±0.3 (n=20), HER2 9.2±0.8 (n=24). Moreover, our targeted SERS NPs allow spatial recognition of each cancer cell type after a single imaging acquisition of the mixed cells. We also demonstrated the ability to non-invasively unmix and localize the presence of all 26 NPs in the liver of a mouse after they were mixed and administered intravenously **(Fig. 1C)**. Finally, SERS imaging of HER2 expression on human tissue sections was validated with gold standard immunohistochemistry (IHC) **(Fig. 1D)**. Tumor areas with stronger IHC coloration demonstrated higher SERS specific-to-nonspecific binding ratios. The Pearson correlation coefficient between SERS binding ratios and IHC color intensity was 0.96 (p=0.05, n=20), indicating strong correlation between the techniques.

Conclusion:
This is the first report presenting an expansive library of 26 NPs, each bearing a unique spectral fingerprint, and revealing the potential of NPs to gain an unparalleled understanding of the spatial relationships between a multitude of cell types using Raman imaging. Our ability to deconvolve a mixture of 26 SERS NPs in a single imaging pixel opens new opportunities to efficiently interrogate heterogeneous molecular expression found within and across patient samples.

Reference
1. Zavaleta, C. L.; Kircher, M. F.; Gambhir, S. S., Raman's "effect" on molecular imaging. J. Nucl. Med. 2011, 52 (12), 1839-1844.
2. Eremina, O. E.; Eremin, D. B.; Czaja, A.; Zavaleta, C., Selecting surface-enhanced Raman spectroscopy flavors for multiplexed imaging applications: Beyond the experiment. J. Phys. Chem. Lett. 2021, 12 (23), 5564-5570.

Oral Presentation

Disclosures: The authors have disclosed no financial interest.

148-Phototherapy of Alzheimer's disease with physically and molecularly produced light

Presenter: Biyue Zhu, Massachusetts General Hospital

Shi Kuang[1], **Biyue Zhu[2]**, Jing Zhang[3], Jun Yang[4], Chongzhao Ran[4]
[1]*Massachusetts General Hospital, Charlestown, MA Massachusetts*

[2]*Massachusetts General Hospital, Boston, MA*
[3]*Harvard Medical School, Charlestown, MA*
[4]*Harvard Medical School*

Over the past decades, classical drug development approaches for Alzheimer's disease have yielded limited success, and this futileness has prompted scientists to seek non-classical approaches. In this report, CRANAD-147 and ADLumin-4 was designed, synthesized and characterized as a novel approache for phototherapy of AD via attenuating Aβ's neurotoxicity. CRANAD-147 contains curcumin scaffold that can bind with the hydrophobicity core of Aβ and diazirine scaffold that can be reacted to produce reactive oxygen species upon light stimulation. ADLumin-4 was designed to activate CRANAD-147 by chemiluminescence resonance energy transfer (CRET) upon binding to the long axis of Aβ fibrils. With irradiation of LED light or with molecularly generated light (dubbed as "molecular light") from chemiluminescence probe ADLumin-4, photolabile CRANAD-147 could cause changes of size properties, structures (sequences) and neurotoxicity of amyloid beta (A*β*) species in vitro. Mass spectra indicated that the photoreaction with photolabile curcumin changed the properties of Aβ via oxidation the vulnerable amino acids such as methione and histidines. In addition, with the assistance from molecular chemiluminescence imaging, the combination of CRANAD-147/LED or CRANAD-147/ADLumin-4 (molecular light) could slow down the accumulation of A*β*s in transgenic 5xFAD mice in vivo. Due to the unlimited capacity of tissue penetration of molecular light in vivo, phototherapy with the combination of photolabile A*β* ligand and molecular light has great potential as an alternative approach for AD drug discovery.

Reference
1. K. C. Moore, Photomed. Laser Surg. 2013, 31, 563-564.
2. a) Y. Zhang, Y. Hao, S. Chen, M. Xu, Front Chem 2020, 8, 770; b) C. Ran, Z. Zhang, J. Hooker, A. Moore, Mol Imaging Biol 2012, 14, 156-162.
3. G. Hong, A. Antaris, H. Dai, Nature Biomedical Engineering 2017, 1, 0010.
4. D. J. Selkoe, Nature 1999, 399, A23-31.
5. a) C. B. Anfinsen, Science 1973, 181, 223-230; b) R. Nelson, M. R. Sawaya, M. Balbirnie, A. O. Madsen, C. Riekel, R. Grothe, D. Eisenberg, Nature 2005, 435, 773-778; c) R. Riek, D. S. Eisenberg, Nature 2016, 539, 227-235.
6. a) R. E. Tanzi, R. D. Moir, S. L. Wagner, Neuron 2004, 43, 605-608; b) B. Das, R. Yan, CNS Drugs 2019, 33, 251-263; c) J. Cummings, G. Lee, K. Zhong, J. Fonseca, K. Taghva, Alzheimers Dement (N Y) 2021, 7, e12179.
7. a) F. Yang, G. P. Lim, A. N. Begum, O. J. Ubeda, M. R. Simmons, S. S. Ambegaokar, P. P. Chen, R. Kayed, C. G. Glabe, S. A. Frautschy, G. M. Cole, J. Biol. Chem. 2005, 280, 5892-5901; b) E. K. Ryu, Y. S. Choe, K. H. Lee, Y. Choi, B. T. Kim, Journal of medicinal chemistry 2006, 49, 6111-6119.
8. a) C. Ran, X. Xu, S. B. Raymond, B. J. Ferrara, K. Neal, B. J. Bacskai, Z. Medarova, A. Moore, J Am Chem Soc 2009, 131, 15257-15261; b) X. Zhang, Y. Tian, Z. Li, X. Tian, H. Sun, H. Liu, A. Moore, C. Ran, J Am Chem Soc 2013, 135, 16397-16409; c) X. Zhang, Y. Tian, C. Zhang, X. Tian, A. W. Ross, R. D. Moir,

H. Sun, R. E. Tanzi, A. Moore, C. Ran, Proc Natl Acad Sci U S A 2015, 112, 9734-9739.
9. X. Zhang, Y. Tian, P. Yuan, Y. Li, M. A. Yaseen, J. Grutzendler, A. Moore, C. Ran, Chem Commun (Camb) 2014, 50, 11550-11553.

Oral Presentation

Disclosures: The authors have disclosed no financial interest.

149-Preclinical evaluation of 68Ga- and 177Lu-radiolabeled integrin αvβ6-targeting peptides

Presenter: Tanushree (Nina) Ganguly, University of California, Davis

Tanushree (Nina) Ganguly[1], Nadine Bauer[1], Ryan A. Davis[2], Rebecca Harris[1], Sven Hausner[3], Yng (Sarah) Tang[4], Julie Sutcliffe[1]

[1]University of California, Davis, Sacramento, CA
[2]University of California, Davis, Sacramnento, CA
[3]UC Davis Health, Sacramento, CA
[4]University of California, Davis, San Jose

Objectives:
The integrin $\alpha_v\beta_6$ is an epithelial specific cell surface receptor that is overexpressed in numerous malignancies including pancreatic ductal adenocarcinomas (PDAC) and is an indicator of poor prognosis [1-5]. Here, we evaluated an $\alpha_v\beta_6$ binding peptide [6], DOTA-5G (Peptide **1**) radiolabeled with Gallium-68 (^{68}Ga, $t_{1/2}$ = 68 min) for positron emission tomography/computed tomography (PET/CT) imaging in mice bearing $\alpha_v\beta_6$ (+) pancreatic xenograft tumors. With the goal to improve the circulation time and renal recycling, and increase tumor uptake, Peptide **1** was further modified with an albumin-binder moiety (ABM) to yield Peptide **2** (DOTA-ABM-5G). **1** and **2** were labeled with Lutetium-177 (^{177}Lu, $t_{1/2}$ = 6.7 days) and evaluated for their therapeutic efficacy [7-8].

Methods:
Peptides **1** and **2** were synthesized using standard Fmoc chemistry on solid phase and their affinity for $\alpha_v\beta_6$ assessed by ELISA. The peptides were radiolabeled with ^{68}Ga and ^{177}Lu and evaluated for *in vitro* cell binding, internalization, and efflux in the $\alpha_v\beta_6$ (+) expressing human pancreatic cancer cell line BxPC-3. *In vivo* PET/CT imaging (^{68}Ga-**1**) and biodistribution studies (^{68}Ga-**1**, ^{177}Lu-**1**, and ^{177}Lu-**2**) were performed in mice bearing BxPC-3 xenograft tumors. Therapeutic efficacy of ^{177}Lu-**2** was determined in mice bearing BxPC-3 tumors: Groups-Saline (Group 1), Peptide **2** (Group 2), 74 MBq ^{177}Lu-**2** (Group 3) and 2 × 37 MBq ^{177}Lu-**2** (Group 4).

Results:
Peptides **1** and **2** demonstrated high affinity for the integrin $\alpha_v\beta_6$ by ELISA (35.6 ± 1 nM and 27.3 ± 4 nM, respectively). ^{68}Ga-**1**, ^{177}Lu-**1**, and ^{177}Lu-**2** were synthesized at 18.5 MBq/nmol molar activity, in >98% radiochemical purity (RCP). Rapid *in vitro* binding (>16% at 1 h) and internalization (>72% of bound at 1 h) of ^{68}Ga-**1**, ^{177}Lu-**1**, and ^{177}Lu-**2** was observed in BxPC-3 cells, with negligible efflux at 1 h. PET/CT imaging showed clear delineation of the BxPC-3 tumors at 1 and 2 h post-injection of ^{68}Ga-**1**, with predominantly renal excretion. The biodistribution studies also demonstrated uptake of ^{68}Ga-**1** in the BxPC-3 tumor (% ID/g): 2.6 ± 0.8, 1 h and 2.03 ± 0.57, 2 h (Figure 1A). Introduction of the ABM in ^{177}Lu-**2** resulted in 3-5-fold increase in tumor uptake and retention over time compared to ^{177}Lu-**1**, (% ID/g at 1 and 72 h – ^{177}Lu-**1**: 1.23 ± 0.19, 0.81 ± 0.16 and ^{177}Lu-**2**: 4.54 ± 0.42, 5.29 ± 0.75; Figure 1B and 1C). Increased blood residence (1 h % ID/g: 0.1 ± 0.03 (^{177}Lu-**1**) vs. 5.36 ± 0.71 ([^{177}Lu-**2**); p = 0.0001) and a 4-fold improvement in BxPC-3-to-kidney ratio at 72 h were also observed (0.14 ± 0.05 (^{177}Lu-**1**) vs. 0.60 ± 0.02 (^{177}Lu-**2**); p = 0.0001). Based on these favorable pharmacokinetics, ^{177}Lu-**2** was evaluated preclinically for therapeutic efficacy. The overall survival of mice treated with ^{177}Lu-**2** was prolonged (median survival - 82 d (Group 3), 113 d (Group 4)) compared to 56 d for the controls (Groups 1 and 2), with groups 3 and 4 having 30% and 43% overall survival respectively, at the end of 120 d (Figure 1D). No notable changes in body weight were observed in any group.

Conclusions:
We have developed and tested a novel theranostic peptide pair targeting integrin $\alpha_v\beta_6$ in a mouse model. ^{68}Ga-**1** successfully imaged $\alpha_v\beta_6$ (+) BxPC-3 tumor and ^{177}Lu-**2** displayed favorable pharmacokinetics and superior therapeutic efficacy, especially on a two-dose regimen. ^{68}Ga-**1**/^{177}Lu-**2** holds promise for targeted imaging and therapy of $\alpha_v\beta_6$ (+) tumors, and warrants further investigation clinically.

Acknowledgements: This work was supported by the Stand Up To Cancer and Lustgarten Foundation Pancreatic Cancer Collective (PCC) New Therapies Challenge Grant (SU2C-AACR-PCC-06-18).

Reference

1. Carcinogenesis 2002, 23, 237.
2. Current Drug Targets 2009, 10, 645.
3. J Clin Invest 2005, 115, 339.
4. Cancer letters 2017, 403, 128.
5. Histopathology 2004, 45, 226.
6. Clin Cancer Res 2019, 25, 1206.
7. Bioconj Chem. 2019, 30, 487.
8. Mol Pharm . 2021, 18, 4437.

Oral Presentation

Disclosures: The authors have disclosed no financial interest.

150-Understanding the dynamics of cellular iron uptake and retention using live cell microscopy and magnetic particle imaging

Presenter: Olivia Sehl, Robarts Research Institute

Olivia Sehl[1], Maryam Berih[2], John Ronald[3], Paula Foster[1]

[1]Robarts Research Institute, London
[2]Western University, Toronto, ON
[3]Robarts Research Institute, London, ON

Abstract body:
Cell tracking with magnetic particle imaging (MPI) provides valuable information on the location and number of therapeutic cells after administration *in vivo*. For MPI detection, cells must be labeled with superparamagnetic iron oxide (SPIO) nanoparticles by co-incubation in cell culture. Transfection agents (TAs) are commonly used to enhance cellular incorporation of SPIO into cells [1]–[3]. Achieving high iron cell labeling permits the sensitive tracking of cells. There have been several longitudinal *in vivo* MPI cell tracking studies [4]–[9], however, cell proliferation is expected to reduce the SPIO per cell. In this study, we use MPI and microscopy to study mechanisms of SPIO uptake and retention in stem cells. These techniques provide complimentary information;

MPI provides quantitative measurements of average iron per cell and microscopy allows for visualization of cell labeling uniformity. Live cell microscopy is used to observe dynamics of SPIO endocytosis and partitioning with cell division, which occurs on the timescale of minutes. Methods: Mesenchymal stem cells were co-incubated with ferucarbotran (VivoTrax^{TM}, Magnetic Insight Inc.) for 4 hours with 60 g/mL protamine sulfate and 3 U/mL heparin [3] in 5 mL serum free low-glucose DMEM. Live cell microscopy was conducted with the Lux3 microscope (CytoSmart Inc.) using a 10x objective every 5 minutes. Then, 5 mL complete media was added for overnight incubation. Cells were washed 3 times with saline then 1 x 10^6 iron-labeled cells were collected for MPI (n = 4). The remaining cells were returned to culture and live cell microscopy was repeated to observe iron partitioning in dividing cells. Cells were collected from culture every day for 5 days for MPI. 2D MPI images were acquired on a Momentum^{TM} system (Magnetic Insight Inc.) with a 5.7 T/m selection field gradient and drive fields 20 mT (X-channel) and 26 mT (Z-channel). A cell cytospin was performed daily to assess iron labeling efficiency with Perl's Prussian blue (PPB) stain [10]. Results: With live cell microscopy, ferucarbotran endocytosis by stem cells can be visualized. Self-assembling nanocomplexes of heparin, protamine, and ferucarbotran form that are approximately 100 - 200 um in diameter (Fig i.). In multiple instances, cells are seen to approach these ferucarbotran clusters and engulf a small portion of the nanocomplex (Fig ii.). The MPI signal generated from ferucarbotran-labeled stem cells diminishes over time (Fig iii.). Quantification from images reveals on day 1, stem cells were labeled with 18 pg iron/cell and the iron loading per cell decreased over time (Fig iv.). Perl's Prussian blue stain shows that on day 1, nearly all cells are labeled with iron but in variable amounts. An overall reduction in cellular iron content is visualized over time (Fig v.). Live cell microscopy shows that iron is shared between daughter cells as cells divide (Fig vi.).

Discussion:

Ferucarbotran is a common cell labeling agent for both MRI and MPI, therefore understanding the uptake and retention mechanisms are valuable. To the best of our knowledge, the phenomenon of detachment and cellular uptake of ferucarbotran clusters from larger nanocomplexes has not been previously reported. The reduction in the amount of iron per cell, resulting from cell proliferation, leads to diminishing MPI cellular sensitivity over time. After 5 days in cell culture, the amount of iron (0.15 pg/cell x 1,000,000 cells = 150 ng) approaches a previously reported detection limit (76 ng) [11]. While MPI can provide direct measurements of SPIO mass, it does not represent the number of cells that are present in longitudinal cell tracking studies. In vivo stem cells are expected to divide much more slowly, still this work can be applied to any proliferative cell type. Overall, this study contributes important knowledge for monitoring SPIO-labeled cells with MPI.

Reference

1. S. Arbab et al., "Efficient magnetic cell labeling with protamine sulfate complexed to ferumoxides for cellular MRI," Blood, vol. 104, no. 4, pp. 1217–1223, 2004.
2. E. Wuerfel et al., "Electrostatically stabilized magnetic nanoparticles - An optimized protocol to label murinet cells for in vivo MRI," Front. Neurol., vol. DEC, no. December, pp. 1–9, 2011.
3. M. S. Thu et al., "Self-Assembling Nanocomplexes by combining Ferumoxytol, Heparin And Protamine For Cell Tracking by MRI HHS Public Access Author manuscript," Nat Med, vol. 18, no. 3, pp. 463–467, 2012.
4. B. Zheng et al., "Magnetic particle imaging tracks the long-term fate of in vivo neural cell implants with high image contrast," Sci. Rep., vol. 5, no. March, pp. 1–9, 2015.
5. B. Zheng et al., "Quantitative magnetic particle imaging monitors the transplantation, biodistribution, and clearance of stem cells in vivo," Theranostics, 2016.
6. P. Wang et al., "Magnetic particle imaging of islet transplantation in the liver and under the kidney capsule in mouse models," Quant. Imaging Med. Surg., vol. 8, no. 2, pp. 114–122, 2018.
7. G. Song et al., "Janus Iron Oxides @ Semiconducting Polymer Nanoparticle Tracer for Cell Tracking by Magnetic Particle Imaging," Nano Lett., vol. 18, no. 1, pp. 182–189, 2018.
8. H. Nejadnik, P. Pandit, O. Lenkov, A. P. Lahiji, K. Yerneni, and H. E. Daldrup-Link, "Ferumoxytol Can Be Used for Quantitative Magnetic Particle Imaging of Transplanted Stem Cells," Mol. Imaging Biol., vol. 21, no. 3, pp. 465–472, 2018.
9. Q. Wang et al., "Artificially Engineered Cubic Iron Oxide Nanoparticle as a High-Performance Magnetic Particle Imaging Tracer for Stem Cell Tracking," ACS Nano, vol. 14, no. 2, pp. 2053–2062, 2020.
10. C. Mcfadden, C. L. Mallett, and P. J. Foster, "Labeling of multiple cell lines using a new iron oxide agent for cell tracking by MRI," Contrast Media Mol. Imaging, 2011.
11. O. C. Sehl and P. J. Foster, "The sensitivity of magnetic particle imaging and

Oral Presentation

Disclosures: The authors have disclosed no financial interest.

151-Ultra-high resolution TOF-DOI Prism-PET brain scanner for accurate quantitative neuroimaging: first experimental brain phantom study

Presenter: Zipai Wang, Stony Brook University

Zipai Wang[1], Xinjie Zeng[1], Wanbin Tan[1], Eric Petersen[1], Xinjie Cao[1], Yixin Li[1], Andy LaBella[1], Anthony Boccia[1], Jinyi Qi[2], Dinko Franceschi[3], Anat Biegon[4], Wei Zhao[1], Amir H. Goldan[1]

[1]*Stony Brook University, Stony Brook, NY*
[2]*University of California, Davis, Davis, CA*
[3]*Stony Brook Medicine, Stony Brook, New York*
[4]*Stony Brook University, Stony Brook*

Introduction:

Positron emission tomography (PET) is an in vivo molecular imaging modality that plays an increasingly important role in neuroimaging. It has the potential to be an early diagnosis tool for brain disorders such as major depressive disorder (MDD) and Alzheimer's disease (AD), thanks to the advances in specific radiotracers that binds to a wide range of brain markers (i.e., [^{11}C]WAY-100635 to 5-HT_{1A} receptor[1] and [^{18}F]MK6230 to tau[2]). However, even the state-of-art brain dedicated PET scanners suffer from the trade-offs among spatial resolution, sensitivity, and system cost. The poor spatial resolution results in partial volume effect (PVE) that causes significant underestimation of binding potentials, especially for small brain structures surrounded by low uptake tissues (i.e., raphe nuclei, hippocampus, and locus coeruleus).[3] On the other hand, the low sensitivity degrades the signal-to-noise (SNR) ratio which leads to noisy parametric images with inaccurate tracer quantification. Thus, there is a growing interest in building a brain PET system that can cost-effectively achieve high sensitivity and ultra-high spatial resolution.

Method:

We have proposed the Prism-PET brain scanner based on our single-ended time-of-flight (TOF) and depth-of-interaction (DOI) capable Prism-PET detector technologies.[4] Our scanner can offer next-generation imaging performance based on 1) conformal

decagon geometry that improves the solid angle coverage and reducing acollinearity blurring, 2) 2-mm FWHM DOI resolution that mitigates the parallax error[5], 3) 274 ps TOF resolution that further boost the effective sensitivity,[6] and 4) ability to correct for inter-crystal scatter (ICS).[7] In this work, we present the first reconstructed images of our prototype scanner (Figure 1.a) using a customized 3D brain phantom with built-in hippocampus and dorsal raphe nuclei (DRN). The prototype scanner consists of 40 detector blocks per transaxial ring and one axial ring, forming an elliptical transaxial FOV of 291 mm (short diameter), 385 mm (long diameter), and an axial FOV of 25.5 mm. Each detector module was composed of 1.5 x 1.5 x 20 mm^3 LYSO crystals arranged in a 16 x 16 array and coupled with 4-to-1 ratios to an array of 3 x 3 mm^3 SiPM pixels. The customized brain phantom was filled with 1.64 mCi of ^{18}F and the activity concentration ratios among the DRN, hippocampus, gray matter, and white matter were 8:3:1:0.25 which simulates the binding potentials of $5HT_{1A}$ radiotracer found in autoradiography study.[1] The energy window was set to 460-560 keV and a 4 ns coincidence window was used for the phantom imaging. The ICS rejection and DOI-rebinning were performed on the list-mode coincidences and the data was reconstructed using 3D-LM-OSEM with TOF and point spread function (PSF) modeling by CASToR.[4,8] The phantom with the same setup was also imaged by Biograph TruePoint PET/CT. We quantified the imaging performance of the two systems by calculating the relative uptake ratio (RUR) value as the average voxel intensity of volume of interest (VOI) versus that of the gray matter.

Results:

The brain phantom images (Figure 1.b&e) prove that our scanner enables accurate visualization and quantification of fine brain structures, with a 4-fold and ~2-fold RUR improvements for the DRN and hippocampus, respectively, compared to the Biograph TruePoint (Figure 1.h). One must notice that the Prism-PET scanner can visualize the 0.8 mm white matter layers of the Hoffman phantom in the coronal view, demonstrating the ultra-high resolution in both transaxial and axial FOVs (Figure 1.b).

Conclusion:

The Prism-PET brain scanner enables quantitative molecular imaging of the human brain, including important brain structures that cannot be accurately resolved with existing PET scanners. The full-scale Prism-PET brain scanner with 12 detector rings will be a promising cost-effective candidate to advance the molecular imaging in both clinical and research areas.

Reference

1. Varnäs K, Halldin C, Hall H. Human brain mapping, 2004, 22(3): 246-260.
2. Therriault J, Pascoal T A, Lussier F Z, et al. Nature Aging, 2022: 1-10.
3. Beliveau V, Ganz M, Feng L, et al. Journal of Neuroscience, 2017, 37(1): 120-128.
4. Wang Z, Cao X, LaBella A, et al. Medical Physics, 2022.
5. LaBella A, Cao X, Petersen E, et al. Journal of Nuclear Medicine, 2020, 61(10): 1528-1533.
6. Cao X, La Bella A, Zeng X, et al. IEEE Transactions on Radiation and Plasma Medical Sciences, 2021.
7. Petersen E W, LaBella A, Howansky A, et al. 2020 IEEE Nuclear Science Symposium and Medical Imaging Conference (NSS/MIC). IEEE, 1-4.
8. Merlin T, Stute S, Benoit D, et al. Physics in Medicine & Biology, 2018, 63(18): 185005.

Oral Presentation

Disclosures: The authors have disclosed no financial interest.

152-A modular approach toward producing nanotherapeutics targeting the innate immune system

Presenter: Anna Ranzenigo, Icahn School of Medicine at Mount Sinai

Anna Ranzenigo[1], Mandy M. T. van Leent[2], Zahi Fayad[2], Willem Mulder[2], Abraham J. Teunissen[2]

[1]Icahn School of Medicine at Mount Sinai
[2]Icahn School of Medicine at Mount Sinai, New York, NY

Immunotherapies controlling the adaptive immune system are firmly established, but regulating the innate immune system remains much less explored. The intrinsic interactions between nanoparticles and phagocytic myeloid cells make these materials especially suited for engaging the innate immune system (1). However, developing nanotherapeutics is an elaborate process that typically needs to be repeated for each specific drug. Here, we demonstrate a modular approach that facilitates efficiently incorporating a broad variety of drugs in a nanobiologic delivery platform. Using a microfluidic formulation strategy, we produced 4 different sizes of apolipoprotein A1–based nanobiologics (20, 35, 65, 120 nm, only the 35 variant is shown; **Fig. 1A**). Nanobiologics were radiolabeled with ^{89}Zr, by functionalizing apoA-I with the chelator deferoxamine (DFO). Pharmacokinetics and biodistribution were monitored by a combination of PET imaging and *ex vivo* gamma counting (**Fig. 1B and 1C**). Flow cytometry was used to reveal their high myeloid cell uptake. Based on these results, we selected the 35 nm-sized nanocarrier for therapeutic studies. Subsequently, we set out to develop a prodrug approach that enhances the therapeutic payload's lipophilicity by functionalizing it with apolar promoieties. Rapamycin (2), diethyl malonate, (+)-JQ1 and GSK J-4, small-molecule inhibitors, were derivatized with lipophilic promoieties, ensuring their seamless incorporation and efficient retention in the lipid-based nanobiologics (comparison between the incorporation of drugs and prodrugs in nanobiologics are reported in **Fig. 1D**). This lipophilic prodrug strategy facilitates incorporating a broad variety of drugs without modifying the nanocarrier, thereby establishing a modular approach for developing nanotherapeutics targeting the innate immune system. To test the rapamycin prodrug-loaded nanobiologics (mTORi-NB), we performed biodistribution, toxicity, and efficacy studies in a mouse model for heart allograft transplantation, revealing significant prolongation of graft survival (**Fig 1E**). To pave the way for clinical translation, we also studied mTORi-NB biodistribution and toxicity in two nonhuman primates. ^{89}Zr-labeled mTORi-NB were intravenously administered and their in vivo distribution was examined using a fully integrated three-dimensional PET/MRI protocol. Dynamic scanning revealed that within the first 20 min after administration, mTORi-NB accumulate in the spleen, liver, kidney, and bone marrow (**Fig. 1F and 1G**). Static whole-body PET/MRI performed 2 and 48 hours after injection allowed quantifying mTORi-NB's biodistribution. Using ex vivo gamma counting of blood samples, we found that mTORi-NB have a blood half-life of ~1 hour and mainly accumulate in the liver, spleen, kidney, and bone marrow 48 hours post injection (**Fig. 1H-L**). Blood analyses showed no signs of liver or kidney damage (**Fig. 1M**). These results indicate that the in vivo behavior and biocompatibility of mTORi-NBs are preserved across species. This study has been published in Science Advances.

Reference

1. W. J. M. Mulder, J. Ochando, L. A. B. Joosten, Z. A. Fayad, M. G. Netea, Therapeutic targeting of trained immunity. Nat. Rev. Drug Discov. 18, 553–566 (2019)
2. S.-C. Cheng, J. Quintin, R. A. Cramer, K. M. Shepardson, S. Saeed, V. Kumar, E. J. Giamarellos-Bourboulis, J. H. A. Martens, N. A. Rao, A. Aghajanirefah, G. R. Manjeri, Y. Li, D. C. Ifrim, R. J. W. Arts, B. M. J. W. van der Veer, P. M. T. Deen, C. Logie, L. A. O'Neill, P. Willems, F. L. van de Veerdonk, J. W. M. van der Meer, A. Ng, L. A. B. Joosten, C. Wijmenga, H. G. Stunnenberg, R. J. Xavier, M. G. Netea, MTOR- and HIF-1α-mediated aerobic glycolysis as metabolic basis for trained immunity. Science 345, 1250684 (2014).

Oral Presentation

Disclosures: The authors have disclosed no financial interest.

153-Transition Metal Heteropolynuclear Complexes as Super-atomic MRI Redox Rulers

Presenter: Jaclyn Brusso, University of Ottawa

Alexandros Kitos[1], Niki Mavragani[1], Raúl Castañeda[2], Zachary Comeau[3], Alexia Kirby[4], Nicholas D. Calvert[5], Francisco Martínez?Santiesteban[6], Timothy J. Scholl[7], Muralee Murugesu[1], Adam Shuhendler[3], **Jaclyn Brusso[1]**

[1]University of Ottawa, Ottawa, ON
[2]New Mexico Highlands University, Las Vegas, New Mexico
[3]University of Ottawa, Ottawa, Ontario
[4]University of Ottawa, Ottawa
[5]University of Ottawa, Orleans
[6]Robarts Research Institute, London, Ontario
[7]Western University, London, Ontario

Background:
A considerable amount of research has been invested into the development of contrast agents based on transition metal complexes that can also potentially overcome nephrogenic systemic fibrosis associated with the use of gadolinium-based contrast agents in patients on dialysis or with severely impaired kidney function. Advantageously, the sensitivity of valence electron configurations of 3d metal ion complexes to their microenvironment allows for the rational design of smart contrast agents capable of reporting a variety of biochemical changes.[1-5]While polynuclear (>2) systems are scarce they offer several advantages (tunability in size, shape and total spin state[6-8]) since the collection of metal ions can act as a single entity – i.e., a super atom. However forming super-atomic contrast agents comprised of robust ligands **must** oppose complex dissociation/speciation in biological media, a challenge remaining to be met.

Methods:
We previously established synthetic methodology to control the topology and nuclearity of Mn, Fe, and Zn complexes using *N*-2-pyrimidylimidoyl-2-pyrimidylamidine (Pm_2ImAm) as ligand.[9-12] We prepared homo- and heterometallic clusters of the general formula $[M_A^{III}M_B^{II}{}_3(Pm_2ImAm)_3Cl_6]\cdot xH_2O$ (**$MnMn_3$** $M_A=Mn^{3+}$, $M_B=Mn^{2+}$, x=5; **$FeMn_3$** $M_A=Fe^{3+}$, $M_B=Mn^{2+}$, x=8; **$FeZn_3$** $M_A=Fe^{3+}$, $M_B=Zn^{2+}$, x=6) (Scheme 1). Contrast agents were evaluated for magnetic and thermogravimetric behaviour, and redox response to common biological reducing (glutathione, ascorbic acid) or oxidizing agents (hydrogen peroxide) by T1w/T2w ratiometric MRI in phantoms *in vitro* and *in vivo* in H460 lung cancer-bearing xenograft mouse models.

Results & Discussion:
All super-atomic clusters were found to have excellent thermal stability ($T_{decomposition}$>250 ºC). Variable temperature dc magnetic susceptibilities of **$FeMn_3$** and **$FeZn_3$** validated that N-imidoylamidine frameworks favor superexchange pathways yielding antiferromagnetic (AF) interactions between central and peripheral metals, yielding the strongest exchange coupling (-11.54 cm^{-1}) for Pm_2ImAm-based complexes (Fig. 1). The varying oxidation states and metal types of our multicentric metal complexes led us to assay the MRI contrast their enhancement properties in the presence of biological reducing and oxidizing agents (Fig. 2). In a redox neutral environment (1´PBS), the average voxelwise ratio of the T_1-weighted to T_2-weighted intensities (T_1w/T_2w) resulted in values of 1.4±0.06 and 1.6±0.03, respectively. Upon reduction by 10 mol-eq. glutathione, T_1w/T_2w values were 4.2±0.29 and 2.8±0.12 for **$FeMn_3$** and **$MnMn_3$**, respectively, while oxidation by 10 mol-eq. of hydrogen peroxide yielded T_1w/T_2w values of 1.4±0.12 and 0.9±0.02. A redox scale was implemented for ratiometric MRI, where voxels with T_1w/T_2w~1.5 represented redox neutral (white), >1.5 indicated reducing (yellow-to-red gradient), and <1.5 indicated oxidizing conditions (white-to-blue gradient) (Fig. 2). Contrary to the other analogs, **$FeZn_3$** did not induce contrast enhancement under any redox conditions, providing strong evidence that the central metal ion does not directly participate in contrast enhancement, and that MR-active peripheral metal ions are necessary to confer the observed contrast enhancement. We applied these contrast agents to map redox status in heterotopic H460 xenografts in mice (Fig. 3). Following intratumoral injection, the extent of contrast agent distribution in tumor tissue was determined by the T_1-weighted image (Fig. 3, blue dashed line). Ratiometric redox mapping with **$FeMn_3$** delineated highly reducing tumor regions (Fig. 3, top row), where **$MnMn_3$** demarcated oxidative tumor microenvironments (Fig. 3, middle row). Importantly, diethyl maleate-mediated glutathione depletion resulted in the loss of reducing but increase in redox neutral and slightly oxidative regions following the administration of **$FeMn_3$** (Fig. 3, bottom row).

Conclusions:
The data presented support the application of **$FeMn_3$** and **$MnMn_3$** as MRI contrast agents capable of mapping tumor redox status through a simple T_1w/T_2w ratiometric approach. The contrast agent design strategy presented here introduces heteropolynuclear transition metal super-atomic complexes suitable for semi-quantitative in vivo MR imaging of tissue redox status and opens up new avenues for non-invasive characterization of the tumor environment by MRI.

Reference

1. Zhang, L. et al. Angewandte Chemie International Edition 56, 16626–16630 (2017).
2. Ratnakar, S. J. et al. J. Am. Chem. Soc. 134, 5798–5800 (2012).
3. Yeo, S. Y. et al. Biochimica et Biophysica Acta (BBA) - Biomembranes 1838, 2807–2816 (2014).
4. Napolitano, R. et al. J. Med. Chem. 56, 2466–2477 (2013).
5. Gündüz, S. et al. Inorg. Chem. 57, 5973–5986 (2018).
6. Di Gregorio, E. et al. ACS Nano 9, 8239–8248 (2015).
7. Wang, Y. et al. Chem. Commun. 47, 3541–3543 (2011).
8. Cage, B. et al. Polyhedron 26, 2413–2419 (2007).
9. Isaacman, S. et al. Polyhedron 24, 2691–2694 (2005).
10. Castañeda, R., Hollingshead, A., Gabidullin, B. & Brusso, J. L. Crystal Growth & Design 17, 6572–6578 (2017).
11. Castañeda, R. et al. European Journal of Inorganic Chemistry 2019, 963–972 (2019).
12. Castañeda, R., Rouzières, M., Clérac, R. & L. Brusso, J. Journal of Materials Chemistry C 8, 4401–4407 (2020). 13. Kitos, A.

A., Mavragani, N., Murugesu, M. & Brusso, J. L. Mater. Adv. 1, 2688–2706 (2020).

Oral Presentation

Disclosures: The authors have disclosed no financial interest.

154-IRDye800CW labeled uPAR-targeting peptide for fluorescence-guided glioblastoma surgery: Preclinical studies in orthotopic xenografts

Presenter: Sorel Kurbegovic, Copenhagen University Hospital Rigshospitalet

Sorel Kurbegovic[1], Karina Juhl[2], Kasper Kildegaard Soerensen[3], Julie Leth[4], Gro Linno Willemoe[5], Anders Christensen[6], Yvonne Adams[7], Anja Ramstedt Jensen[7], Christian von Buchwald[6], Jane Skjøth-Rasmussen[5], Michael Ploug[8], Knud Jørgen Jensen[3], Andreas Kjaer[9]

[1]Copenhagen University Hospital Rigshospitalet, Copenhagen, Denmark
[2]FluoGuide, Denmark
[3]University of Copenhagen, Denmark
[4]University of Copenhagen
[5]Rigshospitalet, Denmark
[6]Rigshospitalet, Copenhagen, Sjaelland, Denmark
[7]University of Copenhagen, Copenhagen, Denmark
[8]University of Copenhagen, copenhagen, denmark, Denmark
[9]Rigshospitalet & University of Copenhagen, Copenhagen, Denmark

Glioblastoma (GBM) is a devastating cancer with basically no curative treatment. Even with aggressive treatment, the median survival is disappointing 14 months [1]. Surgery remains the key treatment and the postoperative survival is determined by the extent of resection [2]. Unfortunately, the invasive growth with infiltrating margins complicates an optimal surgical resection. Precise intraoperative tumor visualization is therefore highly needed and molecular targeted near-infrared (NIR) fluorescence imaging potentially constitutes such a tool. The urokinase-type Plasminogen Activator Receptor (uPAR) is highly expressed in most solid cancers including GBM, breast cancer, head and neck squamous cell carcinoma, pancreatic cancer, and lung cancer [3-7]. The level of expression is correlated to invasion and metastasis, one of the hallmarks of cancer, and accordingly it correlates to the aggressiveness of the cancer. Further, it is highly expressed at the invading front and the adjacent peritumoral activated stroma making it an attractive target allowing accurate margin visualization and tumor delineation [8]. The purpose of this study was to develop and evaluate a new uPAR-targeted optical probe, IRDye800CW-AE344, for fluorescence guided surgery (FGS). We characterized the probe with regard to binding affinity, optical properties, and plasma stability. Further, in vivo imaging characterization was performed in nude mice with orthotopic human patient derived glioblastoma xenografts, and we performed head-to-head comparison within FGS between our probe and the traditional procedure using 5-ALA. Finally, the blood-brain barrier (BBB) penetration was characterized in a 3D BBB spheroid model. The probe effectively visualized GBM in vivo with a tumor-to-background ratio (TBR) above 4.5 between 1 to 12 h post injection and could be used for FGS of orthotopic human glioblastoma xenografts in mice where it was superior to 5-ALA. The probe showed a favorable safety profile with no evidence of any acute toxicity. Finally, the 3D BBB model showed uptake of the probe into the spheroids indicating that the probe crosses the BBB. IRDye800CW-AE344 is a promising uPAR-targeted optical probe for FGS and a candidate for translation into human use.

Reference

1. Delgado-Lopez, P.D. and E.M. Corrales-Garcia, Survival in glioblastoma: a review on the impact of treatment modalities. Clin Transl Oncol, 2016. 18(11): p. 1062-1071.
2. Chaichana, K.L., et al., Establishing percent resection and residual volume thresholds affecting survival and recurrence for patients with newly diagnosed intracranial glioblastoma. Neuro Oncol, 2014. 16(1): p. 113-22.
3. Persson, M., et al., Urokinase-Type Plasminogen Activator Receptor as a Potential PET Biomarker in Glioblastoma. J Nucl Med, 2016. 57(2): p. 272-8.
4. Persson, M., et al., First-in-human uPAR PET: Imaging of Cancer Aggressiveness. Theranostics, 2015. 5(12): p. 1303-16.
5. He, C., et al., Analysis of expressions of components in the plasminogen activator system in high- and low-metastatic human lung cancer cells. J Cancer Res Clin Oncol, 2001. 127(3): p. 180-6.
6. Foekens, J.A., et al., The urokinase system of plasminogen activation and prognosis in 2780 breast cancer patients. Cancer Res, 2000. 60(3): p. 636-43.
7. Cantero, D., et al., Enhanced expression of urokinase plasminogen activator and its receptor in pancreatic carcinoma. Br J Cancer, 1997. 75(3): p. 388-95.
8. Kriegbaum, M.C., et al., Rational targeting of the urokinase receptor (uPAR): development of antagonists and non-invasive imaging probes. Curr Drug Targets, 2011. 12(12): p. 1711-28.

Oral Presentation

Disclosures: The authors would like to disclose that FG001 is an investigational device.

155-Theranostic Iron Oxide Nanoparticles Carrying STAT6 Inhibitor AS1517499 for Reprogramming Tumor-Associated M2-like Macrophages in 4T1 Breast Tumor Mouse Model

Presenter: Yuancheng Li, Emory University School of Medicine

Yuancheng Li[1], Zi Wang[1], Manman Xie[2], Joshua B. Jones[1], Weiping Qian[3], Lily Yang[1], Hui Mao[4]

[1]Emory University School of Medicine, Atlanta, GA
[2]Emory University, Decatur, Georgia
[3]Emory University, Atlanta, Georgia
[4]Emory University School of Medicine, Atlanta, Georgia

While immunotherapy has emerged as a promising treatment strategy for many cancers, most breast cancer types, including triple negative breast cancers (TNBC), are immune "cold" and unresponsive to immunotherapy[1]. As the most prominent immune cells in the tumor microenvironment (TME), tumor-associated macrophages (TAM) more closely resemble the immuno-suppressive M2-like subtype. In contrast, pro-inflammatory M1-like TAM stimulate the TME and render anti-tumor activity. However, chemokines secreted by tumoral and stromal cells polarize the recruited monocytes and macrophages to the pro-tumoral M2 subtype. Although priming "cold" tumors into immune-responsive "hot" ones by reprogramming M2 TAM to M1 has shown potentials in cancer treatment including immunotherapy[2], the targeted delivery of reprogramming agents to the M2 TAM remains a challenge, due to the intrinsic non-specific phagocytosis of

bioengineered drug delivery systems by the mononuclear phagocyte system. We report the application of an anti-biofouling (polyethylene glycol)-*block*-(allyl glycidyl ether) (PEG-*b*-AGE) polymer coated MRI-capable sub-5 nm ultrafine iron oxide nanoparticle (uIONP) functionalized with M2 targeted peptide M2pep (sequence: YEQDPWGVKWWYGGGSKKKC) for targeted imaging of M2 TAM using 4T1 mouse model of TNBC breast cancer with abundant M2 TAM population. Specifically, PEG-*b*-AGE coated uIONP conjugated with M2pep (M2pep-uIONP) is used as a carrier for a signal transducer and activator of transcription 6 (STAT6) inhibitor AS1517499 (AS), which has been reported to repolarize M2 TAM to M1 subtype[3]. The loading efficiency of AS to M2pep-uIONP is 27 wt% determined by UV absorbance of AS at 308 nm. After conjugating with M2pep, M2pep-uIONP/AS can target M2 TAM and delivery AS for M1 repolarization. We validate the targeting specificity of M2pep-uIONP *in vitro* using M2 and M1 macrophages derived from Raw264.7 murine macrophages by interleukin-4 and lipopolysaccharide, respectively. The efficacy of M2pep-uIONP/AS in repolarizing M2 to M1 subtype is firstly confirmed *in vitro* by incubation with induced M2 macrophages for 48 h at the AS dosage of 0.8 μM. Flow cytometry analysis shows 40.6 ± 4.1% of treated cells present M1 phenotype ($CD80^+$/$iNOS^+$), whereas M2pep-uIONP vehicle treated M2 only exhibited 8.95 ± 3.6% conversion to M1 subtype. Labeled with the near infrared (NIR) dye NIR830, M2pep-uIONP/AS is thereby used to probe the M2 reprogramming in xenograft 4T1 breast tumors after intravenous injection to the tumor bearing mice at the AS dosage of 50 and 100 μg/kg body weight. Mice are sacrificed at 1 h, 3 h, 24 h and 48 h to collect the tumors. Immunofluorescence staining of the tumor tissue sections for M1 ($CD68^+$/$CD80^+$ and $CD68^+$/$iNOS^+$) and M2 ($CD68^+$/$CD163^+$ and $CD68^+$/$CD206^+$) TAM are carried out to investigate the change of intratumoral distribution and phenotype of the TAM labeled with NIR830-M2pep-uIONP/AS. The results show that M2pep-uIONP/AS labeled TAM are mainly found near tumor blood vessels (< 30 μm) with predominant M2 phenotype at 1 and 3 h, and migrate > 200 μm away from the blood vessels at 48 h, more importantly, demonstrating M1 phenotype. Meanwhile, the newly infiltrated TAM at 48 h with no M2pep-uIONP/AS remain M2 phenotype. The result of flow cytometry analysis on collected tumors shows that there are 38.7 ± 9.2% and 24.8 ± 8.8% M1 population in total TAM for mice receiving M2pep-uIONP/AS at 100 and 50 μg/kg, respectively. As a control, mice receiving M2pep-uIONP or no treatment only have 15.9 ± 5.8% and 13.2 ± 7.1% M1 population, respectively. In conclusion, M2pep-uIONP/AS has shown the capability in targeted repolarizing immuno-suppressive M2 TAM to pro-inflammatory M1 subtype in the 4T1 breast tumors of mice.

Reference

1. Harbeck N. et al., Nat. Rev. Dis. Primers. 2019, 5, 66.
2. Cassetta L. et al., Nat. Rev. Drug. Discov. 2018, 17, 887.
3. Xiao H. et al., ACS. Cent. Sci. 2020, 6, 1208.

Oral Presentation

Disclosures: The authors have disclosed no financial interest.

156-Molecular Image-guided Protoporphyrin IX Fluorescence Detection and Photodynamic Therapy of Glioblastoma

Presenter: Haini (Hanru) Zhang, Washington University in St. Louis

Haini (Hanru) Zhang[1], Christine M. O'Brien[2], Xiao Xu[3], Suman B. Mondal[4], Mattew Mixdorf[5], Dorota Grabowska[5], Gail Sudlow[6], Brad Manion[5], Kexiang Liang[7], Rui Tang[8], Samuel Achilefu[9]

[1]*Washington University in St. Louis, Dallas, TX*
[2]*Washington University in St. Louis, St. Louis, Missouri*
[3]*University of Texas Southwestern Medical Center, Dallas, Texas*
[4]*Washington University in St. Louis, St Louis, Missouri*
[5]*Washington University in St. Louis, St. Louis, Missour*
[6]*St Louis, MO*
[7]*Washington University School of Medicine, St Louis, MO*
[8]*Washington University School of Medicine, Saint Louis, Missouri*
[9]*UT Southwestern, Dallas*

Glioblastoma is the predominant primary brain malignancy in adults [1]. The 5-year relative survival rate is 22% for patients aged from 20 to 44 years, and an abysmal 6% for 55 to 64 year-old patients [2]. Maximizing the amount of resected tumors is essential to reducing cancer recurrence rate and extending patients' survival. Recent developments in fluorescence image-guided surgery (FGS) holds promise to improve cancer resection with high accuracy by providing real-time visualization of the spatial distribution of tumors, including the difficult infiltrating and diffuse tumors [3, 4]. The US Food and Drug Administration and European Medicines Agency have approved 5-Aminolevulinic acid (5-ALA) in patients with high-grade glioma [5]. Metabolism of exogenously administered 5-ALA to the fluorescent protoporphyrin IX (PpIX) in tumors enables surgeons to distinguish PpIX-fluorescing gliomas from surrounding normal tissue [6-8]. In addition, PpIX is a photosensitizer used in photodynamic therapy (PDT) of tumors [9]. However, PpIX emits weak red fluorescence that must compete with high autofluorescence from biological tissue, diminishing accuracy in its use to identify tumors during surgery [10, 11]. Moreover, the preferred PpIX excitation wavelengths in the 405 nm to 625 nm region confines its FGS and PDT to superficial lesions [12]. In this study, a novel near-infrared (NIR) cancer-targeting contrast agent LS301 [13] visualized by a wearable and head-mounted cancer vision goggle (CVG) [14] has the potential to address these limitations and extend the assessment of deep gliomas for both PpIX-FGS and PpIX-PDT. We demonstrate that LS301 accumulates selectively in delayed brain tumor (DBT) and Uppsala 87 malignant glioma (U87-MG) cells *in vitro*, with maximum uptake at 24 hours post-incubation. Using flow cytometry, fluorescence lifetime imaging, and confocal microscopy, we show that LS301 fluorescence co-localized with that of PpIX. *In vivo,* LS301 fluorescence retained 90% of its maximum signal at 24 hours post-injection in DBT and U87 tumor-bearing BALB/c and Fox Chase SCID Beige mice, respectively. In contrast, PpIX fluorescence declined from 6 hours post-injection of 5-ALA. We discovered that LS301 produced reactive oxygen species when excited in the NIR wavelength, enabling cancer cell death through PDT. We did not observe any adverse events in mice or vital organs during the combination of 5-ALA and LS301 administration, imaging, and PDT. Supplementing LS301 with PpIX fluorescence during glioma surgery is expected to improve image quality and determine the distribution of PpIX to optimize PDT. Dual excitation of both PpIX in the visible and LS301 in the NIR could potentiate PDT effect to eradicate brain tumors. The use of CVG to visualize LS301 during surgery allows for rapid tumor debulking, identify residual tumors, and enhance the precision of excitation light for PDT.

Reference

1. Siegel RL, et al. Cancer statistics, 2022. CA: A Cancer Journal for Clinicians. 2022; 72: 7-33.
2. Ostrom QT, et al. CBTRUS Statistical Report: Primary Brain and Other Central Nervous System Tumors Diagnosed in the United States in 2012-2016. Neuro-oncology. 2019; 21: v1-v100.
3. Barth CW, et al. Fluorescence Image-Guided Surgery - a Perspective on Contrast Agent Development. Proc SPIE Int Soc Opt Eng. 2020; 11222.

4. Lee JY, et al. Intraoperative Near-Infrared Optical Imaging Can Localize Gadolinium-Enhancing Gliomas During Surgery. Neurosurgery. 2016; 79: 856-71.
5. Schwake M, et al. 5-ALA fluorescence-guided surgery in pediatric brain tumors-a systematic review. Acta Neurochir (Wien). 2019; 161: 1099-108.
6. Pablo AV, et al. Quantitative fluorescence in intracranial tumor: implications for ALA-induced PpIX as an intraoperative biomarker. Journal of Neurosurgery JNS. 2011; 115: 11-7.
7. Wei L, et al. Visualization technologies for 5-ALA-based fluorescence-guided surgeries. J Neurooncol. 2019; 141: 495-505.
8. Kaneko S, et al. Fluorescence-Guided Resection of Malignant Glioma with 5-ALA. International Journal of Biomedical Imaging. 2016; 2016: 6135293.
9. Cantisani C, et al. Overview on Topical 5-ALA Photodynamic Therapy Use for Non Melanoma Skin Cancers. International Journal of Photoenergy. 2014; 2014: 304862.
10. Kim CH, et al. Effect of 5-aminolevulinic acid-based photodynamic therapy via reactive oxygen species in human cholangiocarcinoma cells. Int J Nanomedicine. 2011; 6: 1357-63.
11. Juarranz Á, et al. Photodynamic therapy of cancer. Basic principles and applications. Clinical and Translational Oncology. 2008; 10: 148-54.
12. Mahmoudi K, et al. 5-aminolevulinic acid photodynamic therapy for the treatment of high-grade gliomas. J Neurooncol. 2019; 141: 595-607.
13. Shen D, Xu B, et al. Selective imaging of solid tumours via the calcium-dependent high-affinity binding of a cyclic octapeptide to phosphorylated Annexin A2. Nature Biomedical Engineering. 2020; 4: 298-313.
14. Mondal SB, et al. Optical See-Through Cancer Vision Goggles Enable Direct Patient Visualization and Real-Time Fluorescence-Guided Oncologic Surgery. Annals of Surgical Oncology. 2017; 24:

Oral Presentation

Disclosures: The authors have disclosed no financial interest.

157-Mapping Concussion for Early Diagnosis by Molecular MRI

Presenter: Alexia Kirby, University of Ottawa

Alexia Kirby[1], Mojmir Suchy[2], Ryan Daniel[3], Adam Shuhendler[4]

[1]*University of Ottawa, Ottawa*
[2]*Lawson Health Research Institute, London*
[3]*University of Toronto*
[4]*University of Ottawa, Ottawa, Ontario*

Concussion is a form of mild traumatic brain injury (mTBI), defined as complex neurological impairment induced by biomechanical forces without structural brain damage. In Canada, concussions make up 93% of sports-related injuries among children and youth[1]. It is estimated that 1 in 4 adolescences in the United States have experienced a concussion[2]. Currently, the diagnosis of mTBI relies on psychoneurological/cognitive testing via patient interviews, but there does not yet exist an objective diagnostic tool for concussion. Within the emergency department, the lack of consistent guidelines for evaluations of concussion contributes to an estimated 50-90% of patients with undiagnosed mTBI[3]. Symptoms can present days to weeks following injury[4], further amplifying the need for acute diagnosis for management and prognosis of mTBI[5]. The lack of objective diagnostic tools for concussion has identified a need for molecular imaging probes targeted to the diagnosis of mTBI. Downstream injury from mTBI stems from oxidative damage, leading to the production of neurotoxic aldehydes[6]. However, the inability to image aldehydes in live subjects has prevented their exploitation as diagnostic biomarkers. A novel CEST-MRI contrast agent, 5-propargyloxy-2-hydrazinobenzoic acid (PHBA; Fig.1A), has been developed to map aldehyde production *in vivo* following mTBI. PHBA binds rapidly and irreversibly with aldehydes, affording the use of pathology-associated aldehydes as imaging biomarkers for MRI. A new mouse model of closed-head, awake concussion was developed in a strain of aldehyde dehydrogenase 2 knockout ($ALDH2^{-/-}$) mice. While previous mouse models of concussion use anesthetized mice for impact, an awake model not only forgoes the neuroprotective affects of anaesthesia, but also allows for immediate post-impact behaviour evaluation. The use of an electromechanical impactor device allows for highly reproducible cranial impacts. A set of neurological severity score (NSS) tests were used to determine the parameters of impact (velocity, dwell time, and depth). Gadolinium contrast enhanced MRI was used to verify blood-brain barrier integrity after impact. Once a robust model was established, mice were separated into four cohorts (n=4 per group): young (<20 weeks) $ALDH2^{-/-}$, young $ALDH^{+/-}$, old (>65weeks) $ALDH2^{-/-}$, and old $ALDH2^{+/-}$. Mice were either used for MRI or histology. For histology, brains were excised on days 2 or 7 after impact and stained for Iba1 and GFAP. Mice in the imaging cohort underwent NSS, grid walk testing, and MRI before impact for baseline measurements. Immediately after impact, and once the righting reflex was regained, the mice were evaluated again with the NSS and grid walk. CEST-MRI was performed after the injection of PHBA on days 2 and 7 after impact. Signal enhancement significantly increases at two days post-injury and decreases to near baseline by 7 days post-injury in all mice(Fig.1 B,C). GFAP staining, a marker of astrocyte activation, confirms a neuroinflammatory response at 2 days post-injury(Fig.2). The data, although a small sample size, suggest aged mice produce more aldehydes than young mice after concussion, independent of genotype(Fig. 3). The median change in signal enhancement is correlated with deficits in descending motor control (i.e. foot faults) in aged mice, but not young mice(Fig.4). Importantly, the NSS widely used for concussion assessment in mice does not correlate with such sensorimotor deficits. These initial results suggest that mapping aldehydic load post-concussion may be a better predictor of the outcomes of injury than the more broadly but less concussion-specific NSS test battery. These results support the use of aldehydes as an imaging biomarker in a mouse model of concussion. This novel MRI contrast agent represents the first objective diagnostic tool for concussion. If proven safe and effective, these probes may be used in a clinical setting, not only telling that mTBI occurred, but also mapping the location of damage to improve treatment outcomes on an individual patient basis.

Reference

1. CHIRPP, govt of Canada
2. JAMA 2021;325(17):1789-1791
3. Phys Med Rehabil Clin N Am. 2017;28(2):271-286
4. Int Rev Psychiatry 2003;15(4):310-6;5
5. Arch Phys Med Rehabil. 2008 89(8):1550-5
6. Free Radic. Biol. Med.2008;45(4):443-452

Oral Presentation

Disclosures: The authors have disclosed no financial interest.

158-On- or off-rate, which is more important for predicting fibrogenesis molecular MR performance?

Presenter: Hua Ma, Harvard Medical School

Hua Ma[1], Iris Y. Zhou[2], Nicholas Rotile[3], Matthew Drummond[4], Rachel Knipe[4], Samantha Elise Zygmont[5], Avery T. Boice, Eman Akam[6], Huan Wang, Peter Caravan[7]

[1]*Harvard Medical School, Somerville*
[2]*Massachusetts General Hospital, Charlestown, MA*
[3]*Massachusetts General Hospital*
[4]*Massachusetts General Hospital, Boston, MA*
[5]*Massachusetts General Hospital, Charleston, Massachusetts*
[6]*Massachusetts General Hospital, Somervillw, MA*
[7]*Harvard Medical School, Charlestown, MA*

Introduction:
Idiopathic pulmonary fibrosis (IPF) is the most common and most severe type of interstitial lung disease. The presence of oxidized collagen, wherein lysine residues are converted to the aldehyde allysine, is a universal feature of fibrogenesis. Molecular MR imaging of fibrogenesis has the potential for early diagnosis of IPF and for monitoring disease progression and treatment response. Aldehydes can be targeted by hydrazine or oxyamine moieties. Hydrazines typically react faster, but the hydrazone product also hydrolyzes faster than the oxime product formed from oxyamine. In this work, we directly compare hydrazine- and oxyamine-derived Mn-based MR probes in their ability to quantify lung fibrogenesis in a bleomycin-injured mouse model.

Materials and Methods:
The allysine-targeted probes (Figure 1A) were synthesized in 6 steps from the pyclen macrocycle. The condensation kinetics of MnL1 and MnL2 with butyraldehyde and hydrolysis rate constants of the condensation products were measured by UV spectroscopy and HPLC, respectively (25 °C, pH 7.4, PBS). Relaxivities of MnL1 and MnL2 in PBS, BSA solution, and allysine-modified BSA solution were measured at 1.4 T, 37 °C. Protein-bound MnL1 and MnL2 were isolated by ultrafiltration and relaxivities were measured. Lung fibrosis was induced in C57Bl/6 adult male mice by bleomycin instillation and MRI was performed on a 4.7 T Bruker scanner on day 14 post bleomycin injury.[1] Age-matched naïve mice were used as healthy controls. MRI consisted of 3D Ultrashort Echotime (3D-UTE, TR/TE/FA=4 ms/12 µs/16°, 0.6 mm isotropic spatial resolution) images were acquired prior to and dynamically post-injection of 100 µmol/kg contrast agent; 2D RARE (TR/TE=1.5 s/8 ms) and 3D T1-weighted FLASH (TR/TE/FA=10 ms/2.6 ms/30°) images were used to define regions of interest (ROIs) in the lung that excluded vessels and airways. ROIs in the dorsal muscle were also defined as a reference. We averaged the lung-to-muscle ratio (LMR) from 6 UTE image slices to calculate changes in LMR (ΔLMR) at each time point.

Results:
Compared with MnL2, MnL1 reacted 5 times slower with an aliphatic aldehyde (Figure 1B, 12.1 $M^{-1}s^{-1}$ vs. 2.6 $M^{-1}s^{-1}$); however, the oxime formed with MnL2 hydrolyzed 1000 times slower than the corresponding hydrazone product with MnL1 (Figure 1C, 0.8×10^{-6} s^{-1} vs. 1.0×10^{-3} s^{-1}). Relaxivities (Figure. 1D) of MnL1 and MnL2 were similar in PBS ($r_1 = 3$ $mM^{-1}s^{-1}$), consistent with the presence of one coordinated water ligand. Relaxivities were not enhanced in BSA solution indicating weak/no nonspecific protein binding, but dramatically increased in the presence of BSA-Ald, which demonstrates specific binding to the allysine residues. The relaxivity of protein-bound MnL1 and MnL2 were almost 4-times higher than the unbound form, demonstrating a remarkable turn-on effect.
In bleomycin injured mice, both MnL1 and MnL2 showed significantly higher ΔLMR than in naïve mice (Figure 1E,1F). At 60 min post-administration of probes, similar signal enhancement was observed in fibrotic lung (0.13 vs. 0.14). However, the lung signal enhancement generated by MnL1 continued to decline with time, while MnL2 induced persistent signal enhancement to at least 2 hours post-injection.

Conclusion:
The novel hydrazine- or oxyamine-bearing Mn(II) probes MnL1 and MnL2 enable specific binding to allysine, 4-fold turn on in relaxivity upon binding, and show potential for noninvasive imaging of lung fibrogenesis. Imaging of lung fibrogenesis by MnL1 and MnL2 demonstrated that the faster on-rate of MnL1 did not result in higher uptake in the fibrotic lung than MnL2. The faster hydrolysis rate of the MnL1 hydrazone resulted in more efficient lung elimination. Higher hydrolytic stability of the oxime formed by MnL2 resulted in long-lasting signal enhancement in the fibrotic lung, which may be desired for longer acquisitions or when imaging multiple anatomical regions.

Reference

1. Akam, E. A.; Abston, E.; Rotile, N. J.; Slattery, H. R.; Zhou, I. Y.; Lanuti, M.; Caravan, P., Improving the reactivity of hydrazine-bearing MRI probes for in vivo imaging of lung fibrogenesis. Chem Sci 2020, 11 (1), 224-231.

Oral Presentation

Disclosures: The authors have disclosed no financial interest.

159-Bright, water-soluble, near infrared fluorophores for visualization of vital nerve structures enabling two-color imaging for fluorescence-guided surgical applications

Presenter: Antonio Montano, Oregon Health & Science University

Antonio R. Montano[1], Lei G. Wang[1], Anas M. Masillati[2], Connor Barth[3], Nourhan Shams[4], Summer L. Gibbs[1]

[1]*Oregon Health & Science University, Portland, OR*
[2]*Oregon Health & Science University, Portland*
[3]*Inherent Targeting, Portland, OR*
[4]*Oregon Health & Science University, Portland, Oregon*

Injury of peripheral nerves during surgery remains a leading cause of iatrogenic complications and a major source of morbidity affecting all surgical specialties. Prostate cancer, the second leading cause of cancer death among men in the United States, is the most prevalent form of cancer in men. Prostatectomy, surgical removal of the prostate, is the primary mode of therapy for patients with localized prostate cancer. While nerve sparing surgical techniques are practiced, because of extremely limited visibility of the nerve plexus, recognition and conclusive cancer delineation continue to challenge even the most experienced surgeons, with positive surgical margins occurring in up to 21% of patients and nerve damage in up to 60% of patients. This means that not only is the cancer being poorly controlled, but even patients with positive cancer control could still be left with incontinence and/or impotence that often has a severe impact on patient post-operative quality of life. Prostate-specific membrane antigen (PSMA) is a glycosylated type II membrane protein (MW ~110 kDa) that is overexpressed in >90% of all primary prostate cancer lesions, tumor positive lymph

nodes and metastases and is the most well-established, highly specific prostate epithelial cell membrane antigen. A variety of PSMA specific contrast agents have been developed using the small molecule EUK targeting sequence that can be readily labeled for nuclear medicine and fluorescence guided surgery. Clinical trials with these fluorescence agents have demonstrated proof of concept contrast in prostate cancer, paving the way towards fluorescence guided prostatectomy. However, nerve damage still plagues these procedures warranting a two-color fluorescence guided surgery (FGS) solution. Our group has designed and synthesized over 200 oxazine-based near-infrared (NIR) nerve-specific fluorophores with potential applications in FGS. The design of these compounds has provided valuable knowledge regarding the structure-activity relationship (SAR) responsible for nerve-specificity, allowing for further optimization of several lead candidates for specific applications. Our overall strategy is to label both tumor and nerves simultaneously with distinct fluorescent markers, pairing fluorescently labeled PSMA probes, optimized for the 800 nm channel in FGS systems, with a spectrally distinct, water-soluble, nerve-specific agent with emission tuned to the complementary NIR 700 nm channel. Our synthetic strategy, therefore, was aimed at improving key properties relevant to clinical translatability of several promising lead candidates to generate an optimized 700 nm fluorophore for use in two-color prostatectomy. Here, we report the design of a new library of bright, water-soluble, near infrared nerve-specific fluorophores centered around two promising lead candidates from our first published library. Our experimentally acquired knowledge of SAR has guided structural modifications and resulted in a new library of fluorophores, many of which demonstrated improved nerve specificity and *in vivo* brightness, effectively lowering the minimum dose required for generating statistically significant contrast of nerve tissue at the surface and at depth.

Furthermore, through judicious incorporation of solubilizing moieties, we successfully engineered our current lead candidates for improved water-solubility, fully negating the need for formulation development with the added benefit of dramatically improving safety profiles for patient use in the clinic and decreasing the overall cost of clinical translation.

Oral Presentation

Disclosures: The authors have disclosed no financial interest.

160-PET imaging of HER2+ gastric cancer reveals enhanced single-dose antibody-drug potency upon co-administration with statins

Presenter: Emma Brown, Washington University in St. Louis

Emma L. Brown[1], Komal Mandleywala[2], Jason Lewis[3], Patricia M. Ribeiro Pereira[1]
[1]*Washington University in St. Louis*
[2]*Memorial Sloan Kettering Cancer Center, NYC, NY*
[3]*Memorial Sloan Kettering Cancer Center, New York, NY*

Introduction:
Trastuzumab emtansine (TDM1) combines the specific HER2-targeting antibody trastuzumab with the chemotherapy drug emtansine (DM1). Although TDM1 is the standard of care for women with HER2-positive ($HER2^+$) breast cancer, a substantial fraction of patients are refractory to TDM1 and it failed in clinical trials for gastric cancer[1]. Additionally, TDM1-mediated side effects often require lowering the dose or that patient's stop taking the drug in the more severe toxicity cases[2]. Modulation of HER2 surface availability via cholesterol-depleting drugs (Statins) enhances TDM1-tumor uptake, as visualized with immuno-PET, ultimately converting non-responding tumors into responders[2,3,4]. Here, we used HER2-PET imaging to investigate the dosing regime of TDM1 therapy in gastric tumor models, comparing the efficacy of a multi-dose regime, which replicates the clinical standard, to a single-dose regime with and without the co-administration of Statins. We hypothesized that the enhanced potency of TDM1 therapy seen with the co-administration of Statins would enable lowering TDM1 doses while achieving similar therapeutic efficacy.

Methods:
Animals: NCIN87 gastric cells or gastric PDX fragments were s.c. implanted in Balb/c nude or NSG mice (n≥8 mice/cohort). Treatments: Mice received TDM1 (5 mg/kg, i.v.) or saline weekly for 5 weeks (clinical/multi regime) or as a single-dose (**Figure 1A**). Lovastatin (4.15 mg/kg) or saline was orally administered 12 h prior to or at the same time of TDM1 treatment. Radiolabeling: Trastuzumab coupled with the DFO chelator was labeled with the positron emitter zirconium-89. Imaging: HER2 tumoral levels at day 48 post-treatment initiation were monitored via PET/CT images and *ex vivo* biodistribution of [^{89}Zr]Zr-DFO-Trastuzumab (6.66–7.4 Mbq, 45–50 μg protein, >99% RCP). Western blot analysis: Analyses of HER2-mediated signaling pathways were conducted using *ex vivo* NCIN87 tumor extracts excised at day 60 (n=3).

Results:
NCIN87 tumor volumes monitored across a 60-day period from treatment initiation were significantly lower ($P<0.001$) in both Statin-treated TDM1 cohorts, regardless of multi- or single-dose TDM1 administration, than compared to control and TDM1 administration alone (**Figure 1B**). The same observations were made in the gastric PDX model of known clinical resistance to anti-HER2 therapy. Immuno-PET demonstrated decreased uptake of ^{89}Zr-Trastuzumab in NCIN87 tumors upon co-administration with Statins, in both multi- and single TDM1 dosing regimes, indicating TDM1-mediated HER2 depletion at 48 days after therapy initiation (**Figure 1C**). *Ex vivo* biodistribution of the tumors excised from mice after imaging quantified a 1.3-fold decrease in ^{89}Zr-Trastuzumab uptake when Statins were co-administered with TDM1 compared to TDM1 administration alone, which was significant in TDM1 single-dose vs. TDM1/Statin single-dose (P=0.02, **Figure 1D**). Downstream signaling analysis from NCIN87 tumor extracts demonstrated depletion of HER2 and phospho-HER2 following TDM1 co-administration with Statins, in both multi- and single-dose regimes, as well as an 8-fold reduction in phospho-HER3 and a 6-fold reduction in phospho-EGFR in comparison to control tumors. Tyrosine phosphorylation was downregulated in TDM1/Statin multi- or single-dose tumors. Depletion of HER signaling pathways was more successful upon co-administration with Statin compared to TDM1 treatment alone (**Figure 1E,F**). Although TDM1/Statin delayed tumor growth via signaling inhibition, xenograft regrowth arises at 59 days accompanied by an upregulation in phospho-ERK signaling (3-fold induction vs. TDM1 alone; **Persuasive Data**). Ongoing work is exploring phospho-ERK as a resistance mechanism in TDM1/Statin treated tumors.

Conclusions:
This study demonstrates that Statins enhance TDM1 potency in gastric tumor models to such a degree that it enables single-dose administration. Immuno-PET serves as a non-invasive tool to monitor HER2 depletion *in vivo* in response to TDM1 administration. Ongoing work is investigating the possible role of Erk signaling as a resistance mechanism to TDM1/Statin therapeutic strategies and developing combinatorial approaches to prevent or delay the emergence of TDM1 resistance in HER2-expressing tumors.

Reference

1. Oh DY and Bang YJ, HER2-targeted therapies - a role beyond breast cancer. Nat Rev Clin Oncol. 2020;17(1):33-48.
2. Abdel-Qadir H, Bobrowski D, Zhou L, et al. Statin Exposure and Risk of Heart Failure After Anthracycline- or Trastuzumab-Based Chemotherapy for Early Breast Cancer: A Propensity Score–Matched Cohort Study. Journal of the American Heart Association. 2021;10:e018393
3. Pereira PMR, Sharma SK, Carter LM, et al. Caveolin-1 mediates cellular distribution of HER2 and affects trastuzumab binding and therapeutic efficacy. Nat Commun. 2018;9(1):5137.
4. Pereira PMR, Mandleywala k, Monette S, et al. Caveolin-1 temporal modulation enhances trastuzumab and trastuzumab-drug conjugate efficacy in heterogeneous gastric cancer. Nat Commun. 2022. In Press.

Oral Presentation

Disclosures: The authors have disclosed no financial interest.

161-TSPO- and Tau-PET detect neuroinflammation and tau-based accumulation in a novel non-human primate tauopathy model of Alzheimer's Disease

Presenter: Brad Hobson, University of California, Davis

Brad A. Hobson[1], Sean Ott[2], Danielle Beckman[3], John Morrison[3], Abhijit J. Chaudhari[1]
[1]*University of California, Davis, Sacramento, CA*
[2]*University of California Davis, Davis, CA*
[3]*University of California Davis, Davis, California*

Alzheimer's disease (AD) is a devastating, progressive, neurodegenerative disorder that affects more than 6 million Americans [1]. Currently there is a paucity of effective treatments to counteract or slow the progression of AD due in part to the limitations of current preclinical models and tools for studying clinically relevant disease. As a result, the mechanisms underlying the development and progression of AD remain unclear. Recent advancements in viral vector-mediated gene transfer have enabled an inducible, tau-based monkey model of AD that recapitulates the degenerative phase of disease [2]. To-date, however, characterization of this model has been limited spatially and temporally by the high resource costs of terminal histopathological studies. PET with correlative MRI may be particularly well suited to characterize the spatiotemporal progression of AD in this model, and additionally probe candidate mechanisms, such as neuroinflammation and tau accumulation, as these processes can be monitored longitudinally before and after the initiation of disease. Thus, the objective of the present study was to investigate the interaction between adeno-associated virus (AAV)-induced tau expression and local neuroinflammatory responses using tau- and translator protein (TSPO)-PET, respectively, within this emerging monkey tauopathy model of AD. Adult female rhesus macaques (n=5) were administered bilateral injections of AAV expressing a double tau mutation (AAV1-2xTAU; left entorhinal cortex) or empty vector (AAV1-CTR4; right entorhinal cortex) using a surgical stereotaxic navigation system. Tau- and TSPO-PET utilizing the [^{18}F]T807 (T807) radiotracer to assess tau accumulation and [^{18}F]PBR111 (PBR111) to assess neuroinflammation, respectively, were conducted at baseline (prior to injection) and 6-months post AAV administration using a dedicated non-human primate brain PET scanner (pPET, Brain Biosciences). PET data were reconstructed into a single 50-60 min or 80-110 min frames for PBR111 or T807, respectively. PET images were manually registered to corresponding T_1-weighted 3.0T brain MRI scans of each animal, and then normalized into the INIA19 space [3]. Spherical volumes of interest (VOIs) were centered on AAV injection sites within the entorhinal cortex based on surgical planning coordinates, and a third sphere was placed within the cerebellum (reference region). The mean standard uptake value (SUV), and SUV ratio (SUVR) normalized to the cerebellum, were calculated for injection site VOIs using the PMOD software. Statistical analysis included two-way analysis of variance (ANOVA) with Tukey post hoc test to assess differences across imaging time points and hemisphere. At the completion of imaging, animals were taken for correlative histology to evaluate neuroinflammation and signs of AD neuropathology. Co-registered PET and MR images acquired 6 months after AAV injection revealed areas of increased T807 and PBR111 uptake in the left hemisphere that were visually most pronounced at injection sites and spread dorsally and posteriorly along the entorhinal and hippocampal formations. No such lesions were observed on the contralateral location nor was this asymmetry observed in baseline scans of either tracer. Quantitative SUVR analysis revealed significant increases in PBR111 uptake at injections sites in both hemispheres at follow-up compared to baseline (left, $p< 0.001$; right, $p= 0.016$). Uptake of T807 showed a similar trend ($p=0.055$) in only the left hemisphere. Furthermore, 6-months post AAV, PBR111 uptake in the AAV-2xTAU injection site was significantly increased when compared to the contralateral AAV-CTR4 site ($p=0.016$). Again, T807 showed a similar trend ($p=0.0855$), and no such changes were observed between the injection sites at baseline. Collectively, these data suggest localized increases in tau accumulation (detected by T807) drive corresponding neuroinflammation (detected by PBR111) in this non-human primate tauopathy model of AD. Our results strongly suggest that longitudinal Tau- and TSPO-PET warrant further investigation as tools for monitoring AD-related progressive neuropathology.

Reference

1. "2022 Alzheimer's disease facts and figures," Alzheimers Dement, vol. 18, pp. 700-789, Apr 2022.
2. D. Beckman, P. Chakrabarty, S. Ott, A. Dao, E. Zhou, W. G. Janssen, et al., "A novel tau-based rhesus monkey model of Alzheimer's pathogenesis," Alzheimers Dement, vol. 17, pp. 933-945, Jun 2021.
3. T. Rohlfing, C. D. Kroenke, E. V. Sullivan, M. F. Dubach, D. M. Bowden, K. A. Grant, et al., "The INIA19 Template and NeuroMaps Atlas for Primate Brain Image Parcellation and Spatial Normalization," Front Neuroinform, vol. 6, p. 27, 2012.

Oral Presentation

Disclosures: The authors have disclosed no financial interest.

162-CD8 ImmunoPET Visualizes an Early CD8+ Immune Response Induced by Combined Radiation and Anti-CTLA4 Treatment in an Orthotopic Mouse Model of Breast Cancer

Presenter: Elizabeth Germino, City of Hope

Elizabeth Germino[1], Kirstin A. Zettlitz[1], Deirdre La Placa[1], Shichang Li[2], Heather McGee, Terence Williams, Anna M. Wu[1]

[1]*City of Hope, Duarte, CA*
[2]*City of Hope*

Objectives: CD8+ T cells are the main effector cells for immune-mediated anti-tumor responses [1], and CD8+ T cell tumor infiltration

correlates with prognosis and response to immunotherapy across many disease sites [2-4]. Preclinical data have also demonstrated a CD8+ cell-dependent synergistic effect of radiation treatment (RT) combined with checkpoint inhibitors [5-8]. However, as combinatorial strategies are investigated for clinical translation, better prognostic and predictive biomarkers are needed. CD8 immunoPET is being explored for noninvasive, whole body CD8+ cell imaging in early clinical trials [9] but optimal timing for imaging after RT + immunotherapy is unknown and has not been studied in preclinical models, particularly with orthotopic tumors that better approximate the natural tumor immune microenvironment. The purpose of this study is to characterize the intratumoral CD8+ response to RT combined with anti-CTLA4 in an orthotopic mouse model of breast cancer and to test the feasibility of using CD8 immuno-position emission tomography (immunoPET) to visualize this response at an early timepoint after treatment.

Methods:

4T1 tumors were implanted in a mammary fat pad of female BALB/c mice and treated conformally with 8 Gy fractions for 3 consecutive days (X-RAD SmART system) followed by 3 doses anti-CTLA4 (200 micrograms intraperitoneally every third day). Tumors were harvested prior, during and after treatment at multiple timepoints for analysis of CD8 staining by immunohistochemistry (IHC). CD8+ cell density was quantified using Visiopharm software; comparisons were made by one-way ANOVA of log-transformed data, with p values adjusted for multiple comparisons. Single cell suspensions of digested tumors were analyzed by flow cytometry for CD8 and additional immunological markers. For imaging studies, a Zr-89 radiolabeled CD8-specific cys-diabody was injected by tail vein within 24 hours of the final treatment day, or in mice with size-matched untreated tumors, and static images were acquired 24 hours later on a PET/CT scanner (GNext). Mean % injected dose (%ID)/cc for each tumor was calculated from 3 non-overlapping intratumoral regions of interest (ROIs, drawn on CT scans) to mitigate partial volume effects. Activity (%ID/gram, %ID/g) was confirmed with ex vivo biodistribution studies. Unpaired t-test was used for comparisons of treated to untreated mice.

Results:

Tumors treated with RT + anti-CTLA4 (n=14) demonstrated variable but overall increased CD8+ cell density by IHC 24 hours after completing treatment compared to untreated tumors (n=12), mean cell count/mm^2 852 vs 63, p<0.0001; median 590 vs 50, range 40-3484 vs 24-210. Flow cytometry analysis confirmed variability in CD8+ cell infiltration of treated tumors (n=5). Compared to untreated tumors, CD8+ cell density by IHC was not significantly increased in tumors after 1 fraction of RT alone (8 Gy), those treated with RT alone (8 Gy x3) and those harvested 2 weeks after completion of combined treatment. Tumors and tissues enriched for CD8+ cells (including lymph nodes, thymus, and spleen) were visualized with CD8 immunoPET in all mice. Mean %ID/cc for intratumoral ROIs was higher on average for treated vs untreated tumors (6.55 vs 4.91, p=0.0019, n=9 each group). Ex vivo biodistribution studies demonstrated increased %ID/g for treated tumors, n=8, compared to untreated tumors, n=9 (mean %ID/g 3.63 vs 2.25, p=0.0005), consistent with greater CD8+ cell infiltration into treated tumors.

Conclusion:

CD8 immunoPET successfully visualized the intratumoral CD8+ cell response induced by RT + anti-CTLA4 combination therapy as early as 24 hours after completion of treatment in an orthotopic mouse model of breast cancer. CD8 immunoPET will facilitate further studies of longitudinal immune responses in this newly established model for combination therapy with RT + immunotherapy, and will also enable investigation of adjunct therapies for tumors with low CD8+ responses after initial treatment. These preclinical data could inform clinical use of CD8 immunoPET as an early biomarker after RT + immunotherapy in future clinical trials.

Reference

1. Durgeau A et al. Recent advances in targeting CD8 T-cell immunity for more effective cancer immunotherapy. Frontiers in immunology. 2018 Jan 22;9:14.
2. Barnes TA, Amir E. HYPE or HOPE: the prognostic value of infiltrating immune cells in cancer. British journal of cancer. 2017 Aug;117(4):451-60.
3. Gooden MJ et al. The prognostic influence of tumour-infiltrating lymphocytes in cancer: a systematic review with meta-analysis. British journal of cancer. 2011 Jun;105(1):93-103.
4. Paijens ST et al. Tumor-infiltrating lymphocytes in the immunotherapy era. Cellular & molecular immunology. 2021 Apr;18(4):842-59.
5. Demaria S et al. Immune-mediated inhibition of metastases after treatment with local radiation and CTLA-4 blockade in a mouse model of breast cancer. Clinical Cancer Research. 2005 Jan 15;11(2):728-34.
6. Lee Y et al. Therapeutic effects of ablative radiation on local tumor require CD8T cells: changing strategies for cancer treatment. Blood. 2009 Jul 16;114(3):589-95.
7. Gupta A et al. Radiotherapy promotes tumor-specific effector CD8T cells via dendritic cell activation. The Journal of Immunology. 2012 Jul 15;189(2):558-66.
8. Twyman-Saint Victor C et al. Radiation and dual checkpoint blockade activate non-redundant immune mechanisms in cancer. Nature. 2015 Apr;520(7547):373-7.
9. Farwell MD et al. CD8-Targeted PET Imaging of Tumor-Infiltrating T Cells in Patients with Cancer: A Phase I First-in-Humans Study of 89Zr-Df-IAB22M2C, a Radiolabeled Anti-CD8 Minibody. Journal of Nuclear Medicine. 2022 May 1;63(5):720-6.

Oral Presentation

Disclosures: The authors have disclosed no financial interest.

163-Photoacoustic imaging for the detection of endogenous near-infrared biomarkers in high-risk atherosclerotic plaques

Presenter: Martin Schneider, Stanford University

Martin K. Schneider[1], James Wang[2], Caitlin Bell[3], Tom Alsaigh[4], Steven R. Long[5], Nicholas R. Leeper[6], Katherine W. Ferrara[1]

[1]*Stanford University, Palo Alto, CA*
[2]*Stanford University, Palo Alto, California*
[3]*Stanford School of Medicine, CA*
[4]*Stanford School of Medicine*
[5]*University of California, San Francisco, San Fransisco, CA*
[6]*Stanford University, Stanford, California*

Abstract body:

Atherosclerosis is a major cause of mortality and morbidity, due to progression to myocardial infarction and stroke. These complications are caused by thrombotic arterial occlusions localized at the site of high-risk atherosclerotic plaques, and therefore early detection and therapeutic stabilization are urgently needed [1-6]. The goal of this project is to discriminate vulnerable versus stable plaques using non-invasive, non-ionizing photoacoustic (PA) imaging [7,8]. PA signals caused by

near-infrared endogenous chromophores within high- and low-risk human plaques have been evaluated and compared with histological analysis and spatial RNAseq [7,9].

Experimental Design:
An IRB (IRB-50541) approved by the Stanford University Investigator Review Board approved the collection of discarded human carotid plaque specimens from Stanford Hospital. The specimens have been imaged fresh or fixed in 4% PFA for the auto-near-infrared (Auto-NIR) signal in the 670-700nm range, using a commercial PA device (Visualsonics 3100). Afterwards, tissue slides of each plaque specimen were generated and imaged for the endogenous autofluorescence near-infrared (NIR) signal (Cy5). Additionally, slides were processed with histological stains spanning H&E, Masson's Trichome, Picrosirus Red, CD68, αSMA and bilirubin. Spatial RNA sequencing (10x Visium) has been performed on plaque sections. Detected Auto-NIR signals in PA images and histological images were compared with established stains and spatial RNA sequencing results.

Results:
PA 3D imaging of ex vivo human carotid plaque detected areas of high Auto-NIR PA signals (Fig.1a-b). Cross section analysis of PA images and respective stained histological sections showed that the Auto-NIR signal correlates with vulnerable histology markers, such as CD68 and bilirubin (Fig.1c). The PA intensity was significantly enhanced in the vulnerable regions ($p<0.0001$) in comparison to histologically stable regions of the plaque ($n = 22$) (Fig. 1d). We also demonstrated a significant correlation between the naturally-occurring NIR signal, the CD68 macrophage marker ($p<0.0001$) and bilirubin ($p<0.0001$) (Fig. 1e). Other tissue structures such as alpha smooth muscle actin (αSMA), a marker for a healthy and stable artery, were evaluated as a control and correlation with the near-infrared biomarker was significantly lower ($p<0.0001$) (Fig. 1e).

Conclusion:

Photoacoustic imaging detected the $CD68^{+}$ $bilirubin^{+}$ region of pathological atherosclerosis associated with unstable plaque.

Reference

1. Virmani, R., Burke, A. P., Farb, A. & Kolodgie, F. D. Pathology of the vulnerable plaque. J Am Coll Cardiol 47, C13-18, doi:10.1016/j.jacc.2005.10.065 (2006).
2. Falk, E. Pathogenesis of atherosclerosis. J Am Coll Cardiol 47, C7-12, doi:10.1016/j.jacc.2005.09.068 (2006).
3. Virmani, R., Kolodgie, F. D., Burke, A. P., Farb, A. & Schwartz, S. M. Lessons from sudden coronary death: a comprehensive morphological classification scheme for atherosclerotic lesions. Arterioscler Thromb Vasc Biol 20, 1262-1275, doi:10.1161/01.atv.20.5.1262 (2000).
4. Stary, H. C. et al. A definition of advanced types of atherosclerotic lesions and a histological classification of atherosclerosis. A report from the Committee on Vascular Lesions of the Council on Arteriosclerosis, American Heart Association. Circulation 92, 1355-1374, doi:10.1161/01.cir.92.5.1355 (1995).
5. Stary, H. C. et al. A definition of the intima of human arteries and of its atherosclerosis-prone regions. A report from the Committee on Vascular Lesions of the Council on Arteriosclerosis, American Heart Association. Circulation 85, 391-405, doi:10.1161/01.cir.85.1.391 (1992).
6. Libby, P. et al. Atherosclerosis. Nat Rev Dis Primers 5, 56, doi:10.1038/s41572-019-0106-z (2019).
7. Htun, N. M. et al. Near-infrared autofluorescence induced by intraplaque hemorrhage and heme degradation as marker for high-risk atherosclerotic plaques. Nat Commun 8, 75, doi:10.1038/s41467-017-00138-x (2017).
8. Moreno, P. R. Vulnerable plaque: definition, diagnosis, and treatment. Cardiol Clin 28, 1-30, doi:10.1016/j.ccl.2009.09.008 (2010).
9. Kang, S. J. et al. Combined IVUS and NIRS detection of fibroatheromas: histopathological validation in human coronary arteries. JACC Cardiovasc Imaging 8, 184-194, doi:10.1016/j.jcmg.2014.09.021 (2015).

Oral Presentation

Disclosures: The authors have disclosed no financial interest.

164-Enhanced Penetration Of Magnetic Nanoclusters Into Tumors Using Non-linear Magnetic Fields To Improve Diagnosis And Treatment

Presenter: Bian Jang, University of Pennsylvania

Bian Jang[1], Ahmad Amirshaghaghi[2], Zhiliang Cheng[2], Andrew Tsourkas[2]
[1]*University of Pennsylvania*
[2]*University of Pennsylvania, Philadelphia, PA*

Introduction:
Nanoparticles have been widely explored for use in cancer diagnosis and treatment; however, the efficacy is often limited by the inability to penetrate into the tumor due to the dense extracellular matrix (ECM) and the high interstitial fluid pressure (IFP) around tumor cells. A previous paper explored whether a magnetic device comprised of two oppositely polarized magnets could be used to enhance the accumulation and penetration of magnetic nanoparticles within tumor tissues. The use of two oppositely polarized magnetics created a constant magnetic field gradient between the two magnets, thus allowing magnetic nanoparticles to be manipulated at much greater depths than is possible with a single magnet, whereby there is a rapid drop in magnetic field strength with distance from the magnet surface [1]. To further improve upon the 2-magnet device, here we describe an 8-magnet device with a stronger magnetic flux density and magnetic field gradient that is constant in 360 degrees. As the magnetic force on magnetic particles is proportional to the field gradient, the 8-magnet device is able to accelerate the penetration of magnetic nanoparticles into deeply seeded tumors and thus improve both the magnetic resonance imaging (MRI) contrast and treatment efficacy of drug-loaded magnetic nanoparticles.

Materials and Methods:
CoSPIONs are synthesized by seed growth and are encapsulated within the amphiphilic photosensitizer Ce6, forming clusters (Ce6 cluster). Our customized magnetic device was built with 8 neodymium-iron-boron (NdFeB) rare earth element magnets arranged in a cylindrical halbach array. Finite element modeling software, COMSOL, was used to simulate the orientation of the magnetic field and calculate the magnetic field gradient. To calculate the actual magnetic field gradient in three dimensions, we measured the magnetic flux density at different points in the inner space of the device with a gaussmeter. A 0.6% agarose gel tumor phantom was used to study the magnetic forces on clusters placed in the device. *in vivo* MR and *ex vivo* fluorescence images using a syngeneic orthotopic mouse model of 4T1 breast cancer cells were acquired at 24h post-injection (*i.v.*) of Ce6 cluster, dosed at 5 mg Ce6/kg, followed by magnetic exposure.

Results and Discussion:

First, we confirmed the size and uniform morphology of synthesized clusters by transmission electron microscopy (TEM) and dynamic light scattering (DLS). The diameter of CoSPIONs was ~10 nm with a uniform size distribution (Figure A). After the encapsulation into clusters, the size increased to ~60 nm (Figure B). Then, we verified the generation of a sharp zero point at the center of the magnetic device, which was surrounded by uniform field gradients radiating outward (Figure C-F). Next, we evaluated the movement of magnetic clusters through a gel phantom when placed in the 8-magnet device and compared the penetration speed with the 2-magnet device (Figure G-H). Based on MR imaging, it is clear that exposure to the 8-magnet device significantly reduces T2 signal (hypointensity) from Ce6 clusters in tumors (Figure I-J). In addition, tumors from the mice exposed to 8-magnet device show the highest Ce6 fluorescence indicating the improved accumulation of nanoparticles compared with the 2-magnet groups (Figure K-L).

Conclusions:

By using an 8-magnet device, we were able to generate a constant magnetic field gradient with the zero point at the center which exerts a uniform force on the clusters and yields constant velocity in tumor tissues. Our results also proved the possible application of this new system in targeted magnetic delivery and deep tissue penetration, which can result in the improved MR imaging contrast and treatment efficacy of drug-loaded magnetic nanoparticles.

Reference

1. Liu, Jessica F., et al. "Use of oppositely polarized external magnets to improve the accumulation and penetration of magnetic nanocarriers into solid tumors." ACS nano 14.1 (2019): 142-152.

Oral Presentation

Disclosures: The authors have disclosed no financial interest.

165-3D U-Net based internal carotid artery segmentation for derivation of image derived blood input function for human brain dynamic FDG PET

Presenter: Zoraiz Qureshi, University of Virginia

Zoraiz Qureshi[1], Gabriel G. Hyman[2], David Schiff[2], Mark Quigg[3], Miaomiao Zhang[2], Bijoy Kundu[2]

[1]*University of Virginia, Charlottesville*
[2]*University of Virginia, Charlottesville, VA*
[3]*University of Virginia, Charlottesville, Virginia*

Objectives:

Manual segmentation of the internal carotid arteries (ICA) is the current gold standard target for deriving the image derived blood input function (IDIF), which, in turn, is used to calibrate glucose kinetics for human dynamic Fluorine-18 fluorodeoxyglucose positron emission tomography (dFDG-PET). The main objective of this work is to develop a fully automatic pipeline that can facilitate segmentation of ICA, enabling consistent and efficient derivation of image derived blood input function (IDIF).

Materials and Methods:

Dynamic FDG PET (dFDG-PET) of the brain was performed on 35 subjects using a time of flight PET CT scanner to produce a DICOM file that contained a complete four dimensional image of each patient's brain tracer uptake with attenuation correction over time (400 pixels x 400 pixels x 110 slices x 38 timeframes). Dynamic acquisition consisted of an intravenous ~10 mCi tracer injection over 10 seconds with initiation of a 60-minute scan in list-mode format. PET was preceded by non-contrast T1-weighted MPRAGE MRI scans for co-registration. Image pre-processing started with motion correction for the 60-minute acquisition to align and lock the anatomy in the same 3-dimensional space throughout the entire time period. Motion correction of dynamic PET data and co-registration into MRI space were performed as described [1] with bash scripts designed using the FMRIB's Software Library (FSL) tool kit [2-6]. Next, a reference frame containing the ICA was programmatically selected from dFDG-PET data through intensity analysis. This was followed by semi-automatic annotation of both the left and right ICA by localized thresholding using 3DSlicer. A supervised artificial neural network architecture was developed and trained to segment the ICA from the reference frame, allowing for the automatic derivation of the IDIF. Briefly, a 3D U-Net architecture was trained with the reference frame as the input volume and the binary 3D segmentation mask consisting of the model's prediction of the ICA for that dataset as output. The model architecture was defined in Keras TensorFlow with a depth of 2 (number of encoder / decoder blocks) and 16 base convolutional filters in the first layer (~984k model parameters) along with 3D spatial dropout layers of 0.5. Due to computational limitations, for pre-processing, the selected image frames, originally of varying dimensions, were rescaled, systematically padded and cropped to 128x128x128 dimensions. Similarly, the output binary mask (obtained with a decision threshold of 0.5) was post-processed to restore the dataset to its original dimensions. Training was performed over the 35 dFDG-PET datasets using 10-fold cross-validation using the centerline Dice loss function [7], with a batch size of 1 and Adam optimizer with a learning rate of 0.001 for 50 epochs per fold (~8.3 hours total) in Google Colab Pro+ (P100 GPU). 3-fold data augmentation was also applied on the training set for each fold based on rotation, elastic deformation and horizontal flips during training. Downstream IDIFs were computed from the predicted ICA segmentations.

Results:

For generated test set segmentations, average evaluation metrics across the 10 folds show a Dice Similarity Coefficient of 0.737 ± 0.092, Intersection over Union (IoU) of 0.599 ± 0.112, 95% Robust Hausdorff Distance (RHD 95) of 13.479 ± 7.821. The downstream metrics for similarity between ground truth IDIFs and those generated from predicted ICA segmentations had a root mean squared error (RMSE) of 1397.148 ± 777.056 Bq/cc and a mean absolute percentage error (MAPE) of 8.415 ± 3.960 %.

Conclusion:

Despite the limited sample size, this work suggests that the 3D U-Net was effectively able to learn the underlying distribution of the target structure of the ICA and could precisely facilitate the automatic computation of the IDIF for dFDG-PET of the human brain.

Reference

1. Seshadri V, et al. Dynamic FDG-PET in localization of focal epilepsy: A pilot study. Epilepsy Behav. 2021;122:108204.
2. Smith, S.M., Jenkinson, M., Woolrich, et al. Advances in functional and structural MR image analysis and implementation as FSL. Neuroimage 2004; 23: S208-219.
3. Woolrich, M.W., Jbabdi, S., Patenaude, B., et al. Bayesian analysis of neuroimaging data in FSL. Neuroimage 2009; 45:S173-186.

4. Jenkinson, M., Bannister, P., Brady, M. and Smith, S. Improved optimization for the robust and accurate linear registration and motion correction of brain images. Neuroimage 2002; 17: 825-841.
5. Jenkinson, M., Beckmann, C.F., Behrens, T.E., et al. Fsl. Neuroimage 2012; 62:782-790.
6. Jenkinson, M. and Smith, S. A global optimisation method for robust affine registration of brain images. Med Image Anal 2001;5:143-156.
7. Shit, S., Paetzold, J. C., Sekuboyina, A.,et al. clDice-a novel topology-preserving loss function for tubular structure segmentation. In Proceedings of the IEEE/CVF Conference on Computer Vision and Pattern Recognition 2021; 16560-16569.

Oral Presentation

Disclosures: The authors have disclosed no financial interest.

166-A novel radiotracer in conjunction with Cerenkov imaging allows non-invasive monitoring of hepatic myofibroblasts in a mouse model of acute liver injury.

Presenter: Saimir Luli, Newcastle University

Saimir Luli[1], Toni A. Pringle[2], Erik Ramon Gil[3], Jack Leslie[4], Fiona Oakley, James Knight[1]

[1]Newcastle University, Newcastle upon Tyne, Tyne and Wear, United Kingdom
[2]Newcastle University, Newcastle Upon Tyne, United Kingdom
[3]Newcastle upon Tyne, England, United Kingdom
[4]Newcastle University, Newcastle, United Kingdom

Background & Aims:
Chronic liver disease is a major global health care burden[1]. Early diagnosis of liver fibrosis is highly important to improve patient outcomes [2]. Liver biopsy is the gold standard for assessing liver fibrosis. However, the biopsy is invasive, and the sample may not be representative of disease [3]. To address these limitations, a single-chain antibody (C1-3) and *in vivo* fluorescence imaging have successfully been used to assess fibrogenesis in murine models of liver injury [4]. C1-3 is a potent binder of synaptophysin (SYN), a transmembrane protein expressed on scar-forming hepatic myofibroblasts (HM) [5,6]. While *in vivo* fluorescent imaging provides a screening tool, it is limited by autofluorescence and lacks clinical translatability [7]. This study aims to Zirconium-89 [^{89}Zr] labelled C1-3 and determine if it can be used with clinically available positron emission tomography (PET). PET allows the *in vivo* detection of radiopharmaceuticals with high sensitivity and unlimited depth penetration [8].

Methods:
C1-3 and CSBD9 single chain antibodies (ScAb) were generated using phage display. CSBD9 is raised against bacterial protein, therefore, it doesn't recognise mammalian SYN. ScAbs were modified with desferrioxamine and characterised by MALDI-TOF before radiolabelling with ^{89}Zr. C1-3-DFO-[^{89}Zr]Zr and CSBD9-DFO-[^{89}Zr] Zr (60ug/ml) were incubated with activated HM to determine the specificity of C1-3 for SYN. A mouse model of acute liver injury in conjunction with *in vivo* optical (Cerenkov) imaging was applied to determine if C1-3-DFO-[^{89}Zr] Zr can be used as an *in vivo* imaging agent. *In vivo* activation of HM and therefore expression of SYN was induced via an I.P injection of Carbon Tetrachloride (CCl_4). An IVIS® spectrum was applied to visualise radiolabelled ScAbs. *Ex vivo* liver uptake was determined using a gamma counter (Figure 1A). Alpha-smooth muscle actin (α-SMA) staining was performed to assess the number of HM.

Results:
To determine if C1-3 can be used as an imaging agent, ScAbs were conjugated to desferrioxamine (DFO, yield = 70.58 ± 3.34 %) followed by labelling with ^{89}Zr. Stability assays demonstrated that both ScAb complexes, C1-3-DFO-[^{89}Zr]Zr and CSBD9-DFO-[^{89}Zr]Zr were stable in both human and mouse serum (supplemental 1). Cell analysis revealed that the ability of C1-3 to bind to HM was not hindered by radiolabelling. Considering that C1-3 specifically binds to SYN, and SYN is involved in endocytosis, it was not surprising that cell internalisation of C1-3-DFO-[^{89}Zr]Zr was significantly higher compared to control CSBD9-DFO-[^{89}Zr] Zr (Figure 1B). *In vivo* Cerenkov imaging showed that C1-3-DFO-[^{89}Zr] Zr was highly retained in the CCl_4 injured livers compared to oil treated controls where HM are in a quiescent state and the expression of SYN is negligible. In CCl_4 injured mice, the uptake of C1-3-DFO-[^{89}Zr]Zr was preferential compared to CSBD9-DFO-[^{89}Zr]Zr (Figure 1C-D). A limitation of Cerenkov chemiluminescence is the low signal-to-noise ratio due to tissue depth and the inability of the technology to control for photon attenuation. To validate the *in vivo* results, livers were harvested and the injected dose per gram of tissue was assessed. *Ex vivo* Gamma counting revealed that the uptake of C1-3-DFO-[^{89}Zr]Zr was significantly higher compared to CSBD9-DFO-[^{89}Zr]Zr and that C1-3 differentiates between fibrotic and non-fibrotic injury (Figure 1E). Analysis of αSMA (whole mark of HM) staining confirmed that the uptake of C1-3 is specific rather than due to differences in HM numbers between C1-3 and CSBD9 imaged mice (Figure 1F). Our data demonstrate that C1-3 can be used as an *in vivo* imaging agent in conjunction with PET imaging. Because C1-3 is humanised, it has the potential to be used in clinics in the early diagnosis of liver fibrosis and assess antifibrotics.

Reference

1. Asrani, S. K., Devarbhavi, H., Eaton, J. & Kamath, P. S. Burden of liver diseases in the world. Journal of Hepatology vol. 70 (2019).
2. Hydes, T., Brown, E., Hamid, A., Bateman, A. C. & Cuthbertson, D. J. Current and Emerging Biomarkers and Imaging Modalities for Nonalcoholic Fatty Liver Disease: Clinical and Research Applications. Clinical Therapeutics vol. 43 (2021).
3. Bedossa, P. & Carrat, F. Liver biopsy: The best, not the gold standard. Journal of Hepatology vol. 50 (2009).
4. Luli, S. et al. A new fluorescence-based optical imaging method to non-invasively monitor hepatic myofibroblasts in vivo. Journal of Hepatology 65, 75–83 (2016).
5. Elrick, L. J. et al. Generation of a monoclonal human single chain antibody fragment to hepatic stellate cells – a potential mechanism for targeting liver anti-fibrotic therapeutics. Journal of Hepatology 42, 888–896 (2005).
6. Cassiman, D. et al. Synaptophysin: A Novel Marker for Human and Rat Hepatic Stellate Cells. The American Journal of Pathology 155, 1831–1839 (1999).
7. Leslie, J., Robinson, S. M., Oakley, F. & Luli, S. Non-invasive synchronous monitoring of neutrophil migration using whole body near-infrared fluorescence-based imaging. Scientific Reports 11, (2021).
8. Piwowarska-Bilska, H., Supińska, A., Iwanowski, J., Tyczyńska, A. & Birkenfeld, B. PET – advanced nuclear imaging technology for medicine. Pomeranian Journal of Life Sciences 65, (2019).

Oral Presentation

Disclosures: The authors have disclosed no financial interest.

167-Near Infrared Nerve-Specific Probes for Fluorescence Guided Neurosurgery

Presenter: Anas Masillati, Oregon Health & Science University

Anas M. Masillati[1], Lei G. Wang[2], Connor Barth[3], Antonio R. Montano[2], Summer L. Gibbs[2]

[1]*Oregon Health & Science University, Portland*
[2]*Oregon Health & Science University, Portland, OR*
[3]*Oregon Health & Science University*

Iatrogenic nerve injury presents one of the most feared surgical complications and a major source of morbidity across various surgical specialties. A major challenge in skull base surgery is the preservation of cranial nerve integrity, which is required to maintain their critical function and to decrease post-surgical morbidity. Cranial nerves are often intimately associated with tumors of the skull base, where surgery can be curative, but must be balanced against injury risk. Unlike other critical tissues, nerve repair results in negligible, unreliable functional improvement leading to permanent motor or sensory disabilities and chronic neuropathies. During skull base surgery, neurosurgeons rely mainly on their neuroanatomical knowledge, white light visualization and neurophysiological monitoring to identify and visualize the cranial nerves, making preservation extremely challenging especially during minimally invasive procedures. Currently there is no clinically approved method to enhance the visualization of nerve structures intraoperatively, and as a result cranial nerves remain one of the most frequently injured nerve structures across all surgical subspecialities. Recently, our group has developed a library of novel near infrared (NIR) small molecules with demonstrated high specificity and signal to background ratio in the peripheral nerves. Strikingly, it was discovered that a subset of these novel probes can cross the blood-brain barrier (BBB) resulting in varied degrees of cranial nerves specificity. Pharmacokinetic (PK) studies of our lead compounds demonstrated cranial nerve contrast is obtained 30 minutes post systemic administration, and the contrast lasts for > 4 hours post intravenous injection, a PK profile compatible with a variety of neurosurgical interventions. In addition, our lead compounds showed substantial specificity for trigeminal and facial nerves branches, which expands the utility of the obtained contrast to head and neck surgical application as well. Overall, these newly developed NIR nerve-specific compounds will significantly improve nerve identification at depth, enhancing the ability to detect buried cranial nerves, which will be paramount to decreased iatrogenic injury. Finally, the ability of these compounds to cross the BBB and their cranial nerve specificity could solve the unmet clinical need for an intraoperative methodology to enhance identification and visualization of cranial nerves.

Oral Presentation

Disclosures: The authors have disclosed no financial interest.

168-125I-labeled imidazole naphthyridine derivatives as Tau imaging agents in Alzheimer's Disease

Presenter: Tianqing Liu, Beijing Normal University

Tianqing Liu[1], Mengchao Cui[2]

[1]*Beijing Normal University, China*
[2]*Beijing Normal University, Beijing, China, China*

Abstract body:

Tianqing Liu, Mengchao Cui* Key Laboratory of Radiopharmaceuticals, Ministry of Education, College of Chemistry, Beijing Normal University, Beijing 100875, P. R. China

Objectives:
Compared with β-amyloid (Aβ) plaques, abnormal deposition of Tau protein is more positively associated with the degree of cognitive dysfunction in Alzheimer's disease (AD). Thus, developing Tau imaging tracers with excellent characteristics is conducive to enhancing diagnostics and providing more valuable information for disease staging and treatments. In this study, we designed and synthesized a novel probe with satisfying properties for the detection of Tau fibrils.

Methods*:*
Radiosynthesis of ^{125}I-labeled ligands was carried out using corresponding tributyltin precursors. Specific binding to neurofibrillary tangles was confirmed by *in vitro* autoradiography on brain tissues from AD patients (102 years old, female, temporal lobe and hippocampus; 95 years old, female, frontal lobe). Furthermore, to measure the affinity to Tau, we performed the self-blocking study by *in vitro* autoradiography on brain sections in the presence of cold PND-118 with different concentrations. We also assessed its affinity to $A\beta_{1-42}$ aggregates through *in vitro* competitive binding assays using [^{125}I]IMPY as the radioligand. *In vivo* biodistribution was conducted on normal ICR mice (18-20 g, male).

Results:
As shown in **Fig. 1**, specific binding of neurofibrillary tangles was verified by *in vitro* autoradiography and GB-staining on brain sections of AD patients. There is a marked accumulation of radioactive signal on the gray matter of temporal lobe loading with Tau aggregates, which the regional distribution corresponds precisely to the GB-positive Tau pathology. The affinity of Tau was obtained through the displacement curve (IC_{50} = 2.56 nM). What's more, PND-118 displayed poor binding to $A\beta_{1-42}$ aggregates (K_i = 985.07 nM). In biodistribution, [^{125}I]PND-118 exhibited good initial brain uptake (3.2 ±0.71 %ID/g at 2 min) and rapid washout rate (brain $_{2min}$/brain $_{60min}$ = 12.9).

Conclusions:
[^{125}I]PND-118 displayed high affinity to native Tau aggregates at nanomolar scale, high specificity to neurofibrillary tangles against Aβ, and desirable pharmacokinetic characteristics with high initial brain uptake and fast clearance from normal brain regions. Therefore, [^{125}I]PND-118 fulfills the primary criteria for depicting *in vivo* Tau neuroimaging clearly as a promising SPECT radiotracer, further studies of this probe are currently underway.

Acknowledgments: Supported by the National Natural Science Foundation of China (No. U1967221 and 22022601).

Corresponding Author*:* *Tel/Fax: +86-10-58808891. E-mail: cmc@bnu.edu.cn

Oral Presentation

Disclosures: The authors have disclosed no financial interest.

169-D-π-A based trisubstituted alkenes as environment-sensitive fluorescent probes to detect Lewy pathologies.

Presenter: Qi Zeng, Beijing Normal University

Qi Zeng

Beijing Normal University, China

Objectives:
Lewy pathologies, which mainly consist of insoluble α-synuclein (α-syn) aggregates, are the hallmarks of Parkinson's disease and many other neurodegenerative diseases termed "synucleinopathies". Detection of Lewy pathologies with optical methods is of interest for preclinical studies, while the α-syn fluorescent probe is still in great demand. In most synucleinopathies patients, Lewy pathologies are always concomitant with the accumulation of β-amyloid (Aβ) plaques, which makes the development of α-syn fluorescent probes more changeling. In this study, we designed and synthesized a series of D-π-A based trisubstituted alkenes probes and evaluated their capability as potential fluorophores for α-syn pathologies.

Methods:
The probes were directly obtained using Knoevenagel condensation between corresponding aldehydes and acetonitriles. The binding affinities to α-syn and Aβ_{1-42} aggregates were quantitatively measured by *in vitro* ThT competitive binding assay. Fluorescent interaction with synthetic α-syn, Aβ_{1-42} aggregates, and bovine serum albumin (BSA) were measured. *In vitro* fluorescent staining was performed on the brain tissues of the AD patient (88 years old, female) and the PD patient (73 years old female). *Ex vivo* fluorescent imaging was carried out with the ICR mice (4-weeks-old).

Results:
After comprehensive consideration of the biological and optical properties of the probes, TQXN-2 showed high binding affinities ($K_i = 8.20 \pm 1.85$ nM for α-syn and 0.94 ± 0.03 nM for Aβ_{1-42}), significant fluorescent enhancement (26.6-fold with α-syn and 67.6-fold with Aβ_{1-42}), and a satisfying quantum yield (10.4%). Especially, TQXN-2 displayed a 23 nm difference in maximum emission wavelength after binding to α-syn and Aβ fibrils and showed potential in fluorescent discrimination of Lewy pathologies and Aβ plaques at the tissue level. *Ex vivo* fluorescent imaging of ICR mice brains ensured its blood-brain barrier (BBB) penetration.

Conclusions:
We successfully identified a fluorescent probe for α-syn and Aβ. These trisubstituted alkene probes enriched the tools for the fluorescent detection of Lewy pathologies and provided ideas for further developing selective α-syn fluorescent probes. More modifications on this probe are needed to enhance the specific binding over α-syn.

Oral Presentation

Disclosures: The authors have disclosed no financial interest.

170-First-in-human study of a novel uPAR-targeting imaging agent for fluorescent-guided surgery in patients with high-grade glioma

Presenter: Andreas Kjaer, Rigshospitalet & University of Copenhagen

Jane Skjøth-Rasmussen[1], Aleena Azam[2], Karina Juhl[3], Sara A. Ginsborg[2], Martin Kryspin Sørensen[4], Anders Christensen[5], Christine Soelling[4], Carl Christian Larsen[4], Bjarne Winther Kristensen[4], David Scheie[4], **Andreas Kjaer[6]**

[1]*Rigshospitalet, Denmark*
[2]*Rigshospitalet, Copenhagen, Sjælland, Denmark*
[3]*Rigshospitalet, Copenhagen N, Capital Region, Denmark*
[4]*Rigshospitalet*
[5]*Rigshospitalet, Copenhagen, Sjaelland, Denmark*
[6]*Rigshospitalet & University of Copenhagen, Copenhagen, Denmark*

Aim:
To investigate a new urokinase-type Plasminogen Activator Receptor (uPAR)-targeted optical probe for intraoperative visualization of malignant glioma in patients scheduled for neurosurgery.

Design:
Open-label, non-randomized, dose escalation, single-dose administration, multi-center phase I/II clinical trial.

Background:
The principle of using a fluorescent agent for optimizing glioma surgery is well known. ICG-glu-glu-AE105 (FG001) is a novel fluorescent compound that binds specifically to uPAR. uPAR is overexpressed in glioblastoma and facilitates the invasion of the cancer into normal tissue. Hence, uPAR is a suitable target for fluorescence-guided surgery (FGS) to aid surgeons in the delineation of tumor from normal tissue.

Methods:
A pre-designed dose-escalation schedule from 1 to 48 mg FG001 was performed in high-grade glioma patients scheduled for neurosurgery. Safety and efficacy (tumor-to-background ratio; TBR) was the major readout. Biopsies taken from various areas of the tumor/border were histologically analyzed in a blinded manner. These were compared with image readout to evaluate the performance of FG001 to detecting and discriminating cancer from normal tissue. Based on the phase I results, an optimal dose for the phase II study was established.

Results:
In total, 40 patients were administered FG001 in the phase I part of the trial, and the compound was shown to be safe and well-tolerated. No serious drug-related adverse events were reported. The pharmacokinetic (PK) profile for FG001 was assessed for all dose levels. FG001 showed dose-dependent increases in exposure across dose levels in a linear manner. TBR generally increased with dose and peaked at a dose of 36 mg administered the evening before surgery. This dose/time was selected as optimal and all patients revealed a clinically relevant TBR value at this dose.
The histology samples from doses 36 mg and 48 mg administered in the evening before surgery, confirmed that FG001 lights up aggressive brain cancer with high specificity and sensitivity.

Conclusion*:*
FG001, a novel uPAR-targeting drug for image-guided surgery, is safe and well-tolerated. It provides excellent images with high contrast during surgery. Histopathology confirmed the ability to discriminate tumor from non-tumor tissue and thereby the potential for use in fluorescence-guided surgery in patients with high-grade glioma.

Oral Presentation

Disclosures: The authors would like to disclose that FG001 is an investigational device.

171-PD-L1 PET reveals divergent tumor exposure of anti-PD-L1 therapeutics.

Presenter: Akhilesh Mishra, Johns Hopkins Univeristy

Akhilesh Mishra[1], Dhiraj Kumar[2], KULDEEP GUPTA[3], Gabriela Lofland[4], Ajay Kumar Sharma[5], Robert Hobbs[5], Robert F. Dannals[6], Steven Rowe[7], Edward Gabrielson[7], Sridhar Nimmagadda[8]

[1]*Johns Hopkins Univeristy, Baltimore*
[2]*Johns Hopkins University School of Medicine, Baltimore*
[3]*Johns Hopkins Univeristy*
[4]*Johns Hopkins University School of Medicine*
[5]*Johns Hopkins University, Baltimore, MD*
[6]*Johns Hopkins University School of Medicine, Baltimore, Maryland*
[7]*Johns Hopkins University School of Medicine, Baltimore, MD*
[8]*Johns Hopkins Univeristy, Baltimore, MD*

Introduction:
Immune checkpoint protein targeted antibodies (mAb) have transformed cancer treatment but majority of patients do not respond. Although sub-optimal drug exposure is a major contributor to drug resistance, tools to quantify the pharmacokinetics and pharmacodynamics of those mAbs in real-time and at the tumor are few. Here, we explored the concept of using target-centric measurements to gain insights into mAb activity at the tumor. Target levels were measured using a validated radiotracer that exhibits less affinity than the therapeutics so that only unoccupied (or accessible) target levels could be measured during therapy. To demonstrate the concept, we measured immune checkpoint protein programmed death ligand 1 (PD-L1) expression levels using a peptide-based radiotracer, [^{68}Ga]DK223 (K_D=1.01±0.83 nM), during therapy with two FDA approved PD-L1 mAbs avelumab and durvalumab (K_D< 0.7 nM). We quantified accessible PD-L1 levels during therapy by PET and biodistribution studies.

Methods:
To test whether [^{68}Ga]DK223 binds PD-L1 in the presence of mAbs, BFTC909 cells (PD-L1^{high}) were incubated with 1 μCi [^{68}Ga]DK223 in presence (60 nM) or absence of avelumab and durvalumab. To quantify aPD-L1 mAb exposure at the tumor, mice with BFTC909 xenografts (100-200 mm^3) were treated with 10 mg/kg dose of avelumab or durvalumab and [^{68}Ga]DK223 PET (7.4 MBq/mouse) was acquired to measure changes in PD-L1 levels before mAb treatment and every 24 h up to 120 h (n=5-6). Ex vivo biodistribution studies (1.85 MBq/mouse) were performed to validate imaging findings (n=5-6) and mice treated with PBS were used as controls. Accessible PD-L1 levels were calculated by percentage of incubated dose (%ID/g) of treatment groups as a ratio of PBS group.

Results:
In vitro uptake studies showed that [^{68}Ga]DK223 binding to BFTC909 cells (27.9±2.4 percentage of incubated dose (%ID)), reduced to less than 1% in presence of avelumab and durvalumab, indicating that [^{68}Ga]DK223 binds to only accessible PD-L1 during anti-PD-L1 therapy. [^{68}Ga]DK223 PET revealed low uptake of radioactivity in the tumors in treated mice at 24 h after treatment indicating high tumor exposure of avelumab and durvalumab, while high tumor uptake was observed in PBS treated group. Over a 120 h period, avelumab treated mice showed increased [^{68}Ga]DK223 uptake (i.e. high accessible PD-L1) indicating mAb clearance from the tumor. In contrast, [^{68}Ga]DK223 tumor uptake remained low even at 120 h in durvalumab treated mice indicating continued drug exposure at the tumor. In treated mice, we observed 5±3 % accessible PD-L1 during avelumab or durvalumab treatment at 24 h which increased to 50.8±20.0% at 120 h in case of avelumab but remained significantly low for durvalumab (4.4±0.5).

Conclusion:
Our data demonstrate that [^{68}Ga]DK223 PET derived pharmacodynamic measures provide insights into drug exposure at the tumor, thus supporting its use for guiding and optimizing immune checkpoint therapy.

Oral Presentation

Disclosures: The authors have disclosed no financial interest.

172-Deciphering the effects of placental calcification, vasculature, and oxygenation on fetal growth with multi-parametric ultrasound and photoacoustic imaging.

Presenter: Skye Edwards, Tufts University

Skye A. Edwards[1], Ana Branco[2], Mary Wallingford[3], Srivalleesha Mallidi[4]

[1]*Tufts University, Medford, MA*
[2]*Tufts Medical Center, Medford, MA*
[3]*Tufts Medical Center, Boston, Massachusetts*
[4]*Tufts University, Medford*

Background:
Gestational disorders caused by placental vascular dysfunction, such as preeclampsia (PE), are prevalent and can result in adverse pregnancy outcomes. PE occurs in ~4% of all pregnancies and is associated with maternal mortality and preterm birth. Despite scientific advances, underlying mechanisms and progression of PE remain poorly understood. No preventative or curative treatments are available. A major roadblock for early identification of PE is the lack of imaging systems that monitor placenta hemodynamics and oxygenation. Current clinical imaging systems are either harmful due to ionizing sources, too expensive and inaccessible, or provide insufficient data[1]. The structure of the placenta is intertwined with its function and throughout pregnancy there is remodeling of its dynamic structure[2]. We propose the use of combined quantitative ultrasound (QUS) and photoacoustic imaging (USPAI) to characterize the functional and structural changes of the placenta between embryos with and without preeclampsia.

Methods*:*
The Slc20a2 knockout mouse used here displays increased ectopic placental vascular calcification, reduced fetal growth, and decreased postnatal bone mineral density[3,4]. The Slc20a2 knockout, heterozygous, and wild-type placentas were imaged on embryonic day (E) 18.5. *In vivo* and externalized placenta imaging was conducted using Vevo LAZR-X with a 21 MHz transducer (MX250S) to obtain oxygen saturation (sO_2) of the placenta. E*x vivo* imaging of placenta was conducted with a 40 MHz transducer (MX550). Radio frequency data was utilized to investigate spectral parameters, zero slope intercept (ZSI), mid-band fit (MBF), and spectral slope (SS) in relation to ectopic calcification. The placenta genotypes were determined after data collection using yolk sac tissue.

Results:
The *in vivo* scans indicated that the wild-type tissue had a higher sO_2 values than theSlc20a2 knockout tissues. Using the externalized 3D scans, it was discovered that the sO_2 variances between wild-type placenta and heterozygous placenta were significantly different. Our quantitative ultrasound data revealed gene-specific effects and supported that the ZSI and MBF parameters are statistically significant from each other. Qualitatively the MBF and ZSI spectral peaks of the placenta are found to be distinct amongst different genotypes. The spectral peaks, MBF and ZSI are, sparsely distributed around the edges in the wild-type placenta and intensely distributed throughout

the knockout placenta (Fig. 1). The highest of the spectral peaks are localized in obvious calcified areas are found in the labyrinth. Slc20a2 and wild-type SS were statistically significant from the heterozygous placenta.

Conclusions:

Differentiating heterozygous and wild-type placentas using sO_2 values and between three types of placentas using QUS parameters provides strong confidence in the application of USPAI as a novel approach to determining an unhealthy versus a healthy placenta. Building upon the (E) 18.5 gestation data collected here, future work will involve monitoring functional parameters over time including early placentation to support translating the method to early diagnosis of placental vascular diseases.

Reference

1. Nguyen et al., EMJ Radiology. 2020
2. Chengxi et al., Phys. Med. Biol. 2018
3. Wallingford et al., Front Physiol. 2018
4. Correia-Branco et al., Cardiovascular Calcification and Bone Mineralization. 2020

Oral Presentation

Disclosures: The authors have disclosed no financial interest.

173-Cortical Uptake Correlation in Alzheimer's Disease Brain Tissue Sections: Comparative analysis of 3H-Fluselenamyl and 3H-PiB

Presenter: sundaram guruswami, Washington University School of Medicine

Sundaram Guruswami[1], Dhruva Dhavale[2], paul kotzbauer[2], tammie benzinger[2], Vijay Sharma[3]

[1]Washington University School of Medicine, Saint Louis
[2]Washington University School of Medicine
[3]Washington University School of Medicine, St. Lous, MO

Objectives:

As companion diagnostics, Amyloid PET tracers offer versatile noninvasive tools for quantifying the efficacy of disease modifying anti-amyloid therapies for Alzheimer's disease (AD). While radiotracers, such as [^{18}F] Florbetapir, Florbetaben and Flutemetamol are commercially available for β-amyloid (Aβ) imaging, [^{11}C] PiB PET tracer has been rigorously investigated worldwide and continues to be the gold standard for the Aβ) imaging in vivo due to better correlations of imaging data with pathological expression of the disease in autopsy confirmed tissues. Nevertheless, these tracers allow effective detection of fibrillary amyloid plaques (later stage of Aβ pathophysiology). To further embellish PET imaging resources and enable disease-specific imaging at earlier stages, we have reported earlier, the preclinical validation of ^{18}F-Fluselenamyl, a novel PET imaging agent that demonstrated the ability to detect both fibrillary and diffuse plaques and demonstrates unprecedented molecular and disease specificity in human brain sections. To determine whether or not, Fluselenamyl has the ability to map binding patterns of PiB in the cortical regions of the AD human brain sections, we report herein, comparative analysis of ^{3}H-Fluselenamyl and ^{3}H-PiB using saturation binding assays, and in vitro autoradiography experiments.

Methods:

[^{3}H] PiB was purchased commercially and [^{3}H] Fluselenamyl was custom synthesized from ViTrax Radiochemicals by supplying the precursor 6 (Fig 1) synthesized in our lab. Non-Tritiated (Cold) PiB and Fluselenamyl were synthesized in our lab. Brain sections were obtained post-mortem from subjects diagnosed with AD, and subjects with no clinical symptoms of dementia. Saturation binding assays was performed using insoluble fraction obtained from clinically characterized AD tissue sections. Autoradiography experiments were performed by exposing the tissues to GE phosphor screens.

Results:

Using saturation binding assays, [^{3}H]-PiB demonstrated binding average (K_d=2.5 ± 0.3 nM; Bmax = 1152.2 pmol/g; n=3) and [^{3}H]-Fluselenamyl (K_d=4.1 ± 0.6 nM; Bmax = 589 ± 67 pmol/g, n=3) to AD insoluble fraction. Non-specific binding was determined using the cold standards. Binding studies revealed that both tracers likely bind the similar sites, while Kd value of [^{3}H]-PiB is 1.5 times higher than [^{3}H]-Fluselenamyl, it is not explicitly clear, if the higher binding constant of [^{3}H]-PiB could be partly attributed to specific activity differences between both tracers. Next, the auto radiography experiments were performed in AD and control brain sections for comparative analysis of both the tracers. Previous head on comparison using autoradiography experiments, in our lab, showed higher Grey to White Matter ratio of signal corresponding to ^{18}F-Fluselenamyl compared to ^{11}C-PiB in AD brain sections. To warrant effective head-on comparison, the tritiated version of both the agents were used in this study. Accordingly, uptake of [^{3}H]-Fluselenamyl and [^{3}H]-PiB measured via autoradiography experiments following incubation of brain slices, demonstrated higher precision of cortical mapping of both the tracers, which correlates, with the distribution of abundant Aβ plaques detected by fluorescent immunostaining with anti-Aβ antibody (Alexa 647-mHJ 3.4) and was displaceable by excess cold ligands thus suggesting high molecular specificity. In addition, both tracers showed low binding in frontal cortex sections from control cases lacking Aβ pathophysiology. Further correlation of Grey matter retention in AD cases by picking eighteen non-overlapping ROI's over the cortical uptake regions of the autoradiography images minus background for both tracers revealed the mean ratio of PiB to Fluselenamyl activity of 2.5 for AD compared to 5.0 for control, whereas the similar comparison of AD vs control case activity resulted in the mean ratio of 124 for [^{3}H]-PiB and 208 for [^{3}H]-Fluselenamyl respectively. When excess cold was used, we observed ≥ 97% blocking of tracer activity.

Conclusion:

Combined data show that [^{3}H]-Fluselenamyl has both a cortical and white matter uptake comparable to [^{3}H]-PiB. Overall, Fluselenamyl demonstrates Aβ binding profiles desirable for a promising translational imaging agent. Following regulatory approvals, [^{18}F]-Fluselenamyl will undergo first-in human studies at our institution.

Oral Presentation

Disclosures: The authors have disclosed no financial interest.

174-Functional Nerve Imaging Using Near Infrared Nerve-Specific Fluorophores for Enhanced Nerve Repair Surgery

Presenter: Connor Barth, Oregon Health & Science University

Connor Barth[1], Anas M. Masillati[2], Lei G. Wang[3], Antonio R. Montano[3], Summer L. Gibbs[3]

[1]Oregon Health & Science University
[2]Oregon Health & Science University, Portland
[3]Oregon Health & Science University, Portland, OR

Acute peripheral nerve injuries frequently result from penetrating trauma, closed or open fractures, joint dislocations, and high-energy collisions. Nerve crush, stretch or transection can lead to functional deficits ranging from numbness to complete motor and sensory function loss, affecting ~1.6M trauma patients annually. Surgery is the primary treatment for severe peripheral nerve injuries, but finding the optimal timing and approach for surgery remains a challenging dilemma. Currently, surgeons rely mainly on gross visual examination of the nerve during surgery to identify damaged vs. healthy nerve tissue. However, this fails to capture the degree of axonal disruption, leaving ~50% of patients with poor functional recovery outcomes. Surgeons and patients would benefit from a rapid intraoperative assessment of nerve damage to make informed treatment decisions. We have developed a library of first-in-kind near-infrared (NIR) fluorophores that label nerve tissue with high affinity and are undergoing preclinical pharmacology and toxicology testing to facilitate first-in-human (FIH) trials. These fluorophores provide nerve visualization with high contrast at millimeter to centimeter tissue depths in mice, rats, swine, canine, and human specimens. Importantly, fluorescence uptake and retention profiles are decreased in damaged nerve tissue facilitating clear identification between healthy and injured nerve tissues following topical/paint-on or systemic administration. Utilizing this difference, we have developed an objective intraoperative nerve damage assessment methodology that provides rapid contrast between healthy and damaged nerves for real-time nerve repair surgery guidance. Further characterization of the developed methodology in nerve stretch and crush models are underway, including longitudinal studies to assess the ability to diagnose transient vs. permanent nerve injuries and compare with clinical gold standard nerve conduction velocity testing. We believe that the continued development and use of the developed methodology in humans will improve nerve repair surgery and patient outcomes following peripheral nerve injury.

Oral Presentation

Disclosures: The authors have disclosed no financial interest.

175-Targeting CUB domain containing protein 1 (CDCP1) for cancer theranostics

Presenter: Shalini Chopra, University of California, San Francisco

Shalini Chopra[1], Michael J. Evans[2], Sasank Sakhamuri[3], Jie Zhuo[3], James Wells[4], Jonathan Chou[5]

[1]University of California, San Francisco, San Francisco
[2]University of California, San Francisco, San Francisco, CA
[3]University of California San Francisco
[4]University of California, San Francisco
[5]University of California, San Francisco, San Francisco, California

Background:
Radioligand therapy (RLT) is still relatively unexplored in metastatic castration resistant prostate cancer (mCRPC), with much of the focus having been on bone seeking radionuclides and PSMA-directed RLT. Subsets like small cell neuroendocrine prostate cancer (SCNC) are not expected to respond to the current options for RLT. Another genitourinary (GU) cancer type common among men is bladder cancer. Despite recent drug approvals for immune checkpoint inhibitors and antibody drug conjugates targeting Nectin-4 or TROP2, metastatic bladder cancer remains incurable with a dismal five-year survival rate. The lack of treatment options for GU cancers has elevated the urgency to identify new cancer associated targets that can be exploited for RLT. CUB domain containing protein 1 (CDCP1) is a cell surface protein highly overexpressed on the surface of many cancer types with low expression in normal tissues. In this study, we evaluated whether CDCP1 can be a target for cancer theranostics. Our goal was to determine if mCRPC and bladder cancer overexpress CDCP1, and whether CDCP1 can be targeted for treatment with radiolabeled antibodies.

Method:
CDCP1 mRNA levels were evaluated in publicly available RNA-seq data sets. Protein expression was evaluated in patient derived xenografts and cell lysates by immunoblot. Receptor number per cell was defined using a saturation binding assay with 4A06, a recombinant human antibody we recently developed that targets the CDCP1 ectodomain. The feasibility of imaging and treating mCRPC and bladder cancer in vivo was tested with ^{89}Zr-4A06 and ^{177}Lu-4A06 in mouse models.

Results:
CDCP1 expression was observed in 90% of mCRPC biopsies, including SCNC and adenocarcinoma with negligible PSMA expression. Overall, no correlation was observed between CDPC1 and PSMA expression, and modest but significant anticorrelation was observed between CDCP1 and PTEN. CDCP1 mRNA and protein levels were expressed in multiple bladder cancer subtypes. There was a tendency toward higher expression in the basal subtype of bladder cancer. Interestingly, CDCP1 was not correlated with Nectin-4 or TROP2 mRNA. Full length and/or cleaved CDCP1 was expressed in six of seven SCNC PDX samples and expressed in four of five adenocarcinoma PDX samples, including LTL-484 which has low PSMA expression. Bmax values of ~22,000 and ~6,200 fmol/mg were calculated for PC3 and DU145, two PSMA null human prostate cancer cell lines. Protein expression of CDCP1, although not uniformly present in all bladder cancer specimens, was observed in several PDX samples and human cells lines that lacked Nectin-4 and/or TROP2. The cell lines with the highest CDCP1 expression had ~1 x 107 receptors per cell. ^{89}Zr-4A06 PET enabled detection of five human prostate cancer and five bladder cancer xenografts. An antitumor assessment study showed that ^{177}Lu-4A06 significantly suppressed the growth of PSMA null DU145 tumors compared to control and extended overall survival. In case of bladder cancer, the antitumor assessment study showed that fractionated doses of ^{177}Lu-4A06 significantly inhibited the growth of UMUC3 xenografts and improved overall survival. In a representative cohort, 4 of 8 mice experienced complete responses and no tumor regrowth was observed over three months of monitoring.

Conclusions:
We provide the first evidence that CDCP1 can be targeted for RLT in mCRPC and bladder cancer. Combined with the results showing widespread CDCP1 expression in mCRPC including SCNC and low PSMA-expressing models, these data position CDCP1-directed RLT as a potential means to broaden the impact of RLT in prostate cancer. Our data also show that CDCP1 expression does not entirely overlap with Nectin-4 or TROP2, which suggests that CDCP1 directed treatments may have a role in bladder cancer treatment distinct from standard of care. These data sets are the proof of concept that CRPC and bladder cancer can be treated with CDCP1 directed RLT.

Oral Presentation

Disclosures: The authors have disclosed no financial interest.

176-Diffusion-weighted MRI differentiates intraductal papillary mucinous neoplasms from pancreatic cancer: a study in GEM models

Presenter: Miguel Romanello Joaquim, University of Pennsylvania

Miguel Romanello Joaquim[1], Emma Furth[2], Yong Fan[2], Hee Kwon Song[3], Stephen Pickup[2], Cao Jianbo[2], Hoon Choi[2], Mamta Gupta, Deidre McMenamin[2], Cynthia Clendenin[3], Thomas Karasic, Jeffrey Duda, James Gee, Peter O'Dwyer, Mark Rosen[3], Rong Zhou[2]

[1]*University of Pennsylvania, Philadelphia*
[2]*University of Pennsylvania, Philadelphia, PA*
[3]*University of Pennsylvania, Philadelphia, Pennsylvania*

Intraductal papillary mucinous neoplasms (IPMN) are a common precursor to the highly fatal disease pancreatic ductal adenocarcinoma (PDAC), which is the main form of pancreatic cancer. IPMN is considered a premalignant disease, and monitoring tumor progression is recommended over surgical excision for a majority of patients. However, there is ongoing debate regarding the optimal guidelines regarding management and surveillance strategies for IPMN patients [1], and tumor size measurements obtained from anatomic imaging do not provide sufficient information about the potential malignant development of the IPMN lesion. Ideally, a clinical imaging marker would differentiate between IPMN and PDAC and inform the decision between surgery and continued surveillance. Given the changes in the cellular architecture and stromal features during IPMN's transition to PDAC, we hypothesized that diffusion-weighted (DW-) and dynamic contrast-enhanced (DCE-) MRI, two imaging methods sensitive to the tumor microenvironment, could provide quantitative metrics that discern IPMN from PDAC. The transition of IPMN to PDAC has prevalent genetic mutations including activating mutations to the KRAS oncogene and inhibiting mutations to TP53 and SMAD4. Therefore, genetically engineered mouse (GEM) models provide powerful tools to replicate the human diseases in a pre-clinical setting. Mice with KRAS and TP53 mutations ($Kras^{G12D}$: $Trp53^{R172H}$: Pdx1-Cre), also known as KPC, have been shown develop tumors with key characteristics similar to human PDAC [2]. Recent development has also shown that mice with KRAS and SMAD4 mutations ($Kras^{G12D}$: $Smad4^{L/L}$: Ptf1a-Cre), also known as CKS, develop tumors with characteristics similar to human IPMN [3]. Using these two GEM models, we aimed to: (1) compare quantitative DW- and DCE-MRI metrics of KPC and CKS tumors; (2) use immunohistochemistry and pixel classifiers of tumor sections to identify corroborating the differences in MRI metrics; and (3) demonstrate an approach for direct comparison of apparent diffusion coefficient (ADC) maps and cell density maps obtained from hematoxylin and eosin (H&E) staining using ex-vivo MRI and affine transformation. We used radial k-space sampling for the in-vivo MRI protocols due to their robustness to respiratory motion artifacts [4]. We found that two DW-MRI quantitative metrics, ADC and kurtosis index (KI), reliably differentiated KPC tumors (n=44) from CKS tumors (n=20), separating the two groups with almost no overlap (Figure 1). We also showed a clear inverse correlation between the local ADC value and local cell density in KPC tumors ($R=0.327$, $p<10^{-30}$). The same correlation was seen when comparing the KPC and CKS groups (KPC: ADC = 1.66 e-3 mm^2/s, cell density = 7098 $cells/mm^2$; CKS: ADC = 2.24 e-3 mm^2/s, cell density = 6122 $cells/mm^2$). DCE-MRI metrics were not able to separate KPC and CKS tumors as effectively as DW-MRI metrics. However, patterns in parametric maps of K^{trans}, a metric of perfusion from capillaries to tissue, showed that KPC tumors have a highly perfused periphery and low perfused center, in contrast with CKS tumors, which have a more homogeneous perfusion profile. This aligns with patterns of CD31 staining, which shows that KPC tumors have higher microvasculature density on their periphery, and that CKS tumors have a homogeneous distribution of microvasculature. Our results point at both DW- and DCE-MRI as potentially useful tools to identify IPMN's transition to PDAC and to understand the microenvironment of both. DW-MRI quantitative metrics ADC and KI effectively differentiate between two GEM models with similar characteristics to IPMN and PDAC. ADC also provides information about tumor cell density, while K^{trans}, a DCE-MRI metric, provides information on the pattern of microvasculature across the tumor.

Reference

1. Nakamura, M. et al. "Comparison of guidelines for intraductal papillary mucinous neoplasm: What is the next step beyond the current guidelines?" Ann Gastroenterol Surg. 2017. 1(2) 90-98.
2. Hingorani, S.R. et al. "Trp53R172H and KrasG12D cooperate to promote chromosomal instability and widely metastatic pancreatic ductal adenocarcinoma in mice." Cancer Cell. 2005. 7(5) 469-83.
3. Bardeesy, N. et al. "Smad4 is dispensable for normal pancreas development yet critical in progression and tumor biology of pancreas cancer." Genes Dev. 2006. 20(22) 3130-46.
4. Cao, J. et al. "Respiratory Motion Mitigation and Repeatability of Two Diffusion-Weighted MRI Methods Applied to a Murine Model of Spontaneous Pancreatic Cancer." Tomography. 2021. 7(1) 66-79.

Oral Presentation

Disclosures: The authors have disclosed no financial interest.

177-Screening Bacteria-Specific Metabolic Probes for Infection Imaging Using Deuterium NMR/MRI

Presenter: Hecong Qin, University of Chicago

Hecong Qin[1], Aryn A. Alanizi[2], Marina López-Álvarez[3], Sanghee Lee[4], Jeremy Gordon[5], David M. Wilson[5]

[1]*University of Chicago, Chicago, IL*
[2]*University of California San Francisco, CA*
[3]*University of California San Francisco, San Francisco*
[4]*University of California, San Francisco, Gyeonggido, South Korea*
[5]*University of California, San Francisco, San Francisco, CA*

Introduction:

Imaging plays an important role in infection diagnosis, especially for organs where biopsies are inaccessible. However, differentiating sterile inflammation and bacterial infection on imaging exams remains a clinical challenge. Reliable imaging techniques that can detect live bacteria with high specificity *in vivo* could address this unmet clinical need. Bacteria have distinct metabolic profiles from mammalian cells, as they can 1) utilize alternative energy sources such as sugars other than glucose, and 2) produce bacteria-specific metabolites, such as acetate and ethanol. Deuterium Metabolic Imaging is an NMR/MRI technique that allows quantitative study of metabolism of ^{2}H-labeled substrates beyond probe uptakes [1, 2]. We aim to study ^{2}H-labeled sugar and sugar alcohols targeting microorganism-specific metabolism, with the goal to develop new MRI techniques for infection imaging.

Methods and Results:

in vitro ^{2}H NMR-based screening of bacterial metabolism of ^{2}H sugar and sugar alcohols An *in vitro* NMR-based assay in deuterium-depleted depleted media was developed to study bacterial utilization of ^{2}H-labeled sugar probes. *S. aureus* (gram-positive) and *E.*

coli (gram-negative) were cultured in LB agar/broth made with deuterium-depleted water. ^{2}H-labeled sugar (D-glucose, D-mannitol, D-sorbitol, D-arabinose, D-xylose) (1 mg/mL) were introduced to subcultures during the linear growth phase (optical density = 0.3-0.4), then sampled every 20-30 minutes. ^{2}H NMR of heat-killed bacterial culture samples was acquired on an 800MHz spectrometer (Fig. 1A). Both *S. aureus* and *E. coli* showed fastest growth when cultured with [U-^{2}H]glucose-d7, followed by [U-^{2}H]mannitol-d8. Moreover, [U-^{2}H]glucose-d7 culture (Fig. 1C, D) showed greatest and fastest HDO enrichment for both *S. aureus* and *E. coli*, with [U-2H]mannitol-d8 culture (Fig 1. F, G) showing comparable degrees and rates of HDO enrichment. Notably, *S. aureus* showed no metabolism of [U-^{2}H]sorbitol-d8 (Fig 1I), whereas *E. coli* showed delayed and slow metabolism of [U-^{2}H]sorbitol-d8 (Fig. 1J). Moreover, *S. aureus* preferentially produces lactate in addition to acetate, whereas *E. coli* preferentially produces ethanol. No metabolic conversion of D-arabinose (negative control, as bacteria only use L-arabinose) or D-xylose were observed. In summary, bacteria preferentially utilize glucose > mannitol >> sorbitol, as evidenced by their impacts on growth curves and rates of metabolic conversion.
In vivo ^{2}H MR Spectroscopic Imaging (MRSI) of mammalian metabolism of selected ^{2}H sugar and sugar alcohols: MRSI with [U-^{2}H]glucose-d7, [U-^{2}H]mannitol-d8, and [U-^{2}H]sorbitol-d8 was performed on CBA/J mice to study background mammalian metabolism of the selected probes (Fig. 1B). 2D Chemical Shift Imaging (CSI) were performed on a 14.1T MR microimaging system, with a surface RF coil placed on lower-extremity muscles. Baseline scans were acquired before the start of 1-hour infusion of 10-20 mg probes (2.5 uL/min), followed by 1.5-2 hours of dynamic 2D CSI (24 averages/5 minutes per time point). No HDO enrichment was observed in healthy muscle following 10mg [U-^{2}H]mannitol-d8 infusion (Fig. 1H), whereas a 2-fold HDO enrichment was observed following a 20 mg [U-^{2}H]glucose-d7 infusion (Fig. 1E). Moreover, a 3-fold HDO enrichment was observed following a bolus injection of 50mg [U-2H]sorbitol-d8 (Fig. 1K).

Conclusion:
Mannitol was identified as a promising imaging probe targeting bacteria-specific metabolism, as it can be readily utilized by bacteria with minimal background (host) metabolism. Ongoing work focuses on investigating [U-^{2}H]mannitol-d8 MRSI to detect bacterial infection *in vivo*.

Reference

1. De Feyter et al., Sci. Adv. (2018)
2. Aguayo et al., JBC (1988)

Oral Presentation

Disclosures: The authors have disclosed no financial interest.

178-EGFR-targeted fluorescence-guided surgery: differential imaging performance and clinical predictors in solid tumors

Presenter: Quan Zhou, Stanford University School of Medicine

Quan Zhou[1], Michael Iv[1], michael moseley[2]

[1]Stanford University School of Medicine, Stanford, CA
[2]Stanford University, stanford, CA

Background:
As molecular targeted fluorescence imaging emerges as a strategy for intraoperative tumor detection, it is challenging to predict results of clinical studies conducted in different cancers using fluorescent tracers. In this study, clinical fluorescence images in four types of solid tumors using a near-infrared labeled EGFR antibody shared the same imaging pipeline and outcomes were compared against the same criteria. We hypothesized that clinical attributes including tumor biological characteristics and physical imaging conditions contributed to the differential translation of microscopic biomarker expression to macroscopic fluorescence in tumors. While genetic alterations may predict EGFR expression in gliomas[1], biopsies are rarely taken for brain cancer diagnosis in clinical practice. Therefore, radiographic markers on preoperative neuroimages that correlate to biological features in the tumor microenvironment (TME) were examined to stratify patients before surgery for molecular targeted fluorescence imaging.

Methods:
Thirty-five patients with high-grade glioma (HGG, n = 5), head-and-neck squamous cell carcinoma (HNSCC, n = 23), lung adenocarcinoma (LAC, n = 3) or pancreatic ductal adenocarcinoma (PDAC, n = 4) were systemically infused with 50 mg panitumumab-IRDye800, 1 – 3 days prior to surgery. Intraoperative open-field fluorescent images of the surgical field were acquired, where imaging device settings and operating room lighting conditions were tested on tissue-mimicking phantoms. Fluorescence contrast and margin size were measured on resected specimen surface. Antibody distribution and EGFR immunoreactivity were characterized in macroscopic and microscopic histological structures. Integrity of the blood-brain barrier (BBB) was examined via tight junction protein (claudin-5) expression around endothelial cells (ERG) with immunohistochemistry. Stepwise multivariate linear regression of biological variables was performed to identify independent predictors of panitumumab-IRDye800 concentration in tissue. In HGG patients, intraoperative fluorescence intensity and documented biopsy sites were spatially registered via neuronavigation against preoperative contrast-enhanced T1-weighted MRI radiographs[2] that were mapped to dynamic MRI features including forward transfer rate (K^{trans}), relative cerebral blood volume (rCBV) and fractional tumor burden (FTB). Perfusion and tumor density in HGG biopsies were immunohistochemically evaluated by vasculature (CD31) and proliferation (Ki-67) markers.

Results*:*
Optimally acquired at the lowest gain for tumor detection with ambient light, intraoperative fluorescence imaging enhanced tissue-size dependent tumor contrast by 5.2-fold, 3.4-fold and 1.4-fold in HGG, HNSCC and LAC, respectively, but not for PDAC (**Fig. S1A**). Fluorescence contrasts dropped below 1.0 in the wound beds of HGG, HNSCC and LAC, yet remained unchanged for PDAC. Tissue surface fluorescence target-to-background ratio correlated with margin size and identified 93%, 97%, 78% and 48% of at-risk resection margins *ex vivo* in HGG, HNSCC, LAC, and PDAC, respectively (**Fig. S1B**). In 4 mm-thick tissue sections, fluorescence detected tumor with 0.52 – 0.89 areas under the receiver operating characteristic curves. Preferential breakdown of BBB in HGG improved tumor specificity of intratumoral antibody distribution relative to that of EGFR (96% vs 80%) despite its reduced concentration (3.9 ng/mg tissue) compared to HNSCC (8.1 ng/mg) and LAC (6.3 ng/mg) (**Fig. S1C**). Cellular EGFR expression, tumor cell density, plasma antibody concentration and delivery barrier were independently associated with local intratumoral panitumumab-IRDye800 concentration with 0.65 goodness-of-fit for prediction (**Fig. S1D**). *In vivo* fluorescent antibody uptake in HGG tissue biopsies correlated (r = 0.52 – 0.79) to both presurgical radiographic parameters and differential expressions of claudin-5, ERG, CD31, Ki-67 and EGFR (**Fig. S1E**).

Conclusions*:*
In multi-cancer clinical imaging of receptor-ligand based molecular probe, plasma antibody concentration, delivery barrier, as well as

intratumoral EGFR expression driven by cellular biomarker expression and tumor cell density, led to heterogeneous intratumoral antibody accumulation and spatial distribution while tumor size, resection margin, and intraoperative imaging settings substantially influenced macroscopic tumor contrast. TME information from either biopsy immunohistochemistry or dynamic MRI scans could guide patient selection for molecular targeted fluorescence imaging.

Reference

1. Zhou Q, Leonel JC, Santoso MR, Wilson C, van den Berg NS, Chan CT, Aryal M, Vogel H, Cayrol R, Mandella MJ, Schonig F, Lu G, Sambhir SS, Moseley ME, Rosenthal EL, Grant GA. Molecular imaging of a fluorescent antibody against epidermal growth factor receptor detects high-grade glioma. Scientific Reports 11, 5710 (2021)
2. Zhou Q, van den Berg NS, Rosenthal EL, Iv M, Zhang M, Leonel JC, Walters S, Nishio N, Granucci M, Raymundo R, Yi G, Vogel H, Cayrol R, Lee Y, Lu G, Hom M, Kang W, Hayden Gephart M, Recht L, Nagpal S, Thomas R, Patel C, Grant GA, Li G. EGFR-targeted intraoperative fluorescence imaging detects high-grade glioma with panitumumab-IRDye800 in a phase 1 clinical trial. Theranostics 11 (15), 7130-1743 (2021)

Oral Presentation

Disclosures: The authors have disclosed no financial interest.

179-Synthesis of Magnetic Nanoparticle Tracers for High Resolution Magnetic Particle Imaging

Presenter: Jacob Bryan, University of California, Berkeley

Jacob Bryan[1], Benjamin Fellows[2], Javier Mokkarala-Lopez[2], Khadija Yousef[2], Allison Hartley[2], Renesmee Kuo[3], K. L. Barry Fung[4], Prashant Chandrasekharan[5], Steven Conolly[4]

[1]*University of California, Berkeley, Alameda, CA*
[2]*University of California, Berkeley, Berkeley, California*
[3]*University of California, Berkeley*
[4]*University of California, Berkeley, Berkeley, CA*
[5]*University of California, Berkeley, Berkeley*

Magnetic particle imaging (MPI) is a tracer-based imaging modality with comparable applications to nuclear medicine [1-4], but rather than measuring the distribution of radioactive tracers, MPI measures the temporal derivative of the magnetization of super paramagnetic iron oxide nanoparticles (SPIOs) to construct an image with linear contrast, zero background signal, and micromolar sensitivity [5-7]. However, current MPI tracers have poor spatial resolution (~1 mm in an expensive 7T/m gradient). To improve the resolution of MPI one could either increase the gradient strength which comes with significant expense, or one could improve the magnetic susceptibility of the particle tracers. By improving the magnetic susceptibility of the particles, we would thus be able to lower the cost of the MPI gradients. To this end, our lab recently reported on super ferromagnetic iron oxide nanoparticles (SFMIOs) that improve MPI image resolution and sensitivity by over 10-fold [8] and scanner cost by 100-fold. These SFMO magnetic nanoparticles form highly interacting chains that create a steep magnetization derivative. Here, we improved the synthesis of high resolution nanoparticles by implementing a post-oxidation step, which produced the best resolution MPI particles reported in the literature. Previous work demonstrated improved magnetic behavior through oxidation [9-11]. By introducing a post-synthesis oxidation step, we showed more consistent and improved FWHM resolution particles compared to nitrogen (Fig. 1a). After over 150 particles synthesized, we optimized the production of SFMIO particles and discovered a new magnetic nanoparticle that we have deemed high resolution SPIOs (HR-SPIOs) that have ideal magnetic properties. To synthesize high resolution particles more reliably, we use an extended La Mer mechanism by dripping iron oleate precursor for high control over size and morphology [12]. Thereafter, we induce a clustering event and apply a post-synthesis oxidation (Fig. 1b). Magnetic properties were analyzed in our arbitrary waveform relaxometer [13]. SFMIOs show an almost steplike response with applied fields [8]. Unlike SPIOs, SFMIOs form highly interacting chains which enhance the chain's internal magnetic field to boost the sensitivity and resolution. With this novel oxidation procedure, we have produced the highest recorded resolution MPI tracer in the literature (Fig. 1d-g). However, safe encapsulation of these particles to be dispersed in aqueous solution remains a challenge. Since these particles require interaction [8], creating a microbubble encapsulate disrupts their interaction capabilities and degrades their resolution. Despite this challenge, these particles are an enabling technology for affordable MPI imaging. We foresee a 100-fold reduction in scanner cost utilizing SFMIOs once these particles have been encapsulated for in vivo use. Unlike SFMIOs, HR-SPIOs are believed to be noninteracting because they do not have to overcome a coercive field prior to magnetization (Fig. 1f-I). These particles still obtain a 5-fold boost in resolution compared to commercial particles and do not need to form interacting chains. This implies that existing SPIO surface modifications, such as catechol-based polyethylene glycol, could be used [14]. Once surface functionalization is successful, these HR-SPIOs would imply a 25x reduction in scanner cost.

In this work, we have demonstrated that oxidation of magnetic nanoparticles improves the resolution of MPI tracers and significantly reduces scanner costs. By testing our synthesis method on 150 batches, we have created the highest resolution SFMIO nanoparticles reported in the literature. These SFMIOs could reduce the cost of MPI by 100-fold, but encapsulation of these particles and maintaining high interaction remains a challenge. HR-SPIOs, on the other hand, improve the scanner cost of MPI by 25-fold, but don't require a complex encapsulation method. Overall, synthesizing high resolution particles could enable clinical translation of MPI by reducing scanner cost for radiation-free and highly sensitive medical imaging.

Reference

1. B. Gleich and J. Weizenecker, "Tomographic imaging using the nonlinear response of magnetic particles," Nature, vol. 435, no. 7046, pp. 1214–1217, Jun. 2005, doi: 10.1038/nature03808.
2. E. Y. Yu et al., "Magnetic Particle Imaging for Highly Sensitive, Quantitative, and Safe in Vivo Gut Bleed Detection in a Murine Model," ACS Nano, vol. 11, no. 12, pp. 12067–12076, Dec. 2017, doi: 10.1021/acsnano.7b04844. [Online]. Available: https://pubs.acs.org/doi/10.1021/acsnano.7b04844. [Accessed: May 17, 2022]
3. X. Y. Zhou et al., "Magnetic Particle Imaging for Radiation-Free, Sensitive and High-Contrast Vascular Imaging and Cell Tracking," Curr Opin Chem Biol, vol. 45, pp. 131–138, Aug. 2018, doi: 10.1016/j.cbpa.2018.04.014. [Online]. Available: https://www.ncbi.nlm.nih.gov/pmc/articles/PMC6500458/. [Accessed: May 17, 2022]
4. Z. W. Tay, P. Chandrasekharan, X. Y. Zhou, E. Yu, B. Zheng, and S. Conolly, "In vivo tracking and quantification of inhaled aerosol using magnetic particle imaging towards inhaled therapeutic monitoring," Theranostics, vol. 8, no. 13, pp. 3676–3687, Jun. 2018, doi: 10.7150/thno.26608. [Online]. Available: https://www.ncbi.nlm.nih.gov/pmc/articles/PMC6037024/. [Accessed: May 17, 2022]

5. B. Zheng et al., "Magnetic Particle Imaging tracks the long-term fate of in vivo neural cell implants with high image contrast," Sci Rep, vol. 5, no. 1, p. 14055, Sep. 2015, doi: 10.1038/srep14055. [Online]. Available: https://www.nature.com/articles/srep14055. [Accessed: May 17, 2022]
6. B. Zheng et al., "Quantitative Magnetic Particle Imaging Monitors the Transplantation, Biodistribution, and Clearance of Stem Cells In Vivo," Theranostics, vol. 6, no. 3, pp. 291–301, Jan. 2016, doi: 10.7150/thno.13728. [Online]. Available: https://www.ncbi.nlm.nih.gov/pmc/articles/PMC4737718/. [Accessed: May 17, 2022]
7. B. Zheng et al., "Seeing SPIOs Directly In Vivo with Magnetic Particle Imaging," Mol Imaging Biol, vol. 19, no. 3, pp. 385–390, Jun. 2017, doi: 10.1007/s11307-017-1081-y.
8. Z. W. Tay et al., "Superferromagnetic Nanoparticles Enable Order-of-Magnitude Resolution & Sensitivity Gain in Magnetic Particle Imaging," Small Methods, vol. 5, no. 11, p. e2100796, Nov. 2021, doi: 10.1002/smtd.202100796.
9. Z. Yan, S. FitzGerald, T. M. Crawford, and O. T. Mefford, "Oxidation of wüstite

Oral Presentation

Disclosures: The authors would like to disclose that Vivotrax is not approved for distribution in the United States.

180-18F-Labeled PD-L1 Macrocyclic Peptide PET Tracer from Preclinical Studies to Clinical Trials

Presenter: Joonyoung Kim, Bristol Myers Squibb
Joonyoung Kim[1], David J. Donnelly[1], Adrienne Pena[1], Andrea (Olga) O. Shorts, Thomas V. Petrone[1], Erin Cole[2], Yunhui Zhang[3], Kenneth M. Boy[2], Paul M. Scola[2], Daniel J. Tenney[2], Michael A. Poss[2], Matt Soars[2], Sam Bonacorsi[2], Diederik J. Grootendorst[3], Patrick L. Chow[1], Nicholas A. Meanwell[3], Shuyan Du[1]

[1]Bristol Myers Squibb, Princeton, NJ
[2]Bristol Myers Squibb, [3]Bristol Myers Squibb, NJ

Abstract body:
Blockade of the programmed cell death-1 receptor and its ligand (PD-1/PD-L1) signaling pathway has been proven to be one of the most promising immunotherapeutic strategies in oncology [1]. PD-L1 expression has been used clinically as a biomarker for the prediction of response to anti-PD-1/PD-L1 therapies [2]. Multiple antibody-based PD-L1 PET tracers have been published in recent years, but these tracers showed slow clearance, resulting in higher background signals in non-PD-L1 expressing tissues [3]. This study reports the characterization of [^{18}F] BMS-986229 (anti-PD-L1 macrocyclic peptide, 2 kDa), as a novel PD-L1 PET tracer, with the potential for an improved profile of binding, tumor penetration, and clearance.

Methods:
[^{18}F]BMS-986229 was radiolabeled via click-chemistry and assessed for its ability to measure PD-L1 expression. BMS-986189, from the same chemotype series, was also used as a PD-L1 binding blocker of the PET tracer. Tracer binding to PD-L1 positive (L2987) /negative (HT-29) mouse xenograft tumor tissues and human non-small cell lung cancer (NSCLC) tissues was assessed by *in vitro/ex vivo* autoradiography. *In vivo* PET imaging experiments were performed in mice bearing bilateral xenograft L2987 and HT-29 tumors for PD-L1 expression detection (n=4 mice). Target engagement and kinetics with the tracer used mice pre-dosed with the blocker BMS-986189 (n = 58 mice, doses: 0, 0.05, 0.1, 2, 7, 15, 30, 60 mg/kg). To evaluate the ability of the PET tracer to detect various levels of PD-L1 *in vivo*, PET imaging was performed at various times after the blocker had dissociated from PD-L1 over time and was cleared. Longitudinal PET imaging was performed in mice bearing L2987 tumor (n=2 each time-point: at 0, 3, 6, 9, and 21 hours after a single dose, 2 mg/kg) and in the spleen of non-human primates (n=4-6 each time-point: at 0, 2, 24, 74, 146 hours after a single dose, 3.6 mg/kg). In addition, a radiation dosimetry study was performed on 4 NHPs and the radiation effective dose was estimated to support the clinical translation of the tracer.

Results:
In vitro autoradiography of [^{18}F]BMS-986229 showed an 8:1 binding ratio in L2987 vs. HT-29 tumor tissues, more than 90% of which could be blocked with 1 nM of BMS-986189 in human NSCLC tumor sections with high PD-L1 expression. *Ex vivo* autoradiography of tumors showed a 10:1 binding ratio in L2987 vs. HT-29 tumors and the [^{18}F] BMS-986229 signal was penetrant throughout a series of L2987 tumor sections. *In vivo* PET imaging in mice bearing bilateral tumors demonstrated a 5:1 tracer uptake ratio (at 90-100 min after tracer administration) in L2987 vs. HT-29 tumors and demonstrated 83%-93% specific binding within those dose ranges of BMS-986189. In the longitudinal study after a single dose of BMS-986189, L2987 tumor PD-L1 binding went from 3% of tracer bound at 2 hours to 34% at 21 hours. Similarly, monkey spleen PD-L1 binding was 11% at 2 hours but increased to 92% at 146 hours. Target engagement is maintained for this binding series, even though the concentration of the blocker in plasma (time between T_{max} to below low of quantifying) is less than 24 hours. Thus, an optimal profile of fast clearance, but prolonged target binding was seen. Finally, in the dosimetry study, the urinary bladder wall is a dose-limiting organ with an estimated single administration dose of 285 MBq for an average subject.

Conclusion:
This study demonstrates the strong potential of [^{18}F] BMS-986229 as a macrocyclic peptide PD-L1 PET tracer for tumor PD-L1 expression assessment. Clinical studies with [^{18}F] BMS-986229 are currently underway to further evaluate the performance of the tracer in oncology patients treated with immune checkpoint inhibitors.

Reference

1. Pardoll DM. The blockade of immune checkpoints in cancer immunotherapy. Nature Reviews Cancer 2012 April;12:252-264.
2. Brahmer JR, Tykodi SS, Chow LQ, et al. Safety and activity of anti?PD? L1 antibody in patients with advanced cancer. N Engl J Med. 2012;366:2455? 2465.
3. Chatterjee S, Lesniak WG, Gabrielson M, et al. A human antibody for imaging immune checkpoint ligand PD-L1 expression in tumors. Oncotarget. 2016; 7:10215-10227.

Oral Presentation

Disclosures: The authors have disclosed no financial interest.

181-Legumain-Mediated Intracellular Self-Assembly of CES-Theranostic Olsalazine Nanoparticles for Precision Imaging and Treatment of Prostate Cancer

Presenter: Behnaz Ghaemi, Johns Hopkins University School of Medicine

Behnaz Ghaemi[1], Aruna Singh[2], Swati Tanwar[3], Yue Yuan[4], Ishan Barman[5], Michael McMahon[2], Jeff Bulte[1]

[1]Johns Hopkins University School of Medicine, Baltimore
[2]Johns Hopkins University School of Medicine, Baltimore, MD
[3]Johns Hopkins Whiting School of Engineering, Baltimore, MD
[4]University of Science and Technology of China, Baltimore, MD, China
[5]Johns Hopkins Univeristy, Baltimore, Maryland

Introduction:
Cancer therapy may be revolutionized by using specific tumor enzyme-targeted theranostics. The overall aim of this study is to develop a precision-based nanotheranostic platform for prostate cancer that can be monitored by CEST MRI. Exploiting overexpression of enzymes in prostate cancer cells, olsalazine-conjugated peptides were designed to induce self-assembly of olsalazine nanoparticles by the tumor-overexpressed enzymes legumain and furin. Olsalazine is a diaCEST MRI contrast agent with a 9.8 ppm chemical shift from water protons, and acts as a DNA methylation inhibitor anti-cancer agent (1).

Methods:
Synthesis: R6-AAN-CK peptide was synthesized using solid-phase synthesis and subsequently conjugated with olsalazine and 2-cyanobenzothiazole (CBT) to create the peptide-olsalazine-CBT (POC) complex. *Characterization:* Matrix-assisted laser desorption ionization (MALDI) and nuclear magnetic resonance (NMR) were used for peptide characterization. *In vitro and ex vivo immunohistology:* Furin and legumain (over)expression was analyzed in 2D and 3D cell cultures and xenografted tumors. DU145 and LNCaP xenografts were established in Rag2 immunocompromised mice. Aggressive DU145 prostate adenocarcinoma was compared to less-invasive LNCaP tumor cells and RWPE1 normal prostate cells. 3D tumor organoids of prostate cancer were developed and enriched for cancer stem cells up to generation 10 to get the most aggressive clones which were assessed for the expression of legumain, furin and the stemness tumor markers CD133, CD44 and CD24. *In vitro CEST MRI:* After incubation of DU145 with 5 mM POC for 3 h, cells were washed and collected for CEST MRI, performed on a Bruker 11.7 T vertical bore magnetic resonance scanner with a 10-mm birdcage transmit/receive coil.

Results:
In 2D cultures, the levels of legumain and furin expression in DU145 cells were 4- and 3-fold higher than LNCaP and 8- and 6-fold higher than RWPE1 cells, respectively. For 3D tumor spheres, legumain was overexpressed in the periphery while furin was expressed throughout the entire sphere. Legumain and furin expression increased about 6% with each sphere generation accompanied by a 4.5% increase of cancer stem cells according to $CD133^+$, $CD44^{+,}$ and $CD24^-$ expression analysis. Xenografted 5, 15. 50, 75, 100 and 150 mm^3 DU145 tumors showed heterogeneity in furin and legumain expression with overexpressed legumain in peripheral cells correlating with tumor progression stage. CEST MRI of DU145 cells incubated 3h with POC showed 0.2% asymmetric magnetization transfer ratio (MTR_{asym}) increase at 9.8 ppm compared to control cells (incubated with olsalazine only) as a result of legumain expression and consequent intracellular accumulation and retention of Olsalazine.

Conclusion:
Based on a legumain-mediated CBT click condensation reaction followed by intracellular self-assembly of olsalazine nanoparticles, we successfully developed a POC complex for future imaging of drug accumulation and therapeutic response in aggressive vs. non-invasive prostate tumors.

Reference
1. Yuan, Y.; Zhang, J.; Qi, X.; Li, S.; Liu, G.; Siddhanta, S.; Barman, I.; Song, X.; McMahon, M. T.; Bulte, J. W., Furin-mediated intracellular self-assembly of olsalazine nanoparticles for enhanced magnetic resonance imaging and tumour therapy. Nature materials 2019, 18 (12), 1376-1383.

Oral Presentation

Disclosures: The authors have disclosed no financial interest.

182-N-Methyl-D-aspartate receptors (NMDAR) targeted imaging of M1 macrophages in inflammation

Presenter: Yong Hyun Jeon, Daegu Gyeongbuk Medical Innovation Foundation (DGMIF)

Yong Hyun Jeon

Daegu Gyeongbuk Medical Innovation Foundation (DGMIF), Daegu, none, Republic of Korea

The interplay between *N*-methyl-d-aspartate receptors (NMDARs) and macrophage-related inflammation has not been explored, despite several reports on the importance of NMDAR activation in the progression of neurological disorders. We aimed to elucidate the biological role of NMDARs in metabolic reprogramming for M1 polarization of macrophages and their feasibility as a new bio-imaging marker for *in vivo* detection of macrophage-mediated inflammation. We analyzed cellular responses to NMDAR antagonism and small interfering RNAs using mouse bone marrow-derived macrophages treated with lipopolysaccharide (LPS). An NMDAR targeting imaging probe, N-TIP, was produced via introduction of NMDAR antibody and the near-infrared (NIR) fluorescent dye FSD Fluor™ 647. N-TIP binding efficiency was tested in intact and LPS-stimulated BMDMs. N-TIP was intravenously administered to mice with CG and LPS-induced paw edema, and *in vivo* NIR fluorescent imaging was conducted. Anti-inflammatory effects of dexamethasone were evaluated using the N-TIP-mediated macrophage imaging technique. NMDARs were overexpressed in LPS-treated macrophages, subsequently inducing M1 macrophage polarization. Mechanistically, NMDAR-mediated Ca^{2+} accumulation results in LPS-stimulated glycolysis via upregulation of PI3K/AKT/mTORC1 signaling. *In vivo* imaging with N-TIP showed LPS- and carrageenan-induced inflamed lesions at 5 h post-inflammation, and the inflamed lesions could be detected until 24 h. Our N-TIP-mediated imaging technique helped successfully visualize anti-inflammatory effects of dexamethasone in mice with inflammation. This study demonstrates that NMDAR-mediated glycolysis plays a critical role in M1 macrophage-related inflammation. Moreover, our results suggests that NMDARs are a feasible bio-imaging marker for M1 macrophages.

Poster Presentation

Disclosures: The authors have disclosed no financial interest.

183-Evaluation by intravital fluorescent imaging of the angiogenic potential of endothelial cells derived from human pluripotent stem cells (hPSC-ECs) after ischemic injury in mice

Presenter: Valerie Rouffiac, Gustave Roussy

Valerie Rouffiac[1], Alejandra Vargas-Valderrama[2], Tudor Manoliu[3], Karine Ser-Le Roux[1], Georges Uzan[4], Hind Guenou[2]

[1]Gustave Roussy, Villejuif, France, France
[2]Inserm, Villejuif, France
[3]Gustave Roussy, Villejuif, France
[4]Hospital Paul Brousse, Villejuif, France, France

Introduction:
Cardiovascular disorders are a major public health problem. Some of these disorders originate from endothelial dysfunction such as artherosclerosis or thrombosis. Developments of vascular endothelium repair therapies are thus challenging to restore physiological hemorheology and tissue properties. We propose in this study to evaluate by intravital microscopy, hPSC-ECs therapeutic potential to promote angiogenesis after vascular ischemia in mice.

Materials & Methods:
Multiscale intravital imaging of the vascular network was performed through dorsal skinfold chamber. Surgical implantation was done at Day 0 (D0) onto nude mice divided into 3 groups: (G1)- 4 control mice injected with 20 µL PBS with ischemia; (G2)- 7 treated mice injected with 3.105 hPSC-ECs suspended in 20µL of PBS with ischemia; (G3)- 7 treated mice injected 3.105 hPSC-ECs suspended in 20µL of PBS without ischemia. All mCherry-hPSC-ECs were injected close to ischemia induced by thermal cauterization of a macrovessel 15 minutes before cells injection to allow sufficient heat dissipation for preventing cell injuries. Surgical procedure was ended by closing the dorsal chamber with glass coverslips. Mice recovered until D5 and were imaged at D5, D19, D26 and D29 onto a macroscope (AZ100M, Nikon) and a confocal microscope (SP8, Leica) in wildfield and fluorescence mode after 100 µL Dextran-FITC intravenous injection (25µg/µL). Different Dextran-FITC molecular weights from 2000 to 70kDa were used. Acquisition settings were fixed identical as far as possible from D5 to D29. For each day and mouse, fluorescent images were post-processed with Fiji and vascular density was quantified using the skeleton plugin after background subtraction.

Results & Discussion:
An unexpected mortality was observed for all mice after the 2nd Dextran injection for molecular weight ranging from 2000 to 150kDa. In a previous and similar study, multiple Dextran 2000kDa-FITC injections resulted in a 100% survey in C57Bl6 mice. Dextran-FITC molecular weight was thus decreased until 70 kDa in order to reach 0% mice mortality. The number of mice/group was thus reduced to 1, 2 and 2 for G1, G2 and G3 respectively. Despite a reduced number of mice/group, qualitative observations of fluorescent images revealed a migration of hPSC-ECs towards the proximities of blood vessels in the presence of ischemia but also without vessel injury which was confirmed in post-mortem by immunofluorescence. Quantitatively, the number of new vessels did not differ between G1 and G3 with a slight increase of vascular density for G2. Further investigations need to be now conducted in order to: 1- elucidate the “intolerance” of Dextran-FITC ranging from 150 to 2000kDa after 2nd intravenous injection in nude mice, 2- the underlying processes for vessel density increase in presence of hPSC-ECs without ischemia and 3- to confirm the angiogenic potential of hPSC-ECs on a larger cohort of animals.

Reference
1. Proust et al. Stem Cell Res Ther. 2020 May 7;11(1):172

Poster Presentation

Disclosures: The authors have disclosed no financial interest.

184-Potency of the anti-Tumor T Cell Response Induced by Esomeprazole Priming Immune Checkpoint Blockade is Predictable using acidoCEST MRI

Presenter: Renee Chin, University of Texas MD Anderson Cancer Center

Renee Chin[1], Tianzhe Li[1], Jorge De La Cerda[2], F. W. Schuler[3], Shivanand Pudakalakatti[1], Pratip Bhattacharya[1], Sanhita Sinharay[4], Marty Pagel[3]

[1]University of Texas MD Anderson Cancer Center, Houston, TX
[2]MD Anderson Cancer Center, Houston
[3]MD Anderson Cancer Center, Houston, TX
[4]National Institutes of Health

Introduction:
While immune checkpoint blockade (ICB) treatments such as programmed death-1 and cytotoxic T lymphocyte antigen-4 blockade shifted the paradigm of cancer treatment, this ICB combination produces objective response rates of only 35.9% for patients with non-small cell lung cancer,[1] and 58% for melanoma patients.[2] One mechanism allowing tumors to suppress the anti-tumor T cells that drive ICB is the reduction extracellular tumor pH (pHe) to approximately pH 6.4 – 6.9,[3-5] a function inherent to tumor cells due to the Warburg effect. We thus hypothesize that increasing pHe prior to ICB therapy potentiates the T cell-mediated anti-tumor effect of ICB treatment.

In vitro pH sensitizer screening
To interrogate this question, we first screened a panel of six inhibitors that interfere with tumor cell mechanisms that reduce pHe, termed pH sensitizers. We found that esomeprazole significantly reduced the proton efflux rate (PER) of 4T1 cells compared to the other pH sensitizers. Esomeprazole did not significantly affect the PER of B16-F10 cells, making this tumor cell line an ideal model for tumors that are not susceptible to esomeprazole. Furthermore, the ability of esomeprazole to decrease PER in 4T1 cells was not a result of cytotoxicity, as esomeprazole did not significantly reduce cell viability of 4T1 cells or B16-F10 cells. This finding also indicates that the effect of combining esomeprazole and ICB in vivo will not be a result of tumor lysis or increased immunogenic cell death. Lastly, esomeprazole did not inhibit T cell activation in vitro, making it a suitable candidate for combination with ICB in vivo.

Tumor response to esomeprazole and ICB in vivo
When tested on mice bearing orthotopically-implanted 4T1 tumors, esomeprazole was only able to significantly delay tumor growth when delivered one day prior to the beginning of ICB treatment. While the combination of esomeprazole and ICB delayed by one day increased the rate of tumor rejection in mice bearing B16-F10 tumors, there was no significant change in tumor growth. The immune profile of B16-F10 may be responsible for the lack of response, as one day after esomeprazole treatment 4T1 tumors significantly reduce the frequency of Ly6C+ myeloid cells with no change in CD8+ T cell frequency, whereas B16-F10 tumors respond by increasing the frequency of CD8+ T cells with no change in Ly6C+ myeloid cell frequency.
pH response to esomeprazole corresponds to treatment efficacy
AcidoCEST MRI interrogation indicated a correlation between pHe after esomeprazole and tumor control due to ICB, driven by an increase in several activated CD8+ and CD4+FoxP3- T cell subsets whose frequencies increase with pHe, particularly TCF-1. TCF-1-expressing cells amongst both CD8+ and CD4+FoxP3- T cells populations correlated with pHe after esomeprazole treatment.

However, B16-F10 tumor control due to esomeprazole and ICB one day afterwards correlated with change in pHe, rather than pHe following esomeprazole treatment. Also in contrast to the 4T1 tumor results, CD11b+ myeloid cell and CD11c+ dendritic cell frequencies increase with an increase in the change of pH in B16-F10 cells after esomeprazole. Our data suggests that myeloid cell control is integral to the efficacy of increasing pHe in to promote ICB tumor control, as 4T1 tumors respond to esomeprazole by reducing Ly6C+ myeloid cell frequency while B16-F10 tumors do not respond to combination treatment and showed an increase in CD11b+ myeloid cell frequency with an increase in change in pH. Tumoral pHe thus has great potential as a biomarker for ICB success, but the immunotherapeutic combination must also be optimized. The results of our study emphasize the need to better understand individual cancer biology when determining patient treatment with the highest probability of success.

Reference

1. Hellmann, M.D., et al., Nivolumab plus Ipilimumab in Advanced Non-Small-Cell Lung Cancer. N Engl J Med, 2019. 381(21): p. 2020-2031.
2. Hodi, F.S., et al., Nivolumab plus ipilimumab or nivolumab alone versus ipilimumab alone in advanced melanoma (CheckMate 067): 4-year outcomes of a multicentre, randomised, phase 3 trial. Lancet Oncol, 2018. 19(11): p. 1480-1492.
3. Gerweck, L.E. and K. Seetharaman, Cellular pH gradient in tumor versus normal tissue: potential exploitation for the treatment of cancer. Cancer Res, 1996. 56(6): p. 1194-8.
4. Huntington, K.E., et al., Colorectal cancer extracellular acidosis decreases immune cell killing and is partially ameliorated by pH-modulating agents that modify tumor cell cytokine profiles. Am J Cancer Res, 2022. 12(1): p. 138-151.
5. Pilon-Thomas, S., et al., Neutralization of Tumor Acidity Improves Antitumor Responses to Immunotherapy. Cancer Res, 2016. 76(6): p. 1381-90.

Poster Presentation

Disclosures: The authors have disclosed no financial interest.

185-Multispectral optoacoustic tomography to differentiate between lymph node metastases and coronavirus-19 vaccine-associated lymphadenopathy

Presenter: Jan-Malte Placke, Essen University Hospital

Jan-Malte Placke[1], Delphine Mertens[2], Alpaslan Tasdogan[2], Eleftheria Chorti[2], Dirk Schadendorf[2], Selma Ugurel[2], Alexander Roesch[2], Ingo Stoffels[3], Joachim Klode[1]

[1]Essen University Hospital, Essen, Germany
[2]Essen University Hospital, [3]Essen University Hospital, Germany

Introduction:
Worldwide mass vaccination against Covid-19 started in late 2020. Covid-19 vaccines cause benigne hypermetabolic lymphadenopathy. Differentiation between vaccine-associated benigne lymphadenopathy and malignant lymphadenopathy via ultrasound, MRI or FDG PET-CT is not possible, which leads to unnecessary lymph node biopsies, excisions, and even radical lymph node dissections. Therefore, to avoid unnecessary surgery we investigate whether noninvasive multispectral optoacoustic tomography (MSOT) allows a better differentiation between benign and malignant lymphadenopathy.

Patients and methods:
All patients were vaccinated against Covid-19. We used MSOT to image deoxy- and oxyhemoglobin levels in lymph nodes of tumor patients to determine metastatic status. MSOT imaging results were compared with standard Ultrasound and pathological lymph node analysis. Furthermore, the influence of gender, age and time between vaccination and MSOT measurement of lymph nodes on the measured deoxy- and oxyhemoglobin levels in patients with reactive lymph node changes was investigated.

Results:
MSOT identified cancer-free lymph nodes in vivo without a single false negative (32 total lymph nodes), with 100% sensitivity and 50% specificity. A statistically significant higher deoxyhemoglobin content was seen in patients with tumor manifestations in the lymph node ($P=0.02$). There was no statistically significant difference concerning oxyhemoglobin ($P=0.65$). Age, sex, and time between vaccination and MSOT measurement had no statistically significant impact on deoxy- and oxyhemoglobin levels in patients with reactive lymph nodes.

Conclusion:

MSOT measurement could be a useful tool to differentiate between vaccine-associated benign lymphadenopathy and malignant lymph node metastasis based on the deoxygenation level in lymph nodes.

Poster Presentation

Disclosures: The authors have disclosed no financial interest.

186-Sugar Modified Amphiphilic Nano-adjuvant Reverted Tumor Immune Suppression and Ameliorated Peptide Vaccine Induced Anti-tumor Immunity in Cervical Cancer

Presenter: In Kyu Park, Chonnam National University Medical School

In Kyu Park[1], Santhosh K. Rajendrakumar[2], Adityanarayan Mohapatra[3], Yong Yeon Jeong[4], Hansoo Park[5]

[1]Chonnam National University Medical School, Hwasun, South Korea
[2]Chonnam National University Medical School, Hwasun, Jeonnam, Republic of Korea
[3]Chonnam National University, Hwasun, Jeonnam, South Korea
[4]Chonnam National University Hwasun Hospital, Jeonnam, Jeonnam, Republic of Korea
[5]Chung Ang University, Seoul, Seoul, South Korea

Human papilloma virus (HPV), one of the most common cancer-causing viruses, accounts for more than 90% of human anal and cervical cancers. Clinical studies have focused on adjuvant therapy with vaccines to improve therapeutic outcomes in patients with late-stage HPV-related cancers. In the present study, a mannose receptor (CD206) targeting lithocholic acid-modified polyethylenimine (PEI) nano-adjuvant delivering the toll-like receptor 7/8 agonist, resiquimod (R848) (mLAPMi-R848) in HPV E6-and E7-expressing TC1 tumor murine model was developed. Peritumoral administration of mLAPMi resulted in enhanced accumulation in tumor/tumor-draining lymph node and significantly targeting antigen presenting cells like macrophage and dendritic cells. PEI-based nanocarriers can exploit the adjuvant potency of R848 and improve the antitumor immunity. Hence,

co-administration of mLAPMi-R848 along with E6/E7 peptide in TC-1 tumor mice eradicated tumor burden and elicited splenocyte-induced cytotoxicity in TC-1 cancer cells. In a bilateral TC-1 tumor model, administration of mLAPMi-R848 and E6/E7 peptide significantly suppressed both primary and secondary tumor burdens and improved the overall survival rate. Immune cell profiling revealed elevated levels of mature DCs and CD8+T cells but reduced levels of tumor-associated immunosuppressive cells (TAICs) like Myeloid derived suppressor cells and regulatory T (Treg) cells in the distal tumor. Overall, this study demonstrated that mLAPMi-R848 has improved the antitumor immunity of the peptide antigen against HPV-induced cancers by targeted immunodulation of APCs and reducing TAICs. Furthermore, this nano-adjuvant have the potential to offer a new treatment option for patients with cervical cancer and can be applied for the treatment of other HPV induced cancers.

Poster Presentation

Disclosures: The authors have disclosed no financial interest.

187-Towards the clinical development and translation of an integrin ?v?6-targeted peptide for near-infrared fluorescence imaging in pancreatic cancer

Presenter: Okker Bijlstra, Leiden University Medical Center (LUMC)

Okker Bijlstra[1], Friso Achterberg[1], Shadhvi Bhairosingh[2], Ruben Houvast[1], Labrinus van Manen[3], Taryn L. March[4], Sven Mieog[5], Jacobus Burggraaf[6], Willemieke Tummers[7], Alexander Vahrmeijer, Rutger Jan Swijnenburg[8]

[1]*Leiden University Medical Center (LUMC), Leiden, Zuid-Holland, Netherlands*
[2]*Leiden University Medical Center (LUMC), Leiden, Zuid Holland, Netherlands*
[3]*Leiden University Medical Center (LUMC), Leiden, Nederland, Netherlands*
[4]*Leiden University Medical Center (LUMC), Leiden, Leiden, Netherlands*
[5]*Leiden University Medical Center (LUMC), leiden, z-h, Netherlands*
[6]*Centre for Human Drug Research, Leiden, non-US, Netherlands*
[7]*Molecular Imaging Program at Stanford (MIPS), Stanford, CA*
[8]*Amsterdam University Medical Center (UMC), Amsterdam, Noord-Holland, Netherlands*

Introduction:
Complete surgical resection, combined with (neo)adjuvant chemotherapy, remains the only potential curative treatment for pancreatobiliary cancer (PBC) patients[1]. To increase surgical accuracy, a method to detect tumors, metastases and to assess resection margins intraoperatively is essential. Near-infrared (NIR) fluorescence using tumor-specific tracers seems promising[2-5]. However, thus far, none of the probes tested in early phase clinical trials have been considered suitable for incorporation into daily clinical practice. Interesting targets for pancreatobiliary surgery include integrins which regulate various processes in tumor growth, including cellular proliferation, migration and invasion. Integrins are overexpressed on the epithelium in over 80% of pancreatic cancers and cholangiocarcinomas[6]. Among all integrins, specifically integrin ?v?6 resembles an interesting target by virtue of its low expression in most healthy tissues and upregulation in malignant cells. We developed and preclinically validated the integrin ?v?6 targeted tracer R01-MG-IRDye800CW [7]. However the dye appeared to precipitate in the intended solvent (PBS), hampering clinical translation. In this study we describe the translational hurdles needed to be taken before clinical translation of a novel tumor-specific NIR tracer, R01-MG-IRDye800CW, prior to first in-human clinical studies.

Methods:
First, 90:10 propylene glycol (PG):H_2O solution was diluted in PBS in a 2:3 ratio as a novel solvent. The binding properties of the fluorescent dye R01-MG-IRDye800CW dissolved in both PBS and the solvent PG/H_2O:PBS were first tested *in vitro* with fluorescence-activated cell sorting (FACS), and subsequently in a subcutaneous murine model and in a xenograft murine model. For the subcutaneous murine model ten six-week-old nude mice were injected with either $1x10^6$ BxPC-3-Luc2 cells per injection site and five mice were injected with $1x10^6$ HT-29 cells per injection site. After 20 days of tumor growth, five mice carrying HT-29 tumors (cohort A) and five mice carrying BxPC-3-Luc2 (cohort B) tumors received 28.89 ?g (6 nmol) R01-MG-IRDye800CW dissolved in a 100 ?L solution of PG/H_2O-PBS via tail vein injection. Five mice incubated with BxPC-3-Luc2 (cohort C) xenografts received 28.89 ?g R01-MG-IRDye800CW dissolved in 100 ?L PBS. For the orthotopic xenograft murine model, All mice were injected with $1x10^6$ BxPC-3-Luc2 cells in the pancreas. Tumors were grown for 20 days, and all mice received R01-MG-IRDye800CW in 100 ?L PG/H_2O-PBS 24 hours prior to imaging.

Results:
R01-MG-IRDye800CW showed high binding specificity for ?v?6 in the fluorescence-activated cell sorting FACS in both solutions. In the subcutaneous model mean TBRs after 6, 20 and 24 hours were significantly higher in cohort B and C compared to cohort A, 2.52 and 2.33 vs. 1.58, respectively (p=0.005). The TBRs in cohort B were comparable to the TBRs in cohort C after 6, 20 and 24 hours (p=0.700, p=0.200, and p=0.841, respectively). Renal fluorescence signals were analyzed by calculating SBRs for all kidneys in all three cohorts. SBRs were comparable for all groups at each time-point (p=0.133-1.000). Mean *in vivo* and *ex vivo* TBR in the orthotopic mice were 2.57 and 2.04, respectively. Fluorescence intensities in all surrounding organs, the kidneys excluded, were significantly lower than fluorescence intensities in the tumors. Mean *ex vivo* SBRs were 0.93 (p=0.016), 0.69 (p=0.011), 0.22 (p<0.0001), and 0.70 (p=0.002) for the stomach, small bowel, colon and liver, respectively.

Conclusions:
In these final preclinical experiments prior to translation into human subjects we have demonstrated that administration of the fluorescent dye R01-MG-IRDye800 is safe, and both renal clearance and fluorescence properties have not been influenced by altering the solvent. Pending the results of the toxicology study, a phase I/IIa study in healthy volunteers and in patients with potentially resectable pancreaticobiliary cancers will be initiated.

Reference
1. Park W, Chawla A, O'Reilly EM. Pancreatic Cancer: A Review. Jama 2021; 326(9): 851-62.
2. Lu G, van den Berg NS, Martin BA, Nishio N, Hart ZP, van Keulen S, et al. Tumour-specific fluorescence-guided surgery for pancreatic cancer using panitumumab-IRDye800CW: a phase 1 single-centre, open-label, single-arm, dose-escalation study. Lancet Gastroenterol Hepatol 2020; 5(8): 753-64.
3. Hoogstins CES, Boogerd LSF, Sibinga Mulder BG, Mieog JSD, Swijnenburg RJ, van de Velde CJH, et al. Image-Guided Surgery in Patients with Pancreatic Cancer: First Results of a Clinical Trial Using SGM-101, a Novel Carcinoembryonic Antigen-Targeting, Near-Infrared Fluorescent Agent. Annals of surgical oncology 2018; 25(11): 3350-7.

4. Tummers WS, Miller SE, Teraphongphom NT, Gomez A, Steinberg I, Huland DM, et al. Intraoperative Pancreatic Cancer Detection using Tumor-Specific Multimodality Molecular Imaging. Annals of surgical oncology 2018; 25(7): 1880-8.
5. Tummers WS, Miller SE, Teraphongphom NT, van den Berg NS, Hasan A, Longacre TA, et al. Detection of visually occult metastatic lymph nodes using molecularly targeted fluorescent imaging during surgical resection of pancreatic cancer. HPB (Oxford) 2019; 21(7): 883-90.
6. Reader CS, Vallath S, Steele CW, Haider S, Brentnall A, Desai A, et al. The integrin ?v?6 drives pancreatic cancer through diverse mechanisms and represents an effective target for therapy. J Pathol 2019; 249(3): 332-42.
7. Tummers WS, Kimura RH, Abou-Elkacem L, Beinat C, Vahrmeijer AL, Swijnenburg RJ, et al. Development and Preclinical Validation of a Cysteine Knottin Peptide Targeting Integrin ?v?6 for Near-infrared Fluorescent-guided Surgery in Pancreatic Cancer. Clinical cancer research: an official journal of the American Association for Cancer Research 2018; 24(7): 1667-76.

Poster Presentation

Disclosures: The authors have disclosed no financial interest.

188-Hyaluronan-coated Prussian Blue Nanoparticles Relieve LPS-induced Peritonitis by Suppressing Oxidative Species Generation in Tissue-resident Macrophages

Presenter: In Kyu Park, Chonnam National University Medical School

In Kyu Park

Chonnam National University Medical School, Hwasun, South Korea

Excessive inflammatory response during sepsis causes irreversible damage to healthy tissues and results in multi-organ failure. During infection, bacterial endotoxin-triggered inflammatory responses in macrophages facilitate the recruitment of circulating leukocytes, including neutrophils and monocytes. A key component that aggravates the systemic inflammatory response is the generation of stable reactive oxygen species like hydrogen peroxide (H_2O_2). In this study, we present a versatile strategy for reducing the activation of tissue-resident macrophages and preventing leukocyte infiltration in an LPS-induced endotoxemia model. We designed and synthesized hyaluronic acid stabilized Prussian blue (HAPB) nanoparticles and validated their activity in the dismutation of H_2O_2 in LPS-induced tissue-resident macrophages. Hyaluronic acid provided stability and enhanced intracellular uptake of insoluble Prussian blue through the CD44 receptor in the LPS-activated macrophages. Following HAPB administration in an LPS-induced peritonitis murine model, the level of M1 inflammatory macrophage population decreased, and infiltration of neutrophils along with monocytes was suppressed. Overall, we have developed biocompatible Prussian blue nanoparticles that can mitigate inflammatory stress LPS-induced endotoxemia by scavenging the intracellular peroxide production, thereby inhibiting inflammatory cascades in tissue-resident macrophages. Therefore, HAPB nanoparticles may potentially be used as novel nano-stress relievers for sepsis. The nanomaterial may have clinical applicability in sepsis and in other inflammatory diseases involving peroxides as key inflammatory agents.

Poster Presentation

Disclosures: The authors have disclosed no financial interest.

189-Seeing the invisible: radioisotope SWIR Cerenkov luminescence

Presenter: Ben McLarney, Memorial Sloan Kettering Cancer Center

Ben E. Mc Larney[1], Qize Zhang[2], Edwin C. Pratt[1], Magdalena Skubal[1], Elizabeth Isaac[3], Hsu Hsiao-Ting[1], Anuja Ogirala[1], Jan Grimm[1]

[1]Memorial Sloan Kettering Cancer Center, New York, NY
[2]Memorial Sloan Kettering Cancer Center, Kearny, NJ
[3]Memorial Sloan Kettering Cancer Center, New York, New York

Background:
Cerenkov luminescence (CL) is produced when charged particles travel faster than light in a dielectric medium. As the particle travels it polarizes the surrounding molecules, which generate luminescence upon relaxation [1]. CL is UV weighted with an exponential decrease as wavelength increases ($1/\lambda^2$) in the visible and infrared spectrum. [2] Detected CL is correlated to the emitted particles energy upon radioisotope decay, the level of isotope present and is used in astrophysics, nuclear physics, and biomedical imaging.[3] CL imaging (CLI) promises an economical alternative increasing global access to nuclear imaging. CLI is performed in the visible regime is limited by the scattering and absorption of tissue and requires complete ambient light removal.[4, 5] CLI has been employed in a clinical setting for the screening of radioisotope administered patients with high correlation to PET & SPECT, massively reduced costs and rapid acquisition. [5] Theoretically, CL from radioisotopes is also produced in the short-wave infrared (SWIR) spectrum (900 – 1700 nm) but has only been detected from orders of magnitude brighter linear accelerator (LINAC) sources.[6] Radisotope SWIR CLI would overcome many of CLIs current limitations.[7]

Results:
A commercially available SWIR sensor (NIRVana 640 TEC, Teledyne, NJ, USA) and appropriate SWIR lens were used to assess the feasibility of radioisotope SWIR CLI. SWIR CLI could be readily performed with ^{68}Ga and the employed open source and automated processing steps (ImageJ) removed γ strikes, preserved SWIR light detection with SWIR CLI responding linearly to radioisotope levels. Having detected radioisotope SWIR CL, we investigated the detection of other radioisotopes, the SWIR CLI limit of detection, the advantages of SWIR CLI for tissue scatter, and possible *in vivo* applications. SWIR CLI successfully distinguished between four clinical radioisotopes: ^{68}Ga, ^{18}F, ^{89}Zr, ^{131}I and ^{32}P, used in biomedical research (Figure 1A). The relative SWIR radiances provided similar results to visible CLI. A source of ^{68}Ga was imaged during multiple decays (Figure 1B) providing a limit of detection of 7 μCi (0.23 μCi/μl) for ^{68}Ga and conserved linear detection at low radisotope levels. Using suitable acquisition settings and the same phantom we directly compared the IVIS (visible, current CLI gold standard) to SWIR to image a ^{90}Y source through scattering tissue depths. SWIR clearly outperformed visible CLI (Figure 1C). Finally, we assessed SWIR CLIs capability to detect ~200μCi of ^{90}Y labelled silica nanoparticles (SiNPs) in the footpad of mice.[8] The acquisition settings and processing steps removed inherent thermal signatures, providing the first radioisotope *in vivo* SWIR CLI images and accurately locating the source. Four mice injected in a similar fashion are were quantified (Figure 1D,E) with mean signal to background ratios (SBRs) of 3 compared to 1 for a control.

Conclusion & Outlook:
This work outlines the successful approach to detect SWIR CL from 6 radioisotopes via commercially available "off-the"shelf" components. Previously, SWIR CL had only been detected from LINAC sources producing orders of magnitude brighter CL.[6] SWIR CLI performed in a linear manner similar to visible CLI at high and low radisotope levels, is capable of distinguishing the radiance of various radioisotopes, has a current detection limit of 7µCi for ^{68}Ga, showed a comprehensive improvement at imaging through tissue and can detect radisotopes *in vivo* preclinically at clinically relevant levels. Undoubtedly the main limitation of SWIR CLI lies within the sensors inherent dark noise 2 to 3 orders of magnitude higher than EMCCDs and a constant obstacle throughout this work. However, future SWIR CLI iterations employing lower dark noise can readily overcome this obstacle and harness the clear advantages of radisotope SWIR CLI.

Reference

1. Ciarrocchi, E. and N. Belcari, Cerenkov luminescence imaging: physics principles and potential applications in biomedical sciences. EJNMMI physics, 2017. 4(1): p. 1-31.
2. Glaser, A.K., et al., Cherenkov radiation fluence estimates in tissue for molecular imaging and therapy applications. Physics in Medicine & Biology, 2015. 60(17): p. 6701.
3. Ruggiero, A., et al., Cerenkov luminescence imaging of medical isotopes. Journal of Nuclear Medicine, 2010. 51(7): p. 1123-1130.
4. Jacques, S.L., Optical properties of biological tissues: a review. Physics in Medicine & Biology, 2013. 58(11): p. R37.
5. Thorek, D.L., C.C. Riedl, and J. Grimm, Clinical Cerenkov luminescence imaging of 18F-FDG. Journal of Nuclear Medicine, 2014. 55(1): p. 95-98.
6. Cao, X., et al., Observation of short wavelength infrared (SWIR) Cherenkov emission. Optics letters, 2018. 43(16): p. 3854-3857.
7. Carr, J.A., et al., Shortwave infrared fluorescence imaging with the clinically approved near-infrared dye indocyanine green. Proceedings of the National Academy of Sciences, 2018. 115(17): p. 4465-4470.
8. Shaffer, T.M., et al., Silica nanoparticles as substrates for chelator-free labeling of oxophilic radioisotopes. Nano letters, 2015. 15(2): p. 864-868.
9. Bandi, V.G., et al., Targeted multicolor in vivo imaging over 1,000 nm enabled by nonamethine cyanines. Nature Methods, 2022: p. 1-6.

Poster Presentation

Disclosures: The authors have disclosed no financial interest.

190-Full Preclinical Characterization of a Novel Bimodal Probe for Image-guided Surgery of GRPR-positive Cancer

Presenter: Marjolein Verhoeven, Erasmus Medical Center

Marjolein Verhoeven[1], Maryana Handula[2], Lilian van den Brink[3], Corrina de Ridder[1], Debra Stuurman[1], Yann Seimbille[2], Simone Dalm[2]

[1]Erasmus Medical Center, Netherlands
[2]Erasmus Medical Center, Rotterdam, Netherlands
[3]Erasmus Medical Center

Introduction:
Image-guided surgery can aid in precise tumor delineation during surgical procedures and herewith prevent or reduce the occurrence of positive surgical margins. Since surgery remains one of the most widely used treatment options for solid tumors, this imaging-based method has broad applicability. The gastrin-releasing peptide receptor (GRPR) is a promising target for this application, because of its overexpression in several solid tumors, including high-incidence cancers such as prostate and breast cancer. In accordance with this, the GRPR-targeting radiotracer NeoB (Nock BA et al., JNM 2017) was modified to generate a bimodal probe applicable for preoperative nuclear imaging and intraoperative fluorescence guidance. Here, a full preclinical *in vivo* characterization of the bimodal probe is presented, including the pharmacokinetic profile, mass optimization and a proof-of-concept for image-guide surgery.

Materials and Methods:
The bimodal probe DOTA-K(sCy5)-*p*ADA-fQWAVGH-NHCH[$CH_2CH(CH_3)_2]_2$) was synthesized. Studies were conducted in mice xenografted with the GRPR-positive prostate cancer cell line PC-3 on the right shoulder. To determine target specificity, mice were also xenografted with the GRPR-negative small cell lung cancer cell line H69 on the left shoulder in the pharmacokinetic and proof-of-concept studies. To characterize the pharmacokinetic profile of the probe, mice were intravenously injected with ~20 MBq/1 nmol of the indium-111 and sulfo-cyanine5 labeled bimodal probe. After 4 (n=4) and 24 hours (n=4), SPECT/CT and optical imaging was performed using one mouse per group and all mice were included in an *ex vivo* biodistribution study examining both the radioactive and optical signal. The same experimental set-up was used for the mass optimization study, but here mice (n=4 per mass) were injected with three different masses (~20 MBq/0.75, ~20 MBq/1.25 and ~20 MBq/1.75 nmol) and analyzed 24 hours post injection (p.i.). Furthermore, *ex vivo* analyzes on the tumors were performed to localize the nuclear and optical signal within the tissue. Finally, the optimal mass was injected for a proof-of-concept study (n=2) simulating the surgical removal of tumors. Twenty-four hours p.i. a SPECT/CT scan was performed, after which the tumors were resected post-mortem and fluorescent scans were obtained before, during and after surgery.

Results: PC-3 xenografts were clearly visualized on nuclear and optical images with 3.0±0.8% and 2.7±0.7% injected dose/gram (ID/g) radioactivity uptake in the tumor at 4 and 24 hours p.i., respectively. The probe was excreted hepatobiliary and renally with the highest tumor-to-background ratios (TBRs) at 24 h p.i. (tumor-to-blood: 10.6±3.9). Target specificity was demonstrated by the low signal measured in the GRPR-negative tumor (0.5±0.1% ID/g at 24 h). Injection of increasing masses of the probe led to similar TBRs for optical imaging, however, as a result of target saturation the radioactive tumor signal was slightly lower with increasing mass (2.7±0.2% vs. 2.1±0.3% ID/g for 0.75 and 1.75 nmol, respectively). Furthermore, higher liver radioactivity uptake was observed with increasing mass (0.4±0.2% vs. 5.5±1.1% ID/g for 0.75 and 1.75 nmol, respectively). Together, this identifies 0.75 nmol as the optimal mass for further studies. Co-localization of the radioactive and fluorescent signal was observed between organs, but within the sectioned tumor specimens, a stronger fluorescent signal originated from the necrotic core, most likely due to interaction of the dye with dead cells. The mimicked fluorescence guided surgery demonstrated the possibility to clearly visualize the tumor during all surgical steps.

Conclusion:
The GRPR-targeting bimodal probe has favorable pharmacokinetic properties resulting in high TBRs 24 hours p.i. The lowest mass of 0.75 nmol yielded the best TBRs for both imaging modalities. In addition, the bimodal probe has shown promise for image-guided surgery in a simulated surgical situation. Overall, this study demonstrated the potential of the developed bimodal probe for image-guided surgery of GRPR-positive cancer.

Poster Presentation

Disclosures: The authors have disclosed no financial interest.

191-Ga68 PSMA Imaging and Prostate Cancer

Presenter: Jyotsna Rao, Apollo

Jyotsna Rao[1], Alka Chengapa[1], Kalyani Reddy[1]

[1]*Apollo, hyderabad, India*

Aim:
To evaluate the role of Ga68 PSMA in the dignosis and staging of Prostate Cancer

Introduction:
FDG-PET has been used to image prostate cancer but has shown low sensitivity in well differentiated cancers,PSMA has been shown to be more specific in this area. We retrospectively analysed data of patients who were referred by neurologists and oncologists. In patients with suspected prostate cancer in view of elevated PSA and newly diagnosed prostate cancer patients, the age range was 50 years to 85 years. Data from 50 patients was analyzed out of which 38 patients were referred for rising PSA or peristent elevation, scans were reported by two nuclear medicine physicians and a radiologist. Analysis showed 20 patients with PSMA positive prostate tumor with no metastasis,24 patients showed PSMA positive prostate tumor with metastasis, 1 patient with elevated PSA showed no prostate uptake, 5 patients with biopsy proven cancer showed minimal prostate uptake.Our experience shows that Ga68 PSMA imaging is useful dignostic tool in suspected prostate cancer and staging of prostate cancer thus helping in treatment planning

Poster Presentation

Disclosures: The authors have disclosed no financial interest.

192-Evaluation of a Fibronectin-Targeted Imaging Probe for Disease Activity and Treatment Response in a Bleomycin-induced Mouse Model of Pulmonary Fibrosis

Presenter: Soumya Mitra, AbbVie

Soumya Mitra[1], Liang Zhang[1], Yuzhen Wang[1], Jamie Erickson[1], Christine Nelson[2], Heather Knight[2], Munish Puri[1], Meghan Clements[1], Stuart Perper[1], Lucy Phillips[1], Stephen O'Brien[1]

[1]*AbbVie, Worcester, MA*
[2]*AbbVie*

Bleomycin-induced lung injury is a well-accepted animal model of pulmonary fibrosis and widely used in drug discovery programs for idiopathic pulmonary disease. However, to demonstrate the efficacy of anti-fibrotic molecules in this model, there is an increasing need to establish reproducible and quantitative assessments. There exists an unmet need for a quantitative, high-resolution imaging probe to detect pulmonary fibrosis, with special interest in a marker that can differentiate between inflammatory and fibrotic components of disease. Matrix remodeling and overexpression of extracellular matrix proteins, such as collagen and fibronectin, are hallmarks of organ fibrosis. Splice variant of fibronectin extra-domain A, FnEDA, is of particular interest as a target for fibrosis due to its high level of expression in diseased tissue, which is confirmed here using extensive immunohistochemistry in mouse and human lung samples. Supported by these findings, a monoclonal antibody against FnEDA is generated and evaluated as an imaging marker, and the specificity of the probe to assess fibrotic disease activity in the mouse bleomycin model is demonstrated using ^{111}In-SPECT and 800CW-NIR imaging. Further, the uptake of the FnEDA probe in mouse lungs is shown to reduce significantly with treatment response induced with an ALK5 inhibitor. These results are further corroborated and correlated to subsequent downstream assessments in lung tissue sections, including microscopic distribution of the 800CW-labeled FnEDA, histopathology measurements using modified Ashcroft scoring by a pathologist and digital image analysis of collagen content using machine-learning algorithms in whole-slide images. The dataset presented here establishes a strong rationale for further evaluation of the FnEDA probe as an imaging marker of pulmonary fibrosis disease progression and pharmacological response.

Poster Presentation

Disclosures: The authors have disclosed no financial interest.

193-Novel responsive probe for 31P-MR based on oxidation-triggered chemical shift – in vitro and in vivo experiment

Presenter: Natalia Ziółkowska,Institute for Clinical and Experimental Medicine

Natalia Ziółkowska[1], Lucie Wold?ichová[2], Martin Vit[3], Kate?ina Sulková[1], Richard Laga[2], Daniel Jirak[4]

[1]*Institute for Clinical and Experimental Medicine, Prague, Czech Republic*
[2]*Institute of Macromolecular Chemistry, Czech Academy of Sciences, Prague, Czech Republic*
[3]*Technical University of Liberec, Liberec, N/P, Czech Republic*
[4]*Institute for Clinical and Experimental Medicine, PRAHA 4, Czech Republic*

Introduction:
^{31}P-MR is mainly use for assessing various metabolites *in vivo*. Its further potential is tested, but due to high background physiological signal, the imaging requires a specific exogenous probe. Presented polymer [1], is a metal-free phosphorus-containing probe for a specific and functional ^{31}P-MR, because the phosphorothioate group (P=S) in its structure creates a high chemical shift from phosphoester group (P=O). Furthermore, P=S groups are prone to metabolic oxidation by reactive oxygen species (ROS) occurring at higher levels in inflammation and cancer tissue, which makes its signal change a promising functional *in situ* sensor of oxidative stress. In this proof-of-principle experiment, we measured the probe *in vivo* and tested the oxidation-triggered chemical shift.

Methods:
The polymer (pTMPC: Poly[O-(2-(methacryloyloxy)ethyl) O-(2(trimethylamoniumyl)ethyl)phosphorothioate]) was synthesized by controlled radical polymerization technique of the corresponding zwitterionic monomer. MR spectroscopy and imaging were obtained on 4.7T scanner using custom dual ^{1}H/^{31}P RF solenoid (*in vitro*) and surface (*in vivo*) coils. The healthy Balb/C mouse was injected subcutaneously with an aqueous solution of pTMPC (200 μL, c^{P}=100 mmol L^{-1}) into the inner site of left leg and measured using ^{1}H MR imaging (localization) and ^{31}P MR: spectroscopy (single pulse sequence; TR=200ms, scan time=10min) and imaging (CSI; TR=500ms, scan

time=30min). The oxidation-triggered chemical shift (conversion from P=S to P=O) was measured using ^{31}P-MRS (singlepulse sequence; TR=500ms, scan time=5min) by placing the polymer (c^P=10mM) in two oxidative conditions mimicking the inflammatory and tumor tissue: with hydrogen peroxide (H_2O_2; c=20mM; V=0.5mL) and cells suspension (40x10^6 4T1 mouse mammary tumor cell line; V=0.5mL). Quantification of phosphorus P=S MR signal conversion under oxidative stress was obtained using Matlab script. The signal amplitude was averaged from each hour and is presented as a percentage change from the experiment onset.

Results/Discussion:
High content of P=S groups in pTMPC provided a high intensity and chemical shift ($\Delta\delta$=56.07ppm) in ^{31}P-MR at relatively low non-toxic concentrations, making it easily distinguishable from the biological background *in vivo* (Fig.1A). The signal conversion from P=S to P=O over the time accompanied by a significant frequency shift in the ^{31}P-MR spectrum was observed *in vitro* (Fig.1B). pTMPC underwent oxidation and the P=S signal amplitude was reduced by 91.1% (H_2O_2) and 36.0% (4T1). The 4T1 cell line will be used in future *in vivo* experiment on oxidative stress in animal tumor model.

Conclusion:
Novel phosphorus-containing contrast agent showed high sensitivity at ^{31}P-MR and a large chemical shift from biological ^{31}P signal. Add to this the favorable ^{1}H and ^{31}P relaxation times and biocompatibility [1], the probe represents a conceptually new diagnostic for ^{31}P-MR. Furthermore, it can serve as a sensitive ^{31}P-MR sensor of pathological conditions, as it undergoes oxidation-induced structural changes in the presence of ROS.

Acknowledgement: The authors acknowledge financial support from the Ministry of Health of the Czech Republic (grant no. #NU20-08-00095). Institute for Clinical and Experimental Medicine IKEM (IN00023001); Ministry of Education of the Czech Republic through the SGS (project no. 21332/3012) of the Technical University of Liberec.

Reference
1. Kracíková, L., Ziółkowska, N., Androvič, L., Klimánková, I., Červený, D., Vít, M., Jirak, D. Phosphorus-containing Polymeric Zwitterion: A pioneering bioresponsive probe for 31 p-magnetic resonance imaging. Macromolecular Bioscience. 2022; 2100523. doi:10.1002/mabi.202100523.

Poster Presentation

Disclosures: The authors have disclosed no financial interest.

194-Pretargeting of pancreatic cancer with the theranostic pair lead-203 and lead-212

Presenter: David Bauer, Memorial Sloan Kettering Cancer Center

David Bauer[1], Alexa Michel[2], Zachary Samuels[3], Mengshi Li[4], Michael K. Schultz[5], Jason Lewis[3]

[1]Memorial Sloan Kettering Cancer Center, New York City, NY
[2]Memorial Sloan Kettering Cancer Center, Mount Vernon, NY
[3]Memorial Sloan Kettering Cancer Center, New York, NY
[4]Viewpoint Molecular Targeting, Inc., Coraville, IA
[5]University of Iowa, Iowa City, IA

Background:
The carbohydrate antigen 19.9 (CA19.9) is a clinical target (NCT02672917, NCT02687230, NCT03118349) used to screen for primary and metastatic tumors and to evaluate response to therapy in pancreatic ductal adenocarcinoma (PDAC). PDAC is a notoriously lethal disease with a five-year survival rate of less than 10%.[1] The recently identified monoclonal antibody 5B1 is a suitable tumor-targeting vector for CA19.9.[2] The delivery agent was used in a theranostic approach to either carry the diagnostic radionuclide ^{203}Pb or the therapeutic radionuclide ^{212}Pb to the tumor. ^{203}Pb ($t_{1/2}$=2.2 d) is a single-photon emission computed tomography (SPECT) compatible radionuclide, while ^{212}Pb ($t_{1/2}$=10.6 h) is an *in vivo* generator of α-particle emitting daughters – highly effective for inducing fatal DNA double-strand breaks in cancer cells. Due to the short half-life and the high linear energy transfer of ^{212}Pb, quick tumor uptake of the radiotracer and a lower systemic radiation dose for the patient are essential. Pretargeting takes advantage of the antibodies' excellent affinity and specificity and the fast clearance of a small molecule. Here, the trans-cyclooctene (TCO) conjugated antibody 5B1 and the corresponding biorthogonal tetrazine (Tz) unit conjugated to a suitable lead chelator, were employed.

Aim:
This study aimed to investigate different Tz-conjugated lead chelators for their potential to efficiently deliver $^{203/212}Pb$ to a TCO-5B1-pretargeted tumor in a BxPC-3 mouse model.

Methods and Results:
In collaboration with Viewpoint Molecular Targeting®, Inc., four Tz-conjugated lead chelators were synthesized and investigated for radiolabeling with $^{203/212}Pb$, and in vitro stability was tested in human serum. Pretargeting studies were performed *in vitro* (via size exclusion chromatography), testing the bioorthogonal IEDDA (inverse electron demand Diels–Alder) chemistry between 5B1-TCO and tetrazines.
A first pilot study was performed using 100 µg of TCO-5B1 and the radiolabeled tetrazine conjugate [$^{203,212}Pb$]Pb-PSC-PEG7-Tz injected into subcutaneous BxPC-3-xenografted nude mice. A three-day interval was chosen between pretargeting the tumor with 5B1-TCO and injecting the tetrazine. SPECT imaging (^{203}Pb) and a multiple-timepoint biodistribution study (^{212}Pb) were performed, showing a tumor uptake of (4.8 ± 0.9) %ID/g at 24 h post-injection (p.i.). The tumor-to-blood ratio was 4.1 ± 1.0 and the tumor-to-muscle ratio 27.2 ± 8.4 at 24 h p.i. However, a relatively slow kidney clearance was observed for Pb-PSC-PEG7-Tz leading to a kidney uptake of (3.9 ± 0.4) %ID/g at 1 h p.i., and (1.5 ± 0.3) %ID/g at 24 h p.i.

Conclusion and Outlook:
In this study, the pretargeting approach for the matched pair ^{203}Pb and ^{212}Pb is investigated. A first in vivo study showed promising biodistribution for Pb-PSC-PEG7-Tz. This radiotracer carries no overall charge, which might lead to a longer circulation time and slower clearance. In the following studies, the other chelator-tetrazine conjugates, with charges variating from -2 to +2 will be investigated, and a charge clearance profile will reveal the influence of the overall charge on the pharmacokinetics of the radiotracer. The best tetrazine candidate will be considered for a therapy study.

Reference
1. P. Sarantis, et al., Pancreatic ductal adenocarcinoma: Treatment hurdles, tumor microenvironment and immunotherapy. World J Gastrointest Oncol. 2020, 12(2):173-181.
2. S. Poty, et al., Leveraging Bioorthogonal Click Chemistry to Improve 225Ac-Radioimmunotherapy of Pancreatic Ductal Adenocarcinoma. Clin Cancer Res. 2019, 25(2):868-880.

Poster Presentation

Disclosures: The authors have disclosed no financial interest.

195-Radiomic analyses of Contrast enhanced CT (CE-CT) scans for early tumour detection in glioblastoma mouse models and patient datasets.

Presenter: Liam Shiels, Royal College of Surgeons in Ireland

Kate Connor[1], Emer Conroy[2], Kieron White[1], **Liam Shiels[1]**, Simon Keek[3], Abdalla Ibrahim[3], William Gallagher[3], James Clerkin[1], Kieron Sweeney[4], David O'Brien[4], Jane Cryan[4], Josephine Heffernan[4], Philippe Lambin[5], Henry Woodruff[3], Annette Byrne[6]

[1]*Royal College of Surgeons in Ireland, Dublin, Ireland*
[2]*University College Dublin, Ireland*
[3]*Maastricht University, Maastricht, Netherlands*
[4]*Dublin, Ireland*
[5]*Maastricht University*
[6]*Royal College of Surgeons in Ireland, Dublin, Please Select, Ireland*

Background:
Magnetic resonance imaging (MRI) is the gold-standard imaging modality in the glioblastoma (GBM) setting. However, availability of rodent MRI scanners for pre-clinical studies is limited and CT is a more widely available and cost-effective alternative. To study the utility of contrast-enhanced (CE)-CT in rodent GBM models, we optimised CE-CT protocols on two instruments (IVIS$^{SPECTRUM-CT}$;TRIUMPH$^{-X-O-CT}$). and established pipelines for extraction of tumour-specific preclinical CT-derived radiomic features [2-6]. Preclinical tumour-specific features were further studied in an exploratory patient-CT cohort (*n*=11) from The Cancer Imaging Archive (TCIA) to assess species conservation. This study had four aims. A) To identify whether CE-CT may be employed to detect invasive, orthotopic GBM tumours in mice, when MRI is unavailable. B) Establish robust, preclinical GBM CT-specific radiomic workflows on two small animal CT systems. C) Assess whether radiomic features extracted from longitudinal CE-CT scans support earlier detection of tumours and differentiation of tumour from normal tissue. D) Verify putative pre-clinical CT-radiomic classifiers in clinical datasets

Methods:
Two orthotopic, invasive GBM murine models were studied (U87R-Luc2 (*n*=25); NFpp10a-Luc2 (*n*=10) treated +/-temozolomide [TMZ]). Throughout, tumours were monitored *via* bioluminescence imaging. Concurrently, mice underwent CE-CT imaging (IV-iodine/300mg/mL/50kV-scan). Radiomic features were extracted using PyRadiomics. Feature dimensionality was reduced via removal of shape features and Spearman correlation (>0.85; 'Uncorr'). Most informative and non-redundant CT radiomic features were retained. Remaining features were analysed across timepoints (Wk-3,6,9,12), via recursive feature elimination and random forest (RFE; Caret package; Cross-Validated via Repeated CV, 5 fold) or vis Boruta algorithm (random forest). Performance measured as area under the receiver operator characteristic (ROC) curve (AUC). Specifically, normal (Left hemisphere (LH)) and tumour tissue (Right Hemisphere (RH)) were analysed across timepoints (Wk-3,6,9,12), and between treatment (+/-TMZ) groups *via* recursive feature elimination (RFE)[7].

Results:
CE-CT imaging and radiomic pipelines have been established in invasive orthotopic GBM models, on two rodent CT systems (TRIUMPH^{X-O-CT} and IVIS$^{SPECTRUM-CT}$). First, randomised CE-CT scans (*n*=63) were visually assessed, with only 19% of images demonstrating evidence of tumour presence. Unsurprisingly, BLI is significantly more sensitive than CE-CT (by-eye), with tumours detectable at Wk1. Early RH-timepoint (Wk3 *vs* Wk6) comparison, and RH-mid (Wk6) and RH-late (Wk9/12) timepoint comparisons, identified two five-feature classifiers which distinguish between timepoints using the TRIUMPHX^{-O-CT}. These classifiers may represent novel imaging biomarkers for early tumour detection. Next, radiomic analysis of overall LH *vs* RH features identified three 'firstorder TotalEnergy' features which were significantly altered between hemispheres (p<0.001). Finally preclinical features, identified were assessed in the TCIA-GBM patient cohort. Here, 'TotalEnergy' features trended towards increased intensity in tumour *vs* normal tissue. Two features, 'Glszm small area low grey level emphasis' and 'wavelet HLL firstorder Maximum' were also significantly altered between normal and tumour tissue (p<0.05) in the TCIA dataset.

Conclusion:
Overall, radiomic analysis of preclinical CE-CT GBM scans identified putative radiomic signatures which may allow tumour detection (Wk3/Wk6) earlier than is feasible by eye (Wk9/Wk12). Parallel trends in 'TotalEnergy' feature intensity across animal and patient CTs suggest species conservation. Overall CT-derived radiomic features could support early, non-invasive GBM tumour detection.

Reference

1. S. M. Chang, P. Y. Wen, M. A. Vogelbaum, D. R. Macdonald, and M. J. van den Bent, "Response Assessment in Neuro-Oncology (RANO): more than imaging criteria for malignant glioma," Neuro-Oncology Pract., vol. 2, no. 4, pp. 205–209, Dec. 2015.
2. V. Parekh and M. A. Jacobs, "Radiomics: a new application from established techniques," Expert Rev. Precis. Med. Drug Dev., vol. 1, no. 2, pp. 207–226, 2016.
3. S. Sanduleanu et al., "Tracking tumor biology with radiomics: A systematic review utilizing a radiomics quality score," Radiother. Oncol., vol. 127, no. 3, pp. 349–360, 2018.
4. R. J. Gillies, P. E. Kinahan, and H. Hricak, "Radiomics: Images are more than pictures, they are data," Radiology, vol. 278, no. 2, pp. 563–577, 2016.
5. K. M. Panth et al., "Is there a causal relationship between genetic changes and radiomics-based image features? An in vivo preclinical experiment with doxycycline inducible GADD34 tumor cells," Radiother. Oncol., vol. 116, no. 3, pp. 462–466, 2015.
6. P. O. Zinn et al., "A Coclinical Radiogenomic Validation Study: Conserved Magnetic Resonance Radiomic Appearance of Periostin-Expressing Glioblastoma in Patients and Xenograft Models," Clin. Cancer Res., vol. 24, no. 24, pp. 6288–6299, Dec. 2018.
7. A. C. O'Farrell et al., "Implementing systems modelling and molecular imaging to predict the efficacy of BCL-2 inhibition in colorectal cancer patient-derived xenograft models," Cancers (Basel)., vol. 12, no. 10, 2020.
8. D. S. Veres et al., "Radiomic detection of microscopic tumorous lesions in small animal liver SPECT imaging," EJNMMI Res., vol. 9, no. 1, 2019.

Poster Presentation

Disclosures: The authors have disclosed no financial interest.

196-In vitro characterization of a dual-labeled MUC1-targeted immunoconjugate for multimodal PET & near-infrared fluorescence (NIRF) imaging of ovarian cancer

Presenter: Shaniqua Hayes, Memorial Sloan Kettering Cancer Center

Shaniqua Hayes[1], Jason Lewis[2]

[1]*Memorial Sloan Kettering Cancer Center*
[2]*Memorial Sloan Kettering Cancer Center, New York, NY*

In vivo molecular imaging is an indispensable part of screening and symptomatic disease monitoring in cancer management. Positron emission tomography (PET) imaging offers noninvasive whole-body visualization to ascertain the size and location of cancerous tissues. Other modalities such as near-infrared fluorescence (NIRF) imaging allow for rapid, real-time identification of cancerous tissues during fluorescence-guided surgery. The development of agents for preoperative multimodal PET/NIRF imaging would be advantageous in these endeavors due to their complementary nature. This study aims to design, develop, and characterize a multimodal PET/NIRF imaging probe for ovarian cancer based on the AR20.5 antibody, which binds to tumor-associated mucin-1 (MUC1).[1] This goal is founded on the need for imaging tools to noninvasively identify and surgically resect ovarian cancer and improve the overall survival of patients diagnosed with metastatic disease. MUC1 is a highly glycosylated transmembrane glycoprotein expressed on the apical surface of epithelial cells. However, in epithelial ovarian cancer and most other adenocarcinomas, MUC1 is overexpressed and hypoglycosylated. [2, 3] The designed MUC1-targeted immunoconjugate probe, Dual-AR20.5, employs desferrioxamine (DFO) as a chelator for labeling with the radiometal zirconium-89 (^{89}Zr) ($t_{1/2} \approx 3.3$ d) for PET imaging, and the near-infrared fluorophore IRDye 800 ($\lambda_{abs} = 773$ nm, $\lambda_{em} = 792$ nm) for NIRF imaging. AR20.5 has been previously shown to reduce tumor burden in a murine ovarian cancer model using the human ovarian cancer line OVCAR-3, and has also been used to develop a radioimmunoconjugate for the imaging of MUC1-expressing ovarian cancer xenografts in mice using zirconium-89.[4, 5] Here, DFO and IRDye800 were conjugated to lysine residues of AR20.5 to generate the multimodal construct, DFO-IR800-AR20.5, or Dual-AR20.5, with 2.7 +/- 0.1 chelates and 0.93 +/- 0.08 fluorophores per antibody. Dual-AR20.5 was evaluated based on its spectroscopic properties, stability in serum, antigen binding, radiochemical yield, and radiochemical purity. A stability study in human serum revealed that over 96% of [^{89}Zr]Zr-DFO- IR800-AR20.5 remained intact after a 5-day incubation period, indicating a high in vivo stability for [^{89}Zr]Zr-DFO-IR800-AR20.5. [^{89}Zr]-DFO-IR800-Dual-AR20.5 also demonstrated low nonspecific binding, and its binding to MUC1 was effectively blocked by excess unlabeled AR20.5. Furthermore, in vitro studies using the MUC1-expressing OVCAR-3 ovarian cancer cell line confirmed the ability of Dual-AR20.5 to bind to tumor-associated MUC1, and that Dual-AR20.5 retained the spectroscopic properties of IRDye800 for fluorescence imaging. Together, these findings suggest that Dual-AR20.5 is a promising tool for the visualization of MUC1-expressing ovarian cancer with multimodal PET and NIRF imaging.

Reference

1. Movahedin, M., et al., Glycobiology 2017, 27 (7), 677-687.
2. Chen, W., et al., Int J Mol Sci 2021, 22 (12).
3. Deng, J., et al., Cancer Metastasis Rev 2013, 32 (3), 535-551.
4. Qi, W., et al., Hybrid Hybridomics 2001, 20 (5-6), 313-24.
5. Fung, K., et al., Molecules 2020, 25 (10).

Poster Presentation

Disclosures: The authors have disclosed no financial interest.

197-Evaluating Novel Anti-DLL3 Antibodies for Pretargeted ImmunoPET/CT imaging and Radioimmunotherapy

Presenter: Salomon Tendler, Memorial Sloan Kettering Cancer Center

Salomon Tendler[1], David Bauer[2], Kathryn Tully[3], Alexa Michel[4], Zachary Samuels[5], David Andrew[6], John Poirier[7], Charles Rudin[8], Jason Lewis[5]

[1]*Memorial Sloan Kettering Cancer Center*
[2]*Memorial Sloan Kettering Cancer Center, New York City, NY*
[3]*Ratio Therapeutics*
[4]*Memorial Sloan Kettering Cancer Center, Mount Vernon, NY*
[5]*Memorial Sloan Kettering Cancer Center, New York, NY*
[6]*Tri-Institutional Therapeutics Discovery Institute, New York, New York*
[7]*New York University*
[8]*Memorial Sloan Kettering Cancer Center, New York, New York*

Background:
Small cell lung cancer (SCLC) is an aggressive form of lung cancer, with few treatment options. Delta-like ligand 3 (DLL3) has emerged as a viable therapeutic target in SCLC because DLL3 cell surface expression is restricted almost exclusively to malignant tissue. Pretargeting takes advantage of antibodies' excellent affinity and specificity as well as fast clearance of small molecules. This approach allows for early imaging post-administration of the radiotracer and lowers systemic radiation dose to the patient.

Aim:
This study aimed to investigate novel non-internalizing antibodies for pretargeted immunoPET/CT imaging and radioimmunotherapy.

Methods and Results:
In collaboration with the Tri-Institutional Therapeutics Discovery Institute, we screened and assessed 27 antibodies for their internalization rates. Three monoclonal IgG4 antibodies were found to possess low internalization as well as high affinity to the DLL3 receptor: A18, E9, and J8. The pretargeting studies were performed *in vitro* and *in vivo* using the bioorthogonal IEDDA chemistry between trans-cyclooctene (TCO) and tetrazine (Tz). Further optimizing of the pretargeting strategy was tested *in vitro*. The successful click reaction between the different clones conjugated to TCO and [^{64}Cu]Cu-SarAr-Tz was verified by size-exclusion chromatography. A18 and J8 reacted with the tetrazine. However, E9 failed did not show any conversion and was therefore deemed not suitable for in vivo imaging. A pilot study using 100 mg of TCO-conjugated mAb for each of the clones delineated the tumors in H82 xenograft mouse models, and the *ex vivo* tumor-to-tissue ratios ranged between 4 and 6% ID/g. A three-day interval was chosen between injecting the mAb-TCO and the ^{64}Cu-labeled tetrazine ([^{64}Cu]Cu-SarAr-Tz). However, the tumor-to-blood ratio ranged between 1-2% ID/g, indicating a prolonged mAb-TCO circulation.
To achieve an improved tumor-to-blood ratio, the study was repeated with 30 mg TCO-conjugated mAb. However, this resulted in a lower tumor uptake of 1-2% ID/g.
For the last in vivo experiment, the time interval between injecting the mAb-TCO conjugates and the [^{64}Cu]Cu-SarAr-Tz(488-537 mCi, 0.67 nmol) was increased to five days. The immunoPET/CT images were performed 4h and 24h post-injection of the [^{64}Cu]Cu-SarAr-Tz, before concluding the study with an terminal ex vivo biodistribution. The in vivo study showed a tumor uptake of between 2-3% ID/g on the PET/CT images. However, the biodistribution data revealed a tumor-to-blood ratio of 1-3% ID/g.

Conclusion:
This novel study showed the potential of a pre-targeting approach for anti-DLL3 antibodies targeting SCLC.

Poster Presentation

Disclosures: The authors have disclosed no financial interest.

198-Integrin αvβ6 as a Target for Tumor-Specific Imaging of Vulvar Squamous Cell Carcinoma and Adjacent Premalignant Lesions

Presenter: Bertine Huisman, Centre for Human Drug Research

Bertine Huisman[1], Mariette v Poelgeest[2]

[1]*Centre for Human Drug Research, Netherlands*
[2]*Leiden University Medical Center (LUMC), Leiden, Netherlands*

Vulvar squamous cell carcinoma (VSCC) is a rare type of cancer with an incidence of 1.5–2.7 per 100,000 women, necessitating specialized centralized care. However, overall incidence worldwide is increasing. The cornerstone of treatment for VSCC consists of surgery with or without radiochemotherapy. Despite these interventions, high recurrence rates up to 40% and significant morbidity are observed in more than half of the VSCC patients. Morbidity includes genital disfigurement, sexual dysfunction, and psychological problems. In addition, precursor lesions are often found adjacent to the tumor, which are sometimes difficult to identify clinically and therefore not treated adequately. This is at least partially related to the limited ability to distinguish (pre)malignant from normal vulvar tissue. Consequently, better identification and timely recognition of vulvar (pre)malignant lesions may result in prevention of re-excisions, local recurrences, metastases, and associated prognosis. Illumination of neoplastic tissue based on fluorescent tracers, known as fluorescence-guided surgery (FGS), could help resect involved tissue and decrease ancillary mutilation. Clinical studies on various cancer types have shown that FGS improves the recognition of tumor tissue significantly, primarily in cases with incomplete visual and tactile information. Proper identification of tumor-specific targets for molecular imaging is key to the success of FGS. Until now, potential targets for FGS in VSCC have not been studied. The aim of this study was to examine the expression of several targets on vulvar tissues to assess their potential for FGS. The selection of targets was on (i) enhanced expression in vulvar tumors as described in the available literature and (ii) effectiveness of tracers against these targets obtained from studies with other tumor types.
To determine their suitability as a target for tumor-specific imaging in vulvar (pre)malignancies, immunohistochemistry was performed on paraffin-embedded premalignant (high grade squamous intraepithelial lesion and differentiated vulvar intraepithelial neoplasia) and (human papillomavirus (HPV)-dependent and -independent) VSCC tissue sections with healthy vulvar skin as controls. Sections were stained for integrin alphavbeta6 (αvβ6), carbonic anhydrase IX (CAIX), CD44 variant 6 (CD44v6), epidermal growth factor receptor (EGFR), epithelial cell adhesion molecule (EpCAM), folate receptor α (FRα), multidrug resistance-associated protein (MRP1), mucin 1 (MUC1), and urokinase plasminogen activator receptor (uPAR). The expression of each marker was quantified using digital image analysis. H-scores were calculated, and percentages positive cells, expression pattern, and biomarker localization were assessed. In addition, tumor-to-background ratios (TBRs) were established.
TBRs were highest for (pre)malignant vulvar tissues stained for integrin αvβ6 (Figure 1). This conclusion is based on the upregulated homogeneous expression of αvβ6 in VSCCs compared with surrounding stromal tissue and normal squamous epithelium of the healthy control group. αvβ6 showed suitable TBRs in 78% of HPV-independent and 40% of HPV-dependent VSCC patients (Figure 2). TBRs for αvβ6 in premalignancies dVIN and HSIL were lower compared with VSCC, but still above the indicated threshold.
αvβ6 is a promising target for tumor-specific (pre- and intra-operative) molecular imaging of VSCC lesions, which can be hard to distinguish from healthy tissue. For HPV-unrelated VSCCs with adjacent dVIN, that comprise the vast majority of all VSCCs, αvβ6 has shown great potential for precise discrimination at the superficial tissue margins. Further research is needed to validate the use of an αvβ6-targeted probe for FGS of vulvar (pre)malignancies.

Reference

1. Eva, L.J.; Sadler, L.; Fong, K.L.; Sahota, S.; Jones, R.W.; Bigby, S.M. Trends in HPV-dependent and HPV-independent vulvar cancers: The changing face of vulvar squamous cell carcinoma. Gynecol. Oncol. 2020, 157, 450–455.
2. Tan, A.; Bieber, A.K.; Stein, J.; Pomeranz, M.K. Diagnosis and management of vulvar cancer: A review. J. Am. Acad. Dermatol. 2019, 81, 1387–1396.
3. Hinten, F.; Molijn, A.; Eckhardt, L.; Massuger, L.; Quint, W.; Bult, P.; Bulten, J.; Melchers, W.; de Hullu, J. Vulvar cancer: Two pathways with different localization and prognosis. Gynecol. Oncol. 2018, 149, 310–317.
4. Oonk, M.H.; Planchamp, F.; Baldwin, P.; Bidzinski, M.; Brännström, M.; Landoni, F.; Mahner, S.; Mahantshetty, U.; Mirza, M.; Petersen, C.; et al. European Society of Gynaecological Oncology Guidelines for the Management of Patients With Vulvar Cancer. Int. J. Gynecol. Cancer 2017, 27, 832–837.
5. Gaarenstroom, K.N.; Kenter, G.G.; Trimbos, J.B.; Agous, I.; Amant, F.; Peters, A.A.W.; Vergote, I. Postoperative complications after vulvectomy and inguinofemoral lymphadenectomy using separate groin incisions. Int. J. Gynecol. Cancer 2003, 13, 522–527.
6. Vahrmeijer, A.L.; Hutteman, M.; Van Der Vorst, J.R.; Van De Velde, C.J.H.; Frangioni, J.V. Image-guided cancer surgery using near-infrared fluorescence. Nat. Rev. Clin. Oncol. 2013, 10, 507–518.
7. Rosenthal, E.L.; Warram, J.M.; de Boer, E.; Basilion, J.P.; Biel, M.A.; Bogyo, M.; Bouvet, M.; Brigman, B.E.; Colson, Y.L.; DeMeester, S.R.; et al. Successful Translation of Fluorescence Navigation During Oncologic Surgery: A Consensus Report. J. Nucl. Med. 2016, 57, 144–150.
8. Boonstra, M.C.; De Geus, S.W.; Prevoo, H.A.; Hawinkels, L.; Van De Velde, C.J.; Kuppen, P.J.; Vahrmeijer, A.L.; Sier, C.F. Selecting Targets for Tumor Imaging: An Overview of Cancer-Associated Membrane Proteins. Biomarkers Cancer 2016, 8, BIC–S38542.
9. Huisman, B.; Burggraaf, J.; Vahrmeijer, A.; Schoones, J.; Rissmann, R.; Sier, C.; Van Poelgeest, M. Potential targets for tumor-specific imaging of vulvar squamous cell carcinoma: A systematic review of candidate biomarkers. Gynecol. Oncol. 2020, 156, 734–743.

Poster Presentation

Disclosures: The authors have disclosed no financial interest.

199-Assessing Muscle Perfusion in Fatigued Hindlimb Muscle with Contrast Enhanced Ultrasound

Presenter: Jeffrey Morin, Pfizer

Jeffrey Morin[1], Abigail Hunter[1], Yuji Shi[1], Rachel Roth-Flach[2], Dinesh Hirenallur-Shanthappa[1]

[1]*Pfizer, Cambridge, MA*
[2]*Cambridge, MA*

Muscle vasculature plays a critical role in both muscle function and energetics. In many pathologies, poor vascular perfusion and reduced microvascular density can lead to deficits in muscular performance. Assessment of vascular perfusion in skeletal muscle at rest and after contraction is a valuable biomarker to assess muscle blood supply, often measured in the clinic using contrast enhanced ultrasound (CEUS) imaging. The utility of CEUS imaging in assessing skeletal muscle vascular perfusion in the resting and post-contraction state, however, has not been evaluated in preclinical animal models. To test this technique preclinically, external stimulation-induced muscle contraction was used as a localized form of exercise, followed by CEUS imaging to measure vascular perfusion pre and post hindlimb muscle stimulation. The MS-NASH model was used to test this technique, a metabolically driven HFpEF model which demonstrates impaired skeletal muscle perfusion. MS NASH mice were injected intravenously with an ultrasound contrast solution using a perfusion pump, and flow of the contrast through the right hind limb muscle was monitored using ultrasound in nonlinear contrast mode. Following initial imaging at resting state, mice underwent a muscle stimulation protocol aimed at inducing muscle fatigue, then were bolus-infused with contrast agent, and imaged again. Post-stimulation imaging revealed a significant increase in perfusion kinetics (blood volume, wash in rate, fill time). These results suggest contrast imaging with muscle stimulation could provide researchers the ability to study muscle performance in disease models at the vascular level with a clinically translatable modality and open the window of measurability needed to assess therapeutic efficacy in the same models.

Poster Presentation

Disclosures: The authors have disclosed no financial interest.

200-Immunogenicity evaluation and imaging of DHFR as a PET reporter gene in adoptive cellular therapies

Presenter: Mark Sellmyer, University of Pennsylvania

Mark A. Sellmyer

University of Pennsylvania, Philadelphia

Genetically engineered medicines such as chimeric antigen receptor (CAR) T cells have great potential to be the next pillar of medical therapy beyond chemo- and biologic therapies. To develop genetic medicines, new methods to understand their pharmacokinetics (PK) in humans are crucial. It is not feasible to perform traditional PK analysis for "living drugs", because the genes themselves (in the form of DNA or RNA), are not typically responsible for the therapeutic effect. Rather, the protein products of the genes or the cells harboring the engineered genes are the actuators, and thus cannot be measured using standard HPLC or radiolabeled PK experiments. We used a positron emission tomography (PET) reporter gene or "imaging tag" based on the intracellular bacterial enzyme dihydrofolate reductase (eDHFR) that can be paired with radiolabeled versions of trimethoprim (TMP). In this work, we evaluate the potential for immunogenicity using primary human cells and assays geared to assess low affinity and rare T cell clones that may react to eDHFR. We used overlapping pools of 15-mer eDHFR peptides and found that across 9 patients, there was little reactivity compared to EBV and CMV peptide controls. Further, the relative strength of reactivity to the eDHFR peptides was less than that of the viral peptides. Next, we showed that eDHFR iTag harboring CAR T cells were not functionally inferior to unlabeled CAR T cells *in vitro*, and demonstrated strong, selective [^{18}F]-TMP uptake in the eDHFR-expressing CAR T cells. Finally, using a glypican 3 (GPC3) CAR T rodent model and scFv of differing affinity, we performed a feasibility study to non-invasively track proliferation in antigen-harboring xenograft tumors over time with *ex vivo* correlation to anti-CD3 immunohistochemistry. These data demonstrate the potential for non-invasive monitoring of CAR T cells using PET imaging and translational applicability of DHFR / TMP radiotracers.

Poster Presentation

Disclosures: The authors have disclosed no financial interest.

201-Preclinical evaluation of a 68Ga -DOTA-Glypican-3-Adnectin theranostic agent in Glypican-3 expressing tumors in mice

Presenter: Andrea (Olga) Shorts, Bristol Myers Squibb

Andrea (Olga) O. Shorts[1], Joonyoung Kim, Erin Cole[2], Paul Morin[2], Daniel Cohen[2], Sandra Rex-Rabe[2], Ethel Pereira[2], Morvarid Mohseni[2], Sam Bonacorsi[2], Patrick L. Chow, Shuyan Du

[1]*Bristol Myers Squibb, princeton, NJ*
[2]*Bristol Myers Squibb*

Specific hepatocellular carcinoma (HCC) biomarkers and molecular targets hold clinical significance for early diagnosis and development of targeted therapies for patients with HCC, the most common type of primary liver cancer cases [1,2]. Glypican (GPC) are a family of heparan sulfate proteoglycans anchored to cell membrane and Glypican-3 (GPC3) is a cell surface antigen highly expressed on HCC. There is limited GPC3 expression in adult normal liver, but GPC3 expression is at high levels in HCC. It is therefore an attractive target for developing a theranostic platform which combines detection and treatment of both early and advanced diseases [1-3]. The objective of this study was to evaluate the ^{68}Ga-DOTA-GPC3-Adnectin for uptake and specificity in tumor bearing mice. Tumor bearing mice with either H446 (small cell lung cancer line; GPC3+) or Hep3B (HCC line; GPC3+++) were enrolled in the imaging study with a mean tumor volume of 179 ± 34 mm^3 (n=9/tumor line). PET imaging was acquired on the NanoScan PET/CT (Mediso Medical Imaging Systems) along with a low dose CT for attenuation correction and structural definition of organs. Either 75-minute dynamic PET images or 20-minute static PET images (at 40 min after tracer injection) were acquired. To demonstrate selectivity to GPC3 expression in the tumors, mice were injected with either targeted tracer ^{68}Ga-DOTA-GPC3-Adnectin or non-targeted tracer ^{68}Ga-Adnectin to demonstrate selectivity to GPC3+ tumors. Tracer uptake was seen in tumors, kidneys and bladder in both tracers. Specific binding was evaluated using flank muscle as a reference region. Uptake of ^{68}Ga-DOTA-GPC3-Adnectin was observed in both tumor types with higher uptake observed in the Hep3B tumor, consistent with GPC3 expression; SUV of 1.04 ± 0.31 in Hep3B mice vs. 0.23 ± 0.06 in H446 mice. The uptake of ^{68}Ga-Adnectin was low with SUV values of 0.09±0.03 in Hep3B mice and 0.10±0.03 in H446 mice. In summary PET/CT imaging demonstrated successful imaging using 68Ga-DOTA-GPC3-Adnectin with better specific binding and improved tumor to muscle ratio in Hep3B tumor bearing mice vs H446 tumor bearing mice. ^{68}Ga-Adnectin did not show specificity to GPC3. Optimization

would be needed to further test if GPC3 would be a suitable target for radionuclide therapy using GPC3-Adnectin-Theranostic (Lu-177).

Reference

1. Li Y, Zhang J, Gu J, et al., Mol Imaging Biol, 2020 22:134-143
2. Labadie KP, Ludwig AD, Lehnert AL, et al., Scientific Reports, 2021 11:3731
3. Llovet JM, Zucman-Rossi J, Pikarsky E, et al., Nat Rev Dis Primers, 2016, 2:16018

Poster Presentation

Disclosures: The authors have disclosed no financial interest.

202-Modification of hyaluronic acid for CD44 and integrin αvβ6 dual targeting and radio-labeling

Presenter: Hua Zhang, University of California, Davis

Hua Zhang[1], Tanushree (Nina) Ganguly[1], Rebecca Harris[1], Ryan A. Davis[2], Sven Hausner[3], Aaron Mohs[4], Julie Sutcliffe[1]

[1]*University of California, Davis, Sacramento, CA*
[2]*University of California, Davis, Sacramnento, CA*
[3]*UC Davis Health, Sacramento, CA*
[4]*University of Nebraska Medical Center, Omaha, NE*

Introduction:
The targeting capability of hyaluronic acid (HA) to CD44, a cancer cell molecular marker, along with HA's excellent biocompatibility and ease of chemical modification [1], suggests HA will play a role for both cancer imaging and therapy [2]. Although overexpressed in cancers, CD44 is also ubiquitously present throughout the body [3], thereby lowering specificity of HA for CD44-directed tumor targeting. This issue can be circumvented by site-specific modification of HA [4] or by adding another tumor-targeting ligand to achieve simultaneous binding to both targets. The integrin $\alpha_v\beta_6$ is an epithelial-specific cell surface receptor that is highly expressed in a wide range of tumors but has low/undetectable expression in healthy adult tissue [5]. In this study, we synthesized dual targeted agents by combining HA with the $\alpha_v\beta_6$-BindingPeptide ($\alpha_v\beta_6$-BP [6]). Additionally, unlike most HA-based imaging agents reported to date that have used optical probes [7], we explored the feasibility of radiolabeling the HA-constructs with copper-64 for positron emission tomography (PET) imaging [8]. Previous reports suggest that the molecular weight (MW) of HA affects the interaction between HA and CD44 as well as the *in vivo* pharmacokinetics of HA [9, 10], therefore the effects of HA MW was examined with a MW range of 10 - 200 kDa.

Methods:
HA (MW=10, 40, and 200 kDa) was modified with either the DOTA chelator alone for copper-64 labeling, or the $\alpha_v\beta_6$-BP-DOTA conjugate, using strain-promoted alkyne-azide cycloaddition (Fig. 1A). Sulfo-dibenzocyclooctyne (Sulfo-DBCO-PEG-NH_2) was first coupled onto HA's carboxylic acid to yield HA-DBCO. DOTA-Orn(N_3)-$\alpha_v\beta_6$-BP was synthesized by Fmoc solid phase peptide synthesis. Azido-DOTA or DOTA-Orn(N_3)-$\alpha_v\beta_6$-BP were then reacted with HA-DBCO to form HA-DOTA or HA-[$\alpha_v\beta_6$-BP-DOTA], respectively. The radiolabeling of HA_{MW}-DOTA and HA_{MW}-[$\alpha_v\beta_6$-BP-DOTA] was performed with [^{64}Cu]$CuCl_2$ in ammonium acetate buffer (pH 5-6) at 40°C for 30 min at a molar activity of 18.5 MBq/nmol (DOTA). The radiolabeled HA constructs were evaluated *in vitro* for binding and internalization using DX3puroβ6 (CD44+$\alpha_v\beta_6$+) and DX3puro (CD44+$\alpha_v\beta_6$-) cells.

Results:
The formation of HA_{MW}-DBCO, HA_{MW}-DOTA and HA_{MW}-[$\alpha_v\beta_6$-BP-DOTA] was confirmed by UV spectrophotometric analysis. By adjusting the degree of substitution with DBCO for the different molecular weight HAs, HA_{MW}-DOTA and HA_{MW}-[$\alpha_v\beta_6$-BP-DOTA] with about 9 copies of DOTA or [$\alpha_v\beta_6$-BP-DOTA] per HA molecule, respectively, were prepared. For all the HA conjugates tested, the incorporation of copper-64 was ≥85% (iTLC), and the constructs were formulated in PBS (pH = 7) and used without further purification. [^{64}Cu]Cu-[HA_{MW}-DOTA] showed low binding (<12%) and internalization (<3%) to DX3puroβ6 and DX3puro cells, and no selectivity for $\alpha_v\beta_6$ (DX3puroβ6/DX3puro ratio <1.1). Conversely, [^{64}Cu]Cu-[HA_{MW}-[$\alpha_v\beta_6$-BP-DOTA]] showed a high binding (58 - 66%) and internalization (48 - 51% of total radioactivity, 77 - 82% of bound radioactivity) to the DX3puroβ6 cells regardless of the HA MW. The binding of [^{64}Cu]Cu-[HA-[$\alpha_v\beta_6$-BP-DOTA]] in the DX3puro cells decreased with increasing MW of HA: 24, 11, and 5% for 10, 40, and 200 kDa, respectively. As a result, the selectivity for $\alpha_v\beta_6$ increased with increasing MW of HA (Fig. 1B).

Conclusion:
Hyaluronic acid was successfully modified to yield dual targeted (CD44 and $\alpha_v\beta_6$) constructs by conjugating $\alpha_v\beta_6$-BP-DOTA onto HA through strain-promoted alkyne-azide cycloadditions. The resulting constructs were successfully radiolabeled with copper-64. The $\alpha_v\beta_6$-targeted [^{64}Cu]Cu-[HA-[$\alpha_v\beta_6$-BP-DOTA]] demonstrated significantly higher binding to and internalization into DX3puroβ6 cells, as compared to the non-$\alpha_v\beta_6$-targeted analogs. With the molecular weight range of 10 to 200 kDa, the selectivity for $\alpha_v\beta_6$ increased with increasing MW of HA. Given the promising *in vitro* data obtained for [^{64}Cu]Cu-[HA-[$\alpha_v\beta_6$-BP-DOTA]], further investigation into its potential as an *in vivo* PET imaging agent is warranted.

Reference

1. Chen, C., Zhao, S. J., Karnad, A. & Freeman, J. W. The biology and role of CD44 in cancer progression: therapeutic implications. J. Hematol. Oncol. 11, 23, doi:10.1186/s13045-018-0605-5 (2018).
2. Cho, H.-J. Recent progresses in the development of hyaluronic acid-based nanosystems for tumor-targeted drug delivery and cancer imaging. Journal of Pharmaceutical Investigation 50, 115-129, doi:10.1007/s40005-019-00448-w (2020).
3. de la Rosa, J. M. R., Tirella, A. & Tirelli, N. Receptor-Targeted Drug Delivery and the (Many) Problems We Know of: The Case of CD44 and Hyaluronic Acid. Advanced Biosystems 2, doi:10.1002/adbi.201800049 (2018).
4. Bhattacharya, D. S. et al. Sulfation Modulates the Targeting Properties of Hyaluronic Acid to P-Selectin and CD44. ACS Biomater. Sci. Eng. 6, 3585-3598, doi:10.1021/acsbiomaterials.0c00115 (2020).
5. Wu, P. H., Opadele, A. E., Onodera, Y. & Nam, J. M. Targeting Integrins in Cancer Nanomedicine: Applications in Cancer Diagnosis and Therapy. Cancers 11, 24, doi:10.3390/cancers11111783 (2019).
6. Hausner, S. H. et al. Preclinical Development and First-in-Human Imaging of the Integrin alphavbeta6 with 18F alphavbeta6-Binding Peptide in Metastatic Carcinoma. Clinical cancer research: an official journal of the American Association for Cancer Research 25, 1206-1215, doi:10.1158/1078-0432.Ccr-18-2665 (2019).

7. Qi, B. et al. Tuned near infrared fluorescent hyaluronic acid conjugates for delivery to pancreatic cancer for intraoperative imaging. Theranostics 10, 3413-3429, doi:10.7150/thno.40688 (2020).
8. Hai, W. et al. The Labeling, Visualization, and Quantification of Hyaluronan Distribution in Tumor-Bearing Mouse Using PET and MR Imaging. Pharmaceutical Research (Dordrecht) 37, 237, doi:10.1007/s11095-020-02957-y (2020).
9. Wolny, P. M. et al. Analysis of CD44-Hyaluronan Interactions in an Artificial Membrane System INSIGHTS INTO THE DISTINCT BINDING PROPERTIES OF HIGH AND LOW MOLECULAR WEIGHT HYALURONAN. J. Biol. Chem. 285, 30170-30180, doi:10.1074/jbc.M110.137562 (2010).
10. Simek, M. et al. How the molecular weight affects the in vivo fate of exogenous hyaluronan delivered intravenously: A stable-isotope labelling strategy. Carbohydr. Polym. 263, 10, doi:10.1016/j.carbpol.2021.117927 (2021).

Poster Presentation

Disclosures: The authors have disclosed no financial interest.

203-To evaluate the role of the PET-CT in the evaluation of the cutaneous malignancies

Presenter: Sikandar Shaikh, Shadan Institute of Medical Sciences, Kasturba Medical College & IIT Hyderabad

Sikandar M. Shaikh

Shadan Institute of Medical Sciences, Kasturba Medical College & IIT Hyderabad, Hyderabad, India

Cutaneous malignancies are the important and needs to be differentiated from the other skin lesions. Squamous cell carcinoma (cSCC) is the second most common cutaneous malignancy. Usually these pathologies are being evaluated by the CT/MRI . But her it is being evaluated by the FDG-PET/CT for staging of cSCC. Methods: Whole body FDG-PET/CT study is being used for the diagnosis of the and staging of the cSCC were reviewed retrospectively. Lower limb was done separately in the clinical cases The images were quantified by the metabolic activity and quantified by the amount of the FDG uptake by the SUV values. These were evaluated in both the primary and secondary sites . Borderline suspected cases were evaluated by the FDG-PET/CT which was correlated with histopathology and correlated with the follow-up imaging or clinical data . Results: 92 suspected cases of the cSCC patients who underwent the FDG-PET/CT at diagnosis were evaluated. The primary sites in head/neck (n=84), chest (n=4), and foot (n=4). These all patients are having FDG-positive scans and showing the 102 FDG-positive lesions with significant uptake of the (SUV4.3–20.8; mean 5.2). The different positive lesions include 42 nodes, 8 cutaneous lesions, 2 osseous and 2 lung lesion seen in the whole body imaging. Sensitivity, PPV, and accuracy of FDG-PET/CT scan was 100%, 77.5%, and 77.5%, respectively. FDG has detected many lesions and of these 14 additional lesions in 6 patients, compared to CT/MR imaging. Overall, staging FDG-PET/CT detected 18 prior unknown lesions in 10 patients that were proven metastatic disease by histopathology or follow-up; FDG-PET/CT modified management in 5/23 patients (21.7%). Conclusion:
Thus FDG-PET/CT is having very high sensitivity in detection of cSCC lesions, for the evaluation of the small cutaneous and nodal disease and has important role in staging and management of these cancers.

Reference

1. Ebrahimi A, Clark JR, Ahmadi N, Palme CE, Morgan GJ, Veness MJ. Prognostic significance of disease-free interval in head and neck cutaneous squamous cell carcinoma with nodal metastases. Head Neck. 2013;35:1138–1143.

Poster Presentation

Disclosures: The authors have disclosed no financial interest.

204-HDO as a Biomarker of Metabolism of Perdeuterated Glucose

Presenter: Matthew Merritt, University of Florida

Matthew E. Merritt[1], Rohit Mahar[1], Huadong Zeng[1], Anthony Gaiacalone[2], Mukundan Ragavan[3], Thomas H. Mareci[1]

[1]*University of Florida, Gainesville, FL*
[2]*Memphis, TN*
[3]*St. Jude Children's Research Hospital, Memphis, TN*

Deuterium magnetic resonance imaging is a new method for generating metabolic contrast in tissues that does not use ionizing radiation. Experiments with [6,6-$^{2}H_2$]glucose have a specificity advantage, producing methyl deuterated lactate from glycolysis and glutamate/glutamine (glx) enriched at the C4 position after a single turn of the TCA cycle (De Feyter, Behar et al. 2018). However, these signals are relatively low intensity compared to the natural abundance (NA) singly deuterated water (HDO) that is always present. The relative size of these peaks makes chemical shift imaging (CSI) the most suitable means of reading out enrichment, but this acquisition mode is time consuming compared to more standard imaging sequences like gradient recalled echo (GRE). HDO generated from perdeuterated substrates has previously been used to assess whole body fatty acid and glucose metabolism. The general methodology involves administration of the perdeuterated substrate followed by a 3-hour delay to allow body water enrichment to reach pseudo-equilibrium, where the final HDO enrichment is used as a biomarker of whole body metabolic turnover (Votruba, Zeddun et al. 2001). It was hypothesized that administration of perdeuterated ([$^{2}H_7$]glucose) with imaging of the HDO immediately after the injection should produce readouts of tissue specific glycolysis and oxidation in the TCA cycle. Male Sprague-Dawley rats were anesthetized and placed in an 11 T Bruker Biospec imaging system with a 1.2 cm surface coil placed over the brain. Shimming was accomplished by minimizing the NA HDO in the brain using unlocalized 2H spectroscopy. A 1.95 g/kg bolus of perdeuterated glucose was injected via tail vein catheter, and single pulse spectroscopy was used to determine when the glucose began to reach the brain, which was typically within 2-3 minutes. A ^{2}H GRE scan using a 30 degree flip angle, 32-32 pixels, and a 1 cm slice thickness was executed using 256 scans per phase encode for a total time of 13 minutes. A second approach was to perform 2-point Dixon (2PD) imaging to separate the large signals from the perdeuterated glucose and the HDO signal. In some experiments single pulse, unlocalized, ^{2}H spectroscopy was used to measure the HDO enrichment as a function of time post-injection. The ^{2}H spectra following injection of the perdeuterated glucose showed the relatively sharp HDO peak and a large broad resonance associated with the multiple different chemical shifts of the glucose deuterium atoms. Metabolically produced glx was also detected, along with a very small signal

from lactate. As the normal brain is very oxidative, these observations were expected. It was notable that HDO enrichment in the brain went from the natural abundance 13.3 mM (assuming 75% water volume) to an average of 87.5 mM over a 2.5-hour time course. Given the size of the bolus, a final enrichment concentration of 1.35 M in the body water would be expected if the deuterium was incorporated into HDO quantitatively. After an initial jump in HDO enrichment, the signal grew almost linearly from 40 minutes to 150 minutes. GRE images were of notable quality with an in-plane resolution of 0.39 mm^2. The 2PD imaging produced excellent images of the HDO signal alone. Most importantly, for the time window of 8-24 minutes, the HDO signal was observed in a relatively constant 2.5 ratio to the signal associated with the glx component. This suggests that if imaging is executed during this time window, the HDO signal can serve as a biomarker of oxidative metabolism in the brain.

Reference

1. De Feyter, H. M., K. L. Behar, Z. A. Corbin, R. K. Fulbright, P. B. Brown, S. McIntyre, T. W. Nixon, D. L. Rothman and R. A. de Graaf (2018). "Deuterium metabolic imaging (DMI) for MRI-based 3D mapping of metabolism in vivo." Science advances 4(8): eaat7314.
2. Votruba, S., S. Zeddun and D. Schoeller (2001). "Validation of deuterium labeled fatty acids for the measurement of dietary fat oxidation: a method for measuring fat-oxidation in free-living subjects." International journal of obesity 25(8): 1240-1245.

Poster Presentation

Disclosures: The authors have disclosed no financial interest.

205-To evaluate the role of the PET/CT in differentiating tuberculous peritonitis and peritoneal carcinomatosis

Presenter: Sikandar Shaikh, Shadan Institute of Medical Sciences, Kasturba Medical College & IIT Hyderabad

Sikandar M. Shaikh

Shadan Institute of Medical Sciences, Kasturba Medical College & IIT Hyderabad, Hyderabad, India

Objectives:
The Tuberculous peritonitis (TBP) will be closely mimicking peritoneal carcinomatosis (PC). We evaluated the role of the PET/CT in the evaluation of the parietal peritoneum.

Materials and Methods:
This was the retrospective study where the parietal peritoneum was evaluated by the PET/CT . 76 patients with diagnosed tuberculous peritonitis TBP (n=25) and Peritoneal carcinomatosis PC (n=51) were evaluated retrospectively. Different regions of the abdomen were included and different locations were included like right subdiaphragmatic, left subdiaphragmatic, right paracolic gutters, left paracolic gutters, and pelvic regions. The peritoneal involvement was seen in the pelvic and/or right subdiaphragmatic regions suspected of the peritoneal implantation, and also the less-susceptible area for peritoneal implantation, and both uniform distribution. PET features were classified as F18-fluorodeoxyglucose (^{18}F-FDG) uptake in a long beaded line (string-of-beads ^{18}F-FDG uptake) or in a cluster (clustered ^{18}F-FDG uptake) or focal ^{18}F-FDG uptake. The various CT patterns were smooth uniform peritoneal thickening, irregular thickening, or nodules.

Results:
Commonest presentation in the parietal peritoneum is the tuberculous peritonitis compared to the peritoneal carcinomatosis (a) ≥4 involved regions (80.0% vs 19.6%), (b) uniform distribution (67.0% vs 6.9%), (c) string-of-beads ^{18}F-FDG uptake (54.0% vs 8.8%), and (d) smooth uniform thickening (70.0% vs 2.8%) (all $P<0.001$) these were the tuberculous presentations.
The Peritoneal Carcinomatosis in comparison with TBP were (a) distribution (78.4% vs 28.0%), (b) clustered ^{18}F-FDG uptake (56.9% vs 20.0%), (c) focal ^{18}F-FDG uptake (21.6% vs 4.0%), (d) irregular thickening (51.0% vs 12.0%), and (e) nodules (21.6% vs 4.0%) ($P<0.001$, $P<0.05$, $P>0.05$, $P<0.05$, $P>0.05$, respectively).

Conclusion:
Thus, the role of the PET/CT findings in the parietal peritoneum is more useful for the differentiation between the tuberculosis and malignancies

Reference

1. Kinahan PE, Fletcher JW. Positron emission tomography-computed tomography standardized uptake values in clinical practice and assessing response to therapy. Semin Ultrasound, CT MR 2010;31:496–505.

Poster Presentation

Disclosures: The authors have disclosed no financial interest.

206-Influence of proportional change in GTV over PET Radiomic features of Non-Small Cell Lung Carcinoma

Presenter: Grace Mehta, Tata Memorial Hospital

Grace M. Mehta[1], Shreyash Panchal[2], Ashish K. Jha[3], Sneha Mithun[3], Umesh Sherkhane[3], Vinay Jaiswar[3], Biprojit Nath[3], Akhilesh Tripathi[3], Nilendu Purandare[3], Venkatesh Rangarajan[4], Andre Dekker[5], Leonard Wee[5]

[1]Tata Memorial Hospital, Mumbai, India
[2]Tata Memorial Hospital, India
[3]Tata Memorial Hospital, Mumbai, Maharashtra, India
[4]Tata Memorial Hospital, MUMBAI, IN-Mah, India
[5]Maastricht University, Maastricht, Netherlands

Aim:
The Radiomic workflow has several steps such as image acquisition, tumor delineation, pre-processing of the image, feature extraction, feature selection and prediction model development. The image acquisition, tumor delineation, and pre-processing steps impact the reproducibility of radiomic extraction and hence such factors need to be studied in detail. In this study, we have assessed the reproducibility of radiomic features by changing GTV in a controlled manner.

Methodology:
Pre-treatment ^{18}F-FDG PET scans of (n= 28) NSCLC cases were selected for this retrospective study approved by the Institutional Ethics Committee, of our hospital. The SimMD software installed on Advantage Workstation 4.1 (GE Healthcare) was used for the delineation of the tumor. The SUV threshold (42% of SUVmax) method was used to delineate the tumor by an expert imaging medical physicist. The tumor volume was contoured by using a 42% threshold, was named GTV^{100} and saved as an RTSTRUCT file. Further, tumor volume was

reduced to 70% and 30% of GTV^{100} by changing the SUV threshold accordingly and stored as two different RTSTRUCTs i.e., GTV^{70} and GTV^{30} respectively. Three sets of radiomic features (1129) were extracted by using PyRadGUI in-house developed software from all three sets of GTVs. The stability of radiomic features was analyzed using the Intra-class correlation (ICC3) method using psych, library in R (R-4.1.3). Reproducibility of the features was categorized based on ICC3 values i.e., excellent: ICC ≥0.9, good: 0.9>ICC ≥0.75, moderate: 0.75>ICC≥0.5, and poor: ICC<0.5.

Results:

The reproducibility of PET radiomic features was impacted by the change in tumor volume. Out of the total, 237/1129 (21%), 403/1129 (36%), 219/1129 (19%), and 270/1129 (23%) radiomic features had presented excellent, good, moderate, and poor reproducibility respectively.

Conclusion:

Our study suggests that the change in tumor volume impacts the reproducibility of radiomic features substantially. However, 21% of features showed excellent reproducibility, and they need to be investigated further.

Poster Presentation

Disclosures: The authors have disclosed no financial interest.

207-To evaluate the role of the FDG PET-CT in the evaluation of the post operative fever analysis in post operative cases of vascular pathologies .

Presenter: Sikandar Shaikh, Shadan Institute of Medical Sciences, Kasturba Medical College & IIT Hyderabad

Sikandar M. Shaikh

Shadan Institute of Medical Sciences, Kasturba Medical College & IIT Hyderabad, Hyderabad, India

Post operative fever is seen in the various post operative vascular scenarios which can be manifested in various forms like endocarditis, infected aneurysms, or infected vascular prostheses. In this study, we studied the role of the 18Ffluorodeoxyglucose positron emission tomography/computed tomography (18F-FDG-PET/CT) in post operative fever analysis at diagnosis and during follow-up. Methods: Post operative status patients of vascular causes who underwent the surgery an having the symptoms of the fever were studied retrospectively from the June 2017 to December 2021. The clinical data analysis and results were obtained from the 18F-FDG-PET/CT at diagnosis and also at the follow-up and were evaluated and documented . Results: The total, 73 patients who has suspected post operative fever and proven by clinical symptoms of fever were included. 18F-FDGPET/CT scans were performed initially for the diagnosis and this has lead to significant change in the 13.5% in diagnosis. The mortality rate in patients with and without vascular infection diagnosed on the 18F-FDG-PET/CT were 23.8% and 2.1%, respectively (p= 0.001). With the 18F-FDG-PET/CT the modified Duke criteria as major criteria was used with, 17 patients showing the definite endocarditis. For this diagnosis 19.6% of 18F-FDG-PET/CT has changed the line of management . During follow-up, 57.3% of 18F-FDG-PET/CT resulted in treatment modification. Post operative fever and during follow-up leading to the significant change in diagnosis leading to the treatment modification thus providing the significant prognostic information on patient survival.

Reference

1. Fuchs M, Briel M, Daikeler T, et al. The impact of18F-FDG PET on the management of patients with suspected large vessel vasculitis. European Journal of Nuclear Medicine and Molecular Imaging. 2012;39(2):344–353.

Poster Presentation

Disclosures: The authors have disclosed no financial interest.

208-Reproducibility of PET radiomic features of non-small cell lung carcinoma by changing pre-processing parameters

Presenter: Shreyash Panchal, Tata Memorial Hospital

Shreyash Panchal[1], Grace M. Mehta[2], Ashish K. Jha[3], Sneha Mithun[3], Umesh Sherkhane[3], Vinay Jaiswar[3], Biprojit Nath[3], Akhilesh Tripathi[3], Nilendu Purandare[3], Venkatesh Rangarajan[4], Andre Dekker[5], Leonard Wee[5]

[1]*Tata Memorial Hospital, India*
[2]*Tata Memorial Hospital, Mumbai, India*
[3]*Tata Memorial Hospital, Mumbai, Maharashtra, India*
[4]*Tata Memorial Hospital, Mumbai, IN-Mah, India*
[5]*Maastricht University, Maastricht, Netherlands*

Aim/Introduction:

Radiomic feature stability is influenced by various acquisition factors like imaging, image reconstruction and pre-processing steps that affect the final generalizability of the radiomic based prediction model. In this study, we have analysed the reproducibility of PET radiomic features by changing pre-processing parameters i.e., bin width and voxel resampling.

Materials and Methods:

Pre-treatment whole-body 18F-FDG PET/CT scans of 28 patients with non-small cell lung carcinoma (NSCLC) were used in this study. SUV threshold-based (42%) semiautomated delineation of primary lung tumor was performed by an expert imaging medical physicist on an Advantage Workstation (GE Healthcare) using SimMD software and saved as an RT-STRUCT file and named GTV. In-house developed PyRadGUI software was used for radiomic feature extraction. In total five sets of radiomic features were extracted for fixed isotropic voxels (2x2x2 mm^3) by changing bin width to 0.25,0.5,1.0,1.5,2.0 SUV. Similarly, three sets of radiomic features were extracted for fixed bin width (0.5 SUV) by changing isotropic voxel resampling to 1x1x1, 2x2x2, 3x3x3 mm^3.Reproducibility of radiomic features were assessed using intra-class correlation coefficient (ICC3) [excellent: (ICC≥0.90), good: (0.9 >ICC ≥0.75), moderate: (0.75 >ICC ≥0.5), poor: ICC<0.5] using the psych library in R (R-4.1.3).

Results:

The reproducibility of radiomic features was impacted for both the scenarios i.e., change in bin width and change in voxel resampling size. For bin width; 425/1129 (37.64%), 93/1129 (8.23%), 173/1129 (15.32%), and 438/1129 (38.79%) features had excellent, good,

moderate, and poor reproducibility respectively. Similarly, for voxel resampling; 220/1129 (19%), 79/1129 (7%), 148/1129 (13.10%), and 682/1129 (60.40%) features had excellent, good, moderate, and poor reproducibility respectively.

Conclusion:
Our study suggests that pre-processing parameters like bin width and resampling size impact radiomic extraction and very few features remain unchanged. Our study confirms the results of previously published literature hence standard guidelines need to be prescribed and followed by the radiomic community.

Poster Presentation

Disclosures: The authors have disclosed no financial interest.

209-To evaluate the role of the FDG PET CT in the Inflammatory Bowel disease

Presenter: Sikandar Shaikh, Shadan Institute of Medical Sciences, Kasturba Medical College & IIT Hyderabad

Sikandar M. Shaikh

Shadan Institute of Medical Sciences, Kasturba Medical College & IIT Hyderabad, Hyderabad, India

Purpose:
To evaluate the role of the 2-deoxy-2-(^{18}F)fluoro-D-glucose (FDG) uptake on positron-emissions tomography/computed tomography (PET/CT) imaging in the inflammatory bowel disease by using standard uptake value (SUV) levels as an assessment tool

Methods:
This was the retrospective study comprising of the 57 patients suspected to have the inflammatory bowel disease . Whole body PET CT was done after the injection of the FDG Contrast. The quantification is done by the SUV and the analysis is done . The process of the Regions of interest (ROIs) along with the CT images and volumes of interest (VOIs) is done. These VOIs are being analysed based on the anatomical evaluation of the stomach, small bowel and large bowel

Results:
There is the significant correlation between age and average FDG uptake (avg-SUV) of the GI tract (P=.0003) in comparison with the esophagus as the reference of the uptake . The correlations are seen in the sigmoid colon with the (P<.0001), and between the descending colon VOI and the group (P<.0001). There is the intra-operator reproducibility over 3 trials having the coefficient of variation (CV) of .63%. The other inter-operator CV in the few selected patients was 5.6% over the entire GI tract.

Conclusion:
Thus FDG-PET/CT imaging is a promising technique for quantifying bowel inflammation and also used for the management.

Reference
1. Lenze F, Wessling J, Bremer J, et al: Detection and differentiation of inflammatory versus fibromatous Crohn's disease strictures: Prospective comparison of 18F-FDG-PET/CT, MR-enteroclysis, and transabdominal ultrasound versus endoscopic/histologic evaluation. Inflamm Bowel Dis 2012;18:2252-2260

Poster Presentation

Disclosures: The authors have disclosed no financial interest.

210-Impact of change in preprocessing parameters on reproducibility of CT radiomic feature in rectal cancer

Presenter: Shreyash Panchal, Tata Memorial Hospital

Shreyash Panchal[1], Grace M. Mehta[2], Ashish K. Jha[3], Sneha Mithun[3], Umesh Sherkhane[3], Vinay Jaiswar[3], Biprojit Nath[3], Akhilesh Tripathi[3], Nilendu Purandare[3], Venkatesh Rangarajan[4], Andre Dekker[5], Leonard Wee[5]
[1]*Tata Memorial Hospital, India*
[2]*Tata Memorial Hospital, Mumbai, India*
[3]*Tata Memorial Hospital, Mumbai, Maharashtra, India*
[4]*Tata Memorial Hospital, Mumbai, IN-Mah, India*
[5]*Maastricht University, Maastricht, Netherlands*

Aim/Introduction:
Radiomics is a process to extract high throughput quantitative data from medical images which are not appreciable to the expert human eye. These advanced mathematical features have the ability to finitely describe tumor phenotypes. Although radiomic features have shown a strong correlation with clinical outcome, the stability of these features is questionable. Radiomic stability is impacted by various factors like the diverse acquisition parameters, tumor delineation, voxel resampling parameters, and bin-width parameter. In this study, we investigated the reproducibility of CT radiomic features by changing the bin-width and voxel size parameter.

Materials and Methods:
Pretreatment whole-body PET/CT scans of 50 patients with colorectal cancer were used in this study. Contouring of tumor volume on the DICOM data was performed manually by an experienced imaging medical physicist on Philips IntelliSpaceDiscovery workstation in trans-axial view of CT image. The delineated volume for each patient was stored as an RT-STRUCT file and named GTV. Using our in-house developed PyRadGUI software, the radiomic features were extracted. Radiomic features were extracted for voxel size $1 \times 1 \times 1$ mm^3, $2 \times 2 \times 2$ mm^3, $3 \times 3 \times 3$ mm^3 and $4 \times 4 \times 4$ mm^3 keeping the same sigma values as 1, 2, 3mm and bin width 25 .In addition, the variability of features due to different bin widths was evaluated by resampling the bin width to 5, 10, 25, 15, 50 keeping the same sigma values as 1, 2, 3mm and voxel size $2 \times 2 \times 2$ mm^3. Stability of radiomic features was assessed using Intra class correlation coefficient (ICC3) using psych package of R-software: excellent: (ICC≥0.90), good: (0.9 >ICC ≥0.75), moderate: (0.75 >ICC ≥0.5), poor: ICC<0.5.

Results:
Features were extracted for five different bin width for CT. 1032/1093 (94.41%) features showed excellent reproducibility (ICC≥0.90); 10/1093(0.91%) features showed good reproducibility (0.9>ICC ≥0.75); 12/1093 (1.097%) features showed moderate reproducibility (0.75>ICC ≥0.5), 39/1093 (3.568%) features showed poor reproducibility (ICC<0.5). Features were extracted for different isotropic voxel size. 186/1093 (17.01%) features showed excellent reproducibility (ICC≥0.90); 225/1093(20.58%) features showed good reproducibility (0.9>ICC ≥0.75); 277/1093 (25.34%) features showed moderate reproducibility (0.75>ICC ≥0.5), 405/1093 (37.05%) features showed poor reproducibility (ICC<0.5).

Conclusion:
Our study demonstrates the change in bin width do not impact the reproducibility of the CT radiomic features significantly. However, change in voxel size impacts the reproducibility of radiomic features hugely.

Poster Presentation

Disclosures: The authors have disclosed no financial interest.

211-3D High Spatial Resolution/ Thin Slice Rat Brain Venography Based on Wideband QSM MRI

Presenter: Wei-Hao Huang, National Taiwan University

Wei-Hao Huang[1], Po-Wei Cheng[2], Tzu-Yi Wang[1], Chia-Hao Su[3], Jyh-Horng Chen[4]

[1]*National Taiwan University, Taiwan*
[2]*National Taiwan University, Taipei, Taipei, Taiwan*
[3]*Kaohsiung Chang Gung Memorial Hospital, Kaohsiung, Kaoshiung, Taiwan*
[4]*National Taiwan University*

Introduction:
Quantitative Susceptibility Mapping (QSM) is widely applied to different studies, such as neural degeneration diseases, tumor detection, and BOLD-based venography that can observe the vessel regeneration of stroke rat brains. However, the long scanning time of conventional 3D gradient-echo (GRE) limits the high spatial resolution/thin slice QSM venogram and neglects the small blood vessel. Wideband MRI [1] has been proposed to reduce scanning time without additional hardware, and the time saved by Wideband MRI can utilize to acquire high spatial resolution and thinner slice MRI. Therefore, this study aims to use Wideband MRI for a 2-fold high resolution/thin slice 3D rat brain QSM venogram in the same scan time and observe subtle blood vessels.

Materials and Methods:
MR experiments were performed on a Bruker (Ettlingen, Germany) 9.4T animal MR scanner with a 4-channel phase array for signal reception. The 3D conventional GRE and 3D Wideband GRE were performed on Sprague-Dawley (SD) rats with the following parameters: TR/TE = 50/12ms, FOV=20×20×40mm^3, flip angle=20 deg, resolution=156×156×156μm^3 (conventional)/ 78×78×156μm^3 (Wideband high resolution)/ 156×156×78μm^3 (Wideband thin slice), scan time=27min18s. The rats were under normoxia by inhaling mixed gas (20%O_2+80%N_2). The high proportion of deoxyhemoglobin in veins can elevate the contrast of QSM venography. All MR images were reconstructed from raw data using MATLAB (The MathWorks; Natick, MA, USA). The multichannel data used sum-of-square and complex summation algorithms [2] to reconstruct magnitude and phase images. The wrapped phase images were resolved with the 3D path-based unwrapping algorithm [3] and turned into the total field. The background field caused by the air-tissue susceptibility difference was removed by the SHARP [4] algorithm to obtain the local field. Finally, use the MEDI algorithm [5] to calculate QSM from the local field.

Results and Discussion:
The image results of conventional 3D GRE and high resolution Wideband GRE are shown in Fig(a)(b), including the axial view of magnitude images and maximum intensity projection (MIP) of QSM. The spatial resolution improvement resolved the partial volume effect, especially the tiny vessels. The arrows in Fig(a)(b) point out the blood vessels that blur or vanish in the conventional QSM become clearer and manifest after using Wideband MRI. Fig(c) presented the coronal view of the conventional 3D GRE magnitude images and MIP of QSM. Same as Fig(c), Fig(d) included the image results of the thin slice Wideband. The continuity of the cortical vessels of the zoom-in region in Fig(c)(d) enhance obviously because these vessels tilted along the slice acquisition direction (Z-axis). In conclusion, the high resolution/thin slice Wideband QSM increases the capability of small vessels detection.

Conclusion:
In this study, we utilized the Wideband technique to achieve 2-fold spatial resolution/ thin slice 3D GRE in the same scanning time and the size can decrease from 156um to 78um. The high resolution and thin slice rat brain QSM venogram alleviate the partial volume effect and achieve the purpose of subtle vessels detection, which will help for precision medicine. Currently, we combine Wideband MRI and QSM successfully and observe the subtle vessel in high resolution/thin-slice image results. In the future, we will compare the image results to anatomy structure for validation and apply the high resolution/thin slice Wideband QSM to disease models to provide precision quantitative information.

Reference
1. Wu, E.L., et al., Medical physics. (2015)
2. Hammond, K.E., et al., NeuroImage. (2008)
3. Abdul-Rahman, H.S., et al., Appl Opt. (2007)
4. Schweser, F., et al., Neuroimage. (2011)
5. Liu, T., et al., Magn Reson Med. (2011)

Poster Presentation

Disclosures: The authors have disclosed no financial interest.

212-Role of brain SPECT on evaluation of treatment effect of Qigong meditation on brain flow and function among patients with obsession disease

Presenter: Fariba Saddadi, Asia Nuclear Medicine Center

Fariba Saddadi

Asia Nuclear Medicine Center, Tehran, Tehran, Iran

Background and Aim:
Qigong practice is a kind of walking meditation with doing deep breathing and some gentle movements that shows it is good for health and it became very popular in many countries in the world, This dynamic meditation is back to 5000 years ago, that originate mainly at China and little by little became more known and widespread among other countries, including Iran. Nuclear medicine has been showed as a good and reliable imaging modality for detection of any changes in physiology of human body and therefore is a good method and useful device to evaluate any changes in body perfusion and function, specially many disease can be recognized very soon before appearance of any clinical sign and symptoms. We decided to have a survey in this regard and to find the essential qigong effect on patients with obsessive disease by brain SPECT. We chose the obsessives patients because, many of this disease still remained unknown. This clinical symptoms sometimes cannot be differentiated correctly and consequently their therapy encountered with some difficulty. Obsessions is more means as a psychological and behavioral disorders and it seems the prevalence

of this mental disease is increasing. Therapy for those patients is mandatory. But it always therapy is conservative and many of them went for some alternative therapy like yoga, meditation, Taichi,chigong.etc. For behavioural/ mental disease we almost always prescribe to do Shi ba fa Qigong or Yi jin jing qigong cause of its simplicity and easy acceptance of patients and asked them do 2-3 times a week for almost 2-3 months.

Material and methods:
12 patients with obsessive disease, 10 female and 2 male with age range 20-72 years old were selected and enrolled for this study. The main criteria for selection of those patient is their cooperation ability and willingness for doing qigong. Two series of images with Tc99m-ethylene-diamine-tetra-acetic acid Brain SPECT were obtained for each patient. First scan named pre-qigong and the second scan was obtained after practicing Yi ji jing qigong that asked them to do this meditation for 2-3 months. All of those brain scans series was performed with Philips ADAC gamma camera with the same imaging conditions as standard protocols, by injection 25 mCi Tc99m-ECD, for all pre-qigong and post-qigong images and compared to find any changes in brain flow and function if any. The percent value of tracer uptake for both right and left brain cortex for each lobes and also brain nucleus, basal ganglias were evaluated by drawing region of interest (ROI)

Results:
The result shows the cortical perfusion value in pre qigong scan was un-even with mean 0.62 percent of count/pixels activity in temporal, frontals and parietal area. 10/12 patients has asymmetry of tracer activity in their basal ganglias as the same as their deterioration on cortical activity, that more seen in frontal, temporal and parietal. Patient asked doing Yi jin jing qigong for 2-3 months and the post qigong scan shows a definite reduction on that asymmetry of tracer uptake more in cortical and more seen harmonized activity on frontal and parietal cortical tissue. Scan result shows, the perfusion/ function of brain cortex became more even and harmonized as a 0.89 percent of mean count/ pixels without asymmetry of activity, It means after Yi jin jing, the brain tissue reach to more balance rise up to 1.3 times. The same value occurred for their basal ganglia as more activity means better perfusion and function.

Conclusion:
Nuclear medicine has strong role to evaluation of brain perfusion and function and can predict correctly the treatment response it seems that qigong also is a promising therapy for them.

Reference:
Qigong meditation is an ancient method of meditation and calmness that is helpful to have an healthy body,mind and soul, Raharam medical qigong center offers many kind of qigong forms for each specific patients with various brain, body disease and disabilities . You can get in touch with raharamqigong both instagram/ youtubesh . with tel no: +989123075890 and @raharamqigong on instagram.

Poster Presentation

Disclosures: The authors have disclosed no financial interest.

213-Clinical grade [11C]UCB-J radiochemistry by using modified TracerLab FXC Pro

Presenter: Jun-Hyung Park, Molecular Imaging Program at Stanford (MIPS)

Jun-Hyung Park[1], Zhener Zhang[2], Jong H. Yoon[2], Bin Shen[3]

[1]Molecular Imaging Program at Stanford (MIPS), Palo Alto, CA
[2]Stanford University, Palo Alto, CA
[3]Molecular Imaging Program at Stanford (MIPS), Stanford, CA

Objective:
[^{11}C]UCB-J is a tracer that selectively binds to synaptic vesicle glycoprotein 2A (SV2A), which is ubiquitously and homogeneously expressed in presynaptic vesicles across the brain. However, the original C-11 radiochemistry protocols [1][2] were challenged to produce [^{11}C]UCB-J due to C-11 chemistry module difference (Fig. 1a). Therefore, we have re-configured and installed two 3-way valves on the radiosynthesis module to perform [^{11}C]UCB-J production with enhanced efficiency and demonstrate its reliability in a clinical PET/ MR study of schizophrenia.

Methods:
The radiochemistry was performed with [^{11}C]CO_2 produced from the cyclotron, converted to [^{11}C]CH_4 and [^{11}C]CH_3I via reduction and iodination. [^{11}C]CH_3I was trapped in -8 °C DMF and then coupled with a pre-hydrolyzed 3-pyridyl trifluoroborate precursor via Suzuki-Miyaura cross-coupling reaction at 100 °C. In the original [^{11}C]UCB-J protocol, palladium was involved as a catalyst in the reaction. There were precipitates observed after the reaction, which can often cause HPLC injection failure. Two 3-way valves and a 10 mL tube were installed before the HPLC injection port, and this setup allowed to remove palladium particles from the crude mixture by filtration through a PVDF filter (4 mm). Afterward, the crude reaction mixture was injected onto semi-preparative HPLC for purification. The [^{11}C]UCB-J HPLC fraction was formulated in 0.9% NaCl containing no more than 10% ethanol via sterile filtration. Subjects received 10-15 mCi dose intravenously. 90 min Dual-acquisition dynamic 3D PET and MR images were acquired on a PET/MR system.

Results:
Radiosynthesis of [^{11}C]UCB-J was successfully accomplished with reliable reproducibility. [^{11}C]UCB-J was obtained at 86.1±34.3 mCi in 1.4±0.6% radiochemical yield with a specific activity of 7.19±3.4 Ci/ μmol (n=20, decay-corrected to EOS). Both radiochemical and chemical purities were > 99%. Stability tests also showed that prepared doses were stable for 1 hour at ambient temperature. All other QC test results met specified criteria according to USP 823. (Fig. 1b). In the clinical study, we have imaged 20 subjects (10 healthy, 10 with schizophrenia), and one representative whole-brain image of [^{11}C]UCB-J binding is displayed in Fig. 1c.

Conclusion:
We successfully optimized [^{11}C]UCB-J radiochemistry. In this modified setup of the C-11 chemistry module, we achieved reliable radiochemical yield and reproducible high molar activity for clinical use.

Reference
1. Onega M, Chong H, Roble A, Plisson C, Huiban M, Mercier J, Vandergeten M, Passchier J. “Highly improved and GMP compliant synthesis of [11C]UCB-J: in situ generation of Boronic acid precursor” Eur J Nucl Med Mol Imaging. 2017;44 (Suppl 2):S528.
2. Nabulsi B. N, Mercier J, Holden D, Carre S, Najafzadeh S, Vandergeten M, Lin S, Deo A, Price N, Wood M, Lara T, Montel F, Laruell M, Carson R, Hannestad J, Huang Y. “Synthesis and Preclinical Evaluation of C11 UCB-J as a PET Tracer for Imaging the Synaptic Vesicle Glycoprotein 2A in the Brain” J Nucl Med. 2016 May;57(5):777-84

Poster Presentation

Disclosures: The authors have disclosed no financial interest.

214-Hybrid Single Excitation Wideband Spin Echo Diffusion Tensor Imaging (DTI) of Rat Brain

Presenter: Wei-Hao Huang, National Taiwan University

Wei-Hao Huang[1], Po-Wei Cheng[2], Tzu-Yi Wang[1], Jyh-Horng Chen[3]

[1]*National Taiwan University, Taiwan*
[2]*National Taiwan University, Taipei, Taipei, Taiwan*
[3]*National Taiwan University*

Introduction:
Diffusion tensor imaging (DTI) is an MR-based technique that utilizes multi-directions diffusion gradient to measure the water diffusion and track neural fiber direction. With the rise of the concept of precision medicine, the importance of high-resolution/thin slice DTI has increased. However, DTI scanning needs to trade-off between acquisition time, spatial resolution/slice thickness, and image signal to noise ratio (SNR). Therefore, different sacrifices are required depending on the studies. The single excitation Wideband MRI (SE-WMRI) [1] proposed to increase the MR acquisition efficiency is favorable to relieve the limitation aforementioned. Hence, this study aims to combine SE-WMRI with DTI to achieve (1) 2-fold thin slice DTI and (2) 1.3-fold thin slice DTI with 1.5-fold NEX that improves image SNR and slice thickness simultaneous. The scan time of SE-WMRI scannings is the same as the conventional acquisition because of the assistance of SE-WMRI.

Materials and Methods:
MR experiments were accomplished on a Bruker (Ettlingen, Germany) 7T animal MR scanner with a 4-channel phase array. The DTI scanning was performed on Sprague-Dawley (SD) rats. The image parameters are listed below: (1) Conventional Spin echo DTI: slice thickness = 1mm, slice number = 6, TR/TE = 1500/30ms, NEX=2. (2) SE-WMRI spin echo DTI (1.3X thin slice + 1.5X NEX): slice thickness = 0.75mm, slice number = 8, TR/TE = 2000/30ms, NEX=3. (3) SE-WMRI spin echo DTI (2X thin slice): slice thickness = 0.5mm, slice number = 10, TR/TE = 3000/30ms, NEX=2. All scans have same FOV=$30\times30mm^2$, matrix size=128×128, resolution=$234\times234\mu m^2$, scan time=44min. B value = $700s/mm^2$, and use 6 direction diffusion gradient with one set of B-null image. The B-null and diffusion images were reconstructed from raw data using MATLAB (The MathWorks; Natick, MA, USA). The combination of multichannel data used sum-of-square algorithms [2]. The SNR of B-null images was measured by ImageJ. Moreover, the B-null and diffusion images were imported to the DSI studio (Carnegie Mellon University, USA) for fractional anisotropy (FA) analysis.

Results and Discussion:
The conventional B-null image and color FA map are presented in Fig(a) and the SNR of the B-null image is 120.26±2.88. Fig(c) demonstrates the image results of the 2-fold thin slice SE-WMRI DTI. Although with the SE-WMRI benefit, the slice thickness can decrease from 1mm to 0.5mm, the SNR of the B-null image also declined to 85.59±3.47. SE-WMRI can not only apply to single parameter improvement but also upgrade multiple parameters. In Fig(b), the time saved by SE-WMRI improved slice thickness from 1mm to 0.75mm (1.3-fold) and increased the NEX from 2 to 3 (1.5-fold) simultaneously. Moreover, the scan time is 44min which is the same as the conventional scan. The assistance of SE-WMRI implements the thin slice while maintaining the SNR successfully. Follow the equation: $SNR \propto slice\ thickness \times (1-\exp(-TR/T1)) \times \sqrt{NEX}$. The SNR of conventional DTI B-null image is set as 1, the SNR of hybrid SE-WMRI DTI can maintain as 1.09, and 2-fold thin slice SE-WMRI remains 0.72.

Conclusion:
In this study, we utilize the SE-WMRI to achieve the 2-fold thin slice DTI and hybrid DTI with 1.3-fold slice thickness and 1.5-fold NEX improvement in the same acquisition time as conventional DTI. The capability of SE-WMRI that optimizes different parameters depending on the applications makes the flexible DTI parameter setting. Currently, the results demonstrated in this study are based on 2-fold acceleration SE-WMRI. In the future, we will work on the further acceleration of SE-WMRI that benefits the DTI and other MRI-based techniques to supply faster, more accurate image results for helping clinical usage and the research domain.

Reference
1. Wu, E.L., et al., Medical physics. (2015)
2. Hammond, K.E., et al., NeuroImage. (2008)

Poster Presentation

Disclosures: The authors have disclosed no financial interest.

215-Investigation of angiogenesis in cancer initiating cells from remnant living cells of human head and neck squamous cell carcinoma using pDots-NIR II ultrabright molecular imaging

Presenter: Min-Ying Lin, National Yang-Ming Chiao Tung University

Min-Ying Lin[1], Yi-Jang Lee[1]

[1]*National Yang-Ming Chiao Tung University, Taiwan*

Although the death of tumor cells seems to hinder the growth of tumors, it is actually an important mechanism for tumor growth, especially for fast-growing tumors, the higher the proportion of death. The mechanisms that accompany other cells no longer present in tumors are collectively referred to as Cell Loss Factor. Generally, the cell loss rate of human tumors is about 40-90%. The "life and death storm" within the tumor tissue may be the main cause of the tumor's continuous growth, but its mechanism is still unclear. If the cells that can survive smoothly inside the tumor may have their specificity, they can survive in harsh environments. Here we used reporter-gene imaging to track the progression of living cells in tumor model, and ex vivo investigated the properties of this population at late-stage tumor. Cancer stem cells have been considered to be a minority group in tumor tissues, but they have the characteristics of stem cells to differentiate into cancer cells. They are also drug-resistant and radiation-resistant. They are also considered to cause recurrence and metastasis after tumor treatment. This research plan will focus on human head and neck cancer FaDu cells. FaDu xenotransplantation of head and neck cancer cells into nude mice were sacrificed when the tumor grew to the terminal stage (about 1000mm^3). The remnant living cancer cells named FaDu-CSC cells exhibited mainly cancer stem cells properties compared to parental FaDu cells. Using ultrabright biocompatible polymer dots (pDots) with the emission at near infrared II (NIR II) spectrum, the angiogenesis of tumors formed by FaDu-CSC cells were more abundant and irregular than that formed by parental FaDu cells detected by a self-composed 3D multimodality tumor-vessel imaging system. The characteristics of cancer stem cells detected using the novel method of vessel imaging, confirm the identification of human head and neck cancer stem

cells, which will be used as an evaluation platform for tumor treatment methods in the future.

Poster Presentation

Disclosures: The authors have disclosed no financial interest.

216-Computational Modelling of 3D Analytical Magnetic Resonance Imaging (MRI) Phantom based on the Bloch Equation and Relaxation Parameters

Presenter: Michael Dada, Federal University of Technology Minna

Michael O. Dada[1], Bamidele O. Awojoyogbe[2], Iniobong Nicholas Udeme[3]

[1]Federal University of Technology Minna, Minna, Nigeria
[2]Federal University of Technology Minna, Minna, Niger State, Nigeria
[3]Federal University of Technology Minna, Minna, Niger, Nigeria

Introduction:
Numerous acquisition schemes, made possible by the flexibility of k-space encoding are currently in use for clinical imaging. 3D MRI is now center of interesting research efforts as a result of increase in signal-to-noise ratios (SNRs) due to volume excitation and the potential for isotropic voxel dimensions. However, it is important for the development of common and flexible analytical phantom in the Fourier domain (FD) to evaluate the effectiveness of many 3D encoding schemes in simulation studies. To address this problem, Koay et al. (2007) made modifications to the simulated head section produced by Shepp and Logan (1974) by proposing a common and flexible 3D analytical phantom in the FD such that the 3D k-space signal derived from this phantom consists of several ellipsoids that can be analytically expressed. This study is aimed at exploring the possibility of modeling the image space signal intensity within each ellipsoid as a function of MRI parameters such as longitudinal relaxation time (T_1), transverse relaxation time (T_2) and apparent diffusion coefficient (ADC).

Method:
To address this problem, Fourier transform (FT) of an ellipsoid that is centered at the origin of the coordinate system and whose principal directions are aligned parallel to the coordinate axes needs to be found. However, since the ellipsoid is spherical in nature, the excited protons move within this geometry and thus, can be described by the NMR diffusion equation with variable diffusion coefficients. In the rectangular coordinate, this equation is expressed as eqn (1). In this equation, B is the RF magnetic flux, γ is gyromagnetic ratio, $F_0 = M_0/T_1$, $T_0 = (1/T_1) + (1/T_2)$, M_0 is equilibrium magnetization. D_x, D_y and D_z are the spatially dependent diffusion coefficient along the indicated directions. With the assumptions in eqns (2)-(5), the solution to eqn (1) is given by eqn (6). Sampling the transverse magnetization (M_y) at the highest signal amplitude such that $M \approx 0$ (ie, $F_0 \approx 0$) and for a function f (x, y, z) (eqn (7)), the Fourier transform of the function is the same as that of the M_y. This is given as eqn (8) and after further evaluations; we arrive at eqn (9). To specify the 3D diffusion human head phantom for our calculations, we set δ is the pulse time, G_x, G_y and G_z are the RF gradient magnitudes in x, y and z directions respectively. The ADC is set to be D_0. Setting x =y =z =0.0000025 m, δ=0.25 and employing the solutions, we have tables 1-5.

Results and Discussion:
Using the results of the computations, a Python computer program for 2D reconstruction of these data has been developed. Because of the significant differences in the values of the ADC, a direct reconstruction did not return results with noticeable contrasts. This is the reason we did reconstruction for 1/ADC. These results in two dimensions for the relaxation times, ADC and M_y are shown in figure 1. For the 3D reconstruction, we developed a Wolfram Mathematical computer program to reconstruct the computed data as shown in figure 2. As shown in these figures, the phantoms are now dependent on dynamic processes via ADC and deeper tissue contrasts via T_1 and T_2 relaxation times.

Conclusion:
In this study, we have provided modifications to the basic framework for constructing a 3D analytical MRI phantom in the FD which can find applications in comparison of different non-Cartesian encoding schemes and reconstruction methods. Furthermore, the k-space signal for the 3D phantom can be evaluated analytically and sampled according to any chosen k-space trajectory, encoding scheme, dynamic process or contrast parameters. This implies that these phantoms are more realistic.

Reference
1. Koay CG, Sarlls JE, Özarslan E. Three-dimensional analytical MRI phantom in the Fourier domain. MR in Medicine. 2007 Aug; 58(2):430-6.
2. Shepp LA, Logan BF. The Fourier reconstruction of a head section. IEEE Transactions on nuclear science. 1974 Jun; 21(3):21-43.
3. Confidence R, Dada OM, Adesola OA, Awojoyogbe OB. Computational MR Diffusion Tensor Imaging for Probing Human Brain Microstructure. African Journal of Medical Physics, 2019; 1(1), 14-24.

Poster Presentation

Disclosures: The authors have disclosed no financial interest.

217-Computational Magnetic Resonance Spectroscopy using Microsoft Excel Macros

Presenter: Michael Dada, Federal University of Technology Minna

Mayowa Ajilore[1], Iniobong Nicholas Udeme[2], **Michael O. Dada**[3], Bamidele O. Awojoyogbe[4], Taofeeq Ige[5]

[1]Department of Physics, Federal University of Technology, Minna, Niger State, Nigeria
[2]Federal University of Technology Minna, Minna, Niger, Nigeria
[3]Federal University of Technology Minna, Minna, Nigeria
[4]Federal University of Technology Minna, Minna, Niger State, Nigeria
[5]Department of Medical Physics, National Hospital, Abuja, Federal Capital Territory, Nigeria

Introduction:
MRS has the ability to detect N-acetylaspartate (NAA) in the normal brain tissue and citrate in the normal prostate, and their levels decrease once the tumor cells start replacing normal cells. MRS detection of total choline signal has been impressive in the diagnosis and monitoring of brain, breast and prostate cancers. It has also been useful in monitoring of patient’s response to anticancer therapy. However, MRS has lower sensitivities and requires much longer acquisition times and more complex data processing. In addition to this, clinicians are not very much familiar with this technique and thus, limiting the

application of MRS in the clinical setting. In order to overcome this problem, we attempt developing a computational program (macros) with Microsoft excel macros programming for MRS of tissues with fast data processing.

Methods:
For this study, we consider the precessing proton spins [2] within rotating frame of reference. Resonance condition exists at Larmor frequency after RF excitation according to eqn(1) [3]. For spatial variations in the fluid velocity, the Bloch NMR flow equation becomes eqn(2) [3]. If B_1 (x) is applied such that transverse magnetization (M_y) is sampled at maximum magnitude, $M_0 \approx 0$. For spatial velocity expressed as v(x) x/τ, eqn(2) becomes eqn(3). The chemical shift measured in parts per million (ppm) is expressed as eqn(4) [4]; where $\omega = \lambda B$ is the measured angular frequency of the metabolites, $\lambda = 10^6/\omega_0$ and $\omega = \gamma B_0$ is the frequency of the MR system (ppm) and ω_R is resonant frequency of a reference substance. Defining the RF frequency as follows $\omega_1 = \gamma B_1 = \gamma G T_0 \tau x$, and noting $\omega = \omega_0 + \omega_1$. Setting $x = \Omega/(\gamma G \lambda)$, eqn(3) becomes eqn(6). Eqn(6) is an equation transformable to Bessel DE and the solution is given as eqn(7). J_n is Bessel function of the 1st kind, Y_n is Bessel function of the 2nd kind, τ is gradient pulse duration, A_1 and A_2 are constants. Eqn(7) hold only if $(T_0)^2 \geq 4T_g$ ($n \geq 0$). If the frequency of the MR system is in Hertz and since the NMR signal must be measurable at all values of chemical shifts, $A_2 = 0$ while M_y becomes eqn(8).

Results:
Using the result of eqn(8), a Microsoft excel macro has been developed to generate M_y data for different brain tissues (normal and disease-affected) and they produce magnetization profiles according to their unique relaxation times. These relaxation times have been measured at $B_0 = 1.5T$ are given in table 1 [5]. Using table 1, MRS profiles are presented in Figures 1 to 3.

Discussion:
With the computational model presented in this study and the computer program developed, MRS is simply achieved by entering the measured values of T_1 and T_2 relaxation times. Figure 1 gives an illustration of the graphic user interface (GUI), figure 2 gives the MRS profiles of CSF and three different types of brain neoplasms. Figures 3 combines the profiles in figure 2 for the purpose of comparative analysis of normal brain tissue and tumors. As demonstrated in these profiles, the program is not only able to perform tumor diagnosis but also able to provide inter tumor contrast.

Conclusion:
This program is easy to use, highly interactive and the data processing is fast and unambiguous. The advantage of this study is that laboratories that are unable to acquire or maintain magnetic resonance equipments can now perform magnetic resonance diagnosis with straight forward computer programs as long as they find ways of obtaining the required relaxation data (T_1 and T_2). MR relaxometers are cheaper and easier to maintain; they could be used to generate these data.

Reference

1. Lin, G. and Chung, Y.L., 2014. Current opportunities and challenges of magnetic resonance spectroscopy, positron emission tomography, and mass spectrometry imaging for mapping cancer metabolism in vivo. BioMed research international, 2014.
2. Awojoyogbe OB, Dada OM. Mathematical Design of a Magnetic Resonance Imaging Sequence Based on Bloch NMR Flow Equations and Bessel Functions. Chin J Magn Reson Imaging, 2013, Vol 4, No 5.
3. Awojoyogbe OB, Dada OM, Faromika OP, Dada OE. Mathematical Concept of the Bloch Flow Equations for General Magnetic Resonance Imaging: A Review. Concepts in Magnetic Resonance Part A, 2011; Vol. 38A (3): 85–101.
4. Abragam A. The Principles of Nuclear Magnetism. Oxford: Clarendon Press, 1961: pp 48 – 49.
5. Nitz, W.R., Balzer, T., Grosu, D.S. and Allkemper, T., 2010. Principles of magnetic resonance. In Clinical MR Imaging (pp. 1-105). Springer Berlin Heidelberg.

Poster Presentation

Disclosures: The authors have disclosed no financial interest.

218-In vivo imaging of Lenvatinib-induced changes in tumor hypoxia and its relationship to gene expression signatures associated with tumor microenvironment

Presenter: Tapan Nayak, Merck

Xiangjun Meng[1], Eric Muise[2], Wendy Blumenschein[3], Manjiri Sathe[3], Yuchuan Wang[4], Marie Holahan[5], Elaine Pinheiro[6], Doug Linn[6], **Tapan Nayak[7]**

[1]*Merck, West Point, Pennsylvania*
[2]*Merck &Co., Inc, Boston, MA*
[3]*Merck & Co., Inc, San Francisco, CA*
[4]*Merck &Co., Inc, West Point, Pennsylvania*
[5]*Merck & Co., Inc, West Point, Pennsylvania*
[6]*Merck & Co., Inc, Boston, MA*
[7]*Merck, West Point, PA*

Preclinical and clinical studies have demonstrated that anti-angiogenic therapies can lead to hypoxia as a compensatory mechanism which may lead to immunosuppressive microenvironment. Assessment of tumor hypoxia could contribute towards better understanding on how anti-angiogenic therapies can modulate immune microenvironment that can be conducive to cancer immunotherapy. The objective of this study was to assess longitudinal changes in tumor hypoxia by PET imaging in tumor bearing mice treated with Lenvatinib, an anti-angiogenic multi-kinase inhibitor and correlate with molecular changes assessed using RNAseq. Longitudinal PET imaging (baseline, d2 and d7 after start of treatment) was conducted with the clinically used hypoxia PET tracer ^{18}F-FAZA in mice bearing MC38, CT26 or B16F10 tumors treated with either 10 mpk PO Lenvatinib or vehicle control. Tumors were collected at d7 after last PET scans for correlative analyses using RNAseq. In a parallel efficacy study, mice were treated until 16-20 days to determine tumor growth inhibition. In MC38 tumors, normalized tumor hypoxia measured by PET were lower for Lenvatinib group than the control group (2.0 ± 0.3 vs 2.9 ± 0.6, $p = 0.001$, $n \geq 8$) indicative of reduction of tumor hypoxia by Lenvatinib treatment. However, normalized tumor hypoxia in Lenvatinib-treated CT26 tumors were greater than control group (3.8 ± 0.6 vs 2.8 ± 0.3, $p < 0.001$, $n \geq 10$). Similar observation was found in B16F10 tumors, Lenvatinib-treated group had higher normalized tumor hypoxia than control group (2.7 ± 0.4 vs 2.0 ± 0.2, $p < 0.001$, $n \geq 10$) indicative of Lenvatinib induced tumor hypoxia in CT26 and B16F10. The gene expression profiling analysis confirmed the findings from PET, Lenvatinib treatment increased the hypoxia associated genes and modulated HIF downstream target genes in CT26. Lenvatinib treatment resulted in gene expression changes in all 3 tumor models with MC38 showing the most robust effects. Although the gene expression changes were mostly model-specific, a subset of 28 genes were similarly regulated across the 3 models following Lenvatinib treatment, with genes involved in Type 1 IFN pathways enriched in this set. In the efficacy study, 96% tumor growth

inhibition (TGI) was observed in MC38 tumors and 46% and 49% TGI in CT26 and B16F10 tumors respectively. Lenvatinib treatment resulted in decrease tumor hypoxia in MC38 tumors while an increase was observed in CT26 and B16F10 tumors. Analysis from gene expression profiling provided molecular basis behind these changes and further our understanding of role of anti-angiogenics on tumor hypoxia and tumor microenvironment.

Poster Presentation

Disclosures: The authors have disclosed no financial interest.

219-Synthesis of Responsive Paramagnetic-19F Nanoprobes for Detecting Caspase-1 by 19F-MRI Imaging

Presenter: Raana Kashfi Sadabad, Stanford University

Raana Kashfi Sadabad[1], Chih-Liang Chin[2], Melissa Lin[3]

[1]Stanford University, San Mateo, CA
[2]Merck, South San Francisco, CA
[3]Merck company, South San Francisco, California

Fluorine (^{19}F) MRI is a new molecular imaging approach for visualization and quantification of various disease in vivo. In this technique usually a contrast agent based on non-radioactive isotope of fluorine (^{19}F) is used during imaging to monitor, quantify, and stage different disease states [1]. Due to a negligible amount of ^{19}F nuclei in human body, ^{19}F allows for a background-free imaging with a high sensitivity. Current FDA approved ^{19}F contrast agents are based on perfluorocarbons (PFCs) in a lipid-based emulsions. The main drawbacks of these formulations are low stability and poor specificity. More recently, advanced nanoparticles (NPs) with carefully engineered structure and properties are proven effective to carry a high amount of ^{19}F atoms, increase their solubility, delivery efficiency, and signaling properties [2]. Poly (D,L-lactic-co-glycolic acid) (PLGA) is an FDA approved polymer and is one of the most used NP platforms in both drug and contrast agent delivery systems. It can be easily metabolized in vivo, modified with various targeting agents to enhance binding effects, and loaded with a high amount of hydrophobic/hydrophilic drugs/imaging moieties [3]. In this work, we use a PFCs with a cyclic structure named perfluoro-15-crown-5-ether (PFCE) as a tracer for ^{19}F-MRI and incorporate it into PLGA polymers. PFCE holds a high density of ^{19}F nuclei, 20 magnetically equivalent, and provides a strong single resonance peak. But it is not injectable in a free formulation. PLGA polymers would offer several advantages by increasing PFCE solubility, delivering high amount of ^{19}F in vivo, and eventually enhancing contrast-to-noise ratio [4, 5]. We study the feasibility of the PLGA platform to produce a responsive probe with signal-activable function to detect caspace-1 activity. The responsive probe is formed of PFCE in the PLGA polymer core and modified by a Gd^{3+}-conjugated caspase-1 peptide substrate (WEHD) on the particles surface. Due to the paramagnetic relaxation enhancement (PRE) effect of Gd^{3+} complex, the ^{19}F signal can be quenched and subsequently recovered after cleavage of Gd^{3+}-conjugated peptide in the caspase-1 active environment. This approach will allow for sensing caspase-1 by MRI imaging in various inflammatory disease in deep tissues. We evaluated two different PLGA-NHS (Mw ~25KD) and PLGA-PEG-Maleimide (Mw ~20KD) polymers to encapsulate PFCE using water-in-oil emulsion technique. We confirmed formation of uniform particles by dynamic light scattering (DLS) and obtained average particles size of ~200 nm with a low polydispersity index (PDI). We applied ^{19}F NMR spectroscopy to confirm and quantify PFCE encapsulation in the polymeric formulations. Both PFCE-PLGA-NHS and PFCE-PLGA-maleimide samples showed an intense and single sharp fluorine peak at ~92ppm with a high stability compared to pure PFCE. For the PFCE-PLGA-NHS sample, we calculated 16% amount of PFCE encapsulation using ^{19}F NMR. We assessed the ability of the PLGA-NHS and PLGA-PEG-Maleimide polymers to covalently attached to the Gd^{3+}-conjugated caspase-1 peptide substrate. For this purpose, we investigated two different amine-N-hydrosuccinimide (NHS) esters and thiol-maleimide conjugation chemistry to bind the Gd^{3+}-peptide to the PLGA-NHS and PLGA-PEG-Maleimide polymers respectively. We investigated the influence of polymeric structures and various reaction conditions such as different solvents on the efficiency of the conjugation using ^{1}H-NMR. In general, this study opens up a new approach for real-time imaging of caspapse-1 activity in deep tissue of living animals with a high sensitivity and specificity.

Reference

1. F. Chapelin, C.M. Capitini, E.T. Ahrens, Fluorine-19 MRI for detection and quantification of immune cell therapy for cancer, J Immunother Cancer, 6 (2018) 105-105.
2. A. Mali, E.L. Kaijzel, H.J. Lamb, L.J. Cruz, 19F-nanoparticles: Platform for in vivo delivery of fluorinated biomaterials for 19F-MRI, Journal of Controlled Release, 338 (2021) 870-889.
3. F. Danhier, E. Ansorena, J.M. Silva, R. Coco, A. Le Breton, V. Préat, PLGA-based nanoparticles: An overview of biomedical applications, Journal of Controlled Release, 161 (2012) 505-522.
4. C. Jacoby, S. Temme, F. Mayenfels, N. Benoit, M.P. Krafft, R. Schubert, J. Schrader, U. Flögel, Probing different perfluorocarbons for in vivo inflammation imaging by 19F MRI: image reconstruction, biological half-lives and sensitivity, NMR in Biomedicine, 27 (2014) 261-271.
5. M. Srinivas, J. Tel, G. Schreibelt, F. Bonetto, L.-J. Cruz, H. Amiri, A. Heerschap, C.G. Figdor, I.J.M. de Vries, PLGA-encapsulated perfluorocarbon nanoparticles for simultaneous visualization of distinct cell populations by 19F MRI, Nanomedicine (Lond), 10 (2015) 2339-2348.

Poster Presentation

Disclosures: The authors have disclosed no financial interest.

220-Development of a novel double contrast-enhanced CT imaging protocol to monitor metastatic colorectal tumours in pre-clinical models.

Presenter: Ian Miller, Royal College of Surgeons in Ireland

Ian Miller[1], Liam Shiels[1], Kate Connor[1], Thomas Snoeks[1], Annette Byrne[2]

[1]Royal College of Surgeons in Ireland, Dublin, Ireland
[2]Royal College of Surgeons in Ireland, Dublin, Please Select, Ireland

Colorectal cancer (CRC) is the third most diagnosed malignancy in adults. Almost half of patients diagnosed develop metastatic colorectal cancer (mCRC). While Computed Tomography (CT) is a gold-standard imaging modality in this setting, bioluminescence imaging (BLI) represents the default modality in the pre-clinic. However, many preclinical models, including patient derived xenografts (PDX), are not amenable to BLI. Moreover, while orthotopic PDXs may faithfully recapitulate metastatic dissemination evidenced in patients, it remains especially difficult to monitor disease evolution in these models. Overall, use of preclinical CT may assist in the visualization of such tumours. Here, we

have developed a novel double contrast-enhanced CT (CE-CT) method for visualisation of orthotopic CRC tumours and metastases. NSG mice (N=26) were intracaecally implanted with 1x10^6 cells of metastatic CRC cell-line HT29-LUC2 and tumours allowed to develop. Mice were imaged by CE-CT on the Quantum GX2 (Perkin-Elmer) and underwent 4 rounds of CE-CT (90kV, 88µA, Resolution:144µm). 90 minutes preceding CT, iopamidol (iodine-based contrast agent) was administered via oral gavage, contrasting the colon lumen. Prior to imaging, iopamidol was injected intraperitoneally providing contrast in peritoneum, negatively contrasting the intracaecal tumour. To detect metastatic dissemination by CT, metastases were first confirmed by *in vivo* BLI (IVIS Spectrum). A bioluminescence signal was present in lungs of mice. Subsequently, mice were intravenously injected with contrast agent ExiA-160XL (liposomal encapsulated iopamidol) and imaged as before. The contrast agent was specifically taken up in liver and metastatic lesions appeared as dark halos against contrasted liver parenchyma. Moreover, lung metastatic lesions were evident from CT images. At study termination, *ex vivo* BLI confirmed metastatic dissemination to liver and lung in a similar pattern as evidenced in patients. Here we report for the first time the development of a novel contrast-enhanced protocol for the detection and monitoring of orthotopic CRC primary and metastatic tumours. This imaging protocol will be vital for monitoring orthotopic PDX tumours in ongoing studies which aim to establish novel combination treatments for MSS Ras^{mut} mCRC. Pre-clinical and patient mCRC CT data are also being mined to establish radiomic signatures as non-invasive biomarkers to predict response to novel precision medicine treatments.

Poster Presentation

Disclosures: The authors have disclosed no financial interest.

221-Development and validation of radiomic signature for classification of high and low-grade chondrosarcoma: A pilot study

Presenter: Ashish Jha, Tata Memorial Hospital

Ashish K. Jha[1], Prakash Nayak[1], Sneha Mithun[1], Umesh Sherkhane[1], Vinay Jaiswar[1], Biprojit Nath[1], Akhilesh Tripathi[1], Grace M. Mehta[2], Shreyash Panchal[3], Nilendu Purandare[1], Ajay Puri[1], Leonard Wee[4], Andre Dekker[4], Venkatesh Rangarajan[5]

[1]*Tata Memorial Hospital, Mumbai, Maharashtra, India*
[2]*Tata Memorial Hospital, Mumbai, India*
[3]*Tata Memorial Hospital, India*
[4]*Maastricht University, Maastricht, Netherlands*
[5]*Tata Memorial Hospital, Mumbai, IN-Mah, India*

Aim/Introduction:
Chondrosarcomas have diverse clinical and morphological behaviour. The imaging features of chondrosarcomas on magnetic resonance imaging (MRI) are characteristic for definitive diagnosis. Grading of tumour is performed on the pathological diagnosis. This study aims to develop a radiomic signature for grading the tumour on MRI scan.

Materials and Methods:
The study is approved by IEC as a retrospective study with a waiver of informed consent. The pre-treatment MRI scans of 50 chondrosarcomas patients who underwent treatment in our hospital were used in this study. The primary tumour was delineated on T1 images on a 3D slicer by expert imaging physicists and reviewed by an expert ortho-surgeon. In total 1093 radiomic features were extracted from the tumours on T1images. Pathological grade of tumour grade was binarized as Grade 1: 0 (low-grade) and Grade 2 and above: 1 (high-grade). Minority class data balancing is performed using Synthetic Minority Oversampling Technique (SMOTE) in python script. The most appropriate feature was selected using the recursive feature elimination technique (RFE) and random forest (RF) algorithm. The Random Forest model was developed for the classification of the tumour grade using five-fold cross-validation as well as a train-test split.

Results:
A total of eight features were selected using the RFE (table 1). The accuracy of the random forest model on five-fold cross-validation was found to be 0.92(±0.7). The model accuracy and AUC on the test set in the train-test model validation were found to be 0.88 and 0.988 respectively.

Conclusion:
Although it is a preliminary result with very few numbers of patients, our initial result shows the predictive power of radiomic features in the classification of high and low-grade chondrosarcoma. Recruitment of patients in this study is in progress to develop a prediction model on a large data set. Table 1: shows the features selected using RFE for model development

Serial No.	Feature Name
1	'log-sigma-3-0-mm-3D_firstorder_Skewness'
2	'log-sigma-3-0-mm-3D_glrlm_LongRunHighGrayLevelEmphasis'
3	'wavelet-LLH_glcm_Idmn'
4	'wavelet-LLH_glcm_Idn'
5	'wavelet-LLH_glrlm_LongRunHighGrayLevelEmphasis'
6	'wavelet-LLH_gldm_SmallDependenceLowGrayLevelEmphasis'
7	'wavelet-LHH_gldm_SmallDependenceLowGrayLevelEmphasis'
8	'wavelet-LLL_gldm_LargeDependenceHighGrayLevelEmphasis'

Poster Presentation

Disclosures: The authors have disclosed no financial interest.

222-Pretargeted Radioimmunodiagnostic 111In-SPECT & 86Y-PET Versus 18FDG PET Imaging in In Vivo Cell Line & Organoid-Derived Xenograft Models

Presenter: Nicole Aguirre, Memorial Sloan Kettering Cancer Center

Sebastian Chung[1], **Nicole Aguirre**[2], Brett Vaughn[3], Francesco Cambuli[2], Jonathan Bermeo[2], Ahmed Mahmoud[2], Valeria Sgambati[2], Darren Veach[2], Pat Zanzonico[4], Shin Seo[2], Blesida Punzalan[4], Hong-Fen Guo[5], Hong Xu[2], Guangbin Yang[2], Ouathek Ouerfelli[2], Andrea Cercek[2], Garrett Nash[2], Sarah Cheal[5], Karuna Ganesh[2], Steven M. Larson[2], Nai-Kong Cheung[5]

[1]*Memorial Sloan Kettering Cancer Center, New York, MA*
[2]*Memorial Sloan Kettering Cancer Center, New York, NY*
[3]*Memorial Sloan Kettering Cancer Center, New York*
[4]*Memorial Sloan Kettering Cancer Center*
[5]*Memorial Sloan Kettering Cancer Center, New York, New York*

Objectives:
^{18}F-fluorodeoxyglucose (FDG), the most widely used PET/CT radiotracer in oncologic staging and surveillance, has limited sensitivity, particularly in the evaluation of mucinous tumors.[1] A curative, theranostic 3-step pretargeted strategy combining radioimmunodiagnosis (PRID) and radioimmunotherapy (PRIT), both using a glycoprotein A33 (GPA33)-targeting bispecific antibody (BsAb) and a DOTA-based radiohapten has been reported.[2] The sensitivity and specificity of ^{18}FDG PET were compared to that of GPA33-PRID, where PRID used ^{86}Y for PET and ^{111}In for SPECT. Two preclinical *in vivo* tumor models that positively stain for Periodic acid-Schiff (PAS) were used: SW1222 cell line derived xenograft (CDX) colorectal carcinoma model, and CRC107Li, an organoid derived xenograft (ODX) model from colorectal liver metastasis.[3]

Methods:
6-week-old female NSG (NOD.Cg-*Prkdc*^{scid} *Il2rg*^{tm1Wjl}/SzJ) mice were inoculated subcutaneously with 1x10^{6} SW1222 (n=5) or 1 x 10^{5} CRC107Li (n=3). Following 10 days (SW1222) or 4 months (CRC107Li) of tumor growth, mice were injected with 500uCi ^{18}FDG for PET/CT imaging 2 hours post injection (hpi). Mice underwent ^{111}In-GPA33-PRID in week 1 and ^{86}Y-GPA33-PRID in week 2 as follows: at time 0 of each week, 250ug (1.2nmol) anti-GPA33 BsAb was given, followed by 25ug (2.8nmol) CCA16-DOTAY clearing agent 22 hours later, followed by 500 pmol of DOTA-based radiohapten at 26 hours: 9.3MBq ^{111}In “proteus-DOTA”(Pr)[4] for ^{111}In-GPA33-PRID, and 7.4MBq ^{86}Y-aminobenzyl-DOTA (ABD) for ^{86}Y-GPA33-PRID. SPECT/CT and PET/CT images following PRID were obtained at 24hpi of ^{111}InPr and 18hpi of ^{86}Y-ABD, respectively. Following ^{86}Y-PET/CT, tissues were assayed for radioactivity biodistribution. Regions of interest (ROI) were selected based on CT imaging, and the volume average radioactivity of each ROI was compared to tissue radioactivity counted by gamma counter. GPA33 expression on SW1222 and CRC107Li were confirmed by flow cytometry prior to tumor inoculation, and confirmed after tissue dissection by IHC and autoradiography.

Results:
Radioactivity uptake expressed as injected dose per gram of tumor (%ID/g) was consistent across ^{111}In SPECT, ^{86}Y PET and tissue counts for both SW1222 (7.6, 17.6, and 32, respectively) and CRC107Li models (1.9, 3.1, 3.8). There was greater uptake and targeting in SW1222 vs CRC107Li tumors, consistent with the higher GPA33 expression in SW1222 than in CRC107Li as demonstrated by flow cytometry (SW1222 MFI:13471, CRC107Li MFI: 3617). Both models demonstrated high tumor to non-tumor tissues by PRID (see figure) and by biodistribution. The average tumor-to-organ ratios on ^{86}Y-PRIT PET for heart, lungs, and bone were 32.9, 32.3 and 31.4 in SW1222, and 15.0, 11.9, and 12.2 for CRC107Li, respectively. In contrast, the same ratios on ^{18}FDG PET were less than 1: 0.48, 0.64 and 0.42 for SW1222 and 0.45, 0.90 and 0.61 for CRC107Li. In the low antigen density CRC107Li model, sensitivity for tumor detection was similar with the average radioactivity uptake ranging from 1.9-3.8% ID/g for tumors in all imaging modalities (^{18}FDG PET, ^{111}In SPECT, ^{86}Y PET and biodistribution), but PRID strategy demonstrated superior tumor to non-tumor tissues (tumor, heart, lung, kidneys, bone, brain, bladder).

Conclusions:
The feasibility and targeting of DOTA-based PRID in two *in vivo* murine models GPA33-expressing carcinoma, including a patient derived organoid, were demonstrated. The PRID strategy yielded higher contrast of tumor vs non-tumor tissues with ^{111}In-SPECT and ^{86}Y-PET imaging when contrasted with ^{18}FDG PET. Studies evaluating the efficacy of PRIT in these CDX and ODX models are currently underway.

Reference

1. Berger KL, Nicholson SA, Dehdashti F, Siegel BA. FDG PET evaluation of mucinous neoplasms: correlation of FDG uptake with histopathologic features. AJR Am J Roentgenol. 2000 Apr;174(4):1005-8. doi: 10.2214/ajr.174.4.1741005. PMID: 10749239.
2. Cheal SM, Fung EK, Patel M, Xu H, Guo HF, Zanzonico PB, Monette S, Wittrup KD, Cheung NV, Larson SM. Curative Multicycle Radioimmunotherapy Monitored by Quantitative SPECT/CT-Based Theranostics, Using Bispecific Antibody Pretargeting Strategy in Colorectal Cancer. J Nucl Med. 2017 Nov;58(11):1735-1742. doi: 10.2967/jnumed.117.193250. Epub 2017 Jul 13. PMID: 28705917; PMCID: PMC5666642.
3. Ganesh K, Wu C, O'Rourke KP, Szeglin BC, Zheng Y, Sauvé CG, Adileh M, Wasserman I, Marco MR, Kim AS, Shady M, Sanchez-Vega F, Karthaus WR, Won HH, Choi SH, Pelossof R, Barlas A, Ntiamoah P, Pappou E, Elghouayel A, Strong JS, Chen CT, Harris JW, Weiser MR, Nash GM, Guillem JG, Wei IH, Kolesnick RN, Veeraraghavan H, Ortiz EJ, Petkovska I, Cercek A, Manova-Todorova KO, Saltz LB, Lavery JA, DeMatteo RP, Massagué J, Paty PB, Yaeger R, Chen X, Patil S, Clevers H, Berger MF, Lowe SW, Shia J, Romesser PB, Dow LE, Garcia-Aguilar J, Sawyers CL, Smith JJ. A rectal cancer organoid platform to study individual responses to chemoradiation. Nat Med. 2019 Oct;25(10):1607-1614. doi: 10.1038/s41591-019-0584-2. Epub 2019 Oct 7. PMID: 31591597; PMCID: PMC7385919.
4. SM, McDevitt MR, Santich BH, Patel M, Yang G, Fung EK, Veach DR, Bell M, Ahad A, Vargas DB, Punzalan B, Pillarsetty NVK, Xu H, Guo HF, Monette S, Michel AO, Piersigilli A, Scheinberg DA, Ouerfelli O, Cheung NV, Larson SM. Alpha radioimmunotherapy using 225Ac-proteus-DOTA for solid tumors - safety at curative doses. Theranostics. 2020 Sep 14;10(25):11359-11375. doi: 10.7150/thno.48810. PMID: 33052220; PMCID: PMC7546012.

Poster Presentation

Disclosures: The authors would like to disclose that the drugs GPA33 SADA, HER2 SADA, and GD2 SADA are not approved in the United States, the drug Naxitamab is approved, and the drug Omburtamab is an investigational drug.

223-Development and validation of robust CT radiomics signature for predicting 5 year overall survival in Cervical Cancer

Presenter: Ashish Jha, Tata Memorial Hospital

Ashish K. Jha[1], Sneha Mithun[1], Umesh Sherkhane[1], Vinay Jaiswar[1], Shreyash Panchal[2], Grace M. Mehta[3], Nilendu Purandare[1], Sneha Shah[1], Leonard Wee[4], Andre Dekker[4], Venkatesh Rangarajan[5]

[1]*Tata Memorial Hospital, Mumbai, Maharashtra, India*
[2]*Tata Memorial Hospital, India*
[3]*Tata Memorial Hospital, Mumbai, India*
[4]*Maastricht University, Maastricht, Netherlands*
[5]*Tata Memorial Hospital, Mumbai, IN-Mah, India*

Aim/Introduction:
The role of artificial intelligence and radiomics in prediction model development in cancer has been increasing every passing day. Cervical cancer is the 4th most common cancer in women worldwide contributing 6.5% of all cancer types. The treatment outcome of cervical cancer patients varies and individualized prediction of disease outcome is of

paramount importance. The purpose of this study is to develop and validate the digital signature for 5-years overall survival prediction in cervical cancer using robust CT radiomic and clinical features.

Materials and Methods:
Pretreatment clinical features and CT radiomic features of 68 patients, who were treated with chemoradiation therapy in our hospital were used in this study. Radiomic features were extracted using an in-house developed python script and pyradiomic package. Clinical features were selected by the recursive feature elimination technique. Whereas radiomic feature selection was performed using a multi-step process i.e., step-1: only robust radiomic features were selected based on our previous study (Jha AK et.al., 2021), step-2: a hierarchical clustering was performed to eliminate feature redundancy, and as final step-3: recursive feature elimination was performed to select the best features for prediction model development. Four machine algorithms i.e., Logistic regression (LR), Random Forest (RF), Support vector classifier (SVC), and Gradient boosting classifier (GBC) were used to develop 24 models (six models using each algorithm) using clinical, radiomic and combined features. Models were compared based on the prediction score in the internal validation.

Results:
The average prediction accuracy was found to be 0.65±0.05, 0.72±0.09, and 0.77±0.05 for clinical, radiomic, and combined models respectively. The average prediction accuracy was found to be 0.69±0.07, 0.79±0.07, 0.71±0.09, 0.72±0.06 for LR, RF, SVC and GBC models respectively (figure 1).

Conclusion:
Our study shows a strong correlation between robust radiomic signature and 5-year overall survival in cervical cancer patients. However, this model needs to be trained and validated on a larger and external dataset.

Reference

1. Jha AK, Mithun S, Jaiswar V, et al. Repeatability and reproducibility study of radiomic features on a phantom and human cohort. Sci Rep. 2021;11(1):2055. Published 2021 Jan 21. doi:10.1038/s41598-021-81526-8

Poster Presentation

Disclosures: The authors have disclosed no financial interest.

224-Association of androgen receptor expression with glucose metabolic features in triplenegative breast cancer

Presenter: Reeree Lee, Chung-Ang University

Reeree Lee[1], Hongyoon Choi[1], Jin Chul Paeng[2]

[1]Chung-Ang University, Seoul, South Korea
[2]Seoul National University Hospital, Seoul, Korea, Republic of Korea

Background:
Androgen receptor (AR) is a potential therapeutic target in triple-negative breast cancer (TNBC). This study aimed to elucidate the association of AR expression with glucose metabolic features in TNBC.

Methods:
Two independent datasets were analyzed: FDG PET data of our institution and a public dataset of GSE135565. In PET analysis, patients with TNBC who underwent pretreatment PET between Jan 2013 and Dec 2017 were retrospectively enrolled. Clinicopathologic features and maximum standardized uptake value (SUV max) of tumors were compared with AR expression. In GSE135565 dataset, glycolysis score was calculated by the pattern of glycolysis-related genes, and of which association with SUV max and AR gene expression were analyzed.
Results: A total of 608 female patients were included in the PET data of our institution. SUV max was lower in AR-positive tumors ($P < 0.001$) and correlated with lower AR expression (rho = –0.26, $P < 0.001$). In multivariate analysis, AR was a deterministic factor for low SUV max ($P = 0.012$), along with other key clinicopathologic features. In the GSE135565 dataset, AR expression also exhibited a negative correlation with SUV max ($r = –0.34$, $P = 0.001$) and the glycolysis score ($r = –0.27$, $P = 0.013$).

Conclusions: Low glucose metabolism is a signature of AR expression in TNBC. It is suggested that evaluation of AR expression status needs to be considered in clinical practice particularly in TNBC with low glucose metabolism.

Poster Presentation

Disclosures: The authors have disclosed no financial interest.

225-Vasculature on a microfluidic chip to predict PSMA targeted therapies

Presenter: Magdalena Skubal, Memorial Sloan Kettering Cancer Center

Magdalena Skubal[1], Ben E. Mc Larney[1], Anuja Ogirala[1], Camila M. Machado[2], Vladimir Ponomarev[1], Jan Grimm[1]

[1]Memorial Sloan Kettering Cancer Center, New York, NY
[2]Hospital das Clinicas da Universidade de Sao Paulo, Sao Paulo, Brazil

The failure of animal models to predict therapeutic responses in humans is a major problem. Organ on a chip technology with human cells cultured under constant flow can recreate organ level physiology and pathophysiology with high precision and serve as a living avatar for personalized medicine [1]. Prostate-specific membrane antigen (PSMA) overexpression is a characteristic of prostate cancer and is associated with cancer progression, metastasis, and poor prognosis in patients [2,3]. Interestingly, increased expression levels of PSMA are also found on the vasculature of a variety solid tumors [4,5]. Here, using cutting-edge microfluidic organ on a chip technology and human endothelial cells, we have established an innovative approach to investigate PSMA-dependent mechanisms promoting tumor vascularization, where endothelial cells are migrating, coordinating, and organizing themselves into three-dimensional structures similar to those found in a human body. Our preliminary data confirmed that endothelial cells can be activated to sprout, or endothelial cells with elevated PSMA expression levels are more likely to form vessel-like structures. We can alter some of these interactions using PSMA's enzymatic activity inhibitors such as PMPA that impact endothelial cell activation. We hope to gain more understanding of this complex system that reliably bridges the gap between *in vitro* and *in vivo* models and further allows precise studies of cellular and molecular mechanisms driving PSMA-dependent tumorigenesis.

Reference
1. Ingber, D.E., Human organs-on-chips for disease modelling, drug development and personalized medicine. Nature Reviews Genetics, 2022.
2. Ross, J.S., et al., Correlation of primary tumor prostate-specific membrane antigen expression With disease recurrence in prostate cancer. Clinical Cancer Research, 2003.
3. Silver, D.A., et al., Prostate-specific membrane antigen expression in normal and malignant human tissues. Clinical cancer research, 1997.
4. Chang, S.S., et al., Prostate-specific membrane antigen is produced in tumor-associated neovasculature. Clinical Cancer Research, 1999.
5. Nomura, N., et al., Prostate specific membrane antigen (PSMA) expression in primary gliomas and breast cancer brain metastases. Cancer cell international, 2014.

Poster Presentation

Disclosures: The authors have disclosed no financial interest.

226-MRI assessment of abscopal effect induced by radiation/immune checkpoint inhibitor combination therapy in a murine tumor model.

Presenter: Kota Yamashita, National Cancer Institute

Kota Yamashita[1], Shun Kishimoto[1], Jeffrey Brender[1], Devasahayam Nallathamby[1], Kazutoshi Yamamoto[2], Murali Krishna[2]

[1]National Cancer Institute, Bethesda, MD
[2]National Institutes of Health, Bethesda, Maryland

Introduction:
It has been reported that radiation therapy (RT) occasionally causes regression of non-irradiated metastatic lesions, which is called abscopal effect. The radiation-mediated systemic anti-tumor effects are induced by an activation of tumor-specific CD8+ T cells which are primed by antigen-presenting cells that capture tumor-specific antigens from the collapsed tumor. [1 2] Although it has been reported that immunotherapy, especially immune checkpoint blockade (ICB), can enhance abscopal effect, the imaging biomarkers which predict the induction of the abscopal effect have not been investigated to date. [3, 4] Hypoxia is reported to cause T cell exhaustion by inducing a mitochondrial defects. [5] Increased vessel permeability and perfusion may predict the efficacy of ICB.[6] Therefore, in the current study, we investigated pO_2 distribution, permeability and perfusion in the primary/metastatic model tumors treated with the combination therapy to explore the physiological changes in the tumors showing abscopal effect.

Methods:
MC38 colon adenocarcinoma tumor model treated with RT and PD-1 inhibitor were used to evaluate the abscopal effect. $1x10^6$ tumor cells and $2x10^5$ were inoculated subcutaneously into right and left hindlegs of C57BL/6 mice, respectively. In group 1, only right leg tumor was irradiated, and αPD-1 antibody 200 μg was intraperitoneally injected on days 0, 3, and 7 after treatment. In group 2, right leg tumor was irradiated and IgG isotype antibody 200 μg was injected. In group 3 and 4, mice were injected with αPD-1 antibody and IgG isotype antibody, respectively. Imaging studies were performed on both hindleg.
Electron para-magnetic resonance imaging (EPRI) were performed for quantitative intra-tumor pO_2 mapping with high resolution (~0.2mm) by observing the linewidth of the exogenously administered trityl radical probe Oxo63.
Dynamic contrast-enhanced magnetic resonance imaging (DCE-MRI) were performed on a 3T scanner (Bruker BioSpec 3T). T1-weighted fast low-angle shot (FLASH) images were obtained. Gd-DTPA solution was injected through a tail vein cannula. To determine the local concentrations of Gd-DTPA, T1 maps were calculated from three sets of Rapid Imaging with Refocused Echoes (RARE) images, with the acquisitions being made before running the FLASH sequence.
Flowcytometry: To analyze tumor infiltrating lymphocytes (TILs), single-cell suspensions were prepared from left hindleg tumor. The cell surface phenotypes were determined by direct immunofluorescence staining with aCD3, aCD8, and aCD4 antibody and analyzed using FACS Calibur (BD Biosciences). TILs were identified and gated on a forward scatter versus side scatter plot.

Results and Discussion:
Combination treatment of RT and PD-1 inhibitor showed a synergistic effect on MC38 tumor (Fig.1). Flowcytometry showed that CD8+ T cell infiltration in unirradiated tumor increased after the combination of RT and PD-1 inhibitor (Fig.2), suggesting that in vivo synergistical effect was caused by higher CD8+ T cell infiltration. Hypoxic fraction < 10 mmHg (HF10), permeability, perfusion in unirradiated tumor improved after the combination of RT and PD-1 inhibitor (Fig.3 and 4), suggesting that enhanced CD8+ T cell infiltration by the abscopal effect caused the changes in these imaging biomarkers. Interestingly, these biomarkers (high Permeability, Perfusion, and low HF10) before treatment were found to be associated with the extent of induction of abscopal effect (Fig.5), which may imply the mode of tumor cell death by radiation therapy has a significant impact on the induction of abscopal effect.

Conclusion:
Hypoxic fraction < 10 mmHg, permeability, perfusion and CD8+ T cell infiltration in unirradiated tumors improved after the combination of RT and PD-1 inhibitor. Higher permeability/perfusion and lower HF10 in irradiated tumor before treatment was associated with slower unirradiated tumor growth after the treatment. These data can provide imaging biomarkers to predict the successful radiation-induced abscopal effect when treated with PD-1 inhibitor.

Reference
1. Wang, D.; Zhang, X.; Gao, Y.; Cui, X.; Yang, Y.; Mao, W.; Li, M.; Zhang, B.; Yu, J., Research Progress and Existing Problems for Abscopal Effect. Cancer Manag Res 2020, 12, 6695-6706.
2. Henkart, P. A., Lymphocyte-mediated cytotoxicity: two pathways and multiple effector molecules. Immunity 1994, 1 (5), 343-6.
3. Taube, J. M.; Anders, R. A.; Young, G. D.; Xu, H.; Sharma, R.; McMiller, T. L.; Chen, S.; Klein, A. P.; Pardoll, D. M.; Topalian, S. L.; Chen, L., Colocalization of inflammatory response with B7-h1 expression in human melanocytic lesions supports an adaptive resistance mechanism of immune escape. Sci Transl Med 2012, 4 (127), 127ra37.
4. Liu, Y.; Dong, Y.; Kong, L.; Shi, F.; Zhu, H.; Yu, J., Abscopal effect of radiotherapy combined with immune checkpoint inhibitors. J Hematol Oncol 2018, 11 (1), 104.
5. Liu, Y. N.; Yang, J. F.; Huang, D. J.; Ni, H. H.; Zhang, C. X.; Zhang, L.; He, J.; Gu, J. M.; Chen, H. X.; Mai, H. Q.; Chen, Q. Y.; Zhang, X. S.; Gao, S.; Li, J., Hypoxia Induces Mitochondrial Defect That Promotes T Cell Exhaustion in Tumor Microenvironment Through MYC-Regulated Pathways. Front Immunol 2020, 11, 1906.
6. Zheng, X.; Fang, Z.; Liu, X.; Deng, S.; Zhou, P.; Wang, X.; Zhang, C.; Yin, R.; Hu, H.; Chen, X.; Han, Y.; Zhao, Y.; Lin, S. H.; Qin, S.; Wang, X.; Kim, B. Y.; Zhou, P.; Jiang, W.; Wu, Q.; Huang,

Y., Increased vessel perfusion predicts the efficacy of immune checkpoint blockade. J Clin Invest 2018, 128 (5), 2104-2115.

Poster Presentation

Disclosures: The authors have disclosed no financial interest.

227-Systemic Assessment of Autoimmune Inflammatory Arthritis Disease Activity using Total-Body PET/CT with the 18F-FDG radiotracer

Presenter: Abhijit Chaudhari, University of California, Davis

Abhijit J. Chaudhari[1], Yasser G. Abdelhafez[2], Dario Mazza[3], Benjamin Spencer[1], Simon R. Cherry[4], Ramsey D. Badawi[1], Lorenzo Nardo[5], Siba Raychaudhuri[3]

[1]*University of California, Davis, Sacramento, CA*
[2]*UC Davis, Sacramento, CA*
[3]*University of California, Davis, Sacramento, California*
[4]*University of California, Davis, Davis, CA*
[5]*University of California, Davis, Sacramento*

Introduction:
Autoimmune Inflammatory Arthritides (AIA), such as Rheumatoid Arthritis (RA) or Psoriatic Arthritis (PsA), are chronic and systemic disorders that result in significant functional disability and musculoskeletal pain [1,2]. Left undiagnosed for even a few months, AIA may cause permanent musculoskeletal tissue damage. Effective targeted treatments for AIA continue to advance, however, assessment of disease activity is essential for optimizing treatments and improving long-term outcomes [3,4]. Current clinical tools, primarily based on physical exam or structural imaging, are vastly inadequate for evaluating AIA systemic disease activity [5]. Recently developed total-body (TB) PET/CT scanners could help address this challenge by providing objective, molecular-level assessment of tissues across the entire human body [6,7]. In this prospective, first-in-human study, we assessed the performance of an ultra-low-dose ^{18}F-FDG TB-PET/CT acquisition protocol to evaluate systemic joint, entheseal, and nail involvement in AIA. We also report the association of rheumatologic measures derived from standardized outcome instruments with those extracted from TB-PET/CT.

Methods:
Thirty participants (24 with AIA [15 with PsA, 9 with RA] and 6 with osteoarthritis (OA)), were prospectively enrolled in this single-center, observational study. All participants underwent a TB-PET/CT scan on the uEXPLORER scanner (United Imaging Healthcare) for 20 min starting at 40 min after intravenous injection of 78.1±4.7 MBq of ^{18}F-FDG. Evaluation of ^{18}F-FDG uptake was performed from the resulting images for 28 joints (as per the Disease Activity Score-28 [DAS-28] outcome measure) in both AIA and non-AIA groups. In the PsA group, 6 entheses locations (as per the Leeds Enthesitis Index [LEI]) and nails (as per Nail Psoriasis Severity Index [NAPSI] evaluation) were assessed from TB-PET/CT. A rheumatologist blinded to the imaging finding evaluated DAS-28, LEI, and NAPSI within two weeks before the TB-PET/CT scan. Statistical analysis involved correlation measurement (Spearman's ρ) and group comparisons (Mann-Whitney U or Fisher's exact test).

Results:
TB-PET/CT enabled the visualization of ^{18}F-FDG uptake at sites of interest across the entire body in a single bed position, and in the same phase of radiotracer uptake. There was concordance between TB-PET assessments and joint-by-joint rheumatologic evaluation in the AIA and non-AIA cohorts for 69.9% and 91.1% joints, respectively, while an additional 20.1% and 8.8% joints, respectively, deemed negative on rheumatologic examination showed PET-positivity. On the other hand, 10.0% and 0% joints in the AIA and non-AIA cohorts, respectively, were positive on rheumatologic evaluation but negative on TB-PET. Quantitative joint measures from TB-PET in the AIA cohort demonstrated a strong correlation (Spearman's ρ=0.60-0.68, p<0.05) with DAS-28. In the PsA cohort, 10/15 participants presented with enthesitis on TB-PET/CT. Concordance between the LEI and TB-PET/CT assessments was 78%. An additional 19.5% entheses were negative on rheumatologic exam but were positive on TB-PET/CT. On the other hand, 2.5% entheses were positive on rheumatologic exam and negative on PET. When comparing nails in PsA participants, there was concordance between TB-PET/CT and NAPSI evaluation for 82% of the nails. A total of 17% nails considered negative by rheumatologic exam were positive on TB-PET/CT. There were 1% nails that were positive on rheumatologic exam but negative on PET and this mismatch was attributed to intrascan motion.

Conclusion:
Systemic evaluation of hallmark pathologies underlying AIA (as opposed to those in non-AIA) is feasible with a TB-PET/CT system and an ultra-low-dose protocol. TB-PET/CT measures showed an overall positive association with the different clinical scales, and demonstrated the ability to detect pathologies occult on rheumatologic exam. These results provide the foundation for future larger studies to evaluate the possible improvements in AIA systemic assessment via the TB-PET/CT technology.

Reference

1. Aletaha D, Smolen JS. Diagnosis and management of rheumatoid arthritis: a review. JAMA. 2018 Oct 2;320(13):1360-72.
2. Ritchlin CT, et al. Psoriatic arthritis. New England Journal of Medicine. 2017 Mar 9;376(10):957-70.
3. Burmester GR, Pope JE. Novel treatment strategies in rheumatoid arthritis. The Lancet. 2017 Jun 10;389(10086):2338-48.
4. Vivekanantham A, et al Current treatments and recommendations for Psoriatic Arthritis. Best Practice & Research Clinical Rheumatology. 2021 Jun 1;35(2):101680.
5. England BR, et al, 2019 update of the American College of Rheumatology recommended rheumatoid arthritis disease activity measures. Arthritis Care & Research. 2019 Dec;71(12):1540-55.
6. Spencer BA, et al. Performance evaluation of the uEXPLORER total-body PET/CT scanner based on NEMA NU 2-2018 with additional tests to characterize PET scanners with a long axial field of view. Journal of Nuclear Medicine. 2021 Jun 1;62(6):861-70.
7. Chaudhari AJ, et al, Total-Body PET Imaging of Musculoskeletal Disorders. PET clinics. 2021 Jan 1;16(1):99-117.

Poster Presentation

Disclosures: The authors have disclosed no financial interest.

228-Enhanced Therapeutic Effect by Combination of Hyaluronidase and Cytolysin A in the Genetically Engineered Salmonella Typhimurium

Presenter: Khuynh Nguyen Van, Chonnam National University

Khuynh Nguyen Van[1], Dinh Huy Nguyen[2], Hien Ngo Thi Thu[3], Sung-Hwan You[4], Yeongjin Hong[5], Jung-Joon Min[6]

[1]Chonnam National University, Hwasun-gun, Hwasun-eup, Jeonranamdo, South Korea
[2]Chonnam National University, Gwangju, Jeonranamdo, South Korea
[3]Chonnam National University, South Korea
[4]Chonnam National University, Gwangju, Dong-gu, Republic of Korea
[5]Chonnam National University, Hwasun-Gun, Jeollanam-Do, Republic of Korea
[6]Chonnam National University Medical School, Hwasun-gun, South Korea

Recently, bacterial-mediated cancer therapy can be used as an effective delivery system since bacteria can selectively accumulate and proliferate in tumors. However, the complex microenvironmental structure of the tumors might reduce the penetration of bacteria. Thus, depleting the irregular structure of the tumors can increase bacterial colonization, resulting in the enhanced therapeutic effect. However, altering the tumor microenvironment may also facilitate metastasis. Here, we tested the therapeutic effect and impact on cancer metastasis of engineered *Salmonella typhimurium* which can be induced with doxycycline to secrete hyaluronidase to destroy the tumor environment, and cytolysin A to kill cancer cells. Our results indicate that the engineered *Salmonella* can suppress metastasis and the growth of various cancer models such as breast cancers, pancreatic cancers, and colon cancers in mice. Therefore, we suggest that the engineered *Salmonella* can bring an excellent anti-cancer effect and reduce the invasion and metastasis of tumors.

Reference

1. Rosenblum D, Joshi N, Tao W, Karp JM, Peer D: Progress and challenges towards targeted delivery of cancer therapeutics. Nat Commun 2018, 9(1):1410.
2. Zhou S, Gravekamp C, Bermudes D, Liu K: Tumour-targeting bacteria engineered to fight cancer. Nat Rev Cancer 2018, 18(12):727-743.
3. Forbes NS, Munn LL, Fukumura D, Jain RK: Sparse initial entrapment of systemically injected Salmonella typhimurium leads to heterogeneous accumulation within tumors. Cancer Res 2003, 63(17):5188-5193.
4. Fujimori M: Genetically engineered bifidobacterium as a drug delivery system for systemic therapy of metastatic breast cancer patients. Breast Cancer 2006, 13(1):27-31.
5. Kim JE, Phan TX, Nguyen VH, Dinh-Vu HV, Zheng JH, Yun M, Park SG, Hong Y, Choy HE, Szardenings M et al: Salmonella typhimurium Suppresses Tumor Growth via the Pro-Inflammatory Cytokine Interleukin-1beta. Theranostics 2015, 5(12):1328-1342.
6. Bhakdi S, Tranum-Jensen J: Alpha-toxin of Staphylococcus aureus. Microbiol Rev 1991, 55(4):733-751.
7. Nelson KL, Brodsky RA, Buckley JT: Channels formed by subnanomolar concentrations of the toxin aerolysin trigger apoptosis of T lymphomas. Cell Microbiol 1999, 1(1):69-74.
8. Golstein P, Kroemer G: Cell death by necrosis: towards a molecular definition. Trends Biochem Sci 2007, 32(1):37-43.
9. Kennedy CL, Smith DJ, Lyras D, Chakravorty A, Rood JI: Programmed cellular necrosis mediated by the pore-forming alpha-toxin from Clostridium septicum. PLoS Pathog 2009, 5(7):e1000516.
10. Kepp O, Galluzzi L, Zitvogel L, Kroemer G: Pyroptosis - a cell death modality of its kind? Eur J Immunol 2010, 40(3):627-630.
11. Dang LH, Bettegowda C, Huso DL, Kinzler KW, Vogelstein B: Combination bacteriolytic therapy for the treatment of experimental tumors. Proc Natl Acad Sci U S A 2001, 98(26):15155-15160.
12. Walker C, Mojares E, Del Rio Hernandez A: Role of Extracellular Matrix in Development and Cancer Progression. Int J Mol Sci 2018, 19(10).
13. Banerjee S, Modi S, McGinn O, Zhao X, Dudeja V, Ramakrishnan S, Saluja AK: Impaired Synthesis of Stromal Components in Response to Minnelide Improves Vascular Function, Drug Delivery, and Survival in Pancreatic Cancer. Clin Cancer Res

Poster Presentation

Disclosures: The authors have disclosed no financial interest.

229-Cerebral Glutamate MR Imaging in a Rat Forced Swimming Test Model of Depression

Presenter: Do-Wan Lee, University of Ulsan College of Medicine

Do-Wan Lee[1], Dong-Hoon Lee[2], Dong-Cheol Woo[3]

[1]University of Ulsan College of Medicine, Seoul, South Korea
[2]Yonsei University, Wonju, Gangwon-do, South Korea
[3]Asan Medical Center, Seoul, Seoul, Republic of Korea

Introduction:
Depression is a complex psychiatric disorder characterized by persistent and pervasive low mood accompanied by anhedonia, disturbances of sleep and/or appetite, and feelings of sadness [1,2]. Moreover, detecting and evaluating alterations in glutamate levels is important, as it has the potential to be used as an essential key-marker for quantifying cerebral metabolism in depressive disorders. This study aimed to visualize and quantitatively evaluate hippocampal glutamate changes in a rat model of depression using ^{1}H-MRS and glutamate-weighted chemical exchange saturation transfer (GluCEST).

Methods:
Twenty-four rats were randomized into two groups (forced swimming test [FS], n=12; and control, n=12). Rats were individually forced to swim in an open Plexiglas cylinder filled with water up to 40-cm deep [3]. All FS rats were individually subjected to two swimming sessions: an initial pre-swimming trial (15-min), followed 24-h later by a 10-min test.
All MR experiments were performed using a horizontal 7-T preclinical scanner. GluCEST imaging was carried out in a selected single slice in which the hippocampus was well observed using the following parameters: turbo-RARE sequence, slice thickness=1.5-mm, FOV=30×30-mm^2, TR/TE=4200/36.4-ms, RARE-factor=16, and RF saturation pulse (power/length)=3.6-μT/1000-ms. Z-spectra were acquired at 25-frequency offsets from 6 to -6ppm with a step size of 0.5ppm, and the reference image (S_0) [4,5]. To correct for B_0- and B_1-inhomogeneity, water saturation shift referencing Z-spectra (33-frequency offset; ±0.8ppm; 0.05ppm step size; 0.05-μT RF saturation power) [6], and B_1-field map (flip-angle 30° and 60°) [4] were obtained. *In vivo* ^{1}H-MRS data were acquired from a single voxel (12-μL) positioned in the hippocampus using a PRESS sequence (TR/TE=5000/16.3-ms, spectral width=5-kHz, data points=2048, and 256 averages) [7].

The equation for calculating the GluCEST map was as follows: GluCEST(%)=100×(M[−3ppm]–M[+3ppm])/M[−3ppm] where, M[±3ppm] are B_0- and B_1-corrected signals at ±3ppm from water resonance, respectively [4,5]. A ROI was drawn in the hippocampal region for the computation of GluCEST values. The LCModel was used to quantify MRS data. Metabolite concentrations were determined using the unsuppressed water spectrum as an internal reference.
The quantified metabolite concentrations in all spectra were normally distributed (Kolmogorov-Smirnov test of normality, all p>0.2), and independent t-tests were used. Statistical differences were assumed to be significant for p-values below 0.05.

Results and Discussion:
Figure1 shows the magnetization transfer ratio asymmetry (MTR_{asym}) curves and quantified GluCEST-weighted values in the hippocampus of FS and control rats. The average GluCEST value between the left and right hippocampus in FS group was significantly lower (3.67±0.81%) than in controls (5.02±0.44%; p<0.001). Figure2 shows voxel placement in the hippocampal region of rats and presents the spectral fitting results of ^{1}H-MRS in a representative rat from each group. The quantified glutamate concentrations in the hippocampal region were significantly lower in FS rats than in controls (6.560±0.292-μmol/g vs. 7.133±0.397-μmol/g, respectively; p=0.001). Figure3 indicates the calculated multi-parametric MR values in the FS and controls in the hippocampal region. There were no significant differences between two groups. These results might reflect that multi-parametric values do not affect the formation of GluCEST signals in the present study [8]. Figure4 shows reconstructed maps of the quantified multi-parametric MR and GluCEST values overlaid on the corresponding S_0 images from a representative rat in the FS and controls. There was no apparent difference in the multi-parametric MR images in visual inspections, as shown in Fig.3, but remarkable contrasts were observed in the GluCEST maps of the hippocampal region.

Conclusion:
Our findings suggest that GluCEST may provide a unique method to detect and monitor glutamate levels in a rat model of depression. Furthermore, using GluCEST and 1H-MRS techniques may yield greater insight into the neurochemical role of glutamate in various psychiatric disorders.

Reference

1. Zhou X, Liu L, Zhang Y, et al. Metabolomics identifies perturbations in amino acid metabolism in the prefrontal cortex of the learned helplessness rat model of depression. Neuroscience. 2017;343:1–9.
2. Liu L, Zhou X, Zhang Y, et al. The identification of metabolic disturbances in the prefrontal cortex of the chronic restraint stress rat model of depression. Behav Brain Res. 2016;305:148–156.
3. Porsolt RD, Le Pichon M, Jalfre M. Depression: a new animal model sensitive to antidepressant treatments. Nature 1977;266:730–732.
4. Cai K, Haris M, Singh A, et al. Magnetic resonance imaging of glutamate. Nat Med. 2012;18(2):302–306.
5. Lee DH, Woo CW, Kwon JI, et al. Cerebral mapping of glutamate using chemical exchange saturation transfer imaging in a rat model of stress-induced sleep disturbance at 7.0T. J Magn Reson Imaging. 2019;50(6);1866–1872.
6. Kim M, Gillen J, Landman BA, Zhou J, et al. Water saturation shift referencing (WASSR) for chemical exchange saturation transfer (CEST) experiments. Magn Reson Med. 2009;61(6):1441–1450.
7. Tkac I, Starcuk Z, Choi IY, et al. In vivo 1H NMR spectroscopy of rat brain at 1 ms echo time. Magn Reson Med. 1999;41:649–656.
8. Lee DH, Heo HY, Zhang K, et al. Quantitative assessment of the effects of water proton concentration and water T1 changes on amide proton transfer (APT) and nuclear overhauser enhancement (NOE) MRI: The origin of the APT imaging signal in brain tumor. Magn Reson Med. 2017;77(2):855–863.

Poster Presentation

Disclosures: The authors have disclosed no financial interest.

230-Synthesis and preclinical validation of novel NIRF/PDT PSMA-targeted Theranostic probe for image guided surgery and photodynamic therapy of prostate cancer

Presenter: Valentina Dinatale, University of Turin

Valentina Dinatale[1], Rachele Stefania[2], Martina Capozza[3], Henriëtte S. de Bruijn[4], Giorgia Zambito[5], Roisin McMorrow[6], Clemens Lowik[7], Laura Mezzanotte[6], Enzo Terreno[1]

[1]*University of Turin, Torino, Torino, Italy*
[2]*University of Turin, Torino, Italy, Italy*
[3]*University of Turin, Turin, Turin, Italy*
[4]*Erasmus Medical Center, Rotterdam, Rotterdam, Netherlands*
[5]*Erasmus Medical Center, Rotterdam, Zuid-Holland, Netherlands*
[6]*Erasmus Medical Center, Rotterdam, Netherlands*
[7]*Erasmus University Rotterdam, Rotterdam, Zuid Holland, Netherlands*

Introduction:
Prostate cancer (PCa) is the third cause of cancer deaths and affects millions of men globally with high incidence in western countries. Although many different treatment modalities have been proven to be effective in treating localized prostate cancer, radical prostatectomy is still the most accurate way to eradicate localized PCa. However, approximately 20-40% of patients will present biochemical recurrence after the surgery[1]. Prostate-specific membrane antigen (PSMA) is overexpressed in the epithelium of prostate cancer and has been increasingly used as a target for cancer imaging and therapy[2-3]. The aim of this study is to develop PSMA-targeted fluorescent probes that would provide intraoperative image guidance for prostate tumor resection and allow for subsequent interstitial Targeted Photodynamic Therapy (tPDT)[4] to eliminate unresectable or residual tumor lesion.

Methods:
A new bivalent PSMA-targeted Si-phthalocyanine (Pc)-based photosensitizer, functionalized with thiol-Glu-NH-CO-NH-Lys-2-naphthyl-L-Ala-cyclohexane, a well-known PSMA inhibitor, was synthesized (Persuasive data Fig. 3). The cellular uptake of the dye was examined in human PCa cells with different PSMA expression, PC3-PIP (PSMA+) and PC3-FLU (PSMA-), by NIR fluorescent cell binding assay. Photodynamic properties were evaluated in vitro after irradiation with a diode laser at 690 nm (total light fluence: 20 J/cm_2). MTS assay was performed 24h post irradiation. To determine whether ROS generation was involved in contributing to cell death after PDT treatment, fluorescence levels of 2',7'-dichlorofluorescein (DCF) were measured in PC3-PIP and PC3-FLU treated or untreated cells by fluorescence spectroscopy or confocal microscopy. To validate the PSMA-binding specificity of SiPc-$(PSMAi)_2$ and identify the optimal time-point for fluorescence guided surgery and PDT treatment, PC3-PIP and PC3-FLU tumor bearing mice were injected with 10 nmol dose of SiPc-$(PSMAi)_2$ and imaged at 1h, 4h and 24h post injection. After imaging, mice were sacrificed and organs harvested to detect the fluorescence signal.

Results and Discussion:
As shown in Figure 1b, SiPc-$(PSMAi)_2$ probe specifically target PSMA positive PC3-PIP cells displaying a binding proportional to the concentration, whereas a negligible affinity was observed for the PSMA low-expressing PC3-FLU cells (Fig.1a-b). The probe was also evaluated in terms of PDT effect. SiPc-$(PSMAi)_2$ induced a PSMA-specific PDT (Fig. 2a) with a concentration-dependent decrease of cell viability (up to 20,3% at 500 nM) only in the treated PC3-PIP cells but not in control PC3-FLU cells. Treated PC3-PIP cells showed a significant concentration-dependent increase in level of ROS production (up to 4-fold higher at 500 nM) compared to treated PC3-FLU cells (Fig. 2b and Persuasive data Fig. 4). These results clearly demonstrate that SiPc-$(PSMAi)_2$ possesses PSMA-specific phototoxicity and negligible in vitro cytotoxicity in the absence of light irradiation. This probe was preliminary tested on mice bearing PC3-PIP and PC3-FLU tumors showing a significant tumor uptake after the injection of 10 nmol at 4h and 24h (Persuasive data Fig. 5). The kidney and liver uptake were partially due to the route of excretion as well as because a high expression of PSMA was found in many normal tissue types and on endothelial cells of tumor vessels[5]. However, the background toxicity is reduced by the fast clearance rate observed from non-target tissues, the low concentration of PDT agents used, and the tissue or organ specific and focused irradiation required for PDT.

Conclusions:
A novel dye has been designed to be used intraoperatively as dual NIRF/tPDT agent. The probes showed promising results in terms of target affinity, in vitro photo-induced cytotoxicity and in vivo tumor-to-background fluorescence ratio. Future study will be focused on testing in vivo the PDT therapeutic potential of the tumor targeted photosensitizer.

Acknowledgement: PC3-PIP and PC3-FLU cell lines were kindly provided by Prof Martin G. Pomper (Johns Hopkins Medical School, Baltimore, MD)

Reference

1. Tourinho-Barbosa R, Srougi V, Nunes-Silva I, Baghdadi M, Rembeyo G, Eiffel SS, Barret E, Rozet F, Galiano M, Cathelineau X, Sanchez-Salas R. Biochemical recurrence after radical prostatectomy: what does it mean? Int Braz J Urol. 2018 Jan-Feb;44(1):14-21. doi: 10.1590/S1677-5538.
2. Y. Chen, S. Chatterjee, A. Lisok, I. Minn, M. Pullambhatla, B. Wharram, Y. Wang, J. Jin, Z.M. Bhujwalla, S. Nimmagadda, R.C. Mease, M.G. Pomper, A PSMA-targeted theranostic agent for photodynamic therapy, J. Photochem. Photobiol. B Biol. 167 (2017) 111e116, https://doi.org/10.1016/ j.jphotobiol.2016.12.018. 2016 Aug;15(8):1834-44. doi: 10.1158/1535-7163.MCT-15-0722
3. Martina Benešová, Martin Schäfer, Ulrike Bauder-Wüst, Ali Afshar-Oromieh, Clemens Kratochwil, Walter Mier, Uwe Haberkorn, Klaus Kopka, Matthias Eder Preclinical Evaluation of a Tailor-Made DOTA-Conjugated PSMA Inhibitor with Optimized Linker Moiety for Imaging and Endoradiotherapy of Prostate Cancer J Nucl Med . 2015 Jun;56(6):914-20. doi:10.2967/ jnumed.114.14741
4. Xinning Wang, Brian Tsui, Gopolakrishnan Ramamurthy, Ping Zhang, Joseph Meyers, Malcolm E Kenney, Jonathan Kiechle, Lee Ponsky, James P Basilion Theranostic Agents for Photodynamic Therapy of Prostate Cancer by Targeting Prostate-Specific Membrane Antigen Mol Cancer Ther.
5. Chang SS, O'Keefe DS, Bacich DJ, Reuter VE, Heston WD, Gaudin PB. Prostate-specific membrane antigen is produced in tumor-associated neovasculature. Clin Cancer Res. 1999; 5: 2674–2681.

Poster Presentation

Disclosures: The authors have disclosed no financial interest.

231-Preclinical ultrasound cardiovascular imaging: A tool for genetic disease model phenotyping and efficacy assessment

Presenter: James Cao, Sanofi

James Cao[1], Xiaoyou Ying[2], Dinesh Bangari[2], Michelle Potter[2], Laurie Smith[3], Jennifer Nietupski[3], Giulio Tomassy[4], Wei Fan[4], Alex Jayyosi[2]

[1]Sanofi, Newton, MA
[2]Sanofi, Framingham, MA
[3]Sanofi, Cambridge, MA
[4]Sanofi, Waltham, MA

Many rare disease animal models generated with transgenic and gene targeting methods present with altered cardiac structure and function. As a result, high-sensitivity in vivo echocardiography has become an attractive method to evaluate cardiac system phenotype and various therapeutic treatment effect including gene therapy in these models. High frequency echocardiography platform, transthoracic B-mode, M-mode, pulse wave Doppler, ECG kilohertz, VevoStrain, VevoVeso visualization are major imaging methods currently used for assessing cardiac structure and function with great temporal (~msec) and spatial (~0.1 mm) resolutions and relatively high throughput (5 to 15 min per animal). We have used Vevo2100 platform for phenotyping and efficacy imaging of several genetic disease models. Here we present our imaging methods and major conclusions based on these models. 1. Myotonic dystrophy type 1 mouse model (DMSXL): DMSXL mice carry a 45-kb human genomic fragment that includes the mutant DMPK with 1,000-1,600 CTG repeats. DMSXL mouse model recapitulates some of the molecular and clinical features of DM1 phenotype. Phenotyping studies demonstrated that DM1 mice have lower cardiac output, decreased descending aorta diameter and decreased blood flow velocity compared to their wild-type littermates. Furthermore, AAV-mediated muscle targeted expression of engineered artificial microRNA directed against DMPK mRNA treatment reduces toxic DMPK mRNA and improves DM1 model cardiac phenotype compared to untreated mice at two-months post AAV treatment, including the strain and strain rate analysis. 2. Mucopolysaccharidoses type 1-Hurler (MPS I-H) mouse model (Hurler mice): Hurler mice carries a nonsense mutation analogous to the Human severe form of α-L-iduronidase (IDUA deficiency mutation). The homozygous IDUA mutation mice develop cardiac and aortal deficiencies as they age. An AAV vector expressing α-L-iduronidase (IDUA) was administered via single IV injection at 4-5 weeks of age. CV function was measured a half-year post-injection. Substantial aortic dilation improvement was detected and confirmed by histology in the treated cohort. 3. Sickle cell disease model (Towne mice): Towne mice carry several human sickle hemoglobin knock-in genes replacing the endogenous mouse gene. Hearts from Townes mice are grossly enlarged at all time points compared to age matched controls. With increasing age Towne mice (5 weeks, 3 and 6 months), there is an increase in aortic diameter, carotid artery diameter, left ventricular mass, cardiac output, stroke volume with decreases in fractional shortening, ejection fraction as compared to controls and compared to earlier time points. 4. Osteogenesis Imperfecta Mouse Model (OI model G610C mutation): The G610C dominant knock-in OI mouse (Amish) had Glycine to cysteine residue mutation in COL1A2 gene. Cardiac phenotype was profiled at 2-, 6- and 12-months of age. At 2 months age, decreased cardiac output, ejection fraction and descending aorta velocity was observed as compared to matched wild type mice. At 6 months only ejection fraction is lower and no differences at 12 months.

Cardio myofiber changes were seen histologically in OI mice. These applications have demonstrated that ultrasound imaging as a rapid, comparatively inexpensive, non-invasive imaging modality for in-vivo model studies in our early discovery projects.

Poster Presentation

Disclosures: The authors have disclosed no financial interest.

232-High Contrast hypoxia fluorescence imaging in pre-clinical oncology with protoporphyrin IX

Presenter: Brian Pogue, Dartmouth College

Brian Pogue[1], Petr Bruza[2], Arthur F. Pétusseau[2]

[1]Dartmouth College, Hanover, NH
[2]Dartmouth College, Lebanon, NH

Hypoxia imaging in surgery has never been possible to date, but a newly discovered signal from protoporphyrin IX (PpIX) shows that fluorescence can be produced in areas of hypoxia. The molecule PpIX produces a delayed fluorescence signal that is a direct result from low oxygenation, because there is reverse intersystem crossing from the triplet state of the molecule, leading to a long lived red emission. Since the signal comes from the triplet state, that is normally quenched by molecular oxygen, the signal intensity is a direct reporter on the lack of oxygen in tissue. Additionally, since the molecule PpIX is an endogenously produced species from administration of aminolevulinic acid (ALA), it is well tolerated and widely available in a number of pro-drug formulations. The emission signal capture requires a time-gated fluorescence approach, which is achieved by a short pulsed diode laser with a fast off time, followed by a fast on-gated camera. The average irradiance used was just 50 microWatts/cm2 at 635nm wavelength, delivered through a single fiber through a lens based launcher. The camera used was a fast time-gated image intensifier coupled to a CMOS camera with onboard FPGA processing, which had nanosecond level optical gating. The PpIX delayed fluorescence emission lifetime varies from 10s of microseconds to several milliseconds, when going from oxygenated to hypoxic tissue. The production of PpIX is ubiquitous throughout most cells when a patient is given ALA. The demonstration used for this has been in xenograft pancreatic cancer tumors in nude mice, who were given 200 mg/kg ALA in an intraperitoneal administration. After 3-6 hours of incubation, PpIX is known to be highly produced throughout the skin of the mice, and relocates through diffusion and vascular transport to most tissues in the body. The enhanced permeability and retention into the pancreatic cancers is shown, and the delayed fluorescence from PpIX provides very high contrast relative to all normal tissues, which are oxygenated. The quantitative assessment of the signal shows at contrast of 5x-6x in the emission from the pancreatic cancer relative to background normal tissues. PpIX is homogenously present throughout most of the mouse skin and in high concentrations in most organs based upon vascular perfusion.

Poster Presentation

Disclosures: The authors have disclosed no financial interest.

233-Automated segmentation of the lung and individual lung tumors in a genetically engineered mouse model of lung cancer by micro-CT

Presenter: Gregory Ferl, Genentech

Gregory Z. Ferl[1], Kai Barck[1], Jasmine Patil[1], Skander Jemaa[1], Evelyn Malamut[2], Anthony Lima[1], Jason Long[3], Jason Cheng[1], Melissa Junttila[3], Richard Carano[4]

[1]Genentech, South San Francisco, CA
[2]Genentech, Los Angeles, CA
[3]ORIC Pharmaceuticals, South San Francisco, CA
[4]Genentech, San Mateo, CA

Lung cancer is the leading cause of death due to cancer, accounting for an estimated 18 percent of all cancer deaths globally in 2020 [1]. Expression of oncogenic mutant Kras and p53 genes in lung tissues of the $Kras^{Lsl.G12D}$; $p53^{frt/frt}$; adenoCre.FLP genetically engineered mouse model (GEMM) drives development of lung adenocarcinomas resembling human lung cancers, and enables translational preclinical studies focused on treatment of non-small cell lung cancer [2]. GEMMs of lung cancer have been shown to correlate with human tumor growth and response to treatment, providing insight into the development of new therapies [2]. To effectively investigate these GEMMs, micro-CT scans of mouse lungs are used for quantification of lung tumor burden and detection of individual lung tumors as well as longitudinal response of total tumor burden and individual tumors in response to treatment with anti-VEGF antibodies, chemotherapy and small molecule kinase inhibitors [2, 3, 4]. Although manual tissue segmentation has the benefits of simplicity and increased control over the task, both preclinically and clinically, segmentation of the lungs and lung tumors by a human reader is time-consuming and impacted by inter- and intra-reader bias and variability. Automated image segmentation is a broad area of research that aims to replace or augment manual segmentation and reduce bias and variability [5]. While numerous machine learning and deep learning methods have been proposed for segmentation of lungs and lung tumors in clinical CT images, there is a comparatively low number of published pre-clinical studies that have utilized these techniques. Here, we've developed an automated image processing algorithm for segmenting lungs and individual lung tumors in micro-CT scans of the $Kras^{Lsl.G12D/+}$; $p53^{frt/frt}$; adenoCre.FLP genetically engineered mouse model for non-small cell lung cancer. Over 3000 scans acquired from two different scanners across multiple studies were used to train and validate a 3D U-net model to segment the lungs and, subsequently, a Support Vector Machine (SVM) classifier to segment individual lung tumors using a radiomics approach. The trained U-net segments the lungs with a dice coefficient of 0.92 as calculated on hold-out test scans, where the U-net based lung masks show qualitatively excellent agreement with manual segmentation. The U-net lung segmentation algorithm can be used to estimate changes in soft tissue volume within the lungs (primarily tumors and blood vessels), while the trained SVM is able to discriminate between tumors and blood vessels and identify individual lesions. Based on hold-out test scans an F1 score of 0.85 was calculated with respect to the ability of the SVM classifier to correctly identify tumor "objects" generated by watershed segmentation. The trained lung and lung tumor segmentation algorithms 1) significantly reduce time required to perform lung and tumor segmentation, 2) reduce bias and error associated with manual segmentation of images and 3) facilitate identification of individual lung lesions and objective assessment of changes in lung and individual tumor volumes under different experimental conditions. Additionally, we demonstrate that these algorithms can be used to segment micro-CT scans collected from different scanners.

Reference

1. J. Ferlay, M. Ervik, F. Lam, M. Colombet, L. Mery, M. Pin˜eros, A. Znaor, I. Soerjomataram, F. Bray, Global cancer observatory: cancer today. lyon: International agency for research on cancer; 2018 (2020).

2. M. Singh, A. Lima, R. Molina, P. Hamilton, A. C. Clermont, V. Devasthali, J. D. Thompson, J. H. Cheng, H. B. Reslan, C. C. Ho, et al., Assessing therapeutic responses in kras mutant cancers using genetically engineered mouse models, Nature biotechnology 28 (6) (2010) 585–593.
3. K. H. Barck, H. Bou-Reslan, U. Rastogi, T. Sakhuja, J. E. Long, R. Molina, A. Lima, P. Hamilton, M. R. Junttila, L. Johnson, et al., Quantification of tumor burden in a genetically engineered mouse model of lung cancer by micro-ct and automated analysis, Translational oncology 8 (2) (2015) 126–135.
4. M. Merchant, J. Moffat, G. Schaefer, J. Chan, X. Wang, C. Orr, J. Cheng, T. Hunsaker, L. Shao, S. J. Wang, et al., Combined mek and erk inhibition overcomes therapy-mediated pathway reactivation in ras mutant tumors, PloS one 12 (10) (2017) e0185862.
5. K. Marten, F. Auer, S. Schmidt, G. Kohl, E. J. Rummeny, C. Engelke, Inadequacy of manual measurements compared to automated ct volumetry in assessment of treatment response of pulmonary metastases using recist criteria, European radiology 16 (4) (2006) 781–790.

Poster Presentation

Disclosures: The authors have disclosed no financial interest.

234-Disease classification based on features extracted from the Fourier spectrum of CT image: A pilot study

Presenter: Biprojit Nath, Tata Memorial Hospital

Biprojit Nath[1], Akhilesh Tripathi[1], Ashish K. Jha[1], Sneha Mithun[1], Nilendu Purandare[1], Venkatesh Rangarajan[2], Andre Dekker[3], Leonard Wee[3]

[1]Tata Memorial Hospital, Mumbai, Maharashtra, India
[2]Tata Memorial Hospital, Mumbai, IN-Mah, India
[3]Maastricht University, Maastricht, Netherlands

Aim and Objective:
The high throughput extraction of quantitative imaging features from medical images viz radiomics has opened new doors to imaging biomarker research in oncology. Usually, radiomic feature is extracted from original medical images or LoG filtered images, or wavelet transformed images. In this study, we propose the disease classification based on radiomic features extracted from the 2D Fourier Spectrum of CT images.

Methodology:
This study is approved as a retrospective study by the institutional ethics committee (IEC) of our hospital with a waiver of informed consent. In total 90 patients' pretreatment, CT images, 30 patients from each disease group i.e., rectal cancer (Class:0), cervix cancer (Class:1), and lung cancer (Class:2) were used for this study. Two best representative transaxial slices of tumor for each patient were selected by an experienced radiologist and were used for the analysis. The 2D axial slices were reshaped and normalized followed by the forward Fourier transform was performed on an in-house developed python script. The Fourier transformed spectrum is further converted to an 8-bit image on which the mean method of thresholding was performed on ImageJ software. ROI was drawn on the image post thresholding. Subsequently, 33 shape and first-order statistical features were extracted from images. Feature selection was performed using the recursive feature elimination technique using a random forest algorithm. Train and test split of the dataset was performed. A random forest model was developed for multiclass classification on the training dataset and validated on the test dataset.

Results:
Five optimum features were selected using recursive feature elimination. The accuracy of the random forest model validated on test dataset was 0.77, precision (weighted average) was 0.80 and recall (weighted average) was 0.77. Area under the curve- ROC for class 0, 1, 2 are respectively 0.96, 0.90 and 0.90.

Conclusion:
Our preliminary results show excellent predictive power of features extracted from the Fourier spectrum in classifying diseases viz Ca Lung, Ca Cervix and Ca Rectum. This proof-of-concept study will be further validated on external datasets.

Poster Presentation

Disclosures: The authors have disclosed no financial interest.

235-New Somatostatin Receptor 2 (SSTR2)-Targeted Probe for Near-Infrared Fluorescence Guided Meningioma Surgery

Presenter: Merle Weitzenberg, Helmholtz Zentrum Munchen

Merle M. Weitzenberg[1], Gina Fürtjes[2], Oliver Plettenburg[3], Oliver Bruns[4], Volker Neuschmelting[5], Hannes Rolbieski[6]

[1]Helmholtz Zentrum Munchen, Germany
[2]Helmholtz Zentrum München, München, Bayern, Germany
[3]Helmholtz Zentrum Munchen, Hannover, Germany
[4]Helmholtz Zentrum Munchen, München, Bayern, Germany
[5]University Hospital Cologne, Köln, Nordrhein-Westfahlen, Germany
[6]Helmholtz Zentrum Munchen, Munich, Germany

Meningioma are the most common primary tumors of the central nervous system. Tumor resection as first line therapy is often not curing.[1] Recurrences mostly arise at the surgical margin presumably from small tumor lesions that are currently invisible to the surgical eye.[2] Objective of this study is the development of a highly specific and sensitive optical method for intraoperative meningioma imaging in order to make tumor remnants resectable and thus lower recurrence rates.
Labeling of meningioma shall be accomplished by targeting reliably overexpressed somatostatin receptor type 2 (SSTR2) with octapeptide TATE, a synthetic somatostatin analogue.[3] ^{68}Ga-DOTA-TATE is already clinically used for pre- and post-operative diagnostics via SSTR-PET/CT.[4] Due to low spatial resolution and radioactivity of the tracer, PET is not suitable for intraoperative labeling of tumor remnants. Conjugation of TATE to a Near-Infrared (NIR) dye, on the other hand, should allow detection of SSTR2-expressing tissue with high spatial resolution in real time up to few millimeters in depth. Two different heptamethine cyanine dyes were used for conjugation; IRDye®800, a commercially available NIR-dye whose conjugates are currently propelling more than 20 Phase I and Phase II clinical trials,[5] and sNIR, a newly developed NIR-dye. Despite similarities in terms of structure, solubility, net charge and optical properties, sNIR and its TATE-conjugate have higher photostability than IRDye®800 and its TATE-conjugate, both *in vitro* and *in vivo*. The decisive advantage of TATE-sNIR over TATE-IRDye®800, however, is its noticeably faster tissue clearance when injected intravenously in anesthetized mice (compare **Figure A**). Tissue half-life of TATE sNIR (28 ± 2 min, n =

3) is one-sixth of TATE-IRDye®800 (180 ± 42 min, n = 2), indicating that there is a retention of TATE-IRDye®800 that TATE sNIR is not subjected to. Rapid clearance of non and unspecifically bound probe is prerequisite for detection of specifically bound probe in a beneficial target-to-background ratio. Therefore, further experiments were conducted with TATE-sNIR.

TATE-sNIR is stable in aqueous solution up to two weeks when stored at 4 °C in the absence of light. The probe showed high affinity for SSTR2 in a filtration based radioligand competition assay (low nanomolar inhibition constant K_i). To evaluate the ability of labeling SSTR2-expressing tissues *in vivo*, mice were intravenously injected with 4 nmol TATE-sNIR and sacrificed 3 h (equalizing six tissue half-lives) post injection and organs were imaged *ex vivo*. Specific signal uptake was observed in gastric epithelium, pancreas and pituitary gland, which highly express SSTR2 according to immunohistochemistry (IHC). The negative control scrambled TATE-sNIR (not bearing the SSTR2-targeting pharmacophore) did not enrich in these tissues (compare **Figure B**). As proof-of-principle, an orthotopic meningioma mouse model is currently being developed in order to resect tumor tissue using fluorescence guidance. Moreover, washout and blocking experiments with freshly excised human meningioma tissue ex situ are currently conducted.

The preliminary preclinical results demonstrate that the SSTR2-targeted fluorescent probe TATE-sNIR is capable of specifically targeting SSTR2 *in vitro* and *in vivo* potentially enabling sensitive and specific meningioma fluorescence guided surgery in the future.

Reference

1. Goldbrunner, R. et al. EANO guidelines for the diagnosis and treatment of meningiomas. Lancet Oncol. 17, e383–e391 (2016).
2. Lemée, J. M. et al. Extent of Resection in Meningioma: Predictive Factors and Clinical Implications. Sci. Rep. 9, 1–6 (2019).
3. de Oliveira Silva, C. B. et al. Expression of somatostatin receptors (SSTR1-SSTR5) in meningiomas and its clinicopathological significance. Int. J. Clin. Exp. Pathol. 8, 13185–13192 (2015).
4. Boy, C. et al. DGN-Handlungsempfehlung (S1-Leitlinie) Somatostatinrezeptor-PET/CT. (2017). [5] https://www.licor.com/bio/reagents/irdye-800cw-infrared-dyes, accessed 27/04/22.

Poster Presentation

Disclosures: The authors have disclosed no financial interest.

236-Performance evaluation of in-house-developed sensitivity and scatter phantoms

Presenter: Viraj Sawant, Advanced Centre for Treatment, Research and Education in Cancer (ACTREC)

Viraj Sawant[1], Ashish K. Jha[2], Bipin Rawat[2], Sneha Mithun[2], R.S Vishwakarma[3], Sridhar Sahoo[3], T. Palani Selvam[3], Venkatesh Rangarajan[4]

[1]*Advanced Centre for Treatment, Research and Education in Cancer (ACTREC), Mumbai, Maharashtra, India*
[2]*Tata Memorial Hospital, Mumbai, Maharashtra, India*
[3]*Bhabha Atomic Research Centre (BARC), Mumbai, Maharashtra, India*
[4]*Tata Memorial Hospital, Mumbai, IN-Mah, India*

Objective:

Aim of the study is to carry out a performance evaluation of in-house-developed sensitivity and scatter phantoms with the Philips Gemini TOF PET/CT system as per the NEMA NU2-2007 guidelines.

Methods:

According to the NEMA (National Electrical Manufacturers Association) NU-2 2007, sensitivity, scatter fraction, count-rate performance, the accuracy of count losses, and random corrections were evaluated for in-house developed sensitivity and scatter phantoms. System sensitivity was measured by inserting a 70 cm ^{18}F line source in an 80cm tube with an activity concentration of 4.1 MBq in five concentric aluminum sleeves with varying diameters. Scatter fraction and count-rate performance was calculated by analyzing dynamically acquired data of an ^{18}F 565 MBq line-source inside a polyethylene cylinder in 20 cm diameter and 70 cm length. Our results were validated with the reference value provided by the vendor.

Results:

The average system sensitivity recorded is 6819 cps/MBq. (acceptance criteria: >6400 cps/MBq). The scatter fraction of the system is 25.8% (acceptance criteria: <32%. A peak NECR of 106.395 kcps (acceptance criterian: >95 kcps), activity concentration of 18.54 kBq/ml (acceptance criteria: < 20 kBq/ml). The observed maximum true rate is 243 kcps (acceptance criterian: >205 kcps). Conclusion: This study demonstrated that the performance of in-house-developed sensitivity and scatter phantoms is as per the limits specified by the vendor.

Poster Presentation

Disclosures: The authors have disclosed no financial interest.

237-177Lu-LHRH analog as a potential theragnostic agent for prostate cancer

Presenter: Ximena Camacho, Universidad de la República

Ximena Camacho[1], Lucía Alfaya[2], Carolina Perroni[3], Marcos Tassano[4], Mirel Cabrera[5], Ana Laura Reyes[6], Andrea Paolino[7], Marcelo Fernández[1], Pablo Duarte[7], Eduardo Savio[7], Pablo Cabral[1], Juan P. Gambini[8]

[1]*Universidad de la República, Montevideo, Montevideo, Uruguay*
[2]*Universidad de la República, Montevideo, Radiofarmacia, Uruguay*
[3]*University of the Republic, Montevideo, ---Select---, Uruguay*
[4]*Universidad de la República, Montevideo, Uruguay*
[5]*Universidad de la República, Montevideo, ---Select---, Uruguay*
[6]*Mntevideo, Uruguay*
[7]*Montevideo, Uruguay*
[8]*Hospital de Clinicas, Universidad de la Republica, Montevideo, Montevideo, Uruguay*

Introduction:

Prostate cancer (PC) is the most common malignancy in men, accounting for about one quarter of new cancer diagnoses worldwide. Despite several improvements in early detection and management of PC patients, it remains the second leading cause of cancer-related mortality [1]. Luteinizing hormone-releasing hormone receptors (LHRHR) are overexpressed in this pathology, demonstrating that LHRHR could be a molecular target for molecular imaging [2-4]. Therefore, we propose the design, synthesis and preclinical evaluation of an analog of the LHRH peptide (DOTA-Axh-(DLys6)-LHRH), labeled with 177-Lutetium as a potential theragnostic agent for PC. Methodology: 20 ug of DOTA-Axh-(DLys6)-LHRH was radiolabeled with 177LuCl3 (600

MBq) at 90 ºC for 15 min (pH 4.5) for maximum radiochemical yield (≥ 98 %). Final formulation conditions were optimized and analyzed by HPLC. Log D and stability in serum, PBS, EDTA and ammonium acetate 0.5 M (pH 4.5) were evaluated up to 96 hs. In vitro cell binding studies were done in normal prostate cell line RWPE-1 (negative control) and different PC cell lines (PC3, LnCap, DU145) up to 120 min. Biodistribution studies were developed in normal Swiss and in PC3 tumor-bearing Nude mice, up to 4, 24 and 48 h p.i. (n = 4), using a high purity germanium detector (HPGe) (Canberra). SPECT-CT (Mediso) images were carried out the same times that biodistributions studies.

Results:
Radiochemical purity of 177Lu-DOTA-Axh-(DLys6)-LHRH was 98.98 ± 1.42 %, with good hydrophilicity (Log D = - 1.72 ± 0.11) being stable in different in vitro analyzed conditions. Relevant binding affinity and specificity of 177Lu-DOTA-Ahx-(D-Lys6)-LHRH) were observed in different PC cell lines (LnCap, PC3, Du-145) showed relevant membrane-bound results in all of them, with low internalization. We did not observe significant binding affinity in the RWPE-1 cell line with this tracer. Biodistribution and SPECT/CT imaging in normal Swiss mice and PC3 tumor-bearing nude mice revealed high kidney, liver, gastrointestinal uptake and also relevant tumor uptake (tumor-to-muscle ratios of 2.40 ± 0.25, 4.87 ± 0.48 and 3.77 ± 0.85 at 4, 24 and 48 h, respectively).

Conclusions:
Our results suggest that 177Lu-DOTA-Ahx-(D-Lys6)-LHRH represents a potential theragnostic agent for PC.

Reference

1. Leslie SW, Soon-Sutton TL, Sajjad H, Siref LE. Prostate Cancer. 2022 StatPearls; 2022..
2. Hao D, Sun L, Hu X, Hao X. 99mTc-LHRH in tumor receptor imaging. Oncol Lett. 2017;14(1):569-578.
3. Alfaya L, Camacho, X, Cabrera M, et al "Hormona liberadora de la hormona luteinizante (LHRH): potencial agente de oncología molecular". Salud Militar. 2018, 37(2):10-26.
4. Camacho X, Cabrera M, Alfaya L, et al. Development and evaluation of 99mTc-labeled LHRH peptide as potential tumor imaging agent. Journal of Nuclear Medicine. 2017, 58 (1):1024

Poster Presentation

Disclosures: The authors have disclosed no financial interest.

238-Targeting Tumor-Associated Glycans Lewisa/c/x and sialyl-di-Lewisa for Near-infrared Fluorescent (NIRF) Intraoperative Imaging of Pancreatic Ductal Carcinoma: a Preclinical Evaluation

Presenter: Ruben Houvast, Leiden University Medical Center (LUMC)

Ruben Houvast[1], Maurice van Duijvenvoorde[1], Vincent Sier[1], Timo Schomann[1], Mireille Vankemmelbeke[2], Lindy Durrant[3], Bert Bonsing[1], Sven Mieog[4], Peter Kuppen[5], Stijn Crobach[6], Alexander Vahrmeijer, Cornelis F. Sier[7]

[1]Leiden University Medical Center (LUMC), Leiden, Zuid-Holland, Netherlands
[2]Scancell, Nottingham, United Kingdom
[3]University of Nottingham, Nottingham, United Kingdom
[4]Leiden University Medical Center (LUMC), leiden, z-h, Netherlands
[5]Leiden University Medical Center (LUMC), Netherlands
[6]Leiden University Medical Center (LUMC), Leiden, Netherlands
[7]Leiden University Medical Center (LUMC), Leiden, NL, Netherlands

Tumor-targeted molecular imaging may overcome current limitations in preoperative and intraoperative diagnosis and delineation of tumor tissue. Aberrant glycosylation is a hallmark of cancer, potentially providing a new set of tumor-specific targets for molecular imaging (1, 2). Targeting of aberrant glycans on cancer-associated proteins present on the cell membrane may offer significant advantages for molecular imaging over traditional protein targeting, considering their strongly amplified, tumor-specific presence on the outermost layer of the cell and low abundance on healthy tissues (2). Tumor-associated glycans Lewis$^{a/c/x}$ (Le$^{a/c/x}$) and sialyl-di-Lewis^{a} (sdi-Le^{a}), as described by Chua et al. and Tivadar et al., respectively, are highly expressed on gastrointestinal tumors including pancreatic, gastric, colon and rectal cancer, along with a limited expression on healthy surrounding tissues (3, 4). Previous research by our group showed the high potential of Le$^{a/c/x}$ and sdi-Lea as biomarkers for pancreatic ductal adenocarcinoma (PDAC) imaging (5). Subsequently, chimeric (mouse/human) monoclonal antibodies CH88.2 and CH129 were developed to target Le$^{a/c/x}$ and sdi-Le^{a}, respectively. In a proof-of-concept study, we showed that the Le$^{a/c/x}$-targeting tracer CH88.2-800CW allowed clear visualization of human colon carcinoma and pancreatic ductal adenocarcinoma (PDAC) xenografts in immune-compromised mice using near-infrared fluorescence (NIRF) imaging (6). However, the potential of CH129 as a targeting vehicle for NIRF imaging is unknown. The current study therefore provides a comprehensive preclinical evaluation and comparison of CH88.2-800CW and CH129-800CW for NIRF imaging of PDAC, facilitating the clinical translation of Le$^{a/c/x}$ and sdi-Le^{a} targeted NIRF imaging agents.
CH88.2 and CH129 mAbs were conjugated to the NIRF dye IRDye 800CW. Binding of CH88.2-800CW and CH129-800CW was evaluated on multiple human pancreatic cancer cell lines. Subsequently, mice with subcutaneous or orthotopic BxPC-3_luc2 tumors were intravenously injected with 1 nmol (150 µg) of CH88.2-800CW, CH129-800CW or negative control tracer CD20-800CW (chimeric mAb rituximab). Mice were imaged daily until 1 week post injection (subcutaneous models) or at 4 days post injection (orthotopic models) using the preclinical PEARL and clinical Artemis NIRF camera systems. After sacrificing the mice, tumors and organs were resected after which tracer uptake was evaluated ex vivo using the PEARL NIRF imager.
CH88.2-800CW and CH129-800CW showed high binding on BxPC-3_luc2 cells. Administration of CH88.2-800CW and CH129-800CW to BxPC-3_luc2 tumor-bearing mice demonstrated clear tumor delineating fluorescence signal and high tumor-to-background ratios (TBRs) compared to CD20-800CW, suggesting specific CH88.2 and CH129 tumor binding. Next, the NIRF imaging potential of both tracers was evaluated in clinically more relevant orthotopic PDAC models. Using the clinical Artemis NIRF imager, orthotopic PDAC tumors could be clearly delineated with mean TBRs of 2.5±0.3 and 2.9±0.4 at 4 days post injection for CH88.2-800CW and CH129-800CW, respectively, providing high-contrast tumor localization (Figure 1). Ex vivo analysis revealed that fluorescent signals in all tumor lesions were higher compared to healthy organ signals, including the liver and kidneys.
Our study showed that Le$^{a/c/x}$ and sdi-Le^{a}-targeting tracers CH88.2-800CW and CH129-800CW are highly promising agents for NIRF imaging of PDAC. Through this research, we pave the way for a clinical translation of CH88.2-800CW and CH129-800CW, which could improve real-time intraoperative delineation of PDAC and clinical outcomes.

Reference
1. Fuster MM, Esko JD. The sweet and sour of cancer: glycans as novel therapeutic targets. Nat Rev Cancer. 2005;5(7):526-42.
2. Houvast RD, Vankemmelbeke M, Durrant LG, Wuhrer M, Baart VM, Kuppen PJK, et al. Targeting Glycans and Heavily Glycosylated Proteins for Tumor Imaging. Cancers (Basel). 2020;12(12).
3. Chua JX, Vankemmelbeke M, McIntosh RS, Clarke PA, Moss R, Parsons T, et al. Monoclonal Antibodies Targeting LecLex-Related Glycans with Potent Antitumor Activity. Clin Cancer Res. 2015;21(13):2963-74.
4. Tivadar ST, McIntosh RS, Chua JX, Moss R, Parsons T, Zaitoun AM, et al. Monoclonal Antibody Targeting Sialyl-di-Lewis(a)-Containing Internalizing and Noninternalizing Glycoproteins with Cancer Immunotherapy Development Potential. Mol Cancer Ther. 2020;19(3):790-801.
5. Houvast RD, Thijse K, Groen JV, Chua J, Vankemmelbeke M, Durrant LG, et al. An Immunohistochemical Evaluation of Tumor-Associated Glycans and Mucins as Targets for Molecular Imaging of Pancreatic Ductal Adenocarcinoma. Cancers (Basel). 2021;13(22).
6. Houvast RD, Baart VM, Bhairosingh SS, Cordfunke RA, Chua JX, Vankemmelbeke M, et al. Glycan-Based Near-infrared Fluorescent (NIRF) Imaging of Gastrointestinal Tumors: a Preclinical Proof-of-Concept In Vivo Study. Mol Imaging Biol. 2020;22(6):1511-22.

Poster Presentation

Disclosures: The authors have disclosed no financial interest.

239-Body heat activated near-infrared luminescent nanoprobes for in vivo optical imaging of head and neck cancer

Presenter: Jung-Jae Lee, University of Colorado Denver

Jung-Jae Lee[1], Kyoung Nan Kim[1]

[1]University of Colorado Denver, Denver, CO

Introduction:
The main treatment of Head and Neck cancer (HNC) is surgery but surgeons still rely on visual inspection and palpation because current preoperative imaging modalities (e.g., CT, MRI, and PET) lack sufficient resolution to detect microscopic disease - larger than 0.5–1cm to be detectable. Thus, near-infrared fluorescence (NIR FL) probes are widely accepted in fluorescence-guided surgery (FGS) due to low autofluorescence and reduced light scattering, but their limited tissue penetration is still an obvious handicap for clinical translation. Recently, luminescence imaging shows deeper penetration into tissues in vivo with an excellent signal-to-noise ratio (SNR), but the requirement for substrates (e.g., D-luciferin) is an important drawback and current luminescence systems predominantly emit visible light, whose penetration through heterogeneous matrices is limited. Here, we developed novel NIR luminescent nanoprobes and our results in mice clearly demonstrated that luminescent imaging successfully identifies HNC in the orthotopic models: the NIR chemiluminescence (CL) can penetrate deeper into tissues (>4 cm below surface which is several times deeper than can be achieved using planar fluorescence imaging that is currently used) and yield more accurate CL imaging in vivo with an excellent SNR. The nanoprobes are unique because the CL is thermally activated: thus, probes can be stored at low temperature, and their CL is emitted only when they are warmed to body temperature (i.e., a chemical or electrical stimulus is not required). The nanoprobes will significantly advance the combined use of luminescent imaging, to provide improved detection of micrometastatic disease, reduce morbidity of surgery by avoiding unnecessary removal of normal tissue, and serve as a prognostic and predictive biomarker of response to therapy which can guide management decisions for cancer patients.

Materials and Methods:
Chitosan has recently attracted much attention for biomedical applications such as tissue engineering and drug delivery systems due to their high biocompatibility, biodegradability, and bioconjugatable functionality. Here, we have fabricated thermally activated chemiluminescent (CL) and fluorescent (FL) chitosan nanoparticles (CFL CNPs) incorporating NIR dyes and singlet oxygen release agents via carbodiimide chemistry.

Results and Discussion:
The figure shows the results of a typical whole-body imaging experiment with chemiluminescence and fluorescence pixel intensity maps of anesthetized mice at 3h and 24h after tail vein injection of CNPs. There is clear evidence for selective accumulation of CNP and FA-CNP in Head and Neck Cancer (HNC) through FL/CL modes, and the CL from HNC exhibited significantly high intensity without background noise (note that most luciferins have relatively short half-lives of just a few hours). The mice were then sacrificed after 48h and their tissues harvested for ex vivo analysis of probe biodistribution. FL intensity images of the excised tissues confirmed the relatively high tumor selectivity of CNPs. In summary, CNPs can selectively accumulate in HNC in the orthotopic animal model and the results suggest that the floate-conjugated CNP (FA-CNP) more efficiently targets the tumor compared with the non-targeted CNP.

Conclusions:
These results highlight an attractive feature of dual modality probes that enable in vivo optical imaging of cancer. In details, the NIR CFL CNPs can image relatively deep tumor sites in vivo using chemiluminescence mode and subsequently, analyze the microscopic targets within thin histopathology using fluorescence mode. Furthermore, CFL CNPs can be employed for image-guided surgery because current fluorescence-guided surgery images tumors only less than 0.2 cm from the surface but under chemiluminescence mode, CFL CNP is able to identify the deep sites (> 4 cm) within several minutes.

Poster Presentation

Disclosures: The authors have disclosed no financial interest.

240-Prostate-Specific Membrane Antigen Targeted Polymers Enable Improved Tumoral Nanodrug Delivery

Presenter: Niranjan Meher, University of California, San Francisco

Niranjan Meher[1], Gary Ashley[2], Anil P. Bidkar[3], Suchi Dhrona[1], Cyril Fong[4], Shaun Fontaine[2], Denis R. Beckford Vera[1], David M. Wilson[1], Youngho Seo[1], Daniel Santi[2], Henry VanBrocklin[1], Robert R. Flavell[1]
[1]University of California, San Francisco, San Francisco, CA

[2]San Francisco, CA
[3]University of California, San Francisco, San Francisco, California
[4]University of California San Francisco, San Francisco, CA

Background:
The enhanced permeability effect (EPR) has been widely employed for the delivery of nanomedicines to cancer. However, the EPR

effect is heterogeneous and in many cases the delivery to tumors is low.[1,2] Active tumor targeting of nanodrugs has the potential to improve imaging contrast and therapeutic efficacy *in vivo*.[3]

Methods:
To evaluate the targeted deep-tumor uptake of star-PEG nanodrugs beyond EPR mediated tumor accumulation, we designed and synthesized three star-PEG nanodrugs without or with different number of PSMA targeting ACUPA ligands (Fig 1a). The radiometal chelator deferoxamine B (DFB) was also tethered to the nanodrug conjugates for ^{89}Zr labelling and small animal PET imaging. The radiolabeled nanodrugs were evaluated *in vitro* and *in vivo* using PSMA+ PC3-Pip and PSMA- PC3-Flu cell lines and xenografts, respectively.

Results:
The ^{89}Zr labeled star-PEG showed significantly higher *in vitro* binding affinity with a lower dissociation constant (k_d) in PC3-Pip cells with increasing number of ACUPA ligands per molecule (Fig 1b). The *in vivo* PET images and organ biodistribution of mice bearing PSMA(+) PC3-Pip and PSMA(-) PC3-Flu dual xenografts demonstrated around 5.75±0.74 ID% tumor uptake for the non-targeted nanodrug ([^{89}Zr]PEG-DFB4) as a result of the EPR effect (Figure 1c-d). An enhancement in the PSMA positive PC3-Pip tumor uptake was seen in the ACUPA labelled polymers (9.64±0.87 for [^{89}Zr]PEG-DFB3-ACUPA1, 6.69±1.24 for [^{89}Zr]PEG-DFB1-ACUPA3). The autoradiography images showed improved deep-tumor penetration of targeted nanodrugs selectively in PSMA(+) PC3-Pip xenograft (Fig 1e). In contrast, peripheral low tumor accumulation only was observed for the non-targeted nanodrugs in both PSMA(+) PC3-Pip and PSMA(-) PC3-Flu xenografts.

Conclusions and Future Directions:
These data demonstrated a significant improvement in the targeted delivery of nanodrugs with deep-tumor penetration in the presence of PSMA targeting ACUPA ligands (Scheme 1). These PSMA targeted multivalent nanodrugs with high tumor to background ratio could be potentially employed in therapeutic applications.

Reference

1. Denis R. Beckford Vera, Shaun D. Fontaine, Henry F. VanBrocklin, Brian R. Hearn, Ralph Reid, Gary W. Ashley, and Daniel V. Santi, PET Imaging of the EPR Effect in Tumor Xenografts Using Small 15 nm Diameter Polyethylene Glycols Labeled with Zirconium-89. Mol Cancer Ther., 2020,19, 673–679.
2. Jeroen A.C.M. Goos, Andrew Cho, Lukas M. Carter, Thomas R. Dilling, Maria Davydova, Komal Mandleywala, Simon Puttick, Abhishek Gupta, William S. Price, John F. Quinn, Michael R. Whittaker, Jason S. Lewis, Thomas P. Davis, Delivery of polymeric nanostars for molecular imaging and endoradiotherapy through the enhanced permeability and retention (EPR) effect. Theranostics, 2020, 10, 567-584.
3. Thomas S.C. Ng, Michelle A. Garlin, Ralph Weissleder, Miles A. Miller, Improving nanotherapy delivery and action through image-guided systems pharmacology. Theranostics, 2020, 10, 968-997.

Poster Presentation

Disclosures: The authors have disclosed no financial interest.

241-A Single Dose of JAM-A-Targeted Theranostic Agent Affects Proliferation in the Human Breast and Prostate Cancer Xenografts in Vivo

Presenter: Ethan Walker, Case Western Reserve University

Ethan Walker[1], Soumya Turaga[2], Xinning Wang[3], Ramamurthy Gopalakrishnan[1], Sanjeev Shukla[4], Justin Lathia[2], James Basilion[1]

[1]Case Western Reserve University, Cleveland, OH
[2]Lerner Research Institute, Cleveland, Ohio
[3]Case Western Reserve University, Beachwood, OH
[4]University of Florida, Jacksonville, Florida

Introduction:
Prostate and breast cancer are the most prevalent primary malignant human tumors globally. Prostatectomy and breast conserving surgery remain the most common definitive treatment options for the >500,000 men and women per year newly diagnosed with localized prostate and breast cancer in the US [1,2]. Morphological examination is the mainstay of diagnosis, but margin under-sampling of the excised cancer tissue may lead to local recurrence [3,4]. There still exists a clinical need for targeted optical imaging probes that could rapidly and globally visualize cancerous tissues during the surgical procedure.

Methods:
Elevated expression of junctional adhesion molecule-A (JAM-A) on tumor cells and its multiple cancer protumorigenic activity make the JAM-A a candidate for molecular imaging [5,6]. Previously a near-infrared imaging agent, which employed an anti-JAM-A monoclonal antibody (mAb) conjugated to phthalocyanine IR700 dye, was synthesized (*Probe*) and used to identify and visualize heterotopic human prostate and breast cancer mouse xenografts *in vivo* [7]. Here the same model was used to assess the potential for anti-tumor effects of the *Probe*. Briefly, each group of animals harboring human breast (MDAMB-231) or human prostate (PC3pip) tumors was randomly divided into four groups and treated as follows: 1) *Probe* alone (20-µg), 2) *Probe competition*, probe (20-µg) and JAM-A mAb (40-µg) were mixed immediately before i.v. injections, 3) *Norm Ab*, normal non-specific mAb/IR700 conjugates (20-µg), and 4) *IR700* alone (5.0-mg/mL). To assess the effect of the treatment on cancerous tissue, tumors were collected, snap-frozen, sectioned (10-µm) and stained for Cleaved Caspase-3 (Casp-3), minichromosome maintenance protein-2 (MCM2), and phosphorylated-histone H3 (Ser10) markers. Presence, if any, of IR700 in the tumor tissue after treatment was determined by fluorescent microscopy (Leica) in consecutive sections of the tumors.

Results:
The i.v. injected *Probe* confirmed the detection of prostate and breast cancerous tissue by fluorescence imaging *in vivo* (Maestro In Vivo Imaging System, PerkinElmer). After 48-hr of circulation in the mouse a single dose of *Probe* reduced the number of proliferating ($MCM2^+$) and mitotic ($H3^+$) cancer cells *in vivo* as compared to controls. In parallel and in contrast to all controls, the levels of accumulation of the IR700 fluorescence and expression of apoptotic marker (Casp-3) were strongly upregulated in the cancerous tissue only after treatment with Probe.

Conclusion:
This agent demonstrates theranostic characteristics to image the extent of prostate and breast cancer *in vivo*, to suppress cancer cell proliferation, and to set into motion apoptotic machinery 48-hr after a single systemic dose delivery.

Reference

1. S.B. Giordano and W. Gradishar, Breast cancer: updates and advances in 2016, Curr. Opin. Obstet. Gynecol. 29 (2017) 12–17.

2. B.F. Hankey, et al., Cancer surveillance series: interpreting trends in prostate cancer –part I: evidence of the effects of screening in recent prostate cancer incidence, mortality, and survival rates, J. Natl. Cancer Inst. 91 (1999) 1017–1024.
3. G.P. Swanson and J.W. Basler. Prognostic factors for failure after prostatectomy, J. Cancer 2 (2011) 1–19.
4. M. Han, et al., Biochemical (prostate specific antigen) recurrence probability following radical prostatectomy for clinically localized prostate cancer. J. Urol. 169 (2003) 517–523.
5. J.D. Lathia, et al., High-throughput flow cytometry screening reveals a role for junctional adhesion molecule a as a cancer stem cell maintenance factor. Cell reports 6 (2014) 117-129.
6. A.G. Alvarado, et al., Coordination of self-renewal in glioblastoma by integration of adhesion and microRNA signaling. Neuro Oncol. 18 (2016) 656-666.
7. E. Walker, et al., Development of near-infrared imaging agents for detection of junction adhesion molecule-A protein. Transl. Oncol. 14 (2021) 101007.

Poster Presentation

Disclosures: The authors have disclosed no financial interest.

242-Non-invasive bioluminescent imaging of kinase inhibition in living animals

Presenter: Yan Wu, Stanford University

Yan Wu[1], Yichi Su[1], Michael Lin[1], Thomas A. Kirkland[2], Joel R. Walker[3]

[1]Stanford University, Stanford, CA
[2]Promega, Madison, WI
[3]Promega, San Luis Obispo, CA

Kinases are attractive drug targets in neurodegenerative diseases and brain tumors. However, the inability to predict brain concentrations of drugs from their blood concentrations, due to the blood-brain barrier (BBB), presents a major barrier to the efficient testing of kinase inhibitors for these nervous system diseases. [1-4] Existing methods of evaluating the BBB-permeability of a candidate drug require animal sacrifice and biochemical analysis or radioactive labeling, which are expensive, slow, and labor-intensive. [5-6] A faster and less expensive approach to evaluating drug activity in the brain would greatly aid the discovery of effective brain-permeant kinase inhibitors. We describe a novel genetically encoded kinase-modulated bioluminescent indicator (KiMBI) that produces light in response to kinase inhibition. As a first example, we successfully created a KiMBI for ERK inhibition with a 10-fold response amplitude. ERK KiMBI expressed in the brain successfully differentiated between brain permeant and impermeant inhibitors of the MEK-ERK pathway. In both subcutaneous and intracranial tumor xenograft mouse models, ERK KiMBI revealed real-time drug inhibition of the hyperactivated MEK-ER pathway in these cancer cells. Finally, by longitudinal imaging of KiMBI signals, we could assess the kinetics of kinase inhibition following a single-dose injection, a task that would be highly resource-intensive using traditional animal sampling approaches. In summary, we developed KiMBI as a novel method for rapid and non-invasive visualization of the efficacy of kinase inhibitors in living subjects. KiMBI should greatly facilitate the discovery of effective treatments for cancers driven by dysregulated kinase signaling. KiMBIs should provide a generalizable and easy method to rapidly assess the efficacy and pharmacokinetics of kinase inhibitors in the brains of living animals.

Reference

1. L. K. Chico, L. J. Van Eldik, D. M. Watterson, Targeting protein kinases in central nervous system disorders. Nat Rev Drug Discov 8, 892-909 (2009).
2. T. P. Heffron, Challenges of developing small-molecule kinase inhibitors for brain tumors and the need for emphasis on free drug levels. Neuro Oncol 20, 307-312 (2018).
3. V. A. Levin et al., CNS Anticancer Drug Discovery and Development Conference White Paper. Neuro Oncol 17 Suppl 6, vi1-26 (2015).
4. M. D. Prados et al., Toward precision medicine in glioblastoma: the promise and the challenges. Neuro Oncol 17, 1051-1063 (2015).
5. L. Di, E. H. Kerns, G. T. Carter, Strategies to assess blood-brain barrier penetration. Expert Opinion on Drug Discovery 3, 677-687 (2008).
6. A. Traxl et al., Inhibition of ABCB1 and ABCG2 at the Mouse Blood-Brain Barrier with Marketed Drugs To Improve Brain Delivery of the Model ABCB1/ABCG2 Substrate [. Mol Pharm 16, 1282-1293 (2019).

Poster Presentation

Disclosures: The authors have disclosed no financial interest.

243-Imaging analysis of cell-in-cell structures between cancer and NK cells is associated anti-cancer drug resistance

Presenter: Eun Hee Han, Korea Basic Science Institute (KBSI)

Eun Hee Han

Korea Basic Science Institute (KBSI), Cheongju-si, Chungcheongbugdo, South Korea

The cell-in-cell (CIC) phenomenon is known to lead to cell death, and heterotypic CIC structures formed of cancer and immune cells have been observed in tumor tissues. These structures are commonly observed in the tissues of patients with malignant tumors allowing immune evasion. Although many studies have suggested that heterotypic CIC events are involved in the development and progression of multiple tumors, an association with anticancer drug resistance have not been reported. We aimed to assess the feasibility of using heterotypic CICs as a functional biomarker to predict drug resistance. For this, heterotypic CIC structures formed of cancer and NK cells were characterized by microscopic imaging and flow cytometry analysis. NK cells and cancer cells were co-cultured, and CIC and non-CIC populations were separated using a cell sorter. After treatment with anti-cancer drugs, cancer cells that formed heterotypic CICs showed a higher resistance to anti-cancer drugs, including docetaxel, etoposide, doxorubicin, and gemcitabine, than non-CIC cancer cells. We also observed the formation of more CIC structures in cancer cells treated with anticancer drugs than in the non-treated group. Our results confirm the association between heterotypic CIC structures and anticancer drug resistance in CICs formed from NK and cancer cells. These results suggest a novel mechanism underlying immune evasion in heterotypic CIC cancer cells and provide novel insights into the anticancer drug resistance of cancer cells.

Poster Presentation

Disclosures: The authors have disclosed no financial interest.

244-Accumulation of 18F-FDG in the liver in Metabolic Associated Fatty Liver Disease Detected on PET/MRI: A Chinese Population Study

Presenter: Zhaoting Meng, Shanghai Universal Medical Imaging Diagnostic Center

Zhaoting Meng[1], Dandan Zhu[2], Mu Lin[2], Xin Gao[3]

[1]Shanghai Universal Medical Imaging Diagnostic Center, Shanghai, China
[2]Shanghai, China
[3]Universal Medical Imaging Diagnosis Center, Shanghai, Please select an option below, China

Objective:
Metabolic associated fatty liver disease (MAFLD) is a more recent concept developed from non-alcoholic fatty liver disease (NAFLD) that clearly indicates metabolic dysfunction is the primary cause of the type of fatty liver [1]. Prior studies have found that liver steatosis and blood glucose levels can influence ^{18}F-FDG uptake in the liver, a reference tissue used for semi-quantitative assessment [2-4]. However, the results are inconsistent or contradictory, and studies on the hepatic ^{18}F-FDG uptake in patients with MAFLD are still lacking. This study is designed to analyze the hepatic ^{18}F-FDG uptake of the Chinese population with MAFLD and its affecting factors with integrated PET/MRI.

Methods:
A retrospective analysis was conducted on 203 patients who accepted whole-body PET/MRI scanning as well as Liverlab scanning at our center between July 2020 and December 2021. Meanwhile, data of height, body weight, fasting blood glucose (GLU), aspartate aminotransferase (AST), alanine aminotransferase (ALT), alkaline phosphatase (ALP), glutamine transferase (GGT), high-density lipoprotein (HDL), triglyceride (TG), C-reactive protein (CRP) were recorded. According to the MAFLD diagnostic criteria [1], the patients were divided into MAFLD group and non-MAFLD group. The proton density fat fraction (PDFF) and R2water of the right lobe of the liver were calculated automatically. The maximum and average standard uptake value (SUV_{max} and SUV_{mean}), the maximum and average standard uptake value of lean body (SUL_{max} and SUL_{mean}) were obtained on PET images with the same ROI. SPSS v25.0 was used for statistical analysis.

Results:
There were statistically significant differences between MAFLD and Non-MAFLD groups in terms of gender, age, BMI, GLU, PDFF, R2water, AST, ALT, GGT, HDL, TG, CRP, and SUV_{max} ($P < 0.05$). There were no differences in ALP, SUV_{mean}, SUL_{max}, or SUL_{mean} between the two groups ($P>0.05$). SUV_{max} was significantly correlated with BMI(r=0.304), GLU(r=0.174), PDFF(r=0.185), R2water(r=0.177) and ALT(r=0.177) ($P < 0.05$). Stepwise regression analysis showed that BMI had a significant positive effect on SUV_{max}.

Conclusions:
In the Chinese population with MAFLD, there is a significant increase in hepatic uptake of ^{18}F-FDG, and BMI is a major factor in this process.

Reference

1. Eslam M, Newsome PN, Sarin SK, et al. A new definition for metabolic dysfunction-associated fatty liver disease: An international expert consensus statement[J]. J Hepatol, 2020, 73(1):202-209.
2. Dunford A, Keramida G, Singh N, et al. Relationship between regional hepatic glucose metabolism and regional distribution of hepatic fat. Nucl Med Commun. 2019;40(3):212-218.
3. Keramida G, Potts J, Bush J, et al. Hepatic steatosis is associated with increased hepatic FDG uptake. Eur J Radiol. 2014;83(5):751-755.
4. Pak K, Kim SJ, Kim IJ, et al. Hepatic FDG Uptake is not Associated with Hepatic Steatosis but with Visceral Fat Volume in Cancer Screening. Nucl Med Mol Imaging. 2012;46(3):176-181.

Poster Presentation

Disclosures: The authors have disclosed no financial interest.

245-Role of brain SPECT on evaluation of treatment effect of Qigong meditation on brain flow and function among patients with obsessive disease

Presenter: Fariba Saddadi, Asia Nuclear Medicine Center

Fariba Saddadi[1], Reza Shokouhizadeh[2], Faranak Saddadi[3]

[1]Asia Nuclear Medicine Center, Tehran, Tehran, Iran
[2]Asia Nuclear Medicine Center, Tehran, Iran
[3]Vancouvere

Background and Aim:
Qigong practice is a kind of walking meditation with doing deep breathing and some gentle movements that shows it is good for health and it became very popular in many countries in the world, This dynamic meditation is back to 5000 years ago, that originate mainly at China and little by little became more known and widespread among other countries, including Iran. Nuclear medicine has been showed as a good and reliable imaging modality for detection of any changes in physiology of human body and therefore is a good method and useful device to evaluate any changes in body perfusion and function, specially many disease can be recognized very soon before appearance of any clinical sign and symptoms.
We decided to have a survey in this regard and to find the essential qigong effect on patients with obsessive disease by brain SPECT. We chose the obsessives patients because, many of this disease still remained unknown. This clinical symptoms sometimes cannot be differentiated correctly and consequently their therapy encountered with some difficulty.
Obsessions is more means as a psychological and behavioral disorders and it seems the prevalence of this mental disease is increasing. Therapy for those patients is mandatory. But it always therapy is conservative and many of them went for some alternative therapy like yoga, meditation, Taichi,chigong.etc.
For behavioural/ mental disease we almost always prescribe to do Shi ba fa Qigong or Yi jin jing qigong cause of its simplicity and easy acceptance of patients and asked them do 2-3 times a week for almost 2-3 months.

Material and Methods:
12 patients with obsessive disease, 10 female and 2 male with age range 20-72 years old were selected and enrolled for this study. The main criteria for selection of those patient is their cooperation ability and willingness for doing qigong.
Two series of images with Tc99m- ethylene-diamine-tetra-acetic acid Brain SPECT were obtained for each patient.

First scan named pre-qigong and the second scan was obtained after practicing Yi ji jing qigong that asked them to do this meditation for 2-3 months.
All of those brain scans series was performed with Philips ADAC gamma camera with the same imaging conditions as standard protocols, by injection 25 mCi Tc99m-ECD, for all pre-qigong and post-qigong images and compared to find any changes in brain flow and function if any.
The percent value of tracer uptake for both right and left brain cortex for each lobes and also brain nucleus, basal ganglias were evaluated by drawing region of interest (ROI)

Results:
The result shows the cortical perfusion value in pre qigong scan was un-even with mean 0.62 percent of count/pixels activity in temporal, frontals and parietal area.
10/12 patients has asymmetry of tracer activity in their basal ganglias as the same as their deterioration on cortical activity, that more seen in frontal, temporal and parietal.
Patient asked doing Yi jin jing qigong for 2-3 months and the post qigong scan shows a definite reduction on that asymmetry of tracer uptake more in cortical and more seen harmonized activity on frontal and parietal cortical tissue.
Scan result shows, the perfusion/ function of brain cortex became more even and harmonized as a 0.89 percent of mean count/pixels without asymmetry of activity, It means after Yi jin jing, the brain tissue reach to more balance rise up to 1.3 times. The same value occurred for their basal ganglia as more activity means better perfusion and function.

Conclusion:
Nuclear medicine has strong role to evaluation of brain perfusion and function and can predict correctly the treatment response it seems that qigong also is a promising therapy (alternative/complementary) for patients with behavioral disease and nuclear medicine can ascertain the value of such of those treatments.

Reference

1. Wuji Qigong and secret of immortality by stephen benett elliot, International College of Medical Qigong Specializing in Chinese Energetic Medicine brain statistic qigong Dynamic cycles of cognitive and brain development .measuring growth in mind,brain and education, Kurt W. Fischer.A M Batrro, PP 127-150, Cambridge UK, university press (2008).

Poster Presentation

Disclosures: The authors have disclosed no financial interest.

246-Self-Cascade Nanozyme as A pH/GSH-Responsive Ferroptosis Inducer for Tumor Radiosensitization Therapy

Presenter: Qinghe Wu, Shanghai Jiao Tong University

Qinghe Wu[1], Pengli Zhang[1], Mengfei Hou[1], Yifei Jiang[2], Weiqin An[3], Guoping Jia[3], Meng Li[3], Chunfu Zhang[1]

[1]*Shanghai Jiao Tong University, Shanghai, Shanghai, China*
[2]*Shanghai Jiao Tong University, China*
[3]*Shanghai Jiao Tong University*

Introduction:
Ferroptosis serves as a vital role in tumor therapy as it can overcome the resistance of tumor cells to apoptosis [1]. Nanozymes with Fenton/Fenton-like reaction properties are commonly used to induce tumor cells ferroptosis by generating reactive oxygen species (ROS), but its efficacy is substantially neutralized by the insufficient H_2O_2 and excessive GSH in the tumor microenvironment (TME) [2]. Herein, a self-cascade nanozyme consisting of BSA-enclosed Au nanocores and ultrasmall MnO_2 nanodots (BAM) is fabricated. BAM is first found to have glucose oxidase (GOx)-mimic activity. Once accumulated in tumors, BAM can 1) self-supply H_2O_2 by catalyzing endogenous glucose, followed by the production of cytotoxic HO·; 2) efficiently deplete GSH to inactivate GPX4, thus leading to the upregulation of lipid peroxide (LPO) and tumor cells ferroptosis. Combined with the relieved hypoxia and sensitization of Au, ferroptosis-stressed tumor cells become exceptionally vulnerable to X-ray radiation, and radiotherapy completely inhibit the tumor progression.

Materials and Methods:
BAM was prepared by first synthesis of BSA-coated Au nanoclusters (BA), followed by in situ reduction of $KMnO_4$ in BSA corona to generate MnO_2 nanodots surrounding Au nanoclusters. The enzyme-mimicking property of BAM was assessed by commercial detection kits. The pH/GSH-responsive magnetic resonance imaging (MRI) capability of BAM was tested by dispersing BAM into buffer solutions (pH = 6.4, 7.4) with or without GSH. The ferroptosis-inducing capacity of BAM was evaluated by assessing the change of intracellular ROS, GSH and LPO level after incubating 4T1 tumor cells with BAM. The TME-responsive MRI was performed to monitor the tumor-targeting behavior of BAM. The tumor inhibition rate and sensitization of BAM to tumor radiotherapy were investigated on 4T1 tumor-bearing mice with X-ray radiation (6 Gy) after intravenous injection of BAM.

Results and Discussion:
The synthesized BAM has an ultrasmall size (< 5 nm) and unique structure with Au nanoclusters in center and MnO_2 nanodots in surrounding. BAM exhibited fascinating GOx-mimic activity and had excellent thermostability. The relative GPX4 level in 4T1 cells decreased to 48% after treated with BAM (100 mg Mn mL^{-1}) for 12 h. After incubation with BAM, the intracellular ROS and LPO level was upregulated remarkably, and mitochondria were shrunken with dense membranes, indicating the ferroptosis induction in 4T1 cells. BAM exhibited a high tumor targeting efficiency (7.8 %ID/g at 6 h after injection). As a result, the tumor growth was completely inhibited after the mice were treated with BAM + X-ray radiation.

Conclusion:
Our results demonstrated BAM had self-cascade enzymatic property to self-supply H_2O_2, generate HO· and deplete GSH to upregulate intracellular LPO level, efficiently inducing tumor cells ferroptosis. In synergy with the tumor hypoxia alleviation and sensitization of Au, radiotherapy thoroughly inhibited the tumor growth. Overall, the self-cascade nanozyme described here holds great potential as an efficient ferroptosis inducer for sensitization of tumor radiotherapy.

Reference

1. G. Lei, et al., The role of ferroptosis in ionizing radiation-induced cell death and tumor suppression, Cell Res. 30 (2) 146-162.
2. Z. Shen, J, et al., Emerging Strategies of Cancer Therapy Based on Ferroptosis, Adv. Mater. 30 (12) e1704007.

Poster Presentation

Disclosures: The authors have disclosed no financial interest.

247-Amyloid pathology induces the deterioration of systemic neurotransmission; molecular imaging study in APPswe/PS2

Presenter: SE JONG OH, Korea Institute of Radiological and Medical Sciences (KIRAMS)

Se Jong Oh[1], Jae Yong Choi[2]

[1]Korea Institute of Radiological and Medical Sciences (KIRAMS), Seoul, South Korea
[2]Korea Institute of Radiological & Medical Sciences, Seoul, South Korea

Purpose:
Alzheimer's disease (AD) is the most common neurodegenerative disorder.[1] The distinct mechanism of AD is still unclear, and no appropriate treatment strategy has not been developed. Present study aimed to systemically elucidate the effect of Aβ pathology on the major neurotransmission system using positron emission tomography (PET).

Methods:
APPswe/PS2 transgenic mice (21 months of age, AD, n=6) and wild-type mice (WT, n=6) underwent PET and magnetic resonance spectroscopy (MRS). Firstly, ^{18}F-FDG and ^{18}F-florbetaben PET was obtained to elucidate the neuronal integrity and amyloid pathology, respectively. Then, ^{18}F-FPEB and ^{18}F-FMZ PET data were acquired to evaluate the excitatory-inhibitory neurotransmission system. To measure dopamine system, ^{18}F-fallypride PET was performed. Thereafter, MRS experiment was performed. Finally, animals were sacrificed, the $A\beta_{42}$ levels in the brain were also confirmed by immunohistochemical analysis. PET images were analyzed to compute standardized uptake value (SUV) in the brain regions.

Results:
Amyloid PET imaging revealed that radioactivity was 6-12% higher in the AD group than in the WT group, which was validated by IHC. In the cortical and limbic areas, the AD group showed a 25–27% decrease and a 14–35% increase in the glutamatergic and the GABAergic system compared to the WT group. The dopaminergic system in the striatum of the AD group had a 29% decreased striatal uptake compared to that of the WT group. MRS studies also showed a significant reduction of glutamate, N-acetylaspartate, and taurine in the AD group.

Conclusion:
Present work suggested that amyloid pathology is significantly related to the disfunction of neurotransmitter system. Changes in the GABAergic system were prominent, indicating that the inhibitory system may be the most vulnerable to AD pathology.

Reference
1. Serrano-Pozo A, Frosch MP, Masliah E, Hyman BT. 2011. Neuropathological alterations in Alzheimer disease. Cold Spring Harb Perspect Med 1:1–23.

Poster Presentation

Disclosures: The authors have disclosed no financial interest.

248-Assessment of the metabolic biomarkers in a staging murine lung cancer model with concurrent FDG PET/CT and Serum 1H-NMR analysis

Presenter: Yi-hsiu Chung, Linkou Chang Gung Memorial Hospital

Yi-hsiu Chung[1], Cheng-Kun Tsai[1], Tsai-Hsien Hung[1], Ching-Fang Yu[1], Fang-hsin Chen[2], Gigin Lin[2]

[1]Linkou Chang Gung Memorial Hospital, Kawi-Shan, Taoyuan, Taiwan
[2]Linkou Chang Gung Memorial Hospital, Tao-Yuan, AA, Taiwan

Lung cancer is the second leading cancer in the world and spreads to the other organs, frequently. There is a lack of a metabolism platform for diagnosis of primary lung tumors or metastatic tumors. In this study, our aim is to establish a metabolite-based diagnosis platform for lung cancer staging with 18F-FDG PET and 1H-NMR (Nuclear Magnetic Resonance spectroscopy) based serum metabolomics. The nude mice were conducted by surgical orthotopic lung tumor cell implantation with the mixture of H460 (1 x 10^4 cells) and matrigel[1]. The mice were performed 18F-FDG PET/CT scan after implantation in 3 and 5 weeks. Before sacrificing animals, the blood was withdrawn from heart chambers for serum collection. The metabolites in serum for mice with primary lung tumors and metastatic tumors were assessed and analyzed by 1H-NMR system[2]. Histopathologically, the hematoxyline and eosin (H&E) stain and immunofluorescent ki-67 stain were exploiting in validation of tumor proliferation. A receiver-operating-characteristic (ROC) analysis was performed in SUVmean, SUVmax and serum metabolites of the tumor bearing mice. The Results: The 18F-FDG uptake of metastatic tumors is significantly higher than that of primary lung tumors in the metastasis mice (n=4, SUVmean, metastatic tumors 1.97 ± 0.29 v.s. primary lung tumors 1.25 ± 0.38, p <0.05). However, in comparison of 18F-FDG uptake of primary lung tumors in non-metastasis and metastasis mice, there is no significant difference between two groups. The normalized serum pyruvate level in the metastatic mice was significantly lower compared with in the non-metastastic mice (non-mettastatic mice: 0.29± 0.27 v.s. -0.19±0.32,p <0.05). The quantitative expression of fluorescent ki-67 of metastatic tumors is significantly increased compared to that of primary lung tumors (n=3, metastatic tumors 13.41± 1.184 % v.s. primary lung tumors 6.052 ± 1.934 %, $p < 0.05$). The AUCs of SUVmean, SUVmax and tyrosine generated from ROC curves were 0.91, 0.89 and 0.86 with p <0.05, respectively. Conclusion: The metastatic tumors showed high glucose uptake correlated to the increased proliferation and glycolysis. The combination of 18F-FDG PET and 1H-NMR based serum metabolomics demonstrated the feasibility of a metabolism platform for differentiation between primary lung tumors and metastatic tumors. In the future, this platform potentially could provide the metabolic information for the therapeutic strategies of lung cancer.

Reference
1. In the hunt for therapeutic targets: mimicking the growth, metastasis, and stromal associations of early-stage lung cancer using a novel orthotopic animal model. J Thorac Oncol, 2015. 10(1): p. 46-58
2. Metabolic profiling, metabolomic and metabonomic procedures for NMR spectroscopy of urine, plasma, serum and tissue extracts. Nat Protoc, 2007. 2(11): p. 2692-703.

Poster Presentation

Disclosures: The authors have disclosed no financial interest.

249-Dye Labeling for Optical Imaging Biases Drug Carriers' Biodistribution and Tumor Uptake

Presenter: Sarah Schraven, RWTH Aachen University

Sarah Schraven[1], Stefanie Rosenhain[2], Ramona Brueck[3], Tim M. Wiechmann[4], Robert Pola[5], Tomas Etrych[6], Wiltrud Lederle[6], Twan Lammers[7], Felix Gremse[8], Fabian Kiessling[9]

[1]*RWTH Aachen University, Aachen, Germany*
[2]*Institute for Experimental Molecular Imaging, Aachen, North Rhine-Westphalia, Germany*
[3]*RWTH Aachen University*
[4]*Institute for Experimental Molecular Imaging, Aachen, Northrhine-Westfalia, Germany*
[5]*Institute of Macromolecular Chemistry Czech Academy of Sciences, Prague, Prague 6, Czech Republic*
[6]*Prague, Prague 6, Czech Republic*
[7]*RWTH Aachen University Hospital, Aachen, Germany*
[8]*RWTH Aachen University Hospital, Aachen, NRW, Germany*
[9]*RWTH Aachen University, Aachen, NRW, Germany*

Optical imaging with fluorescent dyes is widely used to evaluate biodistribution of drug delivery systems in preclinical research. Although it is known that some dyes can interact with transporters (e.g., organic anion transporting polypeptides (OATPs)), there exists hardly any systematic investigation on the influence of dye conjugation on the biodistribution of macromolecules.[1,2] Therefore, cell uptake, biodistribution and tumor accumulation of four near-infrared dyes (AF750, IRDye750, Cy7 and DY-750) and the respective poly(*N*-(2-hydroxypropyl)methacrylamide)-*co*-aminoethyl-methacrylate (pHPMA)-conjugates (AF750-pHPMA, IRDye750-pHPMA, Cy7-pHPMA and DY-750-pHPMA) are investigated and compared. Hydrophilicity of the free dyes is assessed by high-performance liquid chromatography (HPLC) on a C18 column with an increasing acetonitrile gradient of 0-100 %. Cellular uptake of the fluorescent probes is assessed using a microplate reader. Mice are imaged longitudinal via hybrid micro-computed tomography-fluorescence tomography. HPLC retention times indicate that the dye hydrophobicity is highest for DY-750, followed by Cy7, IRDye750, and lowest for AF750. In vitro studies on A431 tumor cells indicate that more hydrophobic dyes have higher uptake. The more hydrophobic DY-750 has the highest uptake, then, in decreasing order Cy7, IRDye750 and the most hydrophilic dye, AF750, are internalized. Temperature-dependent uptake is observed for Cy7 and DY-750, which reveals an active internalization mechanism, which however, is not strongly related to OATPs. Treatment with OATP-inhibitors (bromosulfophthalein, atazanavir, rifampicin and sincalide) do not result in a significant reduction in uptake, with a decreasing tendency only observed for 17β-estradiol on Cy7 and DY-750. Dye-pHPMA-conjugates show lower cellular uptake than free dyes, with the highest uptake for DY-750-pHPMA, followed by AF750-pHPMA, Cy7-pHPMA and lowest for IRDye750-pHPMA, which is mostly related to dye-hydrophobicity. OATP-blocking experiments with the classical OATP-inhibitor rifampicin do not show a strong reduction; however, 17β-estradiol addition again leads to a slight reduction in dye-pHPMA uptake. In mice, optical imaging indicates that dye hydrophobicity shapes dyes' elimination pathways, leading to renal clearance for AF750, hepatic clearance for DY-750 and mixed clearance for IRDye750 and Cy7. In contrast to the elimination pathways, tumor uptake depends mainly on the dyes blood half-lives, with AF750 and DY-750 having the shortest blood half-lives and lowest tumor accumulation (0.1 h and 0.0 % ID cm^{-3}, and 1.2 h and 0.4 % ID cm^{-3}, respectively) compared with IRDye750 and Cy7 (1.8 h and 3.5 % ID cm^{-3}, and 1.3 h and 3.1 % ID cm^{-3}, respectively). As expected, in vivo, dye-pHPMA-conjugates circulate longer and accumulate stronger in tumors than free dyes. Blood half-lives vary from 6.0 h to 8.6 h and tumor accumulation is in line with the in vitro results (from highest to lowest 5.2 % ID cm^{-3}, 4.1% ID cm^{-3}, 3.1% ID cm^{-3} and 2.6% ID cm^{-3} at 3 h, respectively for DY-750-pHPMA, AF750-pHPMA, Cy7-pHPMA and IRDye750-pHPMA). Interestingly, labeling pHPMA with different dyes leads to an up to threefold different tumor accumulation, which correlates mainly with dyes' hydrophobicity, with the highest difference that is observed between DY-750-pHPMA and IRDye750-pHPMA at 24 h after injection. Dye hydrophobicity also affects the elimination routes of dye-pHPMA-conjugates, as Cy7-pHPMA and DY-750-pHPMA have a higher liver-to-kidney ratio than AF750-pHPMA and IRDye750-pHPMA (1.4-0.5 and 1.1-0.2, respectively). In conclusion, this study shows that labeling of macromolecules like pHPMA, with a labeling rate of only 0.3 mol % dye/pHPMA significantly impacts their biodistribution and tumor uptake. Thus, careful selection of low-interference dyes and further exploration of dye classes is required to reveal reliable results in optical imaging experiments and to avoid potential bias.

Reference

1. Hage, C. et al. Comparison of the Accuracy of FMT/CT and PET/MRI for the Assessment of Antibody Biodistribution in Squamous Cell Carcinoma Xenografts. J. Nucl. Med. 59, 44–50 (2018).
2. Ho, C.-M. et al. Use of indocyanine green for functional assessment of human hepatocytes for transplantation. Asian J. Surg. 35, 9–15 (2012).
3. Gremse, F. et al. Imalytics Preclinical: Interactive Analysis of Biomedical Volume Data. Theranostics 6, 328–341 (2016).

Poster Presentation

Disclosures: The authors have disclosed no financial interest.

250-A PSMA-Targeted Near-Infrared Ratiometric Fluorescence pH Probe for Imaging Prostate Cancer with Enhanced Contrast

Presenter: Xuekang Cai, Peking University First Hospital

Xuekang Cai[1], Jingming Zhang[2], Wenhui Huang[3], Long Yi[3], Xing Yang[4]

[1]*Peking University First Hospital, China*
[2]*Peking University First Hospital*
[3]*Northeastern University, Beijing, China, China*
[4]*Peking University, Beijing, China*

Introduction:

Prostate cancer (PCa) is the most prevalent cancer and the second leading cause of cancer deaths in American males.[1] Advanced optical imaging agents could profit precisive detection of PCa and have potential for fluorescence-guided surgery. The prostate-specific membrane antigen (PSMA) with high expression in the epithelium of most PCa is entitled as one of the most charming targets. Thus, a variety of PSMA-targeted near-infrared (NIR) agents have been widely reported. However, most of the targeted agents were restricted to "always on" NIR dyes (Cy7, IRdye800CW, indocyanine green etc.), with delayed imaging time points and limited optical contrast.[2-3] Few PSMA-targeted activatable fluorescent probes have been reported.[4] Therefore, there is an urgent need to develop activated probes to increase image contrast. In virtue of upregulated glycolysis, the slightly acidic microenvironment (pH 6.2–6.9) is a distinctive feature of tumor. Consequently, pH-activated fluorescent probes have been widely designed for imaging tumor and delineating tumor margin.[5] Among these, ratiometric fluorescence pH

probes could get rid of the factor of local concentration of chromophores owing to self-calibration mechanism and likely provide higher contrast.[6] Here, a PSMA-targeted NIR ratiometric fluorescence pH probe was designed and synthesized based on an oxalyldiaminopropionic acid-urea (ODAP-urea) PSMA inhibitor and a pH-sensitive heptamethine indocyanine dyes (Figure 1 A). Notably, the probe was selectively activated with dual channel of fluorescent emission in PSMA-positive 22Rv1 bearing mice model and fluorescence ratio images were acquired. We reasonably believe that this targeted ratiometric fluorescence pH probe could provide higher optical contrast than traditional “always-on” probes.

Method:
Balb/c nude mice bearing 22Rv1 tumor xenografts were imaged at 1, 2, 4, 10 and 24 h by the IVIS Spectrum Imaging System after tail vein injection of **NIR-pH-ODAP.** Two channel images were acquired using auto-exposure with the following parameters: channel 1 (Ex745nm/Em840nm), channel 2 (Ex535nm/Em700nm). Fluorescence ratio images (channel 1/channel 2) could be calculated and acquired using Living Image 4.3.1 software. The thigh muscle was chose as the background when calculating the tumor-to-background ratio (TBR).

Result:
pH-responsive fluorescent properties of **NIR-pH-ODAP** were illustrated in Figure 1 B. In both channel 1 and ratio channel, tumors were clearly visualized early at 1 h post-injection (Figure 1 C,D). The fluorescence signal in tumor region reached to the peak value at 2-4 h and maintained until 24 h in channel 1. From 1 h to 24 h, the TBR increased in channel 1 from 1.7 to 2.4, and ratio channel from 2.4 to 3.1, respectively (Figure 1 E). The optical contrast in ratio images showed approximately 1.4-fold higher than single channel images.

Conclusion:
The PSMA-targeted NIR ratiometric fluorescence pH probe could detect 22Rv1-tumor at 1 h post-injection, better than PSMA-targeted “always-on” NIR probes reported before. And the ratio channel could achieve higher contrast than single channel imaging. The novel probe has promising potential in intraoperatively delineating PCa and guiding surgery.

Reference

1. Siegel, R. L.; Miller, K. D.; Fuchs, H. E.; Jemal, A., Cancer Statistics, 2021. CA Cancer J Clin 2021, 71 (1), 7-33.
2. Hensbergen, A. W.; van Willigen, D. M.; van Beurden, F.; et al, Image-Guided Surgery: Are We Getting the Most Out of Small-Molecule Prostate-Specific-Membrane-Antigen-Targeted Tracers? Bioconjug Chem 2020, 31 (2), 375-395.
3. Chen, Y.; Minn, I.; Rowe, S. P.; et al, A Series of PSMA-Targeted Near-Infrared Fluorescent Imaging Agents. Biomolecules 2022, 12 (3).
4. Zhang, J.; Rakhimbekova, A.; Duan, X.; et al, A Prostate-Specific Membrane Antigen Activated Molecular Rotor for Real-Time Fluorescence Imaging. Nat Commun 2021, 12 (1), 5460.
5. Voskuil, F. J.; Steinkamp, P. J.; Zhao, T.; vet al, Exploiting Metabolic Acidosis in Solid Cancers Using a Tumor-Agnostic pH-Activatable Nanoprobe for Fluorescence-Guided Surgery. Nat Commun 2020, 11 (1), 3257.
6. Ma, T.; Hou, Y.; Zeng, J.; et al, Dual-Ratiometric Target-Triggered Fluorescent Probe for Simultaneous Quantitative Visualization of Tumor Microenvironment Protease Activity and pH in Vivo. J Am Chem Soc 2018, 140 (1), 211-218.

Poster Presentation

Disclosures: The authors have disclosed no financial interest.

251-Cervical lymph node extemporaneous assessment by new ultra-fast and large field of view confocal microscopy during surgery

Presenter: Muriel Abbaci, Gustave Roussy

Odile Casiraghi[1], Adrien Villard[2], Anne Auperin, Safaa Asmandar[2], Antoine Moya-Plana[2], Ingrid Breuskin, **Muriel Abbaci[3]**

[1]Gustave Roussy, Villejuif, val de marne, France
[2]Gustave Roussy
[3]Gustave Roussy, Villejuif, France

Objective:
To evaluate the diagnostic value of new ultra-fast and large field of view Confocal Microscopy (UFCM) imaging of lymph nodes (LN) in patients with upper aerodigestive tract squamous cell carcinoma, compared to conventional histology (CHi). The UFCM images are artificially colored in purple as frozen sections. This technique would be considered interesting if accuracy based on UFCM images was higher than those on frozen section examination (FSE).

Method:
We carried out an *ex vivo* study on LN from patients N0. The two parts of fresh lymph nodes were stained with acridine orange for 15s, rinsed and imaged with the Histolog-Scanner (UFCM) (SamanTree Medical, Switzerland) during 1 min. With an optical window of 20 cm^2, two parts of several lymph nodes were imaged simultaneously. In postprocessing, all acquired and anonymized UFCM images were independently interpreted by two pathologists (PT1 and PT2) and the “UFCM diagnoses” were compared to CHi.

Results:
We included 11/44 patients, i.e. 64 LN. 8/64 LN were metastatic (N+) on CHi. On UFCM images, PT1 was in accordance with CHi in 93.75% (95% CI= 84.8-98.3%) and PT2, 95.3% (IC95=86.9%-99%). PT1 considered as negative one patient, who was finally N+. The errors were as follows: the metastatic area has escaped the screening of the UFCM image (n=3), a metastasic area has been analyzed as only «suspect » (n=1)

Conclusion:
Inclusions have now reached 44 patients and 206 LN, allowing a robust statistical analysis (in progress). At this stage, the analysis by UFCM seems to be a very promising technique. It could eventually replace the FSE, because its diagnostic reliability seems at least equivalent and its speed processing (5 minutes) constitutes a major asset.

Poster Presentation

Disclosures: The authors have disclosed no financial interest.

252-Radiosynthesis and pilot PET imaging of 2-[11C]methyl glutamate ([11C]AMG)

Presenter: Jun-Hyung Park, Molecular Imaging Program at Stanford (MIPS)

Pablo Buccino Evans[1], **Jun-Hyung Park[1]**, Christopher J. Acosta[2], Katherine L. Lucot[3], Thomas J. Montine, Corinne Beinat[4], Bin Shen[5]

[1]Molecular Imaging Program at Stanford (MIPS), Palo Alto, CA
[2]Stanford University
[3]Stanford University, Stanford, California
[4]Stanford University, Stanford, CA
[5]Molecular Imaging Program at Stanford (MIPS), Stanford, CA

Objective:
We have recently reported the first glutamatergic and GABAergic false neurotransmitters, meaning that these molecules are transported across several membranes, stored in synaptic vesicles where they dose-dependently replace endogenous neurotransmitters and are released upon neuronal membrane depolarization just like the endogenous neurotransmitters; however, they fail to activate receptors [1]. Our glutamatergic false neurotransmitter, the *S* enantiomer of 2-menthylglutamate, does not enter the Kreb's cycle but does enter the glutamate-glutamine cycle where it is rapidly converted to *S*-2-methylglutamine by astrocytes but slowly converted back to 2-methyl glutamate by neurons. Given the unique biochemical and neurochemical properties of *S*-2-methyl glutamate we have synthesized 2-[^{11}C] methyl glutamate ([^{11}C]AMG) and are pursuing it as an imaging agent for L-glutamate transport and L-glutamine biosynthesis in the brain, which has potential to inform on a multitude of neurological conditions.

Methods:
Three individual radiosynthesis modules were used for [^{11}C]AMG radiochemistry. The synthetic route is depicted in Scheme 2. Briefly, [^{11}C] CH_3I was produced from cyclotron delivered [^{11}C]CO_2 via reduction followed by iodination. [^{11}C]CH_3I was transferred and trapped in DMF at -10 °C, then reacted with 3.0 ± 0.5 mg of precursor (E)-di-*tert*-butyl 2-(benzylidene amino)pentanedioate at 80 °C for 5 minutes. Either a mixture of (11bR)- and (11bS)- or (11bR)-Maruoka catalysts (4,4-Dibutyl-4,5-dihydro-2,6-bis(3,4,5-trifluorophenyl)-3H-dinaphth[2,1-c:1´,2´-e]azepinium bromide) were added to catalyze the ^{11}C-methylation and for directing the stereoselectivity towards either the racemic mixture or the (L)-isomer, respectively. [2] After the ^{11}C-methylation reaction was complete, the mixture was injected onto the HPLC for ^{11}C-Intermediate purification. Collected ^{11}C-intermediate was hydrolyzed with 0.55 mL of 12M HCl at 120 °C for 3 minutes. After hydrolysis, the mixture was neutralized with 1M phosphate buffer, and purified by three C18 cartridges. Quality control consisted of pH determination, GC evaluation of residual ethanol and acetonitrile, radiochemical purity, and radiochemical identity through OPA-MPA derivatization. The product was diluted with saline as needed. We completed small animal PET/CT imaging of healthy C57/Bl6 mice (n=4) to determine the brain penetrance and biodistribution of [^{11}C]AMG. 60-min dynamic imaging was completed immediately following intravenous administration of 150 µCi [^{11}C] AMG.

Results and Discussion:
The total [^{11}C]AMG radiosynthesis takes 55 min from EOB, and the average EOS radioactivity for the formulated product was 88±25 mCi with an RCY of 24.7±8.3% (n=3, decay corrected to EOB) Radiochemical purity was consistently higher than 95%, and derivatization with OPA confirmed the structure of [^{11}C]AMG by comparison with non-radioactive racemic 2-methylaminoglutamate-OPA derivative retention time. Residual MeCN was consistently lower than 410 ppm. Dilution with saline prior to animal administration was required due to the high salt concentration of the radiotracer vehicle (1M phosphate buffer, which is needed for neutralizing the HCl). Small animal PET/CT revealed that [^{11}C]AMG appeared to passively cross the intact blood-brain barrier (BBB) and then clear the healthy brain (Fig. 1B). In line with other radiolabeled amino acid derivatives, we observed predominantly renal clearance of [^{11}C]AMG (Fig. 1C).

Conclusion:
We have established a reliable radiosynthesis of [^{11}C]AMG and performed initial imaging in healthy mice. Further development will be focused on the determination of enantiomeric excess of the L-isomer via chiral HPLC. Given the brain penetration and favorable biodistribution of [^{11}C]AMG, future work will focus on its application in animal models of neurodegenerative disease.

Reference

1. AM Wawro, et al. Scientific Reports 2021 (11): 8138
2. A Pekošak, et al. Org. Biomol. Chem., 2017, 15, 570

Poster Presentation

Disclosures: The authors have disclosed no financial interest.

253-Laser Ablation-ICP-MS: A New Imaging Tool to Visualize and Quantify Antibody Distribution in Cancer Cells and Tissue

Presenter: Natasha Patel, King's College London, School of Imaging Sciences and Biomedical Engeneering

Natasha Patel[1], Truc T. Pham[2], Alexander Griffiths[2], Vijay Chudasama[3], Jamie Baker[3], Nicholas Long[3], Michelle T. Ma[4]

[1]King's College London, School of Imaging Sciences and Biomedical Engeneering, London, London, United Kingdom
[2]King's College London, London, London, United Kingdom
[3]University College London, London, London, United Kingdom
[4]King's College London, London, United Kingdom

Abstract Body:
Methodologies that can provide quantitative information on antibody distribution in tissues, and thus infer important biochemical insight, are critically needed. Inductively coupled plasma-mass spectrometry (ICP-MS) and laser ablation-inductively coupled plasma-mass spectrometry (LA-ICP-MS) are highly sensitive analytical techniques capable of quantifying and imaging antibody localisation. To improve upon existing current literature methods, new dibromopyridazinedione conjugation chemistry has been developed to produce robust heavy metal tags that bridge interchain disulphide bonds of antibodies.[1] The clinically-approved therapeutic antibody, trastuzumab, targets human epidermal growth factor receptor 2 (HER2) over-expressed in breast and ovarian cancers. The new chemistry developed has been applied to map trastuzumab distribution in cells and tissue, both quantitively and qualitatively using LA-ICP-MS.

Synthesis:
A novel rhodium-based sarcophagine metal complex attached to a dibromopyridazinedione linker was synthesised (**Fig. A**). Interchain disulphide bonds of trastuzumab were reduced with TCEP, and reacted with the newly synthesised rhodium (Rh) compound. The resulting Rh-sar-trastuzumab immunoconjugate was characterised, by sodium dodecyl sulphate–polyacrylamide gel electrophoresis (SDS-PAGE), electrospray ionisation- mass spectrometry (ESI-MS), and UV-Vis spectroscopy.

In vitro work:
Rh-sar-trastuzumab was incubated with HER2-positive HCC1954 and HER2-negative MDA-MB-231 breast cancer cells for 1 h at 37°C. After washing, cells were fixed with 4% PFA. Rh distribution was imaged with LA-ICP-MS at a spatial resolution of 8 μm.
In vivo work. Rh-sar-trastuzumab (0.5 mg) was administered to mice bearing HCC1954 orthotopic tumours. Mice were culled 72 h post-injection, and the organs dissected, dried and digested in nitric acid and hydrogen peroxide before being analysed for Rh (μg/g dry weight) content by ICP-MS.
Simple and efficient bioconjugation of the rhodium (Rh) metal tag to trastuzumab was readily achieved producing the novel, near-homogenous product, Rh-sar-trastuzumab. LA-ICP-MS analysis revealed significantly higher HER2-specific uptake of metal-tagged antibody in HER2-positive cells relative to HER2-negative cells (3.00 ± 0.68 *vs.* 1.52 ± 0.49 average Rh counts per pixel respectively, $p < 0.0001$; **Fig. B**).
Rh-sar-trastuzumab in HER2-positive tumour-bearing mice at 72 h post-administration was quantified using ^{103}Rh ICP-MS measurements. Rh content was high in HER2 expressing tissues, including the tumour, ovaries and uterine horn, as well as tissue that is known to accumulate IgG antibodies (spleen, liver; **Fig. C**), consistent with reported trastuzumab biodistribution.[2] In animals that were not administered Rh-sar-trastuzumab, negligible amounts of endogenous Rh were recorded for all organs.
In addition to developing a new chemical platform for labelling antibodies with heavy-metal tags, this is the first example of a Rh-tagged antibody that is capable of being imaged and quantified at a cellular level using LA-ICP-MS. This preliminary work provides proof-of-concept, with a future outlook to mapping and quantifying antibody distribution in tissues, and moving from conventional HER2 antibodies to novel antibody-based drugs.
This technology is poised for future integration into the field of imaging sciences, offering a complementary *ex vivo* tool that can be coupled with *in vivo* imaging techniques such as PET.

Reference

1. Bahou C, Richards DA, Maruani A, Love EA, Javaid F, Caddick S, et al. Highly homogeneous antibody modification through optimisation of the synthesis and conjugation of functionalised dibromopyridazinediones. Org Biomol Chem. Royal Society of Chemistry; 2018;16:1359–66.
2. Farleigh M, Pham TT, Yu Z, Kim J, Sunassee K, Firth G, et al. New Bifunctional Chelators Incorporating Dibromomaleimide Groups for Radiolabeling of Antibodies with Positron Emission Tomography Imaging Radioisotopes. Bioconjug Chem. 2021;

Poster Presentation

Disclosures: The authors have disclosed no financial interest.

254-Development of organotypic human vulvar cancer 3D-models as a tool to study anticancer drug efficacy

Presenter: Bertine Huisman, Centre for Human Drug Research

Bertine Huisman[1], Mariette v Poelgeest[2]

[1]*Centre for Human Drug Research, Netherlands*
[2]*Leiden University Medical Center (LUMC), Leiden, Netherlands*

Background:
Although vulvar squamous cell carcinoma (VSCC) is rare, the disease burden is tremendous and prognosis has not improved over the last decades. Current treatment consists of surgery with or without (chemo)radiotherapy and is associated with significant and long-term side effects. To improve current treatments and discover new therapies, more research into VSCC pathogenesis and management is urgently needed. Unfortunately, no proper models are available that mimic human VSCC. Most vulvar cancer research and drug screening programs are performed in tumor biopsies or (transgenic) animal models. Reconstructed 3D-human skin equivalents (HSEs) might be a solution for the issues faced. HSEs are in vitro cultured skin models designed to mimic the characteristics of native human normal or diseased skin as closely as possible. Knowledge of sqaumous cell carcinomas and the crucial tumor microenvironment is essential to mimic VSCCs in vitro. Within the tumour microenvironment (TME) different fibroblast subtypes are present, including papillary fibroblasts (PFs), reticular fibroblasts (RFs) and cancer associated fibroblasts (CAFs). The latter being mostly associated with tumour progression and invasion. Whether PFs, RFs and CAFs also play an important role in VSCC invasion and EMT remains to be determined. Moreover, HSEs can serve as a prediction model to determine the penetration profile of drugs across the skin.

Objectives:
Development of a 3D-organotypic model that mimics normal and malignant vulvar skin for drug screening purposes.

Methods:
Normal and VSCC models were established by seeding primary vulvar keratinocytes or tumor cell lines (A431 and HTB-117) onto dermal matrices harboring PFs, RFs and CAFs. PFs and RFs were isolated from surplus abdominal skin from healthy female donors. CAFs were isolated from cSCC primary tumours obtained from the department of Dermatology. HSE models were firstly cultured for two days under submerged conditions, followed by 2 weeks of culture at air-liquid interface. Next, epithelial morphogenesis was examined by immunohistochemistry and qPCR for e.g., cell activation, proliferation, differentiation and fibroblasts activation biomarkers. In addition, VSCC models were treated with carboplatin and paclitaxel in low and high concententrations in the medium to study their anticancer drug efficacy.

Results:
Human 3D-vulvar models were successfully developed that resemble both normal native vulvar and VSCC. The vulvar models demonstrated the dissimilar effects of PFs, RFs and CAFs in tumor invasion. Furthermore, chemotherapeutic treatments resulted in a significant reduction in tumor-load and invasion.

Conclusions:
This study is the first to our knowledge that showed the successful establishment of ex vivo normal human vulvar 3D skin models which mimic native healthy vulvar tissue. In addition, VSCC cell lines were seeded on a scaffold of normal and cancer-associated fibroblast subtypes. This way 3D full-thickness VSCC-like models were created, harboring both keratinocytes and several types of fibroblasts in a well-controlled microenvironment (Figure 1). The vulvar cancer models revealed the invasive influence of CAFs on VSCC progression. Lastly, shrinkage of the epithelial tumor in the VSCC FTMs was observed after application of chemotherapeutics carboplatin and paclitaxel. These results showed the potency of these 3D ex vivo 3D models as reliable platform for further studies for e.g. drug development in this tumor field.

Reference

1. Tan A, Bieber AK, Stein JA, Pomeranz MK. Diagnosis and management of vulvar cancer: A review. J Am Acad Dermatol [Internet]. 2019 Dec;81(6):1387–96.
2. Vulvar Cancer — Cancer Stat Facts [Internet]. [cited 2021 Dec 28]. Available from: https://seer.cancer.gov/statfacts/html/vulva.html
3. Gaarenstroom KN, Kenter GG, Trimbos JB, Agous I, Amant F, Peters AAW, et al. Postoperative complications after vulvectomy and inguinofemoral lymphadenectomy using separate groin incisions. Int J Gynecol Cancer [Internet]. 2003 Jul ;13(4):522–7.
4. Janson D, Saintigny G, Mahé C, Ghalbzouri A El. Papillary fibroblasts differentiate into reticular fibroblasts after prolonged in vitro culture. Exp Dermatol [Internet]. 2013 Jan;22(1):48–53.
5. M H, M R, F de G, A EG. A shift from papillary to reticular fibroblasts enables tumour-stroma interaction and invasion. Br J Cancer [Internet]. 2018 Apr 1;118(8):1089–97.
6. Their JP. Epithelial-mesenchymal transitions in tumour progression. Nat Rev Cancer [Internet]. 2002 ;2(6):442–54.
7. Lõhmussaar K, Boretto M, Clevers H. Human-Derived Model Systems in Gynecological Cancer Research. Trends in Cancer. 2020 Dec 1;6(12):1031–43.
8. Dongre H, Rana N, Fromreide S, Rajthala S, Bøe Engelsen I, Paradis J, et al. Establishment of a novel cancer cell line derived from vulvar carcinoma associated with lichen sclerosus exhibiting a fibroblast-dependent tumorigenic potential. Exp Cell Res. 2020 Jan 1;386(1):111684.
9. Commandeur S, Ho SH, de Gruijl FR, Willemze R, Tensen CP, El Ghalbzouri A. Functional characterization of cancer-associated fibroblasts of human cutaneous squamous cell carcinoma. Exp Dermatol [Internet]. 2011 Sep;20(9):737–42

Poster Presentation

Disclosures: The authors have disclosed no financial interest.

255-89Zr-ImmunoPET visualizes the optimized pharmacokinetics of anti-PSCA scFv-Fc proteins for radioimmunotherapy of pancreatic cancer

Presenter: Kirstin Zettlitz, City of Hope

Deirdre La Placa[1], Jennifer Chean[1], Felix Salazar[1], Tove Olafsen[2], Anna M. Wu[1], **Kirstin A. Zettlitz[1]**

[1]City of Hope, Duarte, CA
[2]City of Hope, Duarte

Abstract Body:
Most patients with pancreatic adenocarcinoma present with advanced disease (locally or metastatic) and there is a strong need for improved systemic treatment. A promising strategy is the targeted delivery of cytotoxic radioactivity using antibody fragments against tumor-specific antigens, such as prostate stem cell antigen (PSCA). In this study, we use 89Zr-immunoPET to evaluate the in vivo targeting and biodistribution of an anti-PSCA scFv-Fc fusion protein (A2scFv-Fc2DM) with optimized pharmacokinetics for radioimmunotherapy in a xenograft model of pancreatic cancer. The 110 kDa antibody fragment was engineered for rapid blood clearance (double mutant, DM) and gets excreted through the hepatobiliary route, with the goal of reducing toxicity to the bone marrow and the kidneys.

Methods:
The A2scFv-Fc2DM (A2DM) and the wild-type control A2scFv-Fc2 (A2WT) were chelated using a 5-fold molar ratio of p-SCN-Bn-Deferoxamine (SCN-DFO) and radiolabeled with zirconium-89 (89Zr). 89Zr-A2scFv-Fc2DM or 89Zr-A2scFv-Fc2 (10 µg/3.7 MBq) were injected intravenously into nude mice (male and female) bearing subcutaneous Capan-1 tumors (human pancreatic adenocarcinoma endogenously expressing PSCA). A blocking group was co-injected with 10-fold excess of cold A2scFv-Fc2. Static 10 min iPET/CT scans were acquired at 4, 24 and 96 hours post injection (p.i.) and groups of 5 mice were euthanized for ex vivo biodistribution at 24 and 96 h p.i.

Results:
Anti-PSCA scFv-Fc fusion proteins were successfully radiolabeled with efficiencies of 72-98%, resulting in specific activity of about 10 µCi/µg and radiochemical purities of >98%. ImmunoPET showed high uptake of both 89Zr-A2scFv-Fc2DM and 89Zr-A2scFv-Fc2 in the PSCA-expressing Capan-1 tumors. While 89Zr-A2scFv-Fc2DM reached peak uptake at 24 h p.i. (5.3± 2.1 %ID/g), the longer half-life of 89Zr- A2scFv-Fc2 resulted in increased uptake out to 96 h p.i. (9.4+/-0.8%ID/g). The lower activity in the tumors (1.8+/-0.5, %ID/g) in the blocking group at 24 h confirmed antigen specificity of the tracer. Rapid clearance of activity from the blood (heart) and accumulation of activity in the liver was evident for 89Zr-A2scFv-Fc2DM as early as 4 h p.i, confirming the shift toward hepatic clearance. The modulated half-life of 89Zr-A2scFv-Fc2DM resulted in significantly higher tumor-to-blood ratios compared with the control 89Zr-A2scFv-Fc2 (41.1 ± 4.4 vs 0.7 ± 0.1 %ID/g at 96 h p.i.). ImmunoPET/CT images and the ex vivo biodistribution revealed no gender-specific differences or non-specific tissue uptake.

Conclusion:
ImmunoPET as a non-invasive whole body imaging application can inform on in vivo targeting, pharmacokinetics, and clearance of antibody-based therapeutics, and surrogate immunoPET using a positron emitting radionuclide with correlating characteristics can guide the development of radioimmunotherapy. Here, 89Zr-immunoPET of the re-engineered fusion protein A2scFv-Fc2DM confirmed specific targeting to PSCA expressing pancreatic xenografts. 89Zr-A2scFv-Fc2DM cleared through the liver (sparing the more radiosensitive kidneys) and demonstrated rapid blood clearance (reducing hematological toxicity). Thus, A2scFv-Fc2DM could provide an improved therapeutic index for radioimmunotherapy of pancreatic cancer.

Poster Presentation

Disclosures: The authors have disclosed no financial interest.

256-PET imaging of Gal-3BP expression in PDX models

Presenter: Outi Keinaenen, Hunter College

Outi Keinaenen[1], Samantha M. Sarrett[2], Cindy Rodriguez[3], Samantha Delaney[4], Emily Capone[5], Frederic Sauniere[6], Gianluca Sala[5], Stefano Iacobelli[7], Brian Zeglis[8]

[1]Hunter College, New York
[2]City University of New York, New York
[3]City University of New York, Woodhaven, NY
[4]The City University of New York, New York, NY
[5]D'Annunzio University of Chieti - Pescara, Chieti, Italy
[6]Mediapharma srl, Chieti, Italy
[7]MediaPharma Srl, Rome, Italy
[8]Hunter College, New York, NY

Introduction:
Galectin-3 binding protein (Gal-3BP) is a glycoprotein that is overexpressed in a variety of cancers and has been implicated as a marker of tumor progression and poor prognosis in several tumor types, including melanoma, non-small cell lung cancer, head and neck squamous cell carcinoma, and breast cancer. Herein, we report the use of Gal-3BP-targeting radioimmunoconjugate, [^{89}Zr]Zr-DFO-1959, in three different patient-derived melanoma xenograft models.

Methods:
Humanized anti-Gal-3BP antibody 1959 was modified with desferrioxamine (DFO) and labeled with zirconium-89 ($t_{1/2}$ ~ 3.3 d) via standard procedures to produce [^{89}Zr]Zr-DFO-1959. Subsequently, athymic nude mice bearing subcutaneous patient-derived xenografts (PDX) were injected with [^{89}Zr]Zr-DFO-1959 (n=3-4). Three different melanoma PDX models were used: JW-217a, JW-218a, and JW-159a. At 24, 48, 72, 96, and 120 h after the injection of [^{89}Zr]Zr-DFO-1959 (2.6-3 MBq, 70-80 μCi, 5-6 μg), PET images were acquired. At the last imaging timepoint (120 h) the mice were sacrificed, and their organs were collected, weighed, and assayed for radioactivity with a gamma counter calibrated for zirconium-89.

Results:
A radiolabeling yield of >95% was obtained along with a post-purification purity of >99%. In PET experiments, [^{89}Zr]Zr-DFO-1959 clearly delineated Gal-3BP-secreting PDX tissue, reaching optimal tumor-to-background contrast at 120 h. Of the three PDX models, JW-159a showed the highest radioactivity uptake at the tumor, and JW-217a had the lowest uptake, with JW-218a in between. The *ex vivo* biodistribution data confirmed the PET imaging results.

Conclusions:
[^{89}Zr]Zr-DFO-1959 effectively visualized Gal-3BP-secretion in melanoma PDX tissues. Our preliminary results and the expression of Gal-3BP by a variety of cancers make it an enticing target for further development for therapeutics, including antibody-drug conjugates (ADC). We are currently further validating [^{89}Zr]Zr-DFO-1959 in other PDX models and exploring the theranostic value of [^{89}Zr]Zr-DFO-1959 in the context of a Gal-3BP-targeted ADC.

Poster Presentation

Disclosures: Author Stefano Iacobelli is an employee with MediaPharma.

257-Evaluation of the performance parameters on the Biograph Vision PET/CT scanner using the NU2-2012

Presenter: Subhash Kheruka, Sultan Qaboos Comprehensive Cancer Care and Research Centre,

Subhash C. Kheruka[1], ,Naema Al Maymani[2], Noura Al Makhmari[2], Tasnim Al Rahii, Huoda Al Saidi[2], Khulood Al Riyami, Rashid Al Sukaiti[2], Vipin V Jayakrishnan[2]

[1]Sultan Qaboos Comprehensive Cancer Care and Research Centre, Muscat, Oman
[2]Muscat, Oman

Purpose:
To evaluate the performance of the Biograph Vision (Siemens Healthineers) PET/CT system. This new system is based on the Siemens Biograph Vision 600, using the same silicon photomultiplier-based detectors with 3.2×3.2×20-mm lutetium-oxoorthosilicate crystals. The Vision 8 detector rings provide axial field of view (AFOV) of 26 cm, enabling imaging of major organs in one bed position.

Methods:
The new digital PET/CT features silicon photomultiplier (SiPM) based detectors with 3.2 mm lutetium oxyorthosilicate (LSO) crystals and full coverage of the scintillator area. The PET components incorporate eight rings of 38 detector blocks and each block contains 4x2 mini blocks. Each miniblock consists of a 5x5 LSOarray of 3.2x3.2x20 mm crystals coupled to a SiPM array of 16x16 mm, resulting in an axial field of view (FOV) of 26.1 cm. In this study PET/CT system performance will be evaluated conform the NEMA NU 2 2012 standard. The Spatial resolution, sensitivity, count rate performance, scatter correction, Time-of-Flight (TOF) performance, and image quality will be determined. Measurements will be directly compared to results from its predecessor.

Results:
The Biograph Vision shows a NEMA sensitivity of 15.1 kcps/MBq, an axial spatial resolution at Full Width Half Maximum (FWHM) of 3.5 mm at 1 cm offset of the center of the FOV, a NEMA peak NECR of 259 kcps at 32 kBq/mL and TOF timing resolution was 213.7 ps. The overall image contrast seen with the NEMA image quality phantom ranged from 80.79% to 90.86%.

Conclusions: The Biograph Vision is able to meet NEMA standards.

Reference
1. National Electrical Manufacturers Association (NEMA), Standards Publication NU 2-2012, Performance Measurements of Positron Emission Tomographs (NEMA, Rosslyn, VA, 2012).
2. National Electrical Manufacturers Association Performance Measurements of Positron Emission Tomographs. Rosslyn, VA: National Electrical Manufacturers Association; 2018. NEMA Standards Publication NU 2-2018
3. Performance Characteristics of the Digital Biograph Vision PET/CT System Joyce van Sluis, Johan de Jong, Jenny Schaar, Walter Noordzij, Paul van Snick, Rudi Dierckx, Ronald Borra, Antoon Willemsen, Ronald Boellaard Journal of Nuclear Medicine Jul 2019, 60 (7) 1031-1036; DOI: 10.2967/jnumed.118.215418

Poster Presentation

Disclosures: The authors have disclosed no financial interest.

258-Mitochondrion-Tropic Radioconjugates Carrying TPP and PSMA Derivatives: Radiobiological and Imaging Studies in Prostate Cancer Models

Presenter: António Paulo, Instituto Superior Técnico/Universidade de Lisboa

Célia Fernandes[5], Joana Santos[5], Maria Teresa Braz[1], Francisco Silva[1], Paula Raposinho[1], Joana F. Guerreiro[1], Frederik Cleeren[2], Irwin Cassells[3], Filipa Mendes[4], **António Paulo[5]**

[1]Instituto Superior Técnico/Universidade de Lisboa, Lisboa, Portugal
[2]KU Leuven, Leuven, Vlaams-Brabant, Belgium
[3]MOL, Belgium
[4]Bobadela, Portugal, Portugal

[5]*Instituto Superior Técnico/Universidade de Lisboa, Bobadela LRS, Portugal*

In the past few years, there has been a significant interest in the design of new theranostic radiopharmaceuticals targeted at the Prostate-Specific Membrane Antigen (PSMA), which is overexpressed in the majority of prostate cancer (PCa) and its metastases [1]. A variety of PSMA ligands were labeled with different imaging and therapeutic radionuclides, namely with the soft beta minus emitter ^{177}Lu. This intense research work led to the development of ^{177}Lu-PSMA-617, undergoing a Phase III clinical trial to treat metastatic castration-resistant PCa (mCRPC) [1,2]. However, the use of beta minus emitters in targeted radionuclide therapy (TRNT) of cancers has some limitations, such as the nephrotoxicity and beta radiation resistance encountered in a non-negligible number of patients. Auger electron (AE) emitters can be an attractive alternative to circumvent these difficulties and common radionuclides for nuclear medicine imaging applications can be used (e.g. ^{67}Ga, ^{99m}Tc or ^{111}In) [3]. The radiobiological effects induced by AE emitters might include hardly repairable and lethal DNA damage in the targeted tumor cells, if the AEs are emitted in close proximity to a radiosensitive cellular target, such as the nuclear DNA or the mitochondria. In particular, mitochondria-targeted radioconjugates may be an attractive alternative because mitochondrial DNA is damaged by exposure to ionizing radiation, which is also able to elicit other deleterious effects such as ROS production or apoptosis. For this reason, recently, the energized mitochondria of tumor cells started to be studied as a subcellular target for therapeutic AE-emitting radionuclides [4]. Having this in mind, we have designed dual-targeted ^{111}In-DOTA complexes carrying a PSMA inhibitor (PSMA-617 derivative) and a triphenyl phosphonium (TPP) group to promote a selective uptake by PCa cells and their accumulation in the mitochondria, respectively. Conjugates bearing a cathepsin B cleavable linker between the PSMA-617 moiety and the DOTA chelator were also synthesized, aiming at a further enhanced accumulation in the mitochondria upon enzymatic cleavage of the linker. In this way, we expected to obtain AE emitting radioconjugates suitable for a more selective TRT of mCRPC (see Figure 1). In this communication, we describe novel DOTA-based chelators functionalized with PSMA-617 and/or TPP derivatives and their respective ^{nat}In and ^{111}In complexes. The "cold" compounds (ligands and ^{nat}In complexes) were fully characterized by HPLC, ESI-MS and multinuclear NMR analysis. The ^{111}In complexes were obtained by reaction of the different ligands with $^{111}InCl_3$, in high radiochemical yield and purity at high specific activity; their chemical identity was ascertained by HPLC comparison with the cold congeners. All the radiocomplexes showed high *in vitro* stability in physiologic conditions and in the presence of cell culture medium. The biological evaluation included cellular uptake and internalization and PSMA-blocking studies in different cell lines (LNCaP, PC3 PIP and PC3 Flu), subcellular localization experiments and the assessment of radiobiological effects based on the clonogenic survival assay. The PSMA-targeted ^{111}In-radiocomplexes displayed high cellular uptake and internalization in the PSMA-positive PC3 PIP cells while presenting a negligible internalization in the PSMA-negative PC3 Flu cells. In some cases, the radiobiological studies indicated that the complexes compromise the cellular viability in a dose-dependent manner. In summary, the high and specific cellular uptake and internalization in prostate cancer cells displayed by the PSMA-targeted ^{111}In-complexes, as well as their significant radiotoxicity in the same cell lines, are indicative of their potential for Auger therapy of cancer. MicroSPECT imaging studies in PSMA-positive PCa xenografts are underway to assess how the different components (TPP and PSMA-617 pharmacophores, cleavable linker) influence the *in vivo* behavior of the radioconjugates.

Acknowledgements: This work was supported by Fundação para a Ciência e Tecnologia, Portugal (projects UID/Multi/04349/2019 and PTDC /MED-QUI/1554/2020).

Reference

1. E. A. M. Ruigrok, W. M. van Weerden, J. Nonnekens, M. de Jong, Pharmaceutics 2019, 11, 560.
2. S. Rasul, M. Hacker, E. Kretschmer-Chott, A. Leisser, B. Grubmüller, G. Kramer, S. Shariat, W. Wadsak, M. Mitterhauser, M. Hartenbach, A. R. Haug, Eur J Nucl Med Mol Imaging 2020, 47, 713–720.
3. A. Ku, V. J. Facca, Z. Cai, R. M. Reilly, EJNMMI Radiopharmacy and Chemistry 2019, 4, 27.
4. D. Figueiredo, C. Fernandes, F. Silva, E. Palma, P. Raposinho, A. Belchior, P. Vaz, A. Paulo, Molecules 2021, 26(2), 441.

Poster Presentation

Disclosures: The authors have disclosed no financial interest.

259-Maximizing T1-weighted MRI acquisition to detect gadolinium-gold nanoparticles.

Presenter: Michel Modo, University of Pittsburgh

Harmanvir Ghuman[1], Kevin Hitchens[2], Thomas Meade[3], **Michel Modo[2]**

[1]*University of Pittsburgh*
[2]*University of Pittsburgh, Pittsburgh, PA*
[3]*Northwestern University, Evanston, IL*

Developing non-invasive imaging of cell distribution and migration in the brain using MRI remains an important tool to evaluate longitudinally how transplanted and endogenous neural progenitor/stem cells contribute to brain repair. Although T_2-weighted techniques relying on iron oxide-based contrast agents can provide a strong signal that even allows the detection of individual particles, this approach is compromised by false positives (i.e. air bubbles, hemosidrin), as well as a limitation on resolving the exact position of cells within their anatomical context. Gadolinium (Gd)-based T_1-weighted signals provide a unique signal for detection, but the signal attenuation is much lower than with iron-oxide based contrast agents. Engineering of Gd particles with DNA cross-linked on gold (Au) nanoparticles (Gd-DNA@AuNP) can dramatically increase their T1 relaxivity, as well as mitigate T1 quenching upon endocytosis. To achieve a maximum T_1-weighted contrast between Gd-DNA@AuNP and brain tissue, we measure the T1 of Gd-DNA@AuNP in transplanted cells and contrast this with the T1 measured in brain tissue. Considering the Curie point for Gd (19-20 °C), we performed these measurements at different temperatures (14, 18, 20, 22, 26, 30, 34, 38 °C, Figure 1A). The difference in T1 between Gd-DNA@AuNP and brain tissue was 20% greater at 38 °C than at 14 °C. Although there was a higher T1 signal for brain and Gd-DNA@AuNP at 11.7T compared to 9.4T, T1 contrast at 11.7T was only 4% higher compared to 9.4T. Using a design of experiment (DoE) simulation approach to determine optimal repetition time (TR= 50, 100, 500, 1000 ms, Figure 1B) and flip angle (10-90°), we determined that a TR=1000 ms with a flip angle of 90° provided maximum contrast between Gd-DNA@AuNP and brain tissue. These experiments highlight the importance of the image acquisition parameters to ensure maximum T_1-weighted contrast that is required to detect Gd-DNA@AuNP labeled cells for cellular MRI.

Poster Presentation

Disclosures: The authors have disclosed no financial interest.

260-PET Imaging of Pancreatic Cancer in Xenograft-Bearing Mice Using 18F-Labeled rBC2LCN Lectin

Presenter: Yukihito Kuroda, University of Tsukuba

Yukihito Kuroda[1], Kentaro Hatano[2], Osamu Shimomura[1], Hiroaki Tateno[3], Tatsuya Oda[1]
[1]*University of Tsukuba, Japan*
[2]*University of Tsukuba, Tsukuba, Ibaraki, Japan*
[3]*National Institute of Advanced Industrial Science and Technology (AIST), Japan*

Introduction:
Detecting pancreatic cancer in early stage should be the most effective means to improve curative outcomes, but existing imaging modalities, including US, CT and MRI, have been insufficient. Focusing on the hypermetabolism of cancers, [^{18}F]FDG-PET imaging have provided new insight in pancreatic cancer imaging diagnosis, however, its detecting rate, especially of early stage PDAC, have been limited. Researches on antibody-based imaging probes, targeting cancer cell surface protein antigen, are also in the development stage. One promising yet untapped target is the glycan-enriched outer layer of cancer cells known as the glycocalyx. We have previously demonstrated that fucosylated glycans (H type-3 antigens) are expressed in pancreatic cancers and a recombinant lectin, called rBC2LCN, binds to these glycans specifically (Shimomura O, Oda T, et al: Mol Cancer Ther 2018). Here, we developed a novel lectin-based PET probe for molecular imaging of cell surface glycans for pancreatic cancer. In this study, we first engineered ^{18}F-Labeled rBC2LCN lectin and evaluated its behavior in pancreatic cancer xenograft mice.

Material and Methods:
rBC2LCN (16kDa) lectin was labeled with N-succinimidyl-4-[^{18}F] fluorobenzoate ([^{18}F]SFB) which was prepared according to literature (Maeding P, et al: Appl Radiat Isot 2005) in phosphate buffer (pH 8.5). [^{18}F]FB-rBC2LCN thus obtained was purified using gel filtration column (PD-10, GE, Uppsala, Sweden). A pancreatic cancer cell line Capan-1 was used as a model which expresses H type-3 antigens. The biodistribution of the [^{18}F]FB-rBC2LCN was evaluated in athymic nude mice bearing subcutaneous Capan-1 tumors. Static small-animal PET imaging studies (G4, SOFIE, Dulles, VA) were performed to further evaluate *in vivo* tumor targeting and specificity.

Results:
Decay-corrected radiochemical yield of [^{18}F]FB-rBC2LCN was 3.6% ± 0.3% (mean ±SD, n = 5) based on [^{18}F]SFB and radiochemical purity was more than 96%. Dose of the labeled product injected intravenously to mice was 0.32 ± 0.16 MBq which corresponds 59 ± 21 mg. The biodistribution study demonstrated that Capan-1 tumor uptake (6.5 ± 2.0 %ID/g) was high as early as 60 min after injection of [^{18}F]FB-rBC2LCN, and the uptake increased over time (9.6 ± 2.2 and 11 ± 3.9 at 150 and 240 min after injection, respectively). Tumor-to-muscle ratio increased with time up to 15.2 ± 3.7 at 240 min after injection indicating image contrast. Although kidneys (72 ± 23 %ID/g), liver (7.1 ± 1.7 %ID/g) and lungs (7.4 ± 2.9 %ID/g) showed high uptake at 60 min after injection, the uptake of those organs decreased over time. The blood activity concentration of the tracer was also high at 60 min after injection (12 ± 4.4 %ID/g) and decreased over time (6.3 ± 2.1 and 3.8 ± 1.3 at 150 and 240 min after injection, respectively). Bone uptake was very low (below 1.8 %ID/g throughout the study) indicating that defluorinating metabolism was negligible. High-contrast PET imaging of tumors was achieved as early as 60 min after injection, and the contrast became clearer over 240 min, which was consistent with the biodistribution result. [^{18}F]FB-rBC2LCN exhibited moderate blood clearance predominantly through renal excretion.

Conclusions:
The ^{18}F-labeled rBC2LCN lectin represents a new class of tumor-specific probes for PET that are based on targeting cell surface glycans. The [^{18}F]FB-rBC2LCN demonstrated high-contrast small-animal PET imaging of pancreatic cancer xenografts. It could be translated to the clinic for PET of pancreatic cancer.

Acknowledgements: Authors are grateful to the members of AIC Imaging Center for their assistance.

Poster Presentation

Disclosures: The authors have disclosed no financial interest.

261-Pegylated rhodamine as a rapid and persistent contrast agent for glioma imaging in a cryo-imaged in-vivo mouse model

Presenter: Augustino Scorzo, Thayer School of Engineering at Dartmouth

Augustino Scorzo[1], Brook Byrd[2], Rendall R. Strawbridge[3], Scott Davis[2]

[1]*Thayer School of Engineering at Dartmouth*
[2]*Dartmouth College, Hanover, NH*
[3]*Dartmouth College, Lebanon, NH*

The current paradigm for the treatment of intracranial tumors is maximizing the extent of resection (EOR). Even for highly malignant and infiltrative tumor types, such as glioblastoma, increased EOR is correlative to increased overall survival[1-2] . To help maximize EOR, a preoperative MRI (pMRI) is acquired, often using a gadolinium-based contrast agent (GBCA), and these images are co-registered to the patient in the operating room for stereotactic neuro-navigation. Yet, this procedure has limitations arising from the deformation of brain tissue during resection. To help address this challenge, fluorescence guidance has emerged as an important modality for improving EOR. Existing contrast agents (CAs) for fluorescence guidance that are either approved or under investigation for this indication each have their own limitation. ALA-PpIX, approved for this indication, can provide exceptional contrast in many tumors but has shown unpredictable sensitivity to tumor heterogeneity[3], sodium fluorescein can display significant normal tissue uptake, and long-incubation ICG, which provides robust tumor contrast, is often performed using a 24-hr administration schedule, which can be logistically challenging in some settings[4]. In this context, we aim to identify a new agent for fluorescence neurosurgical guidance that displays the following characteristics: (1) high tumor-to-normal contrast within minutes of administration that persists well into the surgical procedure and (2) similar uptake behavior to GBCA's to provide familiar information to neurosurgeons. By using a whole animal hyperspectral fluorescence cryomacrotome co-registered to MRI, we screened several fluorescent candidate agents selected to minimize normal brain uptake and maximize tumor:normal tissue contrast. Herein, we report on a lead candidate, rhodamine conjugated to a small (1 kDa) methoxy-polyethylene glycol (mPEG) chain, which shows high contrast within minutes of administration that persists for at least 90 minutes. Mice containing orthotopic gliomas were positioned

in a specialized MRI coil, and after pre-CA images were acquired, administered a cocktail of contrast agents consisting of a GBCA and multiple fluorescence CA candidates. GBCA images were acquired until a set time at which point animals were euthanized and prepared for multi-channel, hyperspectral cryo-macrotome imaging which produces 3D whole body images of up to four fluorescent agents overlaid on color-RGB volumes at 100-micron resolution[5]. MRI and macrotome volumes were co-registered using fiducial-based registration for comparison between the two modalities. Cohorts were imaged at 10, 40 and 90 min. after administration and tumor:normal metrics assess.
Representative images of the lead candidate agent, mPeg-rhodamine 1kDa (PegRhd1k), and the GBCA in two mice (10 and 40 min. time points) are provided in Fig. 1. Qualitatively, we observed high tumor uptake with a profile that largely matches the GBCA. Quantitative analysis of all three cohorts confirms these observations. At 10, 40, and 90 min. after administration, tumor:normal brain contrast of PegRhd1k was 16.5 (n = 7, σ=9.5), 19.2 (n = 5, σ=2.35) and 12.7 (n = 3, σ=5.34), respectively. Notably, the normal brain signal in all animals was close to that measured in control animals without a fluorophore administered, a major factor in increasing contrast. These results indicate that the PegRhd1k agent provides very high tumor contrast within 10 minutes of administration which persists for at least 90 minutes. These favorable properties support further evaluation and development of this strategy.

Reference

1. Lacroix et al., "A Multivariate Analysis of 416 Patients with Glioblastoma Multiforme."
2. Sanai et al., "An Extent of Resection Threshold for Newly Diagnosed Glioblastomas."
3. Mazurek et al., "Analysis of Factors Affecting 5-ALA Fluorescence Intensity in Visualizing Glial Tumor Cells—Literature Review."
4. Zeh et al., "The Second Window ICG Technique Demonstrates a Broad Plateau Period for near Infrared Fluorescence Tumor Contrast in Glioblastoma."
5. Wirth et al., "Hyperspectral Imaging and Spectral Unmixing for Improving Whole-Body Fluorescence Cryo-Imaging."

Poster Presentation

Disclosures: The authors have disclosed no financial interest.

262-18F-FDG PETCT Image Processing with BSREM Reconstruction Algorithm And Performance Comparison With Conventional Reconstruction Method

Presenter: Pooja Dwivedi, Advanced Centre for Treatment, Research and Education in Cancer (ACTREC)

Pooja Dwivedi[1], Viraj Sawant, Sayak Choudhury[2], Ashish K. Jha[3], Venkatesh Rangarajan[4]

[1]*Advanced Centre for Treatment, Research and Education in Cancer (ACTREC), Mumbai, Maharashtra, India*
[2]*Advanced Centre for Treatment, Research and Education in Cancer (ACTREC), Mumbai, India*
[3]*Tata Memorial Hospital, Mumbai, Maharashtra, India*
[4]*Tata Memorial Hospital, Mumbai, IN-Mah, India*

Purpose:
The aim of the study is to evaluate the PET image processed with variable penalization factor of Block sequential regularized expectation maximization (BSREM) reconstruction algorithm on 5 rings BGO based PETCT system. The evaluation was required to check its performance on the basis of both quantitative and qualitative analysis to improve the overall image quality that will not only promote the diagnostic confidence but also treatment response evaluations. Order Subset Expectation Maximization (OSEM) is a fast and most applied standard PET reconstruction method, however, image noise increases with subsequent iterations and the algorithm is stopped before the images become too noisy. This could lead to inaccuracies for quantitative assessment as the algorithm does not reach full convergence. BSREM reconstruction algorithm allows full convergence of measured and estimated data with point spread function modeling without noise amplification during the image reconstruction process by noise controlling penalty factor.

Method:
In this study, 20 patients' data of 18F FDG PETCT study with confirmed malignancies were retrospectively assessed. For each study one OSEM reconstruction was performed with the standard protocol of 2 iterations, 12 subsets,4.8 mm Gaussian filter, and eight reconstructions with BSREM algorithm of variable β factors from 200 to 600 in the step of 50. To check the performance post image reconstruction process quantitative parameters SUVmax, SUVmean, SUVstd, Noise levels, Signal to Background ratio (SBR), and Signal to noise ratio (SNR) were calculated for each reconstruction method. The comparison was made among different reconstruction methods using statistical methods. Qualitative analysis was also done with visual scoring by two experienced nuclear medicine Physicians. All statistical analyses were performed using Microsoft Excel and IBM SPSS. Descriptive parameters were expressed as mean and SD. A value of $p < 0.05$ was considered statistically significant.

Result:
20 lesions of mean size 1.9±0.7 cm (range 1.2-4.1 cm) was identified. SNR significantly increased on increasing beta value from β 200 to 600 ($p < 0.05$) because the noise was decreasing on increasing beta value. SBR decreased on increasing beta values since SUVmax of lesion decreased on increasing β value. On com with a conventional algorithm noise level of β 200 was similar to OSEM(p=0.1). SBR of β200 to β400 were significantly higher (p<0.05 each) than OSEM whereas β450 500 and 550 doesn't show a significant difference(p>0.05 each) with the only exception of β600 which shows significantly lower SBR than OSEM. Visual scoring results for overall image quality considering both parameters of noise as well as lesion detection, β350 was the preferred choice among both readers with the moderate agreement. (Cohen kappa k = 0.5)

Conclusion:
The study indicates that in the BSREM reconstruction algorithm of PET images higher beta value could be utilized if noise is very high without loss of signal to background level and lower beta values could be beneficial in case of suspicious lesion detection for better lesion delineation where the study suggests the preferable range of 300 to 400. The overall evaluation shows β350 of BSREM is optimum in oncological cases for 18F FDG PET CT in a non-TOF-based PETCT system and it outperforms the conventional reconstruction method.

Reference

1. Jaskowiak CJ, Bianco JA, Perlman SB, Fine JP. Influence of reconstruction iterations on F-18-FDG PET/CT standardized uptake values. J Nucl Med. 2005;46:424–8.
2. Teoh EJ, McGowan DR, Macpherson RE, Bradley KM, Gleeson FV. Phantom and clinical evaluation of the Bayesian penalized likelihood reconstruction algorithm Q. Clear on an LYSO PET/CT system. J Nucl Med. 2015;56(9):1447–52.

3. Ahn S, Ross SG, Asma E, Miao J, Jin X, Cheng L, Wollenweber SD, Manjeshwar RM. Quantitative comparison of OSEM and penalized likelihood image reconstruction using relative difference penalties for clinical PET. Phys Med Biol. 2015 Aug 7;60(15):5733-51. doi: 10.1088/0031-9155/60/15/5733. Epub 2015 Jul 9. PMID: 26158503.
4. Chen, Wei, and Ying Liang. "Impact of BSREM Reconstruction Algorithm on Image Quality and Quantification Accuracy of PET-a Phantom Study." Journal of Nuclear Medicine 62, no. supplement 1 (2021): 3036–3036.
5. Wangerin KA, Ahn S, Wollenweber S, Ross SG, Kinahan PE, Manjeshwar RM. Evaluation of lesion detectability in positron emission tomography when using a convergent penalized likelihood image reconstruction method. J Med Imaging (Bellingham). 2017 Jan;4(1):011002. doi: 10.1117/1.JMI.4.1.011002. Epub 2016 Nov 22. PMID: 27921073; PMCID: PMC5118556
6. Rogasch, Julian M et al. "Reconstructed spatial resolution and contrast recovery with Bayesian penalized likelihood reconstruction (Q.Clear) for FDG-PET compared to time-of-flight (TOF) with point spread function (PSF)." EJNMMI physics vol. 7,1 2. 10 Jan. 2020, doi:10.1186/s40658-020-0270-y

Poster Presentation

Disclosures: The authors have disclosed no financial interest.

263-Relationship between Myocardial Extracellular Volume by Contrast MRI, Percent Fibrosis by Histology, and Glucose Metabolism by 18FDG/PET five days after a Myocardial Infarction in a Canine Model

Presenter: Erik Sistermans, Lawson Health Research Institute

Erik R. Sistermans[1], Haris Smailovic[2], Rebecca Sullivan[3], John Butler[3], Talia Richardson[3], Michael S. Kovacs[3], Gerald Wisenberg[4], Jonathan D. Thiessen[5], Frank S. Prato[2], Ben Wilk[6]

[1]*Lawson Health Research Institute*
[2]*Lawson Health Research Institute, London, Ontario*
[3]*Lawson Health Research Institute, London, ON*
[4]*London, Ontario*
[5]*Lawson Health Research Institute, London*
[6]*Western University, London*

Introduction:
Increases in myocardial extracellular volume (MECV) are often interpreted as existence of scar—presence of clinically important levels of myocardial fibrosis[1]. Increases in MECV can be detected using extracellular contrast agents with MRI[2]. If the increase in fibrosis is focal, a delayed enhancement method can qualitatively detect its presence. However, if the increase in fibrosis is diffuse, quantification of MECV is needed, which requires T1-maps prior to and after contrast administration along with a measure of hematocrit. With advances in T1-mapping, determination of MECV is now more often used to characterize cardiac tissue when diffuse fibrosis is present including tissue remote to the ischemic tissue following myocardial infarction (MI). However, pathophysiological interpretation of MECV measurement requires an understanding of tissue changes that generate changes in MECV and how these evolve with time. We investigated the relationship between the increase in MECV by MRI, tissue inflammation by PET, and extent of tissue fibrosis by histology in dogs, five days after MI.

Methods:
In seven adult female hounds, a MI was induced by permanent ligation of the left anterior descending coronary artery during left thoracotomy. The care and treatment of the animals was in accordance with the University of Western Ontario Council on Animal Care (Animal Use Subcommittee) guidelines. At baseline and five days after MI, hybrid PET/MRI was performed; MECV and metabolic rate of glucose (MRGlu) were assessed during a 150-minute constant infusion of Gd-DTPA at 4 μmol/min/kg and FDG at 170 kBq/min/kg. T1 maps acquired before and after contrast administration allowed the calculation of the MECV, assuming a hematocrit of 0.45[3]. Simultaneous constant infusion of Gd-DTPA and FDG has been shown to be an effective approach to measure the MECV by MRI and the MRGlu by PET[4]. Animals were euthanized and heart tissue samples were collected from four regions: center of infarct, edge of infarct, remote tissue, and right ventricle. Tissue samples were fixed, frozen and embedded in optimal cutting temperature compound, and subsequently sectioned at 5-6 μm thickness[5][6]. They were then stained with Masson's Trichrome Stain. All data points from the seven dogs were grouped into the 4 regions of tissue and statistical analysis was performed using GraphPad Prism (GraphPad Software, La Jolla, CA). Data did not pass normality; therefore, an unpaired and nonparametric Mann-Whitney test was used to compare mean percent fibrosis between tissue regions (Figure 1).

Results:
Percent fibrosis by histology decreased significantly between all regions, from Infarct Center to Infarct Edge to Remote Tissue to Right Ventricle ($p<0.05$, Fig 1). MECV significantly increased with percent fibrosis ($r=0.6740$, $p<0.05$) and with MRGlu ($r=0.7221$, $p<0.05$).

Discussion and Summary:
Although the temporal increase in MECV following MI remains constant in both dogs[7] and humans[8][9] the underlying tissue characteristics are changing with time. For example, Pereira *et al.* (1999) showed that within hours of a MI induced by occlusion/reperfusion injury that the MECV had increases in 30 min to the same values seen months later, even though at 30 min no fibrosis is present whereas at the later time fibrosis tissue content would be significant. Here, we show that by five days the increase in MECV is only partially related to fibrosis. The dependence on inflammation and the observation that even at five days the amount of fibrosis varied between animals (data not shown) suggests that the temporal response to MI varies even between well matched subjects. Hence, to better determine tissue conditions important for patient management, additional imaging methodologies (e.g. T1ρ for fibrosis[10], T2 for edema[2], FDG/PET for inflammation[11]) are needed.

Reference
1. Cheung, E., et al. (2021). Eur J Hybrid Imaging, 5(1).
2. Nakamori, S., & Dohi, K. (2022). J Cardiol. S0914-5087(22)00028-4.
3. Lawrence, J., et al. (2013). PLoS ONE, 8(11).
4. Smailovic, H., et al. (2021). J Nucl Cardiol, 29(3), 1304–1314.
5. McGirr, R., et al. (2011). Regul Pept, 172(1-3), 69–76.
6. Douglas, G.A.F., et al. (2014). Peptides, 54, 81–88.
7. Pereira, R.S., et al. (1999). Magn Reson Med, 42(1), 60–68.
8. Flacke, S.J., Fischer, S. E., & Lorenz, C. H. (2001). Radiology, 218(3), 703–710.
9. Thornhill, R.E., et al. (2006). Magn Reson Med, 55(4), 780–789.
10. Wang, K., et al. (2022). Magn Reson Imaging, 91, 1–8.
11. Wilk, B. et al. (2020). J Nucl Cardiol, 27(6), 2083–2099.

Poster Presentation

Disclosures: The authors have disclosed no financial interest.

264-In vivo characterization of [11C](+3)-MPB binding to mAChR in the brain of living mice

Presenter: Su Bin Kim, Seoul National University

Su Bin Kim[1], Hye Won Kim[1], Byung Seok Moon[2], Byung Chul Lee[3], Hyun Soo Park[4], Sang Eun Kim[5]

[1]*Seoul National University, Seoul, South Korea*
[2]*Ewha Womans University School of Medicine, Seoul, South Korea*
[3]*Seongnam-si, Gyeonggi-do, Republic of Korea*
[4]*Seoul National University Bundang Hospital, Seongnam, Gyeonggi-do, Republic of Korea*
[5]*Seoul National University Bundang Hospital, Seongnam-si, Gyeonggi-do, South Korea*

Background/Aim:
Positron emission tomography (PET) radiotracers targeting muscarinic acetylcholine receptors (mAChR) could have an enormous impact on enhancing therapeutic strategies for various neurological diseases including dementia. (+)N-[^{11}C]methyl-3-piperidyl benzilate ([^{11}C](+)3-MPB) was developed as a PET radiotracer for mAChR. The aim of the present study is to characterize the binding of [^{11}C](+)3-MPB to mAChR in the brain of living mice.

Method:
A total of 24 ICR mice underwent dynamic [^{11}C](+)3-MPB PET/CT studies after treatment with vehicle and different doses of mAChR antagonists, solifenacin and oxybutynin. Regional brain non-displaceable binding potential (BP_{ND}) of [^{11}C](+)3-MPB to mAChR was estimated using a time-course of [^{11}C](+)3-MPB distribution in cortical and subcortical structures and a simplified reference tissue model with cerebellar reference tissue input function. The differences in regional brain BP_{ND} of [^{11}C](+)3-MPB were examined to establish the dose-response relationship in terms of the effective dose (ED_{50}) using non-linear regression analysis for the E_{max} model.

Results/Conclusions:
[^{11}C](+)3-MPB PET quantitatively visualized cortical and subcortical mAChR function and its dose-dependent changes after solifenacin and oxybutynin treatment in the brain of living mice. Solifenacin and oxybutynin showed a maximal 61% and 60% difference compared to BP_{ND} of vehicle treatment for the highest doses of those drugs (10 mg/kg and 1 mg/kg, respectively) in the striatum. ED_{50} across regions ranged 3.67 – 12.54 mg/kg and 0.42 – 1.18 mg/kg for solifenacin and oxybutynin, respectively. *In vivo* quantitative PET analysis of brain mAChR occupancy may provide a fundamental basis for managing therapeutic strategies of potential drugs that exert mAChR antagonism implicated in neurological diseases.

Poster Presentation

Disclosures: The authors have disclosed no financial interest.

265-Preclinical internal radiation dosimetry of [18F]PSMA-1007 and its application for predicting the tumor absorbed dose of PSMA-targeting 177Lu-labeled theranostic tandem

Presenter: Su Bin Kim, Seoul National University

Su Bin Kim[1], Hye Won Kim[1], Hae Young Ko[2], Seon yu Kim[2], In Ho Song[3], Hyun Soo Park[4], Mijin Yun[2], Sang Eun Kim[3]

[1]*Seoul National University, Seoul, South Korea*
[2]*Yonsei University College of Medicine, Seoul, Seoul, Republic of Korea*
[3]*Seoul National University Bundang Hospital, Seongnam-si, Gyeonggi-do, South Korea*
[4]*Seoul National University Bundang Hospital, Seongnam, Gyeonggi-do, Republic of Korea*

Aims/Introduction:
[^{18}F]PSMA-1007 shows similarity in structure, biodistribution, and tumor uptake to the theranostic compound PSMA-617. Thus, [^{18}F]PSMA-1007 and [^{177}Lu]PSMA-617 seem to be a perfect theranostic tandem. This study aimed to predict the absorbed dose in the tumor and non-target organs of [^{177}Lu]PSMA-617 using [^{18}F]PSMA-1007 and an image-based internal radiation dosimetry analysis in prostate cancer xenograft model mice.

Material & Methods:
A total of eight BALB/c mice bearing lymph node carcinoma of the prostate cells underwent [^{18}F]PSMA-1007 PET/CT studies to illustrate the time-courses of distribution in the tumor and various organs. And the virtual PET images mimicking the biodistribution and pharmacokinetics of [^{177}Lu]PSMA-617 were artificially created using [^{18}F]PSMA-1007 PET images by considering the differences in the physical half-life between F-18 and Lu-177. Accordingly, given voxelized-source (PET) and -phantom (CT) images were used in the simulation for radiation transportation and electromagnetic process of radioactive decay of Lu-177 with Geant4 application for tomographic emission (GATE) Monte Carlo simulation software. Finally absorbed doses were calculated from the integral sum of the area under the dose rate curve to complete the image-based internal radiation dosimetry analysis.

Results:
The substantial accumulation of the [^{18}F]PSMA-1007 was shown in the tumor, kidney and salivary glands. The radiation dose of [^{177}Lu]PSMA-617 in the tumor and various organs were visualized and quantified via the energy deposition map (MeV) and the dose distribution map (Gy) by using the virtual PET images, while statistical uncertainties for the estimation were kept below 2%. The absorbed dose of [^{177}Lu]PSMA-617 in the tumor, kidney and salivary glands was predicted at 0.71 ± 0.14 Gy/MBq, 2.80 ± 0.53 Gy/MBq and 0.39 ± 0.06 Gy/MBq, respectively.

Conclusion:
Preclinical dosimetry in prostate cancer xenograft model mice can provide a starting point for the radiobiological interpretation and modeling of the dose distribution for response assessment during targeted radionuclide therapy. The present study suggests the possible application of [^{18}F]PSMA-1007 in the pre-therapeutic dosimetry for [^{177}Lu]PSMA-617.

Poster Presentation

Disclosures: The authors have disclosed no financial interest.

266-Preclinical evaluation of a smart liposomal nanoformulation for immunotargeted and real-time monitored delivery of chemotherapeutic drugs by SPECT imaging

Presenter: Shishu Kant Suman, Bhabha Atomic Research Centre

Shishu Kant Suman[1], Archana Mukherjee[2]

[1]*Bhabha Atomic Research Centre, India*
[2]*Bhabha Atomic Research Centre (BARC), Mumbai, Maharashtra, India*

Objective:
To design a smart liposomal nanoformulation for immunotargeted and real-time monitored delivery of chemotherapeutic drugs at the target site.

Introduction:
Liposomal formulations loaded with chemotherapeutic drugs have shown promising results for drug delivery in clinics [1]. However, smart nanoformulations are desired for targeted delivery and quantitation of the percentage of drug delivered at the target site for optimizing the doses and schedule of cancer treatment. Herein, we report the design, characterization, radiolabeling and preclinical evaluation of ^{99m}Tc labeled liposomes loaded with doxorubicin and decorated with antibodies for targeting HER2 receptor overexpressing cancers.

Methods:
Liposomes were prepared using N-(carbonyl-methoxypolyethylene glycol 2000)-1,2-distearoyl-sn-glycero-3-phosphoethanolamine sodium salt (MPEG-DSPE), cholesterol and 1,2-distearoyl-sn-glycero-3-phosphocholine (DSPC) by using ethanol injection method in acetate buffer. Drug doxorubicin was loaded using the active pH gradient method. After loading of drug, unloaded doxorubicin was removed using dialysis followed by sephadex G-25 exclusion column purification. For evaluating the drug loading efficiency, liposomes were ruptured using triton X-100, and absorbance of doxorubicin was measured at 485 nM using a plate reader and reverse phase-HPLC. For conjugation of doxorubicin loaded liposomes (Lip-Dox) with HER2 receptor targeting monoclonal antibody trastuzumab, liposomes were prepared using maleimide conjugated lipid. Antibodies were modified with Traut's reagent. Maleimide-liposomes and –SH modified antibodies were incubated at a ratio of 1:10 [2]. The formulation was purified for removing unconjugated antibodies using a superdex 200 size exclusion column using PBS. The Lip-Dox conjugated with trastuzumab (Lip-Ab-Dox) was radiolabeled with ^{99m}Tc (DTPA-lipid was utilized in preparing liposomes) using stannous chloride as a reducing agent. The stability of ^{99m}Tc-Lip-Ab-Dox (^{99m}Tc labeled liposomes encapsulating doxorubicin and conjugated with trastuzumab) and ^{99m}Tc-Lip-Dox (^{99m}Tc labeled liposomes encapsulating doxorubicin) was studied. For ascertaining the affinity of ^{99m}Tc-Lip-Ab-Dox against HER2 receptor, cell binding and inhibition studies were carried out in HER2 positive SKBR3 and negative MDA-MB-231 (Human breast cancer) cell lines. *In viv*o comparative evaluation of ^{99m}Tc-Lip-Ab-Dox and ^{99m}Tc-Lip-Dox in SKBR3 xenograft SCID mice was also carried out.

Results:
Liposomes of size 84.2 ± 2.9 nm could be prepared in a reproducible manner. The encapsulation efficiency of doxorubicin into liposomes was found to be 64.9 ± 2.8 %. Radiolabeling with ^{99m}Tc resulted in 100% radiochemical purity of the formulation. The stability of ^{99m}Tc-Lip-Ab-Dox and ^{99m}Tc-Lip-Dox was found to be 99.5 ± 0.3 % in serum and PBS at 37°C and 4°C when studied up to 24 h using thin layer chromatography and saline as mobile phase. ^{99m}Tc-Lip-Ab-Dox showed binding of 28.5 ± 0.2 % in HER2 positive cells. Up to 51.6 % inhibition in the uptake of radiolabeled formulation with 5 µg of unlabeled trastuzumab was observed indicating specificity of the radioformulation. ^{99m}Tc-Lip-Dox showed only 4.3 ± 0.9 % cell uptake and no inhibition was observed. While in similar studies with HER2 negative MDA-MB-231 (breast cancer) cell line, ^{99m}Tc-Lip-Ab-Dox and ^{99m}Tc-Lip-Dox showed 3.2 ± 0.7 % and 3.6 ± 0.5 % binding respectively and no inhibition was observed with unlabeled trastuzumab. This confirms the specificity of ^{99m}Tc-Lip-Ab-Dox for HER2 receptors. In *In vivo* comparative evaluation of ^{99m}Tc-Lip-Ab-Dox and ^{99m}Tc-Lip-Dox in SKBR3 xenograft bearing SCID mice, ^{99m}Tc-Lip-Ab-Dox showed two-fold higher uptake in tumor at 6 h and 24 h as ascertained by SPECT imaging. Results of biodistribution studies also corroborated with the SPECT imaging data. These results reveal the potential of ^{99m}Tc-Lip-Ab-Dox for immunotargeted and real-time monitored delivery of doxorubicin in HER2 positive tumors using SPECT imaging.

Conclusion:
A smart liposomal nanoformulation for immunotargeted and real-time monitored delivery of chemotherapeutic drugs at the target site was successfully formulated and evaluated with encouraging results in preclinical studies. To the best of our knowledge, this is the first attempt to design a target-specific radiolabeled liposomal nanoformulation for immunotargeted delivery and quantitation of drug delivery using SPECT imaging.

Reference
1. Allahou LW, Madani SY, Seifalian A. Investigating the Application of Liposomes as Drug Delivery Systems for the Diagnosis and Treatment of Cancer. Int J Biomater. 2021 Sep 1;2021:3041969.
2. Shi C, Gao F, Gao X, Liu Y. A novel anti-VEGF165 monoclonal antibody-conjugated liposomal nanocarrier system: physical characterization and cellular uptake evaluation in vitro and in vivo. Biomed Pharmacother. 2015 Feb;69:191-200.

Poster Presentation

Disclosures: The authors have disclosed no financial interest.

267-Pharmacological Ascorbate induces transient hypoxia potentiating hypoxia activated prodrug.

Presenter: shun Kishimoto, NIH

Shun Kishimoto[1], Jeffrey Brender[2], Kota Yamashita[2], Kazutoshi Yamamoto[3], Devasahayam Nallathamby[2], Murali Krishna Cherukuri[2]

[1]*NIH*
[2]*National Cancer Institute, Bethesda, MD*
[3]*National Institutes of Health, Bethesda, Maryland*

Purpose:
When ascorbate is administered at high concentration via intraperitoneal or intravenous injection, it is feasible to achieve concentration. At such high concentrations ascorbate can get autoxidized forming active oxygen including superoxide with subsequent dismutation to hydrogen peroxide.(1) (Figure 1) In the current study, we examined local oxygen consumption by the pharmacological ascorbate therapy using treatment sensitive pancreatic ductal adenocarcinoma MIA Paca-2 model and resistant lung carcinoma A549 model and further evaluated the effect of induced hypoxia on the treatment efficacy of hypoxia-activated prodrug evofosfamide therapy.(2)

Methods:
The oxygen consumption rate (OCR) and extracellular acidification rate (ECAR) were analyzed on a XF96 Extracellular Flux Analyzer (Agilent Technology). Twenty thousand cells were plated into each

well of a 96-well plate and cultured overnight. During the measurement of OCR and ECAR, cells were treated with ascorbate (0.1, 1 and 1000 μM) and catalase (100 μg/ml) at time point of 30 minutes and 60 minutes, respectively.
Photoacoustic imaging was performed by scanning tumors with the Visual Sonics Vevo®LAZR System (FUJIFILM VisualSonics Inc., Canada) using a 21-MHz linear array transducer system (central frequency) integrated with a tunable nanosecond pulsed laser. During the scan, mice were anesthetized using isoflurane (1.5–2.5%). Respiration was continuously monitored to ensure the data reproducibility and animal well- being. The tumor area in the sagittal plane of the leg was manually determined from concurrently acquired ultrasound images. In this study, the experiments were performed on a fixed plane depicting the center of the tumor in order to achieve better temporal resolution.

Results:
In both MIA Paca-2 and A549 cells, we could observe the increased OCR right after ascorbate treatment followed by quick decrease, and following catalase treatment cancelled the decrease in OCR and increased the OCR level higher than baseline again. (Figure 2) The result suggested that pharmacological ascorbate caused hydrogen peroxide production resulting in enhanced consumption of oxygen. The following drop in OCR was considered the result of oxidative stress on mitochondrial respiration, which could be rescued by catalase. ECAR decreased after ascorbate treatment and the decrease was stopped by catalase in both cell lines, suggesting that anaerobic fermentation was also downregulated by hydrogen peroxide and the effect persisted after catalase treatment unlike mitochondrial damage.(1,3) The in vivo oxygen consuming effect on both MIA Paca-2 and A549 tumors was examined by photoacoustic imaging (PAI).(Figure 3) As expected, the transient hypoxia for 6-7 min after ascorbate injection was observed in both tumors. Since the changes was not observed in MIA Paca-2 tumors treated with same amount of vehicle, the biphasic sO2 and vasodynamic changes might be induced by the mixed effect of rapid oxygen consumption and ascorbate-induced vasodilation. In both tumor models, we could confirm the significantly improved tumor doubling time in ascorbate + evofosfamide group compared to control group suggesting that adjuvant use of ascorbate can improve the treatment effect of evofosfamide by inducing transient hypoxia. (Figure 4)

Conclusion:
The treatment induced transient but severe hypoxia sensitized both ascorbate-sensitive MIA Paca-2 and ascorbate-resistant A549 tumors to evofosfamide, without increasing toxicity. Since both treatments in the combination therapy are selectively targeting and have shown safe profiles in clinical studies, the combination therapy has a great potential to be safely and positively evaluated in clinical settings in the future.

Reference

1. Chen Q, Espey MG, Sun AY, Lee JH, Krishna MC, Shacter E, Choyke PL, Pooput C, Kirk KL, Buettner GR, Levine M. Ascorbate in pharmacologic concentrations selectively generates ascorbate radical and hydrogen peroxide in extracellular fluid in vivo. Proc Natl Acad Sci U S A 104: 8749-54, 2007.
2. Doskey CM, Buranasudja V, Wagner BA, Wilkes JG, Du J, Cullen JJ, Buettner GR. Tumor cells have decreased ability to metabolize H2O2: Implications for pharmacological ascorbate in cancer therapy. Redox Biol 10: 274-284, 2016.
3. Uetaki M, Tabata S, Nakasuka F, Soga T, Tomita M. Metabolomic alterations in human cancer cells by vitamin C-induced oxidative stress. Sci Rep 5: 13896, 2015.

Poster Presentation

Disclosures: The authors have disclosed no financial interest.

268-Quantification of Effective Dose In Patients From 18F-FDG WBPETCT Study for Radiation Dose Optimization

Presenter: Pooja Dwivedi, Advanced Centre for Treatment, Research and Education in Cancer (ACTREC)

Pooja Dwivedi[1], Vishal Vajarkar, Sayak Choudhury[2], Ashish K. Jha[3], Venkatesh Rangarajan[4]

[1]Advanced Centre for Treatment, Research and Education in Cancer (ACTREC), Mumbai, Maharashtra, India
[2]Advanced Centre for Treatment, Research and Education in Cancer (ACTREC), Mumbai, India
[3]Tata Memorial Hospital, Mumbai, Maharashtra, India
[4]Tata Memorial Hospital, Mumbai, IN-Mah, India

Purpose:
The underline motive of this study was the assessment of radiation dose optimization by quantifying the estimated effective dose in patients from both PET and CT components in 18F-FDG WB PETCT procedure. Another important reason for the study was to make a small effort in providing such data which could help in establishing DRL levels at the regional level as per ICRP recommendations. As it is well-established fact that PET-CT is a valuable medical imaging tool in oncology since combined metabolic and morphological information is provided in a single study however hybrid imaging also brings an increased patient exposure to radiation. With the advancement in imaging technology, it is now easier to track the patient dose along with simple calculation methods which are both practical as well as based on ICRP recommendations and utilized in this study.

Method:
Data of 98 patients with various confirmed malignancies who underwent WB F18 FDG PETCT study were retrospectively studied. Scans were acquired on 5 ring BGO PETCT scanner with 60 minutes uptake period after injecting18F FDG. CT scans were performed under beam collimation of 10mm, pitch 0.938, helical thickness 5mm, rotation time 0.5 sec, and tube voltage of 120 kV. CT dose optimization strategy was adopted by selecting smart mA which uses automatic tube current modulation. PET Scans were acquired in the 3D mode for dose optimization. Estimation of effective (ED) dose from PET component was calculated based on injected activity and Γ dose coefficient as per ICRP128. Effective dose from CT component was estimated as a product of DLP and conversion factors k as per ICRP 102 for various scan protocols The conversion factor k was used as 0.014 and 0.015 mSv/mGy-cm for the chest and trunk respectively according to ICRP publication 102. All the calculations and statistical analyses were performed using Microsoft Excel. Descriptive parameters were expressed as mean and SD.

Results:
Average injected activity of 18F-FDG was 261.57 ± 52.50 MBq in adult patients with a mean weight of 51.92± 10.48 kg. Mean $CTDI_{vol}$ and DLP and corresponding calculated mean estimated effective dose are provided in Supplementary Table. The total calculated ED of CT component from standard protocol which includes CT lung and CT WB was found to be 12.07± 1.25 mSv (range 8.16-15.21 mSv). The calculated mean estimated ED of the PET component was found to be 4.96 ±0.99 mSv (range 3.1-7.6 mSv) which is significantly lower than the dose from CT ($p<0.05$). The total mean effective dose of both

components CT and PET in the standard protocol of WB PETCT is found to be 17.04 ± 1.71 mSv (range 13.43- 21.38 mSv).

Conclusion:
The results indicate that the total mean effective dose from the standard WB PET CT protocol was found to be 17.04 ± 1.71 mSv which is within the range of the global estimated dose with an average of 25 mSv. This shows that dose optimization strategies work well if implemented in a planned manner. The study also reflects that periodic data monitoring and auditing of estimated effective dose is important for the verification of dose optimization strategies adopted.

Reference
1. Huang B, Law MW, Khong PL. Whole-body PET/CT scanning: estimation of radiation dose and cancer risk. Radiology. 2009 Apr;251(1):166-74. doi: 10.1148/radiol.2511081300. Epub 2009 Feb 27. PMID: 19251940..
2. European Commission (EC) (2014) Diagnostic Reference Levels in Thirty-Six European Countries Part 2/2. Radiation Protection n°180.
3. ICRP 106 Publication. Radiation dose to patients from radiopharmaceuticals. Ann ICRP 2007;38:21–4.
4. ICRP publication 102. Ann ICRP. 2007;37:1–79.

Poster Presentation

Disclosures: The authors have disclosed no financial interest.

269-In vivo multimodal imaging of inflammatory bowel disease (IBD) progression in a mouse model

Presenter: Jeffrey Peterson, PerkinElmer

Alexis Stanley[1], Craig McMannus[2], Jen-Chieh Tseng[2], **Jeffrey D. Peterson[2]**

[1]PerkinElmer
[2]PerkinElmer, Hopkinton, MA

Objective:
Inflammatory bowel disease (IBD) is a multifaceted and complex disorder with significant unmet clinical treatment options for patients. The most common forms of idiopathic IBD include Crohn's disease (CD) and ulcerative colitis (UC) with hallmarks of disease that include inflammation of the gastrointestinal tract and reduced [RG1] epithelial barrier function. We hypothesize that non-invasive in vivo imaging techniques can detect, visualize, and quantify disease progression in preclinical IBD models. Two imaging modalities were tested in this study: (1) Ultrasound (3D B-Mode) to measure induced changes from normal intestinal structure; and (2) Fluorescent molecular tomography (FMT), in conjunction with specific imaging probes, to detect parenteral inflammation [RG2] of the gut and responses to known treatments. As each technology aims to visualize and quantify different aspects of the disease, this multimodal imaging approach should facilitate non-invasive assessment of IBD progression in preclinical models.

Methods:
The IBD mouse model was established by administering 4% Dextran Sulfate Sodium (DSS) ad libitum in drinking water to female BALB/c mice, which induces chemical irritation and, ultimately, acute colitis in these mice. The animals were then imaged at various timepoints during the study timeline. Abdominal hair removal and depilation were performed prior to imaging to prevent interference with optical and ultrasound signal. In addition to the untreated control (CTRL) and DSS-treated (DSS) mice, we modulated the disease severity by using dexamethasone (DSS-DEX) and imiquimod (DSS-IMQ). Although widely used as an anti-inflammatory therapeutic, dexamethasone is known to exacerbate acute colitis induced by DSS. Imiquimod, on the other hand, a proinflammatory agonist of TLR7, has been shown to have antibacterial activity and to reduce colon inflammation in this particular model. The DSS-DEX group combined 4% DSS with daily IP injection of 1 mg/kg Dexamethasone; the DSS-IMQ group received 4% DSS with daily imiquimod (IMQ) oral gavages at a dose of 30 mg/kg. 3D B-mode ultrasound images were captured on a Vega imaging system (PerkinElmer Inc.). 3D FMT imaging of tissue inflammation was performed with a FMT4000 imaging system (PerkinElmer Inc.) using IVISense^{TM} Pan Cathepsin 680 (PC 680), a fluorescent probe for cathepsin activity, delivered via the tail vein 24h prior to FMT acquisition. Non-invasive imaging measurements for DSS-induced changes in the thickness of the colon wall and loss of barrier function were validated via H&E staining of fixed and sectioned tissue collected from both the cecum and colon. Histology sections from each study group were scored for disease severity by an independent pathologist.

Results:
Inflammatory bowel disease was observed in all DSS treated groups after 10 days. Hallmarks of disease, including loss of body weight, loose feces, and perianal bleeding, were confirmed by daily observation. Colon diameter (mm) measured on Day 9 by ultrasound showed a significant ~40% increase (student t-test: **P< 0.01) in both the DSS and DSS-DEX cohorts. Interestingly, IMQ protected the colon from acute colitis induced by DSS; DSS-IMQ mice had improved colon diameters as measured by ultrasound and calipers. However, histologic analysis indicated that IMQ did not protect the cecum from elevated leukocyte infiltration, ulceration, or erosion. The increased cathepsin activity in the GI area of the DSS mice was inhibited by DEX but further elevated in the DSS-IMQ mice, suggesting induction of either protective innate immunity or an enhanced wound healing response by IMQ.

Conclusion:
This multimodal strategy provides a novel approach for the non-invasive visualization and quantitative assessment of IBD disease progress in animal models. Additionally, we show that this approach is useful in separately assessing anatomical and molecular phenotypes of IBD before and during response to therapy.

Poster Presentation

Disclosures: The authors have disclosed no financial interest.

270-Novel magnetic vortex nanorings for tumor MRI/PAI/CT diagnosis and PTT-RT synergistic therapy

Presenter: Shuangshuang Guo, Zhengzhou University

Shuangshuang Guo[1], Jianfeng Bao[2], Dandan Fan[2], Miaomiao Chen[3], Zhenyu Ji[3]

[1]Zhengzhou University, China
[2]First Affiliated Hospital of Zhengzhou University, Zhengzhou, Henan, China
[3]Zhengzhou University

Background:

Current cancer treatments have serious limitations, such as surgical resection, chemotherapy, and radiation therapy. Photothermal therapy (PTT) as an adjunct to radiation therapy (RT) can significantly increase tumor regression, and the combination of PTT and RT has been shown to be synergistic. Noble metal nanoparticles such as gold (Au) and silver (Ag) exhibit a unique photophysical phenomenon called localized surface plasmon resonance (LSPR) that enhances their light absorption. Therefore, they are thought to be able to stimulate hyperthermia in cancer cells upon exposure to near-infrared radiation (NIR). Additionally, magnetic nanoparticles (NPs) have been used for magnetic resonance (MR) imaging due to their T_2 shortening effect. [1] Considering all the above properties and capabilities of Fe_3O_4 NPs and AuNPs, they can be combined into a single nanocomposite[2]. Gold-coated iron oxide nanoparticles are under intense investigation as a promising theranostic nanoparticle, as they can be used as a contrast agent for MRI, as well as a sensitizer to enhance the effects of laser and radiofrequency hyperthermia.

Objective:
By combining MRI imaging, PTT, and RT capabilities, an Au NP-coated Fe_3O_4 NP was fabricated to develop promising biocompatible theranostic nanoplatform.

Methods:
A novel magnetic vortex nanoring Fe_3O_4@Au was synthesized. A series of physical and chemical characterizations confirmed the successful construction of Fe_3O_4@Au. The heat generation ability of Fe_3O_4@Au was confirmed under the excitation of 808 nm laser. The cell viability of different concentrations of Fe_3O_4@Au, and the therapeutic effects of PTT and RT were investigated in vitro with MCF-7 cells. Additionally, T_2-weighted MRI was studied *in vitro* and investigated *in vivo* contrast-enhancing capabilities and tumor aggregation behavior. Finally, the effects of different hyperthermia on cancer treatment were evaluated and compared through in vivo animal experiments.

Results:
Fe_3O_4@Au was successfully constructed. By simply reducing ring-Fe_2O_3, uniform hollow magnetite Fe_3O_4 is obtained with excellent magnetic properties. Nanoring Fe_3O_4 coated with Au exhibited strong absorption and photothermal conversion efficiency, and the heat generation capacity, heating rate and peak value were significantly improved. Cell culture results showed that the nanoparticles themselves possess excellent biocompatibility, but have high levels of cytotoxicity upon activation with NIR.

Conclusions:
In conclusion, a novel iron oxide-based theranostic nanosystem was reported for the effective enhancement of MRI-guided photothermal therapy. This work not only demonstrates that the nanoring Fe_3O_4@Au is a highly efficient nanocomposite for imaging-guided photothermal therapy, but also provides a basic guidance for the development of a hollow iron oxide-based multifunctional therapeutic nanoplatform for efficient hyperthermia and monitoring of cancer.

Reference

1. A. Espinosa, R. Di Corato, J. Kolosnjaj-Tabi, P. Flaud, T. Pellegrino, C. Wilhelm, Duality of Iron Oxide Nanoparticles in Cancer Therapy: Amplification of Heating Efficiency by Magnetic Hyperthermia and Photothermal Bimodal Treatment, ACS Nano 10(2) (2016) 2436-2446.
2. N. Eyvazzadeh, A. Shakeri-Zadeh, R. Fekrazad, E. Amini, H. Ghaznavi, S. Kamran Kamrava, Gold-coated magnetic nanoparticle as a nanotheranostic agent for magnetic resonance imaging and photothermal therapy of cancer, Lasers in Medical Science 32(7) (2017) 1469-1477.

Poster Presentation

Disclosures: The authors have disclosed no financial interest.

271-Nanocluster-antibody-drug conjugates (NADC) as an intravesical precision theranostic agent for interstitial cystitis

Presenter: Zhijun Lin, Sun Yat-sen University Cancer Center

Zhijun Lin[1], Jiang Yang[2], Dingxin Liu[3], Jiadong Pang[2]

[1]Sun Yat-sen University Cancer Center, China
[2]Sun Yat-sen University Cancer Center, Guangzhou, Guangdong, China
[3]State Key Laboratory of Oncology in South China Sun Yat-sen University Cancer Center, Guangzhou, China, China

Objective:
Interstitial cystitis (IC) is a long-lasting, complex medical condition currently with no cure. Intravesical IC therapy competently attains a high local concentration of drug payloads to directly contact the afflicted area of the bladder with reduced systemic side effects. However, the low drug retention and bladder elimination during urinary emiction greatly limit therapeutic efficacy. To circumvent the variable pharmacological behaviors of multiple modalities and achieve therapeutic synergy with precision, we developed a versatile theranostic NADC using covalent conjugation that comprises a Tanezumab monoclonal antibody (Tan) targeting the nerve growth factor (NGF), near-infrared fluorescent (NIRF) catalytic enzyme-mimicking gold quantum nanoclusters (AuQCs), and the dihydroorotate dehydrogenase (DHODH) inhibitor, Vidofludimus (Vido). We hypothesize that the hybrid NADC framework presents synergistic therapeutic efficacy in treating IC with high NGF expressions in bladder mucosae by intravesical instillation under NIRF image guidance.

Methods:
Firstly, AuQCs were synthesized from an alpha-lactalbumin (α-LA)-mediated reduction reaction using the HAuCl4 precursor, as reported previously[1]. Secondly, the primary amines of lysine side chains of AuQCs reacted with the NHS ester of Traut's reagent (2-iminothiolane) to afford reactive maleimides. In the meantime, solvent-accessible primary amines of the Tan antibody were similarly modified into sulfo-SMCC, which successively reacted with the maleimide-activated AuQCs. Last, after purification, the remaining unreacted amines were further covalently crosslinked with the benzoic acid of Vido via the classic EDC/NHS reaction to derive the NADC. We then comprehensively characterized the NADC using dynamic light scattering (DLS), transmission electron microscopy (TEM), circular dichroism, biolayer interferometry (BLI), and optical spectroscopies. Furthermore, the nanocluster-to-drug-to-antibody ratio (NDAR) was calculated that maintain balanced efficacy, pharmacokinetics, and toxicity. To investigate the anti-inflammatory effects, we evaluated the NADC in the immortalized human uroepithelial SV-HUC-1 IC model induced with lipopolysaccharide (LPS) and ATP. Time-lapse non-invasive near-infrared fluorescence (NIRF) imaging was conducted in living rats following intravesical instillation of the NADC in the bladder.

To understand the bladder mucosal permeability, flux rates, and body absorption, we tested the transport of NADCs with rat bladder tissues. Finally, the in vivo intravesical treatment using the NADC was verified in the cyclophosphamide (CYP)-induced cystitis rat model.

Results:
The AuQCs-Tan-Vido NADC has a hydrodynamic size of ~40 nm and a negative zeta-potential (-18 mV). Moreover, the NDAR ratio is approximately 5:3:1 for AuQCs:Vido:Tan. The NADC preserved the unique optical properties of AuQCs and enabled NIRF around 700 nm by visible excitation at 500 nm. The high binding affinity constant (KD) to NGF from Tan remained at the same 10^{-9} order of magnitude in the NADC with a similar association and dissociation kinetics as measured by BLI. The NADC coordinately regulated pro- and anti-inflammatory cytokines in the SV-HUC-1 IC model. Further, time-course in vivo NIRF imaging disclosed prolonged bladder retention of NADCs in the rat IC model with an extended half-life compared to the ultrasmall AuQCs. The transmucosal permeability assay verified negligible penetration of NADCs across the bladder tissue. Intravesical administration of NADCs in rats with IC improved the therapeutic efficacy on the mechanical threshold and micturition function by inhibiting expressions of pro-inflammatory cytokines, including the Vido-targeted IL-17A, and the phosphorylation of the NGF receptor, tropomyosin receptor kinase A (p-TrkA).

Conclusion:
Since an effective IC management strategy remains challenging due to its complicated unelusive pathogenesis, the NADC has great theranostic potential with imaging to guide drug administration, doses, and frequencies. The state-of-art NADC framework for diagnosing and treating IC patients with high NGF expressions in the bladder mucosae provides a viable all-in-one polytherapeutic solution. Consequently, IC symptoms, such as mechanical allodynia and micturition function, were significantly mitigated following intravesical administration of NADCs. These preliminary results strongly suggested that the AuQCs-Tan-Vido NADC could serve as a precision IC theranostic agent with alleviated systemic toxicity.

Reference

1. Yang, J. et al. Nat Biomed Eng. 2020; 4(7):686-703.

Poster Presentation

Disclosures: The authors have disclosed no financial interest.

272-Bioprofiling Disease Progression Using In Vivo Fluorescent Imaging in a Mouse Model of Systemic Lupus Erythematosus

Presenter: Jeffrey Peterson, PerkinElmer

Kristine O. Vasquez[1], **Jeffrey D. Peterson[1]**

[1]PerkinElmer, Hopkinton, MA

Systemic Lupus Erythematosus (SLE) in humans is a complex multigenic, systemic disorder that can cause acute or chronic inflammation of multiple organ systems, involving autoantibody production, lymphoid activation/hyperplasia, and nephritis. There are multiple mouse models that capture some of the important hallmarks of human disease, and the MRL MpJ Fas-lpr /J (MRL/lpr) mouse is one of the most commonly used, developing lymproliferation by 16-18 weeks, as well as progressive albuminuria and renal disease, lymphadenopathy, and skin lesions, typically dying at around 20 weeks of age. In contrast, related MRL-MpJ (MpJ) control mice demonstrate mild and slow progressing signs of autoimmunity, generally living for 73 weeks. We tested the use of non-invasive *in vivo* fluorescence imaging techniques to detect, visualize, and quantify disease progression in animal MRL/lpr as compared to MpJ and BALB/c mice. Multiple near infrared (NIR) fluorescent IVISense^{TM} imaging probes (PerkinElmer Inc.) were used to profile inflammatory responses (pan-cathepsin-, matrix metalloprotease-, cathepsin B-, and cathepsin K-activatable probes), kidney function (renin activatable probe), and cell death (Annexin V probe). Fluorescence tomography (3D) and epifluorescence (2D) images were acquired on the FMT4000 (PerkinElmer Inc.) to visualize and quantify tissue signal. MRL/lpr lupus develops spontaneously, and animals were assessed at 16 and 20 weeks for albuminuria and lymphadenopathy. Albuminuria microplate assay readings ranged from 50 to 140 mg/dL at week 20, and 16 week lymphadenopathy scores ranged from 2-5, with brachial or inguinal lymph node sizes from <0.5 cm to >1 cm at 1 to 2 sites. MpJ and BALB/c mice showed no signs of lymphadenopathy or albuminuria. All animals were depilated (light shaving and depilatory cream) the day prior to fluorescent probe imaging to prevent fur interference with fluorescence signal. Imaging probes were injected IV (2 nmol/mouse) every two weeks in separate mouse cohorts, each of which received the same probe injections 6 times over 4-16 weeks. Mice were imaged in 2D and 3D at 4, 8, 10, 12, 14, and 16 weeks to detect biological changes associated with lupus progression, as compared to MpJ and BALB/c mice. All six imaging probes revealed whole body 3D signal increases at 12-16 weeks as compared to BALB/c, in both MRL/lpr and MpJ mice, suggesting systemic basal increases in inflammatory activity. However, total signal could not differentiate between subclinical MpJ and clinical MRL/lpr disease. This suggested that these imaging probes are sensitive enough to detect even low grade lupus progression. Three fluorescent probes in particular, specific for cathepsin B, cathepsin K, and Annexin-V-binding, detected regional tissue differences localized to the spleen, lymph nodes, and kidneys, that had increased signal in MRL/lpr mice as compared to both MpJ and BALB/c controls, i.e. these probes were able to differentiate clinical and subclinical disease. These specific regional signals were very low in BALB/c mice, generally intermediate in MpJ mice, and distinctly elevated in MRL/lpr mice. In addition, the renin-activatable probe detected distinct but low increases in liver signal unique to late stage disease in MRL/lpr mice, suggesting an increase in liver renin-angiotensin system activity in lupus development. In summary, NIR fluorescent imaging strategies using validated imaging probes can provide a novel means for the non-invasive assessment of lupus progression in animal models. In addition, expansion of this approach to other relevant biomarkers may further help to identify critical tissues and biological pathways involved in lupus development or progression.

Poster Presentation

Disclosures: The authors have disclosed no financial interest.

273-Novel macromolecular probe for dual 19F/31P MRI

Presenter: Daniel Jirak, Institute for Clinical and Experimental Medicine

Daniel Jirak[1], Lucie Wold?ichová[2], Martin Vit[3], Natalia Zió?kowska[4], Ladislav Androvic[5], Richard Laga[2]

[1]Institute for Clinical and Experimental Medicine, PRAHA 4, Czech Republic

[2]*Institute of Macromolecular Chemistry, Czech Academy of Sciences, Prague, Czech Republic*
[3]*Technical University of Liberec, Liberec, N/P, Czech Republic*
[4]*Charles University, Prague, N/A, Czech Republic*
[5]*Prague, Czech Republic*

Introduction:
A novel bioresponsive macromolecular probe based on a conjugate of phosphorus-containing zwitterionic polymer with anticancer drug 5-fluorouracil (FU) enabling dual ^{19}F and ^{31}P magnetic resonance imaging (MRI) has been developed. The polymer is characterized by a high content of naturally rare phosphorothioate (P=S) groups in its structure, which oxidize to phosphoesters (P=O) in the presence of reactive oxygen species (ROS) overproduced in tumor and inflamed tissues. This transformation is accompanied by a significant chemical shift detected by ^{31}P MRI [1]. The presence of FU provides the probe not only with a source of fluorine, but also with a potential antitumor effect. In this proof-of-principle experiment, we assessed the MR properties of the probe and performed *in vitro* and *in vivo* ^{19}F/^{31}P MRI measurement of the probe.

Methods:
The phosphorus-containing polymer precursor was synthesized by the controlled radical copolymerization (RAFT) technique of a zwitterionic monomer *O*-(2-(methacryloyloxy)ethyl) *O*-(2-(trimethylamoniumyl) ethyl) phosphorothioate (TMPC) with an amino group-containing monomer *N*-(2-aminoethyl)methacrylamide (AEMA) in the presence of a dithiobenzoate-based chain transfer agent. The resulting probe was generated by attaching a thiazolidine-2-thione-activated FU derivative (5-fluoro-3,4-dihydro-2,4-dioxo-1(2H)-pyrimidinoacetic acid) to AEMA units of the precursor via a stable amide bond. MR relaxometry, imaging and spectroscopy were performed in 4.7T scanner using dual home-made ^{1}H/^{31}P and ^{1}H/^{19}F radiofrequency coils. Laboratory rat was subcutaneously injected in right hind leg by 170 µl dose consisting of polymer dissolved in distilled water.

Results/Discussion:
Both nuclei (^{31}P and ^{19}F) incorporated in the probe possessed optimal T_2 relaxation times for MRI visualization (172 ms for ^{19}F and 83 ms for ^{31}P). This made it easy to visualize them in both aqueous solution phantoms and animal using two independent MR imaging modalities – ^{31}P MRI and ^{19}F MRI (Fig.1). The P=S groups in the probe structure caused a chemical shift of 56.07 ppm enabling separation of phosphorus coming from the probe from naturally occurring phosphorus compounds in the body. Signal from isoflurane anaesthetics does not interfere with the *in vivo* probe's signal in ^{19}F MR, their chemical shift was large (more than 60 ppm).

Conclusion:
The macromolecular probe combining a phosphorus-based polymer and a fluorine-containing antitumor drug was successfully visualized in both phantoms and animal using ^{19}F and ^{31}P MRI. MRI experiments were performed on magnetic fields close to those used in clinical medicine, which opens up the possibility of transition to clinical medicine. The next step in testing the probe will be an *in vivo* experiment on a statistically significant population of mouse models with tumours, aimed at simultaneous reduction of ROS at the tumour site and induction of antitumor effect of FU. We believe that this innovative concept of polymeric theranostics can be used in both the diagnosis and treatment of cancer.

Acknowledgement: The project was partially supported by SGS project no. 21332/3002 of the Technical University of Liberec and by the Ministry of Health of the Czech Republic [NU20-08-00095].

Reference

1. Kracíková L, Ziółkowska N, Androvič L et al. Phosphorus-Containing Polymeric Zwitterion: A Pioneering Bioresponsive Probe for 31 P-Magnetic Resonance Imaging. Macromol Biosci. 2022 Mar 5:e2100523

Poster Presentation

Disclosures: The authors have disclosed no financial interest.

274-Imaging human and canine lung cancer using a phospholipase A2 activatable fluorophore

Presenter: Ritesh Isuri, University of Pennsylvania

Michael C. Hart[1], Drew Ramos[1], Sofya Osharovich[2], Andrea E. Rodriguez[3], Stefan Harmsen[1], David Holt[4], Anatoliy V. Popov[1], Sunil Singhal[5], Jim Delikatny[1], **Ritesh K. Isuri[6]**

[1]*University of Pennsylvania, Philadelphia, PA*
[2]*University of Pennsylvania, Medford, NJ*
[3]*University of Pennsylvania, Philadelphia, Pennsylvania*
[4]*University of Pennsylvania*
[5]*Perelman School of Medicine at the University of Pennsylvania, Philadelphia, PA*
[6]*University of Pennsylvania, Port louis, Savanne, Mauritius*

Introduction:
Lung cancer is the leading cause of cancer-related death in the United States with a 5-year survival rate of less than 20%.[1] Approximately 85% of lung cancers are non-small cell lung cancers (NSCLC) which are primarily treated by surgical resection. NSCLC resections rely on tissue palpation and visual inspection to identify margins. This nonspecific identification leads to roughly 40% of NSCLC patients experiencing disease recurrence.[2,3] Thus, developing targeted imaging agents for the intraoperative detection of NSCLC would improve rates of curative resections by aiding surgeons in identifying malignancies. Cytosolic phospholipase A2 (cPLA2) is overexpressed and hyperactive in NSCLC. A cPLA2 activatable NIR fluorophore, DDAO-arachidonate (DDAO-A) was previously developed for *in vivo* triple-negative breast cancer (TNBC) imaging, but intravenous injections resulted in poor biodistribution and off-target activation of the probe.[4-6] However, DDAO-A exhibited rapid activation kinetics making topical administration of the probe a possible alternative.[4,5] Due to the high cPLA2 expression and mortality rate associated with NSCLC, we hypothesized that DDAO-A would be preferentially activated in human and canine lung cancer tissues when compared to normal lung tissues making it a promising agent for real-time guidance of NSCLC surgical resections and identification of malignant positive margins of resected tissues.

Methods:
Five DBA/2 mice bearing NSCLC derived KLN 205 tumors, were treated intratumorally with DDAO-A, with the control probe DDAO-palmitate (DDAO-P), or with DDAO-P chased by DDAO-A to rescue fluorescence activation. Tumors and flank muscle tissues were excised from the mice and imaged for *ex vivo* fluorescence. Human (n=10) and canine (n=3) normal lung and lung tumor tissues were obtained from patients undergoing lung cancer surgery from our hospital and veterinary school, respectively. Tissues were treated topically with DDAO-A, and fluorescence was measured after 15 min. *Results*: Mice treated with the negative control probe, DDAO-P, exhibited insignificant increases in tumor fluorescence.

DDAO-A chase treatments and initial intratumoral injections resulted in significant increases in the signal-to-noise ratios (SNR) showing strong activation of DDAO-A in tumors with SNRs up to 9.5:1. In 8 out of 10 human and in all canine specimens, tissues exhibited fluorescent tumor-to-normal ratios (TNRs) of at least 2:1 and up to 5.2:1 demonstrating that DDAO-A is preferentially activated in lung tumor tissues.

Discussion:

DDAO-A is preferentially activated by lung tumor tissues in mouse models and in human and canine specimens. TNRs of 2:1 and higher demonstrated tumor selectivity making the probe a promising candidate for the real-time guidance of surgical resections. Additionally, this study demonstrates that the use of human and canine tumor tissue specimens provides a promising alternative to *in vivo* murine studies for fluorophore development. By imaging tumor accumulation in human and canine tumors, fewer mice were needed to verify the effectiveness of DDAO-A for NSCLC imaging. Due to the rapid activation of the probe, topical administration of the fluorophore in surgical cavities and for back table imaging in surgeries could aid surgeons in identifying residual disease without significantly increasing the duration of surgeries. As systemic administration is not necessary for probe application, there are fewer concerns for biodistribution and toxicity

Reference

1. Cancer Facts & Figures. American Cancer Society. 2022. https://www.cancer.org/research/cancer-facts-statistics/all-cancer-facts-figures/cancer-facts-figures-2022.html
2. Kelsey CR, Clough RW, Marks LB. Local recurrence following initial resection of NSCLC: salvage is possible with radiation therapy. Cancer J. Jul-Aug 2006;12(4):283-8. doi:10.1097/00130404-200607000-00006
3. Uramoto H, Tanaka F. Recurrence after surgery in patients with NSCLC. Transl Lung Cancer Res. Aug 2014;3(4):242-9. doi:10.3978/j.issn.2218-6751.2013.12.05
4. Chiorazzo MG, Bloch NB, Popov AV, Delikatny EJ. Synthesis and Evaluation of Cytosolic Phospholipase A(2) Activatable Fluorophores for Cancer Imaging. Bioconjug Chem. Dec 16 2015;26(12):2360-70. doi:10.1021/acs.bioconjchem.5b00417
5. Chiorazzo MG, Tunset HM, Popov AV, Johansen B, Moestue S, Delikatny EJ. Detection and Differentiation of Breast Cancer SubTypes using a cPLA2alpha Activatable Fluorophore. Sci Rep. Apr 16 2019;9(1):6122. doi:10.1038/s41598-019-41626-y
6. Linkous AG, Yazlovitskaya EM, Hallahan DE. Cytosolic phospholipase A2 and lysophospholipids in tumor angiogenesis. J Natl Cancer Inst. Sep 22 2010;102(18):1398-412. doi:10.1093/jnci/djq290

Poster Presentation

Disclosures: The authors have disclosed no financial interest.

275-T2/T2W MRI and 18FDG-PET multimodal imaging of the innate immune response in skeletal muscle and draining lymph node post vaccination in rats

Presenter: Saaussan Madi, GlaxoSmithKline

Saaussan Madi[1], Mary Rambo[2], Tina Skedzielewski[2], Shih Hsun Cheng[3], Tolulope A. Aweda[4], Bhasker Radaram[3], Stephanie Slania[5], Hasan Alsaid, Tammy Lambert[6], Stephane Temmerman[7], Giulietta Maruggi[8], Russell Johnson[8], Beat Jucker[4]

[1]*GlaxoSmithKline, Collegeville*
[2]*GlaxoSmithKline, King of Prussia, PA*
[3]*GlaxoSmithKline, Collegeville, PA*
[4]*GSK, Collegeville, PA*
[5]*Johnson&Johnson*
[6]*Collegeville*
[7]*Rixensart, Belgium*
[8]*Rockville*

Introduction:

The goal of this study was to utilizeT2 /T2W MRI and ^{18}FDG PET multimodal imaging to assess the local innate immune response in skeletal muscle and draining lymph node following vaccination in rats, and to compare two different vaccine platforms (Adjuvant System (AS01B), and Self Amplifying mRNA (SAM)) to better understand the temporal, local immune response profile of these different vaccine platforms and to provide a direct measure of reactogenicity in muscle[1-5].

Methods:

Two groups of Sprague Dawley rats (250-300 g) received 50 ml injections, in the right gastrocnemius muscle, of 1) Adjuvanted vaccine, CMV (gB/pentamer)/AS01B, n=4; 2) AS01B (adjuvant alone), n=2; 3) CMV (gB) SAM LNP (lipid nanoparticle), n=4; 4) LNP alone, n=2.

Group 1 was imaged after the prime vaccine injection (Day 0). Group 2 received a booster vaccine injection (Day 21) and was imaged only after receiving the booster injection. Serial ^{18}FDG PET imaging using a Mediso LFER150 PET scanner was followed by T2/T2W MRI performed on a 4.7T Bruker scanner @ 4, 24, 48, and 72 hr post-injection. Blood was drawn prior to each imaging session for cytokine and antibody titer assessment. All procedures were approved by the Institutional Animal Care and Use Committee of GlaxoSmithKline.

Results:

^{18}FDG PET/CT signal was detected in both right popliteal lymph node (Fig. 1A, B) and right gastrocnemius (Fig. 1C, D) of vaccinated hindlimbs with little to no uptake in contralateral hindlimb. The regions of MRI signal enhancement and ^{18}FDG PET uptake in muscle were similar as can be observed in the coregistered image (Fig. 1E). T2 weighted MRI signal enhancement in skeletal muscle at the site of injection was used as a biomarker of innate immune activation. The right gastrocnemius signal enhancement in the CMV SAM group appeared greater at 24 hr and longer in duration compared with the CMV AS01B group (Fig 1F, G). Similar responses were observed with the AS01B or empty LNP alone. There was no signal enhancement observed in the contralateral hindlimb. The MRI signal enhancement volume in gastrocnemius was increased and duration of enhancement was temporally shifted right in the CMV SAM vs CMV AS01B groups following both Prime and Prime-Boost vaccinations (Fig 1H, I). Total glycolysis in gastrocnemius following ^{18}FDG PET also showed a similar response profile to MRI (Fig. 1J, K). MRI assessed right popliteal lymph node volume was rapidly elevated in both the CMV SAM and CMV AS01B groups (Fig. 1L, M). However, only the AS01B groups showed a robust increase in volume following Prime-Boost administration. Additionally, ^{18}FDG PET signal enhancement and total glycolytic burden in the right popliteal lymph node was higher in CMV SAM vs CMV AS01B groups. Again, only the AS01B groups showed a robust increase in volume following Prime-Boost administration. Correlations were observed between imaging endpoints and cytokine response with IL-6 and IL-13 showing the strongest correlations. However, the imaging endpoints exhibited greater dynamic responses than did the cytokines. Finally, AI/ML radiomics was used to systematically assess a variety of image features, including those based on intensity, shape, and texture, in the right gastrocnemius and draining popliteal lymph

node. These features were correlated with cytokines and mAb titers to identify clusters of features with strong associations.

Conclusion:
In vivo imaging provides direct and sensitive reactogenic readouts by directly visualizing the entire skeletal muscle and draining lymph node. Combining these spatiotemporal imaging approaches with AI/ML & systems vaccinology approaches may better predict immune responses and cellular profiles at site of injection and draining lymph node which may be especially useful in evaluating next generation

Reference

1. Burger et al., Clin Nucl Med 36: 848-853, 2011
2. Coates et al., Clin Nucl Med 42:329-334, 2017
3. McIntosh et al., Am J Roentgenology 217:975-983, 2021
4. Eisenberg et al. Radiology Case Reports 16:3024-3028, 2021
5. Win et al., Front Immunol 11:613496., doi.org/10.3389/fimmu.2020.613496

Poster Presentation

Disclosures: The authors have disclosed no financial interest.

276-Automated synthesis and preliminary imaging results of a sodium glucose co-transporter 2 PET imaging agent, Me 4-[18F] FDG

Presenter: Avinash Bansode, Wake Forest School of Medicine

Avinash H. Bansode[1], Naresh Damuka[2], Ivan Krizan, Mack Miller[1], Krishna Gollapelli[3], Bhuvanachandra Bhoopal, Suzanne Craft[4], Kiran Kumar Solingapuram Sai

[1]Wake Forest School of Medicine, Winston-Salem, NC
[2]Wake Forest School of Medicine, Winston Salem
[3]Wake Forest School of Medicine, Winston salem, NC
[4]Wake Forest School of Medicine, Winston Salem, North Carolina

Introduction:
Metabolic and vascular disorders are powerful risk factors for Alzheimer's disease (AD). Medications used to treat type2 diabetes mellitus (T2DM) could be repurposed as therapeutic agents for AD. Among them, sodium-glucose co-transporter 2 inhibitors (SGLT2is) are an important new class of therapeutic compounds that have attracted considerable interest because of their concomitant effects on metabolism and vascular function in adults with T2DM. While preclinical studies have drawn attention to SGLT2is as possible AD therapeutics, determining *in vivo* levels of SGLT2s will provide critical information on their underlying mechanisms, which could lead to develop novel drug candidates to treat AD symptoms. Direct regulation of SGLT2is in AD brain *in vivo* has not yet been investigated and to examine these changes in the metabolic cascade of AD, it is important to image SGLT2 *in vivo*. Automated radiochemistry of a new SGLT2-based PET radioligand, β-methyl-4-[^{18}F]fluoro-4-deoxy-D-glucopyranoside (Me-[^{18}F]-4FDG) in a commercial radiochemistry module, TRASIS AIO is reported. To validate the radiotracer production, microPET imaging, post-PET biodistribution, and autoradiography studies were performed with Me-[^{18}F]-4FDG in normal/healthy mice.

Methods:
Me 4-[^{18}F]FDG was produced in the TRASIS AIO radiochemistry module following [^{18}F]F$^-$/K$_{222}$/K$_2$CO$_3$-assisted nucleophilic substitution reaction of the corresponding triflate analog (methyl 2.3.6-tri O-acetyl-4-trifluoromethanesulfonate), which was purchased from ABX. Briefly, triflate precursor (1-3 mg) was dissolved in dry acetonitrile (1 mL) and added to the dried [^{18}F]F$^-$/K$_{222}$ reaction vessel. The reaction mixture was heated at 90 °C for 15 min and the residual solvent was evaporated under nitrogen at 110°C. HCl (1N, 1.5 mL) was then added to the dried reaction vial and heated at 110°C for an additional 15 min. The crude reaction mixture was passed through cation, anion, and alumina resins before transfer to the C18 semi prep HPLC column (mobile phase: water). The final radiotracer was directly collected into a sterile vial through a 0.2 µm sterile filter. Me 4-[^{18}F]FDG (150 ± 10 µCi) was intravenously injected via tail vein and 0-60 min dynamic PET/CT brain imaging was performed in normal/healthy male mice (n=4). Post-PET whole-body biodistribution and brain autoradiography studies were performed in the same mice. Tracer uptakes in organs of interest were measured using a γ-counter and expressed as %ID/g tissue. Brain autoradiography studies were performed at baseline and blockade conditions, with nonradioactive Me 4-FDG as the blocking agent.

Results:
Herein simplified and automated the Me 4-[^{18}F]FDG radiosynthesis in the TRASIA AIO module. Me 4-[^{18}F]FDG was produced in high radiochemical purities (~97 ± 2%) in 8 ± 4 % radiochemical yield, with decay corrected to the end of synthesis. Me 4-[^{18}F]FDG was identified using the analytical QC- HPLC system by co-eluting with a standard Me 4-FDG (retention time of 10.0−10.9 min). *In vivo,* microPET/CT images in rodents indicated brain penetration. *Ex vivo* post-PET biodistribution in the same mice showed favorable kinetics, including renal and/or hepatic clearance, non-significant bone uptake (no defluorination), and high target (brain) to non-target (muscle) ratio. Autoradiography data with blockade showed a significant reduction (>80%) of uptake when compared to baseline.

Conclusions:
Our TRASIS AIO-based automated radiochemistry can be directly translated and easily adapted to any commercially available automated modules for human injections. Strong preliminary biological evaluations of Me 4-[^{18}F]FDG in rodents support its high translational potential to image SGLT2s effectively.

Reference

1. Kepe, V., Scafoglio, C., Liu, J., Yong, W. H., Bergsneider, M., Huang, S. C., Barrio, J. R., & Wright, E. M. (2018). Positron emission tomography of sodium glucose cotransport activity in high grade astrocytomas. Journal of neuro-oncology, 138(3), 557–569.

Poster Presentation

Disclosures: The authors have disclosed no financial interest.

277-Multiplex iterative immunofluorescence analysis enables a better understanding of AKT signaling dynamics in living cells

Presenter: Min Xue, University of California, Riverside

Min Xue

University of California, Riverside, Riverside

Kinase signaling networks among cells play crucial roles in many pathophysiological processes, such as tumorigenesis and inflammation.

The temporal patterns of kinase signaling, such as oscillations, and transient or sustained activity, have been found to carry information that controls cellular responses. To understand the kinase signaling dynamics and access a comprehensive perspective of the cellular signaling network, combining single-cell kinase signaling dynamics with multiplex protein analysis is required. However, with conventional immunofluorescence, the number of protein detection is limited. Herein, an iterative immunofluorescence method was developed to address this unmet need. This method utilizes a photocleavable (PC) linker to connect the antibody and fluorophore. After imaging and data acquisition, the PC linker can be cleaved with UV light under a mild condition in the buffer solution. The fluorophore is separated from the antibody and washed away, which allows a new cycle of immunostaining. This approach can be readily combined with the kinase dynamics detection methods. For a proof of concept, cells were first treated using a pair of peptide-based AKT sensors, which enabled continuous analysis of AKT signaling activities under various perturbations. Then, the iterative immunofluorescence method was implemented to quantify eighteen proteins along the AKT pathway. Such exercise allowed a better understanding of AKT signaling dynamics in the context of phenotypical signatures at single-cell resolution.

Reference

1. F. Ji, S. Wang, S. Shao, P. Sarkar, M. Xue, Real-Time Analysis of AKT Signaling Activities at Single-Cell Resolution Using Cyclic Peptide-Based Probes, Biomedical Engineering Technologies 2022, 65-80.
2. S. Shao, Z. Li, H. Cheng, S. Wang, N. G. Perkins, P. Sarkar, W. Wei, M. Xue, A Chemical Approach for Profiling Intracellular AKT Signaling Dynamics from Single Cells, Journal of the American Chemical Society, 2018, 140, 13586-13589.

Poster Presentation

Disclosures: The authors have disclosed no financial interest.

278-In vivo imaging system for intravital cellular-level visualization of mouse brain

Presenter: Pilhan Kim, Korea Advanced Institute of Science and Technology (KAIST)

Jerome Kim[1], Alex Kim[1], Hayden Kwon[1], **Pilhan Kim[2]**

[1]*IVIM Technology, South Korea*
[2]*Korea Advanced Institute of Science and Technology (KAIST), Daejeon, South Korea*

For the investigation of the central nervous system (CNS) and pathogenesis of neuroinflammation, previous studies have been mainly conducted with *in vitro* or *ex vivo* histological analysis. However, the conventional histological analysis has difficulty understanding the 3D spatiotemporal cellular changes of the central nervous system over a long time in the pathological condition because the available information was limited to a single specific time point of tissue harvest. During the last decades, fluorescence microscopy, including confocal and multi-photon microscopy, has been actively utilized for the direct in vivo visualization of dynamic cellular movement in live animal models. However, the cellular-level dynamics in the central nervous system are still poorly understood due to technical limitations [1]. Herein, we optimized the surgical procedure for cranial imaging window implantation with less inflammation and we established the stereotaxic plate with the heating function of maintenance of live animal physiological conditions [2]. By utilizing the IVM-CM intravital imaging system and in vivo fluorescence labeling of target cells, in vivo cellular-level observation of brain vasculature was clearly achieved in the cranial imaging window implanted mouse model. By switching the imaging mode from confocal to two-photon, collagen fibers from detection of second-harmonic generation signal were simultaneously visualized with brain vasculature. In addition, with the ultrafast uniform laser-beam scanning of the IVM-CM imaging system, real-time dynamics of rapidly circulating neutrophils fluorescently labeled in blood vessels were successfully visualized in the brain cortex. Furthermore, longitudinal visualization of brain vasculature in the photothrombosis-induced mouse model was conducted. For phototrombosis induction on the specific brain area, laser beam with 561 nm wavelength was illuminated right after the retro-orbital injection of Rose Bengal [3]. At 4 days after induction of photothrombosis, the damaged vessels with greatly reduced diameter were observed, in comparison with the normal state. To conclude, we established the intravital imaging method for in vivo high-resolution cellular visualization of the brain. We believe that it could be a highly useful tool for a comprehensive understanding of the studies of the central nervous system in pathological condition. Furthermore, it can also be applied for real-time analysis for in vivo drug tests in the various brain disease murine model.

Reference

1. Carmen Hierro-Bujalance, et al., Front. Aging Neurosci. 10:218 (2018).
2. Jingu Lee, et al., Biomedical Optics Express, 11(9): 5132-5146 (2020).
3. Jingu Lee, et al., Glia, 70(5): 975-988 (2022).

Poster Presentation

Disclosures: The authors would like to disclose that IVIM Technology is not approved for distribution in the United States.

279-Deuterated α-ketoglutarate has the potential to detect the isocitrate dehydrogenase 1 mutation in low-grade gliomas

Presenter: Celine Taglang ,University of California, San Francisco

Celine Taglang[1], Georgios Batsios[2], Meryssa Tran[3], Anne Marie Gillespie[3], Sabrina Ronen[1], Pavithra Viswanath[3]

[1]*University of California, San Francisco, San Francisco, CA*
[2]*University of California, San Francisco, San Francisco*
[3]*University of California, San Francisco, San Francisco, California*

Introduction:

The isocitrate dehydrogenase 1 mutation (IDH_{mut}) drives tumorigenesis in low-grade gliomas (LGGs)[1,2]. The wild-type isocitrate dehydrogenase (IDH_{wt}) enzyme converts isocitrate to α-ketoglutarate (α-KG) while IDH_{mut} catalyzes the conversion of α-KG to 2-hydroxyglutarate (2-HG)[3]. ^{1}H-MRS-based detection of 2-HG has been used to determine IDH_{mut} status and assess response to IDH_{mut} inhibitors[4]. However, ^{1}H-MRS detects steady-state metabolism and does not reflect metabolic pathway activity. ^{2}H-MRS following administration of ^{2}H-labeled substrates recently emerged as a novel, clinically translatable method of assessing flux via metabolic pathways[5,6]. The goal of this study was to determine whether ^{2}H-MRS-based assessment of [3,3'-^{2}H]-α-KG

metabolism has the potential to detect IDH_{mut} status and response to IDH_{mut} inhibitors in LGG models.

Methods:

Synthesis of [3,3'-^{2}H]-α-KG**:** To reduce the complexity of ^{2}H-MR spectra, we examined the utility of [3,3'-^{2}H]-α-KG. Specifically, metabolism of [3,3'-^{2}H]-α-KG (2.9 ppm) is expected to produce [3,3'-^{2}H]-2-HG or [3-^{2}H]-2-HG (1.9 ppm; hereafter referred to as ^{2}H-2-HG for clarity) through the action of the IDH_{mut} enzyme. [3,3'-^{2}H]-α-KG was synthesized as previously described using D_2O at basic pH[7].

Cell Culture:

Immortalized normal human astrocytes expressing IDH_{wt} ($NHAIDH_{wt}$) or IDH_{mut} ($NHAIDH_{mut}$) were maintained in Dulbecco's modified Eagles Medium supplemented with 10% fetal calf serum and 2 mM glutamine as described previously[8-10]. IDH_{wt} and IDH_{mut} expression has been confirmed previously[8-10]. For assessment of response to IDH_{mut} inhibition, $NHAIDH_{mut}$ cells were treated with 1 mM BAY1436032 or vehicle-control (DMSO) every 24h for 72h[11].

^{1}H-MRS:

Metabolites were extracted by methanol-chloroform extraction and ^{1}H-MR spectra acquired on a Bruker 500 MHz spectrometer equipped with a Triple Resonance CryoProbe[8-10]. Data was analyzed using Mnova. Peak integrals were calculated, corrected for saturation, and normalized to cell number and to an external reference (trimethylsilyl propionate).

^{2}H-MRS:

Cells were incubated in media containing 10 mM [3,3'-^{2}H]-α-KG for 72h. ^{2}H-MR spectra were acquired from live cell suspensions on a Varian 14.1T scanner using a 16mm ^{2}H surface coil. Data was analyzed in Mnova. Peak integrals were normalized to α-KG, the natural abundance of semi-heavy water (HDO, 4.75 ppm; estimated to be 12.8 mM and quantified from the signal collected from a vial containing saline), cell number and expressed as normalized 2-HG per 10^{12} cells.

Statistical Analysis:

All results are expressed as mean±standard deviation. Statistical significance was assessed using an unpaired two-tailed Student's t-test with $p<0.05$ considered significant.

Results:

[3,3'-^{2}H]-α-KG metabolism to 2-HG can be observed in IDH_{mut} cells: We confirmed the presence of 2-HG in $NHAIDH_{mut}$ but not $NHAIDH_{wt}$ cells by ^{1}H-MRS. Importantly, as shown in the representative ^{2}H-MR spectra, $NHAIDH_{mut}$ cells showed a clear peak at 1.9 ppm corresponding to ^{2}H-2-HG, which was absent in $NHAIDH_{wt}$ cells. Quantification of the data confirmed that $NHAIDH_{mut}$ cells produced significantly higher ^{2}H-2-HG relative to $NHAIDH_{wt}$ cells.

2-HG production from [3,3'-^{2}H]-α-KG can be used to monitor response to IDH_{mut} inhibitors: Next, we examined whether [3,3'-^{2}H]-α-KG can be used to assess response to BAY1436032, an IDH_{mut} inhibitor that reduces 2-HG production in IDH_{mut} glioma cells[11]. As shown in the representative ^{2}H-MR spectra and quantification, ^{2}H-2-HG labeling was significantly reduced by treatment with BAY1436032, confirming that the peak at 1.9 ppm is 2-HG and pointing to the potential ability of [3,3'-^{2}H]-α-KG to assess response to IDH_{mut} inhibitors.

Conclusions:

Our study shows that [3,3'-^{2}H]-α-KG metabolism to 2-HG can be specifically observed in $NHAIDH_{mut}$, but not $NHAIDH_{wt}$, cells. Importantly, 2-HG production from [3,3'-^{2}H]-α-KG is reduced in $NHAIDH_{mut}$ cells following treatment with the IDH_{mut} inhibitor BAY1436032. Further studies in patient-derived IDH_{mut} cells and tumor xenografts are ongoing to determine the utility of [3,3'-^{2}H]-α-KG for *in vivo* imaging of tumor burden and treatment response in LGGs.

Reference

1. Cheng, M., Bhujwalla, Z. M. & Glunde, K. Targeting Phospholipid Metabolism in Cancer. Frontiers in oncology 6, 266, doi:10.3389/fonc.2016.00266 (2016).
2. Glunde, K., Bhujwalla, Z. M. & Ronen, S. M. Choline metabolism in malignant transformation. Nature reviews. Cancer 11, 835-848, doi:10.1038/nrc3162 (2011).
3. De Feyter, H. T., Thomas, M., Ip, K., Behar, K. & de Graaf, R. Delayed mapping of 2H-labeled choline using Deuterium Metabolic Imaging (DMI) reveals active choline metabolism in rat glioblastoma. 2021 Annual Meeting of the International Society for Magnetic Resonance in Medicine (2021).
4. Veltien, A. et al. Simultaneous Recording of the Uptake and Conversion of Glucose and Choline in Tumors by Deuterium Metabolic Imaging. Cancers (Basel) 13, doi:10.3390/cancers13164034 (2021).
5. Mancini, A. et al. Disruption of the beta1L Isoform of GABP Reverses Glioblastoma Replicative Immortality in a TERT Promoter Mutation-Dependent Manner. Cancer cell 34, 513-528 e518 (2018).
6. Giannini, C. et al. Patient tumor EGFR and PDGFRA gene amplifications retained in an invasive intracranial xenograft model of glioblastoma multiforme. Neuro-oncology 7, 164-176 (2005).
7. Kelly, J. J. et al. Oligodendroglioma cell lines containing t(1;19)(q10;p10). Neuro-oncology 12, 745-755, doi:10.1093/neuonc/noq031 (2010).
8. Mazor, T. et al. Clonal expansion and epigenetic reprogramming following deletion or amplification of mutant IDH1. Proceedings of the National Academy of Sciences of the United States of America 114, 10743-10748, doi:10.1073/pnas.1708914114 (2017).
9. Viswanath, P. et al. Mutant IDH1 gliomas downregulate phosphocholine and phosphoethanolamine synthesis in a 2-hydroxyglutarate-dependent manner. Cancer & metabolism 6, 3, doi:10.1186/s40170-018-0178-3 (2018).
10. Viswanath, P. et al. 2-hydroxyglutarate-mediated autophagy of the endoplasmic reticulum leads to an unusual downregulation of phospholipid biosynthesis in mutant IDH1 gliomas. Cancer research, doi:10.1158/0008-5472.can-17-2926 (2018).
11. Viswanath, P. et al. Non-invasive assessment of telomere maintenance mechanisms in brain tumors. Nature communications 12, 92, doi:10.1038/s41467-020-20312-y (2021).

Poster Presentation

Disclosures: The authors have disclosed no financial interest.

280-Developmental complex trauma causes dysfunction of neurotransmission in vivo

Presenter: Jae Yong Choi, Korea Institute of Radiological & Medical Sciences

Jae Yong Choi[1], Namhun Lee[2], Se Jong Oh[2]

[1]Korea Institute of Radiological & Medical Sciences, Seoul, South Korea

[2]*Korea Institute of Radiological and Medical Sciences (KIRAMS), Seoul, South Korea*

Early life stress has a deleterious effect on the development of normal brain development, and as a result, it also induces various psychiatric disorders in adulthood. Previous studies mainly focus on behavioral or molecular biology, but researches on the functional aspects are still limited. The aim of the present study is to elucidate the effect of early life stress on specific neurotransmission—including glutamatergic, GABAergic, and serotonergic systems—by means of positron emission tomography (PET). Early life stress models include single trauma (MS), and complex trauma groups (MRS). Here, MS was generated from maternal separation, and MRS was derived from maternal separation and restraint stress. As a result, the MRS group displayed significant weight loss and depressive/anxiety-like behavioral phenotypes than the MS and control groups. Corticosterone levels in MRS showed a greater extent of decline than in the MS group; however, there was no significant difference in the change of thyroid hormones between MRS and MS. In the PET, the MS and MRS group showed lower brain uptake for GABAergic, glutamatergic, and serotonergic systems compared with the control group. We also confirmed the neuronal degeneration in the stress exposure groups by immunohistochemistry. Taken together, we suggested that early life stress induces dysfunction of neurotransmission in vivo.

Reference

1. Lee N, Oh SJ, Park JW, Nam KR, Kang KJ, Lee KC, Lee YJ, Choi JS, Seok JH, Choi JY."Evaluation of the Effects of Developmental Trauma on Neurotransmitter Systems Using Functional Molecular Imaging". Int J Mol Sci. 2021;22:2522

Poster Presentation

Disclosures: The authors have disclosed no financial interest.

281-Modified PROMISE Criteria for Standardized Interpretation of GRPR-targeted PET

Presenter: Heying Duan, Stanford University

Heying Duan[1], Guido A. Davidzon[1], Farshad Moradi[1], Tie Liang[2], Andrei Iagaru[1]

[1]*Stanford University, Stanford, CA*
[2]*Stanford University, Stanford, California*

Introduction:
There are three different interpretation criteria for prostate-specific membrane antigen (PSMA)-targeted PET. As up to 10% of prostate cancer (PC) do not express PSMA, other targets such as gastrin releasing peptide receptor (GRPR) were evaluated. GRPR-targeted imaging has been increasingly used for initial staging and biochemical recurrence (BCR). We therefore propose a unified interpretation criteria for GRPR-targeted PET based on the Prostate Cancer Molecular Imaging Standardized Evaluation (PROMISE) criteria which was developed for PSMA-PET [1].

Materials and Methods:
Participants who were initially prospectively enrolled in research protocols at our institution, were retrospectively reviewed. One-hundred patients, aged 67.9±7.0 years, underwent ^{68}Ga-RM2 PET/MRI for BCR PC. Two nuclear medicine physicians independently evaluated whole-body and dedicated delayed pelvic PET/MRI according to a modified PROMISE criteria (Table 1). Inter-rater reliability was computed using Gwet agreement coefficient for overall GRPR expression, prostate bed, lymph node stations, skeleton, organ, and final judgement of the scan.

Results:
Prostate specific antigen (PSA) at ^{68}Ga-RM2 PET/MRI was 4.8±13.22 (range 0.2 – 124) ng/mL. The inter-rater reliability were as follows: substantial agreement was seen for GRPR expression (0.70 [95% confidence interval [CI] 0.59, 0.81]) and final judgement (0.65 [95% CI 0.53, 0.78]), and almost perfect agreement was found for the prostate bed in the whole-body (0.87 [95% CI 0.80, 0.94]) and pelvic (0.83 [95% CI 0.75, 0.92]) images as well as for lymph nodes (0.92 [95% CI 0.85, 1.00]), skeleton (0.97 [95% CI 0.93, 1.00]), and organ metastases (0.97 [95% CI 0.93,1.00]). No consensus read was performed yet.

Conclusion:
Interpreting GRPR-targeted PET according to a modified PROMISE criteria showed its reliability with an almost perfect interrater agreement amongst all regions except for GRPR expression and final judgement, where substantial agreement was seen. This proposed standardized reporting system will aid clinicians to decrease the level of uncertainty, especially those who are starting GRPR-targeting imaging at their facility, and clinical trials to uniform evaluation and reporting of GRPR-targeted PET. Prospective studies, especially at initial staging of PC, is needed to support the robustness of this interpretation criteria.

Reference

1. Eiber M, Herrmann K, Calais J, Hadaschik B, Giesel FL, Hartenbach M, et al. Prostate Cancer Molecular Imaging Standardized Evaluation (PROMISE): Proposed miTNM Classification for the Interpretation of PSMA-Ligand PET/CT. J Nucl Med. 2018;59:469-78. doi:10.2967/jnumed.117.198119.

Poster Presentation

Disclosures: The authors have disclosed no financial interest.

282-Hypoxia-responsive luminescent CEST MRI agent for in vitro and in vivo tumor detection and imaging

Presenter: Sanu Karan, Korea Basic Science Institute (KBSI)

Sanu Karan[1], Hyunseung Lee[2], Mi Young Cho[3], Hye Sun Park[4], Eun Hee Han[5], Kwan Soo Hong[6], Jee-Hyun Cho[7]

[1]*Korea Basic Science Institute (KBSI), Cheongju-si, Chungcheongbuk-do, South Korea*
[2]*Korea Basic Science Institute (KBSI), Cheongju-si, South Korea*
[3]*Cheongju-si, Chungcheongbuk-do, Republic of Korea*
[4]*Korea Basic Science Institute (KBSI), Cheongju-si, Chungcheongbuk-do, Republic of Korea*
[5]*Korea Basic Science Institute (KBSI), Cheongju-si, Chungcheongbugdo, South Korea*
[6]*Korea Basic Science Institute (KBSI), Cheongju, South Korea*
[7]*Korea Basic Science Institute (KBSI), Cheongju-si,, South Korea*

Hypoxia is a feature of most solid tumors and a key determinant of cancer growth and propagation. Sensing hypoxia effectively could lead to more favorable clinical outcomes. Here, we report a molecular antenna-based bimodal probe designed to exploit the complementary

advantages of magnetic resonance (MR)- and optical-based imaging. Specifically, we describe the synthesis and evaluation of a dual action probe (**NO_2-Eu**) that permits hypoxia-activated chemical exchange saturation transfer (CEST) MR and optical imaging. In CT26 cells, this **NO_2-Eu** probe not only provides an enhanced CEST MRI signal, but also turns "ON" the optical signal under hypoxic conditions. Time-dependent in vivo CEST imaging in a hypoxic CT26 tumor xenograft mouse model revealed probe-dependent tumor detection by CEST MRI contrast in the tumor area. We thus suggest that dual action hypoxia probes, such as the one reported here, could have a role to play in solid tumor diagnosis and monitoring.

Poster Presentation

Disclosures: The authors have disclosed no financial interest.

283-Monitoring in vivo behavior of size-dependent fluorescent particles as a model fine dust

Presenter: Taewoong Son, Chungnam National University

Taewoong Son[1], Hyunseung Lee[2], Mi Young Cho[3], Hye Sun Park[4], Kwan Soo Hong[5]

[1]*Chungnam National University, Daejeon, South Korea*
[2]*Korea Basic Science Institute (KBSI), Cheongju-si, South Korea*
[3]*Cheongju-si, Chungcheongbuk-do, Republic of Korea*
[4]*Korea Basic Science Institute (KBSI), Cheongju-si, Chungcheongbuk-do, Republic of Korea*
[5]*Korea Basic Science Institute (KBSI), Cheongju, South Korea*

There has been growing concern regarding the impact of air pollution, especially fine dust, on human health. However, it is difficult to estimate the toxicity of fine dust on the human body because of its diverse effects depending on the composition and environmental factors. We focused on the difference in the biodistribution of fine dust according to the size distribution of particulate matter after inhalation into the body to predict its impact on human health. We synthesized Cy7-doped silica particulate matters (CSPMs) having different particle sizes and employed them as model fine dust, and studied their whole-body in vivo biodistribution in BALB/c nude mice. Image-tracking and quantitative and qualitative analyses were performed on the ex vivo organs and tissues. Smaller particles with a diameter of less than 100 nm (CSPM0.1) were observed to be removed relatively rapidly from the lungs upon initial inhalation. Smaller particles were found to spread rapidly to other organs during the early stages of inhalation. The results show in vivo behavioral differences that arisen from particle size. This study might provide with insights on association between CSPM0.1 accumulation in several organs including the lungs and adverse effect to underlying diseases in the organs.

Poster Presentation

Disclosures: The authors have disclosed no financial interest.

284-Near-infrared fluorescent probe activated by nitroreductase for in vitro and in vivo hypoxic tumor detection

Presenter: Hyunseung Lee, Korea Basic Science Institute (KBSI)

Hyunseung Lee[1], Mi Young Cho[2], Sanu Karan[3], Kwan Soo Hong[4]

[1]*Korea Basic Science Institute (KBSI), Cheongju-si, South Korea*
[2]*Cheongju-si, Chungcheongbuk-do, Republic of Korea*
[3]*Korea Basic Science Institute (KBSI), Cheongju-si, Chungcheongbuk-do, South Korea*
[4]*Korea Basic Science Institute (KBSI), Cheongju, South Korea*

Tumor hypoxia is correlated with increased resistance to chemotherapy and poor overall prognoses across a number of cancer types. We present here a cancer cell-selective and hypoxia-responsive probe (**fol-BODIPY**) designed on the basis of density functional theory (DFT)-optimized quantum chemical calculations. Probe **fol-BODIPY** was found to provide a rapid fluorescence 'off-on' response to hypoxia relative to controls, which lack the folate or nitro-benzyl moieties. *In vitro* confocal microscopy and flow cytometry analyses, as well as *in vivo* near-infrared (NIR) optical imaging of CT26 solid tumor-bearing mice, provided support for the contention that **fol-BODIPY** is more readily accepted by folate receptor-positive CT26 cancer cells and provides a superior fluorescence 'off-on' signal under hypoxic conditions than the controls. Based on the findings of this study, we propose that **fol-BODIPY** may have a role to play as a tumor-targeting, hypoxia-activatable probe that allows for direct cancer monitoring both *in vitro* and *in vivo*.

Poster Presentation

Disclosures: The authors have disclosed no financial interest.

285-Elucidation of the dysfunction of amygdala-mPFC circuit in developmental complex trauma model by means of neuroPET

Presenter: Kyung Rok Nam, Korea Institute of Radiological & Medical Sciences

Kyung Rok Nam[1], Se Jong Oh[2], Jae Yong Choi[3]

[1]*Korea Institute of Radiological & Medical Sciences, Nowon, South Korea*
[2]*Korea Institute of Radiological and Medical Sciences (KIRAMS), Seoul, South Korea*
[3]*Korea Institute of Radiological & Medical Sciences, Seoul, South Korea*

Purpose:
Developmental complex trauma is known to be an exacerbation factor for normal brain development, which associated with psychiatric disorders such as anxiety and depression.[1] Previous studies have shown that the amygdala-mPFC circuit plays a key role in stress responses. However, many studies on developmental trauma have mainly focused on the behavioral, and structural changes of the amygdala-mPFC circuit. Therefore, the purpose of the present study was to identify functional changes in the amygdala-mPFC circuit in a developmental complex trauma model using neuroPET.

Methods:
Maternal separation (PND 1-12) and restraint stress (PND 20-26) were used to generate developmental trauma model. The body weight and corticosterone levels were examined in the developmental trauma group (PND 55, n=5) and its age matched control group (n=5). Then, the neuroPET studies of dopaminergic, and serotonergic systems were assessed in both groups. Thereafter, IL-1β, TNF-α, and IL-10 concentrations in the serum were determined using a rat-specific ELISA sandwich assay kit.

Results:

The developmental trauma group showed lower body weights and corticosterone levels compared to the control group. As for the neuroPET aspect, dopaminergic and serotoninergic radioactivities for the developmental trauma group showed 16-32% lower than those for the control group in the amygdala-mPFC circuit. As part of the inflammatory response, trauma leads to changes in proinflammatory cytokines, resulting in upregulation of TNF-α and downregulation of IL-β.

Conclusion:

Overall, our data indicate that developmental complex trauma weakens the serotonergic and dopaminergic systems in the amygdala-mPFC circuit.

Reference

1. M.D. De Bellis, A. Zisk, The Biological Effects of Childhood Trauma, Child Adolesc. Psychiatr. Clin. N. Am. 23 (2014) 185–222. https://doi.org/10.1016/j.chc.2014.01.002.

Poster Presentation

Disclosures: The authors have disclosed no financial interest.

286-Synergistic Cancer Immunotherapy Utilizing Oncolytic Bacteria Secreting Fusion Protein of Interleukin 15 and Heterologous Flagellin B

Presenter: Zhang Ying, Chonnam National University

Zhang Ying[1], Yeongjin Hong[2], Jinhai Zheng[3], Sung-Hwan You[4]

[1]Chonnam National University, South Korea
[2]Chonnam National University, Hwasun-Gun, Jeollanam-Do, Republic of Korea
[3]Chonnam National University, Hwasun, Jeonnam, Republic of Korea
[4]Chonnam National University

Synthetic biology to design the expression system of therapeutic gene(s) in attenuated bacteria is an appealing approach in tumor therapy as bacteria are specifically targeted to tumor tissue [1-3]. In this study, an attenuated *Salmonella typhimurium* deficient of ppGpp biosynthesis (△ppGpp) [4] was designed to express IL15/FlaB, a fusion protein of interleukin 15 (IL15) and flagellin B (FlaB) in the presence of inducer, and named SLpIF. IL15/FlaB secreted from bacterial retained the both bioactivity of FlaB and IL15 *in vitro*. We assessed the anti-tumor effects of engineered bacterial in multiple mouse tumor models, SLpIF showed more efficient tumor growth inhibition and increased survival than treating with bacteria expressing mono-therapeutic gene, SLpFlaB or SLpIL15, in the presence of L-ara. In SLpIF-treated mice, we detected the pronounced shift from an M2-like to an M1-like phenotypes in macrophage as well as higher proliferation and activation in tumor-infiltrated CD8+ T, NK and NKT cells. Moreover, we observed a robust immune memory in ≥50% of the cases rejects tumor re-challenged in SLpIF vaccinated mice. Compared with engineered bacteria expressing IL15/FlaB, we further enhance therapeutic effects with the combination of SLpIF and anti-PD-L1 antibody [5], an immune checkpoint inhibitor, in mice bearing tumors with high malignancy, 4T1 and B16F10. Such mice showed improved tumor suppression and prolong survival. Together, our study provides new insights to design the bacterial-mediated combination cancer immunotherapy.

Reference

1. S.-R. Kang, D.-H. Nguyen, S. W. Yoo, J.-J. Min, Advanced drug delivery reviews 2021, 114085.
2. Y. Guo, Y. Chen, X. Liu, J.-J. Min, W. Tan, J. H. Zheng, Cancer letters 2020, 469, 102.
3. V. H. Nguyen, H.-S. Kim, J.-M. Ha, Y. Hong, H. E. Choy, J.-J. Min, Cancer research 2010, 70, 18
4. J. H. Zheng, V. H. Nguyen, S.-N. Jiang, S.-H. Park, W. Tan, S. H. Hong, M. G. Shin, I.-J. Chung, Y. Hong, H.-S. Bom, Science translational medicine 2017, 9.
5. R. Cubas, M. Moskalenko, J. Cheung, M. Yang, E. McNamara, H. Xiong, S. Hoves, C. H. Ries, J. Kim, S. Gould, The Journal of Immunology 2018, 201, 2273.

Poster Presentation

Disclosures: The authors have disclosed no financial interest.

287-Utility of Ga 68 dotanoc in radiation therapy planning in meningiomas

Presenter: Jyotsna Rao, Apollo

Jyotsna Rao[1], Alka Chengapa[1], Kalyani Reddy[1]
[1]Apollo, hyderabad, India

Mengiomas form 20 percent of all intracranial tumours. They are often located in proximity to critical areas of the brain and tend to recur post operatively which makes accurate radiation therapy planning important. Well differentiated tumours express somatostatin receptors strongly picking up Ga68 dotanoc. This helps in precise tumour volume delineation.Reports of 39 patients were analysed retrospectively. 14 patients had previous surgery and 4 had recurrence. 5 patients had no tissue diagnosis and were presumed to have meningioma. 1 patient had incision biopsy. 1 patient had an FDG pet scan with poor uptake done elsewhere.Patients were scanned one hour after IV injection of the tracer for 15 minutes from vertex to neck with IV contrast unless contrast was contraindicated. Scans were reported jointly by a nuclear medicine physician and radiologist. 25 patients showed high uptake in the lesions with the rest showing no or minimal uptake.The visual impression along with SUV max was reported. Location of the lesions included the optic nerve sheath, the cerebellum, clinoidal and cerebellopontine angle. Incidental uptake was noted in the thyroid in 2 patients and nodal uptake in 1. Conclusion-Ga 68 dotanoc imaging is useful in radiation therapy planning of meningiomas, particularly in view of their location and tendency to recur and will probably help in prognostication as uptake is high in well differentiated tumours.

Reference

1. Ga68 dotatoc for meningioma IMRT Radiation oncology November 18 2009 Gehller, Paulsen et al

Poster Presentation

Disclosures: The authors have disclosed no financial interest.

288-Immuno-PET imaging of inflammatory bowel disease using [89Zr]Zr-DFO-Bz-anti-IL12/23 p40

Presenter: Farzaneh Rezazadeh, Karmanos Cancer Institute

Farzaneh Rezazadeh[1], Nicholas Ramos[1], Allen Saliganan[2], Nerissa T. Viola[1]

[1]*Karmanos Cancer Institute, Detroit, MI*
[2]*Wayne State University, Detroit, MI*

Background:
Inflammatory bowel diseases (IBD), which include both Crohn's disease and ulcerative colitis, are relapsing inflammations of the gastrointestinal tract[1]. It is prevalent in western countries, but incidence is increasing in developing countries[2]. Moreover, about 35-44% of patients administered with immune checkpoint inhibitors experience diarrhea/colitis as an adverse effect, which can be life-threatening if severe[3]. Currently, diagnosis and therapy monitoring of IBD in patients are reliant on endoscopy, which is invasive and cannot provide detailed molecular information. Development of imaging agents that target colitis-specific molecular signatures to provide real-time and quantitative information on the degree of disease severity and response to therapy by patients is clearly needed. Immuno-PET could be used to noninvasive imaging of inflammation in IBD by targeting specific immune effector molecules responsible for inflammation. Herein, we evaluated the diagnostic potential of a ^{89}Zr-labeled murine antibody targeting IL12/23p40, an established key cytokine in the pathogenicity of IBD in a chemically induced mouse model of colitis.

Methods:
Colitis in BALB/c mice was induced by replacing normal drinking water with 3% (w/v) dextran sodium sulfate (DSS) for 7 days. Mice were assessed and weighed daily. The anti-IL-12/23p40 antibody was conjugated to deferoxamine (DFO), labeled with zirconium-89 ($t_{1/2}$ ~ 3.27 d) and injected intravenously on the lateral tail vein on day 5. PET images were acquired at 24-96 h post-injection (p.i.) on healthy and DSS-treated mice. Volume-of-interest (VOI) analyses were performed on large intestines to quantify probe uptake. *Ex vivo* biodistribution of [^{89}Zr]Zr-DFO-Bz-anti-IL12/23 p40 antibody was evaluated at 48 h p.i. A parallel cohort of DSS-treated mice were injected with ^{89}Zr-labeled nonspecific isotype-matched antibody. Specificity of radiotracer for IL12/23 p40 was further investigated via *in vitro* and *in vivo* blocking studies. Serum concentration of IL12/23 p40 at baseline and 5 days after DSS treatment was measured by ELISA. Intestinal tissue damage will be evaluated via H&E and trichrome stains.

Results:
DSS-treated mice showed weight loss beginning on day 6. Colon length was significantly reduced (~26%) in the DSS group compared to control. From the PET images, increased VOIs of [^{89}Zr]Zr-DFO-Bz-anti-IL12/23p40 in colitic mice clearly visualized the large intestines versus healthy controls. Biodistribution demonstrated an enhanced uptake of radiotracer in colon of DSS mice than that in healthy mice (3.0 ± 0.38 %ID/g in DSS group vs. 1.7 ± 0.35 %ID/gr in control group, P<0.01). Competitive binding studies decreased the uptake in the small intestines (1.3 ± 0.2 vs 0.4 ± 0.1, P<0.0001), colon (3.0 ± 0.4 %ID/g vs. 0.8 ± 0.2 %ID/g, P<0.0001) and cecum (1.6 ± 0.5 vs 1.0 ± 0.3 %ID/gr, p <0.01). The results of ELISA revealed elevated IL12p40 in sera on day 5 versus baseline (Day 5: 2.25 ± 0.63 vs. baseline: 1.53 ± 0.46 ng/ml p=0.03).

Conclusions:
We have shown that immuno-PET using ^{89}Zr-labeled antibody directed to IL12/23 p40 detected colonic inflammation in the gut of animals with colitis. The results of this study indicate that IL12/23 p40 may be a promising target for non-invasive imaging of IB.

Reference

1. Abraham C, Cho JH. N Engl J Med. 2009; 361:2066–2078.
2. https://www.thelancet.com/journals/langas/article/PIIS2468-1253(19)30333-4/fulltext
3. https://www.sciencedirect.com/science/article/pii/S2059702920323553):

Poster Presentation

Disclosures: The authors have disclosed no financial interest.

289-scFv-Fc as Vectors for PET Imaging of TRA-1-60-positive Pancreatic Xenograft

Presenter: Farzaneh Rezazadeh, Karmanos Cancer Institute

Farzaneh Rezazadeh[1], Allen Saliganan[2], Nerissa T. Viola[1]

[1]*Karmanos Cancer Institute, Detroit, MI*
[2]*Wayne State University, Detroit, MI*

Background:
TRA-1−60 (TRA) is a pluripotency stem cell marker that is lost upon cell differentiation[1]. TRA is also a marker of malignancy and therapy resistance and its overexpression has been reported in prostate, breast, ovarian, germ cell and tumors and in follicular lymphoma[2]. We previously described ^{89}Zr radiolabeled anti-TRA full-length antibody, and established proof-of-principle studies demonstrating its efficacy in tracking TRA in pancreatic and prostate xenografts[3]. However, smaller fragments of the monoclonal antibody have better favorable pharmacokinetics (PK) and tumor penetration, which shortens the waiting period between infusion and imaging[4]. The aim of this study seeks to develop and compare the specificity and pharmacokinetics of a humanized anti-TRA-scFv-Fc, a smaller fragment of the antibody (~ 110 kDa), separately radiolabeled with Zr-89 ($t_{1/2}$ ~ 3.27 d) and Cu-64 ($t_{1/2}$ ~ 12.7 h) for targeting TRA in BxPC-3 xenografts.

Methods:
Anti-TRA-scFv-Fc was conjugated with deferoxamine (DFO) and 2,2′-(7-(4-isothiocyanatobenzyl)-1,4,7-triazonane-1,4-diyl)diacetic acid (NODA) through an isothiocyanates (NCS) linker for labeling with Zr-89 and Cu-64 respectively. BxPC-3 (5×10^6 cells) were injected subcutaneously (s.c.) on the shoulder of female athymic nude mice. Tumor growth was monitored until volumes reached 150−200 mm^3. Tumor bearing mice were imaged with [^{89}Zr]Zr-DFO-anti-TRA-scFv-Fc from 3–120 h post injection (p.i.). Mice injected with [^{64}Cu]Cu-NODA-anti-TRA-scFv-Fc Bsg were imaged from 3–48 h p.i.. Tissue distributions of both radiotracers were performed in tumor-bearing mice.

Results:
Anti-TRA-scFv-Fc sufficiently labeled with Zr-89 and Cu-64 with a >99% radiochemical purity and specific activity of 0.185 ± 0.01 GBq/mg (5 ± 0.3 mCi/mg). PET images of [^{89}Zr]Zr-DFO-anti-TRA-ScFv-Fc- showed tracer uptake as early as 3 h p.i. (VOI: 4.7 ± 1.6 %ID/mL), which increased over time. The highest tumor uptake was achieved after 120 h (VOI: 17.5 ± 3.5 %ID/mL). PET images of [^{64}Cu]Cu-DFO-anti-TRA-ScFv-Fc exhibited high tumor uptake after 24 and 48 h p.i. Uptake in tumor peaked after 48 h p.i. (VOI: 68 ± 4.2 %ID/mL). Tissue distribution studies revealed that maximal accumulation of [^{89}Zr]Zr-DFO-anti-TRA-ScFv-Fc occurred at 24 h p.i. (12.02 ± 2.6 %ID/g). The probe was retained in the tumor at 72 h (7.5 ± 1.7%ID/g) and 120 h (6.3 ± 2.1%ID/g) p.i.. Blood retention was lower compared

to the Zr-89 labeled full length antibody after 120 h p.i[3]. indicative of the effect of the scFv-Fc's smaller size.

Conclusions:
We have successfully developed radiolabeled anti-TRA-scFv-Fc fragments with retained TRA^+ tumor affinity and especially, rapid pharmacokinetics than the full-length antibody. Studies are underway to develop this tracer for theranostic applications in TRA^+ lesions.

Reference

1. Schopperle WM, et al. Stem Cells. 2007 Mar;25(3):723-30.
2. Reya, T, et al. Nature. 2001; 414, 105–111
3. Jordan M. White, et al. Mol. Pharmaceutics 2020, 17, 1139−1147
4. Jordan M. White, et al. Theranostics. 2021; 11(13): 6293-6314.

Poster Presentation

Disclosures: The authors have disclosed no financial interest.

290-Fully automated whole brain segmentation from T2-weighted MRI brain scans of rats exposed to organophosphates using the U-Net neural network

Presenter: Valerie Porter, University of California, Davis

Valerie A. Porter[1], Brad A. Hobson[1], Brent Foster[2], Pamela J. Lein[3], Abhijit J. Chaudhari[1]

[1]University of California, Davis, Sacramento, CA
[2]Yale University
[3]University of California, Davis School of Veterinary Medicine, Davis, CA, California

Introduction:
Whole brain delineation (WBD) is a common technique used in neuroimaging analysis to alleviate the impact of unwanted, non-brain signals on brain measures of interest.[1] Furthermore, WBD is utilized in brain image pre-processing to improve the accuracy of automated and semi-automated co-registration to other medical images or atlases.[2] A limitation of currently available WBD techniques, particularly in pre-clinical research, is that they perform poorly on brain images that show large deformations due to neuropathology, such as those resulting from organophosphate intoxication (OPI).[3,4] The U-Net convolutional neural network (CNN) has shown promise for brain MRI segmentation in humans and other species.[5,6] We optimized a 2D U-net CNN and evaluated its performance for WBD for MRI scans of a rat model of OPI.

Methods:
The CNN has a modified architecture with 18 (3x3) convolutions (activation function=leaky rectified linear unit (ReLU)), four max pooling operations with zero padding, and two dropout operations to prevent overfitting. Training parameters for the U-Net were optimized, including the learning rate, number of epochs, steps per epoch, and batch size. Our data consisted of T2-weighted MRI rat brain scans (n=120 scans, 59 slices/scan, acquired on a Bruker BioSpec 7T scanner, phased array coil, voxel size: 125x125x500µm, matrix size: 280x200x59). These scans were of adult Sprague Dawley rats in an OPI (diisopropylfluorophosphate (DFP)) study, testing the impact of novel neuroprotective therapies at three timepoints (3-, 7-, and 28-days post-OPI).[7] The treatments tested were midazolam (MDZ), allopregnanolone (ALO), and MDZ and ALO (DUO). Additional groups were vehicle controls (VEH) and untreated DFP-exposed animals (DFP). These data thus presented a wide range of acute and chronic OPI pathologies.[8] Each scan was segmented by an experienced human observer to delineate the whole brain, excluding the olfactory bulb and brainstem. The training and evaluation datasets for the CNN consisted of 100 scans (DFP=23, MDZ=23, ALO=21, DUO=21, VEH=12) and 20 scans (DFP=4, MDZ=4, ALO=4, DUO=4, VEH=4), respectively. MRI scans and manually segmented label data were preprocessed by applying N4ITK bias correction, centering and cropping the volumes to the brain (to [200x200x59]), and down-sampling the resolution of each slice to improve runtime efficiency (to [128x128x59]). Data augmentation (with Medical Open Network for Artificial Intelligence (MONAI)[9]) parameters utilized to improve performance were: shifting each slice (-40,40) pixels in both x- and y- direction, rotating between (-45,45) degrees, flipping the image horizontally and vertically, scaling each slice from (-0.3, 0.3) in the y-direction, shifting the brightness levels by ± 0.5, and adding gaussian noise (mean=1, st. dev.=0.25). The performance of the CNN was tested on the evaluation data via calculating the Dice coefficients of volumetric overlap between the CNN-generated labels and those from manual segmentation.

Results and Conclusion:
The CNN training parameters converged on a learning rate=0.002, number of epochs=125, steps per epoch=20, and batch size=10. The CNN output WBD labels achieved a Dice Coefficient (median[range]) of 0.9836[0.9356-0.9900], indicating excellent segmentation accuracy. Model training accuracy and loss did not improve significantly after 60 epochs, indicating that the CNN was quickly able to find robust segmentation features despite changes in brain volume and signal heterogeneity. However, the model accuracy (percentage of correct pixel values out of the total number of pixels) did marginally improve from 98.08% to 99.07% from epochs 60 to 125. The training runtime was 30 minutes for 150 epochs, while the individual scan segmentation processing took approximately 10 seconds. We conclude that the U-net CNN provided a fully automated, efficient, segmentation approach and achieved a high accuracy. Future research will include examining the applicability of this WBD CNN on other preclinical disease and animal models.

Reference

1. R. Feo, et. al., "Towards an efficient segmentation of small rodents' brains: A short critical review." Journal of Neuroscience Methods, vol. 32, 2019; 82-89.
2. L. Hsu, et. al., "Automatic skull stripping of rat and mouse brain MRI data using U-net." Frontiers in Neuroscience. vol. 14, 2020.
3. M. Lyman, et. al., "Neuroinflammation: the role and consequences." Neuroscience Research, vol. 79, 2014;1-12.
4. W. Chen, et. al., "Role of neuroinflammation in neurodegenerative diseases," Molecular Medicine Reports. 2016;3391-3396.
5. O. Ronneberger, et. al., "U-Net: Convolutional networks for biomedical image segmentation," in International Conference on Medical image computing and computer-assisted intervention. Springer, 2015; 234–241.
6. S. Salehi, et. al., Auto-context convolutional neural network (auto-net) for brain extraction in magnetic resonance imaging. IEEE transactions on medical imaging. 2017 Jun 28;36(11):2319-30.
7. S. Supasai, et. al., "Acute administration of diazepam or midazolam minimally alters long-term neuropathological effects in the rat brain following acute intoxication with diisopropylfluorophosphate." European Journal of Pharmacology, vol. 886, 2020.
8. B. Hobson, et. al., "Magnetic resonance imaging reveals progressive brain injury in rats acutely intoxicated with diisopropylfluorophosphate." Toxicological Sciences. 2017; 342-53.

9. The MONAI Consortium. (2020). Project MONAI. Zenodo. https://doi.org/10.5281/zenodo.4323059

Poster Presentation

Disclosures: The authors have disclosed no financial interest.

291-Mitochondrial pyruvate carrier (MPC)-dependent [3-11C] pyruvate PET imaging driven by androgen receptor in prostate cancer and its role in metabolic changes

Presenter: Chul-Hee Lee, Weill Cornell Medicine

Chul-Hee Lee[1], Nicole Waterhouse[1], Thomas M. Jeitner[2], Clarence Williams, Jr[2], Ruth Fernandez[2], John W. Babich[2], James M. Kelly[3]

[1]*Weill Cornell Medicine, NY*
[2]*Weill Cornell Medicine*
[3]*Weill Cornell Medicine, New York, NY*

Introduction:
Although [^{18}F]FDG (FDG) PET is the most frequently used non-invasive imaging method for oncology, it has poor sensitivity for primary, androgen-sensitive prostate cancer (PCa).[1] PCa undergoes major metabolic changes when it becomes androgen resistant. One significant difference is a reduction in the expression of mitochondrial pyruvate carriers (MPCs), which regulate mitochondrial pyruvate metabolic flux and are regulated by the androgen receptor (AR)[2]. We hypothesize that MPC is critical to the metabolic reprogramming that drives PCa progression and is an imaging biomarker in PCa whose activity can be visualized with [3-^{11}C]pyruvate PET. Our aim was to determine the potential of [3-^{11}C]pyruvate PET to characterize metabolic phenotype in PCa.

Methods:
We compared the uptake and retention of FDG and [3-^{14}C]pyruvate in three prostate cancer cell lines: LNCaP (AR+ and androgen-dependent; AD), C4-2 (AR+ and androgen-independent; AI), and PC-3 (AR- and AI). Furthermore, we examined the relationship between uptake of these probes and the expression of key metabolic regulators using western blot. To determine the role of MPC in pyruvate metabolism, we reduced its expression by treatment of the cells with 100 µM of the MPC inhibitor UK5099 for 72 h and repeated the assays described above. Next, we compared FDG and [3-^{11}C]pyruvate PET in male *nu/nu* mice bearing LNCaP or PC3 xenograft tumors. We synthesized [3-^{11}C]pyruvate *via* [3-^{11}C] alanine using D-amino acid oxidase, alanine racemase, and catalase[3]. Mice were administered 14-16 MBq [3-^{11}C]pyruvate or 7-9 MBq FDG intravenously, and a 60 min dynamic PET acquisition was performed beginning 7-10 min post-injection. Time-activity curves were estimated by drawing a volume of interest (VOI) over the tumors.

Results:
FDG uptake was the highest in PC-3 cells ($p < 0.001$), while [3-^{14}C] pyruvate uptake and retention was greater in LNCaP cells than PC-3 cells ($p < 0.05$). Uptake of each tracer was intermediate in C4-2 cells. These findings were attributed to the high expression of glycolytic proteins in PC-3 cells, *e.g.*, GLUT1, PKM2, LDHA/B, and MCT1, as well as mitochondrial OXPHOS proteins in LNCaP cells, *e.g.*, MPC1/2, PDH complex, and MCT4. Interestingly, except for GLUT1, the expression of glycolytic/OXPHOS proteins in C4-2 cells was similar to that of LNCaP cells. The [3-^{14}C]pyruvate flux in MPC1/2 expressing cells changed after treatment with UK5099, but there was no change in cell viability. In addition to decreased expression of MPC1/2, we found significant changes in LDHA/B and MCT1/4. These changes support the role of MPC as a driver of metabolic change in PCa. [3-^{11}C]Pyruvate was prepared in 18.5 ± 2.2% decay-corrected radiochemical yield and >99% radiochemical purity. PET imaging in xenograft mice confirmed rapid distribution of [3-^{11}C]pyruvate-derived radioactivity to tumors followed by gradual clearance over 60 min. In agreement with our in vitro findings, peak uptake in LNCaP tumors significantly higher uptake than in PC-3 tumors ($p < 0.0001$).

Conclusions:
Our findings support the notion of MPC as a major metabolic regulator in PCa and a driver of PCa progression. We show that pharmacological MPC inhibition in androgen-sensitive cells induces the metabolic phenotype seen in androgen-resistant PCa. Furthermore, these distinct metabolic phenotypes can be distinguished in vitro and in vivo by differential pyruvate uptake. Consequently, we demonstrate the potential of [3-^{11}C]pyruvate PET imaging to monitor AR-driven metabolic changes. This modality may prove to be a useful tool for characterizing the metabolic phenotype of PCa.

Acknowledgments: This work was funded by a Trailblazer R21 Award (R21EB029649-01A1) awarded by the National Institute of Biomedical Imaging and Bioengineering (National Institutes of Health).

References
1. Jadvar H. Is There Utility for FDG PET in Prostate Cancer? Semin Nucl Med. 2016;46:502-506.
2. Bader DA, Hartig SM, Putluri V, et al. Mitochondrial pyruvate import is a metabolic vulnerability in androgen receptor-driven prostate cancer. Nat Metab. 2019;1:70-85.
3. Ikemoto M, Sasaki M, Haradahira T, et al. A New Synthesis of [3-11C]pyruvic Acid using Alanine Racemase. Appl Radiat Isot. 1998;49:1557-1562.

Poster Presentation

Disclosures: The authors have disclosed no financial interest.

292-Double Trouble: Multi-rodent Beds for PET/MR Imaging

Presenter: Christiane Mallett, Michigan State University

Christiane Mallett[1], Kylie Smith[1], Katherine Powell[2], Katarzyna Kempinska[2], Lorenzo Sempere, Jeremy M. Hix[1], Kurt Zinn[1], Erik Shapiro[1]
[1]*Michigan State University, East Lansing, MI*
[2]*Michigan State University, East Lansing, Michigan*

Introduction:
Pre-clinical PET/MR imaging can be expensive and time consuming, so methods to increase throughput are valuable (see also Zhou). If short-lived isotopes are used, multi-animal scanning increases the efficiency of tracer use. We developed new multi-animal imaging beds that integrate into the beds provided by our instrument vendor. The criteria for new beds were that animals were able to be anesthetized, warmed and monitored over long scan times, with access for catheters for dynamic acquisitions.

Methods:
Two multi-animal imaging beds were designed for simultaneous PET/MR imaging. A 4-mouse bed was designed to fit inside an enclosed

bed originally intended for rat imaging and was 3D printed using VeroClear resin (linear attenuation coefficient 9.41x10-2 cm2/g) (Kucuk) on a Stratasys J750. Animals are warmed by warm air (using a system built in by the vendor) and one mouse can be monitored (SAII) . A 2-rodent bed was constructed partially of 3D printed components and partially from a polyvinyl chloride (PVC) pipe (linear attenuation coefficient 8.98x10-2 cm2/g) cut lengthwise to fit on top of the existing rat MRI bed, which was extended 12.5 cm in the Z direction using a 3D printed attachment. The system is modular to allow swapping between sets of animals for repeated imaging with consistent positioning, and includes bite bars and nose cone inserts to stabilize rat or mouse heads. Animals are warmed using warm water circulation and one animal is monitored.

We acquired images on a 7T Bruker BioSpin 70/30 MRI with a 3 ring PET insert with inner diameter of 12 cm. To demonstrate multi-animal imaging capabilities, [F-18]-2-deoxy-fluoroglucose (F-18 FDG, ~5.5 MBq/animal) was injected IV into 4 mice simultaneously through tail vein catheters (3D FISP MRI sequence with 72 mm PET-optimized RF coil), and 2 rats were similarly injected IV with F-18 FDG (~6.1 MBq/animal) (T2TurboRARE MRI sequence with 86 mm RF coil). To measure recovery coefficient and spillover, saline bottles with known activity of F-18 FDG were scanned by PET/MRI for 5 minutes with cold saline in the neighboring positions. High throughput MRI-only of 4 mice with spontaneous pancreatic tumors (T2TurboRARE sequence) was also performed. Animals were anesthetized with isoflurane (1-2%). Images were analyzed in PMOD.

Results:

With the 4-mouse bed, we obtained 4 whole-body PET/MRI images. With the 2-rodent bed, we obtained heart-to-brain PET images, with the whole head covered by MRI. For the 4-mouse bed, 94% of the phantom signal was recovered, compared to 97% with only the vendor bed in place. For the 2-rodent holder, 78% of signal was recovered. Spillover was 0.01-0.67% for the 4-mouse bed, and 0.025% for the 2-rodent bed. We were able to monitor respiration and maintain animal temperature at 37 ± 1 °C for over an hour. These systems decrease scan time and therefore cost by 60-75%. The implementation of these beds did not require any instrument modification.

Conclusions:

Two cost-effective multi-animal imaging beds were built and tested for simultaneous PET/MR imaging in rodents. Recovery coefficient was high for the 4-mouse bed and lower for the 2-rodent bed, but an attenuation map that compensates for the new beds can be created and integrated into the workflow in the acquisition software. Animal health was monitored and maintained while using new beds, which will increase efficiency for data acquisition, reduce scan time, and increase the practicality of using short-lived isotopes.

Reference

1. Kucuk, N., M. Cakir, and N.A. Isitman, Mass attenuation coefficients, effective atomic numbers and effective electron densities for some polymers. Radiat Prot Dosimetry, 2013. 153(1): p. 127-134.
2. Zhou, I.Y., C.T. Farrar, J. Mandeville, M.S. Placzek, N.J. Rotile, C. Molinos Solsona, T. Sasser, S.A. Esfahani, M. Heidenreich, and P. Caravan, Multi-animal simultaneous pet/mr imaging. Bruker BioSpin.

Poster Presentation

Disclosures: The authors would like to disclose that FDG is approved.

293-Two-dimensional projection imaging of a fillable mouse phantom with a single-sided magnetic particle imaging scanner

Presenter: Alexey Tonyushkin, Oakland University

Chris McDonough[1], **Alexey Tonyushkin[2]**

[1]Oakland University
[2]Oakland University, Rochester, MI

Magnetic Particle Imaging (MPI) is a promising molecular imaging modality that uses magnetic nanoparticles (MNPs) as a tracer in applications such as cancer detection, cell tracking, and angiography [1]. There are active efforts to build a human scale MPI scanner by several groups, which are concentrated around brain imaging application [2,3]. There are significant challenges, however, of scaling up such a scanner to a full body size. An alternative approach is to adopt an open geometry design for imaging of a local body region [4]. Such a single-sided design has an advantage of accommodation of all body sizes, lower power consumption, and smaller footprint. The major challenges of the single-sided designs are non-homogeneous fields, limited penetration depths, low sensitivity and spatial resolution that impact their utility. In our prototype of a single-sided scanner we incorporated a field-free line (FFL) topology of the magnetic field to achieve higher sensitivity and robust image reconstruction using back-projection technique as compared to the alternative topology utilizing field-free point (FFP) [5]. Previously, we showed simulations of 2D imaging with our scanner using the back-projection image reconstruction and the experimental 1D imaging showing the capability of the spatial resolution of up to 6 mm with low field gradient [6]. In this work, we present the first 2D imaging of a mouse phantom. In the imaging experiments, we used an anatomical 3D printed fillable mouse phantom (BIOEMTECH) with various organs. Kidneys were filled with 300 µl each of undiluted SPIO Vivotrax+ (MagneticInsight). The phantom was placed on a subject table with the graduated angles corresponding to 22° rotation step and imaged from 0 to 180° with 4 cm x 4 cm FOV in coronal plane at the penetration depth of 17 mm. For each angle position the signal was obtained with the FFL moving back and force and the background was subtracted from the average. A sinogram was collected and back-projected to obtain a 2D image. A separate PSF image was experimentally obtained with the symmetrical point source of a glass bulb placed at the center and containing 18 µl of SPIO. A deconvoluted image was overlaid with the photograph of the mouse phantom to obtain the contour lines of the mouse and the kidneys. The results show the proof of principle of in-plane projection imaging with the single-sided FFL MPI scanner.

Reference

1. N. Panagiotopoulos, et al., "Magnetic particle imaging: current developments and future directions," International Journal of Nanomedicine, p. 3097, apr 2015.
2. E.E. Mason, et al., "Design analysis of an MPI human functional brain scanner," Int J Magn Part Imaging. 3(1), 1703008, (2017).
3. M. Graeser, et al., "Human-sized magnetic particle imaging for brain applications," Nature Communications. 10, 1936, (2019)
4. C. Kaethner, et al., "Asymmetric scanner design for interventional scenarios in magnetic particle imaging," IEEE Trans. Magn. vol. 51, no. 2, Art. no. 6501904, Feb. 2015.
5. K. Grafe, et al., "2D images recorded with a single-sided magnetic particle imaging scanner," IEEE Trans. Med. Imag. vol. 35, no. 4, pp. 1056–1065, Apr. 2016.
6. C. McDonough, et al., "1d imaging of a superparamagnetic iron oxide nanoparticle distribution by a single-sided ffl magnetic par-

ticle imaging scanner," IEEE Transactions on Magnetics, early view, pp. 1–1, 2022.

Poster Presentation

Disclosures: The authors have disclosed no financial interest.

294-Comparison of external butterfly and endorectal coils for sodium MRI of human prostate cancer

Presenter: Josephine Tan, Western University

Josephine L. Tan[1], Jonathan D. Thiessen[2], Timothy J. Scholl[3], Alireza Akbari[3]
[1]*Western University*
[2]*Lawson Health Research Institute, London*
[3]*Robarts Research Institute, London, Ontario*

Background:
Sodium (^{23}Na) MRI is a molecular imaging technique that can detect the increased tissue sodium concentration (TSC) exhibited in several tumour types, including prostate cancer (PCa). In recent work, TSC measured by sodium MRI was shown to significantly correlate with histological lesion grade in human PCa (1). This study employed an endorectal coil and a 3D fast gradient-recalled-echo sequence to acquire sodium images. Although an endorectal coil can facilitate higher imaging signal-to-noise ratio (SNR), it is associated with a limited field of view, increased scan times, gland deformation, and patient discomfort. To address these challenges, this abstract focuses on the development and evaluation of a completely external 'butterfly' surface coil for sodium imaging using a 3D density-adapted radial projection sequence (2).

Objective:
To compare sodium MRI SNR in the human prostate using an externally located butterfly surface coil versus a conventional endorectal surface coil.

Methods:
Two PET-compatible, custom-built radiofrequency systems for sodium MRI were compared using a 3-Tesla PET/MRI scanner (Siemens Biograph mMR).
The first setup consisted of a ^{23}Na transmit body coil, a rigid $^{1}H/^{23}Na$ dual-tuned receive endorectal coil (dimensions=7.2×2.3cm^2, tuning=32.6 MHz), and a flexible anterior receive array for 1H imaging. Sodium images were acquired with a gradient echo sequence (TR=218ms, TE=2.3ms, FOV=20cm^2, resolution=3mm^2, slice thickness=8mm, total scan time=32min) and evaluated in two patients with biopsy-proven PCa (62 and 68 yrs; 95.2 and 77.5 kg; Gleason scores 7).
The second setup consisted of a ^{23}Na transmit/receive butterfly coil (diameter=18cm, tuning=32.6 MHz), and a flexible anterior receive array and spine array for ^{1}H imaging. Sodium images were acquired with a 3D density-adapted radial projection sequence (TR=50ms, TE=0.5ms, FOV=36×36×10cm^3, resolution=5×5×5mm^3, total scan time=27min) and evaluated in a healthy volunteer (28 yrs, 72 kg) and one patient with biopsy-proven PCa (65 yrs, 66.8 kg, Gleason score to-be-determined).
Prostate-specific membrane antigen (PSMA)-PET (3D mode, resolution=4.2×4.2×2.0mm^3, frame duration=20min) was acquired during all patient imaging sessions 2 hours following the administration of [^{18}F]PSMA-1007 (dose=372.7±39.1MBq). Sodium SNR in patient images was calculated for the region defined by 40% of the maximum standardized uptake value (SUV_{max}) of PSMA-PET (3). Sodium SNR in the volunteer image was calculated for a manually-drawn region capturing the whole prostate.

Results and Discussion:
For the first two patients imaged with the endorectal coil, the sodium signal dropped below noise thresholds starting 1cm from the surface of the coil. As a result, the sodium SNR was low (SNR=4.4 and 4.0, respectively) in the primary lesion identified by PSMA-PET (SUV_{max} = 7.8 and 19.9, respectively). There were also difficulties in the insertion of the endorectal coil that resulted in gland deformation, coil ejection, and patient discomfort.
In contrast, the butterfly coil achieved a greater field of view and higher SNR (SNR = 26.8) in the region defined by 40% of SUV_{max} (SUV_{max}=4.7) of the third patient. A lower SNR was observed in the whole prostate of the healthy volunteer (SNR=14.5) using this setup, which is consistent with prior findings of higher TSC in PCa relative to healthy prostatic tissue (1). The prostate peripheral zones in both the patient and volunteer exhibited greater sodium signals compared to the rest of the gland likely due to larger extracellular space and loose stroma (4). Future work will investigate the correlation between TSC in lesions and Gleason grade as determined by whole-mount histopathology.

Conclusion:
This work demonstrates that, in the same scan time, the proposed non-invasive butterfly surface coil can achieve a higher SNR over the whole prostate compared to the endorectal coil for patients with PCa, which may enhance the workflow and applicability of sodium MRI in PCa studies.

Reference
1. Broeke NC, Peterson J, Lee J, et al. Characterization of clinical human prostate cancer lesions using 3.0-T sodium MRI registered to Gleason-graded whole-mount histopathology. J. Magn. Reson. Imaging 2019;49:1409–1419 doi: 10.1002/jmri.26336.
2. Nagel AM, Laun FB, Weber MA, Matthies C, Semmler W, Schad LR. Sodium MRI using a density-adapted 3D radial acquisition technique. Magn. Reson. Med. 2009;62:1565–1573 doi: 10.1002/mrm.22157.
3. Spohn SKB, Kramer M, Kiefer S, et al. Comparison of Manual and Semi-Automatic [18F]PSMA-1007 PET Based Contouring Techniques for Intraprostatic Tumor Delineation in Patients With Primary Prostate Cancer and Validation With Histopathology as Standard of Reference. Front. Oncol. 2020;10:600690 doi: 10.3389/fonc.2020.600690.
4. Barrett T, Riemer F, McLean MA, et al. Quantification of Total and Intracellular Sodium Concentration in Primary Prostate Cancer and Adjacent Normal Prostate Tissue with Magnetic Resonance Imaging. Invest. Radiol. 2018;53:450–456 doi: 10.1097/RLI.0000000000000470.

Poster Presentation

Disclosures: The authors have disclosed no financial interest.

295-Metabolomics Characterizations of Alzheimer's Disease for Human Patients and with Animal Models: The MGH Experiences

Presenter: Leo Cheng, MGH/Harvard

Leo L. Cheng

MGH/Harvard, Charlestown, MA

Currently, a definitive Alzheimer's Disease (AD) diagnosis can only be achieved at autopsy, through pathology examinations of brain tissue. No non- or less-invasive examination can yet diagnose and characterize AD during the patient's life, in turn limiting insights into potential strategies for countering AD modes of progression. Here, using high-resolution magic angle spinning (HRMAS) nuclear magnetic resonance (NMR) spectroscopy, we studied human blood samples obtained from AD and non-AD subjects to reveal potential AD-associated metabolomic changes measurable in blood, and quantified tissue and blood metabolomics for AD and wild-type (WT) mouse models for potential developments of an ex vivo to in vivo translational platform capable of using AD associate endogenous cellular metabolomics profiles for metabolomic imaging to assist with AD diagnosis and, more importantly, contribute to the development of precision treatments. HRMAS MRS-based metabolomics has demonstrated its utility in studies of biofluids for various diseases. HRMAS MRS is uniquely well-suited for analysis of human blood samples due to the small quantity of sample and minimal preparation required. Metabolomic analysis has been proposed as a potential methodology to better investigate and understand the progression of AD. Our investigation focuses on developing AD and non-AD metabolomics differentiating models, including procedures of quality assurance (QA) and quality control (QC) through pooled samples. The quality evaluations and procedures designed for these evaluations are critical for the development of MRS-based metabolomics for various disease of concern. We obtained AD metabolomics results using HRMAS NMR on human blood plasma samples obtained from AD and non-AD subjects, as well as in vivo MRS and ex vivo NMR studies of AD and wild-type (WT) mouse. From the analysis of human serum samples, our study found several metabolites to be significantly correlated with AD compared to controls. We also demonstrated that HRMAS NMR technology has the ability to differentiate diseased from wild-type brain tissue in mice. These results suggest the potential for future translational research with important clinical implications, including comprehensive comparisons of in vivo and ex vivo imaging measurements in animal models and AD diagnostics from a simple, non-invasive blood sample. Establishing connections between in vivo imaging and ex vivo brain tissue and serum measurements will enable us to design in vivo imaging and blood serum evaluation protocols to test age- and AD-associated metabolomic changes in humans, aimed at non-invasively detecting AD onset, development, and progression, monitoring the effects of potential future therapies, as well as understanding AD metabolic mechanisms. In summary, using endogenous cellular metabolomics measured ex vivo from blood samples from human patients and animal models, together with in vivo and ex vivo measurements of animal brain metabolomics, our rigorous, stepwise, and translational approaches evaluate metabolomics correlations between in vivo brain and ex vivo blood from animal models. Advised by thus observed correlations, human AD metabolomics measured from blood samples may be investigated for their relationships with AD brain metabolomics that maybe investigated through in vivo metabolomics imaging.

Poster Presentation

Disclosures: The authors have disclosed no financial interest.

296- Comparison of alternate methods for protein estimation

Presenter: Punita Bhardwaj, Tata Memorial Hospital

Punita Bhardwaj[1], Sneha Mithun[1], Ashish K. Jha[1], Sandeep Yadav[1], Meryl Maria[1], Niha Nisar[1], Merline Babu[1], Kinnari Chitnis[1], Shreyash Panchal[2], Pranjal Dighe[1], Mythili Kameswaran[1], Venkatesh Rangarajan[3]

[1]*Tata Memorial Hospital, Mumbai, Maharashtra, India*
[2]*Tata Memorial Hospital, India*
[3]*Tata Memorial Hospital, Mumbai, IN-Mah, India*

Introduction:
Protein estimation assays used for research applications are classified on the basis of their sensitivity and specificity of detection. Established assays like Bradford's, Lowry's, BCA assay, and UV absorption have been used conventionally for estimation of protein concentrations in samples. This study aims to devise and compare alternate method for protein estimation using HPLC and generating standard curves from the absorbances observed with Bovine Serum Albumin (BSA) and Bovine IgG as standards. Trastuzumab, a monoclonal antibody used for treatment of breast cancer was used as the test sample. It has been observed that the protein concentrations of radiolabeled antibodies differ from its original concentration after radiolabeling. An alternate method for protein estimation in this study explores an additional option for confirmation of the final antibody concentration in such radiolabeling and other test samples.

Method:
Standard solutions of varying known concentrations (750 ng to 100 µg range) were prepared using the commercially available Bovine Serum Albumin (BSA) and Bovine Immunoglobulin (IgG) (Sigma-Aldrich) and chromatograms were generated in the HPLC system (Synthra) using a TSK gel column. The sample volumes were kept constant at 15 µL. A calibration curve was generated by plotting the concentrations versus absorbance and an equation for the best fitted linear regression line was generated. As test samples, different known concentrations of trastuzumab were injected into the HPLC system and chromatograms were generated using the same protocol under identical conditions. Their absolute concentrations were estimated using the equation1 generated for the regression (R1) and its correlation to the known concentration was estimated.
Another calibration curve was generated by plotting known concentrations of Trastuzumab solution at varying known concentrations (150ng to 75µg) versus absorbance at identical conditions as above and the equation for best fit linear regression line generated. Absolute concentration of three blinded concentrations of trastuzumab was estimated using equation2 generated for this regression (R2).

Results:
The percentage error observed between the calculated trastuzumab sample concentration and their known concentrations from R1 was significantly higher at higher concentrations. For R1 average percentage error ± Standard deviation observed was 44.17±24.95 % using the standard curve generated for BSA and 39.13±33.14 % for Bovine IgG. On the other hand, R2 gave more accurate result with an average of 5.3 % (range) error for blinded concentrations with least error at higher concentration (2.7%) and slightly higher error at lowest concentration (6.8%).

Conclusion:
Our study reveals that the concentration of monoclonal antibodies by HPLC best correlates with the standard curve generated with the same antibody. Further studies would deal with the validation of this HPLC method with other standard methods like Lowry's or Bradford's assay for protein estimation.

Poster Presentation

Disclosures: The authors have disclosed no financial interest.

297-Prostate Specific Membrane Antigen Targeted Dextran as a Multiplexed siRNA Carrier for Prostate Cancer Specific Immunotheranostics

Presenter: Zhihang Chen, Johns Hopkins Univeristy

Zhihang Chen[1], Balaji Krishnamachary[2], Yelena Mironchik[3], Sangeeta Ray[1], Martin Pomper[1], Zaver M. Bhujwalla[2]

[1]*Johns Hopkins Univeristy, Baltimore, MD*
[2]*Johns Hopkins University School of Medicine, Baltimore, MD*
[3]*Johns Hopkins University School of Medicine, Baltimore, Maryland*

Exploiting the power of the immune system to eliminate cancer cells has led to exciting advances in cancer treatment in some cancers such as melanoma, but not in prostate cancer (PCa) that continues to cause 20% of cancer-related death in men. The multiple checks and balances built into the immune system are exploited by cancer cells to escape immunesurveillance. The ability to target two or more of these immune pathways concurrently and specifically in PCa cells may provide an effective treatment strategy for advanced prostate cancer. The flexibility of siRNA design and synthesis makes siRNA therapeutics an appealing option for blocking immune checkpoints, especially if they can be specifically delivered to cancer cells to avoid the autoimmune complications of antibody based checkpoint blockade. Prostate specific membrane antigen (PSMA) is a transmembrane protein that is highly expressed by castrate-resistant PCa cells. Here, we demonstrated the ability of a novel PSMA-specific degradable dextran nanocarrier to deliver siRNA to simultaneously downregulate two important immune molecules, PD-L1 and CD46, which are exploited by cancer cells to escape immune surveillance, in PSMA-expressing human PCa cells. These studies pave the way for harnessing the power of the immune system using siRNA therapeutics for effective treatment of advanced PCa in humans. The NP structure and characterization are shown in Fig. 1A. In the NPs, amine groups that electrostatically bind siRNA were conjugated to the dextran scaffold through acetal bonds that were rapidly cleaved in weak acid conditions to release siRNA within cells, while the small molecular PSMA targeting moieties were conjugated to the dextran through a polyethylene glycol (PEG) linker. Imaging and therapy studies with the NP were performed with PC3-PIP (PSMA+), PC3-Flu (PSMA-) cells and with PC3-PIP cells treated with ZJ-43, which is a PSMA blocking agent. Cell imaging studies indicated that the cellular uptake of siRNA NPs in PC3-PIP cells was much higher than that in PC3-Flu cells and PC3-PIP cells treated with ZJ-43. The measurement of fluorescence by flow cytometry confirmed these results. mRNA (Fig.1B-C) and protein analysis indicated that PD-L1 and CD46 siRNA dextran NPs reduced PD-L1 and CD46 levels in PC3-PIP cells. Our data confirm that PSMA targeted dextran NPs can be used as a safe siRNA carrier to effectively reduce PD-L1 and CD46 expression specifically in PSMA expressing PCa cells.

Poster Presentation

Disclosures: The authors have disclosed no financial interest.

298-Implementation of Synthetic Genetic Logic into Tumor-specific Therapeutic Molecules Expression in S. typhimurium

Presenter: Hien Ngo Thi Thu, Chonnam National University

Hien Ngo Thi Thu[1], Dinh Huy Nguyen[2], Sung-Hwan You[3], Khuynh Nguyen Van[4], soyoung Kim[5], Yeongjin Hong[6], Jung-Joon Min[5]

[1]*Chonnam National University, South Korea*
[2]*Chonnam National University, Gwangju, Jeonranamdo, South Korea*
[3]*Chonnam National University*
[4]*Chonnam National University, Hwasun-gun, Hwasun-eup, Jeonranamdo, South Korea*
[5]*Chonnam National University Medical School, Hwasun-gun, South Korea*
[6]*Chonnam National University, Hwasun-Gun, Jeollanam-Do, Republic of Korea*

Previous studies have reported that *Salmonella typhimurium* showed the capability of colonization and active proliferation in tumor tissue, therefore they can be used as a vehicle to deliver anticancer agents for cancer treatment. However, the bio-distribution of bacteria in normal organs may result in toxicity to these normal organs. To address this issue, we engineered synthetic genetic logic based on combination of recombinase system and hypoxia-inducible promoter to express the therapeutic molecules exclusively in the cancerous tissue and not in healthy organs. Additionally, synthetic genetic logic does not require constant recombinase production from the cell to maintain state, resulting in reducing metabolic burden on the bacteria. Recently, we developed a two-plasmid system. The first plasmid contains an irreversible recombinase gene, under the control of the inducible promoter. The second reporter plasmid contains synthetic genetic logic to regulate the reporter gene expression, included two recognition sites of recombinase flanking a hypoxia-inducible promoter in reverse orientation without inducible agent. In the presence of inducible agent, the recombinase expression results in inverting of the orientation of the hypoxia-inducible promoter, which can upregulate the expression of reporter gene in tumor microenvironment. In order to develop our system, firstly by using a constitutive promoter instead of hypoxia-inducible promoter, we optimized the expression of our system. Further experiments using hypoxia-inducible promoter in synthetic logic gate system would be conducted.

Poster Presentation

Disclosures: The authors have disclosed no financial interest.

299-Magnetic, biocompatible FeCO3 nanoparticles for T2-weighted magnetic resonance imaging of in vivo lung tumors

Presenter: Suresh Thangudu, Kaohsiung Chang Gung Memorial Hospital

Suresh Thangudu

Kaohsiung Chang Gung Memorial Hospital, Taiwan

Late diagnosis of lung cancer is one of the leading causes of higher mortality in lung cancer patients worldwide. Significant research attention has focused on the use of magnetic resonance imaging (MRI) based nano contrast agents to efficiently locate cancer tumors for surgical removal or disease diagnostics. Although contrast agents offer significant advantages, further clinical applications require improvements in biocompatibility, biosafety and efficacy. To address these challenges, we fabricated ultra-fine Iron Carbonate Nanoparticles ($FeCO_3$ NPs) for the first time via modified literature method. Synthesized NPs exhibit ultra-fine size (~17 nm), good dispersibility and excellent stability in both aqueous and biological media. We evaluated the MR contrast

abilities of $FeCO_3$ NPs and observed remarkable T2 weighted MRI contrast in a concentration dependent manner, with a transverse relaxivity (r2) value of 730.9 ± 4.8 mM^{-1} S^{-1}at 9.4 T. Moreover, the r2 values of present $FeCO_3$ NPs are respectively 1.95 and 2.3 times higher than the clinically approved contrast agents Resovist® and Friedx at same 9.4 T MR scanner. $FeCO_3$ NPs demonstrate an enhanced T2 weighted contrast for in vivo lung tumors within 5 h of post intravenous administration with no apparent systemic toxicity or induction of inflammation observed in in vivo mice models. The excellent biocompatibility and T2 weighted contrast abilities of $FeCO_3$ NPs suggest potential for future clinical use in early diagnosis of lung tumors.

Reference

1. Thangudu, S., Yu, CC., Lee, CL. et al. Magnetic, biocompatible FeCO3 nanoparticles for T2-weighted magnetic resonance imaging of in vivo lung tumors. J Nanobiotechnol 20, 157 (2022). https://doi.org/10.1186/s12951-022-01355-3

Poster Presentation

Disclosures: The authors have disclosed no financial interest.

300-In vivo magnetic particle imaging of PD-L1 expression with high sensitivity and quantification

Presenter: Yang Du, Institute of Automation, Chinese Academy of Sciences

Yang 洋. Du[1], Jie Tian[2]

[1]Institute of Automation, Chinese Academy of Sciences, ???, Beijing, China
[2]Chinese Academy of Sciences, Beijing, Beijing, China

In vivo molecular imaging techniques, as invaluable tools, enable the new biology finding in preclinical studies, and help to diagnose and provide guidance for the treatment of diseases in clinics. Preclinical and clinical studies to predict response to anti-PD-1/PD-L1 immunotherapy mainly rely on the *in vivo* positron emission tomography (PET), single photon emission computed tomography (SPET), and also fluorescence imaging. However, optical imaging suffers from autofluorescence and image depth limitation. PET imaging suffers from the short half-life of radiotracers and radioactivity. Hence, it is still worth exploring new imaging methods to realize the sensitive detection of PD-L1 expression *in vivo* with no safety concern. Magnetic particle imaging (MPI), as an emerging imaging modality, possesses high sensitivity and image depth, linear quantitativity, positive contrast, almost no background from tissues, and no radiation. Moreover, the iron oxide nanoparticles of MPI are safe for clinical use. Hence, in this study, we developed anti-PDL1 antibody conjugated magnetic-fluorescent hybrid nanoprobe (aPDL1-MFNPs) and carry out the *in vivo* MPI imaging of PD-L1 expression at different tumor xenografts with varying PD-L1 expression levels. The MPI tailored MFNPs-aPDL1 nanoprobe were SPIO encapsulated with semiconducting polymer to produce nanoprobe that both possessed optical and magnetic properties for MPI and fluorescence imaging (FMI), and the aPD-L1 was conjugated to the surface of the nanoparticle to realize the PD-L1 targeting and binding property. The specific and targeted PD-L1 imaging of MFNPs-aPDL1 was demonstrated through comparing with IgG-MFNPs control probe. The CT26 tumors with or without IFN-γ treatment were utilized to provide tumor models with varying PD-L1 expression levels. The MPI imaging of PD-L1 with different expression levels were detailed characterized and quantified, and the *in vivo* FMI was also carried out to confirm and complement with MPI imaging. In addition, the *ex vivo* real-time PCR, western blot and immunofluorescence staining were also performed for further validation of *in vivo* observation of PD-L1 expression. Our study aims to provide an alternative whole body imaging method for the characterization of immune checkpoint molecule expression with high sensitivity and specificity, which may possess the clinical translation potential. Such insights may also facilitate the optimization of existing treatments and in development of new immunotherapeutic agents or combinations.

Poster Presentation

Disclosures: The authors have disclosed no financial interest.

301-Acute and Chronic Vasculature Destruction in Vivo Animal Orthotropic Kidney Tumors Based on Vascular Disrupting Agent (OXi8007) Examined by Optical and Multispectral Optoacoustic Imaging

Presenter: Hashini Wanniarachchi, University of Texas Southwestern Medical Center

Hashini I. Wanniarachchi[1], Regan Schuetze[2], Lorena Arango[2], Cyprian Pavlich[3], Khagendra Hamal[4], Mary Lynn Trawick[3], Kevin Pinney[3], Li Liu[5], Ralph Mason[5]

[1]University of Texas Southwestern Medical Center, Dallas
[2]University of Texas Southwestern Medical Center
[3]Baylor University, Waco, Texas
[4]Waco, Texas
[5]University of Texas Southwestern Medical Center, Dallas, TX

Background:
Vasculature offers an attractive therapeutic target in tumors since disruption causes massive amplification through downstream cell death. Most vascular disrupting agents (VDAs) function by inhibiting microtubule formation, which causes rapid morphological changes, resulting in dramatically increased vessel permeability, cellular detachment, vessel occlusion, and vessel wall damage. Being highly vascular, kidney tumors are expected to be particularly sensitive to VDAs. A promising indole-based molecule (OXi8007) [1,2], structurally inspired by the first generation VDA combretastatin A-4 (CA4), was examined non-invasively for VDA activity, using multispectral optoacoustic tomography (MSOT) and bioluminescence imaging (BLI) and confirmed by histology [3]. Repeat dosing was used to examine tumor growth, as revealed by BLI.

Method:
Luciferase-expressing RENCA tumor cells were implanted orthotopically in the right kidney capsule of syngeneic BALB/c mice. Bioluminescence Imaging (BLI) was applied weekly to assess tumor growth. Once tumors reached about $1x10^7$ photons/s, both dynamic BLI and Multispectral Optoacoustic Tomography (MSOT) were applied to evaluate acute and chronic response to OXi8007 (250 mg/kg) at baseline and 4h post-treatment. Tissue samples were further evaluated through histology. Two groups of mice ($n_{Control} = 5$, $n_{OXi8007} = 9$) were treated with saline or OXi8007 (250 mg/kg IP) respectively, twice a week. BLI images were acquired over several weeks to observe the tumor growth delay.

Data Analysis:
MSOT images were acquired from a single transaxial slice for 15 minutes at a sampling frequency of 10fps at 700, 730, 760, 800, 850,875

nm wavelengths. MSOT image analysis was performed using ViewMSOT software. The Model Linear method was applied to reconstruct images at the optimal speed of sound followed by fluence correction masking the background. Signals were unmixed for HbO_2 and Hb to quantify oxygen saturation (sO_2^{MSOT}) at each pixel. Mean oxygen saturation was calculated for selected ROIs. BLI images were acquired following administration of luciferin subcutaneously and the signal was quantified using Living Image 4.7. Further analysis was conducted using MATLAB (2022a) or Python 3.8. Growth rates were calculated using linear regression on log-transformed total flux with respect to the days after initial treatment using the SciPy package.

Results:
MSOT showed that OXi8007 reduces the oxygenation in the tumor at 4h post-treatment compared to baseline (Fig. B, C). Post-treatment there was reduced oxygen saturation in the tumor and a smaller response to the gas oxygen-breathing challenge compared to baseline. Other organs did not show this depression. The change is emphasized in histograms showing a left shift relative to the oxygen saturation during air/oxygen (Fig. C). BLI signals (Fig. D) reached a peak within 2-6 minutes of luciferin injection (Fig. E). At 4h post-VDA, the BLI signal was reduced to about 2% of baseline, indicating a vascular disruption in a group of mice (n=6; p=0.008). Histology revealed massive hemorrhage 4h following OXi8007 (Fig. E). The treated group showed a statistically slower tumor growth rate compared to the control group (p=0.008) (Fig. F).

Discussion & Conclusion:
BLI effectively revealed acute responses to VDA and allows effective long-term monitoring of tumor growth as well as the impact of VDA in the orthotopic kidney tumor. MSOT revealed changes in tumor oxygenation in real-time based on endogenous signal alone. The promising VDA OXi8007, demonstrated acute vascular disruption and long-term tumor growth delay in orthotopic kidney tumors, as revealed by BLI, MSOT, and histology. MSOT showed selectivity for tumors versus other organs. These results provide further evidence for the utility of combined BLI and MSOT for effectively evaluating novel VDAs [3].

Reference
1. T. E. Strecker et al., "The vascular disrupting activity of OXi8006 in endothelial cells and its phosphate prodrug OXi8007 in breast tumor xenografts.," Cancer Lett., vol. 369, no. 1, pp. 229–241, Dec. 2015, doi: 10.1016/j.canlet.2015.08.021.
2. M. B. Hadimani et al., "Synthesis of a 2-aryl-3-aroyl indole salt (OXi8007) resembling combretastatin A-4 with the application as a vascular disrupting agent.," J. Nat. Prod., vol. 76, no. 9, pp. 1668–1678, Sep. 2013, doi: 10.1021/np400374w.
3. L. Liu et al., "Non-Invasive Evaluation of Acute Effects of Tubulin Binding Agents: A Review of Imaging Vascular Disruption in Tumors," Molecules, vol. 26, no. 9, 2021, doi: 10.3390/molecules26092551.

Poster Presentation

Disclosures: The authors have disclosed no financial interest.

302-MRI-detectable nanocarriers for vaccine delivery

Presenter: Daniel Jirak, Institute for Clinical and Experimental Medicine

Daniel Jirak[1], Lucie Wold?ichová[2], David ?ervený[3], Ladislav Androvic[4], Richard Laga[2]

[1]Institute for Clinical and Experimental Medicine, PRAHA 4, Czech Republic
[2]Institute of Macromolecular Chemistry, Czech Academy of Sciences, Prague, Czech Republic
[3]Technical University of Liberec, Liberec, Czech Republic
[4]Prague, Czech Republic

Introduction:
Various macromolecular delivery systems have been developed to increase the stability and potency of subunit vaccines, but many have not optimal size size and morphology to ensure efficient interaction of antigens with immune cells and accumulate in the body after performing their function. To overcome these limitations, we have introduced new biocompatible polymer-colloidal carriers based on maghemite (γ-Fe_2O_3) nanoparticles coated with poly[N-(2-hydroxypropyl)methacrylamide] (PHPMA) polymers. In this proof-of-principle experiment, we assessed the MR properties of the probe and performed phantom and in vivo ^{1}H MRI measurement of the polymer based nanocarrier.

Methods:
PHPMA polymers (semitelechelic homopolymers, statistical copolymers and di-block copolymer) were attached to the surface of γ-Fe_2O_3 (maghemite) particles via an iron-chelating deferoxamine group linked to the ends of their chains through stable or stimuli-responsive bonds. In addition, a minimal peptide immunogen (V3) derived from the HIV-1 binding site was successfully conjugated to exemplary polymer-colloid systems to demonstrate their suitability for vaccine delivery. To characterize the physicochemical properties of prepared conjugates, dynamic light scattering (DLS) measurements were conducted. The MR properties of the probes were assessed by relaxometry at 1.5 relaxometer (37°C, r_1: saturation recovery sequence, repetition time (TR) = 0.01–10 000ms, echo time (TE) = 0.05ms; r_2: Carr–Purcell–Meiboom–Gill (CPMG) sequence, TR = 10 000ms, TE = 0.05ms). T_1 and T_2 weighted MR images of the phantoms containing the nanoparticles and in vivo measurements were acquired on a 4.7 T scanner using a resonator coil. A standard 2D rapid acquisition with relaxation enhancement (RARE) multi-spin echo MR sequence (T_1w: TR = 294.8ms, TE = 16.7ms, turbo factor = 2 and T_2w: TR = 3300ms, TE = 36ms, turbo factor = 4) for both phantom and in vivo measurement was used. Whistar rats were scanned immediately and 48 hours after administration of polymer into the muscle.

Results/Discussion:
The resulting probes were chemically stable, well-defined nanoparticles characterized by negligible toxicity and suitable hydrodynamic size and shape for efficient uptake by immune cells. DLS studies of maghemite nanoparticles and polymer-coated maghemite nanoparticles determined their size to be around 100 nm. Relaxometry shows a strong effect of iron binding to the probe, r_1 was 4.6L.mmol^{-1}s^{-1} and r_2 was 46.1L.mmol^{-1}s^{-1}, respectively. These excellent MR properties were confirmed by imaging of phantoms, where CNR was much higher compared to CNR of phantoms containing only pure polymer. The quantification from phantom study is summarized in Figure 1.
The polymer bound to the surface of γ-Fe_2O_3 particles (maghemite) was clearly detected as a hypointensive signal also in vivo immediately after its administration (CNR = 77). In the case of pure polymer, we observed a slightly hyperintensive signal (CNR = 25). This illustrates Figure 1. Two days later, we still detected a polymer with maghemite as a strong hypointensive signal (CNR = 65). In contrast, pure polymer was not detected, indicating its removal from the body.

Conclusion:
The resulting materials were stable, well-defined nanoparticles characterized by negligible toxicity and suitable hydrodynamic size and shape for efficient uptake by immune cells; those having polymers attached via stimuli-responsive bonds exhibited rapid decoating upon being incubated in the solutions mimicking reductive environment inside the cells. In addition, the favorable magnetic properties of the nanoparticles enabled their detection by MRI, which can be used to monitor their pharmacokinetics.

Acknowledgements: The Ministry of Health of the Czech Republic (project no. NU20-08-00095) and by the Ministry of Health of the Czech Republic (Institute for Clinical and Experimental Medicine – IKEM, Project IN 00023001).

Poster Presentation

Disclosures: The authors have disclosed no financial interest.

303-IN VIVO EVALUATION OF NEUTROPHILS INFILTRATION IN ACUTE LUNG INJURY BY IMMUNEPET IMAGING

Presenter: María Isabel González-Gutiérrez, Fundación Investigación Biomédica del Hospital Gregorio Marañón

María Isabel González-Gutiérrez[1], Gorka Sobrino[2], Agustín Clemente-Moragón[3], Mario González-Arjona[1], Mónica Gómez-Parriza[2], Borja Ibáñez[3], Manuel Desco[4], Eduardo Oliver[3], Beatriz Salinas[5]

[1]*Fundación Investigación Biomédica del Hospital Gregorio Marañón, Madrid, Spain*
[2]*Centro Nacional de Investigaciones Cardiovasculares (CNIC), Madrid, Spain*
[3]*Centro Nacional de Investigaciones Cardiovasculares (CNIC), Madrid, Madrid, Spain*
[4]*Instituto de Investigación Sanitaria Gregorio Maranon, Madrid, Spain*
[5]*Fundación Investigación Biomédica del Hospital Gregorio Marañón, Madrid, Madrid, Spain*

Introduction:
Neutrophils are one of the first responders at early stages of acute inflammation underlying several pathologies, such as cancer or heart and lung injury[1,2]. Although the modulatory role of these neutrophils in the immune response is known, new non-invasive tools are still needed to gain a deeper understanding of their recruitment process and differentiation into subpopulations in vivo[1]. This work aims to design a novel immunePET specific of the Ly6G GPI protein, expressed in neutrophils, to evaluate its infiltration in acute lung injury, for further application in cardiopulmonary disorders.

Methods:
Chelator p-DFO-Bz-NCS was conjugated to the anti-mouse Ly6G monoclonal antibody (2mg) for 30min at 37ºC and pH 9.0, in a 5-fold molar excess. Resultant product was labeled with [^{89}Zr]Zr-oxalic for 1h at RT and pH 5.5, and then purified using 100KDa Amicon filters. Purity was stablished by radioTLC and antibody integrity was evaluated by immunoblot. For the *in vivo* evaluation of the radiotracer, we used the acute lung injury (ALI) model by direct intratracheal lipopolysaccharide (LPS, n = 5) instillation compared to sham animals (PBS, n = 3). ^{89}Zr-antiLy6G was injected intravenously in all mice after 24h of model induction (95-135µCi, 100µL PBS). *In vivo* PET/CT imaging was performed at 24 and 48h hours post-administration and tracer biodistribution was assessed *in vivo* by imaging quantification and *ex vivo* by gamma-counter.

Results:
^{89}Zr-antiLy6G was synthetized with 41.49 ± 16.55 % radiochemical yield and > 99% purity (Figure 1A), without altering the integrity of the antibody, established by immunoblot. CT imaging confirmed lung injury in ALI model, especially after at latest imaging point, as well as no lung damage to the sham mice. PET imaging revealed significant nuclear signal accumulated in lungs of ALI mice, while activity was mainly located in heart and spleen in sham group (Figure 1B). *In vivo* quantification (Figure 1D) confirmed higher uptake of the tracer in ALI lungs compared to sham after 48h of administration ($4.05 \cdot 10^4 \pm 2.54 \cdot 10^4$ total activity (SUV) in ALI vs. $1.90 \cdot 10^4 \pm 1.27 \cdot 10^4$ total activity (SUV) in sham mice. *Ex vivo* biodistribution (Figure 1C) also supported these results, presenting values of 26.12 ± 4.08 % ID/g in ALI mice lungs vs. 2.72 ± 0.36 % ID/g in sham.

Conclusions:
This work presents a neutrophil selective immunePET tracer and its non-invasive evaluation in acute injured tissues. Results achieved suggest the promising application of this approach for the detection of neutrophil infiltration in cardiopulmonary disorders and cardiovascular pathologies in which exacerbated inflammatory response plays a role, allowing an early stage detection of this phenomenon.

Reference
1. Rosales, C. (2018) Frontiers in physiology, 9, 113;
2. Herrero-Cervera, A. (2022) Cellular & Molecular Immunology, 19(2), 177-191.

Poster Presentation

Disclosures: The authors have disclosed no financial interest.

304-CCR2 Targeting PET/CT Imaging of Pancreatic Ductal Adenocarcinoma and the Metastasis

Presenter: Xiaohui Zhang, Washington University in St. Louis

Xiaohui Zhang[1], Lisa Detering[2], Deborah H. Sultan[3], Hannah P. Luehmann[4], Lin Li[4], Gyu Seong Heo[5], Josie Lesser[6], Marianna Ruzinova[6], Kian-Huat Lim[6], Yongjian Liu[7]

[1]*Washington University in St. Louis, St. Louis, MO*
[2]*Washington University School of Medicine, St. Louis, MO*
[3]*St. Louis, MO*
[4]*Washington University School of Medicine, St. Louis, Missouri*
[5]*Washington University School of Medicine, St. Louis*
[6]*University of Washington School of Medicine*
[7]*Washington University in St. Louis, St. Louis, Missouri*

Objective:
Pancreatic ductal adenocarcinoma (PDAC) is a devastating human cancer and a growing burden to the healthcare system in the United States. The tumor microenvironment of PDAC is heavily infiltrated with myeloid-derived suppressor cells (MDSCs) which express C-C chemokine receptor type 2 (CCR2). The CCR2-bearing MDSCs greatly outnumbers PDAC cells and are the initial cell type accumulating at the earliest stages of distant metastasis which are invisible to conventional imaging modalities and are likely the cause of distant relapse for patients after resection. Therefore, we developed a CCR2 targeting PET

tracer (^{68}Ga-DOTA-ECL1i) and evaluated the PET imaging on PDAC metastasis in mouse models.

Methods:
PET/CT imaging of ^{68}Ga-DOTA-ECL1i was performed in widely adopted hemisplenic injection liver metastasis models (KI) at 1-4 weeks post tumor injection and 16-23 week old genetically-engineered KPC (p48-CRE; LSL-KRas$^{G12D/wt}$; p53$^{flox/flox}$) orthotopic PDAC models and compared to ^{18}F-FDG. Hematoxylin and eosin (H&E) and CCR2 immunohistochemical (IHC) staining were performed to characterize the metastatic lesions. Autoradiography was conducted to confirm the uptake of ^{68}Ga-DOTA-ECL1i in the metastatic sites.

Results:
PET/CT images visualized the PDAC metastases in both liver and lung in KI mice at 1-4 weeks post tumor injection and in the liver of 16-23 week old KPC mice. Quantitative uptake analysis revealed increased liver and lung metastasis uptake in the KI mouse model (liver: from 1.38±0.46%ID/gram ($p<0.05$, n=7) at 1 week to 2.36±0.70%ID/gram ($p<0.005$, n=5) at 4 weeks post tumor implantation; lung (1.15±0.46%ID/gram ($p<0.05$, n=7) at 2 weeks to 1.80±0.43 %ID/gram ($p<0.005$, n=5) at 4 weeks post tumor implantation). ^{68}Ga-DOTA-ECL1i also demonstrated increased liver metastasis uptake in the 16-18 week old (0.82±0.07%ID/gram, $p<0.05$, n=4) and 20-23 week old (1.50±0.62%ID/gram, $p<0.05$, n=4) KPPC mice. In comparison, ^{18}F-FDG PET failed to detect any metastases during the time course study. H&E staining showed metastases in the liver and lung of KI mice, within which immunostaining clearly demonstrated the overexpression of CCR2 as well as CCR2^{+} cell infiltration into the normal liver. Autoradiographic images confirmed the metastatic uptake of ^{68}Ga-DOTA-ECL1i.

Conclusion:
Our data showed the specific expression of CCR2 at metastatic organs, indicating its potential as a biomarker for PDAC metastasis. ^{68}Ga-DOTA-ECL1i PET/CT in KI and KPC models demonstrated its sensitivity and specificity to detect PDAC metastasis.

Research Support: Emerson Collective Fund.

Poster Presentation

Disclosures: The authors would like to disclose that 68Ga-FAPI-46 is an investigational device.

305-Dynamic contrast enhanced-fluorescence imaging quantification of bone viability in lower limb amputation surgery

Presenter: Xinyue Han, Dartmouth College

Xinyue Han

Dartmouth College, Hanover, NH

Introduction:
Tissue viability depends on adequate blood supply, indicated by the perfusion level [1-3]. Bone perfusion level is estimated by the total blood flow in endosteal and periosteal vessels. The low -flow regions of bone are regarded as inviable, and request timely surgical debridement in order to prevent surgical site infection [4, 5]. Fluorescence-guided-surgery is a recently developed technique that using the fluorescent signal to visualize targeted tissue and provide guidance for surgeons. A bone specific tracer kinetic model [6, 7] and texture analysis model [8], based on dynamic contrast enhanced-fluorescence imaging (DCE-FI), can correspond to the level of bone viability. However, there are currently no techniques that can intraoperatively quantify bone viability level quickly and model independently.

Study Design:
Eleven participants with confirmed below knee amputation were included in this study. The study was approved by the Institutional Review Board of the Dartmouth-Hitchcock Medical Center and listed on ClinicalTrials.gov as NCT04250558. Three surgical conditions were created at each patient limb, designed to mimic three decreasing levels of bone viability after trauma, and 0.1 mg/kg indocyanine green (ICG) was intravenously injected in each condition: (1) *baseline (i.e. high viability)*; (2) *osteotomy (i.e. medium viability);* (3) *osteotomy and soft tissue stripping (i.e. low viability).* Time series of fluorescence images and a white-light image were recorded after ICG injection in each condition, using SPY Elite imaging system (Stryker Corp., Kalamazoo, MI, USA). An in-house built ICG pulse dye densitometer has been placed on the patient's finger to acquire an arterial input function (AIF). DCE-FI images were processed by custom MATLAB (The MathWorks, Natwick, MA) programs. In each time series of fluorescence images, three circular Regions-of-interest (ROIs) with same radius were respectively selected at proximal and distal to the osteotomy. For each ROI, model-independent first-pass kinetic parameters: maximum intensity, time-to-peak, ingress slope and egress slope of dye wash-in phase (denoted by *Imax*, *TTP*, *IS* and *ES*, respectively) were extracted from temporal fluorescence intensity (FI) curve (**Fig. 1(a)**) that was averaged over the pixels covered by the ROI. To account for the AIF-dependent effects, tissue temporal FI curves were corrected by replacing the individual AIF with averaged AIF [9].

Results:
First pass parameters *Imax* (**Fig. 1(b)** top) and *IS* (**Fig. 1(b)** bottom) were consistently decreasing as bone viability level decreased, which reflected the importance of maximum capacity of blood volume and transit rate of ICG in blood vessel, respectively, in bone viability. *TTP* and *ES* were not significant factors. As a result, *Imax* and *IS* can be used for classifying the bone viability states. The optimal thresholds for classification were as followed: ROIs with $Imax>120$ and $log(IS)>-1$ are classified as high viability (**Fig. 1(c)** in green), ROIs with $30<Imax<120$ and $-1<log(IS)<2$ are classified as medium viability (**Fig. 1(c)** in yellow), and ROIs with $Imax<100$ and $log(IS)<-0.5$ are classified as low viability (**Fig. 1(c)** in red).

Discussions and Conclusion:
In this human study, quick quantification of bone viability was achieved by using model-independent first pass kinetic parameters from DCE-FI captured intraoperatively. The population variation caused by various cardio functions among participants has been efficiently accounted for by arterial input function correction. This study is the first clinical study that performs DCE-FI in quantifying bone viability. The software and hardware is relatively straight-forward and the later can be 3D printed in a hospital lab.

Reference
1. Marenzana M and Arnett T R, 2013. The key role of the blood supply to bone. Bone Res. 1(1) 203–215.
2. Wootton R, Reeve J and Veall N, 1976. The clinical measurement of skeletal blood flow. Clin. Sci. Mol. Med. 50(4) 261–268.
3. Fujikawa Y, Quinn J M, Sabokbar A, McGee J O and Athanasou N A, 1996. The human osteoclast precursor circulates in the monocyte fraction. Endocrinology 137(9) 4058–4060.
4. Fry D E, Marek J M and Langsfeld M, 1998. Infection in the ischemic lower extremity. Surg. Clin. North Am. 78(3) 465–479.

5. Garwood E R, Moore D, Ewing C, Hwang E S, Alvarado M, Foster R D and Esserman L J, 2009. Total skin-sparing mastectomy: complications and local recurrence rates in 2 cohorts of patients. Ann. Surg. 249(1) 26–32.
6. Elliott J T, Jiang S, Pogue B W and Gitajn I L, 2019. Bone-specific kinetic model to quantify periosteal and endosteal blood flow using indocyanine green in fluorescence guided orthopedic surgery. J Biophotonics 4(8) 206–218.
7. Gitajn I L, Elliott J T, Gunn J R, Ruiz A J, Henderson E R, Pogue B W and Jiang S, 2020. Evaluation of bone perfusion during open orthopedic surgery using quantitative dynamic contrast-enhanced fluorescence imaging. Biomed Opt Express 11(11) 6458-6469.
8. Han X, Demidov V, Vaze V S, Jiang S, Gitajn I L, and Elliott J T, 2022. Spatial and temporal patterns in dynamic-contrast enhanced intraoperative fluorescence imaging enable classification of bone perfusion in patients undergoing leg amputation. Biomed. Opt. Express 13(6), 3171-3186.
9. Elliott J T, Addante R R, Slobogean G P, Jiang S, Henderson E R, Pogue B W and Gitajn I L, 2020. Intraoperative fluorescence perfusion assessment should be corrected by a measured subject-specific arterial input function. J. Biomed. Opt. 25(6) 1–14.

Poster Presentation

Disclosures: The authors have disclosed no financial interest.

306-Effects of BRCA2 loss on PSMA expression in Prostate Cancer.

Presenter: Teja Muralidhar Kalidindi, Memorial Sloan Kettering Cancer Center

Teja Muralidhar Kalidindi[1], NagaVaraKishore Pillarsetty[2], Tullio V. Esposito[3], Goutam Chakraborty[3], Heiko Schöder[2]

[1]Memorial Sloan Kettering Cancer Center, Hastings on Hudson, NY
[2]Memorial Sloan Kettering Cancer Center, New York, NY
[3]Memorial Sloan Kettering Cancer Center, New York City, NY

Background:
Hemizygous and Homozygous deletion of hallmark DNA damage repair (DDR) protein, *BRCA2* in Prostate cancer (PC) are associated with increased risk of aggressive PC, highere rate of distant metastasis and resistance to androgen deprivation therapy (ADT). Clinical data has shown BTCA2/DDR deficiency commonly results in poor prognosis. Lately immunohistochemical analysis of mCRPC patient samples by Paschalis et al. revealed that mutations in DDR genes (in particular *BRCA2* and *ATM*) are associated with increased prostate-specific membrane antigen (PSMA; folate hydrolase, FOLH1) expression on the cell membrane. We wanted to investigate if this upregulation in PSMA expression can be targeted with a dignostic positron emission tomograpy (PET) imaging agents such as [^{68}Ga]-PSMA11 or [^{124}I]-MSK-PSMA1. Therefore, we hypothesized that upregulation of PSMA expression can be used as a marker for *BRCA2* alteration, which can be measured using PET imaging *in vivo*.

Experimental Design:
We analyzed human prostate cancer cell line, LNCaP, at mRNA and protein level and quantified the expression of PSMA using saturation binding assays with [^{124}I]-MSK-PSMA1. Using CRISPR-Cas9, we knocked out *BRCA2* in the castration sensitive cell line LNCaP cells and evaluated its effect on PSMA at the transcriptional and translational level. Saturation binding assay using [^{124}I]-MSK-PSMA1 was performed to measure changes in cell surface PSMA receptor density in LNCaP *BRCA2* knockouts.

Results:
BRCA2 knockout was achieved successfully using CRISPR-Cas9 based methods. Western blot analysis revealed that PSMA levels increase significantly with *BRCA2* loss when *BRCA2* knockouts were compared to control LNCaP cell line. Immunohistochemical analysis confirmed this obervation. Cell binding assays demonstrated that *BRCA2* knockout LNCaP cell lines have about 6 fold higher uptake of the PET tracer [^{124}I]-MSK-PSMA1. *in vivo* studies were planned to demonstrate that *BRCA2* deletion leads to a signficant increase in PSMA signal in mice xenograft models.

Conclusions:
Our results indicate that BRCA2 silencing leads to signficant upregulation of PSMA expression in PC cell lines, which can be imaged using a PSMA targeted PET tracer.

Poster Presentation

Disclosures: The authors have disclosed no financial interest.

307-A Vascularized Organoid On-A-Chip Model for the Investigation of HIF-1-Alpha in Angiogenesis

Presenter: Ngan Phung, Memorial Sloan Kettering Cancer Center

Ngan Phung[1], Magdalena Skubal[1], Ben E. Mc Larney[1], Jan Grimm[1]

[1]Memorial Sloan Kettering Cancer Center, New York, NY

Angiogenesis, the development of new blood vessels from pre-existing ones as a response to hypoxia, plays an important role in tumor growth, progression, and metastasis.[1] Under hypoxic conditions, hypoxia inducible factor 1 alpha, HIF-1-alpha, is stabilized and translocated into the nucleus, resulting in the upregulation of pro-angiogenic factors, such as vascular endothelial growth factor (VEGF) and platelet-derived growth factor (PDGF).[2] Hypoxia is a major therapeutic barrier and is known to be highly correlated with increased tumor resistance to cancer treatments.[3] Most preclinical *in vitro* studies on solid tumors and angiogenesis are done using the conventional two-dimensional (2D) tissue culture system. However, 2D systems as a model are limited, as they lack the organization and complexity of a tumor and do not comprehensively replicate the hypoxic microenvironment within the tumor and vasculature. Here, we have established a three-dimensional co-culture system combining organoids and microvessels to model vasculature in solid tumors on a microfluidic chip. Our preliminary data showed that co-culturing patient derived organoids with endothelial cells on the chip results in a vascular network formation. We propose to model hypoxia-induced angiogenesis and investigate the role of HIF-1-alpha in angiogenesis by co-culturing patient derived colorectal adenocarcinoma cancer organoids and endothelial cells on the microfluidic chips.

Reference
1. Hanahan, D.; Weinberg, R. A., Hallmarks of cancer: the next generation. Cell 2011, 144 (5), 646-74.
2. Makrilia, N.; Lappa, T.; Xyla, V.; Nikolaidis, I.; Syrigos, K., The role of angiogenesis in solid tumours: an overview. Eur J Intern Med 2009, 20 (7), 663-71.
3. Muz, B.; de la Puente, P.; Azab, F.; Azab, A. K., The role of hypoxia in cancer progression, angiogenesis, metastasis, and resistance to therapy. Hypoxia (Auckl) 2015, 3, 83-92.

Poster Presentation

Disclosures: The authors have disclosed no financial interest.

308-In Vivo Photoacoustic and Fluorescence Molecular Imaging of Bacterial Infections

Presenter: Stella Yang, Stanford University

Stella Yang[1], Aimen Zlitni[2], Sanjiv S. Gambhir[2], Tulio A. Valdez[3]

[1]*Stanford University*
[2]*Stanford University, Stanford, CA*
[3]*Stanford University, Palo Alto, CA*

Current methods only measure inflammation (an indirect biomarker of infection, therefore lacking sensitivity and specificity), are highly invasive (requires multiple tissue samples and has a high risk of infection), or can only detect the infection once it is too late (imaging anatomy alone). We propose a targeted bacteria probe as a noninvasive tool that can rapidly diagnose and determine the extent of bacterial infections. Our probe consists of a maltodextrin sugar linked with a fluorescent dye, indocyanine green (ICG) since only bacteria have the transporter that can uptake the sugar and ICG has the best fluorescent and photoacoustic properties. Our fluorescence studies were conducted with SKH1-elite female mice, with 20μL of S. aureus (Xen36) of different CFUs injected subcutaneously as an infected wound model. We used 10nmol / mouse of the maltotriose-ICG probe injected via the tail vein and a sample size of 5 mice. We measured fluorescence with an excitation of 745nm and an 820nm long-pass filter. Our photoacoustic studies were conducted with nu/nu female mice, with the same bacteria just injected into the thigh muscle. We used 10nmol / mouse of the maltotriose-ICG probe and a sample size of 5 mice. We measured with an excitation of 800nm and a Z 250 transducer as the ultrasound probe. These studies were also repeated with fluorescence to complement. Overall, our findings that there is a distinguishable signal at the site of infection with fluorescence imaging as early as 2 hours post-injection and remains visible until 20 hours. Furthermore, with photoacoustic methods, the entire infection in the mouse thigh of 10mm in depth can be imaged. Therefore, we can reliably detect and distinguish bacterial infection from non-bacterial inflammation or any mammalian cells (including cancer) in an accurate and highly specific manner, leading to a novel method for accurately and completely detecting ear infections as well as numerous other bacterial infections.

Poster Presentation

Disclosures: The authors have disclosed no financial interest.

309-New Parahydrogen Hyperpolarized Metabolic Probes for Magnetic Resonance Spectroscopy Imaging

Presenter: Michael Keim, NVision Imaging Technologies GmbH

Michael Keim[1], Martin Gierse[2], Stephan Knecht[3], Pascal Wolff[2], Ilai Schwartz[1]

[1]*NVision Imaging Technologies GmbH, Germany*
[2]*NVision Imaging Technologies GmbH, Baden-Wuerttemberg, Germany*
[3]*NVision Imaging Technologies GmbH, Ulm, Germany*

Melabolic MRI using hyperpolarized ^{13}C nuclei has been becoming a popular tool for the study of metabolic processes and has been used for a variety of applications ranging all the way from tumor treatment response [1] to the study of heart disease [2]. In this modality, the metabolic conversion of biologically relevant tracer molecules is studied by means of MR imaging and spectroscopy. In order to make this modality technically feasible, the signal of these marker molecules needs to be enhanced by several orders of magnitude prior to injection, commonly referred to as hyperpolarization. So far, the most prominent method and gold standard in this field is dissolution Dynamic Nuclear Polarization (d-DNP). However, for many applications, d-DNP is prohibitively expensive, complex and slow. Hyperpolarization of biomolecules using Parahydrogen Induced Polarization (PHIP) is an efficient and cost-effective alternative to the established d-DNP method and was therefore studied as an alternative to d-DNP by several research groups [3,4]. Nevertheless, the d-DNP approach was superior to the PHIP approach due to its broad applicability to various biomolecules. So far, from the metabolites of interest only pyruvate and fumarate could be satisfactorily polarized using the PHIP approach. The most promising technique used to hyperpolarize pyruvate via parahydrogen is called PHIP-SAH (ParaHydrogen Induced Polarization - Side-Arm Hydrogenation). This technique involves a side-arm with an unsaturated bond that is covalently attached to a metabolite and hydrogenated with parahydrogen by the help of a (homogeneous) catalyst. Following the hydrogenation and polarization of the target, the side-arm can be cleaved off selectively, resulting in the hyperpolarized metabolite of interest. The presented results demonstrate the translation of the PHIP-SAH approach to other interesting biomolecules than pyruvate and therefore, extending the portfolio of relevant PHIP-polarizable metabolites with two additional molecules which provide key metabolic insight, namely lactate and α-ketoglutarate. Figure 1 a) and b) shows the hyperpolarized ^{13}C NMR spectrum before side arm cleavage of α-ketoglutarate and lactate respectively. Both probes can be polarized to levels exceeding 10 % with concentrations above 100 mM. Following polarization, both molecules can be cleaved and purified resulting in usable hyperpolarized probes for HP-MRI. These two important probes significantly expand the class of molecules efficiently polarized by PHIP-SAH, and will enable key metabolic insights, as shown in initial in vivo experiments with these probes by d-DNP in preclinical studies.

Reference

1. Day, Sam E., et al. "Detecting tumor response to treatment using hyperpolarized 13 C magnetic resonance imaging and spectroscopy." Nature medicine 13.11 (2007): 1382-1387.
2. Rider, Oliver J., et al. "Noninvasive in vivo assessment of cardiac metabolism in the healthy and diabetic human heart using hyperpolarized 13C MRI." Circulation research 126.6 (2020): 725-736.
3. Knecht, Stephan, et al. "Rapid hyperpolarization and purification of the metabolite fumarate in aqueous solution." Proceedings of the National Academy of Sciences 118.13 (2021).
4. Reineri, Francesca, et al. "Parahydrogen induced polarization of 13 C carboxylate resonance in acetate and pyruvate." Nature communications 6.1 (2015): 1-6.

Poster Presentation

Disclosures: The authors have disclosed no financial interest.

310-Optimization of 18F-labeled anti-HER2 5F7 theranostic treatement of brain tumor metastases using low-level radiation and combined DCE-MRI and PET

Presenter: Daniele Procissi, Northwestern University Feinberg School of Medicine

Daniele Procissi[1], Stephen Jannetti[2], Markella Zannikou[3], Zhengyuan Zhou[2], Darryl McDougald[2], Deepak Kanojia[2], Ganesan Vaidyanathan[2], michael r. zalutsky[4], Irina V. Balyasnikova[5]

[1]*Northwestern University Feinberg School of Medicine, Chicago, IL*
[2]*Duke University, Durham, North Carolina*
[3]*Northwestern University Feinberg School of Medicine, Chiago, Illinois*
[4]*Duke University, Durham, NC*
[5]*Northwestern University, Chicago, Illinois*

Background & Hypothesis:
The ability to detect and treat brain metastases (BM) in breast cancer patients expressing human epidermal growth factor receptor type 2 (HER2) is an urgent medical need[1]. One of the main challenges towards developing efficient BM treatments is associated with the more restrictive brain blood-tumor barrier (BTB) in BMs compared to glioblastomas (GBM), which limits the efficient delivery of therapeutic agents to intracranial lesions[2]. Single-domain antibody fragments (aka V_HH, ~13 kDa) are promising targeting systems for BM lesion theranostics. However, strategies are needed to overcome the BTB and to enable efficient intra-cranial lesion uptake without affecting the surrounding normal brain tissue. Low-dose (< 3-Gy) whole-brain irradiation (WBRT) has been shown, both in mice and humans, to increase brain tumor perfusion and permeability and is considered a viable option to circumvent BTB and enhance uptake of therapeutic agents[3]. This preclinical study evaluates WBRT as a strategy to modulate and alter BM microenvironment with the goal of enhancing tumor uptake of theranostic ^{18}F-labeled anti-HER2 V_HH 5F7[4]. The experimental framework for this study involved a mouse model implanted with HER2-positive BT474BrM3 and use of a combination of non-invasive imaging techniques (MRI and PET/CT)[5] supported by histology flow-cytometry and genetic assays.

Methods:
Mice implanted with BT474Br intracranial xenograft were divided into a control and irradiated group (n=4). Longitudinal non-invasive imaging was conducted following WBRT to evaluate associated changes in tumor perfusion and permeability and to track the migration of ^{18}F-labeled anti-HER2 VHH 5F7 using respectively, dynamic contrast-enhanced MRI (DCE-MRI) and PET/CT. *Ex-vivo* histological and western blot analysis were used to obtain vascular and Her2 expression data.

Results & Discussion:
Panel (i) summarizes DCE-MRI results. (a) Comparison of DCE-MRI derived parametric maps show general increase and more heterogeneity in the irradiated mice group as compared to the control group. Shown in Panel (i)-(b) are representative 3D whole-tumor rendered images from a WBRT and control mice. Use of different treshold windows for rendering enables 3D visualization of tumor microenvironment differences reflecting tumor wide increases in permeability. Panel (i)-(c) depicts quantitative trends of tumor perfusion/permeability data which reflect the transient changes occuring in treated mice as compared to controls. PET results are summarized in Panel (ii). PET uptake images and quantitative analysis show higher tumor uptake of ^{18}F-labeled anti-HER2 5F7 at ~12 days post-radiation in radiation treated mice as compared to controls. The PET-uptake increase and timing is consistent with the corresponding observed increases in permeability measured with MRI. *Ex-vivo* histology and Western Blot (data not shown) were to used to confirm that the observed tumor uptake of labeled antibodies was directly linked to radiation effects and not to changes in Her2 expression.

Conclusion:
The results presented in this study validate the hypothesis that low-level radiation can induce transient changes in tumor microenvironment which improve tumor uptake of single-domain antibody fragments. In addition to validating the potential of a novel theranostic approach the work presented suggests that the combined use of non-invasive DCE-MRI and direct PET imaging of labeled therapeutic antibodies could be used as a tool to optimize novel treatment strategies by providing non-invasive real-time insight into radiation-induced effects on tumor physiology.

Reference
1. Hurvitz SA, O'Shaughnessy J, Mason G, et al. Central Nervous System Metastasis in Patients with HER2-Positive Metastatic Breast Cancer: Patient Characteristics, Treatment, and Survival from SystHERs. Clin Cancer Res. 2019;25(8):2433-2441.
2. Lockman PR, Mittapalli RK, Taskar KS, et al. Heterogeneous Blood–Tumor Barrier Permeability Determines Drug Efficacy in Experimental Brain Metastases of Breast Cancer. Clin Cancer Res. 2010;16:5664-5678.
3. DeAngelis LM, Delattre J-Y, Posner JB. Radiation-induced dementia in patients cured of brain metastases. Neurology. 1989;39:789-789.
4. Pruszynski M, Koumarianou E, Vaidyanathan G, et al. Targeting breast carcinoma with radioiodinated anti-HER2 Nanobody. Nucl Med Biol. 2013;40:52-59.
5. Jakubovic R, Sahgal A, Soliman H, et al. Magnetic Resonance Imaging-based Tumour Perfusion Parameters are Biomarkers Predicting Response after Radiation to Brain Metastases. Clin Oncol. 2014;26:704-712.

Poster Presentation

Disclosures: The authors have disclosed no financial interest.

311-[123I]-KX1, a potential tracer for imaging PARP in pancreatic cancer model

Presenter: Chia Hsin Fan, Chang Gung University

Chia Hsin Fan[1], Chang Pei Ti[2], Yi-hsiu Chung[3], Robert Mach[4], Chi-Chang Weng[5]

[1]*Chang Gung University, Taiwan*
[2]*Linkou Chang Gung Memorial Hospital, Taiwan*
[3]*Linkou Chang Gung Memorial Hospital, Kawi-Shan, Taoyuan, Taiwan*
[4]*University of Pennsylvania, Philadelphia, PA*
[5]*Chang Gung University, Tao-Yuan City, Taiwan*

Aim:
Recently, Poly (ADP-ribose) polymerase (PARP) inhibitors are postulated to have possible therapeutical benefits for the patient with pancreatic cancer. However, the treatment efficacy of theses PARP inhibitors seems to be related with the BReast CAncer (BRCA) gene mutation, which means a predictive biomarker may be helpful for the screening of the suitable patients to receive a PARP inhibitor treatment in the future. As such reason, in the study present herein, an radioiodinated rucaparib derivative ([^{123}I]KX1) was used as a PARP-1 imaging ligand

and applied for the in vivo SPECT imaging on the pancreatic tumor bearing mouse model.

Methods:

For the preparation of the tumor bearing animal model, briefly, Mia-PaCa-2 cells (2x10^6 cells in 200μL PBS) were injected subcutaneously in lower right flank on 4-6 male Balb/c nu/nu mice (9-weeks-old). Four weeks after tumor inoculation, each animal was received a dose of 0.6-0.8 mCi [^{123}I]-KX1 via the tail vein and applied for a 30 min SPECT imaging procedure (1hr after tracer injection). After in vivo imaging studies, all animals were sacrificed and the tumor tissues were dissected for the further autoradiography (ARG) and immunohistochemistry (IHC) examination. The tumor tissue sections with a thickness of 20μm were used for the ex vivo ARG preparation. For the IHC staining on the tumor section, the PARP-1 targeting antibody (9532, Cell Signaling) and the DAB substrate kit (ab64238, abcam) were used tissue staining.

Results:

Four weeks after tumor inoculation, all tumor-bearing animals were used for the in vivo [^{123}I]KX1 SPECT imaging. Based on the imaging acquisition results on the pancreatic tumor bearing mice, the tracer uptakes in the regions of tumor and muscle were 14.3±1.3 and 2.9±0.7, and the tumor-to-muscle ratio is 4.93. For the following ex vivo ARG and PARP-1 IHC results were correlated well with the finding on the SPECT images.

Conclusion:

Taken together, a high tumor-to-muscle ratio of [^{123}I]KX1 on the PARP-1 overexpression pancreatic tumor cells bearing mice demonstrates the this radiotracer may have the potential on the patient selection for PARP inhibitor treatment in the future.

Poster Presentation

Disclosures: The authors have disclosed no financial interest.

312-Near infrared imaging human EGFR positive lung cancers using IRDye800CW-nimotuzumab

Presenter: Wendy Bernhard, University of Saskatchewan

Wendy Bernhard[1], Kris Barreto[2], Ron C Geyer[2], Steven Bharadwaj[1], Darryl Yu[1], Emina Torlakovic[1]

[1]*University of Saskatchewan, Saskatoon, Saskatchewan*
[2]*University of Saskatchewan, Saskatoon, SK*

Introduction:

Epidermal growth factor receptor (EGFR) is overexpressed in many cancers[1]. There are a number of therapeutic antibodies currently used to treat EGFR positive cancers. Nimotuzumab is a humanized therapeutic antibody that targets EGFR. Surgical resection is used to treat many solid tumors including non-disseminated non-small cell lung cancer (NSCLC)[2]. 40-80% of NSCLC overexpress EGFR[3]. Detection of lung cancer during surgery can be difficult when there are deeply located lesions that can be impossible to see by white light alone. Image-guided surgery using a fluorescent probe provides a way to increase detection of tumors during surgery and improve negative resection margins. We are currently recruiting for a clinical trial (NCT04459065) to evaluate an anti-EGFR fluorescent imaging probe in image-guided surgical resection of EGFR positive cancers.

Methods:

The preclinical evaluation of IRDye800CW-nimotuzumab probe has been published[4,5]. We are recruiting for a phase I/II clinical trial in Canada to evaluate this probe in lung cancer surgery. GMP production and quality control specifications of the fluorescent probe were determined. Clinical evaluation was carried out in lung cancer patients eligible for surgical resection. The trial was designed to determine the optimal dose and time for imaging. Participants received an infusion of IRDye800CW-nimotuzumab. Blood, vitals, and lab parameters were collected for safety and pharmacokinetics (PK), and surgical resection was performed following probe injection. The resected tissue was analyzed for fluorescence (from the probe), H&E staining, and for EGFR expression by immunohistochemistry.

Results:

IRDye800CW-nimotuzumab had high uptake in the tumor and a high tumor to background ratio (TBR) compared with normal tissue (Figure 1). The tumor-to-background-ratios (TBRs) were between 5-7 for one participant and up to 30 for the second participant.

Pharmacokinetics were analyzed and IRDye800CW-nimotuzumab probe had a half-life of ~1.6 days. The probe was stable as shown by its ability to bind to EGFR positive cells a few days after injection. Immunohistochemistry of the tumor tissue with an EGFR antibody showed a strong correlation with fluorescence from IRDye800CW-nimotuzumab in tissues. We did not observe related adverse events from the probe.

Conclusions:

In this study, we produced GMP-grade IRDye800CW-nimotuzumab for image-guided surgery of EGFR positive cancers. The probe had high accumulation in NSCLC tumors in humans. This data showed the potential for this probe to be used during surgical resection of NSCLC. We also observed uptake in nearby lymph nodes, highlighting another potential benefit of using this probe during surgery to detect disseminated cancer cells in lymph nodes.

Reference

1. Yewale C, Baradia D, Vhora I, Patil S, Misra A. Epidermal growth factor receptor targeting in cancer: A review of trends and strategies. Biomaterials. 2013; 34:8690–707.
2. Neijenhuis LKA, de Myunck LDAN, Bijlstra OD, Kuppen PJK, Denise E Hilling, et al. Near-Infrared Fluorescence tumor-targeted imaging in lung cancer: A systemic review. Life (Basel). 2022; 2:446
3. Hirsch FR, Varella-Garcia M, Cappuzzo F. Predictive value of EGFR and HER2 overexpression in advanced non-small-cell lung cancer. Nature. 2009; 28:S32-S37
4. Bernhard W, El-Sayed A, Barreto K, Gonzalez C, Hill W, et al. Near infrared fluorescence imaging of EGFR expression in vivo using IRDye800CW-nimotuzumab. Oncotarget. 2018. 9:6213-6227.
5. Bernhard W, Barreto K, El-Sayed A, Gonzalez C, Viswas RS, et al. Pre-clinical study of IRDye800Cw-nimotuzumab formulation, stability, pharmacokinetics and safety. BMC Cancer. 2021. 270

Poster Presentation

Disclosures: The authors have disclosed no financial interest.

313-Whole-Body Distribution of Lipid Nanoparticle mediated mRNA Delivery using Cryo-Fluorescence Tomography (CFT)

Presenter: Guankui Wang, Hopewell Therapeutics, Inc.

Guankui Wang[1], Shuhan Ji[1], Jerry H. Li[1], Changfeng Huang[1], Bevan Bsharah[1], Eli White[2], Antoinette Cordova[2], Qiaobing Xu[1]
[1]*Hopewell Therapeutics Inc., Woburn, MA, USA*
[2]*Emit Imaging, Baltimore, MD, USA*

Lipid nanoparticles (LNPs) have shown great potential for delivering a variety of nucleic acid-based therapeutics[1], especially after FDA approval of mRNA vaccines for conquering the COVID-19 pandemic[2]. However, systemic delivery of nucleic acids with LNPs is more complicated than the intramuscular injection of LNP-mRNA vaccines, given the physiological barriers for organ-specific delivery of different disease-specific gene editorial or mRNA payloads.[3] Recently, LNPs have emerged as a versatile organ-specific delivery carrier for RNA therapeutics[4, 5, 6]. Most efforts in the gene/mRNA delivery field have mainly been focused on improving the delivery efficiency and efficacy of payloads to liver-specific cells[7, 8, 9], because the liver is still the main site for clearing the payloads independent on the delivery system, viral or non-viral[10]. Realizing the importance of expanding the delivery system from liver to other organs to potentially treat other non-liver diseases, we have developed several lead LNP candidates with lung-specific targeting for mRNA delivery.[11] In order to illustrate the whole-body distribution of LNP delivered mRNA, cryo-fluorescence tomography (CFT), an *ex-vivo* molecular imaging technique, was utilized to localize the mRNA expression in specific tissues and cells in the Ai9 transgenic mouse model leveraging the tdTomato gene reporter system. With successful Cre mRNA delivery, the tdTomato gene will be transcribed due to the Cre recombinase activity on the loxP-flanked STOP cassette. Thus, the tdTomato fluorescence intensity will indicate the level of Cre mRNA delivery efficiency mediated by LNPs, in addition to the biodistribution of mRNA LNPs. After 3 days of intravenous injection of Cre mRNA LNPs (0.5 mg/kg mRNA dose), mice were sacrificed and immediately frozen in dry ice and shipped to Emit Imaging for CFT using the Xerra™ imaging platform. The automatic microtome slicing and fluorescence/white light imaging system of the Xerra™ allowed the robust and efficient visualization of the tdTomato signals through the whole mouse. After imaging the sections (20 µm thickness), a 3-dimensional fluorescence image was reconstructed from thousands of individual 2-dimensional images for each mouse. The CFT data have confirmed the Cre mRNA delivery in the liver or lung tissues by the LNPs targeting to those organs, indicating that CFT is a powerful tool to establish the whole-body distribution database for our organ-specific LNP delivery platforms.

Reference

1. Samaridou E., Heyes J., Lutwyche P. Lipid nanoparticle for nucleic acid delivery: current perspective. Adv. Drug Deliv Rev. 2020, 154-155: 37-63.
2. Cross R. Without these lipid shells, there would be no mRNA vaccines for COVID-19. Chemical & Engineering News, 2021, 99, 8.
3. Torres-Vanegas J., Cruz J.C., Reyes L.H. Delivery systems for nucleic acids and proteins: barriers, cell capture pathways and nanocarriers.
4. Andresen J.L., Fenton O.S. Nucleic acid delivery and nanoparticle design for COVID vaccines. MRS Bulletin, 2021, 46, 832-839.
5. Hou X., Zaks T, Langer R., Dong Y. Lipid nanoparticles for mRNA delivery. Nature Reviews Materials, 2021, 6, 1078-1094.
6. Qiu M., Li Y., Bloomer H., Xu Q. Developing biodegradable lipid nanoparticles for intracellular mRNA delivery and genome editing. Acc. Chem. Res., 2021, 54, 21, 4001-4011.
7. Bottger R. et al. Lipid-based nanoparticle technologies for liver targeting. Adv. Drug Deliv Rev. 2020, 154-155: 79-101.
8. Yang T. et al. Efficient hepatic delivery and protein expression enabled by optimized mRNA and ionizable lipid nanoparticle. Bioactive Materials, 2020, 5, 4, 1053-1061.
9. Kim M. et al. Engineered ionizable lipid nanoparticles for targeted delivery of RNA therapeutics into different types of cells in the liver. Science Advances. 2021, 7.
10. Maestro S. et al. Novel vectors and approaches for gene therapy in liver diseases. JHEP Reports, 2021, 3, 4, 100300.
11. Qiu M. et al. Lung-selective mRNA delivery of synthetic lipid nanoparticles for the treatment of pulmonary lymphangioleiomyomatosis. PNAS, 2022, 119, 8.

Poster Presentation

Disclosures: The authors have disclosed no financial interest.

314-Evaluation of reference region based modeling of AT1R antagonist 11C-KR31173 binding in rat kidney

Presenter: Lindsey Drake, Bristol Myers Squibb

Lindsey Drake[1], Erin Cole[1], Andrea (Olga) O. Shorts[2], Gordon Pipes[1], Jeremy Richter[1], Sam Bonacorsi[1], Matt Fronhesier[1], Patrick L. Chow

[1]*Bristol Myers Squibb*
[2]*Bristol Myers Squibb, princeton, NJ*

Cardiovascular complications including heart failure or ischemic heart disease are the leading cause of death in patients with chronic kidney disease. Amongst others, components of the renin angiotensin system, particularly the Ang II type 1 receptor (AT1R), are responsible for blood pressure and electrolyte homeostasis. The AT1R antagonist radioligand, ^{11}C-KR31173, was developed and has been utilized in rodents,[1-3] dog,[2] baboon,[2] pig,[4,5,6,7] and human.[5,7,8] In the myocardium and kidneys,tracer retention has been reported as well as the 2-tissue-compartment model.[5-8] The objective of this work was to establish a reference region and determine suitable graphical models for the estimation of BP_{ND} in rodent kidneys. Dynamic ^{11}C-KR31173 PET images were acquired on the NanoScan PET/CT (Mediso) along with a low dose CT for attenuation correction and structural definition of organs. Based on low protein level expression, muscle and spinal cord were investigated as possible reference regions. Left and right kidney were drawn as regions with established expression of AT1R. Time activity curves (TAC) were exported into PKIN (Pmod4.0) for modeling. Graphical models including Logan reference, linear SRTM, SRTM, and $MRTM_0$ were evaluated. Model selection was based on lowest Akaike Information Criterion (AIC) reduced χ^2 and associated standard error with the estimated parameters. Naïve Sprague Dawley rats were used for the imaging evaluation in three groups (n=6/ group): baseline, valsartan (10 mg/kg) challenge, and vehicle challenge. Valsartan and vehicle challenges were dosed 20 minutes before radiotracer injection. Spinal cord was chosen as the preferred reference region based on time activity curve shape, relatively low inter-subject variability, lack of effect during vehicle and blocking studies, and performance in graphical models. All methods provided reasonable estimates of BP_{ND}, with $MRTM_0$ being favored by lowest AIC. In the highest region of AT1R, kidneys, the estimated BP_{ND} ($MRTM_0$) was reduced ~50% in the valsartan challenge, as expected from literature.[3] In summary, ^{11}C-KR31173 uptake in naïve rats was evaluated for a suitable reference region and establish a robust graphical method for modeling BP_{ND}. Spinal cord and muscle were evaluated as possible reference regions and the spinal cord was better performing. $MRTM_0$ was the best fitting graphical model of those evaluated and provided good fits across

baseline and challenge scans. Graphical models provide simplified, yet robust estimates of specific binding when validated. This allows for target engagement to be performed, without blood sampling, in preclinical species.

Reference

1. Matthews et al. J Nucl Med 2004; 31: 571-574.
2. Zober et al. J of Nucl Med 2006; 33(1): 5-13.
3. Higuchi et al., J of Nucl Med 2010; 51:1956-1961.
4. Xia et al. Hypertension 2008; 51(2): 466-473.
5. Fukushima et al., J Am Coll Cardiol 2012; 60(24):2527-2534.
6. Gulaldi et al., BioMed Research International 2013; Article ID 835859.
7. Feng et al., Medical Physics 2015; 42(11): 6736-6744.
8. Valenta et al., J Am Coll Cardiol Img 2019; 12(9): 1895-1896.

Poster Presentation

Disclosures: The authors have disclosed no financial interest.

315-Targeting the Extracellular Matrix for Non-Invasive PET Imaging of Triple Negative Breast Cancer.

Presenter: Justin Hachey, Weill Cornell Medicine

Justin S. Hachey[1], Silvia Ortona[2], Luciano Zardi[2], Jason Lewis[3]
[1]Weill Cornell Medicine
[2]Genoa, Italy
[3]Memorial Sloan Kettering Cancer Center, New York, NY

Introduction:
Triple negative breast cancer (TNBC) is characterized by lacking expression of the estrogen and progesterone hormone receptors (ER/PR), and human epidermal growth factor receptor 2 (HER2). TNBC comprises approximately 15% of breast cancer diagnoses, and TNBC patients face a worse prognosis than ER+/PR+ and/or HER2+ breast cancer patients [1]. Given the lack of key receptor targets, alternate markers are necessary for identification of TNBC. Fibronectin (FN) is an alternatively spliced extracellular matrix (ECM) protein, and splice variants containing the Extradomain B (EDB-FN) exon are unique to oncogenic tissues, and significantly upregulated in TNBC relative to healthy breast tissues [2, 3]. EDB-FN expression is correlated with increased invasive potential, and increased FN expression is associated with worse overall cancer progression and prognosis in invasive breast cancers [2-4]. IUG-1 is an immunouteroglobin construct that harnesses the targeting scFv regions of the anti-EDB-FN antibody, CGS-1, in combination with the enhanced stability and blood clearance of a uteroglobin backbone [5, 6]. We propose that IUG-1 is a suitable fusion protein construct for the non-invasive PET imaging of TNBC by targeting EDB-FN.

Methodology:
A panel of TNBC cell lines (MDA-MB-231, Hs578T, MDA-MB-468, BT549, MCF7) was screened for EDB abundance *in vitro* utilizing western blotting. A 3D culture system for MDA-MB-231 and Hs578T cell lines was developed to enhance ECM protein expression. EDB-FN abundance was compared between 2D and 3D culturing systems by western blotting. Recombinant human uteroglobin and IUG-1 were bioconjugated to p-SCN-Bn-DFO through non-specific lysine bioconjugation. *In vitro* radioactive ligand binding assay using [^{89}Zr]Zr-DFO-IUG-1 was performed utilizing MDA-MB-231 cells grown in 3D culture. Six to eight week old female NSG mice were xenografted with MDA-MB-231 cells, and tumors were allowed to develop for 2 weeks prior to imaging. 200µCi of [^{89}Zr]Zr-DFO-IUG-1 was administered to mice and PET scans were performed at 4, 24, 48, and 96 hours post-injection. SUVs within tumor ROIs were calculated for each imaging time point.

Results:
Western blotting analysis indicated that invasive mesenchymal stem like subtype TNBC cells MDA-MB-231 and Hs578T displayed the greatest abundance of EDB-FN in 2D culture. 3D culture conditions provided 3.9 and 4.1-fold increases in EDB-FN abundance in MDA-MB-231 and Hs578T cultures, respectively. [^{89}Zr]Zr-DFO-IUG-1 was synthesized with >97% radiochemical yield with a specific activity of ~12µCi/µg. *In vitro* binding assay demonstrated specificity of [^{89}Zr]Zr-DFO-IUG-1 for EDB-FN. *In vivo* PET scans and SUV determination demonstrated enhanced tumor uptake by 24 hours post-injection, with retention of radioligand through 96 hours post-injection in mice bearing MDA-MB-231 xenografts.

Conclusions:
Our findings demonstrate the successful utility and feasibility of [^{89}Zr]Zr-DFO-IUG-1 as a radiotracer for PET imaging of TNBC by targeting a component of the extracellular matrix. We are working to validate EDB-FN targeted imaging for detection of metastatic lesions of TNBC.

Acknowledgement: This work was supported by the NIH R35 CA232130, Small Animal Imaging Core at MSKCC, and Molecular Cytology Core at MSKCC.

Reference

1. Li, X., et al., Triple-negative breast cancer has worse overall survival and cause-specific survival than non-triple-negative breast cancer. Breast Cancer Res Treat, 2017. 161(2): p. 279-287.
2. Vaidya, A., et al., Overexpression of Extradomain-B Fibronectin is Associated with Invasion of Breast Cancer Cells. Cells, 2020. 9(8).
3. Nam, J.M., et al., Breast cancer cells in three-dimensional culture display an enhanced radioresponse after coordinate targeting of integrin alpha5beta1 and fibronectin. Cancer Res, 2010. 70(13): p. 5238-48.
4. Bae, Y.K., et al., Fibronectin expression in carcinoma cells correlates with tumor aggressiveness and poor clinical outcome in patients with invasive breast cancer. Hum Pathol, 2013. 44(10): p. 2028-37.
5. Neri, D., et al., Targeting by affinity-matured recombinant antibody fragments of an angiogenesis associated fibronectin isoform. Nat Biotechnol, 1997. 15(12): p. 1271-5.
6. Ventura, E., et al., Use of Uteroglobin for the Engineering of Polyvalent, Polyspecific Fusion Proteins. Journal of Biological Chemistry, 2009. 284(39): p. 26646-26654.

Poster Presentation

Disclosures: The authors have disclosed no financial interest.

316-Directed evolution of PD-L1 imaging agents by mRNA display

Presenter: Steven Millward, University of Texas MD Anderson Cancer Center

Steven W. Millward[1], Brian Grindel[1], Brian J. Engel[1], Justin Ong[2], Anupallavi Srinivasamani[1], Xiaowen Liang[1], Niki Zacharias Millward[3], Robert C. Bast[4], Michael Curran[5], Terry Takahashi[2], Richard Roberts

[1]*University of Texas MD Anderson Cancer Center, Houston, TX*
[2]*University of Southern California, Los Angeles, CA*
[3]*MD Anderson Cancer Center, Houston*
[4]*MD Anderson Cancer Center, Houston, TX*
[5]*University of Texas MD Anderson Cancer Center, Houston, Texas*

Purpose:
Although durable benefit has been demonstrated with anti-PD-L1 and anti-PD-1 therapies, only a subset of the total patient population responds these interventions. Heterogenous expression of PD-L1 across the tumor, immune, and stromal microenvironments argues for a non-invasive, quantitative, image-based process to evaluate the whole-body status of this receptor for diagnosis and treatment monitoring. There have been numerous efforts to image systemic PD-L1 expression through PET/CT. While radiolabeled anti-PD-L1 antibodies with picomolar target affinity have been developed, these take multiple days to achieve sufficient systemic clearance for high-resolution imaging[1]. In contrast, radiolabeled anti-PD-L1 peptides clear rapidly from circulation yet often lack sufficient affinity and/or specificity for high sensitivity imaging[2]. The triple helix affibody scaffold provides a favorable combination of potential affinity and clearance rate for imaging agent design. In this structured polypeptide, three α-helices assemble into a stable three-dimensional fold with a large binding surface defined by 13 surface-exposed amino acids[3]. These residues can be randomized (e.g. by phage display) to generate a library of affibodies which can be selected for target binding. However, the achievable complexity of phage display libraries (~10^{11} unique sequences) is significantly lower than the possible combinations of the 13 residues that define the affibody binding surface (~10^{17} possible sequences). In contrast, mRNA display[4] can achieve maximal library diversities greater than 10^{15} sequences, increasing the probability of obtaining true antibody-like affinity (< 100 picomolar). However, the affibody scaffold has yet to be adapted for implementation in mRNA display and affibodies have yet to find use as PD-L1 imaging agents.

Procedures:
We generated an mRNA display library in which the 13 residues comprising the affibody binding site were randomized. The resulting library underwent four rounds of selection against the human PD-L1 (hPD-L1) ectodomain followed by 3 rounds of selection against either human or mouse PD-L1 (mPD-L1) ectodomains. Off-rate selections were carried out to enhance the affinity of the final pool. Putative PD-L1 binding affibodies were screened by expressing each clone as a radiolabeled mRNA-Affibody fusion and measuring binding to immobilized hPD-L1 and mPD-L1. Dissociation constants for the highest affinity clones were measured by ELISA and surface plasmon resonance (SPR). Affibody binding to hPD-L1 and mPD-L1 on the surface of CHO cells was quantified by flow cytometry and blockade of the PD-L1:PD-1 signaling axis was measured by bioluminescence imaging (BLI) in a cell-based functional assay. Tumor uptake of the most promising Cy5-labeled PD-L1 affibody in a syngeneic mouse model of lymphoma was assessed by *in vivo* optical imaging.

Results:
mRNA Display selections against both hPD-L1 and mPD-L1 yielded multiple affibody sequences with affinity for both human and mouse isoforms. One clone from the dual-target selection, denoted M1, showed low nanomolar affinity against hPD-L1 and mPD-L1 by SPR and ELISA. Fluorescein-labeled M1 showed similar high-affinity binding against hPD-L1 and mPD-L1 on the surface of CHO cells and inhibited PD-L1:PD-1 signaling at single-digit micromolar concentrations in a cell-based BLI reporter assay. Binding of M1 to hPD-L1 was completely inhibited by atezolizumab confirming that its binding site overlaps that of PD-1. Cy5-labeled M1 showed hPD-L1 selective tumor uptake in the EL4 syngeneic mouse model of lymphoma.

Conclusions:
These results confirm the feasibility of evolving target-specific affibodies by mRNA Display and indicate that specificity for multiple isoforms can be achieved by dual-target selections. The resulting M1 affibody showed low nanomolar target affinity for hPD-L1 and mPD-L1 and could image PD-L1 expression in a fully immune-competent mouse model. These results demonstrate utility of the affibody scaffold in the context of mRNA display and indicate the potential for affibody-based PET imaging agents for the interrogation of PD-L1 expression.

Reference
1. Jagoda, E. M.; Vasalatiy, O.; Basuli, F.; Opina, A. C. L.; Williams, M. R.; Wong, K.; Lane, K. C.; Adler, S.; Ton, A. T.; Szajek, L. P.; Xu, B.; Butcher, D.; Edmondson, E. F.; Swenson, R. E.; Greiner, J.; Gulley, J.; Eary, J.; Choyke, P. L., Immuno-PET Imaging of the Programmed Cell Death-1 Ligand (PD-L1) Using a Zirconium-89 Labeled Therapeutic Antibody, Avelumab. Mol Imaging 2019, 18, 1536012119829986.
2. Kamalinia, G.; Engel, B. J.; Srinivasamani, A.; Grindel, B. J.; Ong, J. N.; Curran, M. A.; Takahashi, T. T.; Millward, S. W.; Roberts, R. W., mRNA Display Discovery of a Novel Programmed Death Ligand 1 (PD-L1) Binding Peptide (a Peptide Ligand for PD-L1). ACS Chem Biol 2020, 15 (6), 1630-1641.
3. Wikman, M.; Steffen, A. C.; Gunneriusson, E.; Tolmachev, V.; Adams, G. P.; Carlsson, J.; Stahl, S., Selection and characterization of HER2/neu-binding affibody ligands. Protein Eng Des Sel 2004, 17 (5), 455-62.
4. Kamalinia, G.; Grindel, B. J.; Takahashi, T. T.; Millward, S. W.; Roberts, R. W., Directing evolution of novel ligands by mRNA display. Chem Soc Rev 2021, 50 (16), 9055-9103.

Poster Presentation

Disclosures: The authors have disclosed no financial interest.

317-3Labeling Dendritic Cells with Magnetic Nanoparticles Tailored for Magnetic Particle Imaging

Presenter: Bo Yu, University of Florida

Bo Yu[1], N'Quel Bonner[1], Ginger Moore[1], Sitong Liu[2], Angelie Rivera-Rodriguez[3], Duane A. Mitchell[4], Carlos Rinaldi-Ramos[4]

[1]*University of Florida*
[2]*University of Florida, Gainesville, Florida*
[3]*Stanford University School of Medicine, Palo Alto, CA*
[4]*University of Florida, Gainesville, FL*

Immunotherapy has emerged as a safe and effective approach to treat some cancers because of reduced side effects, longer post-treatment protection, and potential to treat metastatic disease. Cell-based vaccines using dendritic cells (DCs) have proven to be a safe therapeutic approach although with inconsistent clinical results. DCs must migrate to lymphoid organs to be effective, and the magnitude of anti-tumor response is correlated to DC migration to lymph nodes. Therefore, non-invasive methods to monitor and quantify migration

of adoptive DC therapies would be tremendously helpful in evaluating immune response. Although techniques such as magnetic resonance imaging (MRI), single-photon emission computed tomography (SPECT), and positron emission tomography (PET) have previously been used to track DCs, these techniques are limited by low cell detection sensitivity in the range of 10^4 cells or more. Magnetic particle imaging (MPI) is a novel molecular imaging technology that can sensitively and quantitatively detect iron oxide magnetic tracers *in vivo*. MPI is non-invasive, tomographic and quantitative, has negligible background signal and no practical tissue penetration depth limitations. Compared to other imaging approaches, MPI can achieve higher cell sensitivity. Cell detection sensitivity in MPI is determined by two factors: the properties of tracer used to label cells and tracer uptake. We expect better MPI sensitivity with tracers developed for MPI and improved nanoparticle uptake by DCs. In this study, cellular uptake was evaluated using superparamagnetic iron oxide nanoparticle (SPION) tracers (RL-1) which are tailored for improved MPI sensitivity. Particles were coated with poly(maleic anhydride-*alt*-1-octadecene) (PMAO) to be water-soluble for cell labeling application. The arithmetic volume weighted mean hydrodynamic diameter and standard deviation values of RL-1 tracer were evaluated using dynamic light scattering, which is 79.3 ± 7.2 nm. The MPI maximum signal intensity values for the tracer is 100.9 $mgFe^{-1}$, while the corresponding value is 33.8 $mgFe^{-1}$ for ferucarbotran. The upper limit to label DCs using tracers without compromising viability or functionality was determined by screening SPION concentration and incubation time. Cells were co-incubated with tracers for 1, 2, 4 and 24 hours, while concentrations ranged from 10 – 200 µgFe/mL. Tracer uptake was quantified by MPI, particle intracellular internalization was evaluated by confocal microscopy. The optimal labeling condition was determined to be 50 µgFe/mL for 4 hours incubation, which provided cellular uptake ~ 50 pgFe/cell. Confocal images suggest particles are in vesicle-like structures inside cells. Cell dilution studies demonstrate detection of 10^3 cells with MPI using optimized labeling conditions and imaging under high sensitivity mode.

Poster Presentation

Disclosures: The authors have disclosed no financial interest.

318-MRI/MPI tracking of cerebral homing of intra-arterially injected mesenchymal stem cells

Presenter: Ali Shakeri-Zadeh, Johns Hopkins Univeristy

Ali Shakeri-Zadeh[1], Shreyas Kuddannaya[2], Adnan Bibic[3], Piotr Walczak[4], Jeff Bulte[5]

[1]Johns Hopkins Univeristy, Baltimore
[2]Johns Hopkins University School of Medicine, Baltimore, MD
[3]Kennedy Krieger Institute, Baltimore
[4]University of Maryland, Baltimore, Baltimore, MD
[5]Johns Hopkins University School of Medicine, Baltimore

Introduction:
Several pre-clinical and clinical investigations have shown that stem cell therapy for the central nervous system is a potential strategy for treating a variety of diseases. Intra-arterial (IA) injection into the carotid artery is an appealing delivery route because it avoids initial uptake by systemic organs, allowing large numbers of cells to be delivered directly to the brain (1). Information on the effectiveness of this procedure and the amount of delivered cells is highly desirable for further optimization. In this study, we used magnetic particle imaging (MPI) combined with magnetic resonance imaging (MRI) to track human mesenchymal stem cells (hMSCs) labeled with superparamagnetic (SPIO) nanoparticles *in vivo* (2, 3).

Methods:
Bone marrow-derived hMSCs were magnetically labeled with poly-L-lysine as transfection agent and Resovist® (25 µg Fe/ml). Labeled cells were collected for IA injection into immunodeficient male Rag2 mice (4). Prussian blue staining and a Ferrozine-based spectrophotometric assay were used to assess intracellular iron uptake. Labeled cells were delivered into the brain using 4 separate injections (30,000 cells each) with a time interval of 6 min between each injection (Figure 1A). Whole body 2D MPI was performed before and after each injection using a Magnetic Insight Momentum scanner. Animals were then sacrificed and the heads were imaged *ex vivo* with MRI using a 17.4T vertical bore Bruker Biospec scanner and then with MPI. MR images were acquired using a FLASH sequence with TR=8.4 ms, TE=2.5 ms, NEX=16, FA=5 deg, resolution=0.1 mm, slice thickness= 18 mm, matrix size=150x300x180, and FOV=3x2x1.8 cm. Heads were scanned with MPI using the same FOV as MRI with 55 projections, 3D high resolution mode, and one scan per projection.

Results:
Peri-nuclear accumulation of SPIOs in labeled hMSCs was confirmed (Figure 1B). An amount of 25 pg Fe per cell was measured with a Ferrozine assay. Figure 1C shows representative individual and overlay images of the *ex vivo* MRI and MPI datasets, where a unilateral distribution of labeled hMSCs at the side of IA injection can be seen. Figure 1D shows *in vivo* MP images of a mouse before and after IA injection, where hot spots in brain and lung as well as signal intensity alterations over time are present.

Conclusions:
This successful example MRI/MPI application of *in vivo* tracking of hMSCs may encourage further use of this technique to probe the fate of therapeutic cells after transplantation.

Reference
1. B. Rodríguez-Frutos, et al., Stem cell therapy and administration routes after stroke, Translational stroke research. 2016; 7(5):378.
2. J.W.M. Bulte, Superparamagnetic iron oxides as MPI tracers: A primer and review of early applications. Advanced Drug Delivery Reviews. 2019; 138:293.
3. J.W.M. Bulte, et al., Quantitative "hot-spot" imaging of transplanted stem cells using superparamagnetic tracers and magnetic particle imaging. Tomography. 2015;1(2):91.
4. C. Chu, et al., Hyperosmolar blood–brain barrier opening using intra-arterial injection of hyperosmotic mannitol in mice under real-time MRI guidance. Nature Protocols. 2022; 17, 76.

Poster Presentation

Disclosures: The authors have disclosed no financial interest.

319-PSMA-Targeted Gold Nanoparticles for Photodynamic Therapy of Prostate Cancer in Canine Prostate Cancer Model

Presenter: Xinning Wang, Case Western Reserve University

Xinning Wang[1], Dong Luo[2], Ramamurthy Gopalakrishnan[3], Ethan Walker[3], Thomas Rosol[4], Michael F. Tweedle[5], James Basilion[3]

[1]Case Western Reserve University, Beachwood, OH
[2]Case Western Reserve University, Cleveland, Ohio
[3]Case Western Reserve University, Cleveland, OH
[4]Ohio University, [5]Ohio State University, Columbus, Ohio

Prostate cancer is the most prevalent cancer among men in the United States[1]. Although surgeons are experienced with this disease, radical prostatectomy remains an imperfect intervention. Local and metastatic relapses often occur following surgery of the primary tumor as a result of microscopic tumor deposits left behind[2]. New therapies are needed for the treatment of prostate cancer. Photodynamic therapy (PDT) has been used as a minimally invasive therapy for the treatment of many cancers. A major concern with PDT is off-target tissue accumulation and activation of photosensitizer leading to cell death in normal tissue. Nanoparticles offer great opportunities for precision medicine. Prostate-specific membrane antigen (PSMA) is a unique membrane-bound biomarker which is overexpressed in prostate cancer and neovasculature of many solid tumors[4]. We have developed PSMA-targeted theranostic gold nanoparticles (PSMA-1-AuNPs-Pc158) to selectively deliver the photosensitizer Pc158 to PSMA-expressing cancer cells[5]. While excellent results have been achieved in mouse models, the mouse models are limited to predict therapeutic efficacy and collateral damage to tissues surrounding the prostate because of the small size of the gland. Dogs are ideal large animal models because of their similar anatomy to human and the fact that they are the only laboratory animals that develop prostate cancer similar to men. The objective of this study is to further assess the utility of PSMA-1-AuNPs-Pc158 for surgery and local ablation of prostate tumors using an orthotopic dog prostate cancer model. Immunocompromised dogs were orthotopically injected with 1 million canine prostate cancer cells modified to express human PSMA (Ace1-hPSMA cells) under ultrasound guidance to form tumors within the prostate gland. When the tumors reached appropriate size, dogs received PSMA-1-AuNPs-Pc158 at the dose of 0.1 mg/kg through i.v. injection. The dogs underwent surgery to expose the prostate at 24-hour post injection. The prostates were imaged using a Curadel fluorescence imaging device. Ace1-hPSMA prostate tumors showed bright fluorescent signal, while normal prostate tissue showed minimal fluorescent signal. After imaging, half of the tumor and a small area of normal prostate adjacent to the tumor were exposed to 150 J/cm2 of 672 nm light for PDT treatment, while the remaining tumor and prostate were covered with opaque paper. After PDT, the prostate was imaged again. It was found that fluorescence in the treated area was photobleached, indicating the activation of PSMA-1-AuNPs-Pc158. In contrast, the fluorescence signal in the un-irradiated area remained the same intensity. Two hours after PDT, the dog was euthanized and the prostate was removed for ex vivo imaging. Ex vivo imaging results were consistent with in vivo imaging results: fluorescent signal was only observed in the un-irradiated tumor, while the irradiated area and non-irradiated normal prostate didn't show any fluorescence. Histopathological analysis of the tumor and adjacent prostate showed that in the treated tumor area there was necrosis of the outer region of the tumor cells with additional hemorrhage and acute inflammation. The necrosis extended from 2-4 mm deep. The histology revealed evidence of a treatment effect that included necrosis, hemorrhage, secondary inflammation, and occasionally focal thrombosis in the tumor capsule. Mononuclear inflammation around tumors was consistent with a mild immune reaction from the dog. There was no effect of PDT treatment on the adjacent normal prostate tissue. In summary, our results indicated that the PSMA-targeted PSMA-1-AuNPs-Pc158 can be systemically administered and then selectively accumulate in PSMA-expressing canine orthotopic prostate tumors, but not in normal prostate tissues. Furthermore, PDT of prostate tumor within the gland can be performed without destroying surrounding necessary tissues. PSMA-1-AuNPs-Pc158 have the potential to be used for fluorescence image guided surgery and photo ablation of prostate cancer. Acknowledgements: This research was supported by the National

Reference

1. Siegel, R. L.; Miller, K. D.; Fuchs, H. E.; Jemal, A. Cancer Statistics, 2021., Ca-Cancer J. Clin. 2021, 71, 7-33.
2. Wang, X.; Huang, S. S.; Heston, W. D.; Guo, H.; Wang, B. C.; Basilion, J. P. Development of Targeted Near-Infrared Imaging Agents for Prostate Cancer. Mol. Cancer Ther. 2014, 13, 2595-2606.
3. Van Straten, D.; Mashayekhi, V.; de Bruijn, H. S.; Oliveira, S.; Robinson, D. J. Oncologic Photodynamic Therapy: Basic Principles, Current Clinical Status and Future Directions. Cancers, 2017, 9, 19.
4. Wang, X.; Ramamurthy, G.; Shirke, A. A.; Walker, E.; Mangadlao, J.; Wang, Z.; Wang, Y.; Shan, L.; Schluchter, M. D.; Dong, Z.; Brady-Kalnay, S. M.; Walker, N. K.; Gargesha, M.; MacLennan, G.; Luo, D.; Sun, R.; Scott, B.; Roy, D.; Li, J.; Basilion, J. P. Photodynamic Therapy Is an Effective Adjuvant Therapy for Image-Guided Surgery in Prostate Cancer. Cancer Res. 2020, 80, 156-162.
5. Dong, L.; XinnWang, X.; Walker, E.; Wang, J.; Springer, S.; Lou, J.; Ramamurthy, G.; Burda, C.; Basilion, J. Nanoparticle Yield Increased Drug Uptake and Therapeutic Efficacy Upon Sequential Near-Infrared Irradiation. ACS Nano, 2020, 14, 15193-15203.

Poster Presentation

Disclosures: The authors have disclosed no financial interest.

320-Immunofluorescence specific measurement of differentiation by Cell Profiler software: A new approach to analysis of macrophage/microglia polarization

Presenter: Arpan Mahanty, Hong Kong Polytechnic University

Arpan Mahanty[1], In Young Oh[2], Ka Wing Wan[3], Jung Sun Yoo[2]

[1]Hong Kong Polytechnic University, Hung Hom, Hong Kong
[2]Hong Kong Polytechnic University, Hung Hom, Kowloon, Hong Kong SAR
[3]Hong Kong Polytechnic University, Hung Hom, Kowloon, Hong Kong

The manual process for image recognition and tracking in cell biology is a common and traditional way for ROI based quantification, though it always consumes a lot of time and effort. Even the results have a significant chance to be variant from expert to expert. As the regular strategy for ImageJ based identification is not convenient from the aspect of user's comfort for handling such a huge data. So, for a long decade image scientists are trying to use the various automation platform for image data analysis. Herein, we have represented a Cell profiler software (CPS) based automatic methods for analysis of macrophage and microglial differentiation based on their polarization state. Though, it has been earlier verified that CPS can firmly delineate cell components, biomolecules, and receptor's locations. The current results implied that using CPS can identify objects and analyse quantitatively to distinguish proinflammatory and anti-inflammatory polarizing state of BMDM and murine microglia BV2 cell line. The hypothesis has been reported and established that a single immune cell can polarized to make inflammatory (M1) response reciprocally it can exhibit as anti-inflammatory (M2) polarized form with characterized response. Our present data from constructed pipeline indicate that a

clear detection and differentiation can made from general macrophage and microglia markers labelled image, also from polarization markers CD86 and CD206. Based on database searching and knowledge, this is the earliest study report for CPS based immune cells identification and cytokine-based optimization and quantification. As we reported the increased concentration of inflammatory cytokines (IFN-γ) can leads a differentiation in between inflammatory states with changed morphology and antibody intensity. The CPL based automated pipeline could perform a clear differentiation of interchanging cytokine response of M1 like cells which could corelate AD/PD response based on neuroinflammation condition. On the other hand, considering to cancer dilemma, immune cells act a vital task for prognosis (M2) and suppression (M1). Immunotherapy and immunomodulation in cancer is a hot topic and optimistic scope for cancer therapy and diagnostics. Identification, quantification of TAM and immune modulation through inhibition could be done depending on phenotyping of immune cells. The automation pipeline can be effortlessly acclimated to differentiate polarization state of macrophage and microglias based of their surface and subcellular localization of markers. Our present data from constructed pipeline indicate that a clear detection and differentiation can made from general macrophage and microglia markers labelled image, also from polarization markers CD86 and CD206. Based on database searching and knowledge, this is the earliest study report for CPS based immune cells identification and cytokine-based optimization and quantification. The future research will be needed to illustrate influential differentiation of different cytokines and polarization hitching nature immune cells. Our present finding is approached to be a supportive tool for polarized immune cells identification and their immune response prediction.

Reference

1. Hattori, A., et al., A new approach to analysis of intracellular proteins and subcellular localization using cellprofiler and imageJ in combination. Methods, 2021.
2. Sanz, G., et al., Muscle2View, a CellProfiler pipeline for detection of the capillary-to-muscle fiber interface and high-content quantification of fiber type-specific histology. J Appl Physiol (1985), 2019. 127(6): p. 1698-1709.
3. Ardeshir, R.A., et al., Measurement of DNA damage by CellProfiler software in the liver of Caspian white fish exposed to environmental concentrations of fipronil. Computational Toxicology, 2019. 12.
4. Tollemar, V., et al., Quantitative chromogenic immunohistochemical image analysis in cellprofiler software. Cytometry A, 2018. 93(10): p. 1051-1059.
5. Bray, M.A., M.S. Vokes, and A.E. Carpenter, Using CellProfiler for Automatic Identification and Measurement of Biological Objects in Images. Curr Protoc Mol Biol, 2015. 109: p. 14 17 1-14 17 13.
6. Bray, M.A. and A.E. Carpenter, CellProfiler Tracer: exploring and validating high-throughput, time-lapse microscopy image data. BMC Bioinformatics, 2015. 16: p. 368.
7. Jones, T.R., et al., CellProfiler Analyst: data exploration and analysis software for complex image-based screens. BMC Bioinformatics, 2008. 9: p. 482.
8. Carpenter, A.E., et al., CellProfiler: image analysis software for identifying and quantifying cell phenotypes. Genome Biol, 2006. 7(10): p. R100.

Poster Presentation

Disclosures: The authors have disclosed no financial interest.

321-A quantitative assessment of perfusion of the gastric conduit after esophagectomy using near-infrared fluorescence with indocyanine green

Presenter: Robin Faber, Leiden University Medical Center

Robin A. Faber[1], Hidde Galema[2], Floris Tange[3], Wobbe de Steur[4], Henk Hartgrink[5], Sjoerd Lagarde[2], Pieter van der Sluis[6], Bas Wijnhoven[6], Sven Mieog[7], Cornelis Verhoef[2], Alexander Vahrmeijer, Stijn Keereweer[2], Merlijn Hutteman[2], Denise Hilling[8], Joost Van Der Vorst[9]

[1]*Leiden University Medical Center, Leiden, Zuid-Holland, Netherlands*
[2]*Erasmus Medical Center, Rotterdam, Zuid-Holland, Netherlands*
[3]*Leiden University Medical Center, Netherlands*
[4]*Leiden University Medical Center, Leiden, Netherlands*
[5]*Leiden University Medical Center (LUMC), Leiden, Zuid-Holland, Netherlands*
[6]*Erasmus Medical Center, Rotterdam, Netherlands*
[7]*Leiden University Medical Center (LUMC), leiden, z-h, Netherlands*
[8]*Leiden University Medical Center (LUMC), Leiden, Nederland, Netherlands*
[9]*Leiden University Medical Center (LUMC)*

Introduction:

Anastomotic leakage (AL) can be a severe complication of esophagectomy with gastric conduit reconstruction and occurs in 4 to 30% of patients (1, 2). Poor perfusion of the gastric conduit is a likely an important risk factor for AL. Intraoperative assessment of perfusion of the gastric conduit with near infrared (NIR) ICG-fluorescence angiography (ICG-FA) may help in reducing AL rates but strong scientific evidence is lacking. This may be due to the subjective interpretation of the fluorescence signal, which solely depends on the 'in real-time' interpretation of the surgeon (3). Quantitative NIR ICG-FA can objectively measure the fluorescence signal. This study aims to perform quantitative ICG-FA on gastric conduit reconstructions and to assess perfusion patterns of the gastric conduit.

Methods:

In this prospective study, 20 patients undergoing esophagectomy with gastric conduit reconstruction were included. Before creating the anastomosis, a standardized NIR ICG-FA video of the complete gastric conduit was recorded with the Quest Spectrum V2 fluorescence camera (Quest Medical Imaging, Middenmeer, The Netherlands). Postoperatively, the videos were quantified by plotting time-intensity curves from contiguous regions of interest (ROIs) on the whole gastric conduit (4). The following nine perfusion parameters were extracted from the ROIs: time to max, Imax, ingress rate, max ingress slope, normalized ingress slope, maximum egress slope, and the area under the curve (AUC) 30, 60, and 120 seconds after the peak intensity. Primary outcomes were the time-intensity curves and perfusion parameters of the ROIs. Secondary outcomes were the inter-observer agreement of the subjective interpretation of the ICG-FA videos between the surgeons and the occurrence of anastomotic leakage.

Results:

Based on a total of 424 curves, three distinct perfusion patterns were recognized: pattern 1 (steep inflow and steep outflow); pattern 2 (steep inflow, no/minor outflow); and pattern 3 (slow inflow, no outflow). All curves were categorized in 3 patterns according to the max egress and the time to max. Figure 1A shows the average time-intensity curves of the three perfusion patterns. All perfusion parameters were significantly different between the perfusion patterns. The inter-observer agreement of the subjective ICG-FA video interpretation between the

surgeons was poor (intraclass correlation coefficient (ICC): 0.345). Figure 1B shows all curves from ROIs on the anastomoses stratified by anastomotic leakage. ROIs of locations with anastomotic leakage (n=4) had significant lower median Imax (47.17 vs. 97.69, p=0.007) and max ingress slope (2.34 vs. 7.58, p=0.049) compared to ROIs of locations without leakage.

Discussion:

This is the first study to describe three distinct perfusion patterns of the complete gastric conduit after esophagectomy. The presence of a specific perfusion pattern on the location of the anastomosis possibly has clinical predictive value on AL, but this is yet unclear and should be further evaluated. The poor inter observer agreement of the subjective analysis of the ICG-FA videos between the surgeons underlines the need for quantification of ICG-FA assessment of the gastric conduit.

Reference

1. Voeten DM, Busweiler LAD, van der Werf LR, Wijnhoven BPL, Verhoeven RHA, van Sandick JW, et al. Outcomes of Esophagogastric Cancer Surgery During Eight Years of Surgical Auditing by the Dutch Upper Gastrointestinal Cancer Audit (DUCA). Ann Surg. 2021;274(5):866-73.
2. de Steur WO, Hutteman M, Hartgrink HH. Generalizability of the Results and Concerns About Leakage Rates of the ICAN Trial. JAMA Surg. 2022;157(2):176.
3. Hardy NP, Joosten JJ, Dalli J, Hompes R, Cahill RA, van Berge Henegouwen MI. Evaluation of inter-user variability in indocyanine green fluorescence angiography to assess gastric conduit perfusion in esophageal cancer surgery. Dis Esophagus. 2022.
4. Van Den Hoven P, Goncalves LN, Quax PHA, Van Rijswijk CSP, Van Schaik J, Schepers A, et al. Perfusion Patterns in Patients with Chronic Limb-Threatening Ischemia versus Control Patients Using Near-Infrared Fluorescence Imaging with Indocyanine Green. Biomedicines. 2021;9(10).

Poster Presentation

Disclosures: The authors have disclosed no financial interest.

322-Diazaborine-Based Probes for Selective Peroxynitrite Imaging in Live Cells

Presenter: Dylan Domaille, Colorado School of Mines

Dylan Domaille

Colorado School of Mines, Golden, CO

Reactive oxygen species (ROS) and reactive nitrogen species (RNS) play important roles in inflammation initiation and resolution.(1) While molecular probes for tracking cellular ROS and RNS have been pivotal tools to track these species in cells, commonly used arylboronate/arylboronic-acid based probes struggle to discriminate between two key ROS/RNS: H_2O_2 and peroxynitrite ($ONOO^-$).(2) We hypothesized that the ROS/RNS selectivity of arylboronic acid-based probes could be tuned with neighboring effects. Here, we present a physical organic study that shows cyclization of arylboronic acids to diazaborines (DABs) slows the rate of H_2O_2-mediated oxidation by more than 3,000-fold. However, the cyclized diazaborines oxidize immediately upon addition of peroxynitrite. Thus, DABs enhance kinetic discrimination between H_2O_2 and $ONOO^-$. These results prompted the pursuit of diazaborine-based peroxynitrite imaging probes for chemoselective peroxynitrite detection in live macrophages. We anticipate these results will motivate the development of new DAB-based imaging and chemical biology tools for peroxynitrite-specific applications.

Reference

1. Kvietys PR, Granger DN. Role of reactive oxygen and nitrogen species in the vascular responses to inflammation. Free Radic Biol Med. 2012;52(3):556-592. doi:10.1016/j.freeradbiomed.2011.11.002
2. Zielonka J, Sikora A, Hardy M, Joseph J, Dranka BP, Kalyanaraman B. Boronate probes as diagnostic tools for real time monitoring of peroxynitrite and hydroperoxides. Chem Res Toxicol. 2012;25(9):1793-1799. doi:10.1021/tx300164j

Poster Presentation

Disclosures: The authors have disclosed no financial interest.

323-Cephalofurimazine (CFz): A Brain Permeable Bioluminescent Substrate for NanoLuc based Antares

Presenter: Thomas Kirkland, Promega

Thomas A. Kirkland[1], Joel R. Walker[2], Yichi Su[3], Mary P. Hall[1], Xiang Wu[4], Kerriann Casey[5], Guosong Hong[4], Michael Lin[3]

[1]*Promega, Madison, WI*
[2]*Promega, San Luis Obispo, CA*
[3]*Stanford University, Stanford, CA*
[4]*Stanford University, Palo Alto, CA*
[5]*Stanford University School of Medicine, Stanford, CA*

Non-invasive imaging methods for tracking gene expression, cell growth and migration and other biological events in vivo are indispensable tools for biomedical studies. Bioluminescence imaging (BLI) can achieve sensitive detection with low background *in vivo*, which is desirable for body imaging of small animals. Yet, BLI in the central nervous system (CNS) is challenging because many luciferase substrates show limited permeability of the blood-brain-barrier (BBB). For example, outside of the brain, the Antares reporter, a fusion of the luciferase NanoLuc to the orange fluorescent protein CyOFP, enables highly sensitive bioluminescence imaging when coupled with the substrate fluorofurimazine (FFz). However, FFz suffers from low BBB permeation, limiting its applicability for brain imaging. Here we report the discovery of a new brain-permeant NanoLuc substrate, cephalofurimazine (CFz). CFz paired with Antares produces an order of magnitude more signal from the brain than the standard combination of D-luciferin with firefly luciferase, and matches the peak output of AkaLumine with AkaLuc. The CFz-Antares system will be a powerful imaging tool for preclinical animal models of CNS diseases and could allow for sensitive two-population imaging in the brain when used together with AkaLuc-AkaLumine.

Reference

1. Chu, J., et al. (2016). "A bright cyan-excitable orange fluorescent protein facilitates dual-emission microscopy and enhances bioluminescence imaging in vivo." Nat Biotech 34: 760-767.
2. Su, Y. et al. (2020) "Novel NanoLuc substrates enable bright bioluminescence imaging in animals." Nat Methods 17, 852–860 (2020).

Poster Presentation

Disclosures: The authors have disclosed no financial interest.

324-Quantification of whole-body [18F]AS2471907 PET imaging to assess 11β hydroxysteroid dehydrogenase type 1 enzyme levels in a Zucker Fatty rat model

Presenter: Jason Bini, Yale University School of Medicine

Jason Bini[1], Michael Kapinos[2], Mike (MingQiang) M. Wenn (Zheng)[3], Jordan Strober[4], Kristin Koehl-Carabetta[5], Songye Li[6], Keunpoong Lim[4], Paul R. Emery[6], Jim Ropchan[3], Nabeel Nabulsi[4], Ania Jastreboff[4], Yiyun H. Huang[3], Daniel Vatner[4], Richard E. Carson[3]

[1]Yale University School of Medicine, New Haven
[2]michael.kapinos@yale.edu, New Haven, CT
[3]Yale University, New Haven, CT
[4]Yale School of Medicine
[5]Yale School of Medicine, New Haven, Connecticut
[6]Yale School of Medicine, New Haven, CT

Objectives:
The intracellular enzyme 11β-hydroxysteroid dehydrogenase type 1 (11β-HSD1) catalyzes the conversion of inactive cortisone (11-dehydrocorticosterone in rodents) to active cortisol (corticosterone). [^{18}F]AS2471907 has been used to quantify *in vivo* levels of 11β-HSD1 in brain(1,2,3), liver(3,4) and adipose tissue (AT)(3) in humans and rats. Dysregulation of glucocorticoid action at the tissue level is thought to be a part of the pathophysiology of metabolic diseases. The amount of 11β-HSD1 in tissues, including the liver, brain and adipose tissue, may be a key to understanding obesity and fatty liver disease pathophysiology. As such, a careful characterization of [^{18}F]AS2471907 in an animal model of obesity is needed. With this in mind, we performed PET imaging studies to examine 11β-HSD1 levels in liver, brain, and AT of lean Zucker Fatty (ZF) rats.

Methods:
Four (2M/2F) lean ZF rats (weight 260 ± 80 g; Charles River; Strain 186) were assessed. Rats were injected with [^{18}F]AS2471907 via tail vein (mean ± SD injected dose: 12.6 ± 7.6 MBq; mass: 0.10 ± 0.12 µg). Listmode PET data were acquired for 60 min on the Inveon microPET/CT scanner. At the end of the PET scan, blood was drawn for radioligand metabolite analysis via HPLC, and after sacrifice, the liver was removed for immunoblotting. PET image reconstructions were performed with 3D-OSEM-MAP. An image-derived input function (IDIF) was obtained from a ROI drawn on the abdominal aorta (AA) during early time frames (0-30 s) and was not corrected for partial volume effects. Liver, brain, and AT ROIs were drawn on summed images from 20-50 min and TACs were generated. Volume of distribution (V_T, mL/cm^3) was calculated using the Logan graphical approach (t*=40min) using the AA TAC as the IDIF (Logan IF). Standardized uptake values (SUV) and SUVR (ref region AA) were also calculated. An additional cohort of lean ZF rats (2M/2F; 286 ± 79 g) were injected (15.5 ± 3.6 MBq; mass: 0.11 ± 0.03 µg) to measure liver tissue metabolites. Each rat was sacrificed (n=2 30 min; n=2 60 min) and the liver removed and homogenized for radiolabeled liver tissue metabolite analysis via HPLC.

Results:
A representative SUV PET image (30-60 min) demonstrates high uptake in the liver with moderate uptake in the intrascapular AT and brain (**Fig 1A**). Representative coronal **(Fig 1B)** and axial **(Fig 1C)** SUV PET images (0-30 sec) demonstrate the AA IDIF. Representative time activity curves for AA, liver, AT and brain (**Fig 1D**). HPLC analysis of [^{18}F]AS2471907 demonstrated a mean intact parent fraction of 89% in whole blood at 60 min post injection. Logan IF, SUV and SUVR (ref: AA) quantitative values were measured in liver, AT, and brain (**Table 1**). Liver tissue metabolites were <3% at 30 min and <10% at 60 min post injection. Liver Logan IF values correlated well with 11β-HSD1 protein levels (R^2=0.62), as measured by western blot analysis. Semiquantitative measures of liver SUVR and SUV correlated with Logan IF (SUVR: R^2=0.99; SUV: R^2=0.66).

Conclusions:
These preliminary results suggest that SUV PET images 40-60 min after injection are a suitable quantitative measure in this rodent model of obesity. This is possible given the nature of [^{18}F]AS2471907, which has minimal metabolites in blood and liver tissue allowing use of semi-quantitative measures that correlate well with *ex vivo* protein levels in the liver. Confirmatory studies are in progress in our laboratory.

Reference

1. Bhatt, JCBFM, 2019;
2. Bini, Mol Imaging and Biol, 2020;
3. Bini, IEEE TRPMS, 2021;
4. Bini, SNMMI Annual Meeting, 2020

Poster Presentation

Disclosures: The authors have disclosed no financial interest.

325-A 25 mT Preclinical Electron Paramagnetic Resonance Oxygen Imager and Its Applications to Biomedical Studies

Presenter: Mrignaayni Kotecha, O2M Technologies, LLC

Mrignaayni Kotecha[1], Boris Epel[2]

[1]O2M Technologies, LLC

[2]University of Chicago, Chicago, IL

Oxygen is an important fundamental physiological parameter affecting all aspects of living being. In tumors, hypoxia is one of the most important factors that impact tumor growth, development, aggressiveness, metastasis, and treatment outcome. In tissue engineering and regenerative medicine (TERM), oxygen affects survivability and functionality of artificial tissue grafts and cell encapsulation devices. In type I diabetes, the lack of oxygen to metabolically active islet cells is considered the major roadblock in developing functional islet replacement devices. Therefore, the biomedical field needs a noninvasive unambiguous oxygen imager that can provide three-dimensional maps of partial oxygen pressure (pO_2) in tissues. We report the first commercial preclinical oxygen imager, JIVA-25™, based on electron paramagnetic resonance oxygen imaging (EPROI). EPROI is a non-invasive oxygen mapping method with high precision and absolute accuracy. EPR detects unpaired electron spins subjected to the constant uniform magnetic field by manipulating them using radio-frequency electromagnetic radiation. EPROI uses the relaxation of an injectable non-toxic soluble contrast agent, trityl (OX063 or its deuterated counterpart OX071), for obtaining oxygen maps in tissues. EPROI was used recently for the first successful demonstration of oxygen-guided radiation therapy in a mouse model of tumor (1). JIVA-25™ has been used in studies related to cancer, tissue engineering, and T1D (2-5).

JIVA-25™ is a compact 25 mT EPROI instrument suitable for *in vitro* and small animal *in vivo* (mice) oxygen mapping. JIVA-25™ provides pO_2 maps with a high spatial resolution (up to 0.25 mm *in vitro* or 1 mm *in vivo*), high pO_2 resolution (~1 torr in hypoxic conditions, ~3-5 torr in hyperoxic conditions), and high temporal resolution (1-10 min). An intuitive software, OxyVue™, makes image acquisition, processing, and visualization easy for a new user to adapt. JIVA-25™ has two leading oxygen imaging modalities, inversion recovery electron spin-echo (IRESE) and single point imaging (SPI). Several vertical and horizontal resonators to fit various samples sizes have been developed. JIVA-25™ is fitted with an animal temperature control and respiratory monitor. Overall, we expect that JIVA-25™ will be a unique tool in helping scientists to understand and develop better therapies in cancer, TERM, and T1D.

Reference

1. Epel B, Maggio MC, Barth ED, Miller RC, Pelizzari CA, Krzykawska-Serda M, Sundramoorthy SV, Aydogan B, Weichselbaum RR, Tormyshev VM, Halpern HJ. Oxygen-guided radiation therapy. Int J Radiat Oncol Biol Phys. 2019;103(4):977-84. doi: 10.1016/j.ijrobp.2018.10.041. PubMed PMID: 30414912.
2. Wang L-H, Ernst AU, An D, Datta AK, Epel B, Kotecha M, Ma M. A bioinspired scaffold for rapid oxygenation of cell encapsulation systems. Nat Commun. 2021;12(1):5846. doi: 10.1038/s41467-021-26126-w.
3. Wang L-H, Ernst AU, Flanders JA, Liu W, Wang X, Datta A, Epel B, Kotecha M, Papas K, Ma M. An inverse-breathing encapsulation system for cell delivery. Science Advances. 2021;7:eabd5835.
4. Magana A, Giovanni R, Essien E, Epel B, Kotecha M, Liu S, Mathew MT, Hagarty SE, Bijukumar D. Amniotic growth factors enhanced human adipocyte cell viability and differentiation under hypoxia Journal of Biomedical Materials Research: Part B - Applied Biomaterials. 2022, in press.
5. Viswakarma N, Siddiqui E, Patel S, Hammed S, Schreiber W, Swartz HM, Kotecha M. In Vivo pO2 Assessment in Subcutaneous and Intraperitoneal sites Using Imaging of Solid Oxygen Probe. Tissue Engineering Part C: Methods. 2022;0(ja):null. doi: 10.1089/ten.TEC.2022.0061. PubMed PMID: 35509263.

Poster Presentation

Disclosures: The authors have disclosed no financial interest.

326-Photodynamic Priming and Low Intensity Focused Ultrasound for improving the diagnostic accuracy of monoclonal antibodies in head and neck tumors

Presenter: Chanda Bhandari, University of Texas at Dallas

Chanda Bhandari[1], John Fakhry[2], Ryan Margolis[3], Mawia Khairalseed[3], Junjie Li[4], Kim Samkoe[5], Tayyaba Hasan[6], Kenneth Hoyt[7], Girgis Obaid[1]

[1]*University of Texas at Dallas, Richardson*
[2]*University of Texas at Dallas, Richardson, Texas*
[3]*University of Texas at Dallas*
[4]*University of Texas at Dallas, Allen, TX*
[5]*Dartmouth College, Hanover, NH*
[6]*Massachusetts General Hospital*
[7]*University of Texas at Dallas, Richardson, TX*

Head and neck cancer is the 6th common cancer worldwide and surgical resection is the primary treatment intervention. The current standard of care for surgical resection of the tumor is either surgery based on preoperative imaging or white light-based image guided surgery. However, the ability of these strategies to correctly identify the tumor margin is limited leading to the tumor recurrence in more than 35% of the patients. Recently, the use of fluorescently labeled antibodies that target the surface receptors overexpressed on cancer cells has been found to be promising for effectively assessing the surgical margin due to their ability to specifically localize to tumor regions. However, the long time interval, typically 2-5 days, that the patients have to wait for surgical debulking after the probe is administered is a limitation of this strategy. Sub-therapeutic doses of photodynamic therapy (PDT), also known as Photodynamic Priming (PDP) has the ability to modulate the tumor microenvironment. So, in this study we have shown that PDP increases the diagnostic accuracy (264.2% improvement), fractional tumor coverage (49.5% improvement) and overall tumor delivery (138.6% improvement) of Cetuximab-IRDye800 CW (Cet-IRDye800) that targets EGFR receptors in orthotopic FaDu head and neck tumors. Moreover, Low Intensity Focused Ultrasound (LIUS) was found to synergize with PDP to augment the delivery of IRDye800 conjugate of aPD-L1 antibody (an immune checkpoint inhibitor) into syngeneic head and neck tumors by 300.9%. Thus, PDP, when combined with LIUS, has the potential to synergistically improve the delivery of immune checkpoint antibodies by overcoming the limitations of vascular and stromal barriers in solid tumors.

Reference

1. Obaid, Girgis, et al. "Activatable clinical fluorophore-quencher antibody pairs as dual molecular probes for the enhanced specificity of image-guided surgery." Journal of biomedical optics 22.12 (2017): 121607.
2. Rosenthal, Eben L., et al. "Safety and tumor specificity of cetuximab-IRDye800 for surgical navigation in head and neck cancer." Clinical Cancer Research 21.16 (2015): 3658-3666.

Poster Presentation

Disclosures: The authors have disclosed no financial interest.

327-E7-specific affibody for HPV-positive Head and Neck Cancer

Presenter: Sheryl Roberts, Wayne State University School of Medicine

Sheryl Roberts[1], Cien Huang[2], Dauren Adilbay[3], Delissa Johnson[4], Tara D. Viray[5], Thomas Reiner[6], NagaVaraKishore Pillarsetty[3]

[1]*Wayne State University School of Medicine, Detroit, MI*
[2]*Hunter College, New York, New York*
[3]*Memorial Sloan Kettering Cancer Center, New York, NY*
[4]*Memorial Sloan Kettering Cancer Center, Brooklyn, New York*
[5]*Memorial Sloan Kettering Cancer Center, North Brunswick, NJ*
[6]*Novartis, Switzerland*

Objectives:

Cancers associated with the human papillomavirus (HPV), including oropharyngeal, anal canal, cervical, and vulvar carcinomas are responsible for 5% of all cancers[1]. HPV-positive patients have much better prognosis and treatment responses than HPV-negative patients[2]. HPV derived E7/E6 are drivers of malignancy and expression exists in patient with head and neck squamous-cell carcinomas of (HNSCC)[3]. HPV16/18 subtypes are high-risk, detected in 26% of all HNSCC.

Hence, oncogene E7/E6 with HPV16/18 subtypes is a valuable biomarker for non-invasive imaging and potential therapy. Here, we introduce a novel E7-specific affibody (HPV16 E7-affibody) for the fluorescent imaging of HPV-positive HNSCC.

Methods:
To synthesize the appropriate targeted affibody optimized from a phase display screening and its corresponding wild-type[4], we cloned the genes into pET21b(+) plasmid, transformed, expressed and purified the recombinant protein using bacterial expression system with excellent yields of ~50 mg/L of culture. To develop biomarker probes, we synthesized four fluorescently labeled affibodies, namely Z_{wt}-Cy7.5 and Z_{wt}-IR800CW and HPV16 E7-Cy7.5 and HPV16 E7-IR800CW. HPLC and mass spectrometric methods were used to assess purity and identity of the conjugates. In vivo studies were conducted in HPV+ and HPV- HNSCC cell lines.

Results:
Peptide purity was confirmed with HPLC (>99%). HPLC/electrospray ionization/MS confirmed the identity of all NIR affibodies generated and gave mass-to-charge ratio corresponding to the calculated mass. Probe characteristics and accumulation were assessed in vitro, in vivo and ex vivo using HPV-negative and HPV-positive xenograft mouse models. In vitro studies showed uptake of HPV16 E7-Cy7.5 in HNSCC cell lines but not HPV-negative cell lines which were blockable (20×). The tumor uptake of HPV16 E7-Cy7.5 was observed in mice which was statistically significant than vehicle control and it was blockable (10×).

Conclusions:
We synthesized and characterized HPV16 E7-specific probe. This represents the first step towards the development of companion imaging agents for HPV-positive HNSCC.

Acknowledgements: The authors thank the support of Memorial Sloan Kettering Cancer Center's Animal Imaging Core Facility, Radiochemistry & Molecular Imaging Probes Core Facility, Molecular Cytology Core Facility and the Nuclear Magnetic Resonance Analytical Core Facility. S.R has transitioned from MSK to WSU during this work. This work was supported by National Institutes of Health grants NIH R01 CA204441 (NKP), P30 CA008748, Wayne State University Start-up Fund (SR) and SKI-SRIG-22-1006 (SR).

Reference

1. Parfenov, M.; Pedamallu, C. S.; Gehlenborg, N.; Freeman, S. S.; Danilova, L.; Bristow, C. A.; Lee, S.; Hadjipanayis, A. G.; Ivanova, E. V.; Wilkerson, M. D.; et al. Characterization of HPV and host genome interactions in primary head and neck cancers. Proc Natl Acad Sci U S A 2014, 111 (43), 15544-15549. DOI: 10.1073/pnas.1416074111 From NLM Medline.
2. Ausoni, S.; Boscolo-Rizzo, P.; Singh, B.; Da Mosto, M. C.; Spinato, G.; Tirelli, G.; Spinato, R.; Azzarello, G. Targeting cellular and molecular drivers of head and neck squamous cell carcinoma: current options and emerging perspectives. Cancer Metastasis Rev 2016, 35 (3), 413-426. DOI: 10.1007/s10555-016-9625-1 From NLM Medline.
3. Martinez-Zapien, D.; Ruiz, F. X.; Poirson, J.; Mitschler, A.; Ramirez, J.; Forster, A.; Cousido-Siah, A.; Masson, M.; Vande Pol, S.; Podjarny, A.; et al. Structure of the E6/E6AP/p53 complex required for HPV-mediated degradation of p53. Nature 2016, 529 (7587), 541-545. DOI: 10.1038/nature16481 From NLM Medline.
4. Xue, X.; Wang, B.; Du, W.; Zhang, C.; Song, Y.; Cai, Y.; Cen, D.; Wang, L.; Xiong, Y.; Jiang, P.; et al. Generation of affibody molecules specific for HPV16 E7 recognition. Oncotarget 2016, 7 (45), 73995-74005. DOI: 10.18632/oncotarget.12174 From NLM Medline.

Poster Presentation

Disclosures: The authors have disclosed no financial interest.

328-Development of Highly Sensitive Chemiluminescence Imaging Probes for Amyloid Beta Species

Presenter: Jing Zhang, Harvard Medical School

Jing Zhang[1], Biyue Zhu[2], Jun Yang[3], Chongzhao Ran[3], Chongzhao Ran[4]

[1]*Harvard Medical School, Charlestown, MA*
[2]*Massachusetts General Hospital, Boston, MA*
[3]*Harvard Medical School*
[4]*Massachusetts General Hospital and Harvard Medical School, Boston, MA*

Near infrared fluorescence imaging (NIRF) is one of the most used imaging technologies for preclinical investigations. However, it has several intrinsic limitations, such as low signal-to-noise ratio (SNR) and autofluorescence. By contrast, chemiluminescence imaging can provide very high SNRs and high sensitivity. Although chemiluminescence imaging has been frequently explored in many diseases such as cancers and diabetes, it is rarely applied in the brain disorders including Alzheimer's disease (AD). In our previous study, we reported that ADLumin-1 was a highly sensitive turn-on chemiluminescence probe for amyloid beta (Ab) species. Importantly, we demonstrated that ADLumin-1's light emitting was not dependent on ROS or enzymatic reactions. With ADLumin-1, we found that it could provide 1.80-fold signal difference between transgenic 5xFAD mice and wild type mice.[1] However, ADLumin-1 suffers two apparent shortcomings: a) its chemiluminescence emitting efficiency is low; and b) its emission peak with Ab was around 540 nm, which is not ideal for in vivo NIR imaging to achieve deep tissue penetration. To overcome these drawbacks, we designed and synthesized a series of ADLumin-X (X = 5-9) probes with different substituents that can adjust emission efficiency and wavelength (Figure 1A). We speculated that the rotation of the conjugated double bonds in ADLumin-1 caused its low emission efficiency, due to non-radiative decay. In this regard, in ADLumin-X, we introduced five-member rings (benzofuran and benzothiazole) to restrict the rotation. Indeed, we found that ADLumin-5 could provide over 10-fold enhancement of emitting efficiency and longer emission peak (580nm), compared to ADLumin-1 (Figure 1B). To further extend the emission wavelength, we designed ADLumin-6 via introducing -cyano (-CN) group into ADLumin-5 to reduce the energy level of LUMO and thus to decrease the HOMO-LUMO energy gap. As expected, ADLumin-6's emission peak is longer than that of ADLumin-5 (600nm). We further investigated the signal amplifications of the probes with Ab aggregates in vitro, and found that ADLumin-6 provided the highest amplification, evident by a 118-fold chemiluminescence intensity increasing upon mixing with Aβs

(Figure 1C). In vivo imaging studies with ADLumin-6 showed the differences between 5xFAD and WT were 5.10-fold at 90 min after i.p. injection, which is much higher than that from ADLumin-1 (1.8-fold) (Figure 1D). In summary, through rational design and in vitro testing and in vivo imaging, we demonstrated that ADLumin-6 was a highly sensitive chemiluminescence probe for Aβs in vitro and in vivo, which may have great potential for preclinical animal AD studies in the future.

Reference

1. Yang, J.; Yin, W.; Van, R.; Yin, K. Y.; Wang, P.; Zheng, C.; Zhu, B. Y.; Ran, K.; Zhang, C.; Kumar, M.et al. Turn-on chemiluminescence probes and dual-amplification of signal for detection of amyloid beta species in vivo. Nat. Commun. 2020, 11 (1).

Poster Presentation

Disclosures: The authors have disclosed no financial interest.

329-Dynamic 2-deoxy-D-glucose-enhanced Multispectral Optoacoustic Tomography for Assessing Vasculature Hemodynamics of Breast Cancer

Presenter: Zheng Han, University of Oklahoma Health Sciences Center

Zheng Han[1], Lacey McNally[2]

[1]University of Oklahoma Health Sciences Center, OK
[2]University of Oklahoma Health Sciences Center, Oklahoma City, OK

Background:
Measuring vasculature hemodynamic properties is crucial to gauge the aggressiveness of tumors, as tumors exploit leaky and abundant vasculatures to promote survival and progression [1]. Currently, dynamic contrast-enhanced MRI using gadolinium(Gd)-based agents is the major clinical tool for hemodynamic assessment, but potential Gd toxicity limits its use in patients with impaired renal function [2]. Here we explored the use of an optical probe, IRdye800CW labeled 2-deoxyglucose (2-DG-800), to measure the tumor hemodynamics in multispectral optoacoustic tomography (MSOT).

Methods:
Four female athymic mice bearing 2-LMP orthotropic xenografts were scanned using MSOT inVision 512-TF (iThera Medical GmbH) using 10 Hz laser pulses and wavelengths ranging from 680 to 900 nm. A single-slice axial image was repeatedly acquired at the center tumor position for 4 min and 10 nmol of 2-DG-800 (LI-COR Biosciences) was then i.v. injected in bolus for 1 min. Mice were scanned at a temporal resolution of 15 s for 40 min. MSOT images were reconstructed using the curve-driven-based model-matrix inversion (CDMMI) algorithm using the MSOT-RAFT Matlab package[3]. The two-compartmental extended Tofts model (ETM)[4] (**Eq.1**) and non-linear reference region model (RRM)[5] (**Eq.2**) were used to analyze time-course signal of 2-DG-800. The time-dependent probe concentration in tumor using ETM can be described as:

$$C_{tumor}(t) = v_{plasma} \cdot C_{plasma}(t) + K^{trans} \cdot e^{-t \cdot K_{ep}} * C_{plasma}(t)$$

---(Eq.1)

Where * denotes convolution, and v_{plasma} denotes plasma volume in tumor.
In RRM, $C_{tumor}(t)$, with respect to the probe concentration in reference region $C_{RR}(t)$, can be descried as:

$$C_{tumor}(t) = \frac{K^{trans,tumor}}{K^{trans,\ RR}} \cdot C_{RR}(t) + \frac{K^{trans,tumor}}{K^{trans,RR}} \cdot (K_{ep,RR} - K_{ep,tumor}) \cdot e^{-t \cdot K_{ep,tumor}} * C_{RR}(t)$$

---(Eq.2)

Where $K^{trans,RR}$ denotes the K^{trans} values of the reference region, which was muscle in the current study. Based on the linear relationship between the MSOT signal of 2-DG-800 and the concentration in tissues C(t) can be simply replaced by S(t). The dynamic 2-DG-800 signal in the spinal aorta was referred to as the arterial input function (AIF) which, together with $C_{tumor}(t)$ or $C_{muslce}(t)$, were used to solve the differential equation (Eq. (1)) to estimated rate constant parameters in ETM. In RRM, only $C_{tumor}(t)$ and $C_{muslce}(t)$ were used to solve the relative rate constants. Based on measured rate constants in muscle in ETM, absolute values of tumor parameters were calculated in RRM. Regions of interest (ROIs) of tumor, aorta, and muscle were selected based on MSOT signal at 900 nm (**Fig.1A**).

Results:
Fig.1B shows 2-DG-800 maps of a representative mouse from 5 to 40 min. Injection of 2-DG-800 occurred at around 4 min and at 5 min, spikes of aorta signal became prominent because of 2-DG-800 administration (**Fig.1C**). Tumor and muscle also demonstrated initial increases after injection, followed a plateau, with a higher probe accumulation in tumor than muscle (**Fig.1D**). The ETM and RRM were fitted to the empirical data points in a voxel-wise manner by optimizing the relevant rate constants. The K^{trans} values of voxels in tumor, which is a parameter indicative of vessel permeability, derived from the two models demonstrated strong resemblance (**Fig.1E,F**). Strong correlations can be found for voxel values of K^{trans} (**Fig.1G)** between the two models (correlation coefficient (r^2) = 0.370).

Discussions and Conclusions:
Pharmacokinetic modeling in MSOT is rarely explored [6, 7] because MSOT as an in vivo imaging modality is still at its infancy. Our data support the feasibility of MSOT to characterize tumor hemodynamics using a metal-free probe, 2-DG-800, and two-compartment models including ETM and RRM. The lack of ionizing radiation and the capability to perform MSOT at the bedside give MSOT advantages in monitoring the tumor frequently, thus facilitating timely clinical management of cancer.

Reference

1. Norton, K.A., K. Jin, and A.S. Popel, Modeling triple-negative breast cancer heterogeneity: Effects of stromal macrophages, fibroblasts and tumor vasculature. J Theor Biol, 2018. 452: p. 56-68.
2. Arsenault, T.M., et al., Systemic gadolinium toxicity in patients with renal insufficiency and renal failure: retrospective analysis of an initial experience. Mayo Clin Proc, 1996. 71(12): p. 1150-4.
3. O'Kelly, D., et al., A scalable open-source MATLAB toolbox for reconstruction and analysis of multispectral optoacoustic tomography data. Sci Rep, 2021. 11(1): p. 19872.

4. Sourbron, S.P. and D.L. Buckley, On the scope and interpretation of the Tofts models for DCE-MRI. Magn Reson Med, 2011. 66(3): p. 735-45.
5. Cardenas-Rodriguez, J., C.M. Howison, and M.D. Pagel, A linear algorithm of the reference region model for DCE-MRI is robust and relaxes requirements for temporal resolution. Magnetic Resonance Imaging, 2013. 31(4): p. 497-507.
6. Xiao, T.G., et al., Applying dynamic contrast enhanced MSOT imaging to intratumoral pharmacokinetic modeling. Photoacoustics, 2018. 11: p. 28-35.
7. Hupple, C.W., et al., A light-fluence-independent method for the quantitative analysis of dynamic contrast-enhanced multispectral optoacoustic tomography (DCE MSOT). Photoacoustics, 2018. 10: p. 54-64.

Poster Presentation

Disclosures: The authors have disclosed no financial interest.

330-PET imaging of CD8+ T-cells using 89Zr-Crefmirlimab in healthy Non-Human Primate

Presenter: Shih Hsun Cheng, GlaxoSmithKline

Shih Hsun Cheng[1], Stephen C. Lenhard[1], Heather Haag[2], Shelly Marshall[2], Fang Jia[3], Alessandro Mascioni[4], Ian Wilson[3], Hasan Alsaid[5]

[1]*GlaxoSmithKline, Collegeville, PA*
[2]*GlaxoSmithKline*
[3]*ImaginAb, Inglewood, CA*
[4]*ImaginAb, Inglewood, California*
[5]*GSK, Collegeville, PA*

Introduction:
A $CD8^+$ PET imaging probe using a radiolabeled human CD8 minibody (^{89}Zr-Crefmirlimab, ImaginAb) can help to select effective single or combination immunotherapies in oncology clinical trials [1,2]. $CD8^+$ T-cells are not only a major biomarker in cancer immunotherapy, [3] but they are also a critical biomarker in vaccine development [4]. The COVID-19 pandemic generated significant interest for new vaccine development and the ideal species to understand the immune response to vaccines is the non-human primate (NHP) [5]. This study is the first CD8 PET imaging study in NHPs to provide a non-invasive method of visualizing the biodistribution of $CD8^+$ leukocytes in the lymphatic organs.

Methods:
Two female Cynomolgus NHPs with body weights of 4.25 kg (5.7 years old) and 5.45 kg (5.3 years old) were included in this study. Each NHP received a bolus IV injection of a GMP grade ^{89}Zr-Crefmirlimab (^{89}Zr-Df-IAB22M2C, ~1mCi) in the concentration of 0.18mg/ml for a total dose 0.25mg/kg. The dose calculation was based on the estimated affinity of Crefmirlimab in Cynomolgus NHP. ADA (anti-drug antibody) assay was performed prior to the imaging study to confirm immunogenicity. Full body PET/CT imaging was performed on a Mediso LFER scanner at 17 hours, and on days 2, 5, and 7 post injection. SUVmean uptake of ^{89}Zr-Crefmirlimab was measured in the heart, liver, spleen, kidneys, and lymph nodes.

Results:
The PET images (Figure 1) showed high uptake of ^{89}Zr-Crefmirlimab in the liver, spleen, kidneys, and lymph nodes and a low background uptake in CD8 poor tissues (e.g. muscle and lung). The quantitative SUVmean (Figure 2) showed a decreasing uptake over time in the heart matching the ex-vivo blood uptake (Figure 2A). A steady state uptake was observed in the liver and spleen after the end of the distribution phase (SUV_{mean}: 13.87, and 5.21 on day 5, respectively. Figure 2B). Interestingly, the uptake in the kidney was very high compared to any other organ with a distinguished uptake in the cortex compared to the medulla (SUV_{mean}: 18.44, and 9.95 on day 5, respectively). The SUVmean uptake gradually increased over time in lymph nodes (LNs) with the highest uptake in the cervical LN compared to the axillary and inguinal LNs (SUV_{mean}: 15.4, 9.4, and 9.18 on day 5, respectively. Figure 2B).

Conclusion:
In this study, we assessed the baseline distribution of ^{89}Zr-Crefmirlimab in healthy NHPs. The data confirmed Crefmirlimab has a high uptake in the lymphatic system with a low background which makes it an ideal PET probe to non-invasively monitor whole body biodistribution of CD8+ T-cells for vaccine and infection disease drug development.

Reference

1. Pandit-Taskar N, Postow MA, Hellmann MD, et al. First-in-humans imaging with (89)Zr-Df-IAB22M2C anti-CD8 minibody in patients with solid malignancies: preliminary pharmacokinetics, biodistribution, and lesion targeting. J Nucl Med. 2020;61:512-519.
2. Griessinger CM, Olafsen T, Mascioni A, et al. The PET-tracer (89) Zr-Df-IAB22M2C enables monitoring of intratumoral CD8 T-cell infiltrates in tumor-bearing humanized mice after T-cell bispecific antibody treatment. Cancer Res. 2020;80:2903-2913.
3. Miller, B. C. et al. Subsets of exhausted CD8+ T cells differentially mediate tumor control and respond to checkpoint blockade. Nat. Immunol. 2019;20;326–336
4. Albrecht, L.; Bishop, E.; Jay, B.; Lafoux, B.; Minoves, M.; Passaes, C. COVID-19 Research: Lessons from Non-Human Primate Models. Vaccines 2021; 9; 886.
5. Mohammad Arif Rahman & Marjorie Robert-Guroff Accelerating HIV vaccine development using non-human primate models, Expert Review of Vaccines. 2019;18:1; 61-73

Poster Presentation

Disclosures: The authors have disclosed no financial interest.

331-Quantitative assessment of bowel tissue perfusion using Indocyanine Green near-infrared fluorescence imaging in colorectal surgery.

Presenter: Robin Faber, Leiden University Medical Center

Robin A. Faber[1], Floris Tange[2], Hidde Galema[3], Thomas Zwaan[1], Fabian Holman[4], Tessa van Ginhoven[5], Eva Madsen[6], Koen Peeters[4], Joost Rothbarth[7], Pieter Tanis[6], Cornelis Verhoef[3], Sven Mieog[8], Alexander Vahrmeijer[9], Merlijn Hutteman[9], Stijn Keereweer[3], Joost Van Der Vorst[10], Denise Hilling[4]

[1]*Leiden University Medical Center, Leiden, Zuid-Holland, Netherlands*
[2]*Leiden University Medical Center, Netherlands*
[3]*Erasmus Medical Center, Rotterdam, Zuid-Holland, Netherlands*
[4]*Leiden University Medical Center (LUMC), Leiden, Nederland, Netherlands*

[5]*Erasmus University Rotterdam*
[6]*Erasmus Medical Center, Rotterdam, Netherlands*
[7]*Erasmus University Rotterdam, Rotterdam, Zuid-Holland, Netherlands*
[8]*Leiden University Medical Center (LUMC), leiden, z-h, Netherlands*
[9]*Leiden University Medical Center (LUMC), leiden, Zuid-Holland, Netherlands*
[10]*Leiden University Medical Center (LUMC)*

Introduction:
Anastomotic leakage (AL) is a severe postoperative complication in colorectal surgery with an incidence ranging from 1 to 20% (1). The etiology of AL is known to be multifactorial, in which compromised tissue perfusion is considered as a major contributing factor. In several studies, intraoperative bowel tissue perfusion assessment using near-infrared (NIR) fluorescence imaging with Indocyanine Green (ICG) has demonstrated its potential benefit in the prevention of AL (2). However, the qualitative evaluation of the fluorescence signal could be a limiting factor of the validity and reproducibility of this technique in daily practice (3). Quantitative evaluation of the fluorescence signal holds promise as a more objective and accurate method to assess bowel perfusion (4). Therefore, this prospective cohort study evaluated quantification of bowel tissue perfusion patterns of patients undergoing colorectal surgery by using a standardized NIR fluorescence imaging protocol.

Method:
Twenty (20) patients who underwent oncological colorectal surgery were included in the study. After dissection of the vascular branch, all patients received 5 mg ICG intravenously for intraoperative extracorporeal bowel tissue perfusion assessment according to standard of care. A standardized fluorescence video was recorded for 5 minutes using the Quest Spectrum 2.0 NIR fluorescence imaging system. Fixed camera settings, camera-to-tissue distance and angle of camera on tissue were maintained. Postoperatively, the fluorescence videos were quantified by drawing contiguous ROIs from proximal to distal of the intended anastomosis on the bowel (i.e., ileum, afferent colon and/or efferent colon, depending on the surgical procedure) using the Quest Research Framework quantification software. For each ROI, a time-intensity curve was plotted from which 5 inflow and 5 outflow parameters were derived and analyzed seperately for the ileum, afferent colon, and efferent colon. Furthermore, the inter-observer agreement of the surgeon's subjective interpretation of the fluorescence signal was assessed.

Results:
Thirty (30) percent of the patients underwent a right-sided colectomy (i.e., ileocecal resection or right hemicolectomy), 65% of the patients underwent a left-sided colectomy (i.e., left hemicolectomy, sigmoidectomy or low anterior resection) and 5% of the patients underwent a subtotal colectomy. Based on the quantified time-intensity curves, bowel tissue perfusion could be divided into 3 different perfusion patterns: well perfused, transition zone and poorly perfused. Similar for both the ileum, afferent colon, and efferent colon, the perfusion patterns were characterized by a significantly steeper inflow and outflow slope in the well perfused time-intensity curves compared to the transition zone ($p=<0.001$). Moreover, the time to maximum fluorescence intensity (Tmax) was significantly shorter in the well perfused time-intensity curves ($p=<0.001$). The poorly perfused time-intensity curves only reached its peak intensity after 3 minutes with a slow inflow gradient preceding it (Figure 1). The inter-observer agreement was poor (Intraclass Correlation Coefficient (ICC): 0.368, 95%-CI $0.192 < ICC < 0.580$).

Conclusion:
This prospective cohort study shows that quantification of bowel tissue perfusion is a feasible method to differentiate between well perfused, transition zone and poorly perfused perfusion patterns. In addition, the poor inter-observer agreement of the subjective assessment of the fluorescent signal between surgeons emphasizes the need for quantification of the fluorescence signal. Future studies should examine the correlation between each perfusion pattern and the occurrence of AL.

Reference
1. Arron MNN, Greijdanus NG, Ten Broek RPG, Dekker JWT, van Workum F, van Goor H, et al. Trends in risk factors of anastomotic leakage after colorectal cancer surgery (2011-2019): A Dutch population-based study. Colorectal Dis. 2021;23(12):3251-61.
2. Song M, Liu J, Xia D, Yao H, Tian G, Chen X, et al. Assessment of intraoperative use of indocyanine green fluorescence imaging on the incidence of anastomotic leakage after rectal cancer surgery: a PRISMA-compliant systematic review and meta-analysis. Tech Coloproctol. 2021;25(1):49-58.
3. Karliczek A, Harlaar NJ, Zeebregts CJ, Wiggers T, Baas PC, van Dam GM. Surgeons lack predictive accuracy for anastomotic leakage in gastrointestinal surgery. Int J Colorectal Dis. 2009;24(5):569-76.
4. D'Urso A, Agnus V, Barberio M, Seeliger B, Marchegiani F, Charles AL, et al. Computer-assisted quantification and visualization of bowel perfusion using fluorescence-based enhanced reality in left-sided colonic resections. Surg Endosc. 2021;35(8):4321-31.

Poster Presentation

Disclosures: The authors have disclosed no financial interest.

332-Evaluation of Dotatate-PET After Two Cycles of Peptide Receptor Radionuclide Therapy (PRRT) in Neuroendocrine Tumors (NET)

Presenter: Heying Duan, Stanford University

Heying Duan[1], Hong Song[1], Valentina Ferri[2], George Fisher[3], Shagufta Shaheen[3], Jagruti Shah[4], Judy Nguyen[3], Farshad Moradi[1], Benjamin L. Franc[5], Guido A. Davidzon[1], Andrei Iagaru[1], Carina Mari[1]

[1]*Stanford University, Stanford, CA*
[2]*Stanford University, San Francisco, CA*
[3]*Stanford University, Stanford, California*
[4]*Stanford University, Stanfordq, California*
[5]*University of California, San Francisco, San Francisco, CA*

Aim:
We aimed to evaluate the added information of imaging with DOTATATE-PET after two cycles of peptide receptor radionuclide therapy (PRRT) in patients with somatostatin receptor (SSR)-expressing neuroendocrine tumors (NET).

Methods:
In this retrospective study, 105 patients (54 women and 51 men, 62.5±10.5-year-old) with progressive NET treated with at least two cycles of ^{177}Lu-DOTATATE were included. All patients had DOTATATE-PET (PET/CT or PET/MRI), at baseline, after two cycles, and upon completion of PRRT. RECIST and change in SSR-density were used to evaluate the scans and assess treatment response. If applicable, additional dedicated CT and MRI was obtained and change in tumor marker chromogranin A was recorded. Patients were interviewed about their thoughts of the additional scan midway through the treatment.

Results:
All patients considered the additional DOTATATE-PET very important for peace of mind mid-way through the therapy. After two PRRT cycles, 0/105 (0%) patients showed complete response, and 54/105 (51%) partial response (PR) while 40/105 (38%) had stable disease (SD) with agreement between RECIST and SSR-density. In 11/105 (11%) patients RECIST and SSR-density was discordant. Progressive disease (PD) according to RECIST was seen in 11/11 patients, however, evaluation of SSR-density showed true progression (new lesions) in only 4/11 participants. Follow-up imaging after completion of PRRT proved true progression in these patients while the other 7/11 patients showed PR. These patients were considered to show pseudo-progression (PSP) after two cycles. The pattern of PSP consisted in an overall up-to ~2 mm increase in size of known NET lesions, with/without central necrosis, with/without new stranding, but no new lesions. The SSR-density in these patients showed to be stable or decreased when related to the liver. Chromogranin A was available in 37/105 patients. The change in chromogranin A did not correlate well with response/stability nor progression of disease at 2 cycles.

Conclusion:
Our data show that a DOTATATE-PET after 2 cycles of PRRT provides important reassurance for the patient about the status of the disease as they go through the therapy. No patient showed complete response after 2 cycles of PRRT, clearing concerns about possible overtreatment. DOTATATE-PET is more accurate in assessing treatment response at 2 cycles when RECIST and SSR-density criteria is used, allowing continuation of treatment in patients with pseudo-progression. Change in tumor marker did not correlate well with response/stability nor progression at 2 cycles.

Poster Presentation

Disclosures: The authors have disclosed no financial interest.

333-Peptide receptor radionuclide therapy (PRRT) in unresectable, metastatic pheochromocytoma and paraganglioma

Presenter: Heying Duan, Stanford University

Heying Duan[1], Valentina Ferri[2], George Fisher[3], Shagufta Shaheen[3], Guido A. Davidzon[1], Farshad Moradi[1], Judy Nguyen[3], Benjamin L. Franc[4], Andrei Iagaru[1], Carina Mari[1]

[1]Stanford University, Stanford, CA
[2]Stanford University, San Francisco, CA
[3]Stanford University, Stanford, California
[4]University of California, San Francisco, San Francisco, CA

Introduction:
Pheochromocytoma and paraganglioma (PPGL) are very rare tumors characterized by a heterogenous prognosis. In the setting of unresectable, metastatic PPGL, there is a lack of clear treatment guidelines, and options are very limited. Here we present our initial experience with peptide receptor radionuclide therapy (PRRT) in advanced PPGL.

Methods:
Six patients (1 woman and 5 men, mean±SD: 59.7±11.7-year-old) with progressive, somatostatin receptor (SSR)-expressing PPGL (4 paraganglioma and 2 pheochromocytoma) were treated with ^{177}Lu-Dotatate. ^{68}Ga-Dotatate PET (PET/CT or PET/MRI) was obtained at baseline, after 2 cycles, and after 4 PRRT cycles. Follow-up imaging was performed every 3 months. RECIST and change in SSR-density (based on change in SUV_{max}) were used to evaluate treatment response. Laboratory tests were performed 1 week before each cycle and every 2 months at follow-up. Toxicity was determined based on the National Cancer Institute Common Terminology Criteria for Adverse Events (NCI CTCAE) V5.0. Overall response rate (ORR), disease control (DC) and progression free survival (PFS) were determined.

Results:
All patients underwent 4 cycles of PRRT. After the first cycle, 1/6 (16.7%) and 1/6 (16.7%) patients, respectively, developed neutropenia and lymphopenia grade 3 which resolved in both cases after 1 month. 2/6 (33.3%) patients showed lymphopenia grade 3, 1 and 3 months after the last cycle might also be related to newly initiated radiation therapy after PRRT in both cases. No other grade 3 toxicity was seen, especially regarding liver and renal function. The mean follow-up since PRRT initiation was 21.9±7.4 (range 10.3 – 30.3) months. The Kaplan-Meier curve analysis showed a PFS of 83%, 58% and 39% at 11-month, 15-month and 18-month follow-up since PRRT initiation, respectively. The ORR (complete and partial response [CR, PR]) was 33.3%. DC (CR, PR and stable disease) was 80% at 11-month follow-up.

Conclusion:
Our preliminary data show that patients with unresectable, metastatic PPGL treated with ^{177}Lu-Dotatate show overall good results with a disease control of 80% and PFS of 83% at 11-month follow-up.

Poster Presentation

Disclosures: The authors have disclosed no financial interest.

334-Development of caged melanin precursors that detect enzyme activity with Multispectral Optoacoustic Tomography

Presenter: Xiaofei Liang, MD Anderson Cancer Center

Xiaofei Liang[1], Alyssa Pollard[2], Sanjaya Lokugama[3], Marty Pagel[1]

[1]MD Anderson Cancer Center, Houston, TX
[2]MD Anderson Cancer Center, Smithtown, NY
[3]University of Arizona

Our goal is to improve the localization of solid tumors that express and secrete high levels of protease enzymes.[1] Proteases degrade the extracellular matrix and cellular stroma, increasing tumor proliferation, invasion, and metastasis. More specifically, our research focuses on the detection of tumors with cathepsin B, which is a protease biomarker of malignant tumors.[2]To meet our goal, we have designed a "caged melanin precursor" that is cleaved by cathepsin B, then undergoes spontaneous disassembly, and finally spontaneously polymerizes to form eumelanin (Figure 1). The caged agent cannot form eumelanin prior to cleavage by cathepsin B. This nano-sized eumelanin product strongly absorbs near-infrared light, and therefore can be detected with Multispectral Optoacoustic Tomography (also known as photoacoustic tomography; Figure 2).[3] Pre-clinical MSOT can image an entire torso of mouse tumor models, and clinical MSOT has been used to image many tumor types including breast cancer. We use an innovative Dynamic Contrast Enhanced (DCE) MSOT imaging protocol that can monitor the generation of eumelanin in tumors, which improves the specificity of protease-active tumors vs. normal tissues.[4] Furthermore, the strong pigmentation of eumelanin provides potential to improve surgery of solid tumors (Figure 3). As an analogy, fluorescent contrast agents have been developed that are trapped or activated in tumors with high protease activity.[5]These tumors can then be visualized during

surgery, when the tumors can be imaged with fluorescence imaging instrumentation. Our agent causes eumelanin to accumulate in tumors with high protease activity, causing the tumors to become black. Simple visual inspection, without expensive and cumbersome fluorescence imaging instrumentation, can identify the black tumors against the beige-to-red background of normal tissues. As a longer-term goal, MSOT during surgery has potential to detect melanin-stained tumors as deep as 3 cm below the tissue-exposed surface during surgery.
To meet our objectives, we have completed the synthesis of our agent. Friedel-Craft alkylation of L-tyrosine **6** was performed to introduce a ketone group on the ortho position of the phenol, to provide a stable diphenol structure with different protecting groups **7**. The BOC protecting group was introduced to the free amine group **8** to improve solubility in organic solvent. We performed an oxidation reaction of the ketone by mCPBA **9**, as the ketone is the only group that can be oxidized in this intermediate. Dibenzyl protected groups were introduced on both the acid and phenol substitutes **10**.[6] The BOC protecting group was transformed to a picoliamide group **11**, as the carbonyl and nitrogen on the pyridine ring are required for the cyclization reaction to form the indole ring. The hydrolysis reaction was performed to facilitate the coupling reaction with the peptide linker making the melanin precursor maintained as a monomer in vitro. Cyclization was catalyzed by $Pd(OAC)_2$ on the hydrogen of the benzene ring and the amide of the picoliamide substitute **13**.[7] All of our reactions are similar to previously published reactions. High performance liquid chromatography was used to purify our caged-melanin contrast agent **14**. The polarity of our contrast agent is high, providing good aqueous solubility for upcoming in vivo studies.
We are currently improving the yield of our final product, so that we have material for subsequent DCE MSOT studies that measure Michaelis-Menten kinetics of cathepsin B with our caged melanin precursor.

Reference

1. McIntyre JO, Matrisian LM. Molecular imaging of proteolytic activity in cancer. J Cell Biochem 2003;90:1087–1097.
2. Aggarwal N, Sloane BF. Cathepsin B: multiple roles in cancer. Proteomics Clin Appl 2014;8:427-437.
3. Schwarz M, Buehler A, Aguirre J, Ntziachristos V. Three-dimensional multispectral optoacoustic mesoscopy reveals melanin and blood oxygenation in human skin in vivo. J Biophotonics 2016;9:55-60.
4. Hupple CW, Morscher S, Burton NC, Pagel MD, McNally LR, Cardenas-Rodriguez J. A light-fluence-independent method for the quantitative analysis of dynamic contrast-enhanced multispectral optoacoustic tomography (DCE MSOT). Photoacoustics 2018;10:54-64.
5. Nguyen QT, Olson ES, Aguillera TA, Jiang T, Scadeng M, Ellies LG, Tsien RY. Surgery with molecular fluorescence imaging using activatable cell-penetrating peptides decreases residual cancer and improves survival. Proc Nat Acad Sci USA. 2010;107:4317-4322.
6. Chen C, Zhu YF, Wilcoxen K. An improved synthesis of selectively protected L-dopa derivatives from L-tyrosine. J Org Chem 2000;65:2574-2576.
7. He G, Lu C, Zhao Y, Nack WA, Chen G. Improved protocol for indoline synthesis via palladium-catalyzed intramolecular C(sp2)-H amination. Org Lett 2012;14:2944-2947.

Poster Presentation

Disclosures: The authors have disclosed no financial interest.

335-Visualizing dynamic changes in PD-L1 expression in non-small-cell lung carcinoma with radiolabeled recombinant human PD1

Presenter: Haiming Luo, Huazhong University of Science and Technology

Haiming Luo

Huazhong University of Science and Technology, China

Purpose:
Tumor heterogeneity limits the predictive value of PD-L1 expression and influences the outcomes of the immunohistochemical assay for therapy-induced changes in PD-L1 levels. This study aimed to determine the predictive value of PD-L1 for non-small-cell lung carcinoma (NSCLC), thereby developing imaging agents to non-invasively image and examine the effect of the therapeutic response to PD-L1 blockade therapy.

Methods:
A cohort of 102 patients with lung cancer was analyzed, and the prognostic significance of PD-L1 expression level was investigated. Recombinant human PD-1 ECD protein (rhPD1) was expressed, purified, and labeled with ^{64}Cu for the evaluation of PD-L1 status in tumors. Mice subcutaneously bearing PD-L1 high-expressing tumor HCC827 and PD-L1 low-expressing tumor A549 were used to determine tracer-target specificity and examine the effect of therapeutic response to PD-L1 blockade therapy.

Results:
PD-L1 was proved to be a good prognosis marker for NSCLC, and its expression was correlated with the histology of NSCLC. PET imaging revealed high tumor accumulation of ^{64}Cu-NOTA-rhPD1 in HCC827 tumors (9.0 ± 0.5 %ID/g), whereas it was 3.2 ± 0.4 %ID/g in A549 tumors at 3 h post-injection. The lower tumor uptake (3.1± 0.3 %ID/g) of ^{64}Cu-labeled denatured-rhPD1 in HCC827 tumors at 3 h post-injection ($P<0.001$) demonstrated the target-specificity of ^{64}Cu-NOTA-rhPD1. Furthermore, PET showed that ^{64}Cu-NOTA-rhPD1 sensitively monitored treatment-related changes in PD-L1 expression, and seemed to be superior to [^{18}F]FDG.

Conclusion:
We identified PD-L1 as a good prognosis marker for surgically resected NSCLC and developed a PET tracer ^{64}Cu-NOTA-rhPD1 with high target-specificity for PD-L1.

Innovation:
This study confirmed that PD-L1 is a good prognostic marker for surgically resected NSCLC and our developed ^{64}Cu-labeled rhPD1 derived protein could accurately visualize the dynamic changes in PD-L1 expression in NSCLC tumors, and distinguish PD-L1-positive NSCLC malignancies from negative tumors.

Reference

1. Lu T, Yang X, Huang Y, Zhao M, Li M, Ma K, et al. Trends in the incidence, treatment, and survival of patients with lung cancer in the last four decades. Cancer Manag Res. 2019;11:943-53. doi:10.2147/CMAR.S187317.
2. Sgambato A, Casaluce F, Sacco PC, Palazzolo G, Maione P, Rossi A, et al. Anti PD-1 and PDL-1 Immunotherapy in the Treatment of Advanced Non- Small Cell Lung Cancer (NSCLC): A Review on

Toxicity Profile and its Management. Curr Drug Saf. 2016;11:62-8. doi:10.2174/1574886311207040289.
3. Lantuejoul S, Sound-Tsao M, Cooper WA, Girard N, Hirsch FR, Roden AC, et al. PD-L1 Testing for Lung Cancer in 2019: Perspective From the IASLC Pathology Committee. J Thorac Oncol. 2020;15:499-519. doi:10.1016/j.jtho.2019.12.107.
4. Hartley GP, Chow L, Ammons DT, Wheat WH, Dow SW. Programmed Cell Death Ligand 1 (PD-L1) Signaling Regulates Macrophage Proliferation and Activation. Cancer Immunol Res. 2018;6:1260-73. doi:10.1158/2326-6066.CIR-17-0537.
5. Latchman YE, Liang SC, Wu Y, Chernova T, Sobel RA, Klemm M, et al. PD-L1-deficient mice show that PD-L1 on T cells, antigen-presenting cells, and host tissues negatively regulates T cells. Proc Natl Acad Sci U S A. 2004;101:10691-6. doi:10.1073/pnas.0307252101.
6. Iraolagoitia XL, Spallanzani RG, Torres NI, Araya RE, Ziblat A, Domaica CI, et al. NK Cells Restrain Spontaneous Antitumor CD8+ T Cell Priming through PD-1/PD-L1 Interactions with Dendritic Cells. J Immunol. 2016;197:953-61. doi:10.4049/jimmunol.1502291.
7. Dong W, Wu X, Ma S, Wang Y, Nalin AP, Zhu Z, et al. The Mechanism of Anti-PD-L1 Antibody Efficacy against PD-L1-Negative Tumors Identifies NK Cells Expressing PD-L1 as a Cytolytic Effector. Cancer Discov. 2019;9:1422-37. doi:10.1158/2159-8290.CD-18-1259.
8. Shimoji M, Shimizu S, Sato K, Suda K, Kobayashi Y, Tomizawa K, et al. Clinical and pathologic features of lung cancer expressing programmed cell death ligand 1 (PD-L1). Lung Cancer. 2016;98:69-75. doi:10.1016/j.lungcan.2016.04.021.

Poster Presentation

Disclosures: The authors have disclosed no financial interest.

336-Photoacoustic imaging of multiple anatomical structures in a live mouse for a long duration using a single injectable contrast agent

Presenter: Anjul Khadria, California Institute of Technology (Caltech)

Anjul Khadria[1], Chad Paavola[1], Yang Zhang[2], Samuel Davis, Patrick Grealish[3], Konstantin Maslov[3], Junhui Shi[3], John Beals[3], Sunday Oladipupo[3], Lihong Wang[2]

[1]*California Institute of Technology (Caltech), India*
[2]*California Institute of Technology (Caltech), Pasadena, CA*
[3]*Eli Lilly and Company, Indianapolis, IN*

Simultaneous imaging of anatomical features such as peripheral nerves, blood and lymphatic vessels, and sebaceous glands in live animals for several hours will help improve understanding of diseases, study the effects of therapeutics, and guide molecular optimization in preclinical models.[1,2] Currently available techniques to simultaneously image the above-mentioned features involve either injecting multiple contrast agents, which often interfere with each other, or using mice genetically engineered with fluorescent proteins, which are expensive, time-consuming and not translatable clinically.[3,4] Current approaches to image lymphatic vessels use standalone dyes such as Evans blue or indocyanine green (ICG), which are not photostable, get absorbed by the blood vessels, and cannot be used for long-duration imaging as they clear out in less than 30 – 60 minutes.[5,6] Imaging of peripheral nerves using injectable contrast agents has been challenging and only a few studies have been published that image peripheral nerves through fluorescence imaging.[7,8] Photoacoustic imaging of peripheral nerves has been done only *ex vivo*.[9] Imaging of sebaceous glands on the skin can help study several disorders, such as sebaceous adenoma, sebaceoma, sebaceous carcinoma, etc.[10] A method that utilizes a single injectable contrast agent to simultaneously image several anatomical features will provide an inexpensive, faster, and clinically translatable approach to understand the physiological characteristics of the anatomical structures and associated diseases such as peripheral neuropathy, lymphoma, vasculitis, sebaceoma.[11,12] In this study, we labeled an IgG4 isotype control antibody with the near-infrared sulfo-cy7.5 dye and injected it into a mouse ear to perform simultaneous visualization of peripheral nerves, blood and lymphatic vessels, and sebaceous glands for up to 3 hours using photoacoustic microscopy. We imaged the blood label-free with 559 nm wavelength light while imaging the lymphatic vessels, peripheral nerves, and sebaceous glands through the dye-labeled antibody with 780 nm wavelength light. To enable multi-feature imaging, the lymphatic vessels are visualized outside the injected dye-labeled antibody mass while visualizing the peripheral nerves and sebaceous glands inside the mass. Initially, the peripheral nerves and the sebaceous glands were not visible due to background signals from the dye-labeled antibody. We removed the excess background signals by inspecting the two-dimensional sections from the three-dimensional volume at various depths. The peripheral nerves and sebaceous glands are distinguished from each other through their shapes as the sebaceous glands are circular while the nerves are shaped as long elongated fibers. Peripheral nerves and arteries are aligned together in mouse skin, a feature that enabled us to identify the nerves in our images.[13] We digitally labeled the structures in different colors through image segmentation. The mean photoacoustic signal from both the lymphatic vessel and the peripheral nerve decreased by only ~20% after 3 hours of injection. This was possible because of the slow clearance of the large-size dye-labeled antibody (~ 147 kDa) from the injection site. Apart from imaging the mouse ear, we also injected the sulfo-cy7.4 dye-labeled antibody in the hind-paw of the mouse and observed its deep medial lymphatic vessel and lymph node up to 0.4 cm deep through photoacoustic computed tomography. We did not perform imaging of peripheral nerves and sebaceous glands in deep tissues because the sebaceous glands are present only on the skin and unlike in skin, we have no information about the nerves in deep tissues to help us correctly identify them. Our approach to image multiple features for a long duration will potentially improve preclinical therapeutic optimization, shorten discovery timelines, and enable clinical treatments. Further engineering can be performed on the antibody to bind to specific antigens to enable long-duration imaging of deep and shallow individual structures in live animals.

Reference

1. Hoshida, T. et al. Imaging Steps of Lymphatic Metastasis Reveals That Vascular Endothelial Growth Factor-C Increases Metastasis by Increasing Delivery of Cancer Cells to Lymph Nodes: Therapeutic Implications. Cancer Res. 66, 8065 LP – 8075 (2006).
2. Munn, L. L. et al. Imaging the lymphatic system. Microvasc. Res. 96, 55–63 (2014).
3. Zhu, J. et al. Simultaneous in vivo imaging of blood and lymphatic vessel growth in Prox1–GFP/Flk1::myr–mCherry mice. FEBS J. 282, 1458–1467 (2015).
4. Yamazaki, T. et al. Whole-mount Confocal Microscopy for Adult Ear Skin: A Model System to Study Neuro-vascular Branching Morphogenesis and Immune Cell Distribution. J. Vis. Exp. 57406 (2018).
5. Liu, C. et al. Five-wavelength optical-resolution photoacoustic microscopy of blood and lymphatic vessels. Adv. Photonics 3, 1–10 (2021).

6. Robinson, H. A. et al. Non-invasive optical imaging of the lymphatic vasculature of a mouse. J. Vis. Exp. e4326 (2013).
7. Whitney, M. A. et al. Fluorescent peptides highlight peripheral nerves during surgery in mice. Nat. Biotechnol. 29, 352–356 (2011).
8. Wang, L. G. et al. Near-infrared nerve-binding fluorophores for buried nerve tissue imaging. Sci. Transl. Med. 12, eaay0712 (2020).
9. Matthews, T. P. et al. Label-free photoacoustic microscopy of peripheral nerves. J. Biomed. Opt. 19, 16004 (2014).
10. Shamloul, G. et al. An updated review of the sebaceous gland and its role in health and diseases Part 2: Pathophysiological clinical disorders of sebaceous glands. Dermatol. Ther. 34, e14862 (2021).
11. Kwee, T. C. et al. Imaging in staging of malignant lymphoma: a systematic review. Blood 111, 504–516 (2008).
12. Choi, W. et al. Three-dimensional Multistructural Quantitative Photoacoustic and US Imaging of Human Feet in Vivo. Radiology 303, 467–473 (2022).
13. Mukouyama, Y. et al. Sensory Nerves Determine the Pattern of Arterial Differentiation and Blood Vessel Branching in the Skin. Cell 109, 693–705 (2002).

Poster Presentation

Disclosures: The authors have disclosed no financial interest.

337-Enabling High Sensitivity and Resolution with Optimized Broadband Receive Front End Design for Magnetic Particle Imaging, Spectroscopy, and Relaxometry

Presenter: Quincy Huynh, University of California, Berkeley

Quincy Huynh[1], K. L. Barry Fung[2], Chinmoy Saayujya[3], Kim Hwang Yeo[4], Irati Rodrigo Arrizabalaga[5], Steven Conolly[2]

[1]University of California, Berkeley, Union City, CA
[2]University of California, Berkeley, Berkeley, CA
[3]University of California, Berkeley, Berkeley
[4]UC Berkeley, [5]University of California, Berkeley, Berkeley, California

Introduction:

Magnetic particle imaging (MPI) is a tracer imaging modality that detects superparamagnetic iron oxide nanoparticles (SPIOs). Since its inception [1], MPI has enjoyed a rich developmental history - from its k-space and x-space formulation [2], [3]; to scanner design [4]–[7]; to optimized coil and instrumentation [8]–[11]. Promising clinical applications for MPI include brain imaging [6], [7], [12]; stem cell tracking [13], [14]; immune cell tracking [15]; lung imaging [16]; gastrointestinal bleed imaging [17]; and cancer imaging [18]. Magnetic Particle Spectroscopy (MPS) and Magnetic Particle Relaxometry (MRX) are used to characterize the nanoparticles used in MPI, as well as other biosensing applications [19]. Preclinical MPI, while both highly sensitive and quantitative [citation], has yet to have the resolution for economical human-scale clinical scanner [12], [20]. Novel tracers called Superferromagnetic Iron Oxide (SFMIO) particles show an order-of-magnitude improvement in resolution that would allow for 100-fold decrease in scanner prices. However, these high-resolution tracers show a rich harmonic spectrum showing strong peaks at harmonic numbers well past where common MPI tracers (e.g. VivoTrax, ferucarbotran) have signal above the noise floor, shown in Figure 1 [21]. Therefore, an order of magnitude improvement in resolution with SFMIOs necessitates a corresponding increase in the RX signal bandwidth. This work focuses on optimizing the RX frontend of MPI/MPS/MRX systems to realize this 10-fold increase in bandwidth, while also improving the limit of detection with broadband noise matching and improving dynamic range with a combination of gradiometric cancellation and active compensation of the drive field feedthrough interference.

Methods:

Previous work in MPI broadband noise matching has shown exquisite noise performance down to 100 pV/rtHz voltage noise [9], [10] by increasing the noise matching ratio N by adding more turns or parallel amplifiers. However, increasing N leads to decreasing effective noise bandwidth due to two major factors. The first is that the resonant frequency of the RX coil decreases as the effective inductance increases (winding more turns or using a transformer increases inductance and capacitance) and effective capacitance increases (adding more amplifiers in parallel increases input capacitance). Reported resonance frequencies of 200 kHz to 300 kHz for existing RX coils allow for sufficient bandwidth to reconstruct 10-15 harmonics for VivoTrax (at 20 kHz drive frequency) and other commercial particles, but squander the several remaining harmonics of SFMIOs. The current noise contribution of the preamplifier due to the increasing impedance of the inductive coil over frequency can also become more dominant than the coil noise voltage and noise voltage of the preamplifier. These two factors limit effective noise match bandwidth. This work showcases a design procedure for minimizing RX noise over a desired bandwidth and improve limit-of-detection, with results in Figure 2. Drive field feedthrough interference occurs because of transmit (TX) coil to RX coil coupling. Dynamic range suffers when feedthrough interference is too large since the feedthrough may saturate the RX amplifier before the particle signal is adequately amplified. Previous works have used coil geometry to cancel out the interference by reducing the effective mutual inductance between the TX and RX coils [8], [22], [23]. Previous works have also used active components to analog subtract the feedthrough [11], [24], [25]. These techniques achieve several orders of magnitude more suppression for single tone excitation. This work utilizes this concept for broadband suppression with a combination of an easily shim-able gradiometer for passive compensation and instrumentation amplifier and DAC for active compensation, with results in Figure 3. With an established noise floor and adequate drive field feedthrough suppression, the next design step is to choose an appropriate Analog-to-Digital Converter (ADC) to quantize the particle signal outlined in the supplementary.

Reference

1. B. Gleich and J. Weizenecker, Nature, 2005.
2. J. Rahmer, J. Weizenecker, B. Gleich, and J. Borgert, BMC Med. Imaging, 2009.
3. P. W. Goodwill and S. M. Conolly, IEEE Trans. Med. Imaging, 2010.
4. P. W. Goodwill, K. Lu, B. Zheng, and S. M. Conolly, Rev. Sci. Instrum., 2012.
5. P. W. Goodwill et al., IEEE Trans. Med. Imaging, 2012.
6. E. E. Mason et al., Int. J. Magn. Part. imaging, 2017.
7. M. Graeser et al., Nat. Commun., 2019.
8. G. Bringout and T. M. Buzug, IEEE Trans. Magn., 2015.
9. B. Zheng et al., IEEE Trans. Biomed. Circuits Syst., 2017.
10. M. Graeser et al., Sci. Reports, 2017.
11. D. Pantke et al., Med. Phys., 2019.
12. X. L. C. Wu et al., AJNR Am. J. Neuroradiol., 2019.
13. B. Zheng et al., Sci. Rep., 2015.
14. B. Zheng et al., Theranostics, 2016.
15. P. Chandrasekharan et al., Nanotheranostics, 2021.
16. X. Y. Zhou et al., Phys. Med. Biol., 2017.
17. E. Y. Yu et al., ACS Nano, 2017.
18. E. Y. Yu et al., Nano Lett., 2017.

19. Z. W. Tay et al., Sci. Rep., 2016.
20. Z. W. Tay et al., Biomed Phys Eng Express, 2017
21. Z. W. Tay et al., Small Methods, 2021.
22. A. R. Çağıl, B. Tasdelen, and E. U. Saritas, Int. J. Magn. Part. Imaging, 2020.
23. Q. Huynh et al., Int. J. Magn. Part. Imaging, 2022.
24. T. Q. Bui, W. L. Tew, and S. I. Woods, J. Appl. Phys., 2020.
25. B. Tasdelen et al., Int. J. Magn. Part. Imaging, 2020.

Poster Presentation

Disclosures: The authors have disclosed no financial interest.

338-Imaging tumor extracellular pH using PET/MRI co-agents.

Presenter: Chetan Dhakan, University of Texas MD Anderson Cancer Center

Chetan B. Dhakan[1], Alyssa Pollard[2], Lorenzo Palagi[3], Jorge De La Cerda[4], F. W. Schuler[5], Tyler Pollard[6], Aikaterini Kotrotsou[7], Federica Pisaneschi[8], Marty Pagel[5]

[1]*University of Texas MD Anderson Cancer Center, Houston, TX*
[2]*MD Anderson Cancer Center, Smithtown, NY*
[3]*University of Turin, Italy*
[4]*MD Anderson Cancer Center, Houston*
[5]*MD Anderson Cancer Center, Houston, TX*
[6]*Georgia Institute of Technology, Atlanta, GA*
[7]*University of Texas MD Anderson Cancer Center, Houston, Texas*
[8]*University of Texas MD Anderson Cancer Center, Houston*

Introduction:
Acidosis is a useful biomarker for tumor diagnoses and for evaluating early response to anti-cancer treatments.[1] Despite these useful applications, there are few methods available for non-invasively measuring tumor extracellular pH (pHe), and none are routinely used in clinics.[2] Responsive MRI contrast agents have been developed, and they undergo a change in MRI signal with pH. However, these signal changes are concentration-dependent, and it is difficult to accurately measure the concentration of an MRI contrast agent in vivo.[3] PET/MRI provides a unique opportunity to overcome this concentration dependence issue by using the PET component to report on the concentration of the pH-responsive MRI agent.[4,5]

Hypothesis:
Herein, we hypothesize that simultaneous PET/MRI co-agents can measure tumor pHe, with a precision that depends on the concentration of the MRI co-agent**.** In this work, we synthesized a Gd-based MRI agent,[6] and we have correlated pH with the r_1 relaxivity of the MRI co-agent. We then chelated the same agent with ^{68}Ga to develop ^{68}Ga PET/MRI co-agents, and we chelated the agent with ^{64}Cu to develop ^{64}Cu PET/MRI co-agents. In addition, we synthesized a ^{18}F- and ^{19}F-labeled versions of the Gd-based MRI agent that served as ^{18}F PET/MRI co-agents. We have also developed a procedure that uses MRI r_1 relaxation rate measurements, PET radioactivity measurements, and the ratio of the PET/MRI co-agents administered to the mouse model to determine the r_1 relaxivity of the MRI co-agent, which can then be used to estimate pHe. We used our procedure to measure tumor pHe in a subcutaneous flank model of MIA PaCa-2 pancreatic cancer and 4T1 breast cancer.
Simultaneous ^{68}Ga PET/MRI can measure tumor extracellular pH
We synthesized ^{68}Ga PET/MRI co-agents with high yields and purity, and we used these agents to accurately measure pH in solution. The precision of the pH measurement was dependent on the concentration of the MRI co-agent. At the highest concentration of MRI co-agent (0.8 mM), a standard error of 0.08 pH unit was achieved compared to a gold-standard pH microsensor. These PET/MRI co-agents were used to measure tumor pHe. However, the ^{68}Ga PET co-agent degraded in urine after 20 min, raising potential concerns that the PET agent lacked stability in the tumor.
Simultaneous ^{64}Cu PET/MRI was not able to measure tumor extracellular pH
We synthesized ^{64}Cu PET/MRI co-agents with high yield and radiochemical purity. However, ^{64}Cu is known to de-chelate from DOTA-based ligands and can be easily transchelated by enzymes in the liver, which often leads to high retention of the metal ion in the liver. This was observed in our in vivo PET/MR images with the ^{64}Cu PET co-agent, as validated by radioHPLC of extracted urine post-injection. Therefore, a ^{64}Cu PET agent was an unsuccessful choice for our simultaneous PET/MRI approach.
Simultaneous ^{18}F PET/MRI can measure tumor extracellular pH
We synthesized ^{18}F PET/MRI co-agents with high yield and radiochemical purity. The radiolabeling was performed in less than one hour using an automated synthesizer. We achieved a standard deviation as low as 0.06 pH units in solution. With sufficient co-agent tumor uptake, we measured tumor pHe *in vivo* with a correlation of 0.848 compared to a gold-standard pH microsensor. In addition, the co-agents showed high stability in solution and *in vivo* with no metabolic degradation of the ^{18}F radiolabel.

Conclusion:
These preliminary results showed that tumor acidosis can be evaluated with simultaneous PET/MRI. The ^{18}F PET/MRI co-agents showed the most promising approach. Improvements are needed to more precisely measure MRI r_1 relaxation rates, and to ensure the in vivo stability of the agents.

Reference

1. Gillies, R.J.; Raghunand, N.; Karczmar, G.S.; Bhujwalla, Z.M. MRI of the Tumor Microenvironment. J Magn Reson Imaging 2002, 16 (4), 430-450.
2. Chen, L.Q.; Pagel, M.D. Evaluating pH in the Extracellular Tumor Microenvironment using CEST MRI and other Imaging Methods. Adv Radiol 2015, 2015, 206405.
3. Ekanger, L.A.; Allen, M.J. Overcoming the Concentration-Dependence of Responsive Probes for Magnetic Resonance Imaging. Metallomics 2015. 7 (3), 405-421.
4. Frullano, L.; Catana, C.; Benner, T.; Sherry, A.D.; Caravan, P. Bimodal MR–PET Agent for Quantitative pH Imaging. Angew Chem Int Ed 2010, 49, 2382–2384.
5. Pollard, A.C.; de la Cerda, J.; Schuler, F.W.; Pollard, T.R.; Kotrotsou, A.; Pisaneschi, F.; Pagel, M.D. Radiometal-Based PET/MRI Contrast Agents for Sensing Tumor Extracellular pH. Biosensors 2022, 12 (2) 134.
6. Lowe, M.P.; Parker, D.; Reany, O.; Aime, S.; Botta, M.; Castellano, G.; Gianolio, E.; Pagliarin, R. pH-Dependent Modulation of Relaxivity and Luminescence in Macrocyclic Gadolinium and Europium Complexes Based on Reversible Intramolecular Sulfonamide Ligation. J Am Chem Soc 2001, 123, 7601–7609.

Poster Presentation

Disclosures: The authors have disclosed no financial interest.

339-Novel Self-Assembled Multifunctional Nanoprobe for Preclinical NIR-II Fluorescence Image-guided Breast Cancer Surgery, Enhancement of Radiotherapy Efficacy and Breast Cancer Identification

Presenter: Yong-Qu Zhang

Yong-Qu Zhang[1], Wan-Ling Liu[1], Xiang-Jie Luo[1], Guo-Jun Zhang[1]

[1]*Xiang'an Hospital of Xiamen University, Xiamen, Fujian, China*

Introduction:
Breast conserving surgery (BCS) is the upmost option for patients with early-stage breast cancer. However, due to no clinically effective approach for the evaluation of BCS's margin, positive margin resulting in local recurrence is still a problem. Accordingly, radiation therapy (RT) is a common modality in patients with advanced breast cancer. In addition, there is an urgent need for a multimodal nano-therapy platform for precision cancer drugs. Therefore, a novel self-assembled multifunctional nano-probe ^{Gd}DTPA-HSA@ICG- Bevacizumab (NPs-Bev), is developed to improve fluorescence image-guided surgery and breast cancer RT efficacy. The nano-probe-based NIR-II fluorescence image guidance facilitates complete tumor resection, improves the overall mouse survival rate, and effectively discriminates between benign and malignant breast tissues in spontaneous breast cancer transgenic mice. Moreover, introducing the nano-probe to tumors generated more reactive oxygen species under X-ray irradiation, improved RT sensitivity, and reduced mouse tumor progression. We also found that the probe could accurately identify mouse malignant tissues and normal tissues by rapid in vitro immersion with great clinical transformation potential to identify breast malignant tissues/margins.

Methods:
1. Characterization and biosafety of the probe NPs-Bev were performed.
2. The targeting of the probe was verified by *in vitro* fluorescence co-localization and flow cytometry experiment.
3. MDA-MB-231-luc breast cell tumor-bearing mouse modal was performed to investigate the characterization of the probe.
4. Dynamic MR imaging is respectively used to monitor the boundary of the tumor.
5. Fluorescence image-guided surgery in multiple micro-tumor mouse, spontaneous breast cancer transgenic mice and transplanted tumor model were to evaluated the specificity and sensitivity of guided tumor resection with the probe.
6. In vitro probe immersion and incubation were performed to identify tumor properties.
7. RT sensitization in MDA-MB-231-luc bearing mice to evaluate radiosensitization properties of the probe.

Results:
1. NPs-Bev was successfully synthesized with good dispersibility, stability with high intensity of NIR-II fluorescent and high quality signal of MRI imaging.
2. NPs-Bev could specifically target high expression level of VEGF-A in breast cancer cell lines compared with NPs-IgG.
3. NPs-Bev was able to detected the MDA-MB-231-luc breast cell tumor-bearing mouse models with a tumor-to-muscle ratios of ~6, correspondingly, 2 fold NIR-II FL signal decrease was detected while blocked by unlabeled Bevacizumab. The signal to background ratio of MRI was nearly 3 fold increase in the group NPs-Bev *vs*. NPs-IgG.
4. NPs-Bev was able to detected the multiple micro-tumor mouse and the minimum detectable tumor diameter is about 1mm. The nano-probe-based NIR-II fluorescence image guidance facilitates complete tumor resection, improves the overall mouse survival rate, and effectively discriminates between benign and malignant breast tissues in spontaneous breast cancer transgenic mice (area under the curve = 0.985; 95% confidence interval: 0.965, 1.0).
5. The probe could accurately identify mouse cancer tissues and normal tissues by rapid in vitro immersion (5min), and had great clinical transformation potential to identify intraoperative breast malignant tumor tissues/margins.
6. Tumor elimination efficiency was evaluated for mice that had been intravenously injected with NPs-Bev. The non-irradiated NPs-Bev -treated mice exhibited almost no tumor growth inhibition. However, upon X-ray irradiation, NPs-Bev-treated mice exhibited efficient RT sensitization and remarkably tumor regression compared to the mice that had only received X-ray RT.

Summary:
In summary, this study results present the potential benefits of a novel self-assembled, diagnostic, and therapeutic integrated nanoplatform for the precise breast cancer treatment strategies. Combining multimodal imaging with tumor-targeting strategies can shift the paradigm of surgical oncologic and diagnostic imaging and offer a unique opportunity to improve RT benefits. This study also provides a new method for recognition of malignant breast tissue: a rapid incubation method based on antibody-based nano-probe.

Poster Presentation

Disclosures: The authors have disclosed no financial interest.

340-A comparison of the dual-peak vs. dual-power acidoCEST MRI methods that measure pH

Presenter: Priya Trakru, University of Texas MD Anderson Cancer Center

Priya N. Trakru[1], Tianzhe Li[1], Ananya Sharma[2], Sanhita Sinharay[3], Marty Pagel[4]

[1]*University of Texas MD Anderson Cancer Center, Houston, TX*
[2]*GMC Saharanpur*
[3]*Indian Institute of Science Bangalore*
[4]*MD Anderson Cancer Center, Houston, TX*

Introduction:
The extracellular tumor microenvironment of many solid tumors has high acidosis due to upregulated glycolysis (known as the Warburg effect).[1] The noninvasive imaging of extracellular pH in the tumor microenvironment can be used to improve cancer diagnosis and the evaluations of anti-cancer therapies.[2] Chemical Exchange Saturation Transfer (CEST) MRI can measure pH using an exogenous, diamagnetic agent (known as acidoCEST MRI). The "dual-peak" method measures pH based on a ratio of two CEST signals from **TWO** unique protons on the agent while using **ONE** saturation power.[3] The "dual-power" method measures pH based on a ratio of two CEST signals from **ONE** proton on the agent while using **TWO** saturation powers.[4] We sought to compare the dual-peak vs. dual-power acidoCEST MRI methods to determine which method is best for clinical translation. Furthermore, we sought to determine the optimal saturation power and saturation time for each method. Finally, we sought to determine if the CEST-pH calibrations from either method are independent of concentration, T1 relaxation time, and temperature.

Methods:

We developed 200 samples of iopamidol (Isovue™, Bracco Diagnostics) with 8 pH values ranging from 6.2 to 7.3; 5 concentrations ranging from 5 to 50 mM; and 5 T1 values ranging from 0.4 to 2.0 sec (by doping samples with gadobutrol). We acquired 36,000 CEST spectra with 6 saturation powers ranging from 0.5 to 6 µT; 6 saturation times ranging from 0.5 to 6 sec; and at 5 temperatures ranging from 31°C to 43°C. We fit each spectrum with three Lorentzian lineshapes to obtain the amplitude of the CEST signals at 4.2 and 5.6 ppm, while also accounting for the direct saturation of water at 0 ppm. We then generated CEST-pH calibrations using a ratio of CEST signal amplitudes at 4.2 and 5.6 ppm (the dual-peak method). We also generated CEST-pH calibrations using a ratio of the 4.2 ppm CEST signal amplitude acquired with saturation powers of 2 vs. 4 µT; 1 vs. 4 µT, and 2 vs. 6 µT. We evaluated the precision of each calibration for measuring a range of pH 6.2-7.3.

Results:

CEST signals acquired with 0.5 µT saturation power or 0.5 sec saturation time were too low to be included in our analysis. The Lorentzian lineshape fitting showed outstanding fits for the remaining 25,000 CEST spectra.

Analysis with the dual-peak method showed outstanding correlations between estimated pH and true pH from a benchtop pH meter. Using practical saturation times and powers, the average standard deviation of the pH measurement was 0.04-0.06 pH units, depending on various conditions. This correlation was independent of concentration and T1 relaxation time, and was the same between 31°C and 43°C.

Analysis with the dual-power method showed relatively poor correlations between estimated pH and true pH from a benchtop pH meter. The best average standard deviation of the pH measurement was 0.45 pH units even when using optimal conditions for the comparison of 2 vs. 4 µT saturation power. Comparisons of 1 vs 4 µTand 2 vs 6 µT had even worse performance than 2 vs 4 µT.

Conclusions:

Our results demonstrated that the dual-peak method is superior to the dual-power method. Both methods can estimate pH independent of concentration and T1 relaxation time, and has negligible dependence on temperature between 31-43°C. Finally, a saturation power of 4 µT and saturation time of 3 sec is optimal for the dual-peak acidoCEST MRI method, producing an average standard deviation of 0.04-0.06 pH units for the pH measurement between pH 6.2-7.3.

Reference

1. Warburg O. On the origin of cancer cells. Science 1956;123:309–314.
2. Akhenblit PA, Pagel MD. Recent advances in targeting tumor energy metabolism with tumor acidosis as a biomarker of drug efficacy. J Cancer Sci Therapy 2016, 2016;8:20-29.
3. Chen LQ, Howison CM, Jeffery JJ, Robey IF, Kuo PH, Pagel MD. Evaluations of extracellular pH within in vivo tumors using acidoCEST MRI. Magn Reson Med 2014;72:1408-1417.
4. Longo DL, Sun PZ, Consolino L, Michelotti FC, Uggeri F, Aime S. A general MRI-CEST ratiometric approach for pH imaging: Demonstration of in vivo pH mapping with iobitridol. J Am Chem Soc 2014;136:14333-14336.

Poster Presentation

Disclosures: The authors have disclosed no financial interest.

341-Porphyrin dyes to visualize different cellular organelles through nonlinear optical imaging

Presenter: Anjul Khadria, California Institute of Technology (Caltech)

Anjul Khadria[1], Harry Anderson[2]

[1]*California Institute of Technology (Caltech), India*
[2]*University of Oxford, Oxford, Oxfordshire, United Kingdom*

Imaging organelles in live cells through nonlinear optical imaging will help understand several cellular mechanisms and design targetable therapeutics for a range of diseases.[1] Organic dyes that be used for nonlinear optical imaging absorbing light in the near-infrared (NIR) region based on two-photon excited fluorescence (TPEF) and second harmonic generation (SHG) offer various advantages, such as deep light penetration and reduced background signal.[2,3] Designing and synthesizing photostable dyes that can target different cellular organelles has been a longstanding challenge. Porphyrin-based dyes have been shown to possess excellent nonlinear optical characteristics without significant photobleaching.[4,5] In this work, we show that by engineering the molecular structure of porphyrin dyes, different cellular organelles can be targeted for nonlinear optical imaging. Upon performing live cell imaging in HEK 293T cells, we found that singly-charged cationic porphyrin dye, although amphiphilic, is taken by the cells to label the mitochondria giving bright TPEF signals. However, upon increasing the cationic charge from one to two, we found that the dye stains the endoplasmic reticulum of the cells to give bright TPEF and SHG signals. TPEF signals were also observed from the mitochondria but SHG signals were only visible from the endoplasmic reticulum. After a few hours, the cellular trafficking machinery drove out the dyes from the endoplasmic reticulum to the plasma membrane, generating strong TPEF and SHG signals from the plasma membrane. This is of significance because it is well known that the endoplasmic reticulum is a network of membranous tubules that are involved in lipid synthesis for the plasma membrane.[6] Observing the trafficking of lipids from the endoplasmic reticulum to the plasma membrane through SHG has not been possible before. We further observed that upon increasing the number of cationic groups from two to three, a perfect plasma membrane localization can be attained for several hours in a wide range of cells including cultured rat hippocampal neurons and neurons in mice brain slices. We attached an electron-donor and an electron-acceptor group to the triple-charged dye to make it an electrochromic voltage-sensitive dye, which can further make it useful to measure membrane potentials. We tested the membrane potential efficacy of the triple-charged dyes in live beating cardiomyocytes and found the voltage sensitivity, $\Delta F/F$ to be significantly high at around 60%. Given that the dyes are electrochromic they are extremely fast working in a time scale of nanoseconds to picoseconds, thus exceeding the milliseconds time scale of a typical neuronal action potential by several orders of magnitude.[7] The high voltage sensitivity of the singly-charged porphyrin dye has been demonstrated in lipid bilayers.[8] This is very promising not only in the field of neurobiology but also in cell biology because the doubly-charged dyes that locate in the endoplasmic reticulum can be used to measure potentials in endoplasmic reticula. In preliminary studies, the porphyrin dyes were also seen to generate throng nonlinear optical signals from *E.coli* bacteria thus displaying potential to image and study microbes.

We further engineered the dyes to switch off their TPEF while keeping the SHG on, thus making it purely SHG-based dye that does not undergo any photobleaching. The advantages of SHG-only dyes are: (a) SHG does not cause the production of reactive oxygenated species and (b) SHG signals are not generated from isotropic media.[4] We introduced a copper element in the center of the porphyrin dye which

made it pure-SHG dye and confirmed its efficacy in the HEK 293T cells.[5]

Overall our approach to changing the number of cationic charges in the porphyrin dyes to target and image different cellular compartments offers a huge potential to design more dyes as well as use these dyes to study cellular physiology.

Reference

1. Zhu, H., Fan, J., Du, J. & Peng, X. Fluorescent Probes for Sensing and Imaging within Specific Cellular Organelles. Acc. Chem. Res. 49, 2115–2126 (2016).
2. Marder, S. R. Organic nonlinear optical materials: where we have been and where we are going. Chem. Commun. 131–134 (2006).
3. Pawlicki, M., Collins, H. A., Denning, R. G. & Anderson, H. L. Two-photon absorption and the design of two-photon dyes. Angew. Chem. Int. Ed. 48, 3244–3266 (2009).
4. Reeve, J. E., Anderson, H. L. & Clays, K. Dyes for biological second harmonic generation imaging. Phys. Chem. Chem. Phys. 12, 13484–13498 (2010).
5. Khadria, A. et al. Porphyrin Dyes for Nonlinear Optical Imaging of Live Cells. iScience 4, 153–163 (2018).
6. Schwarz, D. S. & Blower, M. D. The endoplasmic reticulum: structure, function and response to cellular signaling. Cell. Mol. Life Sci. 73, 79–94 (2016).
7. Khadria, A. Tools to measure membrane potential of neurons. Biomed. J. (2022). doi:https://doi.org/10.1016/j.bj.2022.05.007
8. Reeve, J. E. et al. Porphyrins for probing electrical potential across lipid bilayer membranes by second harmonic generation. Angew. Chem. Int. Ed. 52, 9044–9048 (2013).

Poster Presentation

Disclosures: The authors have disclosed no financial interest.

342-In vivo PET imaging of 89Zr-labelled Natural Killer cell trafficking to solid tumour under the influence of a therapeutic antibody

Presenter: Truc Pham, King's College London

Truc T. Pham[1], Alicia Chenoweth[2], Gabriel Osborn[3], Philip J. Blower[4], Sophia Karagiannis[3], Michelle T. Ma[3]

[1]King's College London, London, London, United Kingdom
[2]Cancer Antibody Discovery & Immunotherapy Group, St. Johnâ's Institute of Dermatology, School of Basic & Medical Biosciences, Kingâ's College London, London, United Kingdom
[3]King's College London, London, United Kingdom
[4]King's College London, London, UK, United Kingdom

Introduction:

Natural killer (NK) cells are a component of innate immunity, they can detect and control early signs of cancer without prior sensitisation or immunisation. NK cells can kill cancer cells via a process known as antibody-dependent cell-mediated cytotoxicity (ADCC).[1] In this process, the binding of a tumour-associated antigen (TAA)-specific antibody to the cancer cells recruits NK cells to the tumour site and activates their killing mechanism.[2] This ability has been employed for cancer immunotherapy.[3] PET imaging permits longitudinal *in vivo* tracking and quantification of radiolabelled immune effector cell infiltration.[4] Thus, this study aimed to use PET imaging to demonstrate the recruitment of NK cells within the tumour environment, with and without a therapeutic antibody treatment.

Methods:

NK cells were isolated from healthy human volunteers and expanded *ex vivo*. [^{89}Zr]Zr-oxine was synthesised using a kit.[5] NK cells were radiolabelled with [^{89}Zr]Zr-oxine at RT for 15 min in PBS. Various *in vitro* functions of [^{89}Zr]Zr-oxine labelled NK cells were assessed including viability, proliferation, migration and ADCC using the therapeutic monoclonal trastuzumab antibody against HER2 overexpressing human breast cancer cell lines HCC1954 and SKBR3. Flow cytometry was used to monitor NK cell surface markers. To visualise the effects of trastuzumab treatment on NK cell tumour infiltration *in vivo*, [^{89}Zr]Zr-oxine labelled NK cells were administered intravenously together with a therapeutic dose of trastuzumab (5 mg/kg) to mammary fat pad HCC1954 tumour-bearing NSG mice (n=4). In a control group, tumour-bearing mice were injected with [^{89}Zr]Zr-oxine labelled NK cells and PBS only (n=4). PET imaging was performed on days 1, 3 and 7 post cell injection. Organs were collected at the end of imaging study to further quantify cell biodistribution.

Results:

[^{89}Zr]Zr-oxine was reproducibly synthesised with labelling yields of 92.1±3.5% (n=10) and used to radiolabel *ex vivo* expanded NK cells with moderate labelling efficiencies of 39.4±6.6% (n=23). The radiolabelling did not affect NK cell viability and characteristic CD16/CD56 cell surface expression. ^{89}Zr-labelled NK cells exhibited comparable ADCC functions to those of non-radiolabelled NK cells. Cell migration assay demonstrated that ^{89}Zr-labelled cells presented typical NK migration responses to stimuli.

PET/CT imaging showed that NK cells migrated from lungs to reside mostly in liver and spleen over the 7 days (Figure A). *Ex vivo* flow-cytometric analyses of these mouse tissues detected huCD45$^+$ human leukocytes, which were further confirmed as human CD56$^+$CD16$^+$ NK cells. Bone uptake of ^{89}Zr was observed at all time points. This is a known phenomenon in multiple ^{89}Zr cell tracking studies due to osteotropic properties of weakly chelated ^{89}Zr released from cells. Radioactive signals were visualised and quantified in the tumours of both groups (Figures A and B), with stronger ^{89}Zr signals in trastuzumab-treated group, compared to buffer only controls, especially on days 1 and 3; this effect was less prominent on day 7. *Ex vivo* quantification of ^{89}Zr in tumours on day 7 was consistent with PET imaging data, with ^{89}Zr tumour concentration in trastuzumab-treated mice higher than that of non-treated mice (0.81 ± 0.24 vs 0.66 ± 0.10 %ID/g, n=4/group, respectively).

Conclusion:

Ex vivo expanded NK cells can be radiolabelled with [^{89}Zr]Zr-oxine at levels required for preclinical PET imaging while maintaining their basic cellular and cytotoxic functions. The results showed that NK cells traffic to HER2+ tumour even without trastuzumab and this can be tracked with PET imaging for up to 7 days. Trastuzumab treatment increased HER2+ tumour infiltration by NK cells compared to that in the non-treated group. This study demonstrates the possibility of using PET imaging to track NK cells in real-time and to explore the effects of therapeutic antibodies on NK cell recruitment to solid tumours in cancer immunotherapy.

Reference

1. Ilieva, K. M., Fazekas-Singer, J., Achkova, D. Y., Dodev, T. S., Mele, S., Crescioli, S., Bax, H. J., Cheung, A., Karagiannis, P., Correa, I., Figini, M., Marlow, R., Josephs, D. H., Beavil, A. J., Maher, J., Spicer, J. F., Jensen-Jarolim, E., Tutt, A. N. & Karagi-

annis, S. N. Functionally active Fc mutant antibodies recognizing cancer antigens generated rapidly at high yields. Front. Immunol. 8, 1112 (2017).
2. Miller, S. E., Tummers, W. S., Teraphongphom, N., van den Berg, N. S., Hasan, A., Ertsey, R. D., Nagpal, S., Recht, L. D., Plowey, E. D., Vogel, H., Harsh, G. R., Grant, G. A., Li, G. H. & Rosenthal, E. L. First-in-human intraoperative near-infrared fluorescence imaging of glioblastoma using cetuximab-IRDye800. J. Neurooncol. 139, 135–143 (2018).
3. Shimasaki, N., Jain, A. & Campana, D. NK cells for cancer immunotherapy. Nat. Rev. Drug Discov. 19, 200–218 (2020).
4. Man, F., Lim, L., Volpe, A., Gabizon, A., Shmeeda, H., Draper, B., Parente-Pereira, A. C., Maher, J., Blower, P. J., Fruhwirth, G. O. & T.M. de Rosales, R. In Vivo PET Tracking of 89Zr-Labeled Vγ9Vδ2 T Cells to Mouse Xenograft Breast Tumors Activated with Liposomal Alendronate. Mol. Ther. 27, 219–229 (2019).
5. Man, F., Khan, A. A., Carrascal-Miniño, A., Blower, P. J. & T.M. de Rosales, R. A kit formulation for the preparation of [89Zr]Zr(oxinate)4 for PET cell tracking: White blood cell labelling and comparison with [111In]In(oxinate)3. Nucl. Med. Biol. 90–91, 31–40 (2020).

Poster Presentation

Disclosures: The authors have disclosed no financial interest.

343-Simultaneous evaluations of pH and enzyme activity using a cat-acido-CEST MRI contrast agent with three CEST signals

Presenter: Elijah Gonzalez, MD Anderson Cancer Center

Elijah Gonzalez[1], Alyssa Pollard[2], Xiaofei Liang[3], Chathuri J. Kombala[3], Sanjaya Lokugama[4], Aikaterini Kotrotsou[5], Tianzhe Li[6], Marty Pagel[3]

[1]MD Anderson Cancer Center
[2]MD Anderson Cancer Center, Smithtown, NY
[3]MD Anderson Cancer Center, Houston, TX
[4]University of Arizona
[5]University of Texas MD Anderson Cancer Center, Houston, Texas
[6]University of Texas MD Anderson Cancer Center, Houston, TX

Abstract Body:
The extracellular tumor microenvironment of many solid tumors has high acidosis and high protease activity.[1,2] Simultaneously assessing both characteristics may improve diagnostic evaluations of aggressive tumors and the effects of anticancer treatments. Noninvasive imaging methods have employed Chemical Exchange Saturation Transfer (CEST) MRI to detect enzyme activity (catalyCEST MRI)[3] or to measure pH (acidoCEST MRI).[4] We hypothesized that the designs of catalyCEST and acidoCEST agents can be combined to develop a single cat-acido-CEST agent that can simultaneously measure pH and evaluate protease activity. The design of our cat-acido-CEST agent is based on 4-aminosalicylic acid with a Phe-Lys-PABA ligand.[5] This agent has a CEST signal at 5.0 ppm from the aryl amide that disappears after the agent is treated with cathepsin B, and a second CEST signal at 9.2 ppm from the salicylic acid that is dependent on pH. However, the CEST signal from the aryl amide is also pH-dependent, and enzyme cleavage also changes the CEST signal from the salicylic acid, complicating the separate evaluations of pH and enzyme activity.
To solve this problem, we included a methylsulfonylanthranilic acid moiety that is conjugated to the 4-aminosalicylic acid through a PEG linker.[6] A methylsulfonylanthranilic acid generates a CEST signal at 7.3 ppm that is independent of pH, while the PEG linker insulates the CEST signal of the methylsulfonylanthranilic acid from the proteolytic cleavage of the peptidyl ligand by cathepsin-B. This "control" CEST signal at 7.3 ppm can be directly compared with the pH-dependent CEST signal at 9.2 ppm, and the enzyme-dependent CEST signal at 5.0 ppm.
The synthesis of our cat-acido-CEST agent is convergent. The amino position of 5-hydroxyanthranilic acid was protected by a tert-butoxycarbonyl (boc) group, and the carboxylate position was protected by a benzyl group. One terminal alcohol group of tetraethylene glycol (TEG) was functionalized by a toluenesulfonyl (tosyl) group, and the other terminal alcohol group was functionalized by a propylene group. The unprotected alcohol in 5-hydroxyanthranilic acid then reacted with the tosyl group in the TEG moiety. The salicylic acid moiety was synthesized by a benzyl protection of both the carboxylate group and the phenol group. This adduct was then selectively iodinated at the 5-position by *N*-iodosuccinimide. This salicylic acid moiety will be attached to the conjugated anthranilic acid and TEG moiety by a Suzuki reaction at the alkene group of the TEG moiety and the iodinated position of the salicylic acid. The amino position of anthranilic acid in the coupled moiety will be deprotected, then mesylated. The peptide moiety was synthesized by first coupling a p-aminobenzyl alcohol (PABA) with a lysine amino acid which was commercially protected by a fluorenylmethyloxycarbonyl (fmoc) group at the alpha-amino group and a boc group at the zeta-amino group. Then, the N-terminus of the peptidyl group was deprotected, and a boc-protected phenylalanine was coupled. Finally, the PABA group was functionalized by coupling the alcohol with p-nitrophenol. This peptidyl group will be attached to the mesylated adduct by a substitution of the unprotected amino group of salicylic acid moiety at the p-nitrophenol position. A global deprotection of this adduct using trifluoroacetic acid will yield the desired final product.

Conclusions:
Our cat-acido-CEST MRI contrast agent with two CEST signals at 5.0 and 9.2 ppm can measure pH while also detecting enzyme activity. However, both CEST signals depend on pH and enzyme activity, necessitating a third "control" CEST signal to disentangle the imaging of both biomarkers. The synthesis of our improved cat-acido-CEST MRI contrast agent with a third "control" CEST signal is nearing completion.

Reference
1. Warburg O. On the origin of cancer cells. Science 1956;123:309−314.
2. Buck MR, Karustis DG, Day NA, Honn KV, Sloane BF. Degradation of extracellular-matrix proteins by human cathepsin B from normal and tumour tissues. Biochem J 1992;282:273-278.
3. Hingorani DV, Montano LA, Randtke EA, Lee YS, Cárdenas-Rodríguez J, Pagel MD. A single diamagnetic catalyCEST MRI contrast agent that detects cathepsin B enzyme activity by using a ratio of two CEST signals. Contrast Media Molec Imaging 2016;11:130-138.
4. Chen LQ, Howison CM, Jeffery JJ, Robey IF, Kuo PH, Pagel MD. Evaluations of extracellular pH within in vivo tumors using acidoCEST MRI. Magn Reson Med 2014;72:1408-1417.
5. Kombala CJ, Lokugama SD, Kotrotsou A, Li T, Pollard AC, Pagel MD. Simultaneous evaluations of pH and enzyme activity with a CEST MRI contrast agent. ACS Sensors 2021;6:2535-4544.
6. Song X, Yang X, Banerjee SR, Pomper MG, McMahon MT. Anthranilic acid analogs as diamagnetic CEST MRI contrast agents that feature an intramolecular-bond shifted hydrogen. Contrast Media Molec Imaging 2015;10:74-80.

Poster Presentation

Disclosures: The authors have disclosed no financial interest.

344-PET Imaging of PD-L1 Expression in Gastric Tumor Cells and Host Cells

Presenter: Emma Brown, Washington University in St. Louis

Emma L. Brown[1], Sandeep Surendra Panikar[2], Rachel DeWeerd[3], William L. Smith[3], Zachary T. Fisher[4], Patricia M. Ribeiro Pereira[1]

[1]Washington University in St. Louis
[2]Washington University School of Medicine, St. Luois
[3]Washington University in St. Louis, St. Louis, MO
[4]Washington University School of Medicine, St. Louis, MO

Introduction:
Programmed cell death protein ligand-1 (PD-L1) blockade, including antibody therapeutics, has transformed cancer treatment. However, many patients still do not respond to treatment, particularly in heterogeneous cancers[1]. Although PD-L1 expression is detected in approximately 40% of gastric cancers[2,3], 87% of patients with gastric cancer were non-responders to anti-PD-L1 antibody therapy[4]. PD-L1 expression is highly dynamic and complex; it is highly restricted to lymphocytes, and it is more frequent on immune cells than on tumor cells[5]. The complexity of PD-L1 expression has made it difficult to select tumors which are likely to respond to immune checkpoint inhibitors as biopsy-based diagnostic tests can be inaccurate, due to high spatial and temporal heterogeneity of PD-L1 expression[6]. ImmunoPET using radiolabeled antibodies targeted towards PD-L1 may offer a complementary technique in patient selection for immune checkpoint therapy, as PD-L1 protein levels can be assessed non-invasively in the whole body giving information about PD-L1 in both tumor and host cells[7]. Here, we used two FDA-approved anti-PD-L1 antibodies, Avelumab and Atezolizumab, human and murine PD-L1 cross-reactive to visualize PD-L1 protein levels in gastric cancer and host cells, particularly tumor-associated macrophages (TAMs).

Methods:
Animals: NCIN87 gastric cells were s.c. implanted in athymic nude mice (n=2-3 mice/cohort). Treatments: To deplete macrophages, mice received one dose of clodronate liposomes or neutral liposomes as control (175 µl, i.p.) 48 h before radiotracer injection (**Figure**). Radiolabeling: Avelumab or Atezolizumab coupled with the DFO chelator were labeled with the positron emitter zirconium-89. Imaging: PD-L1 levels at 48 h after radiotracer injection were monitored via PET/CT images and *ex vivo* biodistribution of [^{89}Zr]Zr-DFO-Avelumab (52-56 µCi, 50 µg protein, >98% RCP) or [^{89}Zr]Zr-DFO-Atezolizumab (42-46 µCi, 50 µg protein, >98% RCP). Immunofluorescence: NCIN87 tumor cells were incubated with Avelumab or Atezolizumab labeled with Alexa-488 fluorophore.

Results:
In a head-to-head comparison of antibody biodistribution, measured in *ex vivo* tissues, ^{89}Zr-Avelumab consistently showed higher NCIN87 tumor to organ ratios in major organs (blood, liver, spleen, heart, lungs, bone, lymph nodes) compared to ^{89}Zr-Atezolizumab, with a 2.8-fold higher tumor:heart ratio and over 2-fold higher tumor:lung and tumor:bone ratios (**Persuasive Data A**). The higher binding of Avelumab in NCIN87 cancer cells compared with Atezolizumab was further validated by immunofluorescence. PET imaging similarly displayed a more favorable biodistribution of ^{89}Zr-Avelumab, with higher uptake in NCIN87 gastric tumors compared to ^{89}Zr-Atezolizumab, despite this model typically expressing heterogeneous levels of PD-L1 (**Persuasive Data B**). While ^{89}Zr-Atezolizumab accumulates in liver and spleen due to Fc receptors in liver and PD-L1 expression on splenic lymphocytes, there was minimal NCIN87 tumor accumulation (**Persuasive Data B**). Unlike Atezolizumab, Avelumab has a wild-type Fc region suggesting that Avelumab accumulation in tumors could be a result of interactions with PD-L1 and Fc-γ receptors expressed by TAMs[8]. In our studies, macrophage depletion decreased uptake of ^{89}Zr-Avelumab in tumor, liver spleen and lymph nodes on PET imaging (**Persuasive Data B**). From this preliminary work, ongoing work will assess the distinct interactions of Avelumab with tumor and host cells and the regulation of PD-L1 in these cells that could explain the low response of gastric cancer to PD-L1 antibody therapy.

Conclusions:
This study demonstrates that ^{89}Zr-Avelumab outperforms ^{89}Zr-Atezolizumab in monitoring PD-L1 expression in a gastric tumor model, both *in vivo* and *in vitro*. Macrophages appear to play a role in ^{89}Zr-Avelumab tumor uptake and ongoing studies are using PET to investigate the distinct regulation of PD-L1 in tumor and host cells. ImmunoPET serves as a non-invasive tool to monitor the dynamic PD-L1 expression *in vivo*. Ongoing work is investigating the modulation of systemic and local PD-L1 expression, using ^{89}Zr-Avelumab ImmunoPET as a non-invasive tool to monitor these dynamic processes.

Reference
1. Ribas, A. & Wolchok, J. D. Cancer immunotherapy using checkpoint blockade. Science 359, 1350–1355 (2018).
2. Thompson, E. D. et al. Patterns of PD-L1 expression and CD8 T cell infiltration in gastric adenocarcinomas and associated immune stroma. Gut 66, 794–801 (2017).
3. Muro, K. et al. Pembrolizumab for patients with PD-L1-positive advanced gastric cancer (KEYNOTE-012): a multicentre, open-label, phase 1b trial. Lancet. Oncol. 17, 717–726 (2016).
4. Moehler, M. et al. Phase III Trial of Avelumab Maintenance After First-Line Induction Chemotherapy Versus Continuation of Chemotherapy in Patients With Gastric Cancers: Results From JAVELIN Gastric 100. J. Clin. Oncol. Off. J. Am. Soc. Clin. Oncol. 39, 966–977 (2021).
5. Noguchi, T. et al. Temporally Distinct PD-L1 Expression by Tumor and Host Cells Contributes to Immune Escape. Cancer Immunol. Res. 5, 106–117 (2017).
6. McLaughlin, J. et al. Quantitative Assessment of the Heterogeneity of PD-L1 Expression in Non-Small-Cell Lung Cancer. JAMA Oncol. 2, 46–54 (2016).
7. Bensch, F. et al. (89)Zr-atezolizumab imaging as a non-invasive approach to assess clinical response to PD-L1 blockade in cancer. Nat. Med. 24, 1852–1858 (2018).
8. Arlauckas, S. P. et al. In vivo imaging reveals a tumor-associated macrophage-mediated resistance pathway in anti-PD-1 therapy. Sci. Transl. Med. 9, (2017).

Poster Presentation

Disclosures: The authors have disclosed no financial interest.

345-Development of 2-(diphenylphosphaneyl)phenyl [18F]sulfurofluoridate as a Sulfur-Fluoride Exchange (SuFEx) Building Block for Bioorthogonal Chemistry

Presenter: Mirkka Sarparanta, University of Helsinki

Mirkka Sarparanta[1], Anisa Biti[2], Filip Ekholm[1]

[1]*University of Helsinki, Helsinki, Finland*
[2]*University of Helsinki, Helsinki, Finland, Finland*

Background and Aims:
The sulfur-fluoride exchange (SuFEx) chemistry has been recently reported as a straight-forward approach towards the rapid and mild radiofluorination of a plethora of radiolabeling precursors and radiopharmaceuticals.[1,2] We hypothesized that the rapid, room temperature SuFEx reactions carried out in strictly non-aqueous media could be used to radiolabel triaryl phosphines, the bioorthogonal reactant in the classic Staudinger ligation with azides. Despite the widespread use of the Staudinger ligations in cell labeling, triaryl phosphines have due to their sensitivity remained notoriously difficult to radiolabel, yet alone with fluorine-18 using the S_N2 nucleophilic substitution reactions that typically require basic conditions and elevated temperatures. Specifically, we aimed to harness the advantages of the SuFEx radiolabeling to develop a ^{18}F-radiolabeled triaryl phosphine to facilitate the use of the perfluoroaryl azide (PFAA) Staudinger ligation, the fastest reported Staudinger variation to date (k_2=18 m^{-1} s^{-1}), as a bioorthogonal building block in biomolecular radiofluorination.

Materials and Methods:
The radiolabeling precursor 2-(diphenylphosphaneyl)phenyl sulfurofluoridate (**1**, Scheme 1, A) was synthesized using reported procedures with *ex situ* generated sulfuryl fluoride[3]. For demonstration of feasibility of the PFAA Staudinger ligation with **1**, it was reacted with an in-house synthesized PFAA-mannosamine[4] (**2**, Scheme 1, A), a substrate for metabolic glycoengineering of cells, and the reaction monitored with ^{19}F and ^{31}P NMR. Radiolabeling of **1** with [18F]fluoride was explored using two different conditions in the SuFEx exchange reaction (Scheme 1, B).

Results:
2-(diphenylphosphaneyl)phenyl sulfurofluoridate was successfully synthesized with an overall yield of 76% and reacted with the PFAA-mannosamine in vitro as evidenced by the characteristic 6.24 ppm and 45.47 ppm peaks in the ^{31}P and ^{19}F NMR, respectively. Radiolabeling of **1** with fluorine-18 was first attempted with [^{18}F]fluoride as the $^{18}F^-$/Kryptofix2.2.2/K^+ complex in anhydrous DMSO at 25°C, but as this gave highly variable results, the 0.5 M K_2CO_3 eluent and Kryptofix2.2.2 were replaced with 0.5 M K_3PO_4 and Bu_4NOMs, previously reported optimal for aliphatic radiofluorination of base-sensitive substrates[5]. The latter strategy yielded **[^{18}F]1** with radiochemical conversion (RCC) of 69.1±9.2% starting from 250–800 MBq of fluorine-18 (n=6) determined by HPLC with radiodetection. **[^{18}F]1** was stable in 2% FBS in 1×HBSS up to 120 minutes (84% of radiolabel intact).

Conclusions:
In conclusion, we have successfully developed a stable triaryl phosphine bearing an aryl fluorosulfate moiety for SuFEx radiolabeling for the perfluoroaryl azide Staudinger ligation expanding the selection of fluorine-18- radiolabeled building blocks for bioorthogonal chemistry.

Acknowledgements: Financial support from the Academy of Finland (decision nos. 318422, 320102 and 346122) and the Doctoral Program in Drug Research (DPDR), University of Helsinki is gratefully acknowledged.

Reference
1. Zheng, Q.; et al. J Am Chem Soc 2021, 143, 3753-3763, doi:10.1021/jacs.0c09306.
2. Walter, N.; et al. European Journal of Medicinal Chemistry 2022, 237, doi:10.1016/j.ejmech.2022.114383.
3. Veryser, C.; et al. Org Lett 2017, 19, 5244-5247, doi:10.1021/acs.orglett.7b02522.
4. Sundhoro, M.; et al. Angew Chem Int Ed 2017, 129, 12285-12289, doi:10.1002/ange.201705346.
5. Bratteby, K.; et al. ACS Pharmacol Transl Sci 2021, 4, 1556-1566, doi:10.1021/acsptsci.1c00133.

Poster Presentation

Disclosures: The authors have disclosed no financial interest.

346-SiPM-based confocal laser scanning microscopy for in vivo multicolor NIR-I/-II imaging

Presenter: Tianyu Yan, Xidian University

Tianyu Yan[1], Xinyu Wang[1], Siting Liu[2], Dawei Fan[2], Xinyi Xu[3], Xueli Chen[3]

[1]*Xidian University, China*
[2]*Xi'an, Shaanxi, China*
[3]*Xidian University, Xian, Shaanxi, China*

Confocal laser scanning microscopy (CLSM) has become a valuable tool in biomedical fields due to its excellent performance in spatial resolution and image signal-to-noise ratio (SNR). Using the illumination mode of point-scanning, as well as blocking the signal outside the focal plane from entering the detector by a conjugate pinhole, CLSM can avoid the high background and pixel-to-pixel interference, realizing the axial tomographic microscopy for biological samples. However, the wavelength bands of the current mainstream commercial CLSM solutions are mainly using visible and the first near-infrared (NIR-I, 780-900 nm) light. Due to the scattering and absorption by biological tissues and the endogenous fluorescence background, the deep imaging ability of this CLSM scheme is limited. The second window in the NIR region, NIR-II (900-1700 nm), has gained increasing attention in the biomedical field in recent years because of its lower tissue scattering and autofluorescence background. It has been reported that, by using NIR-II light, point-scanning based confocal/two-photon microscopy can achieve high-quality fluorescence imaging of hundreds of microns inside living animal tissue. Currently, the realization of NIR-II CLSM requires the use of NIR photomultiplier (PMT) made of InGaAs materials. The cost of such PMT is extremely high, with common cost of tens of thousands of dollars, and requires long pre-cooling time to reduce dark current noise to work effectively. In addition, InGaAs PMT requires a supply voltage of several hundred volts and strictly limits the luminous flux to avoid device damage. Most importantly, it lacks the response to visible and NIR-I light. With so many constraints, the quantum efficiency of InGaAs PMT is only 1-3%. Therefore, an efficient and low-cost detector is currently needed to support the popularization of NIR-II CLSM. Silicon photomultiplier (SiPM) is a kind of high-sensitivity detector composed of avalanche photodiode arrays operating in Geiger mode. SiPM has the advantages of small size, low cost, and high reliability, which is considered as an efficient and inexpensive alternative to PMT. The wavelength response range of the NIR-sensitive SiPM can cover NIR-I and part of NIR-II regions. Thus, we used a home-built CLSM and a customized SiPM module to realize a SiPM-based NIR-I/NIR-II multicolor CLSM scheme for the first time, in which the cost of the complete SiPM module is only hundreds of dollars. Using the NIR fluorescent probe, IR-780, as contrast agent, the imaging performance of SiPM and PMT in NIR-I and NIR-II CLSM were compared. Results indicated that the SiPM showed a better image SNR than PMT. Furthermore, SiPM was proved to be sufficient

to support diffraction-limited spatial resolution and efficient detection of low-concentration fluorophores. Finally, by imaging blood vessels inside living mouse tissues, our SiPM-based CLSM scheme can realize the three-dimensional reconstruction and optical sectioning of blood vessels in both NIR-I and NIR-II regions. In conclusion, our work demonstrated the potential of SiPM as an efficient, low-cost detector for *in vivo* multicolor NIR-I and NIR-II fluorescence microscopy.

Poster Presentation

Disclosures: The authors have disclosed no financial interest.

347-Small animal fluorescent signal detection system based on single pixel detectors and multi-channel spatial coding-decoding

Presenter: Dawei Fan,

Dawei Fan[1], Tianyu Yan[2], Ying He[1], Siting Liu[1], Xueli Chen[3]

[1]Xi'an, Shaanxi, China
[2]Xidian University, China
[3]Xidian University, Xian, Shaanxi, China

Small animal fluorescence imaging technology is one of the important technical tools for pre-clinical research in many fields such as gene expression, tumor detection, medical treatment, and drug development. The cores of the technology are specific optical molecular markers and highly-sensitive optical detection devices. To achieve highly-sensitive detection of fluorescence signals, small animal fluorescence imaging technology usually employs scientific-grade-cooled charge-coupled device (CCD) cameras or electron multiplication CCD (EMCCD) cameras with high quantum efficiency as fluorescence signal detectors. However, the sensitivity of CCD or EMCCD in detecting weak fluorescent signals is still slightly inadequate, inducing the problems of long image acquisition time and high cost, which are not conducive to the promotion and wide application of small animal fluorescence imaging technology. Single-point detectors such as silicon photomultiplier tubes (SiPM) offer higher sensitivity and signal gain for faint light detection, while enabling the detection of faint fluorescent signals from live small animals at a lower system cost. Thus, we developed a novel small animal fluorescent signal detection system by using a single-point detector array instead of EMCCD as the fluorescence signal detection module and incorporating the multi-channel spatial encoding capability of the digital micromirror device (DMD). The fluorescent signals on the animal surface are first delivered on the DMD that is divided into several parts determined by the number of SiPM. The projected fluorescence signal is spatially encoded in multiple channels by controlling the pixels of the DMD, after which it is focused on the SiPM array according to the segmentation area of the DMD. Finally it is restored to a fluorescent signal distribution image by a decoding algorithm. To improve the image quality, we use differential coding to reduce the interference of noise on the detection results. The results on mouse tumor models show that the system can clearly image the location, shape and contour size of tumor, demonstrating the potential of the system for the application of fluorescent signal detection in small animal imaging.

Poster Presentation

Disclosures: The authors have disclosed no financial interest.

348-Low-dose EDB Fibronectin Gd-DOTA Probe for Pancreatic Cancer Mouse Model Targeting Magnetic-optical Dual-modality Imaging In Vivo

Presenter: Wenjia Zhang, Peking Union Medical College Hospital

Wenjia Zhang[1], Yang Du[2], Huadan Xue[3], Jie Tian[4]

[1]Peking Union Medical College Hospital, Beijing, Beijing, China
[2]Chinese Academy of Sciences, Beijing, China
[3]Beijing, Beijing, China
[4]Chinese Academy of Sciences, Beijing, Beijing, China

Purpose:

Pancreatic ductal adenocarcinoma (PDAC) is a lethal malignancy worldwide. PDAC is a hypovascular cancer surrounded by a dense stroma, which is recognized as a critical factor of tumor progression through direct effects on cancer cells and indirect effects on the tumor microenvironment[1]. Multimodal molecular imaging of onco-proteins is a promising method for accurate, early detection of the disease. Extradomain-B fibronectin (EDB-FN), a high-expression onco-protein in the tumor extracellular matrix, can realize targeted and effective molecular imaging[2]. Here, we prepared a novel Gd-based contrast agent of EDB-Gd-IRDye800cw to perform fluorescence molecular imaging and molecular MRI, which could complement its advantages. Thus, multi-modal imaging with EDB-targeted contrast agent is a promising strategy for accurate, early and safe detection of PDAC.

Material and Method:
The EDB-FN targeting peptide and near infrared dye IRDye800cw were conjugated to the Gd-DOTA (EDB-Gd-IRDye800cw) for the PDAC-targeting multimodality imaging. Five-week-old BALB/c nude mice were implanted with human pancreatic stellate cells (PSC) and human PDAC cell lines (Bxpc-3) at a ratio of 1:1 to establish the subcutaneous and orthotopic PDAC xenograft models. Mice were intravenously injected with EDB-Gd-IRDye800cw or Gd-DOTA at the Gd concentration of 0.05 mmol/kg, which is merely a half of clinical dose. T1 mapping MRI and fluorescence imaging were performed on both subcutaneous and orthotopic models. The TBR (Tumor background ratio) of fluorescence intensity and the ratio of T1 value reduction (T1d%) were analyzed and compared quantitatively. Histological and immunofluorescence analyses were used as references for ex vivo validation.

Results:
The concentration of EDB-Gd-IRDye800cw showed a linear correlation with fluorescence intensity and T1 relaxation time in vitro. For in vivo T1 mapping MRI, the T1d% showed the most significant difference at 30 minutes post-injection in subcutaneous (EDB-Gd-IRDye800cw group: 68.19±19.18% vs. Gd-DOTA group: 84.99±3.77%, $p< 0.05$) and orthotopic (EDB-Gd-IRDye800cw group: 60.92±19.18% vs. Gd-DOTA group: 96.76±12.21%, $P<0.05$) PDAC xenograft models. For in vivo fluorescence imaging, at 30 minutes post-injection, the TBR of fluorescence intensity showed the most significant difference between two groups (EDB-Gd-IRDye800cw group: 1.11±0.03 vs. Gd-DOTA group: 0.88±0.05, $p=0.002$) in subcutaneous models, while the TBR of fluorescence intensity showed no significant differences between two groups in orthotopic models (EDB-Gd-IRDye800cw group: 1.04±0.04 vs. Gd-DOTA group: 0.95±0.07, $p>0.05$) due to the limited tissue penetration of fluorescence imaging. Immunofluorescence confirmed the targeting of EDB-Gd-IRDye800cw to EDB-FN in both PDAC models.

Conclusion: Our dual-modal imaging findings indicate that fluorescence molecular imaging and molecular MRI could complement its advantages and translation of oncoprotein targeted dual-modal imaging with low-dose EDB-Gd-IRDye800cw to humans, which might provide a promising imaging technique to detect PDAC precisely compared to standard Gd-DOTA contrast agents. Moreover, these findings suggest that EDB-FN targeting MRI might have clinical application to evaluate post-treatment fibrotic changes in the tumor bed and help with clinical management in the future, which traditional CT and MRI are unable to distinguish neoadjuvant chemotherapy induced fibrotic response from residual cancer[3].

Reference

1. N. Hosein, R. A. Brekken, A. Maitra, Nat Rev Gastroenterol Hepatol 2020, 17, 487.
2. Y. Li, Z. Han, S. Roelle, A. DeSanto, R. Sabatelle, R. Schur, Z. R. Lu, Mol Pharm 2017, 14, 3906.
3. D. J. Erstad, M. Sojoodi, M. S. Taylor, V. C. Jordan, C. T. Farrar, A. L. Axtell, N. J. Rotile, C. Jones, K. A. Graham-O'Regan, D. S. Ferreira, T. Michelakos, F. Kontos, A. Chawla, S. Li, S. Ghoshal, Y. I. Chen, G. Arora, V. Humblet, V. Deshpande, M. Qadan, N. Bardeesy, C. R. Ferrone, M. Lanuti, K. K. Tanabe, P. Caravan, B. C. Fuchs, Clin Cancer Res 2020, 26, 5007.

Poster Presentation

Disclosures: The authors have disclosed no financial interest.

349-Quantitative flow cytometry based determination of targeted antibody delivery in an EBC-1 tumor xenograft model using an enzyme-activatable, dual fluorescent biosensor

Presenter: Jason Giurleo, Regeneron Pharmaceuticals

Jason T. Giurleo[1], Travis Shaffer[2], Sai Kiran Sharma[1], Kevin Guley[3], Howard Willett[1], Xiaoxi Ling[4], Sosina Makonnen[1], Shu Mao[1], Frank Delfino[1], John DaSilva[1], Dangshe Ma[5]

[1]Regeneron Pharmaceuticals, Tarrytown, NY
[2]Regeneron Pharmaceuticals, Briarcliff, NY
[3]Regeneron Pharmaceuticals
[4]Regeneron Pharmaceuticals, White Plains, NY
[5]Regeneron Pharmaceuticals, Tarrytown

Leveraging the target specificity of monoclonal antibodies to deliver payloads as antibody-drug conjugates (ADCs) represents an established therapeutic approach for treating advanced cancers with several recent FDA approvals. Interestingly, quantitative determination of antibody uptake and drug delivery in an in vivo setting is limited. To this end, we designed a novel enzyme-activatable, dual fluorescent biosensor, M378, as a quantitative antibody trafficking probe to determine antibody uptake and payload release in tumor cells in vivo. M378 consists of a "click" handle for antibody conjugation and a hexapeptide that serves as a substrate selective for the lysosomal protease cathepsin B, flanked by Alexa Fluor 568 (AF568) and Alexa Fluor 647 (AF647). The spectroscopic properties of M378 are consistent with an excitonic heterodimer and thus, AF568 is extremely well quenched (>98%) until enzymatically cleaved inside target cells. AF647 is partially, but predictably, quenched (~50%) until cleaved and serves as the "always on" beacon to quantify the total antibody present in the system. We hypothesized that by taking advantage of quantitative flow cytometry and applying a straightforward mathematical transformation, we may quantify and delineate in vivo antibody binding and internalization/cleavage in tumor cells as a surrogate detection for payload release. Here we report an in vivo/ex vivo application of M378 conjugated to a clinical-stage METxMET biparatopic antibody, REGN5093, developed at Regeneron (John DaSilva, MCT 2021, NCT04077099), to quantify the absolute number of antibodies delivered to EBC-1 lung cancer cells (antibodies per cell) as well as projected payload released by antibody degradation (payloads per cell). M378 selectivity was assayed against 10 different cathepsin proteases at both lysosomal and early endosomal pH (5.0 and 6.8, respectively). M378 demonstrated selective cathepsin B cleavage at pH 5.0 which is 12-fold greater relative to the next most active enzyme:condition combination tested by comparison of k_{cat}/K_M. REGN5093 conjugates of M378 and AF568 were generated with a dye-to-antibody ratio of 2.1 and 1.9, respectively. REGN5093-M378 demonstrated less than 5% cleavage in mouse serum at 37°C over 7 days as measured by AF568 fluorescence. To determine the in vivo uptake, trafficking and cleavage of REGN5093-M378, 5 million EBC-1 cells (~250,000 copies of antigen (MET) per cell) were implanted into SCID mice and tumor cells allowed to grow to a tumor volume ~150 mm^3. After randomization, animals (n=3) were injected with 3 mg/kg of REGN5093-M378 (dual fluorescence biosensor), REGN5093-AF568 (single color control), or saline (background control). Tumors at 1.5, 6, and 24 hours post-injection were harvested and mechanically dissociated for ex vivo quantitative flow cytometry analysis (Cytek Aurora). To convert qualitative fluorescence values to quantitative results, calibration curves were established using anti-human Fc capture beads (Bangs Laboratories) for both antibody-conjugated M378 and single-color controls (AF568, AF647). The binding capacity of the beads was previously validated in house via a radiolabelled antibody control. For each cell event, fluorescence intensity from the AF568 and AF647 channels were transformed to TOTAL Ab uptake per cell (median ~35,000 antibodies per cell) and CLEAVED biosensor per cell (median ~20,000 antibodies per cell) at the 24-hour time point. We found that cleaved biosensor measured by AF568 intensity, increased from 1.5 to 24 hours. The single color control arm (REGN5093-AF568) independently represented the total Ab uptake and was within ~10% of TOTAL biosensor uptake calculated at each time point. The fraction of biosensor cleaved per cell at 24 hours was approximately 40%. To our knowledge, this is the first report of quantifying absolute antibody uptake and catabolism in an in vivo tumor model. Using biosensor technology as a surrogate for the payload release can be expanded to other targets and/or antibodies to correlate in vivo efficacy with on-target payload delivery.

Poster Presentation

Disclosures: The authors have disclosed no financial interest.

350-Strategy to arrange an apparent failed radiolabelling of leukocytes

Presenter: Silvia Migliari, University Hospital of Parma

Silvia Migliari[1], Linda Davoli[2], Chiara Lazzara[1], Tiziano Graziani, Livia Ruffini[3]

[1]University Hospital of Parma, Parma, Italy
[2]University Hospital of Parma, Parma, italy, Italy
[3]University Hospital Parma Medical Center, Parma, Italy, Italy

Background:
Labeled leukocytes with 99mTc-HMPAO are routinely used for infection imaging. Although cell labeling with 99mTc-HMPAO represents an imaging probe to detect infection sites, the diagnostic efficiency of

the probe is largely influenced by cell manipulation, multidisciplinary interventions (i.e., biologist, technicians) and available technology (i.e., SPECT, SPECT/CT). Two mechanisms have been suggested to be responsible for the retention of 99mTc-HMPAO inside the cell: (1) conversion of the lipophilic 99mTc-HMPAO complex into a hydrophilic complex by reducing agents such as glutathione, and (2) binding of 99mTc-HMPAO to non diffusible proteins and cell organelles. Each 99mTc-HMPAO labeled leukocytes production must be assessed evaluating Labelling Efficacy parameter (LE, %), by measuring the amount of radioactivity of both supernatant (soluble 99mTc-compounds) and pellet (cell-associated 99mTc) of the labeling solution obtained after centrifugation. A LE values comprised in the range 40-80% is advisable, but when LE is <40% the batch is not useful for diagnostic imaging.

Aim:
To developed a strategy to arrange an apparent failed radiolabelling of white blood cells (WBC) using ^{99m}Tc-HMPAO, increasing the LE value.

Methods:
A patient blood sample was collected and then, after a sedimentation of 45 minutes, mixed leukocytes were isolated through a centrifugation of 1000 rpm for 5 minutes.
The lipophilic primary 99mTc-HMPAO complex was obtained after resuspension of HMPAO with freshly eluted sodium 99mTc-pertechnetate and radiochemical purity (RCP) of the radiopharmaceutical was assessed according to manufacture's instructions.
Freshly prepared 99mTc-HMPAO (800-900 MBq) in 1 ml of saline was added to the mixed leukocytes suspension and incubated for 10 minutes at room temperature. The labelling process was stopped by adding 5 ml of NaCl 0,9% (w/v) in the solution. Labelled cells and unbound 99mTc-HMPAO were then separated by centrifugation at 1000 rpm for 5 minutes.
The radioactivity of both supernatant and cell pellet was measured in a dose calibrator, and the efficiency of the labeling method (labeling efficiency, LE) was estimated as the percentage of residual radioactivity in the cells.
To improve the LE value, > 40%, we centrifugated the WBC labelled with 99mTc-HMPAO once again, but using a centrifugation of 1000 rpm for 2 minutes, in order to remove the supernatant. Then we added 99mTc-HMPAO (800-900 MBq) on cell pellet again and after 10 minutes we centrifugated at 1000 rpm for 2 minutes.
The same QC system was followed to assess the validity of the double/repeated labelling of WBC with 99mTc-HMPAO.

Results:
The RCP of 99mTc-HMPAO was 95.56%. LE resulted 10% after the first labelling procedure and 70% after the "arrangement" labelling strategy.

Conclusions:
This strategic labelling method appears safe, reproducible and easy to use in clinical routine for leukocyte labeling, when this radiopharmaceutical production seems to be failed.

Reference

1. Peters AM. The utility of [99mTc]HMPAO-leukocytes for imaging infection. Semin Nucl Med. 1994 Apr;24(2):110-27. doi: 10.1016/s0001-2998(05)80226-0. PMID: 8023168.
2. de Vries EF, Roca M, Jamar F, Israel O, Signore A. Guidelines for the labelling of leucocytes with (99m)Tc-HMPAO. Inflammation/Infection Taskgroup of the European Association of Nuclear Medicine. Eur J Nucl Med Mol Imaging. 2010 Apr;37(4):842-8. doi: 10.1007/s00259-010-1394-4.
3. Erratum in: Eur J Nucl Med Mol Imaging.2010 Jun;37(6):1235. PMID: 20198473; PMCID: PMC2844965.

Poster Presentation

Disclosures: The authors have disclosed no financial interest.

351-Neoadjuvant and adjuvant CAR-T cell therapy for metastases prevention.

Presenter: Mayuresh Mane, Memorial Sloan Kettering Cancer Center

Mayuresh M. Mane[1], Alessia Volpe[1], Juan Zurita[1], Larissa Shenker[1], Vladimir Ponomarev[1]

[1]Memorial Sloan Kettering Cancer Center, New York, NY

Objective:
To demonstrate that monitoring neoadjuvant and adjuvant CAR-T cell therapy together with ex vivo quantification of reporter-tagged circulating tumor cells (CTCs) can be used as reliable indicators for prognostic guidance on development of metastases in murine xenograft tumor models. Introduction: Presence of CTCs has been linked to increasingly poor prognosis in highly metastatic colorectal, prostate and breast cancers [1]. Cancer metastases originate by detachment of tumor cells from the primary tumor site, and spreading to other locations within the body via circulatory and lymphatic systems, as well as direct spread [2]. The carcinoembryonic antigen (CEA) is a glycoprotein that affects cell-to-cell adhesion in cancers [3] and is being used as a tumor-shed prognostic marker for metastatic development. Here, we show that engineered anti-CEA CAR-T cells can deplete CEA-expressing CTCs in the blood as well as tumor "microseeds" and can be used as an adjuvant therapy to prevent the establishment of newer metastases in murine CEA-positive xenograft tumor models.

Experimental Design and Methods:
Healthy donor derived, anti-CEA CAR T cells were engineered to express the anti-CEA CAR with the Cypridina luciferase (exCLuc) bioluminescence reporter, to enable whole-body monitoring of CAR-T cells in vivo. Highly metastatic human colorectal cancer cell line SW620 was modified to uniformly express CEA and Click Beetle Red luciferase reporter (CBRluc). SW620 CEA/CBRluc-expressing tumors were subcutaneously established in mice and were monitored via caliper measurements and BLI, until surgical excision on day 14 post implantation. Anti-CEA CAR-T cells were injected I.V. prior to (72 hours, neoadjuvant) and/or post (48 hours, adjuvant) surgical tumor excision. Blood was collected at regular intervals; separated into cellular and plasma fractions and subjected to the Bright-Glo Luciferase Assay and corelated with whole-body BLI signal.

Results and Discussion:
A delay/absence in development of metastases was recorded in the group of mice treated with anti-CEA CAR-T cells after tumor resection as compared to control mice that only had surgical removal of the primary tumor (at 5 weeks post surgical resection, 25% of the mice had very low detectable signal from metastases in the "post-surgical anti-CEA CAR therapy" group vs 43% of the mice in the control group). The group of mice that received anti-CEA CAR T cell therapy prior to and after surgery had a similar outcome as the control group (40% developed high detectable BLI signal). However, surprisingly,

the group of mice treated with anti-CEA CAR-T cells prior to tumor resection surgery, developed lung metastases sooner than the group of mice that received no CAR-T cell therapy (80% developed high detectable BLI signa, Fig. 1.). High blood CTC levels were associated with elevated BLI signal and earlier onset of metastases in 50% of the mice that progressed after primary tumor removal. Ongoing experiments are aimed towards elucidating the mechanisms of CAR-T cell efficacy in neoadjuvant and adjuvant settings.

Conclusions:

The results indicate that adjuvant adoptive anti-CEA T cell therapy is capable of controlling the development of newer metastases by attacking CTCs and tumor "microseeds". CAR-T cell therapy directed towards the primary tumor, as a form of neoadjuvant therapy, leads to faster establishment of metastases than control mice. The utility of CTC quantification in blood as a tool for predicting metastasis formation is a reliable indicator for prognostic efficacy of CAR-T cell treatment.

Reference

1. Hanahan, D. and R.A. Weinberg, Hallmarks of cancer: the next generation. Cell, 2011. 144(5): p. 646-74.
2. Harouaka, R., et al., Circulating tumor cells: advances in isolation and analysis, and challenges for clinical applications. Pharmacol Ther, 2014. 141(2): p. 209-21.
3. Abdul-Wahid, A., et al., Serum-derived carcinoembryonic antigen (CEA) activates fibroblasts to induce a local re-modeling of the extracellular matrix that favors the engraftment of CEA-expressing tumor cells. International Journal of Cancer, 2018. 143(8): p. 1963-1977.

Poster Presentation

Disclosures: The authors have disclosed no financial interest.

352-Distribution of ICG around colorectal liver metastases: towards real-time intraoperative quantitative tumor margin assessment

Presenter: Tom Dijkhuis, Leiden University Medical Center (LUMC)

Okker Bijlstra[1], **Tom Dijkhuis[2]**, Friso Achterberg[1], Mats Warmerdam[1], Stijn Crobach[2], Alexander Broersen[2], Rutger Jan Swijnenburg[3], Jacobus Burggraaf[4], Jouke Dijkstra[4], Alexander Vahrmeijer, Sven Mieog[5]

[1]Leiden University Medical Center (LUMC), Leiden, Zuid-Holland, Netherlands
[2]Leiden University Medical Center (LUMC), Leiden, Netherlands
[3]Amsterdam University Medical Center (UMC), Amsterdam, Noord-Holland, Netherlands
[4]Centre for Human Drug Research, Leiden, non-US, Netherlands
[5]Leiden University Medical Center (LUMC), Leiden, z-h, Netherlands

Introduction:

Near-infrared (NIR) fluorescence-guided surgery using indocyanine green (ICG) has provided several advantages over conventional white-light imaging in colorectal liver metastases (CRLM) surgery: i.e., improved detection of preoperatively identified lesions, intraoperative identification of additional lesions, and enabling intraoperative tumor margin assessment[1-3]. Therefore, NIR fluorescence imaging using ICG has been implemented as standard-of-care in liver surgery in several hospitals. Tumor margin evaluation is of great importance, as the resection margin after CRLM resection is an important factor in the 5-year survival rate of patients undergoing CRLM surgery[4]. The current use of NIR fluorescence imaging in CRLM surgery is based on a qualitative assessment of the visible fluorescence around the resected tumors, however, to date little is known about the exact behavior of the ICG fluorescence rim. To improve the assessment of the fluorescent rim, a standardized method to quantify fluorescence intensities is mandatory. Therefore, we developed and tested a novel method to quantify fluorescence intensities surrounding CRLM by analyzing the distribution of ICG in patients that received neoadjuvant chemotherapy and patients without neoadjuvant chemotherapy.

Methods:

Patients scheduled for open or minimally-invasive surgical resection for CRLM in a single institution were included. All patients received an intravenous injection of 10 mg of ICG dissolved in water for injection (5 mg/mL) approximately 24 hours prior to surgery. Surgery was performed under intermittent NIR guidance, according to the hospital's protocol. Directly after surgery, the resected specimen was cut into 5 mm bread loaves by a certified pathologist. NIR fluorescence images were acquired from all bread loaves with the PEARL Trilogy imaging system (LI-COR Biotechnology, Lincoln, Nebraska USA). Subsequently, the bread loaf with the largest tumor diameter was included in the dataset for quantification analysis. Tumors were manually delineated by two researchers independently. In MeVisLab (MeVis Medical Solutions AG, Germany) a network was developed to automatically create masks of the tumor- and bread loaf delineations. Tumors were then enlarged automatically with 1 mm steps to create halos up to 10 mm surrounding the tumor. Finally, for each halo the signal-to-background ratio (SBR) was calculated, and the effect of chemotherapy, the location and size of the CRLM on the SBR were studied.

Results:

A total of 32 patients were included in the analysis, of whom 11 (34%) received neoadjuvant chemotherapy and 21 (66%) did not receive chemotherapy. A significant difference in median SBR between the chemotherapy and non-chemotherapy group was found for the halos from 0 mm to 4 mm from the tumor (p-values ranging from <0.001 to 0.020). When discriminating capsular metastases from subcapsular lesions, no significant differences in SBRs (p-values ranging from 0.131 to 1.000) were identified between both groups. Moreover, in this cohort also tumor size did not significantly influence SBRs (p-values ranging from 0.180 to 0.840).

Discussion:

Quantitative fluorescence imaging is a novel and emerging niche in fluorescence imaging. The call for quantification of fluorescent signals has become louder in recent years. For the use of ICG during CRLM surgery several studies tried to analyze the fluorescent rim around CRLM5,6. This study, however, showed the first quantification method to standardize and semi-automatically describe the accumulation of ICG around CRLM. These results showed a high fluorescence intensity close to the tumor which decreased exponentially over distance up to around the background fluorescence intensity at a distance of 10 millimeters from the tumor. Moreover, the use of neoadjuvant chemotherapy significantly influenced the accumulation of ICG close to CRLM suggesting surgeons should interpret qualitative fluorescence signals with caution in different patient categories, and indicating the need for a more patient-tailored approach for the ideal dose and timing of ICG administration or the addition of tumor-specific imaging agents.

Reference

1. Handgraaf HJM, Boogerd LSF, Hoppener DJ, Peloso A, Sibinga Mulder BG, Hoogstins CES, et al. Long-term follow-up after near-infrared fluorescence-guided resection of colorectal liver metas-

tases: A retrospective multicenter analysis. European journal of surgical oncology: the journal of the European Society of Surgical Oncology and the British Association of Surgical Oncology 2017; 43(8): 1463-71.
2. Achterberg FB, Sibinga Mulder BG, Meijer RPJ, Bonsing BA, Hartgrink HH, Mieog JSD, et al. Real-time surgical margin assessment using ICG-fluorescence during laparoscopic and robot-assisted resections of colorectal liver metastases. Ann Transl Med 2020; 8(21): 1448.
3. He K, Hong X, Chi C, Cai C, An Y, Li P, et al. Efficacy of Near-Infrared Fluorescence-Guided Hepatectomy for the Detection of Colorectal Liver Metastases: A Randomized Controlled Trial. Journal of the American College of Surgeons 2022; 234(2): 130-7.
4. Ardito F, Panettieri E, Vellone M, Ferrucci M, Coppola A, Silvestrini N, et al. The impact of R1 resection for colorectal liver metastases on local recurrence and overall survival in the era of modern chemotherapy: An analysis of 1,428 resection areas. Surgery 2019; 165(4): 712-20.
5. Tashiro Y, Aoki T, Hirai T, Koizumi T, Mansou DA, Kusano T, et al. Pathological Validity of Using Near-infrared Fluorescence Imaging for Securing Surgical Margins During Liver Resection. Anticancer research 2020; 40(7): 3873-82.
6. van der Vorst JR, Schaafsma BE, Hutteman M, Verbeek FP, Liefers GJ, Hartgrink HH, et al. Near-infrared fluorescence-guided resection of colorectal liver metastases. Cancer 2013; 119(18): 3411-8.

Poster Presentation

Disclosures: The authors have disclosed no financial interest.

353-Genetic engineering of SIRPα/TIM-3 membrane nanocapsules carrying melanin-gemcitabine in the diagnosis and treatment of pancreatic cancer

Presenter: Zining Zhang, The Affiliated Hospital of Jiangsu University

Zining Zhang[1], Wenyao Wang[2], Hsiang-i Tsai[1], xiongfeng cao[3], Xufeng Pu[2], Haitao Zhu[2], Jianghong Ji[2]

[1]The Affiliated Hospital of Jiangsu University, Zhenjiang, China
[2]Jiangsu University, China
[3]Jiangsu University, Zhenjiang, Zhenjiang, China

Background:
Pancreatic cancer is extremely malignant, cannot easily detected, poorly treated and mostly found in the middle and late stages, with a five-year survival rate of less than 5%. Pancreatic cancer is resistant to its first-line treatment,which is gemcitabine. In addition, pancreatic cancer can inhibit phagocytosis by macrophages through the CD47-SIRPα axis, which generates "don't eat me" signals to macrophages. At the same time, pancreatic cancer can also reduce the cytotoxic effect of CD8+ T cells through the Galectin-9-TIM-3 axis, resulting in immune escape. The use of nanovesicles to deliver drugs for anticancer therapy has been reported in order to address the issue of tumour drug resistance. Molecular imaging probes has also been used in conjunction with nanomaterials to assess the efficacy of tumour therapy using iron tetroxide, melanin, etc.

Objective:
The aim of this study is to determine the cytotoxic effect of TIM-3/SIRPα genetically engineered nanovesicles encapsulated with gemcitabine-melanin sensitized CD8+ T cells on pancreatic cancer cells and to reduce immune escape and phagocytosis by macrophages. The combined treatment of pancreatic cancer by nanomaterials and molecular imaging is achieved through the use of molecular imaging diagnostic modalities and MRI imaging to reflect the therapeutic effect.

Methods:
Firstly, Galectin-9 and CD47 were determined to be overexpressed in mouse orthotopic model of pancreatic cancer. Pancreatic cancer cells overexpressing TIM-3 and SIRPα were constructed, and cell membranes with overexpressed TIM-3 and SIRPα were extracted. Then, melanin nanospheres were synthesized to load gemcitabine and encapsulated with the extracted cell membranes. The killing effect of nanovesicles on pancreatic cancer cells was detected by CCK8 assay in vitro, and T cells and macrophages were respectively co-cultured with pancreatic cancer cells by adding nanovesicles to detect the activity and activity index of T cells and macrophages. Finally, we verified the effect of nanovesicles on pancreatic cancer cells and T cells and macrophages by in vivo, with the aid of melanin for MRI imaging.

Results:
In pancreatic cancer, The expression of Galectin-9 was 18.44 times higher than normal pancreatic tissue ,CD47 was 5.68 times higher than normal pancreatic tissue, and TIM-3 and SIRPα transfection efficiency were significant. The nanovesicles overexpressing TIM-3 and SIRPα enhanced the phagocytosis of pancreatic cancer cells by macrophages and the killing effect of CD8+ T cells on pancreatic cancer. The activity of T cells and macrophages co-cultured with pancreatic cancer cells was significantly enhanced by the addition of nanovesicles. In vivo, MRI imaging using melanin revealed that gemcitabine was the most effective treatment in combination with nanovesicles.

Conclusions:
For the reason that it is difficult to treat pancreatic cancer, the combination of nanomaterials and molecular imaging can significantly improve the outcome of pancreatic cancer treatment. The use of nanovesicles with overexpressed TIM-3 and SIRPα encapsulated with gemcitabine has indeed significantly improved the therapeutic efficacy of pancreatic cancer, solving the problem of unsatisfactory results with gemcitabine alone, as overexpression of TIM-3 and SIRPα enhances the killing effect of CD8+ T cells on pancreatic cells and the phagocytosis of pancreatic cancer cells by macrophages. MRI imaging using melanin provides a sharp edge for the identification of pancreatic cancer treatment effects.

Reference
1. Tsai HI, Wu Y, Liu X, Xu Z, Liu L, Wang C, Zhang H, Huang Y, Wang L, Zhang W, Su D, Khan FU, Zhu X, Yang R, Pang Y, Eriksson JE, Zhu H, Wang D, Jia B, Cheng F, Chen H. Engineered Small Extracellular Vesicles as a FGL1/PD-L1 Dual-Targeting Delivery System for Alleviating Immune Rejection. Adv Sci (Weinh). 2022 Jan;9(3):e2102634.
2. Zhu H, Cao X, Cai X, Tian Y, Wang D, Qi J, Teng Z, Lu G, Ni Q, Wang S, Zhang L. Pifithrin-μ incorporated in gold nanoparticle amplifies pro-apoptotic unfolded protein response cascades to potentiate synergistic glioblastoma therapy. Biomaterials. 2020 Feb;232:119677.

Poster Presentation

Disclosures: The authors have disclosed no financial interest.

354-Activity-based 19F-MRI Sensing of Zn2+: A Novel Strategy for Quantitative Mapping of Cation Dynamics with Ultimate Specificity

Presenter: Lucia M. Lee, Weizmann Institute of Science

Lucia M. Lee[1], Nishanth D Tirukoti[2], Yuki Konishi[3], Amnon Bar-Shir[2]

[1]*Weizmann Institute of Science, Israel*
[2]*Weizmann Institute of Science, Rehovot, Israel*
[3]*Osaka University, Osaka, Japan*

Introduction:
Imaging sensors developed for metal ions are mostly based on specific ion recognition capabilities and non-covalent interactions between the ion of interest and the synthetic probe. Nevertheless, an alternative strategy for ion recognition, one that uses molecular reactivity, is desired to allow (i) ultimate specificity; (ii) detectability of transient changes in ion levels, and (iii) enhanced contrast-to-noise changes. Several examples have shown activity-based fluorescence sensing for Zn^{2+}.[1,2,3] Specifically for these designs, binding zinc mediates hydrolytic cleavage of acetyl groups in the probe, providing a large fluorescence response. Fluorescent imaging however, is not applicable for deep tissue imaging and are not capable for quantitative assessments. Inspired by the activity-based Zn^{2+} sensing strategy and the quantifiability of ^{19}F-MRI signals, we designed a highly reactive but very specific synthetic fluorinated probe for MRI mapping of the Zn^{2+}. Upon binding to Zn^{2+} the synthetic probe is readily hydrolyzed and the resonance of its ^{19}F-functional group is shifted by more than 12 ppm allowing to display Zn^{2+} distribution as an artificial MRI colored map highlighting its ultimate specificity as compared to other metal ions.

Method:
A fluorinated-chelate **LML-1** was synthesized using reductive amination and acetylation methods. Following determination of the T_1 relaxation time of purified **LML-1**, fully recovered ^{19}F-NMR experiments were performed on 11.7 T NMR spectrometer at 25 ^oC and 37 ^oC. To this end, PBS solutions (pH = 7.2) containing 3 mM **LML-1** and 3 mM of either Zn^{2+} or Ca^{2+} were examined to determine the reactivity and half life time ($t_{1/2}$) of **LML-1**. Then, a phantom composed of six tubes was set where each sample tube contained **LML-1** in PBS (pH = 7.2) and one of the examined cations (Ca^{2+}, Mg^{2+}, Na^+, K^+, Zn^{2+} or no cation). The phantom was placed in a 9.4 T MRI scanner and both ^{1}H-MRI and ^{19}F-MRI data were obtained. Two ^{19}F-MRI data sets were acquired with the center frequency O_1 set at -116 ppm (without Zn^{2+} activity) or at -128 ppm (following Zn^{2+} activity).

Results:
The probe **LML-1** containing a Zn^{2+} binding moiety was synthesized, purified and characterized. The ^{19}F NMR of the probe in PBS showed a single ^{19}F signal at -116 ppm (Figure 1a, top). Upon the addition of Zn^{2+} to the solution of **LML-1**, an additional peak of Zn^{2+}-**LML-1** complex was obtained at -128 ppm (Figure 1a, bottom). Within an hour, the probe signal fully converted to the Zn^{2+}-complex ($t_{1/2}$= 10 mins, Figure 1b). The same experiment repeated at 37 ^oC yielded a faster hydrolysis of the acetyl group ($t_{1/2}$= 5 mins, Figure 1c). Importantly, without the addition of Zn^{2+} and upon addition of Ca^{2+} to the **LML-1** solution, only a trace conversion of the fluorinated chelate could be detected after 3 days emphasizing the stability of the probe for a very long time even in aqueous solution. ^{19}F-MRI experiments of a phantom clearly showed the ability to use the activity-based **LML-1** to map Zn^{2+} (-128 ppm, red) with no background signal and differentiate this signal from unreacted **LML-1** (-116 ppm, green) by displaying it in a multicolor ^{19}F-MRI (Figure 1d).

Conclusion:
We showed a conceptually novel approach for mapping Zn^{2+} with MRI. Our approach uses molecular reactivity to provide several advantages, especially: (i) Zn^{2+} specificity; (ii) detectability of transient changes in Zn^{2+} levels; and (iii) enhanced contrast-to-noise changes. We have demonstrated binding Zn^{2+} induces hydrolysis of the acetyl group of the probe, forming a Zn^{2+}-**LML-1** complex with a significant change in the ^{19}F-NMR resonance. We showed the probe is specific to Zn^{2+} compared to other biological relevant cations suggesting its potential ability to image mobile zinc in live cells and tissues

References
1. Chyan, W.; Zhang, D. Y.; Lippard, S. J.; Radford, R. J., Reaction-based fluorescent sensor for investigating mobile Zn2+ in Mitochondria of Healthy versus Cancerous Prostate Cells. Proc. Natl. Acad. Sci. USA 2014, 111(1), 143-8.
2. Zastrow, M.L; Radford, R. J.; Chyan, W.; Anderson C. T.; Zhang, D. Y.; Loas, A.; Tzounopoulos, T.; Lippard, S. J.; Reaction-based Proves for Imaging Mobile Zinc in live Cells and Tissues. ACS Sens. 2016, 1(1), 32-39.
3. Lee, M.; Maji, B.; Manna, d.; Kahraman, S.; Elgamal, R. M.; Small, J.; Kokkonda, P.; Vetere, A.; Goldberg, J. M.; Lippard, S. J; Kulkarni, R. N.; Wagner, B. K.; Choudhary, A., Native Zinc Catalyzes Selective and Traceless Release of Small Molecules in beta-Cells. J. Am. Chem. Soc. 2020, 143(14), 6477-6482.

Poster Presentation

Disclosures: The authors have disclosed no financial interest.

355-Optical redox imaging as a label-free tool for predicting metabolically-targeted therapeutic response in triple-negative breast cancer cells

Presenter: He Nucleus Xu, University of Pennsylvania

He Nucleus N. Xu[1], Allison Podsednik[2], Joseph Baur[2], Julia Tchou[2], David Mankoff[3], Rong Zhou[3], Lin Z. Z. Li[4]

[1]*University of Pennsylvania, Philadelphia*
[2]*Perelman School of Medicine at the University of Pennsylvania, Philadelphia, PA*
[3]*University of Pennsylvania, Philadelphia, PA*
[4]*University of Pennsylvania*

Metabolically-targeted therapy has received increasing research and clinical attention in recent years for its potential for cancers with limited treatment options, such as triple-negative breast cancer (TNBC). TNBC cells are highly heterogeneous with diverse treatment responses. Better understanding of the biological basis of metabolic phenotypes in TNBC is crucial to the clinical translation of metabolically-targeted therapy and new metabolic drug development. As essential coenzymes, the redox pair NAD^+ and NADH together with flavin adenine dinucleotide (FAD and $FADH_2$) redox pair critically support energy metabolism and maintain mitochondrial redox homeostasis. Cancer cells rely heavily on metabolic reprogramming that is critically supported by altered redox status and an increased demand for NAD^+. The biosynthesis of NAD^+ is regulated by the rate-limiting enzyme Nampt in the NAD salvage pathway. When these metabolic pathways are therapeutically inhibited, the cellular redox status is also affected. We hypothesize that metabolic inhibition-induced redox changes can be detected by imaging the intrinsic fluorescence intensities of NAD(P)H and FAD-containing

flavoproteins (Fp), i.e. the well-established label-free optical redox imaging (ORI) technique [1-3]. By employing an inverted wide-field Zeiss fluorescence microscope equipped with proper filters (NADH: excitation (Ex) 370–400 nm, emission (Em) 414–450 nm; Fp: Ex 450–488 nm, Em 500–530 nm; mitoSOX: Ex 370–400 nm and Em 580–610 nm), we performed ORI of 4 TNBC cell lines cultured in glass-bottom dishes and treated with various metabolic inhibitors, chemo-drug Taxol and their combinations. These metabolic inhibitors include FX11 (a specific inhibitor of lactate dehydrogenase A that converts pyruvate to lactate in the last step of glycolysis), CB-839 (a specific inhibitor of the rate-limiting enzyme glutaminase that converts glutamine to glutamate as a critical part of glutaminolysis), and FK866 (a selective Nampt inhibitor). After ORI, we stained the cells with mitoSOX to image mitochondrial reactive oxygen species (ROS). The cells were then fixed, DAPI-stained, imaged, and counted. Our main results include

1. Metabolic phenotype differentiation: ORI differentiated among 4 TNBC lines (Basal-like 1 and 2: HCC1806 and MDA-MB-468; and more aggressive mesenchymal stem-like (MSL): MDA-MB-231 and MDA-MB-436) under basal metabolism or under glycolytic inhibition by FX11 (5 and 10 μM) or glutaminolysis inhibition by CB-839 (1 μM) or NAD^+ biosynthesis inhibition by FK866 (1nM), suggesting MSL types have a higher redox ratio Fp/(NADH+Fp) (more oxidized state) and are less prone to metabolic inhibitor-induced change.
2. Treatment response prediction: strong correlations between ORI responses and growth inhibition induced by various treatments: ***(a)*** all redox indices (NADH, Fp, the redox ratio Fp/(NADH+Fp)) increased with Taxol-induced growth inhibition in HCC1806 cells in a dose-dependent manner; ***(b)*** all redox indices had highly significant positive correlations with enhanced growth inhibition induced by CB-839 (1 μM) + Taxol (1nM) in HCC1806 whereas such correlations were less prominent in MDA-MB-231 cells even treated with a higher Taxol dose of 10 nM; ***(c)*** Fp/(NADH+Fp) had a significant positive correlation with enhanced growth inhibition induced by FX11 (5 μM) + Taxol (10 nM) in MDA-MB-231 cells whereas HCC1806 cells lacked such a correlation; ***(d)*** ORI detected differential responses to FK866+Taxol treatment among sub-types with less prominent redox changes in the more oxidized MSL cells.

Optical redox imaging (ORI) as a label-free live cell imaging technique can accelerate research process by providing real-time, quantitative redox/metabolism measures and the same cells can then be live-stained with fluorescence tracers to get multiple results from just one experiment. Our data are the first to demonstrate that ORI as a label-free tool can differentiate among TNBC metabolic phenotypes and responds to metabolic inhibitions and/or chemo-drug Taxol or their combinations, indicating that ORI may assist in selecting metabolically-targeted drugs for different metabolic phenotypes of TNBC cells. These results warrant further investigations in animal models.

Reference

1. Heikal AA (2010) Intracellular coenzymes as natural biomarkers for metabolic activities and mitochondrial anomalies. Biomark Med 4:241-263.
2. Xu HN, Feng M, Nath K, et al. (2019) Optical redox imaging of lonidamine treatment response of melanoma cells and xenografts. Mol Imaging Biol 21:426-435.
3. Podsednik A, Jiang J, Jacob A, Li LZ, Xu HN (2021) Optical Redox Imaging of Treatment Responses to Nampt Inhibition and Combination Therapy in Triple-Negative Breast Cancer Cells. International journal of molecular sciences 22:5563.

Poster Presentation

Disclosures: The authors have disclosed no financial interest.

356-A Fibroblast Activation Protein Specific Optical Imaging Probe Capable of Imaging Non-small Cell Lung Cancer in Humans.

Presenter: Layla Mathieson, The University of Edinburgh

Layla Mathieson[1], Richard O'Connor[1], Hazel Stewart[1], Paige Shaw[1], Kev Dhaliwal[2], Gareth Williams[1], Alicia Megia-Fernandez[1], Ahsan Akram[3]

[1]The University of Edinburgh, United Kingdom
[2]Queens Medical Research Institute, Edinburgh, Scotland, United Kingdom
[3]University of Edinburgh, Edinburgh, Midlothian, United Kingdom

Optical imaging using a Fibroblast activation protein-α (FAP) specific chemical probe, when combined with clinically compatible fibre-based imaging systems, can provide a readout of FAP activity in NSCLC tumours, which could allow disease-monitoring, prognostication and potentially stratify therapy. FAP is a type II transmembrane glycoprotein of the serine protease family involved in the regulation of extracellular matrix (1). FAP is expressed at minimal levels in healthy tissue but is highly expressed on activated fibroblasts, including cancer-associated fibroblasts (CAFs) in the stroma of epithelial tumours (2). FAP positive CAFs in cancer promote tumour growth and suppression of the anti-cancer immune response. High FAP expression is associated with poor survival and high recurrence rates in ovarian cancer, pancreatic ductal adenocarcinoma and non-small cell lung cancer (NSCLC) (3). FAP, in NSCLC, is associated with a suppressed lymphocyte-dependent immune response, and been shown to be a predictor of worse overall survival (4). We have iteratively developed a FAP cleavable peptide compound (5) which utilises a carboxyfluorescein (FAM) fluorophore with a methyl red quencher as a FRET pairing. The resulting sequence (Lys(MethylRed)-Val-(D)Ser-Pro-Asn-Gln-Gly-Lys(5-FAM)-[Peg_2-(D)$Lys]_3$-NH_2) retains specificity over closely related endopeptidases (prolyl endopeptidase (PREP)), as well as dipeptidyl peptidase IV and a number of matrix metalloproteinases. The sequence remains stable in highly proteolytic environments such as activated neutrophil lysate. Physiological FAP levels were assessed by incubation with CAFs derived from NSCLC patients. CAFs successfully cleaved the sequence with the signal successfully abrogated in the presence of Talabostat, an inhibitor of FAP (mean velocity of 36.5 RFU/min compared to 0.8 RFU/min with Talabostat, N=3, p=0.0127). We determined the FLIM changes following cleavage by FAP and demonstrated a change over time and concentration of FAP. Using a clinically approved video rate fibre based FLIM imaging system, we assessed FAP activity in ex vivo NSCLC (6). NSCLC tissue incubated with the probe demonstrated a baseline mean intensity of 62AU (+/- 16 SEM), increasing to 251AU (+/- 81 SEM) after 40 minutes (p=0.0496, paired t test, N=5). Similarly, the fluorescence lifetime also demonstrated an increase from a baseline mean lifetime of 2.6ns (+/- 0.2 SEM) to 3.3ns (+/-0.2 SEM) after 40 minutes (p=0.0034, paired t test, N=5). Representative images demonstrating the fluorescence intensity and lifetime measurements for the probe using the endomicroscopy system are show in figure 1. Both signals were inhibited in the tumour tissue in the presence of Talabostat. In conclusion, we have developed an optical imaging probe capable of imaging the fluorescence intensity and lifetime of physiological levels of FAP in NSCLC tumour tissue. We have demonstrated the probe is specific for FAP over PREP, DPPIV and MMPs, as well as stability in the presence of activated neutrophil lysate. The resulting

probe is therefore suitable for potential imaging applications in the imaging of NSCLC as well as other inflammatory conditions where FAP is highly expressed.

Reference

1. Liu R, Li H, Liu L, Yu J, Ren X. Fibroblast activation protein. Cancer Biol Ther [Internet]. 2012;13(3):123–9. Available from: http://www.tandfonline.com/doi/abs/10.4161/cbt.13.3.18696
2. Kilvaer TK, Rakaee M, Hellevik T, Østman A, Strell C, Bremnes RM, et al. Tissue analyses reveal a potential immune-adjuvant function of FAP-1 positive fibroblasts in non-small cell lung cancer. PLoS One. 2018;13(2):1–17.
3. Puré E, Blomberg R. Pro-tumorigenic roles of fibroblast activation protein in cancer: back to the basics. Oncogene [Internet]. 2018;37(32):4343–57. Available from: http://dx.doi.org/10.1038/s41388-018-0275-3
4. Liao Y, Ni Y, He R, Liu W, Du J. Clinical implications of fibroblast activation protein-alpha in non-small cell lung cancer after curative resection: a new predictor for prognosis. J Cancer Res Clin Oncol. 2013 Sep;139(9):1523–8.
5. Mathieson L, O'Connor RA, Stewart H, Shaw P, Dhaliwal K, Williams GOS, et al. Fibroblast Activation Protein Specific Optical Imaging in Non-Small Cell Lung Cancer. Front Oncol. 2022;12(March):1–10.
6. Williams GOS, Williams E, Finlayson N, Erdogan AT, Wang Q, Fernandes S, et al. Full spectrum fluorescence lifetime imaging with 0.5 nm spectral and 50 ps temporal resolution. Nat Commun. 2021;12(1):1–9.

Poster Presentation

Disclosures: The authors have disclosed no financial interest.

357-Investigating the efficacy of TRAIL-armored CAR-T cells to improve cancer immunotherapy in Non-Small Cell Lung Cancer

Presenter: Alessia Volpe, Memorial Sloan Kettering Cancer Center

Alessia Volpe[1], Juan Zurita[1], Larissa Shenker[1], Maxim A. Moroz[2], Anna Moroz[3], Prasad S. Adusumilli[1], Dmitri V. Rozanov[4], Vladimir Ponomarev[1]

[1]Memorial Sloan Kettering Cancer Center, New York, NY
[2]Stanford University, Fremont, United States
[3]Stanford University, Stanford, CA
[4]Oregon Health and Science University, Portland, OR

Introduction:
Non-small Cell Lung Cancer (NSCLC) is the most common type of lung malignancy. Mesothelin (MSLN)-specific chimeric antigen receptor (CAR)-T cells can successfully target MSLN expressing NSCLCs either alone or as a combination treatment,[1] but fail to treat MSLN-negative cells. The TNF-related apoptosis-inducing ligand (TRAIL) exhibits a strong anti-tumor activity in preclinical and in clinical settings[2] and is a promising therapeutic molecule for the treatment of lung cancer.[3] However, mechanisms of TRAIL resistance were reported. Radiation therapy and chemotherapeutic drugs can sensitize certain lung cancers to TRAIL-induced apoptosis and greatly enhance cell killing.[4] Here we propose a synergistic approach combining translatable TRAIL-armored CAR-T cell therapy with ionizing radiation and chemotherapy regimens to overcome mechanisms of TRAIL resistance and render the less sensitive A549 human NSCLC cancer more amenable to effective TRAIL-mediated CAR-T therapy.

Methods:
MSLN+/- A549 cells sensitivity to recombinant human (rh)TRAIL was assessed by flow cytometric analysis. Cells were additionally treated with either ionizing radiation or chemotherapy (*e.g.*, doxorubicin) to evaluate their added therapeutic impact. Membrane-bound (MB-) and secreted (s-) TRAILs with active trimerization motifs coupled with a MSLN-directed CAR (M28z) were retrovirally transduced into human T cells. CAR-T cells cytolytic activity was evaluated by *in vitro* killing assays (live/dead staining). CAR-T cells and MSLN+/- targets were engineered with membrane anchored Cypridina luciferase (maCluc), Click Beatle Green luciferase (CBG) and Renilla luciferase (Rluc) bioluminescence reporters, respectively, thereby enabling long-term *in vivo* bioluminescence imaging (BLI) of all three populations within the same animal[5] and the reliable assessment of treatment efficacy.

Results:
MSLN+/- A549 cells showed low sensitivity to rhTRAIL treatment **(Fig.1 A-B)**. Combination of high doses of rhTRAIL (³30 ng/mL) and clinically relevant doses of radiation **(C)** and chemotherapy **(D)** resulted in a significantly enhanced TRAIL-mediated cell killing (30 ng/mL rhTRAIL *vs* 30 ng/mL rhTRAIL + 5 Gy radiation: p=0.0107; 30 ng/mL rhTRAIL *vs* 30 ng/mL rhTRAIL + 0.1 ug/mL doxorubicin: p=0.0122). MB- and s-TRAIL-armored M28z CAR-T constructs were successfully generated in a SFG retroviral vector system **(E)**. While all CAR-T cells killed MSLN+ cells due to anti-MSLN CAR:MSLN engagement **(F)**, only TRAIL-based M28z CAR-T cells with constitutive expression of MB-TRAIL or s-TRAIL were able to kill also MSLN-negative cells **(G)**, thereby proving the added therapeutic benefit of TRAIL. However, the tumoricidal effect was limited by the A549 low sensitivity to TRAIL. Radiation and chemotherapy-induced *in vitro* and *in vivo* sensitization to TRAIL-based CAR-T cells as well as the identification of the most effective regimen (drug/dose combination) are now under evaluation.

Conclusions:
We proved that our new TRAIL-armored MSLN-specific CAR-T cell strategy is superior to the already therapeutic and trialled MSLN-specific CAR-T cells by providing additional proapoptotic stimuli to both antigen positive and negative tumor targets, thereby enhancing anti-tumor targeting and cancer cell killing in a model of NSCLC. As our data also suggest the role of ionizing radiation and chemotherapy (*e.g.*, doxorubicin) to further sensitize NSCLC cells to TRAIL, we are currently exploring their use enhance TRAIL-mediated CAR-T cells treatment. In fact, the central promise of this work is to render patients with advanced NSCLC more amenable to effective TRAIL-armored CAR-T therapy by overcoming TRAIL resistance, thereby improving outcomes.

Acknowledgements: This work was supported by the EIO Fellowship Award from the Center for Experimental Immuno-Oncology and the Tow Foundation Postdoctoral Fellowship from the MSKCC Center for Molecular Imaging and Nanotechnology to A.V., as well as an NIH/NCI grant to V.P.

Reference

1. Adusumilli PS, Zauderer MG, Riviere I, et al. A phase I trial of regional mesothelin-targeted CAR T-cell therapy in patients with malignant pleural disease, in combination with the anti-PD-1 agent pembrolizumab. Cancer discovery 2021 doi: 10.1158/2159-8290. Cd-21-0407 [published Online First: 2021/07/17].

2. Bellail AC, Qi L, Mulligan P, et al. TRAIL agonists on clinical trials for cancer therapy: the promises and the challenges. Rev Recent Clin Trials 2009;4(1):34-41. doi: 10.2174/157488709787047530 [published Online First: 2009/01/20].
3. Skovgard MS, Hocine HR, Saini JK, et al. Imaging CAR T-cell kinetics in solid tumors: Translational implications. Molecular therapy oncolytics 2021;22:355-67. doi: 10.1016/j.omto.2021.06.006 [published Online First: 20210612].
4. Bellail AC, Hao C. TRAIL apoptotic pathway-targeted therapies for NSCLC. Transl Lung Cancer Res 2012;1(2):155-7. doi: 10.3978/j.issn.2218-6751.2012.02.02.
5. Moroz MA, Zurita J, Moroz A, et al. Introducing a new reporter gene, membrane-anchored Cypridina luciferase, for multiplex bioluminescence imaging. Molecular therapy oncolytics 2021;21:15-22. doi: 10.1016/j.omto.2021.03.004 [published Online First: 2021/04/15].

Poster Presentation

Disclosures: The authors have disclosed no financial interest.

358-Rare Earth Nanoprobes Targeting CXCR4 Enhance the Efficacy of Radiotherapy and Radiotherapy Combined with Immunotherapy in Triple Negative Breast Cancer

Presenter: Zi-He Ming, Xiamen University

Zi-He Ming[1], Yong-Qu Zhang[1], Guo-Jun Zhang[2]

[1]Xiamen University, China
[2]Xiang'an Hospital of Xiamen University, Xiamen, Fujian, China

Introduction:
The incidence of breast cancer ranks first among female malignant tumors, especially triple negative breast cancer (TNBC) which has relatively worse outcome owing to lack of effective treatments. It is urgent to find out a method to identify the metastatic tumor in an accurate and intuitive way and try to improve the treatment effect including the radiotherapy and immunotherapy. In patients with radical concurrent radiotherapy and chemotherapy, more than 50% of patients will end up with treatment failure. The main reason is that radiotherapy can only kill sensitive cancer cells, so the sensitivity is the key of curative effect of radiotherapy. Studies showed that high atomic number lanthanide elements, such as lutetium (Lu), can promote tumor cell apoptosis after radiation. In addition, a variety of anti-PD-L1 drugs have been approved to enter the clinic which can benefit patients. But tumor microenvironment (TME) tends to inhibit the activity of human normal immune cells, so immune checkpoint blockade therapy (ICBT) response is low (20-30%), leading to poor therapeutic effect. Studies have shown that radiotherapy can activate TME in patients, improve the response rate of PD-L1 inhibitors, and prolong the survival time of patients. We have successfully synthesized a CXCR4 targeted down conversion luminescence rare earth nanoparticles (RENPs) probe RENPs-AMD3100, which can visually identify and diagnose breast cancer, improve the sensitivity of radiotherapy and enhance the therapeutic effect of immunotherapy.

Methods:
1. Material characterization:Appearance (Transmission Electron Microscope (TEM)), dispersibility, particle size (Dynamic Light Scattering (DLS)), stability, fluorescence emission spectrum (Spectroscope), absorption spectrum and fluorescence penetration were examined to characterize probe. 2. Safety and metabolization of RENPs-AMD3100 in vitro and in vivo: Cytotoxicity assay (CCK8), biological distribution of probes, blood biochemical and pathology of important organs are examined to verify probe safety. 3. Targeting of RENPs-AMD3100 in vitro and in vivo. Untargeted probe RENPs, targeted probe RENPs-AMD3100 and free AMD3100 blocking assays are used to examine the specificity in breast cancer cell lines and tumor-bearing mouse model. 4. Sensitivity of radiotherapy in vitro and in vivo: Cell viability, cell apoptosis and the level of ROS under different doses of radiation, survival rates and tumor volumes of mouse under different treatments. 5. Synergistic effect of radiotherapy and immunotherapy: survival rates and tumor volumes of mouse under different treatments.

Results:
1. RENPs-AMD3100 was successfully synthesized with good appearance, dispersibility, stability with high intensity of NIR-II fluorescent in 1030nm. 2. RENPs-AMD3100 exhibit little damage in breast cancer cell lines and normal breast cell line ($p<0.05$). What's more, this kind of nanoscale materials can metabolize by liver and excrete in 48h. 3. RENPs-AMD3100 could specifically target TNBC cell line and tumor-bearing mouse models, the differences of probes uptake between targeted and untargeted group were very obvious. In the animal models, the tumor to muscle ratio is up to 13, and the fluorescent signal of targeted probe group is about 2 folds than untargeted probe group. 4. RENPs-AMD3100 could increase the sensitivity of radiotherapy by the elements of Lu both in vitro and in vivo.

Summary:
Our synthesized probe RENPs-AMD3100 targeting CXCR4 can visualize the development and metastasis of breast cancer, so as to conduct targeted precision radiotherapy. Moreover, due to the high expression of CXCR4 on the surface of tumor cells, the probe can be specifically enriched on tumor cells, improving the sensitivity of radiotherapy and enhancing the effect of radiotherapy. At the same time, tumor cells will die of immunogenicity after radiotherapy, and expose tumor specific antigens, thus activating the immune microenvironment. In the future, the platform is expected to transform "cold tumor" into "hot tumor" and improve the therapeutic effect of immune checkpoint inhibitors.

Poster Presentation

Disclosures: The authors have disclosed no financial interest.

359-Cucurbituril-adamantane based pretargeted PET with a copper-64-labeled adamantane ligand in xenograft models of pancreatic cancer

Presenter: Vilma Jallinoja, Memorial Sloan Kettering Cancer Center

Vilma Jallinoja[1], Courtney Abbriano[2], Kavita Bhatt[2], David Schlyer[3], Paul Yazaki[4], Brandon Carney[5], Jacob Houghton[6]

[1]Memorial Sloan Kettering Cancer Center
[2]Stony Brook Medicine
[3]Brookhaven National Laboratory
[4]City of Hope, CA
[5]Stony Brook University
[6]Stony Brook University, Stony Brook, NY

Objectives:
In pretargeted nuclear medicine, a target specific macromolecule (e.g. monoclonal antibody; mAb) is radiolabeled *in vivo* with a macromolecule specific radioligand to result in a lower radiation burden to the

healthy tissue compared to the use of a directly radiolabeled macromolecule.[1,2] A promising new pretargeted PET methodology based on the host-guest cucurbit[7]uril-ferrocene (CB7-Fc) chemistry has been recently reported to result in specific tumor uptake and to be feasible with lag times up to 9 days.[3] However, the *in vivo*stability of the formed CB7-Fc complex is compromised after 24 h.[3] We hypothesize, that cucurbit[7]uril-adamantane (CB7-Adma) pretargeted PET platform provides a more suitable host-guest pair (K_a~10^{14}) due to adamantane's higher *in vivo* stability and reported compatibility in humans compared to ferrocene.[4,5] We propose that the higher stability of adamantane guest ligands will result in a more stable host-guest complex *in vivo*.

Methods and Results:

A copper-64-labeled adamantane guest radioligand, [^{64}Cu]Cu-NOTA-PEG_3-Adma (**1**) was developed and studied along with a CB7-modified, carcinoembryonic antigen (CEA) targeting mAb (CB7-M5A) in pretargeting experiments in two subcutaneous xenograft mouse models of pancreatic cancer.

1 was synthesized with high radiochemical yield (98.5±0.7 %) and purity (98.3±1.8 %). Additionally, its measured partition coefficient was -1.9 ± 0.3 and the studied blood half-life in healthy nude mice was 13.8 min. The radioligand was highly stable in bovine plasma at 37 ºC, with 90.6±1.6 % of **1** still intact after 24 h.

The radioligand was studied for *in vivo* pretargeting in two xenograft models of human pancreatic cancer, BxPC3 (CEA+) and MIAPaca-2 (CEA-). The subcutaneous tumor bearing female nude mice were injected with CB7-M5A (0.7 nmol) via the tail vein 72 h prior to the injection of **1** (1.5 nmol, 10.2-13.9 MBq). The mice were imaged with a small animal PET scanner 24 h post radioligand injection followed by *in vivo* biodistribution. Three additional biodistribution cohorts were assigned with BxPC3 xenografts (2, 4 and 8 h) to assess the dosimetry of the imaging strategy. An additional control group involved the injection of only **1** (non-pretargeted) into the tail vein of BxPC3 tumor bearing mice. The tumor uptake of the pretargeted BxPC3 xenograft cohort was significantly higher compared to the pretargeted MIAPaCa-2 or non-pretargeted BxPC3 xenograft cohorts (12.0±0.9 %ID/g; 0.5±0.1 %ID/g; 0.0±0.0; p=0.003). Additionally, the tumor uptake of pretargeted **1** increased over time (2 h: 3.3±0.8 %ID/g & 24h: 12.0±0.9 %ID/g) proving that the formed CB7-Adma complex was highly stable over the monitored 24 h.

A biodistribution of a directly radiolabeled M5A mAb, [^{89}Zr]Zr-DFO-M5A was also studied in both of the xenograft models at 4, 24 and 72 h. Again, the tumor uptake was significantly higher in the BxPC3 xenografts compared to MIAPaCa-2 (53.7±10.0 %ID/g & 7.3 ±0.3 %ID/g at 72 h p.i.; p=0.004). Our findings aligned with our Western Blotting CEA expression experiments of the two cell lines, where MIAPaCa-2 did not show expression of CEA. Excitingly in the BxPC3 xenografts, the tumor-to-blood ratio of the pretargeting approach was only minimally lower compared to [^{89}Zr]Zr-DFO-M5A 5.8±0.4 (24h p.i.) and 7.7±1.1 (72 h p.i.) respectively (p=0.04). Moreover, when the dosimetry of the two approaches were calculated and compared based on their *in vivo* biodistribution data, the red marrow experienced a 70-fold dose reduction with the pretargeting approach compared to the use of [^{89}Zr]Zr-DFO-M5A (0.83 and 57.60 μSv/MBq respectively) making the pretargeting approach a much appealing strategy to utilize for antibody based nuclear medicine.

Conclusions:

The reported studies establish that CB7-Adma driven pretargeting results in excellent antibody PET imaging and high tumor accumulation of the radioligand. The tumor uptake of the adamantane radioligand remained high up to 24 h and the target uptake was dependent on the administration of the tumor targeting CB7-M5A and the specificity of CB7-M5A to the CEA expression of the tumor target.

Reference

1. Jallinoja, V. et al. (2021) DOI: 10.2967/jnumed.120.260687.
2. Altai, M. et al. (2017) DOI: 10.2967/jnumed.117.189944
3. Jallinoja, V. et al. (2022) DOI: 10.1021/acs.molpharmaceut.2c00102
4. Barrow, S.J. et al. (2015) DOI: 10.1021/acs.chemrev.5b00341.
5. Wanka, L. et al. (2013) DOI: 10.1021/cr100264t

Poster Presentation

Disclosures: The authors have disclosed no financial interest.

360-Legumain-Mediated Intracellular Self-Assembly of CES-Theranostic Olsalazine Nanoparticles for Precision Imaging and Treatment of Prostate Cancer

Presenter: Behnaz Ghaemi, Johns Hopkins University School of Medicine

Behnaz Ghaemi[1], Aruna Singh[2], Swati Tanwar[3], Yue Yuan[4], Ishan Barman[5], Michael McMahon[2], Jeff Bulte[1]

[1]Johns Hopkins University School of Medicine, Baltimore
[2]Johns Hopkins University School of Medicine, Baltimore, MD
[3]Johns Hopkins Whiting School of Engineering, Baltimore, MD
[4]University of Science and Technology of China, Baltimore, MD, China
[5]Johns Hopkins Univeristy, Baltimore, Maryland

Introduction:

Cancer therapy may be revolutionized by using specific tumor enzyme-targeted theranostics. The overall aim of this study is to develop a precision-based nanotheranostic platform for prostate cancer that can be monitored by CEST MRI. Exploiting overexpression of enzymes in prostate cancer cells, olsalazine-conjugated peptides were designed to induce self-assembly of olsalazine nanoparticles by the tumor-overexpressed enzymes legumain and furin. Olsalazine is a diaCEST MRI contrast agent with a 9.8 ppm chemical shift from water protons, and acts as a DNA methylation inhibitor anti-cancer agent (1).

Methods:

Synthesis: R6-AAN-CK peptide was synthesized using solid-phase synthesis and subsequently conjugated with olsalazine and 2-cyanobenzothiazole (CBT) to create the peptide-olsalazine-CBT (POC) complex. *Characterization:* Matrix-assisted laser desorption ionization (MALDI) and nuclear magnetic resonance (NMR) were used for peptide characterization. *In vitro and ex vivo immunohistology:* Furin and legumain (over)expression was analyzed in 2D and 3D cell cultures and xenografted tumors. DU145 and LNCaP xenografts were established in Rag2 immunocompromised mice. Aggressive DU145 prostate adenocarcinoma was compared to less-invasive LNCaP tumor cells and RWPE1 normal prostate cells. 3D tumor organoids of prostate cancer were developed and enriched for cancer stem cells up to generation 10 to get the most aggressive clones which were assessed for the expression of legumain, furin and the stemness tumor markers CD133, CD44 and CD24. *In vitro CEST MRI:* After incubation of DU145 with 5 mM POC for 3 h, cells were washed and collected for CEST MRI, performed on a Bruker 11.7 T vertical bore magnetic resonance scanner with a 10-mm birdcage transmit/receive coil.

Results:
In 2D cultures, the levels of legumain and furin expression in DU145 cells were 4- and 3-fold higher than LNCaP and 8- and 6-fold higher than RWPE1 cells, respectively. For 3D tumor spheres, legumain was overexpressed in the periphery while furin was expressed throughout the entire sphere. Legumain and furin expression increased about 6% with each sphere generation accompanied by a 4.5% increase of cancer stem cells according to $CD133^{+}$, $CD44^{+,}$ and $CD24^{-}$ expression analysis. Xenografted 5, 15. 50, 75, 100 and 150 mm^3 DU145 tumors showed heterogeneity in furin and legumain expression with overexpressed legumain in peripheral cells correlating with tumor progression stage. CEST MRI of DU145 cells incubated 3h with POC showed 0.2% asymmetric magnetization transfer ratio (MTR_{asym}) increase at 9.8 ppm compared to control cells (incubated with olsalazine only) as a result of legumain expression and consequent intracellular accumulation and retention of Olsalazine.

Conclusion:
Based on a legumain-mediated CBT click condensation reaction followed by intracellular self-assembly of olsalazine nanoparticles, we successfully developed a POC complex for future imaging of drug accumulation and therapeutic response in aggressive vs. non-invasive prostate tumors.

Reference

1. Yuan, Y.; Zhang, J.; Qi, X.; Li, S.; Liu, G.; Siddhanta, S.; Barman, I.; Song, X.; McMahon, M. T.; Bulte, J. W., Furin-mediated intracellular self-assembly of olsalazine nanoparticles for enhanced magnetic resonance imaging and tumour therapy. Nature materials 2019, 18 (12), 1376-1383.

Poster Presentation

Disclosures: The authors have disclosed no financial interest.

361-The Development of a Dual-Modality (PET/NIRF) Radioimmunoconjugate for Image-Guided Sarcoma Surgery

Presenter: Toni Pringle, Newcastle University

Toni A. Pringle[1], James Knight[2], Saimir Luli[2], Corey D. Chan[3], Kenneth S. Rankin[1], Helen Blair[4]

[1]Newcastle University, Newcastle Upon Tyne, United Kingdom
[2]Newcastle University, Newcastle upon Tyne, Tyne and Wear, United Kingdom
[3]Newcastle University, Newcaslte Upon Tyne, United Kingdom
[4]Newcastle University, Newcastle Upon Tyne, Newcastle Upon Tyne, United Kingdom

Bone sarcomas are devastating primary bone cancers that mostly affect children, young adults, and the elderly [1-3]. These aggressive tumours are associated with poor survival, and surgery remains the mainstay of treatment for localised or resectable bone sarcomas [4, 5]. Surgical resection aims to remove the tumour fully surrounded by healthy tissue to achieve negative tumour margins, whilst maintaining as much healthy tissue as possible to maximise the recovery and functional outcomes for the patient. It is important to achieve negative margins at the first operation as the risk of bone sarcoma recurrence has been found to strongly correlate to the incidence of positive tumour margins after excision [6, 7]. Pre-operative surgical planning is increasingly informed by positron emission tomography (PET) and tumour margin identification during surgery is aided by near-infrared fluorescence (NIRF) imaging, yet these investigations are confounded by probes that lack specificity for sarcoma biomarkers. We report the development of a dual-modal (PET/NIRF) immunoconjugate ([^{89}Zr]Zr-DFO-anti-MT1-MMP-IRDye800CW) that targets MT1-MMP; a matrix metalloproteinase overexpressed in a range of cancers, including sarcoma, and is associated with tumour growth, invasion, metastasis and angiogenesis [8-10]. DFO-anti-MT1-MMP-IRDye800CW and a non-specific IgG control were synthesised by site-selective chemoenzymatic glycan modification (total synthetic yield = 46.15 ± 10.14 %; IRDye800CW degree of labelling = 1.74 0.47). Immunoconjugates were characterised by SDS-PAGE and LCMS which showed localisation of IRDye800CW and DFO to the heavy chain (HC), with the light chain unmodified. The RIC was radiolabelled with ^{89}Zr and isolated in high (>99%) radiochemical purity. Saturation binding and immunoreactivity assays indicted only minor perturbation of binding properties, presenting an immunoreactivity of 96% and a binding affinity (Kd) of 17.4 nM. The ability of the radioimmunoconjugate to selectively bind MT1-MMP was also confirmed via radio-immunostaining of biopsied sarcoma human and mouse tissues. A novel mouse model of dedifferentiated chondrosarcoma based on intrafemoral inoculation of HT1080 wild type or knock-out cells (high and low MT1-MMP expression, respectively) was used to evaluate target binding and biodistribution. Fluorescence and Cerenkov luminescence images acquired 24, 48, and 72 h p.i. of [^{89}Zr]Zr-DFO-anti-MT1-MMP-IRDye800CW showed preferential uptake in HT1080 WT tumours. *Ex vivo* gamma counting revealed that uptake in MT1-MMP-positive tumours (17.64 ± 3.84 %ID/g) was significantly higher than in control groups (P = 0.0006). Taken together, we demonstrate that [^{89}Zr]Zr-DFO-anti-MT1-MMP-IRDye800CW is a promising dual-modal imaging agent for pre-operative surgical planning and intra-operative surgical guidance in sarcoma.

Reference

1. CRUK. Survival for bone cancer. https://www.cancerresearchuk.org/about-cancer/bone-cancer/survival. Accessed 08/11/19.
2. CRUK. Bone sarcoma incidence statistics. https://www.cancerresearchuk.org/health-professional/cancer-statistics/statistics-by-cancer-type/bone-sarcoma/incidence#heading-One. Accessed 09/04/20 2020.
3. Francis M, Dennis N, Charman J, Lawrence G, Grimer R. Bone and Soft Tissue Sarcomas, UK Incidence and Survival: 1996 to 2010. National Cancer Intelligence Network November 2013.
4. Gerrand C, Athanasou N, Brennan B, Grimer R, Judson I, Morland B et al. UK guidelines for the management of bone sarcomas. Clin Sarcoma Res. 2016;6:7. doi:10.1186/s13569-016-0047-1.
5. Casali PG, Bielack S, Abecassis N, Aro HT, Bauer S, Biagini R et al. Bone sarcomas: ESMO-PaedCan-EURACAN Clinical Practice Guidelines for diagnosis, treatment and follow-up. Ann Oncol. 2018;29(Suppl 4):iv79-iv95. doi:10.1093/annonc/mdy310.
6. O'Donnell PW, Griffin AM, Eward WC, Sternheim A, Catton CN, Chung PW et al. The effect of the setting of a positive surgical margin in soft tissue sarcoma. Cancer. 2014;120(18):2866-75. doi:10.1002/cncr.28793.
7. Dickinson IC, Whitwell DJ, Battistuta D, Thompson B, Strobel N, Duggal A et al. Surgical margin and its influence on survival in soft tissue sarcoma. ANZ J Surg. 2006;76(3):104-9. doi:10.1111/j.1445-2197.2006.03615.x.
8. Sato H, Takino T, Okada Y, Cao J, Shinagawa A, Yamamoto E et al. A matrix metalloproteinase expressed on the surface of invasive tumour cells. Nature. 1994;370(6484):61-5. doi:10.1038/370061a0.
9. Bjørnland K, Flatmark K, Pettersen S, Aaasen AO, Fodstad Ø, Mælandsmo GM. Matrix Metalloproteinases Par-

ticipate in Osteosarcoma Invasion. Journal of Surgical Research. 2005;127(2):151-6. doi:https://doi.org/10.1016/j.jss.2004.12.016.

10. Gonzalez-Molina J, Gramolelli S, Liao Z, Carlson JW, Ojala PM, Lehti K. MMP14 in Sarcoma: A Regulator of Tumor Microenvironment Communication in Connective Tissues. Cells. 2019;8(9). doi:10.3390/cells8090991.

Poster Presentation

Disclosures: The authors would like to disclose that the Stryker SPY PHI Camera has been approved.

362-Whole CNS 3D cryo-fluorescent microscopy shows CSF clearance along nasal lymphatics, spinal nerves, and lumbar lymphatics

Presenter: Christian Stokes, Emit Imaging

Christian Stokes[1], Eli White[1], Nicole Bens[2], Praveen Kulkarni[2], Craig Ferris[2], Steven Toddes[1]

[1]Emit Imaging, Baltimore, MD
[2]Northeastern University, Boston, MA

Unwanted proteins and metabolic waste in cerebral spinal fluid (CSF) are cleared from the brain by meningeal and nasal lymphatics, and along blood vessels and the epineural sheath of cranial nerves; however the distribution and clearance of CSF along the subarachnoid space of the entire spinal cord has yet to be determined. It was hypothesized that the anatomical resolution of Cryo-Fluorescence Tomography (CFT) could provide the missing visual evidence of tracer exiting the spinal nerves at each level of the vertebral column. To that end, isoflurane anesthetized mice were infused into the lateral cerebroventricle with 5.0 µl of quantum dots [QdotR 605 ITKTM amino (PEG)] over two mins. Mice were allowed to recover (ca 2-3 min) and remained awake and ambulatory for 5, 15, 30, 60 and 120 min after which they were euthanized, and the entire intact body frozen at -80^{0}. The animals were imaged on Emit Imaging's Xerra at a 35µm isotropic voxel resolution. The Xerra, and CFT in general, section through the animals capturing white light and fluorescent images after each slice to produce high resolution three-dimensional volumes for each animal. 16-bit fluorescent images are acquired with exposure times of 5 ms, 50 ms, 500 ms, 1500 ms and 2500 ms. These images are then combined into a single 32-bit high dynamic range (HDR) image to extend the Xerra's detection limits beyond a single exposure. CFT highlighted the circulation of tracer throughout the ventricular system and central canal of the spinal cord and the entire subarachnoid space of the CNS. Signal could be visualized in the nasal cavity, deep cervical lymph nodes and more superficial submandibular lymph nodes as early as 15 min post infusion. Fluorescent signal could be visualized along the dorsal root ganglia and down the proximal extension of the spinal nerves of the thoracic and lumbar segments at 15 min. Interestingly, there was significant accumulation of tracer in the aortic lumbar lymphatics at the level of the kidneys between 15- 60 min. The dense fluorescent signal in the thoracic vertebrae noted at 5- and 15-mins post infusion was significantly reduced by 30 min. Indeed, all signal in the spinal cord was ostensibly absent by 120 min with the exception of trace amounts in the coccyx. The brain still had some residual signal at 120 min. These data show that Qdots with a hydrodynamic diameter of 20nm rapidly clear from the brain of awake mice. These data also clearly demonstrate the rapid distribution and efflux of trace along a major length of the vertebral column and the potential contribution of the spinal cord and it many pairs of spinal nerves in the clearance of brain waste. One could also consider the notion that bioactive molecules e.g. proinflammatory cytokines and other neural and glial molecules generated in the brain parenchyma could impact systemic physiology by their transported down the epineural sheath of spinal nerves to terminate in extracellular tissue of skin, muscle, and joints.

Poster Presentation

Disclosures: The authors have disclosed no financial interest.

363-Ex vivo human breast cancer visualization by topical application of the cathepsin-activatable fluorescent probe 6QC-ICG

Presenter: Daan Linders, Leiden University Medical Center (LUMC)

Daan G. Linders[1], Okker Bijlstra[2], Ethan Walker[3], Brian Straight[4], Marieke Straver[5], Hans Marten Hazelbag[5], James Basilion[3], Alexander Vahrmeijer

[1]Leiden University Medical Center (LUMC), Netherlands
[2]Leiden University Medical Center (LUMC), Leiden, Zuid-Holland, Netherlands
[3]Case Western Reserve University, Cleveland, OH
[4]Akrotome Imaging, Cleveland, Ohio
[5]Haaglanden Medisch Centrum, The Hague, Netherlands

Background and Aim:
Breast cancer (BC) remains the most frequently diagnosed cancer and the leading cause of cancer-related mortality in females [1]. Treatment of non-metastatic BC consists of surgical resection and, depending on patient and tumor characteristics, systemic and/or radiation therapy [2]. Patient outcomes can be improved by achieving tumor-free resection margins during BC surgery, as this prevents local recurrence and in some cases disease-specific mortality [3-5]. However, a tumor-positive resection margin rate of 4-18% indicates that removal of the tumor using breast conserving surgery (BCS, the preferred method) based on visual and tactile feedback alone can be challenging [6,7]. Evidently, there is an unmet need for a method to determine the presence of residual cancer within the resection cavity at the time of surgery. Tumor-targeted fluorescence imaging during BCS could help to identify residual tumor and guide additional resection. A promising contrast agent for fluorescence-guided BCS is the quenched, protease-activatable probe 6QC-ICG. It consists of an analogue of indocyanine-green (ICG) and a quencher conjugated to a core Cbz-Phe-Lys peptide sequence [8]. The probe is cleaved and activated by the cysteine cathepsins B, L and S, proteolytic enzymes that are highly upregulated in BC cells [9]. Preclinical studies demonstrated that intravenously administered 6QC-ICG can clearly visualize BC and guide tumor resection in an orthotopic mouse-model [8,10]. However, a topical application protocol would be easier to implement in the surgical workflow and would be more patient-friendly than systemic administration. As proof-of-concept, the current study aims to investigate whether topically applied 6QC-ICG is able to visualize human BC ex vivo as a precursor to topical in vivo application during surgery for tumor identification.

Methods:
Female patients with invasive BC or ductal carcinoma in situ (DCIS) scheduled to undergo surgery at the Haaglanden Medical Center, The Netherlands, were enrolled in the study. Patients with a history of surgery on the ipsilateral breast or that received neoadjuvant treatment or intraoperative radiotherapy were excluded. Immediately after resection, the BC specimen was inked, frozen at -80°C for 5 minutes, and sliced into 3-5 millimeter thick slices. Subsequently, 6QC-ICG probe dissolved in Pluronic gel was applied onto the tissue slice with the

macroscopically largest tumor diameter and the two adjacent slices. Different probe concentrations (20, 50, and 100 µM) were tested. After 10 minutes of incubation, the imaging gel was washed off 3-5 times with sterile saline and the tissue slices were dried using sterile gauze. Fluorescent images of the three tissue slices were obtained using the Pearl Trilogy Imaging System. The fluorescence signal in the tumor from each tissue slice was quantified as a tumor-to-background ratio (TBR), defined as the mean fluorescence intensity (MFI) in the tumor divided by the MFI in the surrounding healthy breast tissue. The complete tissue slices were fixed with formalin and embedded in paraffin. Four-µm thick tissue slides were stained for routine H&E histology. Tumor-positive regions were delineated by a pathologist blinded for the fluorescent signal.

Results:
A total of 36 tissue slices of 12 different patients were imaged. Twenty-seven of the 36 tissue slices (75%) were tumor-positive. The 20, 50, and 100 µM probe concentration was used on 2, 15, and 10 of the tumor-positive tissue slices, respectively. The MFI in tumor tissue was significantly higher than in healthy breast tissue (0.036 vs. 0.02, $p < 0.005$). Topically applied 6QC-ICG visualized BC with a mean TBR of 1.8. There was no significant difference in TBR between the different dosing groups.

Conclusions:
These results show that topical application of the cathepsin-activatable fluorescent probe 6QC-ICG can visualize human BC with a considerable contrast to adjacent healthy tissue, indicating its potential for fluorescence-guided BCS.

Reference

1. Bray F, Ferlay J, Soerjomataram I, Siegel RL, Torre LA, Jemal A. Global cancer statistics 2018: GLOBOCAN estimates of incidence and mortality worldwide for 36 cancers in 185 countries. CA Cancer J Clin 2018;68(6):394-424.
2. Waks AG, Winer EP. Breast Cancer Treatment: A Review. JAMA 2019;321(3):288-300.
3. Clarke M, Collins R, Darby S, Davies C, Elphinstone P, Evans V, Godwin J, Gray R, Hicks C, James S and others. Effects of radiotherapy and of differences in the extent of surgery for early breast cancer on local recurrence and 15-year survival: an overview of the randomised trials. Lancet 2005;366(9503):2087-106.
4. Houssami N, Macaskill P, Marinovich ML, Dixon JM, Irwig L, Brennan ME, Solin LJ. Meta-analysis of the impact of surgical margins on local recurrence in women with early-stage invasive breast cancer treated with breast-conserving therapy. Eur J Cancer 2010;46(18):3219-32.
5. Tejera Hernandez AA, Vega Benitez VM, Rocca Cardenas JC, Gutierrez Giner MI, Diaz Chico JC, Hernandez Hernandez JR. Factors predicting local relapse and survival in patients treated with surgery for breast cancer. Asian J Surg 2019;42(7):755-760.
6. McCahill LE, Single RM, Aiello Bowles EJ, Feigelson HS, James TA, Barney T, Engel JM, Onitilo AA. Variability in reexcision following breast conservation surgery. JAMA 2012;307(5):467-75.
7. Brouwer de Koning SG, Vrancken Peeters M, Jozwiak K, Bhairosing PA, Ruers TJM. Tumor Resection Margin Definitions in Breast-Conserving Surgery: Systematic Review and Meta-analysis of the Current Literature. Clin Breast Cancer 2018;18(4):e595-e600.
8. Yim JJ, Tholen M, Klaassen A, Sorger J, Bogyo M. Optimization of a Protease Activated Probe for Optical Surgical Navigation. Mol Pharm 2018;15(3):750-758.
9. Olson OC, Joyce JA. Cysteine cathepsin proteases: regulators of cancer progression and therapeutic response. Nat Rev Cancer 2015;15(12):712-29.
10. Widen JC, Tholen M, Yim JJ, Antaris A, Casey KM, Rogalla S, Klaassen A, Sorger J, Bogyo M. AND-gate contrast agents for enhanced fluorescence-guided surgery. Nat Biomed Eng 2021;5(3):264-277.

Poster Presentation

Disclosures: The authors have disclosed no financial interest.

364-Pharmacokinetics of a Model Antigen from Emulsion-Adjuvanted Vaccines using Nuclear Imaging

Presenter: Tullio Esposito, Memorial Sloan Kettering Cancer Center

Tullio V. Esposito[1], Aidan Wirrick[1], NagaVaraKishore Pillarsetty[2]

[1]*Memorial Sloan Kettering Cancer Center, New York City, NY*
[2]*Memorial Sloan Kettering Cancer Center, New York, NY*

Background:
Emulsions are used as vaccine adjuvants to potentiate and direct the adaptive immune response against co-formulated antigen(s)[1]. Water-in-mineral oil emulsions, such as Freund's adjuvants, are a mainstay in the research setting to induce autoimmunity and antibody production in animal models.[2] Less reactogenic squalene-based oil-in-water emulsions, namely AS03 and MF59, are licensed for use in human vaccines against seasonal/ pandemic influenza and are in advanced phase III clinical trails against SARS-CoV-2 (COVID-19).[3] Despite widespread use, surprisingly little is known about the absorption and distribution of antigens from emulsion-adjuvanted vaccines.[2, 3]Understanding these parameters is fundamental to fully understand the immunology, safety and efficacy profile of a vaccine.[4] This work therefore sought to comprehensively assess the pharmacokinetics of the model antigen ovalbumin (OVA) from oil-in-water and water-in-oil emulsions using fully quantitative nuclear techniques.

Experimental:
OVA was modified with an isothiocyanate derivative of deferoxamine and radiolabeled with ^{89}Zr-oxalate to form ^{89}Zr-DFO-OVA [structural overview in **Figure 1a**]. Radiochemical conversion (RCC) and radiopurity (RCP) were calculated using an instant thin layer chromatography (ITLC) system consisting of a silica-gel impregnated stationary phase and 50 mM EDTA mobile phase. Changes in the molecular weight of the radiotracer were determined with non-reducing sodium dodecyl sulfate polyacrylamide gel electrophoresis (SDS-PAGE). ^{89}Zr-DFO-OVA was formulated for administration by admixing with pre-formed AddaVax (similar to MF59) and AddaS03 (similar to AS03) emulsions or emulsified with Incomplete Freund's adjuvant (IFA) by repeated passage through a 23G syringe. The above formulations, along with a free antigen control, were injected subcutaneously into the dorsal flank of 8-10 week old female C57Bl/6 mice. Serial PET/CT scans were then acquired over 10 days and biodistributions were performed at 1, 4 and 10 days post-injection (n=3-4/ group).

Results:
ITLC analysis of four radiolabeling attempts found RCC to be 93.1 ± 5.7 % and RCP to be 99.2 ± 0.2 % [**Figure 1b**]. A slight upshift in the ^{89}Zr-DFO-OVA band was observed on SDS-PAGE, consistent with the modifications used to radiolabel the protein [**Figure 1c**]. Quantitative analysis of the injection site [**Figure 2**] found that both

AddaVax and AddaS03 significantly enhanced the rate of antigen adsorption compared to the free antigen control over the duration of the study. The absorption of ^{89}Zr-DFO-OVA was also significantly faster in the AddaS03 group relative to AddaVax up to 96 h post-injection. IFA on the other hand significantly delayed antigen absorption from the site of injection compared to the free antigen control over the 10 day study. Tissue concentrations of ^{89}Zr-DFO-OVA in distant organs (lymph nodes, kidney, spleen, liver, blood) were elevated across all time points in the oil-in-water cohorts relative to IFA and the free antigen control [**Figure 3**]. The distribution of ^{89}Zr-DFO-OVA in the lymph nodes was more transient in nature and of higher initial magnitude in the AddaS03 group compared to AddaVax.

Conclusions:

An OVA-based radiotracer was successfully prepared and used to identify key differences in antigen absorption and distribution between commonly used emulsion-based adjuvants. This information is of importance as it can facilitate rationale vaccine design and formulation.

Reference

1. Pulendran, B.; S. Arunachalam, P.; O'Hagan, D. T., Emerging concepts in the science of vaccine adjuvants. Nature Reviews Drug Discovery 2021, 20 (6), 454-475.
2. Stills, H. F., Jr., Adjuvants and antibody production: dispelling the myths associated with Freund's complete and other adjuvants. Ilar j 2005, 46 (3), 280-93.
3. O'Hagan, D. T.; van der Most, R.; Lodaya, R. N.; Coccia, M.; Lofano, G., "World in motion" - emulsion adjuvants rising to meet the pandemic challenges. NPJ Vaccines 2021, 6 (1), 158.
4. Bachmann, M. F.; Jennings, G. T., Vaccine delivery: a matter of size, geometry, kinetics and molecular patterns. Nature Reviews Immunology 2010, 10(11), 787-796.

Poster Presentation

Disclosures: The authors have disclosed no financial interest.

365-Evaluating Antibody to Cell Penetrating Peptide Ratios for Enhanced Cellular Internalisation

Presenter: Toni Pringle, Newcastle University

Toni A. Pringle[1], James Knight[2], Akane Kawamura[1], Oliver Coleman[1]

[1]*Newcastle University, Newcastle Upon Tyne, United Kingdom*
[2]*Newcastle University, Newcastle upon Tyne, Tyne and Wear, United Kingdom*

Monoclonal antibody-based imaging and therapeutic agents are restricted to cell-surface targets primarily due to their inefficient cellular internalisation. Modification of mAbs leading to enhanced cellular translocation can improve both imaging and therapy and expose new intracellular and intranuclear epitopes that were previously out of reach of these agents.[1, 2] This can be achieved through chemical modification of the antibody with a cell-penetrating peptide (CPP), leading to enhanced cell membrane translocation. Determining the optimal CPP to antibody ratio is essential so that the specific antigen recognition of the antibody is not overcome by the non-specific cell penetrating ability of a coupled CPP.[3] Surprisingly, the effects of CPP to antibody ratios on cell specific internalisation has not been closely examined in an stepwise, incremental approach. We report the development of HER-2 targeting antibody-CPP conjugates ([^{89}Zr]Zr-DFO-Her-TAT$_{(0\text{-}5)}$) modified with varying numbers of the cell-penetrating peptide TAT. DFO-Her-TAT, with a TAT degree of labelling between 0 and 5, were synthesized *via* a three-step synthesis beginning with the attachment of dibenzocyclooctyne (DBCO, 0-7 fold molar excess) to lysine residues distributed throughout trastuzumab (Herceptin, Her, yields >78%). Her-DBCO$_{(0\text{-}7)}$ conjugates then underwent a strain-promoted azide-alkyne coupling (SPAAC) reaction with an excess of azide modified TAT (TAT-N_3) to produce Her-TAT with average TAT degrees of labelling between 0-5 (DOL$_{TAT}$, yields >85%). Lysine residues were further modified with DFO to enable ^{89}Zr chelation (yields >80%). The DBCO and TAT degree of labelling was determined by UV/Vis spectroscopy and validated by MALDI-TOF. SDS-PAGE and MALDI-TOF analysis showed multiple bands/peaks, at an increased mass compared to unmodified Herceptin, each due to the attachment of an additional TAT peptide. [^{89}Zr]Zr-DFO-Her-TAT$_{(0\text{-}5)}$ conjugates were isolated in high radiochemical purity (>99%) and were >98% stable serum, mouse serum and PBS over 7 days at 37 C. The extent of internalisation of [^{89}Zr]Zr-DFO-Her-TAT$_{(0\text{-}5)}$ was assessed in SKBR3 and MDA-MB-468 (HER-2 + and - respectively) breast cancer cells. The percentage of internalised dose was found to be dependent upon the DOL$_{TAT}$ at all time-points, with larger DOL$_{TAT}$ leading to a larger internalised dose in SKBR3, and to a lesser extent MDA-MB-468 cells. The internalised dose in SKBR3 cells for RICs with DOL$_{TAT}$ of 0 and 1 are very similar at all time points, suggesting that more than one TAT is required to effectively increase internalisation. Controlling for uptake in MDA-MB-468 cells, the largest increase in internalised dose is observed when increasing the DOL$_{TAT}$ from 1 to 2 (203% at 48 h), followed by 2 to 3 (172% at 48 h). Increasing from DOL$_{TAT}$ 0 to 5 resulted in over 11-fold increase in normalised internalised dose in SKBR3 cells. Cell penetrating peptides can be expensive to purchase, especially with specific handles (such as DBCO) for cargo conjugation. A compromise therefore must be made between the cost of attaching an additional TAT peptide with the effect on internalisation. Therefore, when balancing cost, we believe a minimum of 2, but ideally 3 TAT peptides are required to effectively enhance cell internalisation. The percentage of applied dose that was membrane bound also increased with the DOL$_{TAT}$. The differences between specific and non-specific uptake were found to only be significant between 24 and 48 h with conjugates with a DOL$_{TAT}$ of 2 and above. A decrease in membrane bound dose from 24 to 48 h was observed, which correlates with the large increase in internalised dose observed at this time-point. Unexpectedly, this data suggests similar initial binding of the conjugate to the membrane of both SKBR3 and the non-specific MDA-MB-468 cells, though the non-specific binding was found to decrease at later time-points.

Reference

1. M. Veal, G. Dias, V. Kersemans, D. Sneddon, S. Faulkner and B. Cornelissen, J Nucl Med, 2021, 62, 1537-1544.
2. B. Cornelissen, V. Kersemans, S. Darbar, J. Thompson, K. Shah, K. Sleeth, M. A. Hill and K. A. Vallis, Cancer Res, 2011, 71, 4539-4549.
3. M. Jain, G. Venkatraman and S. K. Batra, European Journal of Nuclear Medicine and Molecular Imaging, 2007, 34, 973-977.

Poster Presentation

Disclosures: The authors have disclosed no financial interest.

366-Effect of pixel size on the microstructural properties of bone using µCT imaging for preclinical and biological research

Presenter: Shyam Hassan, Keck School of Medicine of USC

Shyam F. Hassan[1], Luis Diego Luna Centeno[2], Tautis Skorka[3], Peter Conti[3], Adam Huttenlocker[1], Biren Patel[1], Tea Jashashvili[1]

[1]Keck School of Medicine of USC, Los Angeles, CA
[2]Keck School of Medicine of USC
[3]Keck School of Medicine of USC, Los Angeles, CA, CA

Background and Aims:
Studying trabecular bone microstructural properties (TBMP) is essential in preclinical and biological research. High-resolution micro-computed tomography (Hr-μCT) imaging is one of the most used methods to study these properties and understand biological variation and pathological and treatment effects on bone development or remodeling. Unfortunately, the lack of uniformity in reported results makes it difficult to compare and interpret results across different studies. Several research articles previously addressed the possibility of standardizing the terminology, reporting, and image acquisition parameters [1-2]. The pixel size (PS) dependency, reproducibility, and sensitivity of human subjects have been well established in clinical and research settings [3-7]. The PS choice of the Hr-μCT images is crucial for TBMP. For example, 0.020-0.030 mm images may be acceptable for human trabecular thickness averaging about 0.2 mm [8]. The trabecular thickness of a mouse is about 0.030-0.060 mm. Therefore, studies using mouse models require smaller PS (0.006-0.01 mm) [9-10]. Detailed studies of the effect of PS on the TBMP for small and medium size research animals and how these compare to human TBMP are lacking [9-10]. This study aims to determine whether the PS difference of same-size structures affects the morphological outcome of TBMP when all Hr-μCT acquisition, reconstruction, region of interest (ROI), thresholding, and trabecular analysis parameters remain the same. We also evaluate how TBMP varies among different skeletal sites of the same animal and what constitutes an acceptable PS of Hr-μCT images for effectively calculating TBMP without encountering PS effect on the results.

Methods and Results:
We recognize the expected effects of X-ray parameters and post-μCT acquisition image treatment on the outcomes of TBMP (e.g., the choice of the segmentation algorithm, filtration of the image during reconstruction, and model-independent/-dependent measurements). In this study, all these parameters are standardized across six different skeleton sites (capitate, lateral cuneiform, third metacarpal, and third metatarsal) of one wild cat and two coyotes. Considering the effect of varying ROIs on the BV/TV (bone volume fraction %) and Tb.Th (trabecular thickness mm), we have overlapped all three Hr-μCT scans (i.e., PS of 0.022, 0.035, and 0.045 mm) and used the same ROIs (Table1-2). Figure1 illustrates the Hr-μCT images of the same structures scanned at different PS and the corresponding image intensity profile defined on trabecular bone strides for each scan. The BV/TV and Tb.Th parameters significantly increase with large PS (above 5% difference) (Table1). Our results demonstrate that if the same animal were studied using different pixel sizes, two conflicting results could result depending on skeletal sites (e.g., carpals versus metacarpal at 0.022 and 0.035 mm, Table1). Our analysis also demonstrated that dominance patterns between hindlimb and forelimb are less affected by PS and will deliver more comparable results between different PSs (Table2) [7,9]. The difference between the physical boundary of the trabecular bone from one PS to another is due to the partial volume effect (PVE). This effect depends on the pixel-to-object-size ratio (POSR) (Fig.1).

Conclusions:
The actual size of structures could be used as a guiding factor in which PS can be chosen during Hr-μCT scanning for the given animal model. Published histological measurements of the group's trabecular thickness will be used. If it is unavailable, histological measurements must be required to validate PS choice to avoid a large PVE during an Hr-μCT and prevent aberrant results. Determining POSR is part of our ongoing research. Given that the presented analyses are intriguing and meaningful as they relate to preclinical and biological research study design, we plan to extend our study, investigate different size animals, and validate the results with histological measurements.

Reference

1. Bouxsein, M.L., et al., Guidelines for assessment of bone microstructure in rodents using micro-computed tomography. J Bone Miner Res, 2010. 25:1468-86
2. Irie, M.S., et al., Effect of data binning and frame averaging for micro-CT image acquisition on the morphometric outcome of bone repair assessment. Scientific Reports, 2022. 12: 1424
3. Tjong, W., et al., The effect of voxel size on high-resolution peripheral computed tomography measurements of trabecular and cortical bone microstructure. Medical Physics, 2012. 39:1893-1903
4. Pauwels, R., et al., Effect of exposure parameters and voxel size on bone structure analysis in CBCT. Dentomaxillofac Radiol, 2015. 44:20150078
5. Cooper, D., et al., Effect of voxel size on 3D micro-CT analysis of cortical bone porosity. Calcif Tissue Int, 2007. 80:211-219
6. Christen, P., et al., Voxel size dependency, reproducibility, and sensitivity of an in vivo bone loading estimation algorithm. J R Soc Interface, 2016. 13:20150991
7. Perilli, E., et al., Reynolds, Micro-CT examination of human bone: from biopsies towards the entire organ. Annali dell'Istituto superiore di sanita, 2012. 48:75-82
8. Larrue, A., et al., Synchrotron Radiation Micro-CT at the Micrometer Scale for the Analysis of the Three-Dimensional Morphology of Microcracks in Human Trabecular Bone. PLOS ONE, 2011. 6:e21297
9. Christiansen, B.A., Effect of micro-computed tomography voxel size and segmentation method on trabecular bone microstructure measures in mice. Bone Rep, 2016. 5:136-40
10. Müller, R., et al., Resolution dependency of microstructural properties of cancellous bone based on three-dimensional mu-tomography. Technol Health Care, 1996. 4:113-9

Poster Presentation

Disclosures: The authors have disclosed no financial interest.

367-Biomarker discovery for imaging tumour relevant T cells in non-small cell lung cancer (NSCLC)

Presenter: Lilian Koppensteiner, The University of Edinburgh

Lilian Koppensteiner[1], Layla Mathieson[1], Richard O'Connor[1], Ahsan Akram[2]

[1]The University of Edinburgh, United Kingdom
[2]University of Edinburgh, Edinburgh, Midlothian, United Kingdom

Background:
The immune response to cancer is dependent on functionally efficient cytotoxic T lymphocytes (CTL). Checkpoint inhibition therapy is aimed at reinvigorating local cytotoxic T cells but the rate of immunotherapy failure in NSCLC is as high as 80% in unselected patients.[1] As CTL phenotypes determine the immunological response to therapy, they are an attractive imaging biomarker target. Therefore identifying the extent of cytotoxic lymphocyte infiltration, as a measure of

pre-existing immunity could be used to predict clinical outcome or responsiveness to treatment.[3] In recent years, CD39 has emerged as a marker to identify tumour relevant T cells. Unlike PD1, which may also be expressed on multiple cell types, CD39 expression is lacking in bystander $CD8^+$ T cells and highly expressed in tumour reactive $CD8^+$ T cells in colon cancer and melanoma.[4] Notably, Duhen et al revealed that $CD39^+CD8^+$TIL often co-express the tissue resident memory marker CD103. These DP cells display an exhausted tissue resident memory T cell phenotype that, despite its reduced capacity for effector cytokine production, shows great cytotoxicity against neoplastic cells.[5] **Objective** In order to identify an imaging target to tag tumour relevant T cells in NSCLC, we aimed to analyse upregulated gene expression in T cells in NSCLC, characterize the expression of CD39 and CD103 in the peripheral blood and tumour microenvironment of early NSCLC and corresponding non-cancerous lung tissue (NCL) as well as their spatial expression patterns in tumour-, and stromal areas to understand the imaging significance of $CD39^+CD103^+$ CTL in NSCLC.

Methods & Results:
$CD8^+$ T cells from NCL tissue and tumour tissue were sorted using flow cytometry and analysed using a Nanostring nCounter gene expression assay. Amongst the top differentially expressed genes, we observed a significant upregulation of the CD39 encoding gene ENTPD1 in tumour compared to NCL tissue (log2(fold change) = 3.5, p = 0.001280), illustrating the upregulation of CD39 in $CD8^+$ T cells by the tumour microenvironment. We aimed to further characterize the expression profile of CD39+ cells using flow cytometry of i) primary NSCLC tumour tissue, ii) adjacent NCL and iii) peripheral blood. While we saw a dramatic shift towards CD39+ cells across multiple cell types in tumour- compared to NCL tissue, we found that the expression of CD103 is restricted to lung tissue, where it is mainly expressed by T cells. In the tumour tissue of NSCLC, the majority of $CD39^+CD8^+$T cells are $CD103^+$, and this co-expression was not found in other cell types. Finally, spatial expression patterns of CD39 and CD103 in tumour-, and stroma areas of FFPE tissue microarrays (TMA) were analysed using multispectral imaging of OPAL multiplex Immunofluorescence in a cohort of early untreated NSCLC patients (n=162). In support of our flow cytometry data, the frequency of $CD39^+CD103^+$ cells amongst $CD8^+$ T cells is significantly higher in tumour tissue compared to NCL and while CD8+ T cells only expressing CD39 are sequestered in the stroma, CD39+CD103+ CD8+ T cells were distributed across stroma and tumour areas.

Conclusion:
In conclusion, while CD39 expression is significantly increased across cell types in the tumour tissue of NSCLC compared to NCL and peripheral blood, $CD39^+CD103^+$ cells are absent in the peripheral blood, significantly increased in tumour tissue where they are restricted to $CD8^+$ T cells, and distributed across tumour and stroma areas, making them a good imaging target for evaluating the presence of tumour relevant exhausted T cells that could be rescued by checkpoint inhibition. Testing suitable imaging modalities will be subject to future work.

Reference

1. Assi, H. I., Kamphorst, A. O., Moukalled, N. M. & Ramalingam, S. S. Immune checkpoint inhibitors in advanced non–small cell lung cancer. Cancer 124, 248–261 (2018).
2. Reck, M. et al. Pembrolizumab versus Chemotherapy for PD-L1–Positive Non–Small-Cell Lung Cancer. N. Engl. J. Med. 375, 1823–1833 (2016).
3. Bodor, J. N., Boumber, Y. & Borghaei, H. Biomarkers for immune checkpoint inhibition in non-small cell lung cancer (NSCLC). Cancer 126, 260–270 (2020).
4. Simoni, Y. et al. Bystander CD8+ T cells are abundant and phenotypically distinct in human tumour infiltrates. Nature (2018).
5. Duhen, T. et al. Co-expression of CD39 and CD103 identifies tumor-reactive CD8 T cells in human solid tumors. Nat. Commun. 9, (2018).

Poster Presentation

Disclosures: The authors have disclosed no financial interest.

368-The synthesis and evaluation of 64Cu labeled Neurotensin Receptor antagonists for theranostic application

Presenter: Xinrui Ma, University of North Carolina at Chapel Hill

Xinrui Ma[1], Tao Zhang[1], Muyun Xu[1], German Fonseca Cabrera[2], Zhanhong Wu[1], Zibo Li[1]

[1]University of North Carolina at Chapel Hill, Chapel Hill, NC
[2]UNC-Chapel Hill

Introduction:
Accumulating evidence suggests that neurotensin (NTS) and neurotensin receptors (NTSRs) play key roles in lung cancer progression by triggering multiple oncogenic signaling pathways including PKC/ERK and AKT. Recently, several attempts have been made to synthesize radiometal labeled NTRS agents, most of which demonstrated only moderate tumor uptake and retention. The aim of this study is to develop novel NTSR1 targeted agents for both imaging and therapy applications.

Methods:
A series of NTR antagonists were synthesized with variable propylamine (PA) linker length and different chelators, including [^{64}Cu]Cu-CB-iPA-NT (i=1, 2, 3), [^{64}Cu]Cu-NOTA-2PA-NT, [^{64}Cu]Cu-DOTA-2PA-NT, and [^{64}Cu]Cu-DOTA-2PA-NT-VS. Radiolabeling reactions were performed under 95-degree heating for CB precursors, while 37 degrees for NOTA and DOTA precursors. Western blot was used to determine NTR expression in human lung cancer cell lines. We assessed the candidate compounds' *in vitro* and *in vivo* stability and their binding affinity to H1299 cells. To evaluate the agents' biodistribution properties, small animal PET/CT scans were performed using H1299 xenografts at 2, 4, 24, and 48h post injection.

Results:
NTSR1 was confirmed to have high expression in H1299 cells by western blot. NT-CB-2PA showed good binding affinity towards H1299 cells with IC_{50} to be 3.038 nM. Small animal PET/CT showed prominent tumor uptake, high tumor-to-background contrast, and long tumor retention up to 48 h post injection. The lead agent, NT-CB-2PA, demonstrated 8.41±1.33 %ID/g tumor uptake, which was maintained at 9.72±4.89 %ID/g at 48h. Moderate liver uptake (7.72±4.68 %ID/g at 48h) was observed along with low uptake in most other organs. Compared to NT-CB-2PA, NT-CB-1PA had a lower background including low liver uptake at 24h and 48h after injection (0.27 ± 0.14 %ID/g at 24h and 0.08 ± 0.05 %ID/g at 48h) while tumor uptake remained high (6.06 ± 2.28 %ID/g at 24h and 4.52 ± 1.90 %ID/g at 48h). Meanwhile, CB-3PA showed increased uptake in both tumor and liver.

Conclusions:
Through the side-by-side comparison, CB-2PA-NT was identified as the lead agent for further evaluation based on its high and persistent tumor uptake and moderate liver uptake. The success of this theranostic

approach will not only lead to an accurate imaging-based method to efficiently detect NTSR1 expression in lung cancer (for diagnosis, patient screening, and treatment monitoring), but also the radionuclide-based agent for lung cancer therapy.

Poster Presentation

Disclosures: The authors have disclosed no financial interest.

369-Image Quality in a Range of Isotopes with a new Preclinical PET Insert for Simultaneous PET/MRI

Presenter: Deborah Hill

Deborah Hill[1], Morten Karlsen[2], Cesar Molinos Solsona[3], Carlos Correcher[4], Abel Orero[5], Josep Oliver[6], Emilio Gimenez[6], Antonio J. Gonzalez[7], Thorsten Greeb[8], Todd Sasser[3], Anne Chen[8], Geoffrey Warnock[9], Sven Junge[8], Mette Lauritzen[8], Michael Heidenreich[10]

[1]*Trondheim, Norway*
[2]*Norwegian University of Sceince and Technology, Trondheim, Norway*
[3]*Bruker BioSpin, Billerica, MA*
[4]*Bruker Española S.A., Valencia, Comunidad Valenciana, Spain*
[5]*Bruker Española S.A., La Pobla de Vallbona, Valencia, Spain*
[6]*Bruker Española S.A., Valencia, Spain*
[7]*Institute for Instrumentation in Molecular Imaging, Valencia, Spain*
[8]*Bruker, Ettlingen, Baden-Württemberg, Germany*
[9]*University Hospital Zurich, Zurich, Switzerland*
[10]*Bruker BioSpin, Germany*

Background:
A PET Insert for rats in 30 cm bore MRI scanners was introduced in 2015 and has been fully characterized in Ref [1]. PET Inserts for smaller bore scanners can be used for mouse and rat head imaging, and offer the additional advantage of higher gradient strengths and slew rates beneficial in functional MRI or brain connectivity studies on mice. The work presented here describes a new PET Insert Ref. [2] compatible with 17 cm bore magnets and gradient strengths of up to 900 mT/m. The study provides the assessment of image quality for most relevant PET isotopes and the first in vivo validation using 18F FDG in mice.

Method:
The PET insert is based on continuous LYSO crystals coupled to SiPM. The external and inner diameters is 103 and 60 mm respectively. The FOV is 55×101 mm making it suitable for total body imaging of mice and rat heads applications. The insert was used on a BioSpec 70/20 PET/MR Scanner (Bruker BioSpin), equipped with a BGA12S high power gradient and a PET-optimized 35 mm TR volume coil. Image acquisition, reconstruction and analysis was done using Paravision 360. The image quality using F-18, Cu-64 and Ga-68 isotopes was characterized using a NEMA Image Quality Phantom which was filled with 3.7 MBq, acquired for 20 min PET/MR and processed according to the NEMA standard [3].
The resulting PET list-mode files were reconstructed with three iterative algorithms: MLEM, MAP and OSEM. A voxel size of 0.25 mm was employed in all reconstructions, and the iteration number was individually optimized for best recovery coefficient performance yet maintaining uniformity below 15%.
F-18 FDG PET/MR in vivo experiments were also carried out on mice. Mice were injected with 8 MBq, and images were acquired for 15 min after a 60 min uptake time. MAP reconstructions with 20 iterations and a 0.25 mm voxel were used. Anatomical MRI imaging involved a T1-weighted FISP 3D sequence (TE/TR of 2.6/5.5 ms) and an isotropic voxel size of 200 um. These MRI images were used to provide the attenuation map for quantitative PET reconstructions.

Results:
The table below shows the results of the IQ phantom images for the different isotopes and reconstruction algorithms tested. All reconstruction algorithms provided adequate image quality in all isotopes tested. With F-18, MAP showed the best 1 mm RC performance because it allowed a high iteration number yet maintaining a reasonably low Uniformity. Compared to F-18, Cu-64 and Ga-68 showed a higher increase of noise with increasing iteration number. This can be explained by the fact that the activity employed in all cases was 3.7 MBq, but both Cu-64 and Ga-68 have a lower positron emission probability than F-18. Therefore, their images contained poorer statistical sampling as compared to the F-18 case. For Cu-64, the number of iterations was kept relatively low to avoid noise increasing excessively. In the case of Ga-68, the air spill over ratio was highest, most likely due its long positron range.
The persuasive PET/MR imaging data shows the quality of imaging results using different isotopes. The *in-vivo* PET/MRI imaging show the expected F-18 FDG biodistribution with excellent spatial resolution and the good T1 contrast of the morphological MRI image.

Conclusion:
The image quality of a new PET insert has been assessed with several common PET isotopes for the first time. The performance shown here on both phantoms and in vivo suggests this PET Insert is very useful tool in small rodent imaging.

Reference
1. Willy Gsell, Cesar Molinos, Carlos Correcher, Sarah Belderbos, Jens Wouters, Sven Junge, Michael Heidenreich, Greetje Vande Velde, Ahmadreza Rezaei, Johan Nuyts, Christopher Cawthorne, Frederik Cleeren, Lise Nannan, Christophe M. Deroose, Uwe Himmelreich, Antonio J. Gonzalez. “Characterization of a preclinical PET insert in a 7 Tesla MRI scanner: beyond NEMA testing” Physics in Medicine & Biology July 2020.
2. Antonio Gonzalez, Andrea Gonzalez-Montoro, Marta Freire, Luis Vidal, Liczandro Hernandez, Carlos Correcher, Ramiro Polo, Abel Orero, Gustavo Pastor, Vicente Carrilero, Thorsten Greeb, Sven Junge, Cesar Molinos, Peter Bruyndonckx and Michael Heidenreich. “Performance of a PET/MR Insert for Mice Based on Monolithic Crystals”. Journal of Nuclear Medicine May 2020, 61 (supplement 1) 3123;
3. NEMA NU4-2008: performance measurements of small animal positron emission tomographs. National Electrical Manufacturers Association (NEMA). Rosslyn: National Electrical Manufacturers Association: 2008.

Poster Presentation

Disclosures: Michael Heidenreich is an employee of Bruker Biospin.

370-The Green Lanmodulin-Based Reporter: A Fluorescent MRI Probe used for Rapid Onsite Detection and Accumulation of Rare Earth Elements, Powered by Synthetic Biology

Presenter: Harvey Lee,Michigan State University

Harvey Lee[1], Connor Grady[2], Katie Krell[2], Cooper Strebeck[2], Assaf Gilad[2]

[1]*Michigan State University, East Lansing*
[2]*Michigan State University, East Lansing, MI*

Despite their name, REEs can be quite abundant throughout the Earth's crust, although they're typically spread out in low concentrations to be mined in a cost-effective manner. In this study, we have created a biosynthetically producible recombinant protein that directly indicates binding events via green fluorescence with high specificity for REEs, which can be utilized downstream as an MRI and optical imaging agent upon binding gadolinium. GLamouR is the first of its kind that possesses an optical feedback feature for detecting unbound gadolinium ions, which correlates with chelate stability. REEs can be found in our smartphones, computers, electric vehicles, tanks, missiles, GPS devices, high powered lasers, and even in the Euro banknote. Currently, we are completely reliant on foreign countries for the supply of Rare Earths but are unknowingly polluting our local environment with them. For example, MRI patients excrete more than 90% of their gadolinium dose within the first 24 hours of injection directly into the environment. REEs are not only finding their way into our wastewaters as a form of pollution, but they can also be an untapped source of financial gain when properly mined and processed. To address the adverse effects of REE pollution in the environment, we have constructed a prototype device capable of accumulating Rare Earths from dilute concentrations and indicating the presence or absence of free Rare Earths in solution, for rapid onsite detection and recycling. This device can be easily put together with parts printed off a 3D printer at extremely low cost, and it is anticipated the price point will drop down lower once the designs are finalized and mass-produced with injection molding for scalability to parts of the world with limited resources.

Reference

1. Cotruvo, J. A., Jr.; Featherston, E. R.; Mattocks, J. A.; Ho, J. V.; Laremore, T. N., Lanmodulin: A Highly Selective Lanthanide-Binding Protein from a Lanthanide-Utilizing Bacterium. J Am Chem Soc 2018, 140 (44), 15056-15061.
2. Wahsner, J.; Gale, E. M.; Rodriguez-Rodriguez, A.; Caravan, P., Chemistry of MRI Contrast Agents: Current Challenges and New Frontiers. Chem Rev 2019, 119 (2), 957-1057.
3. Brunjes, R.; Hofmann, T., Anthropogenic gadolinium in freshwater and drinking water systems. Water Res 2020, 182, 115966.
4. Ebrahimi, P.; Barbieri, M., Gadolinium as an Emerging Microcontaminant in Water Resources: Threats and Opportunities. Geosciences 2019, 9 (2).

Poster Presentation

Disclosures: The authors have disclosed no financial interest.

371-Quantitative Intravital Imaging for Real-time Monitoring of Pancreatic Tumor Cell Hypoxia and Stroma in an Orthotopic Mouse Model

Presenter: Michael Edson, University Health Network

Timothy Samuel[1], Sara Rapic[1], Cristiana O'Brien[2], **Michael Edson[3]**, Yonghong(Emily) Chen[3], Ralph DaCosta[1]

[1]*University Health Network, Toronto, Ontario*
[2]*University Health Network, Toronto*
[3]*University Health Network, Toronto, ON*

Pancreatic cancer is a lethal disease with few successful treatment options[1,2]. Tumor hypoxia, an underlying characteristic of pancreatic cancer, has a profound effect on promoting tumor invasion, metastasis, and resistance to chemo-, radio-, and immuno- therapies[3-6]. Recent evidence has shown that the formation of a pronounced proinflammatory stromal tissue can induce tumor hypoxia by disrupting vascular networks[7,8]. Thus, by investigating the spatiotemporal relationship between hypoxia and the pancreatic tumor microenvironment (TME), new therapeutic strategies could be established resulting in a better prognosis of this disease. However, to better understand both the spatial and temporal influence hypoxia has on the TME and vice versa, an *in vivo* model that offers both temporal continuity and sufficient spatial resolution is required. Thus, the hypothesis is that intravital fluorescence microscopy (IVFM) can be used to directly study the pancreatic TME *in vivo* at a cellular resolution over several weeks. A dually fluorescent human pancreatic adenocarcinoma cell line, BxPC3-DsRed hypoxia-response-element (HRE)-GFP, was designed to label the cancer cells and image hypoxia. Hypoxia-induced GFP expression was validated by measuring GFP expression and performing Western blot analysis on cells exposed to hypoxic or normoxic conditions. These BxPC3 cells were orthotopically implanted in an NRG mouse model, and IVFM was performed through a novel surgically implanted pancreatic imaging window. Mice were injected with an Allophycocyanin (APC)-conjugated anti-CD31 fluorescent dye to visualize tumor microvasculature, and second harmonic generation (SHG) microscopy was performed to simultaneously image tumor-associated collagen in the stromal compartment. Intravital fluorescence and SHG imaging of pancreatic tumors were performed using an LSM710 laser-scanning confocal microscope. Fluorescence of the BxPC3 cells (DsRed) and their hypoxia-inducible factor (HIF; GFP) activity, tumor vasculature density, and distance between blood vessels and tumor cells were quantified. To investigate the relationship between tumor-associated collagen fibers and BxPC3 HRE/GFP expression, 50 µm-radius circular regions of interest (ROI) were analyzed along the peritumoral tumor-collagen interface to determine mean GFP fluorescence, SHG intensity, collagen fiber spatial alignment and orientation (relative to the tumor edge). After four weeks, tumors were extracted and embedded for immunofluorescence staining for DsRed (BxPC3 tumor cells), GFP (driven by HIF activity), CD31 (endothelial cells), and two traditional hypoxia markers: pimonidazole and carbonic anhydrase IX (CA9). Pixel intensity-based colocalization analysis was performed on the tissue sections to determine the relationships between BxPC3 HRE/GFP staining, pimonidazole, and CA9. A negative correlation ($R = -0.39$, $p<0.0001$) was determined between tumor vascular density and GFP fluorescence, while a positive relationship was found between GFP fluorescence and distance to the nearest blood vessel ($R = 0.48$, $p<0.0001$). Tissue section staining found that anti-GFP fluorescence had the strongest correlation with anti-CA9 fluorescence, with a mean Pearson correlation coefficient ($\bar{R}$) of 0.84 (SD = 0.09). Anti-pimonidazole and anti-GFP stains had an $\bar{R}$ of 0.74 (SD = 0.09), while anti-PIMO and anti-CA9 stains had an $\bar{R}$ of 0.66 (SD = 0.13). The mean tumor cell GFP fluorescence from IVFM strongly correlates with the tissue sections that stained positive for PIMO ($R=0.89$, $p=0.0003$) and CA9 ($R=0.88$, $p=0.0003$). Furthermore, a weak positive correlation was found between the mean GFP fluorescence and mean SHG intensity ($R = 0.20$, $p<0.0001$) and a weak negative correlation between GFP fluorescence and the orientation of collagen fibers relative to the tumor edge ($\bar{R} = -0.06$, $p<0.0001$). A lower mean GFP fluorescence was detected in the 50 µm-radius ROI where collagen fibers were perpendicular to the tumor edge, compared to those that were parallel (10.41 vs 8.68, $p<0.0001$).
In conclusion, this novel imaging methodology is capable of studying the pancreatic TME *in situ* over time, and the mean BxPC3 HRE/GFP fluorescence is representative of hypoxia throughout the tumor.

Reference

1. McGuigan, A. et al. Pancreatic cancer: A review of clinical diagnosis, epidemiology, treatment and outcomes. World Journal of Gastroenterology vol. 24 4846–4861 (2018).
2. Yabar, C. S. & Winter, J. M. Pancreatic Cancer: A Review. in Gastrointestinal Neoplasia, An Issue of Gastroenterology Clinics of North America (eds. Limburg, P. J. & Dixon, D. A.) vol. 45 (Elsevier Health Sciences, 2016).
3. Pereira, S. P. et al. Early detection of pancreatic cancer. The Lancet Gastroenterology and Hepatology vol. 5 698–710 (2020).
4. Weibel, P., Pavic, M., Lombriser, N., Gutknecht, S. & Weber, M. Chemoradiotherapy after curative surgery for locally advanced pancreatic cancer: A 20-year single center experience. Surgical Oncology 36, 36–41 (2021).
5. Liu, Q., Liao, Q. & Zhao, Y. Chemotherapy and tumor microenvironment of pancreatic cancer. Cancer Cell International vol. 17 1–17 (2017).
6. Jahanban-Esfahlan, R., de la Guardia, M., Ahmadi, D. & Yousefi, B. Modulating tumor hypoxia by nanomedicine for effective cancer therapy. Journal of Cellular Physiology vol. 233 2019–2031 (2018).
7. Provenzano, P. P. & Hingorani, S. R. Hyaluronan, fluid pressure, and stromal resistance in pancreas cancer. Br J Cancer 108, 1–8 (2013).
8. Provenzano, P. P. et al. Enzymatic Targeting of the Stroma Ablates Physical Barriers to Treatment of Pancreatic Ductal Adenocarcinoma. Cancer Cell 21, 418–429 (2012).

Poster Presentation

Disclosures: The authors have disclosed no financial interest.

372-Imaging of CRISPRi-attenuated receptor expression in triple-negative breast cancer models.

Presenter: Alexei Bogdanov, UMass Chan Medical School

Suresh Gupta[1], Eric Schmidt[2], Rahul Pal[3], Anita Leporati[4], Anand T. Kumar[5], **Alexei A. Bogdanov[6]**

[1]UMass Chan Medical School, 55 Lake Ave N., Massachusetts
[2]UMass Chan Medical School, Worcester, Massachusetts
[3]Athinoula A. Martinos Center for Biomedical Imaging, Charlestown, Massachusetts
[4]UMass Chan Medical School, Sterling, MA
[5]Massachusetts General Hospital
[6]UMass Chan Medical School, Worcester, MA

Both advanced imaging probes and improved cancer models are required for non-invasive assessment and monitoring of cancer-relevant therapeutic targets with eventual goal of developing novel anti-proliferative and checkpoint inhibitor therapies. The aims of this study were to: 1) obtain morphologically similar cancer models with diverse levels of relevant therapeutic target (e.g. EGFR) expression using CRISPR interference (CRISPRi); 2) develop and test miniaturized quenched near-infrared (NIR) imaging probes derived from therapeutic antibodies in these models. To achieve attenuation of EGFR expression in TNBC cells an approach requiring a co-expression of specific single-chain guide RNAs (sgRNA) and the inactive dCas9 mutant fused with a Krüppel-associated box (KRAB) repressor (dCas9-KRAB), which partially silences target gene expression was used [1]. To generate single guide RNAs we identified two DNA sequences in *EGFR* gene 5' - upstream of ATG codon of intron I and one sequence specific for downstream DNA of Intron II relative to the Sp Cas9-protospacer associated motif (PAM). Co-expression of sgRNA and dCas9-KRAB cassettes in MB-MDA-231 wild-type (WT) TNBC cells resulted in attenuated levels of EGFR expression in two subpopulations as determined by fluorescence microscopy and FACS analysis. In contrast to parent WT cells, dCas9-KRAB/sgRNA T2.1 cells showed a 10-times lower level of EGFR expression with concomitant decrease of PD-L1 levels in a subpopulation which was isolated as a stable CRISPRi clone. Anti-EGFR mAb binding assays showed a 2-times lower Bmax in T2.1 cells compared to WT TNBC cells and negligible differences in Kd. To obtain a NIR EGFR in vivo imaging probe with improved pharmacokinetics we used sequential conjugation of IRDye 800CW via free cysteine and amino groups of Cetuximab-derived Fab' fragment (Fab'-800CW, Figure A) which enabled linking of 1.9 mol 800CW/mol Fab' with the resultant 800CW fluorescence intensity (FI) quenching by 4.5-5.1 times. IRDye 800CW fluorescence lifetimes (FLT) increased by a factor of 3 after probe internalization and proteolysis by MDA-MB-231 WT TNBC cells as determined by FLT microscopy at two time points (after binding and probe internalization, Figure B). The ability of TNBC cells to bind, internalize and degrade the Fab'-800CW probe was impaired by the CRISPR/dCas9-mediated EGFR expression attenuation because mean NIR FI of EGFR-attenuated (T2.1) vs. WT TNBC cells was significantly different (mean FI=173 ± 27 vs. 138 ± 9 AU, $p<0.01$). The anti-EGFR staining of model tumors revealed higher FI of EGFR positive tumor cells in small mammary WT tumor xenografts compared to their EGFR-attenuated T2.1 counterparts (Figure C). We further explored the ability of Fab'-800CW to differentiate between the WT and CRISPRi-attenuated EGFR expression in orthotopic TNBC tumor models using NIR imaging. The main rationale of testing Fab'-based probes was in achieving sufficiently high tumor/background (muscle) ratios at earlier time points than in the case of the larger IgG fragments or a full-size IgG. Fab'-800CW injection allowed to image thoracic or abdominal orthotopic xenografts in both T2.1 and WT TNBC groups over time (n=4-5/group), Figure D. NIR/CT image registration enabled quantification of FI signals in tissue volumes that were normalized by muscle background. Quantitative analysis of the reconstructed 3D volumes of FI distribution *in vivo* showed that mean tumor/background (muscle) ratio in the range of 2-5 could be achieved at 2 h time point in the WT and the T2.1 (attenuated) tumor group (Figure E). Conclusions: 1) CRISPRi by using dCas9-mediated targeting of KRAB repressor to *EGFR* resulted in TNBC populations which were forming xenografts with attenuated EGFR expression; 2) *in vivo* NIR imaging by using a miniaturized anti-EGFR imaging probe allowed to assess the feasibility of WT and attenuated EGFR expression in experimental tumors at early time points after injection, which is relevant to multiple cancer theranostic approaches.

Reference

1. Jameson NM, Ma J, Benitez J, et al. (2019) Intron 1-Mediated Regulation of EGFR Expression in EGFR-Dependent Malignancies Is Mediated by AP-1 and BET Proteins. Mol Cancer Res 17:2208-2220.

Poster Presentation

Disclosures: The authors have disclosed no financial interest.

373-In vivo measurement of reactive oxygen species (ROS) penetration depth in a cervix cancer model treated with gold nanoparticles and brachytherapy

Presenter: Mariia Kiseleva, Laval University

Marc-André Fortin[1], **Mariia Kiseleva[2]**, Svetlana Selivanova[3]

[1]Université Laval, Québec, QC
[2]Laval University, Sainte-Sophie
[3]Université Laval, Quebec, Quebec

Introduction, Hypothesis, and Objectives:
Brachytherapy is a widely used clinical procedure for the treatment of prostate, breast, eye, and cervical cancer. It consists of the insertion of radioactive implants into tumors, which remain on-site for a period sufficiently long to deliver a lethal dose of radioactivity to cancer cells. Gold nanoparticles (AuNPs) are being developed as powerful radiosensitizers for brachytherapy. Their presence in tumors enhances the radiation effect through the production of low-energy photons and electrons, which increase the dose and lead to the production of ROS that can induce cell death.[1, 2] AuNPs can be administrated either attached at a brachytherapy implant, or using hydrogels, from which they are released within a few hours for diffusion into the tumor. Both the penetration range of AuNPs into the tumor and the production and diffusion of ROS into the cancer tissue must be precisely measured by a comprehensive approach correlating *in vivo* imaging and microscopy data. We hypothesized that AuNPs as radiosensitizers for the treatment of cervical cancer by brachytherapy, could diffuse several hundreds of microns into cancer tissue and produce ROS even further deep into the tissue, with impact on tumor volume control. This study i) reveals the intratumoral penetration depth of AuNPs eluted from a delivery system; ii) measures the ROS diffusion profile; and iii) confirms the impact on tumor volume.

Materials and Methods:
Radioactive implant and hydrogel delivery system: Custom-designed cupola-shaped brachytherapy implants made of biocompatible, 3D-printed polyetheretherketone (PEEK; d=6 mm, h=4.5 mm) containing a ^{125}I source (0.8 mCi; $t_{1/2}$ = 59.5 days; ~28 keV photons), were coated with a biocompatible pluronic F127 (20% w/v) and alginate (0.5% w/v) hydrogel (also 3D-printed, Cellink BioX bioprinter; 2mm-thick lens-shaped coatings). This hydrogel contained fluorescent AuNPs (0.1 mg/ml, core size <6 nm (TEM); hydrodynamic diameter of 18 nm DLS; + Cy5 fluo dye), and allowed a controlled elution *in vivo*(described in [3]).

Animal Study:
The therapeutic effect of AuNPs released from the 3D-printed hydrogel coating, diffusing into the tumors, and producing ROS in the cancer tissue, was studied in NU/NU mice inoculated with HeLa cells (flank tumors). The gel-bearing inserts were administered beneath the tumor by aseptic surgery (Figure 1a) and were visualized with MRI (T_1-w. SE; TE/TR: 13.5/704.2 ms). On day 7 post-surgery, dihydroethidium (DHE; a ROS detection fluorescent probe) was injected in the tumors 30 min before euthanasia (0.1 mg/kg, 50 µL; 5 µL/min; stereotax.). The tumors were extracted, preserved in OCT, sliced from the side in contact with the AuNP-hydrogel and down into the cancer mass (20 mm-thick), and observed in immunofluorescence.

Results:
A strong presence of AuNPs was observed at a depth of at least 125 mm in the tumor (Figure 1b,c), thus revealing the diffusion range of Au NPs into the cancer tissue. However, the amount of ROS generated by the interactions of AuNPs and the ^{125}I photons, was much higher than for controls (^{125}I only), and were very strong at least 900 mm deep in the tumor (Figure 1c) thus confirming the capacity of a single 0.8 mCi conventional brachytherapy seed supplemented with Au NPs, to generate a strong ROS generation thus leading to a reduction of tumor volume in spite of the limited radioactivity of the implant.

Conclusion:
This study reveals precious information about the diffusion range of Au NPs injected from brachytherapy implants (~125 mm), as well as the range of ROS production (~1 mm). Au NPs are being approved as radiosensitizers for clinical use, and therefore the results will be useful to radiooncologists for planning the number of implants, their spacing, and the dose of Au NPs per implant.

Reference
1. Laprise-Pelletier, M., Fortin, M. A. et al., Gold Nanoparticles in Radiotherapy and Recent Progress in Nanobrachytherapy. Adv. Healthc. Mater. 2018, 7 (16), 27, DOI:10.1002/adhm.201701460.
2. Her, S.; Jaffray, D. A.; Allen, C., Gold nanoparticles for applications in cancer radiotherapy: Mechanisms and recent advancements. Adv. Drug Deliv. Rev. 2017, 109, 84-101, DOI:10.1016/j.addr.2015.12.012.
3. Kiiseleva, M, Fortin MA et al, A Three-Dimensional Printable Hydrogel Formulation for the Local Delivery of Therapeutic Nanoparticles to Cervical Cancer. ACS Biomater. Sci. Eng. 2022, 8, 3, 1200–1214.

Poster Presentation

Disclosures: The authors have disclosed no financial interest.

374-Proof of concept of cucurbituril-adamantane host-guest pretargeted PET with fractionated dosing.

Presenter: Amritjyot Kaur, Stony Brook University

Amritjyot Kaur[1], Vilma Jallinoja[2], Courtney Abbriano[3], Kavita Bhatt[3], Paul Yazaki[4], Brandon Carney[5], Jacob Houghton[6]

[1]Stony Brook University, New York, NY
[2]Memorial Sloan Kettering Cancer Center
[3]Stony Brook Medicine
[4]City of Hope, CA
[5]Stony Brook University
[6]Stony Brook University, Stony Brook, NY

Hypothesis:
In pretargeted nuclear medicine, to alleviate the high radiation load often associated with the use of directly radiolabeled macromolecules, a pre-administered target bound macromolecule (e.g., monoclonal antibody: mAb) is labeled *in vivo* with a radiolabeled small molecule (radioligand).[1] In previous work with host-guest cucurbit[7]uril-ferrocene (CB7-Fc) pretargeting studies it was found that as the lag time is increased the tumor uptake decreases.[2,3,4] Adamantane (Adma) guest molecules have higher affinity for the CB7 host molecule compared to ferrocenes[4], which is why we hypothesize that CB7-Adma pretargeting components can generate a more stable host-guest complexation *in vivo*. In the present work, the high affinity non-covalent interaction between a CB7 modified antibody and a [^{68}Ga]Ga-NOTA-PEG$_3$-Adma guest molecule were evaluated in pretargeting studies with lag times of 3 or 6 days as well as with dose fractionation.

Methods:
A novel [^{68}Ga]Ga-NOTA-PEG$_3$-Adma radioligand was developed and characterized. Radioligand's partition coefficient (log D), *in vitro* plasma stability and plasma protein binding was studied. The guest radioligand was evaluated for *in vivo* pretargeting in a xenograft mouse model using a CB7-modified carcinoembryonic antigen

(CEA) targeting full-length antibody (CB7-M5A) as the secondary pretargeting agent. The pretargeting studies included evaluating the target specificity of the pretargeting methodology and studying different pretargeting dosing schedules and regimens. Three experimental cohorts of BxPC3 (CEA+) tumor bearing female nude mice (n=4/cohort) were injected in the tail vein with CB7-M5A (0.7 nmol; 100 mg in 150 mL in PBS7.4). The single dose were administered with [^{68}Ga]Ga-NOTA-PEG$_3$-Adma (1.5 nmol; 11.8 – 15.0 MBq in 150 mL in PBS7.4) via the tail vein either 3- or 6-days post CB7-M5A injection (Group A and B). Group C (Fractionated dose) received an injection of the [^{68}Ga]Ga-NOTA-PEG$_3$-Adma radioligand on day 3 and 6 post CB7-M5A injection. The Group D was injected only with the [^{68}Ga]Ga-NOTA-PEG$_3$-Adma with no prior CB7-M5A injection. All groups were euthanized for *in vivo* biodistribution 4 h post final injection. Additionally, the mice in groups B and C were imaged with a small animal PET scanner 2 and 4 h post radioligand injections.

Results:
The radiochemical yield of the [^{68}Ga]Ga-NOTA-PEG$_3$-Adma was 58.3 ± 9.4%, and its final radiochemical purity was 97.45 ± 1.3% (n = 3). The measured log D of the radioligand was -1.23 ± 0.20. The human plasma protein bound fraction at 60, 120 and 180 min was found to be 10.8 ± 1.04, 12.3 ± 1.32, 15.6 ± 3.86 respectively. The radioligand was highly stable up to 3 h in plasma with 96.74 % of the radioligand remaining intact. The radioligand possessed high gastrointestinal clearance with minimal renal excretion. Pretargeting experiments in subcutaneous BxPC3 tumor bearing nude female mice demonstrated that the tumor uptake of the pretargeted radioligand in group A (p= 0.001), B (p=0.003) and C (p=0.003) was significantly higher compared to Group D. Moreover, there is no significant difference in tumor uptake with fractionated dosing on day 3 and day 6 lag.

Conclusions:
The findings show for the first time that a CB7-Adma driven pretargeting results in excellent tumor uptake. The tumor uptake remained high despite using a longer lag time of 6 days or injecting multiple doses of the Adma radioligand. These exciting results show that the CB7-Adma approach has potential to be used in therapeutic applications with flexible dosing schedules.

Reference

1. Jallinoja, V. et al. (2021) DOI: 10.2967/jnumed.120.260687.
2. Jallinoja, V. et al. (2021) DOI: 10.1021/acs.bioconjchem.1c00280
3. Jallinoja, V. et.al (2022) DOI: 10.1021/acs.molpharmaceut.2c00102
4. Barrow, S.J. et al. (2015) DOI: 10.1021/acs.chemrev.5b0034

Poster Presentation

Disclosures: The authors have disclosed no financial interest.

375-CEST MRI of the ASCT2 transporter in a mouse model of prostate cancer

Presenter: Behnaz Ghaemi, Johns Hopkins University School of Medicine

Behnaz Ghaemi[1], Yuguo Li[2], Martin Pomper[3], Jeff Bulte[1], Peter C. van Zijl[4], Aline Thomas[5]

[1]*Johns Hopkins University School of Medicine, Baltimore*
[2]*Johns Hopkins Univeristy, Baltimore*
[3]*Johns Hopkins Univeristy, Baltimore, MD*
[4]*Johns Hopkins Univeristy, Baltimore, Maryland*
[5]*Johns Hopkins University School of Medicine*

Introduction:
Alanine serine cysteine transporter 2 (ASCT2), the primary transporter for glutamine, is a prognostic marker for many cancers[1-4]. Immunohistochemical grading is the current clinical metric for ASCT2; however, *in vivo* imaging can provide a spatiotemporal profile of this biomarker. Alanine is a well-recognized substrate for ASCT2[5] that has been intravenously injected at a dose of 6 mM into humans for other applications without symptoms[6]. Chemical exchange saturation transfer magnetic resonance imaging (CEST MRI) can detect alanine without modification or the need for specialized equipment through the water-exchanging protons in its amine[7-9]. We investigated the utility of CEST MRI to evaluate ASCT2-mediated transport by comparing DU-145 and LNCaP prostate cancer cells, which have different levels of ASCT2 expression[10, 11].

Methods:
Prostate cancer model: Animal studies were approved by our institutional ACUC. DU-145 (2-3 x 10^6) or LNCaP (3-5 x 10^6) cells were subcutaneously injected into the right flank of male, 6-10 week old Rag2 mice. CEST MRI: Mice were imaged 1-2 months after tumor induction using a Bruker 11.7T horizontal bore spectrometer and an 8-channel phase array coil. Animals were anesthetized with isoflurane (1-2%). Dynamic CEST images were collected at the +3.1 ppm frequency prior to alanine (6 mM, IV) injection and over a period of 60 minutes after injection. CEST enhancement ($\Delta S/S_{0,0\text{-}t}$) was quantified by subtracting the signal (S/S_0) at time t from the signal obtained prior to injection. S_0 was acquired before and after (n = 5 each), then linearly fitted over time. Scan parameters were TR/TE = 10,000/3.49 ms, RARE factor = 32, NA = 20, repetitions = 1, B_1 = 3.6 μT, saturation length = 3 s, matrix size = 48 x 48, slice thickness = 1.5 mm, and field of view = 30 × 30 mm^2.
Statistics: A two-way ANOVA was performed with $p<0.05$ considered significant.

Results:
We first investigated the CEST signal generated by alanine in vitro at cancer-relevant pH values (from 5.3 to 8.3; **Persuasive Figure 1**). For the majority of this range, alanine (20 mM) generated CEST contrast above baseline (PBS). We then quantified the expression of ASCT2 in the prostatic cancer cell lines DU-145 and LNCaP (**Persuasive Figure 2**). The average intensity of ASCT2 in LNCaP was 81% higher than that of DU-145. Since ASCT2 function requires translocation to the plasma membrane[12], we also investigated the intensity across the cellular space. A line profile revealed that the expression at the cell membrane was higher than that in the cytoplasm for both cell lines. It also revealed LNCaP had higher fluorescent intensity compared to DU-145 throughout the cellular space. We then investigated CEST signal enhancement when alanine was administered IV (**Figure 1**). When alanine was administered into mice with DU-145 tumors, CEST signal was near or below baseline levels throughout the scan. When alanine was administered into mice with LNCaP tumors, CEST signal at the +3.1 ppm frequency was enhanced throughout the 60-minute scan. CEST signal was significantly higher in LNCaP compared to DU-145 tumors at 60 minutes (p = 0.012).

Conclusion:
CEST MRI detected the uptake of alanine, a natural ASCT2 substrate. CEST enhancement upon injecting alanine distinguished prostate tumors with differing ASCT2 levels.

Reference

1. Sun, H.-W., et al., GLUT1 and ASCT2 as Predictors for Prognosis of Hepatocellular Carcinoma. PLOS ONE, 2016. 11(12): p. e0168907.
2. Shimizu, K., et al., ASC amino-acid transporter 2 (ASCT2) as a novel prognostic marker in non-small cell lung cancer. British Journal of Cancer, 2014. 110(8): p. 2030-2039.
3. Luo, Y., et al., ASCT2 overexpression is associated with poor survival of OSCC patients and ASCT2 knockdown inhibited growth of glutamine-addicted OSCC cells. Cancer Medicine, 2020. 9(10): p. 3489-3499.
4. Bernhardt, S., et al., Proteomic profiling of breast cancer metabolism identifies SHMT2 and ASCT2 as prognostic factors. Breast Cancer Research, 2017. 19(1): p. 112.
5. Foster, A.C., et al., D-Serine Is a Substrate for Neutral Amino Acid Transporters ASCT1/SLC1A4 and ASCT2/SLC1A5, and Is Transported by Both Subtypes in Rat Hippocampal Astrocyte Cultures. PLOS ONE, 2016. 11(6): p. e0156551.
6. Fernandes, J. and W. Blom, The intravenous L-alanine tolerance test as a means for investigating gluconeogenesis. Metabolism - Clinical and Experimental, 1974. 23(12): p. 1149-1156.
7. Chen, J., et al., Thiol-water proton exchange of glutathione, cysteine, and N-acetylcysteine: Implications for CEST MRI. NMR in Biomedicine, 2020. 33(1): p. e4188.
8. Cai, K., et al., Breast Cancer Redox Heterogeneity Detectable with Chemical Exchange Saturation Transfer (CEST) MRI. Molecular Imaging and Biology, 2014. 16(5): p. 670-679.
9. Walker-Samuel, S., et al., In vivo imaging of glucose uptake and metabolism in tumors. Nature Medicine, 2013. 19(8): p. 1067-1072.
10. Wang, Q., et al., Targeting ASCT2-mediated glutamine uptake blocks prostate cancer growth and tumour development. The Journal of Pathology, 2015. 236(3): p. 278-289.
11. Cardoso, H.J., et al., Glutaminolysis is a metabolic route essential for survival and growth of prostate cancer cells and a target of 5α-dihydrotestosterone regulation. Cellular Oncology, 2021. 44(2): p. 385-403.
12. Console, L., et al., N-linked Glycosylation of human SLC1A5 (ASCT2) transporter is critical for trafficking to membrane. Biochimica et Biophysica Acta (BBA) - Molecular Cell Research, 2015. 1853(7): p. 1636-1645.

Poster Presentation

Disclosures: The authors have disclosed no financial interest.

376-Formulation and Production of Collagen Targeting Protein MRI Contrast Agent for Early Detection of Liver Cancer and fibrosis

Presenter: Brenda-Ruth Mimba, Georgia State University

Brenda-Ruth N. Mimba[1], Dongjun Li[2], zongxiang gui[3], Mani Salarian[4], Jingjuan Qiao, Florence Reddish

[1]Georgia State University, Sugarhill, GA
[2]Georgia State University, Atlant, GA
[3]Georgia State University, Atlanta, GA
[4]Georgia State University, Decatur, GA

Cancer is classified as a chronic disease and deaths caused by cancer are estimated to increase to 11.5 million by 2030. Patient response to treatment and chances of survival improve significantly when cancer is diagnosed at an early stage. MRI is often seen as a superior imaging modality to acquire detailed information about the healthy or diseased state of internal organs. Many contrast agents currently available are severely limited due to their low relaxation rates which increases the chances of metal ion toxicity due to a need for higher doses of administration. A novel class of protein-based MRI contrast agents was created that had high dual relaxivity with the capability to quantitatively target molecular biomarkers with improved specificity which reduces the need for administering a high dose. This study reports the progress in the achievement of high expression of protein using bacteria *E. coli* cells. The purification and refolding of active monomeric hProca32.collagen were further achieved by optimizing various formulation conditions. Several quantitative quality control assays such as ELISA, SEC-HPLC, Mass spectrometry, and relaxivity have been successfully developed. The purified samples have excellent collagen-binding affinity (Kd 0.1-1.3 μM) under physiological conditions and good relaxivity values (30 and 42 $mM^{-1}S^{-1}$ for r1 and r2 respectively) which are 100-folds greater than clinically available contrast agents. The formulated hProCA32.collagen enables early detection of liver cancer and lung fibrosis in mouse models by Precision MRI (pMRI).

Poster Presentation

Disclosures: The authors have disclosed no financial interest.

377-Preclinical imaging of therapeutic alpha-emitters

Presenter: Eleftherios Fysikopoulos

Eleftherios Fysikopoulos[1], Maria Georgiou[2], Maritina Rouchota[2], Efthimis Lamprou[3], George Loudos[4]

[1]Athens, Greece
[2]BIOEMTECH, Greece
[3]BioEmission Technology Solutions, Greece
[4]BIOEMTECH, Athens, Greece

Introduction:
Alpha and beta emitters present a highly potentiality as therapeutic agents in clinics [1], [2]. Novel compounds using radionuclides such as Pb-212, Ac-225, At-211, Ra-223, Lu-177 are increasingly tested in preclinical stage for the development of future emerging radiopharmaceuticals. Quantitative imaging of such compounds is often possible via imaging of gammas produced by complex decay schemes. Understanding the biokinetics of alpha and beta emitting radiopharmaceuticals in preclinical studies is of major importance, in order to evaluate its safety and efficacy [3], [4]. In the current work, we present *in vivo* and phantom imaging studies of Pb-212 and Ac-225.

Materials and Methods:
In vivo animal studies were performed on a dedicated bench top, mouse-sized, planar scintigraphy system (γ-eye^{TM} by BIOEMTECH, Athens, Greece). The ability of the system to quantify activity variations was evaluated through a series of phantom experiments. Gamma rays detection is based on position-sensitive photomultiplier tubes, coupled to a CsI(Na) pixelated scintillator and a high-sensitivity tungsten collimator with parallel hexagonal holes, supporting a wide range of gamma rays emitting isotopes.
For the evaluation of system sensitivity to activity variations three cylindrical phantoms (12 mm in diameter, 8 mm active height) filled with either Pb-212 or Ac-225 were placed in the imaging platform of γ-eye^{TM}. A mouse phantom (Fillable mouse, BIOEMTECH, Greece) filled with the different activities of the aforementioned

isotopes was used to further evaluate system's capability to image accurate activity variations.
In vivo Pb-212 static scans (below 20 min) were performed at different time points, to provide longitudinal information on the distribution on the same animal, while the total administered activity was below 1 Mbq. During imaging, mice were kept under isoflurane anesthesia and under constant temperature of 37° C.

Results:
Phantom studies results show the capability of γ-eye™ imaging scanner to obtain accurate quantitative information of the distribution of alpha emitting radiopharmaceuticals in preclinical studies.
In vivo studies highlight the feasibility of imaging successful tumor targeting using a Pb-212 compound, during scanning times of less than 20 min and a total administered activity of less than one 1 Mbq.

Conclusions:
Noninvasive quantitative imaging of alpha and beta emitting radiopharmaceuticals is feasible via imaging of the gammas and positrons produced of these radionuclides. Understanding its complex decay scheme, an imaging methodology can be derived. Dedicated scintigraphy screening tools allow tracking of these radiopharmaceuticals over time with a potential to accelerate preclinical research.

Reference

1. M. Lassmann et al. Ann.ICRP, 47 (2018)
2. ES Delpassand Targeted et al. J Nucl Med (2022)
3. Y. Seo, Nucl Med Mol Imaging, 53 (2019)
4. Poty S. et al. J Nucl Med, 59 (2018)

Poster Presentation

Disclosures: The authors have disclosed no financial interest.

378-Photoacoustic imaging to elucidate vasculogenic mimicry competence

Presenter: Mariam-Eleni Oraiopoulou, University of Cambridge

Mariam-Eleni Oraiopoulou[1], Thierry L. Lefebvre[1], Thomas Else[2], Eleftheria Tzamali[3], Dominique Laurent-Couturier[4], Cara Brodie[5], Ian Cannell[2], Sarah J. Aitken[6], Gregory Hannon[2], Vangelis Sakkalis[7], Sarah Bohndiek[1]

[1]*University of Cambridge, Cambridge, Cambridgeshire, United Kingdom*
[2]*Cancer Research UK Cambridge Institute*
[3]*Institute of Computer Science, Foundation for Research and Technology - Hellas (FORTH), Greece*
[4]*Cancer Research UK Cambridge Institute, Cambridge, United Kingdom*
[5]*Cancer Research UK Cambridge Institute, United Kingdom*
[6]*University of Cambridge, United Kingdom*
[7]*Institute of Computer Science, Foundation for Research and Technology - Hellas (FORTH)*

Tumour vascularization proceeds through several mechanisms that are genotypically and phenotypically distinct. Vasculogenic mimicry (VM) refers to the appearance of endothelial-like vessels arising from cancer cells [1, 2], a process associated with therapy resistance and has been identified as a driver of metastasis [3]. Here, we investigate the potential of photoacoustic imaging (PAI) to elucidate the spatiotemporal dynamics of VM competence in a murine model of breast cancer. Murine breast tumours were established at the mammary fat pad of BALB/c nude female mice (5-6 weeks old) using 4T1 cells (n= 10 mice) and the derivative clone 4T1-T (n= 10 mice), which has previously been found to demonstrate a higher competence for VM [3]. Response to the anti-vascular agent Axitinib (Generon) was evaluated in a subset of mice (n_{4T1}= 4, $n_{4T1\text{-}T}$= 4). Multi-scale PAI was performed every 2-3 days once the tumour mass was palpable for up to 3 weeks post-implantation. In the treatment groups, Axitinib was intraperitoneally dosed at 50 mg/kg in a scheme 5 days on/ 2 days off. We used commercial raster-scan PA mesoscopy system (RSOM Explorer P50; iThera Medical) with a 532nm laser excitation to assess the vasculature morphology and a PA tomography system (MSOT inVision 256; iThera Medical) to acquire data in the 660-880nm wavelength range to allow discrimination between oxy- and deoxy-haemoglobin. In the final imaging session, an additional gas challenge was applied [4], to further monitor the intratumoural vascular kinetics. VM competence was assessed *ex vivo* by CD31-periodic acid-Schiff (PAS) double staining [5] in order to differentiate between VM and endothelial cells. For the mesoscopic data, a vessel analysis segmentation pipeline [6] and graph analysis was implemented (MATLAB) to further identify and locate morphological features of VM. For the tomographic data, PA image analysis was performed using custom code (Python) to identify the tumour areas and oxygenation status, using the abdominal aorta as a reference. The overall growth rate of the tumours was similar for the 4T1 and 4T1-T VM models, allowing a size-matched comparison throughout the study period. The overall oxygenation in PA tomography was similar for both models, although the 4T1-T model showed a more heterogeneous oxygenation phenotype throughout the time course of the study. No difference was observed in the overall blood content of the models. A 1mm-rim segmentation was applied to look at rim-core disparities. In line with previous results [7], unlike the 4T1 model that shows a uniformly distributed profile, the VM-competent 4T1-T tumours display a rim-core effect that diverges over time (Figure 1A). The response to the anti-vascular treatment was an overall compromised oxygenation status throughout the study for both models.
To further examine the differences in the vascular architecture of the tumour periphery, we analysed the PA mesoscopy (Figure 1B) using graph metrics while maintaining their topology (Figure 1C). A distinct architectural circularity feature emerged that was statistically less apparent in 4T1 tumours relative to the VM-competent 4T1-T tumours. Interestingly, in response to the anti-vascular treatment, the same feature was reduced in both models. Subsequent *ex vivo* validation with immunohistological double staining for endothelial and VM markers (Figure 1D) indicates similar structures that underscore the potential of mesoscopic PA assessment of VM.
Our results demonstrate divergent spatiotemporal oxygenation in a murine cell line tumour model with higher VM competence compared to the parental model. Assessment of the vascular architecture in these models with graphs indicates potential PA biomarkers of VM. These findings will be further validated by co-registering the PA VM characteristics with the histology-proven VM vessels and the Axitinib effect will be further investigated to assess the importance of VM in anti-angiogenic treatment schemes.

Reference

1. Luo, Q., et al., Vasculogenic mimicry in carcinogenesis and clinical applications. Journal of Hematology & Oncology, 2020. 13(1): p. 19.
2. Treps, L., S. Faure, and N. Clere, Vasculogenic mimicry, a complex and devious process favoring tumorigenesis - Interest in making it a therapeutic target. Pharmacol Ther, 2021. 223: p. 107805.
3. Wagenblast, E., et al., A model of breast cancer heterogeneity reveals vascular mimicry as a driver of metastasis. Nature, 2015. 520(7547): p. 358-362.

4. Tomaszewski, M.R., et al., Oxygen Enhanced Optoacoustic Tomography (OE-OT) Reveals Vascular Dynamics in Murine Models of Prostate Cancer. Theranostics, 2017. 7(11): p. 2900-2913.
5. Andonegui-Elguera, M.A., et al., An Overview of Vasculogenic Mimicry in Breast Cancer. Frontiers in oncology, 2020. 10: p. 220-220.
6. Brown, E.L., et al., Quantification of Vascular Networks in Photoacoustic Mesoscopy. Photoacoustics, 2022: p. 100357.
7. Quiros-Gonzalez, I., et al., Optoacoustics delineates murine breast cancer models displaying angiogenesis and vascular mimicry. British Journal of Cancer, 2018. 118(8): p. 1098-1106.

Poster Presentation

Disclosures: The authors would like to disclose that axitinib, RSOM Explorer P50, and MSOT inVision 256 have been approved.

379-18F-Labeling and In Vitro Assessment of Anti-HER2 Cys-Diabody and Minibody Using Perfluoroaryls for PET Imaging

Presenter: Iman Daryaei, TheraCea Pharma

Iman Daryaei[1], Nathan Wright[1], Huong Dang[1], Edmund Marinelli[1]
[1]TheraCea Pharma, Tucson, AZ

Introduction:
Full antibodies (MW>100KDa) have a long circulation time necessitating the use of radioisotopes with long half-lives (e.g. 89Zr). By contrast, cys-diabodies and minibodies (50-75 KDa) display a relatively short blood circulation time (5-10h) that makes them good candidates for ^{18}F labeling because of the better match of the circulation time with it's shorter half-life for positron emmision .[1,3] Traditionally, ^{18}F species from cyclotrons are reacted with other reagents to produce ^{18}F-bearing prosthetic groups that can be used for further chemistry development. The prosthetic groups are then reacted with the target molecule to prepare the ^{18}F radiotracer. This indirect ^{18}F-labeling is a relatively long procedure entailing multiple synthesis and purification steps often with harsh reaction conditions, rendering this approach unsuitable for biologics.[4-6] PFAr (perfluoroaromatic) chemical moieties are reliable chemical entities that can be synthetically conjugated to cys-diabodies and minibodies through cysteine-maleimide and amine-NHS ester conjugation strategies. They are also very good candidates for $^{18/19}$F isotope exchange for 18F-labeling of the final products.[7] The investigators in this study applied this novel and efficient ^{18}F-labeleing strategy on an anti-HER2 cys-diabody and minibody.

Methods:
The anti-HER2 cys-diabody and minibody were obtained from a commercial vendor. Conjugation of maleimide and NHS-ester bearing commercially available Cy5 fluorophores to the anti-HER2 cys-diabody and minibody, respectively, were tested by SDS-Page. Conjugated cys-diabody and minibody bound to HER2-bearing magnetic beads as shown by FACS analysis. Pentafluorosulfanyl chloride was conjugated to a maleimide functional group through a PEG linker. Hexafluoro benzene was conjugated to and NHS ester bearing linker via a sulfide bond. Two different strategies for ^{18}F-lableing were investigated: 1) ^{18}F-labeleing of the PFAr linker before conjugation to cys-diabody or minibody and 2) ^{18}F-labeling of the PFAr linker after conjugation to cys-diabody or minibody. Na^{18}F salt (5-10 mCi) in DMF solvent in the presence of $K_{2.2.2}$ was performed at 40-50ºC in 15-30 min. ^{18}F-labeling of the cys-diabody or minibody bearing PFAr was performed in the presence of Na^{18}F and $K_{2.2.2}$ at 30-37ºC in 15-30 min. ^{18}F-labeling was monitored by HPLC analysis of the reaction mixtureemployinig a radioactive counter detector. Antibody purification kits were used to purify the final products by separating the ^{18}F-labeled products from 18/19F salts and other impurities. Biological reactivity of 18F-PFAr diabody and minibody was evaluated in Sk-Br-3 (HER2 positive) and MDA-MB-231 (control) cell lines.

Results:
Fluorescent bands with matching proteins with MW= 50-55KDa and 70-75KDa confirmed the availability of cysteines in the cys-diabody and lysine(s) in the minibody for conjugation. Moreover, a 2-3 fold shift in intensity of fluorescence signal on HER2 on magnetic beads confirmed that both the cys-diabody and minibody were biologically active after conjugation to maleimide and NHS ester linkers. MALDI Mass Spectroscopy and HPLC with radioactive detection confirmed conjugation and ^{18}F-labeling of the PFAr linkers in both the cys-diabody and minibody. ^{18}F-labeled cys-diabody and minibody showed 2.09 and 1.98, respectively, uptake increase in Sk-Br-3 cell lines (HER2 positive) compared to MDA-MB-231 (control).

Conclusion:
PFAr groups are suitable chemical entities for conjugation and subsequent ^{18}F-labeling of diabody and minibodies. Fast ^{18}F-labeling and simple purification strategy provides the opportunity to prepare ^{18}F-labeling kits in which cold PFAr conjugated to these constructs can be stored for significant periods (weeks or months). This allows the ad hoc preparation of the ^{18}F-labeled constructs, for biological applications, ad hoc by simple 'shake and bake' chemistry.

Reference

1. Carmon KS, Azhdarinia A. Applications of immunio-PET in antibody-drug conjugate development. Mol. Imaging, 2018, 17, 1-10.
2. Shively JE. 18F labeling for immune-PET: where speed and contrast meet. J Nuc. Med., 2007, 48(2), 170-171.
3. Fu R, Carroll L, Yahioglu G, Aboagye EO, Miller PW. Antibody fragment and affibody immunoPET imaging agents: radiolabeling strategies and applications. ChemMedChem, 2018, 13, 2466-2478.
4. Jacobson O and Chen X. PET designated flouride-18 production and chemistry. Curr Top Med Chem., 2010, 10(11), 1048-1059.
5. Krishnan HS, Ma L, Vasdev N, Liang SH. 18F-Labeling of sensitive biomolecules for positron emission tomography. Chem. Eur. J., 2017, 23, 15553-15577.
6. Jacobson O, Kiesewetter DO, Chen X. Fluorine-18 radiochemistry, labeling strategies and synthetic routes. Bioconjugate Chem., 2015, 26, 1−18.
7. Jacobson O, Yan X, Ma Y, Niu G, Kiesewetter DO, Chen X. Novel method for radiolabeling and dimerizing thiolated peptides using 18F-hexafluorobenzene. Bioconjugate Chem., 2015, 26, 2016-2020.

Poster Presentation

Disclosures: The authors have disclosed no financial interest.

380-Tumor-induced metabolic and physiological reprogramming of the spleen in mice

Presenter: James Barnett, Johns Hopkins University School of Medicine

James D. Barnett[1], Marie-France Penet[1], Raj Kumar Sharma[2], Saleem Yousf[3], Andrew D. Brannen[4], Yelena Mironchik[5], Balaji Krishnamachary[1], Zaver M. Bhujwalla[1]

[1]*Johns Hopkins University School of Medicine, Baltimore, MD*
[2]*Johns Hopkins University School of Medicine, Baltmore, MD*
[3]*Johns Hopkins University*
[4]*iThera Medical, Auburn, AL*
[5]*Johns Hopkins University School of Medicine, Baltimore, Maryland*

Introduction:
Cancer-related mortality accounted for approximately 16% of all deaths in 2020 (WHO). Poor tumor control is generally, but not solely, a result of tumor heterogeneity and complex mechanisms of immune evasion in solid tumors [1]. Our focus is to investigate the pro-tumorigenic properties of the tumor macroenvironment (TMaE) – the interactions between the tumor and the host as a multi-organ extension of the tumor microenvironment [2]. Tumorigenesis initiates a program of dysregulated hematopoiesis in the spleen, giving rise to hematopoietic progenitors and stromal cells that promote tumor immune evasion, cancer progression and metastatic cascade [2][3]. Using high resolution ^{1}H magnetic resonance spectroscopy (MRS), we investigated the impact of tumor burden on spleen metabolism in different syngeneic mouse cancer models. Hemodynamic changes were characterized with multi-spectral optoacoustic tomography (MSOT). Understanding how tumorigenesis affects the metabolic function of the spleen will expand our understanding of what shapes the TMaE and how metabolic intervention can be utilized for anticancer treatments.

Method:
Female BALB/c and C57BL/6 mice were inoculated orthotopically with 4T1 (mammary carcinoma) cells and E0771 (mammary carcinoma) cells, respectively. Male C57BL/6 mice were inoculated subcutaneously with Panc02 (pancreatic adenocarcinoma) cells. Uninoculated mice of each strain were used as non-tumor-bearing controls (Ctrl). Once tumor volumes reached approximately 400 – 600 mm^3, Ctrl and tumor-bearing (TB) mice were euthanized, the spleen and other organs were harvested, freeze clamped and stored at -80 °C for further analyses. Cryopulverization of mouse spleens was conducted in liquid nitrogen followed by dual phase extractions. Water-soluble metabolites from aqueous phase spleen extracts were identified through ^{1}H MRS analysis using a Bruker Avance III 750 MHz (17.6T) MR spectrometer. Plasma spectra were acquired using a CPMG pulse sequence. Data acquisition was performed using a 5 mm inverse triple-resonance (TXI) probe. Topspin 3.5 software was used for data processing, analysis and quantification. Metabolite concentrations were calculated using the internal reference sodium trimethylsilyl propionate (TSP), and all metabolite concentrations were normalized to spleen sample weight. Analysis of physiological changes in the spleen during tumorigenesis was performed with MSOT imaging of hemoglobin oxygenation in Ctrl and 4T1-TB BALB/c mice was conducted using an MSOT inVision 512-echo scanner (iThera Medical). Values represent mean ± SEM. Two-tailed Student's t test. *$p \leq 0.05$, **$p \leq 0.01$, ***$p \leq 0.001$ compared to tumor-bearing mice.

Results and Discussion:
Mice bearing 4T1 (n = 4) and E0771 (n = 5), but not Panc02 (n = 7) tumors exhibited splenomegaly (Figure 1A). Figure 1B illustrates the distinct metabolic changes observed in the spleen of all TB mice compared to Ctrl mice of the corresponding strain. These spleen metabolite changes were strikingly different from those identified in the plasma of TB mice, ruling out the possibility of any systemic contributions to spleen metabolism (data not shown). Elevated lactate, glutamate, glutathione, alanine and glycine were common across all groups of TB mice compared to controls (Figure 1C). Spleen metabolism determined for different 4T1 tumor weights revealed that a change in lactate and glutathione metabolism occurred for tumors at 200 - 400 milligrams (data not shown). An overlay of ultrasound and the optoacoustic signals of deoxyhemoglobin (Hb) and oxyhemoglobin (HbO_2) is presented in Figure 1D, revealing a significant reduction (P = 0.016) in oxyhemoglobin saturation in the spleen of 4T1-TB (n = 3) compared to Ctrl (n = 3) mice that may have contributed to the metabolic changes. Our findings highlight the metabolic reprogramming that occurs in the spleen with cancer. These splenic metabolite changes can contribute to immune suppression and to poor prognosis. These findings can be used to develop metabolic strategies coupled with frontline treatments to improve outcome.

Reference
1. Caswell D, et al. BMC Med. 2017
2. Steenbrugge J, et al. Cancer Research. 2021
3. Wu C, et al. JCI. 2018

Poster Presentation

Disclosures: The authors have disclosed no financial interest.

381-Dual E- and P-selectin DNA aptamer for imaging acute bowel inflammation using ultrasound molecular imaging

Presenter: Una Goncin, University of Saskatchewan

Una Goncin[1], Ron C Geyer[1], Steven Machtaler[2]

[1]*University of Saskatchewan, Saskatoon, SK*
[2]*University of Saskatchewan, Saskatoon*

Introduction:
Aptamers are oligonucleotides that bind to various targets with high affinity and specificity. Even with costly modifications, they are efficiently degraded by nucleases in blood and/or rapidly filtrated by the kidneys, leading to limited adoption in molecular imaging. Ultrasound molecular imaging (US-MI) uses microbubbles (MBs) that bind to vascular markers of disease within minutes after injection allowing for rapid disease detection, making it an ideal candidate for aptamer functionalization. Our goal is to create a targeted MB with a dual P- and E-selectin-targeted DNA aptamer (both expressed on activated endothelium for immune cell trafficking) and use it to image murine bowel inflammation.

Methods:
Lipid shell (DSPC, DSPE-PEG2K, and DSPE-PEG2K-DBCO) MBs were activated in perfluobutane-purged vials with a VIALMIX (Fig. 1a). Size and concentration were measured using a Multisizer 4e. A clinically-translatable azide-DBCO reaction was initiated by incubating MBs (containing the lipid-tethered DBCO) with a fluorescent dual P- and E-selectin DNA aptamer (5'-azide-DNA-Apt-3'-Cy3) or Scr aptamer (5'-azide-Scr-Apt-3'; 50 mg per 1x109 MBs) for 20 min at 37°C (Fig. 1b). Confocal microscopy was used to confirm labelling of fluorescent aptamer to MB shell. Acute colitis was induced using 2% TNBS in 3 of 6 Balb/C mice. Mice were imaged using contrast mode on a Vevo3100 US system following i.v. bolus of 1x108 MBs. Each mouse received dual selectin aptamer (DABs) and non-targeted (NTBs) MBs. Images were analyzed using VEVOCQ. Bowels were excised and prepared using a Swiss roll technique for histology and immunofluorescence.

Results/Discussion:
Labelling of MBs with fluorescent dual selectin DNA aptamer was verified with confocal microscopy (Fig 1c). There was a low US-MI signal detected using NTBs (0.40 + 0.26 a.u.) and DABs (0.07 + 0.12 a.u.) in healthy mice (Fig. 1d, e). There was a non-significant increase in US-MI signal in mice with acute colitis using DABs (3.95 + 2.87 a.u.) in comparison to NTBs (1.15 + 0.31 a.u.) (Fig. 1d, e). All 3 mice with acute colitis showed signs of inflammation histologically. Mouse 1 showed severe/necrotic signs of inflammation, with epithelial necrosis and reduced blood flow (Fig. 1f, Persuasive Data), suggesting MBs were severely limited in their ability to accumulate in the bowel, contributing to the low molecular imaging signal. In mice 2 and 3, DABs signal increases along with histological severity (Fig. 1f, Persuasive Data). Mouse 2 showed moderate severity, moderate immune adhesion to vasculature, and patchy perfusion pattern (Fig. 1f, Persuasive Data). Mouse 3 showed moderate-high inflammation with high immune cell adhesion to vessels and uniform, high-uniform perfusion. No healthy mice showed signs of inflammation (Fig. 1f, Persuasive Data). Mice with acute colitis presented with increased P- and E-selectin expression on the vasculature (white arrows; Persuasive Data).

Conclusion:
We constructed a dual P- and E-selectin targeted MB using a fluorescent, dual-selectin DNA aptamer which generated a detectable US-MI signal in mice with acute colitis. Though not significant, the molecular imaging patterns correlated to histological severity and blood flow patterns. This approach for construction is quick, cost-efficient, and represents a new generation of US-MI contrast agents that can be clinically translated.

Poster Presentation

Disclosures: The authors have disclosed no financial interest.

382-Biodistribution of Sotrovimab, a SARS-CoV-2 monoclonal antibody, using PET imaging in cynomolgus monkey

Presenter: Tolulope Aweda ,GSK

Tolulope A. Aweda[1], Shih Hsun Cheng[2], Stephen C. Lenhard[2], Armin Sepp[3], Tina Skedzielewski[3], Chih-Yang Hsu[4], Shelly Marshall[5], Heather Haag[5], Jonathan Kehler[4], Prabhas Jagdale[4], Andrew Gehman[5], Minh Doan[4], Andrew Mayer[4], Peter Gorycki[4], Christophe Colas[6], Brenda Smith[6], Curtis Maier[7], Hasan Alsaid

[1]*GSK, Collegeville, PA*
[2]*GlaxoSmithKline, Collegeville, PA*
[3]*Sheffield, United Kingdom*
[4]*GlaxoSmithKline, Collegeville, Pennsylvania*
[5]*GlaxoSmithKline*
[6]*San Francisco, California*
[7]*Collegeville, Pennsylvania*

Abstract Body:
Sotrovimab (VIR-7831), an engineered human IgG1κ monoclonal antibody (mAb), binds to a conserved epitope of the SARS-CoV-2 spike protein receptor binding domain (RBD) and, neutralizes the virus in vitro[1]. The Fc region of VIR-7831 contains an LS modification (M428L and N434S) to promote neonatal Fc-receptor (FcRn)-mediated recycling and extend its serum half-life[2]. Here, we aimed to evaluate the impact of the LS modification on tissue biodistribution by comparing ^{89}Zr labeled VIR-7831 to its non-LS equivalent, ^{89}Zr-VIR-7831-WT in cynomolgus monkeys using Positron Emission Tomography/Computed Tomography (PET/CT) imaging up to 14 days post treatment.

Methods:
Deferoxamine (DFO) modified VIR-7831 and the non-LS wild-type (VIR-7831-WT) antibodies were radiolabeled with ^{89}Zr and their stability confirmed in 10% monkey serum/PBS for up to 7 days. FcRn and RBD ELISA binding assays were used to confirm that ^{89}Zr labeling did not disrupt RBD or FcRn binding of the antibodies. Full body PET/CT in cynomolgus monkeys was used to compare the tissue biodistribution properties of ^{89}Zr-VIR-7831 and ^{89}Zr-VIR-7831-WT. All major organs were analyzed for absolute concentration (SUV_{mean} uptake) as well as tissue:blood SUV_{mean} uptake ratios, with the focus on the respiratory tract. Serum concentration in blood, tissues and PET data were modeled by physiologically-based pharmacokinetics (PBPK) to evaluate the tissue biodistribution kinetics of VIR-7831 and VIR-7831-WT[3]. Additionally, radiomics features (intensity profiles, shapes and textures) were extracted from the PET images and SUV values to investigate differences between ^{89}Zr-VIR-7831 and ^{89}Zr-VIR-7831-WT[4]. A levelset analysis was performed to analyze the spatial distribution of the ^{89}Zr labeled antibodies with proximity to blood supply.

Results:
^{89}Zr-VIR-7831 and ^{89}Zr-VIR-7831-WT were obtained at radiolabeling yield of 84±3% with ≥95% radiochemical purity and specific activities of 2.87±0.22 mCi/mg and 2.36±0.2 mCi/mg respectively. In vivo, SUV_{mean} uptake in the pulmonary bronchi for ^{89}Zr-VIR-7831 was statistically higher than ^{89}Zr-VIR-7831-WT at Days 6 (3.43±0.55 and 2.59±0.38, respectively), and 10 (2.66±0.32 and 2.15±0.18, respectively), while the reverse was observed in the liver at Day 6 (5.14±0.8 and 8.63±0.89, respectively), Day 10 (4.52±0.59 and 7.73±0.66, respectively), and Day 14 (4.95±0.65 and 7.94±0.54, respectively), Figure 1. The half-life extended ^{89}Zr-VIR-7831 remained longer in circulation than ^{89}Zr-VIR-7831-WT (21.3±3.0 days vs. 16.5±1.1 days), consistent with enhanced FcRn binding. On Day 3, the ^{89}Zr-VIR-7831 group mean tissue:blood ratio in pulmonary bronchi (0.41) and lung tissue excluding air space (0.70) was higher than other respiratory tract tissues, including nasal cavity (0.29), pharynx (0.20), larynx (0.23), trachea (0.16) and total lung (0.25, including air space). PBPK modelling predicted the lung interstitial space to serum ratio to be 0.55 on Day 3. Radiomics analysis showed extracted features with VIR-7831 exhibiting mean-centralized distribution in lungs indicating more uniform uptake than VIR-7831-WT, while the 3D levelset analysis showed significantly higher uptake of ^{89}Zr-VIR-7831 vs ^{89}Zr-VIR-7831-WT in the region closest to the bronchi on Day 6.

Conclusion:
The half-extending LS modified antibody, ^{89}Zr-VIR-7831 remained longer in circulation than ^{89}Zr-VIR-7831-WT correlating with higher tissue concentrations, although only statistically significant in the pulmonary bronchi. The relatively higher local concentration of ^{89}Zr-VIR-7831 in the bronchiolar region was substantiated by physiomic image analysis. The data observed allow insight into tissue distribution and elimination kinetics of mAbs that can guide future biologic drug discovery efforts.

Reference
1. Cathcart AL, et al. bioRxiv. 2021:2021.2003.2009.434607
2. Ko S, et al. BioDrugs. 2021;35:147-157.
3. Sepp A, et al. MAbs. 2020;12:1832861.
4. Cook GJR, et al. International Journal of Radiation Oncology*Biology*Physics. 2018;102:1083-1089.

Poster Presentation

Disclosures: The authors have disclosed no financial interest.

383-Novel Antibody-Targeted Clathrin-Based Superparamagnetic Iron Oxide Nanoprobes for MRI of Dopamine Transporters in Drug Addiction

Presenter: Gordana Vitaliano, McLean Hospital

Gordana Vitaliano[1], Christopher Adam[1], Gonzalo E. Zeballos[1], Kyoko Ohashi[2], Franco Vitaliano[3]

[1]McLean Hospital, Belmont, MA
[2]McLean Hospital
[3]ExQor Technologies, Inc., Boston, MA

Rationale and Objectives:
MRI has high spatial resolution but poor sensitivity for visualization of molecular targets. Superparamagnetic iron oxide (SPIO) contrast agents along with antibodies are used to improve MRI sensitivity and molecular targeting, but they cannot cross an intact blood-brain barrier (BBB) limiting their use for CNS receptor/transporter imaging. Our goal was to enable MR imaging of dopamine transporters (DAT) in drug addiction using novel clathrin-nanoprobes (CNPs) carrying SPIO and anti-DAT-antibodies, which noninvasively pass a BBB and target DAT.

Methods:
DAT-antagonists can be used for diagnosis and treatment of drug addiction, Parkinson's disease and ADHD. DAT-CNPs were synthesized by conjugating anti-DAT-antibody and SPIO (or NHS-Fluorescein) to clathrin using polyethylene glycols at 1:1:1 molar ratio. The size and uniformity of nanoprobe was determined by dynamic light scattering. *C57BL/6J* mice were given intraperitoneal injections of saline or neurotoxic dose of methamphetamine (METH, 30 mg/kg) 24h before MRI. Mice were then given saline or DAT-CNPs intranasally (68pmol, 50μL) 4h before *in-vivo* or *ex-vivo* MRI. Voxel-wise R_2* relaxation rates were obtained at 9.4T using a series of gradient-echo images, and estimated in the striatum (STR), substantia nigra (SN) and visual cortex (vCTX), a control region with low DAT expression.

Results:
DAT-CNPs remained immunoreactive after modifications. The iron stained brain slices showed an accumulation of DAT-CNPs in brain regions rich in DAT (e.g., STR). Fluorescent microscopy demonstrated specific targeting of dopamine brain regions with DAT-CNPs. Confocal laser microscopy confirmed integrity of DAT-CNPs, as clathrin and DAT-antibody fluorescence co-localized in dopamine regions. MRI studies revealed that R_2* values were lower in STR (p=0.0077) and SN (p=0.0023) in METH vs. saline treated mice. R2* values were significantly higher in the STR (p=0.0010) and SN (p=0.0007) compared to vCTX in WT animals that received DAT-CNPs, but not in saline treated animals. DAT-CNPs significantly increased R2* in the STR (p<0.0001) and SN (p=0.0002) compared to saline without significantly altering R2* in the vCTX.

Conclusions:
DAT-CNPs successfully bypassed an intact BBB and noninvasively delivered SPIO contrast agents along with anti-DAT-antibody to the mouse brain, enabling MRI detection of decreased DAT levels in METH toxicity. Hence, clathrin appears to provide a highly efficient nanoplatform for targeted delivery of antibodies and SPIO to CNS. This nanotechnology strategy may lead to development of new neurotheranostics for imaging of molecular changes in brain disorders, for monitoring disease progression and recovery process, and for efficiently treating CNS disorders through targeted delivery of specific antibodies.

Poster Presentation

Disclosures: The authors have disclosed no financial interest.

384-Demonstrating Tumor Vascular Disrupting Activity of the Small-Molecule Dihydronaphthalene Tubulin-Binding Agent OXi6196 as a Potential Therapeutic Agent for Cancer Treatment using BLI in mice

Presenter: Ralph Mason, University of Texas Southwestern Medical Center

Li Liu[1], Regan Schuetze[2], Jeni Gerberich[3], Ramona Lopez[2], Samuel Odutola[4], Rajendra Tanpure[4], Justin Tidmore[5], Amanda Charlton-Sevcik[5], Hans Hammers[2], Payal Kapur[2], Mary Lynn Trawick[4], Kevin Pinney[4], **Ralph Mason[1]**

[1]University of Texas Southwestern Medical Center, Dallas, TX
[2]University of Texas Southwestern Medical Center
[3]University of Texas Southwestern Medical Center, Dallas, Texas
[4]Baylor University, Waco, Texas
[5]Waco, Texas

Background:
Bioluminescence imaging (BLI) is particularly effective for assessment of tumor growth and spread in mice, provided luciferase transfected cells are available. Given that the substrate luciferin must reach the cells for enzyme induced light emission, BLI is also found to effectively reveal vascular disruption [1]. The concept of selectively targeting tumor vasculature as an effective therapy to starve tumors is well established and there continues active research into identifying and developing next generation agents. Various analogs and unique molecules inspired by the first generation vascular-disrupting agent (VDA) combretastatin A-4 (CA4) have been synthesized and preliminary data suggested that the dihydronaphthalene OXi6196 exhibits potent antitumor properties. At concentrations >5 nM OXi6196 causes G2/M cell cycle arrest and monolayers of rapidly growing HUVECs undergo concentration-dependent changes in their morphology. At 0.1 μM OXi6196 disrupts capillary-like endothelial networks pre-established with HUVECs on Matrigel. Since OXi6196 is extremely hydrophobic it has been phosphorylated to generate a water soluble prodrug OXi6197 (Fig. A). We have now examined acute vascular disruption and therapeutic response in two distinct tumor types: orthotopic human MDA-MB-231 breast tumor and syngeneic RENCA kidney tumor in mice.

Method:
OXi6197 was synthesized [2] and tested in cell culture and capillary network assays to verify activity. Luciferase expressing tumor cells were implanted respectively in the mammary fat pad (MDA-MB-231-luc) or right kidney (RENCA-luc) of mice. BLI was applied repeatedly to assess tumor growth. We examined dose response with repeated dynamic BLI measurement at baseline and up to 24 hrs after administering (IP) various doses of OXi6197. Having established that 35 mg/kg caused highly effective acute vascular disruption, we then undertook long-term therapeutic studies with twice weekly doses of 20 or 35 mg/kg.

Results:
Dynamic BLI revealed dose dependent vascular shutdown with >80% signal loss within 2 hrs at doses ≥30 mg/kg and >95% shutdown after 6 h for doses ≥35 mg/kg, which remained depressed by at least 70% after 24 hrs in MDA-MB-231-luc tumors (Fig. b). Twice weekly treatment with OXi6197 (20 mg/kg) caused a significant tumor growth delay (Fig. C). Similar efficacy was observed in orthotopic RENCA-luc

tumors (Fig. D-G), which showed massive hemorrhage and necrosis after 72 hrs (Fig. F).

Discussion & Conclusion:
BLI effectively revealed tumor growth and treatment-induced delay in orthotopic tumors in mice. Following administration of luciferin subcutaneously in the fore back of mice, signal appeared and reached its maximum much more rapidly in the orthotopic kidney tumors compared to breast tumors consistent with more extensive vascularization. In both tumor types bioluminescence was significantly reduced within hours following administration of OXi6197 IP indicative of vascular disruption. Histology confirmed massive hemorrhage and necrosis within 72 hours of administration. Both tumor types showed tumor growth delay when treated with OXi6197 twice weekly. While the breast tumors could have been assessed using calipers, the BLI provided effective insight into the orthotopic kidney tumor growth. These results demonstrate effective vascular disruption at doses comparable to the most effective vascular-disrupting agents suggesting opportunities for further development.

Reference

1. L. Liu, D. O'Kelly, R. Schuetze, G. Carlson, H. Zhou, M.L. Trawick, K.G. Pinney, R.P. Mason, Non-Invasive Evaluation of Acute Effects of Tubulin Binding Agents: A Review of Imaging Vascular Disruption in Tumors, Molecules, 26 (2021) 2551.
2. C.J. Maguire, Z. Chen, V.P. Mocharla, M. Sriram, T.E. Strecker, E. Hamel, H. Zhou, R. Lopez, Y. Wang, R.P. Mason, D.J. Chaplin, M.L. Trawick, K.G. Pinney, Synthesis of dihydronaphthalene analogues inspired by combretastatin A-4 and their biological evaluation as anticancer agents, Medchemcomm, 9 (2018) 1649-1662.

Poster Presentation

Disclosures: The authors have disclosed no financial interest.

385-Deep Learning Segmentation of microCT images of the Mouse Lung in Study of SARS-CoV-2

Presenter: Douglas Rowland, University of California, Davis

Douglas J. Rowland[1], Valerie A. Porter[2], Hongwei Liu[3], Ana Ramirez[1], Mollie Heffner[3], Louise Lanoue[3], Lark Coffey[3], Kent Lloyd[3], Abhijit J. Chaudhari[2]

[1]*University of California, Davis, Davis, CA*
[2]*University of California, Davis, Sacramento, CA*
[3]*University of California Davis, Davis, CA*

Introduction:
Humanized animal models are essential to model SARS-CoV-2 infection and COVID-19 pathophysiology in people. To this end, CRISPR was used to replace the endogenous mouse Ace2 locus with coding sequence (exons 2-19) of the human *ACE2* gene, in murine embryonic stem (ES) cells, effectively creating a humanized knockin of the *ACE2* gene (KI-h*ACE2*) under control of intrinsic mouse regulatory regions while knocking out the mouse *Ace2* gene. *ACE2* expression in KI-hACE2 mice is similar to that in humans with high expression in the lung. SARS-CoV-2 infection and disease progression in KI-h*ACE2* mice were compared to that in transgenic mice in which 8 copies of *ACE2* coding sequence under control of the K18 promoter (K18-ACE2) were randomly inserted into the genome without disrupting mouse *Ace2* expression. Animals at 9, 20, and 28 weeks of age for both KI-h*ACE2* and K18-*ACE2*mice were inoculated with SARS-CoV-2 or mock-inoculated with virus diluent only, and assessed daily for signs of clinical disease including weight loss, and cognitive impairment, ECG, and microCT at regular intervals until 14 days post inoculation. We optimized the U-Net-like convolutional neural network (CNN) for facile and accurate lung segmentation of this large dataset of microCT images.

Methods:
Mice were given saline (PBS) or SARS-CoV-2 B.1.617.2 (delta strain) diluted in PBS intranasally. Infection was confirmed by virus isolation from throat swab, lung, or seroconversion as assessed by detection of neutralizing anti-SARS-CoV-2 antibody on day 14. Mice underwent up to 3 microCT sessions on a QuantumGX-II (Perkin Elmer) in an animal BSL3 that included a 4-minute respiratory gated scan at 90kV and 88mA. With a camera frame rate of 60fps, 14k projections were retrospectively binned into end -expiration and -inspiration images resulting in 172 total images volumes over the entire cohort of animals. Images were reconstructed at 72μm isotropic voxels with a matrix size of 512x512x277. The CNN used was the Sensor3D [1] as implemented in Dragonfly 2022.1 (Object Research Systems Inc.). The CNN has 15 (3x3) time-distributed convolutions (activation function=Conv2D), four time-distributed max pooling and 2 bidirectional convolutional long-short term memory steps. The CNN was trained with a patch size of 64, stride ratio 0.5, batch size 32, a loss function looking at the categorical cross entropy and optimized with the Adadelta function. A linear learning rate was set at 1. Data augmentation by a factor of 5 was implemented (flip, rotation, scaling, brightness change, and gaussian noise). The input size for training datasets were subvolumes of the original dataset at 347x347x277 to improve training time. Two training datasets (1 end inspiration and 1 end expiration) were used to initially test the Sensor3D CNN. Four datasets were used to evaluate the model training (2 end inspiration and 2 end expiration). All six datasets were manually segmented, each taking 6+ hours.

Results and Conclusion:
Due to limited projections in which end inspiration occurs, the reconstructed microCT image has lower signal-to-noise (SNR) than the end expiration (Figure 1A). The model shows good convergence over the two training sessions implemented (session 1 epochs 1-20 and session 2 epochs 21-58, 2 sessions were necessary due to limitations on the computational device, Figure 1B). Results of applying the model to datasets not in the training set were determined to be robust (Figure 1C). The Dice coefficients of overlap between manual and CNN-based segmentations were >0.96 (Figure 1D, E). Also, the true positivity rate was high (0.96). The maximum mismatch was found at the periphery of the lung. We conclude that the deep learning segmentation could present a promising method for lung segmentation, overcoming the subjectivity and resource-intensiveness of manual segmentation.

Reference

1. A. A. Novikov, D. Major, M. Wimmer, D. Lenis and K. Bühler, "Deep Sequential Segmentation of Organs in Volumetric Medical Scans," in IEEE Transactions on Medical Imaging, vol. 38, no. 5, pp. 1207-1215, May 2019, doi: 10.1109/TMI.2018.2881678.

Poster Presentation

Disclosures: The authors have disclosed no financial interest.

386-AI based imaging biomarker development in ADPKD mouse model

Presenter: Snehal Vadvalkar, AbbVie

Snehal Vadvalkar[1], Ansh Sharma[1], Xiaomeng Zhang[2], Kaneli Galiotos[3], Bradley Hooker[3], Dustin Wooten[2], Varsha Mohan[3], Quaisar Ali[3], Ana Basso[3], Eric Mohler[3], Abhishek Pandey[3]

[1]*AbbVie, North Chicago*
[2]*AbbVie, North Chicago, IL*
[3]*AbbVie, North Chicago, Illinois*

Introduction:
Autosomal Dominant Polycystic Kidney Disease (ADPKD) is a common genetic renal disease in which formation and expansion of fluid-filled renal cysts leads to chronic renal injury or failure. Whereas end stage renal failure has been the established clinical endpoint, there may be increasing regulatory acceptance of total kidney volume (TKV) and cystic volume as surrogate endpoints which can be measured non-invasively with imaging modalities such as magnetic resonance imaging (MRI), computed tomography (CT), or ultrasound (US). In the course of our exploration of preclinical models of polycystic kidney disease, we have investigated the automation of this volume calculation via a deep learning model, followed by development of AI based imaging biomarker.

Method:
A 3D U-NET[1] deep learning model was trained using clinical CT images (~200 human kidney CT Images) along with radiologist verified labels made available as part of the kits-19 data challenge. The kidney volume segmentation model was then trained on first time point of a longitudinal study with MRI images acquired from in-house pcy (polycystic) mice (63 mice MRI images), using transfer learning with the weights learned from clinical CT kidney model. The model was then recursively retrained using transfer learning with weights from the previous timepoint and imaging data aggregated over timepoints. After segmentation, additional imaging features were derived from baseline kidney volumes using the pyradiomics python package. Mesh Volume and Total energy were two imaging features that provided best hierarchical clustering results. We then investigated if there was a relationship between imaging features from baseline scans and terminal Biomarker Data. It was observed that biomarkers in one cluster performed better than the other.

Conclusion:
We observe that deep learning can be used successfully in segmenting kidney volumes with a small dataset of 63 mice images while using transfer learning approach calculated from a different imaging modality. Furthermore, the extracted baseline imaging features cluster in two groups, where biomarkers in one group perform well over the other. Future work will investigate if mice cohorts can be predicted as progressor or non-progressor and biological pathways will be investigated based on imaging features[2] and RNA-seq data.

Reference
1. Çiçek, Ö. Abdulkadir, A. Lienkamp, S.S. Brox, T. Ronneberger,O. arXiv:1606.06650,3D U-Net: Learning Dense Volumetric Segmentation from Sparse Annotation,https://doi.org/10.48550/arXiv.1606.06650
2. Rajan Jain, Andrew S Chi, Radiogenomics identifying important biological pathways in gliomas, Neuro-Oncology, Volume 23, Issue 2, February 2021, Pages 177–178, https://doi.org/10.1093/neuonc/noaa290

Poster Presentation

Disclosures: The authors have disclosed no financial interest.

387-Optimization of Chelators of 99mTc-antiCD8 to Assess T Cell Infiltration

Presenter: Lindy Melegari, Yale School of Medicine

Lindy M. Melegari[1], Bernadette Marquez-Nostra[2], Khashayar Rajabimoghadam[3], Felix Salazar[4], Anna M. Wu[4], Chi Liu[4]

[1]*Yale School of Medicine, New Haven, CT*
[2]*Yale University, New Haven, CT*
[3]*Yale University*
[4]*City of Hope, Duarte, CA*

Objectives:
Due to its capacity for antigen-directed cytotoxicity, T lymphocytes have become a central focus for engaging the immune system to fight against cancer. It has been shown, through evidence of their presence in tumor samples from long-surviving patients, that stronger infiltration of CD8+ T cells into solid tumors closely correlates with better treatment outcomes (1). However, some patients do not respond to this type of treatment, or those that do can develop a resistance overtime. Developing non-invasive imaging approaches for monitoring immune cell function and specifically tracking CD8+ T cells during and after therapy would provide diagnosticians tools for assessing therapeutic efficacy. 99mTc is one of the most clinically used radionuclides for SPECT imaging due to its relatively short half-life (t1/2 = 6.01 hr) and its wide availability (2). We hypothesize that imaging CD8+ T cells with this stable and efficient radiocompound will provide insight into the systemic alterations of CD8+ T cell in the tumor microenvironment and in hematopoietic organs such as bone marrow and lymph nodes to understand the effect of immunotherapies on this important immune cell.

Methods:
169 cDb fragment was conjugated via reduced disulfide bond from cysteine residues with different chelators like DOTA, NOTA, DFO and HYNIC. Conjugation was followed by radiolabeling with ^{99m}Tc [Figure 1] to each chelator, yielding a result of [^{99m}Tc]Tc-[chelator]-αCD8-cDb. The efficiency, radiochemical purity and specific activities were assessed in all synthesized conjugation reactions along with antibody conformation analysis using SEC-HPLC and iTLC. The top three chelators were chosen to then test the performance of the different radioconjugates in vivo by immunoSPECT imaging and ex vivo biodistribution. Each conjugate was formulated in 100 μL of sterile PBS containing 300 MBq of SPECT agent. Each dose was injected via tail vein into C57BL/6 mice. The uptake of the radiotracer was assessed in each organ through biodistributioin studies. The selection of the best chelator was chosen based on the highest uptake in T cell rich organs such as lymph nodes and the spleen and the lowest uptake in the liver.

Results:
The top three chelating agents that yielded the highest specific activity were HYNIC, DOTA and DFO. Most chelators achieved >99% radiochemical yield with the exception of NOTA (95%). The highest specific activity was seen in both DFO and DOTA at 200 μCi/μg **[Figure 1a]**. Biodistribution studies resulted in the DFO chelator having the greatest uptake in the lymph nodes and the least uptake in the liver, proving it to be the best selection **[Figure 1b].**

Conclusions:
Selection of this chelator provided us with an optimization technique for further radiolabeling and imaging of CD8+ T cells to track its infiltration in the tumor environment. Herein, we present the first SPECT imaging agent for CD8 which opens a new avenue for non-invasive imgaging using SPECT. Current work includes SPECt imaging of murine models.

Reference

1. Fridman, W., Pagès, F., Sautès-Fridman, C. et al. The immune contexture in human tumors: impact on clinical outcome. Nat Rev Cancer 12, 298–306 (2012). https://doi.org/10.1038/nrc3245
2. Kane SM, Davis DD. Technetium-99m. [Updated 2021 Sep 22]. In: StatPearls [Internet]. Treasure Island (FL): StatPearls Publishing; 2022 Jan-. Available from: https://www.ncbi.nlm.nih.gov/books/NBK559013/?report=classic

Poster Presentation

Disclosures: The authors have disclosed no financial interest.

388-Utilizing fructose metabolism to fuel and image anti-tumor immunity

Presenter: Tanya Schild, Memorial Sloan Kettering Cancer Center

Tanya Schild[1], Rachel Chirayil[2], Quinlan Cullen[3], Nathaniel Kim[1], Kayvan Keshari[4]
[1]*Memorial Sloan Kettering Cancer Center, New York*
[2]*Memorial Sloan Kettering Cancer Center, New York City, New York*
[3]*Memorial Sloan Kettering Cancer Center*
[4]*Memorial Sloan Kettering Cancer Center, New York, NY*

Background:
Our current understanding of immunometabolism and how it contributes to anti-tumor immunity is extremely narrow because we rely on artificial models which do not recapitulate the physiological conditions found *in vivo*. Adding the ability to visualize anti-tumor immunity and the metabolic fluxes both in tumor cells and in immune cells in real time *in vivo* will be extremely important. The field of modulating dietary intake to synergize with cancer therapies is rapidly growing, and new tools are needed to observe if various dietary interventions are relevant[1]. Consumption of fructose, in the form of high fructose corn syrup, is elevated in the western diet, but it is unclear how fructose metabolism influences anti-tumor immunity. Fructose is canonically metabolized in the intestine and the liver and can shunt into glycolysis[2]. In certain tumor types, fructose metabolism becomes deregulated, allowing tumor cells to metabolize fructose to power their biosynthetic processes[3]. Similarly, engineering immune system to be able to efficiently metabolize fructose may help us power immunotherapy to work in difficult to treat cancers, especially in individuals who have high fructose in blood or in the tumor microenvironment.

Results:
We engineered T cells to overexpress a fructose transporter, GLUT5, which is normally not expressed in the immune compartment at high levels. We hypothesized that increased fructose uptake by CD8 T cells will ameliorate exhaustion caused by the glucose-low tumor microenvironment. We utilized the OTI mouse model of anti-tumor immunity where all CD8 T cells are engineered to recognize OVA peptide presented on MHCI[4]. For our tumor model, we chose B16 melanoma cells overexpressing OVA in conjunction with GFP and Luciferase for *in vivo* and *in vitro* imaging[4]. We then designed an assay to measure cancer cell killing *in vitro* using T cells which express GLUT5 coupled to mCherry and B16-OVA-GFP-Luciferase cells (Figure 1a). We quantified live B16 cells post incubation with T cells under various glucose and fructose titrations using luminescence (Figure 1b). We determined that GLUT5 T cells are more efficient in killing under low glucose and fructose conditions, in the range of 1.5-3mM (Figure 1b). We also observed that GLUT5 expression restores T cell glycolytic capacity under fructose to that of unexhausted T cells under glucose replete conditions (Figure 1c). Similarly, GLUT5 expressing T cells proliferated more under high fructose and low glucose conditions, as was assayed through CFSE fluorescent dye incorporation and dilution over three-day period (Figure 1d). Lastly, we are conducting a mouse experiment to measure GLUT5 T cell tumor killing *in vivo* (Figure 1f). We are quantifying the tumor size using luminescence and T2-weighted MRI imaging.

Discussion:
We showed that overexpressing GLUT5 on T cells can be a viable strategy to restore their functionality *in vitro* and *in vivo* under limiting glucose conditions. Ultimately, we want to employ a hyperpolarized ^{13}C fructose probe we are developing in lab to visualize T cell metabolism *in vivo* using hyperpolarized MRI[5].

Acknowledgments: T32 Molecular Imaging in Cancer Biology (MICB) Research Fellowship

Reference

1. Kanarek, N., Petrova, B. and Sabatini, D.M., 2020. Dietary modifications for enhanced cancer therapy. Nature, 579(7800), pp.507-517.
2. Hannou, S.A., Haslam, D.E., McKeown, N.M. and Herman, M.A., 2018. Fructose metabolism and metabolic disease. The Journal of clinical investigation, 128(2), pp.545-555.
3. Krause, N. and Wegner, A., 2020. Fructose metabolism in cancer. Cells, 9(12), p.2635.
4. Vardhana, S.A., Hwee, M.A., Berisa, M., Wells, D.K., Yost, K.E., King, B., Smith, M., Herrera, P.S., Chang, H.Y., Satpathy, A.T. and van den Brink, M.R., 2020. Impaired mitochondrial oxidative phosphorylation limits the self-renewal of T cells exposed to persistent antigen. Nature immunology, 21(9), pp.1022-1033.
5. Keshari, K.R., Wilson, D.M., Chen, A.P., Bok, R., Larson, P.E., Hu, S., Criekinge, M.V., Macdonald, J.M., Vigneron, D.B. and Kurhanewicz, J., 2009. Hyperpolarized [2-13C]-fructose: a hemiketal DNP substrate for in vivo metabolic imaging. Journal of the American Chemical Society, 131(48), pp.17591-17596.

Poster Presentation

Disclosures: The authors would like to disclose that HP pyruvate is an investigational device.

389-Evaluation of the anti-tumor immune response following PSMA-targeted, PSMA-1-Pc413 based PDT

Presenter: Lifang Zhang, Case Western Reserve University

Lifang Zhang[1], Aditi A. Shirke[2], Ramamurthy Gopalakrishnan[2], Ethan Walker[2], Dong Luo[3], Xinning Wang[4], James Basilion[2]

[1]*Case Western Reserve University*
[2]*Case Western Reserve University, Cleveland, OH*

[3]*Case Western Reserve University, Cleveland, Ohio*
[4]*Case Western Reserve University, Beachwood, OH*

Introduction:
Recently, photodynamic therapy (PDT) comes to insights for being a powerful strategy for inducing immunogenic cell death (ICD), thus to alter the tumor microenvironment and enhance the host's anti-tumor immunity [1, 2]. We recently developed a prostate specific membrane antigen (PSMA)-targeted PDT agent, PSMA-1-Pc413, which showed perfectly combines both fluorescence for image-guide surgery (IGS) and highly selective tumor cell killing photodynamic therapy. However, whether PSMA-1-Pc413 based PDT can enhance the host's anti-tumor immune response is unclear. In this study, a mouse prostate cancer cell line TRAMP-C1-hPSMA, which expresses human PSMA, and both immune deficient and immune competent mice were used to evaluate the impact of PSMA-1-Pc413 based PDT on host's anti-tumor immune response.

Methods:
A syngeneic transgenic adenocarcinoma mouse prostate cancer cell line TRAMP-C1-hPSMA, which expresses human PSMA, was used for tumor establishment. TRAMP-C1-hPSMA cells ($2x10^6$ cells in 100ul Matrigel) was implanted subcutaneously either to the flank of immune deficient male BALB/C nude mice or to immune competent male C57BL/6 mice. When tumor size reached $100mm^3$, mice received PSMA-1-Pc413 (0.1nmol/g body weight) through tail vein injection. Maestro images were taken at 24h post PSMA-1-Pc413 injection to show the uptake of PSMA-1-Pc413 in tumors. Then the treatment group of mice were received PDT ($150J/cm^2$ of 672nm light). After PDT, Maestro images were taken immediately to show the photo bleach of fluorescence signal in tumors, which indicates activation of the probe. Tumor growth was then monitored by caliper measurement. Blood was collected at time points of 24h, 72h and 120h for detection of cell death signals released by tumor cells and immunologically important cytokines, such as TNF-alpha, IL-6, IL-10 and IL-1beta, to evaluate the host's anti-tumor immune response.

Results and Discussion:
Maestro images at 24h post injection showed selective accumulation of probe in TRAMP-C1-hPSMA tumors. And fluorescent signals in Nude mice and C57BL/6 mice were comparable (Figure 1A). After PDT, the fluorescence signal on both tumors were photobleached, indicating the activation of PSMA-1-Pc413 probe (Figure 1A). Tumor growth monitoring results from Figure 1B demonstrated that tumors in both Nude mice and C57BL/6 mice were responded to PDT, but significant response was observed in C57BL/6 mice with the complete disappearance of tumors and no recurrence during the two months observation. Tumors in nontreated C57BL/6 mice were continuedly growing. These results indicated the host immune response after PDT was stimulated and which restricted the tumor recurrence. Interestingly, compared to Nude mice, tumors in nontreated C57BL/6 mice were restricted and slowly growing, which may indicate the immune rejection for human PSMA expressing tumor cells in immune competent mice.

Reference
1. Kobayashi, H., et al., Near-infrared photoimmunotherapy of cancer: a new approach that kills cancer cells and enhances anti-cancer host immunity. Int Immunol, 2021. 33(1): p. 7-15.
2. Yang, Y., Y. Hu, and H. Wang, Targeting Antitumor Immune Response for Enhancing the Efficacy of Photodynamic Therapy of Cancer: Recent Advances and Future Perspectives. Oxid Med Cell Longev, 2016. 2016: p. 5274084.

Poster Presentation

Disclosures: The authors have disclosed no financial interest.

390-The right choice of anaesthetics for PET neuroimaging in pigs

Presenter: Aage Kristian Alstrup, Aarhus University Hospital

Aage Kristian O. Alstrup[1], Mette O. Simonsen[2], Mie Ringgaard Dollerup[3]

[1]*Aarhus University Hospital, Aarhus N, Denmark*
[2]*PET-centret, Århus C, Danmark, Denmark*
[3]*Aarhus University Hospital, Aarhus, Denmark*

Introduction:
The right choice of anaesthetics for pig PET neuroimaging protocols is a challenge, as anaesthetics often have major effects on tracer binding and uptake by reducing brain metabolism, affecting the cerebral blood flow or altering enzymes and brain receptors.

Materials and Methods:
For this poster we reviewed the literature on the effects of anaesthesia with PET neuroimaging in pigs. We furthermore reviewed the latest knowledge about practical pig anaesthesia, and illustrated with photos how pig anaesthesia in neuroimaging can be performed.

Results:
Only a few studies have been published. Both [11C]SCH23390 and [11C]MDL100,907 binding, but not [11C]yohimbine, are strongly affected by the choice of anaesthetics used. Furthermore, the kinetics of [11C]SCH23390 are flow-dependent in pigs, whereas this is not the case in primates, including humans. Anaesthesia also reduces cerebral metabolism in pigs measured with the glucose analog, [18F]FDG. The literature review shows that both isoflurane and propofol are useful anaesthetics for long-term anaesthesia of pigs in imaging studies.

Conclusion:
The right choice of anaesthetics for porcine PET neuroimaging may primarily be based on ensuring a sufficient depth of anaesthesia and good animal welfare. The anaesthesia procedures used must always be included in research papers.

Poster Presentation

Disclosures: The authors have disclosed no financial interest.

391-Mapping Nav1.7 Expression in Human Peripheral Nerves.

Presenter: Tara Viray, Memorial Sloan Kettering Cancer Center

Tara D. Viray[1], Dauren Adilbay[2], Delissa Johnson[3], Paula Demetrio de Souza Franca[4], NagaVaraKishore Pillarsetty[2], Thomas Reiner[5]

[1]*Memorial Sloan Kettering Cancer Center, North Brunswick, NJ*
[2]*Memorial Sloan Kettering Cancer Center, New York, NY*
[3]*New York City, NY*
[4]*Memorial Sloan Kettering Cancer Center, New York*
[5]*Novartis, Switzerland*

Introduction: Nerve injury is a debilitating condition affecting over 350 million individuals worldwide. About 51,000,000 surgeries are

performed in the US every year that result in 600,000 accidental nerve injuries. Although trauma is the majority cause of injuries, a previous surgical procedure is attributed as the origin of the neurological symptoms in a quarter of all cases. Intuitively, every surgery aims to preserve nerves whenever possible. However, intraoperatively, these nerves are difficult to visualize even on experienced hands when there is recurrence or post radiation settings. A technology that enables fluorescent visualization of nerves, especially those buried under layers of tissue, would be of great clinical interest. Nav1.7 is a voltage-gated sodium channel found on peripheral pain-sensing neurons. Nav1.7 is also explored as a target to develop effective painkillers with no risk of addiction. (1) Taking advantage of Nav1.7 expression on neurons, we are developing an intraoperative fluorescent agent to identify nerves during surgeries. (2) To clinically translate our agent and identify potential surgeries where our agent can be utilized, we must identify the extent of expression of Nav1.7 in peripheral nerves. This study aims to determine the level of expression of Nav1.7 in peripheral nerves since thorough knowledge of Nav1.7 channels distribution is needed for future clinical translation.

Methods:
Measurements of Nav1.7 positive expression in nerves and organ tissues, such as the thyroid, lung, kidney, and muscle were collected from paraffin-embedded sections. The nerves and organs were resected from 3 female and 3 male specimens which were acquired from United Tissue Network (Phoenix, AZ). The samples were stained using anti- Nav1.7 neuromab clone N86/6, followed by immunohistochemical (IHC) detection. The slides were then viewed using Caseviewer 2.4 at 20x magnification. In each sample, 5 regions of interest (ROIs) in peripheral nerves and tissues were selected manually. Images were further analyzed with an Image J script to determine the percentage of the Nav1.7 positivity when compared to the tissue area.

Results:
Immunohistochemistry shows that the nerve bundles found in the cranial nerve are positively stained dark brown. The average percentage of Nav1.7 expression in the cranial nerve was 33.3%. ± 11.3. There is less expression in the lung and thyroid, where the thyroid was 12.3% ± 3.3 positive. A t-test comparing the nerves and organ tissue showed a significant statistical difference ($p<0.0001$). The nerves show greater expression of Nav1.7 when compared to organ tissue. Across the 6 specimens, the nerves have an average positivity of 15.6% ± 7.7, while the organ tissue expressed 3.2% ± 1.8 positive area. When comparing the nerves found in the arm/leg and torso, the nerves in the neck and torso averaged 27% ± 6.6 positive and the radial, ulnar, median, MCN, tibial, fibular, and femoral averaged 16.4% ± 2.3.

Conclusion:
The data shows that there is a significantly greater expression of Nav1.7 in the nervous system than organ tissues. Nerves found in the neck and abdomen, such as the cranial nerve, obturator, and genitofemoral appear to be great targets for intraoperative markers as these have the high average expression. Clinical application of Nav1.7 can aid in minimizing permanent nerve damage and lessen the recovery time needed from temporary nerve damage due to surgery. Nav1.7 could serve as a potential molecular target on the development of technologies for intraoperative nerve identification.

Acknowledgements: This work was supported by the NIH R01-EB029769 and the support for MSKCC cores from center grant P30CA008748 is acknowledged.

Reference
1. Minett, M., Nassar, M., Clark, A. et al. Nat Commun 3, 791 (2012).
2. Gonzales J, Demetrio de Souza Franca P, Jiang Y, Pirovano G, Kossatz S, Guru N, Yarilin D, Agwa AJ, Schroeder CI, Patel SG, Ganly I, King GF, Reiner T. Bioconjug Chem. 2019 Nov 20;30(11):2879-2888.

Poster Presentation

Disclosures: The authors have disclosed no financial interest.

392-Engineering light-activable liposomes and modulating the tumor microenvironment with photochemical and ultrasound strategies potentiates neoadjuvant chemotherapy and improves image guided surgery

Presenter: Girgis Obaid, University of Texas at Dallas

Girgis Obaid[1], Chanda Bhandari[1], Mina Guirguis[2], Ryan Margolis[3], Kenneth Hoyt[4], Tayyaba Hasan[5], Kim Samkoe[6]

[1]*University of Texas at Dallas, Richardson*
[2]*University of Texas at Dallas, Richardson, Texas*
[3]*University of Texas at Dallas*
[4]*University of Texas at Dallas, Richardson, TX*
[5]*Massachusetts General Hospital*
[6]*Dartmouth College, Hanover, NH*

Light-activable liposomes have proven to be invaluable drug delivery tools for chemotherapy, amongst other anti-cancer agents, with unparalleled spatiotemporal control over drug deposition in solid tumors. In this work, the individual membrane composition of molecular targeted light-activable liposomes was systematically modulated to provide the greatest optical and photochemical activity, drug release properties and tumor specificity (Figure 1). Using light-activable liposomes encapsulating chemotherapy, it was shown that pancreatic tumor growth is controlled by 10-fold with significantly de-escalated chemotherapy doses, and overall survival is doubled. For the first time, it was also shown that the tumor-specific delivery of NIR-labeled monoclonal antibodies is also significantly improved by 130% when the vasculature and stroma of solid head and neck tumors is modulated using a combination of sub-therapeutic photodynamic priming and low-intensity ultrasound therapy. Such tumor modulating approaches hold tremendous potential for improving the diagnostic accuracy of NIR-labeled monoclonal antibodies for image guided surgery by up to 50%. As such, a synergy between light-activable liposome engineering and tumor microenvironmental modulation strategies provide a rational framework for improving both neoadjuvant chemotherapy and image guided surgical debulking of solid tumors.

Reference
1. Guirguis, M., Bhandari, C., Li, J., Eroy, M., Prajapati, S., Margolis, R., Shrivastava, N., Hoyt, K., Hasan, T. and Obaid, G., 2021. Membrane composition is a functional determinant of NIR-activable liposomes in orthotopic head and neck cancer. Nanophotonics, 10(12), pp.3169-3185.
2. Obaid, G., Bano, S., Mallidi, S., Broekgaarden, M., Kuriakose, J., Silber, Z., Bulin, A.L., Wang, Y., Mai, Z., Jin, W., Simeone, D. and Hasan, T. 2019. Impacting pancreatic cancer therapy in heterotypic in vitro organoids and in vivo tumors with specificity-tuned,

NIR-activable photoimmunonanoconjugates: towards conquering desmoplasia?. Nano letters, 19(11), pp.7573-7587.

Poster Presentation

Disclosures: The authors have disclosed no financial interest.

393-[111In]In-CHX-A''-DTPA-αCD68 as a SPECT Agent for Non-Invasive Tracking of Macrophages In Vivo

Presenter: Samantha Katz, Yale University

Samantha Katz[1], Erika Belitzky[1], Alessandra Cavaliere[2], Supum N. Lee[3], Khashayar Rajabimoghadam[1], Michael Liu[3], Albert Sinusas[4], Harriet M. Kluger[2], Bernadette Marquez-Nostra[4]

[1]*Yale University*
[2]*Yale University, New Haven, Connecticut*
[3]*Yale School of Medicine, New Haven, CT*
[4]*Yale University, New Haven, CT*

Objectives:
Tumor-associated macrophages (TAMs) are capable of two contradictory functions: an anti-tumorigenic inflammatory function and a pro-tumorigenic immune-suppressive function. Imaging TAMs can provide understanding of macrophage infiltration and immune response to immunotherapies that modulate macrophage function. Tracking these immune cells non-invasively through SPECT imaging can help monitor individual tumor responses to these immunotherapies, thus potentially saving non-responders the burden of ineffective treatment. CD68 is the clinical biomarker for macrophages and is also present in murine macrophages. Here, we validated CD68 as a SPECT imaging biomarker for murine macrophages by radiolabeling anti-mouse CD68 with In-111, we can track $CD68^+$ macrophages in vivo using SPECT imaging.

Methods:
CD68 expression in murine bone marrow-derived macrophages was validated using immunofluorescence staining. ^{111}In-acd68-IgG was prepared via conjugation of CHX-A''-DTPA to the acd68-IgG followed by radiolabeling with ^{111}In to obtain [^{111}In]In-CHX-A"-DTPA-aCD68. Various in vitro studies were performed including stability, binding affinity, and effect on viability of bone marrow-derived macrophages. Finally, SPECT/CT imaging and biodistribution studies were performed in RENCA tumor models. The SPECT/CT scans were viewed in ITK-Snap. Regions of interest (ROI)s included the heart, tumor, liver, and spleen to determine the mean intensity of uptake. Heart was used as the reference tissue to calculate tumor- or organ-to-heart ratios.

Results:
Radiochemical yield was greater than or equal to 95%. A stability study showed70% or greater intact [111In]In-CHX-A''-DTPA-αCD68 in mouse serum or PBS up to 24 hours post radiolabeling. Binding affinity was determined to have a dissociation constant (KD) of 7.99 ±2.26 nM, and the EC50 ratio for αCD68-DTPA to αCD68 was 1.33. αCD68-DTPA did not affect the viability of macrophages. Biodistribution studies in non-tumor bearing mice showed that the highest uptake in the macrophage-rich spleen was2.00±0.48% ID/organ at 24 hours post injection. In contrast, the uptake of the isotype control(0.44±0.094% ID/organ) at this time point was significantly lower (P = 0.028). Mean intensity of the tumor, 0.0035, and heart, 0.0016, were calculated from analysis of SPECT imaging. The mean tumor to heart intensity ratio is 2.19.

Conclusion:
[111In]In-CHX-A''-DTPA-αCD68 has high stability, binds with high affinity, and binds specifically to CD68. Additionally, [111In]In-CHX-A''-DTPA-αCD68 does not deplete macrophages in vitro.

Reference
1. AnfrayC, UmmarinoA, AndónFT, AllavenaP. Current Strategies to Target Tumor-Associated-Macrophages to Improve Anti-Tumor Immune Responses.Cells. 2020; 9(1):46. https://doi.org/10.3390/cells90100462.
2. Chistiakov, D., Killingsworth, M., Myasoedova, V.et al.CD68/macrosialin: not just a histochemical marker.Lab Invest97,4–13 (2017). https://doi.org/10.1038/labinvest.2016.1163.
3. Perry CJ, Muñoz-Rojas AR, MeethKM, et al. Myeloid-targeted immunotherapies act in synergy to induce inflammation and antitumor immunity.J Exp Med. 2018;215(3):877-893. doi:10.1084/jem.20171435

Poster Presentation

Disclosures: The authors have disclosed no financial interest.

394-Whole body biodistribution and myocardial kinetics of the ketone PET radiotracer 3-[11C]-OHB: A pilot study in domestic pigs

Presenter: Mie Ringgaard Dollerup, Aarhus University Hospital

Mie Ringgaard Dollerup[1], Erik Nguyen Nielsen[2], Mette O. Simonsen[3], Thien Vinh Luong[2], Mikkel Vendelbo[2], Lise Falborg[2], Lars Christian Gormsen[2], Aage Kristian O. Alstrup[4]

[1]*Aarhus University Hospital, Aarhus, Denmark*
[2]*Aarhus University Hospital, Aarhus N, Denmark, Denmark*
[3]*PET-centret, Århus C, Danmark, Denmark*
[4]*Aarhus University Hospital, Aarhus N, Denmark*

Background:
Ketone bodies are increasingly recognized as a quantitatively important source of energy for the brain and heart during times of stress such as long-term fasting, strenuous exercise or heart failure. In the brain, the relationship between circulating ketone bodies and cerebral uptake and subsequent metabolism is roughly linear. However, it is still largely unknown to what extent the heart takes up ketone bodies at various levels of ketonemia and whether ketone bodies are readily oxidized. We therefore performed a series of porcine studies using the previously developed PET radiotracer 3-[^{11}C]OHB to study ketone body metabolism. We specifically aimed to investigate: 1) whether only the endogenously found enantiomer D-3-[^{11}C]OHB is taken up by the heart or whether the L-3-[^{11}C]OHB enantiomer is also metabolized, 2) whole body biodistribution and myocardial D-3-[^{11}C]OHB kinetics, and 3) appearance of the quantitatively most important metabolite [^{11}C]CO_2.

Materials and Methods:
Five female Danish Landrace x Yorkshire crossbred pigs (38-41kg) were studied under various conditions, while under propofol anaesthesia in a non-recovery setup. 1) Using the D- and L- enantiomer of 3-[^{11}C]OHB, 2) Under conditions of low and elevated (~ 3mM) ketone bodies, and 3) compared to the biodistribution of ^{11}C-acetate (dose

483 MBq). All PET scans were obtained using a Siemens Biograph Vision PET/CT system. Pigs were administered 76-410 MBq (median 235 MBq) 3-[^{11}C]OHB and two different image acquisition protocols were subsequently employed: 1) Dynamic imaging of the myocardium for 60 minutes, and 2): D-Whole-body imaging of the entire pig using the built-in feature in the Siemens system (16-20 passes over approximately 70-90minutes). Time-activity curves of 3-[^{11}C]OHB in tissues and organs were drawn using PMOD v4.1 and femoral arterial samples were in a subset of animals drawn to measure blood and plasma activity. Tissue 3-[^{11}C]OHB kinetics were analyzed using a simple 1-tissue compartment model assuming rapid conversion of 3-[^{11}C]OHB to [^{11}C]CO_2. Circulating [^{11}C]CO_2 as a fraction of total blood ^{11}C-activity was estimated by purging [^{11}C]CO_2 from an acidified blood sample under stirring as described previously [1]. Radioactivity in the blood samples were measured with a Hidex Automatic Gamma Counter.

Results:
We observed a significant rapid uptake and subsequent decrease of myocardial ^{11}C-activity after D-3-[^{11}C]OHB administration. Administration of the L-3-[^{11}C]OHB enantiomer resulted in a significantly attenuated myocardial uptake. K1 and k2-values (indicating uptake) after D-3-[^{11}C]OHB administration were comparable in the myocardium regardless of the level of circulating ketone bodies indicating non-saturable ketone kinetics in the heart. In the liver, ^{11}C-activity increased rapidly after D-3-[^{11}C]OHB administration and subsequently decreased slowly for the remaining study, but this was markedly attenuated under conditions of hyperketonemia. Circulating [^{11}C]CO_2 reached 40% of total ^{11}C-acitivity in the blood after 20 minutes and remained constant throughout the duration of the studies. Of interest, ^{11}C-activity increased rapidly in the proximal parts of the duodenum and the distal part of the gastric ventricle 20 minutes after injection of D-3-[^{11}C]OHB possibly indicating appearance of the metabolite [^{11}C]HCO_3^-. This was also observed after injection of ^{11}C-acetate.

Conclusion:
D-3-[^{11}C]OHB is readily taken up by the heart under both conditions of low and elevated ketones further underscoring the notion that ketone bodies act as an important myocardial oxidative substrate. D-3-[^{11}C]OHB undergoes rapid conversion into $^{11}CO_2$, which constitutes a significant fraction of blood radioactivity as soon as 20 minutes after injection necessitating metabolite corrections in kinetic studies. Finally, D-3-[^{11}C]OHB appears to also undergo conversion to [^{11}C]HCO_3^- in the duodenum, resulting in a backflux appearance of the ^{11}C-isotope in the gastric ventricle.

Reference

1. Christensen NL, Jakobsen S, Schacht AC, Munk OL, Alstrup AKO, Tolbod LP, Harms HJ, Nielsen S, Gormsen LC. Whole-Body Biodistribution, Dosimetry, and Metabolite Correction of [11C]Palmitate: A PET Tracer for Imaging of Fatty Acid Metabolism. Mol Imaging. 2017 Jan-Dec;16:1536012117734485. doi: 10.1177/1536012117734485. PMID: 29073808; PMCID: PMC5665104.

Poster Presentation

Disclosures: The authors have disclosed no financial interest.

395-Non-radioactive and sensitive tracking of neutrophils to bone marrow and sites of inflammation using Magnetic Particle Imaging

Presenter: Renesmee Kuo,University of California, Berkeley

Renesmee Kuo[1], K. L. Barry Fung[2], Prashant Chandrasekharan[3], Caylin Colson[2], Quincy Huynh[4], Chinmoy Saayujya[3], Irati Rodrigo Arrizabalaga[5], Mariam Yousuf[3], Steven Conolly[2]

[1]University of California, Berkeley
[2]University of California, Berkeley, Berkeley, CA
[3]University of California, Berkeley, Berkeley
[4]University of California, Berkeley, Union City, CA
[5]University of California, Berkeley, Berkeley, California

Introduction:
The reticuloendothelial system (RES) plays an integral role in the immune system, and it governs the clearance of nanoparticles from circulation. The primary organs associated with the RES include the liver, spleen and bone marrow. Bone marrow is also where new blood cells (e.g., RBCs, WBCs and platelets) originate and get cleared after circulating in the blood for 7 hours (WBCs) to 120 days (RBCs) as illustrated in Fig. 1a. Hence, quantitative imaging of the bone marrow function could benefit immunotherapy, help monitor bone marrow replacement stem cell therapies and evaluate autoimmune disorders. Bone marrow diseases and disorders are most commonly diagnosed via an aspiration or a biopsy, which can be invasive and painful. Imaging techniques like In111 WBC scintigraphy help doctors visualize bone marrow dysfunction noninvasively [1,2], but both involve radiation and lack persistence. Beyond the radiation dose to the patient, there is also a serious concern about the much higher radiation dose to the WBCs themselves. The 70-kg patient's radiation dose during a Tc99m or In111 WBC scan is initially administered to a tiny (~70 mg) mass of WBCs prior to autologous reinjection. This 1-million-fold high radiation dose to WBCs can kill WBCs, adversely affecting targeting efficacy and specificity [3]. CAR-T and CAR-NK cells often cannot survive this radiation dose [4,5].
Magnetic particle imaging (MPI) [6-11] is a new tracer scanning technique that matches the sensitivity, contrast and resolution of Nuclear Medicine but with zero radiation. Here we aim to complement WBC-In111 tracking of WBCs to bone marrow to provide bone marrow function studies with zero radiation damage to patients and zero radiation to the WBCs. MPI uses safe superparamagnetic iron oxide (SPIO) tracers to track cells, and SPIOs do not damage cell viability or functionality (Fig. 1b) [9-14]. Hence, MPI could soon safely and effectively image bone marrow function with none of the pitfalls of scintigraphy or SPECT.

Materials and Methods:
Anti-Ly6G-antibody-conjugated SPIOs (Ab-SPIOs) (IgG1, REA526 clone, Miltenyi Biotec, GmBH) were purified using dialysis prior to in vivo usage. The biodistribution of tracers were imaged with a 6.3T/m field free line (FFL) MPI scanner (projection FOV 10.6 x 6.2 cm, t = 95 s/projection) (Fig. 1c). The scanning bed was mechanically translated in the z-direction in 1 mm increments to complete the imaging trajectory for a single projection. 3D tomography images were acquired post-euthanasia. Forty 2D projection images were acquired at equally spaced angles and reconstructed using a Filtered Back projection method [15]. The images were compared with an X-ray image of the mouse [16]. 10mT/6T/m = roughly 1.4 mm resolution.

Results and Discussion:
Tracers of ferucarbotran (VivoTraxTM) are rapidly taken up in the liver and spleen. Ab-SPIOs, however, bind to neutrophils expressing the corresponding surface antigen. Twenty-four hours post-intravenous (IV) injection of Ab-SPIOs, maximum intensity projection (MIP) MPI images (Fig. 1d-f) showed signal enhancement in bone marrow of the skull, vertebral column, the lower pelvic bones and other RES organs. These results are similar to anti-NCA95-antibody scintigraphy tracers that are traditionally used for neutrophil tracking [17]. Further, MPI

was able to track in situ labeled neutrophils to sites of lipopolysaccharide (LPS)-induced myositis in the right flank of the mouse with high contrast (CNR = 8-13) compared to the contralateral side (figure 1e-f).

Conclusion:
The in vivo Ab-SPIOs targeting of leukocytes highlight MPI's potential to image the immune system. MPI could soon safely and effectively address the pitfalls of scintigraphy. Immunotherapy-MPI could help doctors and researchers diagnose bone marrow disorders and diseases, monitor the success of immunotherapy and screen for early-stage cancers, all without ionizing radiation and with infinite persistence.

Reference

1. Palestro et al., RadioGraphics, 2006;
2. Storey and Arbini, J Magn Reson Imaging, 2014;
3. Chisholm et al., J Nucl Med, 1979;
4. Goodwin, Journal of Nuclear Medicine, 1978;
5. Segal et al. Journal of Nuclear Medicine, 1978;
6. Gleich, B., Weizenecker, Nature 435, 1214–1217 (2005)
7. Yu EY, et al., Nano Letters. 2017;17(3):1648-54
8. Yu EY, et al., ACS Nano. 2017;11(12):12067-76.
9. Chandrasekharan et al., Nanotheranostics, 2021;
10. R Kuo, et al., International Journal on Magnetic Particle Imaging, 2022
11. JJ Gevaert et al., Molecular Imaging and Biology, 2022.
12. Rivera-Rodriguez A et al., Nanotheranostics 2021; 5(4):431-444.
13. Chandrasekharan et al., Theranostics, 2020;
14. Chandrasekharan et al., Br J Radiol, 2018;
15. Konkle et al. Biomedizinische Technik/Biomedical Engineering 2013;
16. Dogdas et al., Phys Med Biol, 2007; [17] Agool et al, Eur J Nucl Med Mol Imaging, 2011.

Poster Presentation

Disclosures: The authors have disclosed no financial interest.

396-ImmunoPET antiGD2 mAb as theranostic agent in B78 melanoma murine model to calculate prescribed absorbed dose of therapeutic radioisotope-mAb.

Presenter: Cynthia Choi, University of Wisconsin Madison

Cynthia Choi[1], David Coleman[2], Zachary Rosenkrans[2], Christopher Massey[2], Caroline Kerr[2], Eduardo Aluicio-Sarduy[2], Carolina de Aguiar Ferreira, Joseph Grudzinski[3], Bryan Bednarz[2], Jonathan W. Engle[2], Zachary Morris[2], Reinier Hernandez[4], Jamey Weichert[5]

[1]*University of Wisconsin Madison, Madison, WI*
[2]*University of Wisconsin-Madison, Madison, Wisconsin*
[3]*University of Wisconsin-Madison*
[4]*University of Wisconsin-Madison, Madison, WI*
[5]*University of Wisconsin-Madison, Madison, WI*

Objective:
Disialoganglioside GD2 is a tumor-associated glycolipid overexpressed in neuroblastomas and melanomas, making it a desirable target for cancer therapy. In this study, anti-GD2 monoclonal antibody dinutuximab (ch14.18, Unituxin®), a clinically approved for immunotherapy in high-risk pediatric neuroblastoma, was radiolabeled to obtain clear immune-positron emission tomography (immunoPET) image of the ^{89}Zr-dinutuximab in syngeneic B78 melanoma mouse model. Through the PET/CT images, radiation dose deposited in tumors vs normal tissue was calculated per unit of injected activity, enabling us to determine the dosage that will limit toxicity and maximize treatment efficacy when the mAb is radiolabeled with therapeutic radioisotope, Yttrium-90 as targeted radionuclide therapy (TRT).

Materials and Methods:
Dinutuximab was radiolabeled with ^{89}Zr ($t_{1/2}$ = 78.41 hr) via conjugation with bifunctional chelator desferrioxamine (DFO). B6 mice were implanted subcutaneously with syngeneic B78 cells, the GD2+ melanoma cancer cell line derived from B16 melanoma cells. Serial PET/CT scans were carried out at 4-, 24-, 71-, and 170-hours post IV injection of ~12 MBq of ^{89}Zr-dinutuximab. In vivo dosimetry was performed using the Monte Carlo-based RAPID platform to calculate the prescribed absorbed dose estimates for ^{90}Y-dinutuximab for B78 tumor.

Results:
^{89}Zr was chosen as the imaging radioisotope due to its positron emission properties and longer half-life that matches the circulation half-life of mAbs. The uptake in tumor started from average concentration of 6.5%ID/g at 4 hours, then peaked at 71 hours with 12%ID/g, and finally decreased to 8.5%ID/g at 170 hours, which was validated through ex vivo gamma counts to be 7.75%ID/g. The normal tissues showed uptake of <11%ID/g which steadily decreased to <5%ID/g at 170 hours except for liver, which was ~6%ID/g. Blood showed the greatest clearance from 17%ID/g at 4 hours which decreased to <2%ID/g at 170 hours and muscle stayed consistently <2.5%ID/g. RAPID platform calculation predicted that to achieve 4 Gy of ^{90}Y-dinutuximab, a therapeutic radioisotope radiolabeled to the same mAb, between 1.55 MBq and 1.15MBq ^{90}Y-dinutuximab should be administered to tumor sized between 50mm^3 and 150mm^3, respectively, in the same B78 murine model.

Conclusions:
The high tumor specificity of ^{89}Zr-dinutuximab shows superior uptake and retention in the tumor vs normal tissue. Calculations of predicted activity necessary to achieve prescribed doses will be utilized for TRT using ^{90}Y-dinutuximab that will limit toxicity and maximize treatment effect. This direct calculation from imaging result to treatment dose can be used in clinical settings to conduct highly accurate and effective image-guided therapy.

Poster Presentation

Disclosures: The authors have disclosed no financial interest.

397-Design and Development of 18F-Labeled Peptides Using Perfluoroaryls for PET Imaging

Presenter: Iman Daryaei, TheraCea Pharma

Iman Daryaei[1], Edmund Marinelli[1], Pavel Safar[2], Chris Nabong[1], Julian Dresler[1]

[1]*TheraCea Pharma, Tucson, AZ*
[2]*TheraCea Pharma*

Introduction:
The half-life of the radionuclide ^{18}F is 109 minutes, long enough to allow incorporation into many molecular species by a wide variety of techniques, yet short enough such that in less than 24 hours there is no need for special collection or cleanup protocols. Other advantages include: a) the 97% positron emission yield, b) the low energy of the

emitted positrons, and, c) the lack of interfering radiations; this results in high-resolution images. In addition, the capability to produce ^{18}F using low energy medical cyclotrons and the large availability of PET scanners calibrated for using ^{18}F make it the most popular nucleus for PET imaging; almost half of all PET radiotracer molecules are based on ^{18}F.[1-3] Traditionally, ^{18}F species from cyclotrons are reacted with other reagents to produce ^{18}F-bearing prosthetic groups that can be used for further chemistry development. The prosthetic groups are then reacted with the target molecule to prepare the ^{18}F radiotracer. This indirect ^{18}F-labeling is a relatively long procedure entailing multiple synthesis and purification steps often with harsh reaction conditions, rendering this approach unsuitable for biologics. Perfluoroaryl (PFAr) compounds are highly reactive electrophiles and useful building blocks for organic synthesis. The reactivity of PFArs is tunable due to substituent effects of other groups on the heavily fluorinated aromatic ring(s), the number and type of the aromatic rings, and the number of fluorine atoms on the rings in the structure. [4-6] PFARs are suitable chemical moieties for ^{18}F-labeling through $^{18/19}$F exchange chemistry.[7] The team applied ^{18}F-labeling via PFAr on HER2 (A9 and LTV), Octreotide, PSMA, duramycin, E-Selectin (DK-12), Fibrin Binding Peptide (FBP), and Granzyme B peptides.

Methods:
A9, LTV, Octreotide, PSMA, and Granzyme B peptides were synthesized by solid phase peptide synthesis using Fmoc-based chemistry. A library of PFArs with different reactivities was used for arylation (Scheme 1). Chemical modification with PFArs was performed while the the peptides were still on the resin. PFArs were conjugated to specific amino acids by site-selective deprotection of the amino acids (Scheme 2). Commercially available Duramycin, DK-12, and FBP peptides were purchased and used for modification with PFAr. ^{18}F-labeling was performed using Na^{18}F salt (5-10 mCi) received from a commercial cyclotron, in aqueous solution (with organic co-solvent) at 30-40°C in 15-120 min. $K_{2.2.2}$ was also added to some of the reactions to increase the yield. C-18 cartridges were utilized to purify the final products by separating the ^{18}F-labeled products from $^{18/19}$F salts and other impurities.

Results:
Modified peptides were successfully synthesized, purified by HPLC, and characterized by LC/MS and MS. ^{18}F-labeling was monitored using a HPLC system equipped with a radioactive counter detector. The chemical modification and PFAr labeling strategy allowed ^{18}F-labeling of the peptides with radiochemical yield of 10-45% (decay corrected) after purification of the ^{18}F-labeled products.

Conclusion:
^{18}F-labeling using this class of heavily fluorinated aromatic rings offers several advantages: 1- Simple purification as only the remaining ^{18}/^{19}F salt will need to be separated, 2- Facile labeling procedures, 3- Cold precursors (with ^{19}F) will have exactly the same biological properties as the ^{18}F-labeled product, and 4- The product can be prepared using kits with high geographical accessibility.

Reference

1. Alauddin MM. Positron emission tomography (PET) imaging with 18F-based radiotracers. Am. J. Nucl. Med. Mol. Imaging, 2012, 2(1), 55-76.
2. Jacobson O and Chen X. PET designated flouride-18 production and chemistry. Curr Top Med Chem., 2010, 10(11), 1048-1059.
3. Krishnan HS, Ma L, Vasdev N, Liang SH. 18F-Labeling of sensitive biomolecules for positron emission tomography. Chem. Eur. J., 2017, 23, 15553-15577.
4. Makosza M, Wojciechowski K. Nucleophilic substitution of hydrogen in heterocyclic chemistry. Chem. Rev., 2004, 104, 2631-2666.
5. Zhang C, Vinogradova EV, Spokoyny AM, Buchwald SL, and Pentelute BL. Arylation Chemistry for Bioconjugation. Angew. Chem. Int. Ed. 2019, 58, 4810– 4839
6. Brittain,WDG, Coxon CR. Perfluoroaryl and Perfluoroheteroaryl Reagents as Emerging New Tools for Peptide Synthesis, Modification and Bioconjugation. Chem. Eur. J. 2021, 27, 1–15
7. Jacobson O, Yan X, Ma Y, Niu G, Kiesewetter DO, Chen X. Novel method for radiolabeling and dimerizing thiolated peptides using 18F-hexafluorobenzene. Bioconjugate Chem., 2015, 26, 2016-2020.

Poster Presentation

Disclosures: The authors have disclosed no financial interest.

398-Brownian superparamagnetic Iron Oxide nanoparticles enable viscosity and binding contrast in Magnetic Particle Imaging

Presenter: Chinmoy Saayujya, University of California, Berkeley

Chinmoy Saayujya[1], Kim Hwang Yeo[2], Quincy Huynh[3], Irati Rodrigo Arrizabalaga[4], Benjamin Fellows[4], Prashant Chandrasekharan[1], Steven Conolly[5]

[1]University of California, Berkeley, Berkeley
[2]UC Berkeley
[3]University of California, Berkeley, Union City, CA
[4]University of California, Berkeley, Berkeley, California
[5]University of California, Berkeley, Berkeley, CA

Abstract Body:
Magnetic Particle Imaging (MPI) is an emerging positive-contrast imaging modality that directly images superparamagnetic iron oxide (SPIO) tracers in the body [1]. The physical and magnetic properties of the MPI tracers govern spatial resolution, sensitivity and contrast. MPI is being evaluated as a nonradioactive complement to Nuclear Medicine. Current MPI applications include Cancer, Stroke, Cell Tracking, WBC-MPI, Pulmonary Embolism Imaging and GI bleeds [2–5]. Here we aim to include a new MPI contrast mechanism: binding and viscosity contrast. Viscosity changes have been measured with cell death and so viscosity contrast could permit an imaging method that assesses therapeutic cell viability [6]. This could be very useful to debug stem cell or CAR-T cell therapies. There currently are no standard *in vivo* biomedical imaging methods that can distinguish bound from unbound tracers or that can assess the viability of therapeutic cells.

How can MPI Sense Binding or Viscosity?
Every SPIO tracer rotates precisely 180 degrees during the MPI scanning process. This rotation occurs via two parallel relaxation mechanisms: Brownian (rotation of the physical SPIO and its shell to align with the field) and Néel (re-alignment of only the SPIO magnetic domain without any physical rotation) [7]. The Brownian rotation time scales linearly with the media's nanoscale viscosity and is thereby sensitive to binding or any mechanical rotation impediment like freezing. Néel relaxation senses neither viscosity nor binding. Here, we experimentally demonstrate that Brownian SPIO relaxation times can measure viscosity.

Objective:
Square wave relaxometry was performed on three commercial SPIO nanoparticles to determine their relaxation time constant versus the

viscosity of the medium [8, 9]. The viscosity of the SPIO solvent (a glycerol-water mixture) was varied by changing the temperature. The measurements were compared to Brownian and Néel relaxation theory. The relationship between relaxation time constant and viscosity was used to determine the dominant mechanism of relaxation and the ability of the SPIO to generate viscosity-based contrast.

Methods:
Aliquots of commercial SPIOs (Micromod Partikeltechnologie GmbH Synomag-D, nanoComposix NanoXact, and Magnetic Insight VivoTrax) are combined with glycerol in a 55-45 ratio (by weight) to yield a viscous tracer solution. The temperature of the solution is varied, using a heating mantle, between 20ºC and 65ºC to generate a viscosity-temperature calibration curve. Viscosity measurements are made using an Ubbelohde type viscometer. Relaxation time constants are obtained by subjecting 40μL of the SPIO-glycerol mixture to a periodic square-wave pulsed magnetic field of amplitude 10mT in an Arbitrary Waveform Relaxometer [8]. The gradiometric receive signal is integrated and fit to a rising exponential function to determine the relaxation time constant. The sample under test is first heated to a set temperature (65ºC) and subsequently cooled under ambient conditions to obtain time-series data of relaxation time constants and temperature. Relaxation time constants are thereby obtained as an indirect function of viscosity.

Results:
We observe distinct mechanisms of relaxation for the two commercial tracers. Synomag-D shows no observable change in relaxation time with viscosity and so its observed behavior matches a Néel SPIO. NanoXact relaxation time varies linearly with viscosity precisely as predicted by Brownian theory. VivoTrax relaxes in a Brownian manner up to a viscosity of 3.0 cP, after which the Néel relaxation mechanism dominates as the faster relaxation mechanism.

Conclusion:
We have successfully demonstrated that MPI can observe both Brownian and Néel relaxation behavior with commercial tracers. We also showed that Brownian SPIOs can measure the viscosity of the tracer medium. This proof of concept experiment paves the way for SPIOs to image binding contrast in MPI scans. This novel contrast mechanism could also be exploited to measure local viscosity, which may predict *in vivo* therapeutic cell viability.

Reference

1. Gleich, Bernhard, and Jürgen Weizenecker. "Tomographic imaging using the nonlinear response of magnetic particles." Nature 435.7046 (2005): 1214-1217.
2. Zhou, Xinyi, et al. "White Blood Cell Tracking with Magnetic Particle Imaging." IWMPI (2019).
3. Zheng, Bo, et al. "Quantitative magnetic particle imaging monitors the transplantation, biodistribution, and clearance of stem cells in vivo." Theranostics 6.3 (2016): 291.(2018): 131-138.
4. Yu, Elaine Y., et al. "Magnetic particle imaging for highly sensitive, quantitative, and safe in vivo gut bleed detection in a murine model." ACS nano 11.12 (2017): 12067-12076.
5. Zhou, Xinyi Y., et al. "First in vivo magnetic particle imaging of lung perfusion in rats." Physics in Medicine & Biology 62.9 (2017): 3510.
6. Dyson, J. E. D., et al. "Kinetic and physical studies of cell death induced by chemotherapeutic agents or hyperthermia." Cell Proliferation 19.3 (1986): 311-324.
7. W. T. Coffey, Y. P. Kalmykov, and J. T. Waldron, The Langevin Equation, 2nd ed. (World Scientific, Singapore, 2004).
8. Tay, Zhi Wei, et al. "A high-throughput, arbitrary-waveform, MPI spectrometer and relaxometer for comprehensive magnetic particle optimization and characterization." Scientific reports 6.1 (2016): 1-12.
9. Tay, Zhi Wei, et al. "Pulsed excitation in magnetic particle imaging." IEEE transactions on medical imaging 38.10 (2019): 2389-2399.

Poster Presentation

Disclosures: The authors have disclosed no financial interest.

399-Evaluating the efficacy of PARPi-FL in detecting patient cervical lesions.

Presenter: Paula Demetrio de Souza Franca, Memorial Sloan Kettering Cancer Center

Paula Demetrio de Souza Franca[1], Dauren Adilbay[2], Sheryl Roberts[3], Tara D. Viray[4], Kieran Evans[5], Marcio Abrahao[6], Snehal G. Patel[5], Kay Park, Jason Lewis[2], Elizabeth Jewell[5], NagaVaraKishore Pillarsetty[2]

[1]*Memorial Sloan Kettering Cancer Center, New York*
[2]*Memorial Sloan Kettering Cancer Center, New York, NY*
[3]*Wayne State University School of Medicine, Detroit, MI*
[4]*Memorial Sloan Kettering Cancer Center, North Brunswick, NJ*
[5]*Memorial Sloan Kettering Cancer Center, New York, New York*
[6]*Escola Paulista de Medicina - Federal University of Sao Paulo, Sao Paulo, Sao Paulo, Brazil*

Introduction:
Despite the increase in human papillomavirus (HPV) vaccination and screening efforts, in 2022, over 14,000 women will be diagnosed with cervical cancer in the USA (1). The agents currently used to delineate cervical lesions during screening procedures (such as acetic acid and/or Lugol's iodine) lack specificity and it can lead to unnecessary cervical excisions. Here we describe the use of a fluorescence-based functional molecular imaging probe PARPi-FL that targets PARP1, a nuclear enzyme overexpressed in cancer and dysplasia (2). We evaluate its use as an optical imaging agent to delineate cervical lesions.

Methods:
To evaluate PARP1 expression's ability to stratify different grades of Cervical Intraepithelial Neoplasia (CIN), immunohistochemistry was performed on 31 banked patient samples. The CIN grade is defined by the amount of immature squamous cell proliferation involving the mucosal thickness, *CIN 1* - involving lower one-third of the thickness (n = 8), *CIN 2* - one-third to two-thirds (n= 5), *CIN 3* - more than two-thirds *(n = 6),* and cancer - trespassing the mucosal basal layer (n= 12). To explore the ability of PARPi-FL to delineate amongst them, 10 patients scheduled to undergo surgical resection (either a cone or a hysterectomy), were accrued. Resected specimens were submerged in a solution of 1,000 nM PARPi-FL in 30% PEG/PBS for 5 minutes followed by a washing step (30% PEG/PBS) for 5 minutes. The median age was 36.5 years old (range 29-63), and 90% were HPV positive. Sixty percent harbored invasive cancer (4 adenocarcinomas and 2 squamous cell carcinomas) and 30% dysplasia (2 CIN 3 and 1 CIN 1). One patient had a lesion completely resected on a previous biopsy. For microscopic investigation, images were acquired using a handheld confocal microscope (FIVE2 Optiscan, Australia) (2). A fluorescence camera (Quest Medical Imaging, Netherlands) was used for macroscopic assessment (3) and the results were correlated with histology.

Results:
Using immunohistochemistry in banked tissue, we observed that PARP1 expression correlated with the different grades of cervical dysplasia. To test if PARPi-FL could be used to access cervical lesions prospectively, a total of 10 women were imaged in the operating room. Confocal microscopy detected the fluorescent signal arising from one layer of cells (the XY-plane), which was ideal for imaging a cellular layer and to confirm PARPi-FL specificity. A fluorescence camera, which allowed verification of fluorescence arising from the bulk of the tissue rather than a monolayer, revealed marked signal increase in tumor (both SCC and adenocarcinoma) and CIN 3 when compared to the normal surrounding tissue. No significant difference in fluorescence signal was observed in CIN 1 and normal tissue. None of the imaged patients harbored CIN 2.

Conclusion:
We demonstrated that fluorescence imaging post topical application of PARPi-FL on the cervix can identify CIN 3 and invasive carcinomas. This molecularly-targeted probe has the potential to serve as a novel diagnostic tool for lesion stratification in cervical cancer screening and serve as a tool for the *in-vivo* assessment of surgical margins, ensuring complete excision of malignant lesions.

Reference

1. Siegel RL, Miller KD, Fuchs HE, Jemal A. Cancer statistics, 2022. CA: a cancer journal for clinicians. 2022;72(1):7-33.
2. Demetrio de Souza Franca P, Guru N, Kostolansky AR, Mauguen A, Pirovano G, Kossatz S, et al. Poly(ADP-ribose)polymerase1: A potential molecular marker to identify cancer during colposcopy procedures. Journal of nuclear medicine: official publication, Society of Nuclear Medicine. 2020.
3. Demétrio de Souza França P, Kossatz S, Brand C, Karassawa Zanoni D, Roberts S, Guru N, et al. A phase I study of a PARP1-targeted topical fluorophore for the detection of oral cancer. European journal of nuclear medicine and molecular imaging. 2021.

Poster Presentation

Disclosures: The authors have disclosed no financial interest.

400-MRSI with co-polarized HP [1-13C]pyruvate and [1-13C] dehydroascorbate reveals differences in brain tumor metabolism in orthotopic mouse models treated with radiation

Presenter: Elizabeth Coffee, Memorial Sloan Kettering Cancer Center

Elizabeth Coffee[1], Nathaniel Kim[2], Marjan Berishaj[1], Paola Porcari[1], Saket Patel[3], Kofi Deh[1], Kayvan Keshari[1]

[1]Memorial Sloan Kettering Cancer Center, New York, NY
[2]Memorial Sloan Kettering Cancer Center, New York
[3]Memorial Sloan Kettering Cancer Center

Introduction:
Noninvasive measurements of tumor metabolism represent an ideal biomarker in the field of neuro-oncology, where an early measurement of response to treatment remains elusive. In this study, we investigated whether co-hyperpolarized [1-^{13}C]pyruvate and [1-^{13}C] dehydroascorbate (DHA) along with Magnetic Resonance Spectroscopic Imaging (MRSI)[1-4] might be a useful method to evaluate differences in brain tumor metabolism in mouse brain. The goal of this study was to evaluate feasibility and to assess for potential metabolic differences between tumors and contralateral brain in both treated and untreated mice.

Methods:
Female athymic Foxn1nu mice (Envigo) aged 7 weeks (n=8, 22-25g) were studied. Animal procedures were performed in accordance with institutional animal care guidelines. Mice underwent stereotactic injection with $3x10^5$ U87 glioblastoma cells in 2ul, 2mm lateral to midline along the bregma, 3mm deep. After 14 days, n=4 mice underwent whole brain radiation with 10Gy. Imaging took place at day 21 +/-3 days for both groups. Each mouse was injected via tail vein over 10s with 225-350μL of co-hyperpolarized 40 mM [1-^{13}C]DHA and 100 mM [1-^{13}C]pyruvate. Both substrates were co-hyperpolarized for two hours (150μL of a 40:60 v/v mixture of monomeric [1-^{13}C]DHA and [1-^{13}C]pyruvate containing 15 mM AH111501 trityl radical) through the SpinLab polarizer (GE) and dissolved in D_2O. MR experiments were performed using a 3T MRI system (Bruker) equipped with a quadrature double-tuned ^{1}H/^{13}C volume coil. The MRI protocol included a T2-weighted fast spin-echo (FSE) sequence for anatomical reference and ^{13}C Chemical Shift Imaging (CSI) sequence (32x32mm^2 field-of-view, 8 slices, 2mm thickness) run 20s after substrate injection. Spectroscopic data were analyzed using a custom Matlab script while metabolic maps were calculated using SIVIC[5]. Statistical analysis was performed using GraphPad Prism (v9.1.1). Normalization for polarization, injected volume and concentration were performed and means were compared using a two-tailed t-test.

Results:
Figure 1 shows the coronal (**A**) view of a mouse brain with the corresponding spectra acquired in each voxel of the brain. **Figure 1B** shows a representative spectrum from a voxel of the overlayed spectrum on the brain showing the metabolites of interest. **Figure 2** demonstrates the overlay of representative metabolite maps, pyruvate (**A**) lactate (**B**), DHA (**C**) and Vitamin C (**D**), with the white dashed circle representing tumor location (obstructed by overlay). Here, the differential lactate and vitamin C generation within the tumors can be appreciated. **Figure 3** compares the normalized means of the concentrations of metabolites (uM). The difference between radiated tumor and the contralateral brain **(A)** reaches significance for lactate (246.4uM±57.03, p=0.02) and vitamin C (47.85uM±13.7, p=0.03). In mice that were not treated with radiation **(B),** this relationship is preserved but did not reach significance. Both radiated tumors **(C)** and radiated brain **(D)** produced lower amounts of all metabolites when compared to untreated counterparts. Differences reached significance in DHA (-665.8uM±144.8, p=0.01) and Vit C (-379uM±110, p=0.04) between tumors **(3C)** and in all metabolites between contralateral brains **(3D)**: pyruvate (-1983uM±757.8, p=0.03), lactate (-802.7uM±212.6, p=0.003), DHA (-745.7uM±160.5, p=0.003), and vitamin C (-270.1uM±72.2, p=0.009).

Conclusion:
These findings further demonstrate the feasibility and sensitivity of this novel technique to examine the metabolism of mouse models of brain tumors. While differences in metabolism were not seen between untreated U87 brain tumors and contralateral brain, a significant decrement in lactate and vitamin C was seen in tumors that were radiated. Further, radiation decreased all metabolite production in both tumors and contralateral brain, suggesting a significant reduction in the global metabolism seen after radiation. This may be secondary to blood-brain-barrier disruption. These data are the starting point for further exploration of tumor metabolism in glioblastoma with potential for revealing an early response to treatment as a noninvasive biomarker.

Reference

1. Keshari, K. R., Kurhanewicz, J., Bok, R., Larson, P. E. Z., Vigneron, D. B., Wilson, D. M. (2011). Hyperpolarized 13C dehydroascorbate as an endogenous redox sensor for in vivo metabolic imaging. PNAS, 150(46), 18606-18611.
2. Bohndiek, S. E., Kettunen, M. I., Hu, D., Kennedy, B. W. C., Boren, J., Gallagher, F. A., Brindle, K. M. (2011). Hyperpolarized [1-13C]-ascorbic and dehydroascorbic acid: vitamin C as a probe for imaging redox status in vivo. JACS, 133(30), 11795-11801.
3. Timm, K. N., Hu, D., Williams, M., Wright, A. J., Kettunen, M. I., Kennedy, B. W. C., Larkin, T. J., Dzien, P., Marco-Rius, I., Bohndiek, S. E., Brindle, K. M. (2017). Assessing oxidative stress in tumors by measuring the rate of hyperpolarized [1-13] dehydroascorbic acid reduction using 13C magnetic resonance spectroscopy. Journal of Biological Chemistry, 292(5), 1737-1748.
4. Qin, H., Carroll, V. N., Sriram, R., Villanueva-Meyer, J. E., von Morze, C., Wang, Z. J., Mutch, C. A., Keshari, K. R., Flavell, R. R., Kurhanewicz, J., Wilson, D. M. (2018). Imaging glutathione depletion in the rat brain using ascorbate-derived hyperpolarized MR and PET probes. Scientific Reports, 8, 7928.
5. Crane, J. C., Olson M. P., Nelson S. J. (2013). SIVIC: Open-Source, Standards-Based Software for DICOM MR Spectroscopy Workflows. Int J. Biomed Imaging, 2013: 169526

Poster Presentation

Disclosures: The authors would like to disclose that HP pyruvate is an investigational device.

401-Development of one-dimensional nanotracer platforms for magnetic particle imaging of lungs

Presenter: Saumya Nigam, Michigan State University

Saumya Nigam[1], Jeotikanta Mohapatra[2], Jabin George[3], Elizabeth Kenyon[4], Hanaan Hayat[4], Bin Gu[5], J. Ping Liu[2], Jinxing Li[5], Ping Wang[5]

[1]*Michigan State University, East Lansing*
[2]*The University of Texas at Arlington, Arlington, Texas*
[3]*The University of Texas at Arlington, Grand Prairie, TX*
[4]*Precision Health Program, East Lansing, Michigan*
[5]*Michigan State University, East Lansing, Michigan*

Recently, Magnetic Particle Imaging (MPI) has emerged as a promising imaging modality and has been garnering significant attention. The imaging devices, MPI scanners based on this technique, are actively attempted to be scaled for human size and use. Its main advantages include being radiation-free and high signal-to-noise ratio. MPI utilizes the non-linear magnetization of the magnetic nanoparticles and generates signals which are processed towards imaging [1]. The current magnetic nanoparticles which are used as tracers of MPI are limited by their suboptimal magnetic properties even though the technique promises high sensitivity and detection. This necessitates the development of high-performance magnetic nanotracers specifically tailored for use in MPI for improving the spatial resolution of *in vivo* imaging [2]. The magnetic properties of these nanotracers are closely related to their intrinsic magnetic anisotropy [3]. Considering shape anisotropy as a unique governing factor, we rationalized that exploring various shapes might help our quest for a tracer with improved performance. Until now, the spherically shaped (zero-dimensional) iron oxide nanoparticles have been the most widely studied MPI tracers. Our work explores the fabrication of one-dimensional iron oxide nanorods and evaluates their performance as MPI tracer towards lung imaging in mice model. The iron oxide nanorods were fabricated by the solution-phase chemical process and characterized by various techniques. The saturation magnetization was assessed using the physical property measurement system (Suppl Fig. 1). The surface of these nanorods were then modified using dextran T-10 (Fig. 1a). After their surface modification, optical emission spectroscopy was used to determine their iron content and relaxation response was evaluated using Momentum™ MPI scanner (Magnetic Insight Inc.) (Suppl Fig. 2). Their relaxation response was further compared with that of VivoTrax® (VTX) for 1 mg/ml of iron (Fig. 1b, c). At a concentration of 0.5 mg/ml, these nanorods were aerosolized using a laboratory nebulizer and exposed to the CD1 mice (12-week-old, male, n=3) for 30 min. The mice were imaged immediately post-administration using Momentum™ MPI scanner with a projection Field Free Line (FFL) operating with a magnetic field gradient strength of 6 x 6 T/m. 3D MPI images with a FOV of 6 cm x 6 cm x 12 cm were acquired with 21 projections for ~30 minutes per mouse in the high-resolution mode. Anatomic X-ray Computed tomographic (CT) images were acquired using the Perkin-Elmer Quantum GX µCT Scanner and MPI images were co-registered using the fiducial markers which identify the position of object/animal in 3D space. The mice were sacrificed after 24 h and vital organs (Brain, Heart, Liver, Lungs, Stomach, Spleen and Kidneys) were excised for imaging *ex vivo* using 2D MPI. All imaging data processing was performed using Horos software (Horosproject.org). The MPI images acquired immediately after delivery identified two positive signal outputs, with substantial intensity from the lungs of the animal. In order to locate the exact origin of the MPI signal, the data was co-registered with CT images. The co-registration revealed the location of the signal in the lungs which was further confirmed by 2D *ex vivo* images of the lungs (Fig. 1d; Suppl Fig. 3). Here, we witnessed the ability of a 1D nanoparticle to act successfully as a MPI nanotracer and their potential towards *in vivo* pulmonary delivery and imaging. When compared to the performance of VivoTrax® at the same iron concentration, the nanorods well exceeded our expectations and their signal intensity was more than 5-fold of VivoTrax®. This study unlocks a dynamic provision of use of anisotropic nanoparticles as MPI tracers which can further help us utilize the technique to it maximum capability. 1D nanoparticles, Anisotropy, Iron oxide nanoparticles, Lung imaging, Magnetic particle imaging, Nanotracers

Reference

1. Hufschmid, R., et al., Nanoscale Physical and Chemical Structure of Iron Oxide Nanoparticles for Magnetic Particle Imaging. physica status solidi (a), 2019. 216(2): p. 1800544.
2. Lu, C., et al., Engineering of magnetic nanoparticles as magnetic particle imaging tracers. Chemical Society Reviews, 2021. 50(14): p. 8102-8146.
3. Bauer, L.M., et al., Magnetic Particle Imaging Tracers: State-of-the-Art and Future Directions. The Journal of Physical Chemistry Letters, 2015. 6(13): p. 2509-2517.

Poster Presentation

Disclosures: The authors have disclosed no financial interest.

402-18F-Fluciclovine PET/CT in Initial Staging of Prostate Cancer

Presenter: Ray Zhang, Stanford University Medical Center

Ray Zhang[1], Andrei Iagaru[2], Benjamin L. Franc[3], Farshad Moradi[2], Carina Mari[2], Guido A. Davidzon[2], Ryusuke Nakamoto[1]

[1]*Stanford University Medical Center, Palo Alto*
[2]*Stanford University, Stanford, CA*
[3]*University of California, San Francisco, San Francisco, CA*

Purpose:
^{18}F-Fluciclovine is a PET radiopharmaceutical that is FDA approved for the detection of prostate cancer recurrence and exhibits higher sensitivity and specificity compared to conventional imaging modalities such as CT or MRI. However, it currently plays a limited role in initial staging of prostate cancer. Given its favorable biodistribution and lower renal and bladder uptake compared to prostate-specific membrane antigen PET radiotracers, which was recently approved, there may be a role for imaging with ^{18}F-fluciclovine for initial staging of prostate cancer.

Materials and Methods:
We performed a retrospective analysis of 64 cases of ^{18}F-fluciclovine PET/CT used for initial staging of prostate cancer from November 2017 to April 2020. Approximately 10.4 ± 0.2 mCi of ^{18}F-fluciclovine was administered intravenously. Three to five minutes after radiopharmaceutical administration, PET/CT scans of the base of skull to midthigh were obtained using the Discovery 690 and Discovery MI PET/CT scanners (GE Healthcare). ^{18}F-fluciclovine PET/CT findings were correlated to pelvic MRI, other imaging modalities such as bone scans, and final pathology.

Results:
The average age of patient was 69.6 ± 1.2 (SEM). Initial pretreatment PSA was 42.0 ± 9.7. All patients had intermediate and high-risk prostate cancer that was confirmed on pathology. Thirty-four patients had MRI of the pelvis $_{\text{demonstrating}}$ PIRADS 4 or 5 lesions. Initial staging ^{18}F-fluciclovine PET/CT scans demonstrated intraprostatic cancer foci in 64 of the patients, locoregional lymph node involvement in 31 of the patients, and distant metastases in 24 of the patients. ^{18}F-Fluciclovine PET/CT resulted in management change in 34.4% of the patients (n=22).

Conclusion:
Initial staging with^{18}F-Fluciclovine PET/CT for prostate cancer correctly identifies intraprostatic cancer in all 64 patients with intermediate to high-grade prostate cancer. ^{18}F-Fluciclovine PET/CT also demonstrates locoregional lymph nodes and distant metastases that changed the management in approximately 34.4% of patients by identifying locoregional and metastatic disease that was not definitively characterized on conventional imaging. ^{18}F-Fluciclovine PET/CT may serve as a useful adjunctive imaging study used in initial staging for prostate cancer patients.

Poster Presentation

Disclosures: The authors have disclosed no financial interest.

403-89Zr-DFO-TAT-anti-γH2AX as a PET biomarker for Radiotheraputic DNA Damage

Presenter: Michael Dimitrov, Memorial Sloan Kettering Cancer Center

Michael Dimitrov

Memorial Sloan Kettering Cancer Center

Pancreatic Ductal Adenocarcinoma (PDAC) is a malignancy with a poor clinical prognosis of less than 10 percent patient survival past five years[1], due to its high vascularization, metastatic potential, and late detection[2]. Many novel targeted cancer treatments, including chemotherapeutic agents and targeted radiopharmaceuticals, induce Double Strand Breaks (DSBs) in the cancerous cells, leading to genomic instability, and ultimately cell death or apoptosis. These treatment paradigms lead to the activation of DNA Damage Response (DDR) cascades, of which H2AX is a critical histone that initiates DNA repair protein recruitment[3]. As a result, anti-γH2AX antibodies have been used extensively as biomarkers of DNA damage in histology[4]. Recently, a Zirconium-89 conjugated anti- γH2AX antibody coupled with a TAT nuclear internalization sequence has been developed as a potential radioprobe for Positron Emission Tomography (PET)[5]. The half-life of chelated ^{89}Zr of approximately 78 hrs. coincides with the biological half-life of the coupled antibodies, allowing for minimal non-target irradiation by the radiopharmaceutical after the treatment period. Previously, the internalization of the ^{89}Zr-DFO-TAT-anti-γH2AX antibody into irradiated breast adenocarcinoma cell lines has been validated[6], as well as the ability of the antibody to monitor nucleic activity of pancreatic cancer cell lines exposed to chemotherapy treatments[7]. The ability of synthesized ^{89}Zr-DFO-TAT-anti-γH2AX antibodies to be used as effective and dose-dependent PET imaging agents during external beam irradiation of xenografted human pancreatic cell lines was assayed in the present study. We optimized the chelation protocol of the radiometal to the antibody complex and subsequently found that given a standard therapeutic irradiation dose sequence, γH2AX is highly significantly overexpressed in human PDAC cells. Further, irradiation led to increased internalization and affinity of the antibody into the cellular nucleus. Finally, we observe that mice which underwent the irradiation sequence express significantly higher tumor signals then controls, particularly 48 hours post injection and when probe administration immediately precedes irradiation.

Reference

1. Miller, K. D., Siegel, R. L., Lin, C. C., Mariotto, A. B., Kramer, J. L., Rowland, J. H., ... & Jemal, A. (2016). Cancer treatment and survivorship statistics, 2016. CA: a cancer journal for clinicians, 66(4), 271-289.
2. Tao, J., Yang, G., Zhou, W., Qiu, J., Chen, G., Luo, W., ... & Zhao, Y. (2021). Targeting hypoxic tumor microenvironment in pancreatic cancer. Journal of Hematology & Oncology, 14(1), 1-25.
3. Kuo, L. J., & Yang, L. X. (2008). γ-H2AX-a novel biomarker for DNA double-strand breaks. In vivo, 22(3), 305-309.
4. Valdiglesias, V., Giunta, S., Fenech, M., Neri, M., & Bonassi, S. (2013). γH2AX as a marker of DNA double strand breaks and genomic instability in human population studies. Mutation Research/Reviews in Mutation Research, 753(1), 24-40.
5. Cornelissen, B., Kersemans, V., Darbar, S., Thompson, J., Shah, K., Sleeth, K., ... & Vallis, K. A. (2011). Imaging DNA damage in vivo using γH2AX-targeted immunoconjugates. Cancer research, 71(13), 4539-4549.
6. Knight, J. C., Topping, C., Mosley, M., Kersemans, V., Falzone, N., Fernández-Varea, J. M., & Cornelissen, B. (2015). PET imaging of DNA damage using 89Zr-labelled anti-γH2AX-TAT immunoconjugates. European journal of nuclear medicine and molecular imaging, 42(11), 1707-1717.
7. Knight, J. C., Mosley, M. J., Bravo, L. C., Kersemans, V., Allen, P. D., Mukherjee, S., ... & Cornelissen, B. (2017). 89Zr-anti-γH2AX-TAT but not 18F-FDG Allows Early Monitoring of Response to Chemotherapy in a Mouse Model of Pancreatic Ductal AdenocarcinomaImaging DNA Damage Response in PDAC. Clinical Cancer Research, 23(21), 6498-6504.

Poster Presentation

Disclosures: The authors have disclosed no financial interest.

404-Cryo-Fluorescence Tomography, not just for cold cuts: analysis and characterization of a quantitative, computationally defined, imaging modality.

Presenter: Christian Stokes, Emit Imaging

Christian Stokes[1], Steven Toddes[1], Eli White[1], Craig Ferris[2]

[1]Emit Imaging, Baltimore, MD
[2]Northeastern University, Boston, MA

Every whole animal imaging modality has an inherent risk of failing to capture a portion or the entirety of a region of interest. Usually, that means the investigator must alter an acquisition parameter or gather a second dataset. With CFT, there is no ability to react or alter the acquisition because the modality is inherently destructive. Further, because the sample needs to be sliced all-the-way through, there is significant time investment required for gathering CFT datasets. But CFTs largest drawbacks of lengthy study time and destructive nature can be leveraged to make it a robust reliable, and consistent system for small animal imaging research. Developing an optical imaging system that is destructive and time consuming by nature required a new approach to both white light and fluorescent acquisitions. A computational approach was devised such that the data produced from a CFT study was guaranteed to produce usable data (barring extreme events like an unexpected hardware failure or severe user error, i.e. having a GFP+ animal and trying to use an IR laser filter combo). Not only does the computational approach allow for improved data quality, but it also allows for data to be reprocessed when improved methods become available.
The mechanical, optical, and computational system is not unique, but the ecosystem that has been built around the system is. A system with as many moving parts as a CFT system necessitates regular calibration in its imaging and mechanical systems. Using the automated nature of CFT, the Xerra is calibrated to its darkfield noise, illumination pattern, and own system movements prior to every study is run. The result is a well calibrated system before any computational techniques are used. As currently deployed, CFT produces: tack sharp images across its acquisitional range 470 nm - 840 nm without optics changes; 32-bit high dynamic range (HDR) fluorescent data sampled from 5 ms to 2.5 s; HDR, color accurate, white light images from laser illumination without a Bayer filter.

Reference

1. Debevec, Paul E. and Jitendra Malik. “Recovering high dynamic range radiance maps from photographs.” SIGGRAPH ’08 (2008).
2. Mathew Brevard, Mohammed Farhoud, Hemi Dimant, Gary Sahagian, Eben Rosenthal, Quang-De Nguyen; Abstract LB-366: Cryo-fluorescence tomography as a new tool in 3D visualization of tumor heterogeneity, metastatic proliferation and immuno-oncology. Cancer Res 1 July 2018; 78 (13_Supplement): LB–366.
3. C. Vinegoni, P. Fumene Feruglio and R. Weissleder, "High Dynamic Range Fluorescence Imaging," in IEEE Journal of Selected Topics in Quantum Electronics, vol. 25, no. 1, pp. 1-7, Jan.-Feb. 2019, Art no. 6801507, doi: 10.1109/JSTQE.2018.2881608.

Poster Presentation

Disclosures: The authors have disclosed no financial interest.

405-Imaging of KRAS G12C mutations employing a novel [124/131I]-AMG510 tracer in murine models.

Presenter: Raik Artschwager,Memorial Sloan Kettering Cancer Center

Raik Artschwager[1], Delissa Johnson[2], NagaVaraKishore Pillarsetty[1]

[1]Memorial Sloan Kettering Cancer Center, New York, NY
[2]Memorial Sloan Kettering Cancer Center, Brooklyn, New York

Introduction:
KRAS is one of the most frequently altered proteins in human cancer. [1] As a member of the GTPase RAS family critically involved in cell signaling a single amino acid mutation in KRAS at codon 12 (p.G12D, p.G12V or p.G12C) can lead to uncontrolled tumor growth. Our aim was to develop a novel PET imaging probe to identify KRAS G12C driven tumors. Long thought to be undruggable, the inactive GDP bound form of mutated KRAS G12C can be covalently targeted by the FDA approved inhibitor Sotorasib (AMG510). [2,3] Herein, we present the radiosynthesis of a novel PET tracer derived from Sotorasib and its *in vitro* and *in vivo* evaluation in KRAS G12C mutant cell lines and tumors.

Methods:
Iodination of AMG510 was performed using chloramine-T and sodium iodide to yield an ortho- and a para-hydroxy iodinated derivative. The [$^{127/124/131}$I]-AMG510 tracers were separated via HPLC and evaluated *in vitro* (internalization and efflux assays) using KRAS G12C mutant H358 and MiaPaca-2 cell lines. *In vivo* PET imaging and biodistribution studies were performed on athymic nude mice bearing tumor xenografts (~300 mm^3) obtained by s.c. administration of 3-5 million cancer cells. For imaging [^{124}I]-AMG510 was administered via tail vein injection (150 µCi) and imaged using an Inveon microPET/CT instrument at different time points. Biodistribution studies were conducted sacrificing mice at different time points to correlate organ uptake.

Results:
The synthesis of the cold [^{127}I]-AMG510 and radiolabeled [$^{124/131}$I]-AMG510 inhibitor was accomplished in good to moderate yields, respectively (60%, RCY: 30%, n = 10). The 2 obtained iodinated derivatives could be separated via preparative HPLC and only one derivative demonstrated preferential binding to KRAS G12C cells in our *in vitro* studies. Efflux studies confirmed retained activity in cell lysates in both used cell lines and stability studies in human serum of the tracer demonstrated its integrity over time. *In vivo* PET imaging and biodistribution studies indicated good uptake in H358 tumor xenografts with uptake values of 0.93 ± 0.1 %ID/g after 0.5 h, 0.54 ± 0.02 %ID/g after 1 h and 0.49 ± 0.05 %ID/g after 2 h, respectively.

Conclusion:
Our results show preserved affinity towards the mutated KRAS G12C protein upon modification of AMG510 with iodine. Cell internalization and efflux studies confirmed retained inhibition and serum stability studies confirmed the inhibitors stability over time. Furthermore, we established the pharmacokinetic profile and demonstrated good tumor targeting in murine models showing that this novel PET tracer has potential for preclinical applications.

Reference

A. K. Kwan et al., J. Exp. Clin. Cancer Res. 2022, 41, 1-23.

B. J. Canon et al., Nature 2019, 575, 217-223.
C. B. A. Lanman et al., J. Med. Chem. 2020, 63, 52–65.

Poster Presentation

Disclosures: The authors have disclosed no financial interest.

406-Monitoring therapeutic cell viability using brownian superparamagnetic iron oxide nanoparticles with Magnetic Particle Imaging

Presenter: Renesmee Kuo, University of California, Berkeley

Renesmee Kuo[1], Irati Rodrigo Arrizabalaga[2], Chinmoy Saayujya[3], Prashant Chandrasekharan[3], Kim Hwang Yeo[4], Benjamin Fellows[2], Steven Conolly[5]

[1]University of California, Berkeley
[2]University of California, Berkeley, Berkeley, California
[3]University of California, Berkeley, Berkeley
[4]UC Berkeley, [5]University of California, Berkeley, Berkeley, CA

Introduction:
Molecular Imaging methods are often used to track therapeutic cells like stem cell and CAR-T cells therapies. Cell tracking methods include MRI with 19F or Superparamagnetic Iron Oxide (SPIO) tags, Ultrasound with microbubble tags, and Nuclear Medicine. Each of these has limitations in persistence, sensitivity, resolution or artifacts. Magnetic Particle Imaging (MPI) is a new imaging method ideal for tracking cells, in terms of sensitivity, penetration, robustness and linear, positive contrast (Fig.1A) [1,2]. Superferromagnetic MPI tracers [3] could soon allow for detecting even 20 labeled cells with 100-micron resolution anywhere in a mouse. An outstanding challenge for all cell tracking methods is distinguishing live from dead cells. Because these methods track an inorganic tag, the live and dead cells are indistinguishable. We demonstrate here, for the first time, promising data showing that MPI can distinguish live from dead cells.
MPI scanning requires a 180-degree rotation of the SPIO. This rotation time is slowed by Neelian and Brownian relaxation constants (Fig.1B) [4]. In Neelian relaxation, only the domain flips, not the entire particle [5], so Neelian SPIOs cannot sense viscosity. With Brownian relaxation, the entire particle flips, so Brownian relaxation scales linearly with the nanoscale viscosity [6]. Since Neel and Brownian relaxation occurs in parallel, we observe the faster of the two. Nonimaging measurements show that cells change their viscosity as they go through apoptosis [7-9]. Here we hypothesize that Brownian MPI particles could measure this change via viscosity sensing and allow us to infer cell viability *in vivo* with MPI.

Materials and Methods:
We used two commercial SPIO nanoparticles: nanoComposix NanoXact (NN) and Magnetic Insight VivoTraxTM (VT) to label LLC1 lung cancer cells. NN was chosen for our Brownian SPIO because we found its relaxation time scales linearly with viscosity. VT was chosen as our Neelian SPIO as its relaxation time does not vary with viscosity. We labeled cells with both SPIOs. In two flasks, cells were incubated with 100 μL of NN and with 300 μL of VT in the other two flasks. After 24 hours, the cells were harvested and washed with a phosphate buffer. The NN and VT labeled cells were divided into two groups. One group was incubated at 37°C (control), and the other group was incubated in a hot water bath at 60°C to induce cell death via hyperthermia for 2 hours. We then performed square wave relaxometry on both groups of cells using an home-built arbitrary-waveform relaxometer [10]. We also prepared two SPIO samples (without cells) by diluting NN and VT with a phosphate buffer in a 1-1 ratio (by weight). Relaxation time constants of all SPIO-labeled cell samples were measured using a periodic pulsed magnetic field with amplitude of 10 mT and 1 kHz frequency [11,12]. We then integrated the received signal and fit it to an exponential function to determine the relaxation time constant using Matlab.

Results and Discussion:
We observe distinct mechanisms of relaxation for the two groups of cells (Fig. 1C). There is a statistically significant change in relaxation time with viscosity changes due to apoptosis for cells labeled with Brownian SPIOs (NN) as hypothesized for Brownian SPIOs. Also as expected for the Neelian SPIO (VT), we observed no change in the relaxation time constant with cell death. These data show great promise for MPI cell tracking using Brownian SPIOs to monitor therapeutic cell viability in real-time.
We plan future applications to exploit Brownian relaxation contrast to allow for distinguishing bound SPIOs (which will have restricted rotation) from unbound SPIOs in an imaging format. This remains an open challenge for medical imaging.

Reference
1. Zheng B, et al., Sci Rep, 2015;
2. Zheng B, et al., Theranostics, 2016;
3. Tay ZW, et al., Small Methods, 2021;
4. Coffey, et al., World Scientific, 2004;
5. Brown WF, Phys. Rev., 1963;
6. Rosensweig R., Journal of Magnetism and Magnetic Materials, 2002;
7. Chandrasekharan et al., WMIC, 2020;
8. Gupta et al., J. Mater. Chem. B, 2016;
9. Xiao, et al., Chemistry—A European Journal, 2020;
10. Tay, ZW, et al., Sci Rep, 2016;
11. Tay ,ZW, et al., IEEE Trans Med Imaging, 2019;
12. Utkur, M., Saritas, EU., Med Phys. 2022; 49: 2590– 2601.

Poster Presentation

Disclosures: The authors have disclosed no financial interest.

407-Positivity rates of Indium-labeled WBC scans for Occult Infection

Presenter: Ray Zhang, Stanford University Medical Center

Ray Zhang[1], Andrei Iagaru[2], Benjamin L. Franc[3], Farshad Moradi[2], Carina Mari[2], Judy Nguyen[4], Guido A. Davidzon[2]

[1]Stanford University Medical Center, Palo Alto
[2]Stanford University, Stanford, CA
[3]University of California, San Francisco, San Francisco, CA
[4]Stanford University, Stanford, California

Purpose:
Tagged-WBC scans are frequently used in the diagnostic workup of occult infections. However, there has been limited research into the diagnostic utility of tagged-WBC scans recently in the era of SPECT-CT. In addition, with the approval of FDG PET/CT for evaluation of occult infections, it is important to understand the advantages and disadvantages of these different approaches in the diagnosis of occult infection to obtain the imaging study most suited for the clinical

indication and patient history. We, therefore, analyzed the positivity rates of tagged-WBC indium scans based on the clinical indication and important patient characteristics like antibiotic use.

Materials and Methods:
Fifty-six tagged-WBC indium scans were performed at Stanford from July 2019 through February 2020. Approximately 700-1100 μCi of In-111 Oxine solution was labeled to patient-derived WBCs and administered intravenously. Images were acquired at 16-30 hours after injection of radiotracer. Planar images were acquired using a large-field-of-view gamma camera, fitted with a medium-energy collimator. SPECT-CT imaging of the appropriate anatomical region was performed based on the clinical history or the planar images using a NM/CT 870 CZT or Discovery 670 Pro scanner (GE Healthcare).

Results:
Out of the fifty six scans, fifty three were performed in the inpatient setting, and three were performed in the outpatient setting. The rate of positivity was 39.3% (22), and the non-diagnostic rate was 8.9% (5). In patients receiving broad-spectrum antibiotics (42), the rate of positivity was 47.6% (20), and the rate of positivity was 21.4% (3) in those who were not on antibiotics (14). The highest rates of positivity were seen in sepsis and/or bacteremia with a positivity rate of 75.0% (9/12). Positivity rates were 17.7% (3/17) for aortic graft infections and endocarditis, 14.3% (1/7) for abdominal infections, 25.0% (2/8) for suspected hardware infections and osteomyelitis, and 50.0% for pneumonia (1/2).

Conclusion:
Tagged-WBC indium scans remains a useful imaging study to identify occult infections with a positivity rate of 39.3% when performed adjunctively with SPECT-CT. Remarkably, the rate of positivity is higher with broad-spectrum antibiotic use (47.6%), and the highest positivity rate is in patients with sepsis and/or bacteremia (75.0%). Knowledge of these rates of positivity based on patient characteristics, and clinical indication may allow clinicians to diagnose and localize occult infections more efficiently.

Poster Presentation

Disclosures: The authors have disclosed no financial interest.

408-A novel PET reporter system using [18F]fluoroestradiol for imaging opsins and other exogenous proteins

Presenter: Michael Michaelides, National Institute on Drug Abuse

Jordi Bonaventura[2], Matthew Boehm[2], Hank Jedema[2], Oscar Solis[2], Marco Pignatelli[2], Xiaowei Song[1], Christopher Richie[1], Shilliang Zhang[1], Hanbing Lu[1], Juan L. Gomez[2], Marisela Morales[2], Omar Gharbawie[2], Martin Pomper[3], Elliot Stein[3], Charles Bradberry[3], **Michael Michaelides[2]**

[1]National Institute on Drug Abuse
[2]National Institute on Drug Abuse, Baltimore, MD
[3]Johns Hopkins Univeristy, Baltimore, MD

Positron emission tomography (PET) can be used to visualize transgenic constructs using reporters and compatible radiotracers but there is a lack of selective PET reporter systems for imaging transgenic constructs in the brain. [^{18}F]fluoroestradiol (FES) is an FDA-approved PET radiopharmaceutical used for detection of breast cancer by binding with high affinity to estrogen receptors (ERs). Optogenetics is a widely used technology that enables the manipulation of target neuronal populations and circuits with precise spatiotemporal control. Optogenetics affords potential for translational research and clinical therapeutics. However, a major constraint is the inability to track opsins longitudinally in a noninvasive and quantitative manner. To address this, we engineered ChRERα (pronounced 'carrera'), a novel chimeric protein comprised of the prototypical opsin Channelrhodopsin-2 (ChR2) and the ligand binding domain (LBD) of the human estrogen receptor alpha (ERα). Experiments in HEK-293 cells show ChRERα retains the original ERα-LBD affinity for binding estradiol and FES. In addition, blue light stimulation (473 nm) in cells transfected with ChRERα elicited photocurrents indistinguishable from cells transfected with ChR2. Adeno-associated virus (AAV)-mediated ChRERα transduction in mouse cortex led to blue-light evoked photocurrents in brain slices. AAV-mediated ChRERα transduction in the ventral tegmental area stimulated locomotor activity upon blue light stimulation in rats indicating ChRERα retains the functional properties of ChR2 in vitro and in vivo. AAV-mediated ChRERα transduction was visualized noninvasively in rats and squirrel monkeys using FES-PET where ChRERα was detected at both the local site of AAV injection in the motor cortex (e.g. neuron cell body) as well as at long-range terminal projection sites (thalamus, controlateral cortex). In monkeys, the neuroanatomical pattern of ChRERα localization using FES-PET predicted functional brain connectivity assessed using resting-state functional magnetic resonance imaging (rsfMRI). Longitudinal tracking with repeated FES-PET scans in the same monkey confirmed opsin brain expression at multiple timepoints throughout a 1.5-year period following AAV-injection and revealed decreases in FES-ChRERα binding at the 1.5 year time point. ChRERα expressing was visualized postmortem using fluorescent and electron microscopy confirming its subcellular localization in the plasma membrane. In sum, ChRERα is the first opsin that can be tracked in a noninvasive and longitudinal manner in the brain of living animals and is expected to facilitate translational and clinical optogenetics applications. Furthermore, this FES-ERα-LBD reporter system comprises a scalable and modular platform for the noninvasive visualization of other opsins and other exogenous proteins. This approach may be adaptable for visualizing a variety of opsins (and other transgenic constructs) to advance the translational potential of optogenetics and related technologies.

Poster Presentation

Disclosures: The authors have disclosed no financial interest.

409-Imaging of endometriosis using cRGD-MN probe in a mouse model

Presenter: Nazanin Talebloo, Michigan State University

Nazanin Talebloo[1], M. Ariadna Ochoa Bernal[2], Elizabeth Kenyon[3], Christiane Mallett[4], Asgerally Fazleabas[2], Anna Moore[5]

[1]Michigan State University, East Lansing
[2]Michigan State University
[3]Precision Health Program, East Lansing, Michigan
[4]Michigan State University, East Lansing, MI
[5]Michigan State University, East Lansing, Michigan

Introduction:
Endometriosis is a chronic, inflammatory, and hormone-dependent gynecological condition which is generally characterized by the presence and growth of ectopic, endometrial-like tissue outside of the uterus mainly in the pelvic area including ovaries, and peritoneal surfaces. This disease affects about 10% of women during their reproductive years[1,2]. No symptom is pathogenic for endometriosis, but it can be

accompanied by multiple symptoms including pelvic pain and infertility [1,3]. The etiology of endometriosis is complex, resulting in a heterogenous disease[4] which makes it difficult to diagnose. Currently, the gold standard for diagnosis of endometriosis is a diagnostic laparoscopy followed by histological confirmation for the presence of glands and stroma. However, due to the risks of this invasive diagnostic procedure, other non-invasive diagnostic methods should be considered. Imaging techniques that are currently used to diagnose endometriosis are ultrasound and magnetic resonance imaging (MRI)[5,6.] Ultrasound is operator-dependent and cannot detect all lesions while MRI can overlook some endometriotic masses[7–13]. Developing targeted contrast agents can help diagnose endometriosis through MRI by increasing the signal difference between lesions and their surroundings[14]. However, no clinically approved MRI targeted contrast agent is available for endometriosis detection[11,15,16]. Angiogenesis plays an important role in the inflammatory response and establishment of lesions [17]. Targeting angiogenesis and cell adhesion in lesions using imaging probes might increase the chances of reliably detecting endometriosis. Since alpha(v)beta3 integrin plays a role in lesion implantation[18] we proposed to use cyclic RGD (c-RGD) peptide for targeting similar to that in cancer[19,20,21]. Here, for the first time, c-RGD conjugated, optically active, iron oxide nanoparticles were used to image endometriotic lesions in a mouse model of endometriosis.

Methods:
Endometriosis was induced by removing one uterine horn and suturing the $2mm^3$ pieces of endometrial tissue to the peritoneal wall of the same female Pgr^{cre}/+Luc/Luc mouse. Progesterone positive tissues including lesions express luciferase in this model which can be imaged with bioluminescence imaging (BLI) to confirm the location of lesions. Dextran-coated iron oxide nanoparticles were synthesized with the previously established co-precipitation method[22] and conjugated with Cy5.5 dye (Cy5.5-MN). c-RGD was conjugated to Cy5.5-MN based on previous reports (RGD-MN)[20]. Nine mice were imaged with 7 Tesla Biospec 70/30 USR (Bruker, Billerica, MA) imaging system, and T2* maps were acquired before and 24 hours after RGD-MN injection (10 mg Fe/kg) with the same parameters. After the imaging sessions, mice were sacrificed, and organs were removed for a biodistribution based on Cy5.5 signal with fluorescence imaging (IVIS Spectrum, Perkin Elmer, Waltham, MA). Inductively coupled plasma-optical emission spectrometry (ICP-OES) was done on digested tissue samples (lesions and muscles) to measure iron content.

Results:
RGD-MN were synthesized and characterized (size:33.2± 5 nm, zeta potential:13 mv, average number of 12 RGD per MN). Although, RGD-MN injected (experimental) and Cy5.5-MN injected (control) groups showed an accumulation of nanoparticles in the lesions which reduced T2 values on MR T2 maps (Fig.1A), animals injected with RGD-MN showed a significantly higher change of T2 values compared to Cy5.5-NP injected group ($p<0.05$; Fig.1B). Biodistribution studies were aligned with the MRI results and showed that while probe accumulation was observed in the lesions of both experimental and control groups, mice injected with RGD-MN exhibited higher probe accumulation and therefore had a significantly higher average signal intensity compared toCy5.5-MN injected group ($p < 0.01$; Fig.1C). ICP-OES results also showed that there was a significantly higher accumulation of iron in lesions from the experimental group compared to the control group ($p <0.01$; Fig.1D).

Conclusion:
RGD-MN can be used as a potential targeted MR imaging probe to image endometriotic lesions noninvasively. This work was supported in part by the NIH HD 099090 to A.F.

Reference

1. Zondervan et al. Endometriosis. Nature Reviews Disease Primers(2018).
2. Malvezzi et al. Endometriosis: current challenges in modeling a multifactorial disease of unknown etiology. J. Transl. Med. (2020).
3. Prentice. Regular review: Endometriosis. BMJ(2001).
4. Child et al. Endometriosis. Drugs(2001).
5. Kinkel et al. Diagnosis of endometriosis with imaging. European Radiology (2006).
6. Chapron et al. Rethinking mechanisms, diagnosis and management of endometriosis. Nature Reviews Endocrinology(2019).
7. Savelli. Transvaginal sonography for the assessment of ovarian and pelvic endometriosis. Ultrasound in Obstetrics and Gynecology(2009).
8. Exacoustos et al. Imaging for the evaluation of endometriosis and adenomyosis.Best Pract. Res. Clin. Obstet. Gynaecol.(2014).
9. Samreen et al. MRI of endometriosis: a comprehensive review. Applied Radiology (2019).
10. Siegelman et al. MR imaging of endometriosis: ten imaging pearls. Radiographics(2012).
11. Zhang et al. Hyaluronic acid-modified magnetic iron oxide nanoparticles for MR imaging of surgically induced endometriosis model in rats. PLoS One(2014).
12. Bianek-Bodzak et al. The importance and perspective of magnetic resonance imaging in the evaluation of endometriosis. Biomed Res Int(2013).
13. Bourgioti et al. MR imaging of endometriosis. Interv. Imaging(2017).
14. Morawski et al. Targeted contrast agents for magnetic resonance imaging and ultrasound. Current Opinion in Biotechnology(2005).
15. Moses et al. Nanomedicines for endometriosis: lessons learned from cancer research. Small(2021).
16. Guo. An overview of the current status of clinical trials on endometriosis. Fertil. Steril.(2014).
17. Kralickova et al. Role of angiogenesis in endometriosis. Pathol Discov(2016).
18. Nothnick et al. miR-451 deficiency is associated with altered endometrial fibrinogen alpha chain expression and reduced endometriotic implant establishment in an experimental mouse model. PLoS One(2014).
19. Danhier et al. RGD-based strategies to target alpha(v)beta(3) integrin in cancer therapy and diagnosis. Mol Pharm(2012).
20. Montet et al. Multivalent effects of RGD peptides obtained by nanoparticle display. J Med Chem(2006).
21. Hu et al. Facile synthesis of RGD peptide-modified iron oxide nanoparticles with ultrahigh relaxivity for targeted MR imaging of tumors. Biomater Sci(2015).
22. Yigit et al. Context-dependent differences in miR-10b breast oncogenesis can be be targeted for the prevention and arrest of lymph node metastasis. Oncogene(2013)

Poster Presentation

Disclosures: The authors would like to disclose that FDG has been approved.

410-Monte Carlo Dosimetry for 67Cu-LLP2A in a BRAFV600E Melanoma Mouse Model from 64Cu-LLP2A PET Imaging Data

Presenter: Michael Bellavia, University of Pittsburgh

Michael C. Bellavia[1], Paul Wickre[2], Joseph Grudzinski[3], Joseph D. Latoche[4], Kathryn Day[5], Ravi Patel[6], Carolyn Anderson [7]

[1]University of Pittsburgh, Columbia, MO
[2]Madison, WI
[3]University of Wisconsin Madison
[4]University of Pittsburgh, Pittsburgh, PA
[5]University of Pittsburgh, Pittsburgh, Pennsylvania
[6]University of Pittsburgh
[7]University of Missouri, Columbia, Missouri

Objective:
In clinical practice, radiopharmaceutical therapy is usually given with a fixed dosing regimen regardless of the individual patient's tumor burden or tumor uptake of the corresponding pretherapy imaging tracer, despite accumulating evidence that more tailored therapy may improve outcomes [1, 2]. We have recently demonstrated avid and selective uptake of LLP2A, a peptidomimetic labeled with Cu-64 ([^{64}Cu]-LLP2A) for positron emission tomography/computed tomography (PET/CT) imaging in a BRAF^{V600E}-mutant subcutaneous melanoma model (BPRα) that simulates clinical melanoma via BRAF inhibitor resistance and overexpression of very late antigen-4 (VLA-4, integrin $\alpha_4\beta_1$) [3]. Towards validation of LLP2A as a theranostic suitable for patient-specific radionuclide therapy, subject-specific doses for the therapeutic (β^- emitting) cognate isotope Cu-67 ([^{67}Cu]-LLP2A) were estimated for the tumor and organs of interest from serial ^{64}Cu-LLP2A PET/CT imaging in melanoma-bearing mice via dose rate correction and Monte Carlo simulation using Torch software (Voximetry, Madison WI).

Methods:
C57BL/6 mice bearing s.c. flank BPRα tumors (n=3, 1m/2f) were injected intravenously with [^{64}Cu]-LLP2A (approximately 12.2 MBq [330 μCi]; 57.2 MBq/nmol) and PET/CT images were acquired at 2, 4, 24, and 48 h post-injection. PET and CT images were co-registered and organ regions of interest (ROIs) were manually contoured in VivoQuant 2021 software (Invicro, Needham, MA USA) for each timepoint per mouse. Organs selected included those enriched in VLA-4 or involved in tracer clearance (tumor, thymus, bone marrow, spleen, kidneys) as well as key non-target organs (lungs, heart, liver, muscle). Matched PET/CT images with their associated ROIs were imported into Torch software v1.1.0.122 and deformably registered across time. ROIs were either propagated from the initial 2 h timepoint across all successive images per mouse or were specific to each timepoint per mouse. The measured time-activity data was integrated per ROI followed by Monte Carlo simulation of Cu-67 radiation transport for the calculation of ROI dose statistics.

Results:
Activity integration in Torch software removes non-overlapping portions of corresponding ROIs across time prior to integration, and 2 h ROI propagation was selected as it was determined to reduce ROI volume less severely than the per timepoint method. For an injected activity of 12.2 MBq (0.33 mCi), the average mean Cu-67 dose (n=3) predicted for the tumor was 0.7 ± 0.06 Gy (mean ± SD), which was significantly greater relative to non-target organs only (heart, lungs, liver) except for the bone marrow (femur). These results largely corroborate our biodistribution studies previously conducted over a similar timeframe in BPRα [3].

Conclusions and Future Work:
Surprisingly, mean predicted tumor dose was low, and not significantly different from that of the kidneys or organs with notable VLA-4 expression (thymus). To ensure accurate and robust ROI dose calculations, further optimization of the dosimetry workflow with Torch will be required.
Future work will compare these results to dose rate integration per ROI. This feature will be included in a later release. Ultimately, we will utilize image-based dosimetry towards tumor dose stratification in a [^{67}Cu]-LLP2A therapy study aimed at maximizing efficacy while avoiding toxicities.

Reference
1. Garske-Román, U., et al., Prospective observational study of (177) Lu-DOTA-octreotate therapy in 200 patients with advanced metastasized neuroendocrine tumours (NETs): feasibility and impact of a dosimetry-guided study protocol on outcome and toxicity. Eur J Nucl Med Mol Imaging, 2018. 45(6): p. 970-988.
2. Violet, J., et al., Dosimetry of (177)Lu-PSMA-617 in Metastatic Castration-Resistant Prostate Cancer: Correlations Between Pretherapeutic Imaging and Whole-Body Tumor Dosimetry with Treatment Outcomes. J Nucl Med, 2019. 60(4): p. 517-523.
3. Bellavia, M.C., et al., PET Imaging of VLA-4 in a New BRAF(V600E) Mouse Model of Melanoma. Mol Imaging Biol, 2022. 24(3): p. 425-433.

Poster Presentation

Disclosures: The authors have disclosed no financial interest.

411-High-resolution iron oxide nanoparticle tracers for sensitive cell tracking using Magnetic Particle Imaging

Presenter: Renesmee Kuo, University of California, Berkeley

Renesmee Kuo[1], Irati Rodrigo Arrizabalaga[2], Chinmoy Saayujya[3], Kim Hwang Yeo[4], Prashant Chandrasekharan[3], Steven Conolly[5]

[1]University of California, Berkeley
[2]University of California, Berkeley, Berkeley, California
[3]University of California, Berkeley, Berkeley
[4]UC Berkeley, [5]University of California, Berkeley, Berkeley, CA

Introduction:
Our immune system plays a key role in cancer, autoimmune diseases, and inflammation. Scintigraphy and SPECT are used clinically to image autologous white blood cells (WBCs) to allow MDs to track a patient's immune response. However, the radioactive tags (Tc99m or In111) are toxic to WBCs, leading to poor specificity [1,2]. Magnetic Particle Imaging (MPI) is a potential breakthrough in medical imaging [3-8]. MPI could soon be ideal for CAR-T and CAR-NK cell tracking, providing a rapid, high-quality, and zero-radiation complement to clinical Nuclear Medicine studies, with no WBC toxicity [7]. The only remaining technical challenge for MPI is its poor resolution (~1.5 mm in a mouse). Hence, it is crucial to design high-resolution, MPI-tailored superparamagnetic iron oxide (SPIO) tracers to scale up MPI scanners to safe and affordable whole-human MPI. Here we show a serendipitous finding that one commercially available tracer (MS1 Synomag®-D) demonstrates significantly better spatial resolution (3.3-fold sharper) when imaged with a weaker drive field [9].

Materials and Methods:
Here we experimentally compare MS1 (Synomag®-D-70nm-plain, micromod Partikeltechnologie GmbH, Germany) to the resolution of MS3 (Synomag®-D-50nm-plain, micromod Partikeltechnologie GmbH, Germany) and VivoTrax (VT) (Magnetic Insight, USA) using

both high and low drive fields. These three commercial SPIOs were characterized for MPI performance using our in-house arbitrary wave relaxometer (AWR) [10]. The point spread functions (PSFs) and peak signals were measured. Point source phantoms for Synomag®-D tracers were created using three tracer-filled 0.3mm I.D. capillary tubes with 1.8mm center-to-center spacing between the tubes. For VivoTrax, larger-sized capillary tubes (0.6mm I.D.) were used to maintain comparable iron quantity (34μg Fe per tube). The phantoms were imaged with a 6.3T/m field-free line MPI scanner. 2D projection images were acquired with a field-of-view of 6.2cm x 3.1cm and with a 20 kHz drive field at 2.0 and 20.0mT drive field. The MPI images were reconstructed using x-space reconstruction algorithms [12-14].

Results:

Multi-amplitude evaluation of Synomag®-D showed superior tracer performance at a low-excitation amplitude [10]. The resolution of MS1 Synomag®-D is 2.9mT/6.3T/m, roughly 460μm at 2mT, compared to VivoTrax (VT) and MS3 Synomag®-D with roughly 1.5mm resolution (Fig.1A&B). However, at 20mT amplitude, the three tracers have comparable resolution (Fig.1C). Figure 1D&E show MPI images of MS1 Synomag®-D at 2mT and VivoTrax at 20mT. At 2mT amplitude, MS1 Synomag®-D point sources are distinct and easily resolved with a 3.3-fold improvement in resolution compared to VivoTrax.

Discussion:

We have experimentally demonstrated a 3.3-fold boost in resolution in MPI using a commercial MPI tracer simply by reducing the drive field amplitude from 20mT to 2 mT [15,16]. This unexpected 3.3-fold boost in magnetic resolution could enable a dramatic cost reduction for future clinical MPI scanners. Because the cost of MPI scanner hardware scales quadratically with gradient strength, a 3.3-fold reduction in gradient strength could reduce the MPI scanner cost by 11-fold [15]. The SNR tradeoffs and nanoscale physics mechanism underlying this resolution boost merit deeper study.

Recently, we demonstrated that superferromagnetic iron oxide nanoparticles (SFMIOs) can provide a 10-fold improvement in resolution and SNR per gram of tracer [17]. However, biocompatible formulations of SFMIOs remain an open challenge whereas the Synomag®-D tracers are already biocompatible and available commercially. So this high-resolution MPI technique shows immediate promise for reducing the cost of clinical MPI scanners and accelerating the adoption of MPI for imaging CAR-T response to immunotherapies.

Reference

1. Chisholm et al., J Nucl Med, 1979;
2. Goodwin, Journal of Nuclear Medicine, 1978;
3. Gleich, B., Weizenecker, Nature 435, 1214–1217 (2005)
4. Yu EY, et al., Nano Letters. 2017;17(3):1648-54
5. Yu EY, et al., ACS Nano. 2017;11(12):12067-76.
6. Chandrasekharan et al., Nanotheranostics, 2021;
7. Kuo R, et al., International Journal on Magnetic Particle Imaging, 2022
8. JJ Gevaert et al., Molecular Imaging and Biology, 2022.
9. Chandrasekharan et al., The British Institute of Radiology, 2018;
10. Tay, ZW, et al., Sci Rep, 2016;
11. Yeo et al., International Journal on Magnetic Particle Imaging, 2022;
12. Konkle et at., Magnetic Particle Imaging, 2012;
13. Konkle et al., Biomedizinische Technik/Biomedical Engineering, 2013;
14. Goodwill and Conolly, IEEE Trans Med Imaging, 2010;
15. Croft et al., Med Phys, 2016;
16. Tay ZW, et al., IEEE Trans Med Imaging, 2019;
17. Tay ZW, et al., Small Methods, 2021.

Poster Presentation

Disclosures: The authors have disclosed no financial interest.

412-Evaluation of MUC13 as a potential theranostic target for colorectal cancer using radioimmuno-PET imaging in a cell line-derived xenograft mouse model

Presenter: Ryan Coll, University of Texas MD Anderson Cancer Center

Ryan P. Coll[1], Mai Lin[2], Xiaoxia Wen[2], Jianbo Wang[2], Murali Yallapu[3], Sheema Khan[3], Meena Jaggi[3], Subhash Chauhan[3], H. Charles Manning[4]

[1]*University of Texas MD Anderson Cancer Center, Houston*
[2]*University of Texas MD Anderson Cancer Center, Houston, Texas*
[3]*McAllen, Texas*
[4]*University of Texas MD Anderson Cancer Center, Houston, TX*

The use of radiolabeled monoclonal antibodies (mAbs) in diagnostic imaging is a promising method towards increasing the accuracy of identifying cancers in patients. By developing mAbs against specific tumor-associated antigens (TAA's), a more intense signal should be observed in tumors where such antigens are over-expressed compared to that seen in healthy tissue. Among numerous TAA's currently being investigated, mucins have been identified as potential targets in epithelial carcinomas.[1] This protein family includes transmembrane glycoproteins, specifically Mucin13 (MUC13) in this study, which are expressed in cells along the epithelial lining of most organs. Though their role in biological processes such as cell signaling and immune response has also been documented,[2] their role in protecting cell surfaces from physiologically harsh environments is commonly recognized due to dense *O*- and *N*-glycosylation of their extracellular tandem repeat domains. Deviated levels of such glycosylation has been observed in epithelial cancer cells, allowing for ligand interaction with cell surface receptors.[3] Furthermore, the overexpression of MUC13 in pancreatic[4] and ovarian cancers[5] renders it a suitable target for radioimmuno-PET imaging. In the research presented, the targeting capability of a radiolabeled novel anti-MUC13 mAb is being tested using in vitro and in vivo colorectal cancer models. The mAb of interest has been bioconjugated with the chelator *p*-isothiocyanatobenzyl-desferrioxamine (*p*-SCN-Bn-DFO) and was radiolabeled with the positron-emitting isotope ^{89}Zr according to literature protocol.[6] The radiolabeling efficiency of purified radiolabeled mAb was determined using radio thin layer chromatography (radio-TLC) and estimation of the average number of *p*-SCN-Bn-DFO chelators bioconjugated to each mAb was made.[7] Further studies are ongoing and include analyzing purity and specific activity by size exclusion high performance liquid chromatography (SE-HPLC), conducting gel electrophoretic experiments to monitor stability of the radiolabeled mAb, measuring the binding affinity to MUC13-overexpressing colorectal cell line HT29 along with comparison to the low MUC13-expressing cell line SW480, and performing in vivo PET imaging of a colorectal cancer xenograft model in athymic nude mice. Accumulation of the ^{89}Zr-radiolabeled anti-MUC13 mAb in MUC13-overexpressing tumors is expected to be observed by PET imaging. Results from this study will also support further investigations into the radiolabeling of the mAb of interest with therapeutic isotopes for the development of radioimmunotherapeutic drug candidates.

Reference

1. Ratan, C.; Cicily K. D, D.; Nair, B.; Nath, L.R. Curr. Cancer Drug Targets 2021, 21, 132-152.

2. Rao, C.V.; Janakiram, N.B.; Mohammed, A. Clin. Cancer Res. 2017, 23, 1373-1378.
3. Hollingsworth, M.A.; Swanson, B.J. Nat. Rev. Cancer 2004, 4, 45-60.
4. Chauhan, S.C.; Ebeling, M.C.; Maher, D.M.; Koch, M.D.; Watanabe, A.; Aburatani, H.; Lio, Y.; Jaggi, M. Mol. Cancer Ther. 2012, 11, 24-33.
5. Chauhan, S.C.; Vannatta, K.; Ebeling, M.C.; Vinayek, N.; Watanabe, A.; Pandey, K.K.; Bell, M.C.; Koch, M.D.; Aburatani, H.; Lio, Y.; Jaggi, M. Cancer Res. 2009, 69, 765-774.
6. Vosjan, M.J.W.D.; Perk, L.R.; Visser, G.W.M.; Budde, M.; Jurek, P.; Kiefer, G.E.; van Dongen, G.A.M.S. Nat. Protoc. 2010, 5, 740-743.
7. Deri, M.A.; Ponnala, S.; Kozlowski, P.; Burton-Pye, B.P.; Cicek, H.T.; Hu, C.; Lewis, J.S.; Francesconi, L.C. Bioconjugate Chem. 2015, 26, 2579-2591.

Poster Presentation

Disclosures: The authors have disclosed no financial interest.

413-Quantitative imaging of drug target availability in live cells and tissues

Presenter: Lei Wang, Oregon Health & Science University

Lei G. Wang[1], Antonio R. Montano[1], Allison Solanki[2], Nathan P. McMahon[1], Ken Tichauer[3], Kim Samkoe[4], Summer L. Gibbs[1]

[1]Oregon Health & Science University, Portland, OR
[2]Ohio State University, Portland, Oregon
[3]Illinois Institute of Technology, Chicago, IL
[4]Dartmouth College, Hanover, NH

Personalized medicine strives to use biomarker-matched molecularly targeted therapies to overcome known resistance mechanisms. However, there is currently no methodology to measure the highly interdependent levels of available molecular drug targets, amount of drug binding and the resulting cellular response in a single dynamic, living system. Intracellular drug target validation and target engagement quantification have proven to be challenging, and all drugs have some degree of non-specific accumulation due to variable drug affinity, biodistribution, pharmacokinetics, and metabolism. Quantification of available drug targets necessitates accounting for both the drug that binds to its target as well as the drug that accumulates in the cells and tissues in a non-specific manner. While fluorescence imaging has long been used to visualize biological specimens, recent years have seen significant advances in the development of synthetic dyes, genetically encoded biosensors, and fluorescent nanomaterials. We have developed a dynamic, fluorescence-based, three-compartment model termed intracellular paired-agent imaging (iPAI). iPAI is a fluorescence-based approach that utilizes fluorophore labeled small molecule therapeutics as imaging agents to measure drug target availability (DTA). Effective performance of the iPAI probe pair to access DTA highly depends on the inert quality and stable fluorescence signal of the fluorophore pair as drug labels. In particular, the ability of a fluorophore to diffuse across a cell membrane non-destructively and provide an unbiased fluorescence signal read-out for the tagged drugs is critical for quantitative imaging in live cells and tissues. Commercially available small molecule fluorophores have been engineered to offer high water solubility via modification of rhodamine and cyanine dyes with multiple sulfonate groups, however these fluorophores are often cell-impermeant as a result of an overall net negative charge. Herein, we report our designed and developed water-soluble and cell-permeable fluorophores, termed OregonFluor (ORFluor). In proof-of-concept studies, we have developed targeted and untargeted versions of the epidermal growth factor receptor (EGFR) tyrosine kinase inhibitor Erlotinib using our novel ORFluor as drug labels. Adapting previously established ratiometric imaging methodology using bio-affinity agents, it is now possible to use small molecule fluorophore labeled therapeutic inhibitors to visualize their targeted proteins intracellularly, providing a chemical tool kit to generate maps of bound and unbound inhibitors at the single-cell level both *in vitro* and *ex vivo*. iPAI platform provides a powerful new opportunity to study numerous other drugs in cells and tissues, resulting in a comprehensive spatial view of drug distribution and binding for improved personalized therapy assessment.

Poster Presentation

Disclosures: The authors have disclosed no financial interest.

414-Contrast-enhanced magnetic resonance imaging (CE-MRI) evaluation of blood-brain barrier permeability in organophosphate intoxicated rats

Presenter: Sydney Baker, University of California, Davis

Sydney Baker[1], Pedro Bernardino[2], Naomi Saito[2], Peter Andrew[2], Jeremy Macmahon[2], Donald A. Bruun[3], Danielle Harvey[4], Pamela J. Lein[3], Joel R. Garbow[5], Abhijit J. Chaudhari[1], Brad A. Hobson[1]

[1]University of California, Davis, Sacramento, CA
[2]University of California, Davis, Davis, California
[3]University of California, Davis School of Veterinary Medicine, Davis, CA, California
[4]Department of Public Health Sciences, University of California, Davis, Davis, California
[5]Washington University School of Medicine, Saint Louis, MO

Organophosphate (OP) intoxication, including nerve-agent or pesticide poisoning, is an ongoing global public health concern [1]. Acute intoxication by OPs is clinically characterized by cholinergic hyperactivation and seizures, potentially leading to long-term cognitive impairment and acquired epilepsy in patients that survive early symptoms [2]. The mechanisms linking acute OP intoxication to long-term effects are unclear, but a proposed pathological mechanism contributing to epileptogenesis is blood brain barrier (BBB) dysfunction [3]. Evidence of BBB leakage was observed in a preclinical model of acute nerve agent exposure [4]; however, this mechanism has not been systematically evaluated as an underlying cause of long-term, OP induced sequelae. Contrast-enhanced magnetic resonance imaging (CE-MRI) is a powerful, non-invasive method of assessing brain injury and BBB integrity in neurological diseases. The objective of the present study was to characterize the extent and duration of BBB dysfunction in a rodent model of acute diisopropylfluorophosphate (DFP) intoxication using CE-MRI. Adult male Sprague-Dawley rats were administered DFP (3.75 mg/kg, s.c.) or vehicle (VEH) (phosphate-buffered saline) followed immediately with atropine sulfate (2 mg/kg, i.m.) and 2-pralidoxime (25 mg/kg, i.m.), and two subsequent doses of midazolam (0.65 mg/kg, i.m.) at 40 and 50 minutes post-DFP intoxication, respectively. Gadobenate dimeglumine (Gd-BOPTA) MRI contrast agent was administered as a step-down infusion *via* tail-vein catheter during imaging [5]. Animals were imaged on a 7T MR scanner at 6 h or longitudinally at 24, 72, and 168 h post-DFP intoxication. The imaging protocol consisted of a T2-weighted scan, T1-weighted pre- and post-Gd-BOPTA scans (22-min apart), and a dynamic T1-weighted scan (DCE-MRI) during Gd infusion (22 min). Five brain regions

(hippocampus, piriform cortex, amygdala, thalamus, and cerebral cortex) were manually segmented on T1-weighted images using AMIRA software. DCE-MRI was motion corrected and image metrics were extracted using PMOD software. Imaging metrics included percent change in regional signal intensity and lesioned volume. After completion of imaging at each timepoint, subsets of DFP and VEH animals were euthanized and brains immunolabeled for albumin as a correlative marker of BBB disruption. For all outcomes, mixed effects models, including animal-specific random effects, were fit to assess differences between exposure groups. Primary factors of interest included exposure (DFP, VEH), brain region (piriform cortex, amygdala, hippocampus, thalamus, cortex) and time point (6 h, 24 h, 72 h, 168 h). Interactions between these factors (exposure, region, time point) were considered and the best model was chosen using Akaike Information Criterion. Compared to vehicle controls, significant increases in signal intensity and lesioned volume were observed in post-Gd images of DFP-intoxicated animals, varying by brain region and time post-exposure. Of note, signal intensity in the piriform cortex was significantly higher in DFP animals compared to VEH animals at all time points ($p<0.02$). Overall, evidence of BBB breakdown was most apparent at 24 h post DFP intoxication, with the hippocampus ($p=0.008$), amygdala ($p<0.001$), thalamus ($p=0.003$), and the piriform ($p<0.02$) and cerebral cortices ($p<0.001$) exhibiting significantly increased signal intensity compared to VEH controls. Lesions on post-Gd images of DFP animals were corresponded spatially with areas of diffuse albumin immunolabeling in brain parenchyma, which further corresponded to areas of T2-weighted hyperintensity previously shown to undergo necrosis and inflammation following acute OP exposure [6]. Collectively, these data indicate clear BBB leakage after acute DFP intoxication, demonstrating CE-MRI as a promising quantification tool of BBB integrity for future evaluation of novel therapeutics aimed at mitigating the effects of acute OP intoxication.

Reference

1. Eddleston, M., et al., Management of acute organophosphorus pesticide poisoning. Lancet, 2008. 371(9612): p. 597-607.
2. Jett, D.A., et al., A national toxicology program systematic review of the evidence for long-term effects after acute exposure to sarin nerve agent. Crit Rev Toxicol, 2020. 50(6): p. 474-490.
3. Marchi, N., et al., Blood-brain barrier dysfunction and epilepsy: pathophysiologic role and therapeutic approaches. Epilepsia, 2012. 53(11): p. 1877-86.
4. Abdel-Rahman, A., A.K. Shetty, and M.B. Abou-Donia, Acute exposure to sarin increases blood brain barrier permeability and induces neuropathological changes in the rat brain: dose-response relationships. Neuroscience, 2002. 113(3): p. 721-41.
5. van Vliet, E.A., et al., Longitudinal assessment of blood-brain barrier leakage during epileptogenesis in rats. A quantitative MRI study. Neurobiol Dis, 2014. 63: p. 74-84.
6. Hobson, B.A., et al., Magnetic Resonance Imaging Reveals Progressive Brain Injury in Rats Acutely Intoxicated With Diisopropylfluorophosphate. Toxicological Sciences, 2017. 157(2): p. 342-353.

Poster Presentation

Disclosures: The authors have disclosed no financial interest.

415-Using Whole Body PET-CT with 18-FDG in the Management of Post-COVID Infections

Presenter: Venkat Ramesh, Apollo Hospitals

Venkat Ramesh[1], Jyotsna Rao[2], Kalyani Reddy[2], Alka Chengapa[2], Suneetha Narreddy[1], Vijay Kumar Chennamchetty[1], P VIshnu Rao[1], Mahathi Kandal[1]

[1]Apollo Hospitals, Hyderabad, Telangana, India
[2]Apollo, hyderabad, India

Background:
Multiple randomised clinical studies have shown that Immunosuppressive agents such as dexamethasone[1], tocilizumab[2] and baricitinib[3] reduce mortality in severe COVID. Hence, their use is strongly recommended in patients in such patients. The use of such immunosuppressive agents predisposes to opportunistic infections (OIs).[4] Furthermore, immunosuppressed patients are susceptible to critical COVID-19[5], and the use of these agents in this population gravely increases the susceptibility to OIs. It is also hypothesised that even mild COVID-19 lowers immunity and is a risk factor for opportunistic infections, especially COVID-19 associated mucormycosis (CAM).[6] The utility of whole-body PET-CT with FDG in the management of post-COVID infections, hitherto unknown, was evaluated by us.

Methods Study Setting:
Tertiary care academic medical centre in Hyderabad, India

Study Design:
Retrospective, Descriptive

Inclusion Criteria:
Patients with PCR proven SARS-CoV-2 infection and referred for Whole Body PET-CT with FDG with/without contrast at the treating physician's discretion.

Exclusion Criteria:
Patients with known malignancy where PET-CT is performed for staging or monitoring.

Results:
A total of 26 patients (21 males and five females) with a mean age of 53.71 years fulfilled the inclusion and exclusion criteria. The average duration of symptoms until initial evaluation (not necessarily PET-CT) was 21.60 days.
The most common provisional diagnosis was 'Fever of unknown origin (FUO)' in 20 patients.
The most common final diagnosis was 'invasive fungal infection (IFI)' in 13 patients (50% of cases). Of this, mucormycosis was diagnosed in 9 patients, COVID-19 associated pulmonary aspergillosis (CAPA) in 2 patients and fungal granulomas (etiological agent unidentified) in 2 patients.
Of the nine patients with mucormycosis, five had pulmonary mucormycosis alone, two had disseminated mucormycosis with pulmonary involvement, and two had rhino-orbital mucormycosis. Thus, out of nine patients with mucormycosis, seven had pulmonary involvement due to Mucorales.
The other diagnosis (in descending order of frequency) was:

1. No cause of fever was identified in 4 patients; fevers resolved spontaneously with non-steroidal anti-inflammatory drugs (NSAIDs).
2. Tuberculosis in 3 patients: 2 patients with lymph node TB and one with disseminated TB with TB meningitis
3. Infective endocarditis in 2 patients
4. 'Recurrent thrombosis', 'reactive lymphadenopathy' and 'nosocomial pneumonia' were diagnosed in one patient.

Twenty-three patients were cured, and three patients died. The diagnosis in these three patients was 1) septic shock secondary to nosocomial pneumonia, 2) Pulmonary mucormycosis, and 3) Disseminated mucormycosis.

Conclusions:

India has seen a massive surge in cases of COVID-19 due to the Delta variant in 2021. Unfortunately, a large number of patients developed post-COVID invasive fungal infections, most commonly COVID-19 associated mucormycosis.[7-10]

The significant burden of fungal infections following COVID-19 is reflected in our study. 50% of patients in our study were diagnosed with an IFI, most of whom had mucormycosis. Pulmonary mucormycosis was the predominant clinical presentation of mucormycosis in our research. This likely reflects a selection bias as pulmonary mucormycosis is challenging to diagnose, and treatment response is difficult to monitor. Hence, the use of Whole Body PET-CT with FDG with/without contrast was employed extensively in patients with unresolved fevers, cough, hemoptysis, dyspnea and increasing oxygen requirements.

Although tuberculosis is extensively seen in India[11], only three patients in our study were diagnosed with tuberculosis. This could be on account of multiple reasons:

1. The predominance of fungal infections post-COVID.
2. Tuberculosis, especially pulmonary tuberculosis, is relatively easier to diagnose.
3. The study was conducted in a tertiary care hospital, so this could represent a selection bias for patients with difficult to diagnose diseases (such as pulmonary mucormycosis).

In our study, Whole Body PET-CT with FDG with/without contrast proved to be a useful diagnostic tool in evaluating FUO following a diagnosis of SARS-CoV-2 infection.

Reference

1. Dexamethasone in Hospitalized Patients with Covid-19. New England Journal of Medicine. 2020;384(8):693-704.
2. Tocilizumab in patients admitted to hospital with COVID-19 (RECOVERY): a randomised, controlled, open-label, platform trial. Lancet (London, England). 2021;397(10285):1637-45.
3. Marconi VC, Ramanan AV, de Bono S, Kartman CE, Krishnan V, Liao R, et al. Efficacy and safety of baricitinib for the treatment of hospitalised adults with COVID-19 (COV-BARRIER): a randomised, double-blind, parallel-group, placebo-controlled phase 3 trial. The Lancet Respiratory Medicine. 2021;9(12):1407-18.
4. Fishman JA. Opportunistic infections--coming to the limits of immunosuppression? Cold Spring Harb Perspect Med. 2013;3(10):a015669-a.
5. Banerjee D, Popoola J, Shah S, Ster IC, Quan V, Phanish M. COVID-19 infection in kidney transplant recipients. Kidney international. 2020;97(6):1076-82.
6. Pal R, Singh B, Bhadada SK, Banerjee M, Bhogal RS, Hage N, et al. COVID-19-associated mucormycosis: An updated systematic review of literature. Mycoses. 2021;64(12):1452-9.
7. Aranjani JM, Manuel A, Abdul Razack HI, Mathew ST. COVID-19-associated mucormycosis: Evidence-based critical review of an emerging infection burden during the pandemic's second wave in India. PLoS neglected tropical diseases. 2021;15(11):e0009921.
8. Nambiar M, Varma SR, Damdoum M. Post-Covid alliance-mucormycosis, a fatal sequel to the pandemic in India. Saudi Journal of Biological Sciences. 2021;28(11):6461-4.
9. Chakrabarti SS, Kaur U, Aggarwal SK, Kanakan A, Saini A, Agrawal BK, et al. The Pathogenetic Dilemma of Post-COVID-19 Mucormycosis in India. Aging and disease. 2022;13(1):24-8.
10. Singh AK, Singh R, Joshi SR, Misra A. Mucormycosis in COVID-19: A systematic review of cases reported worldwide and in India. Diabetes Metab Syndr. 2021;15(4):102146-.
11. Dhamnetiya D, Patel P, Jha RP, Shri N, Singh M, Bhattacharyya K. Trends in incidence and mortality of tuberculosis in India over past three decades: a joinpoint and age–period–cohort analysis. BMC Pulmonary Medicine. 2021;21(1):375.

Poster Presentation

Disclosures: The authors have disclosed no financial interest.

416-Synthesis and evaluation of molecular imaging probes targeting EphA2 receptor

Presenter: Takenori Furukawa, Kyoto Pharmaceutical University

Takenori Furukawa[1], Hiroyuki Kimura[1], Akane Yoshimura[1], Hiroyuki Yasui[2]

[1]Kyoto Pharmaceutical University, Japan
[2]Kyoto Pharmaceutical University, Kyoto, Japan

Background:

Erythropoietin-producing hepatocellular A2 (EphA2) receptor was determined to be particularly overexpressed in cancer cells than in normal cells. Furthermore, the EphA2 receptor has been reported to be expressed in various types of cancer, including breast and prostate cancers, and malignant gliomas [1]. Interestingly, the expression level of EphA2 receptor is increased in high-grade cancers among the same carcinomas, and this is believed to be related to the malignancy of cancers [2]. Therefore, the EphA2 receptor has attracted attention as a target molecule for the diagnosis of cancer. Positron emission tomography (PET) probes using peptides labeled with F-18 [3] and single-photon emission computed tomography (SPECT) probes using antibodies labeled with In-111 [4] have been reported, but small molecule imaging probes for the EphA2 receptor have not yet been reported. So, we decided to develop an imaging probe based on a small molecule. We designed and synthesized novel candidates using computational chemistry based on the results of ALW-II-41-27 as a scaffold, as it was reported to bind to EphA2 receptor kinase with high affinity and also efficiently inhibit cancer progression [5]. As a result, we have developed *N*-(5-((4-((4-ethylpiperazin-1-yl)methyl)-3-(trifluoromethyl)phenyl)carbamoyl)-2-methylphenyl)-5-iodonicotinamide ([^{123}I]ETB), which has potential as a SPECT imaging probe for the EphA2 receptor [6]. In this study, based on the results of [^{123}I]ETB studies, we attempted to develop novel compounds with higher affinity to the EphA2 receptor using computational chemistry.

Method:

Novel compounds (EFT-1 to 7) targeting EphA2 receptor were designed using Molecular Operating Environment. To verify the validity of these calculation results, the designed compounds were synthesized, and their affinities for EphA2 receptor were evaluated. The ability of the synthesized compounds to inhibit EphA2 receptor kinase activity was analyzed using an ADP-Glo™ kinase inhibition assay. Compounds with high kinase inhibitory activity were labeled with radioisotopes, and cellular uptake and organ distribution experiments were performed. For the *in vitro* and *in vivo* evaluation of radiolabeled compounds, the EphA2 receptor-positive U87MG and HT1080 cell

lines were used. Finally, a radiolabeled compound was used for biodistribution experiments in cancer-bearing mice, and SPECT and PET imaging were performed to evaluate whether the compound was useful as an imaging probe.

Result:
From the results of docking simulation, a characteristic interaction was observed between Met695 of EphA2 receptor and the pyridine moiety of ALW-II-41-27. Therefore, ETB and EFT-1 to 7 we designed contain a pyridine ring. Comparison of the measured IC_{50} values results with calculated results from computer simulation showed that there was a close correlation among several compounds (calculated affinity: ALW-II-41-27>ETB>EFT-1>EFT-6, IC50 value: ALW-II-41-27: 419±60 nM, ETB: 578 nM, EFT-1: 1813±399 nM, EFT-6: 88146 nM). In cellular uptake experiments, it was revealed that [^{125}I]ETB and [^{125}I]EFT-1 are taken up by U87MG cells (cell uptake ratio (CUR)/mg protein: ETB: 155±3.9 CUR%/mg, EFT-1: 69±6.1 CUR%/mg at 60 min). The uptake of [^{125}I]ETB into the experimental tumors was clear from reaching 2.2±0.3% ID/g at 240 min post-injection and Tumor/Blood and Tumor/Muscle ratios for each time point (Tumor/Blood = 11.7, Tumor/Muscle = 4.2 at 240 min). Finally, the implanted U87MG tumors in the right limbs of mice were clearly visualized using [^{123}I]ETB in SPECT. Furthermore, this accumulation was inhibited by the pre-administration of ETB.

Discussion:
The compounds designed and synthesized in this study showed a correlation between their affinity for the EphA2 receptor and the calculated values, indicating that the drug design predicted by docking simulation is valid. In the second cycle of evaluation, we succeeded in synthesizing two promising compounds with similar affinities to ALW-II-41-27. At this meeting, we will present the results of cellular uptake experiments, biodistribution experiments, and PET and SPECT imaging experiments of these compounds.

Reference

1. Tandon M. et al, Emerging strategies for EphA2 receptor targeting for cancer therapeutics. Expert Opin. Ther. Targets. 2011;15:31–51.
2. Macrae M. et al, A conditional feedback loop regulates Ras activity through EphA2. Cancer Cell. 2005;8:111–118.
3. Mudd GE. et al, Identification and optimization of EphA2-selective bicycles for the delivery of cytotoxic payloads. J. Med. Chem. 2020;63;4107–4116.
4. Burvenich IJG. et al, Molecular Imaging and Quantitation of EphA2 Expression in Xenograft Models with 89Zr-DS-8895a. J. Nucl. Med. 2016;57;974-980.
5. Martini G. et al, EphA2 is a predictive biomarker of resistance and a potential therapeutic target for improving antiepidermal growth factor receptor therapy in colorectal cancer. Mol. Cancer Ther. 2019;18:845–855.
6. Furukawa T. et al, A putative single-photon emission CT radiotracer for erythropoietin-producing hepatocellular A2 receptor. ACS Med Chem Lett. 2021;12:1238-1244.

Poster Presentation

Disclosures: The authors have disclosed no financial interest.

417-Preclinical assessment of folate receptor-targeted near-infrared photodynamic therapy

Presenter: Winnaung Kuribayashi, National Institutes for Quantum and Radiological Science and Technology

Winnaung Kuribayashi[1], Atsushi Tsuji[2], Aya Sugyo[1], Kenjiro Hanaoka[3], Tatsuya Higashi[1]

[1]*National Institutes for Quantum and Radiological Science and Technology, Chiba, Japan*
[2]*National Institutes for Quantum and Radiological Science and Technology, Chiba, Please Select, Japan*
[3]*Keio University, Tokyo, Japan*

Background:
Photodynamic therapy (PDT) is a minimally invasive therapeutic modality employed in the management of a variety of cancers. To improve the treatment outcome of PDT, it is important to develop a new photosensitizer (PS) with optimal properties for PDT applications. Meanwhile, folate receptor (FR) is a membrane protein that frequently overexpresses in a variety of cancers, accounting for 40% of human cancers and it is a good candidate for tumor-specific targeting and can be exploited for the targeted delivery of PS to cancer.

Aim:
The purpose of this study is to evaluate the therapeutic efficacy of FolateSiR-1, a folate receptor (FR)-targeted, near-infrared (NIR)-sensitive new PS, in animal models.

Methods:
Previously, FolateSiR-1 probe was developed by conjugating a folate ligand moiety to Si-rhodamine derivative fluorophore, through a negatively charged tripeptide linker (*Angew. Chem. Int. Ed.* 59, 6015-6020 (2020). After FR expression in the designated cell lines was examined by western blotting, and the selective binding of FolateSiR-1 to FR was confirmed in FR overexpressing KB cells (FR+) and tumors, by fluorescence microscopy and *in vivo* fluorescence imaging. Low FR expressing OVCAR-3 and A4 cell lines were used as negative controls (FR-). NIR light (635 ± 3 nm)-induced phototoxic effect of FolateSiR-1 on cells was evaluated by cell viability imaging assay. The time-dependent distribution of FolateSiR-1 and its specific accumulation in tumors were determined with *in vivo* longitudinal fluorescence imaging. For evaluation of the phototherapeutic effect of FolateSiR-1, the xenograft tumor-bearing mice were randomly assigned to 4 groups received: (1) intravenous injection of FolateSiR-1 (100 μM) alone, (2) injection of FolateSiR-1 (100 μM) followed by NIR irradiation (50 J/cm^2) at 2 h after injection, (3) only NIR irradiation (50 J/cm^2) and (4) no treatment. Tumor volume measurement was done 2 times per week. Histological and immunohistochemical (IHC) examinations of tumor sections were performed 24 h after the irradiation to check the effect of PDT.

Results:
FR-specific binding of FolateSiR-1 was observed with *in vitro* and *in vivo* fluorescence imaging. Cell viability imaging assay exhibited that NIR-PDT induced cell death. Longitudinal imaging showed that FolateSiR-1 accumulation in tumors reached a peak at about 2 h after injection. *In vivo* PDT conducted at this point caused the tumor growth delay. The relative tumor volumes were significantly reduced in the PDT group compared to the other groups ($P < 0.05$). PDT-treated tumors exhibited the features of necrotic and apoptotic cell death upon hematoxylin-eosin staining and reduction of proliferation marker Ki-67-positive cells upon IHC analysis.

Conclusion:
Our results suggest that FolateSiR-1 has the prospect to be effectively utilized in PDT, and the FR-targeted NIR-PDT can potentially open a new avenue for treatment of FR-overexpressing tumors.

Poster Presentation

Disclosures: The authors have disclosed no financial interest.

418-Ultrasound-enhanced brain delivery of [64Cu]Cu-AAVs assessed by positron emission tomography (PET)

Presenter: Javier Ajenjo, Stanford University

Javier Ajenjo[1], Jai Woong Seo[2], Josquin Foiret[3], Bo Wu[4], Raie Marina[2], Brett Fite[1], Katherine W. Ferrara[2], Corinne Beinat[5]

[1]Stanford University
[2]Stanford University, Palo Alto, CA
[3]Stanford University, Palo Lato, CA
[4]Stanford Universtiy, Palo Alto, CA
[5]Stanford University, Stanford, CA

The use of adeno-associated viruses (AAVs) as a gene transfer platform for the treatment of central nervous system (CNS) disorders, such as neurodegenerative diseases and brain tumors, is a fast-growing approach in molecular medicine.[1] AAVs are non-integrating in vivo vectors with an established clinical safety profile and low pathogenicity. Despite many pre-clinical and in-human trials, few AAV-based gene therapies have been approved for clinical practice. The approved agents, including Luxturna (retinal dystrophy), Zolgensma (spinal muscular atrophy) and Zynteglo (beta thalassemia), rely on naturally occurring AAV serotypes. Challenges for AAV delivery to the brain include the limited efficiency of AAVs in crossing the blood-brain barrier (BBB) and the need to regionally concentrate AAVs encoding for neurotrophic factors. Recent studies focused ultrasound (FUS) mediated delivery of gene therapy have demonstrated its utility to enhance AAV transduction in sonicated regions of the brain.[2] This technique requires a systemic injection of the viral vectors and lipid-based microbubbles, which upon sonication (FUS) oscillate and result in a transient disruption of the BBB. To the best of our knowledge, delivery of viral vectors into the brain has been only assessed by invasive transduction studies.[3] In this study we use PET imaging to quantify the accumulation of AAV9, a naturally occurring AAV serotype with limited BBB transport[4], after unilateral FUS treatment of the brain in murine models (C57BL/6) (Figure 1A, 1B). Biorthogonal conjugation of the AAV9 capsid surface with an in-house designed [^{64}Cu]Cu-(NOTA)$_8$ multichelator[5] allowed non-invasive PET-CT imaging quantitation of viral capsid accumulation in the brain. We find that the accumulation of [^{64}Cu]Cu-AAV9 can be modulated by varying the ultrasound parameters (Figure 1C) and is enhanced in the sonicated region (Figure 1D-E). Mice were insonified under ultrasound guidance with a 1.5 MHz therapeutic array immediately after the injection of 5x10^6 size-isolated lipid microbubbles (mean diameter of 4 microns) and [^{64}Cu]Cu-AAV9 (1x10^{12} vg). Disruption of the BBB was confirmed with 11.7T MRI using T1w imaging with either gadoteridol or gadomer-17, and T2*w imaging confirmed the absence of hemorrhage. Optimal FUS parameters for maximal viral accumulation in target area were: 1.5 MHz, 740 kPa, 1 ms burst per focus position, 5 Hz pulse repetition frequency, 2 min sonication. The maximum accumulation in the treated brain area was 4.6 %ID/cc (estimated by ROI analysis). In conclusion, combined MBs-FUS treatment temporarily disrupts the BBB enhancing AAV9 transduction in targeted areas of the brain and the resulting accumulation has been quantified by PET.

Reference

1. Au, H. K. E., Isalan, M., & Mielcarek, M. Front Med, 8, 809118 (2021). doi:10.3389/fmed.2021.809118.
2. Fischell, J. M., & Fishman, P. S. Front Neurosci, 15, 747726 (2021). doi:10.3389/fnins.2021.747726
3. Concilio, S. C., Russell, S. J., & Peng, K.-W. Molecular Therapy - Oncolytics, 21, 98-109 (2021). doi:10.1016/j.omto.2021.03.006
4. Goertsen, D. et al. Nat. Neurosci. (2021). doi:10.1038/s41593-021-00969-4
5. J. W. Seo et al, Nature Communications. 11 (2020). doi:10.1038/s41467-020-15818-4

Poster Presentation

Disclosures: The authors have disclosed no financial interest.

419-Development of near-infrared imaging agents targeted to the PTPmu tumor biomarker

Presenter: Susann Brady-Kalnay, Case Western Reserve University

Mette Johansen[1], Jason Vincent, Jennifer Major, Andrew Sloan[2], **Susann Brady-Kalnay**[3]

[1]Case Western Reserve University, Cleveland, Ohio
[2]University Hospitals Cleveland Medical Center, Cleveland, Ohio
[3]Case Western Reserve University, Cleveland, OH

Surgical removal of solid tumors is often the first step in cancer treatment. Much effort has been spent recently in developing surgical tools that allow better detection of tumor margins and identification of invasion and metastasis. Recent advances in this area include the development of molecularly-targeted fluorescent imaging agents that aid the surgeon in accurately distinguishing normal from neoplastic tissue in real-time. Of particular importance is the use of Near-Infrared (NIR) fluorophores which provide greater depth of light penetration and are detected at wavelengths where autofluorescence or interference from hemoglobin and other endogenous components is minimal. Glioblastoma (GBM) is among the most challenging tumor types to surgically remove due to its highly invasive and infiltrative characteristics. In GBM, tumor-specific extracellular fragments of PTPmu are generated. PTPmu is a homophilic cell adhesion molecule and a receptor protein tyrosine phosphatase that is normally localized to cell-cell junctions. These PTPmu extracellular fragments remain associated with both the main tumor mass as well as with migratory tumor cells and serve as tumor biomarkers for GBM and other tumor types. Peptides that bind to this PTPmu biomarker were effectively used as recognition and targeting moieties in preclinical imaging of tumors with optical imaging, contrast-enhanced magnetic resonance imaging and ultrasound imaging. In this work, two commonly used NIR fluorophores, indocyanine green (ICG) and IRDye® 800CW, were conjugated to a PTPmu-derived peptide, SBK2, to make tumor-targeted fluorescent imaging agents and evaluated in a preclinical model to determine their potential usefulness for fluorescence-guided resection (FGR). Following injection of NIR-labeled peptides, the labeling of heterotopic human glioma tumors in mice was examined over 24 hours. Results were compared to control scrambled peptides labeled with the same fluorophore. In vivo kidney fluorescence was also examined to characterize biodistribution. To extend and confirm these in vivo findings, tumors were also assessed ex vivo at 24 hours post-injection. In these studies, NIR-conjugated peptides targeted to the PTPmu biomarker recognized tumors with high specificity and favorable kinetics, and show promise for use in the operating room during FGR.

Poster Presentation

Disclosures: The authors have disclosed no financial interest.

420-Development of Optimal PET/CT Imaging Methods for the Diagnosis and Monitoring Disease Progression of Atherosclerosis

Presenter: Mikayla Tamboline, Crump Institute for Molecular Imaging

Mikayla Tamboline[1], Jeffrey Collins[1], John O. 2025[2], Richard Taschereau[1], Arion Chaziioannou[1], Simon Jackson[3], Tayo Ikotun[4], Shili Xu[5]

[1]*Crump Institute for Molecular Imaging, Los Angeles, California*
[2]*Amgen, Thousand Oaks, California*
[3]*Amgen, South San Francisco, California*
[4]*University of California, Los Angeles, Los Angeles, CA*
[5]*David Geffen School of Medicine at UCLA, Los Angeles, California*

In the Western world, cardiovascular disease continues to be the leading cause of death and is the predominant reason for cardiovascular events such as stroke, ischemia, and myocardial infarction (1). Atherosclerosis is a key contributor to these cardiovascular events (2). Using genetically engineered mouse models of disease, microPET using 18F-FDG and 18F-NaF, and microCT has been successfully utilized for non-invasive visualization of disease pathology. 18F-FDG uptake in inflamed plaques measures glucose consumption by activated macrophages within the aorta vessel walls (3). Inflammation triggers calcifying extracellular vesicles (EVs) that are released by macrophages and vascular smooth muscles and microcalcification results from aggregation and fusion of individual EVs. 18F-NaF PET detects this active process via 18F incorporation into areas of calcium deposition (4). Alternatively, the macroscopic presences of calcification associated with atherosclerosis progressive disease can be measured with microCT (2). While each modality measures various hallmarks of disease, they individually have their limitations (3). For these reasons, a comprehensive side-by-side comparison of each imaging assay at various stages of disease has been proposed. It was hypothesized that 18F-FDG and 18F-NaF will serve as early markers of disease while microCT will prove most effective at later disease stage. In this study, 6week old ApoE deficient mice (ApoE -/-) were placed on a high cholesterol diet at weeks 12-20 . Age-matched wildtype C57BI/6 mice fed regular chow were used as the control group. Mice underwent imaging at weeks 12, 15, 18, and 20 weeks of age or 6, 9, 12, and 14 weeks after starting the high cholesterol diet. For 18F-FDG PET studies, images were acquired 3 and 5 hours post tracer injection. For 18F-NaF PET studies, images were acquired at 1 and 3 hours post tracer injection. High-resolution in vivo microCT images were acquired at 80 kVp for 1 minute (100 μm voxel) immediately following PET imaging to visualize micro- and macro-calcification. Images were analyzed using Amide software. For 18F-NaF, a 5x4x2 mm ROI was automatically segmented above the heart using a 1 mm boundary from rib bones, and a signal intensity threshold of 2 %ID/cc. For microCT, a 6x6x4mm ROI with a Hounsfield (HU) value threshold of 350 was used (HU water = 0). For 18F-FDG images, the whole-heart ROI and an aorta were obtained. It was observed that 18F-NaF PET detected atherosclerotic lesions earlier than microCT or 18F-FDG. However, 18F-NaF PET could not monitor disease progression beyond week 18. MicroCT proved effective for monitoring disease progression from weeks 15 – 20 . While 18F-FDG PET signal in the whole heart was unchanged, 18F-FDG accumulation in the aorta of ApoE -/- mice was significantly higher than control at 5 hours post injection at week 12 and week 15, but no significance was observed in weeks 18 and 20. The study reveals that 18F-NaF PET detects disease significantly earlier than other imaging modalities, however high-resolution microCT is best utilized for monitoring late-stage disease.

Reference

1. Bucerius, J., Dijkgraaf, I., Mottaghy, F.M. et al. Target identification for the diagnosis and intervention of vulnerable atherosclerotic plaques beyond 18F-fluorodeoxyglucose positron emission tomography imaging: promising tracers on the horizon. Eur J Nucl Med Mol Imaging 46, 251–265 (2019). https://doi.org/10.1007/s00259-018-4176-z
2. Cocker, M.S., Mc Ardle, B., Spence, J.D. et al. Imaging atherosclerosis with hybrid [18F]fluorodeoxyglucose positron emission tomography/computed tomography imaging: What Leonardo da Vinci could not see. J. Nucl. Cardiol. 19, 1211–1225 (2012). https://doi.org/10.1007/s12350-012-9631-9
3. Schillaci O, Danieli R, Padovano F, Testa A, Simonetti G. Molecular imaging of atheroslerotic plaque with nuclear medicine techniques. Int J Mol Med. 2008 Jul;22(1):3-7. PMID: 18575769.
4. Czernin J, Satyamurthy N, Schiepers C. Molecular mechanisms of bone 18F-NaF deposition. J Nucl Med. 2010 Dec;51(12):1826-9. doi: 10.2967/jnumed.110.077933. Epub 2010 Nov 15. PMID: 21078790; PMCID: PMC3169430.

Poster Presentation

Disclosures: The authors would like to disclose that GNEXT preclinical PET/CT instrument, made by Sofie Biosciences, has been approved.

421-Development of Nanophosphor Excited Oxygen Sensor to Quantify the Oxygen Levels in the Hypoxic Tissue

Presenter: Vigjna Abbaraju, Clemson University

Vigjna Abbaraju[1], Jeffrey Anker[1], Sriparna Bhattacharya[2]

[1]*Clemson University, Clemson, SC*
[2]*Clemson University, Clemson, South Carolina*

Low oxygen (hypoxic) environments play an important role in maintaining the small number of adult stem cells in the human body, such as in bone marrow, and also believed to enable dormant cancer cells to survive and undergo metastasis. Therefore, *in vivo* monitoring of oxygen levels in such tissues is necessary in developing better therapeutic strategies for preventing cancer relapse and improving stem cell treatment. We are developing a novel reversible oxygen sensor to measure the oxygen gradients in the hypoxic tissues using X-rays Excited Luminescent Chemical Imaging (XELCI) system. Oxygen sensor is made of scintillator (top layer) and oxygen dye PDMS films (bottom layer). The focused X-rays when irradiated on the scintillator film ($SrAl_2O_4$ or Gd_2O_2S:Tb particles) generate photons from 430-620 nm with λ_{max}-500 nm in the focal region which excites the oxygen dye film (Platinum(II) tetrakis (pentafluorophenyl) porphyrin or Platinum(II) octaethyl porphyrin ketone) at emission wavelength overlapping with absorbance of oxygen indicator. This results in attenuation in the luminescent spectrum of scintillator at wavelengths absorbed and phosphorescence from indicator dye where the intensity is quenched in the presence of molecular oxygen. Our preliminary results show proof of principle of working of our oxygen sensor under X-ray excitation at varying oxygen environments. Our further studies will focus on acquiring images of the oxygen sensor with changing emission intensities in different oxygen environments through tissue by X-ray scanning the sample placed on a stage, collected using acrylic light guide and detected with

a photomultiplier tube (PMT). In conclusion, our approach could be useful for deep understanding hypoxic tissue microenvironments and give scope for developing better treatment strategies.

Poster Presentation

Disclosures: The authors have disclosed no financial interest.

422-Efficacies of Quantitative Indexes from FDG PET/CT in Prediction of Prognosis in Biliary Cancer

Presenter: Hyun Joo Kim, Korea University

Hyun Joo Kim[1], Jae Seon Eo[2], Hyun Woo Kwon[1]
[1]*Korea University, Seoul, South Korea*
[2]*Korea University Guro Hospital, Seoul, Seoul, Republic of Korea*

Purpose:
Biliary cancers are rare malignancies originating from biliary system, including bile ducts and gallbladder. Since the patients are usually diagnosed at advanced stage, the 5-year survival rates are generally lower than 30%. The purpose of this study was to investigate the effectiveness of quantitative indexes derived from ^{18}F-fluorodeoxyglucose (FDG) positron emission tomography/computed tomography (PET/CT) in the evaluation of biliary cancer and its predictive value.

Method:
A total of 314 biliary cancer patients who performed FDG PET/CT from 2015 to 2021 were retrospectively enrolled. Progression-free survival (PFS) and overall survival (OS) were determined by follow-up PET/CT and clinical record. Maximum standardized uptake value (SUVmax), metabolic tumor volume (MTV), and total lesion glycolysis (TLG) were measured in the primary tumor lesion. The efficacies of these quantitative indexes along with clinical, biochemical factors regarding the prediction of PFS and OS were investigated.

Result:
Quantitative indexes derived from initial PET/CT were useful in predicting recurrence and overall survival. MTV and TLG from initial PET were significant in predicting recurrence ($p = 0.0221$, 0.0198, respectively). In predicting overall survival, SUVmax, MTV, TLG from initial PET were all statistically significant, along with tumor markers of CA19-9 and CEA ($p = 0.0003$, 0.0004, 0.0001, 0.0001, 0.0042, respectively). In multivariate Cox regression analysis, CA19-9 and TLG remained significant in the prediction of OS ($p = 0.0005$ and 0.0160, respectively). Among the 89 recurred patients, CA19-9 at the time of recurrence and MTV, TLG from recurred PET were statistically significant in predicting OS ($p = 0.0001$, 0.0020, 0.0004, respectively).

Conclusion:
Quantitative PET indexes can be used as predictive indicators of prognosis in biliary cancer, especially in predicting overall survival. MTV and TLG of the tumor lesion from initial and recurred PET can be effective in prediction of prognosis in biliary cancer.

Poster Presentation

Disclosures: The authors have disclosed no financial interest.

423-Probing HIV, anti-retroviral drugs, and nicotine interactions via CEST-MRI

Presenter: Gabriel Gauthier, University of Nebraska Medical Center

Gabriel Gauthier

University of Nebraska Medical Center

Background:
The Chemical Exchange Saturation Transfer (CEST) effect, characterized by the exchange of spin saturation from liable proton compounds to those of adjacent water molecules[1], is now being used as a novel Magnetic Resonance Imaging (MRI) contrast agent[1-4]. Through this approach, known as CEST-MRI, it is now possible to probe the body *in vivo* for compounds of interest (including many key metabolites and drugs) that exist in previously unobservable locations and concentrations.[1-4] In our investigation, we used CEST-MRI to study metabolic alterations in the central nervous system (CNS) of mice administrated with combinational antiretroviral therapy (cART) and nicotine. Keywords: CEST, MRI, CEST-MRI, Anti-retroviral, cART, HIV

Materials and Methods:
Twelve C57BL/6 mice were divided into four groups of three. Group 1 was given cART (Dolutegravir (DTG, 51.25 mg/kg/day), Lamivudine (3TC, 250 mg/kg/day), and Abacavir (ABC, 500 mg/kg/day)) for 12 days via oral gavage. Group 2 was injected with nicotine (2 mg/kg/day in 100 uL saline) through i.p. for 12 days. Group 3 was administrated with both cART and nicotine. Group 4 was administrated with the administration vehicle alone and were used as controls. CEST-MRI was performed on a 7 T scanner (Bruker BioSpec, Billerica, MA) with a volume coil for RF transmission and a 4-element array coil for reception. For each scan, data was collected using the RARE sequence, with offsets ranging from -5 to +5 ppm, divided into steps of 0.2 ppm, and utilizing an RF power of 2 uT, and duration of 1 second. CEST data was fitted using 5-pool Lorentzian functions, as demonstrated in a previous study.[5]

Results:
Figures 1A-B represent the fitted metabolite curves in the cortex (CTX) and hippocampus (HIP) at 3.5ppm, with solid lines denoting group-averaged values with mean standard errors. Figure 1C shows the corresponding area-under-curve (AUC) calculated from 1A-B. Contrasting these figures, both nicotine-dosed groups experienced a clear drop in the CEST effect at 3.5 ppm, both relative to their comparable non-nicotine group and overall. The mice administrated with nicotine (1F-G) showed a lower CEST effect than the mice administered with vehicle-only (1D) and cART-only (1E). To aid in the visualization of this trend, color maps of the 3.5 ppm CEST effect in the CTX and HIP are provided for all groups in Figure 1D-G. Knowing that the CEST effect of glutamate occurs at 3 ppm, it seems plausible that the ingestion of nicotine may decrease glial glutamate release. Using a similar technique, the effect of other nicotine-linked metabolites (e.g. myo-inositol/glucose at ~1ppm) can be assessed.

Discussion:
Expanding upon nicotine's well-documented immunocompromising and neuroinflammatory properties[6-8], growing evidence suggests ARVs and nicotine induce a form of mutual metabolic modulation: nicotine can cause altered metabolism of ARVs, altering their pharmokinetics (PK), while ARVs can lead to variable metabolism of nicotine.[9-17] This feedback loop may result in highly variable drug efficacy for a regime that requires consistency. Noting the high incidence of nicotine usage in people living with HIV (PLWH),[18] the nicotine-related metabolite glutamate's crucial role in healthy CNS function, and the troublesome pervasiveness of HIV-associated neurological

disorders (HAND) for PLWH[19], the described study aimed to monitor interactions between ARV, and nicotine with CEST-MRI.
While there are no additional insights into ARV-nicotine interaction, the provided data suggests that regular nicotine use may decrease the secretion of glutamate in the brain in fewer than 12 days, seemingly contradicting previous analyses.[20-22] This contradiction may be due to withdrawal, as nicotine was not administered on the day the CEST scan took place, but this phenomenon warrants additional investigation either way. Follow-up investigations will increase sample size and include additional metabolites of interest.

Reference

1. Ward KM, Aletras AH, Balaban RS. A New Class of Contrast Agents for MRI Based on Proton Chemical Exchange Dependent Saturation Transfer (CEST). Journal of Magnetic Resonance 2000; 143(1):79-87.
2. van Zijl PC, Yadav NN. Chemical exchange saturation transfer (CEST): what is in a name and what isn't? Magnetic resonance in medicine 2011; 65(4):927-948.
3. Liu G, Song X, Chan KW, McMahon MT. Nuts and bolts of chemical exchange saturation transfer MRI. NMR Biomed. 2013 Jul;26(7):810-28. doi: 10.1002/nbm.2899. Epub 2013 Jan 10. PMID: 23303716; PMCID: PMC4144273.
4. Wu B, Warnock G, Zaiss M, Lin C, Chen M, Zhou Z, et al. An overview of CEST MRI for non-MR physicists. EJNMMI physics 2016; 3(1):19.
5. Bade AN, Gendelman HE, McMillan J, Liu Y. Chemical exchange saturation transfer for detection of antiretroviral drugs in brain tissue. Aids 2021; 35(11):1733-1741.
6. Vassallo R, Kroening PR, Parambil J, Kita H. Nicotine and oxidative cigarette smoke constituents induce immune-modulatory and pro-inflammatory dendritic cell responses. Mol Immunol 2008; 45(12):3321-3329.
7. Vassallo R, Tamada K, Lau JS, Kroening PR, Chen L. Cigarette smoke extract suppresses human dendritic cell function leading to preferential induction of Th-2 priming. J Immunol 2005; 175(4):2684-2691.
8. Yanagita M, Kobayashi R, Kojima Y, Mori K, Murakami S. Nicotine modulates the immunological function of dendritic cells through peroxisome proliferator-activated receptor-gamma upregulation. Cell Immunol 2012; 274(1-2):26-33.
9. Durazzo TC, Rothlind JC, Cardenas VA, Studholme C, Weiner MW, Meyerhoff DJ. Chronic cigarette smoking and heavy drinking in human immunodeficiency virus: consequences for neurocognition and brain morphology. Alcohol 2007; 41(7):489-501.
10. Liang H, Chang L, Chen R, Oishi K, Ernst T. Independent and Combined Effects of Chronic HIV-Infection and Tobacco Smoking on Brain Microstructure. J Neuroimmune Pharmacol 2018; 13(4):509-522.
11. Earla R, Ande A, McArthur C, Kumar A, Kumar S. Enhanced nicotine metabolism in HIV-1-positive smokers compared with HIV-negative smokers: simultaneous determination of nicotine and its four

Poster Presentation

Disclosures: The authors have disclosed no financial interest.

424-Dual-channel near-infrared fluorescence imaging for simultaneous identification of lung cancer and intersegmental plane

Presenter: Ok Hwa Jeon

Ok Hwa Jeon[1], Kai Bao[2], Kyungsu Kim[3], Haoran Wang[2], Shinya Yokomizo[4], G. Kate Park[2], Byeong Hyeon Choi[5], Jiyun RHO[6], Chungyeul Kim[7], Hak Soo Choi[8], Hyun Koo Kim[9]

[1]*Seoul, South Korea*
[2]*Gordon Center for Medical Imaging (MGH/HMS), Boston, MA*
[3]*Korea University, South Korea*
[4]*Massachusetts General Hospital, Charlestown, Massachusetts*
[5]*Korea University, Seoul, Other, Republic of Korea*
[6]*Korea University, Seoul, South Korea*
[7]*Korea University Guro Hospital, Seoul, South Korea*
[8]*Massachusetts General Hospital, Boston, MA*
[9]*Korea University Guro Hospital, Seoul, Republic of Korea*

Intraoperative delineation of the tumor with negative margins is the holy grail of cancer surgery. Segmentectomy is preferred for early-stage lung cancer patients due to the preservation of lung function with minimal tissue resection, which requires an accurate detection of the intersegment plane and tumor margins. Herein, we report dual-channel targeted NIR fluorophores for image-guided precise resection of lung tumors with minimal negative margins: cRGD-ZW800-PEG (800 nm channel) for tumor-specific targeting with improved renal clearance and physicochemical stability, whereas ZW700-1C (700 nm channel) for intraoperative discrimination of lung segmental planes. cRGD-ZW800-PEG provided much improved tumor targeting compared with other fluorophores with providing tumor-to-background ratios greater than 3.5 in three animal models of lung cancer. Armed with the dual-channel imaging, our study of fluorescence image-guided surgery enables complete tumor resection with negative margins and has the potential to reduce the recurrence rate and increase the survival rate of cancer patients.

Reference

1. Handgraaf, H.J.M., et al. Real-time near-infrared fluorescence imaging using cRGD-ZW800-1 for intraoperative visualization of multiple cancer types. Oncotarget 8, 21054-21066 (2017). 22.
2. de Valk, K.S., et al. First-in-Human Assessment of cRGD-ZW800-1, a Zwitterionic, Integrin-Targeted, Near-Infrared Fluorescent Peptide in Colon Carcinoma. Clinical cancer research: an official journal of the American Association for Cancer Research 26, 3990-3998 (2020).

Poster Presentation

Disclosures: The authors have disclosed no financial interest.

425-Simultaneous Fluorescence Visualization of Lung Cancer and Intersegmental Planes using Indocyanine Green during Segmentectomy

Presenter: Kyungsu Kim, Korea University

Kyungsu Kim[1], Ok Hwa Jeon[2], Byeong Hyeon Choi[3], Jiyun RHO[4], Jun Hee Lee[5], Beop-Min Kim, Hyun Koo Kim[6]

[1]*Korea University, South Korea*
[2]*Seoul, South Korea*
[3]*Korea University, Seoul, Other, Republic of Korea*
[4]*Korea University, Seoul, South Korea*
[5]*Korea University Guro Hospital, Seoul, South Korea*
[6]*Korea University Guro Hospital, Seoul, Republic of Korea*

Background:
Segmentectomy is a minimal resection surgery required for elderly patients and early-stage lung cancer, in which accurate detection of tumor margins with simultaneous identification of the lung intersegment plane is the key to success.

Purpose:
To assess the feasibility of a technique for simultaneous visualization of lung cancer and intersegment planes by fluorescence imaging using intravenously injected indocyanine green (ICG) at different time points and dose.

Methods:
A rabbit model with lung tumor was established using VX2 cancer cells, and ICG (2 mg/kg) were injected intravenously 12 hours before surgery. After identifying the lung tumor using the fluorescence signal, the pulmonary artery segment supplying the target segment was ligated and ICG (0.5 mg/kg) was injected intravenously. Next, we enrolled 3 consecutive patients scheduled for segmentectomy in the Korea University Guro Hospital, and evaluated the feasibility of a technique for simultaneous visualization of lung cancer and intersegment planes using intravenously injected ICG. The near-infrared (NIR) fluorescent image of lung cancer and intersegment planes was detected both preclinical and clinical study.

Result:
ICG fluorescence imaging simultaneously visualized the lung tumor and the intersegmental plane of the targeted segment in all rabbit models. The resection margin of the lung cancer and intersegmental planes were also successfully determined during surgery in a patient with lung cancer, and the segmentectomy was performed. There were no complications due to ICG.

Conclusion:
Armed with the simultaneous visualization of lung cancer and intersegment planes by fluorescence imaging, image-guided surgery enables complete tumor resection with minimal negative margins that can improve quality of life and increase the survival rate of cancer patients.

Reference

1. Oh Y, Quan YH, Kim M, Kim BM, Kim HK. Intraoperative fluorescence image-guided pulmonary segmentectomy. J Surg Res. 2015 Dec;199(2):287-93. doi: 10.1016/j.jss.2015.05.009. Epub 2015 May 13. PMID: 26115807.
2. Choi BH, Young HS, Quan YH, Rho JY, Eo JS, Han KN, Choi YH, Kim HK. Real-time computed tomography fluoroscopy-guided solitary lung tumor model in a rabbit. PLoS One. 2017 Jun 13;12(6):e0179220. doi: 10.1371/journal.pone.0179220. Erratum in: PLoS One. 2018 Feb 2;13(2):e0192527. PMID: 28609443; PMCID: PMC5469482.

Poster Presentation

Disclosures: The authors have disclosed no financial interest.

426-Optimization of Indocyanine Green for Intraoperative Fluorescence Image-guided Thoracoscopic Resection of Lung Cancer

Presenter: Ok Hwa Jeon

Ok Hwa Jeon[1], Byeong Hyeon Choi[2], Jiyun RHO[3], Jun Hee Lee[4], Beop-Min Kim, Hyun Koo Kim[5]

[1]Seoul, South Korea
[2]Korea University, Seoul, Other, Republic of Korea
[3]Korea University, Seoul, South Korea
[4]Korea University Guro Hospital, Seoul, South Korea
[5]Korea University Guro Hospital, Seoul, Republic of Korea

Objective:
Indocyanine green (ICG) fluorescence imaging has been tried to detect lung cancers during surgery. However, there is no consensus on the optimization of ICG injection for identification of lung cancer. This study aims to find an optimal ICG dose and time for detecting lung cancers in animal models, and further evaluated the feasibility of ICG fluorescence to detect in patients with early-stage of lung cancer.

Methods:
Twenty C57BL/6 mice with lewis lung carcinoma (LLC) footpad cancer and 27 rabbits with VX2 lung cancer were used in this study. These animals received ICG with 0.5, 1, 2, and 5 mg/kg, and the cancers were detected using an in vivo fluorescent imaging system after 3 ,6, 12 and 24h. Forty six patients diagnosed with lung cancer and scheduled to undergo surgery were included. We detected lung cancer and measured the fluorescent signal of lung cancer, and the fluorescence signal in cancer was quantified by the fluorescent signal of tumor-to-normal (TNR) ratio.

Results:
In mouse and rabbit cancer models, intravenous injection of ICG at a dose of 1 mg/kg to 5 mg/kg can detect lung cancer after 6 hours to 24 hours. Among the 46 cases, ICG successfully detected 34 of 36 cases (72%) with the consolidation-to tumor (C/T) ratio >50% (mean TNR was 3.3 ± 1.2), while in 2 cases (4%) failure of the ICG detection was due to the presence of black pigments in the lung cancer tissue. The remaining 11 cases (23%) had C/T ratio ≤50% ICG failed to detect lung cancer.

Conclusions:
ICG with 2 mg/kg before 12 h surgery was the optimal injection method for intraoperative lung cancer detection. Lung cancers with C/T ratio >50% were successfully detected using the ICG image. The detection rate of lung cancer with C/T ratio >50% was 94%.

Poster Presentation

Disclosures: The authors have disclosed no financial interest.

427-Gd(III) complex-backboned branched polymers with high kinetic stability and T1 relaxivity for magnetic resonance angiography

Presenter: Shengxiang Fu, West China Hospital, Sichuan University

Shengxiang Fu[1], min wu[2], Hua Ai[3], Bin Song[1]

[1]West China Hospital, Sichuan University, China
[2]West China Medical Center of Sichuan University, Chengdu, Si Chuan Province, China
[3]Sichuan University, China

Statement of Purpose:
Dendrimers-based polymer contrast agents with high kinetic stability and increased T_1 relaxivity have been widely used in magnetic resonance imaging (MRI). However, most of them were prepared by grafting small molecules contrast agents to the surface of dendrimers,

causing a waste of the internal skeleton, and unsatisfactory increase in T_1 relaxivity. In addition, the tedious synthetic process of dendrimers bringing them the difficulty of achieving sufficient quantity and broad applications in practice. Branched polymers with cascade-branch structures are usually synthesized through simple 'Ax+By' type one-pot polymerization, possessing the same advantages as dendrimers and being considered to be the most ideal alternative to dendrimers for preparation of polymer contrast agents. Herein, DOTA-backboned branched polymers were synthesized by simple 'A_2+B_4' type one-pot polymerization, showing high Gd(III) chelation stability and T_1 relaxivity.

Methods:
1) Four DOTA-backboned branched polymers (G1, G2, G3 and G4) with increasing molecular weights and degrees of branching were synthesized by simple 'A_2+B_4' type one-pot polymerization with two monomers of ethylenediaminetetraacetic dianhydride (A_2) and 1,4,7,10-tetraazacyclododecane (B_4), and then chelating Gd(III) at pH 7.4. 2) the kinetic stability of Gd(III) complex-backboned branched polymers was evaluated by ASIII colorimetric assay at pH 1.5. 3) The T_1 relaxivity (0.5, 1.0 and 3.0 T) and *in vivo* magnetic resonance angiography (MRA, 3.0 T) of Gd(III) complex-backboned branched polymers were then evaluated.

Results:
Free Gd(III) can combine with Arsazo(AS) to form Gd(III)-AS complex which give a new UV absorption peak at 660 nm (Figure 1b), therefore the Gd(III) dissociation percentage of Gd(III) chelates can be calculated from such absorbance value (Figure 1c). After mixing with AS at pH 1.5 for 168 h, Gd(III) was almost completely dissociated from DTPA-Gd and show similar UV absorption value to $GdCl_3$ at 660 nm, due to its low dynamic stability. G4-Gd with the highest molecular weight and degrees of branching show significantly lower absorption value than DTPA-Gd, gadobutrol and other Gd(III) complex-backboned branched polymers, demonstrating its higher dynamic stability. G4-Gd with significantly higher T_1 relaxivity than DOTA-Gd and other Gd(III) complex-backboned branched polymers (Figure 1d), showing clearer magnetic resonance angiography (MRA) (Figure 1e-h).

Conclusions:
Gd(III) complex-backboned branched polymers with high kinetic stability, significantly increased T_1 relaxivity and excellent MRA effect were successfully prepared.

Acknowledgments: The work was supported by National Natural Science Foundation of China (No. 81971571), and Sichuan Foundation for Distinguished Young Scholars (No. 2022JDJQ0049).

Reference
1. S. Langereis, A. Dirksen, T. M. Hackeng, M. H. Van Genderen, E. Meijer, New J. Chem. 2007, 31, 1152;
2. Y. Cao, M. Liu, G. Zu, Y. Kuang, X. Tong, D. Xiong, R. Pei, Polym. Chem. 2017, 8, 1104.

Poster Presentation

Disclosures: The authors have disclosed no financial interest.

428-Light Sheet Fluorescence Microscopy (LSFM) and In Vivo Imaging System (IVIS) Imaging of CRANAD-2 Targeting Aβ Deposits in APP/PS1 Transgenic Mouse Model of Alzheimer's Disease

Presenter: Lei Bi, Fifth Affiliated Hospital of Sun Yat-sen University

Lei Bi[1], Peizhen Ye[1], Guolong Huang[1], Kui Huang[1], Yifan Qiu[1], Yanfang Shen[1], Jianzhong Xian[2], Xiaofang Huang[1], Hongjun Jin[3]

[1]Fifth Affiliated Hospital of Sun Yat-sen University, Zhuhai, China
[2]Fifth Affiliated Hospital of Sun Yat-sen University, Zhuhai, China, China
[3]The Fifth Affiliated Hospital, Sun Yat-sen University, Zhuhai City, Guangdong, China

Introduction:
Light sheet fluorescence microscopy (LSFM) is a fluorescence microscopy technique with an intermediate-to-high optical resolution, but good optical sectioning capabilities. In contrast to conventional microscopy only a thin slice of the sample, LSFM provides axial resolution, restrict photobleaching and phototoxicity to a fraction of the sample and use cameras to record tens to thousands of images per second. LSFM is used for in-depth analyses of large, optically cleared samples and long-term three-dimensional (3D) observations of live biological specimens at high spatio-temporal resolution. In this study, curcumin derivative CRANAD-2, previously reported Aβ-peptide targeting fluorescence imaging probe, was used for LSFM and in vivo imaging system (IVIS) fluorescence imaging to trace the distribution of Aβ deposits in transgenic mouse model of Alzheimer's disease.

Methods:
Twenty-seven-month-old APP/PS1 transgenic AD mice (n = 3) and normal age-matched healthy C57 mice (n = 3) were injected CRANAD-2 (1 mg/kg) through tail vein. AD and healthy mice were performed IVIS fluorescence imaging (PerkinElmer Health Sciences, IVIS Lumina III) for fifty minutes. Then after euthanized animals, the brain tissues were collected, half brains of AD and healthy mice were imaged by LSFM instrument (LaVision Biotec Ultramicroscope II equipped with sCMOS camera, excitation wavelength = 630/30 nm, emission wavelength = 680/30 nm). Meanwhile another half brains were frozen sectioned as 10 μm, histologically stained by CRANAD-2 (50 μmol/L), Thioflavin T (10 μmol/L) and DAPI, and observed by axio observer 7 microscope (ZEISS, Germany).

Results:
Through IVIS fluorescence imaging and quantitative analysis, it was found that CRANAD-2 was high uptake in the brain of AD mice and the corrected total radiant efficiency of AD was twice that of healthy mice (Fig 1B). By the image of LSFM, it was found that CRANAD-2 was not only highly ingested in AD mice, but also centralized distribution in cerebral cortex, hippocampus and cerebellum cortex (Fig 1C). At the same time, tissue fluorescence staining was verified that CRANAD-2 and ThioT were co-localized in AD mice for Aβ deposits (Fig 1D).

Conclusions:
Curcumin derivative CRANAD-2 could directly bind to Aβ aggregation in the central nervous system, and showed significant higher uptake in the brain of AD mice compared to the age-matched healthy controls. LSFM, for the first time showed that CRANAD-2 was centralized distribution in cerebral cortex, hippocampus and cerebellum cortex, which might reveal brain area with high expression of Aβ aggregations.

Reference
1. Ran C, Xu X, Raymond SB, Ferrara BJ, Neal K, Bacskai BJ, Medarova Z, Moore A. Design, synthesis, and testing of difluoroboron-derivatized curcumins as near-infrared probes for

in vivo detection of amyloid-beta deposits. J Am Chem Soc. 2009;131(42):15257-61.
2. Ni R, Villois A, Dean-Ben XL, Chen Z, Vaas M, Stavrakis S, Shi G, deMello A, Ran C, Razansky D, Arosio P, Klohs J. In-vitro and in-vivo characterization of CRANAD-2 for multi-spectral optoacoustic tomography and fluorescence imaging of amyloid-beta deposits in Alzheimer mice. Photoacoustics. 2021;23:100285.
3. Zhang X, Tian Y, Li Z, Tian X, Sun H, Liu H, Moore A, Ran C. Design and synthesis of curcumin analogues for in vivo fluorescence imaging and inhibiting copper-induced cross-linking of amyloid beta species in Alzheimer's disease. J Am Chem Soc. 2013;135(44):16397-409.

Poster Presentation

Disclosures: The authors have disclosed no financial interest.

429-Assessment of silver sulfide nanoparticles as a contrast agent for spectral photon-counting mammography

Presenter: Jessica Hsu, University of Pennsylvania

Jessica C. Hsu[1], Kristen Lau[2], Björn Cederström[3], Mats Lundqvist[4], Andrew A. Maidment[5], David Cormode[2]

[1]*University of Pennsylvania*
[2]*University of Pennsylvania, Philadelphia, PA*
[3]*Philips Healthcare, Kista, Kista, Sweden*
[4]*Philips Healthcare, Kista, Sweden*
[5]*Philadelphia, PA*

Introduction:
Mammography has extended in recent years to include a dual-energy approach, which is based on K-edge imaging. This technique utilizes contrast agents to increase tumor detection in women with dense breasts through weighted subtraction between the low- and high-energy images. However, dual-energy mammography (DEM) requires two sequential exposures at two different energies, leading to higher doses as well as misregistration artifacts from patient movement. On the other hand, spectral mammography, an emerging technology similar to DEM, but making use of photon-counting detectors, provides energy information via a single x-ray exposure. This system uses less radiation than DEM, without impacting image quality, and eliminates motion artifacts associated with DEM. This technique has also been shown to improve contrast-to-noise ratios (CNR) and specificity without contrast injection, resulting in better breast lesion characterization. Currently, contrast-enhanced mammography is performed using iodinated small molecules, but these agents produce sub-optimal contrast due to iodine's relatively high K-edge. Thus, there exists a need to explore novel imaging agents that are explicitly designed for contrast-enhanced photon-counting mammography.

Methods and Results:
Recently, our group identified silver sulfide nanoparticles (Ag_2S-NP) to generate stronger contrast than iodine in DEM, as silver's lower K-edge is well matched to the energies used. We therefore decided to investigate the feasibility of using Ag_2S-NP as a spectral mammography specific contrast agent. In this study, monodisperse, ultrasmall Ag_2S-NP were synthesized by heating a mixture of silver nitrate and glutathione in ethylene glycol (Fig. S1) and were purified via repeated centrifugation. These nanoparticles were characterized using various analytical tools such as TEM, DLS, and zeta potential (Fig. A). They remain well suspended in PBS and serum, proving their robust stability under physiological conditions. The biocompatibility of Ag_2S-NP was evaluated using the LIVE/DEAD assay in five cell lines after 24 hours of treatment. Nearly 100% relative cell viability was observed even at a dose of 1 mg Ag/ml, indicating good biocompatibility (Fig. S2). To evaluate the potential of Ag_2S-NP as a photon-counting mammography contrast agent, a Philips MicroDose SI prototype mammography system was used to image a customized ramp phantom composed of adipose and glandular tissue-equivalent materials. The following acquisition parameters were used: 26-40 kV, 12-24 mAs, and 0.28-0.40 high bin fractions (HBF). Ag_2S-NP with concentrations ranging from 1 to 30 mg Ag/ml along with PBS and water were inserted in the phantom (Fig. B). Analysis of the phantom images shows a linear correlation between Ag_2S-NP concentration and DE signal at each scanning condition (Fig. S3). Ag_2S-NP produce significantly higher CNR than iodine over the concentrations (Fig. S4) and energies used, while iodine signal is not detectable below 35 kV (Fig. C). The imaging sensitivity of Ag_2S-NP is significantly greater than that of iodine, even at energies above iodine's K-edge (Fig. D). The optimal energy for detection of iodine is beyond the clinical mammographic energy range. Lastly, HBF calibration, which determines the threshold energy for count binning, could be further reduced to enhance the contrast of Ag_2S-NP (Fig. E). Therefore, silver can be imaged at lower mammographic energies (< 35 kV) without compromising image quality, which results in radiation dose savings (Fig. S5).

Conclusion:
We have synthesized Ag_2S-NP that have good stability and excellent biocompatibility. When compared to iodine, these nanoparticles provide improved contrast production, dose efficiency and sensitivity in photon-counting mammography at clinically relevant beam energies, demonstrating their utility as a contrast agent for this new technique for breast cancer screening.

Poster Presentation

Disclosures: The authors have disclosed no financial interest.

430-Development of a versatile radiolabeled nanosystem for cancer theranostics

Presenter: Twiany Cruz-Dubois, CERIMED Aix-Marseille Université

Twiany Cruz-Dubois[1], Béatrice Louis[2], Vincent Nail[1], Ahlem Bouhlel[1], Laure Balasse[3], Françoise Dignat-George[3], Ling Peng[3], Philippe Garrigue, Benjamin Guillet, Tom Roussel[4], Adrien Chabert[1], Anaïs Moyon[5]

[1]*CERIMED Aix-Marseille Université, France*
[2]*Aix-Marseille University, Marseille Cedex 07, France*
[3]*Aix-Marseille University, Marseille, France*
[4]*Aix-Marseille University*
[5]*CERIMED Aix-Marseille Université*

Introduction:
The use of nanoparticles as delivery systems has been widely explored for cancer theranostics (1). Dendrimeric nanosystems have become popular as drug-delivery systems due to their size and their capability of self-assembling (2). Due to the Enhanced Permeability and Retention (EPR) effect, the dendrimers preferentially accumulate in tumor tissues (3). We previously developed radiolabeled dendrimers with gallium-68 and indium-111 respectively for PET and SPECT imaging of EPR effect variability in tumors, and successfully added an active targeting towards integrins (4,5). Here, we developed the radiolabeling

of two different self-assembling dendrimeric nanosystems with lutetium-177, and evaluated their stability *in vitro*, in order to follow up on their application for internal vectorized therapy of cancer.

Materials and Methods:
50 µg/50 µL of AD-DOTA or FC11-DOTA were added to 26 µL of 1 mol.L^{-1} ammonium acetate and 10 mg of ascorbic acid, further adding 400 µL of the solution containing [^{177}Lu]$LuCl_3$ (47.7±1.8 MBq and 50.7±1.5 MBq respectively, n=3). pH values were measured. The solution was heated at 58°C for 1h. Radiochemical purity (RCP) was evaluated by radio-thin layer chromatography with mobile phase in 0.1 mol.L^{-1} sodium citrate buffer at the end of radiosynthesis. To evaluate radiolabeling stability, 100 µL of the radiotracer solution were added to 400 µL of human serum, incubated at 37°C, and the RCP was controlled for 30 minutes, 1h, 24h, 48h, and 1 week after incubation.

Results:
The final pH of the radiolabeling solutions was 5. RCP was quantified >95% for [^{177}Lu]Lu-AD-DOTA from the end of radiosynthesis up to 1 week after, in human serum at 37°C. Radiolabeling stability of [^{177}Lu]Lu-FC11-DOTA was confirmed >90% in human serum for up to 1 week. RCP results collide in Table 1.

Conclusion:
The optimal radiolabeling conditions and stability being confirmed, we look forward to the evaluation of the *in vivo* biodistribution and therapeutic effects of lutetium-177-radiolabeled dendrimers in preclinical orthotopic models of glioblastoma and breast cancer.

Reference

1. https://doi.org/10.1002/adhm.201901223
2. https://doi.org/10.3390/pharmaceutics14020224
3. https://doi.org/10.1021/acs.biomac.1c00262
4. https://doi.org/10.1002/smll.202003290
5. https://doi.org/10.1073/pnas.1812938115

Poster Presentation

Disclosures: The authors have disclosed no financial interest.

431-Cellular localization dynamics studies of FtsK in a radioresistant bacterium, Deinococcus radiodurans using confocal microscopy.

Presenter: Shruti Mishra, Bhabha Atomic Research Centre (BARC)

Shruti Mishra[1], Hari Sharan Misra[2], Swathi Kota[2]

[1]*Bhabha Atomic Research Centre (BARC), India*
[2]*Bhabha Atomic Research Centre (BARC), Mumbai, Maharashtra, India*

Deinococcus radiodurans is one of the most radioresistant bacteria with a D10 value of 10kGy. This coccus-shaped bacterium exists in tetrads and has a polyploid multipartite genome which is compactly arranged in a doughnut-shaped toroidal structure. A highly efficient DNA repair mechanism, strong antioxidative stress response and unique genome arrangement are some of the factors thought to be responsible for such an extremophilic nature of *D. radiodurans*. How this complex genome is maintained and its relevance in radiation resistance response is still unknown? FtsK, a multifunctional DNA translocase has been shown to act at the interface of cell division and genome segregation in other bacteria (Griange I, 2010). The genome of *D. radiodurans* R1 encodes a putative FtsK/SpoIIIE family protein (drFtsK). Here, for the first time, *in-vivo* functional characterization of drFtsK in genome segregation and cell division of the bacteria that predominantly occurs as tetrads is reported. To study the role of drFtsK, *ftsK-rfp* knock-in mutant was generated by homologous recombination which expressed fluorescently tagged, biologically functional drFtsK (drFtsK-RFP) under native promoter in *D. radiodurans*. These cells were visualized under confocal microscope. drFtsK-RFP produced various foci on the membrane and the nucleoid with the highest foci density on the septum. Nucleoid arrangement changes over time in exponentially growing *D. radiodurans*. Time lapse imaging of live cells was performed and the dynamics of drFtsK with the genome was studied. The movement of drFtsK-foci with respect to nucleoid separation and new septal formation suggests that drFtsK aligns along the septum (divisional plane) when the nucleoid is in rod shape. The alignment then switches to the new divisional plane (perpendicular to the old one) as the rod shaped nucleoid separates into two ring like structures during cell division. This shows how drFtsK functionally moves during the cell growth of the bacteria. A similar pattern of movement was observed in cells during post irradiation recovery (PIR) period. Co-ordinated action of drFtsK with other proteins like cell division protein (FtsZ) and genome segregation protein (ParA2) was also monitored by expressing these proteins in trans in *ftsK-rfp* knock-in mutants. drFtsK and FtsZ localize together and drFtsK aligns along the developing septum after the FtsZ ring forms there. Different domain deletion mutants of drFtsK were generated and microscopic observation showed changes in the nucleoid arrangement, cell division and cell morphology. All this indicates towards an important role of drFtsK in synchronizing the process of nucleoid separation with septal formation and cell division in a radioresistant bacterium, *Deinococcus radiodurans,* under normal growth conditions as well as post irradiation.

Reference

1. Grainge, I. (2010). FtsK–a bacterial cell division checkpoint?. Molecular microbiology, 78(5), 1055-1057.

Poster Presentation

Disclosures: The authors have disclosed no financial interest.

432-Preclinical study on a colorectal adenocarcinoma mouse model for quantification of lung metastasis

Presenter: Pradip Chaudhari, Advanced Centre for Treatment, Research and Education in Cancer (ACTREC)

Pradip Chaudhari[1], Bhabani Mohanty[1], Sumit Chaudhary[2], Neetinkumar Reddy[2], Amol Magdum[3], Maritina Rouchota[4], Panagiotis Tsialios[4], George Loudos[5]

[1]*Advanced Centre for Treatment, Research and Education in Cancer (ACTREC), Navi Mumbai, Maharashtra, India*
[2]*Hyderabad, Hyderabad, India*
[3]*Hyderabad, Telangana, India*
[4]*BioEmission Technology Solutions, Athens, Greece*
[5]*BIOEMTECH, Athens, Greece*

PET imaging is widely used in oncology research, as it accelerates the development of targeting molecules for novel diagnostic and therapy schemes (1). This study presents a workflow on oncology studies, for quick *in vivo* and *ex vivo* assessment

of novel compounds. *Live* dynamic *in vivo* screening of PET-labelled compounds is used to establish uptake regions, find the optimal accumulation times and quantify the targeting efficiency of compounds. Following the optimal selected parameters, in vivo imaging is performed, and tumor regions are established and quantified. After this is performed, animals are euthanized and selected extracted organs are imaged and quantified, using the same system, to quicky export the %ID/organ, just after the experimental procedure, with no need to wait for the organs to decay. The oncology model is created by injecting intravenously HT-29 colorectal adenocarcinoma cells on nude mice (2). Tumors are allowed to grow for up to 3 weeks. When they are ready, imaging is performed, to study the cancer occurrence sites and the highest accumulation of the clinical tracer [^{18}F]-FDG, with a focus on lung metastasis. Dose of 40 uL, having an average activity of 1 MBq of [^{18}F]-FDG administered intravenously via tail vein for the imaging purpose. The mice are first imaged *in vivo*, and the lung uptake is quantified by delineating regions of interest around the lung and subtracting the heart region. This results in the %ID in the lung for the selected time points. Then the mice are euthanized, and the organs of interest are imaged on the same system (β-eye), to export the %ID in the lung and other organs, through a second method. The two methodologies are compared to achieve more robust results. For all *in vivo* and *ex vivo* scanning, β-eye imaging system (BIOEMTECH, Greece) is employed (3, 4). Results of this study showed successful lung metastasis and a significant difference in quantified tumor tissues, when comparing the treatment group. The rapid establishment of tumour occurrence regions and uptake quantification, along with reduced acquisition and processing time renders this workflow optimised for oncology research.

Reference

1. Chaudhari P. (2021). Preclinical Imaging of Laboratory Rodents. In Nagarajan P, Ramachandra SG, Suresh R (Eds) Essentials of Laboratory Animal Science: Principles and Practices. Singapore; Springer, 2021. Pp 607-630. (ISBN 978-981-16-0987-9)
2. Dhumal A, Bendale K, Chaudhari P. (2019). Preclinical Animal Models for Cancer Research and Drug Discovery. In: Bose K., Chaudhari P. (eds.) Unravelling Cancer Signaling Pathways: A Multidisciplinary Approach. Springer, Singapore: 229-254.
3. Fysikopoulos, E., et al. "β-eye: A benchtop system for in vivo molecular screening of labeled compounds." Applied Radiation and Isotopes 180 (2022): 110034.
4. Rouchota, Maritina, et al. "Optimization of in vivo studies by combining planar dynamic and tomographic imaging: workflow evaluation on a superparamagnetic nanoparticles system." Molecular imaging 2021 (2021).
5. Fysikopoulos, Eleftherios, et al. "Optical to Planar X-ray Mouse Image Mapping in Preclinical Nuclear Medicine Using Conditional Adversarial Networks." Journal of Imaging 7.12 (2021): 262.

Poster Presentation

Disclosures: The authors have disclosed no financial interest.

433-Develop Companion Radiopharmaceutical YKL40 Antibodies as Potential Theranostic Agents for Epithelial Ovarian Cancer

Presenter: Ming-Cheng Chang, Institute of Nuclear Energy Research

Ming-Cheng Chang[1], Chun-Tang Chen[2], Ping-Fang Chiang[2], Yu-Jen Kuo[2], Cheng-Liang Peng[3]

[1]*Institute of Nuclear Energy Research, Taoyuan City, Taiwan*
[2]*Institute of Nuclear Energy Research (INER), Taoyuan City, Taiwan*
[3]*Institute of Nuclear Energy Research, Taoyuan, Taiwan, Taiwan*

Epithelial ovarian cancer (EOC) is usually diagnosed at advanced stage with poor prognosis. Theranostic agent is the current trend of drug development, but it is lacking in EOC. YKL40 is predominantly expressed and involved in the tumorigenesis of EOC. In this study, we developed the companion theranostic agent target to YKL40. We measured the YKL40 expression levels in ascites by ELISA and correlated with the clinical outcomes of EOC patients. We developed the radionuclide labeled In-111/Lu-177-DTPA-YKL40 neutralizing antibodies and investigated the radiochemical purity, SPECT/CT imaging, bio-distribution and therapeutic responses in ovarian cancer xenograft mice. We demonstrated that the YKL40 expression levels in ascites were significantly higher in the EOC patients with serous histologic type, high tumor grade, advanced stage, tumor recurrence, chemo-resistance and tumor related death. The radiochemical purity of In-111/Lu-177-DTPA-YKL40 neutralizing antibodies reached more than 90% after 24 hours of labeling. SPECT/CT imaging showed that significant accumulation of In-111-DTPA-YKL40 antibodies in tumor site of ovarian cancer xenograft mice at 24 hours after administration. Lu-177-DTPA-YKL40 antibodies significantly inhibited tumor growth in ovarian cancer xenograft mice. Our study indicated that In-111/Lu-177-DTPA-YKL40 neutralizing antibodies could be potential companion theranostic agents for EOC patients.

Reference

1. Y.C. Chiang, W.F. Cheng, M.C. Chang, T.P. Lu, K.T. Kuo, H.P. Lin, C.Y. Hsieh, C.A. Chen, Establishment of a New Ovarian Cancer Cell Line CA5171, Reproductive sciences 22 (2015) 725-734.
2. H.W. Lin, Y.C. Chiang, N.Y. Sun, Y.L. Chen, C.F. Chang, Y.J. Tai, C.A. Chen, W.F. Cheng, CHI3L1 results in poor outcome of ovarian cancer by promoting properties of stem-like cells, Endocrine-related cancer, 26 (2019) 73-88

Poster Presentation

Disclosures: The authors have disclosed no financial interest.

434-Propelling discoveries with magnetic imaging: Visualization for precise biomedical applications

Presenter: Kaviarasi Sathyasivam, SASTRA Deemed University

Kaviarasi Sathyasivam[1], Akhilasree Karthikeyan[1], Uma Maheswari Krishnan[1]

[1]*SASTRA Deemed University, Thanjavur, Tamil Nadu, India*

The escalating clinical pathology has necessitated the development of a potential diagnostic imaging technique. Magnetic resonance imaging (MRI) is one of the crucial techniques, essentially used by clinicians in the qualitative assessment of pathological conditions. The MRI principally works on the T1 and T2 relaxation of the protons of water upon magnetization in the target organ. Currently, there is a prioritized need for a safe magnetic contrast agent that could alter the intrinsic property of the target tissue by altering its magnetic relaxivity. This could thereby improve the strategical localization (such as localization of the thrombus in the brain) of the pathology with the preferential enhancement of specificity and sensitivity. Gadolinium-based contrast agents such as gadopentetate are widely employed as

they alter T1 relaxivity consequently improving the resolution of the acquired image. But the major limitations are that gadolinium chelates undergo trans-metallation and ligand exchange leading to the complexation with native proteins and macromolecules. This leads to an ineffective glomerular infiltration subsequently causing renal toxicity. This mandated the development of a novel gadolinium-based magnetic contrast agent that is hypothesized to possess a similar magnetic property with reduced toxicity.
The therapeutic implications of flavonoids are well studied and are found to possess diverse pharmacological properties that at regulated concentrations are potent antioxidants. Complexation of the gadolinium ion with the flavonoid could significantly reduce its associated toxicity. Quercetin and rutin are some of the most powerful antioxidants that can specifically target MMPs were complexed with gadolinium to formulate the Quercetin-Gadolinium (QGd) complex and Rutin-Gadolinium (RGd) complex respectively. Various alkalyted quercetin derivatives are reported to possess similar antioxidant properties and could easily be incorporated into nanocarrier for the targeted delivery. Hence as part of the long-term objective Alkylated Quercetin-Gadolinium (AQGd) complex was also synthesized and was compared with QGd and RGd. Quercetin was alkylated in multi-step reaction and the respective gadolinium complex namely, AQGd, QGd, and RGd was synthesized in-house and was characterized using UV/Visible spectrophotometry. The functional groups for each complex were identified with FT-IR spectroscopy. Thermal properties were studied by thermogravimetry (TG-DTA) and differential scanning calorimetry (DSC). The elemental composition and purity were analyzed with X-ray Photoelectron Spectroscopy (XPS). The stoichiometric mole ratio of the flavonoid and gadolinium was confirmed with Job's continuous variation method. Electrochemical studies were performed to elucidate the biosensing applications. Interestingly, AQGd showed an enhanced sensing application pertaining to the increased electroactive surface area. Magnetic characterization of the complexes was performed with Vibrating Sample Magnetometry (VSM) exhibiting the paramagnetic property. Magnetic imaging property was analyzed in physiological pH and *in vitro* conditions by Phantom agar assay which elucidated the relaxivity of 0.2952 μg mL^{-1} sec^{-1} for QGd and 0.2858 μg mL^{-1} sec^{-1} for RGd under physiological pH. Surprisingly, AQGd exhibited a negative slope with relaxivity of 0.3212 μg mL^{-1} sec^{-1} in physiological pH. Similarly, under the *invitro* condition, the relaxivity was found to be 0.2451 μg mL^{-1} sec^{-1} and 0.2247 μg mL^{-1} sec^{-1}. The *ex vivo* studies also highlight the superior MR contrast properties with QGd. These studies thereby elucidate the enhanced contrast ability in QGd and RGd than that of the alkylated version with reduced cytotoxicity. More focussed studies on QGd and RGd as superior MR contrast agents with relatively reduced cytotoxicity as nanoformulations for targeted delivery for specific biomedical applications are underway.

Reference

1. Kaviarasi, S., Shalini Devi, K.S., Vinoth, P., Sridharan, V., Yuba, E., Harada, A., Krishnan, U.M., 2019. Synthesis, Characterization, and Biomedical Applications of an Alkylated Quercetin–Gadolinium Complex. ACS Biomater. Sci. Eng. 5, 1215–1227. https://doi.org/10.1021/acsbiomaterials.8b01254
2. Muthurajan, T., Rammanohar, P., Rajendran, N.P., Sethuraman, S., Krishnan, U.M., 2015. Evaluation of a quercetin–gadolinium complex as an efficient positive contrast enhancer for magnetic resonance imaging. RSC Adv. 5, 86967–86979. https://doi.org/10.1039/C5RA16405B

Poster Presentation

Disclosures: The authors have disclosed no financial interest.

435-Covalent organic nanosheets as a fluorescence in vivo molecular imaging probe

Presenter: Dong Wook Kim, Inha University

Seok Min Kang[2], Heesu Ahn[1], Ju gyeong Jeong[2], Yong Kwon Kim[2], Yong Jin Lee[3], **Dong Wook Kim[2]**

[1]*Korea Institute of Radiological & Medical Sciences, Nowon, Seoul, South Korea*
[2]*Inha University, Incheon, South Korea*
[3]*Korea Institute of Radiological & Medical Sciences, Seoul, Seoul, Republic of Korea*

Covalent organic frameworks (COFs) have received much interest as a class of emerging crystalline porous polymeric platform for their widespread applications [1]. In particular, COFs possess tremendous potential for biomedical applications due to their good biocompatibility, tunable functionality, enormous porosity, and unique stability [2]. The bulk TpPy COFs were synthesized through Schiff condensation reaction between 1,3,5-triformylglucinol (Tp) and 2,7-diaminopyrene (Py) under solvothermal condition. The bulk TpPy COF materials were isolated as a brownish powder, which is completely insoluble in water and all organic solvents, indicating the formation of a stable polymeric materials. For biomedical applications of bulk material, liquid exfoliation processing (LEP) of TpPy COF was performed to impart water solubility and stability, and the nanosheets (TpPy CONs) were obtained using ultrasonication of bulk TpPy COF dispersed in water for 5 h.
These TpPy CONs showed the favorable properties - such as their enhanced optical characteristic, excellent dispersibility in biological media, low cytotoxicity, and high biocompatibility - to perform further in vivo bioimaging study using them as an optical imaging probe. For in vivo optical imaging study, only 22 μg of the TpPy-CONs dispersed in PBS were injected intravenously into female nude mice bearing a MDA-MB-231 cancer cells on their right thigh. After the injection, in vivo optical images were obtained from the mouse at 1, 3, 12, and 24 h intervals. The in vivo optical image showed a clearly strong fluorescence signal in the tumor site from only 1 h after the injection, which indicates that the TpPy-CONs could be fast accumulated into tumor tissues by EPR effect, showing an excellent optical performance in in vivo fluorescent optical imaging system. Moreover, at all intervals after the injection of the 2D TpPy-CONs, persistently high fluorescent signal intensity was observed on the tumor region without background signal from the normal tissues (Figure).
In summary, these in vivo optical imaging results showed that the TpPy-CONs can be used successfully without any labeling process to visualize the tumor site rapidly owing to their excellent optical property of themselves and EPR effect.

Reference

1. Feng X, Ding X, Jiang D. Covalent organic frameworks. Chem Soc Rev 2012;41:6010-6022.
2. Zhang G, Li X, Liao Q, Liu Y, Xi K, Huang W, Jia X. Water-dispersible PEG-curcummin/amine-functionalized covalent organic framework nanocomposites as smart carriers for in vivo drug delivery. Nat Commun 2018;9:2785

Poster Presentation

Disclosures: The authors have disclosed no financial interest.

436-Employment of the Dual Anti-oxidative and Pro-oxidative Nanoceria in a Nano-cocktail: A Versatile Platform for Theranostics of Inflammatory Diseases and Cancers

Presenter: Hang Ta, Griffith University

Hang T. Ta

Griffith University, Brisbane, QLD, Australia

Background and Novelty:
Nanoceria or cerium oxide nanoparticles characterised by the co-existing of Ce^{3+} and Ce^{4+} that allows self-regenerative, redox-responsive dual-catalytic activities, have attracted interests in biomedical field recently. Depending on surface characteristics and immediate environment, nanoceria exerts either anti- or pro-oxidative effects which regulates reactive oxygen species (ROS) levels in biological systems. Employing the dual-catalytic activities of nanoceria, we have created a novel versatile nano-cocktail comprised of chitosan nanocarrier loaded with nanoceria and superparamagnetic iron oxide nanoparticles (Chit−IOCO) as an effective theranostics material for both inflammatory disease and cancer. Methotrexate (MTX), as a chemotherapeutic agent and a structural analogue of folate, was conjugated to Chit-IOCO to provide synergistic anti-tumour effect and also enable targeted delivery of the material to tumour site.

Methodology:
The chitosan nano-cocktail (Chit-IOCO) loaded with treatment module (cerium oxide nanoparticles) and imaging module (iron oxide nanoparticles) were synthesised by electrostatic self-assembly. MTX was conjugated to Chit-IOCO by carbodiimide chemistry. To enable optical imaging, the nano-cocktails were also labeled with fluorophore Cy5 by carbodiimide chemistry. Mouse models of liver inflammation (CCl_4-treated C57BL/6 mouse) and subcutaneous glioblastoma tumor were employed to evaluate the theranostics capability of the developed nano-cocktail for inflammatory disease and cancer, respectively. Its MRI capability, anti-ROS, anti-inflammatory, anti-fibrosis and anticancer activities were investigated.

Results:
Data showed that Chit-IOCO exhibited the dual pro-oxidative and antioxidative properties similar to nanoceria. The nano-cocktail could act as an antioxidant for inflammatory diseases while performed as a prooxidant for cancers.
Chit-IOCO significantly reduced the expression of ROS, TNF-α and COX-2 in LPS-stimulated macrophages. The nano-cocktail also provided ROS scavenging activities in endothelial cells. Cytotoxicity studies showed that the nano-cocktails inhibited the proliferation of macrophages. Chit−IOCO also exhibited excellent ability as a negative contrast agent in T_2 and T_2*-weighted magnetic resonance (MR) imaging with a high relaxivity of 409.5 mM^{-1} s^{-1} which is comparable to clinically approved agents. It was possible to track the delivery of Chit-IOCO to the inflamed livers of CCl4-treated C57BL/6 mice, demonstrated by a shortened T_2* relaxation time of the livers after injecting Chit-IOCO into mice. In vivo anti-inflammatory and blood tests demonstrated that Chit-IOCO reduced inflammation-related proteins (TNF-a, iNOS and Cox-2) and bilirubin in CCl_4 treated C57BL/6. Histology images indicated that the nano-cocktails reduced fibrosis of CCl4-treated mouse liver and did not affect other organs of the mice.
On the other hand, Chit-IOCO and Chit-IOCO-MTX increased ROS production and triggered cell death in cancer cells. Nanoceria in combination with MTX in the nano-cocktail demonstrated in vitro synergistic anti-cancer effects in U87MG cells with combination index of 0.247. MTX as a structural analogue of folate acted as a ligand targeting tumour biomarker folate transporters that facilitated enhanced uptake of Chit−IOCO-MTX in U87MG cells and also in the subcutaneous tumour. Significant inhibition of tumour growth was observed in U87MG tumour-bearing BaLB/c mice treated with Chit-IOCO and Chit−IOCO-MTX. Tumors from MTX group re-grew after 16 days while those from nano-cocktail groups remained very tiny. Despite significant difference in in-vitro anticancer activity between Chit-IOCO and Chit-IOCO-MTX, significant difference in in-vivo anti-tumour effect between these two nanoparticles was not observed. In vivo MR imaging presented Chit−IOCO-MTX as a potential tumour-targeting and effective MR contrast agent capable of non-invasive monitoring of treatment response. Chit-IOCO-MTX accumulated stronger to tumour site within the first 3 days compared to Chit-IOCO.

Conclusion:
Overall, the developed nano-cocktails exhibited as a promising nanoplatform for (1) the treatment of cancers and other ROS-related, inflammatory diseases, (2) real-time tracking of the drugs administered and (3) monitoring of disease progression. Interestingly, depending on the diseases, this versatile nano-cocktail can act as either an antioxidant or a pro-oxidant that can treat the diseases.

Poster Presentation

Disclosures: The authors have disclosed no financial interest.

437-Anaplastic large cell lymphoma of primary femoral neck on 18F-FDG PET/CT

Presenter: Pengyang Feng, Henan Provincial People's Hospital

Pengyang Feng[1], Yan Bai[2], Zhun Huang[3], Meiyun Wang[1]

[1]*Henan Provincial People's Hospital, China*
[2]*Henan Provincial People's Hospital, Henan, China*
[3]*Henan, China*

Anaplastic large cell lymphoma (ALCL) is a rare, aggressive peripheral T-cell non-Hodgkin's lymphoma (NHL) that is a CD30-positive lymphoproliferative disorder[1]. Primary bone lymphoma (PBL) is a rare extranodal lymphoma that accounts for about 3% of malignant bone tumors[2]. ALCL mainly involves lymph nodes, while involvement of extra-lymph node sites of me sites such as bone is uncommon. PBL lacks the typical manifestations of lymphoma such as lymphadenopathy, fever, night sweats, and weight loss, and mainly manifests as local pain. Therefore, clinical diagnosis of PBL is difficult and easy to be misdiagnosed. ^{18}F-FDG PET/CT is an important functional imaging technique, which has become the standard imaging method for lymphoma staging, evaluating treatment response and predicting prognosis according to the latest lymphoma imaging guidelines[3]. Therefore, a child who was evaluated for pathological metabolism and potential metastasis of primary bone ALK-positive ALCL by ^{18}F-FDG PET/CT was included in the study. The patient fasted for at least 6 hours before scan. the blood glucose level was controlled less than 8.0 mmol/L before intravenous injection of a 4.07MBq/kg dose of ^{18}F-FDG. Image acquisition was performed after 40-60 min of rest. Scanning range: cranial top to lower femur, scanning direction: body to head. PET/CT image showed bone destruction of the left femoral neck and proximal femur with periosteal reaction, surrounding soft tissue mass formation, increased radiological uptake (SUVmax 25.56), and increased metabolism of left pelvic wall and iliac fossa lymph nodes. Needle biopsy showed ALK-positive anaplastic large cell lymphoma, immunohistochemistry showed positive for ALK, CD30, CD3, CD4, CD43, TIA-1, GramB and EMA, CD5, CD20, CD138, EBV-EBER and

PAX5 were negative. PET/CT can provide anatomical and metabolic information of lesions, and can quantitatively evaluate lesions through metabolic parameters such as SUVmax and MTV, which is essential in the management of lymphoma. Our study suggests that lymphoma should also be considered in the differential diagnosis of primary bone tumors.

Reference

1. Fuchs S, Naderi J, Meggetto F. Non-Coding RNA Networks in ALK-Positive Anaplastic-Large Cell Lymphoma. INT J MOL SCI. 2019;20(9).
2. Beal K, Allen L, Yahalom J. Primary bone lymphoma: treatment results and prognostic factors with long-term follow-up of 82 patients. 2006;106(12):2652-6.
3. Jiang Y, Wang L, Zhou W, Gu J, Tian Y, Dong Y, et al. (18)F-FDG PET/CT imaging findings in anaplastic large cell lymphoma, a rare subtype of lymphoma. CANCER IMAGING. 2020;20(1):4.

Poster Presentation

Disclosures: The authors have disclosed no financial interest.

438-Engineering TIGIT/CD40-exosomes encapsulated with calcium to enhance tumor immunity and diagnosis in pancreatic cancer

Presenter: Wenyao Wang, Jiangsu University

Wenyao Wang[1], xiongfeng cao[2], Zining Zhang[3], Hsiang-i Tsai[3]

[1]Jiangsu University, China
[2]Jiangsu University, Zhenjiang, Zhenjiang, China
[3]The Affiliated Hospital of Jiangsu University, Zhenjiang, China

Background:
Pancreatic cancer is of great malignancy, has difficulty in early detection,and immune-related therapies have been largely unsuccessful to date. However, recent research have found that the CD155/TIGIT axis is critical in maintaining immune evasion in PDAC and the combination immunotherapy (TIGIT/PD-1 co-blockade plus CD40 agonism) can elicit profound anti-tumor responses in preclinical models. It has been reported that many cancer cells secrete 10 times more exosomes than normal cells. Exosomes are characterized with small size and good biocompatibility and has a biological targeting ability, it can also be genetically engineered with tumor-targeted proteins, peptides or antibodies for more precise therapeutic drug delivery. Calcium has been reported to stimulate $CD8^+$T cells activity, and calcium overload could induce damage to cancer cells. However, the microenvironment of pancreatic cancer is low concentration of calcium, melanin-nanoparticle could be used for molecular imaging and carrying calcium which has a great potential of diagnosing and treating pancreatic cancer. The main aim is to improve the cytotoxic and targeted effect of $CD8^+$ T cells through TIGIT/CD40-exosomes (TC-EVs), which can be used to assess the therapeutic effect through MRI imaging. The TC-EVs has been reported to deliver drugs for anticancer therapy and address the issue of tumor drug resistance. The calcium-melanin nanovesicles also can be used in conjunction with molecular imaging to assess the efficacy of tumor therapy. Above all, TIGIT/CD40-exosomes encapsulated with calcium-melanin nanovesicles (TC-EVs@CM) could block immune evasion and MR imaging was combined to achieve diagnosis in pancreatic cancer.

Methods:
(1) Pancreatic cancer cells overexpressing TIGIT and CD40 were constructed and exosomes excreted by these cells were collected. (2) Melanin nanospheres were synthesized for loading calcium and encapsulated with the extracted TC-EVs. (3) RT-qPCR, Western Blot and TEM were selected to reflect the feature of TC-EVs, including particle size range DLS, Zeta potential and the expression of TIGIT/CD40.,the TIGIT/CD40-exosomes carried calcium-melanin nanoparticles (CM) were prepared by electrotransformation (4) The cytotoxic effect of TC-EVs@CM on pancreatic cancer cells was detected by CCK8 assay, and T cells were co-cultured with pancreatic cancer cells by adding TC-EVs@CM, and the activity and activity index of T cells were detected through Flow CytoMetry. (5) We verified the effect of TC-EVs on pancreatic cancer cells and T cells in vivo. The TC-EVs@CM were injected into mouse orthotopic model of pancreatic cancer through tail vein. Meanwhile observing the inhibition of tumor growth and the target on TC-EVs@CM through molecular imaging of MRI.

Results:
(1) CD155 was higher expressed in pancreatic cancer than normal pancreatic tissues, CD47 was 5.68 times higher than normal pancreatic tissues. (2) EVs with high TIGIT/CD40 protein expression were prepared from stably overexpressing cell line, and GEM-Melanin were encapsulated by electroporation to prepare TC-EVs@CM. (3) TIGIT/CD40 exosomes can respectively bind to CD155 and CD40L on the surface of pancreatic cancer cells and T cells. (4) In the mouse orthotopic model of pancreatic cancer, TC-EVs@CM can significantly inhibit the growth of pancreatic cancer (5) Magnetic resonance imaging using melanin revealed the best therapeutic effect in the TC-EVs@CM

Conclusion:
The use of TC-EVs@CM can significantly improve the therapeutic effect of pancreatic cancer; Exosomes which extracted by overexpressed CD40 and TIGIT pancreatic cancers can enhance the cytotoxic effect of $CD8^+$T cells, and target pancreatic cancer cells specifically. In this study, we used TIGIT/CD40-exosomes carried calcium-melanin nanoparticles to enhance cytotoxic effect of $CD8^+$T cells, and the feature of nanoparticles probe for molecular imaging. Taken together, the dual target TC-EVs@CM are of great potential in the aspect of pancreatic cancer for future diagnostics and therapeutics, thus realizing clinically transforming.

Reference

1. Freed-Pastor W A, Lambert L J, Ely Z A, et al. The CD155/TIGIT axis promotes and maintains immune evasion in neoantigen-expressing pancreatic cancer - ScienceDirect[J]. 2021.
2. Kamerkar S, Lebleu V S, Sugimoto H, et al. Exosomes facilitate therapeutic targeting of oncogenic KRAS in pancreatic cancer[J]. Nature.

Poster Presentation

Disclosures: The authors have disclosed no financial interest.

439-Improvement of imaging quality using deep learning in fluorescence endoscopy

Presenter: Su Woong Yoo, Chonnam National University Hwasun Hospital

Su Woong Yoo[1], Dat Thanh Le[2], Jung-Joon Min[3], Changho Lee[4]

[1]*Chonnam National University Hwasun Hospital, Hwasun-eup, Hwasun-gun, South Korea*
[2]*Chonnam National University, South Korea*
[3]*Chonnam National University*
[4]*Chonnam National University Medical School, Jeollanam-do, South Korea*

The fluorescence endoscopic system is used in colon cancer research to enable the early detection of the micro-scale tumor with the fluorescence-specific markers in vivo [1]. The excitation light is delivered to the tissue through a light source or biopsy channel via optical fiber. The camera system records the fluorescence signal emitted from the marker with an optical filter to obtain a specific wavelength. In 2020, a dual-scale fluorescence endoscopy (DSFE) system was introduced [2] by combining wide-field fluorescence endoscopy (WFE) which specialized in the early detection of dysplastic lesions with extreme contrast [3], and the confocal fluorescence endomicroscopy (CFEM) which provide high resolution of small colonic mucosa [4]. We used a monochrome scientific CCD camera to obtain the best sensitivity of fluorescence signal from the target area and another RGB (color) CMOS camera to get the white light image of the biologic region (e.g., colon) *in vivo*. Although modulated CMOS image sensor takes several benefits (e.g., higher frame rate, lower cost at same configuration than CCD camera), the sensitivity of CMOS camera is affected by noise coupling of digital integration, which can conflict with the pursuit of image quality. Therefore, we applied deep learning to optimize the advantage of the RGB CMOS camera as well as improve signal efficiency to achieve the quality corresponding to the monochrome CCD camera for the endoscopic system. We prepared a phantom sample containing fluorescein isothiocyanate (FITC) dextran. Then we compared the fluorescence signal of both cameras (CCD and CMOS) with different light intensities (from 0 to 100% of 480 nm LED light) and exposure time (10/50/100/500/1000 ms). The dataset from the CMOS camera (Basler ace, acA1920-40uc, Basler AG, Ahrensburg, German) and a CCD camera (Retiga R1, QImaging, Tucson, AZ, USA) was storage in 16-bit image formation. We successfully applied a conditional generative adversarial network [5] (cGAN) as a conversational model from CMOS-single channel images to target CCD-monochrome images of FTIC-filled tubes. The cGAN followed the standard approach: applied the Adam solver, with a learning rate of 0.0002 and momentum parameter was 0.5 for beta1 and 0.999 for beta 2, the batch size was set to 1, and the number of iterations was 100. The generated image from CMOS-single channel images was compared with the target monochrome CCD camera image by the peak signal-to-noise (PSNR). The result showed the feasibility of applying deep learning to replace the CCD camera with an alternative CMOS camera without compromising signal quality in fluorescence endoscopy. The image improvement technology based on deep learning can be widely used to enhance image qualities with a lower price and mobility in the imaging system.

Reference

1. G. Oh et al., "Intravital imaging of mouse colonic adenoma using MMP-based molecular probes with multi-channel fluorescence endoscopy," Biomedical Optics Express, Vol. 5, Issue 5, pp. 1677-1689, vol. 5, no. 5, pp. 1677–1689, May 2014.
2. S. W. Yoo et al., "Development of Dual-Scale Fluorescence Endoscopy for In Vivo Bacteria Imaging in an Orthotopic Mouse Colon Tumor Model," Applied Sciences 2020, Vol. 10, Page 844, vol. 10, no. 3, p. 844, Jan. 2020.
3. E. Gounaris, Y. Ishihara, M. Shrivastrav, D. Bentrem, and T. A. Barrett, "Near-Infrared Fluorescence Endoscopy to Detect Dysplastic Lesions in the Mouse Colon," Methods Mol Biol, vol. 1422, pp. 137–147, 2016.
4. F. Salvatori et al., "Confocal laser endomicroscopy in the study of colonic mucosa in IBD patients: A review," Gastroenterology Research and Practice, 2012.
5. P. Isola, J. Y. Zhu, T. Zhou, and A. A. Efros, "Image-to-image translation with conditional adversarial networks," Proceedings - 30th IEEE Conference on Computer Vision and Pattern Recognition, CVPR 2017, vol. 2017-January, pp. 5967–5976, Nov. 2017.

Poster Presentation

Disclosures: The authors have disclosed no financial interest.

440-Effect of ACE2 levels and sex on LPS-induced pulmonary inflammation in mice assessed by 18F-DPA-714 PET imaging

Presenter: Neysha Martinez Orengo, National Institutes of Health

Neysha Martinez Orengo[1], Swati Shah[2], Jianhao Lai[3], Maya Lara[4], Eyob Alemu[4], Rekeya Knight[4], Anna P. Lyndaker[4], Alan Kim[4], Cynthia Kim[4], Falguni Basuli[1], Jianfeng Shi[4], Dima A. Hammoud[1]

[1]*National Institutes of Health, Bethesda, MD*
[2]*National Institutes of Health, Bethesda*
[3]*National Institutes of Health, MD*
[4]*National Institutes of Health*

Background:
The importance of evaluating sex differences in the outcomes of different infectious/inflammatory diseases (e.g. tuberculosis, influenza, COVID-19) has become more evident in the past few years [1-3]. Additionally, the ongoing pandemic has renewed the focus on the role of ACE2 in modulating inflammation in response to infection [4]. Thus, in this study, male and female mice with differing levels of ACE2 expression [wild type non-carrier (NC), human ACE2 transgenic/hemizygous (HZ) and ACE2 deficient Knock-out (KO) mice] underwent post-pharyngeal (PP) inoculation of LPS to induce pulmonary inflammation and ^{18}F-DPA-714 PET to assess changes in expression of TSPO, an inflammation biomarker expressed mainly in macrophages and other immune cells.

Methods:
Six to eight-week old male and female mice from each genotype (KO, NC, or HZ) were inoculated with LPS by PP aspiration to induce acute lung injury. LPS was injected at 25mg/kg to avoid the effect of weight differences between groups and genders. Six hours post-LPS inoculation, the mice underwent static PET imaging 30 minutes after tracer injection. Another set of age-matched controls for each cohort also underwent ^{18}F-DPA-714 PET imaging. Images were analyzed to obtain Mean Standardized Uptake values (SUVmean) using MIM. After scanning, serum and whole lung tissues were collected for western blot (WB), cytokine/chemokine, and H&E analyses. Mouse and human ACE2 protein levels were determined by WB. The expression levels of 32 cytokines/chemokines were measured by ELISA. One-way ANOVA tests were used to evaluate differences in ^{18}F-DPA-714 binding and cytokine levels between different cohorts of mice.

Results:
The WB data showed that HZ mice had twice the amount of total ACE2 protein (mouse plus human ACE2) compared to NC, while no ACE2 was identified in KO mice, as expected. All LPS- treated mouse cohorts, male (NCM, KOM, HZM) and female (NCF, KOF and HZF), exhibited expected signs of increased inflammation in the lungs

compared to their respective controls, as evidenced by increased ^{18}F-DPA-714 binding. However, between LPS-treated groups, higher tracer binding was seen in the lungs of mice with normal (NC) or increased expression of ACE2 (HZ) compared to KO mice in both males and females but differences were significant only in female mice (HZF vs KOF p=0.0065). The HZF mice also presented worse hypothermia when compared to HZM. Qualitatively, H&E staining showed increased immune cell infiltration (macrophages and neutrophils) in the lungs and reduction of the alveolar spaces in the HZ groups compared to NC. To understand the local inflammatory milieu, a variety of cytokines/chemokines involved in immune cell activation and recruitment were evaluated. Compared to controls, all the LPS groups showed higher expression of inflammatory cytokines/chemokines. Within LPS cohorts, the HZF mice showed higher levels of MIP1α (p<0.0001), MCP-1 (p=0.0007), KC (p=0.0340), IL-6 (p=0.0.0055), and TNF (p=0.0352) compared to KOF. In males, however, the results were variable and showed no clear trends. There were no major changes in either mouse or human ACE2 protein expression in the lung lysates as result of LPS treatment.

Conclusions:

The extent of immune activation in response to various infections has been shown to be gender dependent, with females generally mounting a stronger immune response than males [5]. Here, PET imaging and cytokine data demonstrate that higher expression of ACE2 is associated with stronger immune cell activation in the lungs resulting in higher local inflammatory responses, especially in female mice. Additionally, worse hypothermia in HZF mice compared to males suggests a stronger systemic reaction to LPS inoculation. Based on these preliminary results in an inflammatory model, further studies in appropriate infection models are warranted to better understand the effect of gender on the induction of inflammation and on disease progression.

Reference

1. Scully, E.P., et al., Considering how biological sex impacts immune responses and COVID-19 outcomes. Nat Rev Immunol, 2020. 20(7): p. 442-447.
2. Klein, S.L. and A. Pekosz, Sex-based biology and the rational design of influenza vaccination strategies. J Infect Dis, 2014. 209 Suppl 3: p. S114-9.
3. Nhamoyebonde, S. and A. Leslie, Biological differences between the sexes and susceptibility to tuberculosis. J Infect Dis, 2014. 209 Suppl 3: p. S100-6.
4. Chaudhry, F., et al., Manipulation of ACE2 expression in COVID-19. Open Heart, 2020. 7(2).
5. Klein, S.L. and K.L. Flanagan, Sex differences in immune responses. Nat Rev Immunol, 2016. 16(10): p. 626-38.

Poster Presentation

Disclosures: The authors have disclosed no financial interest.

441-Preparation and evaluation of a dual imaging agent for computed tomography (CT) and magnetic particle imaging (MPI)

Presenter: Carlos Rinaldi-Ramos, University of Florida
Sitong Liu[1], Anahita Heshmat[2], Izabella Barreto[2], **Carlos Rinaldi-Ramos[2]**

[1]University of Florida, Gainesville, Florida
[2]University of Florida, Gainesville, FL

Introduction:

Magnetic particle imaging (MPI) is a novel biomedical imaging modality that allows non-invasive, tomographic, and quantitative tracking of the distribution of superparamagnetic iron oxide nanoparticle (SPION) tracers. MPI possesses high sensitivity in detecting nanograms of iron. However, it does not acquire anatomical information. Computed Tomography (CT) is a widely used biomedical imaging modality that yields anatomical information at high resolution. A multimodal imaging agent combining the benefits of MPI and CT, resulting in high sensitivity and high spatial resolution with anatomical information, would be of interest. We have previously reported the synthesis of MPI-tailored iron oxide nanoparticles with better sensitivity and resolution compared to commercial tracer ferucarbotran. The high electron density and chemical stability of hafnium oxide (HfO_2, hafnia) make its nanoparticle form a good candidate as a contrast agent for CT, where it could be a more sensitive and affordable alternative to clinical iodine-based contrast agents and research use gold nanoparticle contrast agents. Flash nanoprecipitation is a novel method for formulating polymeric nanoparticles containing hydrophobic cores. Due to its simplicity, scalability, and manufacturability, FNP has been used widely for the preparation of composite nanoparticles. Here we combine MPI-tailored iron oxide nanoparticles with hafnium oxide nanoparticles using flash nanoprecipitation to obtain dual-imaging MPI/CT tracers.

Materials and Methods:

The dual imaging agent was prepared with iron oxide nanoparticles and hafnia nanoparticles synthesized from thermal decomposition, encapsulated in poly(lactic acid)-b-poly(ethylene glycol) (PLA-b-PEG) via flash nanoprecipitation using custom-designed and 3D printed multi-inlet vortex mixers. The dual imaging agents were evaluated for physical size through transmission electron microscopy (TEM) and hydrodynamic size through dynamic light scattering (DLS). The MPI intensity and resolution of the dual imaging agents were evaluated using the MOMENTUM™ MPI scanner RELAX™ module and 2D imaging mode. The CT contrast performance was evaluated using an IVIS® Spectrum In Vivo Imaging System as well as an Aquilion One Genesis and compared to the clinical CT contrast agent OMNIPAQUE (active ingredient, iohexol).

Result and Discussion:

The dual imaging agents were evaluated using TEM and energy dispersive spectroscopy (EDS) to confirm the co-localization of iron oxide nanoparticles and hafnia nanoparticles in one composite nanoparticle. The hydrodynamic diameter was around 130 ± 44 nm, with 72% w/w iron oxide 28% w/w hafnia. The magnetic diameter of the dual imaging agents (13.5 ± 1.0 nm) was slightly smaller than singly coated iron oxide nanoparticles (16.7 ± 3.0 nm). A reduction in saturation magnetization was also observed for the dual imaging agents (57.07 Am^2/kg) compared to the singly coated iron oxide nanoparticles (64.7 Am^2/kg). The reduction of both saturation magnetization and the magnetic diameter may suggest interactions between the nanoparticles inside the composite nanoparticles. The MPI maximum signal intensity for the dual imaging agent is 78 $mgFe^{-1}$, while the corresponding value for ferucarbotran is 28 $mgFe-^{1}$. In terms of resolution, the dual imaging agents had a FWHM of 17.2 mT, while the corresponding value was 11.4 mT for ferucarbotran. The PSF data suggests that dual imaging agents have much better sensitivity than ferucarbotran while having a slightly worse resolution. The X-ray attenuation of the dual imaging agent in both scanners is better compared to OMNIPAQUE.

Conclusion:

The dual imaging agents possess good contrast in both an MPI scanner and a CT scanner, making them the first dual-purpose contrast agent for MPI and CT.

Poster Presentation

Disclosures: The authors have disclosed no financial interest.

442-Evaluation of the angiosome concept in peripheral artery disease patients using near-infrared fluorescence with indocyanine green

Presenter: Floris Tange, Leiden University Medical Center

Floris Tange[1], Bien Ferrari[2], Pim Van Den Hoven[3], Jan Van Schaik[4], Abbey Schepers[4], Carla Van Rijswijk[4], Rutger van der Meer[2], Hein Putter[2], Alexander Vahrmeijer, Jaap Hamming[4], Joost Van Der Vorst[4]

[1]*Leiden University Medical Center, Netherlands*
[2]*Leiden University Medical Center (LUMC), Netherlands*
[3]*Leiden University Medical Center (LUMC), Leiden, Zuid-Holland, Netherlands*
[4]*Leiden University Medical Center (LUMC)*

Introduction:
The angiosome concept is defined as the anatomical territory of a source artery within all tissue layers (1). When applying this theory in peripheral artery disease (PAD) patients' interventional decision making, an attending physician can choose to perform direct or indirect revascularization. For patients suffering from PAD with ischemic wounds, it seems rational to directly target the revascularization to the angiosome that supplies the site of the ulcer. However, the clinical usability of this theory is debatable due to collateral vessel growth, interfering with the borders of the angiosomes (2). This study evaluates whether a difference in quantified near-infrared (NIR) fluorescence perfusion parameters is objectifiable when comparing directly and indirectly revascularized angiosomes.

Methods:
This cohort study included patients undergoing an endovascular or surgical revascularization between January 2019 and December 2021. Pre- and postinterventional NIR fluorescence imaging was performed during a period of 10 minutes. Three angiosomes on the dorsum of the foot were classified; the ATP (hallux), ATA (dorsum) and the mixed angiosome (dig. 2-5). Directly and indirectly revascularized angiosomes were assessed from the electronic patient records. The degree of collateralization was classified based on pre-procedural CT angiography and X-ray angiography by two independent interventional radiologists. The collateral grade was classified as 'substantial' when collaterals were visible for ≥ 25% of the calf length and/or estimated to be ≥ 50% of the corresponding crural artery diameter and/or when objectified as an extensive amount. Time-intensity curves were quantified from the obtained fluorescence measurements using the Quest Research Framework® software in each angiosome set as Regions Of Interest (ROI). Ten in- and outflow parameters were extracted out of these time-intensity curves. The difference in pre- and postinterventional perfusion parameters was described as a percentual change. A subgroup analysis between endovascular and surgical revascularized angiosomes was performed.

Results:
Successful NIR fluorescence measurements were obtained in 52 patients (54 limbs) including a total of 157 angiosomes (121 direct, 36 indirect). Significant improvement of all perfusion parameters in both the directly and indirectly revascularized angiosomes was demonstrated (p-values between <0.001 – 0.007). Within the indirectly revascularized angiosomes, 90.6% of the scored collaterals were rated as significant. When comparing the percentual change in perfusion parameters between the direct and indirect angiosomes, no significant difference was seen in all perfusion parameters (p-values between 0.253 – 0.783). Alongside, no significant differences were seen when comparing percentual changes of perfusion parameters in direct and indirect revascularized angiosomes within surgical (p-values between 0.053 – 0.899), as well as endovascular interventions (p-values between 0.290 – 0.883).

Conclusion:
This study demonstrates a significant postinterventional increase of NIR fluorescence perfusion parameters in both directly and indirectly revascularized angiosomes along with no significant difference when comparing the percentual change of NIR fluorescence perfusion parameters between directly and indirectly revascularized angiosomes. Furthermore, subgroup analysis within endovascular and surgical procedures did not show differences in perfusion parameter changes comparing direct and indirect angiosomes. A possible explanation for the insignificant difference comparing direct and indirect angiosomes postinterventional is the substantial amount of collateral formation in indirect angiosomes. The results of this study suggest that the angiosome concept should be applied with restraint in clinical setting.

Reference
1. Taylor GI, Palmer JH. The vascular territories (angiosomes) of the body: experimental study and clinical applications. Br J Plast Surg. 1987;40(2):113-41.
2. Jongsma. Angiosome-directed revascularization in patients with critical limb ischemia. 2016.

Poster Presentation

Disclosures: The authors have disclosed no financial interest.

443-Near-infrared fluorescence with indocyanine green to predict clinical outcome after revascularization.

Presenter: Floris Tange, Leiden University Medical Center

Floris Tange[1], Pim Van Den Hoven[2], Jan Van Schaik[3], Abbey Schepers[3], Koen van der Bogt[4], Carla Van Rijswijk[3], Hein Putter[4], Alexander Vahrmeijer, Jaap Hamming[3], Joost Van Der Vorst[3]

[1]*Leiden University Medical Center, Netherlands*
[2]*Leiden University Medical Center (LUMC), Leiden, Zuid-Holland, Netherlands*
[3]*Leiden University Medical Center (LUMC)*
[4]*Leiden University Medical Center (LUMC), Netherlands*

Introduction:
Improvement of peripheral perfusion through revascularization is fundamental in the treatment strategy of peripheral artery disease (PAD) patients (1). However, despite successful revascularization, reintervention rates remain high (2). Contemporary postinterventional quality control methods have several limitations and are insufficient in predicting clinical outcome (3). Near-infrared (NIR) fluorescence has already been evaluated as a seemingly promising technique for quality control after a revascularization procedure (4, 5). This study evaluates the potential application of near-infrared fluorescence imaging with indocyanine green (ICG) to quantify perfusion changes and hereby predict the postinterventional clinical outcome.

Methods: This prospective cohort study included patients with valid pre- and postinterventional fluorescence measurements who underwent a technically successful revascularization procedure between January 2019 and December 2021. ICG NIR fluorescence imaging was performed before and within five days following the intervention. Outpatient clinic follow-up was performed at the initial revision moment 6 weeks following the revascularization procedure. A clinical successful outcome was defined as either a substantial improvement of pain free walking distance, reduction or disappearance of rest- and/or nocturnal pain or tendency towards wound - or ulcer healing. Quantification of the ICG NIR fluorescence images was performed using a software tool (Quest Research Framework®) which plotted time-intensity curves from the dorsum of the foot on the treated side. From these time-intensity curves, 5 inflow- and 5 outflow parameters were extracted. Postinterventional perfusion changes were displayed as percentual improvement of perfusion parameter values. Pre- and postinterventional ankle-brachial index and toe pressure measurements were performed. Receiver operating characteristics (ROC) curves were plotted depicting the predictive value of perfusion parameters for a clinically successful outcome.

Results:
Successful ICG NIR fluorescence imaging was performed in 50 patients (52 limbs). A clinical successful outcome following revascularization was described in 45 patients. All inflow parameters showed a significant difference after revascularization in the successful outcome group, while no significant differences were shown in the unsuccessful outcome group (All p-values <0.001; p-values between 0.116 - 0.917 respectively). Four inflow parameters demonstrated significant differences in percentual improvement comparing the successful and unsuccessful outcome groups (p-values within 0.012 – 0.015). No significant difference was observed when comparing percentual changes in outflow parameters and the maximum intensity (Imax) between both outcome groups (p-values between 0.143 – 0.346). The predictive value analysis for a successful outcome of the 4 significant inflow parameters (normalized slope, absolute slope, ingress rate, time to max) displayed area under the curve values between 0.801 and 0.812.

Conclusions:
This study shows a significant improvement in ICG NIR fluorescence inflow parameters in patients with a successful clinical outcome following revascularization. A significant difference was shown when comparing the percentual improvement of these parameters between patients with a successful and unsuccessful outcome. This study underlines the potential of ICG NIR fluorescence in addition to several clinical elements for predicting clinical outcome after revascularization. These statements should be confirmed in future studies, additionally evaluating possible cut-off values for the seemingly reliable inflow parameters.

Reference

1. Gerhard-Herman MD, Gornik HL, Barrett C, Barshes NR, Corriere MA, Drachman DE, et al. 2016 AHA/ACC Guideline on the Management of Patients With Lower Extremity Peripheral Artery Disease: A Report of the American College of Cardiology/American Heart Association Task Force on Clinical Practice Guidelines. Circulation. 2017;135(12):e726-e79.
2. Parvar SL, Ngo L, Dawson J, Nicholls SJ, Fitridge R, Psaltis PJ, et al. Long-term outcomes following endovascular and surgical revascularization for peripheral artery disease: a propensity score-matched analysis. Eur Heart J. 2021;43(1):32-40.
3. Misra S, Shishehbor MH, Takahashi EA, Aronow HD, Brewster LP, Bunte MC, et al. Perfusion Assessment in Critical Limb Ischemia: Principles for Understanding and the Development of Evidence and Evaluation of Devices: A Scientific Statement From the American Heart Association. Circulation. 2019;140(12):e657-e72.
4. Igari K, Kudo T, Toyofuku T, Jibiki M, Inoue Y, Kawano T. Quantitative evaluation of the outcomes of revascularization procedures for peripheral arterial disease using indocyanine green angiography. Eur J Vasc Endovasc Surg. 2013;46(4):460-5.
5. Settembre N, Kauhanen P, Alback A, Spillerova K, Venermo M. Quality Control of the Foot Revascularization Using Indocyanine Green Fluorescence Imaging. World J Surg. 2017;41(7):1919-26.

Poster Presentation

Disclosures: The authors have disclosed no financial interest.

444-Engineering TIGIT/CD40-exosomes encapsulated with calcium to enhance tumor immunity and diagnosis in pancreatic cancer

Presenter: Xufeng Pu, Jiangsu University

Xufeng Pu[1], Zining Zhang[2], Wenyao Wang[1], Hsiang-i Tsai[2], Xiongfeng Cao[3], Haitao Zhu[1]
[1]*Jiangsu University, China*
[2]*The Affiliated Hospital of Jiangsu University, Zhenjiang, China*
[3]*Jiangsu University, Zhenjiang, Zhenjiang, China*

Background:
Pancreatic cancer is of great malignancy, has difficulty in early detection,and immune-related therapies have been largely unsuccessful to date. However, recent research have found that the CD155/TIGIT axis is critical in maintaining immune evasion in PDAC and the combination immunotherapy (TIGIT/PD-1 co-blockade plus CD40 agonism) can elicit profound anti-tumor responses in preclinical models. It has been reported that many cancer cells secrete 10 times more exosomes than normal cells. Exosomes are characterized with small size and good biocompatibility and has a biological targeting ability, it can also be genetically engineered with tumor-targeted proteins, peptides or antibodies for more precise therapeutic drug delivery. Calcium has been reported to stimulate $CD8^{+}$T cells activity, and calcium overload could induce damage to cancer cells. However, the microenvironment of pancreatic cancer is low concentration of calcium, melanin-nanoparticle could be used for molecular imaging and carrying calcium which has a great potential of diagnosing and treating pancreatic cancer. The main aim is to improve the cytotoxic and targeted effect of $CD8^{+}$ T cells through TIGIT/CD40-exosomes (TC-EVs), which can be used to assess the therapeutic effect through MRI imaging. The TC-EVs has been reported to deliver drugs for anticancer therapy and address the issue of tumor drug resistance. The calcium-melanin nanovesicles also can be used in conjunction with molecular imaging to assess the efficacy of tumor therapy. Above all, TIGIT/CD40-exosomes encapsulated with calcium-melanin nanovesicles (TC-EVs@CM) could block immune evasion and MR imaging was combined to achieve diagnosis in pancreatic cancer.

Methods:
(1) Pancreatic cancer cells overexpressing TIGIT and CD40 were constructed and exosomes excreted by these cells were collected. (2) Melanin nanospheres were synthesized for loading calcium and encapsulated with the extracted TC-EVs. (3) RT-qPCR, Western Blot and TEM were selected to reflect the feature of TC-EVs, including particle size range DLS, Zeta potential and the expression of TIGIT/CD40.,the TIGIT/CD40-exosomes carried calcium-melanin nanoparticles (CM) were prepared by electrotransformation (4) The cytotoxic

effect of TC-EVs@CM on pancreatic cancer cells was detected by CCK8 assay, and T cells were co-cultured with pancreatic cancer cells by adding TC-EVs@CM, and the activity and activity index of T cells were detected through Flow CytoMetry. (5) We verified the effect of TC-EVs on pancreatic cancer cells and T cells in vivo. The TC-EVs@CM were injected into mouse orthotopic model of pancreatic cancer through tail vein. Meanwhile observing the inhibition of tumor growth and the target on TC-EVs@CM through molecular imaging of MRI.

Results:

(1) CD155 was higher expressed in pancreatic cancer than normal pancreatic tissues, CD47 was 5.68 times higher than normal pancreatic tissues. (2) EVs with high TIGIT/CD40 protein expression were prepared from stably overexpressing cell line, and GEM-Melanin were encapsulated by electroporation to prepare TC-EVs@CM. (3) TIGIT/CD40 exosomes can respectively bind to CD155 and CD40L on the surface of pancreatic cancer cells and T cells. (4) In the mouse orthotopic model of pancreatic cancer, TC-EVs@CM can significantly inhibit the growth of pancreatic cancer (5) Magnetic resonance imaging using melanin revealed the best therapeutic effect in the TC-EVs@CM

Conclusion:

The use of TC-EVs@CM can significantly improve the therapeutic effect of pancreatic cancer; Exosomes which extracted by overexpressed CD40 and TIGIT pancreatic cancers can enhance the cytotoxic effect of $CD8^{+}$T cells, and target pancreatic cancer cells specifically. In this study, we used TIGIT/CD40-exosomes carried calcium-melanin nanoparticles to enhance cytotoxic effect of $CD8^{+}$T cells, and the feature of nanoparticles probe for molecular imaging. Taken together, the dual target TC-EVs@CM are of great potential in the aspect of pancreatic cancer for future diagnostics and therapeutics, thus realizing clinically transforming.

Reference

1. Freed-Pastor W A, Lambert L J, Ely Z A, et al. The CD155/TIGIT axis promotes and maintains immune evasion in neoantigen-expressing pancreatic cancer - ScienceDirect[J]. 2021.
2. Kamerkar S, Lebleu V S, Sugimoto H, et al. Exosomes facilitate therapeutic targeting of oncogenic KRAS in pancreatic cancer[J]. Nature.

Poster Presentation

Disclosures: The authors have disclosed no financial interest.

445-Engineering SIGLECg/SIRP nanovesicles encapsulated with GEM-Melanin for enhancing tumor immunity and diagnostics in Pancreatic cancer.

Presenter: Jianghong Ji, Jiangsu University

Jianghong Ji[1], Haitao Zhu[1]

[1]*Jiangsu University, China*

Background:

Pancreatic cancer is characterized with great malignant. For the cause of lacking early symptoms and reliable screening methods, which makes it is significantly difficult to treat pancreatic cancer. Gemcitabine (GEM) is the first-line treatment for pancreatic cancer. However, pancreatic tumor tissue is infiltrated with a large number of tumor-associated macrophages (TAMs) that enhances resistance to GEM by releasing pyrimidine nucleosides, further increasing the refractoriness of pancreatic cancer. Among these checkpoint genes, CD24 and CD47 mRNA were higher in pancreatic cancer tissues. The phagocytosis of macrophages was inhibited by CD24-SIGLECg and CD47-SIRPa axes, thus CD24 and CD47 are expected to be new and promising targets for immunotherapy of pancreatic cancer. Meanwhile, MR-targeted nanomaterials can not only improve early diagnosis of pancreatic cancer, but also improve treatment prognosis.

Objective:

The aim of this experiment was to target pancreatic cancer cells by constructing SIGLECg/SIRPa@GEM-Melanin nanovesicles (SS-NVs@GM). The vesicles blocked the "don't eat me" signal on the surface of macrophages, such as CD24-SIGLECg and CD47-SIRPa immune checkpoints, and reduced the drug resistance of pancreatic cancer to GEM. At the same time, MR imaging was combined to achieve diagnosis and to assess the treatment of pancreatic cancer.

Methods:

(1) Extraction of pancreatic cancer cell membranes overexpressing SIGLECg and SIRPa, constructing melanin nanovesicles loaded with GEM, and the SS-NVs biomembrane-derived cell vesicles which obtain GEM were prepared by electrotransformation. (2) RT-qPCR, Western Blot and TEM were selected to reflect the feature of SS-NVs@GM, including particle size range DLS, Zeta potential and the expression of SIGLECg/SIRPa. (3) Performing co-culture of pancreatic cancer cells with macrophages, and observing the phagocytosis of pancreatic cancer cells by macrophages under the effect of SIGLECg/SIRPa nanovesicles (SS-NVs) through fluorescence microscopy. (4) To observe the polarization of macrophages after treating SS-NVs by RT-qPCR and FACS. (5) The SS-NVs@GM were injected into mouse orthotopic model of pancreatic cancer through tail vein. Meanwhile observing the inhibition of tumor growth and the target on SS-NVs@GM through molecular imaging of MRI.

Results:

(1) NVs with high SIGLECg and SIRPa protein expression were prepared from stably overexpressing cell line, and GEM-Melanin were encapsulated by electroporation to prepare SS-NVs@GM.(2) SS-NVs@GM can bind to CD24,CD47 of pancreatic cancer ,enhancing the phagocytosis of the macrophages. (3) Meanwhile, SS-NVs were used to regulate the M1/M2 polarization in the aspect of TAMs. (4) In the mouse orthotopic model of pancreatic cancer, SS-NVs@GM can significantly inhibit the growth of pancreatic cancer . (5) SS-NVs@GM can improve the consequences of molecular imaging such as MRI.

Conclusions:

On account of the difficulty of early diagnosis and great malignancy of pancreatic cancer, it is vital to provide a more precise and efficient remedy to detect and cure the pancreatic cancer. In this study, we used SIGLECg/SIRPa nanovesicles encapsulated GEM-melanin to enhance tumor immunity and the feature of nanoparticles probe for molecular imaging. Taken together, the dual target SS-NVs@GM are of great potential in the aspect of pancreatic cancer for future diagnostics and therapeutics, thus realizing clinically transforming.

References

1. Tsai HI, Wu Y, Liu X, Xu Z, Liu L, Wang C, Zhang H, Huang Y, Wang L, Zhang W, Su D, Khan FU, Zhu X, Yang R, Pang Y, Eriksson JE, Zhu H, Wang D, Jia B, Cheng F, Chen H. Engineered Small Extracellular Vesicles as a FGL1/PD-L1 Dual-Targeting Delivery System for Alleviating Immune Rejection. Adv Sci (Weinh). 2022 Jan;9(3):e2102634.

2. Zhu H, Cao X, Cai X, Tian Y, Wang D, Qi J, Teng Z, Lu G, Ni Q, Wang S, Zhang L. Pifithrin-μ incorporated in gold nanoparticle amplifies pro-apoptotic unfolded protein response cascades to potentiate synergistic glioblastoma therapy. Biomaterials. 2020 Feb;232:119677.

Poster Presentation

Disclosures: The authors have disclosed no financial interest.

446-A comparative study of amide proton transfer weighted imaging and intravoxel incoherent motion imaging in the diagnosis of pathological grade of lung adenocarcinoma and its correlation with SUVmax

Presenter: Pengyang Feng, Henan Provincial People's Hospital

Pengyang Feng[1], Nan Meng[2], Yu Luo[2], Yan Bai[3], Meiyun Wang[1]

[1]Henan Provincial People's Hospital, China
[2]Henan Provincial People's Hospital
[3]Henan Provincial People's Hospital, Henan, China

Synopsis:
^{18}F-FDG PET can be used to diagnose and differentiate tumors [1]. Amide proton transfer-weighted imaging (APTWI) primarily reflects the protein content and acidity information of tissue structures [2]. Intravoxel incoherent motion (IVIM) includes bi-exponential model and stretch-exponential model [3], the former mainly reflects the diffusion and perfusion information of water molecules [4], the latter mainly reflects the heterogeneity of the tissue [5].

Objective:
To compare the value of amide amide proton transfer-weighted imaging (APTWI) and intravoxel incoherent motion (IVIM) imaging in identifying the pathological grade of lung adenocarcinoma, and to assess the correlation between each parameter and the metabolic parameter SUVmax of ^{18}F-FDG PET.

Materials and Methods:
A total of 66 patients with postoperative pathologically confirmed lung adenocarcinoma were prospectively collected. APTWI, IVIM and 18F-FDG PET images were analyzed to measure the magnetization transfer ratio asymmetry (MTRasym [3.5 ppm]), diffusion coefficient (D), false diffusion coefficient (D*), perfusion fraction (f), distributed diffusion coefficient (DDC), diffusion heterogeneity index (α) and maximum standard uptake value (SUVmax). The differences and diagnostic efficacy of each parameter between different grading groups were compared and analyzed, and the correlation between each parameter value and SUVmax was evaluated.

Results:
MTRasym (3.5ppm) and f values in poorly differentiated group were higher than those in moderately/well differentiated group, while D and DDC values were lower than those in moderately/well differentiated group (all $P<0.05$), there was no significant difference in D* and α values between the two groups. The AUC of MTRasym (3.5 ppm), D, DDC, f, α, and D* values for diagnosing the pathological grade of lung adenocarcinoma were 0.858, 0.743, 0.661, 0.645, 0.577, 0.531, respectively. The diagnostic efficiency of MTRasym (3.5 ppm) was significantly higher than that of other parameters except D value ($P < 0.05$). The combination of APTWI and IVIM had the highest diagnostic performance in identifying pathological grade (AUC = 0.973). There was a weak positive correlation between MTRasym (3.5 ppm) and SUVmax value (r=0.396); D and DDC values were weakly negatively correlated with SUVmax value respectively (r=-0.359, -0.249, $P<0.05$).

Conclusion:
Both APTWI and IVIM are effective means to identify the pathological grade of lung adenocarcinoma. The diagnostic efficiency of APTWI parameters is better than IVIM, and some parameters are correlated with SUVmax.

Reference
1. Alçın G, Şanlı Y, Yeğen G, et al. The Impact of Primary Tumor and Locoregional Metastatic Lymph Node SUVmax on Predicting Survival in Patients with Rectal Cancer. Mol Imaging Radionucl Ther. 2020,29(2):65-71. DOI:10.4274/mirt.galenos.2020.40316.
2. Zhang H, Tang X, Lv Y, et al. Amide Proton Transfer-Weighted (APTw) Imaging of Intracranial Infection in Children: Initial Experience and Comparison with Gadolinium-Enhanced T1-Weighted Imaging. Biomed Res Int. 2020,2020:6418343. Published 2020 May 16. DOI:10.1155/2020/6418343.
3. Meng N, Fang T, Feng P, et al. Amide Proton Transfer-Weighted Imaging and Multiple Models Diffusion-Weighted Imaging Facilitates Preoperative Risk Stratification of Early-Stage Endometrial Carcinoma. J Magn Reson Imaging. 2021,54(4):1200-1211. DOI:10.1002/jmri.27684.
4. Lecler A, Duron L, Zmuda M, et al. Intravoxel incoherent motion (IVIM) 3 T MRI for orbital lesion characterization. Eur Radiol. 2021,31(1):14-23. DOI:10.1007/s00330-020-07103-1.
5. Lin L, Xue Y, Duan Q, et al. Grading meningiomas using mono-exponential, bi-exponential and stretched exponential model-based diffusion-weighted MR imaging. Clin Radiol. 2019,74(8):651.e15-651.e23. DOI:10.1016/j.crad.2019.04.007.

Poster Presentation

Disclosures: The authors have disclosed no financial interest.

447-Resolution, sensitivity, and depth enhancement of photoacoustic microscopy with three-dimensional deep learning process

Presenter: Changho Lee, Chonnam National University Medical School

Dat Thanh Le[1], **Changho Lee**[2]

[1]Chonnam National University, South Korea
[2]Chonnam National University Medical School, Jeollanam-do, South Korea

Photoacoustic microscopy (PAM) uses photoacoustic effects to detect absorption property at microscale resolution in high-resolution contrasts and microbiological tissues[1]. Molecules absorb energy from nanosecond pulsed beams and emit a wide band of ultrasound waveform via thermal elastic expansion [2]. The pressure signal is detected by using an ultrasonic transducer. By demonstrating high resolution and giving structural and functional information on the microvasculature, PAM imaging proved deep tissue imaging potential. Depending on the systemic setup, PAM systems may be classified as optical-resolution PAM (OR-PAM) for high spatial resolution and acoustic-resolution PAM (AR-PAM) for higher deep penetration [3]. These multiscale

PAM systems have been used in biomedical imaging applications such as structural imaging, label-free functional imaging, and molecular imaging. The acoustic-resolution PAM (AR-PAM) uses multi-mode fiber to enhance optical energy delivery and reaches a depth of centimeters under biological tissue, however, its lateral resolution is limited due to rough laser focusing. The PAM system turns optical-resolution mode (OR-PAM) with substantial scattering to exhibit a restricted 1 mm penetration depth but tightly focused laser beam with greater spatial resolution than AR-PAM by switching the fiber to single-mode. We applied a Cyclic Consistency Generative Adversarial Networks [4] (CycleGAN) to learn and create the regularities of objects' features in axial scanning (b-scan) to increase the resolution of AR-PAM. The CycleGAN included the inverse transform to examine specific patterns while preserving the benefits of AR-PAM and OR-PAM in three dimensions. OR-PAM and AR-PAM training datasets were created by using leaf phantom. The mean square error (MSE) between the original AR-PAM and the restoration AR-PAM b-scan was used to control the model quality. The generator model can extract from the original AR-PAM b-scan to create an OR-PAM b-scan with greater contrast and similar spatial resolution to the original OR-PAM b-scan after training. The generator model can extract from the original AR-PAM b-scan to create an OR-PAM b-scan with greater contrast and equivalent spatial resolution to the original OR-PAM b-scan after training. In this study, we prepared the dual-mode AR/OR-PAM system with two-lighting channels: 5-um single-core optical fiber (SMF, P1-405BPM, Thorlabs) as OR-PAM laser channel, and 400-um multiple-core optical fiber (MMF, M74L01, Thorlabs) as AR-PAM laser channel. Both laser-beam channels were excited in turn by laser control. The generated acoustic signal was recorded by the ultrasonic transducer (V214-BC-RM, Olympus, Japan) and synchronized with laser control. Using leaf phantom as an experiment sample, we collected around 8000 images of AR-PAM b-scan and OR-PAM b-scan in 02 groups: training and testing group. The b-scan was cropped into 16-bit and 256*256 pixels by each. The CycleGAN was successfully applied by Python coding and PyTorch libraries with followed the standard approach: the number of epochs reach 50 iterations, the Adam solver was applied with a patch size of 1, and the learning rate was set at 0.0002. After training, we extracted the b-scan of the sample and applied the maximum amplitude projection (MAP) to the original AR-PAM, original OR-PAM and generated OR-PAM images from a stack of b-scans, respectively. The results showed the feasibility of applying deep learning to enhance AR-PAM resolution, and sensitivity when keeping the depth enhancement without OR-PAM configuration.

Reference

1. C. Lee, D. Lee, Q. Zhou, J. Kim, and C. Kim, "Real-time Near-infrared Virtual Intraoperative Surgical Photoacoustic Microscopy," Photoacoustics, vol. 3, no. 3, pp. 100–106, Sep. 2015, doi: 10.1016/J.PACS.2015.08.002.
2. C. Liu and L. Wang, "Functional photoacoustic microscopy of hemodynamics: a review," Biomedical Engineering Letters 2022, vol. 1, pp. 1–28, Apr. 2022, doi: 10.1007/S13534-022-00220-4.
3. L. v. Wang, "Multiscale photoacoustic microscopy and computed tomography," Nature Photonics 2009 3:9, vol. 3, no. 9, pp. 503–509, Aug. 2009, doi: 10.1038/nphoton.2009.157.
4. J. Y. Zhu, T. Park, P. Isola, and A. A. Efros, "Unpaired Image-to-Image Translation Using Cycle-Consistent Adversarial Networks," Proceedings of the IEEE International Conference on Computer Vision, vol. 2017-October, pp. 2242–2251, Dec. 2017, doi: 10.1109/ICCV.2017.244.

Poster Presentation

Disclosures: The authors have disclosed no financial interest.

448-Optical high resolution 3D characterisation of the complete Beta-cell mass distribution of the human pancreas

Presenter: Joakim Lehrstrand, Umea University

Max Hahn[1], **Joakim Lehrstrand[2]**, Wayne I. Davies[3], Federico Morini[3], Tomas Alanentalo[3], Olle Korsgren[3], Ulf Ahlgren[4]

[1]*Umea University, Umeå, Vasterbotten, Sweden*
[2]*Umea University, Sweden*
[3]*Umea University, Umea, Vasterbottens lan, Sweden*
[4]*Umea University, Umea, Sweden*

Despite the central role of the islets of Langerhans in regulating blood glucose homeostasis, much information is lacking regarding their global distribution, organisation and physiology within the context of the pancreas as a whole. One major obstacle when implementing modern mesoscopic imaging approaches, such as optical projection tomography (OPT) and light sheet fluorescence microscopy (LSFM), in studies of large tissue volumes is the poor penetration of labelling agents (e.g., primarily antibodies). To circumvent this problem, we have developed an approach to immunolabel and image cubic cm-sized tissue volumes that are mapped to the whole organ. By stitching resultant datasets back into 3D space, much like a 3D jigsaw puzzle in which the position of each piece is known beforehand, we demonstrate how this approach can be successfully used to analyse large volumes of human pancreatic tissue, with high resolution and essentially full freedom of target selectivity using antibody-based labelling. Specifically, we provide the first account of the 3D-spatial distribution and volume of insulin producing β-cells throughout the human pancreas with near cell level resolution and identify previously unrecognised β-cell distribution patterns in the pancreas from donors with long standing Type 1 Diabetes (T1D). Taking advantage of the autofluorescent (AF) properties of the pancreatic tissue, we relate this information to the vascular and ductal network of the gland. Most significantly, our data uncovered the presence of β-cell clusters that are spatially separated from other islet cell types, such as glucagon expressing α-cells. Although the significance of this observation needs to be elucidated, we speculate that these clusters could be associated with regions of compensatory β-cell expansion and/or regeneration. Further, we demonstrate that the uncinate process of the head of the pancreas exhibits the highest remaining β-cell density, which potentially reflects key aspects of disease dynamics. This first whole organ account, at the current level of resolution, may serve as an important advancement towards detailed analyses of endocrine cell identity/function via a wide range of markers in the study of normal pancreas anatomy and pathophysiology.

Reference

1. Sharpe J, Ahlgren U, Perry P, Hill B, Ross A, Hecksher-Sorensen J, Baldock R, Davidson D. Optical projection tomography as a tool for 3D microscopy and gene expression studies. Science. 2002 Apr 19;296(5567):541-5.
2. Alanentalo T, Asayesh A, Morrison H, Loren CE, Holmberg D, Sharpe J, Ahlgren U. Tomographic molecular imaging and 3D quantification within adult mouse organs Nature Methods. 2007 Jan;4(1):31-3.
3. Cheddad A, Svensson C, Sharpe J, Georgsson F, Ahlgren U. Image Processing Assisted Algorithms for Optical Projection Tomography. IEEE Trans Med Imaging. 2012 Jan;31(1):1-15
4. Near infrared optical projection tomography for assessments of ß-cell mass distribution in diabetes research. A. U. Eriksson, C. Svensson, A. Hörnblad, A. Cheddad, E. Kostromina, M. Eriksson, N. Norlin, A. Pileggi, J. Sharpe, F. Georgsson, T. Alanentalo & U. Ahlgren. J Vis Exp, 2013 Jan 12;(71):e50238.

5. Mesoscopic 3D imaging of pancreatic cancer and Langerhans islets based on tissue autofluorescence. Max Hahn, Christoffer Nord, Oskar Franklin, Tomas Alanentalo, Martin Isaksson Mettävainio, Federico Morini, Maria Eriksson, Olle Korsgren, Malin Sund & Ulf Ahlgren. Scientific Reports (2020) Oct 26;10(1):18246.
6. 3D imaging of human organs with micrometer resolution - applied to the endocrine pancreas. Max Hahn, Christoffer Nord, Maria Eriksson, Federico Morini, Tomas Alanentalo, Olle Korsgren & Ulf Ahlgren. Communications Biology, 2021 Sep 10;4(1):1063.

Poster Presentation

Disclosures: The authors have disclosed no financial interest.

449-Development and in vitro evaluation of an RNA aptamer as a PET reporter gene

Presenter: Hasan Babazada, University of Pennsylvania

Hasan Babazada[1], Bryan Chang[1], Soojin Kwon[2], Chatherine Shang[2], Katheryn Lohith[3], Michael Farwell[3]

[1]University of Pennsylvania, Philadelphia, PA
[2]University of Pennsylvania
[3]University of Pennsylvania, Philadelphia PA, PA

Background:
RNA aptamers are artificial oligonucleotides that can be evolved to bind to a specific molecule with high affinity, making them desirable candidates for diagnostic and therapeutic applications. One well-characterized aptamer is a high-affinity tetracycline-binding aptamer that is 71 nucleotides in length. Here we characterized the ligand binding properties of the aptamer with tetracycline and 7-iodosancycline, and assessed the ability of the aptamer, using single and sequential tandem repeats of the aptamer, to accumulate radioiodinated sancycline *in vitro*, when expressed in cancer cells.

Methods:
To evaluate the binding properties of the tetracycline-binding aptamer to 7-iodosancycline, the aptamer was cloned in a pET28 plasmid in between *BglII* and *BamHI* sites operating under a T7 promoter. For precise 3′ ends, the plasmid was linearized at an engineered *PstI* site upstream of *BamHI,* and RNA was transcribed and purified using T7 mScript mRNA production system. The dissociation constant of 7-iodosancycline was determined by fluorimetry together with tetracycline as a positive control. Using the sequence of the tetracycline-binding RNA aptamer, we designed three additional RNA aptamers with 4, 8, and 16 sequential tandem repeats separated by short intervening linkers of 17 randomized nucleotides. These constructs were then stably transduced into a HCT116 mammalian cell line using 3rd generation lentiviral transduction vectors. [124I]-7-Iodosancycline was synthesized via an electrophilic radioiododestannylation reaction. Cell uptake studies were performed using [124I]-7-iodosancycline in transduced and wild-type cells. Blocking studies were performed by incubating cells with tetracycline for 1 hour prior to treatment with [124I]-7-iodosancycline.

Results:
We titrated tetracycline (0.5 nM) and 7-iodosancycline (10 nM) with increasing amounts of RNA and plotted the fractional saturation of compounds as a function of the concentration of free RNA. Using a single binding site model, we calculated a dissociation constant K_d of ~1.2 nM and ~20 nM for tetracycline and 7-iodosancycline respectively (Fig. 1A). The efficiency of stable cell line generation was monitored by the expression of EGFP (Fig. 1B). [124I]-7-Iodosancyline gave a radiochemical yield of 24% ± 2.8% (n=2) with radiochemical purity of >95%. We compared the aptamer expressing HCT116 cells and wild-type control for their ability to concentrate [124I]-7-iodosancycline. [124I]-7-iodosancycline uptake was significantly higher in aptamer-expressing HCT116 cells, when compared to the wild-type control. After 1 hour of incubation, uptake in 1-mer, 4-mer, 8-mer and 16-mer HCT116 cells increased 24%, 69%, 97% and 110% respectively, as compared to wild-type cells. Pre-treatment of cells with tetracycline effectively blocked the uptake of isotope. We found that the uptake pattern increased over time and uptake correlated with aptamer copy number, with the 16-mer construct having the highest uptake (Fig. 1C).

Conclusion:
Cells expressing a tetracycline-binding RNA-aptamer demonstrate greater radiolabeled-sancycline uptake compared to controls, with a positive correlation between the number of aptamer repeats in the reporter gene and cell uptake. The observed dissociation constant of ~20 nM for 7-iodosancycline makes it an excellent potential PET reporter probe. Continued research to translate this technology to the *in vivo* setting may yet provide a powerful tool for diagnostic applications such as cell tracking.

Poster Presentation

Disclosures: The authors have disclosed no financial interest.

450-Milk Small Extracellular Vesicles As Natural Nanoprobes For Tumor Detection By Optical Imaging

Presenter: María Isabel González-Gutiérrez, Fundación Investigación Biomédica del Hospital Gregorio Marañón

María Isabel González-Gutiérrez[1], Ana Santos-Coquillat[2], Sara Sánchez-Redondo[3], Desiré Herreros Pérez[1], Marta Hergueta-Redondo[3], Héctor Peinado[3], Beatriz Salinas[4], Manuel Desco[5]

[1]Fundación Investigación Biomédica del Hospital Gregorio Marañón, Madrid, Spain
[2]Instituto de Investigación Sanitaria Gregorio Maranon, Spain
[3]Spanish National Cancer Research Center (CNIO), Madrid, Spain
[4]Fundación Investigación Biomédica del Hospital Gregorio Marañón, Madrid, Madrid, Spain
[5]Instituto de Investigación Sanitaria Gregorio Maranon, Madrid, Spain

Introduction:
Despite the promising use of synthetic nanoparticles as imaging agents in biomedicine, their translation to the clinic is complex due to some drawbacks associated with their potential toxicity or lack of in *vivo* stability, limiting their use in oncological imaging [1]. Small extracellular vesicles (sEV) are naturally secreted by cells for communication purposes [2] and present physical characteristics close to liposome-like nanoparticles, such as nanometric size or lipid bilayer structure. Together with their natural origin and their intrinsic biological role associated with the development of certain pathologies [3], these small vesicles are postulated as substitutes for traditional nanoparticles in cancer imaging applications. Herein, we present the potential use of fluorescently-labeled milk sEV as natural nanoprobes for tumor imaging, highlighting their capacity to interact with different cells from the tumor microenvironment.

Methods:
sEV were isolated from commercial goat milk by ultracentrifugation and size exclusion chromatography, being characterized by TEM, DLS, NTA and proteomics. The optical labeling of sEV was performed following the methodology previously optimized by our research group [4]. Briefly, 75µg of sEV were covalently labeled with 10µL of SCy7.5-NHS (16.9mM), for 2h at 4ºC and pH 8.5. Resultant nanoprobe was also characterized by TEM, DLS, NTA and flow cytometry. *In vitro* internalization of fluorescent sEV (0.5µg/mL) by 264.7 RAW macrophages, C166-GFP endothelial cells and B16F10-Luc-GFP melanoma cells was evaluated by flow cytometry after 5h, 24h and 48h of incubation. *In vivo* tracking of the nanoprobe in tumor area was assessed in a subcutaneous allograft melanoma model injected in C57BL/6J mice ($5 \cdot 10^5$ B16F10-Luc-GFP melanoma cells/mouse, 1-week *in vivo* growth). Mice were imaged 1h, 5h, 24h, 48h, 72h and 96h after the intravenous injection of the nanoprobe (20µg/100µL), using an IVIS spectrum system. *Ex vivo* fluorescence and luminescence signal in fresh tumors was registered by IVIS and ODYSSEY imaging, 5h and 48h post sEV-administration. Uptake by macrophages and tumor cells was also analyzed and quantified by confocal imaging in excised tumors.

Results:
Milk sEV were fluorescently labeled by covalent binding, reaching high reaction yield (99.9% by flow cytometry) and preserving the original morphology and size distribution of isolated vesicles (Fig 1A). Macrophages and endothelial cells exhibited fast EVs internalization, achieving 99.8±0.1% and 80.4±3.5% of fluorescent positivity after 5h of incubation, respectively. In contrast, tumor cells presented maximum EVs uptake after 48h (Fig 1B). *In vivo* optical imaging showed EVs accumulation in the tumor tissue even 1h post-administration and revealed progressive decrease of the fluorescence signal along time (Fig 1C). *Ex vivo* optical imaging of excised tumors confirmed the nanoprobe uptake by the correlation between bioluminescence from tumor cells and fluorescence from the nanovesicles. Confocal analysis of tissues showed that both tumor-associated macrophages and tumor cells take up sEV, but macrophages exhibited slight increased accumulation of the vesicles (Fig 1D). Quantification of fluorescent signal showed that intensity decreased from 5h to 48h.

Conclusions:
This work presents the potential use of fluorescently-labeled milk sEV as natural nanoplatforms for non-invasive tumor imaging. Fluorescent sEV are rapidly accumulated in primary tumor due to the successful internalization by cells associated to the tumor microenvironment.

Reference
1. van der Meel, Roy, et al. Nature nanotechnology, 2019, vol. 14, no 11, p. 1007-1017.
2. He, Chuanjiang, et al. Theranostics, 2018, vol. 8, no 1, p. 237.
3. Li, Irene; Nabet, Barzin Y. Molecular Cancer, 2019, vol. 18, no 1, p. 1-10.
4. González, María Isabel, et al. Biomedicines, 2021, vol. 9, no 1, p. 81.

Poster Presentation

Disclosures: The authors have disclosed no financial interest.

451-Radiolabelled exosomes as imaging diagnostic tools for early detection of lung metastasis by PET

Presenter: Sara Almeida, University of Coimbra

Sara Almeida[1], Alexandra Isabel Fonseca[2], José Sereno[2], Hugo Ferreira[1], Mariana Lapo-Pais[3], Tânia Martins-Marques[3], Teresa Rodrigues[3], Henrique Girão[3], Celia Gomes[1], Antero Abrunhosa[1]

[1]*University of Coimbra, Portugal*
[2]*alexandraf1996@gmail.com*
[3]*Institute for Nuclear Sciences Applied to Health, Portugal*

Introduction:
Lung metastases (LM) are the leading cause of osteosarcoma (OS)-related death. Current imaging modalities have limited potential in detecting early-stage pulmonary metastasis.[i] Exosomes (EXs) released by tumour cells are major determinants of metastatic organotropism,[ii] and have an intrinsic targeting ability for donor cells, making them potential diagnostic tools and therapeutic vehicles for metastatic lesions.[iii],[iv] Herein, we evaluated the *in vivo* behaviour of EXs by optical and nuclear imaging and their usefulness as non-invasive imaging biomarkers for lung metastasis.

Materials and Methods:
Swiss Fox^{1nu} nude mice were *i.v.* injected with OS cells (143B-Luc+) into the tail vein. Lung metastasis formation was monitored by bioluminescence imaging (BLI) and magnetic resonance imaging (MRI). Exosomes were isolated from the supernatant of 143B cells and radiolabelled with the positron-emitter radionuclide copper-64 ($t_{1/2}$ = 12.7 h, 17.9% β^+, E = 0.653 MeV) via maleimide-thiol conjugation with a bifunctional chelator. Labelling efficiency and stability in biological fluids were assessed. Control and lung metastasis-bearing mice were *i.v.* injected with the radiolabelled EXs and imaged in a micro-PET/MRI at 24 h post-injection. OS-derived EXs were also loaded with DMNPE-caged luciferin or labelled with a near-infrared (NIR) fluorescent dye for optical imaging.

Results:
The surface functionalization via maleimide-thiol conjugation followed by the chelation with ^{64}Cu resulted in a high radiochemical yield of almost 100% and high stability in both PBS and mouse serum at least for 24 h, without affecting the intrinsic features of EXs in terms of morphology, size, or charge or targeting ability for OS cells. Whole-body PET/MRI images obtained 24h after injection showed a clear uptake of EXs in the lung metastatic lesions, which was also observed by near-infrared fluorescence and confirmed by *ex vivo* biodistribution studies by gamma counting. No detectable PET or fluorescent signals was observed in healthy lungs devoid of metastasis, confirming the homing and selective affinity of EXs for homotypic donor cells.

Conclusions:
Exosomes derived from osteosarcoma cells possess an intrinsic homing ability for metastatic lesions and hold great potential as targeted imaging agents for the non-invasive early assessment of lung metastasis by nuclear imaging. The translation of this imaging agent to a clinical set could improve the prognosis of OS patients.

Acknowledgements: FCT: PD/BDE/142929/2018 and PTDC/BTM-SAL/4451/2020. LPCC/LIONS Portugal.

Reference
1. Meazza, C. and Scanagatta, P.Expert Review of Anticancer Therapy, 2016, 16(5), 543-556. doi:10.1586/14737140.2016.1168697.
2. A. Hoshino, B. et al.. Nature, 2015, 527, 329–335. doi:10.1038/nature15756.
3. Zhao Y. et al.. Front. Oncol., 2021, 11, 1-24. doi:10.3389/fonc.2021.743189.

4. Jiang L., Gu Y., Du Y. and Liu J. Mol. Pharmaceutics 2019, 16 (8), 3333–3349. doi: 10.1021/acs.molpharmaceut.9b00409.

Poster Presentation

Disclosures: The authors have disclosed no financial interest.

452-Effect of neoadjuvant therapies on epidermal growth factor receptor (EGFR) expression and EGFR-targeted fluorophore binding in soft-tissue sarcomas

Presenter: Samuel Streeter, Dartmouth College

Samuel Streeter[1], Xiaochun Xu[2], Paul Werth[1], Kim Samkoe[3], Eric Henderson[2]

[1]Dartmouth College, Hanover, New Hampshire
[2]Dartmouth College, Lebanon, NH
[3]Dartmouth College, Hanover, NH

Curative surgery for soft-tissue sarcoma (STS) is ideally performed via a wide local excision, a procedure that removes *en bloc* both the tumor and a surrounding margin of healthy tissue. Neoadjuvant treatments in the form of external beam radiation and/or chemotherapy are often administered preoperatively for STS, usually to neutralize tumor extension and allow for the sparing of critical neurological or vascular structures surrounding the primary tumor. Fluorescence-guided surgery (FGS) is a nascent technology that aims to improve the efficacy of surgical interventions through identification of important tissues or anatomical structures via fluorescent molecules that accumulate in target tissues by local perfusion, metabolism, or molecular binding (1). FGS has been most heavily studied in the operative removal of cancers, most notably in the treatment of malignant gliomas (2) but also in the management of STS (3–5). The epidermal growth factor receptor (EGFR) is overexpressed in 43-78% of STS cases and has proven a useful target for molecular-guided FGS for STS in human xenograft models (6). The fluorophore ABY-029, a synthetic Affibody peptide, Z03115-Cys, labeled with a near-infrared fluorophore, IRDye 800CW, targets the EGFR with high specificity (7). However, to date, STS fluorescence imaging using ABY-029 has occurred in tumors naïve to chemotherapy and radiation. Because of the high frequency of neoadjuvant therapy use in the treatment of STS (8), and the potential for these therapies to modulate tumor receptor expression, a need exists to understand the ability of ABY-029 to effectively label STS in a clinical setting. The goal of this study was to identify the effects of neoadjuvant radiation and doxorubicin chemotherapy on the expression of EGFR in—and thus the binding of ABY-029 to—human STS xenografts in a mouse model. The study workflow is summarized in Figure 1A. Eighty (n=80) female NGS mice (The Jackson Laboratory, Bar Harbor, ME) were used to develop tumor xenografts. Three STS tumor cell lines were compared in this study: MES-SA, an EGFR-negative uterine sarcoma; SK-LMS-1, a uterine leiomyosarcoma; and VA-ES-BJ, an epithelioid sarcoma. Tumor cells were implanted subcutaneously into the right flank of each mouse with an equal volume of Matrigel (Corning Life Sciences, Corning, NY) to maintain cell location and promote cell growth. Four types of treatments—control, radiation, chemotherapy (doxorubicin), and radiation followed by chemotherapy—were given to equally sized cohorts of mice (n=20 each) once the tumor size reached 200 mm^3. After treatment and pre-surgical ABY-029 injection, four types of tissues— adipose, muscle, nerve, and tumor—were harvested from each animal. Fluorescence images were obtained to measure the change in fluorescence signal intensity, which depends on the plasma delivery, tissue density, and receptor expression level. EGFR staining was used as a gold standard for the change in EGFR concentration, and SMA and CD31 IHC staining were used as a gold standard for the change in the vasculature. The resulting correlations between therapy treatments and changes in fluorescence signal were examined. For the three STS cell lines tested, after therapy treatment, no statistically significant reduction in the fluorescence signal intensity was found, including control (Figure 1B). This result indicates positive or no effect on fluorescence signal after different therapies. While tumor-to-background tissue ratios did not exhibit statistically significant differences between treatment cohorts, ratios did vary with the type of sarcoma tumor (data not shown). In conclusion, this work provides the first evidence that neoadjuvant radiation and chemotherapy have insignificant impacts on EGFR expression and ABY-029 binding in human STS xenografts in a mouse model, and as such, represents an important step toward clinical translation of ABY-029 in FGS.

Reference

1. Brian W. Pogue, Eben L. Rosenthal M.D., Samuel Achilefu, Gooitzen M. van Dam, Perspective review of what is needed for molecular-specific fluorescence-guided surgery. Journal of Biomedical Optics 23, 1–9 (2018).
2. W. Stummer, et al., Fluorescence-guided surgery with 5-aminolevulinic acid for resection of malignant glioma: a randomised controlled multicentre phase III trial. Lancet Oncol 7, 392–401 (2006).
3. J. K. Mito, et al., Intraoperative detection and removal of microscopic residual sarcoma using wide-field imaging. Cancer 118, 5320–5330 (2012).
4. David Holt D.V.M., et al., Intraoperative near-infrared fluorescence imaging and spectroscopy identifies residual tumor cells in wounds. Journal of Biomedical Optics 20, 1–14 (2015).
5. J. M. Stahl, et al., The effect of microscopic margin status on survival in adult retroperitoneal soft tissue sarcomas. Eur J Surg Oncol 43, 168–174 (2017).
6. C. Kersting, et al., Pitfalls in immunohistochemical assessment of EGFR expression in soft tissue sarcomas. J Clin Pathol 59, 585–590 (2006).
7. K. S. Samkoe, et al., Preclinical imaging of epidermal growth factor receptor with ABY-029 in soft-tissue sarcoma for fluorescence-guided surgery and tumor detection. J Surg Oncol 119, 1077–1086 (2019).
8. M. J. Spałek, et al., Neoadjuvant Treatment Options in Soft Tissue Sarcomas. Cancers (Basel) 12, 2061 (2020).

Poster Presentation

Disclosures: The authors have disclosed no financial interest.

453-Therapy of Orthotopic glioma with a biomimetic drug delivery system functionalized by liposome loading with PTX

Presenter: XiaoXuan Xu, Southeast University

XiaoXuan Xu

Southeast University, Nanjing, Jiangsu, China, China

The purpose of this work is to establish a bionic smart nano-platform that uses two different modal magnetic resonance imaging agents to achieve dual-modal magnetic resonance imaging of original gliomas in mice, and to identify the location of the lesion. In addition, the high biocompatibility, immune evasion ability and active tumor site

selection of glioma are used to overcome the limitations of the blood-brain barrier (BBB) for glioma. Effective delivery of PTX can improve the efficiency of immunotherapy for glioma, and provide new possibilities for further development of glioma treatment. The carrier of the nano-delivery platform was constructed, and the PTX was encapsulated in. The target activity, biosafety and suitability of the material were tested in vitro experiments, while the corresponding parts and therapeutic effects were tested in vivo. Then the general condition of each group of mice was evaluated, and the improvement of outcome was detected at molecular and protein levels. The nanoparticles showed better targeting ability, that is, higher delivery efficiency to glioma. In addition, in the characteristic acidic microenvironment of tumor, nanoparticles could be degraded "on-demand" to release internal molecules, so as to achieve targeted and precise treatment of tumor. At the same time, bio-membrane-modified nanoparticles showed better biocompatibility, stability, and longer cycle time in the body. The biomimetic intelligent active target nano-therapeutics can significantly improve the outcome and biological safety, and is a feasible method to improve the therapeutic effect of chemotherapy for orthotopic glioma. The design and application of the biomimetic nano-platform may provide a new therapeutic option for immunotherapy of brain tumors.

Reference

1. Mai, W., et al., Cytoplasmic p53 couples oncogene-driven glucose metabolism to apoptosis and is a therapeutic target in glioblastoma. Nature medicine, 2017. 23(11): p. 1342-1351.
2. Tan, A., et al., Management of glioblastoma: State of the art and future directions. CA: a cancer journal for clinicians, 2020. 70(4): p. 299-312.
3. Akintola, O.O. and D.A. Reardon, The Current Landscape of Immune Checkpoint Blockade in Glioblastoma. Neurosurg Clin N Am, 2021. 32(2): p. 235-248.
4. Lim, M., et al., Current state of immunotherapy for glioblastoma. Nat Rev Clin Oncol, 2018. 15(7): p. 422-442.
5. Aldape, K., et al., Challenges to curing primary brain tumours. Nature reviews. Clinical oncology, 2019. 16(8): p. 509-520.
6. Herbst, R.S., et al., Predictive correlates of response to the anti-PD-L1 antibody MPDL3280A in cancer patients. Nature, 2014. 515(7528): p. 563-7.
7. Vom Berg, J., et al., Intratumoral IL-12 combined with CTLA-4 blockade elicits T cell-mediated glioma rejection. J Exp Med, 2013. 210(13): p. 2803-11.
8. Mansurov, A., et al., Collagen-binding IL-12 enhances tumour inflammation and drives the complete remission of established immunologically cold mouse tumours. Nature biomedical engineering, 2020. 4(5): p. 531-543.
9. Qi, Y., et al., Immune Checkpoint Targeted Therapy in Glioma: Status and Hopes. Front Immunol, 2020. 11: p. 578877.
10. Banks, W.A., From blood-brain barrier to blood-brain interface: new opportunities for CNS drug delivery. Nat Rev Drug Discov, 2016. 15(4): p. 275-92.
11. Xue, J., et al., Neutrophil-mediated anticancer drug delivery for suppression of postoperative malignant glioma recurrence. Nat Nanotechnol, 2017. 12(7): p. 692-700.
12. Coureuil, M., et al., A journey into the brain: insight into how bacterial pathogens cross blood-brain barriers. Nat Rev Microbiol, 2017. 15(3): p. 149-159.
13. Zhang, N., et al., Treatment Progress of Immune Checkpoint Blockade Therapy for Glioblastoma. Front Immunol, 2020. 11: p. 592612.
14. Zhang, J., et al., Immunostimulant hydrogel for the inhibition of malignant glioma relapse post-resection. Nat Nanotechnol, 2021. 16(5): p. 538-548.
15. Postow, M.A., M.K. Callahan, and J.D. Wolchok, Immune Checkpoint Blockade in

Poster Presentation

Disclosures: The authors have disclosed no financial interest.

454-Genetically Engineered Salmonella typhimurium Sensing and Responding to Nitric Oxide in Tumor

Presenter: Yeshan Qin, Chonnam National University

Yeshan Qin

Chonnam National University, South Korea

Recent advances in synthetic biology allows the application of engineered bacteria for living diagnosis and therapeutics. In this study, we designed a genetic circuit enables *Salmonella typhimurium* sense and respond to the elevated nitric oxide in the tumor region. Nitric oxide, a vital signaling molecule in the immune system, plays key role in various pathological processes including inflammation and tumor immune response. The formation of NO is catalyzed by nitric oxide synthase (NOS), and the expression of inducible NOS (iNOS) can be regulated by pro-inflammatory cytokines, including IFN-γ, TNF-α and IL-1β, as well as bacterial LPS. In consequence, large amount of NO is synthesized, exceeding the physiological NO production by up to 1000-fold. After the colonization and proliferation of *Salmonella typhimurium* in tumor, both LPS and damaged cancer cells can activate the inflammasome, and induce the infiltration of immune cells, such as neutrophils and macrophages, which can secret pro-inflammatory cytokines, such as TNF-α and IL-1β. To this end, we hypothesized that NO can be used as an inducer for tumor specific gene expression carried by *Salmonella* ppGpp. Therefore, a switch system was constructed utilizing the NO sensor and a DNA recombinase. We demonstrated that our construct can respond to gradient concentration of nitric oxide source DETA/NO *in vitro* and the switch occurred at 50 uM of DETA/NO. I*n vivo* result showed that the switch can be specifically induced in tumor region, and can be inhibited by the iNOS inhibitor, 1400W. Our results demonstrated that NO can be a candidate inducer for tumor specific gene expression carried by *Salmonella typhimurium*.

Reference

1. Engineered E. coli That Detect and Respond to Gut Inflammation through Nitric Oxide sensing, Eric J. Archer, et al., ACS Synth. Biol., 2012, 1, 451-457
2. Two-step enhanced cancer immunotherapy with engineered Salmonella typhimurium secreting heterologous flagellin, Jin Hai Zheng, et al., Sci. Transl. Med., 9, 2017.

Poster Presentation

Disclosures: The authors have disclosed no financial interest.

455-MALDI Imaging of COVID-19 Lipid Storm in Human Lung and Bronchoalveolar Lavage Samples

Presenter: Caitlin Tressler, Johns Hopkins University School of Medicine

Caitlin Tressler[1], Alvaro A. Ordonez[2], Andres Villabona-Rueda[3], Maureen Horton[4], Franco R. D'Alessio[2], David Nauen[2], Kristine Glunde[5]

[1]*Johns Hopkins University School of Medicine, Baltimore*
[2]*Johns Hopkins University School of Medicine, Baltimore, MD*
[3]*Baltimore, Maryland*
[4]*The Johns Hopkins University School of Medicine, Baltimore, MD*
[5]*Johns Hopkins University School of Medicine, Baltimore, Maryland*

Introduction:
The SARS-CoV-2 is a respiratory virus responsible for the COVID-19 pandemic and results in a wide range of severity from mild cold or flu-like symptoms to hospitalization and death. In cases of hospitalization, many patients have to be intubated due to difficulty breathing and excessive fluid in their lungs. Patients who ultimately recover from COVID-19 are often suffer from prolonged pulmonary, cardiac, and neurological symptoms. Immediate, severe disease and long-term symptoms are believed to be a result of a dysregulated immune response. Mechanistic information of the molecular events leading to severe COVID-19 disease and recovery are key in understanding the long-term symptoms and in revealing potential novel treatment strategies.

Methods:
Bronchoalveolar lavage (BAL) and post-mortem lung samples were obtained from consenting patients during the height of the COVID-19 pandemic in 2020. Control lung tissues were obtained from the Johns Hopkins pathology archives. BAL samples were deposited on poly-L-lysine coated indium tin oxide slides using a cytospin centrifuge, and formalin fixed to ensure decontamination of active virus. Lung samples from two patients who had COVID-19 at the time of death and two patients with non-lung affecting illnesses were cryo-sectioned at 10-micron thickness onto ITO slides. Samples were stored at -20 °C until imaging. Samples were sprayed on an HTX M5 sprayer with 40 mg/mL 2,5-dihydroxybenzoic acid in 70% acetonitrile with 0.2% trifluoracetic acid. Samples were imaged at 20-micron spatial resolution in positive ion mode with 200 laser shots per pixel from m/z 0 to 2000. Data was analyzed in FlexImaging and SCiLS Lab software.

Results:
Our patient cohort of BAL samples contains three survivors and 12 deceased patients who were all hospitalized and intubated at the time of sample collection. MALDI imaging of positive ion lipids was collected and analyzed for lipids which are increased in patients who succumbed to COVID-19. Twenty three different lipids were identified ($p > 0.9$) as potential indicators of fatal COVID-19. The top m/z 725.5, tentatively assigned to PA 36:1, was present in the BAL samples of all patients who succumbed to COVID-19 (Fig. 1). Using a receiver operating characteristic curve, this lipid produced an area under the curve (AUC) of 0.97. The second top m/z 760.5 had an AUC of 0.952, with the second highest intensity in many of the deceased patients compared to surviving patients. Further, these two m/z's displayed a high intensity correlation value of 0.82, indicating that these two lipids are frequently occurring together and may be regulated by the same pathway. Finally, in the two post-mortem lung samples examined, one COVID-19 patient lung contained significantly increased PA 36:1 as compared to the control lungs. Lipid storm, which is the significant increase of a variety of lipids, has previously been described in a few studies of COVID-19 plasma samples.

Discussion:
This phenomenon has been suggested to be promoted by the immune response, however, it has not been fully characterized in the lungs. In this pilot study, we have, for the first time, discovered two lipids which are indicative of fatal COVID-19 disease in live patient BAL samples. We have also shown that this finding in BAL samples is partially supported by our observations of elevated lipids in human post-mortem lung samples. Our future work includes increasing our patient cohort of BAL and lung samples, as well as identifying more of the increased lipids to gain a deeper understanding of the phenomenon of COVID-19 induced lipid storm in human lungs.

Reference
1. Surma, S., Banach, M. & Lewek, J. COVID-19 and lipids. The role of lipid disorders and statin use in the prognosis of patients with SARS-CoV-2 infection. Lipids Health Dis 20, 141 (2021).
2. Archambault, A-S, Zaid, Y, Rakotoarivelo, V, et al. High levels of eicosanoids and docosanoids in the lungs of intubated COVID-19 patients. The FASEB Journal. 2021; 35:e21666.
3. Zaid Y, Doré É, Dubuc I, Archambault AS, Flamand O, Laviolette M, Flamand N, Boilard É, Flamand L. Chemokines and eicosanoids fuel the hyperinflammation within the lungs of patients with severe COVID-19. J Allergy Clin Immunol. 2021 Aug;148(2):368-380.e3.

Poster Presentation

Disclosures: The authors have disclosed no financial interest.

456-An MR-based brain template and atlas for optical projection tomography and light sheet fluorescence microscopy

Presenter: Stefanie Willekens, Umea University

Stefanie M. Willekens[1], Federico Morini[1], Anna Överby[1], Ulf Ahlgren[2], Daniel Marcellino[1]

[1]*Umea University, Umeå, Sweden*
[2]*Umea University, Umea, Sweden*

Optical projection tomography (OPT) and light sheet fluorescence microscopy (LSFM) are high-resolution optical imaging techniques, operating in the mm-cm range and are therefore ideally suited for ex vivo 3D whole mouse brain imaging (1,2). Although these techniques exhibit high specificity and sensitivity for their antibody-labeled targets, the anatomical information remains limited. The possibility to anatomically map specific protein expression profiles or pathologic markers, would greatly benefit the application of optical imaging in neuroscience. The first step towards these analyses is to co-register optical brain signals to a reference brain for which detailed annotated brain regions can be readily identified. Therefore, we aimed to develop a novel magnetic resonance (MR)- based brain template and atlas, specifically designed for brains subjected to tissue processing protocols required for 3D optical imaging. Brains were cleared for OPT/ LSFM using BABB (n=10) or DBE (n=9). Afterwards, T1-weighted MR images (MDEFT, TR/TE/TI 3000/3/950ms, 40 mm^3 voxel size) were acquired. Individual images were realigned and averaged using serial longitudinal registration, resulting in a specific BABB and DBE template. Individual DBE brains were then normalized to the BABB template and vice versa. Consequently, final OCUM (BABB size) and iOCUM (DBE size) templates were created by rerunning SLR on all brains (n=19). Both for OCUM and iOCUM, TPMs were created using a 2-step segmentation and DARTEL pipeline. After whole brain immunofluorescent labelling of viral NS5 or cholera toxin (CT), OPT/ LSFM images were acquired. The utility of the templates was investigated by creating fluorescence-MR fusion images and specific anatomical mapping of fluorescent signals. To investigate the effects of clearing on brain size, we created two individual brain templates, one for BABB and one for DBE cleared brains. Segment-based brain volume calculations revealed that DBE-cleared brains (0.308 cm^3 ±

0.009) were significantly smaller than BABB-cleared brains (0.483 ± 0.023 cm^3). Therefore, we created two brain templates containing all images (n=19) namely the Optically Cleared UMeå (OCUM) brain template for BABB brains and the iOCUM brain template for DBE cleared brains. Initially, all individual BABB and DBE cleared brains were co-registered to their respective template and normalized to the opposite template. Next, we created the OCUM and iOCUM by calculating mid-point averages from serial registration of all MR-images in both sizes. Consequently, we created specific tissue segments and tissue probability maps (TPM) using a double segmentation + DARTEL pipeline. Thereafter, we ran the complete process again, using the preliminary tissue priors generated in the previous step, to produce accurate and template specific TPMs for both OCUM and iOCUM. Finally, we normalized the DSURQE atlas to (i)OCUM space to delineate ROIs. Subcortical structures such as deep nuclei and anterior cortical regions were perfectly aligned with (i)OCUM and posterior cortical ROIs were manually adapted on each template. To highlight the applicability of the templates, we created fusion images of optical signals, acquired from BABB and DBE cleared brains, with OCUM and iOCUM. These fusion images allowed exact identification of virus infected brain regions infected. Furthermore, we traced anterograde innervation from the eye using fluorescently labeled CT. We observed clear localization of signal within lateral geniculate nucleus and superior colliculus, a perfect match of brain regions of the visual system, indicating anterograde innervation from the eye towards the visual cortex. Together, our final resources comprise: two mouse brain templates for cleared tissue, their corresponding TPMs, a mouse brain atlas with 336 annotated ROIs and a protocol to create fluorescence-MR fusion images. Thereby, we provide the optical brain imaging community a unique tool allowing anatomical brain mapping optical brain signals.

Reference

1. Dodt, H. U. et al. Ultramicroscopy: three-dimensional visualization of neuronal networks in the whole mouse brain. Nat Methods 4, 331-336, doi:10.1038/nmeth1036 (2007).
2. Sharpe, J. et al. Optical projection tomography as a tool for 3D microscopy and gene expression studies. Science 296, 541-545, doi:10.1126/science.1068206 (2002).

Poster Presentation

Disclosures: The authors have disclosed no financial interest.

457-Development of multimodal 177Lu-DOTA-JR11 analogs for imaging somatostatin receptor expression from the whole-body to the cellular level

Presenter: Nghia Nguyen, Klinikum rechts der Isar

Nghia T. Nguyen[1], Yu Min[2], Sukhen C. Ghosh[3], Wolfgang Weber[4], Ali Azhdarinia[5], Susanne Kossatz[6]

[1]*Klinikum rechts der Isar, München, Bayern, Germany*
[2]*University Hospital Klinikum rechts der Isar, Munich, Bavaria, Germany*
[3]*McGovern Medical School, Institute of Molecular Medicine, Houston, Texas*
[4]*Technical University of Munich, Munich, Baviera, Germany*
[5]*University of Texas Health Science Center at Houston, Houston*
[6]*Klinikum rechts der Isar at TU Munich, Munich, Germany*

Introduction:
Peptide Receptor Radionuclide Therapy (PRRT) with the somatostatin receptor subtype 2 (SSTR2) antagonist ^{177}Lu-DOTA-JR11 has shown promising results for the treatment of neuroendocrine tumors (NET)[1-3]. However, hematologic toxicity occurred when patients received a macroscopic bone marrow dose in the range of 1.5 Gy, which was considered a well-tolerated dose for the agonist ^{177}Lu-DOTA-TATE[2]. We hypothesize that ^{177}Lu-DOTA-JR11 binds with high affinity to a small SSTR2(+) subpopulation of hematopoietic stem cells, exerting increased hematotoxicity compared to agonist-PRRT. Here, our goal was to synthesize multimodal JR11-based analogs with comparable binding characteristics to DOTA-JR11 to enable investigations from the cellular to the whole-body level.

Methods:
We synthesized multimodal DOTA-JR11/TOC analogs by replacing DOTA with the azide-containing cyclen analog, multimodality chelator (MMC)[4], and conjugating DBCO-functionalized dyes using copper-free click chemistry. We conjugated 5 dyes: AF488 and 4 variants of SxCy5 (x=0, 2, 3 or 4 sulfo groups), resulting in MMC(Dye)-JR11/TOC variants that were characterized in comparison to DOTA-JR11/TOC. For *in vitro* experiments, we used HCT116-SSTR2 and -WT (SSTR2 negative) cells. We measured cellular uptake with radioligand assays after ^{177}Lu-labeling. We also determined the binding kinetics using K_D assays. Further characterization of compounds based on their fluorescence was done using microscopy and flow cytometry. Compound sensitivity was determined by analyzing mean fluorescence intensities (MFI). Binding of multimodal analogs (0-25 µM) was compared in cells with varying SSTR2 expression (HCT116-SSTR2 > AR42J > H446 > H69) and HCT116-WT. MMC(Dye)-JR11/TOC analogs were also added to pre-mixed cultures of SSTR2(+)/SSTR2(-) cells to identify the analog with the highest detection sensitivity for SSTR2(+) cell populations. Further analysis of SSTR2-specific binding was performed in CD34+ bone marrow cells obtained via a CD34 isolation kit. All experiments were repeated at least three times.

Results:
Following the successful synthesis of multimodal MMC(Dye)-JR11/TOC analogs, we compared their binding characteristics to DOTA-JR11/TOC. Cellular uptake values and binding specificity of ^{177}Lu-MMC(Dye)-JR11/TOC conjugates were similar to ^{177}Lu-DOTA-JR11/TOC except for the S0Cy5-variants, which showed high non-blockable uptake (*Fig. 1a*). Binding affinity of the ^{177}Lu-MMC(SxCy5)-JR11 series (K_D-values of 16.6 nM, 19.7 nM, 9.7 nM for x=2, 3 or 4, respectively) was similar to DOTA-JR11 (K_D: 9.2 nM). We confirmed via fluorescence microscopy that antagonistic (JR11) and agonistic (TOC) properties were conserved upon dye conjugation (*Fig. 1b*). MFI of MMC(SxCy5)-JR11/TOC conjugates corresponded to SSTR2 expression levels (HCT116-SSTR2 > AR42J > H69 > H446). Flow cytometric characterization further revealed superior detection sensitivity of SxCy5 variants compared to AF488-labelled compounds by up to 5-fold higher MFI at equimolar concentrations. Comparison within the SxCy5-series revealed that reduction of the number of sulfo groups led to a further increase in MFI without a loss in specificity (*Fig. 1c*). Interestingly, the experiment revealed a blockable specific binding of MMC(S0Cy5)-JR11/TOC, in contrast to the radioactive uptake results, thus identifying MMC(S0Cy5)-JR11/TOC as the candidate with highest detection sensitivity. In mixed cell populations, a high SSTR2(+) (HCT116-SSTR2) subpopulation was identified by all multimodal conjugates. Cells with very low SSTR2-expression levels (H69) were still identified from SSTR2(-) cells by MMC(S0Cy5)-JR11 (*Fig. 1d*). This confirms the suitability of our experimental design to potentially identify small SSTR2(+) cell populations in bone marrow samples.

Conclusion:
We have successfully synthesized multimodal variants of clinically used PRRT agents and present these novel agents as valuable tools to investigate cellular binding and to identify potential differences in

bone marrow binding using their multimodal property (fluorescence and nuclear detection). Our ongoing investigation of binding to bone marrow samples may improve our understanding of the hematologic toxicity caused by ^{177}Lu-DOTA-JR11 therapy. Furthermore, we envision the ligands to be helpful for intraoperative imaging of tumor samples to ensure complete resections of NETs.

Reference

1. Strosberg, J., El-Haddad, G. et al. et al., "Phase 3 Trial of 177Lu-Dotatate for Midgut Neuroendocrine Tumors", New England journal of medicine 376, 125-135, (2017).
2. Reidy-Lagunes, D., Pandit-Taskar, N. et al., "Phase I Trial of Well-Differentiated Neuroendocrine Tumors (NETs) with Radiolabeled Somatostatin Antagonist 177Lu-Satoreotide Tetraxetan", Clinical cancer research 25, 6939-6947, (2019).
3. Hennrich U., Kopka K. "Lutathera ®: The First FDA- and EMA-Approved Radiopharmaceutical for Peptide Receptor Radionuclide Therapy", Pharmaceuticals (Basel) 12, 114, (2019).
4. Ghosh, S., Ghosh, P. et al. "Multimodal Chelation Platform for Near-Infrared Fluorescence/Nuclear Imaging", Journal of medical chemistry 56, 406-416, (2013).

Poster Presentation

Disclosures: The authors have disclosed no financial interest.

458-Fluorescence guidance improves accuracy of radiological imaging-guided surgical navigation

Presenter: Samuel Streeter, Dartmouth College

Samuel Streeter[1], Kendra Hebert[1], Paul Werth[1], Kim Samkoe[2], Eric Henderson[3]

[1]*Dartmouth College, Hanover, New Hampshire*
[2]*Dartmouth College, Hanover, NH*
[3]*Dartmouth College, Lebanon, NH*

Imaging-based surgical navigation requires static referencing between the target anatomy and the imaging data provided to the clinical team. Imaging-based navigation is therefore well suited for operations involving relatively static features, such as bony anatomy (1–3). However, these technologies have not translated well to soft-tissue surgery due to an inability to adapt to positional changes during the procedure (4). Soft-tissue sarcomas (STSs) are cancers originating from mesoderm-derived connective tissues (fat, muscle, tendon, ligament, peripheral nerve, and fascia). STSs generally have poor responses to chemotherapy and modest responses to radiation; complete surgical excision of a non-metastatic primary tumor is therefore the only reliable curative treatment (5–8). STSs are optimally removed when the primary tumor is resected with a surrounding margin of normal, non-cancerous tissue through a surgical technique called a *wide local excision* (WLE). In this project, fluorescence imaging, which provides dynamic and real-time tissue recognition (9), was evaluated in combination with conventional imaging-based navigation to guide WLE of validated STS phantom tumors. The hypothesis was that the best performance for WLE would be achieved with a combination of computed tomography (CT), magnetic resonance (MR), and/or fluorescence imaging technologies. Semi-solid, gelatin-based human tissue-simulating phantoms were fabricated (14 cm in diameter, 11 cm in height), each with a cubical 'tumor' inclusion (8 cm^3) containing physiologically accurate concentrations of imaging contrast and fluorophore for an STS (Figure 1A-B). The phantom bulk material had either muscle- or adipose-mimicking optical properties (10). To facilitate CT- and MR-based navigation, each inclusion received a volume-equivalent human dose of 1.25 mL/kg of iohexol (GE Healthcare Inc. Marlborough, MA) and 0.2 mL/kg of gadoterate (Guerbet LLC, Princeton, NJ), respectively. To facilitate fluorescence navigation, inclusions received scaled amounts of IRDye 800CW Carboxylate (Li-Cor Inc., Lincoln, NE) to obtain a 4:1 ratio relative to the phantom stroma, which replicated the adipose- and muscle-to-tumor ratios previously measured in human xenografts and *in vivo* human work for ABY-029 (11). Ten phantoms each—five adipose-based and five muscle-based—were assigned to one of nine groups (90 phantoms total). Eight groups were assigned one or more navigation modalities; one group had no navigation or imaging (Figure 1C). Phantoms were dissected iteratively using all possible combinations of CT, MR, and fluorescence imaging, including control. Phantom groups were presented in random order, and the study dissector—a board-certified orthopaedic surgeon—was blinded to both the location and depth of the inclusions. Data collected were margin accuracy (mean deviation from goal margin of 1 cm, MΔ), margin status (positive or negative), spatial alignment of tumor inclusion with specimen (°), and dissection duration (min). Univariate and multivariate regression were utilized to explore the performance differences between combinations of imaging modalities. Margin accuracy was higher for combined navigation modalities compared to individual navigation modalities, and accuracy was highest with combined CT and fluorescence navigation (MΔ = 1.9 mm, SD = 1.6 mm) as compared to any alternative single or combination of navigation technologies (Intercept = 4.87 mm, B = -2.83 mm, Student's t-test $p = 0.045$). Specimen-tumor alignment was also highest with combined CT and fluorescence navigation (M = 3.4°, SD = 3.5°) as compared to any alternative single or combination of navigation technologies (Intercept = 13.63°, B = -9.83°, Student's t-test $p<0.001$) and improved overall with combined navigation modalities. At present, imaging-based navigation has limited application to guiding STS operations due to its inability to compensate for positional changes during surgery. This work indicates that fluorescence guidance enhances the accuracy of imaging-based navigation and may be best viewed as a synergistic technology, rather than a competing one.

Reference

1. S. Zausinger, et al., Intraop computed tomo with integrated navigation system in spinal stabilizations. Spine (Phila Pa 1976) 34, 2919–2926 (2009).
2. L. Jeys, et al., Can computer navigation-assisted surgery reduce the risk of an intralesional margin and reduce the rate of local recurrence in patients with a tumour of the pelvis or sacrum? Bone Joint J 95-B, 1417–1424 (2013).
3. N. Kaku, et al., Comparison of Cup Setting Angle Accuracy between CT-Based and CT-Free Navigation in the Same Patients with Crowe's Classification I or II Hip Dysplasia. Clin Orthop Surg 13, 144–151 (2021).
4. K.-C. Wong, S.-M. Kumta, Use of Computer Navigation in Orthopedic Oncology. Curr Surg Rep 2, 47–47 (2014).
5. S. A. Rosenberg, et al., The treatment of soft-tissue sarcomas of the extremities: prospective randomized evaluations of (1) limb-sparing surgery plus radiation therapy compared with amputation and (2) the role of adjuvant chemotherapy. Ann Surg 196, 305–315 (1982).
6. J. Itami, et al., High-dose rate brachytherapy alone in postoperative soft tissue sarcomas with close or positive margins. Brachytherapy 9, 349–353 (2010).
7. O. Cahlon, et al., A postoperative nomogram for local recurrence risk in extremity soft tissue sarcomas after limb-sparing surgery without adjuvant radiation. Ann Surg 255, 343–347 (2012).
8. J. Wang, et al., Postoperative intensity-modulated radiation therapy provides favorable local control and low toxicities in

patients with soft tissue sarcomas in the extremities and trunk wall. Onco Targets Ther 8, 2843–2847 (2015).
9. K. E. Tipirneni, et al., Oncologic Procedures Amenable to Fluorescence-guided Surgery. Ann Surg 266, 36–47 (2017).
10. S. L. Jacques, Optical properties of biological tissues: a review. Phys Med Biol 58, R37-61 (2013).
11. K. S. Samkoe, et al., Preclinical imaging of epidermal growth factor receptor with ABY-029 in soft-tissue sarcoma for fluorescence-guided surgery and tumor detection. J Surg Oncol 119, 1077–1086 (2019).

Poster Presentation

Disclosures: The authors have disclosed no financial interest.

459-Radiolabeled spherical nucleic acids as potential theranostic agents

Presenter: Tatsiana Auchynnikava, University of Turku

Tatsiana Auchynnikava[1], Antti Äärelä[2], Olli Moisio[2], Heidi Liljenbäck[3], Putri Andriana[3], Imran Iqbal[3], Xiang-Guo Li[3], Pasi Virta[2], Anne Roivainen[3], Anu J. Airaksinen[3]

[1]*University of Turku, Finland*
[2]*University of Turku, Turku, Finland*
[3]*Turku PET Centre, Turku, Finland*

Introduction:
Spherical nucleic acids (SNAs) have great potential as multipurpose theranostic agents for combined drug delivery and diagnostics. Compared to linear oligonucleotides (ON), they have several advantages, e.g. efficient cellular uptake, higher resistance to nuclease degradation, and lower immune response[1,2]. In addition, they can be monofunctionalized to allow site specific radiolabeling using bioorthogonal chemistry[3]. Here, we report the synthesis and biological evaluation of three radiolabeled SNAs, namely [^{18}F]**1** (containing phosphodiester (PO) backbone), [^{18}F]**2** (containing PO backbone and folate moiety), and [^{18}F]**3** (containing phosphorothioate (PS) backbone), and their comparison with radiolabeled single-stranded linear ON [^{18}F]**4**.

Methods:
[^{18}F]FDG-tetrazine ([^{18}F]**5**) was produced from glucose-free [^{18}F]FDG via oxime formation with N-(4-(1,2,4,5-tetrazin-3-yl)benzyl)-2-((((2S,3S,4R)-2-(fluoro-^{18}F)-3,4,5,6-tetrahydroxyhexylidene)amino)oxy)acetamide. From equal up to 4 times excess of TCO-SNAs or TCO-ON was used for the inverse electron demand Diels-Alder reaction with [^{18}F]**5** (5 min at r.t.). After centrifugal filtration (Amicon Ultra-0.5 mL, 30K, 14,5000 $\times g$ for 5 min, 3 repetitions) and formulation into 0.01M RNase-free phosphate-buffered saline (pH 7.4) the final product was analyzed with radio size exclusion chromatography and radio thin layer chromatography. *In vivo* and *ex vivo* biological evaluation was performed in (s.c.) tumor-bearing mice (HCC1954 breast cancer cells, female Rj:Athymic-Foxn1$^{nu/nu}$, 8-10 weeks old) using 60-min dynamic PET/CT imaging followed by *ex vivo* radioactivity counting of the harvested tissues.

Results:
[^{18}F]**5** was produced with 3.6% ± 0.8 radiochemical yield (RCY) (n = 6), molar activity of 148.9 ± 37.2 GBq/μmol (n = 4) and radiochemical purity (RCP) >95%. The reaction between [^{18}F]**5** and TCO functionalized structures [^{18}F]**1-3** yielded in RCY of 86.4% ± 16.7 (n = 9) and RCP >99%. Biological evaluation revealed that replacement of PO backbone with PS in the antisense ON sequence of SNA prolonged blood circulating radioactivity: the blood SUVs for [^{18}F]**3** and [^{18}F]**1** at 60 min post-injection were 2.9 ± 0.6 (n = 6) vs 0.6 ± 0.1 (n = 4), P = 0.003. As expected, the single stranded linear ON [^{18}F]**4** had the shortest circulating radioactivity (blood SUV 0.4 ± 0.1, n = 6 at 60 min p.i.). However, the addition of folate moiety was able to slightly prolong circulation of the PO backboned SNA (blood SUV 1.7 ± 0.6, n = 7 at 60 min p.i.). *Ex vivo* data confirmed the slowest elimination of [^{18}F]**3** from blood and rapid urinary excretion of other compounds.

Conclusions:
After successfully radiolabeling three SNAs structures and two control compounds, we were able to reveal their differences in distribution biokinetics by *in vivo* PET/CT imaging. The main finding included a positive effect of PS backbone introduction to SNA structure on the blood tracer circulation.

Acknowledgments: The authors would like to thank Aake Honkaniemi for PET/CT imaging support. The project was funded by the Academy of Finland (decision 343608), Jane and Aatos Erkko Foundation, and the University of Turku Graduate School.

Reference
1. Kapadia CH, Melamed JR, Day ES. Spherical Nucleic Acid Nanoparticles: Therapeutic Potential. BioDrugs. 2018;32(4).
2. Li H, Zhang B, Lu X, et al. Molecular spherical nucleic acids. Proc Natl Acad Sci U S A. 2018;115(17):4340-4344.
3. Gulumkar V, Äärelä A, Moisio O, et al. Controlled Monofunctionalization of Molecular Spherical Nucleic Acids on a Buckminster Fullerene Core. Bioconjugate Chemistry. 2021;32(6).

Poster Presentation

Disclosures: The authors have disclosed no financial interest.

460-ChoKα-targeted NIR fluorophore for optical surgical navigation in canine patients with spontaneous lung cancer

Presenter: Sofya Osharovich, University of Pennsylvania

Sofya Osharovich[1], Michael C. Hart[2], Stefan Harmsen[2], Anatoliy V. Popov[2], Sunil Singhal[3], David Holt[4], Jim Delikatny[2]

[1]*University of Pennsylvania, Medford, NJ*
[2]*University of Pennsylvania, Philadelphia, PA*
[3]*Perelman School of Medicine at the University of Pennsylvania, Philadelphia, PA*
[4]*University of Pennsylvania*

Choline Kinase α (ChoKα) is an established cancer biomarker associated with an aggressive phenotype, high histological tumor grade, and poor clinical outcome in many human cancers. ChoKα is overexpressed in 60% of human lung tumors.[1-3] ChoKα catalyzes the phosphorylation of choline to generate phosphocholine, a precursor of the cell membrane phospholipid, phosphatidylcholine (PtdCho).[4] The intraoperative standard of care for identifying tumors is finger palpation and visual inspection along with the aid of preoperative scans. However, this approach is insufficient, as surgeons often miss occult lesions which results in local recurrence in up to 40% of patients and a significantly reduced 5-year survival.[5-6] This problem can be mediated with the use of fluorophores for optical surgical navigation. Presently, there are a

limited number of FDA-approved targeted NIR fluorophores and none that target ChoKα. JAS239 (l_{ex}: 745 nm, l_{em}: 775 nm) is a novel near-infrared (NIR) fluorescent ChoKα inhibitor that binds to the active site of ChoKα, competitively inhibiting phosphocholine production[7]. JAS239 can be used to target ChoKα-overexpressing tumors for optical surgical navigation. Large animals, such as dogs, are excellent models of human disease, as they are exposed to the same environment as their owners and have disease onset and resolution similar to humans. In this study, canine patients with spontaneous operable lung adenocarcinomas were recruited into an informed consent clinical trial. Patients (n=7) received 0.25, 0.5, or 1 mg/kg JAS239 24 hours prior to intraoperative imaging to determine the optimal dose. The VisionSense Imaging System was used to image the lung tumors *in situ*and *ex vivo* as well as involved lymph nodes. After tumor resection, the tumors were imaged on the back bench and sections of the tumors were cut and imaged. Cut pieces of the tumors were imaged on the LI-COR PEARL and submitted to pathology for H&E and ChoKα immunohistochemistry (IHC). Intraoperative tumor imaging showed clear margin delineation with tumor to background ratios (TBR) of 2 (0.25 mg/kg), 6 (0.5 mg/kg), and 4 (1 mg/kg). IHC showed heterogeneous ChoKα expression, similar to humans. The purpose of this preliminary clinical trial is to establish the optimal dosing and timing for imaging JAS239 in canine lung tumors. Patients receiving 0.5 mg/kg JAS239 yielded the highest TBR values due to the low background signal in normal lung tissue compared to tumor. Future studies will evaluate the efficacy of JAS239 for detecting tumor margins, locoregional metastases and from other primary cancers, involved lymph nodes, and ChoKα levels. The ultimate goal of this study is translation of JAS239 for optical surgical navigation in human lung cancer patients.

Reference

1. Cuadrado, A., et. al. “Phosphorylcholine: a novel second messenger essential for mitogenic activity of growth factors.” Oncogene 8.11 (1993): 2959-2968. PMID: 8414498.
2. Molina, A., et. al. "Expression of Choline Kinase Alpha to Predict Outcome in Patients with Early-stage Non-small-cell Lung Cancer: A Retrospective Study." The Lancet Oncology 8.10 (2007): 889-97. PMID: 17851129.
3. Molina, A., et. al. "Overexpression of Choline Kinase Is a Frequent Feature in Human Tumor-derived Cell Lines and in Lung, Prostate, and Colorectal Human Cancers." Biochemical and Biophysical Research Communications 296.3 (2002): 580-83. PMID: 12176020.
4. Arlauckas, S., et al. “Choline Kinase Alpha—Putting the ChoK-Hold on Tumor Metabolism.” Progress in Lipid Research, vol. 63, 2016, pp. 28–40., PMID: 27073147.
5. Klimberg V., et al. “Assessing margin status.” Surg. Oncol. 8.2 (1999): 77–84. PMID: 10732959.
6. Sienko, A., et al. “Frozen Section of Lung Specimens.” Archives of Pathology & Laboratory Medicine 129.12 (2005): 1602-1609.
7. Arlauckas, S., et al. “Direct Inhibition of Choline Kinase by a Near-Infrared Fluorescent Carbocyanine.” Molecular Cancer Th

Poster Presentation

Disclosures: The authors have disclosed no financial interest.

461-Detection of endometriosis lesions using Gd-based collagen I binding probe a in a mouse model of endometriosis

Presenter: Nazanin Talebloo, Michigan State University

Nazanin Talebloo[1], M. Ariadna Ochoa Bernal[2], Elizabeth Kenyon[3], Christiane Mallett[4], Asgerally Fazleabas[2], Anna Moore[5]

[1]*Michigan State University, East Lansing*
[2]*Michigan State University*
[3]*Precision Health Program, East Lansing, Michigan*
[4]*Michigan State University, East Lansing, MI*
[5]*Michigan State University, East Lansing, Michigan*

Introduction:

Endometriosis is a gynecological disorder that is characterized by the presence of endometrial-type mucosa, consisting of stroma and glands, outside the uterus. This disease affects women of reproductive age and can be accompanied by serious symptoms including pain, and infertility [1–3]. Endometriotic lesions include ovarian, peritoneal, and deep infiltrating lesions,[4,5] found in the pelvic area [1,6]. Currently, the gold standard in diagnosis of endometriosis is a diagnostic laparoscopy which is an invasive method normally followed by histological verification of stroma and glands presecnce[7]. However, due to the risks of this procedure, other non-invasive diagnostic methods including magnetic resonance imaging (MRI) and ultrasound should be considered [8,9]. Due to the limitations of these imaging techniques, developing targeted contrast agents can help with the diagnosis through MRI by better differentiating lesions from their surroundings[10]. The lack of success in developing diagnostic targeted imaging probes shows that a better understanding of endometriosis is needed. Endometriotic lesions are wounds undergoing repeated tissue injury and repair which leads to collagen production and fibrosis[11]. The consistent presence of smooth muscle components and fibrosis in all lesion forms can define endometriosis as a fibrotic condition in which endometrial stroma and epithelium can be identified[12]. Fibrosis is characterized by excess deposition of collagens, primarily type I collagen[13,14]. Previous studies have identified a peptide directed against collagen type I, which was modified with Gd(DTPA) to serve as a Gd-based MRI probe (EP-3533)[15,16] and detect fibrosis in liver and heart[17–20]. We propose for the first time, to use it for detection of fibrotic endometriotic lesions in mouse model of endometriosis.

Methods:

Endometriosis was induced by removing one uterine horn of female mice, mincing it in sterile PBS, and injecting back into the peritoneal cavity. A second group of mice were ovariectomized and after recovery, one uterine horn was removed, and tissue samples were obtained from it that were sutured to the peritoneal wall. In these *Pgr* $^{cre/+}$*Rosa26* $^{mTmG/+}$ mouse models, lesions can be visualized by the progesterone receptor (Pgr)-positive cells which express green fluorescent protein (GFP). In vivo, T_1-weighted dynamic contrast-enhanced MRI was done by acquiring a series of baseline images followed by bolus injection of EP-3533(10umol/kg) to mice (n=6), through a tail vein catheter within seconds. Imaging continued for 55 minutes post-injection with a 1-minute temporal resolution. Percent MRI signal enhancement was calculated for each time point based on distributed regions of interest over lesion lining and was normalized to the baseline. After mice were sacrificed, ex vivo fluorescence imaging was performed to confirm the location of GPF-expressing lesions in the peritoneal cavity using fluorescence imaging (IVIS). Collected lesions were sectioned and stained with Masson’s Trichrome Stain to assess the collagen content of tissues with microscopy.Inductively coupled plasma-optical emission spectrometry (ICP-OES) was also done on digested tissue samples to measure the gadolinium content.

Results:

MR T1-weighted images showed an increase in signal intensity of lesion lining, caused by specific binding of gadolinium-based EP-3533(Fig.1A). MRI signal enhancement was increased by about 20

% relative to the baseline and was higher than muscle signal used as control(Fig.1.B). Normally, the initial signal enhancement is unspecific, and as it clears out, the specific accumulation increases the signal. Ex-vivo fluorescence imaging confirmed the location of lesions(Fig.1.C). Stained lesion sections confirmed the presence of collagen(Fig1.D). Based on ICP results gadolinium content was significantly higher in the lesions compared to the muscle which was consistent with the MRI findings(Fig.1.E).

Conclusion:
For the first time, a collagen I binding probe was used to image lesions in a mouse model of endometriosis. This work was supported in part by the NIH HD 099090 to A.F.

Reference

1. Zondervan et al. Endometriosis. Nature Reviews Disease Primers(2018).
2. Malvezzi et al. Endometriosis: current challenges in modeling a multifactorial disease of unknown etiology. Journal of Translational Medicine(2020).
3. Prentice. Regular review: Endometriosis. BMJ(2001).
4. Rolla. Endometriosis: advances and controversies in classification, pathogenesis, diagnosis, and treatment. F1000Res 8, F1000 Faculty Rev(2019).
5. Alimi et al. The Clinical Anatomy of Endometriosis: A Review. Cureus(2018).
6. Parasar, Ozcan & Terry. Endometriosis: Epidemiology, Diagnosis and Clinical Management. Curr Obstet Gynecol(2017).
7. Hsu et al. Invasive and noninvasive methods for the diagnosis of endometriosis. Clin Obstet Gynecol(2010).
8. Kinkel et al. Diagnosis of endometriosis with imaging: a review. European Radiology(2006).
9. Chapron et al. Rethinking mechanisms, diagnosis and management of endometriosis. Nature Reviews Endocrinology(2019).
10. Morawski, Lanza & Wickline. Targeted contrast agents for magnetic resonance imaging and ultrasound. Current Opinion in Biotechnology(2005).
11. Zhang, Duan, Olson, Fazleabas & Guo. Cellular changes consistent with epithelial–mesenchymal transition and fibroblast-to-myofibroblast transdifferentiation in the progression of experimental endometriosis in baboons. Reproductive sciences(2016).
12. Vigano et al. Time to redefine endometriosis including its pro-fibrotic nature. Human Reproduction(2018).
13. Hosper et al. Epithelial-to-mesenchymal transition in fibrosis: Collagen type I expression is highly upregulated after EMT, but does not contribute to collagen deposition. Experimental Cell Research(2013).
14. Polasek et al. Molecular MR imaging of fibrosis in a mouse model of pancreatic cancer. Sci Rep(2017).
15. Caravan et al. A lysine walk to high relaxivity collagen-targeted MRI contrast agents. Chemical communications(2009).
16. Caravan et al. Collagen-targeted MRI contrast agent for molecular imaging of fibrosis. Angewandte Chemie International Edition 46, 8171–8173 (2007).
17. Polasek et al. Molecular MR imaging of liver fibrosis: a feasibility study using rat and mouse models. J Hepatol(2012).
18. Zhu et al. Combined magnetic resonance elastography and collagen molecular magnetic resonance imaging accurately stage liver fibrosis in a rat model. Hepatology(2017).
19. Caravan et al. Collagen-targeted MRI contrast agent for molecular imaging of fibrosis. Angewandte Chemie(2007).
20. Helm et al. Postinfarction myocardial scarring in mice: molecular MR imaging with use of a collagen-targeting contrast agent. Radiology(2008).

Poster Presentation

Disclosures: The authors would like to disclose that FDG has been approved.

462-Breast cancer specificity assessment of tumor targeted Nano-, Encapsulated Manganese Oxide (NEMO) particles

Presenter: Celia Martinez de la Torre, West Virginia University

Celia Martinez de la Torre[1], Dhruvi M. Panchal[2], Kasey Freshwater[2], Margaret Bennewitz[1]

[1]West Virginia University, Morgantown, WV
[2]West Virginia University, Morgantown, West Virginia

Gadolinium chelates are the gold standard contrast agents for breast magnetic resonance imaging (MRI), but their MRI constant signal and lack of specificity results in high background and misdiagnosis. This lack of targeting makes it challenging to differentiate between benign and malignant breast masses, resulting in high false-positive rates of up to 25%. We have developed an enhanced contrast agent that utilizes tumor-targeted pH-sensitive manganese oxide (MnO) nanoparticles, which in physiological pH, produce low signal ("OFF"). After cancer cell uptake and digestion within low pH endosomes/lysosomes, the MnO dissociates into Mn^{2+}, turning the MRI signal "ON." Nano-, Encapsulated Manganese Oxide (NEMO) particles were synthesized by the encapsulation of nanocrystalline MnO within poly(lactic-co-glycolic acid) (PLGA) and poly(ethylene glycol) (PEG) via single emulsion. The nanocrystals and nanoparticles were chemically and physically characterized by TEM, XRD, FTIR, SEM, and DLS. After characterizing the particles, a fluorescent tumor-targeting peptide against underglycosylated mucin-1 (uMUC-1) was attached through click chemistry using copper (I) as the catalyst. MUC-1 was chosen as a tumor target, as it is overexpressed and underglycosylated on breast cancer cells, but not on benign or healthy cells. The uMUC-1 conjugated NEMO particles were characterized with DLS to assess hydrodynamic size (~190 nm) and fluorescence to ensure attachment of the targeting peptide. Before evaluating the cellular uptake of the NEMO particles, different control and breast cancer cell lines were characterized for expression of MUC-1 and uMUC-1 via flow cytometry. MCF10A (control), BT20 (triple negative), and T47D (luminal A) were selected for particle specificity studies, as their expression varied from no uMUC-1 (MCF10A) up to 85% uMUC-1+ cells (T47D). Cells were exposed to targeted NEMO particles (1.6 µg of Mn/mL) for 30 minutes, followed by an MRI scan of the cell pellet and collected media. The change of R_1 (ΔR_1) between the control group (only exposed to media) and the nanoparticles-exposed group was calculated post imaging. In the case of cell pellets, no expression of uMUC-1 resulted in a negligible response of NEMO particles on MRI, where MCF10A labeled with NEMO particles had no increase in R_1. In contrast, BT20 and T47D labeled with NEMO particles had an increase in R_1 of 16% and 54%, respectively, compared to unlabeled cells. The signal enhancement of T47D cells (uMUC-1+) due to NEMO particle dissolution was significant compared to MCF10A cells (uMUC-1-) in just 30 minutes. No significant difference was observed in ΔR_1 when the media content of NEMO particle labeled cells was imaged with MRI. The lack of contrast enhancement in the media indicated that 30 minutes is not enough time for labeled cells to start ejecting Mn^{2+} out into the media. In conclusion, in vitro studies showed that higher uMUC-1 breast cancer cell expression promoted NEMO particle uptake, dissolution into Mn^{2+} and a bright T_1 MRI signal, which did not occur in uMUC-1- control cells. Lastly, T47D tumor-bearing mice were injected with targeted NEMO particles (7.5 mg/kg), and MRI scans were performed

pre-injection (baseline) and 1, 2, 4, and 24hr post-injection to assess the variation in MRI signal in the tumor. After 1hr and 2hr, the MRI signal intensity increased by ~37% compared to baseline, followed by a slight decrease to ~18% above baseline at 24hr. Additionally, through abdominal MRI scans, signal intensity was visualized in the liver and kidneys after NEMO particle injection, highlighting possible elimination via these routes. Future biodistribution studies will be performed to correlate MRI signal to Mn organ content. Overall, targeted NEMO particles caused an increase in T_1 MRI signal in breast cancer cells expressing uMUC-1+ in vitro and in vivo, and further study is warranted to compare its sensitivity and specificity to Gd-chelates.

Poster Presentation

Disclosures: The authors have disclosed no financial interest.

463-Generating MRI reporter genes using a Protein Optimizing Evolving Tool (POET)

Presenter: Alexander Bricco, Michigan State University

Alexander R. Bricco[1], Iliya Miralavy[2], Shaowei Bo[3], Or Perlman[4], Christian Farrar[5], Michael T. McMahon[6], Wolfgang Banzhaf[2], Assaf Gilad[7]

[1]Michigan State University, East Lansing
[2]Michigan State University, East Lansing, Michigan
[3]Johns Hopkins University School of Medicine, Baltimore, Maryland
[4]Tel Aviv University, Tel Aviv, Israel
[5]Massachusetts General Hospital, Charlestown, MA
[6]Kennedy Krieger Institute, Baltimore, Maryland
[7]Michigan State University, East Lansing, MI

Introduction:
Reporter genes for Magnetic Resonance Imaging (MRI) would allow genes to be measured in a non-invasive and safe manner, paving the way for translational use in human subjects. One of the best mechanisms for generating such a reporter gene is Chemical Exchange Saturation Transfer (CEST), which generates contrast without addition of outside metals and allows for the contrast mechanism to be controlled. Previous CEST reporter genes[1,2]can be further optimized via protein evolution but have proven difficult to improve using typical protein optimization engineering methods. We hypothesized that these limitations could be overcome via application of machine learning. To achieve this goal, we utilized Genetic Programming (GP) which is a field in computer science studying algorithms inspired by biological evolution. GP is a powerful technique that evolves models to difficult tasks and has been used in the past to in array of biological studies.

Methods:
We have thusfar performed 10 generations of development for peptides with a CEST peak at 3.6 ppm. For the peptides we started with training data obtained from prior literature values of 12 amino acid long peptides. In each generation of development, POET was used to predict 10 peptides, which were then synthesized by a Genscript (Piscataway, NJ). We dissolved the peptides to a concentration of 5 mg/mL in PBS and were imaged on 7T preclinical MRI (Bruker) at 37 C, TR 10 s, T_{sat} 4s, B_{sat} 4.7 μT with conditions as described before[3]. The experimental results would then be added into the training data and the genetic program would then develop predictive models and predict proteins based on the new information learnable from the increase in data. Exchange rate (K_{ex}) was determined using QUEST[4]. Each sample was scanned alongside a sample of Poly-L-Lysine (PLL), which served as a control and standard. PLL was chosen due to its relation to the Lysine Rich Protein (LRP) which is the current state of the art CEST reporter gene[1].

Results:
The first peptides developed using POET were mostly insoluble, with only one peptide which was able to dissolve and produce contrast. The next two Later generations showed steadily increased contrast. Later generations level out in terms of median and maximum contrast, however, across all generation, 42 peptides were discovered that produce greater contrast than PLL (figure 1). More importantly, several peptides that produce contrast that is substantially higher than PLL were identified. When the exchange rate (K_{ex}) – the hallmark of a good CEST agent) was measure using QUEST, some selected peptides show K_{ex} as high as 822 Hz which is ~2 fold of PLL (K_{ex}=479).

Discussion:
This mechanism has shown the ability to discover new peptides that have challenged the current understanding about what chemical properties allow MRI contrast to be generated. Although the training data, and prior research was focused on peptides that were both positively charged and basic, POET had led to the discovery of CEST agents that are neutral in charge and pI but produce more contrast than PLL.

Conclusion:
The contrast of the peptides generated by POET produce substantially more contrast than PLL after a few generations of using the program. Meanwhile, selected peptides developed using POET, that showed superior contrast can be assembled into a new MRI reporter gene improving its sensitivity over previous generations of reporters.

Reference
1. Gilad, A. A. et al. Artificial reporter gene providing MRI contrast based on proton exchange. Nat Biotechnol 25, 217-219 (2007).
2. Farrar, C. T. et al. Establishing the Lysine-rich Protein CEST Reporter Gene as a CEST MR Imaging Detector for Oncolytic Virotherapy. Radiology, 140251, doi:10.1148/radiol.14140251 (2015).
3. McMahon, M. et al. New "multicolor" polypeptide diamagnetic chemical exchange saturation transfer (DIACEST) contrast agents for MRI. Magnetic Resonance in Medicine 60, 803-812 (2008).
4. McMahon, M. T. et al. Quantifying exchange rates in chemical exchange saturation transfer agents using the saturation time and saturation power dependencies of the magnetization transfer effect on the magnetic resonance imaging signal (QUEST and QUESP): Ph calibration for poly-L-lysine and a starburst dendrimer. Magnetic resonance in medicine 55, 836-847, doi:10.1002/mrm.20818 (2006).
5. Grantham, R. Amino Acid Difference Formula to Help Explain Protein Evolution. Science 185, 862-864 (1974).

Poster Presentation

Disclosures: The authors have disclosed no financial interest.

464-Monitoring pH via Ultrasound Luminescence Chemical Imaging for Early Detection of Implant Associated Infection

Presenter: Vigjna Abbaraju, Clemson University

Sriparna Bhattacharya[1], Gretchen Schober[2], Unaiza Uzair[3], **Vigjna Abbaraju[3]**, Jeffrey Anker[3]

[1]*Clemson University, Clemson, South Carolina*
[2]*Clemson University, Central, SC*
[3]*Clemson University, Clemson, SC*

Orthopedic implants and other medical devices are susceptible to infection by bacterial biofilms which are resistant to antibiotics and the host's immune system. Monitoring the local biochemical environment for early detection of infection is important in developing therapeutic strategies for successful treatment of infection. Therefore, there is a need to develop tools for *in vivo* monitoring of chemical changes, such as pH and oxygen concentration in tissues near implanted devices, that could serve as early indicators of infection. We developed a chemical imaging technique designed to probe the biochemical environment on the implant surface using focused ultrasound pulses to generate luminescence in a mechanoluminescent film ($SrAl_2O_4$:Eu,Dy microparticles in PDMS) that can be imaged through tissue. After an initial UV excitation, the films emitted green phosphorescence afterglow at 520 nm, and when an ultrasound beam irradiated this film, it luminesced more brightly. Turning the ultrasound ON and OFF modulated the luminescence at the focal spot. The mechanoluminescent film was spray coated with pink colored fluorescent paint to shift the emission wavelength from ~520 nm to ~603 nm. This emission overlapped with the absorption spectrum of the pH indicator dye, bromothymol blue, reducing the luminescence at alkaline pH. The technique was applied to image changes in the luminescence spectra of the above spray coated film in different pH environments through a light scattering media. By moving the sample on a stage, the ultrasound was scanned across it, and the pH dependent emitted light was collected with a liquid light guide and detected with a photomultiplier tube (PMT). The time dependent intensity was converted into an image given the stage position using custom MATLAB scripts. Our preliminary results show images with a spatial resolution limited by the ultrasound focal spot size (~3 mm) through the creamer solution. In conclusion, we demonstrated proof of principle for pH imaging through scattering media using ultrasound modulated mechanoluminescence. We expect this approach could be useful for studying, detecting, and monitoring implant associated infection.

Poster Presentation

Disclosures: The authors have disclosed no financial interest.

465-Development of Novel Glypican-3 specific Diabody for Molecular Imaging of Hepatoma

Presenter: Stanley Fayn, National Institutes of Health

Stanley Fayn[1], Freddy E E. Escorcia[2], Paden King[3]

[1]*National Institutes of Health*
[2]*National Cancer Institute, Bethesda, MD*
[3]*NIH/NCI*

Primary liver cancer is the second most common cause of cancer-related death, having around a 20% 5-year absolute survival period[1]. Hepatocellular Carcinoma (HCC) is the most common form of liver cancer, accounting for around 90 percent of cases worldwide[2]. To date, there have been no clinically approved HCC-specific imaging probes developed that would allow for early detection, improved diagnosis, and post-treatment surveillance of the disease. Glypican-3 (GPC3) is a heparin sulfate proteoglycan that is overexpressed in 75-90% of HCC lesions and represents a promising target for tumor-selective diagnostics[3]. Here, we design, engineer, and characterize a novel GPC3-specific diabody-based positron emission tomography (PET) imaging agent for HCC. A VL-VH single-chain variable fragment (scFv) yeast surface display library was used to identify scFvs specific to both murine and human GPC3. The lead scFv was engineered as a homodimeric diabody: DB49. Target binding was determined and confirmed by biolayer interferometry and flow cytometry. DB49 was conjugated to deferoxamine and radiolabeled with Zirconium[Zr]-89. A radioligand binding assay determined a Kd of 2.5 nM for human GPC3. An ex vivo biodistribution study with the [^{89}Zr]Zr-DFO-DB49 tracer was performed in nu/nu athymic mice with HepG2 subcutaneous tumors. Tumor uptake measured by percent injected activity per gram tissue (%IA/g) were 4, 5, and 5, at 1, 3 and 24 h post injection (p.i.), respectively, suggesting good target engagement in GPC3 expressing tumors. Liver and kidney uptake were 6, 7, 5, and 55, 79, and 63 %IA/g, respectively, at 1, 3 and 24h p. i. Our findings suggest that the novel diabody DB49 can specifically bind to GPC3-expressing tumors, however, optimization is needed to lower uptake in clearance organs and improve tumor-to-background ratio prior to translation.

Reference

1. Bray, F. et al. Global cancer statistics 2018: GLOBOCAN estimates of incidence and mortality worldwide for 36 cancers in 185 countries. CA Cancer J Clin 68, 394-424, doi:10.3322/caac.21492 (2018).
2. Llovet, J. M., Kelley, R. K., Villanueva, A., Singal, A. G., Pikarsky, E., Roayaie, S., Lencioni, R., Koike, K., Zucman-Rossi, J., & Finn, R. S. Hepatocellular carcinoma. Nature reviews. Disease primers, 7(1), 6. https://doi.org/10.1038/s41572-020-00240-3 (2021).
3. Wang, H. L., Anatelli, F., Zhai, Q. J., Adley, B., Chuang, S. T., & Yang, X. J. Glypican-3 as a useful diagnostic marker that distinguishes hepatocellular carcinoma from benign hepatocellular mass lesions. Archives of pathology & laboratory medicine, 132(11), 1723–1728. https://doi.org/10.5858/132.11.1723 (2008).

Poster Presentation

Disclosures: The authors have disclosed no financial interest.

466-Creatine Chemical Exchange Saturation Transfer (CrCEST) MRI Reproducibility in healthy adults at 3T

Presenter: KASTUREE CHAKRABORTY, St. Jude Children's Research Hospital

Kasturee Chakraborty[1], Zane Coleman[1], Ayaz Khan[2], Shubo Wang[3], Pat Hanby[1], Donald Wallace[1], Zoltan Patay[1], Puneet Bagga[4]

[1]*St. Jude Children's Research Hospital, Memphis, Tennessee*
[2]*St. Jude Children's Research Hospital, Memphis*
[3]*Memphis, Tennessee*
[4]*St. Jude Children's Research Hospital, Memphis, TN*

Synopsis:
CrCEST MRI indirectly measures creatine (Cr) by exchanging amine protons with free water in skeletal muscle. While 2D CrCEST was performed before in adults, no studies showing its reproducibility have been published. Here, we show that gastrocnemius muscles in the calf are candidates for reproducible CrCEST data in plantar flexion movement. Introduction Oxidative phosphorylation (OXPHOS) plays an essential role during muscle metabolism. Phosphocreatine (PCr) converts into Cr to support ATP synthesis during OXPHOS. This conversion is usually measured using 31P MRS but has a limited spatial resolution. A complementary method to 31P MRS is CrCEST MRI

which can perform muscle group specific estimation of relative free creatine concentrations with high spatial resolution. This technique can be used as an important tool to study mitochondrial bioenergetics in vivo in tissues with high energy demand, including exercising skeletal muscle. The objective of this current study is to understand the reproducibility of the CrCEST based creatine decay post exercise in healthy adults.

Methods:
Fourteen healthy adults (M7, F8, Age:39.13 ± 9.8 yrs) were scanned (written consent from all participants, approved by local IRB) for CrCEST imaging using plantar flexion exercise on a programmable MR compatible pneumatical ergometer (Trispect, Ergospect) at 45 BPM for 2 min. CrCEST contrast was measured in a 10 mm thick transverse slice placed in the right calf for two minutes before exercise and for eight minutes after exercise on a 3T scanner (Siemens, PRISMA). For CrCEST imaging, the calf was placed inside 15-channel knee coil. Water saturation was collected with shift reference (WASSR) and B maps for B0 and B1 correction. Six images were acquired over 24 s intervals with saturation frequency offsets of ±1.5, ±1.8, and ±2.1 ppm. A 500 ms saturation pulse train was applied consisting of five 99.6 ms Hanning windowed pulses with 150 Hz B1 amplitude separated by a 0.4 ms inter-pulse delay. A fat saturation pulse was applied, followed by a single-shot spoiled gradient-echo readout with centric encoding, flip angle 10°, FOV 160x160 mm, matrix 128x128, TR 6.0 ms, TE 3 ms, slice thickness 10mm.4 Regions of interest (ROIs) were placed in the major calf muscle groups: lateral gastrocnemius (LG), medial gastrocnemius (MG), soleus (sol), and tibialis anterior (TA), After 15 minutes of rest outside scanner, the subject repeated exercise for second time. Both scans were processed on MATLAB for CrCEST mapping and creatine recovery time constant (tCr). 1H MRS was also performed in the LG and Sol muscle groups, and data was processed with LCModel using unsuppressed water signal as reference. Intramyocellular lipid (IMCL), extramyocellular lipid (EMCL) concentrations were measured. Additionally, we measured muscle fat fraction (FF) using the 2-point-Dixon MRI.

Results and Discussion:
MRI and 1H MRS Data from all fourteen participants was used for testing reproducibility of this method in skeletal muscle groups involved in plantar flexion exercise. Due to lack of engagement during exercise, TA and sol had a high variance in creatine recovery constant (tCr) and were excluded from this analysis. Among all subjects, the average tCr in the LG and MG are 148.9 ±106.2 and 105.1 ± 77.9 sec, respectively. Figure1 shows baseline and post-exercise CrCEST recovery maps in one subject. Both LG and MG muscle groups were found to be good candidates for testing reproducibility of CrCEST method. The variation in tCr was higher in MG than LG. We found a negative association of IMCL/EMCL ratio with age. This can be explained by increased metabolism, energy expenditure and growth in young subjects. Further, lower FF was found to be associated with higher IMCL concentration, found in athletes.

Conclusion: Post plantar flexion exercise, both muscles (LG and

Reference

1. Chance et al. (1955) J Biol Chem. 217(1):409-427.
2. Sedivy et al. (2019) J Appl Biomed.17(2):91-98.
3. Kogan et al. (2014) J Magn Reson Imag. 40(3):596-602.
4. DeBrosse et al.(2016) JCI Insight.1(18):e88207.
5. Kim et al. (2009) Magn Reson Med. 61(6):1441-1450.
6. Kogan et al. (2014) Magn Reson Med. 71(1):164-172.
7. Wilson NE. ExerciseCEST. Zenodo. (2016).
8. Brennan et al. (2021). Frontiers in Physiology 12.
9. Klepochová et al. (2018). Frontiers in Physiology 9: 300.

Poster Presentation

Disclosures: The authors have disclosed no financial interest.

467-An Anatomically Correct 3D-Printed Mouse Phantom for Magnetic Particle Imaging Studies

Presenter: Nicole Sarna, Vanderbilt University

Nicole S. Sarna[1], Leyda Marrero-Morales[2], Ryan DeGroff[2], Angelie Rivera-Rodriguez[3], Sitong Liu[4], Andreina Chiu Lam[2], Hayden Good, Carlos Rinaldi-Ramos[2]
[1]Vanderbilt University, Nashville, TN
[2]University of Florida, Gainesville, FL
[3]Stanford University School of Medicine, Palo Alto, CA
[4]University of Florida, Gainesville, Florida

Introduction:
Magnetic Particle Imaging (MPI) is a novel imaging modality that enables non-invasive quantitative visualization of the distribution of biocompatible superparamagnetic iron oxide nanoparticle (SPION) tracers. The nonspecific accumulation of SPIONs in the liver upon systemic administration is a common occurrence in nanomedicine and can affect MPI signal from tracers accumulated in neighboring organs. This study aimed to evaluate the effect of nonspecific accumulation of SPIONs on MPI signal sensitivity in brain tumor and breast tumor models using anatomically correct 3D-printed mouse phantoms. While MPI already contributes to advancing the ethical principles of replacement, reduction, and refinement (3Rs) as a non-invasive imaging modality, these phantoms serve to further optimize the planning and execution of *in vivo* experiments.

Methods:
The 3D-printed phantoms were based on the Digimouse 3D whole body mouse atlas and modified to incorporate cavities representative of a liver, brain tumor, and orthotopic breast cancer tumor placed in anatomically correct locations, allowing evaluation of the effect of precise doses of MPI tracer (**Figure 1**) [1]. An in-house synthesized and optimized MPI tracer, RL1, was used, as it exhibits ~3 times better MPI sensitivity than the commercial tracer, ferucarbotran [2]. To illustrate their use, a constant tracer iron mass typical for in vivo applications was present in the liver for the breast (200 µgFe) and brain tumor (10 µgFe) model, while a series of decreasing tracer iron mass was placed in the tumor region. MPI scans were acquired in 2D and 3D high sensitivity (HS) and high sensitivity/high resolution (HSHR) modes using a MOMENTUM^{TM} imager and CT scans were acquired for 3D image registration. A thresholding algorithm was used to define regions of interest (ROI) in the scans and the tracer mass in the liver and tumors was calculated by comparison of the signal in their respective ROI against that of known mass fiducials that were included in each scan.

Results:
An accurate approach to quantify tracer mass in a ROI in an anatomically correct mouse phantom was demonstrated based on comparison of calculated tracer mass to known tracer mass in the brain and breast tumor cavities, while a constant tracer mass resided in the liver cavity. Additionally, it was demonstrated that the limit of detection in MPI is sensitive to the details of tracer distribution in the subject, as it was found that a greater tracer mass in the liver cavity resulted in poorer sensitivity in tumor regions. The smallest tracer mass detected in the tumor cavity for the breast cancer model was 6.41 µgFe in 2D HSHR and HS scan modes (mSNR = 4.5, 3.4) and 1.60 µgFe in 3D HSHR scans (mSNR = 6.4). Furthermore, the results demonstrate that this

approach to image analysis provides accurate quantification of tracer mass.

Conclusion:

The results suggest MPI experimental parameters can be successfully iterated and analyzed for a brain and breast tumor murine model to evaluate impact of liver accumulation on MPI sensitivity and to assess the accuracy of MPI quantification methods [3]. It is shown that anatomically correct phantoms can mimic results from in vivo studies and help answer important questions regarding the most suitable MPI data acquisition conditions, image analysis methods, and SPION dose experimental parameters, prior to animal experimentation. The capabilities of this 3D-printed anatomically correct mouse phantom are extensive, as it is possible to modify the phantom using CAD software to simulate a variety of disease models.

Reference

1. Dogdas B, Stout D, Chatziioannou AF, Leahy RM. Digimouse: a 3D whole body mouse atlas from CT and cryosection data. Phys Med Biol. 2007;52(3):577-587. doi:10.1088/0031-9155/52/3/003
2. Liu S, Chiu-Lam A, Rivera-Rodriguez A, et al. Long circulating tracer tailored for magnetic particle imaging. Nanotheranostics. 2021;5(3): 348-361. doi:10.7150/ntno.58548
3. Sarna NS, Marrero-Morales L, DeGroff R, et al. An anatomically correct 3D-printed mouse phantom for magnetic particle imaging studies. Bioeng Transl Med. 2022; e10299. doi:10.1002/btm2.10299

Poster Presentation

Disclosures: The authors have disclosed no financial interest.

468-18F-FDS PET imaging as a novel biomarker to detect and monitor E. coli infection in a murine model of complicated pyelonephritis

Presenter: Hyunsoo Shin, Johns Hopkins Univeristy

Camilo A. Ruiz-Bedoya[1], **Hyunsoo Shin[2]**, Dylan Boone[3], Patricia De Jesus[4], Kelly Flavahan[5], Alvaro A. Ordonez[6], Sanjay K. Jain[1]

[1]Johns Hopkins Univeristy, Baltimore, MD
[2]Johns Hopkins Univeristy, Baltimore
[3]Johns Hopkins Univeristy, Baltimore, Maryland
[4]Johns Hopkins University School of Medicine, Upper Marlboro
[5]Johns Hopkins University School of Medicine
[6]Johns Hopkins University School of Medicine, Baltimore, MD

Background:

Acute pyelonephritis (APNs) is a type of urinary tract infection commonly caused by ascending infection of the urinary tract by bacteria, mainly by *Escherichia coli.* Although uncomplicated APNs can be easily diagnosed based on symptomatology and treated, such is not the case for complicated APNs. This can induce sepsis, acute renal failure (ARF), and renal and perinephric abscesses. Imaging modalities (e.g., US and CT) are utilized to help with diagnosis, identify underlying factors (e.g., renal obstruction) and detect renal parenchyma involvement in high-risk patients (e.g., lack of response to antibiotic treatment, recurrent pyelonephritis, renal transplant). 2-^{18}F-Flurodeoxysorbitol (^{18}F-FDS) is a novel imaging agent capable of visualizing infections caused by Enterobacterales bacteria (*E. coli*, *Klebsiella*, etc.) and a non-invasive agent for functional renal imaging. ^{18}F-FDS PET/CT has shown the potential to measure split renal function and detect anatomical abnormalities, ARF, and renal obstructions. However, there is a lack of knowledge about its role in renal or perirenal abscesses. Thus, the current study evaluated if ^{18}F-FDS could also be used as a PET tracer to detect and monitor treatment response in a murine model of renal abscesses.

Methods:

CBA/J mice (male, 6 to 8 weeks old) were injected on the right inferior renal pole with 6 Log_{10} colony forming unit (CFU) of *E. coli* (ATCC 25922 or Xen-14) or PBS in 50μL after surgical right-flank incision. ^{18}F-FDS was generated from commercially available ^{18}F-FDG. After 45-hour incubation, mice were injected with 3.6 ± 0.2 MBq of ^{18}F-FDS (3-4 mice/group) via a tail vein injection. A 20 min static PET scan was performed using the nanoScan PET/CT (Mediso), 3-hours post-injection. Low-dose CTs were subsequently acquired for attenuation correction. One mouse was imaged before and after completion of ceftriaxone (5 mg/kg bid SQ) treatment for seven days. Images were reconstructed and coregistered using VivoQuant, version 3.5, and spherical VOIs were drawn to measure PET activity in the inferior right and left renal pole. Kidneys were harvested after imaging to measure colony-forming units (CFUs), H&E staining and IVIS Lumina LT for bioluminescence.

Results:

Mice develop localized inflammation with extensive infiltration of polymorphonuclear cells. The bacterial burden was 8.9 ± 5 Log_{10} CFU, 45 hours after *E. coli* incubation. ^{18}F-FDS shows local uptake in the inferior right renal pole (site of injection), with a significantly higher uptake compared to control mice ($P < 0.05$). Xen-14 *E.* coli corroborated localized bioluminescence on the site of injection. ^{18}F-FDS uptake decreased substantially (comparable to the control group) after seven days of ceftriaxone (antibiotic) treatment.

Conclusion:

In a murine model of complicated renal infection, ^{18}F-FDS PET/CT detected and monitored localized *E. coli* renal abscesses with low background noise and differentiated between sterile inflammation and infection. These results suggest that ^{18}F-FDS could be used as a novel radiotracer in imaging complicated APNs. Further human data is required to validate these findings.

Reference

1. Wakabayashi, H., et al. Initial Preclinical Evaluation of 18F-Fluorodeoxysorbitol PET as a Novel Functional Renal Imaging Agent. J Nucl Med 57, 1625-1628 (2016).
2. Werner, R.A., et al. Novel Functional Renal PET Imaging With 18F-FDS in Human Subjects. Clin Nucl Med 44, 410-411 (2019).
3. Ordonez, A.A., et al. Imaging Enterobacterales infections in patients using pathogen-specific positron emission tomography. Sci Transl Med 13(2021).

Poster Presentation

Disclosures: The authors have disclosed no financial interest.

469-A Novel and Potential Site for Islet Organoid Transplantation: Brown Adipose Tissue

Presenter: Aixia Sun, Michigan State University

Aixia Sun[1], Hanaan Hayat[2], Elizabeth Kenyon[2], Tahnia Quadri[1], Deanna Tarleton[1], Christiane Mallett[3], Wen Li[1], Jinda Fan[3], Aitor Aguirre[3], Ping Wang[1]

[1]*Michigan State University, East Lansing, Michigan*
[2]*Precision Health Program, East Lansing, Michigan*
[3]*Michigan State University, East Lansing, MI*

Introduction:
Transplantation of human induced pluripotent stem cell (hiPSC) derived islet organoids is a promising cell replacement therapy for type 1 diabetes (T1D) [1-3]. It is important to improve the efficacy of islet cell transplantation by investigating new transplantation sites with high vascularization and enough accommodation, which would support graft survival with a high capacity for oxygen delivery [4,5]. Based on these requirements, we have identified brown adipose tissue (BAT) has a potential site of interest [6,7]. We hypothesized that transplantation of islet organoids into the BAT will extend islet organoid graft survival.

Methods:
A stably-expressing transgenic human induced pluripotent stem cell line (hiPSCs-L1) was generated constitutively expressing luciferase. Luciferase expression was verified using bioluminescence imaging (BLI) with the IVIS SpectrumCT (Perkin Elmer). Luciferase-expressing hiPSCs were differentiated into islet organoids according to the established protocols[8]. After 21days of differentiation, islet organoids were tested for typical islet markers, including insulin and glucagon by qPCR and immunofluorescence. Islet organoids (20 IEQ) were tested using the IVIS *in vitro.* We transplanted islet organoids (20 IEQ) into the BAT left lobe of NOD/scid mice (12-week-old, female, n=4, the Jackson Laboratory) as BAT group. The same amount of islet organoids was transplanted under the left kidney capsule (KC) of NOD/scid mice (12-week-old, female, n=4, the Jackson Laboratory) as a control group. These two groups were followed up by BLI at day 1, 7, 14, 28, 35, 42, 49, 56, and 63 post transplantation. Quantitative assessment of the BLI signal intensity of grafts was performed using the Living Image software. Islet organoids grafts were collected and processed for histological studies at 14 days post-surgery.

Results:
Differentiated islet organoids expressed islet cell markers of insulin and glucagon at both the RNA and protein levels. Islet organoids derived from luciferase expressing iPSC-L1 were detected *in vitro* by BLI after culturing with 150μg/mL luciferin (supplemental Fig. 1). Islet organoids were successfully transplanted into the left lobe of BAT of NOD/scid mice and were detected by BLI (Fig. 1A, supplemental Fig. 2). The BLI signals were detected from all recipients including both BAT and control group on the first day post transplantation after injection of luciferin at a dose of 150 mg/kg. During the study, the BLI signal gradually decreased, both in the BAT and the KC group. However, the graft BLI signal intensity under the left KC decreased substantially faster than those from the BAT, on day 63 post transplantation, there was no detectable BLI signal from the KC mice, while the graft BLI signal of the BAT group remained (Fig. 1A, supplemental Fig. 3). Immunofluorescence staining of islet organoid graft in BAT displayed the presence of functional organoid grafts as confirmed by staining for insulin and glucagon (Fig. 1B).

Conclusion:
Our results demonstrated that in comparison to the transplantation site of under kidney capsule, BAT enhances islet organoid graft survival. The successful BAT transplantation of islet organoids strongly suggests the BAT is a potential desirable site for islet organoid transplantation for T1D therapy.

Reference
1. Nidheesh Dadheech, A M James Shapiro. Human Induced Pluripotent Stem Cells in the Curative Treatment of Diabetes and Potential Impediments Ahead. Adv Exp Med Biol. 2019;1144:25-35.
2. Adam Ramzy, David M Thompson, Kirsten A Ward-Hartstonge et al. Implanted pluripotent stem-cell-derived pancreatic endoderm cells secrete glucose-responsive C-peptide in patients with type 1 diabetes. Cell Stem Cell. 2021 Dec 2;28(12):2047-2061.e5.
3. A M James Shapiro, David Thompson, Thomas W Donner et al. Insulin expression and C-peptide in type 1 diabetes subjects implanted with stem cell-derived pancreatic endoderm cells in an encapsulation device. Cell Rep Med. 2021 Dec 2;2(12):100466.
4. Poppy Addison, Karina Fatakhova, Horacio L Rodriguez Rilo. Considerations for an Alternative Site of Islet Cell Transplantation. J Diabetes Sci Technol. 2020 Mar;14(2):338-344.
5. Erwin Ilegems, Per-Olof Berggren. The Eye as a Transplantation Site to Monitor Pancreatic Islet Cell Plasticity. Front Endocrinol (Lausanne). 2021 Apr 23;12:652853.
6. Joseph D White, Revati S Dewal, Kristin I Stanford. The beneficial effects of brown adipose tissue transplantation. Mol Aspects Med. 2019 Aug; 68:74-81.
7. Jessica D Kepple, Jessie M Barra, Martin E Young et al. Islet transplantation into brown adipose tissue can delay immune rejection. JCI Insight. 2022 Feb 22;7(4):e152800.
8. Felicia W Pagliuca, Jeffrey R Millman, Mads Gürtler et al. Generation of functional human pancreatic β cells in vitro. Cell. 2014 Oct 9;159(2):428-39.

Poster Presentation

Disclosures: The authors would like to disclose that FDG has been approved.st

470-A feasibility study of theranostic agents development and cone-beam x-ray luminescence computed tomography (CB-XLCT) design

Presenter: Yu-Hong Wang, National Yang Ming Chiao Tung University

Yu-Hong Wang[1], BO-HAO LEE[1], Jyh-Cheng Chen[1], Tse-Ying Liu[1] David Shih-Chun Jin[1], Yu-Hong Wang[1,2], Pei-Shan Chen[1], Bo-Hao Lee[4], Chia-Lun Tsai[3],Tien-Ai Ji[3],Tien-Yu Wu[3], Jyh-Cheng Chen[1], Snow H. Tseng[3] and Tse-Ying Liu[4]

[1]*National Yang Ming Chiao Tung University, Taiwan, ROC*
[2]*Institute of Biophotonics, National Yang Ming Chiao Tung University, Taiwan, ROC*
[3]*Graduate Institute of Photonics and Optoelectronics, National Taiwan University, Taiwan, ROC*
[4]*Department of Biomedical Engineering, National Yang Ming Chiao Tung University, Taiwan, ROC*

The goal in this study was to develop a small-animal cone-beam x-ray luminescence computed tomography (CB-XLCT) prototype to provide dual modality imaging including computed tomography and optical tomography, which is under low-dose (60 kVp, 0.1 mA) CT mode to reduce the radiation dose. Besides, laser irradiation has been removed to simplify optical tomography via novel optical nanoparticle probe, which is excited by x-ray radiation. In order to improve image quality, there are four aspects breakthroughs described below:
First, theranostic agents apply rare earth-doped crystals with defects induced by lanthanides with good optical and chemical stability, low

toxicity, and narrow emission band provides suitable conditions for biomedical applications. The NaGdF4 dual-modality tracer nanoparticles were used because they have best down-conversion materials with the best luminous efficiency due to their large bandgap, low phonon energy, and high luminescence quantum yield. Additionally, the Gd is a high atomic number element with good X-ray absorption and is an element of a CT contrast agent, furthermore, its visible light properties range of around 600 +/- 20 (nm) wavelength can be emitted under X-ray excitation. It can be used as a multimodal theranostic agent for XLCT imaging and therapy.
Second, the fluorescence diffused optical tomography (FDOT) uses fluorescence as a light source for medical imaging which is highly scattering. In order to simulate the scattering and absorption of light in biological tissue, the diffusion equation to simulate the transmission of light has been used. A FDOT forward model established by utilizing Monte Carlo simulation and NIRFAST [3,4] as the inverse model whose regularization process uses the modified Tikhonov minimization to simulate its optics. The simultaneous algebraic reconstruction technique (SART) using iterations to achieve the allowable value. These solved optical parameters in three-dimensional space can help us to specificity the specific biomarkers.
Third, micro-CT system keeps the original matrix size of in 1944 × 1536 without binning. X-ray tube provides 50–80 kVp characteristic X-ray beams. The system calibration applies line-beads phantom to obtain the system calibration parameters to calibrate the system and calibration parameters are calculated by tracking the position of the steel ball at each angle. The global center of rotation (gCOR) method [5] is used too to calibrate the image again in the sinogram to remove the artifacts caused by any offset. To improve image quality, AI de-noise model was developed and applied to achieve low-dose imaging before reconstruction to maintain image quality. The calibrated projections are reconstructed using FDK and SIRT methods via ASTRA toolbox [6] to achieve good CT images.
Finally, this system applied co-centric rotation design to let both CT and optical tomography simultaneously registered to easily fuse the hybrid images. It opens a new feasibility to observe the change of dual-modality system design.

Reference

1. Zhang, Wenli, et al. "Sub-10 nm water-dispersible β-NaGdF4: X% Eu3+ nanoparticles with enhanced biocompatibility for in vivo x-ray luminescence computed tomography." ACS applied materials & interfaces 9.46 (2017): 39985-39993.
2. Ren, Yufu, et al. "PEGylated β-NaGdF4/Tb@ CaF2 Core/Shell Nanophosphors for Enhanced Radioluminescence and Folate Receptor Targeting." ACS Applied Nano Materials 2.6 (2019): 3718-3727.
3. Jermyn, Michael, et al. "Fast segmentation and high-quality three-dimensional volume mesh creation from medical images for diffuse optical tomography." Journal of biomedical optics 18.8 (2013): 086007.
4. Dehghani, Hamid, et al. "Near infrared optical tomography using NIRFAST: Algorithm for numerical model and image reconstruction." Communications in numerical methods in engineering 25.6 (2009): 711-732.
5. Zhang, Hanqing, et al. "zOPT: an open source optical projection tomography system and methods for rapid 3D zebrafish imaging." Biomedical optics express 11.8 (2020): 4290-4305.
6. Bleichrodt, Folkert et al. "Easy Implementation of Advanced Tomography Algorithms Using the ASTRA Toolbox with Spot Operators." Numerical algorithms 71.3 (2016): 673–697. Web.

Poster Presentation

Disclosures: The authors have disclosed no financial interest.

471-In vivo real-time imaging of microvasculature injury following acute myocardial ischemia/reperfusion injury in the beating murine heart using fiberoptic confocal laser endomicroscopy

Presenter: Shengjie Lu, National Heart Centre Singapore

Shengjie Lu[1], Jasper Chua[2], Su Yin Chaw[3], Ann-Marie Chacko[4], Derek Hausenloy[3]

[1]*National Heart Centre Singapore, Singapore, Singapore*
[2]*Singapore, Singapore*
[3]*Duke-NUS Medical School, Singapore, Singapore, Singapore*
[4]*Duke-NUS Medical School, Singapore, Singapore*

Background/Introduction:
Acute myocardial infarction (AMI), and the heart failure which often follows, are among the leading causes of death and disability worldwide. Microvascular obstruction (MVO), due to damage to the coronary microvasculature is a key determinant of heart failure and poor outcomes following AMI, and there is currently no treatment for preventing MVO. Real-time *in vivo* imaging of MVO in the beating rodent heart is challenging due to the compromised spatial and temporal resolution from movement artifacts. In this study, we apply, for the first time, a fiber-optic confocal laser endomicroscopy (CLM) to real-time image the macro- and microvasculature in the beating murine heart subjected to acute ischemia/reperfusion injury (IRI) in order to image the development of MVO and provide a pre-clinical platform for testing novel therapeutic agents for preventing MVO post-AMI.

Methods:
An *in vivo* murine acute myocardial IRI model (45 min regional ischaemia with temporary ligation of left coronary artery (LCA) and 30 min reperfusion) was applied. At 10 min prior to ischaemia, 150 µl Dextran-FITC (150 kDa, 10 mg/ml) was injected retro-orbitally (RO), and then CLM imaging with a flexible miniprobe (ProFlex S-1500 Probe with CellVizio CLM system, Mauna Kea Technology, France) was applied to the epicardial surface at multiple positions at 5 min post-injection (baseline), 30 min post-ischaemia and 30 min post-reperfusion.

Results:
We firstly confirmed visualization of the macro- and microvasculature at various positions on the epicardial surface of the beating heart. Then, we induced acute myocardial ischemia by ligating the left coronary artery (LCA) and imaged the heart after 30 min ischaemia, and observed reduced microvasculature blood flow below the LCA ligation as evidenced by reduced presence of FITC in within the vessels. Importantly, the microvasculature in the non-ischemic myocardium above the ligation was unaffected. Furthermore, after 45 min of ligation we released the ligature to induce myocardial reperfusion and imaged the heart at 30 min reperfusion. We were able to visualise areas of reduced microvasculature flow due to MVO as evidenced by patchy of reduce FITC imaging within the vessel and damaged to the microvasculature as evidence by leakage of FITC signal outside the vessel. By 60 min reperfusion some of the vessels had regained blood flow, but some areas of reduced FITC signal persisted and leakiness of microvasculature had worsened.

Conclusion:
In conclusion, we have demonstrated for the first time real time *in vivo* imaging of the coronary microvasculature in the beating murine

heart subjected to acute IRI and demonstrate the development of MVO and damaged to the microvasculature with leakage of dye out of the vessels and into the cardiac interstitium, thereby providing a pre-clinical platform to testing novel therapeutic agents for preventing MVO post-AMI.

Acknowledgements: This work was supported by the Singapore Ministry of Health's National Medical Research Council (OF-YIRG: MOH-000230), and SingHealth Duke-NUS Academic Medicine Centre (AM grant: AM/TP014/2018).

Poster Presentation

Disclosures: The authors have disclosed no financial interest.

472-Shifting paradigm: Initial investigation & in vitro evaluation of High relaxivity, Non-Gadolinium Multimodal Theranostic Agents

Presenter: CuhaWijay Sathiyajith, Cardiff University

CuhaWijay Sathiyajith

Cardiff University, Cardiff, South Glamorgan, United Kingdom

Abstract Body:
Inspired by the success of preparing dual-modal imaging agents based on DTPA analogues, we embarked on the preparation based on EDTA bisamides, targeting transition metal complexes. More specifically, we synthesized and characterized Manganese and Copper complexes with 4-(aminomethyl)pyridine and 2-aminoanthraquinone as fluorescent auxiliary groups.

Aim:
Development of a highly scalable, Gd-free, Multimodal Theranostic agent based on EDTA bisamide functionalized with a fluorophore. The diagnostic arm should have high relaxivity for MRI Imaging and high sensitivity for Optical imaging with equal/higher thermodynamic stability than commercial contrast agents, along with the anticancer activity.

Material & Methods:
EDTA bisamide of 4-(aminomethyl)pyridine (**L^1**) was synthesized by the slow addition of the 4-(aminomethyl)pyridine solution to a solution of the EDTA bisanhydride. Subsequently, both the *in-situ* complexation and the solid complexes of manganese and copper of **L^1** were prepared. The potential of **L^1** for magnetic resonance imaging/Optical Imaging (MRI/OI) was evaluated by measuring (a) thermodynamic stability by stability constants with potentiometric titrations; (b) R_1 relaxivities by NMR relaxivity studies (c) spectrophotometric investigations d) therapeutic activity by Molecular docking.

Results: Mn-L^1 and **Cu-L^1**
obtained good yields (77% & 93%). **Mn-L^1** has performance comparable to the commercially available gadolinium-based contrast agents and it is higher than a clinically approved manganese-based contrast agent. Specifically, **Mn-L^1** exhibited relaxivity of 3.52 $mM^{-1}s^{-1}$ (30 MHz, 37 °C) and high overall stability constant for its **Zn-L^1** (16.03). Furthermore, the sharp break exhibited in the NMRD titration profile of **L^1** with Mn (II) indicated a 1:1 complex formation and substantiates a higher association constant. The photophysical characterization confirmed a higher Stokes shift (7355 cm−1) and the ability of **L^1** to act as an *on-off* type for Cu (II). Time-resolved fluorescence investigations (TCSPC) indicated the potentiality of **L^1** for live-cell imaging. Modeling studies exhibited the affinity of **L^1** for Human aurora B kinase, and serum albumin (HSA).

Conclusion:
Water-soluble Manganese complexes of EDTA bisamide of 4-(aminomethyl)pyridine could serve as potential non-gadolinium-based MRI contrast agent and/or PET agent. Additionally, they could act as fluorescent sensors with potential applications in biology and medicine. *In silico* modeling studies indicate that **L^1** has a strong affinity for HSA and that it may effectively inhibit Aurora B Kinase with associated anticancer activity. **MnL^1** and **CuL^1** as PET/OI imaging agents are also envisaged. Further conclusions of this unique research will be presented at the conference.

Reference
1. C. Sathiyajith, A. J. Hallett and P. G. Edwards, Results Chem., 4, 100307, (2022).
2. 2. C. Sathiyajith, A.J. Hallett, A.J. Amoroso and P.G. Edwards, RSC Adv. 7, 38463, (2017).

Poster Presentation

Disclosures: The authors have disclosed no financial interest.

473-Detectability of lesions containing 89Zr-labelled cells under realistic clinical imaging conditions

Presenter: Ferdia Gallagher, University of Cambridge

Laura M. Lechermann[1], Roido Manavaki[2], Tim Fryer[2], Daniel Gillett[3], Luigi Aloj[2], Iosif Mendichovszky[4], **Ferdia Gallagher[2]**

[1]*University of Cambridge - Department of Radiology, Cambridge, United Kingdom*
[2]*University of Cambridge, Cambridge, Cambridgeshire, United Kingdom*
[3]*University of Cambridge, Cambridge, United Kingdom*
[4]*Cambridge University Hospital NHS Foundation Trust, Cambridge, United Kingdom*

Introduction:
In vivo tracking of labeled cells can be used to non-invasively improve the accuracy, efficacy and safety of immunomodulatory treatments and cell therapies. Zirconium-89 ($t_{1/2}$ = 78.4 h) has emerged as a promising radioisotope for direct cell labeling and *in vivo* cell imaging using positron emission tomography (PET) [1]–[3]. The aim of this work was to assess detectability of ^{89}Zr-labeled cells under realistic clinical imaging conditions. To achieve this, spheres containing ^{89}Zr-labeled cells with different cell densities were imaged in air using PET. The data from the sphere acquisitions were combined with patient data from whole-body oncology PET scans to generate artificial lesions within clinically-realistic background distributions. Lesions were located within both the lung and liver, and the relationship between contrast-to-noise ratio (CNR) as a metric of detectability, and labeled cell density (LCD) or specific activity (SA) was investigated.

Methods:
To produce the spheres (n=3) containing ^{89}Zr-labeled cells, Jurkat cells were labeled with 556 kBq of [^{89}Zr]Zr(oxinate)$_4$ for 20 min at room temperature. The ^{89}Zr-labeled cells were subsequently transferred into 3 vials and the cell specific activity [kBq/10^6 cells] was measured using a well counter. ^{89}Zr-labeled cells were entrapped in

alginate beads [4],[5] and transferred into 3D printed spheres of different diameters (1, 2, 3 cm) with similar cell numbers and specific activities. Through inspection of the whole-body scans, the spheres were imaged for 20 min at locations within the PET field-of-view that matched disease-free regions of the lung and liver. Five patients who underwent PET/MR (SIGNA; GE Healthcare) approximately two hours after administration of 4.2 ± 0.3 MBq/kg ^{18}F-FDG were included in this investigation. These were used as a surrogate for whole-body scans of ^{89}Zr-labeled cells which will be acquired in future clinical studies.
Lesion absent (LA) and lesion present (LP) images were reconstructed using time-of-flight ordered-subsets expectation-maximization (3 iterations, 16 subsets, transaxial filter 5mm, standard axial filter) in Duetto v2.03 (GE Healthcare). To produce the LP images, sinograms from the clinical ^{18}F-FDG and ^{89}Zr-labeled cells scans were fused. To avoid quantification errors arising from incorrect attenuation correction, the ^{89}Zr-labelled cells sinograms were multiplied by the corresponding attenuation sinogram of the clinical ^{18}F-FDG scan prior to fusion.
For each lesion, contrast was evaluated by calculating: LP/LA – 1. Adjusting the acquisition duration used for the ^{89}Zr-labeled cells sinograms, effectively simulated spheres of different specific activity. For each contrast level, contrast-to-noise ratio (CNR) was determined and classified using the Rose criterion (i.e. CNR=5). The detection probability of ^{89}Zr-labeled cells as a function of the product of SA and LCD was estimated through logistic regression. The lower limit of detection (LLD) was defined as the LCD required for a detection probability of 50%.

Results:
The spheres contained $0.67 \pm 0.04 \times 10^6$ ^{89}Zr-labeled cells with a SA of 21.4 ± 0.4 kBq/10^6-cells. **Fig. 2** shows example images of lesions together with relationships between detection probability and LCD at various SA values. Due to the lower noise level in the lung, higher detection probability values were obtained with lower LCDs than in the liver. At the LLD, for SA values ranging from 3-30 kBq/10^6 cells, LCDs of 0.2-1.1×10^6 cells/ml were required in the lung vs. 0.2-1.7×10^6 cells/ml in the liver. These LCD values at the LLD are 2-3 orders of magnitude higher than those reported for similar experiments conducted in air [6].

Conclusion:
This study assessed the detectability of ^{89}Zr-labeled cells in realistic clinical imaging scenarios by lesion implantation into clinical scan data, thereby taking account of the noise propagation and quantification issues present in clinical scanning. Compared to our previous results that assessed cellular detectability *in vitro*, significantly higher labeled cell densities were required for *in vivo* imaging.

Reference

1. Asiedu KO, Koyasu S, Szajek LP, Choyke PL, Sato N. Bone marrow cell trafficking analyzed by 89Zr-oxine positron emission tomography in a murine transplantation model. Clin Cancer Res. 2017;23(11):2759-2768.
2. Man F, Lim L, Volpe A, et al. In Vivo PET Tracking of 89 Zr-Labeled Vγ9Vδ2 T Cells to Mouse Xenograft Breast Tumors Activated with Liposomal Alendronate. Mol Ther. 2019;27(1):219-229.
3. Weist MR, Starr R, Aguilar B, et al. PET of adoptively transferred chimeric antigen receptor T Cells with 89Zr-Oxine. J Nucl Med. 2018;59(10):1531-1537.
4. Smidsrød O, Skjåk-Bræk G. Alginate as immobilization matrix for cells. Trends Biotechnol. 1990;8(C):71-78.
5. Andersen T, Auk-Emblem P, Dornish M. 3D Cell Culture in Alginate Hydrogels. Microarrays. 2015;4(2):133-161.
6. Lechermann LM, Manavaki R, Attili B, et al. Detection limit of 89Zr-labeled T cells for cellular tracking: an in vitro imaging approach using clinical PET/CT and PET/MRI. EJNMMI Res. 2020;10:82.

Poster Presentation

Disclosures: The authors have disclosed no financial interest.

474-Physiotherapy induced changes in corticospinal tract of ischemic stroke patients assessed by MRI

Presenter: Dushyant Kumar, All India Institute of Medical Sciences (AIIMS)

Dushyant Kumar[1], Rajesh Mishra[1], Priyanka Bhagat[1], Surbhi Kaura[2], Padma Srivastava[1], Rama Jayasundar[3]

[1]*All India Institute of Medical Sciences (AIIMS), New Delhi, Delhi, India*
[2]*All India Institute of Medical Sciences (AIIMS), Delhi, Delhi, India*
[3]*All India Institute of Medical Sciences (AIIMS), New Delhi, India, New Delhi, Delhi, India*

Introduction:
Stroke is a leading cause of disability worldwide and affects economy and work productivity of countries.[1] Stroke rehabilitation plays a major role in stroke management and physiotherapy is the conventional technique for this. The present study evaluates the effect of physiotherapy in post-stroke rehabilitation by Magnetic Resonance imaging (MRI)

Materials and methods:
Eleven first-ever stroke patients (18-60 years) with ischemia in left hemisphere were enrolled for the study after obtaining approval from Institute Ethics Committee. Qualified physiotherapists gave standard physiotherapy to all patients for one hour every day for six consecutive months. National Institutes of Health Stroke Scale was determined at 0, 3 and 6 months post-intervention. Diffusion Tensor Imaging (DTI) was carried out at 3T (Philips MR scanner) using the following parameters: repetition time - 12,210 ms, echo time - 83 ms, acquisition matrix - 112 x 110, flip angle - 90^0, number of slices - 66, gradient direction - 32. DTI images were acquired and processed with FSL 5.0.9. Color coding of tractography pathways was based on a standard red-green-blue (RGB) code that was applied to the vector in each brain area (red for right to left, blue for dorsal to ventral, and green for anterior to posterior). Comparisons between groups (pre- and post-physiotherapy) for longitudinal changes were carried out.

Results:
Percentage improvement in NIHSS score was observed for all the patients after three (71.5%) and six (80%) months of physiotherapy. Representative images of processed DTI data (Fig. 1) show the physiotherapy induced mean changes in fractional anisotropy (FA) of corticospinal tract for left and right hemisphere separately. While the FA of left corticospinal tract decreased between 3 and 6 months post intervention, it increased in the right corticospinal tract. This shows that the contralateral region has taken over the activity resulting in increase in its CST tract fractional anisotropy.

Conclusion:
Physiotherapy plays a major role in post-stroke rehabilitation. Although there are reports on physiotherapy induced changes in physiological

functions,[2] to the best of our knowledge there are no MR studies, in particular to assess the white matter changes effected by physiotherapy in post-stroke recovery. The current study has shown for the first time the changes induced by physiotherapy in the corticospinal tract in post-stroke recovery using DTI. The study has shown that DTI can play a crucial role in understanding the effects of physiotherapy in post-stroke recovery.

Reference

1. World Health Organization, Global Strategy for the Prevention and Control of Noncommunicable Diseases. Report by the Director General. A 53/14 Fifty-third World Health Assembly, May 2000.
2. Carvalho R, Azevedo E, Marques P, Dias N, Cerqueira JJ. Physiotherapy based on problem-solving in upper limb function and neuroplasticity in chronic stroke patients: A case series. J Eval Clin Pract. 2018; 3: 552-560.

Poster Presentation

Disclosures: The authors have disclosed no financial interest.

475-ExiTron™ BAT, a novel contrast agent visualising activated brown adipose tissue (BAT) by CT imaging

Presenter: Claudia Genger, nanoPET Pharma GmbH

Claudia Genger[1], Eva Jolanthe Koziolek[2], Danielle Franke[2], Alexander Kraupner[2], Andreas Briel[2]

[1]nanoPET Pharma GmbH, Germany
[2]nanoPET Pharma GmbH, Berlin, Berlin, Germany

Introduction*:*
In 2016 more than 1.9 billion adults (>18 years of age) were considered overweight, 650 million categorised as 'obese' (World Health Organisation, 2017). Obesity develops when calorie uptake exceeds energy expenditure, with excess energy being stored in fat. Researchers have identified adipose tissue (i.e., fat) as essential in weight regulation and have distinguished between at least two forms: white adipose tissue (WAT), and brown adipose tissue (BAT). In mammals, BAT is the primary tissue involved in energy expenditure and non-shivering thermogenesis, and its amount and activation level regulate the utilisation of excessive calories for thermogenesis rather than fat storage in WAT. Various biomedical imaging techniques have been utilised to study the morphology and function of BAT *in vivo,* such as positron emission tomography (PET), computed tomography (CT), magnetic resonance imaging (MRI), contrast-enhanced ultrasound (CEUS), or various optical techniques [1-3]. BAT activity *in vivo* is commonly measured by PET-CT scans using 2-[^{18}F]-fluoro-2-deoxy-D-glucose (^{18}F-FDG) to assess glucose utilisation linked to BAT mitochondrial respiration [2,3]. Subjects are exposed to ionising radiation, and different degrees of BAT activation combined with poor reproducibility of FDG PET-CT in measuring BAT glucose metabolism lead to a high result variability [4,5]. As no CT contrast agent for BAT is available to date, our study focuses on the potential of visualising and quantifying BAT in mice using CT combined with a novel CT contrast agent, ExiTron™ BAT (Viscover™, *nanoPET Pharma* GmbH, Berlin, Germany), a nanoparticulate imaging agent with high iodine content.

Methods:
In a pilot study, old (1+ year) and young mice (8 weeks) were compared after BAT activation through short-term cold exposure (12h) versus no BAT activation. CT imaging was performed using the nanoScan® PET/CT scanner (Mediso) with fixed parameters for all groups (helical scan, 360 projections, 900 ms exposure time, 1:4 binning, Butterworth filter).
CT scans of the upper mouse body (head and thorax) were performed prior and at specific time points after intravenous injection of the mice with ExiTron™ BAT (dose 1050 mg iodine/kg body weight, i.e., 125 µL per 25 g mouse).
Post analysis was performed by placing region of interest (ROI)s in the lower neck region where BAT is located and compared to ROIs in lung tissue (control).

Results*:*
Using ExiTron™ BAT, activated BAT in young mice was clearly visualised and uptake measured in Hounsfield units (HU) (Fig. 1A, C). As old mice have little to no BAT, the uptake of ExiTron™ BAT after activation was only slightly increased compared to the younger counterpart (Fig.1B). Liver contrast was increased equally in young and old animals, confirming that the lack of signal was related to the lack of BAT tissue in old mice and indicating the clearance of the contrast agent via the hepatic route. In animals with no BAT activation through short-term cold exposure BAT was not visualised regardless of age however that may be due to limitations of the scanning device and the used parameters.

Conclusion:
Using ExiTron™ BAT, BAT can be clearly visualised in young mice after short-term cold exposure, thereby presenting an alternative method to imaging BAT without radioactive tracers. In animals where BAT was not activated or present, no significant increase in signal was registered, which is to be expected and confirms the validity of the pilot study results.

Reference

1. Chen, Y.I., et al., Anatomical and functional assessment of brown adipose tissue by magnetic resonance imaging. Obesity (Silver Spring), 2012. 20(7): p. 1519-26.
2. Cypess, A.M., et al., Identification and importance of brown adipose tissue in adult humans. N Engl J Med, 2009. 360(15): p. 1509-17.
3. van Marken Lichtenbelt, W.D., et al., Cold-activated brown adipose tissue in healthy men. N Engl J Med, 2009. 360(15): p. 1500-8.
4. Sampath, S.C., et al., Imaging of Brown Adipose Tissue: State of the Art. Radiology, 2016. 280(1): p. 4-19.
5. Crandall, J.P., et al., Repeatability of brown adipose tissue measurements on FDG PET/CT following a simple cooling procedure for BAT activation. PLoS One, 2019. 14(4): p. e0214765.

Poster Presentation

Disclosures: The authors have disclosed no financial interest.

476-Acute Nicotine-Free E-cigarette Vapor Exposure Modulates Immune Response in Murine Lung Vasculature

Presenter: HASSAN ALKHADRAWI, West Virginia University

Hassan Alkhadrawi[1], Hunter Snoderly[2], Dhruvi M. Panchal[2], Margaret Bennewitz, Kelly Weaver[1]

[1]West Virginia University, Morgantown, WV
[2]West Virginia University, Morgantown, West Virginia

E-cigarette vapor (ECV) exposure led to lung damage and a spate of sudden deaths in recent years. E-cigarette or vaping use-associated lung injury has typically been linked to the presence of specific flavorants or contaminants in e-liquid, such as vitamin E acetate. However, here we show that inflammatory cellular responses occur in the pulmonary vasculature and alveolar spaces in response to short-term, acute exposure to ECV generated from e-liquid without nicotine or flavoring. The goal of this study is to characterize subclinical pathologies resulting from ECV exposure in order to better predict the risks of chronic use, which may emerge as the phenomenon of vaping ages. Specifically, we investigated the role of blood cells including neutrophils and platelets in lung injury induced by ECV exposure. Neutrophils are the most abundant type of white blood cells, and when stimulated, release neutrophil extracellular traps (NETs). These webs of extruded DNA fibers are decorated with proteolytic enzymes and enable inflammatory positive feedback loops, vessel damage, and clot formation. Platelets, which are commonly known to cause clotting responses, bind to neutrophils to form occlusive neutrophil-platelet aggregates (NPAs). Female BALB/c mice underwent 3 consecutive hours/day of ECV exposure (1 puff/min at 30 watts, 50% vegetable glycerin (VG)/ 50% propylene glycol (PG)), for 3 days. Control mice were exposed only to room air. Analytes were collected from mice at 3 different time points following exposure: immediately after the final exposure (t=0hrs), one day later (t=24hrs), and 2 days later (t=48hrs). Intravital imaging of the pulmonary lung vasculature (n=5 mice per group) was performed at each time point. Fluorescent labels were retro-orbitally injected to stain vasculature (FITC dextran), neutrophils (Pacific Blue), platelets (AlexaFluor647 CD49b), and DNA (SYTOX orange) (**Figure 1A**). Neutrophil and platelet presence was assessed by measuring count and overall area, respectively. NPAs were defined as any object containing both CD49b+ and Ly6g+ signal. Results indicated a significant increase of neutrophils and NPAs in all ECV treated mice. Interestingly, an increase in platelets was observed only in mice either immediately after or 48 hours after ECV exposure, suggesting two different mechanisms for acute and persistent platelet stimulation following ECV exposure (**Figure 1B**). Whole blood and bronchoalveolar lavage fluid (BALF) were collected from a subset of ECV-exposed and control mice (n=5 per group) at each timepoint. Cell populations in whole blood and BALF were characterized using a ProCyte Dx Hematology Analyzer. Lungs were collected from n=3 mice, fixed in formalin, sectioned, and stained with hematoxylin and eosin (H&E). Cell counts from ProCyte analysis were not significantly altered in BALF or plasma for any ECV-exposed groups compared to control; however, a non-significant increase in lymphocyte presence in BALF was noted t=24hrs after exposure, possibly indicating lung inflammation. Although an increase in neutrophils was not observed via ProCyte in peripheral whole blood, the increased presence of neutrophils observed in intravital imaging suggests this is a highly localized response. Lastly, plasma and BALF were analyzed to assess the presence of cell free DNA, oxidative stress, myeloperoxidase- a component of NETs, and inflammatory cytokines. Results of these assays are pending. Overall, our preliminary data indicate a complex immune response occurs upon acute exposure to ECV that persists in the pulmonary vasculature for at least 3 days after cessation of exposure. This work will not only serve to better inform the public of the risks of e-cigarette use, but will also be beneficial to clinicians in characterizing newly emergent pathologies resulting from e-cigarette usage.

Poster Presentation

Disclosures: The authors have disclosed no financial interest.

477-Heteronuclear magnetic resonance J-spectroscopy of hyperpolarized metabolites with a microfluidic diamond quantum sensor on picoliter volumes

Presenter: Thomas Unden, NVision Imaging Technologies GmbH

Philipp Neumann[1], **Thomas Unden[2]**, Stephan Knecht[1], Christophoros Vassiliou[3], Ilai Schwartz[4], Nico Striegler[4], Michael Keim[4], John Blanchard[3], Martin Gierse[5], Jochen Scheuer[3], Jochen Scharpf[3]

[1]*NVision Imaging Technologies GmbH, Ulm, Germany*
[2]*NVision Imaging Technologies GmbH, 89081, BW, Germany*
[3]*NVision Imaging Technologies GmbH*
[4]*NVision Imaging Technologies GmbH, Germany*
[5]*NVision Imaging Technologies GmbH, Baden-Wuerttemberg, Germany*

Abstract body:
In this study the combination of a microscopic NV-diamond-based NMR quantum sensor, a hyperpolarized [1-13C]Fumarate solution and microfluidic sample delivery enables NMR detection of liquids in picoliter volumes in single shot NMR measurements. Heteronuclear J-spectroscopy confirms hyperpolarized [1-13C]Fumarate nuclear spins. In the future these proof-of-concept experiments might enable NMR-based recording of metabolic processes in single cells.

Instrumentation and workflow of the system:
The NMR probe is based on an ensemble of negatively charged nitrogen vacancy (NV) centers in diamond.[1-3] The NV centers are located in a ten micrometer thick diamond layer that is in direct contact with the liquid sample. A 10-micrometer-diameter laser beam excites and thus initializes those NV centers' electron spins that participate in NMR detection. This way the active sensor region is defined to be a roughly 10 micrometer round spot within the 10 micrometer thick NV diamond layer. A microwave pulse sequence turns the NV electron spins into adjustable narrowband quantum probes for the AC magnetic field generated by the nuclear spins of interest. Finally, the NV electron spins' state and thus the NMR signal is encoded in the NV center fluorescence level that is triggered by readout laser pulses. The NMR detection volume is roughly given by the size of the sensor region of a picolitre. The NMR experiments take place in a 0.1T electromagnet at room temperature. Radiofrequency and microwave pulses are applied with a millimeter coil and a transmission line close by. To load the detection volume of the magnetometer with liquid NMR samples, a microfluidic chip is placed on top of the diamond. Within seconds, the analyte can be transferred to the magnetometer and can be measured. Furthermore, hyperpolarized liquids can be inserted without losing significant amounts of the polarization. Current focus of the investigation is the metabolite Fumarate. To boost SNR hyperpolarized [1-13C] Fumarate in D2O solution is used. First, Fumarate is polarized in house based on parahydrogen induced polarization (PHIP) methods and then transferred to the detection volume of the quantum magnetometer via the microfluidic chip and then detected. Hyperpolarized Fumarate can continuously be delivered and detected. Relaxation times of hyperpolarized proton and carbon nuclei are in the tens of seconds. The future application of this instrument is the study of metabolic processes at the single cell level on the timescale of seconds. J-spectroscopy can then allow studying biochemical conversion processes. This could enable better diagnostics and drug development. To achieve this, high resolution NMR spectroscopy with high SNR on picoliter volumes is necessary.

NMR of hyperpolarized protons in fumarate:
The following figure shows a NMR spectrum of protons in a 50mM D2O solution of hyperpolarized [1-13C]Fumarate acquired in a single shot measurement of about one second. The corresponding nuclear polarization is on the order of 10%, which is many orders of magnitude higher than thermal polarization at 100mT and room temperature. The

main signal comes from about one picolitre volume and its SNR is about 50. The spectrum shows the signal right after preparation of the hyperpolarized sample. Step by step more of the liquid sample is then pumped to the sensor and more spectra are acquired and changes of the spectra are monitored.

Spectroscopy of 1H-13C-J-coupling in hyperpolarized [1-13C] Fumarate:

The following figure shows the JHC-coupling spectrum of hyperpolarized [1-13C]Fumarate. Again a 50mM solution of hyperpolarized Fumarate is first prepared, then transferred to the detection system and then measured in a single run (1s acquisition). The NMR protocol bases on a KDD protocol[4] applied on the proton and carbon channel to refocus inhomogeneities but still keeping the J-coupling between both spin species. Between pulses again a 20ms wait time was used. The expected JCH-coupling of [1-13C]Fumarate is observed.

Reference

1. Bucher, D. B. et al. High Resolution Magnetic Resonance Spectroscopy Using Solid-State Spins. Nature 555, 351–354 (2018).
2. Smits, J. et al. Two-dimensional nuclear magnetic resonance spectroscopy with a microfluidic diamond quantum sensor. Sci. Adv. 8 (2019).
3. Arunkumar, N. et al. Micron-Scale NV-NMR Spectroscopy with Signal Amplification by Reversible Exchange. PRX Quantum 2, 010305 (2021).
4. Souza, A., Álvarez, G. & Suter, D. Robust Dynamical Decoupling for Quantum Computing and Quantum Memory. Phys. Rev. Lett. 106, 240501 (2011).

Poster Presentation

Disclosures: The authors have disclosed no financial interest.

478-Pre-Clinical Characterization of a Novel [89Zr]-Labeled CXCR3-Targeting PET Imaging Probe

Presenter: Chanelle Hunter, University of Alabama at Birmingham

Chanelle Hunter

University of Alabama at Birmingham, Birmingham, AL

Background:

Immuno-Positron Emission Tomography (iPET) is a noninvasive imaging modality that combines the quantitative spatial resolution of PET with the target specificity of immune-based radiotracers for improved clinical diagnostics and management. iPET imaging agents for markers on the surface of T cells and other effector molecules have been used to determine the presence and quantity of immune cells in the tumor microenvironment. However, while identifying the presence of these cell types is valuable, these agents do not provide any information on functional status. Currently, no effective means to noninvasively quantify functional effector cells, such as the activated T-helper 1 (Th1) type immune cells, exists to monitor checkpoint inhibitor responses. Therefore, the development of novel imaging probes targeting biomarkers on Th1 activated immune cells will aid in the understanding of immune activation in cancer and improve the prediction and tracking of therapeutic responses throughout treatment. Chemokine receptor CXCR3, a transmembrane G-protein coupled receptor, is highly expressed on immune cells during active Th1 signaling and enriched in the tumors of mice that respond to immunotherapy.[1] Further, highlighting the importance of spatial localization, levels of CXCR3-positive cells in the blood counterintuitively show a marked decrease in responders to immunotherapy, suggesting active infiltration into tumors to facilitate cell killing, although this has not been directly observed.[2] The aim of this study was to develop an [89Zr]-labeled monoclonal antibody PET probe and observe the effects of tumor development on CXCR3-expressing cell biodistribution, as well as the early effects of immunotherapy administration. Characterization of these CXCR3-targeting antibodies in the context of TH1 response will provide a framework for the development of novel chemokine radiotracers, as well as give insights into the biological distribution of CXCR3 mediated cellular trafficking that has yet to be elucidated.

Methods:

Monoclonal anti-mouse CXCR3 was conjugated to bifunctional chelator p-SCN-Bn-DFO and radiolabeled to produce [89Zr]-DFO-anti-mCXCR3 using standard antibody modification techniques.[3] Using a syngeneic tumor model, C57BL/6 mice (n=8 total, n=2 untreated, n=2 non-tumor bearing) were injected subcutaneously with MC38 murine colorectal cancer cells in the upper right flank. A combination of anti-mouse-PD-1 (programmed cell death protein 1) and anti-mouse CTLA-4 (cytotoxic T lymphocyte-associated protein 4) was administered to the treatment group by intraperitoneal injection every 3 days, beginning 9 days post-implantation. Probe biodistribution and clearance were noninvasively imaged by injection of 0.74-1.11 MBq of [89Zr]-anti-mCXCR3 and performing PET imaging 24-, 48-, and 168-hours post-injection. Statistical analyses were conducted through Student's t-tests.

Results:

The resulting images show uptake in tumors, secondary lymphoid organs such as the spleen and lymph nodes and liver through which antibody-based probes are cleared, demonstrating a clear delineation between stores of CXCR3-expressing cells and areas of potential non-specific uptake. PET imaging was utilized to assess changes in CXCR3 accumulation after immunotherapy. Mice treated with combination therapy had an average tumor uptake signal of 42529.97±16921.85 BQML compared to 25356.46±4118.21 BQML in the untreated group. Along with the increase of CXCR3-expressing cells at the tumor site, mean uptake signal obtained Day 6 post-injection demonstrated decreases in lymphoid tissues (46334.57±8915.94 BQML in the spleen) and blood volume (4748.28±3250.93 BQML) following treatment compared to the untreated groups (62054.70±8838.92 BQML and 14101.67±1697.92 BQML, respectively).

Conclusions:

The outcome of this study is the first CXCR3-targeted PET imaging probe used to noninvasively observe the effects of immunotherapy on effector cell biodistribution. This data correlates with previously shown findings that immunotherapy further drives CXCR3+ cells into the tumor compartment while depleting secondary reservoirs in responders. Ongoing studies are being conducted to further elucidate the predictive capabilities of CXCR3-PET imaging in the pursuit of a novel clinically relevant probe.

Reference

1. Chow MT, Ozga AJ, Servis RL, et al. Intratumoral Activity of the CXCR3 Chemokine System Is Required for the Efficacy of Anti-PD-1 Therapy. Immunity. 2019;50(6):1498-1512.e5.
2. Han X, Wang Y, Sun J, et al. Role of CXCR3 signaling in response to anti-PD-1 therapy. EBioMedicine. 2019;48:169-177.
3. Zeglis, B.M., Lewis, J.S. The Bioconjugation and Radiosynthesis of 89Zr-DFO-labeled Antibodies. J. Vis. Exp. 2015; 96;e52521, doi: 10.3791/52521.

Poster Presentation

Disclosures: The authors have disclosed no financial interest.

479-Design and Synthesis of NIR I & II Dyes for Biological Imaging

Presenter: Chathuranga Rathnamalala, Mississippi State University

Chathuranga Rathnamalala

Mississippi State University, Starkville

NIR I and II dyes are desirable for deep tissue imaging due to the deeper penetration of NIR I&II light, less tissue damage, and high spatial resolution from the low autofluorescence in the NIR I &II regions. Xanthene-based dyes were widely explored for cellular imaging due to their outstanding photophysical properties and stimuli responses; however, their photophysical properties lie in the visible region. Xanthene-based dyes have been modified to achieve absorption and emission wavelengths in NIR I and II regions by changing the bridged oxygen atom of the xanthene scaffold to silicon and phosphors and extending the π-conjugation. Our group has designed a NIR-II dye based on the donor-acceptor-donor strategy, which was prepared in three synthetic steps. The dye, rhodindolizine, absorbs at 920 nm and emits at 1092 nm, where the xanthene scaffold acts as the acceptor and the indolizine moiety as the donor. The dye displayed a high molar absorptivity of 97,500 $M^{-1}cm^{-1}$ with 200 nm stokes shift in dichloromethane. The quantum yield (F) of the dye was 0.03% in DCM relative to the cyanine standard dye. Based on this donor-acceptor-donor design strategy, we have discovered another NIR dye based on a thienylpiperidine donor (XanthCR-880). While this dye boosted photophysical properties shy of the NIR-II region, it was more chemically stable than the previous rhodindolizine dye. XanthCR-880 was prepared in three synthetic steps and showed an intense photoacoustic signal at 880 nm. XanthCR-880 showed a high molar absorptivity of 88900 M^{-1} cm^{-1} with a weak emission peak (λem 960 nm DMSO) in the NIR-II region. Exceptional photostability and biological compatibility with reduced glutathione and proline liver esterase revealed the dye's suitability for in vivo imaging. XanthCR-880 was used in a multiplex imaging experiment with a BODIPY reference dye (λabs = 688 nm, ε = 78300 M^{-1} cm^{-1} measured in CHCl3). The maximum attainable imaging depth of the dye was 4 cm with a tissue overlay application. We have also prepared asymmetric dyes with indolizine, pyrrole, and indole donors. The main goal of this project is to enhance the chemical stability of the dyes using a rhodol-like scaffold while maintaining the photophysical properties in the NIR-I region. While these asymmetric dyes absorb and emit in the NIR-I region, they were more chemically stable than the symmetric version.

References

1. Thienylpiperidine Donor NIR Xanthene – Based Dye for Photoacoustic Imaging, Rathnamalala, C. S. L.; Pino, N. W.; Herring, B. S.; Hooper, M.; Gwaltney, S. R.; Chan, J.; Scott, C. N., Thienylpiperidine Donor NIR Xanthene-Based Dye for Photoacoustic Imaging. Organic Letters 2021, 23 (19), 7640-7644
2. Donor – Acceptor - Donor NIR II Emissive Rhodindolizine Dye Synthesized by C-H bond functionalization, Rathnamalala, C. S. L.; Gayton, J. N.; Dorris, A. L.; Autry, S. A.; Meador, W.; Hammer, N. I.; Delcamp, J. H.; Scott, C. N., Donor–Acceptor–Donor NIR II Emissive Rhodindolizine Dye Synthesized by C–H Bond Functionalization. The Journal of Organic Chemistry 2019, 84 (20), 13186-13193.

Poster Presentation

Disclosures: The authors have disclosed no financial interest.

480-Intra- and Inter-Tumor Somatostatin Receptor Expression Heterogeneity on Ga-68 DOTATATE PET/CT Predicts the Response to Lu-177 Therapy in Neuroendocrine Tumor Patients

Presenter: Camila Gadens Zamboni, University of Iowa

Camila Gadens Zamboni[1], Ayca Dundar[1], Bradley Loeffler[1], Sarah Bell[1], Stephen Graves[1], Michael Graham[2], Yusuf Menda[1], Janet Pollard[1], Ahmad Shariftabrizi[3]

[1]*University of Iowa*
[2]*University of Iowa, IA*
[3]*University of Iowa, Iowa City, Iowa*

Background:
Lu-177 Peptide Receptor Radionuclide Therapy (PRRT) is recently approved for advanced neuroendocrine tumors (NETs) which express somatostatin receptors (SSRTs), evaluated using Ga-68 DOTATATE PET/CT [1]. Several controversies still exist regarding the detailed radiomics interpretation of Ga-68 DOTATATE PET/CTs, including the relative prognostic importance of tumor volume, somatostatin receptor expression, and tumor heterogeneity in NET patients [2-4], which would help in more precise selection and management of these patients. In the current study, pre-therapy 68-Ga-DOTATATE radiomic features were evaluated as biomarkers of treatment response and toxicity in NET patients undergoing PRRT.

Methods:
NET patients with Ga-68 DOTATATE PET/CT scans prior to Lu-177 PRRT at our institution were retrospectively evaluated. Radiomic features were evaluated using a specifically designed workflow "Ga-68 Dotatate Lesion ID" (MIM Software Inc.) which relies on the PET-edge and PETedge+ software capabilities for lesion delineation and radiomic feature extraction (including whole-body and organ-specific tumor volume and somatostatin receptor expression, and whole-body and lesional radiomic metrics related to tumor heterogeneity. The endpoints included overall survival (OS), short-term post-PRRT(1-9 months) progression-free survival(PFS), and treatment-related toxicities. Cox regression models were used to assess the effects of radiomic variables on PFS and OS. Logistic regression models were used to assess the effects of radiomic variables on the odds of PRRT-related toxicities.

Results:
Sixty-nine patients were included in the final analysis. At a median follow-up of 20.8 months, 3-year overall survival was 80%. Median and 9-month short-term post-PRRT progression-free survival were 5.1 months and 14%, respectively. Increasing values of the standard deviation (SD) of the SUVbw coefficient of variation across lesions in the whole body was associated with better PFS. Increasing values of the mean and median of the skewness across lesions in the whole body was associated with better OS. In bone lesions, increasing values of SD of the MinSUVbw, MeanSUVbw, and MedianSUVbw was associated with poorer PFS. In liver lesions, increasing values of the SD of the TotalSUVbw and spleen-corrected Receptor Expression was associated with poorer PFS, while increasing values of the SD of the spleen-corrected Receptor Expression was associated with poorer OS. In nodal lesions, increasing values of the maximum and SD of the kurtosis was associated with better PFS. Increasing values of the mean and maximum of MaxSUVbw, the mean, median, and maximum

of MeanSUVbw, the mean, median, and maximum of the MedianSUVbw, the mean and maximum of the SUVbw SD, the mean and median of skewness, the mean, maximum, and median of the SUVbw coefficient of variation, and the maximum liver-corrected SUVmean In nodal lesions were associated with better OS. Increasing values of the total nodal tumor volume, SD of the liver-corrected MeanSUVbw, and maximum of the spleen-corrected MeanSUVbw in nodal lesions were associated with increased odds of nausea/vomiting. Increasing values of the SD of the MeanSUVbw, and the maximum and SD of the MedianSUVbw across lesions in the whole body were associated with increased odds of abdominal pain. Increasing values of the maximum of the spleen-corrected Receptor Expression in liver lesions were associated with decreased odds of experiencing diarrhea. Increasing values of several heterogeneity indices were associated with decreased odds of post-PRRT fatigue.

Conclusion:
Intra- and inter-tumor receptor expression heterogeneity on Ga-68 DOTATATE/TOC PET/CT can determine which NET patients are more probable to benefit from PRRT. Neither the whole body or organ-specific tumor volumes, nor the degrees of whole body somatostatin receptor expression were predictive of favorable PRRT response, implying that receptor expression heterogeneity is a more valid biomarker for precision medicine PRRT.

Reference
1. Strosberg J, El-Haddad G, Wolin E, Hendifar A, Yao J, Chasen B, et al. Phase 3 Trial of 177Lu-Dotatate for Midgut Neuroendocrine Tumors. N Engl J Med. 2017 Jan 12;376(2):125-135.
2. Hou J, Yang Y, Chen N, Chen D, Hu S. Prognostic Value of Volume-Based Parameters Measured by SSTR PET/CT in Neuroendocrine Tumors: A Systematic Review and Meta-Analysis. Front Med (Lausanne). 2021 Nov 26;8:771912.
3. Bezzi C, Mapelli P, Presotto L, Neri I, Scifo P, Savi A, et al. Radiomics in pancreatic neuroendocrine tumors: methodological issues and clinical significance. Eur J Nucl Med Mol Imaging. 2021 Nov;48(12):4002-4015.
4. Laudicella R, Comelli A, Liberini V, Vento A, Stefano A, Spataro A, et al. [68Ga]DOTATOC PET/CT Radiomics to Predict the Response in GEP-NETs Undergoing [177Lu]DOTATOC PRRT: The "Theragnomics" Concept. Cancers (Basel). 2022 Feb 16;14(4):984.

Poster Presentation

Disclosures: The authors have disclosed no financial interest.

481-BSREM And OSEM Reconstructions Effects On PET Radiomics Features Variability And Robustness Assessment

Presenter: Pooja Dwivedi, Advanced Centre for Treatment, Research and Education in Cancer (ACTREC)

Pooja Dwivedi[1], Vishal Vajarkar, Sayak Choudhury[2], Ashish K. Jha[3], Venkatesh Rangarajan[4]

[1]*Advanced Centre for Treatment, Research and Education in Cancer (ACTREC), Mumbai, Maharashtra, India*
[2]*Advanced Centre for Treatment, Research and Education in Cancer (ACTREC), Mumbai, India*
[3]*Tata Memorial Hospital, Mumbai, Maharashtra, India*
[4]*Tata Memorial Hospital, Mumbai, IN-Mah, India*

Background and Aim:
PET Radiomic feature extraction and analysis by assessing tumour heterogeneity on the basis of pixels or voxel information may improve diagnosis, treatment options and outcomes However there are certain issues which are identified in PET radiomic studies that indicated the dependency of textural features on various factors such as acquisition, image reconstruction, tumour segmentation method which needs to be addressed .Therefore the main focus of the study was to evaluate the variability of PET Radiomics features extracted from different PET reconstruction algorithms and identifying the most robust features under such condition.

Method:
Study involves 17 retrospective data of 18F-FDG PETCT patients with confirmed breast malignancy . Each raw data from list mode was reconstructed twice using conventional Ordered subset expectation maximization (OSEM) and Block sequential expectation maximization (BSREM) reconstruction algorithm respectively with standard clinical settings as per recommended guidelines. Texture indices evaluation was performed with IBSI complaint software, ROI was drawn by 3D tool with 40 % threshold, intensity discretization was processed with 64 bins with absolute scale bounds between 0 and 20 for each data set. PET radiomic features were extracted including conventional PET parameters: SUVmax, SUVmean, SUVpeak, SUVstd, SUVSkewness, SUVKurtosis, TLG; shape-based feature Sphericity and Textural feature: gray-level co-occurrence matrix (GLCM) n=7, gray-level run length matrix (GLRLM)n=4, gray-level zone length matrix (GLZLM) n=4 and neighbourhood gray-level different matrix (NGLDM)n=3. The variability of each radiomic features extracted from two reconstructions methods was calculated by determining Coefficient of variation (CV) and divided into four groups according to the range of variation to determine the most robust radiomic feature.

Result:
22 lesions were identified and total 37 PET radiomic features were extracted. Statistical Textural analysis resulted 40.5 % percent features with COV $\leq$ 5% whereas 27% features showed higher variability with COV >20% and remaining features shows small and intermediate variability.

Conclusion:
Study indicated that textural features can vary with the reconstruction method adopted and therefore it might influence quantitatively for radiomic signature identification .Textural features with least variability between different reconstruction methods could be considered robust for reproducible tumour quantification specifically if collaborated with other institutes for radiomic studies.

Reference
1. Ha S, Choi H, PaengJC, Cheon GJ. Radiomics in Oncological PET/CT: a Methodological Overview. Nucl Med Mol Imaging. 2019;53(1):14-29. doi:10.1007/s13139-019-00571-4
2. Chicklore S, Goh V, Siddique M, Roy A, Marsden PK, Cook GJ. Quantifying tumour heterogeneity in 18F-FDG PET/CT imaging by texture analysis. Eur J Nucl Med Mol Imaging. 2013 Jan;40(1):133-40. doi: 10.1007/s00259-012-2247-0. Epub 2012 Oct 13. PMID: 23064544.
3. Hatt, Mathieu et al. “Characterization of PET/CT images using texture analysis: the past, the present… any future?.” European journal of nuclear medicine and molecular imaging vol. 44,1 (2017): 151-165. doi:10.1007/s00259-016-3427-0
4. van Velden FH, Kramer GM, Frings V, Nissen IA, Mulder ER, de Langen AJ, Hoekstra OS, Smit EF, Boellaard R. Repeatability of Radiomic Features in Non-Small-Cell Lung Cancer [(18)F]FDG-PET/CT Studies: Impact of Reconstruction and Delineation. Mol

Imaging Biol. 2016 Oct;18(5):788-95. doi: 10.1007/s11307-016-0940-2. PMID: 26920355; PMCID: PMC5010602.

5. Yan J, Chu-Shern JL, Loi HY, Khor LK, Sinha AK, Quek ST, Tham IW, Townsend D. Impact of Image Reconstruction Settings on Texture Features in 18F-FDG PET. J Nucl Med. 2015 Nov;56(11):1667-73. doi: 10.2967/jnumed.115.156927. Epub 2015 Jul 30. PMID: 26229145.
6. Kinahan, Paul E., et al. "The QIBA profile for FDG PET/CT as an imaging biomarker measuring response to cancer therapy." Radiology 294.3 (2020): 647-657.

Poster Presentation

Disclosures: The authors have disclosed no financial interest.

482-Nanodelivery of endotoxin derivative drugs by ferumoxytol sensitizes murine melanoma tumors to monoclonal antibody immunotherapy

Presenter: Evan Stater, Memorial Sloan Kettering Cancer Center

Evan Stater[1], Elizabeth Isaac[2], Hsu Hsiao-Ting[1], Valerie Ann Longo[1], Jan Grimm[1]

[1]Memorial Sloan Kettering Cancer Center, New York, NY
[2]Memorial Sloan Kettering Cancer Center, New York, New York

Targeted monoclonal antibody immunotherapies (mAb) have revolutionized cancer treatment; however, many patients are non-responders to these therapies, necessitating their incorporation into combination therapy strategies. We sought to develop a translatable immunotherapeutic agent to facilitate mAb therapies by activating antigen-presenting cells (APC), which possess anti-tumoral effector functions that can both facilitate the mechanistic action of co-administered therapeutic mAb, and induce direct APC-mediated tumor cell killing. We identified bacterial lipopolysaccharides (LPS) and derivative compounds as capable APC activator agents to co-administer alongside mAb immunotherapy. Feraheme (ferumoxytol, FH), an FDA-approved iron oxide nanoparticle drug, demonstrated the capacity to non-covalently encapsulate derivatives of LPS into the exterior carbohydrate shell. The most successful drug cargo candidate, MPLA, could easily be integrated into FH using a simple loading procedure that facilitated stable and non-covalent drug-particle association, forming a unitary nanoscale delivery vehicle with theranostic potential. FH with MPLA payload was a potent activator of APC, upregulating antigen-presenting complexes and T cell costimulatory signal proteins at therapeutically relevant concentrations. Alone, the immunotherapeutic mAb FGK4.5, an agonistic binder of the CD40 receptor, has been shown to have poor efficacy against tumors of the B16F10 model of murine melanoma, mirroring the insufficiency of many immunotherapeutic mAb as monotherapies in human patients. Combining FGK4.5 treatment with concurrent administration of APC-activating MPLA-loaded nanoparticles resulted in significant improvements in both tumor proliferation rates and survival duration compared to FGK4.5 monotherapy. This result demonstrates the potential of our immunostimulatory nanoparticle to sensitize cancers which are otherwise refractory to mAb immunotherapies, potentially expanding their therapeutic application potential to a greater number of patients and cancer types.

Poster Presentation

Disclosures: The authors have disclosed no financial interest.

483-Therapeutic Efficacy of Adoptively Transferred T Cells Labeled with Optimized Magnetic Particle Imaging Tracer

Presenter: Angelie Rivera-Rodriguez, Stanford University School of Medicine

Angelie Rivera-Rodriguez[1], Bo Yu[2], Hayden Good[3], Sitong Liu, Lan B. Hoang-Minh[4], Duane A. Mitchell[4], Carlos Rinaldi-Ramos[4]

[1]Stanford University School of Medicine, Palo Alto, CA
[2]University of Florida
[3]University of Florida, Gainesville, Florida
[4]University of Florida, Gainesville, FL

Advances in adoptive cell transfer (ACT) immunotherapies make these one of the most promising treatments for patients with cancer. ACT following lymphodepletive conditioning regimens has emerged as one of the most effective treatment strategies against advanced malignant melanoma, with remarkable objective clinical responses greater than 70% for patients with refractory metastatic disease.[1] Despite ACT being successful against melanomas and blood cancers, such as leukemia and lymphoma, this therapy has faced challenges in treating solid tumors and invasive central nervous system malignancies, such as malignant gliomas.[2] Clinical responses are dependent on the localization and persistence of transferred T cells to areas of invasive tumor growth, in addition to inconsistencies due to variation in cell source and preparation, and route of administration. However, many fundamental questions regarding the *in vivo* biodistribution of cell therapies remain unanswered. Non-invasive and longitudinal biomedical imaging has the potential to answer these questions and improve the safety and success of cell therapies.[3] Magnetic Particle Imaging (MPI) is a biomedical imaging technology that enables the non-invasive visualization of the distribution of biocompatible superparamagnetic iron oxide (SPIO) tracers.[4, 5] MPI has been used for proof-of-principle studies to track cells such as macrophages, stem cells, dendritic cells, cancer cells, and T cells. While results are promising in terms of labeling and cell tracking using MPI, most past work has been performed using commercial tracers not tailored for MPI in terms of sensitivity and resolution. In this work we report the use of a new MPI tracer, RL-1, synthesized through thermal decomposition with molecular oxygen.[6] RL-1 tracer is 3 times better in MPI signal per iron mass compared to commercial tracer ferucarbotran. RL-1 particles were coated using poly(maleic anhydride-*alt*-1-octadecene) (C_{18}-P, PMAO). PMAO was used to grant colloidal stability to the SPIOs in water by covering the hydrophobic oleic acid coating on the SPIO with an amphiphilic polymeric shell.[7] PMAO coating provides a negative surface due to the hydrolyzed carboxylic groups formed by the ring-opening of the maleic anhydrides, and it can therefore be used for *ex vivo* cell labeling. RL-1 PMAO coated MPI tracers were evaluated for the *ex vivo* labeling of tumor-specific T cells. Different labeling strategies provided different degrees of labeling with the MPI tracer, without affecting their viability, phenotype, or cytotoxic function. We were able to detect at least 5,000 T cells labeled with RL-1 PMAO tracer, showing a remarkable 10x improvement compared with T cells labeled using commercial unoptimized tracer ferucarbotran. Nanoparticle fate after labeling with RL-1 was evaluated *in vitro*, providing insights on particle dilution, exocytosis, or degradation. Also, we evaluated the long-term accumulation and exposure of free-SPIOs and labeled T cells in mice, and their effect on complete blood count and chemistry panels for liver toxicity. The therapeutic efficacy of labeled T cells was assessed in two mouse models of melanoma, B16F10 OVA and $B16_{KVP}/^{Db}$, demonstrating that therapeutic efficacy of T cells is not affected by the nanoparticle labeling. While *in vivo* MPI signal was not observed in the tumor, MPI signal was detected in the tumor *ex vivo* for labeled T cells but not for free-SPIO control group. These results suggest that particle resolution

and large liver signal are challenges to *in vivo* T cell tracking to the tumor, and further particle optimization is needed. Despite these limitations, our results suggest that MPI is an attractive approach to study both *in vitro* and *in vivo* fate of SPIO tracers and that labeling T cells with SPIO do not affect their *in vivo* therapeutic efficacy.

Reference

1. Phan, G.Q. and S.A. Rosenberg, Adoptive cell transfer for patients with metastatic melanoma: the potential and promise of cancer immunotherapy. Cancer Control, 2013. 20(4): p. 289-97.
2. Rivera-Rodriguez, A., et al., Tracking adoptive T cell immunotherapy using magnetic particle imaging. Nanotheranostics, 2021. 5(4): p. 431-444.
3. Sehl, O.C., et al., A Perspective on Cell Tracking with Magnetic Particle Imaging. Tomography, 2020. 6(4): p. 315-324.
4. Gleich, B. and J. Weizenecker, Tomographic imaging using the nonlinear response of magnetic particles. Nature, 2005. 435(7046): p. 1214-7.
5. Zhou, X.Y., et al., Magnetic particle imaging for radiation-free, sensitive and high-contrast vascular imaging and cell tracking. Curr Opin Chem Biol, 2018. 45: p. 131-138.
6. Liu, S., et al., Long circulating tracer tailored for magnetic particle imaging. Nanotheranostics, 2021. 5(3): p. 348-361.
7. Di Corato, R., et al., Water solubilization of hydrophobic nanocrystals by means of poly(maleic anhydride-alt-1-octadecene). Journal of Materials Chemistry, 2008. 18(17): p. 1991-1996.

Poster Presentation

Disclosures: The authors have disclosed no financial interest.

484-Targeted PET imaging detects CCR2 and FAP in cardiac injury mouse models to visualize the inflammation-fibrosis axis

Presenter: Gyu Seong Heo, Washington University School of Medicine

Gyu Seong Heo[1], Junedh M. Amrute[2], Hannah P. Luehmann[3], James Thackeray[3], Frank M. Bengel[4], Robert Gropler[5], Kory Lavine[2], Yongjian Liu[6]

[1]*Washington University School of Medicine, St. Louis*
[2]*Washington University School of Medicine, St. Louis, MO*
[3]*Washington University School of Medicine, St. Louis, Missouri*
[4]*Hannover Medical School, Hannover, N/A, Germany*
[5]*Washington University in St. Louis, Saint Louis, MO*
[6]*Washington University in St. Louis, St. Louis, Missouri*

Objectives:
Inflammation and fibrosis are essential for tissue repair after cardiac injury. However, excessive and chronic inflammatory and fibrotic reactions contribute to the pathogenesis of adverse left ventricular (LV) remodeling in heart failure. Recent data suggest that the C-C motif chemokine receptor 2 positive (CCR2+) pro-inflammatory monocytes/macrophages and fibroblast activation protein positive (FAP+) fibroblasts play important roles within the inflammation-fibrosis axis in the injured heart. The goal of this study was to determine the sensitivity and specificity of ^{68}Ga-DOTA-ECL1i and ^{68}Ga-FAPi-46 detecting CCR2 and FAP, the two key mechanistic elements for the inflammation-fibrosis axis in mouse cardiac injury models, as well as the dynamic correlation between the heart uptake of the two tracers following the injury and remodeling process. We further assessed the potential of the two radiotracers to detect treatment response after IL-1β neutralizing antibody therapy to modulate inflammation, and correlated tracer uptake with treatment outcome.

Methods:
Dynamic PET/CT scans were performed at 45-60 min post tail vein injection of either CCR2 tracer, ^{68}Ga-DOTA-ECL1i (day 3) or FAP probe, ^{68}Ga-FAPi-46 (day 6 or 7) in two mouse models of cardiac injury including left anterior descending coronary artery (LAD) ligation-induced myocardial infarction (MI) and Angiotensin II/Phenylephrine (AngII/PE) infusion-caused cardiac fibrosis and hypertrophy. IL-1β neutralizing antibody or isotype control antibody were injected a day before osmotic pump implantation and on day 2 and 5 post infusion in the AngII/PE model. The injured hearts were collected on day 7 for histology, immunostaining, RT-PCR and flow cytometry analysis.

Results:

CCR2 PET in MI mice at day 3 post infarction showed significantly higher tracer accumulation in the infarct zone (1.53 ± 0.18 %ID/g, n=4) identified by ^{18}F-FDG PET/CT compared to remote zone (0.94 ± 0.10 %ID/g, $p<0.0001$, n=4) and naïve heart (0.58 ± 0.10 %ID/g, $p<0.0001$, n=4). FAP PET at day 7 displayed intense tracer uptake with a comparable spatial pattern to CCR2 signal at day 3. Quantitative analysis demonstrated significantly higher ^{68}Ga-FAPi-46 uptake in the infarct area (1.92 ± 0.36 %ID/g, n=4) than that in the remote zone (1.34 ± 0.19 %ID/g, $p<0.05$, n=4) and naïve heart (0.47 ± 0.16 %ID/g $p<0.0001$, n=4). Importantly, ^{68}Ga-DOTA-ECL1i signal correlated well with ^{68}Ga-FAPi-46 uptake ($r = 0.70$, $p = 0.03$), suggesting the crosstalk between the two biomarkers in the inflammation-fibrosis axis following heart injury. Consistent with the data obtained in the MI model, the uptake of both CCR2 and FAP tracers were elevated in the hearts of AngII/PE mice compared to sham models. Following IL-1β antibody treatment, cardiac uptake for each tracer decreased compared to isotype control antibody-treated animals, indicating sensitivity of CCR2 and FAP PET to anti-inflammatory therapy and subsequent modulation of fibroblast activation. Tissue characterization validated the upregulation of CCR2 and FAP in the injured hearts, which was further confirmed by RT-PCR and flow cytometry. The treatment efficiency of IL-1β was confirmed by reductions in myocardial fibrosis.

Conclusions:
Both CCR2- and FAP-targeted PET imaging showed sensitive and specific detection of inflammation and fibrosis, respectively in murine cardiac injury models. The correlation between CCR2 and FAP signals suggests interaction of these cell types in cardiac injury responses. Moreover, the application of these imaging approaches permits the detection of modulation of the inflammation-fibrosis axis by IL-1β inhibition to mitigate cardiac injury suggesting these targeted molecular imaging could not only provide patient selection method for immunomodulatory therapy, but also monitor their treatment response.

Poster Presentation

Disclosures: The authors would like to disclose that 68Ga-FAPI-46 is an investigational device.

485-Maximization of cucurbit[6]uril hyperpolarized chemical exchange saturation transfer with saturation pre-pulse train optimization at 3 T clinical MRI

Presenter: Vira Grynko, Lakehead University

Vira Grynko[1], Yurii Shepelytskyi[2], Tao Li[3], Hannah Aalto[4], Iulian Ruset[5], Mitchell S. Albert[2]

[1]*Lakehead University, Thunder Bay*
[2]*Lakehead University, Thunder Bay, Ontario*
[3]*Thunder Bay Regional Health Research Institute, Thunder Bay, Ontario*
[4]*Lakehead University*
[5]*Durham, New Hampshire*

Introduction:
Hyperpolarized (HP) chemical exchange saturation transfer (HyperCEST) MRI molecular imaging allows combining the spatial resolution of MRI with a PET-like sensitivity[1,2]. The HyperCEST effect was explored with numerous macrocycles[3–7]. Recently, cucurbit[6]uril (CB6) has been utilized for in vivo HyperCEST imaging[2,8]. Although in vivo CB6 biodistribution imaging was performed at 3.0T[2] and 9.4 T[8], imaging pulse sequence optimization was not performed for maximization of the observed HyperCEST effect. In this work, we demonstrated HyperCEST effect maximization in various concentrations of CB6 solutions in PBS by utilizing different saturation radiofrequency (RF) pulse trains and the lowest detectability limit of CB6 at 3.0T in a clinical whole-body MRI scanner.

Methods:
The present study was conducted with naturally abundant ^{129}Xe polarized up to 56% using a XeBox-10E polarizer (Xemed LCC, USA). CB6 samples in phosphate-buffered saline (PBS) (pH 7.4) of various concentrations (1mM, 0.4mM, 0.25mM, 0.1mM, 25uM, and 10uM) were placed into glass fritted vessel. Spectroscopic measurements were performed using a clinical Philips Achieva 3.0T MRI scanner with a custom-made quadrature RF coil. HyperCEST depletion spectra were acquired during continuous bubbling of the HP ^{129}Xe gas through the CB6 solution in the glass phantom. Four different RF saturation pre-pulse trains were used for HyperCEST spectroscopy: 3-lobe sinc (3LS) pulses, sinusoidal pulses, block pulses, and hyperbolic secant (hypsec) pulses. The overall saturation duration of 480ms was constant for all pulses. The 3LS, sine, and block trains consisted of 16 individual pulses of 30ms duration, whereas hypsec pulse train had 12 individual pulses 40ms each. The range of flip angles (FA) from 90° to 1800° was tested for each saturation pulses. The resonance frequency of HP ^{129}Xe dissolved in the solutions was set a 0ppm. The frequency range for 3LS saturation pulse pulse was set from -149 to 50ppm with a step of 3ppm. Sinusoidal and block pulses were applied in the same range with a step of 2ppm. Hypsec saturation pulses had a step of 12ppm and were applied from -144ppm to 50ppm. Dynamic HyperCEST spectroscopy was performed using the following parameters: TR/TE=10s/0.25ms, receiver bandwidth (BW)=32kHz, 2048 sampling points. Data was initially processed in MATLAB 2021b (MathWorks, USA) and further postprocessed in OriginPro 2021b (OriginLab Corp, USA).

Results and Discussion:
The HyperCEST depletion spectra of CB6 after application of sinusoidal depolarization pulses of various angles are shown in Fig.1A. The HyperCEST depletion occurred at the known resonance frequency of HP ^{129}Xe encapsulated in CB6 (-70ppm). Increasing FA for the 16x30ms sinusoidal pre-pulse from 540° to 1200° boosted HyperCEST effect up to 96%. The HyperCEST effect of four different pre-pulse trains with a FA of 1200° for 1mM CB6 is demonstrated on Fig.1B. The results were close for all pulse trains (98% depletion) except the hypsec pulse, which showed a depletion of 92%.
HyperCEST depletion at various FA is illustrated for 3LS, sine, block and hypsec pulses on Fig.1C. A maximum depletion of 98% was reached at 800° FA for the 3LS pulse, while the sine, block and hypsec pulses demonstrated the highest HyperCEST effect at FA higher than 1200°. Changes in the HyperCEST effect with varying CB6 concentrations are shown in Fig.1D. The efficiency of 3LS pulses was the highest over the whole range of concentrations.
Overall, the HyperCEST detection limit for conventional 3LS saturation pulses was found to be 0.025mM, which is 10 times lower than previously was reported[9]. Flip angle adjustment allowed maximization of the HyperCEST effect for CB6 molecules.

Acknowledgements: This study was funded by an NSERC Discovery grant (RGPIN-2017-05359). YS was supported by a MITACS Elevate postdoctoral fellowship (IT25574). VG was supported by an Ontario Trillium Scholarship.

Reference
1. Schroder L, Lowery TJ, Hilty C, Wemmer DE, Pines A. Molecular Imaging Using a Targeted Magnetic Resonance Hyperpolarized Biosensor. Science (80). 2006;314(5798):446-449. doi:10.1126/science.1131847
2. Hane FT, Li T, Smylie P, et al. In vivo detection of cucurbit[6]uril, a hyperpolarized xenon contrast agent for a xenon magnetic resonance imaging biosensor. Sci Rep. 2017;(3):41027. doi:10.1038/srep41027
3. Hane FTFT, Fernando A, Prete BRJBRJ, et al. Cyclodextrin-Based Pseudorotaxanes: Easily Conjugatable Scaffolds for Synthesizing Hyperpolarized Xenon-129 Magnetic Resonance Imaging Agents. ACS Omega. 2018;3(1):677-681. doi:10.1021/acsomega.7b01744
4. Fernando PUAI, Shepelytskyi Y, Cesana PT, et al. Decacationic pillar[5]arene: A new scaffold for the development of 129Xe MRI imaging agents. ACS Omega. 2020;5(43):27783-27788. doi:10.1021/acsomega.0c02565
5. Hill PA, Wei Q, Eckenhoff RG, Dmochowski IJ. Thermodynamics of xenon binding to cryptophane in water and human plasma. J Am Chem Soc. 2007. doi:10.1021/ja072965p
6. Schnurr M, Joseph R, Naugolny-Keisar A, et al. High Exchange Rate Complexes of 129 Xe with Water-Soluble Pillar[5]arenes for Adjustable Magnetization Transfer MRI. ChemPhysChem. 2018;20(2):246-251. doi:10.1002/cphc.201800618
7. Du K, Zemerov SD, Hurtado Parra S, Kikkawa JM, Dmochowski IJ. Paramagnetic Organocobalt Capsule Revealing Xenon Host-Guest Chemistry. Inorg Chem. 2020;59(19):13831-13844. doi:10.1021/acs.inorgchem.9b03634
8. McHugh CT, Kelley M, Bryden NJ, Branca RT. In vivo hyperCEST imaging: Experimental considerations for a reliable contrast. Magn Reson Med. 2021;(August):1-10. doi:10.1002/mrm.29032
9. Hane FT, Smylie PS, Li T, et al. HyperCEST detection of cucurbit[6]uril in whole blood using an ultrashort saturation Pre-pulse train. Contrast Media Mol Imaging. 2016;11(4):285-290. doi:10.1002/cmmi.1690

Poster Presentation

Disclosures: The authors have disclosed no financial interest.

486-FDG-PET/CT investigation of the pathology of a SARS-CoV-2 VSV pseudotype and its role as an oncological imaging confounder

Presenter: Brianna Kelly, Dalhousie University

Brianna C. Kelly[1], Drew DeBay[2], Christa Davis[3], Matthew Strugari[4], Bassel Dawod[5], Christopher Richardson[6], Kimberly Brewer[7]

[1]*Dalhousie University, Halifax, NS*
[2]*Cubresa Inc., Halifax, Nova Scotia*

[3]IWK Health Centre, Halifax, Nova Scotia
[4]Biomedical Translational Imaging Centre (BIOTIC), Halifax, NS
[5]Biomedical Translational Imaging Centre (BIOTIC), Halifax, Nova Scotia
[6]Dalhousie University, Halifax, Nova Scotia
[7]Dalhousie University, Halifax

Introduction:
The ongoing pandemic caused by SARS-CoV-2 has resulted in over 500 million cases and 6 million deaths as of May 1st, 2022[1]. While significant progress has been made, there are still several unknowns regarding the pathology of COVID-19, particularly with the constant emergence of variants. Furthermore, the SNMMI (Society of Nuclear Medicine and Molecular Imaging) has reported that omicron is a major confounder of cancer diagnostics that use fluorodeoxyglucose positron emission tomography (FDG-PET) by mimicking FDG uptake seen in malignant cells to a greater extent than previous variants[2]. Infectious diseases also cause an increase in FDG uptake due to inflammatory processes needing high energy[3,4]. There is a critical need for research into how COVID-19 impacts the body and how this could interfere with routine medical imaging. While FDG-PET/CT has been used clinically to assess COVID-19 infection on a case-by-case basis, this is one of the first uses of the technique in preclinical research into the pathology and features of COVID-19 disease. This study uses FDG-PET/CT imaging of a GFP + vesicular stomatitis virus (VSV) pseudotype (VSVΔG S) expressing the spike (S) protein from SARS-CoV-2 to assess infection in a containment level (CL-2) environment.

Methods:
K18 hACE2 mice in a C57BL/6 background obtained from Jackson Laboratories were used for this study. The mice were split into four groups; naïve control, mock infection (saline), low titre infection ($5X10^4$PFU), and high titre infection ($1X10^5$ PFU). Infection was performed using intranasal instillation of 30μL concentration virus or saline carrier (mock infection) to mimic the human route of infection better. Mice were imaged on days 4, 11, 18, 25, and 32 post-infection. On scan days, each mouse received 500μCi injections of FDG 30 minutes before scans. Scans were done using the Cubresa NuPET BIO and a Trefoil CT run at 70Kvh and magnification 1.36. At termination, a complete organ harvest was performed on all mice, and biological assays were performed to investigate levels of VSVΔG S and various immune cells in different tissues.

Results:
Levels of GFP in different organ homogenates were compared as a marker of infection level, with the spleen and the lymph nodes indicating significantly higher GFP in the infected groups (Supp data). This suggests that GFP is a valid marker of infection with VSVΔG S. In both infected groups, there was also increased FDG concentration in the heart, kidneys, lungs, and brain compared to the control groups (Figure 1). This suggests a robust inflammatory response following infection with VSVΔG S. Flow cytometry was used to investigate the immune cell populations in several organs. In particular, the lungs and lymph nodes showed increased levels of granulocytes in infected groups. Neutrophils have previously been linked to increased FDG uptake, corresponding to the increase observed in the lungs[5,6]. There were also higher CD4+ T cells in the spleen, lymph nodes, blood, and lungs in infected groups.

Conclusions:
Notably, the organs found that show FDG increases are also those reported previously to be targeted by SARS-CoV-2. The presence of high levels of neutrophils also supports an inflammatory mediated cause of increased FDG. Increased levels of CD4+ T cells could be either inflammatory or regulatory, with further studies planned to characterize them. This data focuses on the original spike protein from SARS-CoV-2, but the omicron, delta, and alpha spikes will also be tested to determine the unique features of each variant. Finally, these data represent a critical first step in the validation of VSVΔG S as a CL-2 model of SARS-CoV-2.

Reference
1. WHO. WHO Coronavirus (COVID-19) Dashboard. https://covid19.who.int/ (2022).
2. Morton, W. SNMMI warns of omicron's impact on PET/CT scans. (2022).
3. Mochizuki, T. et al. FDG Uptake and Glucose Transporter Subtype Expressions in Experimental Tumor and Inflammation Models. J. Nucl. Med. 42, 1551 LP – 1555 (2001).
4. Love, C., Tomas, M. B., Tronco, G. G. & Palestro, C. J. FDG PET of Infection and Inflammation. RadioGraphics 25, 1357–1368 (2005).
5. Rodrigues, R. S. et al. 18 F-fluoro-2-deoxyglucose PET informs neutrophil accumulation and activation in lipopolysaccharide-induced acute lung injury. Nucl. Med. Biol. 48, 52–62 (2017).
6. Eibschutz, L. S. et al. FDG-PET/CT of COVID-19 and Other Lung Infections. Semin. Nucl. Med. 52, 61–70 (2022).

Poster Presentation

Disclosures: The authors have disclosed no financial interest.

487-Does engineering the membranes of NIR-activable photodynamic liposomes affect their functionality in orthotopic head and neck cancer?

Presenter: Nimit Shah, University of Texas at Dallas

Nimit Shah[1], Mina Guirguis[2], Chanda Bhandari[3], Junjie Li[4], Menitte Eroy[5], Ryan Margolis[4], Kenneth Hoyt[6], Tayyaba Hasan[7], Girgis Obaid[3]

[1]University of Texas at Dallas, Dallas, TX
[2]University of Texas at Dallas, Richardson, Texas
[3]University of Texas at Dallas, Richardson
[4]University of Texas at Dallas
[5]University of Texas at Dallas, Dallas, Texas
[6]University of Texas at Dallas, Richardson, TX
[7]Massachusetts General Hospital

Photosensitizer-lipid conjugates with liposomal formulations have emerged as more stable platforms for photodynamic-based cancer therapies. They have been shown to increase the integrity of the construct with exceptional optical, phototherapeutic and photochemical properties. In this study we explored the functional impact of liposomes with two different membrane composition. Two different compositions include liposomes containing lipid conjugates of the clinically approved photosensitizer benzoporphyrin derivative (lipo-BPD) and liposomes containing lipid conjugates the clinically tested photosensitizer IRDye 700DX (lipo-IRDye 700DX). Computational predictions helped confirm the membrane inserting confirmation for lipo-BPD and the membrane protruding conformation for lipo-IRDye700DX. Results indicated that the lipo-IRDye 700DX have superior photochemical properties, such as high reactive molecular species generation and higher fluorescence intensity when compared to lipo-BPD. The lipo-IRDye 700DX was 5 times more efficient in comparison to lipo-BPD in generating reactive molecular species. It also showed 12 times faster burst release of the agents entrapped within when photoactivated.

While lipo-BPD showed a sustained release when photoactivated using a 690 nm wavelength of light, also it exhibited 10 times higher phototoxicity in FaDu (human head and neck) cancer cells. Lipo-BPD also demonstrated 7.16 times greater tumor selective delivery compared to lipo-IRDye700 DX in an orthotopic mouse model of FaDu head and neck tumors. This suggests that a greater emphasis on the membrane composition is critical when engineering and designing light-activable liposomes, as composition evidently results in unprecedented effects on their functionality and therapeutic indices.

Reference

1. Guirguis,M., Bhandari, C., Li, J., Eroy, M., Prajapati, S., Margolis, R., Shrivastava, N., Hoyt, K., Hasan, T. & Obaid, G. (2021). Membrane composition is a functional determinant of NIR-activable liposomes in orthotopic head and neck cancer. Nanophotonics, 10(12), 3169-3185. http://doi.org/10/1515/nanoph-2021-0191

Poster Presentation

Disclosures: The authors have disclosed no financial interest.

488-Preclinical Development of 89Zr-DFO-Isatuximab as a Novel ImmunoPET Tracer for CD38-targeted Imaging of Multiple Myeloma and Other Hematological Malignancies

Presenter: Natalia Herrero Alvarez, Memorial Sloan Kettering Cancer Center

Natalia Herrero Alvarez[1], Tara D. Viray[2], Alexa Michel[3], Jason Lewis[4]

[1]*Memorial Sloan Kettering Cancer Center*
[2]*Memorial Sloan Kettering Cancer Center, North Brunswick, NJ*
[3]*Memorial Sloan Kettering Cancer Center, Mount Vernon, NY*
[4]*Memorial Sloan Kettering Cancer Center, New York, NY*

Introduction:

Multiple myeloma (MM) represents the second most prevalent hematological malignancy, accounting for 1% of all cancers and 13% of hematological tumors, and the most common primary tumor of the skeleton. [1] Disease almost always evolves from a premalignant precursor condition which then develops into asymptomatic or smoldering myeloma (SMM). Despite the availability of new therapeutic approaches, MM remains incurable and prognosis depends on a clinician's ability to monitor disease progression and assess treatment efficacy. Applying an optimized methodology to the clinic will lead to greater personalization in treatment plans, thereby improving response rates and survival. [2] Thus, a sensitive method of detecting, localizing, and measuring tumor burden is urgently needed. Targeted PET imaging is a powerful imaging tool for these unmet clinical needs, as a noninvasive means to determine tumor burden, monitor treatment response and rule out minimal residual disease (MRD). Among recently discovered therapeutic targets, CD38 has proven an excellent biomarker due to its high expression in aberrant lymphoid and myeloid cells relative to normal cell populations.[3] Furthemore, CD38 is currently being evaluated as a potential therapeutic target for certain solid cancers. [4] We aim to rationally develop and validate new agents for CD38-directed PET imaging of MM and extend them to other CD38-positive hematological malignancies, including lymphomas. We have recently reported the synthesis, preclinical evaluation, and first-in-human clinical translation of 89Zr-DFO-daratumumab for the noninvasive CD38-targeted imaging of MM.[5] Isatuximab is the latest FDA-approved CD38-targeting antibody. This work is to study the potential of 89Zr-labeled Isatuximab as a tracer for CD38 immunoPET imaging and whether it would be a suitable alternative and/or counterpart to daratumumab as very distinct mechanisms of action and binding modes have been reported between these two mAbs. Here, we present its radiolabeling and the results of its in vitro and in vivo evaluation in two murine models of hematoligical disease. Finally, a preliminary in vitro evaluation of our tracer targeting in a solid cancer model is included.

Methods:

Conjugation of DFO-chelator to isatuximab was followed by zirconium-89 radiolabeling. Binding potential of newly 89Zr-DFO-isatuximab was firstly quantified using our optimized magnetic bead assay and further evaluated through more detailed cellular assays. In vitro stability was determined in PBS and human serum over 144h. MM1S and Daudi cell lines were selected for in vitro and in vivo evaluation. NSG mice were subcutaneously xenografted or intravenously injected for the disseminated model of disease. Tumor burden was monitored by bioluminescent imaging. Healthy animals were used as a control. Small PET imaging with [89Zr]Zr-DFO-isatuximab (7.4 MBq/mouse) was conducted on an Inveon microPET/CT instrument. 89Zr-DFO-daratumumab was evaluated in parallel for direct comparison. Biodistribution studies were conducted by sacrificing mice at discrete time points. Accumulation of the tracer in the bone lesions was further confirmed by autoradiography imaging. Ex vivo flow cytometry of the bone marrows was used to verify CD38 expresion in diseased animals.

Results:

89Zr-DFO-isatuximab was produced with high specific activity (0.37 MBq/μmol), radiochemical yield (>90%), and purity (>99%). In vitro studies confirmed the binding potential and the high stability of the tracer. In vivo imaging demonstrated extraordinary contrast and uptake in tumor lesions for both MM and lymphoma models. Specificity was assessed both in blocking studies and in a healthy cohort. Time-course biodistribution confirmed the progresive increase of 89Zr-DFO-isatuximab in leg stime-course biodistributon study confirmed the progresive increase of 89Zr-DFO-Isatuximab uptake in bone marrow and squeleton which reached the maximum at 120h. Our data suggested 89Zr-DFO-isatuximab performs just as well as, or better than, 89Zr-DFO-daratumumab.

Conclusions:

These findings show the excelent potential of 89Zr-DFO-isatuximab as a selective immunoPET agent for sensitive detection of MM and lymphoma lesions, and therefore, the possibility to further develop a platform for targeted radiotherapy.

Reference

1. Siegel, R.L., K.D. Miller, and A. Jemal, Cancer statistics, 2016. CA: A Cancer Journal for Clinicians, 2016. 66(1): p. 7-30.
2. Ulaner, G.A. and C.O. Landgren, Current and potential applications of positron emission tomography for multiple myeloma and plasma cell disorders. Best Practice & Research Clinical Haematology, 2020. 33(1): p. 101148-101148.
3. Van De Donk, N.W.C.J. and S.Z. Usmani, CD38 antibodies in multiple myeloma: Mechanisms of action and modes of resistance. Frontiers in Immunology, 2018. 9(SEP): p. 1-12.
4. ing Jiao, Ming Yi, Linping Xu, Qian Chu, Yongxiang Yan, Suxia Luo & Kongming Wu (2020) CD38: targeted therapy in multiple myeloma and therapeutic potential for solid cancers, Expert Opinion on Investigational Drugs, 29:11, 1295-1308
5. Ulaner, G.A., et al., CD38-targeted Immuno-PET of Multiple Myeloma: From Xenograft Models to First-in-Human Imaging. Radiology, 2020. 295(3): p. 606-61.

Poster Presentation

Disclosures: The authors have disclosed no financial interest.

489-PET imaging of Aspergillus fumigatus infection using 89Zr labeled anti-laminarin antibody Fab fragments

Presenter: Swati Shah, National Institutes of Health

Swati Shah[1], Jianhao Lai[2], Eyob Alemu[3], Neysha Martinez Orengo[4], Maya Lara[3], Anna P. Lyndaker[3], Alan Kim[3], Cynthia Kim[3], Falguni Basuli[4], Jianfeng Shi[3], Dima A. Hammoud[4]

[1]*National Institutes of Health, Bethesda*
[2]*National Institutes of Health, MD*
[3]*National Institutes of Health*
[4]*National Institutes of Health, Bethesda, MD*

Background:
Despite increasing mortality and morbidity associated with invasive fungal infections, especially those caused by *Aspergillus fumigatus* (AF), timely and accurate diagnosis remains challenging. The fungal cell wall contains distinctive layers of glycoproteins and polysaccharides such as glucans and chitin, which can serve as unique identifiers of fungal infection within the host system[1]. Antibodies that can bind with high specificity and affinity to various fungal cell wall components could be radiolabeled for the development of potential PET ligands. Full antibodies however have significant drawbacks such as long circulation times, slow clearance from the liver and high background signal. Antibody fragments, on the other hand, retain the desirable high binding characteristics of full antibodies but possess favorable pharmacokinetics for imaging[2]. In this study, Zirconium-89 (^{89}Zr) labeled Fab fragments generated from a full antibody against laminarin (a soluble form of β-1,3 glucan) and an isotype control were evaluated in mouse models of AF infection.

Methods:
The Fab fragments were generated by digesting a commercially available rabbit anti-laminarin antibody (Biorbyt #orb421066) and the isotype antibody using a Fab preparation kit and their purity was assessed by SDS PAGE. The affinity of the specific Fab fragment binding to laminarin was measured by biolayer interferometry (BLI) assay on an Octet K2 system. Two aspergillus infection models were used for PET imaging: (1) thigh myositis infection established by intramuscular (IM) inoculation of live or heat-killed (HK) AF spores (2) pulmonary infection induced by post-pharyngeal (PP) aspiration of AF spores. Additionally, two sterile inflammation models were developed, by IM injection of 150ug LPS in the thigh and by repeated PP aspiration of 200ug polyinosinic:polycytidylic acid (poly (I:C)) into the lungs of CD-1 mice. ^{89}Zr labeled anti-laminarin or isotype control Fab fragments were intravenously injected into untreated, AF infected, or mice with sterile inflammation, followed by PET/CT at 6 and 24 hours post-injection. Biodistribution was performed after the final scan at 24 hours. Confirmation of fungal infection in infected mice was provided by GMS staining of the tissues.

Results:
BLI assay demonstrated that anti-laminarin Fab fragments bound to laminarin with a $K_d = 22$ nM. The labeled full anti-laminarin and isotype antibodies accumulated similarly in areas of fungal and sterile myositis suggesting leakage due to increased endothelial permeability rather than actual binding. On the other hand, PET imaging of the myositis mice showed significantly higher accumulation of the laminarin Fab ligand in the thigh muscle with live AF when compared to LPS inoculation at both 6 and 24 hours (%ID/g at 24 hours: 0.99±0.19 vs. 0.67±0.21, P = 0.037) while there was little to no retention of the isotype fragments (%ID/g at 24h: 0.41±0.04, P = 0.0001). Similarly, in the pneumonia models, higher uptake of laminarin Fab was seen in lung consolidations of the infected mice compared to that of poly (I:C) treated mice or uninfected controls up to 24 hours. Low binding of the isotype fragments in the AF models indicated that the PET signal in the live aspergillus was due to specific binding of the laminarin Fab to the fungal wall. Biodistribution studies were consistent with the PET results.

Conclusions:
We have shown that ^{89}Zr labeled specific anti-laminarin Fab fragments bind specifically to Aspergillus in both the myositis and pneumonia models when compared to uninfected controls and sterile inflammation models, and when compared to isotype Fab, suggesting that this tracer is a promising candidate for the detection of Aspergillus and possibly other fungal pathogens. This study also provides evidence that targeting other fungal cell wall components could yield additional markers for PET imaging, thereby improving the diagnostic capabilities of deep-seated fungal infections.

Reference
1. Gow, N.A.R.; Latge, J.P.; Munro, C.A. The Fungal Cell Wall: Structure, Biosynthesis, and Function. Microbiol Spectr 2017, 5, doi:10.1128/microbiolspec.FUNK-0035-2016.
2. Fu, R.; Carroll, L.; Yahioglu, G.; Aboagye, E.O.; Miller, P.W. Antibody Fragment and Affibody ImmunoPET Imaging Agents: Radiolabelling Strategies and Applications. ChemMedChem 2018, 13, 2466-2478, doi:10.1002/cmdc.201800624.

Poster Presentation

Disclosures: The authors have disclosed no financial interest.

490-Contrast Enhanced Ultrasound Imaging of Ovarian Cancer

Presenter: Marie-France Penet, Johns Hopkins University School of Medicine

Marie-France Penet[1], Saoirse Teevan-Kamhawi[2], Sean Wood[2], Meiyappan Solaiyappan[3], Balaji Krishnamachary[1], Santosh Yadav[4], Dmitri Artemov, Alexander L. Klibanov[5]

[1]*Johns Hopkins University School of Medicine, Baltimore, MD*
[2]*University of Virginia*
[3]*Johns Hopkins University School of Medicine, Baltimore, Maryland*
[4]*Johns Hopkins University School of Medicine*
[5]*University of Virginia, Charlottesville, VA*

Introduction:
There is a need for discovery of new and robust methods that will facilitate ovarian cancer early detection. Currently, there is no clear recommendation for ovarian cancer screening in an asymptomatic population. Multiple large-scale studies have failed to demonstrate adequate sensitivity and specificity for non-contrast transvaginal ultrasound (TVUS) to warrant its use in screening for ovarian cancer. Targeted contrast enhanced ultrasound (TCEUS) can provide functional information at the cellular and molecular levels that could improve cancer early detection. Folate receptor (FR), that is overexpressed in 90% of ovarian cancer will be targeted here. Microbubbles (MBs), typically used as ultrasound (US) contrast agent, are confined within the vasculature due

to their large diameter. Nanobubbles (NBs), characterized by a smaller diameter, can extravasate into the tumor, while still being visible with US, with modest backscatter, allowing targeting tumor cell surface biomarkers by direct contact. Acoustic signal of the NBs accumulating in the tumor could be improved by inflating them with sequential administration of nanodroplets (NDs) (1). Our goal is to develop an efficient contrast agent for ovarian cancer detection, easily translatable to the clinic.

Methods:
FR-targeted and non-targeted gas-filled micro- and nanobubbles were prepared from perfluorobutane by amalgamation of the aqueous medium that contained micellar distearoylphosphatidylcholine (DSPC), polyethylene glycol (PEG) stearate and (in case of targeted particles) folate-PEG-DSPE. Targeted and non-targeted liposomes were prepared by nuclepore filtration from DSPC, cholesterol, folate-PEG-DSPE (omitted in control) and DiI dye. Untargeted perfluoro-15-crown-5 NDs (20% v/v, ~250 nm diameter) were prepared by probe sonication in the aqueous medium that contained DSPC and PEG2000-DSPE (2:1 mass ratio). Two different orthotopic ovarian cancer models were used. OVCAR3 and IGROV1 tumors were implanted in nude female mice by performing a microsurgical implantation of a small tumor tissue within the ovary. US imaging was performed using a Siemens Acuson Sequoia C512 system equipped with a 15L8 probe operated in CPS mode. MRI data were acquired using a 7T preclinical MR instrument with a 75/40 mm $^{1}H/^{19}F$ volume coil. After imaging, mice were euthanized, tumors were excised and fixed in formalin for histology. H&E, CD31 and FR staining were done on 5um thick slices following standard protocols.

Results:
Efficacy of FR targeting was assessed in vitro using folate-decorated liposomes incubated with IGROV1 cells and confirmed by fluorescence spectroscopy; folate-mediated binding exceeded binding of control liposomes by an order of magnitude. In vivo US contrast signal could be detected in OVCAR3 and IGROV1 orthotopic tumors for both FR-targeted and untargeted bubbles. Representative images obtained in both tumor types at different time points are shown in Figure 1. Heterogeneity in tumor uptake has been observed and could be related to differences in tumor vasculature and presence of necrosis. Delivery of fluorinated NDs was assessed by ^{19}F MRI after i.v. injection in orthotopic IGROV1 tumor-bearing mice. At 1h post-injection, ^{19}F MR signals could be detected mostly in the blood, with traces present in the liver. At 4h and 24h post-injection, most of the signal was located in the liver. No signal was detected in the tumor *in vivo* and *ex vivo*. As it could be due to the low sensitivity of MR detection, fluorescent probes will be added to the next formulation to assess the delivery by optical imaging. IHC staining confirmed differences in vasculature and folate receptor of both tumor types.

Discussion:
We aim to improve US sensitivity and specificity of cancer detection by developing a novel combination of targeted NBs and liquid fluorocarbon NDs, that will act in concert, to increase acoustic response. Our ongoing studies are an important step towards improving the sensitivity and specificity for early detection of ovarian cancer that could also be used for screening in high-risk women.

Acknowledgement: This work was supported by Hopkins ICTR Nexus and Emerson Collective.

Reference

1. Brambila et al, Langmuir, 2020, 36:2954-65

Poster Presentation

Disclosures: The authors have disclosed no financial interest.

491-Unsupervised machine learning to evaluate therapeutic outcome in ischemic stroke

Presenter: Adrian Mannel, Werner Siemens Imaging Center

Adrian Mannel[1], Kristin Patzwaldt[1], Dhaval Khunt[2], Salvador Castaneda Vega[3]

[1]Werner Siemens Imaging Center, Germany
[2]Werner Siemens Imaging Center, Tuebingen, Baden-Wuerttemberg, Germany
[3]University of Tuebingen, Tuebingen, Baden-Wuerttemberg, Germany

Introduction:
Ischemic stroke (IS) is a devastating disease that claims more than 15 million lives worldwide each year. Identification and localization of lesions is crucial to confirm diagnosis, objectively evaluate clinical trials and plan neuromodulation therapy. It was previously shown that the combination of apparent diffusion coefficient (ADC) and T2-Weighted (T2W) images can be used to successfully segment ischemic strokes in rats using gaussian mixture models (GMM) [1]. Moreover, it was shown that the GMM-segmented stroke volume at 24 h strongly correlates to the histologically verified stroke volumes at 1-week post-stroke. In this study, it was hypothesized that the GMM model can be used to longitudinally detect and measure therapeutic changes in stroke volume over time.

Methods:
IS was induced in rats (n=53) followed by ADC and T2W measurements after 24 h and 1 week using MRI. One group of animals (n=17) was treated bi-daily with Ambroxol for 5 days starting shortly after stroke on-set. The control group (n=36) was treated with vehicle solution. GMM was applied to the 24 h ADC and T2 images and stroke regions were predicted as previously described [1]. Dice similarity coefficient (DSC) was calculated to compare the similarity of the segmentation results to ground truth data (manual regions at 1-week post stroke).

Result:
The stroke volume of both groups showed a significant difference a 24 h and 1 week post-stroke induction ($p < 0.05$) (Fig A). The first row of Figure 1B shows these results in a joint probability map using all animals, where the difference in stroke extension between both groups can be clearly observed. Perfectly consistent with previously published results, the ML-segmentation at 24 h of vehicle-treated stroke animals shows a very high similarity to the 1-week stroke lesion, demonstrating that the 24 h GMM-Workflow indeed predicts final stroke volume. In stark contrast the DSC of Ambroxol-treated animals is greatly affected by the therapy over time, since the volume reduction significantly alters the shape of the predicted region at 1 week (Fig 1C). This is further quantified in the shrinkage of the lesions (from 24 h to 1 week) in Fig 1D.

Discussion:
The findings confirm that this GMM-Workflow can be used to reliable segment stroke lesions. Moreover, the segmentation can be used to detect changes and evaluate therapeutic changes in stroke volume.

Reference

1. Castaneda-Vega, Salvador, et al. "Machine learning identifies stroke features between species." Theranostics 11.6 (2021): 3017.

Poster Presentation

Disclosures: The authors have disclosed no financial interest.

492-Image-guided validation of combining intraarterial infusion with focused ultrasound mediated blood brain barrier disruption

Presenter: Alessandra Ali, Columbia University PET Center

Alessandra Ali[1], Andrei Molotkov[2], Akiva Mintz[3], Cheng-Chia Wu[4]
[1]*Columbia University PET Center, New York, NY*
[2]*Columbia University PET Center, New York, New York*
[3]*Columbia University, New York, New York*
[4]*Columbia University Irving Medical Center (CUIMC), New York, NY*

Purpose:
Glioblastoma (GBM) is the most common malignant primary adult brain tumor with a poor prognosis and median survival of fewer than 2 years[1]. Focused ultrasound (FUS), in conjunction with microbubbles, is an emerging method that can potentially enable drugs to reach the infiltrating GBM cells outside the natural BBB-permeable core. While FUS can increase BBB penetration of systemically administered therapies, significant challenges remain, including low concentration of drug it allows into the brain. We hypothesize that combining FUS with intraarterial (IA) cerebral infusion can significantly enhance drug concentration in the brain while avoiding the non-selective toxicity associated with previous attempts of using IA delivery using non-selective BBB opening (e.g., mannitol).

Material and Methods:
Mouse serum albumin (ALB, MilliporeSigma, MA, USA) was labeled with Cy7 or Cy5.5 nearinfrared (NIR) fluorescent dye according to manufacturer instructions (Lumiprobe, MD, USA). DEFINITYVR microbubbles were prepared according to manufacturer instructions (Lantheus Medical Imaging, Inc., Billerica, MA, USA). FUS was applied to the right cerebral hemisphere of the mouse brain. Localization of the ultrasound beam with the brain was achieved using stereotactic localization of skull landmarks with a brain atlas-guided FUS (RK50, FUS Instruments, Toronto, Canada). Cy7ALB was injected intracarotid through an internal carotid artery catheter. Cy5.5ALB was injected intravenously (IV) to confirm BBB permeabilization. 3D Optical/CT images were acquired using MILabs 3D optical scanner (MILabs, NL) 24 h after Cy7ALB administration.

Results:
We demonstrated that FUS opens BBB for up to 48 hrs. Intracarotid artery injection of Cy7ALB considerably increased ALB concentration in the brain after FUS compared with IV injection after FUS. 3D optical/CT imaging demonstrated precise localization of the IA infused NIR-labeled albumin and confirmed its co-localization with the FUS-targeted BBB disruption.

Conclusion:
Our data using 3D optical/CT after FUS-mediated BBB disruption demonstrated the potential of IA cerebral infusion to increase drug concentration versus standard IV infusion. Thus, molecular imaging with labeled therapeutic candidates can play a valuable role in preclinically validating the potential of combining IA cerebral perfusion with FUS for therapies that do not normally cross the BBB.

Reference
1. Chen, B., Chen, C., Zhang, Y. et al. Recent incidence trend of elderly patients with glioblastoma in the United States, 2000–2017. BMC Cancer 21, 54 (2021). https://doi.org/10.1186/s12885-020-07778-1

Poster Presentation

Disclosures: The authors have disclosed no financial interest.

493-Quantification of hyperpolarized [1-13C]pyruvate-to-[1-13C] lactate flux in two acute myeloid leukemia cell lines with a three-well micro-slab coil

Presenter: Thomas Ruan, Memorial Sloan Kettering Cancer Center

Thomas L. Ruan[1], Geonhui Lee[2], Claudia Wong[2], Kofi Deh[3], Sang-moo Jeong[4], Kayvan Keshari[3]

[1]*Memorial Sloan Kettering Cancer Center*
[2]*Johns Hopkins University, Baltimore, Maryland*
[3]*Memorial Sloan Kettering Cancer Center, New York, NY*
[4]*Johns Hopkins Univeristy, Baltimore, Maryland*

Introduction:
Magnetic resonance spectroscopy (MRS) of hyperpolarized (HP) ^{13}C-enriched molecules has emerged as a powerful technique for quantifying metabolic flux rates in real time[1]. In particular, the generation rate of [1-^{13}C]lactate from HP [1-^{13}C]pyruvate is being investigated as a biomarker for cancer metabolism. In vitro HP MRS experiments typically require a high number of cells (on the order of 10^7), restricting capacity to probe multiple conditions or measure flux in rare or difficult-to-grow cell types. Building on previous work developing miniaturized dual-tuned ^{1}H/^{13}C microcoil detector circuits for sensitive detection of HP [1-^{13}C]pyruvate flux in small volume cell samples[2,3], we have designed a microcoil that allows simultaneous detection of hyperpolarized metabolic fluxes in multiple cell suspension samples.

Methods:
Magnetic field B_Z simulations showed that an elongated micro-solenoid, or micro-slab, design had improved field homogeneity and magnitude compared to a micro-solenoid coil(Figure A). A sample holder with three wells of 50 mL volume each was 3D-printed, then wound with 28-gauge magnetic wire to create a ^{13}C-sensitive transmit/receive coil (Figure B). The microcoil was completed with picofarad-range adjustable capacitors for tuning and matching the circuit. A ^{1}H-sensitive single loop coil was also implemented on the circuit board for sample visualization and shimming. A 1-dimensional chemical shift imaging (CSI) sequence (9 voxels) was used to spatially resolve spectra from the three wells. Spectra were acquired with a dynamic resolution of 1 second, allowing quantification of the HP [1-^{13}C]pyruvate-to-[1-^{13}C]lactate flux rate in units of pmol*sec^{-1}*(10^5 cells)$^{-1}$ (Figure C).

Results:
This novel microcoil platform was used to measure metabolic flux rates in two models of acute myeloid leukemia, MOLM13 and NOMO1. NOMO1 cells were found to generate HP [1-^{13}C]lactate from [1-^{13}C] pyruvate at a faster rate than MOLM13, in agreement with high-field ^{1}H NMR measurements of secreted lactate levels in cell culture

media (Figure D). This increase in HP [1-^{13}C]lactate flux rate may be driven by the ratio of redox cofactors NADH and NAD^+, which is elevated in NOMO1 cells compared to MOLM13 cells. The microcoil device was also used to measure the increase of pyruvate metabolism in MOLM13 cells upon treatment with AB199, a BCL-2 inhibitor which raises the NADH/NAD^+ ratio in MOLM13 cells (Figure E), demonstrating the device's capacity to assay drug response.

Discussion:

We have developed a microcoil that can measure hyperpolarized pyruvate-to-lactate flux rates in multiple cell suspension samples simultaneously. This three-well microcoil can detect differences in pyruvate metabolism between cancer cell lines and upon drug treatment. We are currently using the improvement in throughput given by this platform to more efficiently profile metabolic kinetics of other tumor cell models, including but not limited to protein overexpression and knockdown, and substrate concentration modulation.

Reference

1. Kurhanewicz, et al. Neoplasia, 2018
2. Jeong, et al. Sci Adv, 2017
3. Lees, et al. NMR Biomed, 2020

Poster Presentation

Disclosures: The authors would like to disclose that HP pyruvate is an investigational drug.

494-CC chemokine receptor 2-targeted molecular imaging of inflammatory response associated with immune checkpoint inhibitor in atherosclerosis

Presenter: Lanlan Lou, Washington University in St. Louis

Lanlan Lou[1], Hannah P. Luehmann[2], Lisa Detering[3], Xiaohui Zhang[4], Gyu Seong Heo[5], Josie Lesser[6], Deborah H. Sultan[7], Yongjian Liu[3]

[1]*Washington University in St. Louis*
[2]*Washington University School of Medicine, St. Louis, Missouri*
[3]*Washington University in St. Louis, St. Louis, Missouri*
[4]*Washington University in St. Louis, St. Louis, MO*
[5]*Washington University School of Medicine, St. Louis*
[6]*University of Washington School of Medicine*
[7]*St. Louis, MO*

Background:

Immune checkpoint inhibitors (ICIs) have led to a dramatically improved survival of cancer patients. However, this usage has resulted in increased clinical reports of immune-related adverse events especially in cardiovascular system including myocardial infarctionand ischemic stroke, reasonably due to aggravated atherosclerosis. It is known that macrophages especially CC chemokine receptor 2-positive (CCR2+) proinflammatory macrophages play central roles in the initiation, progression and complication of atherosclerosis. To determine the ICI treatment caused variation of CCR2+ macrophages in atherosclerosis and gain more insight into the mechanism of ICI related adverse effect, we use ^{64}Cu-DOTA-extracellular loop 1 inverso (ECL1i), a radiotracer to track CCR2+ monocytes and macrophages using positron emission tomography (PET) in mouse atherosclerosis models following ICI treatment.

Methods:

^{64}Cu-DOTA-ECL1i PET was used to image CCR2+ monocytes and macrophages in apolipoprotein E knock-out (ApoE$^{-/-}$) and low density lipoprotein receptor knock-out (LDLR$^{-/-}$) atherosclerosis mouse models with wild type C57BL/6 mice as controls. All the ApoE$^{-/-}$ and LDLR$^{-/-}$ mice were fed with high fat diet for 8 weeks and treated with programmed cell death protein 1 (PD1) antibody or isotype control IgG or saline up to 16 weeks. CCR2 PET imaging was performed at 8 and 16 weeks post treatment to track the variation of proinflammatory macrophages following PD1 antibody administration. Histopathology, flow cytometry and real-time polymerase chain reaction (RT-PCR) were performed at each time point to characterize CCR2 variations in the collected aortic sinuses from mice.

Results:

In contrast to wild type mice, both ApoE$^{-/-}$ and LDLR$^{-/-}$ mice revealed significantly elevated ^{64}Cu-DOTA-ECL1i uptake at aortic arches relative to the weak signals acquired with ^{18}F-FDG, demonstrating the superiority and specificity of CCR2 tracer detecting atherosclerotic plaques. In ApoE$^{-/-}$ mice at 8 weeks post PD1 antibody treatment, CCR2 PET (SUV=0.64±0.07, n=6) showed significantly higher signals than that determined in saline (SUV=0.49±0.09, $p<0.01$, n=9) or IgG (SUV=0.43±0.06, $p<0.0001$, n=10) treated ApoE$^{-/-}$ mice. In wild type mice, no difference was observed with or without PD1 antibody treatment after 8 weeks. At 16 weeks post PD1 antibody treatment, the uptake difference between PD1 antibody treated group and control groups were further increased, which further confirmed the PD1 antibody treatment aggravated inflammatory response in atherosclerosis, as well as the time dependence of the treatment effect. Histopathological analysis demonstrated further elevated immune cells infiltration and enlarged plaques in the aortic arches of PD1 antibody treated mice compared to the saline or IgG treated mice. Quantitative immunostaining showed significantly higher expression of CCR2+ cells in PD1 antibody treated ApoE$^{-/-}$ mice compared to control groups, which was further confirmed by flow cytometry and RT-PCR analyses. All these data indicated the adverse inflammatory response associated with PD1 antibody treatment in atherosclerotic mice. Moreover, we performed the same studies in LDLR$^{-/-}$ mice and observed similar results, which further supported our hypothesis.

Conclusion:

Our results demonstrated the potential of ^{64}Cu-DOTA-ECL1i as a targeted molecular imaging probe to detect ICI-induced aggravation of cardiovascular disease in cancer patients.

Poster Presentation

Disclosures: The authors would like to disclose that 68Ga-FAPI-46 is an investigational device.

495-The synthesis and evaluation of a brain penetrant PARP1 tracer [18F]Pamiparib in rodents and nonhuman primates

Presenter: jie tong, Yale University

Jie Tong[1], Baosheng Chen[2], Jiwei Gu[3], Mike (MingQiang) M. Wenn (Zheng)[3], Santosh Reddy Alluri[3], Chao Zheng[2], Daniel Holden[2], Zachary Felchner[3], Li Zhang[2], Michael Kapinos[4], Jim Ropchan[3], Nabeel Nabulsi[5], Richard E. Carson[3], Yiyun H. Huang[3], Jason (Zhengxin) Cai[2]

[1]*Yale University, New Haven*
[2]*Yale School of Medicine, New Haven, CT*
[3]*Yale University, New Haven, CT*
[4]*michael.kapinos@yale.edu, New Haven, CT*
[5]*Yale School of Medicine*

Objectives:
Altered expression of Poly (ADP-ribose) polymerase-1(PARP1), an enzyme that is involved in multiple cellular functions has been pursued as a therapeutic target for many cancers. The development of PARP1 PET tracers that can provide noninvasive approaches to evaluate the PARP1 expression in vivo is expected to support the choice of therapeutics. As a specific PARP inhibitor, Pamiparib has being investigated in phase III clinical trials as a maintenance therapy in platinum-sensitive ovarian cancer and gastric cancer [1]. Here, we report the synthesis, in vitro and in vivo evaluation of [^{18}F]Pamiparib as a brain penetrant PARP PET tracer in mice, rats and non-human primate (NHP).

Methods:
Pamiparib standard and the borate radiolabeling precursor were synthesized according to the reported procedures with minor modification [1, 2]. Briefly, radiosynthesis of [^{18}F]Pamiparib was carried out using one-pot, two-step strategy, i.e., Cu-mediated radiofluorination, followed with acid facilitated cyclization. Stability of [^{18}F]Pamiparib was tested in dose solution and in PBS at 37 °C. Lipophilicity was determined by the shake flask method. Biodistribution was performed in healthy male Balb/c mice at 30 min and 60 min post tracer injection (p.i.). Metabolism of the tracer was evaluated in the rat plasma and brain homogenate at 60 min and 90 min p.i. Self-blocking study was carried out in rats and the brains were collected for ex vivo autoradiography (AR). The binding specificity was also evaluated in the brains samples of mice, rats and nonhuman primate using in vitro AR. Quantitative NHP brain PET was performed to calculate the brain-to-plasma ratio at equilibrium, a.k.a. volume of distribution (V_T).

Results:
[^{18}F]Pamiparib was synthesized with decay-corrected radiochemical yields of 2 ± 1.4%, molar activity of 127 ± 7 GBq/μmol with radiochemical purities of ≥93% (n = 6). [^{18}F]Pamiparib was unstable under alkaline conditions, but relatively stable in both final dose solution (9% of ethanol in 0.9% saline) and in PBS (PH=7.4). Measured LogP value was 2.44 (n = 4). Relatively high uptake of [^{18}F]Pamiparib was found in the spleen (Fig 1. a). Ex vivo autoradiography and metabolism study in rats indicated the brain penetration of [^{18}F]Pamiparib and minimal radio-metabolites in the brain(Fig 1. b, d). [^{18}F]Pamiparib is metabolized slowly in NHP, with parent fraction of 80% at 120 min p.i. (Fig 1. c). The binding of [^{18}F]Pamiparib to PARP1 is specific as the signal is completely blocked in the brain sections of mice, rats and nonhuman primates using the unlabeled Pamiparib (Fig 1. e). The monkey brain time-activity curve fits well with one-tissue compartment model, generating V_T of 3 in the brain, confirming the brain penetration of [^{18}F]Pamiparib, albeit PET images showed mainly peripheral tracer uptake.

Conclusions:
We have synthesized [^{18}F]Pamiparib, and demonstrated its specific binding with PARP-1 in rodent and monkey brain sections and showed a moderate metabolic stability in rat plasma through in ex vivo and in vitro studies. Further investigations of [^{18}F]Pamiparib as a PARP1 PET imaging probe are needed, including in vitro binding assay, and imaging studies in animal models of oncology and neurodegenerative diseases.

Acknowledgments: The authors thank the professional technical support by the Yale PET Center staff.

Reference

1. Wang, H.; Ren, B.; Liu, Y.; Jiang, B.; Guo, Y.; Wei, M.; Luo, L.; Kuang, X.; Qiu, M.; Lv, L.; Xu, H.; Qi, R.; Yan, H.; Xu, D.; Wang, Z.; Huo, C.-X.; Zhu, Y.; Zhao, Y.; Wu, Y.; Qin, Z.; Su, D.; Tang, T.; Wang, F.; Sun, X.; Feng, Y.; Peng, H.; Wang, X.; Gao, Y.; Liu, Y.; Gong, W.; Yu, F.; Liu, X.; Wang, L.; Zhou, C. J. Med. Chem, 2020, 63, 15541-15563.
2. Guibbal, F.; Isenegger, P. G.; Wilson, T. C.; Pacelli, A.; Mahaut, D.; Sap, J. B. I.; Taylor, N. J.; Verhoog, S.; Preshlock, S.; Hueting, R.; Cornelissen, B.; Gouverneur, V. Nature Protocols, 2020, 15, 1525-1541.

Poster Presentation

Disclosures: The authors have disclosed no financial interest.

496-Effects of BRCA2 loss on PSMA expression in Prostate Cancer

Presenter: Teja Muralidhar Kalidindi, Memorial Sloan Kettering Cancer Center

Teja Muralidhar Kalidindi[1], Tullio Esposito[1], Heiko Schoder[1], Rahim Hirani[2], Goutam Chakraborty[2,3], Naga Vara Kishore Pillarsetty[1]

[1]Department of Radiology, Memorial Sloan Kettering Cancer Center
[2]Department of Medicine, Memorial Sloan Kettering Cancer Center
[3]Department of Urology and Center of Excellence for Prostate Cancer, Tisch Cancer Institute, Icahn School of Mount Sinai

Background:
Hemizygous and Homozygous deletion of hallmark DNA damage repair (DDR) protein, *BRCA2* in Prostate cancer (PC) are associated with increased risk of aggressive PC, highere rate of distant metastasis and resistance to androgen deprivation therapy (ADT). Clinical data has shown BTCA2/DDR deficiency commonly results in poor prognosis. Lately immunohistochemical analysis of mCRPC patient samples by Paschalis et al. revealed that mutations in DDR genes (in particular *BRCA2* and *ATM*) are associated with increased prostate-specific membrane antigen (PSMA; folate hydrolase, FOLH1) expression on the cell membrane. We wanted to investigate if this upregulation in PSMA expression can be targeted with a dignostic positron emission tomogrpay (PET) imaging agents such as [^{68}Ga]-PSMA11 or [^{124}I]-MSK-PSMA1. Therefore, we hypothesized that upregulation of PSMA expression can be used as a marker for *BRCA2* alteration, which can be measured using PET imaging *in vivo*.

Experimental design:
We analyzed human prostate cancer cell line, LNCaP, at mRNA and protein level and quantified the expression of PSMA using saturation binding assays with [^{124}I]-MSK-PSMA1. Using CRISPR-Cas9, we knocked out *BRCA2* in the castration sensitive cell line LNCaP cells and evaluated its effect on PSMA at the transcriptional and translational level. Saturation binding assay using [^{124}I]-MSK-PSMA1 was performed to measure changes in cell surface PSMA receptor density in LNCaP *BRCA2* knockouts.

Results:
BRCA2 knockout was achieved successfully using CRISPR-Cas9 based methods. Western blot analysis revealed that PSMA levels increase significantly with *BRCA2* loss when *BRCA2* knockouts were compared to control LNCaP cell line. Immunohistochemical analysis confirmed this obervation. Cell binding assays demonstrated that *BRCA2* knockout LNCaP cell lines have about 6 fold higher uptake of the PET tracer [^{124}I]-MSK-PSMA1. *in vivo* studies are planned to demonstrate that *BRCA2* deletion leads to a signficant increase in PSMA signal in mice xenograft models.

Conclusions:
Our results indicate that BRCA2 silencing leads to signficant upregulation of PSMA expression in PC cell lines, which can be imaged using a PSMA targeted PET tracer.

Poster Presentation

Disclosures: The authors have disclosed no financial interest.

497-18FDG PET/CT imaging of Marburg virus-infected guinea pigs to assess disease pathophysiology and vaccine efficacy

Presenter: Jianhao Lai, National Institutes of Health

Jianhao Lai[1], Lisa Evans DeWald[2], Sanhita Sinharay[3], Swati Shah[4], Yu Cong[5], Timothy Cooper[5], Jing Qin[3], Jeffrey Solomon[6], Jurgen Seidel[7], Kurt Cooper[2], Philip Sayre[8], David Thomasson[9], Irwin Feuerstein[9], Matthias Schnell[10], Dima A. Hammoud[11], Reed Johnson[12]

[1]*National Institutes of Health, MD*
[2]*Integrated Research Facility at Fort Detrick*
[3]*National Institutes of Health*
[4]*National Institutes of Health, Bethesda*
[5]*Integrated Research Facility at Fort Detrick, Frederick, MD*
[6]*National Cancer Institute, Frederick*
[7]*National Cancer Institute, Bethesda, MD*
[8]*National Institute of Allergy and Infectious Diseases, Fort Detrick, MD*
[9]*Integrated Research Facility at Fort Detrick, Frederick, Maryland*
[10]*Thomas Jefferson University*
[11]*National Institutes of Health, Bethesda, MD*
[12]*National Institutes of Health, Frederick, Maryland*

Background:
The Marburg virus (MARV) belongs to the family *Filovirideae* family and is known to cause lethal hemorrhagic fevers in humans with high case fatality rates[1]. To date, there are no approved vaccines or antivirals and given the severity of disease, countermeasure testing is dependent upon animal models. Guinea pigs have been shown to be an appropriate animal model to study MARV disease (MVD) since their pathophysiologic representations of lesions, serum biochemical changes and coagulopathies are similar to humans [2]. Molecular imaging can be used in this setting to better understand disease pathophysiology and assess the usefulness of therapeutic and preventative measures. Here we describe the use of ^{18}Fluorodeoxyglucose positron emission tomography with computed tomography (FDG-PET/CT) to characterize disease progression and organ involvement in guinea pigs and test the efficacy of a newly developed rabies-virus based MARV bivalent vaccine (FiloRAB3)[3] to control infection.

Methods:
Hartley guinea pigs were challenged intraperitoneally with a target dose of 1,000 plaque forming units of mouse-adapted Marburg virus. After challenge, a cohort of guinea pigs were evaluated for clinical signs of disease progression until euthanasia criteria were met. Major organs were collected at different time points for immunohistochemistry (IHC) staining and RNA in situ hybridization against MARV glycoprotein and matrix protein (VP40). In another cohort, FDG-PET/CT imaging was performed at baseline, 3 and 6 days after infection. Longitudinal changes in FDG uptake across scans were assessed for each organ using repeated-measures one-way ANOVAs. Liver and spleen tissue viral titers were measured by plaque assay and correlated to Standard Uptake Values (SUV) values in respective organs at euthanasia. In the vaccine study, FiloRAB3 was intramuscularly injected on Days -82 and -40 (two doses) or -68, -54, and -40 (three doses) before infection. FDG-PET/CT was performed on Day -12 (baseline) before infection, Day 3 and Day 10 after infection.

Results:
Mouse-adapted MARV was 93% lethal in Hartley guinea pigs at 1,000 PFU following intraperitoneal inoculation. Clinical signs of MVD were observed in the guinea pigs starting from day 5-6 with animals reaching endpoint criteria between 6-10 days post exposure. IHC staining indicated that MARV infection began in liver and spleen at day 3 and later spread to other organs such as kidney (interstitial macrophages), and brain choroid plexus/meninges around day 6-7. FDG PET imaging exhibited an analogous increase in liver and spleen glucose metabolism at days 3 and 6 when compared to baseline, suggesting viral replication and activated immune cells associated with disease progression in these organs. The SUV values showed significant positive correlations with tissue viral titers of liver ($r=0.85$; $p=0.0005$) and spleen ($r=0.74$; $p=0.006$). In the vaccine study, there were no differences in FDG uptake between 2 and 3 dose regimen cohorts. However, vaccinated guinea pigs had significantly moderated increase in FDG uptake in the liver and spleen on day 10 compared to unvaccinated animals on day 6. This was accompanied by undetectable viral loads in blood and tissues and survival of all vaccinated animals.

Conclusion:
Progressive increased FDG uptake in the liver and spleen of MARV-infected guinea pigs was observed in unvaccinated guinea pigs following MARV inoculation, corresponding to viral replication and immune activation. FiloRAB3-vaccinated subjects, on the other hand, showed only mildly increased FDG uptake in both organs compared to unvaccinated animals, along with significantly improved survival. Using molecular imaging, namely FDG-PET, we were able to noninvasively monitor host response to MARV infection in real time using a small animal model of MARV, as well as assess the efficacy of FiloRAB3-MARV vaccine. Molecular imaging can be used in other infections for similar purposes, especially in the setting of developing and optimizing vaccine strategies.

Reference
1. Brauburger, K.; Hume, A.J.; Muhlberger, E.; Olejnik, J. Forty-five years of Marburg virus research. Viruses 2012, 4, 1878-1927, doi:10.3390/v4101878.
2. Shifflett, K.; Marzi, A. Marburg virus pathogenesis - differences and similarities in humans and animal models. Virology journal 2019, 16, 165, doi:10.1186/s12985-019-1272-z.
3. Keshwara, R.; Hagen, K.R.; Abreu-Mota, T.; Papaneri, A.B.; Liu, D.; Wirblich, C.; Johnson, R.F.; Schnell, M.J. A Recombinant Rabies Virus Expressing the Marburg Virus Glycoprotein Is Dependent upon Antibody-Mediated Cellular Cytotoxicity for Protection against Marburg Virus Disease in a Murine Model. Journal of virology 2019, 93, doi:10.1128/JVI.01865-18.

Poster Presentation

Disclosures: The authors have disclosed no financial interest.

498-Preclinical theragnostic approach for Alzheimer´s Disease and other Tauopathies based on novel p-Tau monoclonal antibodies.

Presenter: Marta Aramburu-Núñez, Health Research Institute of Santiago de Compostela

Tomas Sobrino[1], **Marta Aramburu-Núñez[2]**, Noemí Gómez-Lado[3], Lara García-Varela[4], Antía Custodia[1], Laura Vázquez-Vázquez[4], Juan Sebastián Ruíz[5], Daniel Romaus-Sanjurjo[1], Alberto Ouro Villasante[2], Pablo Aguiar[4]

[1]Health Research Institute of Santiago de Compostela, Santiago de Compostela, A Coruña, Spain
[2]Health Research Institute of Santiago de Compostela, Santiago de Compostela, Spain
[3]University of Santiago de Compostela, Santiago de Compostela, A Coruña, Spain
[4]Santiago de Compostela, A Coruña, Spain
[5]Ourense, Ourense, Spain

Objective:
Alzheimer's disease (AD) and other tauopathies, such as Frontotemporal dementia, are leading cause of dementia and loss of autonomy in the elderly, implying a progressive cognitive decline and limitation of social activities. Currently, there is not an effective method for the early diagnosis and treatment of AD and tauopathies. This study suggests an theragnostic approach based on the importance of phosphorylated tau protein (p-Tau) in the early pathophysiological processes of AD. Our strategy was based on the development of a theragnostic monoclonal antibodies (mAb) and their fragments focused on p-Tau detection, in order to provide *in situ* diagnostic and therapeutic effects.

Methods/Results:
We have developed a novel p-Tau mAb. Our design was based on p-Tau mAb or its fragments doped with deferoxamine for radiolabelling with PET radiotracers (Zirconium-^{89}) and fluorescence dies. Non-toxic effects (up to concentrations of p-Tau mAb greater than 100 ug/mL) were observed *in vitro* in both endothelial (bEnd.3) and primary neurons cell cultures by LDH, MTT, and IP/Annexin and Mitochondrial membrane potential. Radiolabelling of p-Tau mAb and its fragments for PET studies was performed with ^{89}Zr. In vivo results in PS19 transgenic mice shows that the ^{89}Zr-pTau_mAb and 89Zr_Fg_pTau-mAb are stable in circulation up to 10 days, without toxic effects, but the amount reaching the brain is <0,.2%.

Conclusions and Discussion:
This study shows a novel theragnostic mAb that specifically recognize very-early molecular markers of AD and tauopathies (p-Tau), and can be detected by means of non-invasive imaging methodologies (PET) and eventually provide a therapeutic action if needed. These theragnostic agents have non-toxic effects in vitro and in vivo, are stable in circulation, but the amount reaching the brain is <0.2%. Therefore, new formulations are needed in order to enhance crossing the blood-brain barrier.

Poster Presentation

Disclosures: The authors have disclosed no financial interest.

499-99mTc-Radiolabeled Doxycycline a Theranostic for Intramyocardial Delivery for Modulation of Post Myocardial Infarction Remodeling

Presenter: Supum Lee, Yale School of Medicine

Supum N. Lee[1], Stephanie Thorn[2], Selen Uman[3], Shawn Ahn[4], Rachel Burns[4], Brandon Bingham[4], Christy Hawley[4], Bernadette Marquez-Nostra[2], Jason Burdick[2], Albert Sinusas[2]

[1]Yale School of Medicine, New Haven, CT
[2]Yale University, New Haven, CT
[3]Perelman School of Medicine at the University of Pennsylvania, Philadelphia, Pennsylvania
[4]Yale University School of Medicine, New Haven, Connecticut

Purpose/Background:
Following myocardial infarction (MI), cardiac remodeling is mediated by matrix metalloproteases (MMP) (1). Intramyocardial injections of hydrogels to the MI and peri-MI region following MI can not only provide mechanical support to improve regional and global function but also serve as a vehicle for local sustained intramyocardial delivery of therapeutic drugs such as doxycycline, an MMP inhibitor which has been shown to reduce adverse remodeling in patients with acute MI (2,3). The incorporation of iodine and ^{99m}Tc-labeled doxycycline (^{99m}Tc-DOX) would allow for in vivo tracking of the initial local delivery and biodistribution of a theranostic hydrogel post-injection via SPECT/CT imaging (4). We have developed a hydrogel composed of two components, adamantane-modified hyaluronic acid (Ad-HA) and cyclodextrin-modified hyaluronic acid (CD-HA), which combine to form a supramolecular gel that can encapsulate both Iohexol, a CT contrast agent, and ^{99m}Tc-DOX as a novel theranostic (5). The purpose of this study is to evaluate the delivery and release kinetics of iodine and ^{99m}Tc-DOX incorporated in a theranostic hydrogel (THA) following intramyocardial delivery in hearts without and with MI.

Methods:
MIs were induced in Yorkshire pigs (n=3) via percutaneous balloon occlusion of the LAD for 90 minutes. Pigs returned 3 days post-MI for intramyocardial delivery of the THA and serial SPECT/CT imaging. Control pigs (n=3) received no MI before THA delivery. 10 mg doxycycline-hyclate was labeled with 2.22 GBq [$^{99m}TcO_4$]$^-$ in a one-pot reaction containing ascorbic acid, tin (II) chloride, and saline. The ^{99m}Tc-DOX and Iohexal were loaded into the hydrogel: Ad-HA was constituted in 200 mg/mL Iohexol, while CD-HA was constituted in an equal volume of ^{99m}Tc-DOX. Under anesthesia the THA was delivered via an apical window as nine 100 µL injections in a 3x3 grid into the MI region. Following injection of the THA, serial SPECT and CT images were acquired on a GE Discovery 570 SPECT/64-slice CT scanner at 30 minutes, 1, 2, 3, and 4 hrs post-injection. SPECT images were co-registered with CT angiographic images and the activity in the whole left ventricle of each pig heart was quantified using image analysis software (Carimas). CT images were analyzed for retention of Iohexol by quantifying Hounsfield units (HU) within regions of interest drawn over the sites of injection. Animals were euthanized and the hearts were excised for histological analysis and gamma well counting.

Results:
The Iohexol contrast agent allowed high resolution CT visualization of the site of THA delivery although washed out rapidly from the myocardium (retention of 30% for both control and MI hearts, Figure A, C). In contrast, the ^{99m}Tc-DOX was retained in the myocardium, with an average 4-hour retention of 100% and 75.3% for control hearts and MI hearts, respectively (Figure A, B).

Conclusion:
We developed a THA for modulation of post-MI remodeling that was imageable with hybrid SPECT/CT imaging. The encapsulation of Iohexol in the THA can be used to verify local intramyocardial delivery under fluoroscopic and/or CT guidance, while ^{99m}Tc-DOX demonstrated local retention for sustained local delivery for targeted MMP inhibition.

Reference

1. Mukherjee R, Brinsa TA, Dowdy KB, Scott AA, Baskin JM, Deschamps AM, et al. Myocardial infarct expansion and matrix metalloproteinase inhibition. Circulation 2003;107:618-25
2. Wu T, Liu W. Functional hydrogels for the treatment of myocardial infarction. NPG Asia Materials 2022;14:9
3. Cerisano G, Buonamici P, Valenti R, Sciagra R, Raspanti S, Santini A, et al. Early short-term doxycycline therapy in patients with acute myocardial infarction and left ventricular dysfunction to prevent the ominous progression to adverse remodelling: the TIPTOP trial. Eur Heart J 2014;35:184-91
4. Uman S, et al. Imaging of Injectable Hydrogels Delivered into Myocardium with SPECT/CT. Adv Healthc Mater 2020;9:e2000294
5. Mealy JE, Rodell CB, Burdick JA. Sustained Small Molecule Delivery from Injectable Hyaluronic Acid Hydrogels through Host-Guest Mediated Retention. J Mater Chem B 2015;3:8010-9

Poster Presentation

Disclosures: The authors have disclosed no financial interest.

500-Myeloperoxidase PET imaging of myocardial infarction

Presenter: Cuihua Wang, Massachusetts General Hospital

Cuihua Wang[1], Matthias W. Zeller[2], Edmund Keliher[3], Gregory R. Wojtkiewicz[2], Kevin P. Maresca[3], Leonard Buckbinder[3], Aaron D. Aguirre[2], John W. Chen[2]

[1]*Massachusetts General Hospital, Charlestown, MA*
[2]*Massachusetts General Hospital, Boston, MA*
[3]*Pfizer, Cambridge, MA*

Background:
Myeloperoxidase (MPO) is a highly oxidative heme-containing enzyme that plays an important role in the pathophysiology of myocardial infarction (MI). As such, MPO can be a prognostic and risk stratification marker and a potential therapeutic target in cardiovascular diseases. We have developed an MPO-activatable PET probe (^{18}F-MAPP) with high specificity and sensitivity to MPO activity. In this study, we aimed to use ^{18}F-MAPP PET imaging to detect myocardial infarction and monitor treatment effect in a rodent model.

Methods:
Synthesis: The synthesis of ^{18}F-MAPP has been automated in two steps.[1] *In vivo* imaging: ^{18}F-MAPP imaging was performed in a mouse model of MI to validate the efficacy of ^{18}F-MAPP and the capability of ^{18}F-MAPP to monitor the treatment effect using an irreversible MPO inhibitor, PF-2999 (50 mg/kg) or vehicle via oral gavage twice daily for 48 hours after MI, followed by PET imaging 2 hours after the last dose (n=5-6 per group). *Ex vivo:* Autoradiography of heart sections was performed after PET imaging.

Results:
The synthesis of ^{18}F-MAPP includes the radiolabeling of the precursor and subsequent deprotection of the Boc group with a radiochemical yield of 47% after decay correction in about 80 min (Figure 1A). The binding mechanism, sensitivity, and specificity of ^{18}F-MAPP to MPO were previously validated both *in vitro* and *in vivo* in mouse models of Matrigel implant and cutaneous inflammation.[1] ^{18}F-MAPP PET imaging of MI found 42% reduction of ^{18}F-MAPP uptake in mice treated with 50 mg/kg of PF-2999 compared to that treated with vehicle (Figure 1B and C, $p < 0.001$, SEM, one-tail t-test). *Ex vivo* autoradiography showed that the uptake of the heart slices with MI treated with PF-2999 was 51% reduced compared to that treated with vehicle (Figure 1D, $p = 0.05$, SEM, one-tail t-test).

Conclusion:
Molecular imaging with the activatable ^{18}F-MAPP probe can detect oxidative stress and track treatment changes in MI by targeting MPO activity.

Reference

1. Wang C*, Keliher E*, Zeller MWG, Wojtkiewicz GR, Aguirre AD, Buckbinder L, Kim HY, Chen JQ, Maresca K, Nahrendorf M, Chen JW. An activatable PET-imaging radioprobe Is a dynamic reporter of myeloperoxidase activity in vivo. Proc. Natl. Acad. Sci. USA,116 (24), 11966-11971, 2019. doi: 10.1073/pnas.1818434116.

Poster Presentation

Disclosures: The authors would like to disclose that PF-2999 and 18F-MAPP are investigational devices.

501-Pertechnetate dynamics and SPECT protocol optimization in a NIS reporter labeled model of cancer

Presenter: Joseph Merrill, Cold Spring Harbor Laboratory

Joseph R. Merrill[1], Tae Moon Chung[2], Libia Garcia[3], Scott Lyons[2]

[1]*Cold Spring Harbor Laboratory, Woodbury, NY*
[2]*Cold Spring Harbor Laboratory, Cold Spring Harbor, NY*
[3]*Cold Spring Harbor Laboratory, Cold Spring Harbor, US-NY*

Imaging with reporter transgenes has transformed preclinical cancer research by amplifying signal over noise and readily enabling dynamic measures of specific biological processes or cell populations *in vivo* that would otherwise be undetectable. Although less mainstream than optical reporters, imaging with reporters like sodium iodide symporter (NIS), linked to nuclear imaging modalities, offers distinct experimental advantages. These include decreased signal attenuation and scatter, which in turn enable high resolution, tomographic images with the potential for superior quantification. Here we use SPECT imaging to characterize the whole-body dynamics of the iodide analogue [^{99m}Tc]pertechnetate in a mouse model of NIS-labeled metastases, with the goal of protocol optimization and validation of quantification. Performance of NIS-SPECT is then compared with the current state-of-the-art FDG-PET. In total ten NSG mice were transplanted via tail vein implantation with luciferase- and NIS-labeled FC1245 murine pancreatic cancer cells, with successful development of lung metastases determined by bioluminescent imaging. The mice were then scanned with one or more of the following imaging protocols; tail vein *iv* injection of approximately 50MBq pertechnetate followed by two hour dynamic SPECT (n = 4), *iv* injection of pertechnetate followed by static SPECT at 60 minutes (n = 1), *iv* injection of pertechnetate 30 minutes after *ip* injection of 2mg of the NIS blocking agent sodium perchlorate followed by two hour dynamic SPECT (n = 1), *iv* injection of pertechnetate after sodium perchlorate followed by static SPECT at 60 minutes (n = 2), *iv* injection of pertechnetate followed by static SPECT at 60 minutes (n = 1), subcutaneous injection

of pertechnetate followed by repeated static SPECT over two hours (n = 5), *iv* injection of [^{18}F]FDG followed by two hour dynamic PET (n = 1), and *iv* injection of FDG followed by static PET at 40 minutes (n = 2). Fourteen regions of interest (ROIs) were semi-manually contoured and mean uptake (SUV_{mean}) calculated at each imaging timepoint to determine the kinetics and biodistribution of tracer between plasma, clearance routes, endogenous NIS-expressing organs, and NIS-transduced tumors. Pertechnetate uptake was clearly shown to be specific for labeled tumor cells, as well as organs of interest known to endogenously express NIS. The 2mg dose of sodium perchlorate effectively blocked pertechnetate uptake with significantly lower mean SUV in the tumor, stomach, salivary glands and thyroid (all $p < 0.01$). There was no significant difference in mean uptake at 60 minutes post-injection between the tail vein *iv* and subcutaneous injection routes for any organs analyzed. Similarly, tumor-to-background (liver) ratios were not significantly different. In the dynamic *iv* pertechnetate-SPECT scans, contrast-to-noise (CNR) and signal-to-noise (SNR) continuously increased over the first two hours of uptake due to both continued uptake of tracer in the tumor and clearance from liver. Overall, tumor uptake in the *iv* pertechnetate-SPECT scans (12.0 ± 3.0 SUV_{mean}) as compared to FDG-PET (1.5 ± 0.2 SUV_{mean}) was significantly higher ($p < 0.01$), which led to significantly higher tumor-to-background ratio ($p < 0.01$). Thus, for this model of lung metastases expressing the NIS reporter gene, NIS-SPECT with [^{99m}Tc]pertechnetate offered improved sensitivity and lesion conspicuity compared to FDG-PET.

Reference

1. Wang Y, Kung AL (2015) 18 F-FDG-PET/CT Imaging of Drug-Induced Metabolic Changes in Genetically Engineered Mouse Lung Cancer Models. Cold Spring Harb Protoc 2015:pdb.prot078246. https://doi.org/10.1101/pdb.prot078246
2. Franken PR, Guglielmi J, Vanhove C, et al (2010) Distribution and dynamics of (99m)Tc-pertechnetate uptake in the thyroid and other organs assessed by single-photon emission computed tomography in living mice. Thyroid 20:519–526. https://doi.org/10.1089/thy.2009.0213
3. Zuckier LS, Dohan O, Li Y, et al (2004) Kinetics of Perrhenate Uptake and Comparative Biodistribution of Perrhenate, Pertechnetate, and Iodide by NaI Symporter–Expressing Tissues In Vivo. Journal of Nuclear Medicine 45:500–507
4. Dohán O, De la Vieja A, Paroder V, et al (2003) The sodium/iodide Symporter (NIS): characterization, regulation, and medical significance. Endocr Rev 24:48–77. https://doi.org/10.1210/er.2001-0029

Poster Presentation

Disclosures: The authors have disclosed no financial interest.

502-Preclinical validation of 3-D focused ultrasound-mediated cetuximab delivery for improved treatment of head and neck cancer

Presenter: Ryan Margolis, University of Texas at Dallas

Ryan Margolis[1], Brian Trinh[1], Menitte Eroy[2], Junjie Li[1], Girgis Obaid[3], Kenneth Hoyt[4]

[1]*University of Texas at Dallas*
[2]*University of Texas at Dallas, Dallas, Texas*
[3]*University of Texas at Dallas, Richardson*
[4]*University of Texas at Dallas, Richardson, TX*

Head and neck cancer (HNC) is among the most common malignancy and has a profound impact on human health and quality of life. While systemic chemotherapy is often used during treatment, the presence of dysfunctional tumor microvascularity can impede effective drug delivery. To overcome this physical limitation, application of focused ultrasound (FUS) with the use of an intravascular microbubble (MB) contrast agent has been shown to improve microvascular permeability and local drug extravasation. In this research, we explored the preclinical use of a novel three-dimensional (3-D) FUS therapy system as a proposed method for improved drug delivery in HNC. Our customizeable 3-D FUS system uses a programmable research scanner (Vantage 256, Verasonics Inc) equipped with a dual transducer configuration for interleaved ultrasound imaging and therapy. Both the imaging and therapeutic transducers are 128 element arrays with center frequencies of 3.5 and 2.0 MHz, respectively. The latter is a concentric array that enables beam steering in volume space. Athymic nude mice were subcutaneously implanted with HNC cells (FaDu). Tumors were allowed to grow for about 4 wk before being randomly divided into two groups, namely, cetuximab +/- FUS ($N = 4$ per group). For animals that received FUS therapy, each received a tail vein bolus injection of MBs (50 µL; Definity, Lantheus Medical Imaging) prior to exposure. FUS therapy was performed at a peak negative pressure of 0.7 MPa, pulse repetition frequency of 10 Hz, duty cycle of 10%, exposure duration of 5 min. The treatment plans incorporated the various tumor sizes, thus the number of focal zones and repetitions per focal zone were different for each subject and treatment plan. IRDye750 (LiCOR Biosciences) was conjugated to cetuximab using established methods and administered once per wk for three wks. A dosing regimen of 3.30 $mg \cdot kg^{-1}$ was used for the first dose and 2.07 $mg \cdot kg^{-1}$ for each of the two subsequent doses, which is a clinically-relevant dosing protocol. For monitoring IRDye750-labeled cetuximab accumulation within the tumor volume, *in vivo* optical imaging (Pearl Trilogy, LI-COR Biosciences) was performed at day 0 (baseline), 1, 3, 7, 14, 21, and 28. The main experimental endpoint was animal survival. After imaging on day 28, all animals were humanely euthanized and tumors were excised for histological analysis. A review of experimental data found no differences in baseline tumor size for any of the cetuximab +/- FUS therapy group animals ($p = 0.99$). Assuming *in vivo* optical measurements represent intratumoral drug accumulation, animals treated with cetuximab + FUS exhibited fluorescent signals at least 120% higher than those animals treated with cetuximab alone. Survival curves revealed animals that received cetuximab + FUS therapy lived on average 3.5 d longer than those treated with cetuximab alone (13.5 vs 10 d). Histological analyses of tumor tissue found increased levels of apoptosis and decreased proliferation for animals that received the cetuximab + FUS therapy. Overall, this research validated the preclinical use of 3-D FUS-mediated cetuximab delivery for improved treatment of HNC.

Poster Presentation

Disclosures: The authors have disclosed no financial interest.

503-Multimodal imaging of pancreatic cancer in a preclinical model

Presenter: Ying Zhao, Karolinska Institute

Ying Zhao[1], Fei Ye[2], Sandra Oerther[3], Mamoun Muhammed[4], Moustapha Hassan[5]

[1]*Karolinska Institute, Huddinge, Sweden*
[2]*Huddinge, Stockholm, Sweden*
[3]*Karolinska Institute, Stockholm, Stockholm, Sweden*
[4]*Stockholm, Stockholm, Sweden*
[5]*Karolinska Institute, Stockholm, Sweden*

Introduction:
Pancreatic ductal adenocarcinoma (PDAC) is the fourth leading cause of cancer-related death worldwide, with a 5-year overall survival of less than 8%. PDAC is among the types of cancer that are most difficult to treat, mainly due to late diagnosis and its refractory behavior towards current treatment protocols. Certainly, accurate *in vivo* animal models that can mimic patient disease progression and treatment outcomes are necessary tools to develop new therapeutics and biomarkers for PDAC. Furthermore, early diagnosis of PDAC utilizing multimodal imaging techniques may therefore offer early treatment and hence decrease mortality and morbidity.

Methods:
Among all the preclinical models, the genetically engineered mouse (GEM) model KPF (FSF-Kras G12D/+; Trp53 frt; Pdx1-Flp), is highly similar to PDAC in humans in terms of malignant progression, metastases and chemo-resistance property. In the present investigation, we applied multimodality imaging techniques in KPF mice to obtain quantitative anatomical, functional, and molecular information about pancreatic tumors. To improve the early diagnosis using a multimodality imaging approach, we also developed a contrast agent of composite nanoparticles (NPs) composed of a gold nanorod core covered by a layer of mesoporous silica that was finally coated with gadolinium oxide carbonate-shell (AuNR-SiO2-Gd). We investigated the new contrast agent and its application in PDAC mouse model.

Results:
By combining the results obtained from different imaging modalities including ultrasound imaging (US), photoacoustic imaging (PAI), magnetic resonance imaging (MRI), and positron emission tomography (PET), we were able to: 1) Follow the tumor development at an early stage, 2) Quantify the tumor size, 3) Measure the tumor perfusion, 4) Determine the tumor hypoxia, and 5) Measure the tumor metabolism rate. It has been well characterized in patients that tissue hypoxia is a signature of PDAC, which contribute to the development of chemo-resistance and tumor metastasis. In addition, PDAC has an extensive tumor-stromal component that results in a disorganized vasculature and a physical barrier to drug delivery. As compared to PDAC patients, our results indicated the same signatures of PDAC tumors in KPF mice, as illustrated by quantitative imaging from multiple modalities. Furthermore, the new contrast agent(AuNR-SiO2-Gd) was investigated as a triple modal contrast agent for MRI, CT, and PAI for the diagnosis of PDAC in KPF mice. The present results showed that AuNR-SiO2-Gd is poorly distributed into the tumor but highly accumulated in the surrounding soft tissues which most probably is due to the poor vascularization of the tumor. The difference in biodistribution has resulted in a negative contrast within the tumor area in both CT and PAI, while a positive contrast was observed in MRI in both T1- and T2-weighted.

Conclusion:
Multimodality imaging techniques in combination with multimodal contrast agent allows early diagnosis and accurate and precise detection of PDAC progression. Furthermore, this combination will allow us to evaluate the treatment efficacy. Such a strategy could enable early diagnosis and personalized therapy which in turn will benefit the clinical outcome and enhance the life quality of PDAC patients.

Poster Presentation

Disclosures: The authors have disclosed no financial interest.

504-Multiscale NIR-SWIR Fluorescent Imaging of Tumor Microenvironment Vascular Function

Presenter: Chris Hansen, Medical College of Wisconsin

Chris Hansen[1], Benjamin Gantner[2], Amit Joshi[1]

[1]*Medical College of Wisconsin, Milwaukee, WI*
[2]*Medical College of Wisconsin, Milwaukee, Wisconsin*

Introduction:
Clinical breast cancer studies have correlated tumor vascular perfusion kinetics with response to therapy and patient survival (PMID: 20429756). The tumor microenvironment (TME) plays a large role in tumor growth and perfusion, and while the tumors are relatively well characterized, host vascular phenotypes are not. Consomic xenograft (CXM) models are a model to elucidate the effects of host genetics on xenograft tumors (25172839). The focus of this study is on the perfusion kinetics of the FDA approved infrared dye indocyanine green (ICG) in CXM with both commercial and patient derived xenograft triple negative (PDX-TN) breast cancer cell lines. ICG has an absorption and emission spectra that spans the NIR-I and tails into the NIR-II or SWIR spectra (29626132). This enables it to be used with both silicon and InGaAs detectors, allowing for high sensitivity imaging at low concentrations and excitation power, while also exploiting the higher spatial resolution due to reduced scattering in the SWIR spectrum. Tumor vasculature can be imaged via both intravital microscopic and whole-body infrared fluorescence imaging techniques on a variety of sensor types with ICG.

Materials and Methods:
CXM rats included both salt sensitive Sprague-Dawley ($SS^{IL2R\gamma}$) and consomic $SS.BN3^{IL2R\gamma}$ (Brown Norway chromosome 3) strains. Xenograft cell lines included MDA-MB-231 (231), a patient derived triple negative breast cancer cell line, and ZR75.1 ER positive (ER+). For both whole-body and intravital microscopic imaging, animals were injected intravenously via tail vein with ICG (0.75mg/kg, MP Biomedicals) and simultaneously imaged. For whole body, a NIRvana 640ST InGaAs focal plane array camera (Princeton Instruments), equipped with a 25mm lens (Navitar, DO-25, 0.95 f-stop), with an 1100nm long pass filter (ThorLabs), excited by 808nm diode laser (~5mW/cm2), was used with a frame rate of 10.6 fps for 6 minutes. For microscopic imaging, a Nikon A1R spinning disk confocal with 730nm laser excitation and 780-860nm emission bandpass, using a 25x objective. Respiratory motion correction was performed with MATLAB (MathWorks Inc.). All animal protocols were reviewed and approved by the Medical College of Wisconsin, Institutional Animal Care and Use Committee, where these experiments were performed.

Results and Discussion:
Previously, $SS.BN3^{IL2R\gamma}$ rats were shown to have greater permeability and retention and subsequently better therapeutic outcomes as compared to $SS^{IL2R\gamma}$ (28567545, 29552392, 32373218). Overall pharmacokinetic trends were conserved in both strains of rat across 231, PDX-TN, and ER+ tumors of comparable size despite the differences in vascular scale, parental cell line and imaging parameters such as dye bolus injection rate, spectral window, and imaging setup (Fig 1. A). These relative trends hold true even in the stromal microvasculature and tissue—albeit on a much faster time scale compared to the bulk tumor (Fig 1. B). The broad spectral band of ICG allows it to be used as a SWIR fluorescence contrast agent for greater spatial resolution compared to the traditional NIR-I band, and even allows for excitation wavelengths as low as 730nm enabling its use on instruments designed for far red fluorophores (Fig 1. C-E). The perfusion kinetics of ICG based on host vascular phenotype provides insight into the probable transport of pharmacologic and nanocarrier based therapeutics and their subsequent dose and duration dependent response.

Conclusions: Multiscale imaging of tumor vasculature allows for the observation of vascular perfusion kinetics at both the bulk organ and microvascular levels, confirming that relative trends in host vascular phenotype are conserved across tumor type and scale.

Poster Presentation

Disclosures: The authors have disclosed no financial interest.

505-Quality by Design applied to the development and optimization of novel nanoimaging probes for vascularized composite allotransplantation

Presenter: Lu Liu, Duquesne University

Jelena M. Janjic[1], Caitlin Crelli[2], Michele Herneisey[1], **Lu Liu**, Anneliese Troidle[1], Lesley Foley[3], Kevin Hitchens[4], Yalcin Kulahci[5], Fatih Zor[6], Vijay S. Gorantla[5]

[1]*Duquesne University, Pittsburgh, PA*
[2]*Duquesne University, Pittsburgh, North Carolina*
[3]*University of Pittsburgh School of Medicine, Pittsburgh, Pennsylvania*
[4]*University of Pittsburgh, Pittsburgh, PA*
[5]*Wake Forest Institute for Regenerative Medicine, Winston Salem, North Carolina*
[6]*Wake Forest Institute for Regenerative Medicine*

Vascularized Composite Allotransplantation (VCA) has emerged as a novel reconstructive and restorative option for patients with severe tissue defects and disfigurement with encouraging overall immune, functional, and graft survival outcomes. Conventional/standard immunosuppression regimens have prolonged VCA graft survival, but in most cases, standard baseline immunosuppression is still unable to totally prevent acute (AR) or chronic (CR) rejection and graft deterioration. Diagnosis and management of AR in VCA relies on protocol or for-cause superficial skin biopsies that do not reflect deep tissue immune responses (that may include CR). Routine deep biopsies are invasive and pose risk to vital neurovascular structures. There is thus an imminent need for non-invasive tools that enable reliable, reproducible, quantitative, and objective diagnosis and monitoring of rejection in deep graft tissues otherwise inaccessible by skin biopsy. Novel nanoprobes capable of immunolabeling multiple cell populations *in vivo*, can shed critical insights into the dynamics, kinetics, intensity and spatial patterns or progression of cellular VCA rejection across deep and superficial tissues as well as objectively quantifying responsiveness or resistance of rejection to immunosuppressive therapy. Furthermore, distinct multispectral nanoimaging can provide unprecedented insights into immune cell dynamics and turnover during acute and chronic rejection in VCA. Such nanoimaging strategies can help in discovery of novel cellular targets for optimizing precision or personalized immunosuppression in VCA. We demonstrate novel nanotechnology designed to allow VCA clinicians to accurately assess the timing, evolution, intensity and distribution of cellular rejection or immune cell activity in superficial and deep tissues. Ultimately this approach will allow true treatment personalization and evaluation of the therapeutic response to immunosuppression, monitor patient compliance to medications, and prognosticate graft outcomes through predictive imaging biomarker models. In order to develop safe, noninvasive, immune cell specific and multispectral nanoprobes we reached into the Quality by Design (QbD) methodology toolbox. Although the development of biomedical nanotechnology continues to accelerate, it continues to meet challenges that may prevent clinical translation and commercialization. Specifically, insufficient quality control in early product development and/or an incomplete understanding of the impact of the manufacturing process on product physicochemical properties can hinder nanomedicine reproducibility and scale-up. We demonstrated by MR and NIRF imaging, for the first time, that the spatial distribution and anatomical localization of macrophage mediated inflammation/infiltration in superficial and most importantly deep tissues in rodent and large animal models of VCA. Notably, the signal intensity and distribution of nanoprobe labeled host macrophages infiltrating into the graft during Grade 2 acute rejection (AR) confirmed that AR is not homogenous, but rather heterogenous and involves discrete zones in superficial and deep tissues in VCA. We also demonstrated that QbD methodology is essential for the development of multimodal nanoprobes. We also show that MRI and NIRF imaging results from both *in vivo (large and small animals)* and *ex vivo* studies can be incorporated into QbD strategies for nanoprobe optimization. In summary, we present here details of how QbD can be utilized to optimize manufacturing processes and assure quality of nanoimaging products. We demonstrated proof of concept multispectral and multimodal imaging in a rodent and primate VCA models. We also showed the potential for further expansion of QbD to complex biomaterial manufacturing and its transformative power on personalized medicine.

Poster Presentation

Disclosures: The authors have disclosed no financial interest.

506-Systematic Degradation and Toxicity Analysis of Copper-Based Semiconductor Nanomaterials

Presenter: George Katsarakes, Boston University

George P. Katsarakes[1], Allison Dennis[2], Xingjian Zhong[1]

[1]*Boston University*
[2]*Boston University, Boston, Massachusetts*

Introduction:
Near-infrared (NIR) active semiconductor nanocrystals (NCs) have promising applications in biomedical imaging in vivo due to their excellent optical features, such as narrow fluorescence spectra, high brightness, and emission tunability [1]. Direct bandgap materials such as quantum dots (QDs) can produce bright and specific fluorescence upon broad excitation, while doped semiconductor materials with localized surface plasmon resonance (LSPR) are widely adapted for photoacoustic imaging [2]. However, there is a dearth of information pertaining to their safety for clinical translation. Early NCs were made with intrinsically toxic ions such as cadmium and lead, motivating the development of materials with safer components for in vivo imaging. In recent studies, particles have been synthesized with seemingly safer elements like copper and indium; however, CIS has been shown to have unexpectedly high levels of toxicity [3]. Thus, there is an urgent need to thoroughly evaluate the degradation properties and toxicity of copper-based biodegradable nanocrystals.

Materials and Methods:
We have tested copper indium sulfide (CIS) QDs along with copper sulfide (Cu2S) and two versions of copper iron sulfide (CFS) NCs. Particles were synthesized via the hot injection method, where instant nucleation is triggered at high temperatures by injecting an organometallic reagent, typically elemental sulfur dissolved in coordinating ligands such as oleylamine; this method allows us to modify the size of the resulting NCs by altering the reaction length and temperature. We employed a variety of analytical techniques, including spectrophotometry for observation of absorbance spectra, microwave plasma atomic emission spectroscopy (MP-AES) to determine elemental

concentrations and ratios, and X-ray diffraction (XRD) along with small-angle X-ray scattering (SAXS) to confirm structure, composition, and size. We also conducted degradation studies where first, particles are left to degrade in either simulated body fluid (SBF) or artificial lysosomal fluid (ALF) in a 37°C incubator, and after centrifugation with ethanol to disrupt the micelles, the ratio of particles remaining in NCs (which form the pellet) to degraded particles (which become suspended in the supernatant) can be determined through MP-AES. Finally, we completed cell viability experiments using ATP assays, where cells are examined after sitting in a solution of NCs and phosphate-buffered saline (PBS) for 24 hours to determine the percentage of viable cells after exposure to NCs at varying concentrations.

Results and Discussion:
The degradation analysis procedure we used gave us specific data on the kinetics of particle degradation in SBF and ALF (Fig. 1A), providing a quantitative method to evaluate particle interactions with cells. The viability assays suggested that, as supported by previous data, CIS is highly toxic to cells even at low concentrations (20 μg/mL), while Cu2S and bornite CFS showed moderate toxicity and chalcopyrite CFS had low toxicity (Fig. 1B). In combination with the degradation studies, it is clear that all four particles degrade significantly in biological fluids and cause different levels of toxicity based on their composition.

Conclusions:
Our research so far has demonstrated that, contrary to the expectation that swapping toxic heavy metals for less harmful elements would reduce QD toxicity, CIS still has significant toxic effects that are not well understood and are likely directly linked to degradation, specifically the ion leaching that occurs as NCs degrade. Chalcopyrite CFS, however, could be a viable candidate for a low toxicity QD. In our continuation of this study, we will further examine the exact relationship between degradation and toxicity using our degradation analysis data, which will enable us to conduct cell viability tests with partially degraded particles at specific degradation ratios. We also plan to examine the means of toxicity produced by indium (e.g. ROS generation and DNA damage) as well as potential mitigatory methods.

Reference

1. Resch-Genger, Ute, et al. "Quantum Dots versus Organic Dyes as Fluorescent Labels." Nature Methods, vol. 5, no. 9, 2008, pp. 763–775., https://doi.org/10.1038/nmeth.1248.
2. Gellini, Cristina, and Alessandro Feis. "Optothermal Properties of Plasmonic Inorganic Nanoparticles for Photoacoustic Applications." Photoacoustics, vol. 23, 2021, p. 100281., https://doi.org/10.1016/j.pacs.2021.100281.
3. Joshua C. Kays et. al., Shell-Free Copper Indium Sulfide Quantum Dots Induce Toxicity in Vitro and in Vivo. Nano Letters, 2020. 20(3).

Poster Presentation

Disclosures: The authors have disclosed no financial interest.

507-Photoacoustic assessment of in vivo blood oxygenation in the brains of mice with cachexia induced by a pancreatic cancer xenograft

Presenter: Saleem Yousf, Johns Hopkins University

Saleem Yousf[1], Marie-France Penet[2], Andrew D. Brannen[3], Balaji Krishnamachary[2], Yelena Mironchik[4], Zaver M. Bhujwalla[2]

[1]*Johns Hopkins University*
[2]*Johns Hopkins University School of Medicine, Baltimore, MD*
[3]*iThera Medical, Auburn, AL*
[4]*Johns Hopkins University School of Medicine, Baltimore, Maryland*

Cancer-induced cachexia causes a cascade of metabolic and functional changes in body organs resulting in morbidity, mortality and inability to withstand treatment [1]. Cachexia is observed with high frequency in pancreatic ductal adenocarcinoma (PDAC) [2]. Over the last decade, we have actively investigated metabolic changes induced by cachexia-inducing PDAC xenografts that have identified significant metabolic changes in the brain, plasma and other organs [3,4]. Multispectral optoacoustic tomography (MSOT) or photoacoustic (PA) imaging is an emerging non-invasive hybrid modality that combines the advantage of high contrast and spectral specificity of optical imaging with the high spatial resolution and penetration depth of ultrasound imaging. Here, for the first time, we used MSOT imaging to identify blood oxygenation changes in the brain associated with cachexia. MSOT imaging provided the ability to investigate changes in hemodynamics as well as changes in the size of organs. The studies were performed using non-tumor bearing mice (n=3), mice with non-cachexia inducing Panc1 tumors (n=3), and mice with cachexia-inducing Pa04C tumors (n=4). Eight-week-old male immunodeficient nude mice were inoculated in the right flank with 2×10^6 cancer cells. Mice were scanned once tumors were ~ 315 and 448 mm^3 for Pa04C and Panc1, respectively. MSOT imaging was performed using the iThera MSOT InVision 512-echo scanner (iThera Medical, Munich, Germany). MSOT data were acquired at wavelengths of 700 nm, 730 nm, 760 nm, 800 nm, 860 nm, 900 nm with 10 averages per wavelength. A linear regression method was used to perform multispectral processing using ViewMSOT software version 4.0. MSOT images were reconstructed from the raw data using a back-projection algorithm at a resolution of 75 μm. Regions of interest (ROIs) were manually drawn based on concurrently acquired b-Mode ultrasound images of the brain to determine the spectral signal and the corresponding size. Mean values of SO_2 obtained from a ROI manually drawn in each slice to cover the brain were obtained to determine the total mean SO_2, obtained as HbO_2/total Hb for each mouse. Representative mSO_2 images of brain are presented in Figure 1A. The analyzed MSOT brain data indicated that the mean SO_2 was higher in brains of Pa04C tumor bearing mice than in normal and non-cachectic mice (Figure 1B) suggesting that blood oxygenation was higher in the brains of mice with cachexia-inducing Pa04C tumors. Representative b-mode ultrasound images used to determine organ size are presented for the brain in Figure 1C. By determining the brain area in each slice we found that the mean size of the brains in mice with Pa04C tumors was lower (474 ± 10 mm^3) than normal mice (494 ± 3 mm^3) and mice with Panc1 tumors (515 ± 17 mm^3) (Figure 1D). These preliminary data highlight the potential applications of noninvasive MSOT imaging to understand the impact of cancers and cancer-induced cachexia in altering organ hemodynamics. These data expand our understanding of how cancers impact the body. These studies can be translated to human applications designed to investigate cancer-induced hemodynamic changes in superficial tissues accessible with MSOT imaging.
Support from NIH R01 CA253617, R35 CA209960, R01 CA82337, P30 CA006973 and S10 OD028486 is gratefully acknowledged. We thank Mr. Gary Cromwell for inoculating the tumors.

Reference

1. Biswas Anup K, Acharyya Swarnali. Cancer-Associated Cachexia: A Systemic Consequence of Cancer Progression. Annual Review of Cancer Biology 2020; 4: 391-411.
2. Mueller Tara C, Burmeister Marc A, Bachmann J, Martignoni Marc E. Cachexia and pancreatic cancer: Are there treatment options? World Journal of Gastroenterology 2014; 20: 9361-9373.

3. Winnard PT, Jr., Bharti SK, Sharma RK, Krishnamachary B, Mironchik Y, Penet MF et al. Brain metabolites in cholinergic and glutamatergic pathways are altered by pancreatic cancer cachexia. Journal of cachexia, sarcopenia and muscle 2020.
4. Sharma RK, Bharti SK, Winnard PT, Jr., Penet MF, Zaver M Bhujwalla. Lung and kidney metabolism altered by cancer-induced cachexia. Cancer Research 16 supplement 2020; 80: 1625-1625.

Poster Presentation

Disclosures: The authors have disclosed no financial interest.

508-Novel combination of PARP inhibitor olaparib with the vascular disrupting agent NOV202 reduces tumor growth in BRCA1/2 mutated prostate cancer xenografts.

Presenter: Evangelia Sereti, Lund University

Evangelia Sereti[1], Anders Bjartell[2], Stefan Rehnmark[3], Marita Högberg[3]

[1]*Lund University, Malmö, Sweden*
[2]*Lund University, Malmö, Skåne, Sweden*
[3]*Noviga Research AB, Södertälje, Sweden*

Introduction and Objectives:
Prostate cancer therapeutic landscape has been rapidly evolved the last years however, metastatic castration-resistant prostate cancer (mCRPC) remains an incurable malignancy with poor clinical outcome and poor prognosis. A high percentage (20-25%) of mCRPC patients harbor homologous recombination repair (HRR) defects, with *BRCA1/2* mutations representing the most frequent events. Several recent clinical trials have shown that mCRPC patients with HRR deficiencies responded well to poly (ADP-ribose) polymerase inhibitors (PARPi). The PARPi olaparib was found to significantly improve survival in patients with *BRCA1/2* mutated mCRPCand recently the FDA approved olaparib for mCRPC patients harboring HRR alterations. Although robust data exist for PARPi as monotherapy in selected patients, there is a clinical need for combinational therapeutic approaches to improve the efficacy of PARPi and overcome or prevent PARPi resistance. NOV202 is a novel vascular disrupting agent (VDA) with strong anti-proliferative effect in a large panel of cancer cells. The aim of this study is to evaluate if NOV202 could improve the *in vivo* efficacy of olaparib in prostate cancer xenografts with and without BRCA1/2 mutations.

Materials and Methods:
Prostate cancer-based xenografts were developed from cell lines with different *BRCA1/2*mutation profile. Luciferase-transfected human PC3 (*BRCA1/2* wildtype) or human DU145 (*BRCA1/2* mutated) cell lines were inoculated subcutaneously in male NMRI nude mice. Animals were treated with olaparib (100 mg/kg), NOV202 (30 mg/kg), or their combination for 21 days, followed by either 1 or 2 weeks of no treatment. Tumor growth and response to therapy were monitored by non-invasive bioluminescence optical imaging (BLI) and tumor size was also measured by caliper. During the experiment, a 25-parameter blood analysis, including hemoglobin concentration, red and white blood cells, and neutrophil granulocytes was performed weekly.

Results:
Olaparib and NOV202, as single drug treatments, induced tumor growth inhibition in both cell lines tested. Compared to monotherapy, the combination of olaparib with NOV202 exerted significant synergistic effect in the *BRCA1/2* mutated xenograft (DU145) in contrast to *BRCA1/2* wildtype xenograft (PC3), where no significant synergistic effect was observed. The combinational effect continued for 2 weeks post-treatment period.

Conclusions:
Single agent treatment with the VDA agent NOV202 and with olaparib reduced tumor growth in prostate cancer xenografts regardless of the *BRCA1/2* mutation profile *in vivo*. Interestingly, the anticancer efficacy of olaparib was significantly increased when combined with NOV202 only in the *BRCA1/2* mutated xenografts, which represents an option to increase the efficacy of PARPi in patients with *BRCA1/2* mutations. A clinical trial of this combination is planned.

Poster Presentation

Disclosures: The authors have disclosed no financial interest.

509-Evaluation of hetero-bislanthanide complexes for MRI and optical imaging

Presenter: Emilie Brun, University of Ottawa

Emilie Brun[1], Neerav Mullur[2], Nan Liu[3], Mojmir Suchy[4], Anna Marriott[5], Hannah Ehler[5], James Rioux[5], Kimberly Brewer[6], Eva Hemmer[3], Adam Shuhendler[2]

[1]*University of Ottawa, Ottawa, ON*
[2]*University of Ottawa, Ottawa, Ontario*
[3]*University of Ottawa, Ottawa*
[4]*Lawson Health Research Institute, London*
[5]*Biotics Research Canada, Halifax, NS*
[6]*Dalhousie University, Halifax*

Introduction:
Lanthanides are known to have both magnetic resonance imaging (MRI) and optical properties, which make them interesting to explore as multimodal contrast agents. Gadolinium-based chelates has been widely used as contrast agent for MRI, where the chelate limits any toxicity in vivo derived from the free metal ion [1]. Lanthanides-organic complexes showed favourable luminescent characteristics that can be employed in fluorescence imaging [4]. Lanthanides, from europium to lutetium were used to create hetero-bislanthanide complexes in a controlled 1:1 ratio in order to begin to explore their properties towards their use in application as contrast agents to enzymatic activities [2] or for cell labelling [3]. Both longitudinal and transverse water proton relaxivities were calculated for each bis-lanthanide compound to identify any interesting properties as MRI contrast agents. Optical properties of a combination of some of these lanthanides were also evaluated, with strong fluorescence enabled by the energy transfer of the ligand to the lanthanide ions [4].

Methods:
BOC-cysteine-(tBu)-phenyldiamine was coupled with DOTA, and this compound was used to chelate 9 different lanthanides. In parallel, DOTA-2-cyanoquinoline compound was used to form chelates of gadolinium. Using these two parts capable of rapidly forming a thiazoline ring, 10 different bis-lanthanides complexes were generated (figure 1). T_1 and T_2 images, and relaxivities were acquired on a 3T MRI at 5 different concentrations (0.02–0.6 mM), and the T_1/T_2 intensity ratio

was mapped. The optical analysis was realized by photoluminescence spectroscopy on 4 different compounds at a 1 mM concentration.

Results:

The synthesis of the bis-lanthanide molecule is realized first by preparing the 2 individual components followed by an uncatalyzed “click” reaction to produce the desired bislanthanide complex with precise control to yield a 1:1 lanthanide ratio. Gadolinium is one of the most commonly used lanthanides as MRI contrast agent, [5] leading us to hypothesize that the highest r_1 was expected for the GdGd bis-lanthanide complex (**3b**). However, according to the results that were repeated twice for each compound at each concentration, it appears that the hetero-bislanthanide complex comprising GdTm (**3g**) provided the largest relaxivities. The remaining bis-lanthanide compounds presented lower relaxivity results that were indistinguishable from each other (figure 2). While thulium (Tm^{3+}) is less used than gadolinium as contrast agent, one previous report showed an application in tumor cell labelling [6]. Absorbance, excitation, and emission spectra were acquired on EuGd, EuYb, EuEu and LuLu complexes, where Eu^{3+} is on the DOTA-quinoline moiety. This aromatic heterocyclic compound is known to absorb between 220 and 350 nm [7], resulting in the intense peak around 250 nm on the absorbance spectrum (figure 3A). Excitation spectra were performed on one compound, EuGd, since all these complexes have the same ligand. An emission wavelength of 617 nm was fixed, which is the characteristic emission of the Eu^{3+} ion [8]. That’s why, an intense signal can be observed at 360 nm at this specific wavelength, suggesting that it excited the molecule in a way that maximizes the 617 nm emission wavelength (figure 3B).

Conclusion:

Unexpectedly, the hetero-bislanthanide complex Gd-Tm showed higher relaxivities when compared to the other samples, even higher than Gd-Gd. With the optical analysis, europium (III) showed a luminescence where its emission is highly dependent of the chemical environment.

Reference

1. Lacerda S, Toth E, ChemMedChem Rev 2017, 12:883-894.
2. He J et al., J. Am. Chem. Soc. 2016, 138:2913-2916.
3. Zheng Q et al., J. Am. Chem. Soc, 2005, 127,46:16178-16188.
4. Yip Y-W et al., Inorg. Chem. 2012, 51,13:7013-7015.
5. Washner J et al., Chem. Rev., 2019, 119 :957-1057.
6. Reifschneider O et al., Anal. Chem. 2015, 87 :4225-4230.
7. Dos Santos GC et al., J. Fluoresc., 2017 27 :271-280.
8. Hussain R et al., Opt Express, 2014, 22,7 :7744-7755.

Poster Presentation

Disclosures: The authors have disclosed no financial interest.

510-Tracking the functionality of kidney ischemic-reperfusion injury and fibrosis using photoacoustic imaging

Presenter: Eno Hysi, St. Michael’s Hospital

Eno Hysi[1], Xiaolin He[2], Luisa Ulloa-Severino[2], Caitriona McEvoy[2], Darren Yuen[2], Michael Kolios[3]

[1]St. Michael’s Hospital, Toronto, Ontario
[2]St. Michael’s Hospital, Toronto
[3]Ryerson University, Toronto

Introduction:

Ischemic-reperfusion injury (IRI) is a well-known phenomenon that occurs during kidney transplant surgery following establishment of flow in the donated graft. It can have detrimental impacts in the outcomes of the transplant, leading to delayed graft function, rejection and irreversible fibrosis affecting longevity [1]. There are no reliable molecular biomarkers in the serum and urine which can predict the occurrence of IRI. To address this, we propose the use photoacoustic (PA) imaging to visualize the functionality of kidneys post-IRI. Specifically, PA imaging algorithms were developed to assess the status of oxygen saturation (sO_2), total hemoglobin (HbT) and collagen deposition in a preclinical IRI model. A novel respiratory-corrected PA imaging algorithm that can accurately estimate these crucial biomarkers in a longitudinal fashion in-vivo.

Methods: Ex-vivo:

A spectral unmixing algorithm was developed to separate the PA signal contributions of kidney collagen from oxy and deoxyhemoglobin [2, 3]. A VevoLAZR-X preclinical PA imaging system operating at 15 MHz and 680-930 nm illuminations imaged the longitudinal buildup of kidney fibrosis in a unilateral ureteral obstruction (UUO) model (Suppl. Fig. 1a). The left ureter was surgically obstructed for 7 and 14 days to induce increasing degrees of fibrosis. The right (normal) and left (fibrotic) kidneys were resected at each timepoint (n = 5/timepoint), imaged ex-vivo and histologically stained for collagen. **In-vivo:** IRI was induced by clamping the renal arteries of 24 mice for 25 mins (n=8 sham, n=24 IRI). The kidneys were imaged in-vivo pre-surgery and D1/D7/D14 post-surgery and the algorithms validated ex-vivo were implemented to estimate the relevant biomarkers longitudinally. Corrections for the respiratory motion was achieved by monitoring the fluctuating electrical impedances in the mouse paws and applying a gating to the PA data (Fig. 1a). Histological analysis estimated the degree of tubular injury (marker of inflammation) and collagen content (marker of fibrosis) following the IRI.

Results and Discussion:

Suppl. Fig. 1b shows increasing levels of fibrosis in both PA and histological images as the ureter is obstructed for longer periods of time. A strong correlation was observed between the PA estimates of collagen and gold standard histology measures (Suppl. Fig. 1c, r = 0.98). These ex-vivo findings suggest that our novel PA approach can accurately quantify fibrosis levels [4].

To assess the accuracy of the respiratory motion correction algorithm, we measured the overlap of the kidney region of interest during multi-frame acquisitions. A 0.94 average dice similarity coefficient suggested that the gating algorithm accurately corrected for respiratory-induced motion (Suppl. Fig. 2a). This high level of accuracy was observed in the longitudinal mouse kidney sO_2 readings over two weeks (2-3% variation/mouse/timepoint, Suppl. Fig. 2b).

This algorithm also performed well during longitudinal imaging of IRI mice. Specifically, IRI kidney sO_2 on D1 decreased by 10% due to inflammation-induced changes in blood flow (Fig. 1b). Collagen gradually increased by 1.5x at D7 relative to pre-surgery before doubling by D14 (Fig. 1c) while HbT gradually decreased throughout the experiment (Fig. 1d). The sO_2 drop in D1 correlated strongly with the increase in collagen by D14 (Fig. 1e). The increase in PA collagen scores corresponded to the buildup of fibrosis associated with IRI and was very well correlated with histology (r=0.96, Fig. 1f). The drop in HbT observed in D1 also correlated very strongly with the tubular injury scores measured in the kidneys (r=0.97, Fig. 1g), suggesting that these imaging biomarkers are capable of quantifying degree of inflammation occurring early post-IRI. Taken together, the findings show that PA imaging can monitor the physiological changes that occur following IRI in-vivo, contributing to the assessment of IRI in the transplant setting.

Reference

1. Emerging medical imaging techniques for the assessment of delayed graft function: A narrative review E Hysi, H Kaur and A Young (2021) Canadian Journal of Kidney Health and Disease 8, 1-14
2. Photoacoustic imaging of kidney fibrosis for assessing pre-transplantation organ quality E Hysi, X He, MN Fadhel, T Zhang, A Krizova, M Ordon, M Farcas, K Pace, V Mintsopoulous, WL Lee, MC Kolios and DA Yuen (2020) The Journal of Clinical Investigation Insights 5(10): e136995, 1-16
3. Imaging of renal fibrosis E Hysi and DA Yuen (2020) Current Opinion in Nephrology and Hypertension 29(6), 599-607
4. A tutorial in photoacoustic microscopy and tomography signal processing methods E Hysi, MJ Moore, EM Strohm and MC Kolios (2021) Journal of Applied Physics 129(14), 141102-1-23

Poster Presentation

Disclosures: The authors have disclosed no financial interest.

511-MOEMS based confocal fluorescence and photoacoustic microscope

Presenter: Bo Li, Michigan State University

Bo Li[1], Aniwat Juhong[2], Wibool Piyawattanametha[3], Wen Li[4], Aaron Wasserman[5], Brett Volmert[1], Xiang Liu[1], Aitor Aguirre[1], Cheng-you Yao, Zhen Qiu[1]

[1]*Michigan State University, East Lansing, MI*
[2]*Michigan State University, East Lansing*
[3]*King Mongkut's Institute of Technology Ladkrabang, Bangkok, Bangkok, Thailand*
[4]*Michigan State University, East Lansing, Michigan*
[5]*Michigan State University, East lasing, MI*

To have a comprehensive biomedical imaging result, multimodality imaging systems are desired by researchers. In here, we present an integrated transparent nanophotonic ultrasonic detector micro-orings (MRRs) and Micro-opto-electro-mechanical systems (MOEMS) based confocal fluorescence and photoacoustic microscope system[1]. An Electrostatic MOEMS scanner has been selected for 2D beam steering. For the laser excitation source, we fiber-coupled a 488nm CW laser and a 532 ns pulse laser into the single mode fiber (SMF) to excite the fluorescence signal and acoustic signal at the imaging target. For the signal collection, the single axis confocal microscope setup was selected. The fluorescence signal will be collected with the same SMF and passes through the long-pass dichroic mirror into the PMT. To minimize the system size, the MRRs ultrasonic sensor was selected and attached under the objective lens to detect the photoacoustic signals. Due to the transparent property of the sensor, the excitation laser beam can easily pass through the quartz substrate to land on the imaging target surface. For the imaging target, the genetically modified zebrafish with GFP (TgBAC: tcf21: NLS-EGFP) at backbone area and mCherry at heart region (Tg:-5.1myl7: DsRed2)can be used for the confocal microscope imaging. The blood and melanin inside the fish body can be excited to generate the photoacoustic signals by 532nm nanosecond pulse laser. With the dual excitation laser channels, two imaging modalities can be achieved simultaneously.

References

1. Li, H. et al. Disposable ultrasound-sensing chronic cranial window by soft nanoimprinting lithography. Nature communications 10, 1-9 (2019).

Poster Presentation

Disclosures: The authors have disclosed no financial interest.

512-Accuracy of 18F-Sodium fluoride PET imaging quantification in a murine model of CAVD

Presenter: Azmi Ahmad, Yale University School of Medicine

Azmi A. Ahmad[1], Mean Ghim[1], Jakub Toczek[1], Kiran Gona[1], Devi Ojha[2], Gunjan Kukreja[1], Zawwad Raza[1], Mehran Sadeghi[1]

[1]*Yale University School of Medicine*
[2]*Yale School of Medicine, New Haven, Connecticut*

Objectives:
Calcification is a pathological feature of cardiovascular disease. Calcific aortic valve disease (CAVD) is a progressive disease that results in fibrocalcific remodeling of the aortic valve leaflets and can lead to hemodynamically significant aortic stenosis. Patients with bicuspid aortic valve (BAV) experience calcification at a younger age, as compared to those with tricuspid aortic valve (TAV). Discoidin, CUB and LCCL domain-containing protein 2 (DCBLD2) is reduced in patients with aortic stenosis, and DCBLD2 deficient mice develop BAV and CAVD with hemodynamically significant aortic stenosis. Accordingly, these animals provide a clinically relevant model to study CAVD progression and reversal. The calcification process may be imaged with ^{18}F-Sodium Fluoride ([^{18}F]-NaF) positron emission tomography (PET). The purpose of this work was to evaluate accuracy of [^{18}F]-NaF PET quantification in *Dcbld2*$^{-/-}$ mice.

Methods:
Following echocardiography to assess aortic valve anatomy and physiology, young (3–4-month, n=5) and old (19-20-month, n=8) *Dcbld2*$^{-/-}$ mice were injected with 0.5±0.06 mCi of [^{18}F]-NaF and PET imaging was performed for 10 min at 80 min post-injection. Contrast (Exitron nano-12000)-enhanced computed tomography (CT) images acquired prior to PET imaging were used to draw a region of interest over the aortic valve, and SUVmax values were determined on fused PET/CT images. Valvular [^{18}F]-NaF uptake was confirmed 48-72 hours later by quantitative autoradiography performed at 1 hr post-[^{18}F]-NaF injection, and aortic valve tracer uptake was quantified as % injected dose/cm^2. Additional organs were harvested to assess [^{18}F]-NaF biodistribution. Aortic valve phenotype was subsequently determined by histological analysis.

Results:
[^{18}F]-NaF uptake was higher in older mice as measured by in vivo PET/CT ($P < 0.05$) and ex vivo autoradiography ($P < 0.05$). There was a significant correlation between aortic valve [^{18}F]-NaF uptake quantified by in vivo PET/CT and ex vivo autoradiography (Pearson $R = 0.72$, $P < 0.01$). 3 out of 8 older *Dcbld2*$^{-/-}$ mice were identified as BAV. Mice with BAV had reduced leaflet separation and higher aortic valve velocity ($P < 0.05$). Additionally, the highest aortic valve signal in both PET and autoradiography was from the BAV mice. No significant difference was present in the cardiac apex, lung, liver, spleen, kidney, bone, and blood NaF activity between BAV and TAV.

Conclusions:
Dcbld2$^{-/-}$ mice develop aortic stenosis and valvular calcification as detected by echocardiography and [^{18}F]-NaF PET/CT, respectively. Valvular [^{18}F]-NaF signal increases with age and can be accurately quantified on in vivo PET/CT images. This approach facilitates preclinical testing and development of novel therapeutic agents for CAVD.

Poster Presentation

Disclosures: The authors have disclosed no financial interest.

513-Quantitative T2 relaxation time magnetic resonance imaging of fibrosis in a rat model of inflammatory bowel disease

Presenter: Una Goncin, University of Saskatchewan

Una Goncin[1], Lumeng Cui[2], Kirstin Olsen[3], Emily Mcwalter[3], Steven Machtaler[4]

[1]University of Saskatchewan, Saskatoon, SK
[2]Siemens Healthineers, Burnaby
[3]University of Saskatchewan, Saskatoon, Saskatchewan
[4]University of Saskatchewan, Saskatoon

Introduction:
Inflammatory bowel disease (IBD) is characterized by chronic bowel wall inflammation and ulceration. Due to the relapsing nature of disease, improper wound healing can lead to stenosis (known as strictures) and unpredictable deposition of fibrotic tissue[1]. Determining whether the stricture is primarily from active inflammation or fibrosis is important clinically as treatment is either medical or surgical, respectively[2]. We lack an imaging approach that can quantitively assess bowel fibrosis in patients with IBD. Magnetic resonance imaging offers high quality 3D morphological images and assessment of macromolecular changes in tissue that has the potential to aid in early detection of disease prior to any gross anatomical changes[3,4]. Our objective is to use a novel quantitative MRI sequence (quantitative double echo in steady state; qDESS)[5,6] to image and quantify bowel fibrosis using a rat model of chronic IBD. This approach has the potential to aid in assessing disease progression, response to therapy, and development of strictures.

Methods:
Sprague-Dawley rats (n=6) were chemically induced with bowel fibrosis using 3-one-week cycles of 4% dextran sulfate sodium (DSS), separated by 14 days of normal drinking water[7]. These rats continued normal drinking water for a minimum 14 days prior to MRI to ensure no active inflammation was present. The remaining rats (n=4) received normal drinking water over a 4-week period prior to imaging. Two rats were loaded at a time in a 16-channel transmit-receive wrist coil and imaging using a modified qDESS sequence[8] (voxel size: 0.3125*0.3125*3 mm^3 with an average scan time of 7 min). T_2 relaxation time maps were generated for each animal using an Extended Phase Graph (EPG) formalism to approximate the relationship between the two DESS signals to a max, achieving T_2 relaxation time estimates. The mean T_2 value from the four ROIs (excluding bowel lumen) was calculated. Bowels were excised for histology and collagen content quantification.

Results:
Rats with bowel fibrosis maintained their weight and displayed symptoms associated with IBD including irritability, bloody stool, and anal bleeding in some cases. All MR images were interpretable (Fig. 1A). Histological investigation showed evidence of immune cell infiltration and increase in collagen deposition in fibrotic rats (Fig. 1A). There was a significant decrease in T_2 signals ($p < 0.001$) in rats with fibrosis (18.2 ± 3.4 ms) in comparison to healthy rats (29.5 ± 3.5 ms; Fig. 2). This is consistent with a significant increase in collagen content in rats with fibrosis (0.16 ± 0.05 mg/ml) than healthy rats (0.08 ± 0.01 mg/ml; Fig. 3). There was a strong negative correlation (r = -0.835) between T_2 relaxation values and collagen content.

Conclusions:
There was a significant decrease in mean T_2 relaxation time in rats with bowel fibrosis that correlated well with increased collagen content. These data suggests that we can identify and quantitatively measure intestinal fibrosis in patients with IBD. This approach can benefit patients by providing a tool that can be used to track disease progression and facilitate timely and accurate treatment decisions.

References
1. Zappa, M. et al. Which magnetic resonance imaging findings accurately evaluate inflammation in small bowel Crohn's disease? A retrospective comparison with surgical pathologic analysis. Inflamm Bowel Dis 17, 984-993, doi:10.1002/ibd.21414 (2011).
2. Rieder, F., Zimmermann, E. M., Remzi, F. H. & Sandborn, W. J. Crohn's disease complicated by strictures: a systematic review. Gut 62, 1072-1084, doi:10.1136/gutjnl-2012-304353 (2013).
3. Raya, J. G., Ruiz, A. & Ferizi, U. Revisiting the experimental base of compositional biomarkers: A meta-analysis study. Proc International Society for Magnetic Resonance in Medicine (2017).
4. Blumenkrantz, G. & Majumdar, S. Quantitative magnetic resonance imaging of articular cartilage in osteoarthritis. Eur Cell Mater 13, 76-86, doi:10.22203/ecm.v013a08 (2007).
5. Staroswiecki, E., Granlund, K. L., Alley, M. T., Gold, G. E. & Hargreaves, B. A. Simultaneous estimation of T(2) and apparent diffusion coefficient in human articular cartilage in vivo with a modified three-dimensional double echo steady state (DESS) sequence at 3 T. Magn Reson Med 67, 1086-1096, doi:10.1002/mrm.23090 (2012).
6. Welsch, G. H. et al. Rapid estimation of cartilage T2 based on double echo at steady state (DESS) with 3 Tesla. Magn Reson Med 62, 544-549, doi:10.1002/mrm.22036 (2009).
7. Wirtz, S., Neufert, C., Weigmann, B. & Neurath, M. F. Chemically induced mouse models of intestinal inflammation. Nat Protoc 2, 541-546, doi:10.1038/nprot.2007.41 (2007).
8. Sveinsson, B., Chaudhari, A. S., Gold, G. E. & Hargreaves, B. A. A simple analytic method for estimating T2 in the knee from DESS. Magn Reson Imaging 38, 63-70, doi:10.1016/j.mri.2016.12.018 (2017).

Poster Presentation

Disclosures: The authors have disclosed no financial interest.

514-Development of genetically engineered reporters to noninvasively detect protease activity in vertebrate animals

Presenter: Asish Ninan Chacko, University of California, Santa Barbara

Asish Ninan Chacko

University of California, Santa Barbara

Proteases modulate the function and abundance of target proteins by cleaving them in defined amino acid sites. In doing so, proteases regulate a variety of physiological and pathological processes [1] ranging from apoptosis [2] and cell differentiation [3] to tumor invasion [4] and neural degeneration [5]. A rich toolbox of sensors has been developed for monitoring protease activity in live cells using genetically encoded fluorescent and bioluminescent reporters [6]. However, these techniques are limited only to optically accessible preparations because of the poor penetration of light through deep, scattering tissue. Consequently, we lack technologies for probing protease activity in a preclinical context, i.e., in living animals. We address this challenge by developing genetically encoded reporters to detect, localize, and monitor protease activity with magnetic resonance imaging (MRI). These reporters are based on water channels known as aquaporins [7], which our lab has previously introduced as a sensitive, metal-free class of MRI-detectable reporter genes that generate contrast by altering the rate of water exchange across the cell membrane. Our general approach is based on engineering aquaporins by fusing peptide-based degradation tags, which may be conditionally removed using protease-based cleavage. This approach allows us to modulate the abundance and membrane localization of aquaporins based on protease activity, thereby providing us with a mechanism to image proteases with diffusion-weighted MRI diffusion-weighted MR. Initial proof-of-concept experiments are focused on establishing the proposed technique by imaging the activity of a model protease (tobacco etch virus protease) in mammalian cell lines. Building on this groundwork, we will extend this approach to monitor biologically relevant proteases (including caspases, furins, and FAP). Finally, we will demonstrate the *in vivo* applicability of this technique by showing that we can use our genetic sensors to image protease activity in animal models of tumor growth.

Reference

1. Klein, T.; Eckhard, U.; Dufour, A.; Solis, N.; Overall, C. M. Proteolytic Cleavage—Mechanisms, Function, and "Omic" Approaches for a Near-Ubiquitous Posttranslational Modification. Chemical Reviews 2017, 118 (3), 1137–1168. https://doi.org/10.1021/acs.chemrev.7b00120.
2. Zhivotovsky, B.; Burgess, D. H.; Orrenius, S. Proteases in Apoptosis. Experientia 1996, 52 (10-11), 968–978. https://doi.org/10.1007/bf01920106.
3. Mitschke, J.; Burk, U. C.; Reinheckel, T. The Role of Proteases in Epithelial-To-Mesenchymal Cell Transitions in Cancer. Cancer and Metastasis Reviews 2019, 38 (3), 431–444. https://doi.org/10.1007/s10555-019-09808-2.
4. Kolkhorst, V.; Stürzebecher, J.; Wiederanders, B. Inhibition of Tumour Cell Invasion by Protease Inhibitors: Correlation with the Protease Profile. Journal of Cancer Research and Clinical Oncology 1998, 124 (11), 598–606. https://doi.org/10.1007/s004320050221.
5. Bai, G.; Pfaff, S. L. Protease Regulation: The Yin and Yang of Neural Development and Disease. Neuron 2011, 72 (1), 9–21. https://doi.org/10.1016/j.neuron.2011.09.012.
6. Fernández-Fernández, Á. D.; Van der Hoorn, R. A. L.; Gevaert, K.; Van Breusegem, F.; Stael, S. Caught Green-Handed: Methods for in Vivo Detection and Visualization of Protease Activity. Journal of Experimental Botany 2019, 70 (7), 2125–2141. https://doi.org/10.1093/jxb/erz076.
7. Mukherjee, A.; Wu, D.; Davis, H. C.; Shapiro, M. G. Non-Invasive Imaging Using Reporter Genes Altering Cellular Water Permeability. Nature Communications 2016, 7 (1), 13891. https://doi.org/10.1038/ncomms13891.

Poster Presentation

Disclosures: The authors have disclosed no financial interest.

515-Light-sheet microscopy Imaging of cardiac organoids with beating pattern analysis.

Presenter: Aniwat Juhong, Michigan State University

Aniwat Juhong[1], Bo Li[2], Brett Volmert[2], Xiang Liu[2], Yonatan Lewis-Israeli[3], Cheng-you Yao, Wen Li[3], Aitor Aguirre[2], Wibool Piyawattanametha[4], Zhen Qiu[2]

[1]*Michigan State University, East Lansing*
[2]*Michigan State University, East Lansing, MI*
[3]*Michigan State University, East Lansing, Michigan*
[4]*King Mongkut's Institute of Technology Ladkrabang, Bangkok, Bangkok, Thailand*

We demonstrate a custom-made light-sheet microscope based on tunable structured illumination (SI) frequencies [1] for cardiac organoid imaging [2]. The tunable SI is created by a grating light valve (GLV), which is a reflective, high-speed 1D spatial light modulator capable of switching at hundreds of kHz. The pattern switching mechanism of the GLV is sufficiently fast to support the camera-limited frame rate. By using this approach, we can fully leverage a high-speed camera to acquire fluorescence images without sacrificing resolution. Moreover, the system is capable of cylindrically focusing a laser beam suitable for manipulating the light-sheet beam. We show that a fluorescence cardiac organoid image with cellular resolution can be acquired by our custom-made light-sheet microscope. In addition, we implement three image processing algorithms to help characterize the beating patterns of the sequential cardiac organoids' images. The first algorithm is based on image segmentation employed to evaluate overall beating patterns. The segmented area is changed following organoids' beating. The second algorithm is the Lucas-Kanade function optical flow [3]. The algorithm is used to determine the vector field of the localized beating characterization of the organoid. Lastly, the third algorithm is the Farneback function [4] optical flow utilized for single cell/particle tracking enabling parametric array tracking such as the trajectory, velocity, acceleration, and distance of a moving cell of the cardiac organoid.

Reference

1. Landry, Joseph R., et al. "Tunable structured illumination light sheet microscopy for background rejection and imaging depth in minimally processed tissues." Journal of biomedical optics 24.4 (2019): 046501.
2. Lewis-Israeli, Yonatan R., Aaron H. Wasserman, Mitchell A. Gabalski, Brett D. Volmert, Yixuan Ming, Kristen A. Ball, Weiyang Yang et al. "Self-assembling human heart organoids for the modeling of cardiac development and congenital heart disease." Nature communications 12, no. 1 (2021): 1-16.
3. Baker, Simon, and Iain Matthews. "Lucas-kanade 20 years on: A unifying framework." International journal of computer vision 56.3 (2004): 221-255.
4. Farnebäck, Gunnar. "Two-frame motion estimation based on polynomial expansion." Scandinavian conference on Image analysis. Springer, Berlin, Heidelberg, 2003.

Poster Presentation

Disclosures: The authors have disclosed no financial interest.

516-Site-selective imaging of carbonylation in live cells and tissues using novel small molecule-clickable fluorescent probes

Presenter: Ozlem Dilek, University of the District of Columbia

Ozlem Dilek[1], Akeem Franklyn[2], Talejha Shirley[2], Julio Argueta[3], Moshe Levi[4]

[1]*University of the District of Columbia, Washington, DC*
[2]*University of the District of Columbia, Washington, District of Columbia*
[3]*Washington, District of Columbia*
[4]*Georgetown University, Washington, District of Columbia*

Carbonylation is a process which indicates the reactive carbonyl groups present in biomolecules due to oxidative reactions induced by reactive oxygen species. Carbonylated proteins, lipids and nucleic acids have been intensively studied and often associated with onset or progression of oxidative stress related diseases--including fibrosis, cardiovascular disease, diabetes, Alzheimer's disease, neuroinflammation and cancer.[1] Tumor tissues and cancer cells are critically known to have higher ROS levels compared to surrounding healthy tissue but ROS-induced specific protein carbonylation and its unique role in cancer progression/suppression are poorly understood.[2,3] To understand underlying carbonylation pathways and biological relevance, it is essential to design site-selective clickable fluorescent probes[4] to image carbonylation system. Newly designed probes should have certain chemical and photophysical characteristics for successful imaging: high stability, less toxicity, fast kinetics, good spectral properties such as large Stokes shifts, reasonable quantum yields, red or blue shift on absorption and emission spectra. In this work, we highlighted designing of novel small molecule probes[5] for targeting carbonyl moieties in live cells using a click reaction to produce a fluorescent product. Organic synthesis, spectroscopic and confocal microscopy methods were performed. Our results showed that newly synthesized probes can selectively image and differentiate the exogenous and endogenous ROS induced carbonylation profile in different renal cancer cell lines. Use of a click chemistry method to monitor carbonylation with a fluorescent probe has proven itself to be superior in satisfying many criteria (e.g., biocompatibility, selectivity, simplicity, yield, stability, and so forth); our results will therefore provide a powerful simple probe technology that can image carbonyl moieties in biological systems. As such, these agents have great potential to overcome some limitations of conventional optical imaging including the reduction of background signal derived from autofluorescence or the enhancement of tissues that are deep to the skin.Therefore, our small molecule-clickable probe design strategy will allow clinicians to solve long-term diagnostics challenges for future biomedical imaging applications.

Reference

1. Betteridge, what is oxidative stress? Metabolism. 2000, 49 (2), 3–8. B.
2. Halliwell, Oxidative stress and cancer: have we moved forward? Biochemical Journal. 2007, 401 (1), 1–11.
3. R. Ahmad, A.K. Tripathi, P. Tripathi, S. Singh, R.K. Singh, Malondialdehyde and protein carbonyl as biomarkers for oxidative stress and disease progression in patients with chronic myeloid leukemia, In Vivo. 2008, 22
4. Mukherjee K., Chio I.T., Sackett L. D., Bane SL. Detection of oxidative stress-induced carbonylation in live mammalian cells. Free Radic Biol Med. 2015 Jul 20; 84:11-21.
5. Erkan H. Dilek O. et al., Sci. Rep, 2020, 10, 7668.

Poster Presentation

Disclosures: The authors have disclosed no financial interest.

517-Evaluation of the benefits of a PET imaging-guided apelin-based therapeutic strategy of a preclinical model of stroke

Presenter: Tatiana Geara, CERIMED Aix-Marseille Université

Tatiana Geara[1], Oriane Nachar[2], Nicolas Hugues[2], Adrien Chabert[2], Béatrice Louis[3], Laure Balasse[4], Vincent Nail[2], Ahlem Bouhlel[2], Anaïs Moyon[5], Jerome LAURIN[5], Françoise Dignat-George[5], Philippe Garrigue, Benjamin Guillet

[1]*CERIMED Aix-Marseille Université, Marseille, France*
[2]*CERIMED Aix-Marseille Université, France*
[3]*Aix-Marseille University, Marseille Cedex 07, France*
[4]*Aix-Marseille University, Marseille, France*
[5]*CERIMED Aix-Marseille Université*

Aim/Introduction:
Ischemic stroke is a major cerebrovascular disease usually resulting in death or disability among the aging population. [1] Recent literature reported that administration of apelin-13 during the hyperacute phase of ischemia/reperfusion induces early neuroprotective effects by reducing neuronal death and the volume of the infarction. Different doses and different routes of administration are reported.[2] Mid- or late-term benefits have not been evaluated. Our team previously developed a PET radiotracer, [^{68}Ga]Ga-AP747, for evaluating the tissue expression of apelin receptor (so-called APJ receptor). [^{68}Ga]Ga-AP747 microPET/CT exhibited a massive and sustained overexpression of APJ in the ischemic hemisphere starting from day 2 up to day 8 after cerebral ischemia in rats and a negative prognostic value on later neurocognitive recuperation on day 17. Considering the overexpression window of APJ and postulating that APJ was overexpressed in response of a lack of endogenous apelin-13, this study aimed at investigating the effect of two therapeutic strategies based on the repeated exogenous supplementation with apelin-13 in a rat model of transient focal cerebral ischemia.

Materials and Methods:
A 60-min middle cerebral artery occlusion (tMCAO) was induced in middle-aged female Sprague Dawley rats (6-8 months, 300-400 grams) followed by reperfusion.[3] Animals were divided into sham, non-treated MCAO, and two different apelin-treated groups (3-day or 10-day treatment). Apelin-13 (ap13) (50µg/kg;1µg/µL) was daily injected into the tail vein 5 min after reperfusion.
Blood brain barrier (BBB) permeability, APJ receptor expression, and angiogenesis were respectively evaluated and quantified by [^{99m}Tc]Tc-DTPA microSPECT/CT on days 2 and 8 post-MCAO (29.2 ± 1.3 MBq/200ml, IV, 30 min after injection), [^{68}Ga]Ga-AP747 microPET/CT on days 3 and 5 respectively for the apelin-treated groups 3-days and 10-days (11.60 ± 0.41 MBq /200µL, IV, 120 min after injection) under 2% isoflurane anesthesia. Cerebral metabolism and viability were assessed through [^{18}F]-FDG microPET/CT on day 17 post-MCAO (13.04 ± 0.70 MBq/100µL, IV, 45 min after injection). Quantitative region-of-interest (ROI) analysis of the PET and SPECT images was performed using VivoQuant software with the help of a rat brain atlas.[4] Activity inside each ROI was quantified in cortex, hippocampus and caudate putamen and expressed as ipsilateral-to-contralateral (i/c) ratios.
Neurological function was graded using the modified neurological severity score (mNSS). Novel Object Recognition test (NOR) was used to evaluate cognitive recovery.[5]

Results: Scoring with mNSS confirmed the intensity of cerebral ischemia repercussion on neuromotor function on day 1 ($mNSS_{ap13\text{-}3d}$=11±1.8; $mNSS_{ap13\text{-}10d}$=10±1.4; $mNSS_{MCAO}$=11.2±2.1). On days 7 and 14, ap13-3days treated group showed an improved recovery compared MCAO group ($mNSS_{day7}$=5.2±2.4; $mNSS_{day14}$=2.6±1.60; $*p_{day7}=0.2933$, $*p_{day14}=0.0132$, n=9).
The permeability of BBB decreased on day 2 and 8 comparing treated groups to MCAO group
[^{68}Ga]Ga-AP747 on days 3 and 5 showed a decreased signal in ap13-3d, significant in ap13-10d, compared to MCAO group.
Moreover, ap13 treatment has a significant protective effect on cerebral perfusion and cell viability at day 17 compared to MCAO group.
Ap13-3d group revealed an increased discrimination index on day 16 compared to that of MCAO group.

Radiotracer	[^{99m}Tc]Tc-DTPA			[^{68}Ga]Ga-AP747				[^{99m}Tc]Tc-DTPA			[^{18}F]-FDG		
Day	2			3		5		8			17		
Group	MCAO	ap13-3d	ap13-10d	MCAO	ap13-3d	MCAO	ap13-10d	MCAO	ap13-3d	ap13-10d	MCAO	ap13-3d	ap13-10d
Mean i/c signal	1.52	1.28	1.24	4,77	2,68	3.18	1.72	1.50	1.26	1.15	0.85	0.93	0.96
±SD	0,23	0.21	0.11	2,62	1,83	1.66	0.68	0.34	0.19	0.13	0.09	0.07	0.08
p-value$^{(1)}$		*$*p=0.0342$*	*$**p=0.0169$*		*$p=0.0507$*		*$*p=0.0443$*		*$*p=0.0456$*	*$**p=0.0023$*		$*p$=0.0463	$*p$=0.0145
n	9	9	8	14	9	9	8	9	9	8	14	9	8

$^{(1)}$ compared to MCAO group

Conclusion:
The decreased [^{68}Ga]Ga-AP747 microPET/CT signal at day5 post-MCAO, after ap13 treatment, highlights the imaging predictive potential of the expression of the APJ receptor. This study provides valuable data showing beneficial neuroprotective effects of a novel innovative therapeutic strategy based on daily repeated IV injections of apelin-13 for post-stroke recovery, guided by [^{68}Ga]Ga-AP747 microPET/CT of APJ overexpression.

Reference

1. doi:10.1016/S1474-4422(19)30415-6
2. doi:10.1016/j.jchemneu.2020.101886
3. doi:10.1097/ALN.0b013e3181a1fe68
4. Luc Zimmer and al.© Copyright CERMEP Imagerie du vivant, 2012-2017. V2.0
5. doi:10.1016/j.hest.2020.09.001

Poster Presentation

Disclosures: The authors have disclosed no financial interest.

518-An in Vitro Study for Improving Transplanted Pancreatic Islet's Viability and Functionality

Presenter: Everett Baxter, Michigan State University

Everett Baxter[1], Assaf Gilad[2], Erik Shapiro[2], Christiane Mallett[2]

[1]*Michigan State University, East Lansing*
[2]*Michigan State University, East Lansing, MI*

Background:
9.5% of the global population are Type 1 Diabetic (T1D) and struggle to maintain glycemic control4,5. Due to how severe these hyperglycemic and hypoglycemic conditions can be, an innovative strategy known as pancreatic islet transplantation (islets) from the pancreas was utilized to circumvent these complications 6. Transplanted islets usage is needed for a small subset of Type 1 Diabetics and occurs only so often 8. To support and monitor the viability of these islets, a chemical from the indigenous Ayahuasca plant called harmine has been shown to promote cell division in HEK293 cells7. Our approach is to use harmine as a substrate that can be transported by a genetically modified Organic Anion Transporter Polypeptide (OATP1B3) to rejuvenate these islet pancreatic beta cells by inhibiting dual-specificity tyrosine phosphorylation-regulated kinase 1a (dyrk1a) inhibitor (Figure 1) 2. Dyrk1a phosphorylates Nuclear Factor Activated T cells c1(NFATc1), which prevents translocation to the nucleus to initiate the transcription of different cyclin dependent kinases 3. In addition, OATP1B3 is also known to transport MRI contrast agent Gd-EOB-DTPA (EOVIST), this can be helpful for tracking the fate of the transplanted cells 1. Not enough harmine can penetrate the cells without a transporter. To improve uptake of harmine, human oatp1b3 transporters are used to increase the uptake of harmine. Therefore, we hypothesize that mutated OATP1B3 mediated cellular uptake of Harmine allows for model HEK293 cells to increase viability further and functionality.

Methods:
To create the Wild Type transporter, the SLCO1B3 gene was cloned into pcDNA3.1 vector using NEBuilder 2X HIFI Assembly. After assembly with confirmation from colony PCR (using NEBuilder Quick Load Taq Polymerase) purified plasmids were then sequenced at the Azenta company. Mutations made in the SLCO1B3 gene were done via random mutagenesis (Aligent GeneMorph ii Random Mutagenesis kit), then used similar cloning methods to assemble mutants/vectors together. Furthermore, assembled mutants were then sequenced. Wild Type (WT) OATP1B3 plasmid were then transiently transfected in HEK293 cells using lipofectamine 3000 kit. To validate expression of the WT OATP1B3 transporter, Indocyanine Green (ICG) was induced in HEK293 cells with 0.1uM of ICG for 5 mins versus a control and negative control group. Analysis was done via SPARK TECAN plate reader and Cytation 5 microscope. To validate Transport of harmine, 0.1 uM of harmine was added to negative control, mutant OATP1B3, and WT OATP1B3. A Student's T Test was used for analysis of significance after using Cytation 5 microscope and SPARK Tecan fluorescent plate reader for validating uptake assay.

Results:
Wild Type OATP1B3 was successfully cloned into pcDNA3.1 backbone and shown at expected base pairs of 2kb with no mutations (Figure 2). Wild Type OATP1B3 plasmids were able to transport 0.1uM of ICG 24 hours post lipofectamine 3000 transfection with wells compared to negative control (no OATP1B3 plasmids with ICG) (Figure 1).

Discussion:
Subsequent re-translocation of NFATc1 due to dephosphorylation is expected to increase the cell's viability and functionality. Based on the

results, it is possible that using a WT OATP1B3 will allow for the use of harmine in treating T1D however, there is still a need for Improving the conditions of random mutagenesis to create next generation mutants. Our next goal is creating more mutants of OATP1B3 gene reporters that can track the viability of HEK293 cells. Once viability is checked in HEK293 cells, a similar process will soon to be completed in RINm5f insulinoma cells.

Reference

1. Nystrom, N. N.; Hamilton, A. M.; Xia, W.; Liu, S.; Scholl, T. J.; Ronald, J. A., Longitudinal Visualization of Viable Cancer Cell Intratumoral Distribution in Mouse Models Using Oatp1a1-Enhanced Magnetic Resonance Imaging. Invest Radiol 2019, 54 (5), 302-311.
2. Patrick, P. S.; Hammersley, J.; Loizou, L.; Kettunen, M. I.; Rodrigues, T. B.; Hu, D. E.; Tee, S. S.; Hesketh, R.; Lyons, S. K.; Soloviev, D.; Lewis, D. Y.; Aime, S.; Fulton, S. M.; Brindle, K. M., Dual-modality gene reporter for in vivo imaging. Proc Natl Acad Sci U S A 2014, 111 (1), 415-20.
3. Gwack, Y. et al., A genome-wide Drosophila RNAi screen identifies DYRK-family kinases as regulators of NFAT. National Library of Medicine National Center for Biotechnology Information. 2006, https://doi.org/10.1038/nature04631
4. Mobasseri, M. et al., Prevalence and incidence of type 1 diabetes in the world: a systematic review and meta-analysis. Health Promotion Perspectives. 2020; 10(2): 98–115. Published online 2020 Mar 30. doi: 10.34172/hpp.2020.18
5. Rickels, M.; Robertson, P., Pancreatic Islet Transplantation in Humans: Recent Progress and Future Directions. Endocrine Reviews, Volume 40, Issue 2, April 2019, Pages 631–668, https://doi.org/10.1210/er.2018-00154
6. Edmond, R et al., Five-Year Follow-Up After Clinical Islet Transplantation. Diabetes 2005;54(7):2060–2069 https://doi.org/10.2337/diabetes.54.7.2060
7. Wang et al., A high-throughput chemical screen reveals that harmine mediated inhibition of DYRK1A increases human pancreatic beta cell replication. Nature Medicine, Volume 21, number 4, April 2015.
8. Bruni et al., Islet cell Transplantation for the treatment of type 1 diabetes: recent advances and future challenges. Diabetes Metab Syndr Obes. 2014; 7: 211–223. Published 2014 Jun 23. DOI: 10.2147/DMSO.S50789

Poster Presentation

Disclosures: The authors would like to disclose that FDG has been approved.

519-Immune-Cell-Mediated Tumor Targeting Mechanism with NIR-II Fluorescence Imaging

Presenter: Homan Kang, Massachusetts General Hospital

Homan Kang[1], Hak Soo Choi[2]
[1]*Massachusetts General Hospital, Boston, Massachusetts*
[2]*Massachusetts General Hospital, Boston, MA*

Objective:
The strategy of structure-inherent tumor targeting (SITT) with cyanine-based fluorophores is getting more attention because no chemical conjugation of targeting moieties is required. However, the targeting mechanism behind SITT has not yet been well explained. Here, we demonstrate that heptamethine cyanine-based fluorophores possess not only targetability of tumor microenvironments without the need for additional targeting ligands but also NIR-II imaging capabilities.

Methods:
The TAIC-mediated tumor targeting mechanism was confirmed by flow cytometry and histological studies, *in vivo* NIR-II fluorescence imaging, and 3D tomographic imaging.

Results:
Among the tested, the NIR-II capability of SH1 allows for deep tissue imaging *in vivo* such as bone marrow, cerebral vasculature, and blood vessels in tumors with improved resolution. With TAIC-mediated tumor-targeting, SH1 provided diverse tumor targetability with a high tumor-to-background ratio (TBR) ranging from 9.5 to 47 in pancreatic, breast, and lung cancer mouse models upon a single bolus intravenous injection. Using the state-of-the-art TriFoil InSyTe FLECT/CT imaging device, the fate of SH1 could be followed in real-time in full 3D in tumor-bearing animal models.

Conclusion:
In this study, inspired by our recent success in the development of organ- or disease-specific fluorophores, we designed and synthesized TAIC-targeted fluorophore SH1 as a SITT agent for intraoperative NIR-II fluorescence imaging. The NIR-II capability of SH1 along with the InGaAs camera built-in NIR-II imaging system greatly facilitated image quality permitting the observation of signals in deep tissues and significantly improved the sensitivity in intraoperative cancer surgery. The SH1 fluorophore can reach a high TBR (9 to 47 in various cancer types) in tumor sites in comparison with healthy tissue. Furthermore, SH1 can also be used to detect small lesions such as metastatic tumors. Thus, SH1 presents itself as a promising cancer-targeting agent which will have a bright future in intraoperative optical imaging.

Poster Presentation

Disclosures: The authors have disclosed no financial interest.

520-Targeting Tumor Heterogeneity with Multi-RTK Clicking Antibodies

Presenter: Sandeep Surendra Panikar, Washington University School of Medicine

Sandeep Surendra Panikar[1], Nai C. Keltee[2], Patricia M. Ribeiro Pereira[3]

[1]*Washington University School of Medicine, St. Luois*
[2]*Washington University School of Medicine, St. Louis, Missouri*
[3]*Washington University in St. Louis*

Objective:
Dysregulated surface availability of Receptor Tyrosine Kinases (RTKs), co-activation mechanisms, and other biological aspects[1,2-3] result in a heterogeneous response of tumors to targeted therapies. Previous studies have shown that RTK-targeted positron emission tomography (PET) annotates changes in RTK membrane dynamics and protein expression that inform tumor response to targeted therapies[4]. Here our study is focused on modifying FDA-approved antibodies [Herceptin (Trast: Anti-HER2), Perjeta (Per: Anti-HER2), Vectibix (Pan: Anti-EGFR)] to develop a strategy for targeting multi-RTK in preclinical models that resemble clinical tumor heterogeneity. We have developed antibody pairs that click at the surface of RTK-expressing tumors and allow measuring dynamic processes of RTK heterogeneous expression and co-activation during tumor response to targeted therapies.

Methods:
Bioconjugation: Anti-RTK antibodies (Trast, Pan, Per) were conjugated with the clickable moieties Trans-Cyclooctene (TCO) or Tetrazine (Tz) through conjugation of the primary amino groups of antibodies with NHS esters of TCO or Tz. The ratio of TCO or Tz to antibodies was optimized to maintain click efficiency and antibody specificity. Immunofluorescence and Endocytic Trafficking: Anti-RTK antibodies were labeled with Alexa488, Alexa594, or pHrodo dyes to monitor cellular localization and internalization of the clicking pairs on cancer cells. Radiolabeling: Anti-RTK-Tz antibodies were conjugated with the DFO chelator and labeled with the positron emitter zirconium-89. PET/CT imaging: [^{89}Zr]Zr-DFO-antibody conjugated with tetrazine was administered at 24 h after tail vein injection of anti-RTK-TCO antibodies targeting single or multi-RTKs. PET/CT images were acquired on a Inveon or Mediso scanner at 48 h post-injection of [^{89}Zr]Zr-DFO-antibody (320 μCi, 80 μg protein, >98% RCP). Animals: Gastric, breast, or epidermoid cancer xenografts (NCIN87, A431, MDA-MB-468, SkBr3) or patient-derived xenografts were subcutaneously inoculated in athymic nude mice.

Results:
Here we show that biorthogonal reactions enable selective and rapid formation of covalent bonds between pairs of antibodies (**Fig1A-B**). The antibody click strategy consists of an anti-HER2 antibody, an anti-EGFR antibody, and the clickable moieties Tz and TCO containing a protein labeling site with varied lengths of polyethylene glycol linkers. Additional binding studies demonstrate that antibody specificity is maintained after antibody modification with clickable moieties. Antibody click pairs co-localize at the surface of cancer cells within the first 24 h and are efficiently internalized between 48 to 72 h (**Suppl Fig1A**). Additional assays using the pHrodo dye that fluoresces only upon internalization demonstrate effective antibody internalization at 48 h after incubation (**Suppl Fig1B**). Antibody-clicking pairs targeting multi-RTKs result in a ~2.5-fold increase in tumor binding when compared with antibody pairs targeting a single RTK (p=0.001) (**Suppl Fig1C**). Together, our preclinical studies provide proof of concept for a novel approach to increase antibody targeting and accumulation in heterogeneous cancers.

Conclusions:
This study demonstrates a strategy for targeting tumor heterogeneity by using biorthogonal click chemistry. We show that antibody clicking pairs simultaneously targeting EGFR and HER2 receptors enhance antibody accumulation when compared with targeting a single RTK. Ongoing work in our laboratory is now exploring the use of antibody-clicking pairs in multiplex bioimaging and to improve the treatment of a wide field of heterogeneous cancers (**Suppl Fig1D**).

Reference

1. Chegu, A.; Panikar, S. S.; Pereira, P. M. R., Mini-Review: Antibody-Pet of Receptor Tyrosine Kinase Interplay and Heterogeneity. Nuclear Medicine and Biology 2022, 108-109, 70-75.
2. Pereira, P. M. R.; Mandleywala, K.; Ragupathi, A.; Carter, L. M.; Goos, J. A. C. M.; Janjigian, Y. Y.; Lewis, J. S., Temporal Modulation of Her2 Membrane Availability Increases Pertuzumab Uptake and Pretargeted Molecular Imaging of Gastric Tumors. Journal of Nuclear Medicine 2019, 60, 1569.
3. Pereira, P. M. R.; Sharma, S. K.; Carter, L. M.; Edwards, K. J.; Pourat, J.; Ragupathi, A.; Janjigian, Y. Y.; Durack, J. C.; Lewis, J. S., Caveolin-1 Mediates Cellular Distribution of Her2 and Affects Trastuzumab Binding and Therapeutic Efficacy. Nature Communications 2018, 9, 5137.
4. Pereira, P. M. R., et al., Caveolin-1 Temporal Modulation Enhances Trastuzumab and Trastuzumab-Drug Conjugate Efficacy in Heterogeneous Gastric Cancer. bioRxiv 2021, 2021.07.13.452260. (In press Nature Communications)

Poster Presentation

Disclosures: The authors have disclosed no financial interest.

521-In Vivo Imaging of Cancer Cell- and Vessel-Size to Assess Chemo-Radiation Treatment Response in Pediatric Ependymoma Models

Presenter: Natalie Serkova, University of Colorado Anschutz Medical Campus

Natalie J. Serkova[1], Jenna Steiner[2]

[1]University of Colorado Anschutz Medical Campus, Aurora, CO
[2]University of Colorado, Aurora, CO

Introduction:
Ependymoma (EPN) is an aggressive pediatric brain tumor that contributes significantly to poor overall outcomes in children[1]. The benefits of chemotherapy in pediatric patients with ependymoma have not been defined[2], and EPN treated with surgery and radiation therapy can still recur in 23-66% of patients[3]. Our group has previously established aggressive behaviors of EPN, including high tumor cellularity, cytological anaplasia, high mitotic index, tumor necrosis, and the presence of inflammatory cells such as M2-type myeloid cells[4]. The purpose of this study is to develop and optimize an advanced mpMRI protocol (cell-size, vessel-size and inflammation imaging) to characterize the phenotype and chemo-radiation treatment (CRT) response in an orthotopic mouse of patient-derived xenografts (PDX) of pediatric EPN.

Methods:
Female severely immune deficient (SCID) mice were used for intracranial orthotopical inoculation of disaggregated tumors from pediatric EPN patients (n=22). Once the intracranial tumor reached at least 5 mm^3, the animals were assigned to a placebo and CRT groups (10 Gy radiation plus 30 mg/kg 5-fluorouracil). All radiation treatment was perform of the animal image-guided precision XRAD irradiator, using MRI and CT guided EPN localization. For each MRI session, the animal were inserted into a Bruker 9.4 Tesla BioSpec MRI scanner with a Bruker mouse head array RF cryo-coil. Each session consisted of an mpMRI protocol based on the following optimized sequences:

- high resolution T2w turboRARE (sagittal and axial) for tumor volume
- diffusion weighted imaging (DWI) for tumor necrosis and edema
- selective size imaging using filters via diffusion times (SSIFT)
- vessel size imaging (VSI) (fast T2* during 10 mg/kg iron-oxide ferumoxytol injection)

- quantitative T2maps (qT2) for inflammation (before and 24hr after ferumoxytol injection).

Analytical methodologies included (i) conventional volumetric analysis, apparent diffusion coefficient (ADC) values and T2 relaxation times using ParaVision NEO software; in-house MATLAB simulations to calculate SSIFT iAUC, vessel size imaging (VSI) and density indices (Q) $VSI = 0.424(D/gDcB_0)^{1/2} (DR_2^*/DR_2)^{3/2}$ [mm] and $Q = DR_2/(DR_2^*)^{2/3}$ [$sec^{-1/3}$] The qT2 were repeated 24 hours after SPION injection. This protocol was performed before CRT, immediately after CRT, and two weeks after CRT.

Results:
High-resolution turboRARE T2w-MRI (48 microns in-plane resolution) was able to detect EPN lesion in cerebellum as small as 0.2 mm; the median tumor volumes at the baseline were 21±12 mm^3. They also revealed increased blood vessel densities (0.54±0.12), high SSIFT iAUC (7.1±1.2) indicative for EPN cell size of 14±3 microns, and low ADC values (as low as $0.58x10^{-3}$ mm^2/s) in EPN as compared to the normal cerebellum. The 5-day CRT with 2Gy/day and 30 mg/kg 5-FU resulted in a significant decrease in the tumor volumes (Figure 2), accompanied by the increased ADC values and decreased SSIFT iAUC and cell size two weeks after CRT. Interestingly, the most immediate response, seen on ferumoxytol-enhanced VCI and qT2 (-4 ms median), seen as soon as 2 days after the CRT, was related to a decreased blood vessel density and an increased presence of inflammatory macrophages and microglial cells in irradiated EPN.

Discussion:
Orthotopically implanted PDX EPN xenografts closely mimic histological features, anatomical location and radiological features of the primary tumors. Our advanced mpMRI protocol followed by novel MATLAB algorithm analysis allows for a unique characterization of pediatric EPN as well as assessing the tumor response to a clinically relevant CRT protocol in a mouse model. A significant decrease in vessel size density and an increase in inflammatory cells were seen as soon as 2 days after CRT. The late response (2 weeks post CRT) is characteristic by decreased ADC values and cell size, resulting in significantly decreased tumor volumes.

Reference

1. Merchant TE. Current Clinical Challenges in Childhood Ependymoma: A Focused Review. J Clin Oncol. 2017;35: 2364-2369.
2. Timmermann B, Kortmann RD, Kuhl J, et al. Role of radiotherapy in anaplastic ependymoma in children under age of 3 years: results of the prospective German brain tumor trials HIT-SKK 87 and 92. Radiother Oncol. 2005;77: 278-285.
3. Byer L, Kline CN, Coleman C, Allen IE, Whitaker E, Mueller S. A systematic review and meta-analysis of outcomes in pediatric, recurrent ependymoma. J Neurooncol. 2019;144: 445-452.
4. Pierce AM, Witt DA, Donson AM, et al. Establishment of patient-derived orthotopic xenograft model of 1q+ posterior fossa group A ependymoma. Neuro Oncol. 2019;21: 1540-1551.

Poster Presentation

Disclosures: The authors have disclosed no financial interest.

522-Development of a theranostic agent for image-guided delivery of temozolomide to SSTR2 expressing cells

Presenter: Solmaz AghaAmiri, University of Texas Health Science Center at Houston

Solmaz AghaAmiri[1], Sukhen C. Ghosh[2], Servando Hernandez Vargas[3], Daniel Halperin[3], Ali Azhdarinia[3]

[1]University of Texas Health Science Center at Houston, Houston, TX
[2]McGovern Medical School, Institute of Molecular Medicine, Houston, Texas
[3]University of Texas Health Science Center at Houston, Houston

Objectives:
Temozolomide (TMZ) is a DNA damaging agent that produces high response rates in neuroendocrine tumors (NETs) when the DNA repair enzyme, known as O6-methylguanine DNA methyltransferase (MGMT), is inactivated. When given at high doses, TMZ therapy can exhaust MGMT activity and its associated resistance mechanisms, but also produces dose-limiting toxicities. Since nearly all NETs overexpress the somatostatin receptor subtype 2 (SSTR2), we hypothesized that a receptor-targeted TMZ analog could produce high intratumoral drug concentrations while avoiding systemic toxicity. Accordingly, we converted the clinically approved radiotracer ^{68}Ga-DOTA-TOC into a radiolabeled peptide-drug conjugate (PDC) for SSTR2-targeted delivery of TMZ and report on the utility of the radioactive label for characterizing receptor-binding properties, pharmacokinetics, and tissue biodistribution.

Methods:
The PDC was synthesized by replacing DOTA with a multimodality chelator (MMC) to permit site-specific modification, attaching a modified TMZ analog to the MMC, and conjugating the payload moiety to TOC on solid-phase. The product, tumor-targeted TMZ (ttTMZ), was labeled with $^{67/68}$Ga and evaluated using radioligand assays to determine SSTR2 binding, specificity, and internalization of the drug-receptor complex in cell lines with varying SSTR2 expression. Cytotoxicity and MGMT inhibitory effects of ttTMZ were evaluated in IMR-32 cells (SSTR2+). To investigate SSTR2-targeting *in vivo*, positron emission tomography (PET) was performed 1h after injection of ^{68}Ga-ttTMZ in H69 xenografts in the presence and absence of a blocking agent. To further evaluate specificity and biodistribution at pharmacologically active drug concentrations, we performed a dose-escalation study with ^{67}Ga-ttTMZ in (i) mice bilaterally implanted with HCT116-WT (SSTR2-negative) and HCT116-SSTR2 (transfected, high SSTR2) cells and (ii) mice implanted with IMR-32 cells (endogenous SSTR2). Resected tissues were weighed and gamma counting was performed to quantitatively measure drug biodistribution as injected activity per gram of tissue (%IA/g) at 3h p.i.

Results:
ttTMZ was efficiently produced with chemical and radiochemical purities >90% and >95%, respectively. Cell-based experiments showed that the specific binding of ^{67}Ga-ttTMZ was similar to ^{67}Ga-DOTA-TOC and correlated with SSTR2 expression. In HCT116-SSTR2 cells that highly overexpress SSTR2, 14.8±4.8% of ^{67}Ga-ttTMZ and 17.0±4.2% of ^{67}Ga-DOTA-TOC were taken up by cells. Markedly less accumulation was observed in cell lines with lower SSTR2 expression. SSTR2 selectivity was further demonstrated in blocking studies where tracer binding was reduced by nearly 90% when co-incubated with octreotide. Acid-washing experiments demonstrated internalization of ^{67}Ga-ttTMZ after receptor-binding, indicating retention of agonist properties following chemical modification. Results from the cell cytotoxicity study in IMR-32 cells demonstrated that the PDC inhibited cell growth in a dose-dependent manner that was similar to free TMZ, with the IC50 values of 81.6 and 75.6 μM for free TMZ and ttTMZ, respectively. Western blot analysis showed that ttTMZ reduces MGMT levels in a dose-dependent manner compared to untreated cells. Similar results were seen with fTMZ and O6-Benzylguanine (O6BG)-a well-characterized pseudo-substrate for MGMT. PET imaging in H69

xenografts showed a notable accumulation of ^{68}Ga-ttTMZ in tumors, which was reduced by 1.2-fold in blocking studies. Similar SSTR2 selectivity was seen in the dual implant model as shown by >5-fold higher uptake in the SSTR2-positive tumors compared to SSTR2-negative tumors. The tissue distribution profile of ^{67}Ga-ttTMZ was analogous to ^{68}Ga-DOTA-TOC: high tumor uptake, rapid elimination through the kidneys, and low signal in normal tissues. This pattern was also observed in dose escalation studies and demonstrates the preferential uptake of ttTMZ in tumors in a therapeutic setting.

Conclusion:

We developed a novel drug conjugate that selectively causes toxicity and MGMT depletion in SSTR2-expressing cells. Direct radiolabeling of ttTMZ provided quantitative evidence of SSTR2 mediated binding and biodistribution analysis in animal models. These findings demonstrate the utility of developing a radiolabeled drug conjugate and may guide optimization strategies.

Reference

1. Whalen KA, et al. Targeting the Somatostatin Receptor 2 with the Miniaturized Drug Conjugate, PEN-221: A Potent and Novel Therapeutic for the Treatment of Small Cell Lung Cancer. Mol Cancer Ther. 2019 Nov;18(11):1926-1936. doi: 10.1158/1535-7163.MCT-19-0022. PMID: 31649014. Copy
2. Cho HY, et al. NEO212, temozolomide conjugated to perillyl alcohol, is a novel drug for effective treatment of a broad range of temozolomide-resistant gliomas. Mol Cancer Ther. 2014 Aug;13(8):2004-17. doi: 10.1158/1535-7163.MCT-13-0964. Epub 2014 Jul 3. PMID: 24994771.
3. Hernandez Vargas S, et al. Specific Targeting of Somatostatin Receptor Subtype-2 for Fluorescence-Guided Surgery. Clin Cancer Res. 2019 Jul 15;25(14):4332-4342. doi: 10.1158/1078-0432.CCR-18-3312. Epub 2019 Apr 23. PMID: 31015345; PMCID: PMC6675459.

Poster Presentation

Disclosures: The authors have disclosed no financial interest.

523-Design and characterization of an optimized somatostatin analog for fluorescence-guided surgery

Presenter: Sukhen Ghosh, McGovern Medical School, Institute of Molecular Medicine

Sukhen C. Ghosh[1], Servando Hernandez Vargas[2], Solmaz AghaAmiri[3], Michael P. Luciano[4], Martin J. Schnermann, Ali Azhdarinia[2]

[1]*McGovern Medical School, Institute of Molecular Medicine, Houston, Texas*
[2]*University of Texas Health Science Center at Houston, Houston*
[3]*University of Texas Health Science Center at Houston, Houston, TX*
[4]*National Cancer Institute, Frederick, MD*

Introduction:

Surgical resection is the main treatment for pancreatic neuroendocrine tumors (pNETs) and can be curative if tumors are completely removed. However, the small size of these tumors, presence of multifocal lesions, and lymph node metastases complicate intraoperative localization and margin detection. Fluorescence-guided surgery (FGS) has shown increasing clinical utility for intraoperative visualization of tumors and can increase complete resections while also improving safety by avoiding unnecessary damage to normal tissues [1]. Given the overexpression of the somatostatin receptor subtype 2 (SSTR2) on pNETs, we used the clinically approved radiopharmaceutical ^{68}Ga-DOTA-TOC as the foundation for a first-generation intraoperative imaging agent with excellent tumor-targeting properties but notable non-specific binding [2]. Here, we used the charge-balanced near-infrared fluorescent (NIRF) dye FNIR-Tag [3] to produce a second-generation agent, MMC(FNIR-Tag)-TOC, with superior tumor specificity and contrast.

Methods:

The SSTR2-targeting peptide TOC was conjugated to a multimodality chelator (MMC) on solid-phase. Conjugation of IR800 (negatively charged) or FNIR-Tag (charged balanced) was performed in solution phase *via* copper-free click chemistry, and dual labeling with $^{67/68}$Ga was carried out as previously described (2). Spectral analysis and physicochemical properties were conducted to measure the optical properties and cLogP values of the conjugates. To evaluate the binding properties of MMC(FNIR-Tag)-TOC in cells, we performed flow cytometry (100 nM, 1 h incubation) and radioactive uptake (10 nM, 1 h incubation) studies in the presence or absence of 100-fold competitor (octreotide) and used the IR800 counterpart as a control. We selected HCT116-WT (SSTR2-), HCT116-SSTR2, BON-SSTR2, and NCI-H69 cells based on their varying SSTR2 expression levels. For *in vivo* studies, a dually implanted HCT116-SSTR2/WT xenograft model was injected with 2 nmol of agent per mouse of non-radioactive MMC(IR800)-TOC or MMC(FNIR-Tag)-TOC (n=5/agent) and imaged at 1 and 3 h p.i. Key tissues were resected for *ex vivo* imaging and histological characterization. After euthanasia, 1 mouse was randomly selected from each group for cryo-fluorescence tomography (Emit Imaging).

Results/Discussion:

Both conjugates were synthesized with high chemical (>90% as shown by HPLC) and radiochemical yield (>95% as shown by radioHPLC). Spectral analysis showed that both conjugates have excitation and emission peaks in the NIR region, with MMC(FNIR-Tag)-TOC having a slightly blue-shifted spectra ($\lambda maxem\ \lambda_{max}^{em}$ = 788 nm) compared to MMC(IR800)-TOC ($\lambda maxem\ \lambda_{max}^{em}$ = 795 nm). Both conjugates had the same fluorescence quantum yield (Φ_F) of 0.13 in PBS. Flow cytometry results were largely in agreement with radioligand experiments and showed SSTR2-mediated binding for both agents, along with a significantly higher degree of non-specific binding with the IR800 analog in blocking studies and in cells that lack SSTR2. Dual labeling revealed that the binding characteristics of ^{67}Ga-MMC(FNIR-Tag)-TOC more closely resembled those of ^{67}Ga-DOTA-TOC (positive control) in different SSTR2 expressing cell lines, suggesting that FNIR-Tag is the more favorable fluorescent label for highly specific tumor targeting. This observation was also evident during pharmacokinetic evaluation in mice where we observed notably lower background signal for charge-balanced MMC(FNIR-Tag)-TOC. While the IR800 analog had ~30% higher tumor accumulation, it also exhibited 2 to 4-fold higher off-target binding that ultimately led to higher TBRs for MMC(FNIR-Tag)-TOC. Histological and mesoscopic analyses of FFPE sections further confirmed the *in vivo* and *ex vivo* imaging results.

Conclusions:

Our findings show that dye charge plays an important role in the specific binding of SSTR2-targeted FGS agents. The charge-balanced dye FNIR-Tag led to the development of a novel fluorescent somatostatin analog with remarkably lower background signal and higher tumor specificity than the IR800 counterpart. As a result, we discovered an enhanced approach for targeting SSTR2-expressing tumors that may

enable detection and removal of tumors which may be missed by standard surgical techniques.

Reference

1. Hernot, S., et al., Lancet Oncol., (2019), DOI: 10.1016/S1470-2045(19)30317-1
2. Hernandez Vargas, S., et al., Clin. Cancer Res., (2019), DOI: 10.1158/1078-0432.CCR-18-3312
3. Luciano, M. P., et al., ACS Chem. Biol., (2019), DOI: 10.1021/acschembio.9b00122

Poster Presentation

Disclosures: The authors have disclosed no financial interest.

524-Innovative theranostic agents for PET imaging and treatment of prostate cancer using a single chelator-minibody conjugate

Presenter: Khanh-Van Ho, University of Missouri

Khanh-Van Ho[1], David Tatum[2], Lisa Watkinson[3], Terry Carmack[3], Fang Jia[4], Alessandro Mascioni[5], Darren Magda[6], Carolyn Anderson [7]

[1]University of Missouri, Columbia
[2]Lumiphore, Berkeley, CA
[3]Harry S. Truman Memorial Veterans Hospital, Columbia, MO
[4]ImaginAb, Inglewood, CA
[5]ImaginAb, Inglewood, California
[6]Lumiphore, Berkeley, California
[7]University of Missouri, Columbia, Missouri

Prostate-specific membrane antigen (PSMA) is an exceptional biomarker for prostate cancer, one of the most common malignancies in men. PSMA is expressed on almost all prostatic tumors, and its expression positively correlates with castration resistance and progression to metastatic disease. A small-molecule radioligand therapeutic, Pluvicto®, targets PSMA and has recently been approved by the FDA for previously treated metastatic castration-resistant prostate cancer, but salivary gland toxicity remains a challenge. In the present study, Lumi804, a macrocyclic bifunctional chelator based on four 1-hydroxypyridin-2-one (1,2-HOPO) coordinating units, was conjugated to IAB2MA, a minibody targeting PSMA that does not localize in the salivary glands. The conjugate was radiolabeled with Zr-89 for PET imaging and Lu-177 for targeted radiopharmaceutical therapy of prostate cancer. For both isotopes, quantitative radiolabeling of the Lumi804-IAB2MA conjugate was achieved at ambient temperature in under 30 min at a molar activity of 7.4 MBq/nmol. This is in contrast to ^{177}Lu-DOTA-IAB2MA, where only approximately 60% radiolabeling was achieved at 37 °C. Leveraging Eu(III) as a luminescent surrogate metal ion, the binding affinity of Eu-Lumi804-IAB2MA was measured in PSMA-positive 22RV1 prostate cancer cells by time-resolved luminescence, demonstrating that the high binding affinity of the conjugate to PSMA was retained ($K_d = 1.1 \pm 0.2$ nM). Biodistribution of ^{177}Lu-Lumi804-IAB2MA was determined in PSMA-positive PC3-PIP tumor-bearing mice. Tumor uptake was 8.1 ± 1.4% ID/g at 24 h and slowly decreased by 96 h post-injection (3.9 ± 0.9% ID/g). The ^{177}Lu-minibody cleared the blood after 24 h, with tumor:blood ratios reaching 282 ± 75 at 96 h. Kidney uptake was 4.7 ± 1.0% ID/g at 24 h, clearing to 0.4 ± 0.1% ID/g at 96 h. PET imaging with Zr-89 and targeted radiopharmaceutical therapy with Lu-177 labeled minibody studies are underway. Data thus far suggest Lumi804 is a versatile chelator allowing for one PSMA-targeted chelator-minibody conjugate for labeling with multiple radiometals for imaging and therapy.

Poster Presentation

Disclosures: The authors have disclosed no financial interest.

525-Intra-observer reliability of 99mTc- DMSA planar scintigraphy vs. SPECT/CT imaging in the detection of renal cortical defects.

Presenter: Nsreen RA Mohamadien, Assiut University

Nsreen RA Mohamadien[1], Marwa S Mohamed[2], Mohamed A Mekkaway[2], Waleed A Diab[2]

[1]Assiut University, Egypt
[2]Assiut University, Assiut, Egypt

Background:
Although ^{99m}Tc-dimercaptosuccinic acid (DMSA) planar scintigraphy is the best method for assessing renal cortical scarring, especially in children, the value of single-photon emission computed tomography/computed tomography (SPECT/CT) is unknown.

Aim:
The aim of this study was to detect the intra-reader reliability of ^{99m}Tc-DMSA planar scintigraphy vs. SPECT/CT imaging in patients with suspected renal cortical scars.

Materials and Methods:
This prospective study included patients with clinically suspected renal cortical scars. The 99mTc-DMSA planar images were obtained approximately 3 hours after I.V injection of approximately 185 MBq of the tracer. The SPECT/CT images were taken immediately after the planar one. The images were independently interpreted by an experienced nuclear medicine physician who was blinded to both clinical data and the results of other imaging modalities. Both images were scored as 0; no defects, 1; equivocal, 2; positive defects and the results of both modalities were compared. The reader repeated the reading six months later to assess the intra-reader reliability of both imaging techniques.

Results:
Ninety-three patients (55 males and 38 females, mean age: 31.9 ± 18.5 years) with a total of 186 kidneys were recruited in this study. The first planar readings revealed 42 defects, 27 equivocal and 117 normal kidneys, while the second reading revealed 40 defects, 31 equivocal and 115 normal kidneys. 64 defects and 122 healthy kidneys were found in the first SPECT/CT reading, while the second reading found 63 defects and 123 healthy kidneys. The first and the second planar readings agreed in the reading of 168 kidneys and disagreed in the reading of 18 kidneys with Cohen's kappa value of 0.820 (P<.01) While those of SPECT/CT images agreed in the readings of 173 kidneys and disagreed in the readings of 13 kidneys, with a Cohen's kappa value of 0.850 (P<.01).

Conclusion:
The intra-reader reliability of ^{99m}Tc-DMSA SPECT/CT scanning was superior to that of the conventional planar imaging in detecting renal cortical scars.

Poster Presentation

Disclosures: The authors have disclosed no financial interest.

526-Automated Synthesis of 18F-Fluselenamyl: Novel Amyloid PET Imaging agent for the Detection of Alzheimer's Disease at Earlier Stages

Presenter: sundaram guruswami, Washington University School of Medicine

Sundaram Guruswami[1], Chris Bognar[2], Nerissa Brame-Torrey[3], Tammie Benzinger[4], Michael Nickels[5], Vijay Sharma[6]

[1]*Washington University School of Medicine, Saint Louis*
[2]*Washington University in St. Louis, saint louis, MO*
[3]*Washington University in St. Louis, MO*
[4]*Washington University School of Medicine*
[5]*Washington University School of Medicine, St. Louis, MO*
[6]*Washington University School of Medicine, St. Lous, MO*

Objectives:
Molecularly specific tracers that detect diffuse plaques, a preclinical manifestation of Aβ pathophysiology (included in revised NIAAA criteria) for detecting AD, can provide tools to assess plaque burdens and quantify efficacy of therapeutic interventions in vivo. Currently available clinical agents, such as Avid 45, GE-067, AZD 4694 allow detection of fibrillary amyloid plaques (later stage of Aβ pathophysiology). To further embellish imaging resources and enable disease-specific imaging at earlier stages, we have reported earlier, the preclinical validation of ^{18}F-Fluselenamyl. Herein, we report automated synthesis of ^{18}F-Fluselenamyl under GMP conditions.

Methods:
[^{18}F] Fluselenamyl was synthesized using GE TRACERlab FX2N-1 automated modules (**Fig 1**) under GMP compliance followed by quality analysis using standard Quality Control (QC) procedures. For QC studies, calibration curve was generated with the cold standard (non radiolabeled Fluselenamyl) on the Dionex U-3000 HPLC equipped with an UV absorbance detector (254 nm) using C_{18} column Phenomenex Luna C 18, particle size 5 µm, 250×4.6 mm) that was eluted with a isocratic mobile phase composed of 55% Acetonitrile / 45% Water with 0.1 M ammonium formate over fifteen minutes. [^{18}F] Fluselenamyl was synthesized with high radiochemical yield and purity. The radioactive peak corresponding to the product was detected approximately 17 minutes after injection into semi preparative C_{18} column eluted with a mobile phase of Acetonitrile/ 0.1 Ammonium Formate Buffer (3/ 2) flowing at a rate of 3.0 mL/min. The total preparation time for the tracer was approximately 80 minutes, with a radiochemical yield of 19-20% (n=3). The radiochemical purity is 100 %. Further QC analysis, confirmed the peak of interest corresponding to the [^{18}F] Fluselenamyl was detected at 11 min that matched with the retention time of the cold standard with 100% radiochemical purity and high specific activity.

Conclusion:
Fluselenamyl is currently undergoing regulatory approvals for human studies. This methodology (described herein using GE-TRACElab FX2N-1 module for its production under GMP conditions) will be used for production of clinical doses needed for performing first-in-human studies.

Poster Presentation

Disclosures: The authors have disclosed no financial interest.

527-Imaging Heterogeneous Lung Fibrosis in IPF and COPD using Precision MRI (pMRI) enabled by collagen-targeted Protein Contrast Agent

Presenter: Dongjun Li, Georgia State University

Dongjun Li[1], Oluwatosin Y. Ibhagui[2], Sophia Bamphia[3], Brenda-Ruth N. Mimba[4], Hongwei Han[3], Guangda Peng, Maureen Beebe[5], Jingjuan Qiao[3], Mani Salarian[6], Malvika Sharma, Bin Dong[3], Shanshan Tan[7], Yiting Xu[3], Hua Yang[8], Ganesh Satyanarayana[3], Shenghui Xue[3], Ravi Chakra C. Turaga[3], Yan Hai[3], Yuguang Meng[3], Khan Hekmatyar[3], Xiangming Ji, Zhi-ren Liu[9], Jenny Yang[3]

[1]*Georgia State University, Atlant, GA*
[2]*Georgia State University, atlanta, Georgia*
[3]*Georgia State University, Atlanta, GA*
[4]*Georgia State University, Sugarhill, GA*
[5]*Georgia State University, Canton, GA*
[6]*Yale University, New Haven, CT*
[7]*Johns Hopkins Univeristy, Towson, MD*
[8]*Emory University, Atlanta, GA*
[9]*Biology Department, Atlatna, Georgia*

Chronic lung diseases, such as idiopathic pulmonary fibrosis (IPF) and chronic obstructive pulmonary disease (COPD) are major leading causes of death worldwide with very poor prognosis. Heterogeneous distribution of collagen, mainly type 1 collagen, associated with excessive collagen deposition plays pivotal role in progressive remodeling of the lung parenchyma to chronic exertional dyspnea for both IPF and COPD. To date, there are no noninvasive and quantitative diagnostic tools with sufficient sensitivity to detect early-stage lung fibrosis during disease progression and monitor treatment response. Therefore, to address the pressing need, here we report the development of human collagen-targeted protein MRI contrast agent (hProCA32.collagen) to specifically bind to collagen 1 overexpressed in multiple lung diseases. Here we report that hProCA32. collagen and its surface modification variants all exhibit significantly improved r1 and r2 relaxivity, strong Gd^{3+} binding affinity and metal selectivity. The effect of surface modification on metal binding, collagen binding specificity overall different types of collagen, protein stability, and relaxivity have also examined using various spectroscopic methods. The robust detection of early and late-stage lung fibrosis with stage-dependent MRI SNR increase with good sensitivity and specificity using newly established progressive bleomycin-induced IPF mice model and nicotine-induced COPD mice model. Spatial heterogeneous mapping of usual interstitial pneumonia (UIP) pattern with key features closely mimicking human IPF including cystic clustering, honeycombing and traction bronchiectasis were noninvasively detected by multiple MR imaging techniques and verified by histological correlation. We further report the detection of heterogeneous expression of collagen in lung airway at different stages of an electronic cigarette induced COPD mice model by hProCA32.collagen enabled pMRI, validated by histological analysis. We also demonstrated that surface modification of ProCA32. collagen results in alteration of PK and PD profile in vivo revealed by pMRI and ICP-OES. The developed hProCA32.collagen is expected to have strong translational potential in noninvasive detection and staging of lung diseases and facilitating effective treatment to halt further chronic lung disease progression.

Reference
1. Yang J J et al. Journal of the American Chemical Society, 2008, 130(29):9260-7.
2. Xue, S., et al. Proceedings of the National Academy of Sciences of the United States of America 112.21(2015):6607-12
3. Salarian, Mani, et al." Nature communications 10.1 (2019): 1-14.

Poster Presentation

Disclosures: The authors have disclosed no financial interest.

528-Translational Studies of Silver Sulfide Nanoparticles as a Novel Contrast Agent

Presenter: Katherine Mossburg, University of Pennsylvania

Katherine Mossburg[1], Jessica C. Hsu[1], Sarah Shepherd[1], Yuxi Dong[2], David Issadore[1], Michael Mitchell[1], Andrew Tsourkas[3], David Cormode[3]

[1]University of Pennsylvania
[2]University of Pennsylvania, Philadelphia, Pennsylvania
[3]University of Pennsylvania, Philadelphia, PA

Introduction:
Inorganic nanoparticles have been explored for many biomedical applications, but often fail to be clinically translated due to insufficient clearance or safety. Recent work has identified sub-5 nm silver-sulfide nanoparticles (SSNP) as a promising multimodality imaging contrast agent[1] with improved contrast generation compared with iodinated agents for dual-energy mammography.[2] SSNP may be especially well-suited to diagnostic breast cancer imaging, where supplemental screening methods are needed to overcome limitations of mammography for women with dense breasts. These nanoparticles have been shown to be renally clearable and avoid retention in reticuloendothelial system (RES) organs, indicating that they could have good safety profiles. Because these nanoparticles have potential for clinical use as a contrast agent, translational studies to determine long-term safety and monitor the distribution of SSNP will be necessary. In addition, developing a reproducible and scalable synthetic method will be required.

Methods:
SSNP with an average diameter of 3.4 ± 0.6 nm were synthesized using a polycarbonate staggered herringbone microfluidic chip (Figure A-B)[3]. They were administered intravenously to mice, which were then scanned with a microCT scanner at several timepoints over the next 24 hours to visualize circulation and clearance. Also, within that time frame, blood was collected to evaluate the pharmacokinetics of the SSNP. The mice were monitored and observed for three months after administration of the contrast agent. At 1-, 14-, 28-, and 81-days post-injection, mice were sacrificed, and their organs were collected for analysis of biodistribution of SSNP, clinical blood chemistry, and histology. Additionally, a microfluidic chip of similar design, but made of PDMS, allowing for the synthesis to be scaled up to 256 times the current production rate, was investigated.

Results:
CT scans indicated high contrast soon after injection, followed by rapid clearance, with most visible contrast depleted within one hour (Figure C). During the three-month study, treated mouse weights did not significantly differ from their control counterparts and no behavioral differences were observed (Figure D). Pharmacokinetic data showed a distribution half-life of 12 min, followed by an excretion half-life of 22.8 hours (Figure E). This is consistent with the observations made in the CT scans and indicates that the imaging window will be long enough to be clinically useful. The 3.4 nm SSNP showed high clearance (77% injected dose) initially, but no significant additional clearance at the longer time points (Figure F). As expected, most remaining SSNP were contained to the RES organs. No toxicity was observed in the histological samples or the clinical blood chemistry values (Figure G-H). The PDMS-based microfluidic chip was shown to produce similar nanoparticles to the polycarbonate chip and can be parallelized to produce up to 256 times the current nanoparticle yield (Figure I).

Conclusions:
These studies have indicated high levels of renal clearance and good biocompatibility of SSNP, as well as potential for a substantial scale up in production, resulting in improved chances of clinical translation. Further work will aim to improve long-term clearance and investigate parallelized microfluidic chip production.

Reference
1. Hsu, J. C. et al. An all-in-one nanoparticle (AION) contrast agent for breast cancer screening with DEM-CT-MRI-NIRF imaging. Nanoscale 10, 17236–17248 (2018).
2. Hsu, J. C. et al. Renally excretable and size-tunable silver sulfide nanoparticles for dual-energy mammography or computed tomography. Chem. Mater. 31, 7845–7854 (2019).
3. Hsu, J. C. et al. Effect of Nanoparticle Synthetic Conditions on Ligand Coating Integrity and Subsequent Nano-Biointeractions. Applied Materials & Interfaces. 13, 58401-58410 (2021).

Poster Presentation

Disclosures: The authors have disclosed no financial interest.

529-Role of KDR-Targeted Ultrasound Molecular Imaging in the Characterization of Ovarian Masses: Correlation with Histopathology

Presenter: Neha Antil, Stanford University

Neha Antil[1], Ahmed El Kaffas[2], Ann Folkins[3], Huaijun Wang[4], Teri A Longacre[3], Amelie Lutz[4]

[1]Stanford University, Mountain View, CA
[2]Stanford University, San Jose, CA
[3]Stanford University, Stanford, California
[4]Stanford University, Stanford, CA

Purpose:
To characterize ovarian masses (OMs) on ultrasound molecular imaging (USMI) using a clinical-grade contrast agent (Kinase insert domain receptor [KDR]-targeted contrast microbubble [MB_{KDR}]] that is targeted at the KDR, one of the key regulators of neo-angiogenesis in cancer) and correlate with gold standard surgical histopathology (HPE).

Material and Methods:
USMI was performed in 24 women (age 48 to 79 years) with complex OMs after meeting the eligibility criteria and obtaining informed consent in a HIPAA-compliant IRB-approved study. The complex OM was first identified on B-Mode US and a plane showing a solid component (target lesion) was then selected for further evaluation. While imaging in dual mode with B-mode and contrast mode side-by-side, MB_{KDR} (BR55, Bracco, [0.03, 0.05 and 0.08 mL/kg of body weight]) were manually injected over 10 seconds followed by 10 mL saline flush. Imaging was obtained starting with initial 45 seconds acquisition to capture the wash-in phase of MB_{KDR}, followed by 10 second acquisition every 2 mins until 30 minutes post injection. Blood pressure, ECG, oxygen levels, heart rate, CBC, and metabolic panel were obtained before and after MB_{KDR}administration. Surgery for these OMs were performed within a 2-week interval following imaging. Tumor regions overlying the imaged target lesions were marked by the surgeon for

accurate correlation on histology. Qualitative and Quantitative USMI analysis was performed by two radiologists in consensus with 9 and 15 years of experience, who were blinded to final HPE diagnosis. Both radiologists visually assessed the presence of focal enhancement and graded into three-grade visual scale: strong (well-defined and strong visual stationary targeted imaging signal), weak (enhancement is weak but considered stationary), or no enhancement (no focal stationary targeted imaging signal). For quantitative USMI analysis, ROI was drawn over the target lesion and mean contrast signal intensity was calculated and recorded using the in-house built software (ITK-SNAP). USMI analysis was then correlated with HPE results.

Results:

Twenty two out of 24 (92%) lesions were confirmed in the ovaries on surgical HPE. 2/24 (8%) lesions were intraoperatively found outside the ovaries (leiomyoma and hematosalpinx) and, therefore, were excluded from the analysis. 13/22 (59%) lesions were malignant with a mean size of 5.38 cm (range, 1.2 to 10.0 cm); while 1 of the malignant lesions was a metastasis from a neuroendocrine GI tumor. 9/22 (41%) lesions were benign with a mean size of 1.86 cm (range, 0.7 to 3.7cm). Overall, Qualitative USMI analysis showed a sensitivity of 76.92% (10/13), specificity of 77.78% (7/9), PPV of 83.33% (10/12) and NPV of 70% (7/10), while quantitative USMI analysis showed a sensitivity of 100% (13/13), specificity of 88.89% (8/9), PPV of 92.85% (13/14) and NPV of 100% (8/8), when compared to gold standard HPE. None of the malignant lesions was miscategorized as a benign lesion.

Conclusion:

KDR-targeted USMI quantitative analysis shows promising results that allow non-invasive accurate characterization of ovarian masses. Larger studies are needed for further validation.

Reference

1. Neha Antil, Amelie Lutz. Ovarian cancer-Current Status of Blood Biomarker and imaging Screening strategies. Medical Research Archives 2020, 8; 2375-1924.
2. Willmann JK, Bonomo L, Testa AC, Rinaldi P, Rindi G, Valluru KS, et al. Ultrasound molecular imaging with BR55 in patients with breast & ovarian lesions: First-in-human results. J Clin Oncol. 2017;35(19):2133–40.
3. Lutz AM, Bachawal S V., Drescher CW, Pysz MA, Willmann JK, Gambhir SS. Ultrasound molecular imaging in a human CD276 expression-modulated murine ovarian cancer model. Clin Cancer Res. 2014;20(5):1313–22.
4. Lutz AM, Willmann JK, Drescher CW, Ray P, Cochran F V., Urban N, et al. Early diagnosis of ovarian carcinoma: Is a solution in sight. Radiology. 2011;259(2):329–45.
5. Willmann JK, Lutz AM, Paulmurugan R, Patel MR, Chu P, Rosenberg J, et al. Dual-targeted contrast agent for US assessment of tumor angiogenesis in vivo. Radiology. 2008;248(3):936–44.
6. Lutz AM, Willmann JK, Cochran F V., Ray P, Gambhir SS. Cancer screening: A mathematical model relating secreted blood biomarker levels to tumor sizes. PLoS Med. 2008;5(8):1287–97.
7. Willmann JK, Cheng Z, Davis C, Lutz AM, Schipper ML, Nielsen CH, et al. Targeted microbubbles for imaging tumor angiogenesis: assessment of whole-body biodistribution with dynamic micro-pet in Mice. Radiology. 2008;249(1):212–9.

Poster Presentation

Disclosures: The authors have disclosed no financial interest.

530-Photodynamic therapy based on Ce6-loaded PVCL nanoparticles inhibits tumor growth

Presenter: Judit Morla-Folch, Icahn School of Medicine at Mount Sinai

Judit Morla-Folch[1], Jingxing Shao[2], Jianhong Wang[2], Jessica Chimene[3], Tomas Post[4], William Wang[3], Willem Mulder[3], Jan van Hest[2], Abraham J. Teunissen[3]

[1]*Icahn School of Medicine at Mount Sinai, New York*
[2]*Eindhoven University of Technology, Eindhoven, Netherlands*
[3]*Icahn School of Medicine at Mount Sinai, New York, NY*
[4]*Radboud University, Nijmegen, Netherlands*

Photodynamic Therapy (PDT) is a minimally invasive clinical treatment that is approved by both the Food and Drug Administration and by the European Medicine Agency as curative therapy for precancer lesions and solid tumors and as palliative therapy for advanced malignancies.[1] PDT is based on a photosensitizer (PS), light, and molecular oxygen. Exciting a PS using (laser) light stimulates its reaction with the surrounding O_2 to produce various reactive oxygen species (ROS). PDT-generated ROS subsequently damage tumor cells and induce inflammation evoking strong immunological response.[2] Recently, PDT has been combined with immunotherapy (e.g., CTLA-4 and PD-L1 immune check-point inhibitors) showing that PDT stimulates immune responses by promoting tumor antigen presentation, thus increasing the response rates to checkpoint blockade antibodies.[3] Porphyrins are the most investigated family of photosensitizers for PDT since they possess high quantum yield in $^1O_2$ production, and they have a broad chemical diversity.[4] However, their high hydrophobicity which leads to aggregation in aqueous media and consequently a decrement on their photodynamic yield challenges their application in PDT. To overcome these challenges, we have designed photosensitizer-loaded nanoparticles that can be efficiently delivered to tumors by peritumoral *(p.t.)* injection. Specifically, we have prepared poly(*N*-vinylcaprolactam) (PVCL) nanogels through precipitation polymerization, loaded with Ce6, a porphyrin-derived photosensitizer[5]. Dynamic light scattering and Scanning electron microscopy showed that our nanoparticles have an average size of 220 nm with a low polydispersity index (PDI < 0.1) and colloidal stability of > 1 month. After characterizing our PVCL nanogels, we set out to study their tumor uptake employing optical imaging. BALB/c mice were inoculated with 4T1 cells (breast cancer) and seven days later administered with PVCL nanoparticles (*p.t.* at 1.5 mg Ce6 photosensitizer/kg). Tumor fluorescence intensity reached its maximum at two hours post-injection, indicating that this is likely the optimal timepoint for PDT (**Figure 1A**). We treated similarly inoculated mice and 7 days later treated them using either PBS (control) or PVCL nanoparticles, n=10. After two hours, tumors were irradiated (660nm, 100mW for 5 minutes). Subsequent monitoring of tumor growth (by daily caliper measurements) revealed a significant lower tumor growth rate for PDT treated mice versus control (**Figure 1B**). In addition, in vivo imaging data from before and after the PDT treatment points out the photostability and low photodegradation rate of PVCL nanogels after laser irradiation (**Figure 1C**). Ex vivo imaging from sliced tumors 10 days later nanoparticle administration also showed fluorescence emission at the 660 nm region, demonstrating the presence of PVCL nanoparticles. Our data strongly suggests that PVCL nanoparticles display high accumulation and long-term retention in the tumor. Moreover, these nanoparticles under 660 nm irradiation inhibit the tumor growth while non-treated tumor grow more significantly. Therefore, Ce6-loaded PVCL nanoparticles represents a promising platform for PDT treatments. In this line, we are currently working on the combination if this nanoparticle-based PDT with checkpoint blockade therapy in order to potentiate the antitumor therapeutic efficacy.

Reference
1. Dolmans, D. E. J. G. J.; Fukumura, D.; Jain, R. K. Photodynamic Therapy for Cancer. Nat. Rev. Cancer 2003, 3 (5), 380–387.
2. Henderson, B. W.; Gollnick, S. O.; Snyder, J. W.; Busch, T. M.; Kousis, P. C.; Cheney, R. T.; Morgan, J. Choice of Oxygen-Conserving Treatment Regimen Determines the Inflammatory Response and Outcome of Photodynamic Therapy of Tumors. Cancer Res. 2004, 64 (6), 2120–2126.
3. Yuan, Z.; Fan, G.; Wu, H.; Liu, C.; Zhan, Y.; Qiu, Y.; Shou, C.; Gao, F.; Zhang, J.; Yin, P.; et al. Photodynamic Therapy Synergizes with PD-L1 Checkpoint Blockade for Immunotherapy of CRC by Multifunctional Nanoparticles. Mol. Ther. 2021, 29 (10), 2931—2948.
4. Ethirajan, M.; Chen, Y.; Joshi, P.; Pandey, R. K. The Role of Porphyrin Chemistry in Tumor Imaging and Photodynamic Therapy. Chem. Soc. Rev. 2011, 40 (1), 340–362.
5. Sun, B.; Chang, R.; Cao, S.; Yuan, C.; Zhao, L.; Yang, H.; Li, J.; Yan, X.; van Hest, J. C. M. Acid-Activatable Transmorphic Peptide-Based Nanomaterials for Photodynamic Therapy. Angew. Chemie Int. Ed. 2020, 59 (46), 20582–20588.

Poster Presentation

Disclosures: The authors have disclosed no financial interest.

531-Improved Glioblastoma Survival and Increased Monocyte Infiltration in Female Mice Treated with anti-PD-1 and TMZ

Presenter: Vlora Riberdy, Dalhousie University

Vlora Riberdy[1], Caroline Fitz[2], Brianna C. Kelly[3], Christa Davis[4], Bassel Dawod[5], Anna Marriott[6], Kimberly Brewer[2]

[1]Dalhousie University
[2]Dalhousie University, Halifax
[3]Dalhousie University, Halifax, NS
[4]IWK Health Centre, Halifax, Nova Scotia
[5]Biomedical Translational Imaging Centre (BIOTIC), Halifax, Nova Scotia
[6]Biotics Research Canada, Halifax, NS

Introduction:
Glioblastoma is an aggressive form of brain cancer with poor long-term survival even with surgical resection and radiation[1]. The majority survive less than a year[1], with a two-year survival rate of 26-33%[2]. The use of novel immunotherapies in combination with chemotherapy temozolomide (TMZ) has shown promising results with glioblastoma[1,2]. Tumour-associated macrophages (TAMs) are associated with tumour growth and poor prognosis[3]. TAMs preferentially take up iron oxide contrast agents, making them an ideal target for imaging. Gadolinium (Gd) contrast agents extravasate into brain tissue when the blood-brain barrier (BBB) is damaged. Magnetic Resonance Fingerprinting (MRF) is a specialized magnetic resonance imaging (MRI) sequence capable of simultaneous T_1, T_2, and T_2^* relaxation measurements[4]. This sequence was used to make concentration maps of iron-labelled TAMs and Gd. In this project, we studied both male and female mice implanted with an orthotopic glioblastoma model and treated with the checkpoint inhibitor anti-PD-1 and the chemotherapy TMZ. We used MRI to follow tumour progression and evaluate TAMs and BBB damage (via Gd uptake) and flow cytometry to monitor immune cell infiltration.

Methods:
Fifteen female mice and fifteen male C57BL/6 mice (5 mice/treatment group) were intracranially implanted with $5x10^4$ gl261 glioma cells. Treatment groups were as follows: 1) untreated/control, 2) treated with anti-PD-1 (200 µg/kg/mouse/dose every 3 days for up to 8 doses) or 3) treated with anti-PD-1 and TMZ (25 µg/kg/mouse/day for 10 days). Mice received MRI brain scans twice weekly (pre- and post-contrast) for up to 6 weeks. Scans included an anatomical T_2-weighted FSE and MRF. Mice received an injection of 100 µL SPIO Rhodamine B (Biopal) 24 hours before the post-contrast scan and injections of MultiHance (gadobentate dimeglumine, Bracco) during the post-contrast scan prior to MRF imaging. Flow cytometry (FC) was performed on brains and spleens upon termination to evaluate the infiltration of immune cells into the brain/tumour, including CD8+ and CD4+ T cells and inflammatory monocytes ($CD11b+/Ly6c^{hi}$).

Results:
Female mice treated with either anti-PD-1 alone, or a combination of anti-PD-1 and TMZ had significantly higher survival than female control mice and all male mice ($p<0.05$). Female mice treated with the combination therapy also had significantly higher percentages of inflammatory monocytes in the brain compared to any group of male mice, and control female mice. However, male mice generally had higher percentages of CD8+ T cells in the brain, particularly following combination treatment. The overall concentration of Gd in the brain (including tumour if present) was plotted over time for each of the groups in female mice (Fig. 1C) (male data still being analyzed). In both untreated and anti-PD-1 treated mice, there was a drop in Gd mass on day 21, which generally corresponded to when tumours began to significantly increase in size. In contrast, mice treated with the combination group had a slower and steadier rise in Gd mass throughout the study. Total Fe mass (a measure of putative SPIO-labeled monocytes) was also compared to tumour volume in female mice. Only mice treated with anti-PD-1 had increasing iron masses strongly positively correlated with increasing tumour volumes. For other mice, there was not a clear correlation between the two.

Conclusions:
In this study, we examined how sex and immunotherapies interacted in a C57BL/6 mouse model of glioblastoma using imaging and biological assays. Female mice had better survival in response to combination therapy, with more inflammatory monocytes, but a lower percentage of CD8+ T cells, indicating that the T cells present in male mice were likely exhausted. MRF has also begun to give us an indication of how macrophage numbers are changing over time, as well as how Gd infiltration due to BBB damage changes over time.

Reference
1. Walid M et al. Prognostic Factors for long-term survival after glioblastoma. Perm J. 2008;12(4).
2. Fernandes C et al. Current standards of care in glioblastoma. In: Glioblastoma. Codon Publications. 2017;197-241.
3. Ma J et al. Macrophages/Microglia in the Glioblastoma Tumor Microenvironment. Int J Mol Sci. 2021;22(11):5775.
4. Marriott A, et al. Simultaneous quantification of SPIO and gadolinium contrast agents using MR fingerprinting. MRI. 2021;79:121-129.

Poster Presentation

Disclosures: The authors have disclosed no financial interest.

532-Data driven identification of targets for fluorescence-guided surgery in non-small cell lung cancer

Presenter: Lisanne Neijenhuis, Leiden University Medical Center (LUMC)

Lisanne Neijenhuis[1], Ruben P. Meijer[2], Annette Zeilstra[2], Sophie Roerink[2], Shadhvi Bhairosingh[3], Denise Hilling[4], Sven Mieog[5], Peter Kuppen[1], Cornelis F. Sier[6], Jerry Braun[6], Jacobus Burggraaf[7], Alexander Vahrmeijer, Danielle Cohen, Merlijn Hutteman

[1]Leiden University Medical Center (LUMC), Netherlands
[2]Leiden University Medical Center (LUMC), Leiden, Zuid-Holland, Netherlands
[3]Leiden University Medical Center (LUMC), Leiden, Zuid Holland, Netherlands
[4]Leiden University Medical Center (LUMC), Leiden, Nederland, Netherlands
[5]Leiden University Medical Center (LUMC), Leiden, z-h, Netherlands
[6]Leiden University Medical Center (LUMC), Leiden, NL, Netherlands
[7]Centre for Human Drug Research, Leiden, non-US, Netherlands

Background:
Intraoperative identification of lung tumors can be challenging, in particular in lung parenchyma sparing resections or after induction therapy. Tumor-targeted fluorescence-guided surgery can provide surgeons with a tool for real-time intraoperative tumor detection. This study evaluated cell surface biomarkers, partially selected via data driven selection software, as potential targets for fluorescence-guided surgery in non-small cell lung cancers; adenocarcinomas (ADC), adenocarcinomas in situ (AIS), and squamous cell carcinomas (SCC).

Patients and methods:
Formalin-fixed paraffin-embedded tissue slides of resection specimens from 15 patients with ADC and 15 patients with SCC were used and compared to healthy tissue. Molecular targets were selected based on two strategies: (1) a data driven selection using > 275 multi-omics databases, literature, and experimental evidence and (2) availability of a fluorescent targeting ligand in advanced stages of clinical development. The selected targets were: Carbonic anhydrase 9 (CAIX), Collagen Type XVII Alpha 1 Chain (Collagen XVII), Glucose transporter 1 (GLUT1), G Protein-Coupled Receptor 87 (GPR87), Transmembrane Protease Serine 4 (TMPRSS4), carcinoembryonic antigen (CEA), epithelial cell adhesion molecule (EpCAM), folate receptor alpha (FRα), integrin αvβ6 (αvβ6) and urokinase-type plasminogen activator receptor (uPAR). Tumor expression of these targets was assessed by immunohistochemical staining. A total immunostaining score (TIS, range 0-12), combining percentage and intensity of stained cells was calculated. Statistical differences in staining between healthy lung and tumor tissue were sought with the Wilcoxon signed rank test. The most promising targets in ADC were explored in six AIS tissue slides to explore stage dependency.

Results:
Statistically significant differences in TIS between healthy lung and tumor tissue for ADC samples were found for CEA, EpCAM, FRα, αvβ6, CAIX, Collagen XVII, GLUT-1 and TMPRSS4, and of these CEA, CAIX and Collagen XVII were also found in AIS. For SCC EpCAM, uPAR, CAIX, Collagen XVII and GLUT-1 were found to be overexpressed.

Conclusion:
EpCAM, CAIX and Collagen XVII were identified using concomitant use of data driven selection software and clinical evidence as promising targets for intraoperative fluorescence imaging for both major subtypes of non-small cell lung carcinomas.

Poster Presentation

Disclosures: The authors have disclosed no financial interest.

533-Deep Learning based framework for quantitative estimation of Standard-Count [18F]-FDG PET from in-vivo preclinical Low-Count [18F]-FDG PET images

Presenter: Kaushik Dutta, Washington University in St. Louis

Kaushik Dutta[1], Richard Laforest[2], Abhinav Jha[3], Kooresh Shoghi[4]

[1]Washington University in St. Louis, University City, MO
[2]St. Louis, Missouri
[3]Washington University in St. Louis, St Louis, Missouri
[4]Washington University School of Medicine, St. Louis

Objective:
Low-Count preclinical PET image acqusition can be achieved either by lowering the dose of radiolabeled agent or by shortening scan, with numerous benefits in terms of animal logistics, maintaining integrity in longitudinal studies and increased throughput. However, low count PET imaging leads to reduced photon count with low signal-to-noise ratio (SNR), poor image quality, lesion contrast and variability in quantification. This study aims to address this tradeoff between loss of SNR and low-count statistics by developing a deep-learning framework for generating quantitatively accurate standard-count PET (SC-PET) from low-count PET (LC-PET) and analyze qualitative and quantitative performance of the framework.

Methods:
This study utilized Patient Derived tumor Xenograft (PDX) implanted in the mammary fat pad. FDG-PET imaging was performed using Siemens Inveon PET/CT scanner. Ten minute static images 50 minutes post injection of FDG were used to obtain PET images at different statistics levels i.e. SC-PET (corresponding to 10 minutes frame) and LC-PET (corresponding to 30 seconds frame i.e. 1/20th of SC-PET events). To design the deep learning framework, we utilized three different architectures i.e. Residual U-Net (RU-Net) [1], Dilated U-Net (D-Net) [2] and Attention-based Residual-Dilated Network (Attention RD-Net) [3]. The RU-Net and D-Net architecture consists of basic encoder-decoder block similar to U-Net [4], while the Attention RD-Net utilizes short-depth linear combination of Enhanced Attention Module (EAM). The EAM units consists of dilated layers of different dilation rates followed by series of convolution layers, a global pooling component and short residual interconnections between modules. While the dilated structure helps preserving the resolution by large-scale feature observation maintained by same size receptive field without increasing network components, the residual blocks facilitates faster propagation of feature information across network modules. Among the thirty-eight mice subjects used for this study, twenty-six were used for training the network and hyperparameter optimization and remaining twelve for testing the performance of the framework. The performance of the DL-generated SC-PET images were compared to several existing denoising methods, including Non-Local Means (NLM) [5] and Block Matching and 3D Filtering (BM3D) [6] in terms of qualitative metrics i.e. structural similarity index metric (SSIM), peak signal-to-noise ratio (PSNR) and normalized root mean square error (NRMSE). Task-specific quantitative analysis of the DL-framework was performed on the lesion of interest using mean standardized uptake value (SUV_{Mean}).

Bias in performance was calculated with respect to original SC-PET images. The total workflow is depicted in Fig. 1A.

Results:
The DL-based framework generated SC-PET images with visually improved image quality and lesion contrast compared to the non-DL approaches and LC-PET as depicted in Fig. 1B. RU-Net, D-Net and Attention RD-Net based denoising performed significantly better ($p<0.05$) than NLM and BM3D in all three qualitative metrics of performance i.e. SSIM, PSNR and NRMSE (Fig. 1 C-E). All network architectures exhibited similar SUV_{Mean} for the analyzed tumor-lesions which were highly correlated with SC-PET ($\rho=0.97$, $p\leq0.05$) and the average SUV_{Mean} bias with respect to SC-PET are 3.13±2.32%, 3.51±3.06% and 3.07±1.84 respectively for RU-Net, D-Net and Attention RD-Net generated SC-PET images. The combination of residual interconnections and dilated layer with feature attention mechanism ensured equivalent performance for Attention RD-Net even with lesser epochs and shallow network structure.

Conclusion:
The proposed DL architectures of the framework performed significantly better than non-DL methods in generating quantitatively accurate SC-PET images from LC-PET equivalent. The generated SC-PET images had enhanced qualitative metrics indicating comparable image quality as corresponding SC-PET images by suppressing noise. The DL-based methods also exhibited nominal SUV_{Mean} bias thus indicating the feasibility of using DL-based SC-PET images for better lesion detection, quantification and diagnosis.

Reference

1. Xu, J., et al. 200x Low-dose PET Reconstruction using Deep Learning. 2017. arXiv:1712.04119.
2. Spuhler, K., et al., Full-count PET recovery from low-count image using a dilated convolutional neural network. Medical Physics, 2020. 47(10): p. 4928-4938.
3. Anwar, S. and N. Barnes. Real image denoising with feature attention. in Proceedings of the IEEE/CVF international conference on computer vision. 2019.
4. Ronneberger, O., P. Fischer, and T. Brox, U-net: Convolutional networks for biomedical image segmentation. Lecture Notes in Computer Science (including subseries Lecture Notes in Artificial Intelligence and Lecture Notes in Bioinformatics), 2015. 9351: p. 234-241.
5. Dutta, J., R.M. Leahy, and Q. Li, Non-local means denoising of dynamic PET images. PLoS One, 2013. 8(12): p. e81390.
6. Dabov, K., et al., Image denoising by sparse 3-D transform-domain collaborative filtering. IEEE Transactions on image processing, 2007. 16(8): p. 2080-2095.

Poster Presentation

Disclosures: The authors have disclosed no financial interest.

534-Targeted detection/imaging of prostate cancer by SPMR and MRI using anti-PSMA peptide functionalized iron oxide nanoparticles

Presenter: Marie Zhang, Imagion Biosystems

Marie Zhang[1], Varahenage Y. Perera[1], Kathirvel kandasamy[2], Eric Smith-nguyen[2], Daniel Inglese[2], John White[3]

[1]*Imagion Biosystems, San Diego, CA*
[2]*Imagion Biosystems, San Diego, California*
[3]*Imagion Biosystems, Inc., San Diego, CA*

Background:
Iron oxide nanoparticles (NPs) have been used in a variety of preclinical and clinical cancer detection/imaging applications. Here we show that targeted superparamagnetic iron oxide nanoparticles (SPION) can be used for *in vivo* detection by two different imaging methods. Superparamagnetic Relaxometry (SPMR) is a highly sensitive *in vivo* detection technology that is able to differentiate the magnetic signature of nanoparticles bound to tumor cells from unbound nanoparticles. Same targeted SPIONs accumulated in tumor are able to provide molecular magnetic resonance imaging (MRI) contrast as well. The purpose of the study is to develop biomarker target–specific imaging probes for image-based diagnosis and treatment monitoring by both SPMR and MRI. Recently, anti-PSMA PET tracer have been reported to be effective in detecting prostate cancer as well as its metastasis. However, using non-radioactive materials to achieve the same targeting capability as the anti-PSMA PET agent as well as obtaining anatomical information at the same time using MRI is more desirable.

Results:
Our anti-PSMA peptide conjugated nanoparticles consist of a 25nm Fe_3O_4 core covered by a polymer shell with polyethylene glycol (PEG) and peptide covalently attached on the surface. The overall size of nanoparticles is 60-70nm with PDI <0.1 as measured by DLS. Size and magnetic property uniformity of SPION are essential for signal strength by SPMR measurement as well as for potential achieving diagnostic utility using MRI. Our results have shown that our anti-PSMA peptide conjugated nanoparticles can distinguish high, medium and null PSMA expression cell lines, such as LnCAP, 22RV1, PC3 respectively in an *in vitro* cell based assay by SPMR, demonstrating good sensitivity, specificity and selectivity. Based on SPMR quantitation, approximate 5-10 µg of nanoparticle were detected when incubating with 1x10^6 PSMA+ cells for 24 hours. *In vivo* study using xenograph model with LnCAP and 22RV1 implanted subcutaneously on the flank region of male athymic nude mice demonstrated sufficient tumor accumulation of anti-PSMA peptide conjugated nanoparticles, measurable by *ex vivo* tumor detection using SPMR. Preliminary time point study also indicated nanoparticle accumulation were observable starting at 6 hours and increasing in amount upto 24 hours. Using a PEG NP (without the target ligand) as control for the mice study have shown minimum NP tumor accumulated were observed, demonstrating the specificity of the nanoparticles *in vivo*. Organ distribution study indicated that anti-PSMA nanoparticles mostly accumulated in liver and spleen as these nanoparticles were cleared through these two organs. Other organs such as brain, heart, lung didn't show appreciable accumulation. Kidney had minor accumulation, likely due to the fact that a subset of kidney cells was reported to contain PSMA expression based on earlier studies in the literature. MRI studies using this type of conjugated nanoparticles have shown they produced excellent T2 and T2* contrast. The repeat of same type of xenograph model used in the SPMR study is currently under the way using MRI as an alternative *in vivo* detection method with images taken pre- and post- dosing of the nanoparticles. Give the specificity and sufficient accumulation of nanoparticles demonstrated in the SPMR study, it is expected that MRI will show similar performance with additional anatomical information.

Conclusion:
Our anti-PSMA peptide nanoparticles provide targeted and specific delivery to cancerous tissue and generate measurable signal by SPMR. Furthermore, demonstration of these anti-PSMA peptide nanoparticles generating tumor specific contrast in MRI is currently under the way. These studies lay the groundwork for use of bio-safe magnetic particles

as a detection and contrast agent for early prostate cancer detection to minimize the needs of invasive biopsies as well as potential utility for monitoring therapy response.

Poster Presentation

Disclosures: The authors have disclosed no financial interest.

535-A machine learning framework for stratifying high vs. low notch-DLL4 expressing host microenvironment for breast cancer bearing subjects

Presenter: Shayan Shafiee, Medical College of Wisconsin

Shayan Shafiee[1], Mykhaylo Zayats[2], Jonathan Epperlein[2], Sergiy Zhuk[2], Amit Joshi[1]

[1]Medical College of Wisconsin, Milwaukee, WI
[2]IBM Research Europe, Dublin, Ireland, Dublin, Ireland

Introduction:
Nanomedicine and macromolecule drug delivery rely on the enhanced permeation and retention effect in solid tumors, and crosstalk between malignant tumor cells and the non-malignant TME contributes to tumor growth, drug delivery, and therapy efficacy (PMID: 25540894). Delta Like Canonical Notch Ligand4(DLL4) is a protein-coding gene that is responsible for developing blood vessels and plays a role in tumor angiogenesis. With Consomic rat strains differing in inherited levels of DLL4 in host stroma, we have shown that the degree of DLL4-dependent dysfunctional angiogenesis affects tumor growth and metastasis, drug delivery, and therapy response (PMID: 32373218). Herein, we propose a machine learning framework to identify and classify hosts with low and high levels of DLL4 expression on tumor endothelium based on the kinetic NIR fluorescence imaging with Indocyanine green dye. The overall objective is to identify tumor-bearing animals likely to respond to DLL4 directed therapies.

Materials and Methods:
We generated two rat strains, Salt sensitive (SS) with high systemic DLL4 expression and consomic(inbred strains containing a whole chromosome from another strain in their genome) SSBN3 with third chromosome substitution from Brown Norway with low DLL4 expression. We also constructed two novel SSBN3 congenic(inbred strains containing a given genomic region in their genome) xenograft host strains (MV, MW) by introducing segments of BN chromosome 3 into the genetic background of the parental SS strain, such that MV inherited DLL4 locus from SS and MW from BN. A whole body imaging platform for rats was developed, and all four strains bearing identical tumors were imaged. MDA-MB-231 (231), triple negative breast cancer, was used as a Xenograft cell line. Animals were injected intravenously via tail vein with ICG (0.75mg/kg, MP Biomedicals) and simultaneously imaged using a PIMAX4 ICCD camera(Princeton Instruments), equipped with a 25mm lens (Navitar, DO-25, 0.95 f-stop), with an 830nm long pass filter (ThorLabs), excited by 785nm diode laser (~5mW/cm2), was used with a frame rate of 10.6 fps for 6 minutes. Respiratory motion correction was performed with Fourier-Wavelet methods, MATLAB (MathWorks Inc.). Tumor ROIs were automatically drawn on principle component decomposed images using a 2D cross-correlation mapping algorithm. Pixels' intensity was averaged from the ROIs, and a single time series was recorded. Data from tumor-bearing SS and SSBN3 rats were used to refine the features and train the classifier. The framework's performance was validated on MV and MW strains (Figure 1. C, L, O). We characterized dynamic perfusion patterns using several features in the NIR time-series. Best pairs of features in terms of performed sensitivity, specificity, and accuracy were selected by a two-step procedure, recursive feature elimination(RFE), and Exhaustive Feature Selection(EFS) by training classifiers for selecting two out of four features selected in the first step (PMID: 35308965). After feature selection, the classification algorithm becomes a standard binary classification problem, with feature selection as a subproblem. Finally, we implemented an experimental framework to validate the features by combining tumor detection, feature extraction, and classification algorithms.

Results:
The performance of the tumor detection algorithm was visually validated, and all the ROIs passed the inspection. The classifier's accuracy, precision, sensitivity, and specificity over the training run in classifying MW and MV as belonging to their respective DLL4 parent strain were 0.84, 0.98, 0.70, and 0.99, respectively, and the sensitivity and specificity were 91.7 and 95, respectively, over the validation run.

Conclusion:
We have demonstrated that whole body non-invasive NIR imaging can discriminate identical tumors based on the differential DLL4 expression in TME using an ML framework with high sensitivity and specificity. If developed for dynamic MR imaging used clinically, similar methods will enable patient stratification for DLL4 targeted therapies.

Reference
1. PMID: 25540894
2. PMID: 32373218
3. PMID: 35308965

Poster Presentation

Disclosures: The authors have disclosed no financial interest.

536-Using Optical Imaging to Assess Antibody–Drug Conjugate Linker Chemistry

Presenter: Syed Usama, National Cancer Institute - Frederick

Syed Usama[1], Martin J. Schnermann[2]

[1]National Cancer Institute - Frederick, Frederick, MD
[2]National Cancer Institute, Frederick, MD

Antibody drug conjugates (ADCs) are an emerging targeted drug delivery approach that benefits from combination of the exceptional specificity of antibodies and the potency of small molecule therapeutics. To date more than 11 ADCs have received FDA approval. A critical component of this approach is the linker domain between the antibody and the drug payload. An ideal ADC linker should be stable in plasma circulation, but it should release payload quickly in tumors. ADCs are conventionally assessed by examining tumoricidal activity and toxicity profiling. While these methods are important benchmarks, they provide only indirect insights into the site and mechanism of drug release. Optical imaging can provide a straightforward means to assess the *in vivo* targeting of therapuetic strategies. Fluorogenic probes are critical tools in chemical biology that respond to biological stimuli. To date most fluorogenic probes are limited to the ultraviolet or visible light region, which can limit applications to *in vitro* setting. This restricts the application of the fluorogenic probes to biochemical assays. To overcome this challenge, we have developed a new class of fluorogenic probes based on the heptamethine cyanine scaffold, the most broadly

used near-infrared (NIR) chromophore. These compounds result from modification of heptamethine norcyanines with stimuli-responsive carbamate linkers. The resulting cyanine carbamates (CyBams) exhibit exceptional turn-ON ratios (~170×) due to dual requirements for NIR emission: carbamate cleavage through 1,6-elimination and chromophore protonation. We demonstrated the utility of this CyBam approach to quantitatively compare the linker component of ADCs. We compare a panel of several common cathepsin (valine-citrulline, alanine-alanine) and disulfide (hindered and non-hindered) ADC linkers using Panitumumab (anti-EGFR mAb) and m276SL (anti CD276 mAb) in triple negative breast cancer tumor models. These studies indicate that cathepsin-cleavable linkers provide dramatically higher tumor activation relative to hindered or non-hindered disulfides, an observation that is only apparent with in vivo imaging. This strategy enables quantitative comparisons of cleavable linker chemistries in complex tissue settings with implications across the drug delivery landscape. This approach is well positioned to investigate other linker strategies and homogeneous labeling strategies. We also anticipate this strategy can be readily extended to analyze the impact of mAb engineering strategies. Going forward, we anticipate that CyBams could provide insights that directly inform the development of ADCs.

References

1. https://pubs.acs.org/doi/abs/10.1021/jacs.1c02112;
2. https://pubs.acs.org/doi/abs/10.1021/jacs.1c10482;

Poster Presentation

Disclosures: The authors have disclosed no financial interest.

537-Visualization of Key determinants for Nonalcoholic Fatty Liver disease by Precise MRI (pMRI)

Presenter: zongxiang gui, Georgia State University

Zongxiang Gui[1], Jingjuan Qiao, Dongjun Li[2], Khan Hekmatyar, Yuguang Meng, Hua Yang[3], Shirong Wang[4], Brenda-Ruth N. Mimba[5], Sophia Bamphia, Mani Salarian[6], Oluwatosin Y. Ibhagui, Ravi Chakra C. Turaga, Hang Shi[4], Hans Grossniklaus[3], Zhi-ren Liu[7], Jenny Yang

[1]*Georgia State University, ATLANTA, GA*
[2]*Georgia State University, Atlant, GA*
[3]*Emory University, Atlanta, GA*
[4]*Georgia State University, Atlanta, Georgia*
[5]*Georgia State University, Sugarhill, GA*
[6]*Georgia State University, Decatur, GA*
[7]*Biology Department, Atlatna, Georgia*

The largest and fastest-growing population at risk for developing hepatic fibrosis are individuals with nonalcoholic fatty liver disease (NAFLD). There are urgent unmet medical needs for early detection and quantifying of multiple biomarkers in NFAD and its progression from obesity to fibrosis, and cancer, metastasis. In addition, we also need an imaging methodology for stratifying patients, quantification of treatment, and drug discovery by noninvasive longitudinal measurements. Our goal is to improve the detection and mapping of key determents in steatosis, inflammation, and fibrosis, define prognosis, measure treatment impact, and facilitate drug discovery using Precision MRI (pMRI) enabled by our pioneered novel protein MRI contrast agents including hProCA32.Collagen, which specifically targets collagen 1. Here, we will report our progress in optimizing imaging methodology (pulse sequences and parameters) to overcome motion artifact and fat background and maximize signal-to-noise ratio, and sensitivity. Imaging methods for tempo-spatial quantification/detection of inflammation, steatosis, fibrosis, vascularity, and fibrotic stroma were developed using several animal models. We have shown that heterogamous distribution and steatosis formation and progression are largely controlled by DNA methylation using ten-eleven translocation methylcytosine dioxygenase 2 knock out (Tet2 KO) KO mice. ProCA32.collagen is able to detect the formation of collagen locked at pre-fibrosis and steatosis stage using both T1-map and T2-map taking advantage of unique properties of high r1 and r2 relaxivity. In addition, ProCA32.collagen is able to map severe fibrosis due to alteration of lipolysis using the Comparative Gene Identification-58 knock-out (CGI-58 KO) liver fibrosis mouse model. Our pMRI further reveals that heterogeneous distribution of steatosis and fibrosis largely alter liver vascular structure associated with disjointed angiogenesis. We also report a detailed spatial correlation of revealed imaging features with established segmented methods including liver function, fat content, and histological analysis. hProCA32.Collagen enabled pMRI is expected to have strong application in monitoring liver fibrosis progression, response to treatment, and facilitating drug discovery.

Reference

1. Salarian, Mani, et al. "Early detection and staging of chronic liver diseases with a protein MRI contrast agent." Nature communications 10.1 (2019)
2. Xue, S. et al. Protein MRI contrast agent with unprecedented metal selectivity and sensitivity for liver cancer imaging. Proceedings of the National Academy of Sciences 112, 6607-6612 (2015).
3. Yang, Jenny J., et al. "Rational design of protein-based MRI contrast agents." Journal of the American Chemical Society 130.29 (2008): 9260-9267.
4. Tan, S. et al. Chemokine receptor 4 targeted protein MRI contrast agent for early detection of liver metastases. Science Advances 6, eaav7504 (2020).

Poster Presentation

Disclosures: The authors have disclosed no financial interest.

538-Targeting Tumor-Associated M2-like Macrophages in a Patient-derived Xenograft Model of Glioblastoma Using Sub-5 nm Iron Oxide Nanoparticles

Presenter: Zi Wang, Emory University School of Medicine

Zi Wang[1], Yuancheng Li[1], Joshua B. Jones[1], Zhaobin Zhang[1], Hui Mao[2]

[1]*Emory University School of Medicine, Atlanta, GA*
[2]*Emory University School of Medicine, Atlanta, Georgia*

Glioblastoma (GBM) is one of the most aggressive malignant tumors in the central nerve system with limited treatment strategy and extremely poor prognosis[1]. The emerging immunotherapy approaches that have shown promising results in many cancers are also explored for treating several brain cancers. In tumor immune microenvironment (TIME), tumor-associated macrophages (TAM) are the most abundant immune-related cells, responsible for tumor initiation, growth and metastasis[2]. In brain tumors, TAM stemming from tissue-resident macrophages (microglia) and recruited monocytes can be classified into pro-inflammatory M1 and pro-tumoral M2 subtypes[3]. As most TAM present M2 phenotype, which attenuates the efficacy of immunotherapies by

secreting immunosuppressive cytokines, stimulating regulatory T cells to suppress immune response, down-regulating PD-1 expression, and inhibiting antitumor actions mediated by T cells[4], theranostic approaches for targeting M2 TAM in GBM render the possibilities of imaging and image-guided therapeutics delivery to modulate the immuno-suppressive TIME in GBM. However, the effective delivery of theranostic agents to the intracranial tumors protected by the blood brain barrier (BBB) and/or blood tumor barrier (BTB) remains one major obstacle[5]. In addition, mononuclear phagocyte system that clears bioengineered theranostic agents through non-specific phagocytosis[6] makes the M2-subtype-specific targeting to GBM more challenging, whereas agents targeting general TAM in GBM have been reported, such as Ferumoxytol, an FDA-approved dextran-coated iron oxide nanoparticle (IONP), for magnetic resonance imaging (MRI) of TAM activities. We have developed an antibiofouling polymer (polyethylene glycol)-*block*-(allyl glycidyl ether) (PEG-*b*-AGE) coated sub-5 nm ultrafine iron oxide nanoparticles (uIONP) with T1-T2 dual MRI contrast effect, and shown that RGD-conjugated uIONP can effectively extravasate tumor blood vessels and target the U87MG cancer cells overexpressing $\alpha_v\beta_3$ integrin in an orthotopic GBM mouse model[7]. In this abstract, we took advantage of the antibiofouling properties of PEG-*b*-AGE coating in blocking non-specific phagocytosis to enable the ligand-mediated active targeting to M2-TAM, after conjugating with an M2-targeted peptide M2pep (sequence: YEQDPWGVKWWY GGGSKKKC). To better recapitulate the human GBM microenvironment, we used an orthotopic patient tissue-derived xenograft (PDX) mouse model of GBM for evaluating the M2pep-uIONP probe. M2pep-uIONP labeled with the near-infrared (NIR) dye NIR830 (NIR830-M2pep-uIONP) were validated for the targeting specificity to M2 macrophages in vitro before the in vivo study using mice bearing PDX GBM tumors through intravenous (i.v.) administration at a dosage of 10 mg Fe/kg body weight. NIR imaging showed observable signals in the tumors at 1 and 3 h, but not at 24 h (Fig. 1A). The region of interest analysis of T_2-weight MRI images of mouse brains at 24 h showed 10.3 ± 4.4% (N = 3) signal drop (Fig. 1B), which supports the NIR imaging result. Immunofluorescence (IF) staining of the brain tumor tissues for M2 TAM ($CD68^+$/$CD206^+$) showed a highly co-localized distribution of M2 TAM with NIR830 signals (Fig. 1C). The IF results indicated 1) NIR830-M2pep-uIONP successfully entered the PDX GBM tumors, and 2) specific M2 TAM targeting by NIR830-M2pep-uIONP. In summary, our results confirmed the delivery of M2pep-uIONP into the orthotopic PDX GBM tumors and their capability in targeting M2 TAM. The developed M2 TAM specific targeting approach will allow us to explore the M2-targeted theranostic application for GBM immunotherapy in the future.

Reference

1. Thakkar J. P., et al., Cancer Epidemiology and Prevention Biomarkers 2014, 23.10, 1985-1996.
2. Chen YB, et al., Journal of biomedical science 2019, 26.1, 1-13.
3. Jun M, et al., International journal of molecular sciences 2021, 22.11, 5775.
4. Duan Z, et al., Signal transduction and targeted therapy 2021, 6(1), 1-21.
5. Yan C., et al., Advanced drug delivery reviews 2012, 64.7,640-665.
6. Gustafson, H. H., et al., Nano today 2015, 10.4, 487-510.
7. Li YC, et al., ACS applied biomaterials 2020, 3(7), 4335-4347.

Poster Presentation

Disclosures: The authors have disclosed no financial interest.

539-Transmembrane pH gradient imaging in gliomas

Presenter: Daniel Coman, Yale University

Sandeep Kumar Mishra[1], Jelena Mihailovi?[1], Fahmeed Hyder[2], **Daniel Coman[1]**

[1]*Yale University, New Haven, CT*
[2]*Yale University, New Haven, Connecticut*

Purpose: Development of an MR-based platform for transmembrane pH gradient imaging in gliomas.

Introduction:
A unique feature of the tumor microenvironment is *extracellular acidosis in relation to intracellular milieu* (Warburg effect)**[1]**. Metabolic reprogramming in tumors results in overproduction of H^+ ions and lactate, which are extruded from the cells to support tumor survival and progression. The difference between intracellular pH (pH_i) and extracellular pH (pH_e) is much larger in tumors than normal tissue**[2]**. The most aggressive and metastatic phenotypes have tumor pH_e in range of 6.2-7.0**[3, 4]**, and tumor pH_i is either neutral or alkaline**[1]**. Cancer cells require an alkaline pH_i to sustain the function of intracellular machinery essential for glycolysis (i.e. glycolytic enzymes)**[5, 6]** . Moreover, controlling the transmembrane pH difference represents an essential therapeutic target**[7]**, and could regulate drug entry into cells**[4, 8]**. Measuring the transmembrane pH gradient (DpH=pH_i–pH_e) would be beneficial clinically by providing a tool for assessing tumor aggressiveness, monitoring treatment efficacy, guiding localized drug delivery, and understanding tumor responsiveness.

Methods:
Fischer 344 rats were implanted with RG2 tumors, which were allowed to grow to 2-3 mm diameter. For the MR scans, the animals were anesthetized (1-2% isoflurane), positioned in a 3D-printed animal holder and artificially ventilated (70% N_2O, 30% O_2). An intraperitoneal line was inserted for $TmDOTP^{5-}$ infusion (15µl/min for 90 minutes). A water-heating pad was used to maintain the body temperature in the physiological range (36–37 °C) throughout the experiment. The body temperature was measured with a rectal optical probe. The MR data was obtained on a 9.4T Bruker (Billerica, MA, USA) horizontal-bore spectrometer. pH_i was measured with Amine and Amide Concentration-Independent Detection (AACID)**[9]** before $TmDOTP^{5-}$ infusion using an echo-planar spin-echo imaging sequence with an FOV of 32mm×32mm, 1 slice of 1mm thickness, a TR of 8s, and an image matrix of 64×64, for a voxel resolution of 0.5mm×0.5mm×0.5mm. A 4s continuous-wave of 1.5µT was used for saturation of 70 offset frequencies specifically chosen to accurately define the amide/amine peaks. pH_e was measured with Biosensor Imaging of Redundant Deviation in Shifts (BIRDS)**[10]** using a 3D chemical shift imaging (CSI) sequence with a FOV of 25mm×15mm×25mm, 1089 spherical encoding steps, TR=5ms, and a voxel resolution of 1x1x1mm^3. The pH_e was calculated from the H2, H3 and H6 chemical shifts of $TmDOTP^{5-}$.**[10]** The pH_e images were resampled using bilinear interpolation to match the 0.5mm×0.5mm×0.5mm resolution of pH_i maps from AACID.

Results:
For both BIRDS and AACID the pH_e (**Fig.1A**) and pH_i (**Fig.1B**) images were overlaid on the T_1–weighted images to localize the RG2 tumors and delineate normal brain regions. The results show a significantly lower pH_e (6.7±0.2) in RG2 tumors compared to normal brain (7.2±0.1, p<0.001, **Fig.1A**). The pH_i was only slightly higher in tumors (7.5±0.2) compared to normal brain (7.3±0.2, p<0.01**, Fig.1B**). As a

result, the transmembrane pH gradient was significantly higher inside the RG2 tumors (0.7±0.2) when compared to normal brain (0.1±0.1, p<0.001**, Fig.1C**).

Discussion:

This work establishes an MR-based platform for transmembrane pH gradient imaging in brain tumors. Because most tumors are hyperglycolytic and possess a large transmembrane pH gradient, decreasing this gradient may serve as a functional biomarker for positive therapeutic outcome.

Reference

1. Gatenby RA, Gillies RJ. Why do cancers have high aerobic glycolysis? Nat Rev Cancer 2004. 4(11): p. 891-9.
2. Gerweck LE. The pH difference between tumor and normal tissue offers a tumor specific target for the treatment of cancer. Drug Resist Updat 2000. 3(1): p. 49-50.
3. Mahoney BP, Raghunand N, Baggett B, Gillies RJ. Tumor acidity, ion trapping and chemotherapeutics. I. Acid pH affects the distribution of chemotherapeutic agents in vitro. Biochem Pharmacol 2003. 66(7): p. 1207-18.
4. Raghunand N, Mahoney BP, Gillies RJ. Tumor acidity, ion trapping and chemotherapeutics. II. pH-dependent partition coefficients predict importance of ion trapping on pharmacokinetics of weakly basic chemotherapeutic agents. Biochem Pharmacol 2003. 66(7): p. 1219-29.
5. Park SJ, Smith CP, Wilbur RR, Cain CP, Kallu SR, Valasapalli S, Sahoo A, Guda MR, Tsung AJ, Velpula KK. An overview of MCT1 and MCT4 in GBM: small molecule transporters with large implications. Am J Cancer Res 2018. 8(10): p. 1967-1976.
6. Harguindey S, Polo Orozco J, Alfarouk KO, Devesa J. Hydrogen Ion Dynamics of Cancer and a New Molecular, Biochemical and Metabolic Approach to the Etiopathogenesis and Treatment of Brain Malignancies. Int J Mol Sci 2019. 20(17).
7. Gerweck LE. Tumor pH: implications for treatment and novel drug design. Semin Radiat Oncol 1998. 8(3): p. 176-82.
8. Larsen AK, Escargueil AE, Skladanowski A. Resistance mechanisms associated with altered intracellular distribution of anticancer agents. Pharmacol Ther 2000. 85(3): p. 217-29.
9. McVicar N, Li AX, Gonçalves DF, Bellyou M, Meakin SO, Prado MA, Bartha R. Quantitative tissue pH measurement during cerebral ischemia using amine and amide concentration-independent detection (AACID) with MRI. J Cereb Blood Flow Metab 2014. 34(4): p. 690-8.
10. Coman D, Trubel HK, Rycyna RE, Hyder F. Brain temperature and pH measured by (1)H chemical shift imaging of a thulium agent. NMR Biomed 2009. 22(2): p. 229-39.

Poster Presentation

Disclosures: The authors have disclosed no financial interest.

540-IRDye800CW labeled uPAR-targeting peptide for fluorescence-guided glioblastoma surgery: Preclinical studies in orthotopic xenografts

Presenter: Sorel Kurbegovic, Copenhagen University Hospital Rigshospitalet

Sorel Kurbegovic[1], Karina Juhl[2], Kasper Kildegaard Soerensen[3], Julie Leth[4], Gro Linno Willemoe[5], Anders Christensen[6], Yvonne Adams[7], Anja Ramstedt Jensen[7], Christian von Buchwald[6], Jane Skjøth-Rasmussen[5], Michael Ploug[8], Knud Jørgen Jensen[3], Andreas Kjaer[9]

[1]Copenhagen University Hospital Rigshospitalet, Copenhagen, Denmark
[2]Rigshospitalet, Copenhagen N, Capital Region, Denmark
[3]University of Copenhagen, Denmark
[4]University of Copenhagen
[5]Rigshospitalet, Denmark
[6]Rigshospitalet, Copenhagen, Sjaelland, Denmark
[7]University of Copenhagen, Copenhagen, Denmark
[8]University of Copenhagen, copenhagen, Denmark, Denmark
[9]Rigshospitalet & University of Copenhagen, Copenhagen, Denmark

Glioblastoma (GBM) is a devastating cancer with basically no curative treatment. Even with aggressive treatment, the median survival is disappointing 14 months [1]. Surgery remains the key treatment and the postoperative survival is determined by the extent of resection [2]. Unfortunately, the invasive growth with infiltrating margins complicates an optimal surgical resection. Precise intraoperative tumor visualization is therefore highly needed and molecular targeted near-infrared (NIR) fluorescence imaging potentially constitutes such a tool. The urokinase-type Plasminogen Activator Receptor (uPAR) is highly expressed in most solid cancers including GBM, breast cancer, head and neck squamous cell carcinoma, pancreatic cancer, and lung cancer [3-7]. The level of expression is correlated to invasion and metastasis, one of the hallmarks of cancer, and accordingly it correlates to the aggressiveness of the cancer. Further, it is highly expressed at the invading front and the adjacent peritumoral activated stroma making it an attractive target allowing accurate margin visualization and tumor delineation [8]. The purpose of this study was to develop and evaluate a new uPAR-targeted optical probe, IRDye800CW-AE344, for fluorescence guided surgery (FGS). We characterized the probe with regard to binding affinity, optical properties, and plasma stability. Further, in vivo imaging characterization was performed in nude mice with orthotopic human patient derived glioblastoma xenografts, and we performed head-to-head comparison within FGS between our probe and the traditional procedure using 5-ALA. Finally, the blood-brain barrier (BBB) penetration was characterized in a 3D BBB spheroid model. The probe effectively visualized GBM in vivo with a tumor-to-background ratio (TBR) above 4.5 between 1 to 12 h post injection and could be used for FGS of orthotopic human glioblastoma xenografts in mice where it was superior to 5-ALA. The probe showed a favorable safety profile with no evidence of any acute toxicity. Finally, the 3D BBB model showed uptake of the probe into the spheroids indicating that the probe crosses the BBB. IRDye800CW-AE344 is a promising uPAR-targeted optical probe for FGS and a candidate for translation into human use.

Reference

1. Delgado-Lopez, P.D. and E.M. Corrales-Garcia, Survival in glioblastoma: a review on the impact of treatment modalities. Clin Transl Oncol, 2016. 18(11): p. 1062-1071.
2. Chaichana, K.L., et al., Establishing percent resection and residual volume thresholds affecting survival and recurrence for patients with newly diagnosed intracranial glioblastoma. Neuro Oncol, 2014. 16(1): p. 113-22.
3. Persson, M., et al., Urokinase-Type Plasminogen Activator Receptor as a Potential PET Biomarker in Glioblastoma. J Nucl Med, 2016. 57(2): p. 272-8.
4. Persson, M., et al., First-in-human uPAR PET: Imaging of Cancer Aggressiveness. Theranostics, 2015. 5(12): p. 1303-16.
5. He, C., et al., Analysis of expressions of components in the plasminogen activator system in high- and low-metastatic human lung cancer cells. J Cancer Res Clin Oncol, 2001. 127(3): p. 180-6.
6. Foekens, J.A., et al., The urokinase system of plasminogen activation and prognosis in 2780 breast cancer patients. Cancer Res, 2000. 60(3): p. 636-43.

7. Cantero, D., et al., Enhanced expression of urokinase plasminogen activator and its receptor in pancreatic carcinoma. Br J Cancer, 1997. 75(3): p. 388-95.
8. Kriegbaum, M.C., et al., Rational targeting of the urokinase receptor (uPAR): development of antagonists and non-invasive imaging probes. Curr Drug Targets, 2011. 12(12): p. 1711-28.

Poster Presentation

Disclosures: The authors would like to disclose that FG001 is an investigational device.

541-Highly NIR-II Scattering Gold Superclusters for Optical Coherence Tomographic Molecular Imaging

Presenter: Nicholas Calvert, University of Ottawa

Nicholas D. Calvert[1], Joshua S. J. Baxter[2], Lora Ramunno[2], Sabaa Rashid[2], Jaspreet Walia[2], Pierre Berini[2], Benjamin Hibbert[3], Eva Hemmer[4], Adam Shuhendler[5]

[1]*University of Ottawa, Orleans*
[2]*University of Ottawa*
[3]*University of Ottawa Heart Institute*
[4]*University of Ottawa, Ottawa*
[5]*University of Ottawa, Ottawa, Ontario*

Introduction:
Near-infrared II (900 – 1700 nm, NIR-II) imaging is important in biological systems as it facilitates high tissue penetration and spatial resolution due to limited light attenuation by scattering with biomolecules[1]. Biocompatible nanomaterials capable of NIR-II imaging would enable novel investigations of biomolecular changes in living subjects. These materials would particularly impact optical coherence tomography (OCT), the main clinical tool for identifying atherosclerotic plaques and evaluating arterial stents[2]. OCT signal relies on backscattered NIR-II light and is limited to anatomical imaging as it lacks a purposeful contrast agent[2].Current investigational contrast agents provide some image brightening, but rely on localized surface plasmon resonance (LSPR) from less cytocompatible non-noble metals, or are composed of biocompatible plasmonic materials (i.e., gold) in nanoarchitectures limiting their safety *in vivo*[3–5]. Gold superclusters (AuSCs), an assembly of individual AuNPs into one large clustered particle, have demonstrated NIR-II absorbance, but result in AuNCs with poor morphology and limited aqueous dispersibility, precluding biomedical applications[6]. Synthesis of stable, homogeneous, and aqueously-dispersible AuNCs could be a potent NIR-II contrast agent.

Methods:
We have developed a new synthetic methodology for metal NCs applicable to plasmonic nanoparticles of a variety of different metals, including our novel gold superclusters (AuSCs), designed with optimal OCT contrast properties. Our AuSC synthetic method relies on controlled aggregation of oleylamine-coated AuNPs via solvophobic interactions with n-butanol, which is stabilized and transferred into an aqueous solution through successive Myrj52 coatings. A variety of imaging and optical techniques were used to characterize size, shape, and internal structure of AuSCs, which were used to create a finite-difference time domain (FDTD) model to define AuSC architecture by comparing simulated and experimental LSPR interactions. Finally, AuSCs were evaluated by clinically relevant *in vivo* OCT imaging to determine their effectiveness as an OCT contrast agent.

Results and Discussion:
Our 3-step methodology (Fig. 1A) demonstrates how successive coatings with an amphiphilic polymer (Myrj52) formed stable, solvophobically assembled clusters, a result of Van der Waal's interactions with oleylamine and Au-C=O coordination. Myrj52 stacking facilitated the transfer of single-coated AuSCs into aqueous media. Synthesis resulted in AuSCs with median size 419 nm (Fig. 1B), an LSPR peak at 1350 nm (equal to center wavelength of the OCT instrument, Fig. 1C), and consistent spherical morphology (Fig. 1D). An FDTD model derived from experimental data gave simulated spectra (Fig. 2B) with high similarity to those obtained experimentally (Fig. 2A). This also elucidated the primary LSPR interaction is through scattering of NIR-II photons (Fig. 2C). OCT images of AuSCs in equal concentration to 15 nm and 500 nm AuNPs (non-clustered, Fig. 3) showed a much higher level of signal (3-fold and 13-fold, respectively). An arterial phantom constructed from AuSC and 15 nm AuNP-doped agarose was used to evaluate the signal and spatial resolution enhancement, and higher in both cases for AuSCs (Fig. 4). Finally, an OCT imaging catheter was inserted into a Sprague-Dawley abdominal aorta rat for clinical imaging: the artery was flushed with saline (Fig. 5A), 0.5 mg/mL AuSCs were introduced locally via imaging catheter (Fig. 5B), the artery was flushed again (Fig. 5C). This procedure allows elucidation of *in vivo* AuSC contrast levels and their ability to be cleared from the site of investigation.

Conclusion:
Our AuSCs have demonstrated their ability to enhance image contrast in the NIR-II regime, especially with OCT, while remaining aqueously dispersible; one of the few materials of their kind. The coating group can be easily functionalized to create versatile molecular targeting groups. Additionally, the synthetic methodology developed is applicable to a wide range of metals which could lead to an entirely new class of contrast agents across a variety of imaging modalities.

Reference
1. Cao J, Zhu B, Zheng K, et al. Recent Progress in NIR-II Contrast Agent for Biological Imaging. Front Bioeng Biotechnol. 2020;7(January):1-21. doi:10.3389/fbioe.2019.00487
2. Brezinski ME. Current Capabilities and Challenges for Optical Coherence Tomography as a High-Impact Cardiovascular Imaging Modality. Circulation. 2011;123(25):2913-2915. doi:10.1161/CIRCULATIONAHA.111.034272
3. Xu Y, Zhou B, Zhuang C, Zhou J, Chen H, Deng S. High-Aspect-Ratio Plasmonic Heterostructures for In Vivo Enhanced Optical Coherence Tomography Imaging in the Second Near-Infrared Biological Window. Adv Opt Mater. 2020;8(15):1-8. doi:10.1002/adom.202000384
4. Marin R, Lifante J, Besteiro L V., et al. Plasmonic Copper Sulfide Nanoparticles Enable Dark Contrast in Optical Coherence Tomography. Adv Healthc Mater. 2020;9(5):1901627. doi:10.1002/adhm.201901627
5. Zhao Y, Wang Y, Ran F, et al. A comparison between sphere and rod nanoparticles regarding their in vivo biological behavior and pharmacokinetics. Sci Rep. 2017;7(1):4131. doi:10.1038/s41598-017-03834-2
6. Kwon N, Oh H, Kim R, et al. Direct Chemical Synthesis of Plasmonic Black Colloidal Gold Superparticles with Broadband Absorption Properties. Nano Lett. 2018;18(9):5927-5932. doi:10.1021/acs.nanolett.8b02629

Poster Presentation

Disclosures: The authors have disclosed no financial interest.

542-Tracking macrophages in diabetic neuropathy with two-color nanoemulsions by near-infrared fluorescent imaging and microscopy

Presenter: LU LIU, Duquesne University

Jelena M. Janjic[1], James Nichols[2], Hoang Vu Pham[2], Caitlin Crelli[3], **Lu Liu**, Andrew Shepherd[2]

[1]Duquesne University, Pittsburgh, PA
[2]University of Texas MD Anderson Cancer Center, Houston, Texas
[3]Duquesne University, Pittsburgh, North Carolina

Background:
The Millennium Cohort Study, launched in 2001 (which includes all service branches and components), revealed significant prevalence of obesity and diabetes in service members. A major and irreversible complication of diabetes is diabetic peripheral neuropathy (DPN), which can lead to significant disability and loss of quality of life. The current treatments achieve significant DPN pain relief in only half of the patients affected. An additional challenge in the treatment of DPN is that current therapies do not necessarily support nerve repair, which is critical for restoration of function and reduced pain. The impact of poorly-managed DPN is a significant unmet military healthcare problem that lacks a comprehensive strategy to address current treatment deficiencies.
Our prior and ongoing work confirms that DPN is associated with macrophage accumulation near terminals (i.e. in skin) and in the proximal nerve. Based on these findings, we predict that noninvasive tracking of macrophage accumulation along the peripheral nervous system may generate functional insights into the progression of DPN, and suggest therapeutic targets related to development of neuropathy and sensory dysfunction in diabetes.

Methods:
Near-infrared fluorescence (NIRF)-dye loaded macrophage targeted nanoemulsions were injected intravenously into wild-type or type 2-diabetic mice (Leprdb/db males, 8 weeks of age). NIRF fluorescence was captured non-invasively using IVIS Lumina imaging. Tissues were perfusion fixed, sectioned and stained for macrophage and neuron-specific antibodies and analyzed using confocal microscopy.

Results:
NIRF signatures could be detected in footpads using noninvasive whole-animal imaging up to 8 weeks after a single injection, demonstrating the feasibility of this approach. No effect of NIRF nanoemulsion exposure or uptake on macrophage viability was observed in vitro. In immunohistochemistry, robust uptake of NIRF-NE was observed in CD68+ and Iba1+ macrophages in skin, in the tissues surrounding the sciatic nerve and the dorsal root ganglion. Interestingly, NIRF signal was not observed in the sciatic nerve trunk or spinal cord, suggesting a difference of resident macrophages/microglia in their propensity for NIRF-NE uptake, or the inability of NIRF-NEs to cross a cellular barrier in these anatomical locations. Despite the lower effective dose per unit weight in Leprdb/db mice, significant increases in macrophage density were observed when compared to the same tissues in wild-type mice. Such alterations were associated with development of behavioral changes that are indicative of sensorimotor dysfunction (von Frey test, Catwalk assay).

Conclusions:
In summary, the NIRF imaging signatures in our macrophage-targeted nanoemulsions could be used in future as a drug delivery system, as well as serving as a durable indicator of the site of drug delivery, as well as how long drug combinations are present in specific target cells. There is currently a lack of understanding of DPN pain, neuroinflammation and poor regeneration found in diabetes. The molecular imaging incorporated into NIRF-NE platforms could provide insights into these relationships that can drive further treatment development.

Poster Presentation

Disclosures: The authors have disclosed no financial interest.

543-Imaging Anaplerosis in Heart Failure by PET

Presenter: Juan Azcona, Weill Cornell Medicine

Juan A. Azcona[1], Alejandro Amor-Coarasa[2], Chul-Hee Lee[3], Thomas M. Jeitner[4], Camille Daviaud[5], Claire Vanpouille-Box[5], James M. Kelly[6]

[1]Weill Cornell Medicine, New York
[2]Albert Einstein College of Medicine, Bronx, New York
[3]Weill Cornell Medicine, NY
[4]Weill Cornell Medicine
[5]Weill Cornell Medicine, New York, New York
[6]Weill Cornell Medicine, New York, NY

Abstract body:
The healthy, functional heart relies on mitochondrial oxidation of palmitate to fuel the TCA cycle. An initial consequence of heart failure is the inactivation of palmitoyl-CoA mitochondrial transporters [1]. To compensate, cardiomyocytes rely on TCA cycle anaplerosis to meet their energetic demands [2]. Short chain fatty acids (SCFA) can enter mitochondria independently of fatty acid shuttling systems and serve as some of the many substrates used during this metabolic shift. Propionate is a unique SCFA as it is not β-oxidized to acetyl-CoA, for which the enzymes are saturated by the metabolic flux in mitochondria. By contrast, propionate is metabolized to succinate *via* a separate pathway and used as a substrate for Complex III in the electron transport chain [3]. The first step for SCFA catabolism is the formation of fatty acyl-CoA intermediates which are catalyzed by acyl-CoA synthetases. Acyl-CoA synthetase short-chain family 1 (ACSS1) is most highly expressed in the heart and converts propionate to propionyl-CoA [4,5]. Moreover, both the expression and enzymatic activity of ACSS1 are upregulated in the failing heart [5-7]. The upregulation of ACSS1 and the increased demand for SCFA which occur during heart failure will promote the uptake and metabolism of 2-[^{18}F] fluoropropionate (FPA). We hypothesize that the differential uptake of [^{18}F]FPA by the heart can be imaged by PET, and further be used to diagnose incipient heart failure which precedes pathological and irreversible tissue remodeling. We addressed our hypothesis by studying the substrate behavior of FPA for ACSS1, and by metabolic profiling HepG2 cells incubated with FPA. We also successfully imaged heart uptake of [^{18}F]FPA in mice by PET.

Methods:
ACSS1 activity was determined by colorimetric pyrophosphate assay. FPA metabolites were determined by LC/MS in HepG2 cell lysates. Racemic [^{18}F]FPA was synthesized from methyl-2-bromopropionate by standard nucleophilic substitution in dry acetonitrile. The ester was hydrolyzed to the acid with 5M HCl and the ensuing product purified by HPLC in pure saline. This solution was directly administered intravenously to mice. In one experiment, *nu/nu* mice (n=2) were injected with 250-500 µCi (9.25-18.5 MBq) of [^{18}F]FPA, and a 60 min dynamic PET scan was immediately acquired, followed by 15 min static acquisitions at 2 h and 4 h post injection (p.i.). In a parallel experiment, *nu/nu* mice (n=2) were pre-treated with MCT inhibitor

AZD3965 and imaged by the same protocol. In a separate experiment, male C57BL/6J mice (n=4) were irradiated with 3 x 8 Gy using an arc beam and a 3 x 3 mm collimator with the isocenter on the heart. Seven weeks after conclusion of the irradiation, mice were administered 200-250 μCi (7.4-9.25 MBq) [^{18}F]FPA and a 60 min dynamic PET scan was immediately acquired, followed by a 15 min static acquisition at 3 h p.i. [^{18}F]FPA uptake was determined by drawing a volume of interest (VOI) over tissues including, heart, brain, liver, kidney, muscle, and bone, and expressed as injected activity/tissue volume.

Results:
The kinetic characteristics for the reaction of ACSS acting on acetate ($K_m = 4.94$ mM, $V_{max} = 0.25$ nmols/sec), propionate ($K_m = 24.20$ mM, $V_{max} = 0.19$ nmols/sec), and 2-fluoropropionoate (V = 0.05 nmols/sec) were determined. Free CoA is depleted in HepG2 cells incubated in 10 mM propionate (4.4 ± 1.2-fold) or 10 mM FPA (3.09 ± 0.96-fold). We observed high uptake of [^{18}F]FPA in the hearts of mice by PET. Inhibition of MCT by AZD3965 significantly decreased [^{18}F]FPA uptake in all tissues but the heart and kidneys. Cardiac uptake of [^{18}F]FPA increased in mice with external beam irradiation-induced cardiomyopathy relative to the control subjects, although this difference was not statistically significant.

Reference

1. Osorio JC, Stanley WC, Linke A, Castellari M, Diep QN, Panchal AR, Hintze TH, Lopaschuk GD, and Recchia FA (2002) Impaired myocardial fatty acid oxidation and reduced protein expression of retinoid X receptor-α in pacing-induced heart failure. Circulation 106:606–612.
2. Bedi KC, Snyder NW, Brandimarto J, Aziz M, Mesaros C, Worth AJ, Wang LL, Javaheri A, Blair IA, Margulies KB, and Rame JE (2016) Evidence for Intramyocardial Disruption of Lipid Metabolism and Increased Myocardial Ketone Utilization in Advanced Human Heart Failure. Circulation 133:706–716.
3. Wang Y, Christopher BA, Wilson KA, Muoio D, McGarrah RW, Brunengraber H, and GF Zhang (2018) Propionate-induced changes in cardiac metabolism, notably CoA trapping, are not altered by l-carnitine. Am J Physiol Endocrinol Metab 315:E622–E633.
4. Fujino T, Kondo J, Ishikawa M, Morikawa K, and Yamamoto TT (2001) Acetyl-CoA Synthetase 2, a Mitochondrial Matrix Enzyme Involved in the Oxidation of Acetate. J Biol Chem 276:11420–11426.
5. Yoshimura Y, Araki A, Maruta H, Takahashi Y, and Yamashita H (2017) Molecular cloning of rat acss3 and characterization of mammalian propionyl-CoA synthetase in the liver mitochondrial matrix. J Biochem 161:279–289.
6. Colak D, Kaya N, Al-Zahrani J, Al Bakheet A, Muiya P, Andres E, Quackenbush J, and Dzimiri N (2009) Left ventricular global transcriptional profiling in human end-stage dilated cardiomyopathy. Genomics 94:20.
7. Lu Y, Wang Y dong, Wang X ya, Chen H, Cai Z jun, and Xiang M xiang (2016) SIRT3 in cardiovascular diseases: Emerging roles and therapeutic implications. Int J Cardiol 220:700–705.

Poster Presentation

Disclosures: The authors have disclosed no financial interest.

544-Non-invasive Mapping of molecular determinants for multiple cancer and metastatic aggressiveness by Precision MRI (pMRI)

Presenter: Jenny Yang, Georgia State University

Jenny Yang[1], zongxiang gui, Shanshan Tan[2], Jingjuan Qiao[1], Dongjun Li[3], Oluwatosin Y. Ibhagui[4], Hua Yang[5], Khan Hekmatyar[1], Yuguang Meng[1], Nan Wang[6], Yibin Xie[6], Phillip Z. Sun[7], Ekihiro Seki[8], Debiao Li[9], Hans Grossniklaus[5]

[1]*Georgia State University, Atlanta, GA*
[2]*Johns Hopkins Univeristy, Towson, MD*
[3]*Georgia State University, Atlant, GA*
[4]*Georgia State University, atlanta, Georgia*
[5]*Emory University, Atlanta, GA*
[6]*Cedars-Sinai Medical Center, Los Angeles, California, USA*
[7]*Yerkes National Primate Research Center, Atlanta, GA*
[8]*Cedars-Sinai Medical Center, Los Angeles, California*
[9]*Cedars-Sinai Medical Center*

Introduction:
The liver is the most common organ for metastases of various malignancies, especially for pancreatic ductal adenocarcinoma (PDAC), colorectal cancer (CRC), and uveal melanoma (UM). We have found that UM, PDAC, and CRC, share similar pathological growth patterns, suggesting common liver metastasis processes that include formation, predisposition for metastases (pre-met), and formation of pro- and post-metastatic niches for early and late stages of metastasis. Non-alcoholic fatty liver disease (NAFLD) has been reported to significantly increase liver metastasis by orchestrating a pre-metastatic niche with activated hepatic stellate cells (HSCs) and tumor-associated infiltrated immune cells. To date, the detection and characterization of the dynamic changes/interactions of metastasis-associated molecular signatures at multiscale levels *are poorly understood. The investigation of the key molecular signatures including* chemokine receptor CXCR4, and its interaction with its natural ligand CXCL12 (SDF-1) and fibrotic stroma collagen *in regulating the metastasis process largely depends on segmented biochemical and histological approaches that* cannot capture heterogeneity and dynamic expression of these molecular biomarkers.

Results and Conclusion:
In this study, we first demonstrated the chemokine receptor CXCR4, and its interaction with its natural ligand CXCL12 (SDF-1) plays a crucial role in organ specific metastasis progression and outcome. CXCR4 and CXCL12 expression are highly upregulated in liver metastasis and are significantly enhanced in NAFLD. We report the recent development of our pioneered novel class of protein-based MRI contrast agents targeted to CXCR4, CXCL12, and collagen (hProCA32.CXCR4, hProCA32.CXCL12 and hProCA32.collagen) using Precision MRI (pMRI). We also shown that They exhibit high dual relaxivities that are 5-10 folds of Eovist and Multihance at both 1.4T and 7.0T. They have strong affinity and specificity to molecular biomarkers expressed in cancer cells and tumor without perturbing downstream signaling. We have demonstrated that hProCA32.CXCR4 and hProCA32.collagen have enabled early detection and stage of liver metastasis from uveal melanoma, ovarian cancer, colon cancer with much-improved sensitivity and specificity compared with non-targeted agents and Eovist. Using multitasking methodology with high temporal resolution dynamic imaging of the contrast enhancement process without sacrificing spatial resolution[1], we have demonstrated the rapid detection of liver metastasis of colon cancer with further improved detection sensitivity by overcoming motion artifacts. The CXCL12 targeted MRI contrast agent (hProCA32.CXCL12) enables the delineation of the micro-vessel (sinusoid space) structure of the liver using pMRI. We discovered that high fat largely alters liver sinusoid structure with a microenvironment pro-metastasis. Further optimizing of our novel imaging methodology and protein contrast agents will provide a comprehensive, longitudinal view of the key determinants of liver metastasis dormancy, progression, and prognosis, and insight into how the

imaging tool is useful to understand the mechanism of cancer metastasis in normal and fatty liver. Development of molecular imaging tools and agents will impact subclinical detection, staging, and treatment for metastasis from multiple cancers.

Reference

1. Xue, S. et al. Protein MRI contrast agent with unprecedented metal selectivity and sensitivity for liver cancer imaging. Proceedings of the National Academy of Sciences 112, 6607-6612 (2015).
2. Mani, Hua Yang, Shanshan Tan, Jingjuan Qiao, Yiting Xu, Zongxiang Gui, Yuguang Meng, Bin Dong, Guangda Peng, Oluwatosin Y. Ibhagui, Weiping Qian, Jimmy Lu, Zezhong Li, Guimin Wang. Jinping Lai, Lily Yang, Hans E. Grossniklaus, and Jenny J. Yang. Non-invasive detection and complementary diagnostic of liver metastases via chemokine receptor 4 imaging, Cancer Gene therapy, (2021) Feb 10. doi: 10.1038/s41417-022-00433-w. Online ahead of print. PMID: 35145271
3. Yang, Jenny J., et al. "Rational design of protein-based MRI contrast agents." Journal of the American Chemical Society 130.29 (2008): 9260-9267.
4. Tan, S. et al. Chemokine receptor 4 targeted protein MRI contrast agent for early detection of liver metastases. Science Advances 6, eaav7504 (2020).
5. Christodoulou, A.G., et al. Magnetic resonance multitasking for motion-resolved quantitative cardiovascular imaging. Nat Biomed Eng 2, 215-226 (2018).

Poster Presentation

Disclosures: The authors have disclosed no financial interest.

545-First-in-humans fluorescence ratiometric aperture imaging to detect close margins in head and neck cancer resection surgery

Presenter: Cody Rounds, Illinois Institute of Technology

Cody Rounds[1], Jaron de Wit[2], Jasper Vonk[3], Floris J. Voskuil, Jennifer Vorjohan[4], Sophia Nelson[5], Brooke Villinski[4], Allyson Trang[4], Ken Tichauer[1], Max J. Witjes[3]

[1]Illinois Institute of Technology, Chicago, IL
[2]University Medical Center Groningen, Groningen, Netherlands
[3]University Medical Center Groningen, Groningen, Groningen, Netherlands
[4]Illinois Institute of Technology, Chicago, Illinois
[5]Illinois Institute of Technology, Warrenville, Illinois

In 2018 alone, it is estimated that there were nearly 1 million new cases of head and neck squamous cell carcinoma (HNSCC) worldwide. This number is only rising, as it is estimated cases will increase 30% over the next decade.[1] Of those who were eligible for surgical intervention, up to 20-50% of patients are estimated to have been sent home after surgery without the entirety of their primary tumor removed.[2] To address this, research groups are exploring the use of molecularly-specific fluorescent probes to increase contrast between healthy and diseased tissue intraoperatively — providing real-time information to surgeons about the molecular status of potentially abnormal tissue in addition to traditional visual/tactile inspection[5]. Currently, reported methods in the literature show promising results, yet a major recurrent challenge has been the accurate classification of "close" surgical margins in the 2-5-mm thickness range[4]. To address this, we are employing a "ratiometric" approach — similar to that proposed by Quan and Ramanujam[3], where each sample is imaged at two numerical apertures, termed "open" and "closed" images. A pixel-by-pixel ratio of the images is then calculated, with the intention of constructing a 3D "depth-of-fluorescence map" of a sample's surface. This method leverages the differences in photon scattering profiles when emitted from varying depths by taking advantage of the distinct photon angular distribution profiles owing to the anisotropic, forward scattering nature of photon propagation in tissue. Our initial investigations explored this idea using monte carlo based simulations of fluorescent inclusions in a tissue "cuboid" situated at varying distances from the surface (1-5 mm). By leveraging the differences in photon scattering profiles at different depths, we demonstrated that it is possible to extract information about a fluorescent signal's depth of origin. Upon verification of the concept's utility via simulations, a custom-built widefield fluorescent imaging device with a large range of possible numerical apertures was constructed. A custom NIR quantum-dot phantom with depth resolution was then imaged and analyzed. Finally, the prototype system was deployed in an ongoing clinical trial (**NCT03923881)** where clinical data from 3 HNSCC samples were imaged and analyzed, followed by subsequent comparison to H&E pathology data to assess accuracy of the measurements. This ratiometric analysis shows a stronger correlation between pixel intensity and true margin depth than imaging at a high or low numerical aperture alone.

Reference

1. Johnson, D.E., Burtness, B., Leemans, C.R. et al. Head and neck squamous cell carcinoma. Nat Rev Dis Primers 2, 92 (2020). https://doi.org/10.1038/s41572-020-00224-3
2. Orosco RK, Tapia VJ, Califano JA, et al. Positive Surgical Margins in the 10 Most Common Solid Cancers. Sci Rep. 04 2018;8(1):5686. doi:10.1038/s41598-018-23403-5
3. Quan, L., & Ramanujam, N. (2002). Relationship between depth of a target in a turbid medium and fluorescence measured by a variable-aperture method. Optics Letters, 27(2), 104-106.
4. van Keulen S, van den Berg NS, Nishio N, et al. Rapid, non-invasive fluorescence margin assessment: Optical specimen mapping in oral squamous cell carcinoma. Oral Oncol. 01 2019;88:58-65.
5. Rosenthal EL, Warram JM, de Boer E, et al. Safety and Tumor Specificity of Cetuximab-IRDye800 for Surgical Navigation in Head and Neck Cancer. Clin Cancer Res. Aug 2015;21(16):3658-66. doi:10.1158/1078-0432.CCR-14-3284

Poster Presentation

Disclosures: The authors have disclosed no financial interest.

546-Design and Synthesis of [18F]NTRX-07, a Novel Imaging Agent to Assess Microglial Activation in the Central Nervous System

Presenter: Chunying Wu, Case Western Reserve University

Chunying Wu[1], Zhiqiang Xia[1], Junqing Zhu[1], George Wang[2], Tony Giordano[3], Yanming Wang[1]

[1]Case Western Reserve University
[2]Phillips Academy Andover, Andover, Massachuset
[3]NeuroTherapia Inc, Cleveland, Ohio

Microglia play a critical role in CNS immune responsiveness. Microglial dysregulation has been linked to a number of neurodegenerative diseases, including, Alzheimer's disease (AD), Parkinson's disease, multiple sclerosis, ALS, and Huntington's disease. Currently, several

imaging markers of neuroinflammation have been developed. However, many of such imaging agents exhibited suboptimal cellular specificity and low signal-to-noise ratios with limited overall success in the clinical setting. The goal of this study is to develop a more sensitive imaging marker by design and synthesis of an F-18 radiolabeled NTRX-07 developed by NeuroTherapia for in vivo studies of microglial activation in the central nervous system. For F-18 labeling of NTRX-07, a tin precursor was first prepared through a palladium-catalyzed tandem dihydro benzofuran cyclization/ Suzuki-coupling approach[1,2]. Radiosynthesis was carried out through a reaction of anhydrous potassium fluoride complex ([^{18}F]KF) with a solution of the trimethyltin precursors dissolved in N, N-Dimethylacetamide (DMA) in the presence of copper triflate. The identity of [^{18}F]-NTRX was confirmed by co-injection of non-radioactive reference compound NTRX on analytical HPLC with a radiochemical purity of >99%. Following the radiosynthesis, PET imaging of [^{18}F]NTRX was performed using a Siemens Inveon microPET/CT scanner. For anatomic localization, CT co-registration was applied. Thus, prior to PET imaging, a CT scout view was taken to ensure either the brain or most of the vertebrae, were placed in the co-scan field of view (FOV) where the highest image resolution and sensitivity are achieved. Approximately 3.7-7.4 MBq of [^{18}F]NTRX was injected through the tail vein, and dynamic microPET data acquisition was performed in a list mode immediately. During the scans, the body temperature and respiration of the anesthetized rats were monitored and maintained. Once the dynamic acquisition was done, a CT acquisition scan was performed for attenuation correction. Quantitative image analysis of the radiotracer uptake in the spinal cord and the brain were performed using Carimas II software. This program allows a region of interest (ROI) to be extrapolated from the reconstructed microPET image frames, allowing the quantification of the SUV in a specific region. Based on the PET and CT co-registered images, brain, heart, liver, lung, kidney, and muscle were then defined as an ROI. The radioactivity data were decay-corrected and normalized by the bodyweight of the mice and the amount of the radiotracers injected. Radioactivity concentration in the organs is expressed in terms of standard uptake value (SUV) and percentage of injected dose per gram of the organ (ID%/g) as a function of time. The time-activity curve (TAC) in various organs was obtained. As shown in Figure 1, [^{18}F]NTRX-PET showed a promising biodistribution in wild-type mice. The uptake in the brain increased as a function of time and reached a plateau at 90 min post-injection while the uptake in the liver gradually decreased. No significant uptake was observed in the kidney, heart, lung, and muscles as expected. Further studies are underway to explore the utility of [^{18}F]NTRX as a novel imaging agent in various disease models associated with neuroinflammation.

Reference

1. M. Naguib; P. Diaz; J.J. Xu; F. Astruc-Diaz; S. Craig; P. Vivas-Mejia; D.L. Brown British Journal of Pharmacology 155, 1104–1116 (2008)
2. Magali Szlosek-Pinaud; Philippe Diaz; Jean Martineza; Frederic Lamatya Tetrahedron 63, 3340–3349 (2007)
3. Z. Luo; M. Naguib Tetrahedron Letters 53, 3316-3318 (2012)

Poster Presentation

Disclosures: The authors have disclosed no financial interest.

547-Application of a minimized fluorescence sensor in intraoperative surgical guidance with a urokinase-type plasminogen activator receptor-targeted probe

Presenter: Cheng Wang, University of California San Francisco

Cheng Wang[1], Shih-Wei Chuo[1], Micah Roschelle[2], Charles Craik[3], Mekhail Anwar[4]

[1]University of California San Francisco
[2]University of California, Berkeley, Berkeley, CA
[3]University of California, San Francisco, San Francisco, California
[4]University of California, San Francisco, San Francisco

Molecular targeted fluorescence agents aiming at enabling surgeons to visualize tumors intraoperatively and perform precise resections have been developed over years. However, intraoperative fluorescence imaging systems are typically bulky with sophisticated optical lenses, which limit their maneuverability for microscopic residue tumor detection in the resection bed. A chip-scale fluorescence sensor has been developed for microscopic tumor detection. The optics-free sensor is only 2 mm thick and has a 2x4.4mm field of view which minimizes form-factor and achieves great maneuverability when integrated with surgical robots. In addition, the field of view of the sensor can be scaled up without compromising the resolution which is absolutely not the case in the lensed system. The angle-selective gratings and contact imaging enable the collection of photons emitted from the pixel location, which limit the light scattering and provide high-resolution images. With custom-designed filters, this sensor collects light in the near-infrared range which facilitates its translation into fluorescence-guided surgery. The residual tumor burden correlates with the rate of cancer recurrence, which every surgeon wants to avoid in surgical excision. The high rates of recurrence are prone to happen in aggressive cancer types. Triple-negative breast cancer, for example, recurs in 40 percent of patients despite treatment. The recurrence in hard-to-treat cancer types leads to poor patient outcomes and low survival rates. Therefore, probes for the malignant cancer diagnosis are urgently needed. It's been shown that Urokinase-type plasminogen activator receptor (uPAR) expression reflects the increased invasion and metastasis and is associated with a poor prognosis in several cancer types. As an attractive diagnosis and therapeutic target, uPAR is expressed at low levels in healthy tissues but at high levels in malignant tumors. In this study, we use a humanized anti-uPAR antibody (2G10) conjugated with IRDye 680LT as the probe and the chip sensor to intraoperatively detect microscopic residue tumors. As a proof-of-concept, we implanted two breast cancer MCF-7, an undetectable uPAR expression cell line, and MDA-MB-231, which overexpress uPAR, in the flank of 8 mice. 2G10-IRDye 680LT was injected through the tail vail when the tumor size reaches 1 cm. After 72 hours of injection, the tumor was imaged by IVIS Spectrum in vivo. Ex-vivo imaging of the tumor and surrounding normal tissue were performed by both IVIS Spectrum and chip-sensor. We found that the chip sensor achieved a comparable diagnostic ability with IVIS Spectrum. In the next step, we plan to take the chip-sensor into the clinical trial as the margin assessment method after surgical resection. We believe the sensor has the potential to improve the complete removal of microscopic residual disease during surgical resection.

Poster Presentation

Disclosures: The authors have disclosed no financial interest.

548-Reference targets for the translation of fluorescence guided surgery systems

Presenter: Alberto Ruiz,Dartmouth College

Alberto Ruiz[1], Ethan LaRochelle[2]

[1]Dartmouth College, Hanover, NH
[2]QUEL Imaging, White River Junction, VT

The emerging clinical use of targeted fluorescent agents has led to a shift in intraoperative imaging practices that overcome the limitations of human vision. However, in contrast to established radiological methods, no appropriate performance specifications and standards have been developed in fluorescence-guided surgery (FGS).[1,2] As the field of FGS expands, there is a wider range of imaging systems indicated for the same uses, such that there is a compelling need for standards that enable system characterization, performance monitoring, and intersystem comparisons.[1,3–5] The performance of imaging systems can affect surgical decision-making,[2,6] so knowledge of their performance capabilities is especially relevant given the real-time surgical decisions that are made with these systems. Here, we discuss the development and design of indocyanine green reference targets that mimic application-specific fluorescence spectra for FGS system standardization. These targets test: 1) varying concentration sensitivity (0.3 - 1000 nM), 2) tissue-equivalent-depth sensitivity (0.5 – 6 mm), 3) fluorescence spatial resolution (using a negative 1951 USFA test chart), and 4) varying optical property (absorption and reduced scattering) effects on fluorescence intensity output. The targets were used to characterize pre-clinical and clinical systems to determine performance variations, demonstrating the ability to provide cross-system comparisons. These targets are now commercially available in an effort to help expedite FDA 510K approvals and reduce the development cost of FGS devices. The design has also been expanded for the use of methylene blue and OTL-38 fluorescence system characterization. Collaborations with academic and industry partners are ongoing to continue to iterate on target design and provide the necessary tools to bring standardization to the field of FGS. The targets described are the first set of commercially available references, with over 20 sets provided to FGS partners. On-going work in standardizing the image processing pipelines, providing radiometric calibration, and establishing a medical-device grade quality management system for manufacturing are on-going. Collaboration between academic, industry, and regulatory stakeholders will play a key role in the adoption of imaging standards within fluorescence guidance.

Reference

1. M. Koch, P. Symvoulidis, and V. Ntziachristos, "Tackling standardization in fluorescence molecular imaging," Nature Photonics 12(9), 505 (2018) [doi:10.1038/s41566-018-0221-5].
2. M. Koch and V. Ntziachristos, "Advancing Surgical Vision with Fluorescence Imaging," Annual Review of Medicine 67(1), 153–164 (2016) [doi:10.1146/annurev-med-051914-022043].
3. D. Gorpas et al., "Benchmarking of fluorescence cameras through the use of a composite phantom," JBO 22(1), 016009 (2017) [doi:10.1117/1.JBO.22.1.016009].
4. B. Zhu et al., "Determining the Performance of Fluorescence Molecular Imaging Devices Using Traceable Working Standards With SI Units of Radiance," IEEE Transactions on Medical Imaging 35(3), 802–811 (2016) [doi:10.1109/TMI.2015.2496898].
5. B. W. Pogue and M. S. Patterson, "Review of tissue simulating phantoms for optical spectroscopy, imaging and dosimetry," JBO 11(4), 041102, International Society for Optics and Photonics (2006) [doi:10.1117/1.2335429].

Poster Presentation

Disclosures: The authors have disclosed no financial interest.

549-68Ga-Galmydar: Semi-Automated GMP-Production for Clinical Studies

Presenter: Jothilingam Sivapackiam, Washington University School of Medicine

Jothilingam Sivapackiam[1], chris bognar[2], nerissa brame-torrey[3], Thomas H. Schindler[4], Pamela Woodard[4], Michael Nickels[1], Vijay Sharma[5]

[1]Washington University School of Medicine, St. Louis, MO
[2]Washington University in St. Louis, Saint Louis, MO
[3]Washington University in St. Louis, MO
[4]Washington University in St. Louis
[5]Washington University School of Medicine, St. Lous, MO

Myocardial Perfusion Imaging (MPI) plays an important role in the noninvasive assessment of Coronary Artery Disease (CAD). For wider deployment of PET imaging resources to enable quantitative detection of CAD, ^{68}Ga-Galmydar, an ultrasensitive probe shows rapid uptake and sustained retention within the myocardium and Pgp (ABCB1) and BCRP (ABCG2)-mediated excretion from the liver in rodent models to enable high contrast myocardium imaging. ^{68}Ga-Galmydar provides a functional readout of mitochondrial status within myocytes. We recently gained FDA approval for performing first in human studies. For consistent supply of high-quality radiotracer needed for performing clinical studies, we have developed a semi-automated method for ^{68}Ga-Galmydar production under Good Manufacturing Practice (GMP)-compliant conditions in our cyclotron facility at the institution. For the production of the radiotracer, the $^{68}GaCl_3$ was eluted from a generator using 0.1M HCl, the eluted mixture was passed through a cation exchange column to remove tracer metal impurities, and finally, pure $^{68}GaCl_3$ was eluted with 0.02M HCl in acetone/water mixture. Reaction parameters, such as buffer conditions, pH range, reaction temperature and time, the volume of the reaction solution, and purification were optimized for radiolabelling. ^{68}Ga-Galmydar was obtained by heating 25 µg of precursor ligand at pH 6 for 15 min at 95° C. Semi-automated synthesis resulted in overall decay-corrected reaction yields of about 70% within 30 min. Production yields for each synthesis were calculated to monitor the performance and efficiency of the radiochemical synthesis. Conclusion: This methodology allows a semi-automated and efficient production of ^{68}Ga-Galmydar under GMP conditions. It has been used successfully for the preparations of clinical doses needed for performing human studies.

Reference

1. Sharma, V., et al., PlosOne, 2014, 9, e109361
2. Sivapackiam, J., Nucl. Med. Biol., 2016, 43, 191-197
3. Sivapackiam, J., et al., Med. Chem. Commun., 2017, 8, 158
4. Sivapackiam, J., et al., Nucl. Med. Biol., 2018, 59, 29-35
5. Sivapackiam, J., et al., PLoS ONE 14(5): e0215579
6. Sivapackiam, J., et al., Curr. Cardiol. Rep., 2020, 22, 62.

Poster Presentation

Disclosures: The authors have disclosed no financial interest.

550-ImmunoPET Imaging of CD69 Visualizes T-cell Activation and Predicts Survival following Immunotherapy in Murine Glioma.

Presenter: Sarah Vincze, University of Pittsburgh

Sarah R. Vincze

University of Pittsburgh, Pittsburgh, PA

Cytotoxic T-cells are key mediators of autoimmune disease, cancer immunotherapy responses, and host immunity in infections.

Noninvasive monitoring of T-cell activity in patients is therefore critical for elucidation of disease mechanisms and therapeutic responses. While the presence of $CD8^+$ cytotoxic T-lymphocytes (T-cells) provides insight on disease pathology, the presence of CD8 alone is insufficient to demonstrate T-cell function. Upon T-cell activation, CD69, a C-Type lectin protein, is transiently expressed on the surface of T-cells and may serve as a marker for T-cell activity. Our aim is to use immunoPET imaging to accurately measure CD69 expression on cytotoxic T-cells in a syngeneic glioma model, following immunotherapy, and correlate the expression to survival. We anticipate non-invasive monitoring of immunotherapeutic efficacy. To monitor T-cell activation as a surrogate of response to immunotherapy in murine glioma models, an anti-mouse CD69 antibody, was conjugated with DFO and radiolabeled with ^{89}Zr. PET/CT imaging, with and without immune checkpoint inhibitor (ICI) therapy (anti-PD-1/anti-CTLA-4 antibody), was performed in syngeneic GL261 mouse gliomas. Flow cytometry and immunostaining of *in vitro* activated T-cells and *ex vivo* isolated tissues were used to validate targeting of CD69. Single-cell RNA sequencing (scRNAseq) of dissociated glioma tissues from patients receiving or not receiving checkpoint inhibitor immunotherapy were compared for CD69 expression on multiple T-cell phenotypes. *In vitro*, human and mouse T-cells rapidly upregulated CD69 upon activation. In a murine glioma model, CD69 expression significantly increased on tumor infiltrating T cells (TILs) upon ICI treatment. scRNAseq demonstrated elevated CD69 expression on effector and memory T-cell populations, in patients treated with ICI compared with patients not treated with ICI. immunoPET studies with ^{89}Zr-DFO-anti-CD69 delivered via tail vein to glioma-bearing mice demonstrated significantly higher tracer uptake in the tumors of ICI treated mice compared with controls (p=0.000781). Notably, ICI treated mice demonstrated a significant positive correlation between survival and tracer standard uptake values (SUV) by PET imaging at 72 hours post-tracer injection (r=0.9837; p=0.0025), and opposing results were identified for the control group (r=-0.9937; p=0.0063). Conclusion: $CD8^+$ T cell activation in response to immunotherapy was quantified with anti-CD69 expression using immunoPET in a murine glioma model, which reflected real time changes in $CD8^+$T cell infiltration after checkpoint immunotherapy. Together with data demonstrating elevated CD69 on T-cells from ICI treated patients vs. untreated patients, this study shows the potential for incorporation of immunoPET to determine patient response to immunotherapy.

Poster Presentation

Disclosures: The authors have disclosed no financial interest.

551-Quantitative Methodology for Fluorescence-Guided Robotic Surgery

Presenter: Logan Stone, University of Birmingham

Logan Stone[1], Shilpa M. Rao[2], Manuel Lora Gonzalez[3], Hari Jeyarajan[3], Carissa Thomas[3], Jason Warram[4]

[1]*University of Birmingham, Birmingham*
[2]*University of Alabama at Birmingham Heersink School of Medicine, Birmingham, AL*
[3]*Birmingham, AL*
[4]*University of Alabama at Birmingham, Birmingham, AL*

Introduction:
Oropharyngeal squamous cell carcinoma (OPSCC) has been shown to over express epidermal growth factor receptor (EGFR), making it a targetable biomarker for fluorescently-labeled monoclonal antibodies such as panitumumab-IRDye800, which can be used during fluorescence-guided trans oral robotic surgery (TORS). Although antibody-based fluorescence-guided surgery is being evaluated in several late-stage trials, the typical classification used to define the fluorescence in imaging tissue includes “solid”, “moderate”, or “vague”. These anecdotal classifications are insufficient when guiding surgical care in advanced stage trials and should be supported by specific criteria for determining positive fluorescence (1-3).

Methods:
During a phase 2 clinical trial evaluating panitumumab-IRDye800 fluorescence-guided TORS of OPSCC, consenting patients (n=6) with biopsy-confirmed OPSCC received 50mg panitumumab-IRDye800 48 hours prior to surgery. Intraoperative fluorescence images were acquired using the onboard fluorescence camera. Representative frames from the Da Vinci Xi robot video were selected via custom MATLAB software and quantified using ImageJ ROI manager. To achieve a standardized fluorescence ratio (SFR) for comparison, fluorescence counts from areas of interest were collected and divided by fluorescent counts acquired from the fluorescing robot manipulator instrument within the same field of view. The areas of interest were then correlated with histology and an SFR threshold was identified that delineated tumor from normal tissue.

Results:
For each patient, 10 total ‘sequences’ were extracted containing pathologist verified tumor, negative margins, normal mucosa and the wound bed. From the frames extracted from those sequences, a total of 9,177 pixels were extracted and quantified using ImageJ. Counts for tumor (51.33 ± 10.96), normal mucosa (10.97 ± 6.56) and negative margins (15.60 ± 4.13) were recorded. From those values, a SFR was calculated for tumor (13.09 ± 26.24), which was significantly greater than negative margin (1.11 ± 0.49, p<0.0001) and normal tissue (1.14 ± 1.01, p<0.0001). Using an SFR threshold of 2.0 yielded a sensitivity of 90% and specificity of 100% for detecting OPSCC during quantitative fluorescence-guided TORS.

Conclusion:
This technique can be used for future surgeries to reveal cancerous tissue, ensuring more accurate and precise resection of the tumor and thus increasing the probability of negative margins.

Reference
1. Warram, J.M., et al., A ratiometric threshold for determining presence of cancer during fluorescence-guided surgery. J Surg Oncol, 2015. 112(1): p. 2-8.
2. Marston JC, Kennedy GD, Lapi SE, Hartman YE, Richardson MT, Modi HM, Warram JM. Panitumumab-IRDye800CW for Fluorescence-Guided Surgical Resection of Colorectal Cancer. J Surg Res. 2019 Jul;239:44-51. doi: 10.1016/j.jss.2019.01.065. Epub 2019 Feb 22. PMID: 30798171; PMCID: PMC6488377.
3. Gao RW, Teraphongphom N, de Boer E, van den Berg NS, Divi V, Kaplan MJ, Oberhelman NJ, Hong SS, Capes E, Colevas AD, Warram JM, Rosenthal EL. Safety of panitumumab-IRDye800CW and cetuximab-IRDye800CW for fluorescence-guided surgical navigation in head and neck cancers. Theranostics. 2018 Mar 28;8(9):2488-2495. doi: 10.7150/thno.24487. PMID: 29721094; PMCID: PMC5928904.

Poster Presentation

Disclosures: The authors have disclosed no financial interest.

552-Fibroblast activation protein-α expressing cancer associated fibroblasts in syngeneic mouse models and their depletion by near-infrared photoimmunotherapy

Presenter: Jiefu Jin, Johns Hopkins University School of Medicine

Jiefu Jin

Johns Hopkins University School of Medicine, Baltimore, MD

Introduction:
As the most abundant stromal cells in the tumor microenvironment (TME), cancer associated fibroblasts (CAFs) play diverse roles in cancer progression and metastasis.[1] A subset of CAFs that express fibroblast activation protein alpha (FAP-α) have protumorigenic and immune suppressive functions.[2] Thus, FAP-α is an attractive molecular target for cancer imaging and treatment, especially in stromal-rich desmoplastic cancers.[3] Here, we established several syngeneic mouse models to examine the presence of murine FAP-α expressing CAFs and their relations with $CD4^+$ and $CD8^+$ T lymphocytes. As an extension to our previous near-infrared photoimmunotherapy (NIR-PIT) studies,[4] we selected a mouse monoclonal antibody with high affinity and specificity to murine FAP-α to conjugate with the phthalocyanine dye IR700 for NIR-PIT. The resultant antibody conjugate FAP-α-IR700 was evaluated for the selective elimination of FAP-α expressing fibroblasts in culture and in syngeneic mouse models following NIR-PIT.

Method:
Anti-FAP-α mouse monoclonal antibody (FAP5) and its IgG isotype control were conjugated with IR700 to form FAP-α-IR700 and IgG-IR700, respectively. Murine NIH-3T3 fibroblasts were lentivirally transduced using a lentiviral vector, pMA3211, containing murine FAP-α cDNA to obtain 3T3-FAP cells. Syngeneic tumor models were established in the mammary fat pad for 4T1, E0771, and EMT-6 tumors or in the mouse flank for CT-26, MC-38 and Panc02 tumors. For *in vivo* NIR-PIT studies, once tumor volume reached approximately 400 mm^3, 100 µg of FAP-α-IR700 was injected *i.v.* on day 0 and day 3 ($n \geq 4$ per group). Light was delivered at 200 J/cm^2 24-h following each injection. Mice were sacrificed on day 6 and tumors were resected and processed for flow cytometry, western blotting and immunohistochemistry studies. IgG-IR700 and PBS-injected mice were used as controls.

Results and Discussion:
Murine FAP-α overexpression was validated in transduced NIH-3T3 fibroblasts (termed 3T3-FAP) by RT-PCR and western blotting (Fig. S1). Mouse monoclonal antibody FAP5 demonstrated specific binding to murine FAP-α on 3T3-FAP cells (Fig. 1a), and the resultant conjugate FAP-α-IR700 showed FAP-α-specific cell killing by NIR-PIT that exhibited concentration and exposure-dose dependence (Fig. 1b, c). Co-culturing Balb/3T3 fibroblasts with 4T1 or CT26 cells resulted in an increase of murine FAP-α levels (Fig. S2a), enabling activated fibroblasts to be specifically eliminated by FAP-α-IR700-based NIR-PIT (Fig. S2b). Murine FAP-α expressing CAFs in syngeneic mouse tumors displayed a range of fractions as well as FAP-α expression levels (Fig. 1d). $CD4^+$ T lymphocytes in tumors positively correlated with $CD8^+$ T lymphocytes, and negatively correlated with the FAP-α fraction (Fig. S3, 4). FAP-α-rich CT26 tumors had negligible $CD4^+$ or $CD8^+$ T lymphocytes, while FAP-α-poor Panc02 tumors had the highest amount of $CD4^+$ or $CD8^+$ T lymphocytes, consistent with the immune suppressive role of FAP-α+ CAFs. *In vivo*, however, we did not detect an FAP-α+ cell fraction-dependent increase of fluorescence intensity of FAP-α-IR700 in tumors, or a significant reduction of FAP-α+ CAFs or a change in immune cells following NIR-PIT (data not shown). This was most likely due to the relatively low FAP-α expression levels in mouse tumors (Fig. 1d, e) that limited detection and cell killing. Once high FAP-α+ CAFs were isolated and enriched from CT26 tumors, FAP-α+ CAFs viability significantly decreased with NIR-PIT (Fig. 1f, g) although with a higher antibody and light exposure dose not achievable *in vivo*. Our data confirm the importance of FAP-α+ CAFs as an immune suppressive target in cancer, but also highlight the requirement of high FAP-α expression for successfully imaging and eliminating FAP-α+ CAFs in tumors. Supported by NIH R35 CA209960, P41 EB024495 and Emerson Collective Cancer Research Fund

Reference
1. Prakash, J. et al. Trends Cancer. 2016;
2. Kieffer, Y. et al. Cancer Discov. 2020;
3. Puré, E. et al. Oncogene. 2018;
4. Jin, J. et al. Sci Rep. 2016, Cancers. 2021.

Poster Presentation

Disclosures: The authors have disclosed no financial interest.

553-Granzyme B Specific Probe for the Imaging of Viral and Bacterial Infections

Presenter: Apurva Pandey, University of California, San Francisco

Apurva Pandey[1], Shalini Chopra[2], Sasank Sakhamuri[3], Michael J. Evans[1], Simon Cleary[4], David M. Wilson[1]

[1]*University of California, San Francisco, San Francisco, CA*
[2]*University of California, San Francisco, San Francisco*
[3]*University of California San Francisco*
[4]*University of California, San Francisco, CA*

Currently, the clinical diagnosis of bacterial and viral infections of the bone (osteomyelitis), muscles (myositis) and lungs (influenza) are based on assessment of several non-specific symptoms such as skin findings, fever, and pain. There is an urgent unmet need for non-invasive tools that can localize and identify deep-seated infections as well as those that reveal an ongoing effective host response to viral and bacterial pathogens. Nuclear imaging tracers are ideally suited to detect small quantities of infected tissue and immune responses in-vivo can meet the need for faster, more accurate and specific tools to diagnose infections. Granzymes (GZM) are a class of serine proteases (A, B, H, K, M) involved in host defense best characterized as pro-apoptotic effectors against cancer cells or infected cells. Secreted granzymes also persist in extracellular space to perform non-cytotoxic signaling functions essential for life. Therefore, targeting granzymes could be a powerful way to both reveal the presence of occult infection while estimating the productivity of the immune response in real time. We hypothesize that a peptide activated by granzyme B (DOTA-GRIP-B), radiolabeled with ^{64}Cu ($t_{1/2} = 12.7$ h, PET) can take advantage of the granzyme targeting peptide and accumulate in sites of infection with high specificity and could also provide a readout of units of enzyme activity in vivo. The ~13h half-life would enable studies over a long window of time post injection to identify the optimal time point for imaging. We have successfully studied ^{64}Cu-DOTA-GRIP-B in a flu (viral infection) and myositis (bacterial infection) model. Radiolabeling with ^{64}Cu produced the radiochemical complex with > 95% radiochemical yield and purity. ^{64}Cu-DOTA-GRIP-B was injected in WT Bl6 mice inoculated with different live and heat-killed bacterial strains.

Subsequent imaging and biodistribution revealed granzyme specific uptake in live bacteria. Control studies in GzmB KO mice confirmed the specificity of ^{64}Cu-DOTA-GRIP-B for granzyme B. The probe was also injected into mice instilled with H1N1 PR8. Biodistribution revealed significantly elevated uptake in lungs for WT mice as compared to GZMB KO mice. Additional in-vivo experiments are currently ongoing, and results will be presented.

Reference

1. ACS Cent. Sci. 2021, 7, 10, 1638–1649

Poster Presentation

Disclosures: The authors have disclosed no financial interest.

554-MR based phenotyping in tandem with autonomic function evaluation in healthy volunteers

Presenter: CHETNA BANGA, All India Institute of Medical Sciences (AIIMS)

Chetna Banga[1], Preeti Bhosle[2], Dushyant Kumar, K.K Deepak[1], Dinu Chandran[1], Rama Jayasundar[3]

[1]All India Institute of Medical Sciences (AIIMS), New Delhi, Delhi, India
[2]All India Institute of Medical Sciences (AIIMS), New Delhi, India
[3]All India Institute of Medical Sciences (AIIMS), New Delhi, India, New Delhi, Delhi, India

Introduction:
With the growing demand for precision medicine, phenotyping has become as important as genotyping to identifying risk groups for specific diseases and for customizing diet and lifestyle.[1] The horizon of precision medicine has expanded beyond genotyping to areas such as molecular profiling, proteomics and phenotyping, providing new opportunities for developing dynamic multi-scale models of individual health.[2] Phenotyping includes physical, functional and physiological characteristics. This study has evaluated physical and functional phenotyping with MR-based body composition analysis and resting state fMRI (R-fMRI), respectively and physiological phenotyping with autonomic functions such as heart rate variability and hand grip.[3]

Material and Methods:
Volunteer recruitment: The study was carried out after Ethical clearance from the Institute. Healthy volunteers (n=18) of both genders, aged between 20-35 years were enrolled for the study after taking written informed consent. *MR studies:* The studies were carried out at 3T (MR Scanner, Philips). mDIXON- Quant sequence was used for evaluating the subcutaneous fat of abdomen and thigh regions[4]. The following acquisition parameters were used FOV- 400x329x188 mm^3, voxel- 2x2.5x5 mm^3, matrix- 200x312x74. R-fMRI are carried out using a FOV of 230x230x153 mm^3, voxel of 3x3x3 mm^3 and a matrix of 240x240x51. *Autonomic reactivity studies:* Parasympathetic reactivity studies involved deep breathing (change in heart rate, ratio of exhalation and inhalation), head up tilt and sympathetic reactivity included head up tilt, hand grip test and cold pressor test. Post-hoc analysis was done for scoring. *Data analysis:* Volunteers were categorized according to their BMI values lean (< 18.5 kg/m^2), normal (18.5-25 kg/m^2) and overweight (25.1-30 kg/m^2). R-fMRI data was analyzed using FreeSurfer (v6.0), CONN and SPM software.

Results:
Figure 1 shows representative MR images (R-fMRI, abdomen and thigh regions) from the three groups of volunteers. Out of the 18 volunteers 11 were in the normal category, 3 in lean and 4 in overweight. The percentage volumes of subcutaneous fat were different in the 3 groups-abdomen (69% lean, 81% normal and 86% overweight) and thigh (77% lean, 84% normal and 87% overweight). As observed with the MR data, clear differences between lean, normal and overweight group of volunteers were observed in the following autonomic function parameters-change in heart rate, exhalation: inhalation ratio and rise in diastolic BP during cold compressor test (CPT).Table 1 shows all parameters which showed differences between the three volunteer groups, with the values from the lean and overweight groups on either side of the normal.Differences were observed in R-fMRI data as well, although further studies are required for interpretation.

Conclusion:
This study has evaluated the physical, functional and physiological phenotyping in healthy volunteers and has shown clear distinction in their values. Further in-depth analysis and studies are underway.

Reference

1. König IR, et al. What is precision medicine? Eur Respir J, 50, 1700391, 2017.
2. Dudley JT, et al. Personalized medicine: from genotypes, molecular phenotypes and the quantified self, towards improved medicine. Pac Symp Biocomput, 342-346, 2015.
3. Ziemssen T and Siepmann T. The Investigation of the Cardiovascular and Sudomotor Autonomic Nervous System-A Review. Frontiers Neurol, 10, 1-13, 2019.
4. Zhang Y, et al. Reliability of measuring the fat content of the lumbar vertebral marrow and paraspinal muscles using MRI mDIXON-Quant sequence. Diagn Interv Radiol, 5, 302-307, 2018.

Poster Presentation

Disclosures: The authors have disclosed no financial interest.

555-Improved Dynamic In Vivo pH Imaging Using Hyperpolarized 13C-bicarbonate

Presenter: Xiaoxi Liu, University of California, San Francisco

Xiaoxi Liu[1], Changhua Mu[2], Ying-Chieh Lai[2], Robert A. Bok[3], Yaewon Kim[2], Jeremy Gordon[3], Robert R. Flavell[3], Peder E. Larson[3]

[1]University of California, San Francisco
[2]University of California, San Francisco, San Francisco, California
[3]University of California, San Francisco, San Francisco, CA

Acid-base balance is a critical signal present in many pathological states, such as inflammation, ischemia, cancer, and renal disease. [1,2] The extracellular pH is mainly controlled by the interconversion between bicarbonate and carbon dioxide (CO_2).[3] Prior work has shown that in vivo pH can be imaged with hyperpolarized ^{13}C-bicarbonate.[4,5] However, the non-renewable hyperpolarized ^{13}C-bicarbonate has limited T_1 relaxation(~60s) and short T_2^* relaxation(~65ms)[6], and limits the achievable spatial resolution. Additionally, the ^{13}C-bicarbonate signal is highest in the aorta[4], which challenges the accuracy of pH imaging due to point spread function blurring and motion-induced image artifacts. To overcome these limitations, in this study, we designed a metabolite-specific gradient echo (MS-GRE) spiral

sequence with flow suppression technique[7] to analyze the dynamic pH imaging with hyperpolarized ^{13}C-bicarbonate probe on the rat kidneys and mouse tumor. The MS-GRE spiral sequence with flow suppression was implemented on a 3T clinical GE MRI scanner using RTHawk scanner control software. We added a bipolar gradient in the arterial flow direction between the spectral-spatial selective pulse and spiral readout to suppress the vascular signal arising from bicarbonate and CO_2 spins. The animal studies were performed on kidneys of two healthy Sprague-Dawley rats and tumor of transgenic adenocarcinoma of the mouse prostate(TRAMP) model. Data were acquired by a $^{1}H/^{13}C$ transceiver single-channel birdcage coil. The hyperpolarized ^{13}C-bicarbonate was injected via tail vein in 12s, and the acquisition started at 3s since injection began. At each timepoint, the acquisition order is CO_2-bicarbonate, with a 0.4s temporal resolution(0.2s/metabolite). In the first rat experiment, flow suppression was not applied. As a result, the bicarbonate and CO_2 area-under-curve image had ring-like aliasing artifacts which were caused by the high bicarbonate aorta signal. The dynamic pH curve was calculated by the mean signal of kidney region at each time point, using Henderson-Hasselbalch equation[4]. In the dynamic pH maps, ring-like artifacts occurred in the first 15s which affected the accuracy of pH measurement on the kidneys. However, with the bipolar gradient to suppress high aorta signals, the ring artifacts can be suppressed in both bicarbonate and CO_2 images (Figure). Thus, the partial-volume effects with kidney voxels were reduced through the application of a bipolar gradient that reduced the vascular signal. Thus, no off-resonance ring-like artifacts were visible. Compared with the bicarbonate images, the CO_2 images had lower SNR, due to the perfusion effect and CO_2 as a downstream metabolite. Thus, a spiral readout was used to reduce the TE to improve the SNR of CO_2 signal. The dynamic pH curves of two kidneys were measured by the mean of bicarbonate and CO_2 signals in the kidney region (orange circle) and showed a similar phenomenon. The measured pH started at 7.0, then increased to 7.6 (similar to the pH of the injected solution), and then went back to 7.0 at 23s. This suggests dynamic pH measurements are monitoring the acid-base balance function of the kidneys, where the relatively large volume of injected solution increases the pH but then it is restored to normal levels. In TRAMP study, the cardiac and tumor dynamic signal and pH values were measured. No obvious artifacts were found in both bicarbonate and CO_2 data. In the tumor region, the measured pH increased from 6.6-7 to ~7.8 and did not later decrease, showing a clearly different phenomenon from the rat's kidneys.

This study used MS-GRE spiral to improve the SNR of bicarbonate and CO_2 with short T_2^* and used bipolar gradients to suppress the high bicarbonate signal in the vessel. With the improved image quality and high temporal resolution, the dynamic in vivo pH of different organs can be accurately measured to monitor dynamic regulation of pH.

Reference

1. Adrogué, Horacio J., and Nicolaos E. Madias. "Management of life-threatening acid–base disorders." New England Journal of Medicine 338.1 (1998): 26-34.
2. Grinstein, Sergio, Carol J. Swallow, and Ori D. Rotstein. "Regulation of cytoplasmic pH in phagocytic cell function and dysfunction." Clinical biochemistry 24.3 (1991): 241-247.
3. Mellanby, John. "Thrombase—its preparation and properties." Proceedings of the Royal Society of London. Series B, Containing Papers of a Biological Character 113.781 (1933): 93-106.
4. Gallagher, Ferdia A., et al. "Magnetic resonance imaging of pH in vivo using hyperpolarized 13C-labelled bicarbonate." Nature 453.7197 (2008): 940-943.
5. Korenchan, David E., et al. "Using bidirectional chemical exchange for improved hyperpolarized [13C] bicarbonate pH imaging." Magnetic resonance in medicine 82.3 (2019): 959-972.
6. Ma, Junjie, et al. "Cardiac measurement of hyperpolarized 13C metabolites using metabolite?selective multi?echo spiral imaging." Magnetic resonance in medicine 86.3 (2021): 1494-1504.
7. Gordon, Jeremy W., et al. "Application of flow sensitive gradients for improved measures of metabolism using hyperpolarized 13C MRI." Magnetic resonance in medicine 75.3 (2016): 1242-1248.

Poster Presentation

Disclosures: The authors have disclosed no financial interest.

556-An Integrin αvβ6 Binding Peptide-Drug-Conjugate for Tumor Targeted Drug Delivery

Presenter: Ryan Davis, University of California, Davis

Ryan A. Davis[1], Tanushree (Nina) Ganguly[2], Rebecca Harris[2], Sven Hausner[3], Luciana Kovacs[4], Julie Sutcliffe[2]

[1]*University of California, Davis, Sacramnento, CA*
[2]*University of California, Davis, Sacramento, CA*
[3]*UC Davis Health, Sacramento, CA*
[4]*University of California, Davis, Berlin, Berlin, Germany*

Objective:

Many cancer therapies exhibit high systemic off-target toxicities resulting in severe side effects and poor quality of life. To reduce off-target toxicity, therapeutics are often combined with a tumor-targeting moiety for selective targeting and killing.[1,2] The integrin a_vb_6 is a cell surface receptor that is highly expressed on many cancers and is specifically targeted by the a_vb_6 Binding Peptide (a_vb_6-BP) which was developed in our lab.[1,3] Monomethyl auristatin E (MMAE) is a potent antimitotic therapeutic, but cannot be used as a drug by itself due to its high toxicity. With the goal of developing an a_vb_6 selective peptide drug conjugate, the a_vb_6-BP was linked to MMAE via a cathepsin cleavable linker,[4-6] and radiolabeled with copper-64 to form the peptide drug conjugate [^{64}Cu]PDC-**1** (**Fig**. **A**). Affinity, efficacy, and pharmacokinetics of the PDC were tested *in vitro* and *in vivo*.

Methods:

The a_vb_6-BP was synthesized with an *N*-terminal cysteine (C) for maleimide-coupling to the cathepsin cleavable linker on MMAE and a DOTA chelator for radiolabeling with copper-64 to yield [^{64}Cu]PDC-**1**. Integrin a_vb_6-affinity was evaluated by ELISA against the latency associated protein and the [^{64}Cu]PDC-**1** was tested for stability in mouse and human serum (1, 4, 24 h; 37°C). Cell binding and internalization was examined in DX3puroβ6 (a_vb_6+), DX3puro (a_vb_6-), and pancreatic BxPC-3 (a_vb_6+) cells. Cytotoxicity was tested by WST-1 assay (controls: C-a_vb_6-BP and MMAE) and apoptosis was correlated to caspase-3/7 activity. *In vivo* (PET/CT & biodistribution) of [^{64}Cu]PDC-**1** was done in a paired DX3purob6/DX3puro and a BxPC-3 xenograft tumor mouse model. Therapeutic efficacy of [^{Nat}Cu]PDC-**1** (6 mg/kg, 0.88 μmol/kg) was evaluated in mice bearing xenograft tumors of either DX3purob6 or DX3puro treated with 4 doses (on days: 1,3,5,7) [controls: saline; [^{Nat}Cu]-C-a_vb_6-BP (6 mg/kg, 1.12 μmol/kg); MMAE(0.3 mg/kg, 0.42 μmol/kg)].

Results:

The modification of the a_vb_6-BP with MMAE did not affect a_vb_6-affinity (IC_{50}: PDC 18±2 nM *vs* DOTA-a_vb_6-BP 28±3 nM). [^{64}Cu]PDC-**1** was obtained in >98% radiochemical purity and exhibited high stability in human serum (1-4 h >98%, 24 h 89%), but degraded quickly

in mouse serum (1 h 89%, 4 h 49%, 24 h 3%). The [^{64}Cu]PDC-**1** showed a_vb_6-dependent cell binding (DX3puroβ6 67.0±2.3%, BxPC-3 62.0±1.0%; DX3puro 4.4±0.1%). The PDC showed a_vb_6-dependent cytotoxicity (EC_{50}: DX3purob6 0.058±0.003 nM, BxPC-3 65.1±10.6 nM, DX3puro >5 nM), while free MMAE exhibited high cytotoxicity to all the cell lines (EC_{50}, ≤0.5 nM). The caspase-3/7 activity for the PDC was also a_vb_6-selective with >5 times higher activity at 24 h in the DX3purob6 cells relative to the untreated control and no observed change in activity in the DX3puro cells. The PET/CT imaging and biodistribution of [^{64}Cu]PDC-**1** showed a_vb_6-selective tumor targeting (% ID/g, 4 h: DX3purob6 4.46±0.91; BxPC-3 4.61±1.44; DX3puro 0.56±0.12; **Fig. B** & **C**). Therapeutic efficacy of [^{Nat}Cu]PDC-**1** was a_vb_6-targeted with prolonged survival of DX3purob6 tumor bearing mice (median survival 77 days) compared to the equally treated DX3puro (median survival 49 days). All controls had a median survival of 37 days (**Fig. D**).

Conclusions:
Combining the cytotoxic MMAE with the integrin a_vb_6-Binding Peptide resulted in a_vb_6-dependent cell binding, internalization, and cytotoxicity. The [^{64}Cu]PDC-**1** demonstrated good pharmacokinetics and a_vb_6-targeted tumor uptake. The [^{Nat}Cu]PDC-**1** displayed promising *in vivo* therapeutic efficacy, warranting future evaluation of a_vb_6-targeted drug therapies.

Reference

1. Theranostics, 2011, 1, 189;
2. Annu. Rev. Med., 2013, 64, 15;
3. Clin Cancer Res, 2019, 25, 1206;
4. J. Med. Chem., 1981, 24, 479;
5. Bioconjug. Chem., 2002, 13, 855;
6. Mol. Cancer Ther., 2016, 15, 958.

Poster Presentation

Disclosures: The authors have disclosed no financial interest.

557-Prediction of motor and non-motor disease progression in early Parkinson's Disease using I-123 Ioflupane SPECT imaging and non-imaging features with machine learning.

Presenter: Sebastian Obrzut, Oregon Health and Science University

Sebastian Obrzut[1], Sandhya Bodapati[2], Roma Panchal[3], Peter Abraham[3]
[1]*Oregon Health and Science University, San Diego, CA*

[2]*Western University of Health Sciences*
[3]*Department of Radiology, University of California San Diego School of Medicine, San Diego, CA*

Introduction:
I-123 Ioflupane Single Photon Emission Tomography (SPECT) brain imaging is utilized to evaluate the degeneration of dopaminergic neurons in the nigrostriatal pathway in patients with Parkinson's disease (PD) and other Parkinsonian disorders. Prediction of PD progression has been challenging due to the heterogeneity of motor and non-motor symptoms that patients develop, such as bradykinesia, tremor, depression, and sleep changes associated with this neurodegenerative disease. Prior studies utilized neural networks to improve the prognostication of motor outcomes, assessed with Unified Parkinson's Disease Rating Scale III (UPDRS III), in PD patients based on I-123 Ioflupane SPECT brain imaging and several non-imaging features. The aim of this study is to predict both motor and non-motor outcomes (total UPDS) with machine learning (ML) using SPECT brain imaging and optimally selected non-imaging features from a large set of baseline clinical data.

Materials and Methods:
Parkinson's Progression Markers Initiative (PPMI) database was queried and yielded 422 patients (mean age = 61.6 +/- 9.7, 276 men, 146 women) with abnormal I-123 Ioflupane SPECT imaging and early PD. Generalized linear mixed model (GLMM) for longitudinal measurements was fitted to PPMI data with initial total UPDRS, gender, age, minimum putamen Striatal Binding Ratio threshold of 0.53 (minSBR-putamen), 3-6 month time intervals (t) over 42 months, and the interaction between t and minSBRputamen as fixed effects. Intercepts with t were designated as random effects, varied by subject. Change in total UPDRS over t was the response variable. 46 baseline features in PPMI database were evaluated for incorporation into machine learning (ML) models for prediction of total UPDRS change at 42 months based on highest Maximum Relevance Minimum Redundancy (MRMR) scores. Areas Under Receiver Operating Characteristic Curves (ROC AUCs) and accuracy (ACC) were evaluated for each ML model after training with 25% hold-out and 5-fold cross validation.

Results:
266/422 (63%) of PD patients progressed at 42 months based on an increase in total UPDRS scores, with mean total UPDRS change of 14.1 +/- 18.2 in all PD patients. Based on GLMM, minSBRputamen (p=0.046429) and gender (p=0.024905) were more predictive of change in total UPDRS over t compared with initial total UPDRS (p = 0.093533), age (p=0.61237) and t (p=0.059829). There was no significant interaction between minSBRputamen and t (p=0.16776). 5 of 46 baseline features were selected for incorporation into machine learning (ML) models for prediction of total UPDRS change at 42 months, which include: UPDRS III (MRMR = 0.0198), The Questionnaire for Impulsive-Compulsive Disorders in Parkinson's Disease (QUIP, MRMR = 0.0174), gender (MRMR = 0.0034), handedness (MRMR = 0.0013) and mean putamen Striatal Binding Ratio threshold of 0.53 (aveSBRputamen, MRMR = 0.0008). The following performance measures were obtained for ML models for prediction of total UPDRS change at 42 months: bi-layered neural network (ACC = 79.1%, AUC = 0.65), fine gaussian support vector machines (ACC = 77.9%, AUC = 0.63) boosted trees (ACC = 75.6%, AUC = 0.62), narrow neural network (ACC = 75.6%, AUC = 0.59) and tri-layered neural network (ACC = 74.4%, AUC = 0.48) using 5 of 46 baseline PPMI features with highest MRMR.

Conclusions:
I-123 Ioflupane SPECT can be helpful in prediction of both motor and non-motor disease progression in early PD using ML, when combined with non-imaging features. Additional investigations are needed that include prodromal patients to allow for earlier clinical interventions and to improve disease prognostication.

Reference

1. Asenbaum S, Brücke T, Pirker W, Podreka I, Angelberger P, Wenger S, Wöber C, Müller C, Deecke L. Imaging of dopamine transporters with iodine-123-beta-CIT and SPECT in Parkinson's disease. J Nucl Med. 1997 Jan;38(1):1-6.
2. Schwarz J, Linke R, Kerner M, et al. Striatal Dopamine Transporter Binding Assessed by [I-123]IPT and Single Photon Emission Computed Tomography in Patients With Early Parkinson's Disease: Implications for a Preclinical Diagnosis. Arch Neurol. 2000;57(2):205–208.
3. Catharina Sjödahl Hammarlund, Albert Westergren, Ingrid Åström, Anna-Karin Edberg, Peter Hagell, "The Impact of Living

with Parkinson's Disease: Balancing within a Web of Needs and Demands", Parkinson's Disease, vol. 2018, Article ID 4598651, 8 pages, 2018.
4. Iwabuchi, Y., Kameyama, M., Matsusaka, Y. et al. A diagnostic strategy for Parkinsonian syndromes using quantitative indices of DAT SPECT and MIBG scintigraphy: an investigation using the classification and regression tree analysis. Eur J Nucl Med Mol Imaging 48, 1833–1841 (2021).
5. Jeong EH, Sunwoo MK, Hyung SW, Han SK, Lee JY. Correlation of Dopaminergic Denervation and the Progression of Autonomic Dysfunctions in Different Clinical Subtypes of Parkinson's Disease. Parkinsons Dis. 2021 Nov 26;2021.
6. Shiiba T, Arimura Y, Nagano M, Takahashi T, Takaki A. Improvement of classification performance of Parkinson's disease using shape features for machine learning on dopamine transporter single photon emission computed tomography. PLoS One. 2020 Jan 24;15(1).
7. Matthew P Adams, Arman Rahmim, Jing Tang. Improved motor outcome prediction in Parkinson's disease applying deep learning to DaTscan SPECT images. Comput Biol Med. 2021 May;132:104312.
8. Jing Tang, Bao Yang, Matthew P Adams, Nikolay N Shenkov, Ivan S Klyuzhin, Sima Fotouhi, Esmaeil Davoodi-Bojd, Lijun Lu, Hamid Soltanian-Zadeh, Vesna Sossi, Arman Rahmim. Artificial Neural Network-Based Prediction of Outcome in Parkinson's Disease Patients Using DaTscan SPECT Imaging Features. Mol Imaging Biol. 2019 Dec;21(6):1165-1173.

Poster Presentation

Disclosures: The authors have disclosed no financial interest.

558-A novel peptide-based radiotracer targeting programmed death ligand-1 with improved pharmacokinetics and specificity

Presenter: Dhiraj Kumar, Johns Hopkins University School of Medicine

Dhiraj Kumar[1], Akhilesh Mishra[2], Kuldeep Gupta[3], Gabriela Lofland[4], Ajay Kumar Sharma[5], Robert Hobbs[5], Robert F. Dannals[6], Steven Rowe[7], Edward Gabrielson[7], Sridhar Nimmagadda[8]

[1]*Johns Hopkins University School of Medicine, Baltimore*
[2]*Johns Hopkins University, Baltimore*
[3]*Johns Hopkins University*
[4]*Johns Hopkins University School of Medicine*
[5]*Johns Hopkins University, Baltimore, MD*
[6]*Johns Hopkins University School of Medicine, Baltimore, Maryland*
[7]*Johns Hopkins University School of Medicine, Baltimore, MD*
[8]*Johns Hopkins University, Baltimore, MD*

Introduction:
Antibodies targeting immune checkpoint proteins programmed death ligand-1 (PD-L1) and its receptor PD-1 form the backbone of cancer therapy. Enrichment of patients for those therapies is based on evaluation of PD-L1 expression in tumors by immunohistochemistry (IHC) that provides a snapshot of PD-L1 levels at a single timepoint from a small area of a tumor. However, heterogeneity seen in PD-L1 levels within and across patients and in response to therapy underscore the need for non-invasive tools. To evaluate total PD-L1 levels and their dynamics non-invasively, we report the development of a new Gallium-68 labeled peptide-based high affinity radiotracer, [^{68}Ga]DK223, for positron emission tomography (PET). To establish in vitro and in vivo PD-L1 specificity of [^{68}Ga]DK223, we performed biodistribution and imaging studies in multiple tumor models derived from triple negative breast cancer (TNBC) and urothelial carcinoma (UC).

Methods:
[$^{69/70}$Ga]DK223 affinity for human PD-L1 was measured by surface plasmon resonance. TNBC and UC cells were screened by flow cytometry for PD-L1 expression and receptor density. In vitro binding assays were performed by incubating 1 million cells with 1 μCi of [^{68}Ga]DK223. To study pharmacokinetics of [^{68}Ga]DK223, PET (200 μCi) and ex vivo biodistribution studies (80 μCi) were performed at 5, 30, 60 and 90 minutes in NSG mice bearing MDAMB231 and SUM149 TNBC xenografts (n=4-5). To establish in vivo selectivity, 50 mg/kg of non-radioactive DK223 was used for blocking studies. PD-L1 specificity of [^{68}Ga]DK223 was validated in NSG mice bearing BFTC909 and SCaBER UC xenografts (n=4-5). IHC was performed on harvested tumors to corroborate imaging findings. Ex vivo biodistribution data was used to perform dosimetry calculations using OLINDA/XEM software.

Results:
[$^{69/70}$Ga]DK223 binds PD-L1 with a KD of 1.01±0.83 nM. In vitro uptake of [^{68}Ga]DK223 in MDAMB231, SUM149, BFTC909 and SCaBER cells was expression dependent, and correlated with surface PD-L1 density (R^2=0.937). [^{68}Ga]DK223 PET revealed high accumulation of radioactivity in MDAMB231 TNBC xenografts (PD-L1^{high}) as early as 5 minutes with highest contrast reached at 60 min with tumor-to-muscle and tumor-to-blood ratios of 74.21±14.6 and 5.75±0.77, respectively. Non-radioactive DK223 reduced [^{68}Ga]DK223 uptake in MDAMB231 tumors by 99% (P<0.0001) confirming the selectivity of the radiotracer. In imaging and biodistribution studies, highest [^{68}Ga]DK223 uptake was observed in BFTC909 (21±2.1 %ID/g), followed by MDAMB231 (11±1.6 %ID/g) tumors with minimal uptake in SCaBER and SUM149 tumors (1.11±0.31 %ID/g). PD-L1 IHC showed intense immunoreactivity in BFTC909 tumors followed by MDAMB231 and least immunoreactivity in SCaBER and SUM149 tumors, validating PET findings. Human dosimetry estimates indicate that a 20 mCi administered dose will lead to <5 rem effective exposure.

Conclusion:
Our data demonstrate that [^{68}Ga]DK223 is a high affinity PD-L1 specific radiotracer that provides high contrast images within 60 minutes of administration. [^{68}Ga]DK223 exhibits sensitivity to detect variable PD-L1 levels in vivo.

Poster Presentation

Disclosures: The authors have disclosed no financial interest.

559-Unexpected Bone Uptake of an EuK-based NIR-II PSMA Imaging Probe

Presenter: Longfei Zhang, Beijing Normal University

Longfei Zhang[1], Mengchao Cui[2]

[1]*Beijing Normal University, Beijing, Beijing, China*
[2]*Beijing Normal University, Beijing, China, China*

Objectives:
Owing to the high affinity toward prostate-specific member antigen (PSMA), a focused biomarker of prostate cancer (PCa), Glu-urea-Lys (EuK) moiety has been widely used in the development of PCa

targeting probes and therapeutics. However, in the modification of our previous reported EuK-based PSMA probe **PSMA-1092**[1], in which we attempt to improve the imaging performance by increasing the number of side-chain conjugated EuK moiety from 2 to 4. The new NIR-II PSMA tetramer, **bone-1064** demonstrated unexpectedly strong bone uptake, which has never been reported in previous similar probes, inspiring us to investigate the mechanism of bone uptake.

Methods:
The structure and optical properties of **bone-1064** (**Figure 1a**) were fully characterized by spectrum-based methods. The quantitive binding affinity was determined by a competitive binding assay using lysate of LnCAP cell. *In vivo* NIR-II imaging, *ex vivo* biodistribution studies, and *ex vivo* micro-imaging were implemented on normal nude mice (male, balb/c) or tumor-bearing mice (male, balb/c, LnCAP cell) to test the biological properties.

Results:
The absorption and emission maxima of **bone-1064** in DMSO are 715 nm and 1064 nm (**Figure 1b**), respectively, with a large stokes shift (370 nm). A competitive binding assay revealed that **bone-1064** displayed a high affinity toward PSMA (K_i = 90 pM). After 6 h post-injection of **bone-1064** (5.0 mg/kg), the skeleton of nude mice could be distinguished from surrounding muscles with a sharp contour, and the highest signal-to-background ratio (SBR) of bone was obtained at 24 h post-injection as 10.22 (**Figure 1c**). Moreover, in *in vivo* blocking study, no obvious difference in imaging quality could be detected between the control (injected **bone-1064**, 5.0 mg/kg) and blocking group (co-injected with 592.4 mg/kg of **DCFPyL**) at any time points post-injection, indicating that PSMA did not participate the bone uptake of **bone-1064**. After 24 h post-injection, *ex vivo* fluorescence micro-imaging was carried out on frozen slices obtained from mice's hind limbs. As shown in **Figure 1d**, the distribution of fluorescence signal was consistent with that of hydroxyapatite, which was further confirmed by the counterstain with a commercially available Mason staining kit, indicating the hydroxyapatite is the binding site of **bone-1064**.

Conclusions:
All these preliminary results indicated that the bond with hydroxyapatite is the reason for the intense bone uptake of **bone-1064**, which displayed good performance in skeleton imaging. Further studies on this probe are currently underway. **Acknowledgements:** Supported by the National Natural Science Foundation of China (No. U1967221 and 22022601).

Corresponding Author: *Tel/Fax: +86-10-58808891. E-mail: cmc@bnu.edu.cn

Reference

1. Long, Z. et al. J. Med. Chem. 2021, 64, 7735–7745.

Poster Presentation

Disclosures: The authors have disclosed no financial interest.

560-Development of Specialized Magnetic Resonance Acquisition Techniques for Human HP [13C,15N2]Urea + [1-13C]Pyruvate Simultaneous Perfusion and Metabolic Imaging

Presenter: Xiaoxi Liu, University of California, San Francisco

Xiaoxi Liu[1], Shuyu Tang[2], Changhua Mu[3], Hecong Qin[4], Di Cui[5], Ying-Chieh Lai[3], Andrew Riselli M.[5], Romelyn Delos Santos[6], Lucas Carvajal[7], Daniel T. Gebrezgiabhier[1], Robert A. Bok[6], Hsin-Yu N. Chen[6], Robert R. Flavell[6], Jeremy Gordon[6], Daniel Vigneron[6], John Kurhanewicz[6], Peder E. Larson[6]

[1]*University of California, San Francisco*
[2]*Los Altos, California*
[3]*University of California, San Francisco, San Francisco, California*
[4]*University of Chicago, Chicago, IL*
[5]*University of California San Francisco, San Francisco, California*
[6]*University of California, San Francisco, San Francisco, CA*
[7]*San Francisco, CA*

Hyperpolarized ^{13}C MRI has become essential for the characterization, treatment selection, and monitoring treatment response of tumors.[1] It offers the unique capability to simultaneously image perfusion and metabolism using co-hyperpolarized [1-^{13}C]pyruvate and [^{13}C,$^{15}N_2$] urea.[2] In the previous study, the co-polarization procedure of [1-^{13}C] pyruvate and [^{13}C,$^{15}N_2$]urea on a clinical SPINlab DNP polarizer has been demonstrated the feasibility in pre-clinical study.[3] In this study, we developed and demonstrated the in vivo feasibility of a specialized acquisition strategy for co-hyperpolarized [1-^{13}C]pyruvate and [^{13}C,$^{15}N_2$]urea to provide high SNR and improved spatial resolution, which was tested in simulation, validated in phantoms and animal models, before being applied in a first-in-human study demonstrating feasibility in the prostate. The strategy developed for co-hyperpolarized [1-^{13}C]pyruvate and [^{13}C,$^{15}N_2$]urea uses a metabolite-specific 2D gradient echo (2D-GRE) for pyruvate and its metabolic products, and interleaved with a metabolite-specific 3D balanced steady-state free precession (3D-bSSFP) sequence[4,5] for [^{13}C,$^{15}N_2$]urea with improved SNR due to refocusing and its long T_2 relaxation time.[4,6] The sequence illustration of 3D-bSSFP urea sequence was shown in Figure1. The proposed sequence was implemented on an MR 3T GE scanner (Waukesha, WI) using a commercial software (RTHawk, HeartVista, CA). To measure the excitation profile of the urea-specific pulse, phantom experiments were performed on a ^{13}C-urea phantom with a single-channel ^{13}C transceiver birdcage coil. The animal study was performed on a healthy adult Sprague-Dawley rat with two identical injections of co-hyperpolarized [1-^{13}C]pyruvate and [^{13}C,$^{15}N_2$] urea to compare the metabolite-specific 3D-bSSFP with conventional hyperpolarized metabolite-specific 2D gradient recalled echo (2D-GRE) sequences[7]. To demonstrate imaging feasibility in patients, a pre-surgical patient with localized prostate cancer was recruited. Data from the human prostate were acquired using a clamshell transmit coil and a double-tuned ^{1}H/^{13}C endorectal coil. The two acquisition methods were compared on a rat's kidney, liver, and cardiac slices. In the field map, the heart slice exhibits a much larger B_0 inhomogeneity. Due to the longer readout time, the heart has a sharper edge that corresponds better with the anatomical image in the 3D-bSSFP images. Even when B_0 inhomogeneity is small, the vessel signal acquired by 3D-bSSFP has a sharper edge in the kidneys and liver slices than data acquired by 2D-GRE because of the J_{CN} coupling of [^{13}C,$^{15}N_2$]urea. With the measurement, the 3D-bSSFP urea sequence shows an approximately 2.5-fold SNR improvement over the 2D-GRE urea sequence, demonstrating a substantial improvement in performance. In the human prostate cancer study, a real-time frequency calibration was applied to calibrate based on the pyruvate frequency prior to the metabolite imaging acquisition. All three metabolite images showed a higher total signal in the tumor than that in the contra-lateral healthy-appearing prostate region. Comparing the pyruvate with urea, urea images showed higher relative signals in the vessels within the rectal wall. This phenomenon shows the difference in information between metabolite imaging and perfusion imaging. In the dynamic metabolite signal intensity curve, the tumor signals of both pyruvate and urea reach their peaks

at around 10.4s after acquisition. As to maximal signal intensity, the tumor voxel was approximately 2.5 times higher than the contralateral healthy-appearing prostate.

In this study, the highly efficient method for imaging co-hyperpolarized ^{13}C pyruvate and urea was validated in human studies. Using a 3D-bSSFP strategy for urea provided higher image quality compared to a conventional GRE approach, with animal studies demonstrating sharper images and ~2.5-fold SNR improvement. In the first-in-human study, the excellent results demonstrated the feasibility of using co-hyperpolarized ^{13}C pyruvate and urea. This work lays the foundation for future human studies to achieve high-quality, high-SNR, simultaneous metabolism and perfusion imaging.

Reference

1. Hanahan D, Weinberg RA. Hallmarks of cancer: The next generation. Cell. 2011;144(5):646-674. doi:10.1016/j.cell.2011.02.013
2. von Morze C, Larson PEZ, Hu S, et al. Investigating tumor perfusion and metabolism using multiple hyperpolarized 13C compounds: HP001, pyruvate and urea. Magnetic Resonance Imaging. 2012;30(3):305-311. doi:10.1016/j.mri.2011.09.026
3. Qin H, Tang S, Riselli AM, et al. Clinical translation of hyperpolarized 13C pyruvate and urea MRI for simultaneous metabolic and perfusion imaging. Magnetic Resonance in Medicine. 2022;87(1):138-149. doi:10.1002/mrm.28965
4. Reed GD, von Morze C, Bok R, et al. High resolution 13C MRI with hyperpolarized urea: In vivo T2 mapping and 15N labeling effects. IEEE Transactions on Medical Imaging. 2014;33(2):362-371. doi:10.1109/TMI.2013.2285120
5. Milshteyn E, von Morze C, Gordon JW, Zhu Z, Larson PEZ, Vigneron DB. High spatiotemporal resolution bSSFP imaging of hyperpolarized [1-13C]pyruvate and [1-13C]lactate with spectral suppression of alanine and pyruvate-hydrate. Magnetic Resonance in Medicine. 2018;80(3):1048-1060. doi:10.1002/mrm.27104
6. Tang S, Bok R, Qin H, et al. A metabolite-specific 3D stack-of-spiral bSSFP sequence for improved lactate imaging in hyperpolarized [1-13C]pyruvate studies on a 3T clinical scanner. Magnetic Resonance in Medicine. 2020;84(3):1113-1125. doi:10.1002/mrm.28204
7. Gordon JW, Vigneron DB, Larson PEZ. Development of a symmetric echo planar imaging framework for clinical translation of rapid dynamic hyperpolarized 13C imaging. Magnetic Resonance in Medicine. 2017;77(2):826-832. doi:10.1002/mrm.26123

Poster Presentation

Disclosures: The authors have disclosed no financial interest.

561-Detection of ALA-induced Ferritin in Active Area of Glioblastoma Multiforme Using In Vivo Animal Quantitative Susceptibility Mapping: A Comparison with Contrast Enhancement

Presenter: anita ebrahimpour, Tehran University of Medical Sciences

Anita Ebrahimpour[1], Nader Riyahi Alam[1], Mehdi Khoobi[1], Mahboubeh Masoumbeigi[2]

[1]Tehran University of Medical Sciences, Tehran, Iran
[2]Tehran University of Medical Science, Tehran, Tehran, Iran

Glioblastoma Multiforme (GBM) is a common tumor of the brain with a difficult diagnosis. Recent imaging studies have tried to find an effective technique to achieve the best segmentation of tumor volume. A major method for GBM evaluation is gadolinium-based contrast enhancement (CE) in magnetic resonance imaging (MRI) (1). Since this method has a poor indication of volumes of metabolically active tumors leading to necrosis area enhancement (2) that results in making mistakes for active tumors and creating difficulty for auto-segmentation of GBM, the development of imaging methods to detect metabolically active areas of tumors is very worth to be addressed. Recently, fluorescence imaging (FI) of GBM using 5-aminolevulinic acid (ALA) was approved as proper navigation for intraoperative visualization of metabolically active tumor accumulated with ALA-induced fluorescent protoporphyrin IX (PpIX) (3). However, leakage of PpIX into blood, choroid plexus, and ventricular wall are some difficulties to use PpIX clinically. In this regard, a novel "ALA+iron supplement"-based MRI method (4, 5) was newly introduced to detect metabolically active areas of GBM outside of surgery, using quantitative susceptibility mapping (QSM). Although the accumulation of ferritins in glioblastoma cells and MRI contrast induced by ferritin in tumor area was properly detected GBM, the ability of this method to discriminate the metabolically active area of tumor from the necrosis region was not demonstrated yet. Therefore, the main aim of this study was to evaluate the ability of discrimination between metabolically active and necrosis areas of GBM using QSM in comparison with CE using a rat case report. To create the C_6 GBM models, male Wistar rats (6–8 weeks, weighing 220–250 g) were used. For anesthetized rats, a C_6 cell suspension (1.5×10^6 C_6 in 8 μL of saline) was injected into the right frontal lobe at a 5mm depth from the outer border of the cranium, using a Hamilton syringe. After two weeks, the tumors were evaluated using MRI. To achieve the T_2*-weighted magnitude and phase images of GBM, a 3D multi-echo gradient-echo sequence (SWI) was performed after administration of "ALA + FAC'. Moreover, to achieve the post-contrast T_1-weighted magnitude images of GBM, a 2D T_1-weighted turbo spin-echo (TSE) sequence was performed after intravenous injection of gadolinium-containing contrast agent (Dotarem (Gd-DOTA)). The susceptibility estimation of GBM was performed using the QSM algorithm. The image processing steps for in vivo QSM including brain mask of magnitude (Mag) with MIPAV software, phase unwrapping using laplacian method, local field map using PDF, and susceptibility estimation with MEDI algorithm were performed (4). The results demonstrated a clear enhancement in the necrosis area of GBM using CE while no enhancement was shown using QSM. However, a significant enhancement was observed only in the active area of the tumor using QSM (Figure 1).

In the "ALA+FAC" method, the signal loss and susceptibility enhancement in the T_2*-weighted magnitude and susceptibility map was only observed in the active area of the tumor due to the accumulated superparamagnetic ferritin clusters (4) while in the necrosis area was shown no enhancement due to the lack of metabolic activity for the heme signaling pathway. While, in T_1- weighted imaging using dotarem, a clear enhancement was observed in the necrosis area since the extracellular distribution of paramagnetic ions (gadolinium) was imaged.

In conclusion, ferritin-based imaging (ALA+iron supplement) using QSM as metabolic imaging could present more reliable discrimination between necrosis and active tumor.

Reference

1. Robert P, Vives V, Grindel A-L, et al. Contrast-to-dose relationship of gadopiclenol, an MRI macrocyclic gadolinium-based contrast agent, compared with gadoterate, gadobenate, and gadobutrol in a rat brain tumor model. Radiology. 2020;294(1):117-126.
2. Nelson SJ. Multivoxel magnetic resonance spectroscopy of brain Tumors1. Molecular cancer therapeutics. 2003;2(5):497-507.
3. Kaneko S, Kaneko S. Fluorescence-guided resection of malignant glioma with 5-ALA. International journal of biomedical imaging. 2016;2016.

4. Ebrahimpour A, Tirgar F, Hajipour-Verdom B, et al. Detection of glioblastoma multiforme using quantitative molecular magnetic resonance imaging based on 5-aminolevulinic acid: in vitro and in vivo studies. Magnetic Resonance Materials in Physics, Biology and Medicine. 2022;35(1):3-15.
5. Ebrahimpour A, Riahi Alam N, Khoobi M. The potential of 5-aminolevulinic acid as a contrast agent in MR imaging: challenges and opportunities. Journal of Sciences, Islamic Republic of Iran. 2021;32(1):15-28.

Poster Presentation

Disclosures: The authors have disclosed no financial interest.

562-PA

Presenter: Derick Rosario Berríos, Perelman School of Medicine at the University of Pennsylvania

Derick Rosario Berríos[1], Johoon Kim[2], David Cormode[2]

[1]Perelman School of Medicine at the University of Pennsylvania, Philadelphia, PA
[2]University of Pennsylvania, Philadelphia, PA

Purpose:
Ulcerative colitis (UC) is a chronic inflammatory bowel disease (IBD) characterized by symptoms of bloody diarrhea, abdominal cramps, vomiting, and fatigue. UC affects approximately 1.6 million individuals in the United States. Computed tomography (CT), used in conjunction with contrast agents, is the gold standard for imaging the gastrointestinal tract (GIT). Iodinated small molecules and barium sulfate suspensions are commonly used in the clinic for imaging the GIT However, iodine-enhanced CT image quality is very poor for imaging the abdomen in obese patients and is not ideal for imaging UC due to its non-specificity for areas of inflammation. Thus, there is a compelling need for the development of new contrast agent strategies for imaging GIT with UC. Nanoparticles have been the focus of much attention as CT contrast agents, since it is relatively easy to synthesize them with different sizes and coatings, which can provide specificity to different types of disease sites. A fundamental question for novel contrast agents for IBD is what size of nanoparticle is the most ideal. Therefore, in this project we evaluated the effect of nanoparticle size on accumulation in a dextran sodium sulfate induced colitis (DSS-induced colitis) mouse model.

Methods and Materials:
Gold nanoparticles (AuNP) are well-established as CT contrast agents and their size can easily be controlled in a wide range, therefore we used spherical AuNP with mPEG to determine the effect of different sizes ranging from 5 to 80nm. To synthesize the 5 nm we used a modified Turkevich method by reducing gold chloride with sodium borohydride, while the 15 nm and 25nm AuNP were synthesized using the unmodified Turkevich method. However, for the larger AuNP sizes, a seeded growth synthesis method employing gold chloride and hydroquinone was used (Fig. A). The nanoparticles were characterized using TEM, UV-vis spectroscopy, DLS, and SEM/EDX. Contrast production was evaluated via phantom imaging using clinical CT (Siemens Force), and a microCT (Molecubes, Gent, Belgium) imaging systems. *In vivo* accumulation and biodistribution studies were performed in a murine model with acute DSS-induced colitis.

Results:
Gold nanoparticles with different core sizes (5,15, 25, 50, and 80 nm) were successfully synthesized (Fig. B) and the physicochemical properties of the resulting formulations was analyzed. In addition, histology studies confirm that the murine mouse model contracted acute colitis after 8 days of DSS treatment (Fig. C). Nanoparticles were administered to the mice via gavage. The mice were then imaged using a conventional microCT scanner at several timepoints (Fig. D). We observed that the gold nanoparticles provide enough contrast to visualize the gastrointestinal tract over 2 hr and furthermore we observed nanoparticles accumulation in areas of inflammation (Fig. E). Finally, the biodistribution was examined via analysis of imaging data (Fig. E) and ICP-OES.

Conclusions:
Our results have shown that NPs are a promising contrast agent for imaging the GIT with IBD. The development of NP for imaging IBD can facilitate the use of clinical CT in the diagnosis of IBD. Future studies will explore the synthesis and testing of novel contrast agents that can simultaneously image and treat ulcerative colitis.

Reference

1. Gajendran, M. et al. A comprehensive review and update on ulcerative colitis,. Disease-a-Month 65, 100851 (2019).
2. Moura, F. A., de Andrade, K. Q., dos Santos, J. C. F., Araújo, O. R. P. & Goulart, M. O. F. Antioxidant therapy for treatment of inflammatory bowel disease: Does it work? Redox Biol. 6, 617–639 (2015).
3. Shivashankar, R., Tremaine, W. J., Harmsen, W. S. & Loftus, E. V. Incidence and Prevalence of Crohn's Disease and Ulcerative Colitis in Olmsted County, Minnesota From 1970 Through 2010. Clin. Gastroenterol. Hepatol. (2017). doi:10.1016/j.cgh.2016.10.039
4. Feagan, B. G. et al. Vedolizumab as induction and maintenance therapy for ulcerative colitis. N. Engl. J. Med. 369, 699–710 (2013).
5. A., Kuester, D., Malfertheiner, P. & Schneider-Stock, R. Oxidative stress in ulcerative colitis-associated carcinogenesis. Pathol. Res. Pract. 204, 511–524 (2008).
6. Fitzgerald, P. F. et al. CT image contrast of high-Z elements: Phantom imaging studies and clinical implications. Radiology (2016). doi:10.1148/radiol.2015150577
7. Lambert, J. W. et al. An intravascular tantalum oxide-based CT contrast agent: Preclinical evaluation emulating overweight and obese patient size. Radiology (2018). doi:10.1148/radiol.2018172381
8. Cormode, D. P., Naha, P. C. & Fayad, Z. A. Nanoparticle contrast agents for computed tomography: A focus on micelles. Contrast Media Mol. Imaging (2014). doi:10.1002/cmmi.1551
9. Dhall, A. & Self, W. Cerium oxide nanoparticles: A brief review of their synthesis methods and biomedical applications. Antioxidants 7, 1–13 (2018).
10. Naha, P. C. et al. Dextran-Coated Iron Oxide Nanoparticles as Biomimetic Catalysts for Localized and pH-Activated Biofilm Disruption. ACS Nano 13, 4960–4971 (2019).
11. Hu, G. et al. Nanoparticles targeting macrophages as potential clinical therapeutic agents against cancer and inflammation. Frontiers in Immunology (2019). doi:10.3389/fimmu.2019.01998
12. Cormode, D. P. & Fayad, Z. A. Nanoparticle contrast agents for CT: Their potential and the challenges that lie ahead. Imaging in Medicine (2011). doi:10.2217/iim.11.17
13. Dong, Y. C. et al. Effect of Gold Nanoparticle Size on Their Properties as Contrast Agents for Computed Tomography. Sci. Rep. (2019).

Poster Presentation

Disclosures: The authors have disclosed no financial interest.

563-Evaluation of TSPO radiotracer [18F]FEPPA in mouse models of acute Zika and Dengue infection-associated inflammation

Presenter: Arun Ganasarajah, Duke-NUS Medical School

Arun Ganasarajah[1], Carla Bianca Victorio[1], Ann-Marie Chacko[1], Jing Yang Tham[2], Joanne Ong[2], Rasha Msallam[3], Satoru Watanabe[3], Subhash Vasudevan[3], Wisna Novera[3]

[1]Duke-NUS Medical School, Singapore, Singapore
[2]Duke-NUS Medical School, Singapore, Singapore, Singapore
[3]Duke-NUS Medical School, Singapore

Objective:
Zika virus (ZIKV) and dengue virus (DENV) are mosquito-borne viral infections with sustained worldwide disease burden over the last decade and persist as major global public health threats [1-3]. These viral infections trigger host innate immune responses associated with increased expression of the translocator protein (TSPO) [4]. ZIKV disease is associated with neurological disease and neuroinflammation [5], while DENV infections are known for systemic vascular and tissue inflammation with liver involvement [6, 7]. Despite the continued public health threat of DENV and ZIKV, there are no effective antivirals and vaccines available [8]. This emphasises the need for imaging biomarkers that correlate with disease progression, predict response to therapy, and rapidly inform go or no-go decisions in drug evaluations to address the real clinical need for infectious disease-related imaging biomarkers [9]. In this study, we evaluate the potential of the TSPO radioligand [^{18}F]FEPPA [10] to detect, monitor, and differentiate inflammatory responses associated with acute ZIKV and DENV infection using a transgenic mouse model.

Methods:
AG129 transgenic mice infected with either DENV or ZIKV were injected with 2 MBq [^{18}F]FEPPA at late-stage disease. *Ex vivo* biodistribution (BioD) studies were performed and complemented with digital autoradiography (DAR) imaging using tissue sections or whole-mount tissues. TSPO immunohistochemistry (IHC) and flow cytometry (FC) were used to confirm molecular expression profiles and define the tissue immune landscape. Markers of disease severity—such as tissue viral burden and pro-inflammatory cytokine expression—were also measured. For PET/CT imaging, mice infected with either ZIKV or DENV were injected with 30MBq [^{18}F]FEPPA and imaged to identify global and tissue specific changes in tracer uptake *in vivo*.

Results:
BioD and DAR studies revealed 5-fold increased [^{18}F]FEPPA liver uptake at late DENV disease relative to mock-infected tissues (p = 0.005), which correlated with increased viral burden and pro-inflammatory cytokine expression in the tissue. This contrasted with [^{18}F]FDG-PET, where no change in liver uptake was noted despite significant dengue disease burden in the tissue [11]. *Ex vivo* studies also revealed 3.6-fold increased tracer uptake in ZIKV-infected brains relative to mock-infected tissue, and this correlated with surges in viral burden and pro-inflammatory cytokines (? = 0.84; p = 0.001). Brain tissues exhibited global elevated TSPO expression by IHC, which was primarily driven by myeloid-derived cells as uncovered by FC. In the ZIKV-infected mouse brains, PET/CT revealed mild increase in [^{18}F]FEPPA uptake, though not as pronounced as observed with BioD and DAR. Similarly, [^{18}F]FEPPA-PET/CT in DENV-infected mice showed modest increase in tracer uptake in the lungs and liver and was not as striking as seen in *ex vivo* assays.

Conclusions:
[^{18}F]FEPPA studies revealed distinct tissue biodistribution patterns that could differentiate DENV from ZIKV disease. [^{18}F]FEPPA is primarily detecting ZIKV-associated neuroinflammation and increased brain TSPO expression. In contrast, [^{18}F]FEPPA in DENV infections detect specific liver and lung uptake signatures which may be related to host immune response driven by myeloid cell. Efforts are underway to evaluate [^{18}F]FEPPA as a treatment response biomarker.

Funding support:
This research was supported by Singapore's Health and Biomedical Sciences (HBMS) Industry Alignment Fund Pre-Positioning (IAF-PP) grant H18/01/a0/018 (AMC) administered by the Agency for Science, Technology and Research (A*STAR), Singapore National Medical Research Council (NMRC) Open Fund Young Individual Research Grant OFYIRG15nov062 (SW).

Reference

1. Pierson TC, Diamond MS. The emergence of Zika virus and its new clinical syndromes. Nature. 2018;560:573-81. doi:10.1038/s41586-018-0446-y.
2. Puntasecca CJ, King CH, LaBeaud AD. Measuring the global burden of chikungunya and Zika viruses: A systematic review. PLoS Negl Trop Dis. 2021;15:e0009055. doi:10.1371/journal.pntd.0009055.
3. Chen Y, Li N, Lourenco J, Wang L, Cazelles B, Dong L, et al. Measuring the effects of COVID-19-related disruption on dengue transmission in southeast Asia and Latin America: a statistical modelling study. Lancet Infect Dis. 2022;22:657-67. doi:10.1016/S1473-3099(22)00025-1.
4. Zheng Y, Liu Q, Wu Y, Ma L, Zhang Z, Liu T, et al. Zika virus elicits inflammation to evade antiviral response by cleaving cGAS via NS1-caspase-1 axis. EMBO J. 2018;37. doi:10.15252/embj.201899347.
5. Panganiban AT, Blair RV, Hattler JB, Bohannon DG, Bonaldo MC, Schouest B, et al. A Zika virus primary isolate induces neuroinflammation, compromises the blood-brain barrier and upregulates CXCL12 in adult macaques. Brain Pathol. 2020;30:1017-27. doi:10.1111/bpa.12873.
6. Fernando S, Wijewickrama A, Gomes L, Punchihewa CT, Madusanka SD, Dissanayake H, et al. Patterns and causes of liver involvement in acute dengue infection. BMC Infect Dis. 2016;16:319. doi:10.1186/s12879-016-1656-2.
7. Samanta J, Sharma V. Dengue and its effects on liver. World J Clin Cases. 2015;3:125-31. doi:10.12998/wjcc.v3.i2.125.
8. Byrne AB, Garcia CC, Damonte EB, Talarico LB. Murine models of dengue virus infection for novel drug discovery. Expert Opin Drug Discov. 2022;17:397-412. doi:10.1080/17460441.2022.2033205.
9. Jain SK. The Promise of Molecular Imaging in the Study and Treatment of Infectious Diseases. Mol Imaging Biol. 2017;19:341-7. doi:10.1007/s11307-017-1055-0.
10. Vignal N, Cisternino S, Rizzo-Padoin N, San C, Hontonnou F, Gele T, et al. [(18)F]FEPPA a TSPO Radioligand: Optimized Radiosynthesis and Evaluation as a PET Radiotracer for Brain Inflammation in a Peripheral LPS-Injected Mouse Model. Molecules. 2018;23. doi:10.3390/molecules23061375.
11. Chacko AM, Watanabe S, Herr KJ, Kalimuddin S, Tham JY, Ong J, et al. [18F]FDG as an inflammation biomarker for imaging dengue virus infection and treatment response. JCI Insight. 2017;2. doi:10.1172/jci.insight.93474.

Poster Presentation

Disclosures: The authors have disclosed no financial interest.

564-Squaraine-based PSMA Probe for NIR-II Imaging and Intraoperative Tumor Resection

Presenter: Xinlin Wang, Beijing Normal University

Xinlin Wang[1], Longfei Zhang[2], Mengchao Cui[3]

[1]*Beijing Normal University, China*
[2]*Beijing Normal University, Beijing, Beijing, China*
[3]*Beijing Normal University, Beijing, China, China*

Objectives:
To date, glutamic acid-based PSMA targeting probes have been extensively reported, and the potential of these agents has proven to attract high demand for new scaffolds with improved biological properties. In this study, we designed a near-infrared (NIR) II fluorescent PSMA probe to develop new inhibitor scaffolds by replacing glutamate with an artificial amino acid containing a squaraine moiety.

Methods:
Probe **1d** (Figure 1A) was prepared by condensation reaction between two squaraine-based PSMA binding pharmacophores and the NIR-II fluorophore bearing benzobis(1,2,5-thiadiazole) moiety via amide bonds[1]. The inhibition constant (K_i) of **1d** to PSMA were evaluated by a fluorescence-based NAALADase assay. NIR-II imaging (808 nm laser excitation, 1100 nm long-pass filter, and 400 ms exposure time) was performed in 22Rv1 tumor-bearing mice after i.v. administration of **1d** (0.42 μg/kg body weight). The feasibility of **1d** in intraoperative fluorescence image-guided precise tumor resection was confirmed in a living 22Rv1 tumor-bearing mouse under anesthesia at 24 h postinjection of **1d**.

Results:
Probe **1d** displayed high affinity to PSMA (K_i = 1.07 ± 0.43 nM), which was comparable with [^{18}F]DCFPyL (K_i = 1.36 ± 0.12 nM) under the same assay conditions. The NIR-II imaging demonstrated that **1d** accumulated in the 22Rv1 tumor, which can distinguish from surrounding tissue with good contrast after 24 h postinjection (Figure 1B). The intraoperative fluorescence image-guided tumor resection was precisely conducted (Figure 1C). The skin was first dissected to expose the tumor (Figure 1C b,c,d). Then the tumor was resected (Figure 1Ce,f), which was thought to be completely removed by visible inspection.

Conclusions:
We designed and synthesized a squaraine-based NIR-II PSMA probe for prostate tumor imaging and image-guided intraoperative tumor resection. Probe **1d** displayed high affinity to the recombinant PSMA protein. NIR-II imaging studies confirmed that the 22Rv1 tumor could be distinguished by **1d**, demonstrating its potential for precise prostate tumor resection in clinical practice.

Corresponding Author: *Tel/Fax: +86-13811995064. E-mail: cmc@bnu.edu.cn

Acknowledgments: This work was funded by the National Natural Science Foundation of China (No. 22022601 and U1967221).

Reference
Longfei Zhang, Xiaojing Shi, Yuying Li, et al: Visualizing Tumors in Real Time: A Highly Sensitive PSMA Probe for NIR-II Imaging and Intraoperative Tumor Resection. Journal of Medicinal Chemistry. 2021, 64, 7735−7745.

Poster Presentation

Disclosures: The authors have disclosed no financial interest.

565-Analysis of Magnetic Resonance Relaxation Rates and Cellular Iron Content in Mammalian Cells Expressing Essential Magnetosome Genes

Presenter: Qin (Daisy) Sun, Lawson Health Research Institute

Qin (Daisy) Sun[1], Prushoth Vivekanantha[2], Salvan Hassan[3], Moeiz Ahmed[4], Neil Gelman[5], Terry Thompson[6], Frank S. Prato[5], Donna Goldhawk[5]
[1]*Lawson Health Research Institute, London, ON*
[2]*McMaster University, Hamilton*
[3]*Western University, London, Ontario*
[4]*Western University, London*
[5]*Lawson Health Research Institute, London, Ontario*
[6]*St Joseph's Health Care London, London, Ontario*

Introduction:
With superb spatial and temporal resolution, magnetic resonance imaging (MRI) has great potential to track cellular activities that define early stages of disease [1]. To improve molecular imaging techniques, we are developing MRI reporter gene expression based on the magnetosome. In magnetotactic bacteria (MTB), magnetosome formation compartmentalizes iron biominerals in membrane-enclosed vesicles [2]. While this process is regulated by numerous genes, we have selected a subset (*mamE, mamB, mamI*, and *mamL*) deemed essential for initial stages of magnetosome formation [1]. While MamB, MamI, and MamL have roles in designating the magnetosome vesicle, they may also provide docking site(s) for additional proteins, such as MamE, that facilitate biomineralization [1-3]. Biosynthesis of magnetosome-like nanoparticles in mammalian cells would provide an endogenous, magnetic resonance (MR) contrast agent under genetic control [4], for long-term molecular imaging of cellular and molecular activities throughout the cell's life cycle.

Hypothesis:
Essential magnetosome proteins interact in any cell type to form rudimentary magnetosome-like nanoparticles and genetically-controlled contrast for molecular MRI.

Methods:
MTB genes *mamE, mamB, mamI,* and *mamL* were cloned from *M. magneticum* sp. AMB-1 genomic DNA by PCR and inserted into vectors with fluorescent protein tags (pEGFP or ptdTomato) to create Mam fusion proteins. In the MamI+MamL co-expression system, GFP-MamI was paired with FLAG-MamL expressed using pSF-EMCV-FLuc by adding a FLAG tag through PCR. All constructs were then stably expressed in human MDA-MB-435 melanoma cells using antibiotic selection and fluorescence-activated cell sorting. Appropriate protein expression was confirmed with western blotting and confocal microscopy, and protein-protein interactions were confirmed with the co-immunoprecipitation assay. Cells were cultured in the presence and absence of iron supplementation (250 μM ferric nitrate/medium). At harvest, cells were either mounted in a gelatin phantom for MRI at 3 Tesla (Biograph mMR) or analyzed by mass spectrometry [5]. A

custom MATLAB-based program was used to obtain relaxation rates. Analysis of variance (ANOVA) and Tukey's post-hoc test were performed in GraphPad Prism 9. A nonlinear regression was used to assess the correlation between total cellular iron content and relaxation rate.

Results:
In the absence of iron supplement, total transverse relaxation rates (R2*) of mammalian cells expressing MamE, MamB, MamI, MamL, or MamI+MamL (Fig. 1) were no different than parental controls. However, in the presence of iron supplement (+Fe), only cells expressing MamB, MamI, or MamL showed a significant increase in R2* while MamI+MamL co-expression or MamE alone did not. The same results were obtained with R2. Examination of R2′ (R2* − R2) indicated significant increases in iron-supplemented cells expressing MamI and MamL but not MamB. Interestingly, a comparable increase in elemental iron content was recorded in MamE-, MamI- and MamL-expressing cells in response to iron supplementation. These data show a moderate correlation between R2* and total cellular iron content ($r^2 = 0.42$), with the iron-specific R2′ component contributing more to Pearson's correlation than R2 ($r^2 = 0.36$ vs 0.10, respectively).

Discussion & Conclusions:
To better understand the components of bacterial magnetosome structure and how their assembly impacts MRI relaxation rates, we are characterizing 4 essential magnetosome proteins (MamE, MamB, MamI, MamL), expressed alone and in combination in mammalian cells. When expressed separately, 3 of 4 genes (MamB, MamI, MamL) impart MR-visible iron-handling properties to a human melanoma cell line. However, co-expression of MamI+MamL reduces transverse relaxation rates and elemental iron content, suggesting a regulatory effect of magnetosome gene combinations. The nature of this regulation not only depends on total iron content but also on cellular organization of iron, as demonstrated by MR-silent MamE expression. Future work will examine the potential of MamB and MamE to interact with the MamI-MamL complex and augment cellular MR parameters.

Reference

1. Goldhawk DE, Gelman N, Thompson RT, Prato FS. In: Design and Applications of Nanoparticles in Biomedical Imaging, Bulte JWM, Modo MMJ, Eds. Springer International Publishing, Cham, 2017; 187-293.
2. Uebe R, Schuler D. Magnetosome biogenesis in magnetotactic bacteria. Nat Rev Microbiol 2016; 14; 621-637.
3. Quinlan A, Murat D, Vali H, Komeili A. The HtrA/DegP family protease MamE is a bifunctional protein with roles in magnetosome protein localization and magnetite biomineralization. Mol Microbiol 2011; 80;1075-1087.
4. Sun Q, Prato FS, Goldhawk DE. In: Bioimaging: Imaging by Light and Electromagnetics in Medicine and Biology, Ueno S, Ed. CRC Press & Taylor Francis Group, 2020; 201-214
5. Sengupta A, Quiaoit K, Thompson RT, Prato FS, Gelman N, Goldhawk DE. Biophysical features of MagA expression in mammalian cells: implications for MRI contrast. Front Microbiol 2014; 5; 1-9.

Poster Presentation

Disclosures: The authors have disclosed no financial interest.

566-Glutamate Level based Short Term Human Brain Plasticity following Visual Memory Learning using ER-MRS and EEG Modalities: Simultaneous Metabolic and Electrophysiological Studies

Presenter: Hossein Mohammadi, Isfahan University of Medical Sciences, Isfahan, Iran

Hossein Mohammadi[1], Nasim Dadashi[2], Nader Riyahi Alam[3], Shahriyar Jamshidi[2], Abbas Rahimi[4], Iman Adibi[5], Shaghayegh Karimi[4]

[1]*Isfahan University of Medical Sciences, Isfahan, Iran, Isfahan, Iran*
[2]*Department of Bioimaging, School of Advanced Technologies in Medicine, Isfahan University of Medical Sciences(IUMS), Isfahan, Iran, Isfahan, Isfahan, Iran*
[3]*Tehran University of Medical Sciences, tehran, Iran*
[4]*Tehran University of Medical Sciences, Tehran, Tehran, Iran*
[5]*Department of Neurology, School of Medicine, Isfahan University of Medical Sciences(IUMS), Isfahan, Iran, Isfahan, Isfahan, Iran*

Introduction:
Learning of new information involves changes at the synaptic level (1). Memory is the encoding, storage, and retrieval of learned information. The study of human memory and learning at the molecular level have been limited to several studies and were accomplished mostly using one modality (2-4). Studies using MRS demonstrated the role of Glutamate in human memory (5-7). Glutamate is released by approximately 80% of synapses and is considered an essential substance in learning and memory. In the prefrontal cortex, NMDA receptors of glutamate are important for working memory (8). It is demonstrated that glutamate release and electrical activity and the hemodynamic response of neurons are dependent on each other (9). Based on the above information the Glutamate dynamic concentration levels in human memory learning and the electrophysiological and hemodynamic response are related to each other and to study them, simultaneous event-related MRS-EEG-fMRI modalities were performed in this study.

Materials and methods:
participants: 10 healthy right-handed participants (6 females; average age = 27.43) were included in this study who had normal or corrected to normal vision and had no involvement with any other diseases and history of brain diseases.

Data acquisition
was obtained as follows: firstly 64 channel MR compatible EEG cape and electrodes were inserted on the volunteer's head. Then EEG impedances were checked to be lesser than 10 k0hm. The subject head was placed inside the MR scanner and 64 channel Hydrogen coil was inserted. A response device is given to the right hand of the subject. Afterward, a high-resolution T1 weighted image was acquired then simultaneous MRS-EEG data were acquired while Strenberge's short-term memory task was presented (fig 1 A). Each trial of the task had 4 parts: Encoding, Retention, Response, and Rest. In the encoding, a list of letters was presented. In the retention, a cross was presented. In the answer, a letter is displayed that was either inside the previous list or not. if the letter is inside the list subjects must press the button, otherwise, they do not press any button, as a negative answer. All parts of the task were triggered by numbers so we can separate every part of the data in the analysis. MRS signals were acquired by 3 tesla Siemens Prisma MR scanners and using PRESS sequences (TR=2000, TE=40 ms, and NEX=96). Voxel size was 8 cm3 (2*2*2 cm) which was located on the right Dorsolateral prefrontal (DLPFC) and parieto-occipital cortex. Finally, fMRI-EEG data was acquired similar to above with the difference that this time it was fMRI-EEG instead of MRS-EEG. For fMRI, an EPI sequence with TR= 2000 and TE= 30 ms was implemented.

Data analysis: MRS signals: water signal was removed, then apodization was employed to reduce background noise and finally, LCmodel

quantification using QUEST functionality was applied. EEG signals: a cut-off frequency of 0.5-40 Hz applied and gradients artifacts removed using PCA. fMRI signals: Slice timing, Realignment, Normalizing, and Smoothing accomplished respectively. Results: glutamate concentration level is elevated in encoding and response phases. This difference is higher in the Prieto-occipital cortex (fig 1 B). Increased activity in alpha and beta bands in encoding and response phases was observed mostly in the right prefrontal, temporal and parieto-occipital areas. Bold signal activation also confirmed these areas. Connectivity analyses on fMRI-EEG demonstrated connections between frontal, occipital, and right DLPFC and hippocampus (fig 1 C-F).

Conclusion:

This study demonstrates that the glutamate levels are correlated with increased EEG activity and BOLD signals and also indicates that there are connections between right frontal and Prieto-occipital areas during human fast visual memory learning.

Reference

1. Kennedy MB. Synaptic signaling in learning and memory. Cold Spring Harbor perspectives in biology. 2016;8(2):a016824.
2. Nishitani N. Dynamics of cognitive processing in the human hippocampus by neuromagnetic and neurochemical assessments. Neuroimage. 2003;20(1):561-71.
3. Floyer-Lea A, Wylezinska M, Kincses T, Matthews PM. Rapid modulation of GABA concentration in human sensorimotor cortex during motor learning. Journal of neurophysiology. 2006;95(3):1639-44.
4. Gonzales MM, Takashi T, Eagan DE, Tanaka H, Vaghasia M, Haley AP. Indirect effects of elevated body mass index on memory performance through altered cerebral metabolite concentrations. Psychosomatic medicine. 2012;74(7):691.
5. Apšvalka D, Gadie A, Clemence M, Mullins PG. Event-related dynamics of glutamate and BOLD effects measured using functional magnetic resonance spectroscopy (fMRS) at 3 T in a repetition suppression paradigm. Neuroimage. 2015;118:292-300.
6. Stanley JA, Burgess A, Khatib D, Ramaseshan K, Arshad M, Wu H, et al. Functional dynamics of hippocampal glutamate during associative learning assessed with in vivo 1H functional magnetic resonance spectroscopy. Neuroimage. 2017;153:189-97.
7. Lally N, Mullins PG, Roberts MV, Price D, Gruber T, Haenschel C. Glutamatergic correlates of gamma-band oscillatory activity during cognition: a concurrent ER-MRS and EEG study. Neuroimage. 2014;85:823-33.
8. Li F, Tsien JZ. Memory and the NMDA receptors. The New England journal of medicine. 2009;361(3):302.
9. Purves D, Augustine GJ, Fitzpatrick D, Hall W, LaMantia A-S, White L. Neurosciences: De Boeck Supérieur; 2019.

Poster Presentation

Disclosures: The authors have disclosed no financial interest.

567-Development of in vivo microbial tracking system using avidin-expressing bacteria

Presenter: Jin Hee Im, Chonnam National University Hospital

Jin Hee Im[1], Seong Young Kwon[2]

[1]Chonnam National University Hospital, South Korea
[2]Chonnam National University Medical School, South Korea

A novel imaging system for in vivo bacterial tracking using bacteria expressing streptavidin which binds specifically to biotin develop . To enhance the expression level in bacteria and solubility of streptavidin, constructed the expression plasmid for monomeric streptavidin-rhizavidin recombinant (mSA) gene fused with maltose-binding protein (MBP) protein at its N-terminus. Ribosome binding site (RBS) sequence for the fused gene was selected from its library to get the efficient expression. As a result, the plasmid was designed that the fused gene was driven by pBAD promoter. E. coli MG1655 was transformed with the plasmid, and named MG1655 R2P-mSA. Bacteria were orally administered to mice. The expression of fused streptavidin was induced using L-arabinose immediately or 1 hour after bacterial administration. One hour after L-arabinose administration, a biotinylated fluorescent dye was intravenously injected to obtain optical images of bacteria. Optical signals were observed only in the intestines of mice with L-arabinose induction but not in those with fluorescent dye injection only or without L-arabinose induction after bacterial administration. In ex vivo imaging of the intestine, signal was stronger in the mice with immediate L-arabinose induction than in those with induction 1 hour after bacterial administration. The number of bacteria in the intestine was similar among both of mice regardless of L-arabinose induction times. Western blot analysis showed that the expression of fused streptavidin and its biotin binding were observed only in intestines with L-arabinose induction. Taken together, novel tracking system to visualize bacterial distribution in vivo using streptavidin and biotinylated optical dye developed . It is expected that this system is useful to monitor specific microorganisms administered into the body as real time.

Reference

1. Zhao, M., et al., Tumor-targeting bacterial therapy with amino acid auxotrophs of GFP-expressing Salmonella typhimurium. Proc Natl Acad Sci U S A, 2005. 102(3): p. 755-60.
2. Yu, Y.A., et al., Visualization of tumors and metastases in live animals with bacteria and vaccinia virus encoding light-emitting proteins. Nat Biotechnol, 2004. 22(3): p. 313-20.
3. Lim, K.H., et al., Stable, high-affinity streptavidin monomer for protein labeling and monovalent biotin detection. Biotechnol Bioeng, 2013. 110(1): p. 57-67.
4. Daniel, C., et al., Bioluminescence imaging study of spatial and temporal persistence of Lactobacillus plantarum and Lactococcus lactis in living mice. Appl Environ Microbiol, 2013. 79(4): p. 1086-94.

Poster Presentation

Disclosures: The authors have disclosed no financial interest.

568-Enhanced Reversibly Photoswitching Upconversion Nanoparticles for Background-free Photoacoustic Molecular Imaging

Presenter: Cheng Liu, Stanford University

Cheng Liu[1], Xianchuang Zheng[1], Tingting Dai[2], Huiliang Wang[3], Xian Chen[4], Bing Chen[5], Tianying Sun[6], Feng Wang[5], Steven Chu[7], Jianghong Rao[1]

[1]Stanford University, Stanford, CA
[2]Stanford University, Menlo Park, CA
[3]University of Texas at Austin, Austin, Texas
[4]Shenzhen University, Shenzhen, Guangdong, China
[5]City University of Hong Kong, Hong Kong, Hong Kong, China
[6]Sun Yat-sen University, Guangzhou, Guangdong, China
[7]Stanford University, Palo Alto, California

Photoacoustic (PA) imaging, an emerging new non-ionizing imaging modality, overcomes the depth and resolution limits of conventional optical imaging by combining optical excitation and acoustic detection. This exciting feature has stimulated strong interest and prompted the use of PA to visualize biological structures at various scales ranging from organelles, and cells to organs at the clinically relevant depth, expanding its application in pre-clinical and clinical studies. PA contrast can be generated from highly light-absorbing endogenous molecules like hemoglobin (Hb) and the exogenous contrast agents, including but not limited to: organic dyes, proteins, gold nanoparticles, carbon nanotubes, and conjugating polymer nanoparticles. However, the high intrinsic background signals from blood and pigments in the body have significantly compromised the sensitivity of PA imaging with exogenous contrast agents. Several strategies have been explored to improve PA imaging sensitivity, including optimizing the optical excitation or acoustic detection in the imaging system, enhancing the brightness of exogenous contrast agents, employing more efficient signal unmixing strategies, and using nonlinear PA imaging techniques. A new attractive direction is to develop PA probes that can be temporally modulated by light to induce changes in the PA signal, a strategy similarly used for modulating the fluorescence signals of the probe by light to remove background in the "optical lock-in detection" method. Assuming the PA background remains little change between pre- and post-modulation, the background suppression can be performed for every pair of PA images from each modulation cycle. In our previous work, we have developed a novel reversibly photoswitchable nanoprobe (PS-Probe) by encapsulating the core/shell upconversion nanoparticles (UCNPs) and photoswitchable small molecules (3ThacacH) with an amphiphilic polymer for super-sensitive molecular photoacoustic (PA) imaging.[1] By employing a conventional PA imager, we can detect 0.05 nM of the nanoprobes in hemoglobin solutions; and 5×10^3 labeled cancer cells within 20 photoswitching cycles. The nanoprobes can be fully photoswitched ON by a 980 nm laser (average power density 3 W cm^{-2}) in 1 minute. However, the photoswitching speed will decrease when reducing the power density. Furthermore, we have observed a reverse-way photoswitching phenomenon when the power density is lower than 1 W cm^{-2}. At higher power densities, the dominant emissions of UCNPs are ultraviolet and drive the photoswitchable 3ThacacH from open to the closed form, which is the forward direction of the reversible photoswitching ways. The blue light generated from the same core/shell UCNPs at lower power densities will become dominant and trigger the photoswitchable 3ThacacH molecules from closed to open form, which is the reverse direction of the reversible two-way photoswitching. Therefore, in order to drive forward-direction photoswitching at a relatively lower power density, we propose to quench the blue light emission by incorporating a blackhole quencher Tide Quencher 1 (TQ1) into our existing photoswitchable nanoprobe (PS-Probe), as shown in **Scheme 1**.

In this work, we have found that the photoswitching speed of the PS-Probe with TQ1 (PS-Probe-TQ1) under a lower power density CW980 irradiation (1 W cm^{-2}) is even faster than that of the PS-Probe without TQ1 quencher under a higher power density CW980 irradiation (3 W cm^{-2}). After incorporating the TQ1 quencher, we can detect 0.05 nM of the nanoprobes (PS-Probe-TQ1) in hemoglobin solutions with 10 photoswitching cycles. Compared with our reported PS-Probe, the new PS-Probe-TQ1 has 1) enhanced the photoswitching-ON speed, 2) lowered the photoswitching-ON power density, and 3) reduced the photoswitching cycle numbers.

Reference

1. Cheng Liu, Xianchuang Zheng, Tingting Dai, Huiliang Wang, Xian Chen, Bing Chen, Tianying Sun, Feng Wang, Steven Chu, and Jianghong Rao. "Reversibly Photoswitching Upconversion Nanoparticles for Super-Sensitive Photoacoustic Molecular Imaging." Angewandte Chemie (2022): e202116802. (selected as the Very Important Paper (VIP), less than 5% in Angew)

Poster Presentation

Disclosures: The authors have disclosed no financial interest.

569-Up regulation of NK cell activity and inhibition of AKT/mTOR pathway enhances therapeutic outcome in Salmonella mediated cancer therapy

Presenter: AKHIL VENU, Chonnam National University

Akhil Venu[1], Jung-Joon Min[2]

[1]Chonnam National University, Hwasun, Jeonnam, South Korea
[2]Chonnam National University Medical School, Hwasun-gun, South Korea

Tumor- homing oncolytic bacteria show promise as a treatment for solid tumors However, the overall response rate varies and the bacteria-host interaction is not well understood., underscoring the need to gain mechanistic and immunological detail about the treatment response. Here we transcriptionally profile tumors from MC38 colon cancer bearing-mice during bacterial infection with the genetically engineered *Salmonella typhimurium* ΔppGpp strain to gain valuable information about tumor regression. We grouped the mice into a moderate response (MR) or a Well response (WR) group according to the therapeutic effect observed compared to PBS- treated group. Our results indicated the NK cell mediated killing and down regulation of AKT/mTOR pathway is elevated in (WR) compared to (MR). Further combination of therapeutic drugs induce NK cell mediated cytotoxicity and inhibit AKT/mTOR pathway to enhance therapeutic efficacy of *Salmonella*

Poster Presentation

Disclosures: The authors have disclosed no financial interest.

570-Deuterium metabolic imaging and hyperpolarized 13C-MRI of the normal human brain at clinical field strength reveals differential cerebral metabolism

Presenter: Joshua Kaggie, University of Cambridge

Joshua Kaggie[1], Alixander Khan[2], Tomasz Matys[3], Matthew Locke[3], Ines Horvat-Menih[4], Rolf Schulte[3], Ashley Grimmer[3], Elizabeth Latimer[3], Amy Frary[2], Martin Graves[5], Mary McLean[6], Ferdia Gallagher[5]

[1]University of Cambridge, Cambridge, United Kingdom
[2]University of Cambridge, United Kingdom
[3]University of Cambridge
[4]Department of Radiology, University of Cambridge, Cambridge, United Kingdom
[5]University of Cambridge, Cambridge, Cambridgeshire, United Kingdom
[6]Cancer Research UK Cambridge Institute, Cambridge, Cambridgeshire, United Kingdom

Background:
Deuterium metabolic imaging (DMI) and hyperpolarized ^{13}C-pyruvate MRI (^{13}C-HPMRI) are two emerging methods for non-invasive and non-ionizing imaging of tissue metabolism. Imaging cerebral metabolism has potential applications in cancer, neurodegeneration, multiple sclerosis, traumatic brain injury, stroke, and inborn errors of metabolism. Here we directly compare these two non-invasive methods at 3 T for the first time in humans and show how they simultaneously probe both oxidative and non-oxidative metabolism.

Methods:
DMI was undertaken 1-2 hours after oral administration of [6,6'-$^{2}H_{2}$]glucose, and ^{13}C-MRI was performed immediately following intravenous injection of hyperpolarized [1-^{13}C]pyruvate in ten and nine normal volunteers within each arm respectively. Ten subjects were imaged 57-136 min following oral ^{2}H-glucose administration using a static 3D MRSI with the following parameters: field-of-view (FOV) = 32 cm, matrix = 10x10x10, TR = 120 ms, flip angle = 90°, 5000 Hz, 544 points, scan duration = 10 min, 2504 transients distributed according to a Hamming filter and repeated twice. Unlocalized MR spectra were also acquired prior to and following the MRSI with the following parameters: flip = 90°, TR = 1 s, 128 averages, 5000 Hz, 2048 points, total scan duration = 2 min 8 s.
Nine normal volunteers in the ^{13}C-HPMRI were injected with an intravenous bolus of [1-^{13}C]pyruvate: 0.4 mL/kg of ~250 mM pyruvate, up to 40 mL at rate of 5 mL/s as described previously (Grist et al., 2019). The ^{13}C-pyruvic acid was hyperpolarized using a SpinLab hyperpolarizer (Research Circle Technology, Albany NY, USA). ^{13}C-MRI was performed using a dual-tuned 16-rung ^{13}C/^{1}H quadrature transmit/receive head coil (Rapid Biomedical, Rimpar, Germany), with a 30 cm diameter and 24 cm rung length.

Results:
DMI was used to generate maps of deuterium-labelled water, glucose, lactate, and glutamate/glutamine (Glx) and the spectral separation demonstrated that DMI is feasible at 3 T. ^{13}C-HPMRI generated maps of hyperpolarized carbon-13 labelled pyruvate, lactate, and bicarbonate. The ratio of ^{13}C-lactate/^{13}C-bicarbonate (mean 3.7 ± 1.2) acquired with ^{13}C-HPMRI was higher than the equivalent ^{2}H-lactate/^{2}H-Glx ratio (mean 0.18 ± 0.09) acquired using DMI. These differences can be explained by the route of administering each probe, the timing of imaging after ingestion or injection, as well as the biological differences in cerebral uptake and cellular physiology between the two molecules.

Conclusions:
DMI and ^{13}C-HPMRI are two emerging techniques for non-invasively probing these alternative aspects of carbohydrate metabolism which could have important implications for evaluating cerebral energy utilization in health and disease. However, the way in which these techniques differ in probing human brain metabolism has not been studied previously. One of the major challenges in undertaking a direct comparison between the two techniques in humans is that ^{13}C-HPMRI is usually undertaken at 3 T, which allows good spectral separation of metabolites while maintaining a sufficiently long relaxation time for the hyperpolarized signal to enable detection of both the injected hyperpolarized substrate and the subsequently formed metabolites (Vaeggemose et al., 2021).
The results demonstrate these two metabolic imaging methods provide different yet complementary readouts of oxidative and reductive metabolism within a clinically feasible timescale. Furthermore, as DMI was undertaken at a clinical field strength within a ten-minute scan time, it demonstrates its potential as a routine clinical tool in the future.

Poster Presentation

Disclosures: The authors have disclosed no financial interest.

571-Creating a Favorable Microenvironment for HyperCEST Amplification: A Liposomal Design for Accelerated Depolarization without Negative Side Effects for Xe MRI

Presenter: Leif Schroeder, German Cancer Research Center (Deutsches Krebsforschungszentrum, DKFZ)

Leif Schroeder[1], Jan Oliver Jost[2]

[1]*German Cancer Research Center (Deutsches Krebsforschungszentrum, DKFZ), Heidelberg, Germany*
[2]*German Cancer Research Center (Deutsches Krebsforschungszentrum, DKFZ)*

Introduction:
The sensitivity of MRI with hyperpolarized ^{129}Xe can be boosted to picomolar in vitro sensitivity by the HyperCEST approach [1] that relies on chemical exchange saturation transfer (CEST) between functionalized Xe (transiently bound to a reporter molecule) and free Xe. The exchange conditions (amount and release rate of bound Xe) are crucial for efficient build-up of the CEST contrast under in vivo conditions [2]. To this end, the original approach for functionalized Xe reporters with individual hosts providing single hydrophobic cavities must be revisited for further translation of the method towards clinical applications. Improved exchange kinetics and a platform for flexible synthesis/assembly routes would be highly beneficial to address targets that have been previously inaccessible for MRI. **Methods:** This study investigated a liposomal design that includes a HyperCEST-active lipopeptide for insertion into POPC liposomal nanocarriers (NCs). The peptide carries cryptophane-A mono-acid (CrA-ma) as a well-studied Xe cage. CrA-ma has been coupled to a Lys side chain close to the palmitic acid to ensure that the hydrophobic cage can insert into the phospholipid bilayer. The HyperCEST performance was compared relative to an equivalent of free CrA-ma and the impact of different CrA loads was studied with adjusted NC concentration to maintain the overall cage concentration constant. Xe MRI and CEST spectroscopy was performed with a home-build polarizer for spin exchange optical pumping and precise Xe dissolution delivery.

Results:
Liposomes with different formulations regarding lipopeptide load (20 mol% vs. 2 mol%) showed significant improved HyperCEST build-up compared to an equivalent of free CrA-ma. Quantitative analysis of the z-spectra reveals that the depolarization rate is increased within the micro-environment of the NC membrane while the negative side effect of line broadening does not occur. An offset of ~200 Hz is sufficient to cause significant loss of CEST effect, thus illustrating the sharp CEST response. This preserves high spectral selectivity and avoids the need for increased saturation power that usually comes with faster exchange [3]. The overall performance of different formulations can be quantified by the net depolarization time, τ. NCs with 20 mol% lipopeptide were ca. 17-fold more efficient than CrA-ma at comparable cage concentration. A lower cage load (2 mol%) yielded further improvement by another factor of 5. PEGylation and insertion of 10 mol% cholesterol did not have a negative impact on the observed saturation responses and can thus be used for tuning the membrane conditions. Overall, the carriers with low cage load performed ca. 100-fold better than unfunctionalized CrA-ma. NCs with 2 mol% lipopeptide were chosen for MRI experiments and yielded a strong CEST response where the equivalent of free CrA-ma remained undetectable.

Discussion and Conclusion:
The environment provided by the NC membrane ensures a high local Xe concentration to participate in chemical exchange and an efficient release from the cage into the immediate lipid environment. Overall, the excellent gas turnover in the membrane is not linked to line broadening when detecting the Xe outside the membrane. This provides excellent HyperCEST conditions for Xe MRI with a switchable contrast. This first generation of the proposed carriers already provides an improvement of ca. 2 orders of magnitude. NCs with lower cage load are surprisingly efficient as they presumably avoid the problem of back-exchange of already depolarized Xe. Further tuning of the cage load and of the membrane composition might lead to additional improvements. Overall, this study illustrates the wide parameter space that is now available when incorporating CrA-labelled lipopeptides into liposomal carriers. The functionalization of such nanocarriers will be investigated in an upcoming study.

Reference

1. Schroder, L., Lowery, T. J., Hilty, C., Wemmer, D. E. & Pines, A. Molecular Imaging Using a Targeted Magnetic Resonance Hyperpolarized Biosensor. Science 314, 446–449 (2006).
2. McHugh, C. T., Kelley, M., Bryden, N. J. & Branca, R. T. In vivo hyperCEST imaging: Experimental considerations for a reliable contrast. Magn. Reson. Med. 87, 1480–1489 (2022).
3. Kunth, M., Witte, C., Hennig, A. & Schröder, L. Identification, classification, and signal amplification capabilities of high-turnover gas binding hosts in ultra-sensitive NMR. Chem. Sci. 6, 6069–6075 (2015).

Poster Presentation

Disclosures: The authors have disclosed no financial interest.

572-Changes in the transchelation kinetics and the release of Gd3+ ions from GBCAs induced by GAGs as endogenous binding partners from the ECM in the presence of competing divalent ions.

Presenter: Patrick Werner, German Cancer Research Center (Deutsches Krebsforschungszentrum, DKFZ)

Patrick Werner[1], Patrick Schuenke[2], Matthias Taupitz[3], Leif Schroeder[1]

[1]*German Cancer Research Center (Deutsches Krebsforschungszentrum, DKFZ), Heidelberg, Germany*
[2]*Berlin, Germany*
[3]*Charite University Medicine Berlin, Berlin, Germany*

Introduction:
Gd^{3+} deposition sites [1-6] in various tissues after injections of gadolinium-based contrast agents (GBCA) have been discussed repeatedly over the last decade. Nevertheless, insights about the underlying biochemical mechanism and about the kinitixs of competing chelation mechanisms that lead to a retention of these toxic metal ions remain still elusive. Potential substances to enlighten missing aspects could be glycosaminoglycans (GAGs) that represent a major component of the extracellular matrix (ECM) throughout the body. The goal of this study was to elucidate the influence of a variable heparin content on the stability of GBCAs in the presence of divalent ions.

Methods:
Sample solutions containing 0-100 µM of heparin and 0.125-4 mM $ZnCl_2$ in combination with five linear GBCAs (150 µM) were investigated. All time-resolved MR measurements were performed at 9.4 T. R_1 measurements at 25 °C were performed using a dephasing recovery sequence. All R_1 values reflect ROI-averaged values from corresponding R_1 parameter maps.

Results:
Upon interaction between GBCAs and Zn^{2+}, a part of the GBCAs is replaced with a higher relaxivity contribution of Gd^{3+} in H_2O or with a re-chelated form (Gd^{3+}@GAG complexes)[7] (Fig.1). The results show that the time constants for the transmetallation process not only differ between the different GBCAs but also vary for different $ZnCl_2$ concentrations. Furthermore comparing the time constants for the transchelation process in heparin solutions with the transmetallation process in H_2O reveals that these kinetics differ significantly: the sole transmetallation process occurs on the order of minutes and increased slightly with increasing $ZnCl_2$ concentrations. The full transchelation, however, progresses on the order of hours to weeks and decrease with increasing $ZnCl_2$ concentrations.

Discussion:
By using time-resolved MR relaxometry, it could be shown that the Zn/GAG ratio has a decisive influence to favor fast or slower exchange kinetics during the transchelation process. A high Zn/GAG ratio leads to a more efficient transchelation process. Due to the higher $ZnCl_2$ concentration, there are on average more Zn^{2+} ions available (unbound, outside the GAG-structure) and as a consequence this leads to faster initial transmetallation of the central Gd^{3+} ion. The entire transchelation of Gd^{3+} to heparin takes up to several days to reach a new chemical equilibrium, in contrast to the relatively rapid displacement of Gd^{3+} by Zn^{2+} in the absence of competing chelators. This vastly different time span highlights the complexity of the situation and arises from the competition for binding sites between Gd^{3+} ions and other cations for both the parent GBCA chelator and the binding sites of heparin. It could be concluded that for small $ZnCl_2$ stimuli, the transmetallation is the limiting step and not the availability of binding sites for the subsequent chelation of dissociated Gd^{3+} to GAGs. Under such conditions, the Zn^{2+} ions are sufficiently prevented from initiating the transmetallation of the central Gd^{3+} ion by their own binding to heparin. It could be shown that the measured time constants decrease significantly with strong $ZnCl_2$ stimuli. Overall, Gd^{3+} outperforms Zn^{2+} in terms of binding to heparin, and the released Gd^{3+} ions are apparently not limited in finding a binding site and forming the macromolecular Gd-GAG complexes.

Conclusion:
The results show that GAGs seem to have an important two-fold effect on the stability of GBCAs in the presence of $ZnCl^2$. On the one hand, they foster the thermodynamic instability of intact GBCA by sequestering Gd^{3+} from a disfavored intermediate. But at the same time, the GAG's interaction with competing ions can suppress the initial attack which leads to a reduced kinetic instability.

Acknowledgement: This research was funded by the Deutsche Forschungsgemeinschaft (DFG, German Research Foundation)—Grant No. 289347353(GRK 2260) and Koselleck Grant No. 316693477 (SCHR 995/5–1). Support by the Dieter Morszeck Stiftung is also gratefully acknowledged.

Reference

1. Laurent, S., Elst, L. V, Copoix, F. & Muller, R. N. Stability of MRI paramagnetic contrast media: a proton relaxometric protocol for transmetallation assessment. Invest. Radiol. 36, 115–22 (2001).
2. Taupitz, M. et al. Gadolinium-containing magnetic resonance contrast media: investigation on the possible transchelation of Gd3+ to the glycosaminoglycan heparin. Contrast Media Mol. Imaging 8, 108–16 (2013).
3. Gianolio, E., Gregorio, E. Di & Aime, S. Chemical Insights into the Issues of Gd Retention in the Brain and Other Tissues Upon the Administration of Gd-Containing MRI Contrast Agents. Eur. J. Inorg. Chem. 2019, 137–151 (2019).
4. Kanda, T., Ishii, K., Kawaguchi, H., Kitajima, K. & Takenaka, D. High signal intensity in the dentate nucleus and globus pallidus on unenhanced T1-weighted MR images: relationship with increasing cumulative dose of a gadolinium-based contrast material. Radiology 270, 834–41 (2014).
5. Kanda, T. et al. High Signal Intensity in Dentate Nucleus on Unenhanced T1-weighted MR Images: Association with Linear versus Macrocyclic Gadolinium Chelate Administration. Radiology 275, 803–9 (2015).
6. Radbruch, A. et al. Gadolinium retention in the dentate nucleus and globus pallidus is dependent on the class of contrast agent. Radiology 275, 783–91 (2015).
7. Werner, P., Taupitz, M., Schröder, L., & Schuenke, P. An NMR relaxometry approach for quantitative investigation of the transchelation of gadolinium ions from GBCAs to a competing macromolecular chelator. Scientific Reports, 11(1), 1-13 (2021).

Poster Presentation

Disclosures: The authors have disclosed no financial interest.

573-A novel analytical approach for clinical outcome prediction in diffuse large B-cell lymphoma by [18F]FDG PET/CT

Presenter: Xiaohui Zhang, Second Affiliated Hospital Zhejiang University School of Medicine

Xiaohui Zhang[1], Lin Chen[2], Han Jiang[3], Xuexin He[4], Jing Wang[4], Teng Zhang[5], Shuang Wu[6], Rui Zhou[7], Chentao Jin[7], Kai Zhang[8], Cheng Zhuo[9], Hong Zhang[10], Mei TIAN[7]

[1]*Second Affiliated Hospital Zhejiang University School of Medicine, Hangzhou, Zhejiang, China*
[2]*Second Affiliated Hospital Zhejiang University School of Medicine, China*
[3]*Fujian Medical University Union Hospital, China*
[4]*Zhejiang University, China*
[5]*Second Affiliated Hospital of Zhejiang University, Hangzhou, Zhejiang Province, China*
[6]*Zhejiang University, Hangzhou, Zhejiang*
[7]*Zhejiang University, Hangzhou, Zhejiang, China*
[8]*Zhejiang University School of Medicine, Hangzhou, Zhejiang, China*
[9]*Zhejiang University, Hangzhou, Zhejiang Province, China*
[10]*Zhejiang University, Hangzhou, Zhejiang 310009, China*

Purpose:
This study aimed to develop a novel analytical approach based on 2-deoxy-2-[^{18}F]fluoro-D-glucose positron emission tomography/computed tomography ([^{18}F]FDG PET/CT) radiomic signatures (RS) and International Prognostic Index (IPI) to predict the progression-free survival (PFS) and overall survival (OS) of patients with diffuse large B-cell lymphoma (DLBCL).

Methods:
We retrospectively enrolled 152 DLBCL patients and divided them into a training cohort ($n = 100$) and a validation cohort ($n = 52$). A total of 1245 radiomic features were extracted from the total metabolic tumor volume (TMTV) and the metabolic bulk volume (MBV) of pretreatment PET/CT images. The least absolute shrinkage and selection operator (LASSO) algorithm was applied to develop the RS. Cox regression analysis was used to construct hybrid nomograms based on different RS and clinical variables. The performances of hybrid nomograms were evaluated using the time-dependent receiver operator characteristic (ROC) curve and Hosmer-Lemeshow test. The clinical utilities of prediction nomograms were determined via decision curve analysis. The predictive efficiency of different RS, clinical variables and hybrid nomograms were compared.

Results:
The RS and IPI were identified as independent predictors of PFS and OS, and were selected to construct hybrid nomograms (Fig. 1a, b). Both TMTV- and MBV-based hybrid nomograms had significantly higher values of area under the curve (AUC) than IPI in training and validation cohorts (all $P < 0.05$), while no significant difference was found between TMTV- and MBV-based hybrid nomograms ($P > 0.05$). Hosmer-Lemeshow test showed that both TMTV- and MBV-based hybrid nomograms were well-calibrated. Decision curve analysis indicated that the hybrid nomograms had higher net benefits than IPI. Both MBV- and TMTV-based hybrid nomograms demonstrated a more distinct risk stratification than IPI, with larger differences between subgroups and improved hazard ratios (log-rank $P < 0.05$) (Fig. 1c, d).

Conclusion:
The hybrid nomograms combining RS with IPI could significantly improve survival prediction in DLBCL. Radiomic analysis on MBV may serve as a potential approach for prognosis assessment in DLBCL.

Poster Presentation

Disclosures: The authors have disclosed no financial interest.

574-Spatiotemporal Dynamic Changes of Neuroinflammation-associated Cognitive Aging Treated by Young Plasma

Presenter: Yan Zhong, Second Affiliated Hospital of Zhejiang University

Yan Zhong[1], Youyou Zhou[1], Xiaoqing Xing[2], Yu Liu[3], Peili Cen[2], Mei Tian[4], Hong Zhang[5]

[1]*Second Affiliated Hospital of Zhejiang University, China*
[2]*Zhejiang University, China*
[3]*Second Affiliated Hospital Zhejiang University School of Medicine, China*
[4]*Zhejiang University, Hangzhou, Zhejiang, China*
[5]*Zhejiang University, Hangzhou, Zhejiang 310009, China*

Background:
Deficits in glucose availability and microglial activation-related neuroinflammation are characteristic of the aged brain that contribute to age-associated cognitive impairment. Previous studies suggested that changes in glucose metabolism of microglia underlie their response to inflammation. This study aimed to investigate the therapeutic effects

of young mice plasma (YMP) on spatiotemporal dynamic biomedical changes and neuroinflammation based on ^{18}F-fluorodeoxyglucose positron emission tomography (^{18}F-FDG PET) imaging.

Methods:
Aged (19-month-old) C57BL/6 mice were systemic infusion of YMP or phosphate buffered saline (PBS) every three days for 8 weeks. ^{18}F-FDG PET imaging and cognitive behavioral tests including open field, contextual fear conditioning test were conducted after treatment. The effect of YMP on the expressions of key cognitive-related proteins and inflammatory cytokines was assessed by Western blots and RT-qPCR. In addition, an age-like microglia model was established and the cellular glucose metabolism profiles were evaluated by ^{18}F-FDG PET imaging, gamma counter and glycolysis/mitochondrial stress test.

Results:
YMP treatment enhanced the glucose metabolism in the bilateral hippocampus and thalamus, improved the expression of cognitive-related proteins BDNF, PSD95 and Synapthin1, inhibited the secretion of inflammation cytokines IL-6 and TNF-α in aged mice brain. Behavioral results showed that aged mice treated with YMP exhibited an improved cognitive performance. Further in vitro studies demonstrated that YMP rather than aged mice plasma (AMP), significantly restored the mitochondrial function, reduced cellular glucose uptake and promoted a shift in energy metabolism from glycolysis to oxygen phosphorylation in aged microglia, which contributed to suppressing microglia-induced inflammatory response.

Conclusions:
Our findings discover the effects of YMP in reprogramming glucose metabolism to suppress neuroinflammation and restore cognition in aged mice. ^{18}F-FDG PET imaging provides a new insight for evaluating the therapeutic effects underlying YMP treatment against aging or neuroinflammation-related disorders.

Poster Presentation

Disclosures: The authors have disclosed no financial interest.

575-Dual-Small Interfering Ribonucleic Acid Delivery via B7H3 targeted polymeric micelles for Pancreatic Ductal Adenocarcinoma therapy

Presenter: Xin Chen, Southeast University

Xin Chen[1], Ying Zhang[2], Jia Wei Du[3], Jinbing Xie[4], Jianqiong Zhang[2]

[1]*Southeast University, China*
[2]*Southeast University, Nanjing, Jiangsu, China*
[3]*Institute of life sciences, Key Laboratory of Developmental Genes and Human Diseases, Nanjing, Jiangsu, China*
[4]*Southeast University, Nanjing, Jiangsu Province, China*

Background:
Pancreatic ductal adenocarcinoma (PDAC) is among the deadliest human malignancies with a 5-year survival rate of less than 8%. Unfortunately, lack of effective treatment and predictive targets, multiple therapies including immune checkpoint inhibitors are ineffective in PDAC. To combat this issue, RNA interference (RNAi) offers a new and potent gene therapy technique.

Methods:
We engineered non-viral polymeric vectors Mal-Peg-Poly(L-Lysine) with targeting peptides and therapeutic siRNAs to treat xenograft of pancreatic cancer mouse models, cy7.5 NIR dyes coupled to nanoparticle surfaces for visual imaging of B7H3. Phage display identified peptides that bind to the B7H3. Literature review and bioinformatics methods adopted to explore potential therapeutic targets in PDAC.

Results:
Polymeric micelles targeted with B7H3–binding LTP peptide efficiently homed to and accumulated at the site of tumorigenesis in mice. We have identified a molecule of the EGFR signal pathway, betacellulin (BTC), involved in the resistance of pancreatic cancer cells to inhibitors of signal transducer and activator of transcription 3 (STAT3). Combined inhibition of BTC and STAT3 is a potential strategy for the treatment of PDAC. Taking advantage of the established Polymeric micelles, siRNAs targeting BTC and STAT3 were efficiently delivered to tumor tissue and consequently blocked the expression of STAT3 and BTC in tumor. Furthermore, dual suppression of STAT3 and BTC inhibited tumor progression significantly by promoting apoptosis in tumor cells compared with other control treatment groups.

Conclusions:
A non-viral polymeric vector Mal-Peg-Poly(L-Lysine) platform targeted B7H3 in PDAC and delivered siRNAs for signal pathway proteins STAT3 and BTC, suppressed tumor growth in subcutaneous xenograft of pancreatic cancer mouse models and enabled molecular imaging of B7H3 in tumors

Poster Presentation

Disclosures: The authors have disclosed no financial interest.

576-Quantitative methods using long-lived phantoms to cross-calibrate preclinical and clinical PET scanners

Presenter: Paul Kinahan,University of Washington
Adrienne Lehnert[1], Robert Miyaoka[1], Mark Muzi[1], Delphine Chen[2], Andrey Fedorov[3], Christina Baik[1], A. McGarry Houghton[4], **Paul E. Kinahan**[1]

[1]*University of Washington, Seattle, WA*
[2]*University of Washington, Seattle, Washington*
[3]*Harvard Medical School, Boston, Mass.*
[4]*Fred Hutchinson Cancer Research Center, Seattle, WA*

Purpose:
Although immune checkpoint inhibitor (ICI) therapy has been a tremendous clinical benefit for some NSCLC patients, only ~20% of NSCLC patients respond to anti-PD1/PDL1 therapy. Using PET co-clinical imaging to improve ICI therapies for NSCLC is challenged in part by a lack of quantitative preclinical PET imaging methods that are linked to quantitative clinical PET imaging methods. To address this we are developing methods using novel long-lived phantoms that can cross-calibrate preclinical and clinical PET scanners accuracies better than the 11% (human) and 16% (mice) coefficient of variation [1,2].

Methods:
We used a previously developed 68Ge/68Ga PET cross-calibration phantom (the 'Xcal') with a 9-month half-life [3,4]. The Xcal phantom was used to demonstrate multi-site cross-calibration for 19 PET scanners at nine hospitals over a 14-month period [5]. This study demonstrated that even using the same dose calibrator for scanner calibration and dose measurement still led to errors in standardized uptake values (SUVs) and absolute estimates of radiotracer uptake measurements. The size of the Xcal phantom is convenient for imaging in our

preclinical PET scanner (Inveon PET/CT) and we have used this for repeatability measurements, longitudinal measurements, and cross-calibration with our clinical PET/CT scanner (GE DMI). To test cross-calibrating the preclinical and clinical PET scanners, we used several Xcal sources with different activity levels acquired over several years, thus with different levels of activity. We measured Xcal phantom data for our clinical PET scanner over a 1-year period, calibrated to a traceable NIST standard. We then used

Results:

The measured coefficient of variation (CoV) for the dose calibrator standard (that was coupled to the Xcal phantom), after correction for radioactive decay, was under 0.1%. For the Xcal phantom itself, the measured image values were within ±2% of the expected value over the 1 year time period. We found that with an Xcal source strength of 200 to 500 uCi it is possible to cross-calibrate the preclinical and clinical PET scanners with the same phantom. The single-day test-retest scans on the pre-clinical PET/CT were very consistent with <1% stdev. There was, however, a 9% bias when compared to the same phantom is scanned on the clinical PET/CT scanner. This has been shown to potentially arise from different sources that can be mitigated [6]. The source of this bias is under investigation.

Conclusions:

For reliable measurements of radiotracer uptake in co-clinical trials using PET imaging, longitudinal cross calibration studies are essential. This is facilitated with the use of long-lived NIST traceable sources that are in the operational range of both classes of scanners, which is 200 to 500 uCi.

Reference

1. Kinahan PE et al.. The QIBA Profile for FDG PET/CT as an Imaging Biomarker Measuring Response to Cancer Therapy. Radiology. 2020;294:647-657. PMCID: PMC7053216. PMID: 31909700.
2. Dandekar M et al. Reproducibility of 18F-FDG microPET studies in mouse tumor xenografts. J Nucl Med. 2007;48:602-607. PMCID: PMC4161128. PMID: 17401098.
3. Byrd DW et al. Evaluation of Cross-Calibrated 68Ge/68Ga Phantoms for Assessing PET/CT Measurement Bias in Oncology Imaging for Single- and Multicenter Trials. Tomography. 2016;2:353-360. PMCID: PMC5214172. PMID: 28066807.
4. Doot RK, et al. Biases in Multicenter Longitudinal PET Standardized Uptake Value Measurements. Transl Oncol. 2014;7:48-54. PMCID: PMC3998681. PMID: 24772207.
5. Byrd D et al. Measuring temporal stability of positron emission tomography standardized uptake value bias using long-lived sources in a multicenter network. J Med Imaging (Bellingham). 2018;5:011016. PMCID: PMC5753626. PMID: 29322068
6. Lockhart CM, et al Quantifying and reducing the effect of calibration error on variability of PET/CT standardized uptake value measurements. J Nucl Med. 2011;52:218-224. PMCID: PMC4491194. PMID: 21233174.

Poster Presentation

Disclosures: The authors have disclosed no financial interest.

577-Development and validation of a predictive nomogram based on Parameters of PET/CT to Diagnose Hepatocellular Carcinoma with Cachexia

Presenter: Xinxiang Li, Zhongda Hospital, Southeast University

Xinxiang Li
Zhongda Hospital, Southeast University, China

Objective: The aim of this prospective study was to develop a nomogram to estimate hepatocellular carcinoma (HCC) with cachexia.

Methods:

In this study, a total of 212 HCC patients before preoperation who underwent PET/CT from two medical center was divided into the training and validation cohorts. Clinical features, PET/CT parameters (SUVmax, SUVmin, SUVavg, SUVpeak, SULmax, SULmin, SULavg, SULpeak) of liver, pancreas, perirenal fat, subcutaneous fat, and erector spine muscle were analyzed. Logistic regression analyses were applied to select independent variables associated with HCC with cachexia in the development cohort that the predictive nomogram was built. The area under the receiver operating characteristic curve (AUC), calibration slope and decision curve analysis were used to assess the nomogram performance.

Results:

132 patients (52 with and 80 without cachexia) were in the training cohort and 80 patients (32 with and 48 without cachexia) were in the validation cohort. Alpha-fetoprotein (AFP) >100 ng/mL (Odds Ratio [OR], 2.76; 95% CI: 1.03, 7.39; p=0.04), tumor size (OR, 2.24; 95% CI: 1.08, 4.65; p=0.03), SUVmax of liver (OR, 2.68; 95% CI: 1.17, 6.16; p=0.02), SULmin of perirenal fat (OR, 2.34; 95% CI: 1.13, 4.82; p=0.02), SULmin of subcutaneous fat (OR, 2.42; 95% CI: 1.03, 5.67; p=0.04) were independently associated with HCC with cachexia. The nomogram from training set showed good discrimination (AUC, 0.77 [95% CI: 0.68, 0.86]) and calibration abilities (calibration slope, 1) in the two validation cohorts.

Conclusion:

This multivariate nomogram using clinical characters and PET/CT parameters may help estimate the probability of HCC with cachexia.

Reference

1. Bruggeman AR, Kamal AH, LeBlanc TW, et al. Cancer Cachexia: Beyond Weight Loss. J Oncol Pract. 2016 Nov;12(11):1163-1171.
2. Nakamoto R, Okuyama C, Ishizu K, et al.Diffusely Decreased Liver Uptake on FDG PET and Cancer-Associated Cachexia With Reduced Survival. Clin Nucl Med. 2019 Aug;44(8):634-642.
3. Blauwhoff-Buskermolen S, Langius JAE, Becker A, et al. The influence of different muscle mass measurements on the diagnosis of cancer cachexia. J Cachexia Sarcopenia Muscle. 2017 Aug;8(4):615-622.

Poster Presentation

Disclosures: The authors have disclosed no financial interest.

578-CRISPR/Cas9-based Study of Dynamics and Function of Transplanted Human Induced Pluripotent Stem Cell-derived Cardiomyocytes

Presenter: Shuang Wu, Zhejiang University

Shuang Wu[1], Yuanxue Gao[2], Jiayue Pan[3], Jingjing Shi[2], Hong Zhang[4], Mei Tian[5]

[1]*Zhejiang University, HangZhou, China*
[2]*Zhejiang University, HangZhou, HangZhou, China*
[3]*Zhejiang University, China*
[4]*Zhejiang University, Hangzhou, Zhejiang 310009, China*
[5]*Zhejiang University, Hangzhou, Zhejiang, China*

Purpose:
To investigate the post-transplantation behaviour and therapeutic efficacy of human urinary-induced pluripotent stem cell-derived cardiomyocytes (hUiCMs) in infarcted heart by molecular imaging approaches. Methods We used clustered regularly interspaced short palindromic repeats/CRISPR-associated nuclease 9 (CRISPR/Cas9) technology to integrate a triple-fusion (TF) reporter gene into the AAVS1 locus in human urine-derived hiPSCs (hUiPSCs) to generate TF-hUiPSCs that stably expressed monomeric red fluorescent protein for fluorescence imaging, firefly luciferase for bioluminescence imaging (BLI) and herpes simplex virus thymidine kinase for positron emission tomography (PET) imaging. All experiments were performed following protocols of the Institutional Animal Care and Use Committee (IACUC) of Zhejiang University School of Medicine (Protocol No. #ZJU20190062).

Results:
Transplanted cardiomyocytes derived from TF-hUiPSCs (TF-hUiCMs) engrafted and proliferated in the infarcted heart as monitored by both BLI and PET imaging and significantly improved cardiac function. Under ischaemic conditions, TFhUiCMs enhanced cardiomyocyte (CM) glucose metabolism and promoted angiogenic activity.

Conclusion:
This study established a CRISPR/Cas9-mediated multimodality reporter gene imaging system that can determine the dynamics and function of TF-hUiCMs in myocardial infarction, which is helpful for investigating the application of stem cell therapy.

Poster Presentation

Disclosures: The authors have disclosed no financial interest.

579-68Ga-Galuminox: A PET Tracer for Imaging Mitochondrial ROS Activity

Presenter: Jothilingam Sivapackiam, Washington University School of Medicine

Jothilingam Sivapackiam[1], Karishma Muthukumar[1], Dequan Zhou[1], Robert Gropler[2], Andrew Gelman[2], Vijay Sharma[3]

[1]*Washington University School of Medicine, St. Louis, MO*
[2]*Washington University in St. Louis, Saint Louis, MO*
[3]*Washington University School of Medicine, St. Lous, MO*

The overproduction of ROS mediates the pathogenesis of numerous diseases, such as pathogenesis of numerous diseases, such as cardiovascular disease, diabetes, atherosclerosis, asthma, Alzheimer's disease, psoriasis, rheumatoid arthritis, and acute lung injury (ALI). Previously, we have reported preclinical validation of Galuminox, a molecularly specific probe to monitor ROS-mediated inflammation through multiple bioassays, and demonstrated its ability to image inflammation in an acute lung injury model. Using live-cell fluorescence imaging, we also showed its localization in the mitochondria of cells. To confirm unambiguously, if previously observed intracellular uptake profiles of Galuminox in human alveolar basal epithelial (A549) cells at macroscale are observed at tracer concentrations, herein, we report cellular uptake of ^{68}Ga-Galuminox under identical conditions and show its localization within mitochondria of A549 cells following treatment with LPS. Galuminox was obtained via reaction of $^{68}GaCl_3$ and the precursor ligand, purified on Phenomenex Strata-X-C cartridge, and analyzed using radio-HPLC. To evaluate the cellular accumulation studies, A549 cells were plated and incubated with serum-deprived media (starvation), LPS (5µg/mL), Mitomycin C (0.5µg/mL) or vehicle for 24h at 37°C under a continuous flux of 5% CO_2, and treated with either ^{68}Ga-Galuminox or its unlabeled counterpart Galuminox (20 µM; 60min). For radiotracer cell assays, net uptake was quantified $(\text{fmol} \times (\text{nM}_0)^{-1} \times (\text{mg protein})^{-1})$. For identification of radiotracer in mitochondria of cells, (5-fold higher activity; 100 µCi/mL) was incubated A549 cells (10 fold higher number of cells plated in a flask) at 37°C for 60 min either in the presence or absence of LPS in the control buffer. A549 cells were fractionated for mitochondria, using Tom 22-mediated immunomagnetic bead positive selection followed by counting of mitochondrial fractions for γ activity, and finally^{68}Ga-Galuminox uptake was quantified. For Fluorescence imaging, images were acquired using a Nikon A1R scanning confocal microscope with a 20x objective utilizing a 405 nm laser line using NIS-Elements software. The cellular uptake of Galuminox was quantified and analyzed using Image J. Compared with vehicle-treated controls, ^{68}Ga-Galuminox shows 3-, 8-, and 12-fold higher accumulation in nutrient-deprived (starvation), LPS-, and Mitomycin C treated A549 cells. Compared to LPS-induced ROS, a much higher uptake of ^{68}Ga-Galuminox with a lower dose of mitomycin-C could be attributed to the presence of a higher density of functionally impaired mitochondria in the cytoplasm of cells due to the inhibition of mitophagy, a mechanism for shuttling of damaged mitochondria to lysosomes. Furthermore, ^{68}Ga-Galuminox shows 2.5-fold higher retention within mitochondria (obtained through Tom 22-mediated immunomagnetic bead positive selection) of LPS-treated A549 cells compared to buffer treated counterparts. The latter data show direct evidence of localization of ^{68}Ga-Galuminox within mitochondria following LPS-induced ROS in human lung epithelial A549 cells. Taken together, ^{68}Ga-Galuminox shows uptake profiles in A549 cells similar to those earlier reported in fluorescence bioassays indicating a good correlation between fluorescence and radiotracer bioassays.

Conclusion:
Following further biochemical validations in vivo, ^{68}Ga-Galuminox could provide a noninvasive imaging agent for interrogating ROS-mediated pathogenesis in diseased models.

Reference
1. Sivapackiam, J. et al., Redox Biol., 2020, 101690
2. Fox, G. C. et al., Mol. Cancer Ther. 2021, 20, 1183

Poster Presentation

Disclosures: The authors have disclosed no financial interest.

580-Synthesis and Biological Properties of No-Carrier-Added 4-Borono-2-18F-fluorophenylalanine (18F-FBPA) Compared with Carrier-Added 18F-FBPA

Presenter: Ting-Yu Chang, National Yang Ming Chiao Tung University

Ting-Yu Chang[1], Wen-Yi Chang[1], Wen-Hsiang Hong[2], Sie-Ong Lau[3], Chun-Yi Wu[4]

[1]*National Yang Ming Chiao Tung University, Taipei, Taiwan*
[2]*National Yang-Ming Chiao Tung University, Taipei, Taipei, Taiwan*
[3]*National Yang Ming Chiao Tung University, Taipei, Taipei, Taiwan*
[4]*National Yang Ming Chiao Tung University, Taipei, Taiwan, Taiwan*

Objective:
This study aims to develop a new method to produce no-carrier-added (NCA) 4-borono-2-^{18}F-fluoro-phenylalanine (^{18}F-FBPA). Regarding there is no study to compare the difference in biological characteristics between NCA and carrier-added (CA) ^{18}F-FBPA, we determined the effect of the amount of non-radioactive FBPA in the in vitro cellular uptake and in vivo imaging studies.

Methods:
Starting from 4-bromo-2-nitrobenzaldehyde, NCA ^{18}F-FBPA was prepared via radiofluorination, alkylation, borylation, and hydrolysis. Cellular uptake studies, microPET imaging, and biodistribution studies were conducted to characterize the biological properties of NCA and CA ^{18}F-FBPA.

Results:
The radiochemical yield of NCA ^{18}F-FBPA was 12±6 (decay corrected) with a radiochemical purity of >98% and specific activity of 56 MBq/nmol in a 100-min synthesis. The in vitro accumulation of NCA ^{18}F-FBPA was significantly higher than that of CA ^{18}F-FBPA in either SAS or CT-26 cells. The uptake of NCA ^{18}F-FBPA, as well as CA ^{18}F-FBPA, dramatically declined after the inhibition of the L-type amino acid transporter (LAT-1). However, there was no apparent difference in tumor uptake between NCA and CA ^{18}F-FBPA-injected tumor-bearing mice. The results obtained from biodistribution studies were in accordance with the findings derived from microPET imaging. The fraction of the intact NCA ^{18}F-FBPA in plasma and urine at 1-h post-injection was more than 90%, indicating its high in vivo stability.

Conclusion:
We successfully prepared NCA ^{18}F-FBPA via a new nucleophilic substitution route, having the potential to be automated, with an acceptable radiochemical yield and radiochemical purity. We also demonstrated that the high specific activity of NCA ^{18}F-FBPA resulted in higher cellular uptakes but equivalent in vivo tumor accumulation with CA ^{18}F-FBPA

Poster Presentation

Disclosures: The authors have disclosed no financial interest.

581-Evaluation of PSMA-Targeted Squaraine Dye in a Murine Model of Prostate Cancer

Presenter: Yimin Chen, Beijing Normal University

Yimin Chen[1], Yuying Li[1], Xi Gao[2], Mengchao Cui[3]

[1]*Beijing Normal University, Beijing, Beijing, China*
[2]*Beijing Normal University, China*
[3]*Beijing Normal University, Beijing, China, China*

Objectives:
Prostate cancer (PCa) is the most common cancer-related malignancy in older men worldwide, with a high mortality rate[1]. To solve the problems of positive margins and other complications during radical prostatectomy, it is necessary to develop suitable optical imaging probes to distinguish tumor from normal tissue during surgery. Prostate-specific membrane antigen (PSMA) is a membrane-bound glutamate carboxypeptidase II overexpressed in PCa[2 3]. In this study, two Glu-Ureido-Lys pharmacophores with high affinity to PSMA were conjugated to the squaraine fluorophore for *in vivo* imaging and intraoperative guidance in tumor-bearing mice.

Methods:
The PSMA-targeted squaraine dye **SQ-CN-PSMA** was synthesized by a simple and effective condensation reaction between the fluorophore and two Glu-Ureido-Lys pharmacophores (Figure 1C). The binding constants (K_i) of **SQ-CN-PSMA** to PSMA was determined by a fluorescence-based NAALADase assay. *In vivo* optical imaging was investigated in mice bearing subcutaneous 22Rv1 tumor xenograft after injection of **SQ-CN-PSMA** (2 nmol) with or without DCFPyL (2 μmol) inhibition at different time points.

Results:
The excitation and emission spectra of **SQ-CN-PSMA** showed suitable optical properties for *in vivo* imaging. A competitive binding assay revealed high binding affinities towards PSMA ($K_i = 0.34 \pm 0.17$ nM). At 4 h postinjection, the tumor was clearly distinguished from surrounding tissue with good contrast (TNR = 3.28 ± 0.66, Figure 1A and B), and high image quality was maintained in the subsequent time with a higher TNR value (11.08 ±1.59 for 24 h, Figure 1B). In addition, the *in vivo* blocking experiment well proved that **SQ-CN-PSMA** is a specific ligand for PSMA (Figure 1A and B).

Conclusions:
We successfully synthesized a novel PSMA-targeted squaraine dye, **SQ-CN-PSMA**, which displayed excellent optical and biological properties toward PSMA.

Corresponding Author: *Tel/Fax: +86-13811995064. E-mail: cmc@bnu.edu.cn

Acknowledgment: This work was funded by the National Natural Science Foundation of China (No. 22022601 and U1967221)

Reference
1. R. L. Siegel, K. D. Miller, H. E. Fuchs and A. Jemal, CA: A Cancer Journal for Clinicians, 2022, 72, 7-33.
2. D. S. O'Keefe, S. L. Su, D. J. Bacich, Y. Horiguchi, Y. Luo, C. T. Powell, D. Zandvliet, P. J. Russell, P. L. Molloy, N. J. Nowak, T. B. Shows, C. Mullins, R. A. Vonder Haar, W. R. Fair and W. D. W. Heston, Biochimica et Biophysica Acta (BBA) - Gene Structure and Expression, 1998, 1443, 113-127.
3. W. Wang, F. Tavora, R. Sharma, M. Eisenberger and G. J. Netto, Urol Oncol, 2009, 27, 525-528.

Poster Presentation

Disclosures: The authors have disclosed no financial interest.

582-Informatics Structures for Quantitative Co-clinical Imaging

Presenter: Paul Kinahan, University of Washington
Andrey Fedorov[1], Robert Miyaoka[2], Mark Muzi[2], Delphine Chen[3], Christina Baik[2], Adrienne Lehnert[2], A. McGarry Houghton[4], **Paul E. Kinahan[2]**

[1]*Harvard Medical School, Boston, Mass.*
[2]*University of Washington, Seattle, WA*

[3]*University of Washington, Seattle, Washington*
[4]*Fred Hutchinson Cancer Research Center, Seattle, WA*

Purpose:
Although immune checkpoint inhibitor (ICI) therapy has been a tremendous clinical benefit for some NSCLC patients, only ~20% of NSCLC patients respond to anti-PD1/PDL1 therapy. Using PET co-clinical imaging to improve ICI therapies for NSCLC is challenged in part by a lack of informatics structures that enable the collection, analysis, and sharing of quantitative pre-clinical and clinical PET imaging data. We are developing methods that allow sharing data and resources on co-clinical trials by extending the DICOM standard for pre-clinical small animal imaging with DICOM-compliant structures that provide necessary quantitative meta-data

Methods:
We are leveraging methods recently developed for standardized representations using the nearly universal Digital Imaging and Communications in Medicine (DICOM) standard. DICOM is a comprehensive standard that contains metadata identifying and relating individual objects, and follows a common data model. Thus, unlike other image formats that may be more convenient for a specific research task, DICOM allows for interoperability between image analysis tools and reusability of analysis results for other purposes, i.e., in accordance with the FAIR (Findable, Accessible, Interoperable, Reusable) principles [1,2].
While DICOM is well-known as a means of transferring and storing medical images, it also supports collecting information about images. This has the key benefit that additional meta-information about images (needed for quantitative analysis) can be stored in a DICOM database long with the images using a variety of DICOM objects. These include SEG: DICOM Segmentation object for ROI definition and labeling of anatomical structures, such as primary tumor or liver. SR: DICOM Structed Report for tracking clinical and quantitative data. RWVM: DICOM Real-World Value Mapping objects encode mapping of the image-specific SUV factor that is needed for normalization of the images and subsequent processing. These objects can also be updated or extended as needed to capture data from additional image analyses. The use of DICOM objects combined with the Healthcare API implemented in Google Cloud Platform also facilitates the creation of DataStudio dashboards that provide interactive real-time information on available images and their associated meta-data. Such dashboards have been created for the NCI Imaging Data Commons and the Medical Imaging and Data Resource Center (MIDRC).
We have implemented a first step with DICOM objects that can be modified for use with preclinical images to correctly capture and transfer quantitative information in a tracible manner. Initial results are with DICOM RT Structure Sets (RT STRUCT) for region of interest (ROI) definition and evaluation.

Results:
An RT STRUCT object defined on a commercial MiM platform was used to define an ROI for an FDG-avid region of a lung tumor evident in the PET image of a WT mouse. From this the image mean and max. values, volume etc. were calculated. The RT STRUCT object was transferred to two open source DICOM analysis platforms: Horus and 3Dslicer and the image values were successfully re-computed. However, our preliminary results indicate that DICOM images from preclinical PET scanners do not always contain the needed (or correct) information for quantitative imaging. Suggested guidelines on the use of PDX models in preclinical research list over 40 metadata fields that should be captured and tracked to support research results, which we are in the process of adding.

Conclusions:
The use of the DICOM objects as informatics structures for co-clinical imaging enables collecting necessary information about the images. This information can be stored in DICOM systems, taking advantage of a broadly implemented and actively supported standard. In addition, the use of DICOM supports the open-source data dashboards, of which there are now several instances for both clinical and pre-clinical collections.

Reference
1. Wilkinson MD et al. The FAIR Guiding Principles for scientific data management and stewardship. Sci Data. 2016;3:160018. PMCID: PMC4792175. PMID: 26978244.
2. A. Fedorov et al., “Quantitative Imaging Informatics for Cancer Research.,” JCO Clinical Cancer Informatics, vol. 4, pp. 444–453, 2020, doi: 10.1200/cci.19.00165.

Poster Presentation

Disclosures: The authors have disclosed no financial interest.

583-Total-Body Preclinical PET Imaging using Gapless DOI Detectors

Presenter: Tiantian Li, University of California, Davis

Xuezhu Zhang[1], **Tiantian Li[2]**, Qian Wang[3], Simon R. Cherry[1], Junwei Du[4], Jinyi Qi[1]

[1]*University of California, Davis, Davis, CA*
[2]*University of California, Davis*
[3]*University of California, Davis, Davis, California*
[4]*University of California, Davis, Davis*

PET scanners with depth-of-interaction (DOI) detectors can achieve high uniform spatial resolution across the field-of-view (FOV). We have previously developed a detector based on a gapless curved scintillator array to reduce the dead space between detector modules and hence improve the photon detection sensitivity [1]. It can measure the DOI for high-resolution imaging using SiPM arrays coupled to both ends of scintillator arrays with finely segmented and long scintillator elements. Here we propose a total-body (TB) preclinical PET scanner that uses gapless curved LYSO arrays for both high-resolution and high-sensitivity imaging. In this work, we perform simulation and image reconstruction study of the small-animal TB-DOI PET. The system has an inner ring diameter of 16 cm and an axial FOV of 25 cm. It consists of 16 detector blocks transaxially and 8 block rings axially with each module consisting of a curved shape 30 × 30 LYSO crystal array with a pitch size of 1.05 × 1.06 (transaxial × axial) mm^2 at the front and 1.44 × 1.06 mm^2 at the back, and a crystal thickness of 30 mm. There is no gap or dead space in-between blocks transaxially and axially except the 50 μm Toray reflector and 10 μm optical grease. We modeled the gapless scanner in SimSET using the cylindrical PET configuration. The DOI resolution was modeled by blurring the photon detection position with a Gaussian function of 2.5 mm FWHM and discretized into 12 DOI bins with a bin width of 2.5 mm. A list-mode image reconstruction was developed to take advantage of the statistical and physical models of the long axial PET [2]. The system response was modeled in the image-domain using a spatially variant point spread function (PSF) model, which was obtained by simulating and reconstructing point source scans in the center transaxial plane and along the axial axis. The resolution models were decoupled into separable

transaxial and aixal PSF kernels for image reconstruction. A uniform cylinder source covering the whole FOV was simulated to calculate the normalization factors for quantitative image reconstruction. The proposed TB-DOI scanner forms more than 500 billion LORs. To reduce the storage size and increase the statistics of the normalization factor in each individual LOR, we took advantage of the geometric symmetry of the scanner and calculated a compressed 4D normalization sinogram (shown in Table 1 & 2), with a size less than 20 MB. We performed a series of simulations using various phantoms including a cylinder source, point sources, and MOBY (mouse whole-body phantom) to evaluate the performance of the proposed scanner. The image reconstructions of the simulated data with and without DOI were compared. The results show that the image resolution was greatly improved by the DOI information and the incorporation of the PSF can further improve the image quality. It demonstrates the benefits of using both DOI and the PSF model. In conclusion, we proposed a high-resolution and high-sensitivity total-body preclinical PET scanner using gapless curved crystals and DOI capable detectors. We developed the image reconstruction method to achieve high-resolution quantitative imaging. The reconstruction method can be extended to other systems with DOI. We will conduct more phantom studies for the evaluation and optimization of the proposed scanner.

Reference

1. Du J, et al. "Design and evaluation of gapless curved scintillator arrays for simultaneous high-resolution and high-sensitivity brain PET". Phys Med Biol 2019
2. Zhang X, et al. "Quantitative image reconstruction for total-body PET imaging using the 2-meter long EXPLORER scanner". Phys. Med. Biol. 2017

Poster Presentation

Disclosures: The authors have disclosed no financial interest.

584-3D MRSI using co-polarized HP [1-13C]pyruvate and [1-13C] dehydroascorbate reveals differences in compartmentalized metabolism in the murine brain

Presenter: Paola Porcari, Memorial Sloan Kettering Cancer Center

Paola Porcari[1], Saket Patel[2], Marjan Berishaj[1], Elizabeth Coffee[1], Kofi Deh[1], Nathaniel Kim[3], Kayvan Keshari[1]

[1]*Memorial Sloan Kettering Cancer Center, New York, NY*
[2]*Memorial Sloan Kettering Cancer Center*
[3]*Memorial Sloan Kettering Cancer Center, New York*

Introduction:
In this study, we investigated whether co-hyperpolarized [1-^{13}C]pyruvate and [1-^{13}C]dehydroascorbate (DHA) along with 3D Magnetic Resonance Spectroscopic Imaging (MRSI)[1-4] might be a useful method to evaluate differences in compartmentalized metabolism in mouse brain. Two brain regions were investigated, the thalamus (THA, gray matter) and the corpus callosum (CC, white matter), with the goal to evaluate the feasibility of the method and assess potential metabolic differences.

Methods:
Female C57Bl/6J mice (Harlan Laboratories, Indianapolis, IN, USA) aged 22 weeks (n=3, 22-25g) were used in this study. Animal procedures were performed in accordance with MSK Institutional Animal care guidelines. Following tail vein cannulation, each mouse was injected over 10s with 200µL of co-hyperpolarized 40 mM [1-^{13}C] DHA and 100 mM [1-^{13}C]pyruvate. Both substrates were co-hyperpolarized for two hours (150µL of a 40:60 v/v mixture of monomeric [1-^{13}C]DHA and [1-^{13}C]pyruvate containing 15 mM AH111501 trityl radical) through the SpinLab polarizer (GE Healthcare) and dissolved in 13 ml D_2O. After dissolution, the sample was collected in a flask containing an equimolar amount of sodium acetate to neutralize the pyruvic acid. MR experiments were performed using a 3T MRI system (Bruker, Billerica, MA) equipped with a 40 mm inner-diameter, quadrature double-tuned ^{1}H/^{13}C volume coil. The MRI protocol included a T2-weighted fast spin-echo (FSE) sequence for anatomical reference and a multi-slice ^{13}C 2D-Echo-Planar-Spectroscopic-Imaging (EPSI) sequence (TR/TE = 900/3.5 ms, 32 x 32 mm^2 of field-of-view, 6 slices of 3.5mm thickness), which is run 25s after the substrate injection simultaneously with the effect of the substrate in the brain. Both sequences were repeated for the reference scan (6M ^{13}C-urea phantom). Spectroscopic data were analyzed using a custom Matlab script while metabolic maps were calculated using SIVIC[5]. A region-of-interest (ROI)-based analysis was performed to evaluate differences between gray (Thalamus, THA) and white matter (Corpus Callosum, CC). Statistical analysis was performed using GraphPad Prism (version 9.1.1).

Results:
Figure 1 shows the coronal (**A**), axial (**B**) and sagittal (**C**) views of a mouse brain (upper panel) with the corresponding spectra acquired in each voxel of the brain (lower panel). A representative spectrum from a voxel of the overlayed grid on the brain showing the main metabolites is reported in **figure 1D**. The overlay of representative metabolite maps (**Figure 2**), pyruvate (**A**, upper panel) and lactate (**A**, lower panel), and DHA (**B**, upper panel) and Vitamin C (**B**, lower panel), on the anatomical proton image demonstrates differential lactate and vitamin C generation, respectively. The comparison of the hyperpolarized metabolites between two different regions of the brain (**Figure 3B-C**, **3E-F**), thalamus (THA - gray matter) and corpus callosum (CC – white matter), show statistically significant differences in pyruvate and DHA levels in the two brain regions (n=3, $P<0.05$) (**Figure 3B,E**). Moreover, the Lactate / Pyruvate and Vitamin C / DHA ratios were determined in both brain regions (**Figure 3D,G**), showing differential metabolism in these compartments, suggesting redox mediated differences.

Conclusion:
Our findings show the feasibility and sensitivity of this novel methodology to reveal differences in the compartmentalized metabolism of murine brain. We observed significant differences in pyruvate and DHA in the thalamus and corpus callosum. Given that generation of hyperpolarized lactate is mediated by NAD^+-dependent metabolism and vitamin C by NADPH, this work suggests differential redox compartmentalization in these regions of the murine brain. This is a first step to better understand the metabolic pathways in the mouse brain with the prospect to extend the investigation through neurological and oncological pathologies with a future possible translation into humans.

Reference

1. Keshari, K. R., Kurhanewicz, J., Bok, R., Larson, P. E. Z., Vigneron, D. B., Wilson, D. M. (2011). Hyperpolarized 13C dehydroascorbate as an endogenous redox sensor for in vivo metabolic imaging. PNAS, 150(46), 18606-18611.
2. Bohndiek, S. E., Kettunen, M. I., Hu, D., Kennedy, B. W. C., Boren, J., Gallagher, F. A., Brindle, K. M. (2011). Hyperpolarized [1-13C]-ascorbic and dehydroascorbic acid: vitamin C as a probe for imaging redox status in vivo. JACS, 133(30), 11795-11801.
3. Timm, K. N., Hu, D., Williams, M., Wright, A. J., Kettunen, M. I., Kennedy, B. W. C., Larkin, T. J., Dzien, P., Marco-Rius, I., Bohndiek, S. E., Brindle, K. M. (2017). Assessing oxidative stress in tumors by measuring the rate of hyperpolarized [1-13]

dehydroascorbic acid reduction using 13C magnetic resonance spectroscopy. Journal of Biological Chemistry, 292(5), 1737-1748.
4. Qin, H., Carroll, V. N., Sriram, R., Villanueva-Meyer, J. E., von Morze, C., Wang, Z. J., Mutch, C. A., Keshari, K. R., Flavell, R. R., Kurhanewicz, J., Wilson, D. M. (2018). Imaging glutathione depletion in the rat brain using ascorbate-derived hyperpolarized MR and PET probes. Scientific Reports, 8, 7928.
5. Crane, J. C., Olson M. P., Nelson S. J. (2013). SIVIC: Open-Source, Standards-Based Software for DICOM MR Spectroscopy Workflows. Int J. Biomed Imaging, 2013: 169526

Poster Presentation

Disclosures: The authors would like to disclose that HP pyruvate is an investigational device.

585-In vivo fluorescence and photodynamic activation of a novel, receptor-independent porphyrin-lipid nanoparticle

Presenter: Tiffany Ho, University of Toronto
Tiffany Ho[1], Lili Ding[2], Juan Chen[3], Jiachuan Bu[4], Gang Zheng[5]

[1]University of Toronto, Toronto
[2]University Health Network, Toronto
[3]University Health Network, Toronto, ON
[4]University Health Network, Toronto, Ontario
[5]Princess Margaret Cancer Centre, Toronto, Ontario

Photodynamic therapy (PDT) involves the combination of non-toxic photosensitizers and light, which in the presence of oxygen allows for the generation of reactive oxygen species (ROS) for cell and tissue destruction. PDT is an attractive cancer treatment modality as light can be spatially focused to the tumour area, which can also confine the photosensitizer activation to the tumour region. This allows for local tumour ablation while sparing the surrounding healthy tissue. Porphysomes (PS) are composed of porphyrin-lipid building blocks (>80 000 porphyrins per particle) that self-assemble into liposome-like nanoparticles [1]. The high density of porphyrin photosensitizers within the PS structure makes them great nano-agents for fluorescence imaging applications and photonic-based therapies [1]. However, compared to conventional nanoparticle receptor-targeting strategies, conventional (non-targeting) PS formulations appear to have limited PDT application due to its poor cellular uptake in cancer cells [2-3]. Ethylenediaminetetraacetic acid (EDTA) is considered an absorption enhancer and has been reported to promote the penetration of various agents through the epithelium of various tissues [4-6]. It has also been reported to interact with and induce the fluidization and temporary permeability of lipid membranes [7], which may offer a novel strategy to improve nanoparticle cell uptake and therapeutic efficiency. We have recently developed a new generation of PS nanoparticles (NPS) which utilize an EDTA-nanoparticle mediated strategy as a novel approach for enhancing nanoparticle accumulation within cancer cells and to overcome the current PDT limitations of PS. We found that NPS was able to significantly enhance the intracellular accumulation of PS in KB cervical cancer cells after 6 hours of incubation, with significant *in vitro* PDT efficacy occurring as early as 3 hours post-incubation. Herein, we report our evaluation of the *in vivo* tumour fluorescence activation, biodistribution, and PDT efficacy of NPS compared to PS in subcutaneous KB-tumour bearing mice. NPS showed rapid tumour accumulation and fluorescence activation as early as 1-hour post-injection compared to PS where tumour fluorescence was observable after 6 hours post-injection. Maximal *in vivo* tumour fluorescence activation for both NPS and PS was observed at 24 hours post-injection. The results of a biodistribution study suggested that the maximal tumour accumulation of NPS and PS occur at 3-hour post-injection. *In vivo* tumour fluorescence imaging in a hamster-cheek carcinogenesis model also demonstrated rapid NPS tumour-specific fluorescence activation as early as 15 minutes post-systemic administration, which was sustained up to 24 hours, while PS demonstrated much weaker tumour fluorescence at all timepoints. The unquenching of intact NPS and PS into their monomeric porphyrin-lipid components enable fluorescence imaging and ROS generation upon laser irradiation for PDT applications; therefore, our results encourage further investigation into the *in vivo* PDT efficacy of NPS compared to PS at drug-light-intervals less than 24 hours, where differences in the fluorescence activation of NPS and PS appear to be the most prominent. An *in vivo* PDT efficacy study suggested that NPS possessed higher PDT efficacy with a short 3-hour drug-light-interval compared to PS, where a higher rate of tumour ablation and mouse survival was observed in mice that received NPS compared to PS. This work aims to introduce our novel NPS nanosystem, which utilizes a novel EDTA-nanoparticle mediated strategy to improve the uptake of porphysomes in cancer cells as a promising agent for PDT applications in cancer treatment. Our work also encourages future investigations into determining the potential generalizability of this EDTA-nanoparticle mediated strategy to improve other nanomedicine formulations that possess similar limitations.

Reference

1. J. F. Lovell, S. Jin, E. Huynh, H. Jin, C. Kim, J. L. Rubinstein, W. C. Chan, W. Cao, L. V. Wang and G. Zheng, "Porphysome nanovesicles generated by porphyrin bilayers for use as multimodal biophotonic contrast agents," Nature Materials, vol. 10, pp. 324-332, 2011.
2. C. S. Jin, L. Cui, F. Wang, J. Chen and G. Zheng, "Targeting-triggered porphysome nanostructure disruption for activatable photodynamic therapy," Adv Healthc Mater, vol. 3, no. 8, pp. 1240-9, 2014.
3. K. K. Ng, M. Takada, C. S. Jin and G. Zheng, "Self-Sensing Porphysomes for Fluorescence-Guided Photothermal Therapy," Bioconjugate Chem, vol. 26, no. 2, pp. 345-351, 2015.
4. P. W. Morrison and V. V. Khutoryanskiy, "Enhancement in corneal permeability of riboflavin using calcium sequestering compounds," Int J Pharm, vol. 472, no. 1-2, pp. 56-64, 2013.
5. Z. Jassim and E. Jasim, "A review on strategies for improving nasal drug delivery systems," Drug Invention Today, vol. 10, no. 1, pp. 2857-2864, 2018.
6. Q. Yu, Z. Wang, P. Li and Q. Yang, "The effect of various absorption enhancers on tight junction in human intestinal Caco-2 cell line," Drug Dev Ind Pharm, vol. 39, no. 4, pp. 587-597, 2013.

Poster Presentation

Disclosures: The authors have disclosed no financial interest.

586-Infusion of zinc-sensitive agents for imaging β-cell function does not alter glucose stimulated insulin secretion

Presenter: A. Dean Sherry, Advanced Imaging Research Center

Eul hyun Suh[1], Sara Chirayil[2], **A. Dean Sherry[3]**

[1]University of Texas Southwestern Medical Center, Dalls
[2]University of Texas Southwestern Medical Center, Dallas, Texas
[3]Advanced Imaging Research Center, Dallas, TX

Glucose-stimulated insulin secretion (GSIS) from pancreatic β-cells plays a crucial role in regulation of blood glucose levels.[1] Recent studies have shown that not all pancreatic islets respond equally to an increase in blood glucose[2] and, even within an individual islet, not all β-cells release insulin simultaneously.[3] We have previously demonstrated that glucose stimulated zinc secretion (GSZS) can be detected as "hot spots" in the tail of rat pancreas *in vivo* and that not all islets respond equally to an increase in plasma glucose.[4,5] This imaging method offers the opportunity to monitor individual islet function in pancreas during progression of type 2 diabetes and may prove useful in evaluating new drugs providing that the method can be shown to be completely non-invasive. In an *in vivo* imaging study of non-human primates,[5] a different high affinity Zn^{2+}-responsive MRI agent was infused continuously, and blood insulin and C-peptide levels were found to be higher during infusion of the Zn^{2+}-binding agent compared to a control agent. This suggests the agent itself may have an impact on release of insulin. In the current study, two different gadolinium-based zinc-responsive agents, one with higher (GdL_1) and another with lower affinity (GdL_2) for Zn^{2+} ions,[4] were compared to evaluate the potential impact of these agents on insulin secretion. We have previously reported that both GdL_1 and GdL_2 can detect Zn^{2+} secretion from β-cells in the pancreas tail (Figure 1). In different groups of animals, GdL_1 or GdL_2 were infused with glucose at a rate of 22.5 mL/min over 30 min. A cocktail of glucose (2.75 mmol/kg) plus either GdL_1 or GdL_2 (0.01 mmol/kg) was infused into a jugular vein in anesthetized rats (Sprague Dawley, 300~350 g). Blood samples were collected at time 0, 5, 15, 30 min during infusion *via* a tail vein, and analyzed for glucose, insulin, and Zn^{2+} at each time point. The blood glucose level (mg/dL) was quantified using a glucose meter, insulin (μU/mL) was measured using commercially available kits, and Zn was m^{2+} measured by inductively coupled plasma mass spectrometry (ICP-MS). Plasma glucose levels increased gradually from ~100 mg/dL to ~350 mg/dL during infusion of either GdL_1 and GdL_2. As expected, insulin also increased from ~4 to ~ 60 μU/mL in parallel with plasma glucose in both studies while plasma Zn^{2+} did not increase significantly in either group. In conclusion, both higher (GdL_1) and lower affinity (GdL_2) Zn^{2+}-responsive MRI agents successfully detect the β-cell function *in vivo* while our preliminary findings indicate there were no differences in plasma insulin or Zn^{2+} levels after continuous infusion of either agent. Further experiments are underway to compare the ability of the two agents to differentiate first responder islets from all islets.

References

1. Harcourt, B.E., et al., Coming full circle in diabetes mellitus: from complications to initiation. Nat Rev Endocrinol 9,113-123 (2013).
2. Salem V, et al. Leader β-Cells Coordinate Ca2+ Dynamics Across Pancreatic Islets In Vivo. Nat Metabol. (2019) 1:615–29.
3. Benninger RKP, et al., The Physiological Role of b-Cell Heterogeneity in Pancreatic Islet Function. Nat Rev Endocrinol (2022) 18:9–22.
4. Thapa, B., et al. Imaging β-Cell Function Using a Zinc-Responsive MRI Contrast Agent May Identify First Responder Islets. Frontiers in Endocrinology 12 (2022).
5. Clavijo Jordan, V., et al. Imaging Beta-Cell Function in the Pancreas of Non-Human Primates Using a Zinc-Sensitive MRI Contrast Agent. Frontiers in Endocrinology 12 (2021).
6. Martins, A.F., et al. Imaging Insulin Secretion from Mouse Pancreas by MRI Is Improved by Use of a Zinc-Responsive MRI Sensor with Lower Affinity for Zn2+ Ions. J Am Chem Soc 140, 17456-17464 (2018).

Poster Presentation

Disclosures: The authors have disclosed no financial interest.

587-99mTc- DMSA renal cortical scintigraphy: Direct comparison of planar, SPECT and SPECT/CT imaging in the detection of renal cortical defects.

Presenter: Nsreen RA Mohamadien, Assiut University

Nsreen RA Mohamadien[1], Mohamed A Mekkaway[2], Marwa S Mohamed[2], Waleed A Diab[2]

[1]*Assiut University, Egypt*

[2]*Assiut University, Assiut, Egypt*

Background:

Planar scintigraphy using ^{99m}Tc-dimercaptosuccinic acid (DMSA) is the best tool for assessing renal scarring, particularly in youngsters, but the utility of single-photon emission computed tomography/computed tomography (SPECT/CT) is not well established.

Aim:

The aim of the current study was to compare the value of planar, SPECT, and SPECT/CT imaging using ^{99m}Tc-DMSA in the detection of renal cortical scarring.

Patients and Methods:

In this prospective trial, patients with clinically suspected renal cortical abnormalities were included. Planar images of ^{99m}Tc-DMSA were taken approximately 3 hours after intravenous injection of 185 MBq of the tracer. After the planar scans, SPECT/CT images were taken. The images were analyzed by a trained nuclear medicine physician who was blinded to both clinical data and other imaging results. Each image set was scored as 0; no detectable defects, 1; single defect, 2; multiple defects, and finally the results of each modality were compared against each other.

Results:

A total of 186 kidneys from ninety-three patients were recruited in this study (55 males and 38 females, mean age: 31.9 $\pm$ 18.5 years). On lesion based analysis, planar images revealed 5 single and 7 multiple defects, SPECT images revealed 17 single and 40 multiple defects while SPECT/CT images revealed 5 single and 11 multiple defects. Planar and SPECT images agreed in the reading of 131 kidneys and disagreed in the readings of 55 ones ($P < .01$). Planar and SPECT/CT images agreed in the reading of 152 kidneys and disagreed in the readings of 34 ones ($P < .01$). Out of the 17 single defects detected by SPECT imaging only 5 were proved to be scar in the SPECT/CT images and the remaining 12 lesions were corresponding to a solitary cortical cyst in the CT images. Only 11/40 cases with positive multiple defects in the SPECT imaging were proved to be scar in SPECT/CT images and the remaining lesions were corresponding to either multiple cortical cysts or hydro-nephrotic changes. Four kidneys with multiple defects in the SPECT/CT images were found to be normal in planar readings and this was attributed to increased renal background activity and decreased renal function.

Conclusion:

In patients with suspected renal cortical scarring, ^{99m}Tc- DMSA SPECT/CT imaging was superior to both planar and SPECT imaging as it decreased the number of false-positive readings of SPECT and the false-negative readings of the planar method.

Keywords: ^{99m}Tc- DMSA, Planar, SPECT/CT, Cortical defects, Renal.

Poster Presentation

Disclosures: The authors have disclosed no financial interest.

588-Elucidating Organelle Compartmentation of Breast Cancer Metabolism to Understand Whole-Tumor PET Data

Presenter: Christopher Hensley, University of Pennsylvania Health System

Christopher T. Hensley[1], Prashanth Padakanti[2], Christina Dulal[2], Hoon Choi[2], Austin Pantel[3], Hsiaoju S. Lee[4], David Mankoff[2], Rong Zhou[2]

[1]*University of Pennsylvania Health System*
[2]*University of Pennsylvania, Philadelphia, PA*
[3]*Hospital of the University of Pennsylvania, Philadelphia, PE*
[4]*University of Pennsylvania, Philadelphia, Pennsylvania*

Introduction:
FDG is widely used for imaging glucose metabolism in cancer. Glutamine metabolism is altered in tumors with comparable importance to glucose metabolism. A subset of cancers demonstrate glutamine "addiction," presenting a possible tumor-specific target. CB-839 is an inhibitor of the first step in glutamine catabolism which involves the enzyme glutaminase (GLS). The use of CB-839 in combination with taxol chemotherapy was furthered to phase II clinical trials in triple negative breast cancer (TNBC) without limiting toxicity. However, efficacy was highly variable, obviating the need for a biomarker of response. A more mechanistic understanding of glutamine "addiction" would improve the design of molecular imaging agents. Glutamine metabolism involves both redox pathways in the cytosol and anaplerotic pathways in the mitochondria. Kinetic analyses have been performed on positron emission tomography (PET) metabolite analogs, specifically glutamine analogs (2S,4R)-4-[18F]fluoroglutamine ([18F]4F-Gln) and [5-11C] glutamine, as well as glutamate analog (4S)-4-(3-[18F] fluoropropyl)-L-glutamate ([18F]4F-FSPG). These kinetic analyses support the hypothesis that glutamate arising from mitochondrial glutamine metabolism is stored in mitochondrial pools as a "buffer" to mediate oxidative stress from proliferation or chemotherapies that induce oxidative stress like paclitaxel. We propose that analyzing the subcellular distributions of [18F]4F-Gln, FSPG, 13C glutamine and 13C glutamate both in vitro and in vivo will confirm this mitochondrial glutamate pool hypothesis (Lee et al., 2019).

Methods and Materials:
To further assess glutamine metabolism compartmentation, we are developing and testing an expansion of the modeling approach used for non-metabolized [18F]4F-Gln by performing kinetic analysis of administered [5-11C] glutamine and downstream metabolites ([5-11C] glutamate and [11C] CO2). This analysis will guide the design and interpretation of experiments utilizing a preclinical model of breast cancer used by our group to model [18F]4F-Gln PET tracer data. Subcellular isolation protocols will be employed to compare cytosolic and mitochondrial 13C and PET glutamine and glutamate pools, with and without CB-839, in vitro, with validation experiments in flank xenograft tumors in vivo.

Results:
[5-11C] glutamine kinetic modeling has been conducted to further support a two-compartment model of glutamine metabolism (Figure 2B). The isolation method has been validated by western blot analysis of the subcellular fractions. Conclusions: Analysis of subcellular metabolic compartmentation in both modeling and experimentation can provide underlying mechanistic insight into whole tumor tracer data.

Clinical Relevance/Application:

If successful, this project will improve translational efforts in developing and interpreting the results of PET tracers of glutamine metabolism as biomarkers of treatment response in TNBC.

Reference

1. Yang, Chendong, et al. "Glutamine oxidation maintains the TCA cycle and cell survival during impaired mitochondrial pyruvate transport." Molecular cell 56.3 (2014): 414-424.
2. Lee, Hsiaoju S et al. "A PET Glutamate Analogue to Measure Cancer Cell Redox State and Oxidative Stress: Promise and Paradox." Cancer research vol. 79,4 (2019): 701-703. doi:10.1158/0008-5472.CAN-18-4034.
3. Viswanath, Varsha et al. "Kinetic Modeling of 18F-(2S,4R)4-Fluoroglutamine in Mouse Models of Breast Cancer to Estimate Glutamine Pool Size as an Indicator of Tumor Glutamine Metabolism." Journal of nuclear medicine: official publication, Society of Nuclear Medicine vol. 62,8 (2021): 1154-1162. doi:10.2967/jnumed.120.250977.

Poster Presentation

Disclosures: The authors have disclosed no financial interest.

589-Fifth metatarsal morphological variation to customize screw sizing prior to operative care of Zone II, Jones fracture

Presenter: Luis Diego Luna Centeno, Keck School of Medicine of USC

Luis Diego Luna Centeno[1], Tea Jashashvili[2]

[1]*Keck School of Medicine of USC*
[2]*Keck School of Medicine of USC, Los Angeles, CA*

Metatarsal fractures are common injuries among athletes, of which the fifth metatarsal (MT5) is the most commonly injured bone[1]. Zone II (Jones) fractures are located at the proximal metaphyseal-diaphyseal junction of MT5. They account for significant morbidity and high delayed union, nonunion and refracture rates in general, as well as long term impediments in function[2]. Operative management, primarily percutaneous intramedullary screw fixation, is the treatment of choice, especially in professional athletic populations, due to lower failure rates and faster return to function, resulting in minimal deconditioning[3,4]. Nonunion of Zone II fractures is mostly related to poor vascularization. In addition, variations in fifth metatarsal medullary canal diameter, bone length, apical height, and angle of curvature pose challenges to successful selection of intramedullary screw for fixation of Zone II fractures[5]. Due to complexity in regional anatomy of the Zone II area of MT5 the selection of surgical screws based on size is essential for optimal healing and maximal return of functionality. Anatomical variations of MT5 have similarly been shown to affect functionality after intramedullary screw fixation[6]. Previous research confirmed that differences in morphology determined by 2D radiographic measurements have been significantly correlated with patient-reported physical function scores[6]. The main goal of the present study is to use 3D morphometric measurements for optimal preoperative screw sizing and screw placement during percutaneous fixation of Zone II fractures. Variation for each measurement in different populations will be assessed and compared to previously published radiographic and CT measurements[6,7]. If our results demonstrate large variation for each measurement, a protocol

that could describe individual measurements of 3D renderings of MT5 will be proposed. Additionally, this protocol will allow customization of screw sizing prior to operative care of Zone II fractures. Coefficient of variation (CV) as a measure of relative variability is used to assess the morphological variation of MT5 (Fig.1). The study sample (n~300) consists of diverse archeological [e.g.,8,9] and recent [e.g.,10,11] materials from geographically diverse human populations. Micro-CT, and CT images were acquired to generate 3D surface renderings, which were then measured using Amira 3D 2021.2 and VGSTUDIO Max 2022.1 software (Fig.1). The data were analyzed using JMP Pro 16 (2021 SAS, Inc.). Analysis of variance (ANOVA) was performed to evaluate the difference between groups with the Tukey-Kramer HSD post hoc test (α=0.05). Here, we report preliminary results from three different geographic populations. Results show that CV for lateral curvature height (LCH) and medullary width (MW) were large in all studied groups (i.e., 40.77 (27.82), 52.49 (17.44), and 53.50 (38.27) for LCH (MW), respectively), while CV for the angle of tilt (AT) from the major axis of MT5 for each respective populations was small (1.05, 0.4, and 1.3). ANOVA showed the statistically significant result for AT (p=.028) and MW had a non-statistically significant, but expressed p-value of 0.051. Morphometric variation in MT5 is consistent with prior literature using 2D radiographic measurements[11]. Our results also differ from previous research[6,7], where MW had lower variation and no statistical significance between males and females studied[7]. Additionally, absolute values of our 3D measurements show differences from previously published 2D measurements[7], possibly related to the problem of plane of section of 3D structures. In this regard, our method delivers precise measurements for given morphology and illustrates the importance of acquiring individual measurements for screw sizing prior to operative management of Zone II fractures. The importance of individual measurements for positive surgical outcome is reinforced by the lack of significant correlation between most of the studied measurements.

Acknowledgments: We thank the IAS, Keck School of Medicine, University of Southern California. The Free Access Decedent Database is funded by the National Institute of Justice grant number **2016-DN-BX-0144**

Reference

1. Cakir, H. et al. Archives of Orthopaedic and Trauma Surgery 131, 241-245, (2011).
2. Bowes, J. & Buckley, RWorld J Orthop 7, 793-800, (2016).
3. Hunt, K. J. & Anderson, R. B. The American Journal of Sports Medicine 39, 1948-1954, (2011).
4. Le, M. & Anderson, R. Curr Rev Musculoskelet Med 10, 86-93, (2017).
5. Khurana, A. et al. Foot Ankle Int 41, 1537-1545, (2020).
6. Nayak, R., Barrett, J., Patel, M. S., Barbosa, M. P. & Kadakia, A. R. J Orthop Surg Res 16, 209-209, (2021).
7. DeSandis, B. et al. Foot & Ankle International 37, 528-536, (2016).
8. Cameron, M. E. & Pfeiffer, S. South African Journal of Science 110, 2013-0369 (2014).
9. L'Abbé, E. N., Coetzee, F. P. & Loots, M. A. The South African Archaeological Bulletin 63, 28-36, (2008).
10. Dayal, M. R., Kegley, A. D. T., Štrkalj, G., Bidmos, M. A. & Kuykendall, K. L. American Journal of Physical Anthropology 140, 324-335, (2009).
11. Edgar, H. J. H. et al. (University of New Mexico, 2020).

Poster Presentation

Disclosures: The authors have disclosed no financial interest.

590-The application of [123I]NaI as a surrogate radiopharmaceutical for the pre-therapeutic dosimetry in differentiated thyroid cancer with [131I]NaI: A preclinical study using the xenograft model mouse

Presenter: Su Bin Kim, Seoul National University

Su Bin Kim[1], Hye Won Kim[1], In Ho Song[2], Hyun Soo Park[3], Sang Eun Kim[2]

[1]*Seoul National University, Seoul, South Korea*
[2]*Seoul National University Bundang Hospital, Seongnam-si, Gyeonggi-do, South Korea*
[3]*Seoul National University Bundang Hospital, Seongnam, Gyeonggi-do, Republic of Korea*

The pre-therapeutic dosimetry with surrogate radiopharmaceuticals helps to maximize therapeutic responses for tumors while minimizing the possible hazard to healthy tissues in the targeted radionuclide therapy. The present study aimed to investigate the theranostic surrogacy of [^{123}I]NaI for [^{131}I]NaI in the differentiated thyroid cancer (DTC) using the xenograft model mouse in terms of the pharmacokinetics and absorbed dose estimates. We prepared a total of eight DTC subcutaneous xenograft mice bearing sodium-iodide symporter (NIS) expressing human thyroid carcinoma cells (K1-NIS cells). Those mice underwent sequential SPECT/CT scans at multiple time points according to the physical half-life of each radionuclide to fully elucidate the time course of the distribution including the elimination after the administration of [^{123}I]NaI and [^{131}I]NaI. Biodistribution and pharmacokinetics of each radiopharmaceutical in the tumor and various organs were examined using SPECT/CT images. And a Monte Carlo simulation using voxelized-source (SPECT) and -phantom (CT) was performed for radiation transportation and the electromagnetic process of radioactive decay to estimate the absorbed doses. *In vitro* high iodide (^{125}I) uptake in K1-NIS cells led to the substantial uptake of [^{123}I]NaI and [^{131}I]NaI in the tumor. The biodistribution and pharmacokinetics of [^{131}I]NaI in the tumor and various organs were marginally similar to the [^{123}I]NaI, while the difference increased over time. The absorbed dose as the integral sum of the area under the normalized dose rate curve was significantly affected by the extent of the extrapolated terminal fraction of the curve. [^{123}I]NaI exhibited a surrogacy in terms of the biodistribution and pharmacokinetics in the tumor and various organs for [^{131}I]NaI in the mice xenograft model of differentiated thyroid cancer. However, the pre-therapeutic dosimetry of [^{131}I]NaI using [^{123}I]NaI in the tumor could be problematic when estimating the absorbed dose including the period of the terminal phase of the pharmacokinetics.

Poster Presentation

Disclosures: The authors have disclosed no financial interest.

591-Tracking multiple FDG labeled single cells in vivo with Positron Emission Tomography

Presenter: Hieu Nguyen, Stanford University

Hieu T. Nguyen[1], Neeladri Das[2], Syamantak Khan[3], Arutselvan Natarajan[4], Guillem Pratx[5]

[1]*Stanford University*
[2]*Stanford University, CA*
[3]*Stanford University, Palo Alto, CA*
[4]*Stanford University, Satnford, CA*
[5]*Stanford University, Stanford, CA*

In vivo imaging tools plays a crucial role in elucidating cell trafficking in biological systems. Several imaging techniques have been explored to study the kinetic patterns of cell circulation at the single-cell level. However, these techniques are often limited by low sensitivity and temporal resolution,[1,2] shadow penetration depth,[3,4] and blood background signal.[5] Recent work has demonstrated the feasibility of tracking the migration of individual live cells *in vivo* using Positron Emission Tomography (PET).[6] However, this method is labor-intensive and cannot track more than 1 cell per animal. We thus report several improvements in the tracking workflow. First, we demonstrate a novel algorithm (PEPT-EM) to track multiple single cells simultaneously within the same scan. Second, we developed an optimized cell labeling protocol that uses FDG, bypassing the need for nanoparticle radiochemistry and improving tracking accuracy thanks to the lower positron range of ^{18}F compared to ^{68}Ga. Third, we investigated the use of a microfluidics-based device to select and dispense single cells prior to *in vivo* injection. The study's overall goal is to expand the application of PET for tracking single cells *in vivo*. We employed a novel and simple workflow to prepare viable radiolabeled single cells using a microfluidic-based single-cell dispenser device. Murine cancer cell lines (B16-F10 and 4T1) were cultured in a 6-well plate and incubated in culture media containing FDG (20 mCi/2 ml) for 45 minutes. Residual free FDG was removed after the incubation period, and cells were stained with viability dye Calcein AM (5 nM) for 10 minutes. Viable single cells were selectively dispensed based on the Calcein AM signal using a microfluidic-based instrument. The radioactivity of individual single cells was characterized by gamma counting. We utilized a high-sensitivity microPET scanner to image various low-activity single cells in vials (4 – 32 Bq/cell) and in a BalB/C mouse after tail vein injection (~12 Bq/cell). Finally, we adapted an algorithm previously developed for fluid mechanics investigations (PEPT-EM)[7] to enable simultaneous tracking of multiple low-radioactivity cells. Following radiolabeling, 92% of the cells were alive, as evidenced by Calcein AM staining. Using a single-cell dispenser device, we isolated single live cells with radioactivity up to 56 Bq for B16 and 26 Bq for 4T1 cells. The radioactivity in B16 is 70% higher than that of 4T1, likely because of their bigger size. Single FDG-labeled cells in vials could be visualized as low as 12 Bq in the standard OSEM-reconstructed PET images, whereas the more sensitive PEPT-EM algorithm could detect cells labeled with as low as 4 Bq FDG. Additionally, the 3D locations of cells derived by PEPT-EM matched the position of the vial seen on the corresponding CT image. We also observed that the variances of the Gaussian mixture model used on the PEPT-EM algorithm decreased significantly from 25 mm^2 at initialization to 0.85-1.16 mm^2 at convergence after 30 iterations. To track 4T1 cells in a BalB/C mouse, we divided the imaging time (10 minutes) into three 3-minute periods and reconstructed the cells location within each interval. The cells positions were within the PET system's resolution of around 1.5 mm, suggesting these cells were likely static after being trapped within the lung capillaries following tail-vein injection. This study demonstrates the feasibility of a new and simple workflow to radiolabel and isolate single cells and a novel application of the PEPT-EM algorithm to simultaneously and accurately track multiple low-activity single cells *in vivo*. Unlike previous methods, this study uses widely available FDG as the labeling tracer, enabling a more straightforward dissemination of this technique. We are currently cell tracking method to elucidate the kinetic patterns of cell circulation *in vivo*.

Reference

1. Heyn, C. et al. In vivo MRI of cancer cell fate at the single-cell level in a mouse model of breast cancer metastasis to the brain. Magn Reson Med 56, 1001–1010 (2006).
2. Hinds, K. A. et al. Highly efficient endosomal labeling of progenitor and stem cells with large magnetic particles allows magnetic resonance imaging of single cells. Blood 102, 867–872 (2003).
3. Thurber, G. M. et al. Single-cell and subcellular pharmacokinetic imaging allows insight into drug action in vivo. Nat Commun 4, 1504 (2013).
4. Dutta, R. et al. Real-Time Detection of Circulating Tumor Cells in Living Animals Using Functionalized Large Gold Nanorods. Nano Lett. 19, 2334–2342 (2019).
5. Deán-Ben, X. L. et al. Deep tissue volumetric optoacoustic tracking of individual circulating tumor cells in an intracardially perfused mouse model. Neoplasia 22, 441–446 (2020).
6. Jung, K. O. et al. Whole-body tracking of single cells via positron emission tomography. Nature Biomedical Engineering 4, 835–844 (2020).
7. Manger, S., Renaud, A. & Vanneste, J. An expectation–maximization algorithm for positron emission particle tracking. Review of Scientific Instruments 92, 085102 (2021).

Poster Presentation

Disclosures: The authors have disclosed no financial interest.

592-Rapid maturation and efficient integration of new-generation forebrain human NPCs in injured adult rat sensory cortex

Presenter: Xiao He, Zhejiang University

Xiao He[1], Jiadong Chen[2], Peili Cen[3], Li Shen[4], Mengjiao Tu[3], Fei Huang[4], Mei TIAN[1], Hong Zhang[5]

[1]*Zhejiang University, Hangzhou, Zhejiang, China*
[2]*Zhejiang University School of Medicine, Hangzhou, Zhejiang, China*
[3]*Zhejiang University, China*
[4]*Zhejiang University*
[5]*Zhejiang University, Hangzhou, Zhejiang 310009, China*

Background:
Cortical progenitor cell transplantation has great potential for treating neurological diseases that affect the cortex by replacing lost neurons and repairing damaged brain circuits (1). Currently, the prolonged maturation (4–6 months) of transplanted cortical neural progenitors significantly hinders understanding of neural replacement mechanisms and its clinical translation (2-5). In order to achieve functional maturation and synaptic integration more efficiently, we generate a new generation of forebrain human neural precursor cells (hNPCs) based on an optimized rosette neural aggregate (RONA) differentiation protocol for ischemic cortical stroke in a rat model.

Methods:
To characterize comprehensively the fate of the transplanted cells, the snRNA-seq analysis was performed to reveal the cell types and differentiation patterns. Immunoelectron microscopy, electrophysiology, and virus tracing were used to confirm that forebrain hNPCs achieved efficient functional maturation and synaptic integration. Further, we performed molecular imaging and behavioral studies to assess the proof of concept that new-generation forebrain hNPCs transplantation has therapeutic effects in the stroke-injured brain.

Results:
The snRNA-seq and histological analysis results showed that the forebrain hNPCs derived from human iPSC possessed efficient cortical neuronal differentiation after transplantation. Furthermore, the hNPCs-derived cortical neurons exhibited high maturity and efficient synaptic integration of neural circuitry in the host brain at the early

stage (7-11 weeks) after transplantation. In addition, the transplanted forebrain hNPCs can promote metabolic recovery, reduce infarct volume of infarct regions as well as promote motor recovery and prevent the onset of chronic post-stroke seizure.

Conclusions:
Taken together, this study provides convincing evidence that these new-generation forebrain hNPCs have considerable advantages regarding maturation and functional integration in lesioned adult murine sensory cortices. This has important implications for preclinical studies of neural replacement mechanisms and clinical translation for neurological diseases affecting the cortex such as Stroke, Huntington disease, Alzheimer disease and amyotrophic lateral sclerosis.

Reference

1. S. Palma-Tortosa, B. Coll-San Martin, Z. Kokaia, D. Tornero, Neuronal Replacement in Stem Cell Therapy for Stroke: Filling the Gap. Frontiers in cell and developmental biology 9, 662636 (2021).
2. S. Palma-Tortosa et al., Activity in grafted human iPS cell-derived cortical neurons integrated in stroke-injured rat brain regulates motor behavior. Proceedings of the National Academy of Sciences of the United States of America 117, 9094-9100 (2020).
3. D. Tornero et al., Synaptic inputs from stroke-injured brain to grafted human stem cell-derived neurons activated by sensory stimuli. Brain: a journal of neurology 140, 692-706 (2017).
4. D. Tornero et al., Human induced pluripotent stem cell-derived cortical neurons integrate in stroke-injured cortex and improve functional recovery. Brain: a journal of neurology 136, 3561-3577 (2013).
5. C. R. Nicholas et al., Functional maturation of hPSC-derived forebrain interneurons requires an extended timeline and mimics human neural development. Cell stem cell 12, 573-586 (2013).

Poster Presentation

Disclosures: The authors have disclosed no financial interest.

593-Targeting Prostate Specific Membrane Antigen For Fluorescence Image Guided Surgery Of Breast Cancer

Presenter: Aditi Shirke, Case Western Reserve University

Aditi A. Shirke

Case Western Reserve University, Cleveland, OH

Introduction:
Breast cancer is the most common cancer in women with cancer.org projecting 276,480 new cases of invasive breast cancer and 42,170 deaths in 2020. With current screening techniques, cancers are caught earlier, and most patients are candidates for breast conserving surgery (BCS) to remove the cancer [1]. Incomplete resections occur in 20-60% of BCS using current surgical tumor visualization technologies often leading to repeat surgeries[2]. This data demonstrates that there is an unmet clinical need for technologies that identify cancerous tissues in the margins of BCS specimens and real-time surgical methods of cancer tissue resection. Prostate Specific Membrane Antigen (PSMA) is known to be overexpressed in prostate cancer and has also is significantly overexpressed on neovasculature of many solid *human* tumors, including breast tumor neovasculature and breast cancer cells[2]. Previously, we combined a potent Photo Dynamic Therapy (PDT), Pc413, and a highly selective PSMA inhibitor, PSMA-1, invented in our lab, to develop a theranostic agent that can selectively identify and destroy prostate cancer (PCa) both *in vitro* and *in vivo* to improve fluorescence image guided surgery (FIGS) for prostate cancer [3] and demonstrated that PDT can be used as an effective adjuvant therapy after FIGS of prostate cancer resulting in reduced PSMs, lower tumor recurrence and extended animal survival following surgery. In this application we will utilize PSMA-Pc413, a theranostic agent, to determine if FIGS followed by PDT can improve the approach to breast cancer management. We additionally hypothesize that an immune system activation in response to PDT will lead to reduced local and distant metastases formation in our immune competent syngeneic mouse model.

Materials and Methods:
Four. adult, female BALB/c mice were orthotopically implanted with 4T1-Luc tumors ($5x10^3$ cells) and allowed to grow. After approximately 2.5 weeks (~$275mm^3$ tumor). They then received 0.5mg/kg of PSMA-1-Pc413 through tail vein injection and either treated with PDT (no surgery) or tumor excision without PDT to simulate conventional BCS. 16-18 days later, any tumors and lungs were excised and tumor nodules quantified. Serum was extracted and levels of IL-?1 before and 72 hours after either PDT only or WLS only were analyzed. To validate PSMA expression in the 4T1 model, orthotopic tumor tissue underwent immunofluorescence staining. Tumor tissues were co-incubated with PSMA-1- Alexa488 (synthesized in the lab) and goat anti-rabbit CD31-specific antibody overnight at 4^oC. After washing, tissues were incubated with goat anti-rabbit AlexaFluor594 and analyzed.

Results and Discussion:
We have demonstrated an orthotopic syngeneic mouse model of breast cancer where PSMA is overexpressed on the neovasculature of 4T1 breast cancers in BALB/c mice. Strong PSMA expression was observed in tumor tissues, which was blocked in the presence of excess amount of PSMA-1 ligand (Fig.1A). PSMA expression was found to be co-localized with CD31, indicating PSMA's expression in tumor vasculature. These data support the feasibility to use PSMA-1-Pc413 to highlight tumor for FIGS and PDT of breast cancer. In Fig. 1C, animals that received PDT had approximately 50% less metastatic lesions in the lungs than did animals that had the tumors surgically removed - corroborated visual counting of nodules through fluorescence imaging. Additionally, There was a dramatic increase in IL-b1 serum concentration 72 hours after PDT treatment (no IL-?1 was detected for WLS only mice), intimating inflammasome activation following PDT. These data suggest that PDT reduces local and distant metastases formation which could be due to stimulation of an immune response and activates immune surveillance against the metastatic potential of the 4T1 primary tumor.

Conclusion:
This work will lay the foundation for development of this agent towards clinical BCS and has the potential to dramatically impact current surgical procedures.

Reference

1. Katipamula, R., J Clin Oncol 27, 2009, 4082-4088
2. Jeevan, R., BMJ 345, 2012, e4505
3. Wang, X., Cancer research 80, 2020, 156-162

Poster Presentation

Disclosures: The authors have disclosed no financial interest.

594-Preclinical Evaluation of [64Cu/67Cu]NOTA-HFn as a Theranostic Agent for Radioiodine Refractory Differentiated Thyroid Cancer

Presenter: Renwei Zhou,Fifth Affiliated Hospital of Sun Yat-sen University

Renwei Zhou[1], Yanfang Shen[2], Ying Wang[1], Hongjun Jin[3], Lei Bi[4]

[1]Fifth Affiliated Hospital of Sun Yat-sen University, China
[2]Fifth Affiliated Hospital of Sun Yat-sen University
[3]The Fifth Affiliated Hospital, Sun Yat-sen University, Zhuhai City, Guangdong, China
[4]Fifth Affiliated Hospital of Sun Yat-sen University, Zhuhai, China

Introduction:
The diagnosis and treatment of radioiodine refractory differentiated thyroid cancer (RAIR-DTC) has been a great challenge in clinical practice due to the cancer cells no longer trap iodine. Transferrin receptor 1 (TfR1), a 95kDa homodimeric transmembrane glycoprotein, is related to DNA synthesis and cellular proliferation through iron uptake. Despite the correlative study of TfR1 in other cancer types suggesting its diagnostic and prognostic value, whether TfR1 plays a role in RAI-RDTC remains to be explored. Ferritin is a natural iron-storage protein assembled by the interaction of 24 polypeptide subunits which creates a spherical conformation that makes it a good candidate as drug delivery system. Heavy ferritin chain (HFn) is a natural (504kDa) ligand for TfR1, capable of specific and tight binding to TfR1. Therefore, we proposed to radiolabel HFn with Copper-64 that allows for positron emission tomography (PET) imaging and targeted Copper-67 radiotherapy of RAIR-DTC.

Materials and Methods:
The expression and distribution of TfR1 in BCPAP papillary thyroid carcinoma cell line was tested by western blot and cellular immunofluorescence. The NOTA-HFn was radiolabeled in a pH 5.2 NaAc buffered environment with $^{64}CuCl_2$.The uptake of [^{64}Cu]NOTA-HFn in BCPAP cell was evaluated by cell uptake assay and the prolonged-time PET imaging was performed at 1,6,12,24 and 36h postinjection of [^{64}Cu]NOTA-HFn to the BCPAP tumor-bearing mice. The expression of TfR1 in BCPAP tumor tissues and patients' tumor tissues were verified by immunohistochemistry.

Results:
The western blot results showed that TfR1 was higher expression in BCPAP than that of FTC-133 and TPC-1(**Figure 1 A**), and the immunofluorescence confirmed the positive expression of TfR1 in the BCPAP tumor(**Figure 1 B**). In the cell uptake assay, a significant reduction in radioactivity accumulation (over 2-fold in 5h after incubation) was observed by blocking BCPAP cells with unlabeled HFn(**Figure 1 C**). PET imaging of BCPAP tumor-bearing mice revealed clear tumor imaging, the highest tumor uptake was 0.31 ±0.05% ID/g and the best tumor-to-muscle ratio was 5.44 ±0.48(**Figure 1 D,E**). The tracer revealed receptor-specific tumor accumulation, which was illustrated by effective blocking via coinjection with a blocking dose of unlabeled HFn(**Figure 1 D,E**). The radioactivity accumulation of liver and kidney was high, indicating that [^{64}Cu]NOTA-HFn was mainly excreted by the liver and kidneys(**Figure 1 D**). The results of immunohistochemistry confirmed that TfR1 was positive in BCPAP tumor-bearing mice and clinic patients' tumor tissues(**Figure 1 F**).

Conclusion:
The current results showed that [^{64}Cu]NOTA-HFn was a good radiolabeled probe for imaging of TfR1 overexpression radioiodine refractory differentiated thyroid cancer. It offers potentials as a novel PET radiotracer for imaging and even [^{67}Cu] radionuclide therapeutic agent for TfR1-positive tumors.

Poster Presentation

Disclosures: The authors have disclosed no financial interest.

595-Organelle Interaction Networks are a Hallmark of Breast Cancer Cells

Presenter: Ling Wang, Albany Medical College

Ling Wang[1], Joshua A. Goldwag[2], Megan Bouyea[1], Niva Maharjan[1], Xavier Intes[1], Uwe Kruger[3], Margarida M. Barroso[1]

[1]Albany Medical College, Albany, NY
[2]Albany Medical College, Southbury, CT
[3]Rensselaer Polytechnic Institute (RPI), Troy, NY

Genomics and proteomics have been central to identify tumor cell populations but accurate approaches to classify subtypes are still lacking. Herein, we developed a new methodology to accurately classify cancer cells based on their organelle interaction networks. This methodology integrates artificial intelligence (AI) and imaging methods to quantify the spatial context of organelle interaction networks, specifically their subcellular location and inter-organelle relationships (topology). We obtained the very high accuracy of a panel of human breast cancer cells, and non-cancerous mammary epithelial cells, grown as 2D monolayer cells or 3D tumor spheroid cells using early endosomes - mitochondria interaction networks. Topology parameters generated the highest accuracy (99.6%) indicated that organelle interaction networks are a highly precise classifier to differentiate cell lines of differing subtype and aggressiveness and cell lines grown in 2D vs. 3D models. These novel findings lay the groundwork for using organelle interaction network's topological profiling as a fast and efficient method for phenotyping breast cancer function as well as a discovery tool to advance our understanding of cancer cell biology on a subcellular level.

Poster Presentation

Disclosures: The authors have disclosed no financial interest.

596-Functional Imaging of Prostate Cancer Tissue Using Optical Coherence Tomography

Presenter: Ping Yu, University of Missouri

Ping Yu[1], Lixin Ma[1]

[1]University of Missouri, Columbia, MO

Introduction:
Optical imaging for site-specific cellular targeting is important in the drug development. Here we report a high-resolution and high-speed optical coherence tomography (OCT) method as preclinical functional imaging to track metastatic cancer cells. OCT uses a low coherence interferometry to acquire depth-resolved images from biological tissues [1]. OCT normally provides a morphological imaging depending on the intensity signals from the light scattering [2]. We develop a dual band OCT with the capability of spectroscopic imaging in combination of a speckle autocorrelation technique to track the cellular movement. This

technique has its advantage in detecting cancer cells since time-dependent speckle is sensitive to the movement of scatters inside the tissue.

Methods:
The imaging system consists of two super-luminescence light emission diodes with wavelengths of 750 nm and 840 nm, respectively. A fiber-based Michelson interferometer is used in Fourier domain OCT. A high-speed line scan camera (Basler, spL2048-140km) is used to acquire the data. The imaging system has an axial resolution of 8 mm and lateral resolution of 20 mm. Two methods are used for high-speed OCT imaging [3]. A parallel thread method that the control, acquisition, process and display run in parallel and the data are flawed between threads using data queues through producer-and-consumer loops. The second method is to accelerate the imaging speed using a graphics processing unit. The system provides an imaging speed of 60 Hz with a frame size of 1024´1000. Suppose OCT image has an intensity distribution I(x, y, z, t) for each wavelength where x and y are the lateral directions and z is the depth direction. An algorithm is developed for the speckle imaging where the frames are acquired at the same location of z. 5 points along x and y directions are averaged to reduce the position uncertainty of speckle. Autocorrelation is performed along the time dimension for each position x and y using the developed algorithm. Severe combined immunodeficient (SCID) mice (age 6–8 weeks; approximately 20 g, Taconic, Germantown, NY) are surgically implanted with cancer cells into the prostate to induce orthotopic prostate cancer models.

Results:
Fig. 1(a) shows OCT image of prostate tumor tissue along x and z directions. Skin and void structures can be observed. The weak vertical line corresponds to the zero cross in the interferometer. We have an effective way to remove the mirror image [3]. The color of the image corresponds to different wavelength. The same tissue is cut to thin slices for the histological images using an optical microscope, as shown in Fig. 1(b). Similar tissue structures can be observed in both images, and the metastatic cancer cells are stained as blue in the histology. By using the autocorrelation technique, the cancer cell movement can be studied (Fig.1 (c) and (d)). Fig. 1(e) and (f) compare the OCT images from prostate tumor tissue and muscle. Due to the orientation of fibers, the color in OCT represents the polarization of optical signals from the muscle. In OCT image of prostate tumor tissue, more colored areas can be found in the deeper location corresponding to muscle tissue. The OCT images are acquired in multiple locations along the y direction. The data sets can be used to reconstruct the images in the x and y plane (Fig. 1(g)).

Discussion:
The spectroscopic OCT developed in this work can be used to differentiate the tissue types, as shown in the difference between the muscle and prostate tumor tissues. The cellular movement of the cancer cells makes contribution to the moving speckle in high-speed OCT imaging. Therefore, the developed technology will be able to track cancer cells in preclinical imaging.

Reference

1. D. Huang, E. A. Swanson, C. P. Lin, et al., "Optical coherence tomography," Science 254, 1178 (1991).
2. J. Izatt, et al., "Introduction to the feature issue on the 25year anniversary of optical coherence tomography," Biomedical Optics Express. 8, 3289-3291 (2017).
3. M. Zhang, L. Ma, and P. Yu, "Three-dimensional full-range dual-band Fourier domain optical coherence tomography accelerated by graphic processing unit," IEEE Journal of Selected Topics in Quantum Electronics, 25, 1-6 (2019).

Poster Presentation

Disclosures: The authors have disclosed no financial interest.

597-Hyperspectral Imaging of NIR-II-Emitting Nanosensors for Lysosomal Function

Presenter: Daniel Heller, Memorial Sloan Kettering Cancer Center

Daniel Heller[1], Mijin Kim, Chen Chen, Prakrit Jena

[1]*Memorial Sloan Kettering Cancer Center, New York, New York*

Lysosomes have emerged as essential signaling centers that govern cell growth, division, and differentiation, as well as catabolic activity. We developed near infrared II (NIR-II)-emitting nanosensors for lysosomal metrics, including pH and lipids, that are dysregulated in many conditions including cancers, neurodegenerative diseases, and metabolic disorders. To measure the emission changes of the nanosensors, we developed new spectroscopic and imaging methods, including NIR-II hyperspectral imaging capabilities of both live cells and mice, high-throughput spectroscopy of live cells, and a fiber optic probe-based instrument for rapid, single-point spectroscopy in animals. Our nanosensors are derived from single-walled carbon nanotubes that emit highly photostable NIR-II fluorescence that is uniquely sensitive to local perturbations. In addition, covalent sp3 defects (often called organic color centers, OCCs) on carbon nanotubes confer unique near-infrared fluorescent properties to nanotubes, including emission bands with increased quantum yield and new chemical sensitivities. The nanosensors, interrogated using the new instruments, enable: 1) quantitative measurements of endolysosomal lipid accumulation in cells and animal models of lysosomal storage diseases, atherosclerosis, fatty liver disease, and cancer, and 2) quantitative lysosomal pH measurements in tumor models, and pharmacodynamic measurements upon drug perturbations.

Poster Presentation

Disclosures: The authors have disclosed no financial interest.

598-A radiation-driven liquid-based detection system for predicting radiotherapy outcomes on prostate carcinoma

Presenter: Shao-peng Chen, National Yang Ming Chiao Tung University

Shao-peng Chen[1], Hui-Yen Chuang[2]

[1]*National Yang Ming Chiao Tung University, Taiwan*
[2]*National Yang Ming Chiao Tung University, Taipei City, Taiwan, Taiwan*

Object:
Radiotherapy is one of mainstream therapeutic tools for cancer treatment. Specific cancer biomarkers are often used for monitoring treatment response but could not accurately reflect the outcomes promptly and are limited to specific cancer types. Although imaging examinations can also monitor treatment response; however, the first image is often taken several weeks after the first irradiation. Furthermore, imaging results are often confounded by various conditions ended up with different outcomes. Thus, a universal tool that can apply to most cancers with high sensitivity and specificity would be helpful.

Ionizing radiation (IR) rapidly upregulates several genes potentially serving as promoters to drive constructs encoding reporter genes to monitor radiotherapy outcomes. Here we aimed to generate a reporter platform driven by IR-sensing promoters for tracking outcomes and potentially predicting prognosis after radiotherapy in prostate cancer at early time points.

Methods:
IR-inducible proteins were detected by Western blot in human prostate cancer cell lines LNCaP and PC-3 that received different doses of ionizing radiation. The IR-activatable promoter systems were established by co-encoding secreted reporters in SBE or ARE-driven constructs and connecting the relationship between transcriptional activity and cell-killing effects. The reporter expressions were determined by luminescence measurement and ELISA respectively. The short-term cell-killing effects were evaluated by MTT and CCK-8 assay.

Results:
Western blot showed that cells showed increased IR-responsive protein expression after being exposed to fractionated and single doses of radiation over time. Meanwhile, cytotoxicity assays reveled that cell viabilities of both PC-3 and LNCaP cells were reduced in a dose-dependent manner after IR treatment. Next, we constructed SBE (smad binding elements) and ARE (antioxidant response elements) as promoter driven downstream liquid-base synthetic biomarkers (Gluc and hCG) as plasmid probes. Subsequently, PC-3 and LNCaP cells stably transfected with these constructs to compare the levels of these synthetic biomarkers treated with different radiation doses, and correlated the biomarker levels and final treatment responses.

Conclusion:
This study demonstrated the potential of using constructs driven by the radiation-activatable promoters to reveal the correlation between the liquid-based reporter outputs and cellular responses post the irradiation. The strategy could be considered for further translational research to help physicians to find out the treatment outcomes at early time points and make the right decision for the following medical care. Hopefully, the patients would have better outcomes and quality of life as our platform being validated and tested in future.

Poster Presentation

Disclosures: The authors have disclosed no financial interest.

599-High performance T1–T2 dual-modal MRI contrast agents based on the vortex nanoring coated with gadolinium

Presenter: Jianfeng Bao, First Affiliated Hospital of Zhengzhou University

Jianfeng Bao

First Affiliated Hospital of Zhengzhou University, Zhengzhou, Henan, China

Nowadays, about 30% of magnetic resonance imaging (MRI) exams need contrast agents (CAs) to improve the sensitivity and quality of the images for accurate diagnosis. However, clinically available CAs usually reduce the longitudinal relaxation time (T1) but rarely change the transverse relaxation time (T2). Here, a multi-functional nano-agent with ring-like vortex-domain iron oxide as core and gadolinium oxide as shell (vortex nanoring Fe3O4@ Gd2O3, abbreviated as VNFG) was firstly designed and prepared for highly enhanced T1-T2 dual-modality magnetic resonance imaging (MRI)-guided magnetic thermal cancer therapy. After thorough characterization, the core-shell structure of VNFG was confirmed. VNFG shows both high longitudinal rate (R1=25.02 mM-1s-1[Gd]) and transverse relaxation rate (R2=138.41 mM-1 s-1[Fe]) on the clinical available MRI scanner with field strengths of 3.0 T, as well as an ideal low ratio(R2/R1=5.53). Moreover, the excellent heat generation property (SAR=984.26 W/g) of the proposed VNFG under alternating magnetic fields was firmly demonstrated. Furthermore, both in vitro and in vivo studies have revealed a good preliminary indication of VNFG's biological compatibility, dual-modality enhancing feature and antitumor efficacy. This work demonstrates that the proposed core-shell structured VNFG is designed and successfully synthesized through coating gadolinium oxide onto the surface of the nanorings Fe3O4 with the connection of thermostable PEI The obtained VNFG effectively reduces both T1 and T2 time while maintaining an appropriate R2/R1 ratio. On the other hand, the VNFG also shows high magneto-thermal conversion efficiency due to the magnetic vortex structure of the ring shape core. We carefully conducted the in vitro and in vivo experiments, and the results further demonstrate that the synthesized VNFG has negligible toxicity, remarkable T1-T2 dual-modality MRI tumor enhancement capacity, and highly efficient antitumor effects. We believe the proposed VNFG in this study will provide potential diagnostic nanoplatforms for precise diagnosis and effective tumor treatment in pre-clinic studies.

Reference
1. Y.X. Zhao, X.-J. Liang, Comprehensive understanding of magnetic hyperthermia for improving antitumor therapeutic efficacy, Theranostics 10(8) (2020) 3793-3815.
2. K. Mahmoudi, A. Bouras, D. Bozec, R. Ivkov, C. Hadjipanayis, Magnetic hyperthermia therapy for the treatment of glioblastoma: a review of the therapy's history, efficacy and application in humans, International Journal of Hyperthermia 34(8) (2018) 1316-1328.
3. E. Kita, T. Oda, T. Kayano, S. Sato, M. Minagawa, H. Yanagihara, M. Kishimoto, C. Mitsumata, S. Hashimoto, K. Yamada, N. Ohkohchi, Ferromagnetic nanoparticles for magnetic hyperthermia and thermoablation therapy, Journal of Physics D: Applied Physics 43(47) (2010) 474011.
4. M. Bañobre-López, A. Teijeiro, J. Rivas, Magnetic nanoparticle-based hyperthermia for cancer treatment, Reports of Practical Oncology & Radiotherapy 18(6) (2013) 397-400.
5. Y. Piñeiro, Z. Vargas, J. Rivas, M.A. López-Quintela, Iron Oxide Based Nanoparticles for Magnetic Hyperthermia Strategies in Biological Applications, European Journal of Inorganic Chemistry 2015(27) (2015) 4495-4509.
6. Y.-J. Lu, E.-Y. Chuang, Y.-H. Cheng, T.S. Anilkumar, H.-A. Chen, J.-P. Chen, Thermosensitive magnetic liposomes for alternating magnetic field-inducible drug delivery in dual targeted brain tumor chemotherapy, Chemical Engineering Journal 373 (2019) 720-733.
7. R.J. Wydra, P.G. Rychahou, B.M. Evers, K.W. Anderson, T.D. Dziubla, J.Z. Hilt, The role of ROS generation from magnetic nanoparticles in an alternating magnetic field on cytotoxicity, Acta Biomaterialia 25 (2015) 284-290.

Poster Presentation

Disclosures: The authors have disclosed no financial interest.

600-Enzymatic Radiosynthesis of [18F]-labelled alpha-Diglucosides and Their Use as Bacteria-Specific Imaging Tracers

Presenter: Alexandre Sorlin, University of California, San Francisco

Alexandre Sorlin[1], Aryn A. Alanizi[2], Sarah Rabbitt[3], Marina López-Álvarez[4], David M. Wilson[5]

[1]*University of California, San Francisco*
[2]*University of California San Francisco, CA*
[3]*University of California San Francisco, San Francisco, California*
[4]*University of California San Francisco, San Francisco*
[5]*University of California, San Francisco, San Francisco, CA*

Currently there are only a few positron emission tomography (PET) methods to image living bacteria *in vivo.* Existing radiotracers such as 2-deoxy-2-[^{18}F]-fluoro-$_{D}$-glucose ([^{18}F]-FDG) are inadequate to detect bacterial infection due to lack of specificity. Lately some diagnostic strategies to target living bacteria include metabolism-targeted PET tracers. One approach is to target maltodextrin ($_{D}$-glucose units with 1->4 alpha linkage), which are energy sources for bacteria. These oligosaccharides are taken up by maltodextrin transporters, which are not present in mammalian cells. This feature can be used to develop tracers specific to bacteria. The reported ^{18}F-labeled carbohydrate 6-[^{18}F]-fluoromaltose, 6-[^{18}F]-fluoromaltotreose have shown bacteria uptake but require lengthy precursor synthesis. There is potential for using routinely produced ^{18}F-FDG as prosthetic to develop maltodextrin-based analogs. We report the one step enzymatic synthesis of 2-deoxy-2[^{18}F]-fluoromaltose ([^{18}F]-FDM) derived from readily available [^{18}F]-FDG. This method also yields 2-deoxy-2-[^{18}F]-fluoronigerose ([^{18}F]-FDN) as radioactive by-product. Both radiotracers were easily isolated in short time and studied *in vitro*. [^{18}F]-FDM showed high uptake with *K. pneumoniae*, and [^{18}F]-FDN showed high incorporation in *S. Aureus*. Preliminary *in vivo* studies using myositis model showed incorporation of [^{18}F]-FDN tracer in infected muscle with *S. Aureus.*

Poster Presentation

Disclosures: The authors have disclosed no financial interest.

601-PET and DTI provide complementary information in the whole central nervous system of rats with contusion spinal cord injury

Presenter: William Mennie, Yale School of Medicine

William D. Mennie[1], Baosheng Chen[2], Takuya Toyonaga[2], Chao Zheng[2], Daniel Coman[3], Jelena Mihailovi?[3], Xingxing Wang[4], jie tong[5], Stephen M Strittmatter[4], Richard E. Carson[3], Yiyun H. Huang[3], Jason (Zhengxin) Cai[2], Balayeva Tutukanhim[6]

[1]*Yale School of Medicine, New Haven*
[2]*Yale School of Medicine, New Haven, CT*
[3]*Yale University, New Haven, CT*
[4]*Yale Alzheimers Disease Research Center, New Haven, Connecticut*
[5]*Yale University, New Haven*
[6]*Yale University School of Medicine*

Introduction:
Traumatic spinal cord injuries (SCI) are the result of damage to vertebral columns. By analyzing axon fiber integrity, measured by Diffusion Tensor imaging (DTI), and the density of synaptic vesicle glycoprotein 2A (SV2A), which is ubiquitously expressed in all presynaptic terminals and can be quantified via PET, this research aims to map the axonal and synaptic changes at the acute to transitional phases of SCI in rats, the understanding of which is crucial to the treatment of SCI. We also sought to track the synaptic dynamics in the whole CNS from day 1 to day 10 post-injury and correlate the SV2A changes with DTI metrics at day 10 post-injury to establish a framework for longitudinal preclinical study comparing these changes on a system-wide and cellular level over the critical recovery period (up to 11 weeks) and provide a highly translational paradigm to evaluate treatment effects of experimental interventions in animal models.

Materials and methods:
PET scans were conducted on day 1 and 10 in-vivo, and an ex-vivo DTI scan on day 10. Subjects include four Sprague-Dawley rats which were given a mild contusion injury between T6 and T7 vertebrae using a MASCIS impactor (10g, 25mm), and four age and sex matched sham controls (n=8).
Rats were scanned with [^{18}F]SDM-8, a highly effective SV2A radiotracer[1] (15~22 MBq, i.v.) for 60 minutes at 1 and 10 days post injury under anesthesia with isoflurane under Inveon PET/CT scanner. SUVR from the 30-60 minutes post injection using cervical spinal cord as the reference region was used in the quantitative analysis (Figure 4).
Ex vivo DTI images were collected using tissues collected at day 10. Full brains and spinal cord sections from T5-T9 were scanned on a 9.4 T horizontal bore magnet, and DTI experiments were performed using a Stejskal-Tanner spin-echo diffusion-weighted sequence[2]. The diffusion tensor was calculated as previously described4. The fractional anisotropy (FA), apparent diffusion coefficient (ADC) and Diffusion Encoded Color (DEC) maps were generated with BioImage Suite[3].

Results:
Compared to sham controls, FA decreased by 27.3% (±3.2) (Fig. 1a) while SV2A tracer uptake at the same site of injury decreased 25% (±8%) (Fig. 1c) on day 10. Rostral and caudal to the site of injury, DTI shows that axon structure remains mostly unchanged at the 10 day period below the site of injury.
However, PET tracer uptake decreased significantly caudal to the point of injury (Fig 1b, 1c). Change in the lower thoracic region was observed decreasing at an average of 23 ± 9% in the SCI group over 10 days. The trend in change over time is consistent with prior literature [REF]. This suggests the cascading effect of neuron death below the site of injury can be measured with SV2A PET.
In the brain, compared to sham controls, the SCI group showed significant changes in FA values at the internal capsule (IC) and primary motor-sensory (M1S1) regions (Fig. 1d); while the SV2A PET data showed a notable trend of change in brain regions (Fig 1e) but did not reveal statistically significant values in this area. Further research is required as change over time is expected.

Conclusions:
Our pilot multimodality DTI and SV2A PET imaging approach yielded complementary data regarding the spinal cord injury's effects on axonal microenvironment and synaptic dynamics in spinal cord injured rats. With further preclinical validations and translation, this novel imaging approach is expected to provide better ways to predict patients' functional recovery and evaluate treatment effects in clinical trials of novel interventions.

Reference
1. Li S, Cai Z, Wu X, Holden D, Pracitto R, Kapinos M, Gao H, Labaree D, Nabulsi N, Carson RE, Huang Y. Synthesis and in Vivo Evaluation of a Novel PET Radiotracer for Imaging of Synaptic Vesicle Glycoprotein 2A (SV2A) in Nonhuman Primates. ACS Chem Neurosci. 2019 Mar 20;10(3):1544-1554. doi: 10.1021/

acschemneuro.8b00526. Epub 2018 Nov 16. PMID: 30396272; PMCID: PMC6810685.
2. Duque A, Coman D, Carlyle BC, Bordner KA, George ED, Papademetris X, Hyder F, Simen AA. Neuroanatomical changes in a mouse model of early life neglect. Brain Struct Funct. 2012 Apr;217(2):459-72. doi: 10.1007/s00429-011-0350-9. Epub 2011 Oct 8. PMID: 21984312; PMCID: PMC3664301.
3. Papademetris X, Jackowski MP, Rajeevan N, DiStasio M, Okuda H, Constable RT, Staib LH. BioImage Suite: An integrated medical image analysis suite: An update. Insight J. 2006;2006:209. PMID: 25364771; PMCID: PMC4213804.

Poster Presentation

Disclosures: The authors have disclosed no financial interest.

602-Towards Brownian relaxation MPI to enable real-time binding and cell viability sensing

Presenter: Kim Hwang Yeo, UC Berkeley

Kim Hwang Yeo[1], Irati Rodrigo Arrizabalaga[2], Chinmoy Saayujya[3], K. L. Barry Fung[4], Molly Ced[5], Varoon Aluri[2], Anuj Raichura[2], Melissa Kim[2], Prashant Chandrasekharan[3], Benjamin Fellows[2], Steven Conolly[4]
[1]*UC Berkeley*

[2]*University of California, Berkeley, Berkeley, California*
[3]*University of California, Berkeley, Berkeley*
[4]*University of California, Berkeley, Berkeley, CA*
[5]*University of California, Berkeley, Salinas, California*

Introduction:
Cell tracking today can be performed with Nuclear Medicine (e.g., RBC-Tc99m, WBC-In111) and MRI (e.g., SPIO-T2*, 19F MRI). However, none of these cell imaging tracer modalities can sense whether the cells they are tracking are actually still alive. Similarly, these imaging methods can only distinguish bound from unbound tracers by waiting for washout. However, washout time can exceed the binding duration. Here we outline how Brownian viscosity sensing could enable real-time *in-vivo* binding and cell viability sensing for the first time — and without any radiation.

Theory:
Iron oxide magnetic nanoparticles (MNP) are the tracers used in Magnetic Particle Imaging (MPI) [1,2]. Some are already FDA or EU safety approved (e.g., Resovist, Ferumoxytol). During the inductive sensing of MPI, the MNP moments rotate 180 degrees via two relaxation pathways in parallel, Brownian and Neélian. Because the two rotation paths occur in parallel, the shorter relaxation mechanism governs the overall measured relaxation time. The Brownian relaxation time, τ_B, of a MNP governs the physical rotation of the entire MNP, including its shell. Hence, Brownian relaxation senses any obstruction to rotation, including viscosity and binding. Mathematically, the Brownian relaxation time scales linearly with the hydrodynamic volume of the MNP, V_H, and linearly with the (dynamic) viscosity, η, of its immediate surround [3]. $\boldsymbol{\tau_B = (3\eta V_H)/(k_B T)}$ **[Eq. 1]** Because the Brownian time constant scales linearly with viscosity we asked if we could exploit it to measure viscosity as a first proof-of-concept experiment.

Materials and Methods:
Other research groups have previously demonstrated quantitative mathematical models to predict the viscosity of glycerol-water solutions as a function of concentration and temperature [4,5]. To test MPI viscosity measurements, we dispersed MNPs into various glycerol-water solutions and measured the rotation relaxation time using our home-built Arbitrary Waveform Relaxometer (AWR) [6]. A viscosity range of 1cP to 6cP was used, close to the viscosity range of blood [7]. Two different particles were analyzed in this work: NanoXact® (NN) and Vivotrax (VT). Glycerol-water samples corresponding to 1cP to 6cP at room temperature (300 K) were prepared according to the model. For relaxation time measurements a 1kHz square wave with field strengths up to 12mT were measured with the AWR [8]. Temperature was recorded with a fiber optic thermometer starting at 330 K, and repeated relaxometry scans were performed at field strengths of 2mT, 4mT, and 10mT (n=5) until the particles cooled to room temperature. Theoretical viscosities based on [4,5] were calculated and relaxation times were computed via a custom NLLS fitting algorithm.

Results:
We observed a linear time constant variation with the concentration of glycerol, ($R2 = 0.996$) for one MNP (NanoXact®), as seen in Fig. 1a, clearly indicating Brownian relaxation behavior. Fig. 1b shows how relaxation times vary with both viscosity and temperature and Fig. 1c shows the measured relaxation time against theoretical viscosity.

Discussion and Conclusion:
This was a successful proof of concept non-imaging experiment. It is possible to expand this to an imaging experiment using either Pulsed MPI [8] or conventional MPI [9]. Moreover, these are promising results for measuring binding or cell viability. We plan to use this technique to measure cell viability because there is a dramatic intracellular viscosity change during cell death as observed in Kuimova et al. [10]. We also plan to use this technique to probe *in-vivo* binding as prior works [11,12] showed that pulsed MPI relaxometry can accurately distinguish between bound and unbound MNPs.

Reference
1. Gleich B. & Weizenecker J., Nature 2005
2. Goodwill P. et al., IEEE Transactions on Medical Imaging, 2010
3. Rosensweig R., Journal of Magnetism and Magnetic Materials, 2002.
4. Chenf N.-S., Industrial & Engineering Chemistry Research, 2008
5. Volk, A. & Kähler, C.J., Experiments in Fluids, 2018
6. Tay, ZW. et al., Scientific Reports, 2016
7. Nader, E. et al., Frontiers in Physiology, 2019
8. Tay, ZW. et al., IEEE Transactions on Medical Imaging, 2019
9. Croft L. R. et al., IEEE Transactions on Medical Imaging, 2012
10. Kuimova M.K. et al., Nature Chemistry, 2009
11. Yao Lu et al. International Journal of Hyperthermia, 2020
12. Hensley D. PhD dissertation, University of California, Berkeley, 2017.

Poster Presentation

Disclosures: The authors have disclosed no financial interest.

603-Comparison of tumor EGFR expression in patients undergoing fluorescence-guided Trans-Oral Robotic Surgery with panitumumab-IRdye800

Presenter: Shilpa Rao, University of Alabama at Birmingham Heersink School of Medicine

Shilpa M. Rao[1], Logan Stone[2], Manuel Lora Gonzalez[3], Hari Jeyarajan[3], Carissa Thomas[3], Jason Warram[4]

[1]*University of Alabama at Birmingham Heersink School of Medicine, Birmingham, AL*
[2]*University of Birmingham, Birmingham*
[3]*Birmingham, AL*
[4]*University of Alabama at Birmingham, Birmingham, AL*

Background:
Epidermal growth factor receptor (EGFR) is a transmembrane tyrosine kinase receptor responsible for intra-cellular signaling and cell survival.[1] EGFR is overexpressed in most head and neck mucosal squamous cell carcinomas (SCC)[2] and is associated with poor outcomes and reduced survival.[4] Recent studies have also shown increased radiosensitivity of Oropharyngeal squamous cell carcinoma (OPSCC) with increased EGFR expression.[5] To this effect, we determine the variability in EGFR densities in OPSCC with immunohistochemistry (IHC), which can be correlated clinically with fluorescence imaging during trans-oral robotic surgery (TORS).

Methods:
Patients undergoing TORS for OPSCC as standard of care were recruited. Consenting patients received panitumumab-IRDye800 intravenously 48 hours prior to surgery. Fluorescent images were taken during surgery with near infrared technology present in the Da Vinci Xi robot camera. Images were processed with ImageJ™, and raw values of tumor and tumor to background ratio (TBR) were obtained. Postoperatively, the tumor specimen was imaged for fluorescence with a closed-field scanner and histological slide scanner to confirm the presence of fluorescence followed by TBR calculation with Image studio™. EGFR expression was confirmed with IHC. The presence of tumor was confirmed with histopathology and the EGFR density assessed.

Results:
The EGFR expressions in tumor samples from the two patients were quantified as low and high by a head and neck pathologist. The raw counts of the tumor with intra-operative fluorescence imaging ranged from 42.71-58.67. The TBR for the patient with low IHC was 2.52 ± 0.24 with intra-operative fluorescence imaging, 2.59 ± 0.43 with closed-field scanner and 2.08 ± 0.51 with histological slide scanner. The TBR for the patient with high IHC was 2.99 ± 0.01 with intra-operative fluorescence imaging, 10.78 ± 0.87 with closed-field scanner and 5.43 ± 2.20 with histological slide scanner.

Conclusion:
Fluorescent imaging can detect the presence of tumor despite low expression of EGFR in OPSCC.

Reference

1. Kriegs M, Clauditz TS,Hoffer K, Bartels J, Buhs S, Gerull H, Zech HB, Bußmann L, Struve N, RieckmannT, Petersen C, Betz CS, Rothkamm K, Nollau P, Münscher A. Analyzing expression and phosphorylation of the EGF receptor in HNSCC. Sci Rep. 2019 Sep19;9(1):13564. doi: 10.1038/s41598-019-49885-5. PMID: 31537844; PMCID:PMC6753061.
2. Rosenthal EL, Warram JM, de Boer E, et al. Safety and Tumor Specificity ofCetuximab-IRDye800 for Surgical Navigation in Head and Neck Cancer. Clin Cancer Res. Aug 152015;21(16):3658-66. doi:10.1158/1078-0432.Ccr-14-3284
3. Sivarajah S, Kostiuk M,Lindsay C, Puttagunta L, O'Connell DA, Harris J, Seikaly H, Biron VL. EGFR as a biomarker of smoking status and survival in oropharyngeal squamous cell carcinoma. J Otolaryngol Head Neck Surg. 2019 Jan 10;48(1):1. doi:10.1186/s40463-018-0323-6. PMID: 30630536; PMCID: PMC6327450.
4. Sweeny L, Dean NR, MagnusonJS, Carroll WR, Helman EE, Hyde SO, Desmond RL, Rosenthal EL. EGFR expression in advanced head and neck cutaneous squamous cell carcinoma. Head Neck. 2012May;34(5):681-6. doi: 10.1002/hed.21802. Epub 2011 Jul 7. PMID: 21739514;PMCID: PMC3193876.
5. Alsahafi EN, Thavaraj S,Sarvestani N, Novoplansky O, Elkabets M, Ayaz B, Tavassoli M, Legends MF. EGFR overexpression increases radiotherapy response in HPV-positive head and neck cancer through inhibition of DNA damage repair and HPV E6 downregulation.Cancer Lett. 2021 Feb 1;498:80-97. doi: 10.1016/j.canlet.2020.10.035. Epub 2020Oct 31. PMID: 33137407.

Poster Presentation

Disclosures: The authors have disclosed no financial interest.

604-In vivo imaging of inflammatory protease activity in preclinical and human atherosclerosis using LUM015, a translatable fluorescence molecular imaging agent

Presenter: Mohamad Kassab, Massachusetts General Hospital

Mohamad B. Kassab[1], Andrew Thrapp, Joseph A Gardecki, Osman O Ahsen, Yoichiro Kawamura, Adam Mauskapf[2], Graham Spicer, Evangelia Gavgiotaki, Aditya Kumar, Maya Modi, Ara L Bablouzian, Aidan Burbridge, Paola Leon, Benjamin Child, Guillermo J Tearney, Farouc Jaffer

[1]*Massachusetts General Hospital, Boston, MA*
[2]*Massachusetts General Hospital, Boston, Massachusetts*

Background:
Novel translatable imaging approaches are needed to identify high-risk atherosclerosis plaque inflammation, a major driver of coronary artery disease (CAD) events. Therefore, in this study, we assess the ability of Lumicell (LUM015), a clinical near-infrared fluorescence (NIRF) molecular imaging agent used for intraoperative cancer detection, to illuminate cathepsin protease inflammatory activity in atherosclerosis.

Methods:
In vitro LUM015 was incubated with human monocyte-derived macrophages (MDMs) and imaged by fluorescence microscopy (FM) 24 hours to assess macrophage inflammatory activity. Next surgically excised human carotid plaques (N=8) incubated with LUM015 in culture media were imaged by catheter-based NIRF-OCT (ex. 647+/-1 nm, em. 708/75 nm), fluorescence reflectance imaging (FRI, ex. 625+/-17 nm, em. 708/75 nm), FM, and histopathological analysis. In vivo signal was detected in cholesterol-fed balloon-injured rabbits (N=5). The rabbits were image 6-24 hours after LUM015 injection (6.2 mg/kg i.v.) using in vivo NIRF-OCT and intravascular ultrasound (IVUS) imaging to assess plaque inflammation and burden. Spatial distribution of macrophages, cathepsin S, and LUM015 signal were evaluated by immunohistochemistry staining.

Results:
Imaging of MDMs revealed LUM015 NIRF signal activation, generating an average NIRF intensity at 6 and 24 hours of 7.9 ± 1.5 and 14.5 ± 2.40 (arbitrary units), respectively ($p<0.05$ vs. pre-incubation signal). The ratio of mean FRI signal intensity of excised human plaques at 6

and 24 hours was 2.9±1.3 and 4.1 respectively, indicating LUM015 activation over time (p<0.05 vs. pre-incubation signal). In rabbits, in vivo intravascular NIRF-OCT pullbacks at 6 and 30 hours showed activation of LUM015 signal (target-to-background ratio of 2.7 ± 1.2 and 2.9 ± 2.1, respectively). On fluorescence microscopy, plaque LUM015 associated with both macrophages-positive areas (r=0.63, P=0.02) and cathepsin S positive areas (r=0.48, P=0.04) by immunohistochemistry staining.

Conclusion:

In preclinical and clinical atherosclerosis studies, we found that LUM015 generated NIRF signal and enabled in vivo imaging of atherosclerotic plaque cathepsin protease activity. LUM015 may offer a novel, clinically translatable approach to image coronary plaque inflammation in CAD patients.

Reference

1. Yoo, H., Kim, J., Shishkov, M. et al. Intra-arterial catheter for simultaneous microstructural and molecular imaging in vivo. Nat Med 17, 1680–1684 (2011). https://doi.org/10.1038/nm.2555
2. Whitley, M. J., Cardona, D. M., Lazarides, A. L., Spasojevic, I., Ferrer, J. M., Cahill, J., Lee, C. L., Snuderl, M., Blazer, D. G., 3rd, Hwang, E. S., Greenup, R. A., Mosca, P. J., Mito, J. K., Cuneo, K. C., Larrier, N. A., O'Reilly, E. K., Riedel, R. F., Eward, W. C., Strasfeld, D. B., Fukumura, D., … Brigman, B. E. (2016). A mouse-human phase 1 co-clinical trial of a protease-activated fluorescent probe for imaging cancer. Science translational medicine, 8(320), 320ra4. https://doi.org/10.1126/scitranslmed.aad0293

Poster Presentation

Disclosures: The authors have disclosed no financial interest.

605-PET imaging of mesothelioma in mouse models with a novel CD146 targeting human monoclonal antibody

Presenter: Jun Li, University of Virginia

Jun Li[1], Ping Chen[2], Yang Su[3], Bin Liu[4], Jiang He[5]

[1]University of Virginia, Charlottesville
[2]University of Virginia School of Medicine, Charlottesville, Virginia
[3]University of California San Francisco, San Francisco, California
[4]University of California, San Francisco, San Francisco, California
[5]University of Virginia, Charlottesville, VA

Purpose/Background:

Most current imaging and targeted radionuclide therapy for mesothelioma under development are targeting mesothelin, which is only expressed in epithelioid subtype of mesothelioma. CD146 is overexpressed in both epithelial and sarcomatous subtypes of mesothelioma, presenting a novel opportunity for targeted imaging and radiotherapy (1,2). A novel fully human monoclonal antibody M40 was developed to selectively bind to CD146. The goal of this study is to test if 89Zr labeled M40 antibody can detect mesothelioma tumor in vivo in a mouse xenograft model.

Methods:

The human monoclonal antibody M40 was conjugated with DFO followed by labeling with 89Zr to produce 89Zr-DFO-M40. 89Zr-DFO-M40 was evaluated in vitro for cell binding with MSTO-211 mesothelioma tumor cells. MST-211H mesothelioma tumor cells were implanted subcutanousely in mice. The tumor animals received 89Zr-DFO-M40 only in the study group or 10 fold of amount of cold antibody M40 prior to 89Zr-DFO-M40 in the blocking control group. The animals underwent PET imaging at 1 day, 3 day, and 5 days post-injection of 89Zr-DFO-M40 and were euthanized for biodistribution after final PET imaging on day 5.

Results:

89Zr-DFO-M40 was produced in > 95% yield and >98% radiochemistry purity after purification. In vitro cell studies confirmed 89Zr-DFO-M40 retained high tumor cell binding. 89Zr-DFO-M40 specifically detected the MSTO-211H tumor and showed higher tumor uptake in animals of study group at all time-points from 1 day to 5 days post-injection compared to the blocking control group. 89Zr-DFO-M40 showed the highest uptake in tumor while the background levels or blood-driven uptake in the rest of organs or tissues. The uptake in tumor, but not normal organs, is reduced in the presence of excess cold antibody M40, demonstrating the tumor targeting specificity of this human monoclonal antibody.

Conclusion:

89Zr-DFO-M40 has demonstrated specific tumor targeting in vivo and is promising for PET imaging of mesothelioma.

Reference

1. Bidlingmaier S, He J, Wang Y, An F, Feng J, Barbone D, Gao D, Franc B, Broaddus VC, Liu B. Identification of MCAM/CD146 as the target antigen of a human monoclonal antibody that recognizes both epithelioid and sarcomatoid types of mesothelioma. Cancer Res. 2009 Feb 15;69(4):1570-7.
2. Salisbury T, Churg A. CD146 immunohistochemical staining for the separation of benign from malignant mesothelial proliferations. Virchows Arch. 2021 Nov;479(5):1047-1050.

Poster Presentation

Disclosures: The authors have disclosed no financial interest.

606-Biomimicking optical phantoms for fluorescence guided surgery device development

Presenter: Alberto Ruiz, Dartmouth College

Alberto Ruiz[1], Ethan LaRochelle[1]

[1]Dartmouth College, Hanover, NH

The development of biomimicking optical phantoms for fluorescence guided surgical (FGS) systems could help expedite the development of new clinical indications. The advantages of these targets are providing "ground truth" fluorescence imaging for application-specific anthropomorphic geometries to help replace the need for biological samples during the pre-clinical device design and verification process. Here we discuss the development of 1) anthropomorphic phantoms and 2) perfusion visualization targets for FGS devices. Techniques that translate computed tomography (CT)/magnetic resonance imaging (MRI) scans into 3D-printed fluorescent targets have been developed. Anthropomorphic phantoms relevant to three different types of fluorescence-guided surgery have been designed and prototypes were manufactured: a micro-CT of an ex vivo breast lumpectomy, a CT of a liver tumor, and an MRI of soft tissue sarcoma. The use of photopolymer-based 3D printing allowed the manufacturing of these

anthropomorphic phantoms with mimicking tissue optical properties that contain fluorescence inclusions. The optical properties of the three phantoms (i.e., ??a, ??s ') were determined with reference to literature. Presented are also perfusion-mimicking targets to study fluorescence depth resolution and dynamic flow. Fluorescence contrast agents, like indocyanine green (ICG), are primarily used to visualize perfusion, but subsurface structures can scatter or absorb fluorescence causing a blurring in the resulting image. This objective develops phantoms that can be used to characterize an imaging system's ability to resolve small vessel shapes and structures at increasing depths in tissue-mimicking material. Two designs for the perfusion phantoms were finalized which consisted of a 1) Serpentine pattern that allows for imaging at various fixed depths and 2) a wedge target design that includes a "V" flow channel at an incline to allow for imaging continuous depth changes. These targets were manufactured using both solid inclusions and a dynamic flow design. The aim of these phantoms is to help study the depth resolution of FGS devices and develop new image processing algorithms to "de-blur" imaged vessels. The dynamic flow targets can facilitate the visualization of new and existing fluorescent agents with application-specific optical spectra.

Reference

1. A. J. Ruiz et al., "3D printing fluorescent material with tunable optical properties," Sci Rep 11(1), 17135 (2021) [doi:10.1038/s41598-021-96496-0]
2. A. J. Ruiz et al., "Indocyanine green matching phantom for fluorescence-guided surgery imaging system characterization and performance assessment," J. Biomed. Opt. 25(05), 1 (2020) [doi:10.1117/1.JBO.25.5.056003]
3. S. L. Jacques, "Optical properties of biological tissues: a review," Phys. Med. Biol. 58(11), R37–R61 (2013) [doi:10.1088/0031-9155/58/11/R37]
4. B. Z. Bentz et al., "Printed optics: phantoms for quantitative deep tissue fluorescence imaging," Opt. Lett. 41(22), 5230 (2016) [doi:10.1364/OL.41.005230]

Poster Presentation

Disclosures: The authors have disclosed no financial interest.

607-Ultrasound imaging of endothelial cell anergy with PDL1-targeted microbubbles

Presenter: Negar Sadeghipour, Stanford University

Negar Sadeghipour[1], Farbod Tabesh[2], Ramasamy Paulmurugan[3], Ahmed El Kaffas[4]

[1]Stanford University, Menlo Park, CA
[2]Stanford University School of Medicine, Palo Alto, CA
[3]Stanford University School of Medicine, Stanford, CA
[4]Stanford University, San Jose, CA

Background:
Immune checkpoint inhibitors (ICIs) have resulted in unprecedented treatment effects in some patients, but remain ineffective in over 50% of patients. The immunosuppressive effects of the endothelial 'barrier' (also termed endothelial cell (EC) anergy) is one important reason for poor ICI outcomes in some patients, and is related to EC surface expression of immunosuppressive markers (i.e. PD-L1) that deter effector T cells; identifying patients with such EC markers could help select patients for ICIs, and spare non-responders. Purpose: Our ultimate goal is to develop ultrasound molecular imaging (UMI) strategies to image pro- and anti-immune markers on endothelial cells, to help guide ICIs. Here, we present developments and validation that PD-L1 expression on ECs can be imaged using UMI.

Methods:
We first studied the expression of PD-L1 on the surface of ECs with FACS analyses. We also tested the expression of PD-L1 in baseline, interferon-γ (IFN-γ), and Rapamycin treated cells, with the goal of replicating the immunogenic state of ECs in the tumor microenvironment. MS1 ECs, as well as 4T1, B16 and CT26 cancer cells, were treated with IFN-γ (25 ng/mL; promotes PD-L1) or Rapamycin (1 nM; inhibits PD-L1) and tested for PD-L1 expression after 48 hours. We also carried out a migration study where we cultured CT26 in the bottom and MS1 cells in an insert of a trans-well plate and added mouse bone marrow cells (BMC; replicating T-cells in tumor microenvironment where IFN-γ can be elevated) on top of MS1 cells. We collected cells from each compartment and compared the baseline expression of PD-L1 by FACS analyses to assess the IFN-γ response. We then used target-ready streptavidin conjugated lipid shelled microbubbles to image the expression of PD-L1 on ECs in immunocompetent mice. For this, we implanted 3 × 106 CT26 cells (murine colon carcinoma cell line) into the lower flank of Balb/c mice. The tumors were allowed to grow and reach 5 mm/diameter before imaging. On the day of imaging, isotype (MBiso) and PD-L1-targeted (MBPDL1) microbubbles were prepared by adding 20 ?g of biotinylated Rat IgG2b or PD-L1 to target-ready MicroMarker, respectively to prepare isotype control and PD-L1 MBs. Tumors were imaged on Vevo2100 US system by placing a catheter in the tail vein. A total of 50 ?l of microbubbles (30e6 bubbles/mouse) diluted in 150 ?l of saline were injected. Isotype microbubbles were injected and imaged for 6 minutes and then a burst signal was applied. We injected PD-L1-targeted microbubbles 20 minutes after the first injection, and imaged in the same order. Perfusion signals as well as differential targeted enhancement values (dTE) were quantified.

Results:
For in vitro experiments, the level of PD-L1 expression in the ECs increases similar to cancer cells after treatment with IFN-γ (Fig. 1a). The western blotting analyses showed that the expression of PD-L1 increases by up to 5-fold on the ECs treated with IFN-γ, which was higher than the increase in CT26 and 4T1 cells (Fig. 1b). Moreover, when BMCs migrate through endothelial cells toward cancer cells in a trans-well culture, the level of PD-L1 expression increases in both cancer cells and cancer ECs (Fig. 1c). For in vivo experiments, our preliminary results demonstrate elevated dTE signal in animals imaged with MBPDL1 (~5.35 a.u,, n = 3) vs. MBiso (~3.4 a.u., n =3). In 3D, qualitative images showed extensive enhancement of targeted signal 5 min after injection throughout the tumor, in most planes only for MBPDL1 imaging; this was not noted in MBiso (Fig. 1d). Minimal signal was observed in any animals with non-targeted MBs. We were able to observe the expression of PD-L1 on the endothelial cells by immunofluorescence staining (Fig.

Reference

1. Rodig N, Ryan T, Allen JA, Pang H, Grabie N, Chernova T, Greenfield EA, Liang SC, Sharpe AH, Lichtman AH, Freeman GJ. Endothelial expression of PD-L1 and PD-L2 down-regulates CD8+T cell activation and cytolysis. Eur J Immunol. 2003;33(11):3117–3126. doi:10.1002/eji.200324270 PMID: 14579280
2. Ding Q, Lu L, Zhou X, Zhou Y, Chou K-Y. Human PD-L1-over-expressing porcine vascular endothelial cells induce functionally suppressive human CD4+CD25hiFoxp3+ Treg cells. J Leukoc Biol. 2011;90(1):77–86. doi:10.1189/jlb.1210691 PMID: 21498584

3. Rodig N, Ryan T, Allen JA, Pang H, Grabie N, Chernova T, Greenfield EA, Liang SC, Sharpe AH, Lichtman AH, Freeman GJ. Endothelial expression of PD-L1 and PD-L2 downregulates CD8+T cell activation and cytolysis. Eur J Immunol. 2003;33(11):3117–3126. doi:10.1002/eji.200324270 PMID: 14579280

Poster Presentation

Disclosures: The authors have disclosed no financial interest.

608-Ultrasound molecular imaging of immune markers expressed on endothelial cells in a tissue-mimicking phantom

Presenter: Negar Sadeghipour, Stanford University

Negar Sadeghipour[1], Ramasamy Paulmurugan[2], Ahmed El Kaffas[3], Farbod Tabesh[4], Kogulan Paulmurugan[4]

[1]*Stanford University, Menlo Park, CA*
[2]*Stanford University School of Medicine, Stanford, CA*
[3]*Stanford University, San Jose, CA*
[4]*Stanford University School of Medicine, Palo Alto, CA*

Background/Purpose:
Ultrasound molecular imaging (UMI) using targeted-microbubbles is being developed for the detection and monitoring of various cancers and cardiovascular inflammation in pre-clinical models; one of the unique attributes of UMI is that it can exclusively image endothelial cell. Pre-clinical animal models are non-ideal for optimizing targeted binding of microbubbles, including conjugation and/or identifying new endothelial targets. There is currently a need for a platform to help accelerate testing and development of UMI targeted microbubbles, especially as new molecular targets. The purpose of this study was to design and test a UMI imaging phantom to address this need. More specifically, we designed and developed a two-channel phantom that allows to compare targeted and isotype microbubbles simultaneously under similar conditions. The phantom was also designed with a channel size that allows the microbubbles to flow and bind to attached endothelial cells, with user-defined control flow-rate.

Methods:
We have developed a tissue mimicking phantom to study the binding of molecularly targeted microbubbles to cell surface target proteins *in vitro*. After testing and optimizing initial prototypes, we designed the phantom in AutoCAD (Fig. 1a) and printed it on a Ultimaker S5 3D printer (Fig. 1b). The phantom consists of two parallel channels of 5 mm in diameter. Two small tubes were placed to create the channels mimicking vascular structure. The phantom has flat surface top and bottom with a 2×3 cm scanning window and a depth of 2 cm where the channels are right in the middle of that depth. The phantom consists of three layers. The bottom and top layer consist of agar and the middle layer in the field of view was filled with agarose (2% agarose in complete cell culture media) mixed with murine endothelial cells, MS1, at a concentration of 3×10^6 cells/mL. Each layer was added after allowing the last layer to solidify. The cells were allowed to grow for one week inside the phantom in the incubator at 37? and 5% CO_2. The culture medium inside the channel was changed every other day. We confirmed the presence of cells covering inside channels by staining with Hoechst33342 and imaging the layers of the gels in Celigo imaging system under bright field and Blue (477/470) channels. We then prepared PD-L1-targeted and IgG-isotype microbubbles. Lipid shelled (fixed-ratio of lipids i.e.DPPC, DPPA, and PEG5000 PE (mole ratio 10:80:8) hydrated with 2 mL buffer solution with propylene glycol, glycerol) microbubbles were made in microfluidic system. The bubbles were injected through phantom channels at a given velocity (200 ?l/min) for 5 minutes using an injection pump. We then washed the channel with PBS for 5 minutes at the same speed. 3D images and bubbles binding and washing were recorded pre- and post- microbubble injection. For quantitative analyses, ROI was drawn over the channels along the field of view and mean contrast signal intensity was calculated and recorded using VevoCQ software.

Results:
The results showed that MS1 cells were attached in the inner walls of the channels (Fig. 1c). The quantification of signal intensities in 10 different planes showed that the enhancement in targeted channel was on average 2 fold higher than in the isotype control channel (Fig. 1 d-e). The phantom is currently under further investigation to demonstrate the effect of changing flow rates and different concentrations of injected microbubbles and wash time on the binding results.

Conclusion/Discussion: The designed two-channel phantom can be used to image the binding of microbubbles to cells attached to the surface channels.

Poster Presentation

Disclosures: The authors have disclosed no financial interest.

609-Investigation of angiogenesis in cancer initiating cells from remnant living cells of human head and neck squamous cell carcinoma using pDots-NIR II ultrabright molecular imaging

Presenter: Min-Ying Lin, National Yang-Ming Chiao Tung University

Min-Ying Lin[1], Hsueh-Yen Yu[1], Guan Zeng[1], Syue-Liang Lin[1], Yang-Hsiang Chan[2], Huihua Kenny Chiang[2], Muh-Hwa Yang[2], Yi-Jang Lee[3]

[1]*National Yang-Ming Chiao Tung University, Taiwan*
[2]*National Yang Ming Chiao Tung University*
[3]*National Yang Ming Chiao Tung University, Taipei, Taiwan*

Although the death of tumor cells seems to hinder the growth of tumors, it is actually an important mechanism for tumor growth, especially for fast-growing tumors, the higher the proportion of death. The mechanisms that accompany other cells no longer present in tumors are collectively referred to as Cell Loss Factor. Generally, the cell loss rate of human tumors is about 40-90%. The "life and death storm" within the tumor tissue may be the main cause of the tumor's continuous growth, but its mechanism is still unclear. If the cells that can survive smoothly inside the tumor may have their specificity, they can survive in harsh environments. Cancer stem cells have been considered to be a minority group in tumor tissues, but they have the characteristics of stem cells to differentiate into cancer cells. They are also drug-resistant and radiation-resistant. They are also considered to cause recurrence and metastasis after tumor treatment. Ethnic group. Previously, we have successfully obtained the remaining cells with the characteristics of cancer stem cells from the cells that survived in the terminal stage after the mouse breast cancer was implanted in mice and allowed to grow naturally. But it is still unclear whether the same phenomenon can be observed in human tumor cells or tumor cells in other mice. This research plan will focus on human head and neck cancer FaDu cells. FaDu xenotransplantation of head and neck cancer cells into nude mice were sacrificed when the tumor grew to the terminal stage (about

1000mm^3). The remnant living cancer cells named FaDu-CSC cells exhibited mainly cancer stem cells properties compared to parental FaDu cells. Using ultrabright biocompatible polymer dots (pDots) with the emission at near infrared II (NIR II) spectrum, the angiogenesis of tumors formed by FaDu-CSC cells were more abundant and irregular than that formed by parental FaDu cells detected by a self-composed 3D multimodality tumor-vessel imaging system. The characteristics of cancer stem cells detected using the novel method of vessel imaging, confirm the identification of human head and neck cancer stem cells, which will be used as an evaluation platform for tumor treatment methods in the future.

Poster Presentation

Disclosures: The authors have disclosed no financial interest.

610-PET imaging of active infection in a rat model of discitis

Presenter: Marina López-Álvarez, University of California San Francisco

Marina López-Álvarez[1], Aryn A. Alanizi[2], Matthew F. L. Parker[3], Michael A. Ohliger[4], Joanne Engel[3], David M. Wilson[4]

[1]*University of California San Francisco, San Francisco*
[2]*University of California San Francisco, CA*
[3]*University of California San Francisco, San Francisco, CA*
[4]*University of California, San Francisco, San Francisco, CA*

Introduction:
A reliable imaging modality to probe live bacterial infection is still an unmet clinical need as the current methods of detection rely on indirect measurements of infection like morphologic changes or host immune response [1]. We have demonstrated that radiolabeled D-amino acids (DAA) are specific markers for live bacterial infections *in vivo* [2]. Our continued pursuit of developing D-amino acids as PET imaging agents has led us to ^{11}C-D-alanine, which has demonstrated accumulation into examples of gram-positive and gram-negative bacteria in vivo in a murine myositis model. One of our current focuses is further evaluated ^{11}C-D-alanine in more clinically-relevant models. In this report, we describe the evaluation of a number of different bacteria specific tracers of bacterial infection *in vivo* vertebral discitis osteomyelitis (VDO) model [3].

Methods:
D-[^{11}C]-alanine was synthesized in two steps using an adapted procedure used for L-alanine [4]. [^{11}C]para-aminobenzoic acid was synthesized in a single step from a commercially available Grignard reagent [5]. [^{18}F]fluorodeoxysorbitol was synthesized in a single step from [^{18}F]fluorodeoxyglucose. [6] D-[^{11}C]-methionine was synthesized in from the homo-cysteine precursor [7]. A VDO rat model was established by injection of a bioluminescent laboratory strain of *S. aureus* in between two vertebrae on the rat tails. The growth of the bacteria was monitored using optical imaging. All images were obtained on Day 4 with different tracers.

Results:
All tracers were synthesized in greater than 95% purity. Optical imaging validated growth of bacteria sequestered to the region of injection. Pilot studies of the VDO model show Day 3 to be ideal for early imaging time point. 150 μCi of dose was used for all fluorine-18 tracers and 800μCi of dose were used for all carbon-11 tracers. D-Ala and PABA both demonstrate 5 to 10-fold increase of tracer over heat-killed and background. D-Met showed only a 2-fold increase in live over heat-killed and background. Gallium Citrate showed accumulation in both live and heat-killed regions. FDS showed no uptake in any region as consistent with its selectivity for gram negative pathogens.

Conclusions:
Several PET tracers have been successfully evaluated in a VDO rat model. The preliminary results suggest both PABA and D-Ala to be promising new tracers for direct detection of live bacterial infection for VDO infections.

Reference

1. Baker JC, Demertzis JL, Rhodes NG, Wessell DE, Rubin DA. Radiographics: a review publication of the Radiological Society of North America, Inc. 2012, 32, 1959–1974.
2. Stacy GS, Kapur A. Radiologic clinics of North America. 2011, 49, 1261–1286.
3. Palestro CJ. Seminars innuclear medicine. 2015, 45, 32-46.
4. Gafter-Gvili, A. et al. QJM: monthly journal of the Association of Physicians, (2014).
5. Neumann KD, Villanueva-Meyer JE, Mutch CA, Flavell RR, Blecha JE, Kwak T, Sriram R, VanBrocklin HF, Rosenberg OS, Ohliger MA, Wilson DM. Sci Rep. 2017, 7, 7903.
6. Ning X, Seo W, Lee S, Takemiya K, Rafi M, Feng X, Weiss D, Wang X, Williams L, Camp VM, Eugene M, Taylor WR, Goodm M, Murthy N. Angew. Chem. Int. Ed. 2014, 53, 14096.
7. Filp U, Pekosak A, Poot AJ, Windhorst AD. Tetrahedron. 2016; 72, 655-6557.
8. Pekosak A, Rotstein BH, Collier TL, Windhorst AD, Vasdev N, Poot AJ. Eur. J. Org. Chem. 2017; 1019-1024.
9. Ordonez AA, Parker MFL, Miller RJ, Plyku K, Ruiz-Deboya CA, Tucker EW, Luu JM, Dikeman DA, Lesniak WG, Holt DP, Dannals RF, Miller LS, Rowe SP, Wilson DM, Jain SK. JCI insight. 2022; 7, 1, e154117.
10. Weinstein EA, Ordonez AA, DeMarco VP, Murawski AM, Pokkali S, MacDonald EM, Klunk M, Mease RC, Pomper MG, Jain SK. Sci Transl Med. 2014 Oct 22;6(259):259ra146.
11. Stewart MN, Parker MFL*, Jivan S, Luu JM, Huynh TL, Schulte B, Seo Y, Blecha JE, Villanueva-Meyer J, VanBrocklin H, Ohliger M, Rosenberg O, Wilson DM. ACS Infectious Diseases. 2020; 6 (1) 43-49.

Poster Presentation

Disclosures: The authors have disclosed no financial interest.

611-Utilizing click chemistry for infection PET imaging by fluorine-18 labeling of azide- modified bacteria

Presenter: Aryn Alanizi, University of California San Francisco

Aryn A. Alanizi[1], Matthew Parker[2], Alexandre Sorlin[3], Marina López-Álvarez[4], David M. Wilson[5]

[1]*University of California San Francisco, CA*
[2]*University of California, San Francisco, San Francisco, California*
[3]*University of California, San Francisco*
[4]*University of California San Francisco, San Francisco*
[5]*University of California, San Francisco, San Francisco, CA*

Introduction:
Using Positron Emission Tomography (PET) to image bacterial infection is an emerging field that has celebrated several recent successes,

including recent advances in carbon-11 labeled D-amino acids for infection imaging.[1] A major goal is to evolve this into fluorine-18 amino acid derivates, however, this has proven challenging to date. Alternatively, we have investigated indirect PET labeling methods to bio-orthogonally detect bacteria in vitro using click chemistry with azido D-amino acids. Here we report [^{18}F]FB-Sulfo-DBCO, a PET ligand for strain-promoted azide-alkyne cycloaddition (SPAAC) reactions.

Methods:

Radiotracer Synthesis [^{18}F]SFB was prepared using an automated published method and reacted with the commercially available Sulfo-DBCO precursor in the presence of DMF and base.[2] [^{18}F]FB-Sulfo-DBCO was purified and isolated using HPLC purification. Identity was confirmed by comparison to the cold standard, which was synthesized using analogous methods. C-terminus amino acid modification Commercially available D-Az-Ala was modified at the C- terminus to chemically synthesize D-Az-AlaOMe. D-Az-Ala was protected with Boc_2O and a methyl ester moiety was added via esterification followed by Boc_2O removal. Chemical identity was confirmed by ^{1}H and ^{13}C NMR analysis.

In Vitro Uptake Assay Azide metabolites (final conc. 5mM) were added to a 1% dilution of an overnight culture and incubated together for 1 hour. The cultures were pelleted and washed with washing buffer. 50?Ci of [18F]FB-Sulfo-DBCO was added and reacted for 1 hour. The pellets were separated and washed with buffer. The pellets and filtrates were individually analyzed on a gamma counter. SPAAC ligation is reported as % of signal.

Results/Discussion:

In this study, we developed a high-throughput click chemistry assay to label bacteria with [^{18}F]FB- Sulfo-DBCO and evaluated its performance in vitro using D-azido-alanine (D-Az-Ala), a modified D-amino acid metabolite that plays an essential role in peptidoglycan synthesis and cell wall remodeling. Using this assay, we saw 7 times greater SPAAC ligation to *S. aureus* cultures incubated with D-Az-Ala and [^{18}F]FB- Sulfo-DBCO compared to bacteria incubated with D-alanine (D-Ala) (Figure 1B). However, it remains unclear as to where D-Az-Ala localizes despite the role D-Ala plays in maintaining the structural rigidity of peptidoglycan. Though gram-positive bacteria have a characteristic thick layer of peptidoglycan, no trend seems to emerge amidst a panel of gram-positive and gram-negative bacteria where gram-negative *A. baumannii* ligates [^{18}F]Sulfo-DBCO better than gram-positive *L. monocytogenes* despite its characteristically thick gram-specific peptidoglycan contents (Figure 1C).

To better understand the selectivity of our radiotracer, a series of azide-bearing linear amino acids (Figure 1B) were incubated with *S. aureus* to correlate amino acid side chain length and stereocenter with bacteria incorporation. D-Az-Ala, the least modified amino acid metabolite, maintained the greatest uptake amidst longer side chain lengths; however, these metabolites demonstrated a significant difference in elevated SPAAC ligation to bacteria compared to D-Ala (Figure 1B). Further amino acid modifications were performed at the C-terminus where a methyl ester D-Az-Ala (D-Az-AlaOMe) derivative was tested in *S. aureus* (Figure 1D). Minimal SPAAC ligation indicates little incorporation of D-Az-AlaOMe or incoporation at an unfavorable location for [^{18}F]FB-Sulfo-DBCO to ligate, but provides useful insight pertaining to bacterial tolerance of modified D-amino acids.

Conclusions:

The new PET tracer, [^{18}F]FB-Sulfo-DBCO, readily labels bacteria when incubated with azide-amino acid click partners. The success of incorporating a fluorinated radiotracer into bacteria holds promise for expanding clinical infection imaging by extending the tracer half-life to 120 minutes, a huge improvement from the currently existing ^{11}C tracers. Moreover, this bio-orthogonal technique offers great potential in guiding the development of the next generation of ^{18}F PET tracers to target unique pathological bacteria strains.

Reference

1. Parker, Matthew F.L. et al. Sensing Living Bacteria in Vivo Using d-Alanine-Derived 11C Radiotracers. ACS Central Science 2020 6 (2), 155-165
2. Lazari, M. et al. Fully Automated Production of Diverse 18F-Labeled PET Tracers on the ELIXYS Multireactor Radiosynthesizer Without Hardware Modification. J. Nucl. Med. Technol. 42, 203 (2014).

Poster Presentation

Disclosures: The authors have disclosed no financial interest.

612-Metabolic Characterization of Patient-derived Xenograft Models of Clear Cell Renal Cell Carcinoma

Presenter: Deepti Upadhyay, University of California San Francisco

Deepti Upadhyay[1], Joao Piraquive[2], Hongjuan Zhao[3], Rosalie Nolley[4], Robert A. Bok[5], James D. Brooks[6], Donna Peehl[2], John Kurhanewicz[5], Renuka Sriram[2]

[1]*University of California San Francisco, California*
[2]*University of California, San Francisco, San Francisco, California*
[3]*Stanford University, Stanford, California*
[4]*University of California San Francisco, San Francisco, California*
[5]*University of California, San Francisco, San Francisco, CA*
[6]*Stanford University, Stanford, CA*

Introduction:

Predictive preclinical models of renal cell carcinoma (RCC) are needed to improve all aspects of clinical management from diagnosis to prognosis to treatment. Dysregulated metabolism is strongly implicated in the development and progression of RCC[1], however, the metabolism of preclinical models has not been investigated thoroughly. Thus, the present study focused on metabolic characterization of patient derived xenografts (PDX) and matched PDX cell culture-derived xenografts (XEN) using hyperpolarized (HP) ^{13}C magnetic resonance imaging (MRI) and nuclear magnetic resonance (NMR) based stable isotope resolved metabolomics.

Methods:

Five RCC PDXs (PDX047, PDX054, PDX068, PDX072 and PDX093) were established from a fresh sample of a clear cell RCC primary tumor implanted under the subrenal capsule of RAG2-/-γC-/- mice. XEN were generated from cells culture from PDX tumors implanted into the mice. All MRI studies were performed on a preclinical 3T Bruker system. T_2-weighted ^{1}H anatomical MR images were acquired using TurboRARE sequence. A ^{13}C dynamic MR spectra post- infusion of [1-^{13}C] pyruvate were acquired with a dual tuned ^{1}H/^{13}C volume coil using 2D chemical shift imaging. The glycolytic activity in tumors was evaluated by calculating the lactate-to-pyruvate area under the curve (L/P AUC). For metabolomics studies, PDX and XEN tumors were labeled by injecting [U-^{13}C] glucose into the tail vein of host mice every 15 minutes for a total labeling time of 45 minutes. Intracellular metabolites were extracted from homogenized tissues using cold methanol:water:chloroform and the aqueous fraction was isolated, lyophilized, and resuspended in D_2O with TSP. 1D and 2D NMR spectra

were acquired on 800 MHz Bruker Avance I equipped with a 5-mm triple resonance TXI cryoprobe. Determination of steady-state metabolite concentrations and fractional enrichment will be accompanied by ^{13}C isotopomer modeling using tcaCALC software.

Results:
Hyperpolarized [1-^{13}C] pyruvate metabolic imaging of RCC PDXs and XENs: Representative maps of the conversion of pyruvate to lactate (L/P AUC ratio), derived from hyperpolarized [1-^{13}C] pyruvate MRI, were overlaid on T2-weighted images (Figure1A). L/P AUC maps show inter-tumoral differences in glycolysis among PDXs (Figure1B), however, differences in glycolytic rate was not statistically significant. Further, we compared the L/P AUC between the PDX and matched XEN. XEN054 and XEN093 showed higher glycolytic activity compared to PDX054 and PDX093, respectively, however, there was no significant difference in L/P AUC ratio between PDX072 and XEN072 (Figure1C-1E). NMR based stable isotope resolve metabolomics: Heat map showing the comparison of steady sate metabolite level among PDXs (Figure1F&1G). The results indicated metabolic heterogeneity among PDXs of different clinical and pathological stages. Further, our results showed that the metabolic features of PDX047, PDX054 and PDX093 were significantly different from corresponding XEN047, XEN054 and XEN093, respectively, however, steady state metabolite levels were similar between PDX072 and its derived XEN072 (Figure1H-1K). Moreover, lactate FE was significantly higher in PDX047 and lower in PDX093 compared to derived XEN047 and XEN093, respectively (Figure1L&1O), while no significant difference was observed in lactate FE between PDX054 and XEN054 and between PDX072 and XEN072 (Figure1M&1N). Furthermore, 13C isotopomer modeling using tcaCALC showed that glucose flux through the TCA cycle is different between PDX047 and XEN047 and between PDX054 and XEN054, however, was similar between PDX072 and XEN072 and between PDX093 and XEN093 (Figure1P).

Conclusion:
Considering that dysregulated metabolism is a hallmark of cancer, it is critical to determine the metabolic fidelity of patient-derived models to the human disease. Both hyperpolarized [1-^{13}C] pyruvate metabolic imaging and NMR-based stable isotope resolved metabolomics results suggest that PDX are authentic models of metabolism of clear cell RCC, but that even short-term culture modifies the metabolic phenotype of RCC cells that is not restored by returning cells to an *in vivo* environment.

Reference

1. H.I. Wettersten, A.A. Hakimi, D. Morin, C. Bianchi, M.E. Johnstone, D.R. Donohoe, J.F. Trott, O.A. Aboud, S. Stirdivant, B. Neri, R. Wolfert, B. Stewart, R. Perego, J.J.Hsieh, R.H. Weiss, Cancer Research, 2015,75, 2541–2552.

Poster Presentation

Disclosures: The authors have disclosed no financial interest.

613-Glucocorticoid receptor expression/occupancy measurement in vivo with 18F-YJH08

Presenter: Hyunjung Kim, University of California San Francisco

Hyunjung Kim

University of California San Francisco

Introduction:
Glucocorticoid receptor (GR) is expressed in almost every normal tissue and some solid tumors. Previously, we developed ^{18}F-YJH08 for GR imaging, and it showed that ^{18}F-YJH08 can detect GR expressions in multiple tissues. In this study, we report measuring GR expression/occupancy by drugs in mice with ^{18}F-YJH08, which is the critical to defining an optimal drug dose.

Methods:
C57Bl6 mice were received the vehicle or several GR modulators, such as the antagonists ORIC-101 (75 mg/kg, BID, for 3 days), CORT125281 (100 mg/kg, for 5 days), RU486 (80 mg/kg, for 3 days) and agonist dexamethasone (50 mg/kg, for 3 days), prior to the radiotracer injection. And, mice bearing PC3 xenografts in the renal capsule were treated with vehicle or dexamethasone. Biodistribution data were collected at 30 min post injection of ^{18}F-YJH08. Autoradiography was performed post mortem. Tissues were collected, sectioned and mounted on glass slides and the slides were developed by phophorimager and processed using software.

Results:
Biodistribution results showed that one of the antagonists ORIC-101 significantly suppressed ^{18}F-YJH08 binding in the brain, brown fat, adrenal glands, heart and lungs while agonist dexamethasone reduced radioligand binding in nearly every tissues. RU486 significantly reduced ^{18}F-YJH08 uptake in the adrenal gland and CORT125281 reduced the radioligand uptake in the jejunum. The tumoral uptake at 30 min post injection was ~2% ID/g in the renal capsule tumors and specific binding was confirmed with dexamethasone. Autoradiography of a tumor-bearing kidney section showed that the tumor retained higher levels of radiotracer compared to normal kidney parenchyma.

Conclusions:
The results of this study showed that the ^{18}F-YJH08 enables measurement of GR expression/occupancy by agonist and antagonists in both normal and tumor mice. A first in human study evaluating ^{11}C-YJH08 in patients with metastatic castration resistant prostate cancer is currently underway.

Reference

1. ACS Chem. Biol. 2020, 15, 1381-1391
2. Mol. Pharmaceutics 2022, 19, 704-709

Poster Presentation

Disclosures: The authors have disclosed no financial interest.

614-18F-FPEB PET/MR Image of mGluR5 Expression with Major Depression Disorder Towards Development of a Potential Biomarker.

Presenter: Chuning Dong, Second Xiangya Hospital of Central South University

Chuning Dong[1], Xiaowei Ma, Yunhua Wang

[1]*Second Xiangya Hospital of Central South University, Changsha, Hunan, China*

Abstract body:
Abnormal of glutamate system is thought to be involved in major depressive disorder (MDD). 18F-FPEB PET/MR, as a neuroimaging,

could assess dynamic chance in metabotropic glutamate subtype 5 receptors (mGluR5) in depression patients. The purpose of this study was to evaluate the location and degree of impaired mGluR5 availability in MDD patients. In order to provide clinical guidance for diagnosis and treatment.

Methods:
18 patients and 12 healthy controls underwent 18F-FPEB PET/MR scan. Nondisplaceable binding potentials (BPND) were calculated to reflect the change of mGluR5 availability.

Results:
The findings showed the average 18F-FPEB BPND values were significant lower in MDD patients than healthy controls in several regions, including in basal ganglia, orbital gyrus, superior frontal gyrus, etc. After whole cortex analysis, we found different cluster in bilaterally prefrontal cortex, anterior cingulate cortex, basal ganglia, and temporal gyrus between patients and healthy controls. These cluster had good diagnostic efficiency, the AUC of left temporal gyrus could be 0.806.

Conclusion:
The results of this study showed a clinical evaluation of 18F-FPEB to investigate, and mGluR5 availability could be a potential biomarker for diagnose and therapy in MDD patients.

Poster Presentation

Disclosures: The authors have disclosed no financial interest.

615-In vivo I-123-FP-CIT SPECT Imaging of dopaminergic neuron degeneration in an a-synuclein preformed fibrils induce PD animal model

Presenter: Yi-Pei Ho, Chang Gung University

Yi-Pei Ho[1], Chi-Chang Weng[2], Yi-hsiu Chung[3], Jin-Chung Chen[4], Chang Pei Ti[5], Yu-Ting Huang[4]

[1]*Chang Gung University, Taiwan*
[2]*Chang Gung University, Tao-Yuan City, Taiwan*
[3]*Linkou Chang Gung Memorial Hospital, Kawi-Shan, Taoyuan, Taiwan*
[4]*Chang Gung University, Tao-Yuan, Please Select, Taiwan*
[5]*Linkou Chang Gung Memorial Hospital, Taiwan*

Aim:
Parkinson's disease (PD) is postulated to be related with the abnormal alpha-synuclein (a-syn) inclusions within the affected dopamine neurons. Several a-syn preformed-fibrils (PFFs)-treated animal models have recently been proposed and applied for behavior or immunohistochemistry experiments. However, the preformed-fibrils (PFFs) injection methods are continuously under discussion. To provide a better understating of the animal model preparation protocol and its effectiveness, in this present study an intrastriatal PFFs injected animals were prepared and in vivo imaged the dopamine neuron loss status with I-123-FP-CIT in different time points.

Methods:
The PFFs-treated and saline-treated mice (C57BL/6 male, 5-8 weeks old) were intracranially injected with a dose of 8 ug of PFFs or saline in both sides of striatum. And then a 30-min static SPECT scan was performed 60 min after i.v. injection of I-123-FP-CIT (0.4-0. 6mCi) in different time points (1, 3, 6 months after surgery). To verify the dopamine neuron degeneration condition in different brain area, the ex vivo autoradiography (ARG) was also performed in line with the time points of the in vivo imaging procedure. For the further comparison the relationship between a-syn aggregation with dopamine neuron loss, and the related immunohistochemistry (IHC) using different antibodies (anti-pS129 and anti-TH) were used in the study.

Results:
I-123-FP-CIT SPECT imaging results showed an obvious dopamine neuron loss in the PFFs-treated animal group 6-month after treatment (~50% dopamine neuron loss compared to the saline-treated group). However, the PFFs induced dopamine neuron loss in the substantial nigra area was not as much as the data in the striatum (only 20% of the tracer uptake) based on the ex vivo ARG. The followed IHC images (TH) displayed the similar results found in the ARG and the pS129 IHC results showed the a-syn deposition is mainly present in the PFFs injected sites.

Conclusion:
I-123-FP-CIT SPECT can visualize the dopamine neuron degeneration on the intrastriatal PFFs-injected PD animals 6-month after injection. Taken together, I-123-FP-CIT SPECT imaging may serve as a potentially useful platform to monitor the therapeutic effect of new drugs aiming for PD treatment in the future.

Poster Presentation

Disclosures: The authors have disclosed no financial interest.

616-Phthalocyanine-Blue Nanoparticle-Assisted White Light Endoscopy for Improved Detection of Colorectal Cancer

Presenter: Ahmad Amirshaghaghi, University of Pennsylvania

Ahmad Amirshaghaghi[1], Wen-Chi Chang[2], Margie L Clapper[2], Bonirath Chhay[1], Zhiliang Cheng[1], Andrew Tsourkas[1]

[1]*University of Pennsylvania, Philadelphia, PA*
[2]*Fox Chase Cancer Center, Philadelphia, PA*

Introduction:
Patients with inflammatory bowel disease (IBD) are at an increased risk of developing colorectal cancer (CRC). The current standard of care for surveillance of IBD has relied on white light endoscopy (WLE). However, there are still dysplastic lesions that are not visible to the naked eye using conventional WLE equipment. Dye-based chromoendoscopy (DBC) is an adjunct technique that has been investigated to enable endoscopists to visualize the colorectal mucosa better. However, inflammatory polyps exhibit similar dye uptake as the surrounding tissues, and dyes used in most studies do not significantly improve the recognition of tumor margins from the surrounding tissues. Here, we developed phthalocyanine (PC) blue-based nanoparticles, resulting in an increased detection rate and improved delineation of tumor margins. These nanoparticles could enable clinicians to distinguish between higher risk and lower risk patients and allow the colon to be more effectively cleared of dysplasia by reducing the likelihood of occult lesions that can grow and progress into a more threatening process.

Material & Methods:
Various hydrophobic derivatives of the phthalocyanine (PC) dyes (e.g., with and without alkyl groups) were loaded into polymeric micelles, composed of the amphiphilic diblock copolymer poly (ethylene glycol)-co-poly(caprolactone) (PEG-PCL), via oil-in-water emulsions. The

PC nanoparticles were characterized by UV-absorption spectroscopy and dynamic light scattering (Figure 1A, B). The stability of the PC nanoparticles was assessed in PBS and sodium cholate buffer by monitoring leakage of PC dyes and the hydrodynamic diameter as a function of time. The cytotoxicity of PC nanoparticles to 4T1 and HT-29 cells was then examined via an MTS cell proliferation assay. The contrast-enhancing capabilities of PC-blue nanoparticles were tested in a murine flank tumor model, using 4T1 cells and adenomatous polyposis coli $(Apc)^{+/Min}$ mice that spontaneously develop multiple colorectal adenomas (Figure 1C, D). Frozen section analysis was used for the final diagnosis of tissue samples (Figure 1E, F, G).

Results and Discussion:
PC-blue nanoparticles demonstrated size stability in water and PBS with high loading capacity (>90%), high retention after dialysis (>90% in 24 hrs in sodium cholate buffer), and narrow-size distribution (PDI < 0.2). No toxicity was evident upon incubation with 4T1 and HT-29 cells up to a concentration of 100 ug/mL. Twenty-four hours post-injection of 20 mg/kg PC-blue nanoparticles (based on PC dye weight) into $(Apc)^{+/Min}$ mice revealed clear demarcation of tumor margins in the excised colon and small intestine tissues, with efficient blue dye accumulation in polyps.

Conclusion:
We successfully prepared PC nanoparticles that enable high-contrast imaging of the mucosal surface without the use of special optical imaging equipment (e.g., fluorescence, OCT), making it a quick and safe option to improve the likelihood of complete resection and reducing the need for follow-up surgeries.

Poster Presentation

Disclosures: The authors have disclosed no financial interest.

617-Molecular imaging of VLA-4 in hypoxia-induced vaso-occlusive crisis in sickle cell disease mice

Presenter: Nishi Yadav,University of Missouri

Qin Zhu[1], Carolyn Anderson [2], Joseph D. Latoche, Enrico Novelli[3], Sina Tavakoli[4], Kathryn Day[3], Lynda Ihrig[3], **Nishi Yadav[5]**

[1]University of Pittsburgh, pittsburgh, PA
[2]University of Missouri, Columbia, Missouri
[3]University of Pittsburgh, Pittsburgh, Pennsylvania
[4]University of Pittsburgh, Pittsburgh
[5]University of Missouri, Columbia, MO

Background:
Sickle cell disease (SCD) is an inherited hemoglobinopathy that affects 100,000 Americans, mostly of African descent, and millions worldwide.[1,2] Vaso-occlusive crisis (VOC) is characterized by acute pain in areas of microvascular occlusion, and is the main cause of hospitalization in SCD.[3] Hyperadhesion of blood cells to the endothelium and to one another is critical to VOC.[4] Very late antigen-4 (VLA-4 or integrin ?4?1) mediates the adhesion of white blood cells (WBC) and reticulocytes to the endothelium, and could therefore be harnessed as an imaging biomarker of VOC. Previous work in our lab has shown that the VLA-4 peptidomimetic PET tracer ^{64}Cu-CB-TE1A1P-LLP2A (^{64}Cu-LLP2A) can quantitatively and in real time image VOC induced by lipopolysaccharide (LPS) in a SCD mouse model.[5] However, VOC is frequently triggered by hypoxia in humans with SCD, so, to further validate our imaging strategy, we investigated whether ^{64}Cu-CB-LLP2A could image hypoxia-induced VOC in SCD mice.

Methods:
Non-GMP grade LLP2A-PEG$_4$-CB-TE1A1P was purchased from Auspep. ^{64}Cu-LLP2A was injected via the tail vein in mice (SCD and non-SCD; n=10/group; 50% female) at the dose of 200 µCi per animal. Baseline PET/CT images were acquired at 1h, 4h, and 24h post-injection (p.i.). After one week, all mice were challenged with 1 hour of hypoxia (FiO_2=0.07) followed by 1 hour of normoxia (FiO_2=0.21) in an animal chamber (Biospherix Ltd, Parish, NY), a treatment known to cause vaso-occlusion.[6] PET/CT images were acquired at 1h, 4h and 24 h p.i. by using a small animal Inveon Preclinical PET/CT scanner (Siemens). PET image standard uptake values (SUVs) for the humerus and femur, typical sites of vaso-occlusive pain in humans, were measured using IRW software (Siemens). Complete blood count analysis was conducted at baseline and after hypoxia challenge. Blood was collected through the facial vein under anesthesia and placed in EDTA-coated tubes. Hemoglobin, hematocrit, WBC, neutrophil, and platelet counts were determined by using the VetScan HM5 analyzer (Abaxis, Union City, CA). The humeri and femurs were collected and fixed in 4% PFA for 24 h. They were then washed with PBS and kept in 10% EDTA buffer for 3 weeks before paraffin mounting and sectioning at Magee-Womens research institute histology and microimaging core for histology imaging.

Results:
The SCD mice showed uptake of ^{64}Cu-LLP2A post-hypoxia challenge in the humerus and femur at both baseline and after hypoxia challenge. SUV ratios at 1 h p.i in the humerus and entire femur compared to muscle in SCD mice were increased over baseline, whereas the control mice did not show any significant change in uptake. Among the three imaging time points, the 1h timepoint showed the most pronounced uptake, which indicates that the effect of ischemia/reoxygenation on the expression of VLA-4 wanes after 1 hour. This is in keeping with a prior report showing that VOC peaked after 1 h of reoxygenation and declined thereafter.[7]

Conclusions:
- ^{64}Cu-LLP2A can be helpful to image hypoxia-induced VOC in SCD mice.
- Increased VLA-4 uptake identifies areas of hyperadhesion and vaso-occlusion in SCD mice and should be investigated in humans with SCD.

Reference
1. Hassell KL. Population estimates of sickle cell disease in the U.S.Am J Prev Med. 2010;38(4suppl):S512-S521.
2. Piel FB, Patil AP, Howes RE, et al. Global epidemiology of sickle haemoglobin in neonates: a contemporary geostatistical model-based map andpopulation estimates.Lancet. 2013;381(9861):142-151
3. Brousseau DC, Owens PL, Mosso AL, Panepinto JA, Steiner CA. Acute care utilization and rehospitalizations for sickle cell disease. JAMA. 2010;303(13):1288-94. Epub 2010/04/08. doi: 10.1001/jama.2010.378. PubMed PMID: 20371788.
4. Sundd P, Gladwin MT, Novelli EM. Pathophysiology of sickle cell disease. Annu Rev Pathol. 2019;14(1):263-292
5. Perkins LA, Nyiranshuti L, Little-Ihrig L, Latoche JD, Day KE, Zhu Q, Tavakoli S, Sundd P, Novelli EM, Anderson CJ. Blood Adv. 2020 Sep 8;4(17):4102-4112.
6. Gutsaeva DR, Montero-Huerta P, Parkerson JB, Yerigenahally SD, Ikuta T, Head CA. Molecular mechanisms underlying synergis-

tic adhesion of sickle red blood cells by hypoxia and low nitric oxide bioavailability. Blood. 2014;123(12):1917-26. doi: 10.1182/blood-2013-06-510180. PubMed PMID: 24429338; PMCID: PMC3962164.
7. John D Belcher, Hemchandra Mahaseth, Thomas E Welch, Asa E Vilback, Khalid M Sonbol, Venkatasubramaniam S Kalambur, Paul R Bowlin, John C Bischof, Robert P Hebbel, Gregory M Vercellotti. Am J Physiol Heart Circ Physiol, 2005 Jun;288(6):H2715-25. doi: 10.1152/ajpheart.00986.2004.

Poster Presentation

Disclosures: The authors have disclosed no financial interest.

618-Ketohexokinase-mediated fructose metabolism is lost in hepatocellular carcinoma and can be leveraged for metabolic imaging

Presenter: Quinlan Cullen, Memorial Sloan Kettering Cancer Center

Quinlan Cullen[1], Nathaniel Kim[2], Sui-Seng Tee[3], Kayvan Keshari[4]

[1]*Memorial Sloan Kettering Cancer Center*
[2]*Memorial Sloan Kettering Cancer Center, New York*
[3]*University of Maryland School of Medicine, Baltimore, Maryland*
[4]*Memorial Sloan Kettering Cancer Center, New York, NY*

Introduction:
Metabolic rewiring is a hallmark of cancer. The aggressive proliferation characteristic of malignancy is dependent on opportunistic utilization of available carbon sources, particularly in the glucose-poor tumor microenvironment. The sweetest of all natural sugars, fructose is mainly metabolized by the intestine and liver, independently of insulin. While entry of glucose into glycolysis via hexokinase and phosphofructokinase is tightly regulated, canonical fructose metabolism comprises phosphorylation by ketohexokinase (KHK) to form fructose-1-phosphate (F1P), then cleavage by aldolase B to form glycolytic intermediates without regulation by glycolytic feedback mechanisms. Expression of KHK during dysfunction has been poorly studied. Altered activity has been shown in clear cell renal cell carcinoma (1) and hepatocellular carcinoma (HCC) (2), but mechanisms remain largely unclear. Preliminary studies by our group revealed a uniform downregulation of KHK in murine and human liver cancer as well as in liver cancer cell lines, particularly in HCC patient samples and cell lines (3). If indeed KHK activity is altered in disease states, characterization and detection of this dysfunction may represent diagnostic opportunities.

Methods:
Stable KHK overexpression: The pCDH-EF1??-MCS-T2A-RFP-Puro plasmid was used to produce lentivirus expressing endogenous KHK. Stable transfectants were selected by incubating with puromycin dihydrochloride (2 µg/mL) for 3 days. Expanded populations were then sorted and collected based on red fluorescent protein expression using a FACS Aria Flow Cytometer.
Metabolic tracing studies: Cells were incubated with isotopically labeled fructose for 4 hours, washed, and lysed with 80% methanol. F1P was detected via NMR. All other metabolites were detected via LC-MS using a Q Exactive Orbitrap Mass Spectrometer coupled to a Vanquish UPLC; metabolites were separated using a SeQuant ZIC-HILIC column.
HP fructose MRI: Mice were anesthetized with 1.5% isoflurane and loaded in a Bruker 3T MRI equipped with a dual tune $^{1}H/^{13}C$ coil. 250 µL HP [2-^{13}C, U-^{2}H]-fructose in D_2O was injected intravenously over 10 s via the implanted tail catheter. An axial 2D CSI sequence was used to acquire HP fructose MRS; data was acquired immediately after completion of injection with 20° constant flip angle, 6.75 mm x 5.625 mm resolution, 36 mm by 30 mm FOV, 10 mm slab thickness, 8x8 image size, and 1.67 Hz per points spectral resolution.

Results and Discussion:
Compared to the hepatoblastoma cell line HepG2, HCC cell line Huh7 exhibited reduced fructose consumption and fructose-derived F1P production, and reduced ability to proliferate in fructose as the sole carbon source (**Figure A**). In HCC cell lines, overexpression of KHK tagged with GFP caused cell death when cells were incubated in fructose (**Figure B**), as well as increased fructose-derived F1P production and decreased production of fructose-derived glycolytic intermediates and TCA cycle markers, and a reduced total ATP pool (**Figure C**). These *in vivo* findings suggest that loss of KHK activity in HCC is necessary for cell survival and proliferation, likely due to KHK-mediated consumption of ATP.
A [2-^{13}C, U-^{2}H]-fructose probe was developed to probe fructolysis *in vivo* via hyperpolarized magnetic resonance spectroscopy. Perdeuteration of [2-^{13}C]-fructose and dissolution in D_2O increased the utility of this probe by nearly quadrupling its relaxation time T_1 (**Figure D**). In an autochthonous AST model of murine liver cancer that allows tumors to form within their physiological environment, injection of HP [2-^{13}C, U-^{2}H]-fructose demonstrated similar uptake but reduced F1P production in malignant tissue compared to normal liver (**Figure E**). These results demonstrate reduced KHK activity in HCC *in vivo*. Together, this data suggests that loss of KHK may present an opportunity for diagnostic strategies. The unique ability of HP MRS to noninvasively detect fructose metabolic flux through KHK introduces clinical potential for detection of dysfunction in tissues that normally metabolize fructose.

Reference
1. J. S. Hwa, H. J. Kim, B. M. Goo, H. J. Park, C. W. Kim, K. H. Chung, H. C. Park, S. H. Chang, Y. W. Kim, D. R. Kim, G. J. Cho, W. S. Choi, K. R. Kang, The expression of ketohexokinase is diminished in human clear cell type of renal cell carcinoma. Proteomics 6, 1077–1084 (2006).
2. D. A. Wheeler, L. R. Roberts; Cancer Genome Atlas Research Network. Electronic address, N. Cancer Genome Atlas Research, Comprehensive and Integrative Genomic Characterization of Hepatocellular Carcinoma. Cell 169, 1327–1341.e1323 (2017).
3. S. S. Tee, N. Kim, Q. Cullen, R. Eskandari, A. Mamakhanyan, R. M. Srouji, R. Chirayil, S. Jeong, M. Shakiba, E. R. Kastenhuber, S. Chen, C. Sigel, S. W. Lowe, W. R. Jarnagin, C. B. Thompson, A. Schietinger, K. R. Keshari. Ketohexokinase-mediated fructose metabolism is lost in hepatocellular carcinoma and can be leveraged for metabolic imaging. Science Advances 8, eabm7985 (2022).

Poster Presentation

Disclosures: The authors would like to disclose that HP pyruvate is an investigational device.

619-Milk Small Extracellular Vesicles As Natural Nanoprobes For Tumor Detection By Optical Imaging

Presenter: María Isabel González-Gutiérrez, Fundación Investigación Biomédica del Hospital Gregorio Marañón

María Isabel González-Gutiérrez[1], Ana Santos-Coquillat[2], Sara Sánchez-Redondo[3], Desiré Herreros Pérez[1], Marta Hergueta-Redondo[3], Héctor Peinado[3], Beatriz Salinas[4], Manuel Desco[5]

[1]Fundación Investigación Biomédica del Hospital Gregorio Marañón, Madrid, Spain
[2]Instituto de Investigación Sanitaria Gregorio Maranon, Spain
[3]Spanish National Cancer Research Center (CNIO), Madrid, Spain
[4]Fundación Investigación Biomédica del Hospital Gregorio Marañón, Madrid, Madrid, Spain
[5]Instituto de Investigación Sanitaria Gregorio Maranon, Madrid, Spain

Introduction:
Despite the promising use of synthetic nanoparticles as imaging agents in biomedicine, their translation to the clinic is complex due to some drawbacks associated with their potential toxicity or lack of in *vivo* stability, limiting their use in oncological imaging [1]. Small extracellular vesicles (sEV) are naturally secreted by cells for communication purposes [2] and present physical characteristics close to liposome-like nanoparticles, such as nanometric size or lipid bilayer structure. Together with their natural origin and their intrinsic biological role associated with the development of certain pathologies [3], these small vesicles are postulated as substitutes for traditional nanoparticles in cancer imaging applications. Herein, we present the potential use of fluorescently-labeled milk sEV as natural nanoprobes for tumor imaging, highlighting their capacity to interact with different cells from the tumor microenvironment.

Methods:
sEV were isolated from commercial goat milk by ultracentrifugation and size exclusion chromatography, being characterized by TEM, DLS, NTA and proteomics. The optical labeling of sEV was performed following the methodology previously optimized by our research group [4]. Briefly, 75µg of sEV were covalently labeled with 10µL of SCy7.5-NHS (16.9mM), for 2h at 4ºC and pH 8.5. Resultant nanoprobe was also characterized by TEM, DLS, NTA and flow cytometry. *In vitro* internalization of fluorescent sEV (0.5µg/mL) by 264.7 RAW macrophages, C166-GFP endothelial cells and B16F10-Luc-GFP melanoma cells was evaluated by flow cytometry after 5h, 24h and 48h of incubation. *In vivo* tracking of the nanoprobe in tumor area was assessed in a subcutaneous allograft melanoma model injected in C57BL/6J mice ($5 \cdot 10^5$ B16F10-Luc-GFP melanoma cells/mouse, 1-week *in vivo* growth). Mice were imaged 1h, 5h, 24h, 48h, 72h and 96h after the intravenous injection of the nanoprobe (20µg/100µL), using an IVIS spectrum system. *Ex vivo* fluorescence and luminescence signal in fresh tumors was registered by IVIS and ODYSSEY imaging, 5h and 48h post sEV-administration. Uptake by macrophages and tumor cells was also analyzed and quantified by confocal imaging in excised tumors.

Results:
Milk sEV were fluorescently labeled by covalent binding, reaching high reaction yield (99.9% by flow cytometry) and preserving the original morphology and size distribution of isolated vesicles (Fig 1A). Macrophages and endothelial cells exhibited fast EVs internalization, achieving 99.8±0.1% and 80.4±3.5% of fluorescent positivity after 5h of incubation, respectively. In contrast, tumor cells presented maximum EVs uptake after 48h (Fig 1B). *In vivo* optical imaging showed EVs accumulation in the tumor tissue even 1h post-administration and revealed progressive decrease of the fluorescence signal along time (Fig 1C). *Ex vivo* optical imaging of excised tumors confirmed the nanoprobe uptake by the correlation between bioluminescence from tumor cells and fluorescence from the nanovesicles. Confocal analysis of tissues showed that both tumor-associated macrophages and tumor cells take up sEV, but macrophages exhibited slight increased accumulation of the vesicles (Fig 1D). Quantification of fluorescent signal showed that intensity decreased from 5h to 48h.

Conclusions:
This work presents the potential use of fluorescently-labeled milk sEV as natural nanoplatforms for non-invasive tumor imaging. Fluorescent sEV are rapidly accumulated in primary tumor due to the successful internalization by cells associated to the tumor microenvironment.

Reference
1. van der Meel, Roy, et al. Nature nanotechnology, 2019, vol. 14, no 11, p. 1007-1017.
2. He, Chuanjiang, et al. Theranostics, 2018, vol. 8, no 1, p. 237.
3. Li, Irene; Nabet, Barzin Y. Molecular Cancer, 2019, vol. 18, no 1, p. 1-10.
4. González, María Isabel, et al. Biomedicines, 2021, vol. 9, no 1, p. 81.

Poster Presentation

Disclosures: The authors have disclosed no financial interest.

Publisher's Note Springer Nature remains neutral with regard to jurisdictional claims in published maps and institutional affiliations.